European Commission

Proceedings of the 10th International Conference on NDE in Relation to Structural Integrity for Nuclear and Pressurized Components

1-3 October 2013, Cannes, FRANCE

Edited on behalf of the organizing committee by Michel Bièth

Joint Research Centre

EUR 26577 EN

Proceedings of the 10th International Conference on

NDE in Relation to Structural Integrity for Nuclear and Pressurised Components

1 - 3 October, 2013 – Cannes, FRANCE

Edited on behalf of the Organising Committee
by Michel Bièth

European Commission

The mission of the JRC-IET is to provide support to European Union policies and technology innovation to ensure sustainable, safe, secure and efficient energy production, distribution and use and to foster sustainable and efficient transport in Europe

European Commission
Joint Research Centre
Institute for Energy and Transport

Contact information: Michel BIETH
Address: Institute for Energy and Transport, P.O. Box 2, 1755 ZG Petten, The Netherlands
E-mail: michel.bieth@ec.europa.eu
Tel.: +31-224-565157
Fax: +31-224-565637

http://iet.jrc.ec.europa.eu/
http://www.jrc.ec.europa.eu/

JRC89268

EUR 26577 EN

ISBN 978-92-79-36758-8(pdf)
ISBN 978-92-79-36759-5(print)

ISSN 1831-9424(online)
ISSN 1018-5593(print)

Doi 10.2790/17225(online)

Luxembourg: Publications Office of the European Union

Table of Contents

Preface to the Conference Proceedings

We are very pleased to introduce the proceedings of the Tenth International Conference on NDE in Relation to Structural Integrity for Nuclear and Pressurised Components.

As for previous conferences, the theme was the link between the information provided by NDE and the use made of this information in assessing structural integrity. In this context, there is a need to determine NDE performance against structural integrity requirements through a process of qualification. There is also a need to develop NDE to address shortcomings revealed by such qualifications or otherwise. Finally, the links between NDE and structural integrity require strengthening in many areas so that NDE is focussed on the components at greatest risk and provides the precise information required for assessment of integrity. These were the issues addressed by the papers presented at the conference. The level of interest in the subject matter of the conference was maintained from previous events and 161 suitable papers were submitted for presentation at the conference. This required the programme to be organised in three parallel sessions, each on a specific theme, to provide each paper with sufficient time for presentation and to accommodate all of them within the overall time allocated.

A major conference theme was related to the links between NDE and structural integrity. One of the three sessions contained all the qualification and structural integrity papers, including those on risk-informed inspection. This session also included papers on NDE reliability, material properties measurement and mathematical predictions of inspection performance through modelling. A second session was devoted to the theme of development of new inspection methods. The third session was concerned with inspections of specific reactor components. Two developments noted at the previous conferences in Yokohama, Berlin and Seattle were the increased number of papers on the subjects of austenitic and bi-metallic weld inspection and also the use of phased arrays. These were also well represented in the programme of the conference in Cannes and are clearly topics which continue to arouse a high level of international interest. Sixteen countries were represented in the final programme from Europe, America and Asia.

In the event, the conference was highly successful. The 161 presented papers maintained the high promise suggested by the written abstracts and the programme was chaired in a professional and efficient way by the session chairmen who were selected for their international standing in the subject. The number of delegates, at 400, was also highly gratifying, showing the high level of international interest in the subject. This is also indicated by the large number of countries, 24, represented by the delegates.

These Proceedings provide the permanent record of what was presented. They indicate the state of development at the time of writing of all aspects of this important topic and will be invaluable to all workers in the field for that reason.

Finally, it is appropriate that we record our thanks to our fellow members of the Organising Committee and we are also indebted to those who served as chairmen. Without their support, the conference could not have been the success that it was. We also acknowledge the authors themselves, without whose expert input there would have been no conference.
We would also like to record our appreciation for the work of the coordinator - Confédération Française pour les Essais Non Destructifs (COFREND) in making all the excellent arrangements for the conference. Their efforts made a great contribution to its success. We also acknowledge the important contribution of Georgiana Beldie in assembling the conference proceedings.

The continuing success of this conference series means that planning can now proceed with confidence for the next event to be held in Jeju Island, South Korea, 19-21 May 2015.

Dr. Michel Bièth

10th International Conference on NDE in Relation to Structural Integrity for Nuclear and Pressurised Components

This conference, the 10th in a series on NDE in relation to structural integrity for nuclear and pressurised components, was held in October 1-3, 2013, Cannes, FRANCE. The scientific programme was produced by the European Commission's Joint Research Centre, Institute for Energy and Transport (EC-JRC/IET) and the conference was coordinated by the Confédération Française pour les Essais Non Destructifs (COFREND). The first conference, under the sole responsibility of EC-JRC was held very successfully in Amsterdam, 20-22 October 1998, the second was locally organized by the EPRI NDE Center in New Orleans, 24-26 May 2000, the third by Tecnatom in Seville, 14-16 November 2001, the fourth by BINDT in London, 6-8 December 2004, the fifth by EPRI NDE Center in San Diego, 10-12 May 2006, the sixth by MAROVISZ in Budapest, 8-10 October 2007, the seventh by JAPEIC and JSM in Yokohama, 12-14 May 2009, the eighth by DGZfP in Berlin, 29 September - 1 October 2010, and the ninth by the EPRI NDE Center in Seattle, 22-24 May 2012.

The theme of this conference series is to provide the link between the information originated by NDE and the use made of this information in assessing structural integrity. In this context, there is often a need to determine NDE performance against structural integrity requirements through a process of qualification or performance demonstration. There is also a need to develop NDE to address shortcomings revealed by such performance demonstration or otherwise. Finally, the links between NDE and structural integrity require strengthening in many areas so that NDE is focussed on the components at greatest risk and provides the precise information required for assessment of integrity. These were the issues addressed by the papers selected for the conference.

Country	papers	participants
France	49	171
United States	32	37
Germany	15	24
Japan	14	19
Canada	12	11
United Kingdom	8	29
Finland	5	18
Sweden	5	25
South Korea	4	9
Spain	4	8
Belgium	3	10
Croatia	3	4
Ukraine	3	2
Czech Republic	2	3
Russian Federation	1	1
Switzerland	1	12
Denmark	0	3
Hungary	0	1
Italy	0	1
Mexico	0	1
Netherlands	0	5
Saudi Arabia	0	3
Slovakia	0	2
Slovenia	0	1

161 papers (130 in Amsterdam, 135 in New Orleans, 142 in Seville, 106 in London, 139 in San Diego, 126 in Budapest, 157 in Yokohama, 137 in Berlin, 160 in Seattle) of high scientific value were presented during the three conference days. The result was highly gratifying. The papers covered the full range of issues that the Technical Organising Committee, composed of representatives from Europe, USA and Japan, wished to address and were of a very high standard. The topical importance of performance demonstration, and primary circuit component inspection should be mentioned. The attraction of this event can be estimated by the international nature of the authors and the participants (see table). In Cannes, 24 countries (24 in Amsterdam, 23 in New Orleans, 31 in Seville and in London, 19 in San Diego, 24 in Budapest, 16 in Yokohama, 28 in Berlin, 19 in Seattle) from Europe, America, and Asia were represented during the conference.

The scientific sessions were chaired in a professional way by delegates who were selected for their internationally recognised standing in the subject. A total of 400 registered delegates (see table & graph), against 241 in Amsterdam, 258 in New Orleans, 285 in Seville, 221 in London, 268 in San Diego, 242 in Budapest, 269 in Yokohama, 323 in Berlin and 298 in Seattle were also highly pleased and expressed their satisfaction, indicating the high level of international interest in the subject. All presented papers are edited, and these proceedings provide a permanent record of the state of development, at the time of writing, of all aspects of this important topic and will be invaluable to all workers in the field.

During the conference, an exhibition of NDT equipment for the nuclear and pressure vessel industries was held, open to conference delegates. As this tenth successful conference has continued the path opened by the Amsterdam, New Orleans, Seville, London, San Diego, Budapest, Yokohama, Berlin and Seattle conferences, the planning can now proceed with confidence for the next conference to be held in Jeju Island, South Korea, 19-21 May 2015.

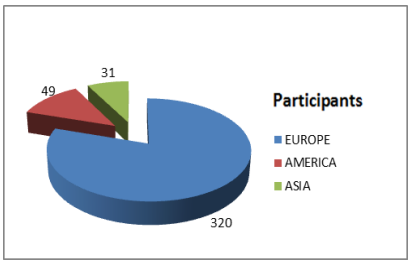

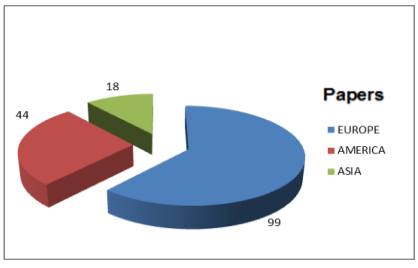

International Organising Committee

Michel Bièth
EUROPEAN COMMISSION
JRC-Institute for Energy and Transport
P.O. Box 2
1755 ZG Petten
THE NETHERLANDS
michel.bieth@ec.europa.eu

Greg Selby
EPRI NDE CENTER
1300 W.T. Harris Boulevard
Charlotte, NC28262
USA
gselby@epri.com

Toshiyuki Takagi
INSTITUTE OF FLUID SCIENCE
Tohoku University
2-1-1 Katahira Aoba-ku
Sendai 980-8577
JAPAN
takagi@ifs.tohoku.ac.jp

French Conference Committees

French Organizing Committee

Etienne Martin
Chair of French Organizing Committee
EDF
2 rue Ampère
93206 Saint Denis
FRANCE
etienne.martin@edf.fr

Nadia Beckerich
COFREND
1 rue Gaston Boissier
75024 PARIS 15ème
FRANCE
n.beckerich@cofrend.com

Jean Pierre Gustin
COFREND
1 rue Gaston Boissier
75024 PARIS 15ème
FRANCE
president@cofrend.com

Pierre Husarek
COFREND
1 rue Gaston Boissier
75024 PARIS 15ème
FRANCE
husarek@sofranel.com

Anne-Marie Roy
COFREND
1 rue Gaston Boissier
75024 PARIS 15ème
FRANCE
contact@amroy-consulting.com

French Technical Committee

Bernard Bisiaux
Chair of Conference Scientific Committee
VALLOUREC
60 Route de Leval
BP 20149
59620 Aulnoye-Aymeries
France
bernard.bisiaux@vallourec.fr

Philippe Benoist
M2M
1 rue de Terre Neuve
91940 LES ULIS
FRANCE
p.pichard@m2m-ndt.com

Pierre Calmon
CEA Saclay
91191 Gif sur Yvette Cedex
FRANCE
pierre.calmon@cea.fr

Bertrand Chassignole
EDF R&D
77848 Moret Sur Loing
FRANCE
bertrand.chassignole@edf.fr

Frederic Lesage
WESTINGHOUSE EUROPE
86 rue de Paris
BP 7
91401 Orsay Cedex
FRANCE
lesagef@westinghouse.com

Mireille Rapin
AREVA
76 Rue des Gémeaux
94583 Rungis
FRANCE
mireille.rapin@areva.com

10th International Conference on NDE

1– 3 October 2013

Cannes, France

Technical programme and contents

Tuesday, October 1st, 2013

08:30	Welcome/Safety Message					
09:00	Opening Plenary Session Debate					
09:40	TU.0.P.1 - Activities and Future Trends of the European Network for Inspection and Qualification Etienne Martin - EDF France, Oliver Martin - EC JRC Netherlands, Russ Booler - AMEC UK, Tony Walker - Rolls-Royce Submarines UK *Presented by Etienne Martin (pg 19)*					
10:00	TU.0.P.2 - Present Status of Nuclear Power Plants in USA Greg Selby - EPRI, USA; *Presented by Greg Selby* (pg 25)					
10:20	TU.0.P.3 - Present Status of Nuclear Power Plants in Japan Toshiyuki Takagi – Innovative Energy Research Center, Institute of Fluid Science, Tohoku University, JAPAN *Presented by Toshiyuki Takagi (pg 26)*					
10:40	BREAK					
	SESSION A	**PG**	**SESSION B**	**PG**	**SESSION C**	**PG**
	INSPECTION QUALIFICATION I		**PIPING INSPECTION - EMBEDDED PIPES**		**STEAM GENERATOR PRIMARY I**	
	TU.1.A.		**TU.1.B**		**TU.1.C**	
	Co-Chairpersons: Tommy Zetterwall, SQC - Sweden Philippe Ashwin, EPRI - USA		**Co-Chairpersons:** Juraj Neupauer, Slovenské Elektrarne - Slovakia Lionel Delannoy, GE - France		**Co-Chairpersons:** Joel Martens, AREVA - France Bertrand Chassignole, EDF - France	
11:00	TU.1.A.1 - Comparison between NDE qualification standards and practices in different countries *P. Jardet, M. Dib, EDF Qualification Body, France*	**28**	TU.1.B.1 - Buried pipe internal diameter inspection tool *M. Sapia, P. Doverspike, GE Hitachi Nuclear Energy, USA*	**150**	TU.1.C.1 - FORERUNNER – efficient and smart solution for SG inspection *P. Mateljak, D. Liebl, Z.Č. Cvjetičanin INETEC, Croatia*	**272**
11:20	TU.1.A.2 - The role of NDT in a UK structural integrity safety case for high integrity components *J. Fasham, J. Pearce, A. Goodfellow, EDF Energy NNB Genco, UK*	**35**	TU.1.B.2 - The inspection of visually inaccessible areas of containment liners and shells utilizing advanced nondestructive examination techniques *J. J. Wall, EPRI, USA* *B. P. Hohmann, T. C. Esselman, T. T. Taylor, Lucius Pitkin, USA*	**151**	TU.1.C.2 - Historical comparison of steam generator tubing eddy current data concurrent with vessel inspections *T. O'Dell, T. Woller, N. Larsen, ZETEC, USA*	**280**
11:40	TU.1.A.3 - Setting realistic tolerances on equipment substitution for conventional, PAUT and TOFD ultrasonic methods *E. Choi, CANDU Owners Group, Canada* *T. Armitt, Lavender Int. NDT Consultancy Services, UK* *P. Ciorau, Tetra Tech Energy Division, Canada*	**44**	TU.1.B.3 - Inspection technique for BWR core spray thermal sleeve weld *J.L. Fisher, G. Light, J. Crane, A. Parvin,* *Southwest Research Institute, USA* *Yoshimasa Sugawara, Tokyo Electric Power Company, Japan*	**165**	TU.1.C.3 - AIDA – the eddy current analysis software *F. Sauriat, AREVA, France* *R. Vojvodic, B. Everett, AREVA, USA*	**285**

12:00	TU.1.A.4 - UT qualification and site feedback on dissimilar metal welds of WWER type NPPs in the Czech republic *L. Horacek, I. Buldra, UJV Rez, Czech Republic* *P. Mares, Centrum vyzkumu Rez Czech Republic*	**53**	TU.1.B.4 - Testing of buried pipes by SLOFEC™ technique in combination with a motor-driven crawler system *W. Kelb, KontrollTechnik, Germany*	**172**	TU.1.C.4 - Steam generator AVB gap measurement by UT and ET *S.W. Glass, M. Boudreaux, R. Vojvodic, J. Wyatt, AREVA, USA*	**292**
12:20	TU.1.A.5 - Generic image quality quantification based on adapted ISO standards for VT system qualification *Y. Caulier, M. Taglione, A. Clay, R. Sancenot, AREVA, France*	**59**	TU.1.B.5 - Nondestructive evaluation of wall thinning of carbon steel using Pulsed Eddy Current technique *D.G. Park , M.B. Kishorea, K.H. Kim , D.H. Lee, Korea Atomic Energy Research Institute, South Korea* *M.B. Kishore, C.G Kim, Chungnam National University, South Korea*	**184**	TU.1.C.5 - A review of real time visualization of eddy currents in a small bore-piping system using solid-state Hall sensor arrays *J. Lee, C. S. Angani, J. Kim, M. Le, Chosun University, South Korea* *Hwa Sik Do, KEPCO, South Korea*	**298**
12:40	**LUNCH**					
Time	**SESSION A**	**PG**	**SESSION B**	**PG**	**SESSION C**	**PG**
	INSPECTION QUALIFICATION II		**PIPING INSPECTION I**		**STEAM GENERATOR PRIMARY II**	
	TU.2.A.		**TU.2.B**		**TU.2.C**	
	Co-Chairpersons: Patrice Jardet, EDF - France Ladislav Horacek, UJV - Czech Republic		**Co-Chairpersons:** Fabienne Rupin, EDF - France Ari Koskinen, VTT - Finland		**Co-Chairpersons:** Eric Lecour, Westinghouse - France Mireille Rapin, AREVA - France	
02:00	TU.2.A.1 - Qualification of invessel visual examination for kernkraftwerk Leibstadt (KKL) and kernkraftwerk (KKM) Mühleberg plants *J. Lindberg, EPRI, USA* *R. Schwammberger, Kernkraftwerk Leibstadt, Switzerland* *P. Graedel, BKW FMB Energie, Switzerland*	**70**	TU.2.B.1 - Applications of new-generation portable phased array systems for truly efficient inspections *P. Tremblay, L. Enenkel, ZETEC NDT Solutions, Canada*	**191**	TU.2.C.1 - NDE of sleeves and sleeved tubes *R. Bienentreu, E. Lecour, F. Lesage, J.L. Renaud, Westinghouse Electric Company*	**307**
02:20	TU.2.A.2 - Qualification of ultrasonic and eddy current techniques to examine the CRDH (control rod drive housing) of a Swiss NPP *F. Fernández, P. Gómez, A. García, J. Sánchez, Tecnatom, Spain*	**77**	TU.2.B.2 - Portable piping thickness measurement system *J.L. Fisher, K. Bartels, A. Schaefer, Southwest Research Institute, USA* *E. Shiina, T. Shimomura, T. Hamano, IHI, Japan*	**198**	TU.2.C.2 - A retrospective – 10 years of intelligent ECT system experience *T. Hasebe, T. Shichida, N. Kawase, T. Matsuura, K. Kawata, M. Kurokawa, Mitsubishi Heavy Industries, Japan,* *J. Siegel, SOLNEX, USA*	**308**
02:40	TU.2.A.3 - Use of advanced simulation tools: some examples in the French qualification process for ultrasonic applications *C. Hubert, S. Deydier, L. De Roumilly, EDF- CEIDRE, France* *E. Lhuillier, B. Chassignole, EDF- R&D, France*	**85**	TU.2.B.3 - Advanced NDE systems for in-service inspections, new scanners combined with adapted UT phased array *F.Mohr, F. Wolfsgruber, G.Guse, AREVA, Germany*	**202**	TU.2.C.3 - Array probe evaluation by Westinghouse *D. Stepnick, Westinghouse Electric Company, USA*	**316**

03:00	TU.2.A.4 - A plenary view on the reliability of NDE-systems *C. Mueller, M. Bertovic, D. Kanzel, M. Skender, BAM, Germany* *R. Holstein, DGZfP , Germany* *J. Pitkanen, Posiva Oy, Finland*	**94**	TU.2.B.4 – Volumetric inspection of welds using the total focus method *R.L. Ten Grotenhuis, C.M. Moes, A. Hong, A. Sakuta, Ontario Power Generation, Canada*	**211**	TU.2.C.4 - Single pass analysis using dual sensor techniques and automated analysis methods *N. Cardillo, ZETEC, USA*	**321**
03:20	TU.2.A.5 - Dissimilar metal welds inspection qualification in Spain *I. Real, Iberdrola Generacion, Spain* *G. Bollini, Tecnatom, Spain* *L. Francia, UNESA, Spain,* *S. Perez, Iberdrola Generacion, Spain,* *J. Julio Jimenez, CN Almaraz Trillo, Spain*	**95**	TU.2.B.5 - Reconstruction of phased array techniques from the full matrix capture data set *R.L. Ten Grotenhuis, J.X. Zhang, A Sakuta, A. Hong, Ontario Power Generation, Canada*	**220**	TU.2.C.5 - Array probe implementation (SMX) on EDF steam generator tubes *Q. Mistral EDF - CEIDRE, France* *T. Charret, J.Martens AREVA, France*	**329**
03:40	**BREAK**					
Time	**SESSION A**	**PG**	**SESSION B**	**PG**	**SESSION C**	**PG**
	INSPECTION QUALIFICATION POD		**PIPING INSPECTION - WELDING**		**STEAM GENERATOR**	
	TU.3.A.		**TU.3.B**		**TU.3.C**	
	Co-Chairpersons: Frédéric Jenson, CEA - LIST, France Christina Mueller, BAM - Germany		**Co-Chairpersons:** Russ Booler, AMEC - UK Philippe Benoist, M2M - France		**Co-Chairpersons:** Marko Budimir, Inetec - Croatia Samuel Glass, AREVA - USA	
04:00	TU.3.A.1 - Application of "CIVA" software for modelling WWER-1000 reactor pressure vessel UT with SK-187 system from outer surface *I. Kadenko, R. Iermolenko, A. Kadenko, N. Sakhno Nondestructive Examination Training and Certification Facility, Ukraine*	**97**	TU.3.B.1- Safety related service water piping assessment for nuclear power stations *R. Royer, K. Rach, A. Crompton, D. Keene, Structural Integrity Associates, USA*	**231**	TU.3.C.1 - TSP blockage of steam generator monitoring method by intelligent ECT *T.Hasebe, Y. Kohashi, , T.Shichida, N.Kawase, T.Matusura, K.Kawata, Mitsubishi Heavy Industries, Japan*	**335**
04:20	TU.3.A.2 - CANDU owner's group risk-informed inservice inspection pilot study *P. O'Regan, EPRI, USA, Paul Lafreniere, CANDU Owner's Group, Canada* *M. Rezaie-Manesh, Ontario Power Generation, Canada,* *S. Chesworth, Structural Integrity, USA*	**104**	TU.3.B.2 - Simulation of ultrasonic inspection of dissimilar metal welds using ray-based approaches *H. Lourme, A. Gardahaut, K. Jezzine,F. Jenson, CEA - LIST, France* *G. Cattiaux, T. Sollier, IRSN, France*	**236**	TU.3.C.2. - Probe based on a giant-magneto-resistance (GMR) sensor for the thickness measurement of magnetic deposit on steam generator tubes *S. Paillard, B. Marchand, J. M. Decitre, CEA Tech, France* *M. El Guedri, EDF- STEP, France*	**343**
04:40	TU.3.A.3 - NDE errors associated with flaw sizing and growth estimates *L. Obrutsky, R. Lakhan, J. Lei, D. Horn, AECL, Canada*	**115**	TU.3.B.3 - Ultrasonic imaging and sizing of stress corrosion cracks in welded austenitic components using the synthetic aperture focusing technique *H. Rieder, A. Dillhöfer, M. Spies, Fraunhofer-Institut Für Techno-Und Wirtschaftsmathematik Itwm, Germany* *S. Dugan, MPA, Universität Stuttgart, Germany*	**243**	TU.3.C.3 - Tube support plate clogging and secondary side deposit: performance evaluation using simulation and site results *N. Le Lostec, Y. Kernin, C. Ferré, J.l Martens, AREVA, France* *D. Dumay, EDF- CEIDRE, France*	**344**

05:00	TU.3.A.4 - POD calculation on a radiographic weld inspection with CIVA 11 RT module *D. Tisseur, M. Costin, CEA - LIST, France* *S Fournier, C. Reece, EDF - CEIDRE, France* *A. Schumm, EDF - R&D, France*	**123**	TU.3.B.4 - Development and qualification of a procedure for the mechanized ultrasonic examination of structural weld overlays *V. Chardome, M. Plateau, V. Van Brabant, J. Cermak, Vinçotte, Belgium*	**251**	TU.3.C.4 - Utilizing NDE information to support long term steam generator deposit management strategies *J. C. Le Querre, Westinghouse, France* *S. Wozniak, Westinghouse, USA*	**353**
05:20	TU.3.A.5 - Observer pod for radiographic testing *D. Kanzler, C. Müller, M. Bertovic, U. Ewert, BAM, Germany* *J. Pitkänen Posiva Oy, Finland*	**130**	TU.3.B.5 - Dissimilar metal weld examination assessment process *P. Sullivan, J. Hayden, C. McDonald, Structural Integrity Associates, USA*	**256**	TU.3.C.5 - Steam generator secondary side televisual inspections *E. Lecour, G. Gaillard, J.L. Renaud, Westinghouse Electric Company, France*	**354**
05:40	TU.3.A.6 - A legacy of probability of detection (POD) *Ward D Rummel D&W Enterprises, USA*	**135**	TU.3.B.6 - New plant challenge – pre-service volumetric examination of a heavy-wall dissimilar metal weld involving a cast stainless steel base material *R. D. Rishel and J. Monaco, WesDyne International, USA*	**263**	TU.3.C.6 - Sizing of magnetite pile on steam generator tubing with two-probe eddy current technique *J. Tarja, L. Kari, VTT Technical Research Centre of Finland*	**361**
06:00	TU.3.A.7 - Optimization of quantitative digital radiography for sizing the depth of circumferential cracks in boiler waterwall tubes: latest developments *S. Walker, EPRI, USA* *B. Jackson, M. Cronin, H. Vaillancourt, Intertek AIM, USA* *S. Paterson, PIKA Solutions, USA* *R. Seals, R.I. Seals, Inc., USA*	**143**			TU.3.C.7 - From concept to reality: performance of steam generator inlet/outlet nozzle dissimilar metal weld examinations from the inside surface *C. M. Barrera, S. Todd, R. Villagomez, IHI Southwest Technologies, USA* *W. A. Jensen NextEra Energy, USA*	**367**
Wednesday, October 2, 2013						
Time	**SESSION A**	**PG**	**SESSION B**	**PG**	**SESSION C**	**PG**
	INSPECTION QUALIFICATION III		**PIPING INSPECTION II**		**REACTOR PRESSURE VESSEL I**	
	WE.1.A		**WE.1.B**		**WE.1.C**	
	Co-Chairpersons: Bernard Bisiaux, Vallourec - France Toshihiro Yamamoto, Japeic - Japan		**Co-Chairpersons:** Pierre Calmon, CEA - LIST, France Gerd Dobmann, IZFP Fraunhofer - Germany		**Co-Chairpersons:** Etienne Martin, EDF - France Clarisse Poidevin, CEA - LIST, France	
08:10	WE.1.A.1 - Qualification of end of manufacturing non destructive examination for high integrity components *JL Gobert, F Lasserre, M Jambon, JM Crauland, AREVA, France*	**376**	WE.1.B.1 - A new method for driving 128CH matrix phased array probes with a very compact and high performance solution *G. Dao, Advanced OEM Solutions, USA*	**527**	WE.1.C.1 - A review of inspections conducted on Belgian reactor pressure vessels affected by hydrogen flaking *Ph. Dombret, A.S. Bogaert, F. Somville, Tractebel Engineering, Belgium*	**702**

08:30	WE.1.A.2 - Qualification of the ultrasonic inspections of vacuum vessel welds of the ITER reactor *F. Fernández, A. García, M.C. Pérez, R. Martinez-Oña Tecnatom, Spain, G. Pirola, Ansaldo Nucleare, Italy, A. Dans, A. Bayón, F4E, Spain*	**383**	WE.1.B.2 - Ultrasonic phased array: application to a coarse-grained stainless steel component examination *G. Garzino, J.M. Paris, AREVA, France*	**531**	WE.1.C.2 - Ultrasonic examination of hydrogen flaking in large forgings: from validation to site inspection *D. Moussebois, Laborelec, Belgium* *T. Pasquier, AREVA , France*	**710**
08:50	WE.1.A.3 - Spanish methodology for steam generator inspection qualification *A.G. Bueno, Tecnatom, Spain* *L. Francia, UNESA, A.E. Industria Electrica, Spain* *J. J. Jimenez, Almaraz, Trillo NPPs, Spain* *J. Torrens, Asco, Vandellos NPPs, Spain*	**389**	WE.1.B.3 - Flaw detection in highly scattering polycrystalline material: improvement of the performances by the use of phased array probes and smart filtering technique *F. Rupin, S. Shahjahan, B. Chassignole, EDF - R&D, France* *A. Aubry, A. Derode, Institut Langevin, Université Paris Diderot, ESPCI, France*	**537**	WE.1.C.3 - Inspection of the reactor pressure vessel wall looking for hydrogen flakes at Ringhals using qualified UT – immersion technique *T. Sjö, J. Benitez, DEKRA Industrial AB, Sweden*	**719**
09:10	WE.1.A.4 - Red dye penetrant testing qualification for the in-service inspection of French nuclear power plant components - overview of current practices *C. Caperaa, Y. Forestier, L. Quemard, EDF-CEIDRE, France* *M. P. Leyris, EDF-CNEPE, France*	**392**	WE.1.B.4 - Study of three-dimensional phased array ultrasonic inspection technique for flaw imaging *M. Tooma, H. Mori, A. Nishimizu, So Kitazawa* *Hitachi Research Laboratory, Hitachi, Japan* *K. Ehara, M. Koike, Hitachi-GE Nuclear Energy, Japan*	**544**	WE.1.C.4 - Comparison of Pre- and In-service inspection techniques in Belgium and Germany against the backdrop of ultrasonic indications found at the reactor pressure vessel of Doel-3 *A. Erhard, BAM, Germany* *S. Dugan, X. Schuler, Materialprüfungsanstalt Universität Stuttgart, Germany*	**726**
09:30	WE.1.A.5 - Qualification and implementation of a NDT based on phased array for the on-site inspection of boiler tubes of coal fired power plants *F. Deneuville, A. Ayoub, Vallourec, France* *P. Cornaton, J. Delemontez, A. Pawlak, EDF, France,*	**400**	WE.1.B.5 - Defect detection and sizing trials using the total focusing method and scattering coefficient matrix with a linear phased array *S. Wedge, L. Carter, A. Rogerson, NDT, AMEC Clean Energy, UK* *J. Zhang, B. Drinkwater, Bristol University, UK*	**545**	WE.1.C.5 - Ultrasound & submarine advancements for RPV internals baffle bolt inspection *S.W. Glass, B. Thigpen, AREVA,USA* *A. Bleuze, E. Brau, AREVA, France*	**735**
09:50	WE.1.A.6 - Effect of the different artificial flaw type in qualification purposes from the point of view of the inspection company *M. Vavrous, K. Markulin, INETEC, Croatia* *M. Kemppainen, I. Virkkunen, K. Miettinen, Trueflaw, Finland* *R. Paussu, J. Pirinen, Fortum Power and Heat Oy, Finland*	**409**	WE.1.B.6 - Phased array transducer optimization for complex nuclear component inspection *A. Vanhoye, O. Casula, CEA - LIST, France* *D. Moussebois, Laborelec, Belgium*	**555**	WE.1.C.6 - Ultrasonic inspection of baffle to former bolts in pressurized water reactors *M. Bolander, L. Alerts, C. Bies, F. Bonitz Westinghouse Electric, Germany* *R. S. Devlin, P. Minogue, WesDyne International,USA*	**742**
10:10	**BREAK**					

Time	SESSION A	PG	SESSION B	PG	SESSION C	PG
	INSPECTION QUALIFICATION IV		**PIPING INSPECTION (Nozzles / Complex)**		**SG & BOP**	
	WE.2.A		**WE.2.B**		**WE.2.C**	
	Co-Chairpersons: Evan Choi, Candu Owners Group - Canada John Taggart, AMEC - UK		**Co-Chairpersons:** Olivier Dupond, EDF - France Diego Molpeceres, Tecnatom - Spain		**Co-Chairpersons:** Jimmy Ponton, CEGELEC - France François Deneuville, Vallourec - France	
10:30	WE.2.A.1 - Needs for massive mock ups and challenges in manufacturing of them for qualification purposes *J. Pirinen, R. Paussu, V. Nikula Fortum Power and Heat Oy, Finland* *I. Virkkunen, M. Kemppainen, K. Miettinen, Trueflaw, Finland*	**418**	WE.2.B.1 - Advanced inspection technique from inside surface for dissimilar metal weld of steam generator nozzle *Y. Tsuruta, T. Yamaguchi, T. Shichida, T. Matsuura, S. Kawanami, Mitsubishi Heavy Industries, Japan*	**564**	WE.2.C.1 - Non invasive heat exchanger tube inspection using two modalities of pulse reflectometry *N. Amir, Y. Harel, Acousticeye, USA*	**753**
10:50	WE.2.A.2 - Position control of stress corrosion cracking using welding bead *B. Lee, Y. Woo, Korea Aerospace University, South Korea*	**427**	WE.2.B.2 - CRDM nozzles cracking of reactor head in Korea *E. Doh, Y. Kim, J. Kim, G. Lee, KEPCO KPS, South Korea*	**575**	WE.2.C.2 - Manufacture and non-distructive tests of high pressure stainless steel feedwater heater tubes *P. Gerard, Valtimet, France*	**754**
11:10	WE.2.A.3 - Differences in indications of different artificially produced flaws in non-destructive examination *A. Koskinen, E. Leskelä VTT, Technical Research Centre of Finland*	**428**	WE.2.B.3 - Development of an ultrasonic inspection method for the internal corner region of a pipe to dome nozzle on a nuclear component *P. Sévrain, P. Bergalonne, Comex-Nucleaire, France* *N. Hankinson, K. Quirk Phoenix ISL, UK*	**576**	WE.2.C.3 - Helium leak testing: a complementary SG inspection technique. Technology and lessons learned *F. Lesage, B. Bittard, L. Riquelme, Westinghouse Electrique, France* *H. Henaff, EDF- CEIDRE, France*	**755**
11:30	WE.2.A.4 - Current status of Japanese performance demonstration in FY 2012 *H. Shohji, K. Hide, K. Watanabe, Central Research Institute of Electric Power Industry, Japan*	**436**	WE.2.B.4 - Development of a flexible cross wound eddy current array probe for weld inspection *A. Lamarre, B. Lepage, Olympus NDT Canada*	**584**	WE.2.C.4 - Helium leak test in line: enhanced reliability for heat exchanger tubes *M. Lheureux, P. Gérard, Vallourec, France*	**756**
11:50	WE.2.A.5 - Usability of the inspection procedure - human factors approach *M. Bertovic, C. Mueller, BAM, Germany* *U. Ronneteg, SKB Swedish Nuclear Fuel and Waste Management Co, Sweden* *B. Fahlbruch, Tuv Nord Systems, Germany*	**442**	WE.2.B.5 - Eddy current probes based on magnetic sensors for complex nuclear parts inspection *B. Marchand, JM. Decitre, CEA-LIST, France* *G. Cattiaux, T. Sollier, IRSN- DSR, France*	**585**	WE.2.C.5 - Pipes for life - an NDE inspection of AGR boiler tubes *C. R Bird, D. Maclennan, Doosan Babcock, UK*	**762**
12:10	WE.2.A.6 - New ISO norm for titanium welded tubes *P. Gerard, Valtimet, France*	**443**	WE.2.B.6 - Development of ultrasonic and eddy current testing techniques for curved structures *T. Miura, S. Yamamoto, N. Kobayashi, J. Senboshi, S. Ueno, M. Ochiai, I. Chida, H. Adachi and S. Yamamoto, Toshiba, Japan*	**593**	WE.2.C.6 - Discussion of the use of remotely operated manipulators and VPN technology for eddy current testing field projects *C. J. Speas, ANATEC, USA*	**772**
12:30	**LUNCH**					

Time	SESSION A	PG	SESSION B	PG	SESSION C	PG
	ALTERNATIVES TO RT		**MODELLING (T6/T6.1) I**		**REACTOR PRESSURE VESSEL II**	
	WE.3.A		**WE.3.B**		**WE.3.C**	
	Co-Chairpersons: David Tisseur, CEA - LIST, France Raymond Ten Grotenhuis, Ontario Power Generation Inc. - Canada		**Co-Chairpersons:** Andreas Schumm, EDF - France Toshiyuki Takagi, Tohoku University - Japan		**Co-Chairpersons:** Philippe Dombret, GDF Suez - France Colin Bird, Doosan - UK	
02:00	WE.3.A.1 - Use of combined UT advanced techniques in lieu of conventional UT associated to radiography for end of manufacturing of primary component circumferential welds *F. Lasserre, J.Y. Gourdin, J.M Crauland, M. Jambon, AREVA, France* *D. Verspeelt, D. Marois, ZETEC NDT Solutions, Canada*	**445**	WE.3.B.1 - Numerical simulations of ultrasound NDE: a hybrid model with improved efficiency by a new boundary forcing method *E. A. Skelton, R. V. Craster W. Choi, , M. J. S. Lowe, Imperial College, UK*	**602**	WE.3.C.1 - Development of new manipulators for PWR and BWR nozzle inspection *M. Wendel, T. Sjö, DEKRA Industrial, Sweden*	**776**
02:20	WE.3.A.2 - Development and implementation of advanced UT techniques in lieu of manual UT and RT for the inspection of narrow gap welds during manufacturing of primary component circumferential welds *P. Tremblay, D. Verspeelt, D. Marois, B. Cliche, ZETEC NDT Solutions, Canada* *J. M. Crauland, M. Jambon, F. Lasserre AREVA, France*	**455**	WE.3.B.2 - The reconstruction of three-dimensional rough surfaces for ultrasonic NDE modelling *W. Choi, E. Skelton, M.J.S. Lowe1, R. Craster, Imperial College, UK*	**610**	WE.3.C.2 - Application of overlapped skew scan technique for nozzle inner radius using phased array *T. Hamano, S. Matsuda, E. Shiina, R. Horikoshi, N. Shiokawa, IHI, Japan*	**784**
02:40	WE.3.A.3 - The challenge of replacing radiographic by ultrasonic testing on thin austenitic pipes *M. Bolander, A.M. Clairouin-Blais, E. Compagnon, R. Jansohn, WesDyne International*	**464**	WE.3.B.3 - Overview of the recent developments on grain-scale modeling to simulate ultrasonic scattering with a 2D finite element code *P. E. Lhuillier, C. Trottier, S. Shahjahan , F. Rupin, B. Chassignole, T. Fouquet, EDF - R&D, France* *I. Zeriouh EDF- CEIDRE, France*	**619**	WE.3.C.3 - RPV nozzle inner radius (NIR) inspection with a 5 axis robot: development, qualification and implementation on french reactors *P. Ancrenaz, E. Brau, AREVA* *S. Deydier, L. Truchetti, B. Ruos, EDF*	**792**
03:00	WE.3.A.4 - Encoded phased array ultrasonic testing of socket welded joints *J. Hall, J. Fred Hall, J. Devers, T. Blechinger, ANATEC, USA*	**473**	WE.3.B.4 - Modeling inspection of steam generator tubes in CIVA platform: prediction of industrial EC probe response (X-Probe® and +Point® eddy current probes) *S. Paillard, A. Skarlatos, E. Demaldent, CEA - LIST, France* *T. Sollier, G. Cattiaux, IRSN, France*	**628**	WE.3.C.4 - New developments for automated nozzle inner radius and piping inspections *D. Eargle,R.Rishel, WesDyne International, USA*	**798**

03:20	WE.3.A.5 - Radiographic source ejection reductions by ultrasonic techniques for some in-service inspections *F. Vivier, C. Reece, EDF - CEIDRE, France* *L. Blarel, EDF- UTO, France*	**474**	WE.3.B.5 - Axial probe eddy current inspection of steam generator tubes near anti-vibration bars: performance evaluation using finite element modelling *L. Maurice, EDF - CEIDRE, France* *V. Costan, P. Thomas, EDF - R&D, France*	**638**	WE.3.C.5 - Multielement ultrasound and eddy current integrated probe for non-destructive evaluation of nuclear reactor pressure vessel head penetrations *M. Budimir, N. Pavlović, R. Gracin, M. Kekelj, INETEC, Croatia*	**803**
03:40	WE.3.A.6 - Linear accelerator for the inspection of cast iron components *G. Mannessiez, L. Woisel, CEP Industrie-Bureau Veritas, France* *M. Hernandes, XsCell, USA*	**480**	WE.3.B.6 - The use and validation of the OPERA simulator for eddy current simulation modelling *J. Taggart, A. Kyrieleis, AMEC, UK*	**645**	WE.3.C.6 - Guide tube inspection *M.Montero, M.Grataloup, P.Blachon, CEGELEC, France*	**810**
04:00	**BREAK**					
Time	**SESSION A**	**PG**	**SESSION B**	**PG**	**SESSION C**	**PG**
	MATERIAL PROPERTIES/ALTERNATIVE RT		**MODELLING (T6/T6.1) II**		**REACTOR PRESSURE VESSEL III**	
	WE.4.A		**WE.4.B**		**WE.4.C**	
	Co-Chairpersons: Frédéric Lesage, Westinghouse - France Patrick Tremblay, ZETEC NDT Solutions - Canada		**Co-Chairpersons:** Steve Mahaut, CEA-LIST, France Anton Erhard, BAM - Germany		**Co-Chairpersons:** Torbjörn Sjö, DEKRA – Sweden, Rudolf Schwammberger, Kernkraftwerk Leibstadt AG, Switzerland	
04:20	WE.4.A.1 - Qualification of a butt-weld inspection using phased array in lieu of radiography *B. Dormoy, ALSTOM POWER, France* *J. Delemontez, T. Le Guevel, EDF, France*	**482**	WE.4.B.1 - A modeling approach to optimise IP response for large wall thicknesses *A. Schumm, EDF - R&D, France* *D. Tisseur, CEA - LIST, France* *F. Mathy, CEA - LETI, France*	**653**	WE.4.C.1 - Development of a fuel rod guided wave inspection system *J.L. Fisher, S. Vinogradov, E. Laiche, Southwest Research Institute, USA* *K. Krzywosz, EPRI, USA*	**818**
04:40	WE.4.A.2 - Multi-point strain measurement using FBG-OTDR optical fiber sensor *K. Saruta Japan Atomic Energy Agency, Japan* *T. Kobayashi, University of Fukui, Japan*	**490**	WE.4.B.2 - Experimental study for the validation of CIVA predictions in TOFD inspections *R. Raillon, G. Toullelan, M. Darmon, CEA - LIST, France* *S. Lonne, EXTENDE, France*	**660**	WE.4.C.2 - Experimental and analytical evidence of using nonlinear ultrasonic testing to monitor radiation damage *K. H. Matlack, J. Kin, L. J. Jacobs, Georgia Institute of Technology, USA* *J. J. Wall, EPRI, USA* *J. Qu, Northwestern University, USA*	**825**
05:00	WE.4.A.3 - Flaw growth evaluation for deep surface flaw based on FFS code procedure *F. Iwamatsu, K. Miyazaki, Hitachi Research Laboratory, Hitachi, Japan,* *M. Mochizuki, Osaka University, Japan*	**497**	WE.4.B.3 - Recent computer modeling activities and achievements in PAUT applications *L. Horacek, UJV Rez, Czech Republic* *P. Mares, Centrum vyzkumu Rez, Czech Republic* *V. Kopal, CEZ Czech Republic*	**668**	WE.4.C.3 - Development and deployment of bottom mounted instrumentation (BMI) nozzle inspection *O. Burat, M. Taglione, F. Jacquinot, AREVA, France* *C. Gibert, EDF- CEIDRE, France*	**826**
05:20	WE.4.A.4 - ND-characterization of ageing phenomena - development of sensors for ISI and SHM *G. Dobmann, Fraunhofer-IZFP, Germany*	**506**	WE.4.B.4 - Generic GTD-Kirchhoff scattering model for the ultrasonic response of planar defects *M. Darmon, R. Raillon, V. Dorval, S. Chatillon, CEA - LIST, France* *L. Fradkin, Sound Mathematics, U.K*	**675**	WE.4.C.4 - A computerized system for the advanced inspection of reactor vessel studs and nuts by combined multi-frequency eddy current and ultrasonic technique *W. Kelb, KontrollTechnik, Germany* *J. M. Sarteel, CapTech, France* *R. Leriche, CEGELEC, France*	**834**

05:40	WE.4.A.5 - Non-destructive detection of dealloying in Cu-Al alloys using ultrasound *R.Royer, Structural Integrity Associates, INC.,USA* *C. Searfass, Jason Van Velsor, Jeff Milligan*	**513**	WE.4.B.5 - Investigations on the critically refracted longitudinal wave for optimized use in the NDT/E field *W. K. Yaacoubi, S. Yaacoubi, Institut de Soudure, France*	**684**	WE.4.C.5 - Mechanized NDE on reactor pressure vessel (BWR) nozzles at nuclear power plant Leibstadt 2012 *I.Vinzelberg, Westinghouse Electric, Germany* *R.Schwammberger, H.Lipke, Nuclear Power Plant, Switzerland*	**847**
06:00	WE.4.A.6 - NDE tools selection for components' state characterization during NPP unit commissioning and operation *Arzhaev , A.I., Blokhin, V.N., Derij, V.P., Makhanev, V.O., Podlatov, M.A., Atomtechenergo, Russia* *Dub, A.V., Razygraev, A.N., Razygraev, N.P.,CNIITMASH, Russia* *Pasmanik, L.A., Smirnov, INCOTEX, Russia*	**520**	WE.4.B.6 - Optimization of the full matrix capture parameters of ultrasonic transmit–receive array data for non-destructive characterization of defects *F. Koubaydatt, S. Chaki, S. Hariri, M. Douai, TPCIM, France* *B. Dupont, F. Berthelot, F. Koubaydatt, CETIM, France*	**692**	WE.4.C.6 - Mechanized inspection of core shroud support legs at Forsmark 1-from idea to inspection with manipulator Nemo *J. Danielsson, Westinghouse, Sweden*	**857**
Thursday, October 3, 2013						
Time	**SESSION A**	**PG**	**SESSION B**	**PG**	**SESSION C**	**PG**
	ADVANCED TECHNOLOGIES		**CONCRETE**		**REACTOR PRESSURE VESSEL IV**	
	THU.1.A		**THU.1.B**		**THU.1.C**	
	Co-Chairpersons: Martin Bolander, Westinghouse - Sweden Frédéric Lasserre, AREVA - France		**Co-Chairpersons:** Etienne Martin, EDF - France Gerd Dobmann, IZFP Fraunhofer - Germany		**Co-Chairpersons:** Andreas Schumm, EDF - France Thierry Pasquier, AREVA - France	
08:10	THU.1.A.1 - Advanced 3D visualization and analysis of phased array UT inspection data *G. Maes, J. Berlanger, D. Reilly, D. Richard, ZETEC , Canada*	**859**	THU.1.B.1 - FDR for non destructive evaluation: inspection of external post-tensioned ducts and measurement of water content in concrete *F. Visco-Comandini, G. Six, F. Sagnard, Université Paris Est, France* *T. Bore, D. Placko, SATIE, ENS Cachan, CNRS, France* *S. Delepine-Lesoille, Andra, France* *F. Taillade G. Moreau, J .Salin , EDF - R&D, France*	**949**	THU.1.C.1-ARCHER- advanced system for RPVH inspection and repair *S. Galošić, T. Tomašić, I. Vuković, A. Bakić, INETEC, Croatia*	**1025**
08:30	THU.1.A.2 - Innovative practical phased-array adaptive focusing applied to the compensation of a weld cap profile *A. Lamarre, J. Habermehl, Olympus NDT, Canada*	**869**	THU.1.B.2 - Condition assessment of pressure pipelines in nuclear power plants: a case for non-destructive evaluation of concrete pressure pipes *E. Padewski, III, P.E., Pure Technologies, USA* *M. Wrigglesworth, A. Somani, Pure Technologies, Canada*	**956**	THU.1.C.2 - Evaluation of the performance of computed radiography systems with different sources and different configurations *J. Banchet, A. Peterzol, B. Bader, AREVA, France* *C. Caperaa, V. Didier, EDF - CEIDRE, France*	**1032**
08:50	THU.1.A.3 - Autocoverage – an automated assessment of the coverage achieved in inspection of a nozzle inner radius by UT beams *T Cherraben, D Cornez, B J Dikstra, Doosan Babcock, UK*	**870**	THU.1.B.3 - Remote controlled vehicle for inspection of vertical concrete structures *J. Lindberg, M. Guimaraes, EPRI, USA*	**963**	THU.1.C.3 - Results from nondestructive examination of PWR vessel internals *J. Spanner, EPRI, USA*	**1044**

09:10	THU.1.A.4 - Zone sensitivity optimization for the ultrasonic inspection of complex 3D geometries using CIVA software *B. Chapuis, F. Jenson, CEA - LIST, France* *F. Vivier, L. De Roumilly, EDF - CEIDRE, France* *B. Chassignole, P.E. Lhuillier, EDF - R&D, France*	**876**	THU.1.B.4 - Advanced methods for sampling and analysis of post-tensioned concrete tendon greases *R. Wurzbach, MRG Labs, USA*	**967**	THU.1.C.4 - Flaw handbook development for VVER-1000 RPV inlet nozzle area *N. Sakhno, O. Kharytonov, I. Kadenko, Nondestructive Examination Training and Certification Facility, Ukraine* *O. Kharytonov, O. Kutzenko, Taras Shevchenko National University of Kyiv, Ukraine*	**1049**
09:30	THU.1.A.5 - Dynamic tracking of ultrasonic probe and real-time volumetric ray-tracing as a support to manual phased-array inspection of complex components *A. Lamarre, J. Habermehl, Olympus NDT, Canada*	**884**	THU.1.B.5 - Determining material properties of concrete components: elastic parameters and compressive strenght *D. Algernon, S. Feistkorn, M. Schrrer, SVT Swiss Association for Technical Inspections, Switzerland*	**968**	THU.1.C.5 - Core mapping process *L. Blondel, European PWR Reactor Services, France* *Rob Wheeler, Newton Research Labs, USA*	**1058**
09:50	THU.1.A.6 - Advances in ultrasonic flaw characterisation *L. Carter, Allan Rogerson, AMEC, UK*	**885**	THU.1.B.6 - Non-destructive evaluation of steel-concrete mock-ups *H. Wiggenhauser, J. Wöstmann, S. Schulze, BAM, Germany* *K. Barry, M. Guimaraes, D. Scott, J. Lindberg, EPRI,USA* *J. Lareau, Westinghouse, USA*	**969**	THU.1.C.6 - Development of high resolution X-ray CT technique for irradiated fuel assembly *A. Ishimi, K. Katsuyama, H. Kodaka, H. Furuya, Japan Atomic Energy Agency, Japan*	**1059**
10:10	**BREAK**					
Time	**SESSION A**	**PG**	**SESSION B**	**PG**	**SESSION C**	**PG**
	EMERGING TECHNOLOGIES		**CONCRETE - CANISTER (T8.2)**		**SURFACE EXAMINATION**	
	Co-Chairpersons: André Lamarre, Olympus NDT - Canada Dominique Moussebois, Laborelec - Belgium		**Co-Chairpersons:** Jean Salin, EDF - France Philippe Dombret, GDF Suez - France		**Co-Chairpersons:** Marko Budimir, INETEC - Croatia Filippo D'Annucci, Westinghouse - France	
	THU.2.A		**THU.2.B**		**THU.2.C**	
10:30	THU.2.A.1 - Improvement of an acoustic sensor dedicated to the internal gas characterization of a LWR nuclear fuel rod in a hot laboratory facility *JY. Ferrandis, G. Lévèque, E. Rosenkrantz, Southern Electronic Institute, CNRS, France* *J.C. Segura, R. Blachier, EDF - SEPTEN, France* *G. Thouvenin, M. Martino, EDF - DCN, France*	**895**	THU.2.B.1 - Applicability evaluation of ultrasonic testing for lid welding of stainless steel canister of concrete cask *H. Shohji, M. Goto, K. Shirai, Central Research Institute of Electric Power Industry, Japan*	**977**	THU.2.C.1 - Asessing reliability of remote visual testing-results of a round robin exercise *P. Ramuhalli, Pacific Northwest National Laboratory, USA* *J. Lindberg, J. Landrum, EPRI, USA* *A. Diaz, M. T. Anderson, Pacific Northwest National Laboratory, USA*	**1066**
10:50	THU.2.A.2 - Property study on EMAT's with visualization of ultrasonic propagation *T. Yamamoto, T. Furukawa, I. Komura* *Japan Power Engineering and Inspection Corporation, Japan* *R. Urayama, T. Uchimoto, T. Takagi, Tohoku University, Japan*	**902**	THU.2.B.2 - Development of phased array ultrasonic techniques for the cast iron insert for the Swedish spent nuclear fuel *U. Ronneteg, T. Grybäck, SKB, Sweden* *R. Risberg, Barend van den Bos, Exova Materials Technology, Sweden* *M. Bertovic, BAM, Germany*	**984**	THU.2.C.2 - Advances in three dimensional measurements in remote visual inspection *J. J. Le Corre, GE Measurement&Controls, France* *E. Hubben, GE Measurement&Controls, USA*	**1067**

11:10	THU.2.A.3 - Detection of incipient SCC damage in primary loop piping using fiber optic strain gages *B. K. Jackson, D. Bosko, M. T. Cronin, J, W. Warwick, Intertek AIM, USA* *J. J. Wall EPRI, USA*	**910**	THU.2.B.3 - Test block for inspection trials of disposal canister of spent fuel *R. Paussu, Fortum Power and Heat Oy, Finland* *J. Pitkänen, Posiva Oy, Finland*	**993**	THU.2.C.3 - Advanced DC-pulse technology for MT testing and demagnetization of steel components *P. Hirsch, HPT Hirsch Prueftechnik GmbH, Germany*	**1068**
11:30	THU.2.A.4 - Ultrasonic transducers for sodium cooled reactors *J.F.Saillant, O.Martin, S.Charrier, J.Sibilo, AREVA, France* *F.Baqué, CEA- DEN, France*	**920**	THU.2.B.4 - Investigation of detectability of cracks in anchor bolts for application of phased array ultrasonic testing *S. Lin, Hiroyuki Fukutomi, Central Research Institute of Electric Power Industry, JAPAN*	**1001**	THU.2.C.4 - Defect detection using an optimized and innovative processing technique of thermography images *M. S. Benmoussat, K. Spinnler, Fraunhofer iis, Erlangen, Germany* *M. S. Benmoussat, M. Guillaume, Ecole Centrale Marseille, Institut Fresnel, CNRS, France* *Y. Caulier, AREVA, France*	**1074**
11:50	THU.2.A.5 - Validation of a high resolution X-ray technique within the PARENT program *L. Hammar, H. Wirdelius, Chalmers University of Technology, Sweden*	**926**	THU.2.B.5 - Defect sizing using PA-ultrasonic testing and acceptance in copper lids, tubes and welds for disposal canister *J. Pitkänen, Posiva Oy, Finland* *A. Lipponen, H. Raiko, D. Braddock, VTT, Finland* *G. Brekow, BAM, Germany*	**1008**	THU.2.C.5 - New system “SOKRAT” for WWER-1000 reactor pressure vessel visual testing from outer surface *I. Kadenko, R.Iermolenko, V.Petryshyn, N.Sakhno, Nondestructive Examination Training and Certification Facility, Ukraine*	**1085**
12:10	THU.2.A.6 - Proposal for NDT strategies to assess the structural integrity of nuclear pipings *S. Yaacoubi1, W. K. Yaacoubi, P. Dainelli, Institut de Soudure, France* *D. Chauveau, and M. Riethmuller, Institut de Soudure Industrie, France*	**933**	THU.2.B.6 - Application of ultrasonic stress measurement to preload assessment on already tightened bolts *H. Walaszeka, P. Bouteilleb, CETIM, France*	**1018**	THU.2.C.6 - New approach of clean NDT for applications in nuclear industry *A. Pelletier, S. Besson, IXTREM, France* *E. A. Crescenzo, CONVERGENCE INNOVATIONS, France*	**1091**

TABLE OF AUTHORS

PLENARY SESSION

ACTIVITIES AND FUTURE TRENDS OF THE ENIQ NETWORK

Etienne Martin, EDF France, Oliver Martin, EC JRC Netherlands,
Russ Booler, AMEC UK, Tony Walker, Rolls-Royce Submarines UK

Abstract

The European Network for Inspection and Qualification (ENIQ) is a network dealing with the reliability and effectiveness of non-destructive testing (NDT) for nuclear power plants (NPP). ENIQ is driven by European nuclear utilities and is working mainly in the areas of qualification of NDT systems and risk-informed in-service inspection (RI-ISI). Since its establishment in 1992 ENIQ has performed two pilot studies and has issued nearly 50 documents making it one of the main contributors to today's global qualification guidelines for in-service inspection (ISI). In the last two years the network saw a number of changes. In 2012 ENIQ entered the newly established international R&D association on Gen II / III reactors NUGENIA as its 8th technical area (out of eight). Following the integration into NUGENIA ENIQ members rewrote the ENIQ roadmap and included a number of challenges facing its members in the next couple of years. These challenges will result into new projects in the coming years and some of them are currently under preparation. Also a new ENIQ task group was established recently, the Task Group for Inspection Qualification Bodies (TGIQB). It should serve as an exchange forum for IQBs. This paper describes the recent development, current activities and future trends of ENIQ.

1. Objectives and Organisation of ENIQ

The European Network for Inspection and Qualification (ENIQ) is a network dealing with the reliability and effectiveness of non-destructive testing (NDT) for nuclear power plants (NPP). ENIQ is driven by European nuclear utilities and is working mainly in the areas of qualification of NDT systems and risk-informed in-service inspection (RI-ISI). Since its establishment in 1992 ENIQ has performed two pilot studies [1] [2] and has issued nearly 50 documents. Among them are the two ENIQ framework documents, the "European Methodology for Qualification of Non-Destructive Testing" [3] and the "European Framework Document for Risk-Informed In-Service-Inspection" [4], 11 recommended practices [5-14] and a significant number of technical reports and discussion documents. ENIQ is recognized as one of the main contributors to today's global qualification guidelines for in-service inspection (ISI).

To achieve its goals ENIQ has three task groups. Beside the two already existing task groups, the Task Group for Qualification (TGQ) and the Task Group for Risk (TGR) a new task group was established in 2013, the Task Group for Inspection Qualification Bodies (TGIQB). The latter should serve as an exchange forum for IQBs. Beside the TGs ENIQ has a steering committee (SC), which is the decision making body of ENIQ. The SC approves all the documents drafted inside the TGs, but also serves as an exchange forum for ISI related issues in NPPs. The SC has twelve voting members who are entirely coming from European utilities with one vote per country. Voting members come from Belgium, Czech Republic, Finland, France, Germany, Hungary, The Netherlands, Slovakia, Spain, Sweden, Switzerland and the United Kingdom. Additionally the SC has non-voting members (observers) from Canada, USA, and the chairpersons of the three task groups and additional representatives of European utilities, ISI vendors, IQBs or research organisations.

The European nuclear industry entered a period of significant change and this prompted the SC in 2010 to initiate an internal discussion to determine the industry's vision and objectives regarding ENIQ's future role and activities.

This exercise resulted in the issuing of a strategy document, entitled the "ENIQ 2020 Roadmap" [15] and the decision of ENIQ voting members to integrate ENIQ into NUGENIA (www.nugenia.org), which is an European based R&D association on Gen II & III reactors founded in November 2011. NUGENIA combines the activities of four previous networks and technical working groups (TWG). These are:

- the international network on severe nuclear accidents SARNET (www.sar-net.eu),
- the European network on plant life management NULIFE,
- the TWG on Gen II & III reactors of the Sustainable Nuclear Energy Technology Platform (SNETP, www.snetp.eu) and
- ENIQ

NUGENIA has now 80 members with all major European nuclear organisations among them. NUGENIA has 8 technical areas (TAs) with ENIQ being one of them (TA8). Following the integration into NUGENIA ENIQ has recently updated its roadmap [15] and included a number of technical challenges facing its members in the coming years.

2. Challenges of ENIQ

2.1 NDT Qualification

After joining NUGENIA ENIQ re-wrote its roadmap published in early 2011 and added a number of new challenges. These are briefly explained in the following paragraphs.

There is a trend to replace film based industrial radiography with computed radiography (CR) and this requires to understand the relative performances of CR and film based radiography. An advantage of CR is its linear detection characteristics and the resulting ability to reduce the radiation exposure, which in turn reduces inspection times and the potential radiological hazard. Since the detection, processing and interpretation of both methods differ considerably, there are many technical aspects that need to be explored. TGQ is currently preparing a comprehensive study on the performance of CR with the aim to identify the essential parameters that affect the performance of CR thereby providing a consistent approach to inspection design and the production of technical justifications (TJs). Another aim of the study is to identify the different aspects for qualification of a CR application.

Ultrasonic phased array provides significant improvements for a wide range of applications compared to conventional ultrasonic testing (UT). These cover the ability to generate several fixed beam angles from within a single probe, beam focussing and the provision of detailed defect characterisation through signal processing. The current approach for qualifying ISI using phased arrays is to apply the same principles and processes as for conventional methods on a case by case basis. With the increasing use of phased array there is substantial benefit to be gained through a more formalised approach. The essential parameters for phased array are more numerous and complex than for conventional UT and extensive studies are required to ensure inspection reliability in practice.

Guided waves UT (GWUT) is seen as a promising ISI method, but no independent assessment of this method has been performed yet. Such an evaluation would be useful for an informed decision making process on the relevance of deployment of this technique and to identify the different aspects that are required for the qualification of the method.

NDT inspection simulation software is widely used as a first step in the development of inspection procedures and sometimes as the final step in verifying inspection capabilities of a technique for defect detection, because of the relatively little costs involved compared to experimental verification using mock-ups. An independent assessment to verify the accuracy of existing NDT inspection simulation software would be useful in evaluating the relevance of their output for the qualification of NDT Systems.

High density polyethylene (HDPE) is a promising alternative to cast iron for piping systems of tertiary cooling systems of NPPs, since HDPE is not subject to corrosion and erosion degradation discovered among cast iron piping. The greatest challenge concerning HDPE is its accurate and reliable ISI. A study to investigate the reliability of ISI methods for HPDE would be beneficial.

The integrity of concrete structures of NPPs, in particular the containments, receives more interest inside the nuclear community with lifetime extension of operating NPPs. This includes ISI of concrete, which is more complex compared to metallic components. The development of an evaluation process on the reliability of commercially available inspection techniques and the implementation of a qualification process for these techniques for concrete components would be beneficial.

The European Methodology for inspection qualification [3] was initially designed as a framework that would enable each country to establish its own detailed practices that matched the specific national requirements (regulatory, plant type, resources, etc.). Whilst being extremely successful in achieving this objective, the inevitable specific nature of the qualification processes has introduced significant obstacles in the ability to transport qualifications between countries. ISI vendors that have qualified their inspection systems in one country are then required to repeat the qualifications in another country even if the plant is similar. Consequently, one of the major tasks faced by ENIQ is to understand the technical barriers that preclude the transport of qualifications between countries and to overcome these. To identify these barriers TGQ has previously carried out a survey and is currently preparing a pilot study on mutual recognition of ISI qualifications.

2.2 Risk-Informed In-Service Inspection

Probability of Detection (PoD) curves are a tool to quantify the reliability of NDT systems and they are slowly finding their way into the nuclear industry. The need to quantify the output of inspection qualification has become more important, especially as structural reliability modelling and quantitative RI-ISI methodologies become more common and the PoD provides a metric for quantifying ISI reliability. Despite recent progress in the development of PoD methodologies adequate guidance on the use of PoD for practitioners is still missing.

Despite RI-ISI is well established an analysis on its role for defence-in-depth and an assessment on the achievable level of risk reduction with RI-ISI is still missing. Another challenge related to RI-ISI is RI pre-service inspection (PSI) for new build in view of the on-going and planned new build of NPPs in Europe.

2.3 Inspection Qualification Bodies

The main challenges for TGIQB are the mutual recognition of qualified inspections and the improvement of inspection qualification practices, in particular the development of a consensus on the design of practical trials and production of test pieces for qualification of ISI procedures and personnel, an investigation on the wider aspects of NDT model validation, the establishment of a consistent approaches for the re-qualification of NDT systems and personnel and provision of a consistent approach to the assessment of NDT simulation.

3 Current Activities and Project Proposals of ENIQ

3.1 Task Group for Qualification

TGQ launched a survey in 2011 to identify the barriers that preclude transfer of inspection qualifications from one country to another. The survey involved a questionnaire on different aspects of inspection qualification. Beside a section with general questions (e.g. if ENIQ Methodology is followed, which codes & standards are followed, etc.) the questionnaire contained sections with questions on regulatory requirements, IQB requirements, test pieces and practical trials, use of modelling, utilisation of foreign validations and personnel qualification. The questionnaire was sent to one organisation per country with ENIQ members, either IQB or utility, and with one exception all countries replied. The received answers and the experience of ENIQ members suggest that transfer of inspection qualifications between countries may not be as difficult as initially anticipated. TGQ

members agree that an in-depth study (pilot project) is required to identify the barriers precluding the transfer of inspection qualifications between countries.

Following the survey TGQ members are currently preparing a pilot study on mutual recognition of inspection qualifications between countries (acronym: MUREC). The aim of the project is to understand the technical barriers that preclude the transfer of inspection qualifications between countries and to find methods or procedures to overcome them. The launch of MUREC is foreseen for early 2014 and the project will have a duration of four years. The first stage of the project involves a comparison of the inspection requirements and inspection specifications of different countries. This task will take a year. In the second and main stage of the project each participant is requested to perform a qualification on a simple case (real or fictitious) according to his national rules, guidelines and methodologies. In the third and last stage of the project the results of these qualifications are compared with each other and recommendations are formulated.

Another project that is currently under preparation by TGQ is a comprehensive study on the performance of computed and digital radiography (CR & DR, acronym: COMRAD). The aim of this study it to identify the essential parameters that affect the performance of CR / DR and thus provide a consistent approach to inspection design and production of technical justifications. The launch of COMRAD is foreseen for early 2014 and the project should have a duration of two years. The first stage of the project is a review of the state-of-the-art of CR / DR and identification of key aspects that determine their performance. The second stage of the project is the writing of a recommended practice on qualification of CR and DR, which is the final output of the project.

3.2 Task Group on Risk

TGR is currently drafting a report on the lessons learned from the application of RI-ISI to European NPPs 0. It summarizes the experience and lessons learned from the application of RI-ISI, either full applications and/or pilot studies, to European NPPs. The report covers the experience from 30 reactors from 10 different countries. Among the reactors are different types and designs, such as boiling water reactors (Asea-Atom, GE) and pressurized water reactors (AREVA, Westinghouse, VVER). Publication of the report is foreseen for 2014.

Another major task of TGR in 2011 and 2012 was a comprehensive study on PoD curves. This study had two aims. The first aim was to summarize the state-of-the-art of PoD curves and its application to RI-ISI in the nuclear industry. The second aim was an in-depth investigation on the influence of sample size and other factors on the hit/miss probability of PoD curves. The later involved a comprehensive study using Monte-Carlo simulations. The comprehensive study on PoD curves resulted into two ENIQ reports 0 0, a conference article 0 and a peer-reviewed article 0.

Figure 1: ENIQ publications resulting from comprehensive study on PoD curves.

Based on the above study TGR is currently preparing a project on approaches for developing PoD curves for RI-ISI applications (acronym: DevPoD). The aim of the project is the evaluation and validation of different methods for developing PoD curves for NDT systems and to identify the most robust among these. DevPoD should start in early 2014 and should have a duration of four years.

In addition TGR is currently preparing a project on justification of risk reduction through ISI (acronym: REDUCE). The aim of the project is to quantify the benefits from ISI and to indicate levels of risk reduction that can be expected from ISI. REDUCE should start in early 2014 and will have a duration of three years.

3.3 Task Group on Inspection Qualification Bodies

TGIQB is a newly established ENIQ task group and had its inaugural meeting during the 2013 NUGENIA Forum in March in Budapest. TGIQB is intended as an exchange forum for IQBs on issues facing them. The members of the task group either come from IQBs or from organisations that work closely with IQBs, e.g. utilities. The task group has issued its terms of reference defining the functioning of the group. During the second meeting of TGIQB, which will be organised in Leibstadt NPP, Switzerland in December 2013, members of the task group coming from IQBs are requested to give presentation on their organisations including current issues facing them at the moment. From these future projects of the task group are defined. Possible topics are re-qualification of NDT systems, human factors in qualification including re-qualification of ISI personnel, NDT model validation and substitution of ISI equipment in terms of tolerances.

4 Summary

ENIQ entered the newly established international R&D association on Gen II / III reactors NUGENIA in 2012 to become one of NUGENIA's eight technical areas (8th TA). Following the integration into NUGENIA ENIQ rewrote its roadmap and included a number of challenges facing its members in the next couple of years. These challenges will result into new projects in the coming years and some of them are currently under preparation. Their topics are mutual recognition of inspection qualifications between countries, performance of computed and digital radiography, development of PoD curves for RI-ISI applications and justification of risk reduction through ISI. Another recent development in ENIQ was the establishment of a new task group, TGIQB, which should serve as an exchange forum for IQBs. With its on-going and new activities ENIQ will maintain its role as one of the main contributors to today's global qualification codes and guidelines for ISI.

References

[1] ENIQ, Final Report of the 1st ENIQ Pilot Study, ENIQ Report no. 20, EUR 19026 EN, 1999.

[2] ENIQ, Final Report of the 2nd ENIQ Pilot Study, ENIQ Report no. 27, EUR 22539 EN, 2006.

[3] ENIQ, European Methodology for Qualification of Non-Destructive Testing – Issue 3, ENIQ Report no. 31, EUR 22906 EN, 2007.

[4] ENIQ, European Framework document for Risk-Informed In-Service Inspection, ENIQ Report no. 23, EUR 21581 EN, 2005.

[5] ENIQ RP1: Influential / Essential Parameters – Issue 2, ENIQ Report no. 24, EUR 21751 EN, 2005.

[6] ENIQ RP2: Strategy and Recommended Contents for Technical Justifications – Issue 2, ENIQ Report no. 39, EUR 24111 EN, 2010.

[7] ENIQ RP4: Recommended Contents for the Qualification Dossier, ENIQ Report no. 13, EUR 18685 EN, 1999.

[8] ENIQ RP5: Guidelines for the Design of Test Pieces and Conduct of Test Piece Trials, ENIQ Report no. 42, EUR 24866 EN, 2011.

[9] ENIQ RP6: The Use of Modelling in Inspection Qualification – Issue 2, ENIQ Report no. 45, EUR 24914 EN, 2011.

[10] ENIQ RP7: Recommended General Requirements for a Body operating Qualification of Non-Destructive Tests, ENIQ Report no. 22, EUR 20395 EN, 2002.

[11] ENIQ RP8: Qualification Levels and Approaches, ENIQ Report no. 25, EUR 21761 EN, 2005.
[12] ENIQ RP9: Verification and Validation of Structural Reliability Models and associated Software to be used in Risk-Informed In-Service Inspection Programmes, ENIQ Report no. 30, EUR 22228 EN, 2007.
[13] ENIQ RP10: Personnel Qualification, ENIQ Report no. 38, EUR 24112 EN, 2010.
[14] ENIQ RP11: Guidance on Expert Panels in RI-ISI, ENIQ Report no. 34, EUR 22234 EN, 2008.
[15] ENIQ, The ENIQ 2020 Roadmap, ENIQ Report no. 43, EUR 24803 EN, 2011.
[16] NUGENIA, The NUGENIA Roadmaps, to be published.
[17] ENIQ TGR Technical Report: Risk-Informed In-Service Inspection: Lessons Learned from Application to European Nuclear Power Plants, ENIQ Report no. 48, in draft.
[18] C. Annis, L. Gandossi, ENIQ TGR Technical Report: Probability of Detection Curves: Statistical Best Practices, ENIQ Report no. 41, EUR 24429 EN, 2010.
[19] C. Annis, L. Gandossi, ENIQ TGR Technical Report: Influence of Sample size and other Factors on the Hit/Miss Probability of Detection Curves, ENIQ Report no. 47, EUR 25200 EN, 2012.
[20] C. Annis, L. Gandossi, O. Martin, "Optimal Sample Size for Probability of Detection Curves ", Proceedings of the 3rd Int. Conf. on Nuclear Power Plant Life Management, 14th – 18th May 2012, Salt Lake City, USA, paper no. CN-194-070.
[21] C. Annis, L. Gandossi, O. Martin, "Optimal Sample Size for Probability of Detection Curves ", Nuclear Engineering and Design, 262, 2013, pp. 98-105.

PRESENT STATUS OF NUCLEAR POWER PLANTS IN USA

Greg Selby, NDE Center EPRI, USA

The US nuclear power fleet continues to operate with an overall capacity factor greater than 90%. In the past year, however, five units have been closed or their imminent closure has been announced. Some of the closures have resulted from the need for repairs that would have been so expensive that the plants would no longer have been economically viable. Others are closing because they are not economically viable in their local electricity markets in competition with low-cost natural gas. All of these closures illustrate the vulnerability of nuclear power plants to high operating costs, in a competitive electricity market. US utilities are making every effort to reduce their cost, particularly operation and maintenance costs, to the maximum extent that is consistent with safety. Part of this cost pressure affects NDE. At a time when recent NDE failures have highlighted the need for improved reliability, the cost of NDE must be reduced. Improved technology and improved training must be key elements in delivering higher reliability with fewer people, less radiation dose, and lower mobilization costs.

PRESENT STATUS OF NUCLEAR POWER PLANTS IN JAPAN

Toshiyuki Takagi, Innovative Energy Research Center,
Institute of Fluid Science, Tohoku University, JAPAN

Two years on from the Fukusima Daiichi site accident, the order for the cessation of all nuclear power plants (with the exception of Ohi-3/4), continues. The former Nuclear and Industry Safety Agency (NISA) issued 30 regulatory requirements in response to the events at Fukushima, and the facilities have since carried out the necessary work and implemented the prescribed measures, including tsunami-resistant walls, emergency operation centers and mobile DG.

However, a new regulatory body, the Nuclear Regulation Authority (NRA), came into effect September 2012. The NRA is preparing to enact new regulatory standards, which are very strict compared with international standards. The life of a nuclear power plant is limited to 40 years by law. This can be extended to 20 years in certain circumstances, and requires special safety checks.

Additional examinations are also required, including non-destructive examinations of reactor pressure vessel belt lines and the nozzle corners of primary coolants.

It is my desire that nuclear power stations re-start operation as soon as possible, accompanied by the implementation of rational safety measures.

INSPECTION QUALIFICATION I

COMPARISON BETWEEN NDE QUALIFICATION STANDARDS AND PRACTICES IN DIFFERENT COUNTRIES

P. Jardet, M. Dib, EDF Qualification Body, France

ABSTRACT

Nowadays NDE qualification is required for in service inspections of nuclear pressurized components in most countries where nuclear power plants are being exploited. But regulatory requirements, methodologies, and practices are more or less different.

After a reminder of the origin and evolution of NDE qualification, the aims of this paper are to:

- present and compare the main existing methodologies and standards such as ASME, ENIQ, RS-EM,
- present the ISI qualification status in different countries, including regulatory requirements, applied standards, scopes of qualification, types of qualification body...
- compare practices,
- point out common areas but also the main differences
- identify possible ways for harmonization.

ORIGIN AND EVOLUTION OF NDE QUALIFICATION

The reliability issue of ultrasonic testing for nuclear pressure vessels emerged in 1965 from the US Pressure Vessel Research Committee (PVRC), an NDE programme was therefore engaged. The " Marshall Commitee", expert group in fracture mechanics established its recommendations about the size of the defects to detect on the Reactor Pressure Vessel welds, firstly in 1976, and then in 1982. International programmes were engaged to do blind comparisons of the results obtained by different teams on the same mock-ups containing induced defects.

These programmes, PISC I (1974-1978), PISC II & III (1981-1994), UKAEA Defect Detection Trials (1980-1983) and HSST showed significative differences between teams and techniques, and showed shortcomings as much as satisfactory pratices as these results were compared to the destructive results of the defects.

The need to insure the reliability of NDE clearly appeared and different qualification approaches and associated referentials were launched and developped worldwilde :

- Recommendations in the UK 1982 LWRSG report;
- Appendix VIII of ASME Code Section XI from 1989 to present;
- US Perfomance Demonstration Initiative (PDI) from 1992 to present
- Creation of the European Network for Inspection Qualification (ENIQ) in 1992, which has established and updated the ENIQ qualification methodology since 1995;
- RSE-M french code has included the NDE qualification since 1997;
- ...

Meanwhile regulators have progressively required ISI qualification since the 1980s in different countries.

MAIN EXISTING METHODOLOGIES AND STANDARDS

As seen above, the main existing references for ISI qualification for nuclear pressurized components are the ASME code section XI (appendix VIII), the ENIQ Methodology and the RS-EM code (Appendix 4.3). One can also quote the IAEA Methodology for WWER NPP, which essentially follows the ENIQ Methodology, and the ASME section V (Article 14), followed in certain countries (e.g. Canada) to complete ASME section XI and/or ENIQ Methodology.

A comparison on the main items between ASME XI Appendix VIII, ENIQ Methodology, and RSE-M Appendix 4.3 is given in the table 1.

item	ASME XI Ap. VIII	ENIQ Methodology	RSE-M Ap. 4.3
Scope	UT examination used to detect and size flaws (mainly fatigue craks)	Any inspection method or technique used for detecting, sizing, locating a specified type of defect	Any inspection method or technique used for : - detecting, sizing, locating a specified type of defect, - or for surveillance purpose when no specified defects are postulated
Input information	- Component Type - NDE Procedure - Equipement description	- objectives of the inspection qualification - full description of the component to be inspected - types, dimensions, orientations, location and morphologies of defects to be detected and/or sized - inspection performance to be achieved - qualification level - NDE procedure, equipment and personnel requirement	- objectives of the inspection - description of the component to be inspected - type of qualification: - Conventional (no defect suspected) - General (postulated defect situation) - Specific (defects observed) - General/Specific: types, dimensions, orientations, location and morphologies of defects to be detected and/or sized - Conventional: prescriptive standard to be applied, type of reflector used to express the sensitivity (Flat Bottom Hole, Notche…) -inspection performance to be achieved - NDE procedure, equipment and personnel requirement
Technical Justifications (TJ)	No TJ required	For providing convincing evidence that the inspection procedure is capable of meeting the requirements. TJ could include : - Measurement on practice or development test pieces - Physical reasoning - Feedback from field experience - Previous qualification - Results from modelling - Laboratory studies -…	Distinction is made between the NDE Technique (instrumentation, probe..), and the in-the-field inspection (accessibilty, robotic if used…). TJ for NDE Technique provides evidence that the Technique is capable of meeting the requirements. TJ could include : - Measurement on practice or development test pieces - Physical reasoning - Feedback from field experience - Previous qualification - Results from modelling - Laboratory studies -… TJ for implementation in field conditions include robot specifications, accessibility and geometric data.

Practical Trials, Test Pieces	Blind pratical trials are required. The Test pieces shall meet precise requirements in terms of dimensions, type of flaws (e.g. craks, semi-elliptic notches), and number and size of these flaws. These requirements are only depending on the component. The acceptance criteria are defined in terms of mimimum of flaws detected and maximum of false calls for detection, and RMS error for sizing.	It is considered preferable to perform open practical tests for procedure/equipment qualification. Blind practical tests should be perform for personnel qualification. Test pieces may replicate the component in size and geometry, however simpler test pieces can also be used (results need to be extrapolated using justifications).	Open pratical trials are required for General or Specific Qualification. The number and the type of defects contained in the Test pieces are justified case by case, in accordance with the TJ. The trials acceptance criteria are also defined cas by case in accordance with TJ.
Qualification Type, Level	No different type or level	3 defects situation are considered : specific (defects have been found), postulated and unspecified. Only specific and postulated situation are subject to qualification. Qualification level is determined by the utility. It is an input information for the qualification.	3 types of qualification: conventional (no defect supected), general (postulated defect) and specific (defect have been found). No level defined, but TJ is sufficient for conventional qualification.
Qualification of Equipment, NDE Procedure	Equipement, NDE procedure and personnel are not qualified separately.	NDE procedure and equipement can be qualified by TJ, open trials or both.	Required
Qualification of Personnel	See above	If required, through one or combination of : - certification through a national NDE personnel certification scheme - theoretical and/or open practical examination - blind trials	Not required. The NDE procedure shall precise whether specific personnel qualification is required. If required, the content of the qualification is documented (training, tests…).
Qualification Body	Not specified.	Required Three types of QB are possible : - An independant third party organisation - Part of a utility organisation set up on a long-term basis - An ad-hoc body set up for a particular inspection.	Required The QB quality system is required to comply the ISO 17020 standard.

Table 1: Comparison between ASME XI Ap.VIII, ENIQ Methodology, and RSE-M Ap. 4.3

To summarize and conclude, there are significative differences between ASME XI Ap. VIII requirements and both ENIQ Methodology and RSE-M Ap. 4.3. Furthermore, if we except the situation of unspecified defect, RSE-M Ap. 4.3 complies the ENIQ Methodology recommendations.

PRESENT ISI QUALIFICATION STATUS IN DIFFERENT COUNTRIES AND PRACTICES COMPARISON

Based on the answers received from 14 countries (see figure 1) to a questionnaire sent in february 2012 to the ENIQ members or participants, elements are now available for a better knowledge of the ISI qualification status and practices in those countries.
One should note that the following elements are only the results analysis of the answers by the authors and are subject to mistakes due to their understanding of the answers.

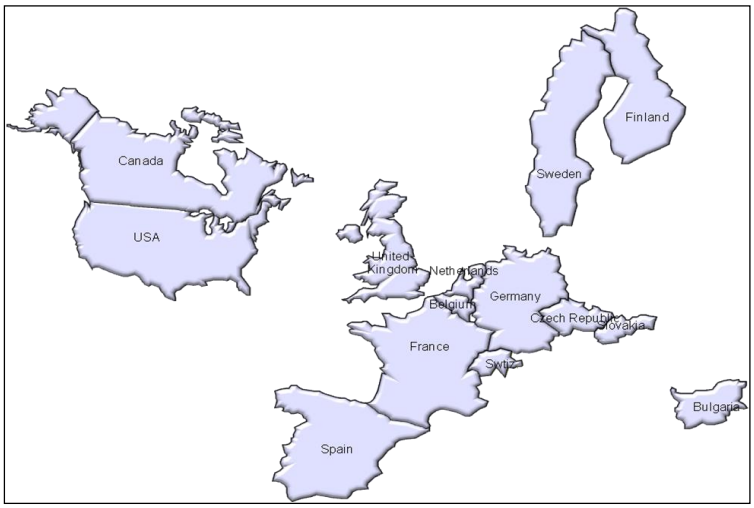

Figure 1: countries ansewring to ENIQ questionnaire

Hereafter presented in map form from figure 2 to figure 7, the main topics concerning ISI qualification in the different countries.

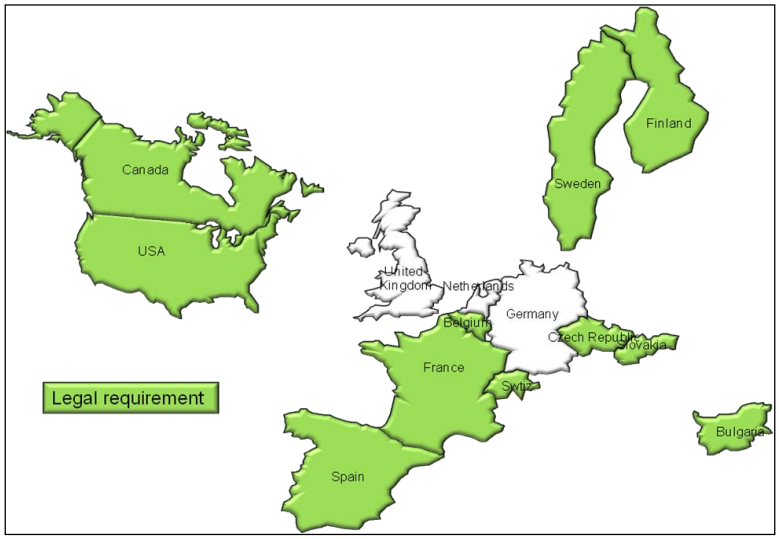

Figure 2: Status of requirement

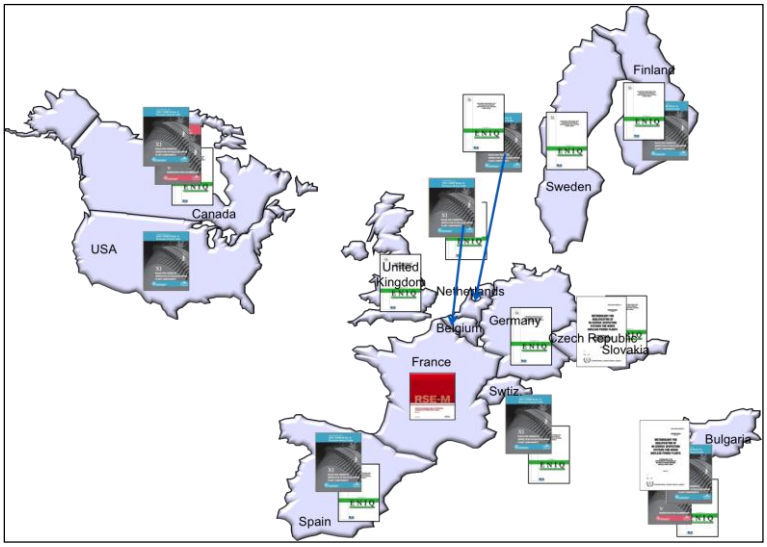

Figure 3: Codes & Standards followed

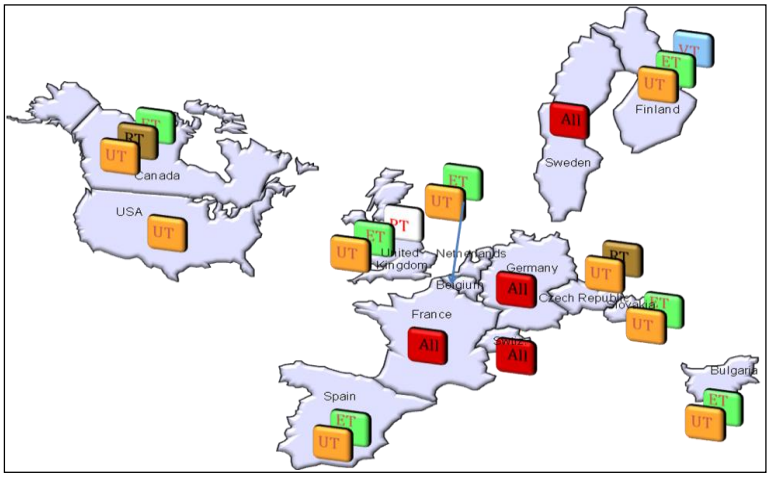

Figure 4: NDT methods included in the scope of qualification

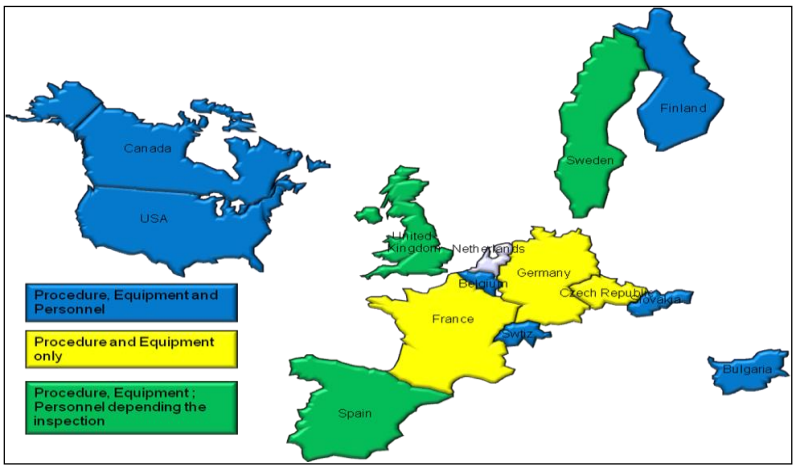

Figure 5: Scope of the qualification

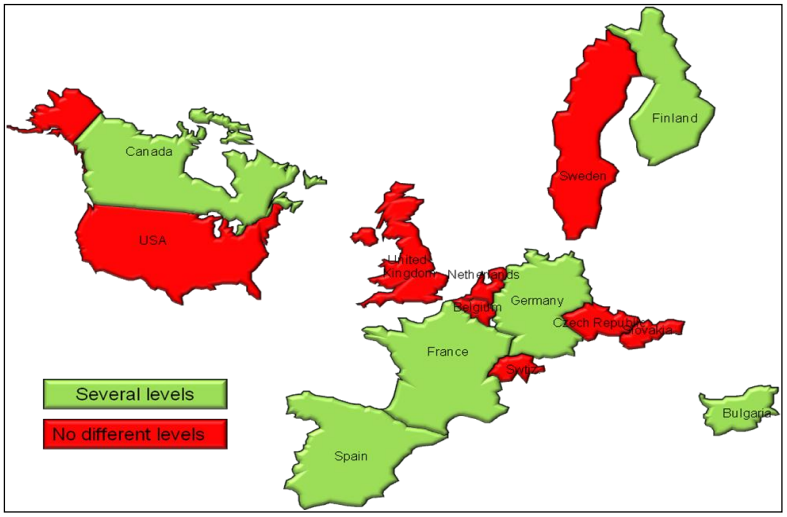

Figure 6: Different levels of qualication

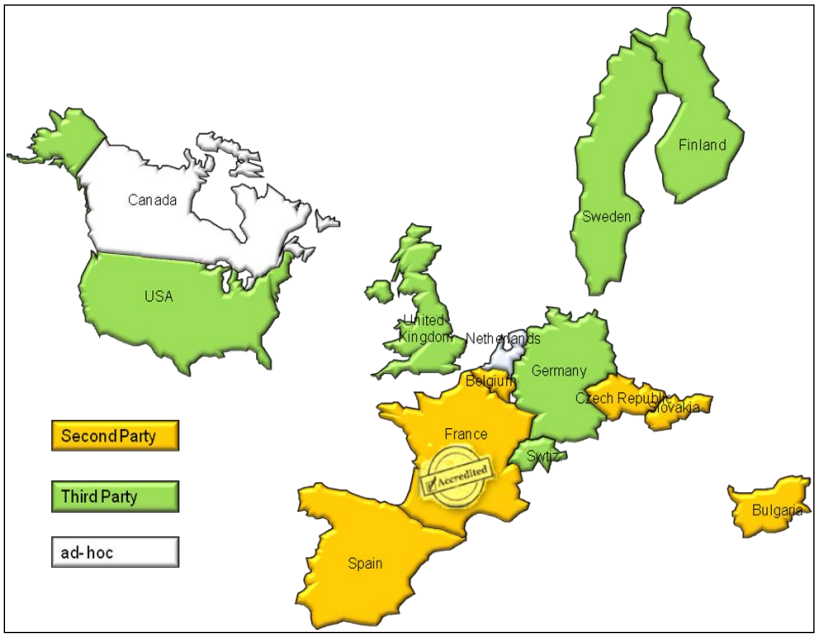

Figure 7: Type of Qualification Body

The differences of qualification practices between countries are a consequence of the local regulations, the standards followed, and local cultures.
Most countries have adopted the ENIQ Methodology, either as a complement to ASME XI (sometimes required by local regulation) or as the main reference. This success of the ENIQ methodology is probably due to its flexibility, which however leads to practice differences.
As an example of topics of pratice differences :

- way to define the objective and input information such as performance target, defaults target, characteristics of the component,
- the levels/types of qualification,
- performance criteria for detection (POD, quantitative, deterministic…)

- performance criteria for sizing (RMS, uncertainty…)
- balance between TJ and practical trials,
- basis for the design of the test pieces and the defects (imposed, justified, use of the concept of worst case defects…)
- …

WAYS FOR HARMONIZATION

The final purpose in term of harmonization would be a straight transfer of qualifications between countries, but before reaching this objective different issues should be investigate.
First of all tranfert of qualification supposes that the inspection requirements for a similar component are the same between countries. Perhaps, efforts could be made to standardize the contain of the inspection requirements (component description, defect characteristics…).
Secondly, if a recognised way to conduct qualification was defined between QBs, it would then be easier for a vendor to submit part of a qualification dossier (e.g. TJ) from one country to an another one.
A first step could be to identify the elements of qualification dossiers that could be easily transferred or used between countries (e.g. technical evidences, test pieces design, modelling…).

CONCLUSION

The overwiew of the current status of ISI qualification in different countries and practices comparison, shows that there are common areas but also significant differences. These differences are obstacles to be overcome to transfer qualification between countries.
There is a real interest to find and develop ways of harmonization in order to facilitate, at least the use of elements of a qualification dossier from one country to another.

REFERENCES

1) Allan Rogerson, A personal perspective on the early developments in inspection qualification and reliability assessment in the nuclear industry and comparison with similar developments in other industries, Proceedings of the 9th International Conference on NDE in Relation to Structural Integrity for Nuclear and Pressurised Components – May 2012 – Seatlle
2) ASME Section XI 2011a
3) ENIQ Methodology third edition 2007
4) RSE-M In-Service Inspection Rules for Mechanical Components of PWR Nuclear Islands - AFCEN, 2010

THE ROLE OF NDT IN A UK STRUCTURAL INTEGRITY SAFETY CASE FOR HIGH INTEGRITY COMPONENTS

J. Fasham, J. Pearce, A. Goodfellow, EDF Energy NNB Genco, UK

Abstract

Nuclear regulation in the UK is based on a non-prescriptive approach whereby each licensee is responsible for justifying the safety of its plant at each stage of design, construction, commissioning, operation and decommissioning (the safety case). The regulator will assess the safety case against technical arguments, international best practice and historical precedent, amongst other considerations.
This paper sets out in general terms a licensee's perspective on the requirements placed on NDT when used to support Structural Integrity safety case claims of High Integrity Components. This covers such notions as multi-legged safety cases, diversity, redundancy, capability assessment and inspection qualification, along with how these are implemented in practice.

1. Introduction

From the perspective of a vendor or supplier used to a relatively prescriptive regulatory background, the goal-setting nature of UK nuclear regulation can be difficult to comprehend. With no explicit requirements set down in law relating to the use of NDT, it is not always apparent where a licensee is deriving its demands from, and it can be difficult for the licensee to convey the full implications of regulator expectations and interpretations of principles as relate to NDT.
This paper is intended to present a licensee's perspective on working in this environment, by setting out the process by which UK law is interpreted through the Nuclear Site Licence Conditions and the licensee's Safety Case to derive explicit requirements relating to NDT, which can then be specified to, and implemented by, the vendor or other organisations.

2. Background to the notion of a UK Safety Case

In broad terms, a Safety Case is the full suite of documentary justification used to support the safe operation of a nuclear power plant. This includes the claims being made on the safety of the plant, the arguments that allow such claims to be made, along with the necessary evidence to substantiate them. All submissions to the relevant safety authority are considered to form part of the safety case. The legislative background to safety cases in the UK is expanded upon below, along with practical considerations that need to be taken on board in developing and respecting a safety case.

2.1 Nuclear Installations Act and Nuclear Site Licence

In the UK, any entity wishing to operate a nuclear installation must obtain a Nuclear Site Licence (NSL) in accordance with the Nuclear Installations Act (NIA) 1965, as amended. The NSL is awarded to a licensee by the Office for Nuclear Regulation (ONR – currently an agency of the UK Government's Health and Safety Executive, HSE), which is also the body responsible for ensuring compliance with the conditions of the licence. Attached to each NSL is a standard set of 36 Licence Conditions (LC) with which the licensee must comply [1].
Amongst these LC is LC14 relating to Safety Documentation.

This sets out the requirements for the documentation the licensee must produce to justify the safety of the plant at all stages from design, through manufacturing, construction, commissioning and operation, to decommissioning. Considerations when developing the Safety Case are described in sub-section 2.2 below.

In addition, LC19 relates to the construction and erection of new plant, and allows the regulator to prevent the licensee progressing without their explicit consent. Consequently, in relation to NDT, if the regulator were not satisfied with the arrangements a licensee has in place regarding the inspection of new plant, they have the legal power to prevent a licensee from progressing beyond certain specified project milestones until such concerns are addressed. For the regime of in-service inspections, LC28 provides the regulator with certain powers in relation to the arrangements the licensee puts in place for ISI as part of the overall programme of Examination, Maintenance, Inspection and Testing (EMIT). An illustrative structure of hierarchy and interdependencies is given pictorially in Figure 1.

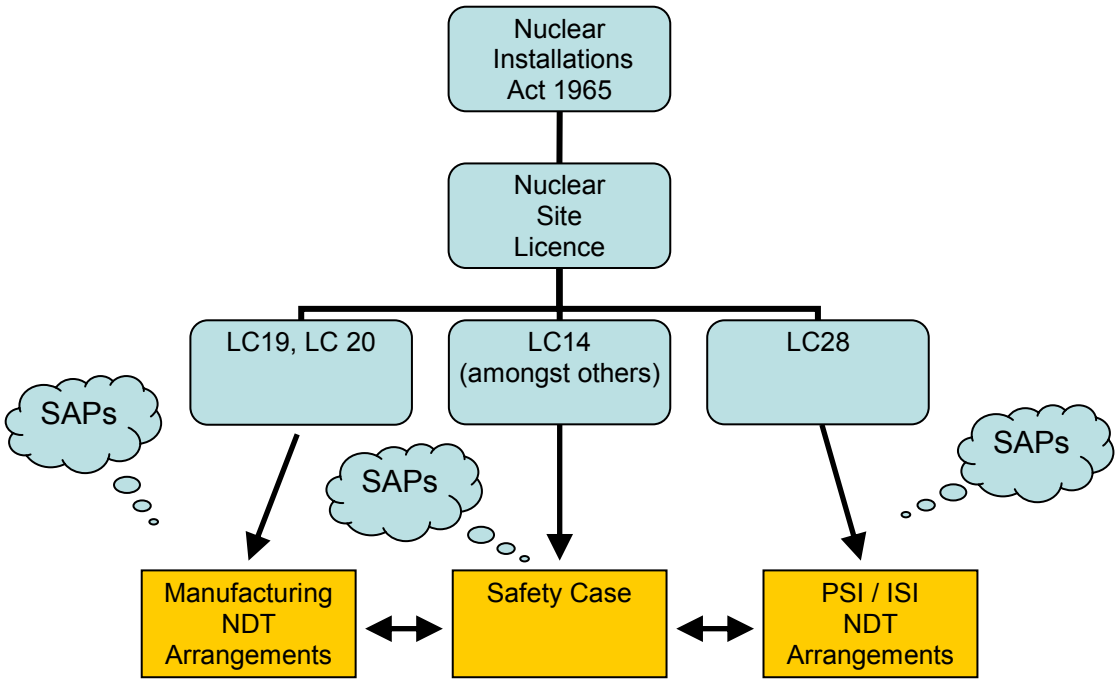

Figure 1 –Illustrative outline of the relationships between the UK legal framework, safety case and NDT arrangements

2.2 Developing a Safety Case

When developing a Safety Case, regular interactions between the licensee and regulator take place at various levels, from senior management down to the working level of licensee engineers and ONR inspectors. When assessing the adequacy of a Safety Case, ONR inspectors will have in mind their Safety Assessment Principles (SAPs) [2]. In applying the SAPs, ONR inspectors will draw heavily on historical precedent and the available scientific and technical information to assess submissions.

In addition to the nuclear-specific SAPs, it must be borne in mind that a nuclear installation is subject to the broader scope of health and safety legislation in the UK, as enacted under the Health and Safety at Work Act etc 1974 (HSW74). Therefore concepts such as reducing risk to a level as low as reasonably practicable (the ALARP principle) are just as applicable [3], although this is likely to be applied more rigorously in the nuclear industry due to the varying levels of risk that society accepts according to the industry or activity [4]. Whilst there are limits set for the level of risk that is just tolerable to workers and the public, the ALARP principle applies in particular to risks that are considered to be tolerable (i.e. a level of risk lying between broadly acceptable and unacceptable).

Therefore a licensee is legally obliged to continue to explore options to reduce risk further even where the "just tolerable" limit is reached. In cases where the effort to do so is not in gross disproportion to the benefit gained, available options should be implemented until risks are so low as to be considered broadly acceptable by society.

2.3 Adhering to the Safety Case

Many of the arrangements invoked by the Safety Case will be enshrined in company procedures to ensure compliance with a number of Licence Conditions, and the likelihood is that ONR will impose a requirement that no change is made to these without their agreement. Therefore adherence to the Safety Case effectively becomes legally binding so as to ensure compliance with the licensee's NSL, under NIA65. In some circumstances, non-adherence to Safety Case requirements could be construed as a contravention of HSW74, giving ONR, as part of the HSE, powers to issue improvement notices or prohibition notices. For a construction project, this can lead to lengthy delays in the construction schedule, whilst for an operating station, this could lead to an extended period of lost production.

3. High Integrity Safety Case

In general, good plant design is based on having several physical barriers between a hazard and any worker or member of the public to whom that hazard may cause a danger. The greater the potential consequences of the realisation of the risk presented by the hazard, the greater the efforts that should be taken to reduce the likelihood of the risk being realised through provision of additional lines of defence or other mitigating measures.

For some components, notably certain parts of the primary circuit of a PWR, producing an adequate safety justification will place very exacting demands on one particular barrier. In addition to the pressure boundary role of the primary circuit, this results from the potentially very large magnitude of the consequences of failure of these components and the resultant very low failure frequencies which must be achieved and demonstrated. Due to the high quality and relatively small numbers of sufficiently similar vessels in the world, no reliable actuarial statistics can be used. Consequently, a conservative deterministic approach has been adopted to provide conceptual defence in depth, through the development of multi-legged safety cases to support High Integrity or Incredibility of Failure claims. Such claims are made where the probability of failure must be so low as to be effectively discounted from further safety analyses.

A claim of High Integrity for a component is not a straightforward one to make, and requires a lot of work to support it. The ONR SAPs explicitly state that this is an onerous way to build a Safety Case. Each leg of the Safety Case should be robust in itself, and the legs should be as independent of one another as possible, so that a deficiency in one leg does not undermine the arguments presented in the other legs.

The UK Technical Advisory Group on the Structural Integrity of High Integrity Plant (TAGSI) has suggested one such way in which a multi-legged SI Safety Case can be constructed [5]. In this approach, highly reliable manufacturing NDT is used to support the Design and Manufacture leg, as well as provide input (along with highly reliable PSI) to the Failure Analysis leg. Highly reliable NDT is then required in-service to support the Forewarning of Failure leg. It should be noted that TAGSI also find that this is not the only structure that could be used, provided that each leg is constructed conceptually independent from the others, and that each leg is sufficiently robust.

4. NDT within a High Integrity Safety Case

As described above, the details of how a multi-legged safety case will be built may vary, but the underlying principles will remain the same. Of interest to this paper, there will always be an element or leg which calls on highly reliable NDT at the manufacturing stage, and an element or leg which requires highly reliable NDT during the service life of the plant.

These are required in order that it can be demonstrated that the plant enters life as defect-free as possible, and that the plant remains free from defects of concern throughout the whole duration of its life.

Consequently, it falls on the licensee's Inspection / NDT Engineers to define what constitutes highly reliable NDT, as well as to provide guidance on practical means of achieving this. The sub-sections below present the potential strategies that can allow such claims of highly reliable inspection.

4.1 Achieving highly reliable inspections

Before looking in detail at how highly reliable inspections may be achieved, some discussion is necessary as to the use of the terms "Capability", "Reliability" and "Confidence" in how they are being applied to NDT in this paper.

Capability refers to the inherent ability of the inspection to detect the target defects, and is due to the physical limitations of the inspection method and its interaction with the defects, the physical properties of the material being inspected, and the physical and electrical properties of the essential equipment used. Capability is assessed assuming perfect implementation of the procedure, so does not address human aspects or any problems surrounding inspection environment.

Reliability is used to mean the ability of the overall system to detect the target defects, so considers the inherent capability of the inspection, its implementation and the human factors that surround the implementation. Additionally, the term reliability is sometimes applied to the overall inspection regime for a component, i.e. the combination of repeated and / or different inspections. This latter point is addressed later.

Confidence is used to mean the degree of certainty with which claims can be made on the reliability and capability of the inspection.

To illustrate these differences, the addition of a favourably angled probe to an inspection would increase its inherent capability, whilst the reliability would then be improved by ensuring that the use of this new probe is adequately included in the procedure and that the operators are suitably trained in the updated procedure. The confidence in claiming higher levels of capability and reliability can then be obtained through qualifying the inspection, noting that qualification will have no impact on the inherent capability of the inspection. (Whilst it is often said that qualification is about improving confidence, not reliability, it is worth adding that it may have an indirect effect on the reliability of the inspection through ensuring better procedures are produced and that more rigorous training regimes are in place.)

In the following subsections, different means of achieving and demonstrating the high reliability of an inspection, with a high degree of confidence, are outlined. In order to provide adequate confidence in the reliability of the NDT necessary to support a High Integrity claim, it will usually be necessary to use an appropriate combination of the options below.

4.2 High confidence in inspection capability

It is essential that the capability of ultrasonic inspections is thoroughly assessed and underwritten. Activities leading to this include:

- use of established codes and standards;
- proper definition of inspection performance requirements;
- effective inspection design;
- critical assessment of inspection procedures;
- comparison with and evidence from the qualification of previous similar inspections on similar components;
- written Technical Justifications / Capability Statements;
- Inspection Qualification by independent body;
- practical demonstration, proving of technique / equipment, using representative test pieces;
- experience, training and qualification of inspection personnel.

Since Inspection Qualification and the demonstration of an inspection's performance by Capability Statements are such important processes in supporting claims of highly reliable NDT, these are expanded upon in the following sub-sub-sections.

4.2.1 Inspection Qualification

The principal means of gaining confidence in the capability and reliability of an inspection is to submit it to a process of formal qualification. In the UK, expectation is that such a qualification for the most safety-significant plant would be conducted by a third-party body, and would be compliant with the well-established methodology developed by the European Network for Inspection Qualification (ENIQ) [6].

As a result, the process will entail an appropriate mix of Technical Justification (TJ) involving physical reasoning, modelling and results of similar previous studies, along with any necessary parametric trials, procedure trials and operator trials. Procedure trials are typically "open", in that the operators are aware of the details of the defects in the test piece being inspected, and operator trials are typically "blind", in that such information is not available. However, the appropriate mix of open and blind trials depends on the elements the Qualification Body wish to examine, so neither should the terms "procedure trial" and "open trial", nor "operator trial" and "blind trial", be used synonymously.

Whilst the importance of maintaining independence of the legs of a high integrity structural integrity Safety Case has been previously stressed, it is equally important to note how Inspection Qualification fits in to the broader structural integrity arguments. Inspections are qualified to demonstrate their ability to detect defects of structural concern. This is obtained by using a Fracture Mechanics Assessment approach to determine a life-limiting defect size, accounting for through-life crack growth (mainly driven by fatigue). A qualified defect size is then chosen to provide a sizeable margin (typically 2) between these two sizes. The nature of defects to be detected is based on history of previous defects produced in similar components.

4.2.2 Capability Statement approach to demonstrating high capability

Where the safety significance of a component still requires that the inspections conducted on it are demonstrably highly capable, but less confidence needs to be shown of this high reliability (perhaps because of greater defect tolerance in a component, or a qualified defect size so large as to present no real concerns over detection capability) alternative approaches can be used. One of the usual means by which this is handled by UK licensees is through the preparation of Capability Statements. The level of rigour applied to such documents will vary according to the safety significance of the plant being inspected.

The most rigorous demonstrations will be very comparable to the TJ of a full qualification, although likely to exclude recourse to conducting any additional practical trials, and prepared with the recommendations of ENIQ RP2 [7] in mind. Likewise, it would typically lead to an iterative process whereby recommendations emerging from the Capability Statement would be fed back to the development of the inspection and procedure, to ensure that an adequate level of performance is achieved. This level would typically be applied to areas of High Integrity components for which a full qualification has been deemed unnecessary, but for which freedom from a specific population of defects still needs to be demonstrated and an objective-based inspection applied.

As the safety significance of the part being inspected decreases, so would the level of rigour applied to the assessment of NDT capability. For lower safety classes, the emphasis moves to demonstrating the level of performance that would be expected where an inspection compliant with a code or standard is used. Such Capability Statements would typically be applicable to a large number of components within certain bounds of product type or configuration, material and size.

For an inspection underwritten by a Capability Statement, confidence in the reliability of the inspection can be gained through giving adequate consideration to the other factors discussed in the later sub-sections.

4.3 High confidence in the competence and aptitude of the inspection personnel

The personnel performing the inspections must be suitably qualified and experienced, hold prerequisite qualifications and certification, be specifically trained and familiarised with the inspection procedure to be used. If required by the Inspection Qualification process, the operators must additionally pass qualification tests, which may include blind trials.

Whilst the prerequisite certification will almost certainly involve training, assessment and work experience requirements consistent with ISO 9712 (or formerly EN 473), such schemes are typically too generalised to provide the necessary confidence in the competence of personnel to a level consistent with a highly reliable claim on the NDT. Therefore there is the need to introduce more specific training programmes and qualifications. The level will vary according to the claims placed on the inspection, with inspections subject to formal qualification requiring the operators to be qualified via blind trials on a given procedure for a specific component.

4.4 Quality of implementation

A highly capable inspection procedure will only become a highly reliable inspection in practice if it is implemented correctly. The necessary high level of quality of implementation is established and maintained through the following arrangements:

- the inspections must be performed by an organisation with effective management and QA systems, such as demonstrated by means of ISO 9001 accreditation;
- the effectiveness of the management and QA systems should be confirmed by internal and external audit, demonstrating visible control of procedures, personnel activities with respect to their qualifications, equipment calibration, control of documents and inspection reports;
- the inspection personnel must be suitably experienced, trained, qualified and certificated (as above);
- the inspection personnel should receive an appropriate level of effective supervision, checking on procedural adherence, equipment compliance, etc.;
- surveillance and monitoring, witnessing and audit of inspections, sample audit by repeat inspection, review of inspection reports;
- client or third-party witnessing of inspections and compliance assessment.

4.5 Diversity and Redundancy

In accordance with established engineering practice, a principal means of improving reliability of a system is through the addition of elements of redundancy and diversity. Redundancy is targeted at meeting the Single Failure Criterion, whereby the failure of just one part of a system must not cause the overall system to fail, whilst diversity aims to provide protection against common cause failure. In a system, these could either be added at a component level to improve the reliability of the system itself, or could replicate the entire system, to improve the overall reliability of the function the system is expected to perform.

By analogy, it is possible to incorporate elements of redundancy and diversity into an inspection regime both at the level of improving the performance of an individual inspection, or in improving the overall reliability of the programme of inspections, and indeed these terms are explicitly mentioned in the SAPs in relation to NDT (principle EMC 29). In the former case, taking as an example a manual ultrasonic inspection, the addition of beams giving rise to different beam-defect interactions can be regarded as adding some diversity. This addresses concerns surrounding the avoidance of some common cause failures, in that the different scans are not reliant on the same response mechanisms.

Redundancy can be incorporated into an individual procedure through the addition of beams which provide a similar response from the target defects as beams that are already well-oriented for such an inspection.

This helps meet the Single Failure Criterion as the operator will have multiple opportunities to detect a defect, and one moment's inattention, poor coupling or misaligned scanning should not lead to the full inspection from missing a relevant signal. This is a particularly useful approach when a certain beam angle is clearly identified as being well adapted for the detection of defined defects of concern.

At the level of the overall inspection programme, redundancy can be included through the use of a repeated inspection of the component, using the same inspection procedure as the original inspection. The choice of whether to involve independent operators (possibly from a different organisation from that performing the original inspection) requires taking a number of aspects into account. Such considerations would include the relative merits of familiarity with the procedures versus the independence of motivation provided by an alternative organisation, and the balance would need to be judged as appropriate.

Provided that adequate redundancy is included in the procedure itself as part of a highly capable inspection, the approach of having a repeat of the overall inspection is not generally regarded as a proportionate response, given the limited gains in reliability compared to the additional effort involved. However, in some circumstances, such as where the ability to implement the original inspection reliably has not been adequately demonstrated, this can provide a means of augmenting the overall reliability of the inspection programme.

Diversity can be brought into an overall programme of inspections through the use of more than one method, or through using distinct techniques within the same method, e.g. an automated TOFD inspection along with a manual pulse echo inspection. It should be noted that this should be regarded as contributing to diversity, rather than providing full diversity, as these will not necessarily exactly replicate the full functionality of the original inspection. Nonetheless, it is usual to provide some level of diversity in an inspection programme, such as through exploring for surface-breaking defects with both appropriate probes in the ultrasonic examination and through using a surface method such as dye penetrant or magnetic particle inspection. Similarly, diverse means of inspecting for embedded defects can arise from a radiographic inspection conducted at an earlier stage of manufacture than a later ultrasonic inspection.

It is important to understand any limitations to these diverse methods, so as to identify any defects within the defect population which are not adequately covered. Additional reassurance should then be sought from one of the alternative strategies above that sufficient diversity and redundancy exists elsewhere to support the highly reliable detection claims for every defect to which such claims apply.

4.6 Automation

In a number of circumstances, it may be possible or desirable to implement automated inspections in place of manual ones. For ISI on nuclear plant, there is a clear advantage in terms of dose reduction to the inspection personnel, but there are a number of other benefits as listed in Table 1 below, alongside some of the principal disadvantages. Whilst this table is focussed on ultrasonic inspections, much of this will also be true for other methods, particularly eddy-current inspection.

Benefits	Disadvantages
• Improved reliability • Improved repeatability • Better at handling complex geometries (e.g. nozzles) • Can access inspection sites that cannot be reached by a manual inspection • Remote operation and dose reduction • Permanent digital data record for future comparison / reference	• Considerable development time and cost • No on-site flexibility to manipulate probe to maximise response from off-angle defects • Increased training requirements • Reduced pool of operators • Bespoke equipment and software often required

Table 1 – Benefits and disadvantages of automated ultrasonic inspections

In addition to the technical advantages for any given inspection, there is also the ease with which the data can be interpreted by more than one operator. This allows for improved claims on control of the quality of implementation of the inspection, along with the level of redundancy. In addition, such repeat interpretation can be conducted off-line, thereby having less of an impact on scheduling, particularly during outages. The quality of the data acquisition can be assessed from the data obtained, so that a repeat of the physical inspection on the plant is only required where identified by any concerns with the data quality.

4.7 Human factors

Several aspects relating to human factors have already been addressed under the inspection personnel sub-section. However, beyond the performance of individual operators, there are some elements which apply more broadly to human factors within the NDT system. The areas discussed below are not intended to present an exhaustive list, but to identify the type of considerations to be taken, and draw from recent assessments undertaken across industries beyond the nuclear sector such as through the Programme for the Assessment of NDT in Industry (PANI) [8].

In terms of ergonomics, where it is possible to manipulate the plant to be inspected, this should be done in such a way as to make the inspection as straightforward for the operators as possible. Where it is not possible to manipulate the plant, especially for ISI, appropriate scaffolding or other platforms should be used to make the inspection surfaces as easily accessible as possible. This helps to reduce operator fatigue from inspecting in awkward positions and allows the inspection to be implemented in the best possible conditions, e.g. for ultrasonic inspections, the operator should be readily able to see both scanning surface and flaw detector screens simultaneously.

Shift patterns should be adapted to ensure adequate rest for operators. Within the EU, this is enshrined in the Working Time Directive. Tasks performed on different shifts should also be appropriate for the time of day, so that, whilst it might be appropriate to acquire data on a night shift (or required, in the case of radiography), interpretation of the results should be performed on a day shift.

Time pressure should be reduced by realistic scheduling of the inspections, with extra time allocated for more complicated inspections, such as ultrasonic examination of austenitic components. Time pressure also arises from the hazardous or uncomfortable nature of the inspection environment, so measures should be taken, where possible, to reduce any factors encouraging the operator to rush the inspection. Examples might be to provide additional shielding or automate the inspections in areas of high radiation dose-rate.

Many of the human factors can be controlled through producing inspection procedures with clearly written, unambiguous instructions, which are logically structured and simple to follow. They should provide systematic, step-wise instructions for the operators to implement.

5. Conclusions

The requirement to implement highly reliable NDT in the UK nuclear industry has been presented, following the legislation through the Nuclear Site Licence Conditions and the regulator’s Safety Assessment Principles to the Safety Case and arrangements the licensee builds and must adhere to.

The means by which high confidence can be demonstrated in the high reliability of the inspections have been outlined, namely:

- Demonstration of the inspection capability (Inspection Qualification or Capability Statement as required);
- Demonstrating the competence and aptitude of the inspection personnel;
- Quality of implementation of the NDT;
- Sufficient diversity and redundancy within the inspections;
- Automation of the inspections;
- Broader human factor considerations.

6. References

[1] Licence condition handbook, HSE-ONR, 2011,
Web version: www.hse.gov.uk/nuclear/silicon.pdf

[2] Safety assessment principles for nuclear facilities, HSE, 2006,
Web version: www.hse.gov.uk/nuclear/saps/

[3] Reducing risks, protecting people: HSE's decision making process, HSE Books, 2001, Web version: www.hse.gov.uk/risk/theory/r2p2.pdf

[4] The tolerability of risk from nuclear power stations, The Stationery Office, 1992, Web version: www.hse.gov.uk/nuclear/tolerability.pdf

[5] Bullough R, Burdekin F M, Chapman O V J, Green Y R, Lidbury D P G, Swingler J N, Wilson R, "The demonstration of incredibility of failure in structural integrity safety cases", Int J Pressure Vessels and Piping 2001 78(8) 539-52

[6] Seldis T, Eriksson A, European methodology for qualification of non-destructive testing (third issue), ENIQ Report no 31, 2007, EUR 22906 EN

[7] Seldis T, ENIQ Recommended Practice 2 – Strategy and recommended contents for Technical Justifications, ENIQ Report no 39, 2010, EUR 24111 EN

[8] McGrath B, Programme for the assessment of NDT in industry – PANI 3, Research Report 617, HSE Books, 2008. Web version: http://www.hse.gov.uk/research/rrpdf/rr617.pdf

SETTING REALISTIC TOLERANCES ON EQUIPMENT SUBSTITUTION FOR CONVENTIONAL, PAUT AND TOFD ULTRASONIC METHODS

E. Choi, CANDU Owners Group, Canada
T. Armitt, Lavender Int. NDT Consultancy Services, UK
P. Ciorau, Tetra Tech Energy Division, Canada

ABSTRACT

The paper presents a new approach to set realistic tolerances on equipment substitution for detection and sizing of cracks in pressure components based on inspection specification. The following aspects will be presented:

- Tolerances on conventional UT equipment substitution for center frequency, bandwidth, pulse length, refracted angle and gain-in reserve
- Tolerances on PAUT features probe, wedge, and test piece velocity compared to reference block velocity
- Tolerances on TOFD parameters, namely PCS offset.

Examples are given for different inspection scenarios for detecting and sizing fatigue cracks. Recommended tolerances are presented based on experimental work, field data and basic principles of UT method. Tolerances for a procedure qualification shall be set based on its scope, not arbitrary, based on ASME XI or other national/international standards. Tolerances quoted are given for clearly resolvable individual defects. Unresolved multiple flaws would not be sizable to tolerances quoted in this paper. Separate tolerances will be discussed with respect to UT, PAUT and TOFD

Introduction

Inspection Qualification process is a complex, costly and long-term process. It addresses a large variety of issues based on Inspection Specification, components specific issues to be inspected: geometry, thickness, access, environmental issues, equipment, procedure, influential and essential parameters, human factor and qualification process on representative mock-ups-just to mention some of most important ones. Most ISI vendors and regulators refer to EPRI PDI program and ASME V/XI Articles / Appendices (ref.1-3), which set minimum requirements for qualification process, including essential parameters (variables) and conditions for equipment checking and substitution. A long list of ASTM Guidelines/Standard practices and ASME Code Cases how to use PAUT in S- and/or E-scan were published within the last decade (ref.4-8). PAUT is an emerging technology, with a fast-pace developing new pieces of hardware, software and accessories (beam simulation, scanners, new type of probes) to solve the needs of ISI in nuclear and/or turbine conventional inspections. Re-qualification process is based on technical justification and fitness-for-service (inspection) approach. The diversity of UT equipment and PAUT hardware/software led to new approaches of inspection qualification/equipment equivalency.

Parallel activities took place at OPG (9-10) and EPRI (ref.11-14), which issued reports and technical justifications for equipment/software equivalency for PAUT application for large-scale turbine components and piping welds (ref.15).

Different approaches are presented in USA for TOFD method (ref.16-17).

In spite of these make-sense approaches, few standards are dealing with realistic tolerances on main system features, in such a way to keep the main scope of inspection (detection, location, sizing, nature, orientation and patter) within the accepted tolerances by IS or fitness-for-service documents related to specific component.

The present paper is dealing with all three aspects of UT inspection: conventional, PAUT and TOFD, trying to stress the logical approach how to set realistic tolerances based on inspection scope.

Conventional UT

Conventional UT is still a reliable inspection method for weld inspection (ref.18). Redundancy of two angles and a freedom of probe movement may outperform a one-line scanning from one side with PAUT, namely for skewed and branched SCC. Partial qualification of conventional UT may be performed as a detection, length sizing and location tool. Discrimination between geometric indications and weld flaws must also be included in the procedure, in order to avoid the false calls or missed flaws. Tolerances on equipment substitution were developed in mid'80s by PNL-Battelle-USA (ref.19), studying the amplitude variation for the worst-case scenario of a large reflector for specular mode reflection. It was a strong belief in USA and Europe that a tighter tolerance on probe and UT instrument (system) will contribute to a repeatable response of flaw amplitude within ±2dB. Our experimental results regarding the frequency measurement methods (target, distance, method, etc.), including the 10% absolute tolerance between *system- to-system* concluded (ref.20) the ASME XI tolerances ***are un-realistic and impossible to be met*** (see Table 1).

Table 1: Factors affecting experimental errors for center frequency and relative bandwidth (ref.18).

Transducer feature		Maximum deviations/experimental errors due to: [%]								
		Wedge angle	Cable length	Pulser type	Pulser set-up	Probe design	Probe family	Metal path	Exp error	Total
2.25	F_c	1.4	5.0	6.0	1.7	6.4	10	1.5	1.0	14.5
	BW	3.9	15.7	5.1	15.2	19.7	12.3	12.1	8.0	35.6
3.5	F_c	0.8	5.7	3.7	1.8	2.7	4.3	1.5	1.0	8.9
	BW	1.7	10.0	5.8	9.6	10.7	7.4	4.4	8.0	21.9
5.0	F_c	0.8	6.9	5.1	5.1	19.6	12.5	4.2	1.0	25.7
	BW	5.7	22.0	8.2	25.0	18.5	28.5	8.7	8.0	50.0

Other sources of errors (ref.21-22) are more important for amplitude response and flaw characteristics (length, location, height, orientation).
The ENIQ process for inspection qualification based on inspection specification (IS) and classification of influential parameters improved the process of procedure validation qualified for a specific task. The following example (see Figure 1) illustrates a partial qualification procedure for ***detection and length sizing*** using different frequencies, but with the same end effect: flaw was detected, located and measured within specified tolerances, acceptable by IS.

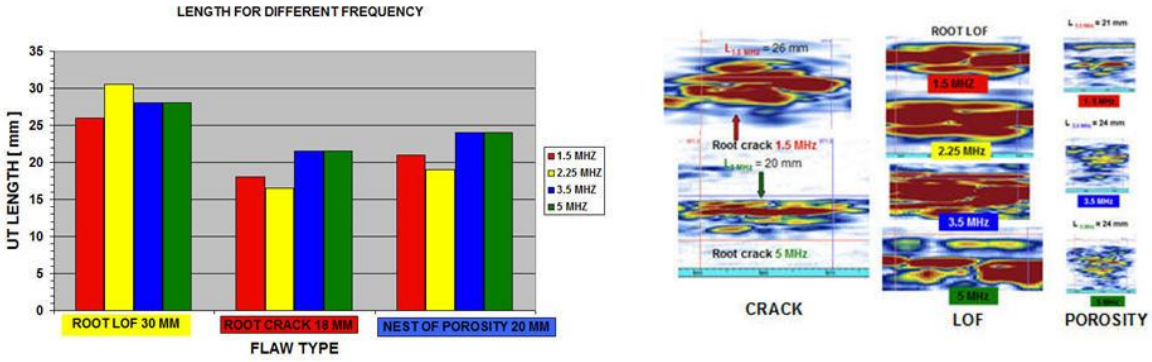

Figure 1: Example of detection and length sizing of root crack, root LOF and nest of porosity by conventional UT probes of 12.7 mm / 45ºT ; frequency range: 1.5 MHz – 5 MHz.

Crack height sizing based on back-scattering tip echo diffraction depends on waveform duration. Our results (ref.22) demonstrated the capability of crack height sizing by a large variety of probes (diameters, frequency, damping factor), under the condition to have enough gain in reserve for corner trap detection and a 3:1 (10 dB) or greater SNR for crack tip versus general noise (see Figure 2).
If the IS requirements for crack height are h > 3 mm, with a specific RMSE (let's say ± 2 mm), a large variety of probes with a waveform duration > 1 μs may be used. Appendix VIII- Article 4110 pct.i) may be used as an option for system characterization and equivalency.

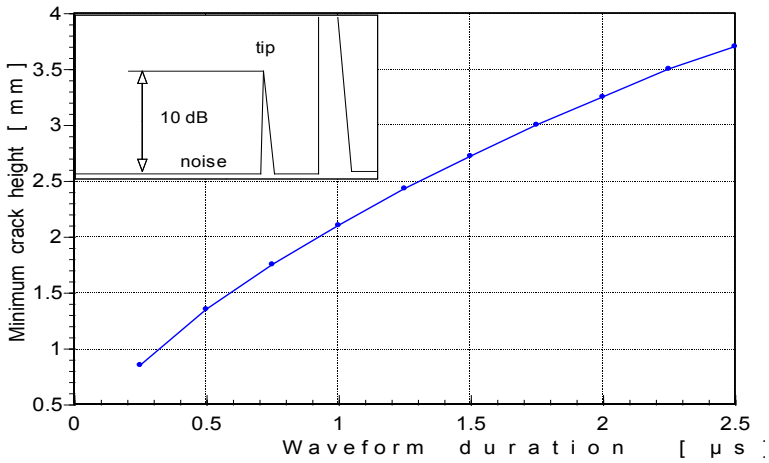

Figure 2: Dependence of crack height on waveform duration-conventional probes.

We suggest the following values for:

- useful gain-in-reserve vs DAC curve > 34 dB
- refracted angle tolerance: ± 2º
- center frequency tolerance: ± 15% to ± 25% vs manufacturer value
- waveform duration: ± 30%, but < 2.5 μs
- SNR $_{\text{crack tip}}$ > 3:1 (10 dB)

These features may be tighter or relaxed, based on specific IS requirements. Using 1.5λ probes of higher frequency (>7 MHz) may be limited to thickness > 40 mm due to small gain-in-reserve, higher scattering and low SNR for crack tip. Our experimental data (ref.23) provided a chart with minimum crack height sized by tip-echo back-scattering using medium-damped probes (see Figure 3).

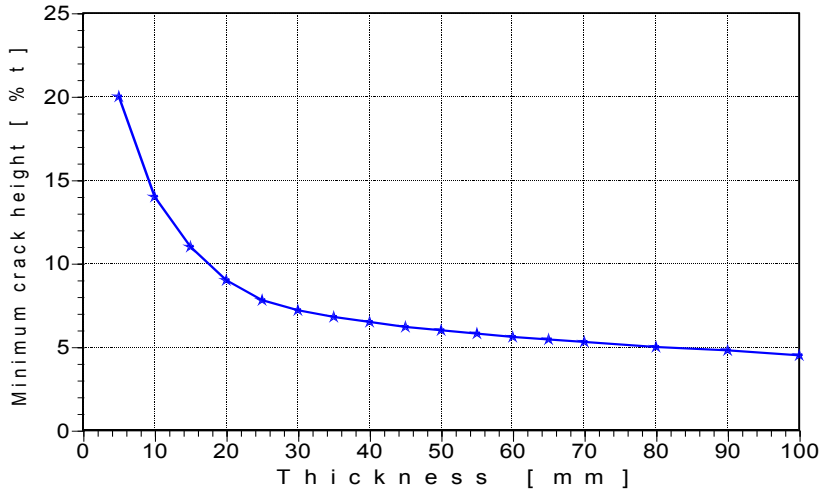

Figure 3: Example of minimum crack height sized by tip-echo back-scattering by medium damped piezo-composite mono-crystal probes.

In conclusion: equipment substitution and system performance shall be based on IS requirements and a realistic assessment of essential variables tolerances. A technical justification with experimental evidence will allow a diversity of UT machines and probes to detect, to size and to locate weld flaws within acceptable tolerances.

A short demo to the customer and regulator (open/blind trial) will increase the confidence of all parties. Using the tolerances of ASME XI Appendix VIII-Art.4000 will limit the problem-solving capability. Some measurements can't be met not even for the same family of probe type. Relaxing the tolerances for a double-reason: experimental errors and sizing cracks with h>3 mm will give an overlapping domain and a make-sense choice for ISI vendor: use the best probe with a good detection power and better SNR for crack tips. An example on a 25% tolerance on center frequency in combination with 30% tolerance on waveform duration is presented in Figure 4.

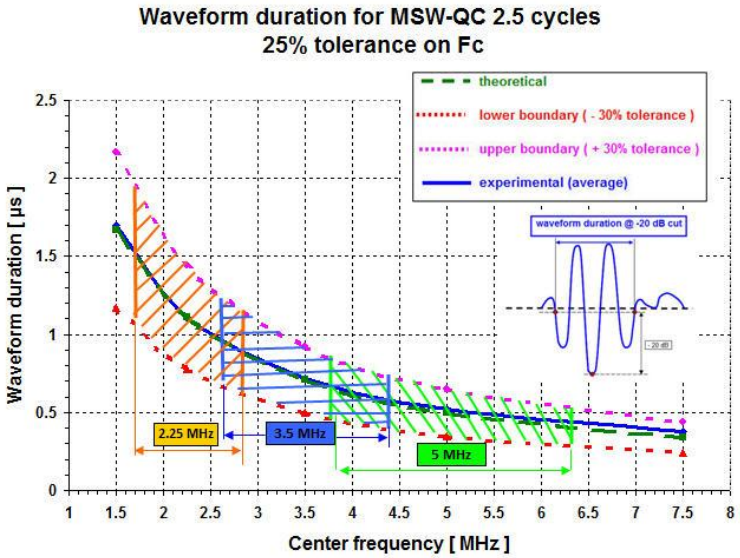

Figure 4: Example of overlapping frequency domains for medium-damped probes of 2.5 cycles.

This approach was used to detect and size weld flaws as per Figure 1, using a range of frequency 1.5-5 MHz. Height sizing and axial resolution was based on higher frequency range (3.5-5 MHz) and shorter waveform duration(< 1µs).

PAUT

PAUT method was quick approved by the customers and regulators because of the three main futures:

- is still a pulse-echo technique using a large variety of angles (redundancy)
- could easily relate the UT results to the part by S-scan display (overlay)
- is using "focused beams' and has a better SNR (detection and sizing of small mis-oriented cracks)

The main weapon of PAUT is the flaw ***PATTERN*** . The same concept based on IS requirements must be applied to PAUT tolerances, namely for S-scan calibration. It is very important to set realistic tolerances on depth, angle range, index/scan readings, gain-in-reserve vs DAC, SNR for crack tips based on acceptable tolerances from an IS or specific OEM procedure. Table 2 illustrates a 4-class event in PAUT applications:

detection only

- sizing within ± 0.5 mm tolerances
- sizing within ± 1.0 mm tolerances
- sizing within ±2.0 mm tolerances

Table 2: Example of tolerance range based on inspection scope for PAUT.

Parameter	Tolerance vs calibration			
	Detection	Sizing **[± 2 mm]**	Sizing **[± 1 mm]**	Sizing **[±0.5 mm]**
Wedge angle	±3°	±2.5°	±1.5°	±0.7°
1-st el. height	±2 mm	±1.5 mm	±1 mm	±0.6 mm
Wedge velocity	±80 m/s	±70 m/s	±50 m/s	±30 m/s
Angular resolution	1°	0.8°	0.5°	0.2°
Test piece velocity	±150 m/s	±120 m/s	±80 m/s	±30 m/s
Index	±15 mm	±12 mm	±10 mm	±5 mm
Sampling A-scans	320	360	640	>640

Another example from turbine components inspection was presented in ref. 24. Some tolerances may be too tight, but in turbine components cases they are crucial for a reliable large-scale inspection. The ***conservative*** values are:

- Wedge velocity: ± 50 m/s
- Wedge angle: ± 1.0°
- Height of 1st element:± 1 mm
- Probe pitch: ± 50 microns for $F_c \geq 6.5$ MHz
- Probe pitch: ± 100 microns for F_c = 3.5 MHz – 6 MHz
- Test piece velocity: ± 80 m/s
- Angular resolution: < 0.5°

In this approach OPG was aiming to detect and size cracks within ±0.7 mm and location of indications within ± 2mm.

Few PAUT practitioners are using the correct number of sampling along the A-scan, in order to deduce the pixel error (ref.25). A combination of independent events – all tolerated to the best of manufacturer/practitioner-may lead to an overall sizing capability of ± 1.1 mm or higher (see Figure 5).

Figure 5: Example of error trend due to independent events, such as point quantity, angular resolution, wedge angle, wedge velocity, and probe pitch tolerances (from ref.25).

Another aspect which is misleading the PAUT practitioners is calibration aspects: velocity, wedge delay, ACG/TCG, encoders) versus the reality of PAUT application. If you want to keep the pattern and use 2-3 types of waves in a single mid-size 1-D probe, you will have to give up some information from the pattern for the sake of calibration process. Few PAUT practitioners are aware about the effective beam aperture, the power steering and the fact a complex set-up may in fact contain 2-3 velocities (L-, T,-and Surface).

Figure 6 demonstrates the sizing of SCCs from surface-waves domain to mode-converted domain, using a ***calibrated pattern*** within ±2 mm tolerances (ref. 26). The beam was totally divergent; some of focal depths were in the wedge!

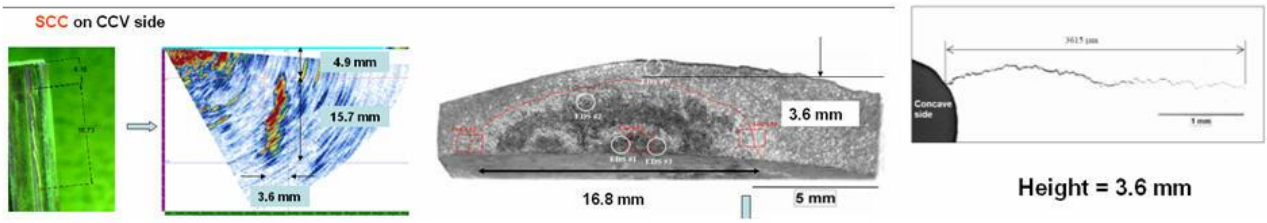

Figure 6: Example of SCC detection and sizing by PAUT using a complex set-up and confirmation of cracks parameters by MP and fracture mechanics. PAUT called 16 x 4 mm (conservative decision), with a ligament of 5 mm (ref.26).

TOFD

The TOFD method was accepted by ASME and UE based on Code Case 2235 and experimental results during different programs, such as PISC II-III and DNV. European and US standards (ref.30-35) detail the procedural steps for a good-practice in applying the TOFD in lieu of radiography or as a quick one-pass weld scanning. It is well-known the limitations of TOFD method (dead zones due to lateral waves, back-wall, LL/TL/LT loci). Examples in Figure 7 to Figure 11 concluded ***the detection*** is a challenge for ID surface breaking cracks with height < 4 mm and ligament < 3 mm. A PCS off-set of more than 10 mm versus 2/3t flaw center may lead to a dead zone and unreliable inspection (see also ref.37-38). The same problem does not exist for OD cracks where conversely cracks located offset to the scan axis become extended in time resulting in significant oversizing.

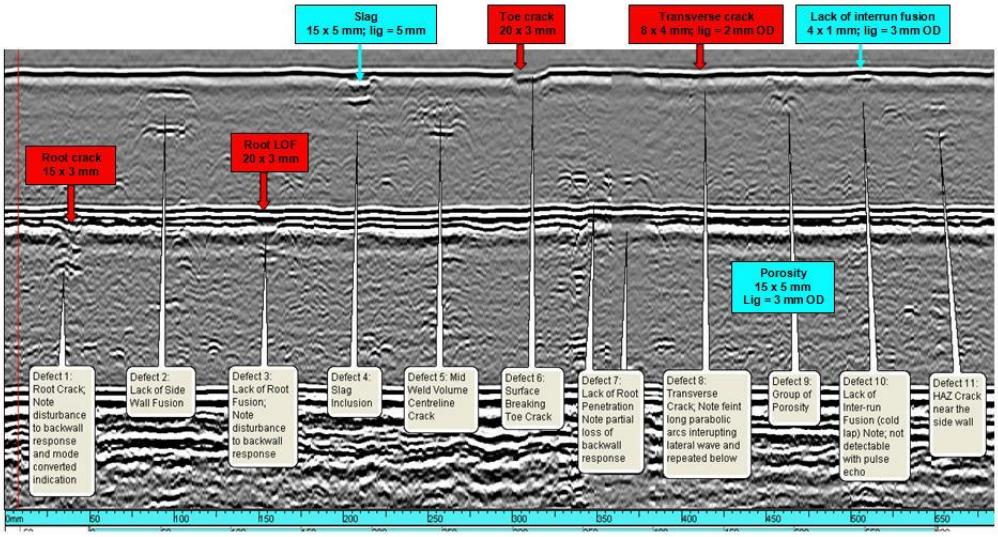

Figure 7: TOFD results for 11 implanted flaws in a welded mock-up of 25 mm. Flaws #1, #3, #6 and 8 are difficult to be detected and sized due to lateral waves and back-wall echoes.

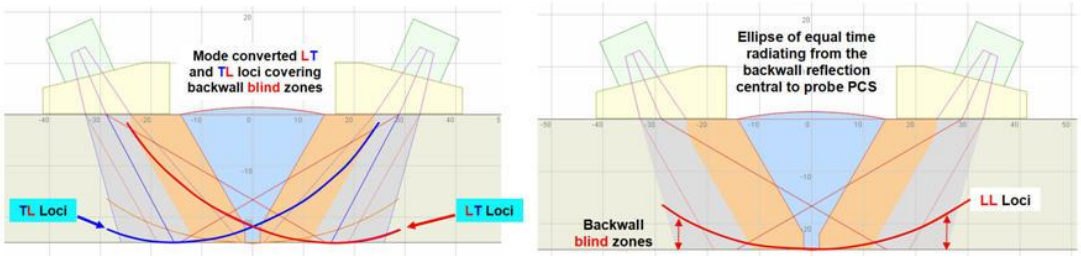

Figure 8: Example of modeling the blind zones for TL/LT loci (left) and LL back wall reflection (right).

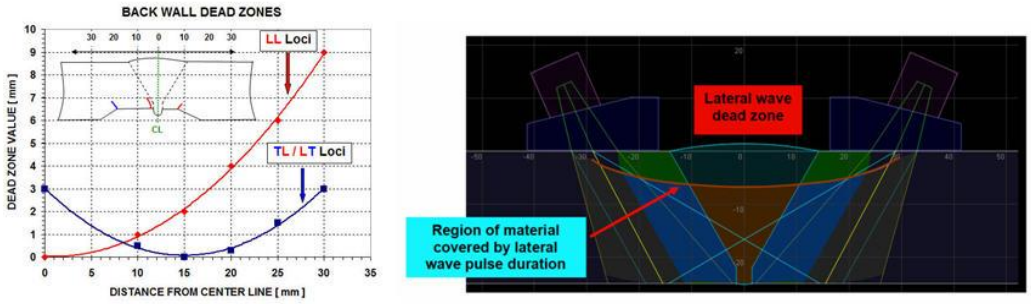

Figure 9: Example of back wall dead zones for t=25 mm and PCS offset ± 30 mm (left) and lateral wave dead zone (right). Removal of lateral waves may increase the information about the OD ligament.

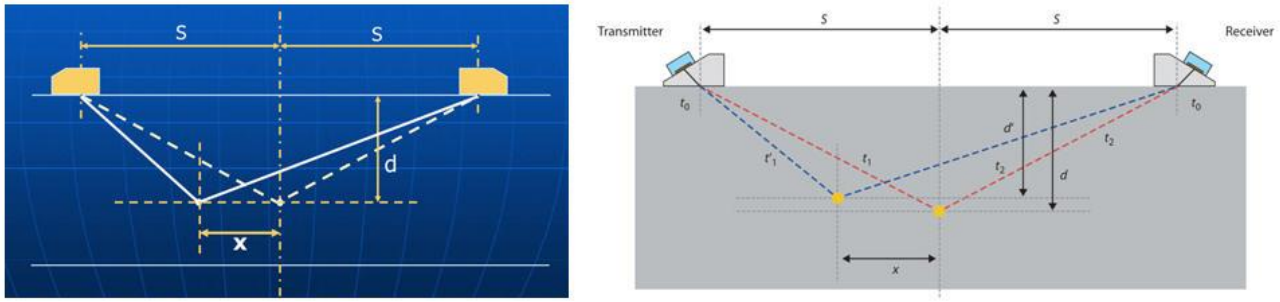

(courtesy OlympusNDT-Waltham-USA)

Figure 10: Principle of location error (mono-crystal-left) and height (PAUT-TOFD-right) due to TOF loci.

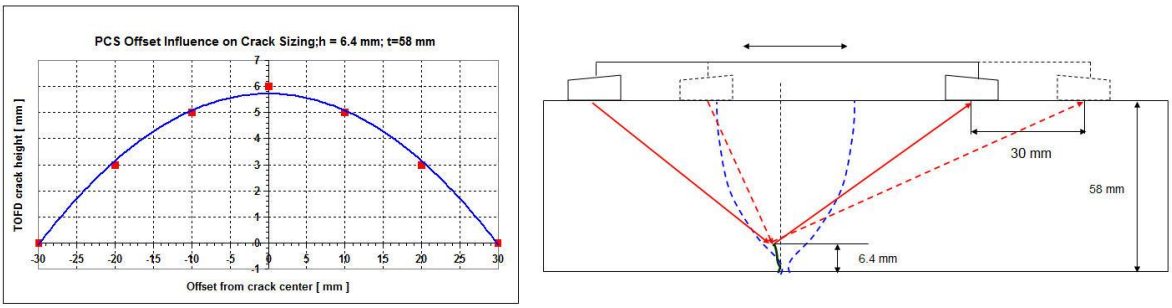

Figure 11: Example of crack undersizing due to probe offset versus crack center line.

Tolerances for PCS offset shall be < 10 mm for an undersizing of 1 mm. A combination with time delay in the couplant, index migration and actual velocity value will contribute to an overall undersizing by more than 2 mm. Use of parallel scans is recommended to eliminate off axis errors. It is highly recommended that multiple offset scans are used to inspect welds with the cap unground. Improved precision in defect size is obtained by measuring the scan which imaged the defect at the shortest arrival time. Data analysts are able to open multiple scan files and make comparative arrival time measurements to ascertain the true defect location and size.

Concluded Remarks and Recommendations

Setting realistic tolerances on essential parameters which might affect inspection results shall be based on IS requirements and its acceptable tolerances for length, height, ligament, location and orientation (ref.27). Assessing the possibilities and limitations of PAUT setting (ref.28-29) will lead to a realistic detection and sizing within achievable tolerances. TOFD tolerances may also be specific to the task (see ref.36-39), but a basic ***do-don't*** line must be drawn in setting the TOFD parameters to meet these requirements(detection, sizing accuracy, flaw positioning). Some hints to reduce the sizing errors and flaw location are given in ref.40-42, but the height error could still reach 20% of the actual crack height.

A value of ±1 mm accuracy for ID surface-breaking crack height with a repeatability of ±0.3 mm ***is unrealistic*** to be achieved in the field unless parallel scans conducted across the weld, cap dressed flush, where the location of crack is known and ***time-of-flight errors are < 0.1 μs***. Flaws in the root area, in counterbore, misalignment and closer to the ID/OD surfaces within 3 mm ligament are very difficult to be detected and characterized unless a diversity and/or a combination of two methods/scanning types are not used. Cracks with height 5-8 mm were not detected in one blind trial by TOFD. It is not recommended that TOFD method be used as a stand-alone method to replace RT. TOFD has inherent defect detection and sizing problems for OD and ID cracks. Crack detection is possible when centered on to an ID crack. Scans off-center to ID cracks can lead to defects being missed or significantly undersized. Surface breaking cracks at the OD will be plotted erroneously deep when they are located off center to the PCS. Taking into account the operator variability, a more realistic tolerance of ±3 mm is recommended for TOFD method when non-parallel scans are solely used (ref.37, 38 and 40). Improved precision with TOFD can be obtained by using very high sampling rates >100MHz, high frequency highly damped transducers, PCS values set to focus at defect locations and use of parallel scans across the defect eliminating off-axis defect errors. Tolerances could be relaxed for PE and PAUT for detection and are very tight for TOFD. SCC/fatigue crack sizing and plotting in stress areas for turbine components require tighter tolerances than ASME XI. More experimental evidence is needed to draw a generic class-based tolerances for essential parameters on all three methods based on ENIQ/ASME approach.

References

1. ASME V-Art.4-2010:Ultrasonic Examination for Welds;
2. ASME V-Art.14-2010: Examination System Qualification
3. ASME XI-2010:Mandatory Appendix VIII-4000: Performance Demonstration for Ultrasonic Examination Systems-Essential Variables Tolerances
4. ASTM vol. 03.03-2011:"Standard Guide-Evaluating Performance Characteristics of Phased-Array Ultrasonic Examination Instruments and Systems" , *ASTM E 2491-08*
5. ASTM vol. 03.03-2011:"Practice for Contact Ultrasonic Testing of Welds Using Phased Arrays" *ASTM E 2700-09*
6. ASME V: "Case 2541 - Use of Manual Phased Array Ultrasonic Examination" 2010
7. ASME V:" Case 2557 Use of Manual Phased Array S-Scan Ultrasonic Examination Per Article 4 Section V" - 2010
8. ASME V:" Case 2558 Use of Manual Phased Array E-Scan Ultrasonic Examination Per Article 4 Section V" – 2010
9. Ciorau, P.: "Phased Array Equipment Substitution-Practitioner Approach for Large-Scale Turbine Inspection"- *ndt.net*- vol. 12, no.6 (June 2007)
10. Ciorau, P.: "A novel checking technique for probe characterization and phased array system performance assessment*"*, *ndt.net* vol.12, no.6 (June 2007)
11. Dennis, M.: "Nondestructive Evaluation: Ultrasonic Instrument Equivalency Demonstration Through Technical Justification"-*EPRI report 1016663*-Dec.2008
12. Dennis, M.:" Nondestructive Evaluation: Ultrasonic Instrument Equivalency Demonstration Through Technical Justification"-*EPRI report 1019114*-Dec.2009
13. Dennis, M.:" Nondestructive Evaluation: Ultrasonic Instrument Equivalency Demonstration Through Technical Justification"-*EPRI report 1021151*-Dec.2010
14. Case N-780 Alternative Requirements for Upgrade, Substitution, or Reconfiguration of Examination Equipment When Using Appendix VIII Qualified Ultrasonic Examination Systems Section XI, Division 1-April 2010 (*ASME XI proposal*)
15. EPRI:" Nondestructive Evaluation: Procedure for Manual Phased Array Ultrasonic Testing of Piping" – *EPRI Report 1016650*-Aug.2008
16. ASTM 2773-04: Standard Practice for Use of the Ultrasonic Time of Flight Diffraction (TOFD) Technique
17. ASME V-Art.4-Mandatory Appendix III and Non-mandatory Appendix L
18 Armitt,T.:"Phased Array not the Answer to Every Application*"- Proceedings ECNDT, paper We3.1.3*-Berlin, Sep-2006; *ndt.net* – no.11-2006
19. Hockey,R.L., Green,E.R., Diaz, A.A.: "The effect of equipment bandwidth and centre frequency changes on ultrasonic inspection reliability: Are model results too conservative?" in proc. *Rev.of Quantitative NDE*, vol.10B, pp.2251-2258, Plenum press, New York, 1991.

20. Ciorau,P., Bevins,B, Mahil, K.: "Frequency response measurements of shear-waves transducers employed for in-service inspection of nuclear components"-*British Journal NDT*, vol.37, no.2, Feb.1995, pp.93-100.
21 CEGB OED/STN/87/20137: "CEGB Code of Practice for Ultrasonic Measurement Errors Assessment"-*CEGB-UK*, May 1987
22. Ciorau, P.:" Random and systematic factors affecting peak amplitude level in ultrasonic inspection of welded joints" - *Canadian Journal of NDT* , vol. 17, no.3, 1995, pp. 14-20.; *Doc. IIW-Vc-923-97/OE*
23. Ciorau,P., et.al.: "Contribution to detection and sizing fatigue cracks in pipe welds"- *Canadian Journal of NDT*, Part 1: Time-of-flight diffraction techniques, vol.19, no.1, Jan. 1997, pp.18-22.
24. Poguet, J., Ciorau,P. :" The Influence of PAUT Parameters on Crack Height, Location and Pattern" Proceedings *8th Int. Nucl. NDE Conf.-paper Th. 3.B.2.*- Berlin-Sep 2010; *3rd COG-CINDE ISI Conf*-Markham-June 2010; *ndt.net*, vol.15, no.12-Dec. 2010 (with ppt)
25. Armitt, T., Ciorau, P., Coulas, J.:" A contribution to quantifying the sources of errors in PAUT"-Proceeding of the *9th NDE Conf.-Seattle*, May 22-24, 2012
26. Ciorau,P., Pullia, L.:" "How Reliable is Your Call? OPG Phased Array Ultrasonic Inspection Experience on Siemens- Parson Turbine Blade Roots 2001-2007"- ndt.net – vol. 12, no. 6 (June 2007) / *10-th EPRI Turbine Workshop-Phoenix-Aug.13-15-2007*.
27 ***ENIQ Report nr.24:"Recommended Practice 1: Influential/Essential Parameters-EUR 21751 EN-2005
28. Armitt,T.: "Measurement and sizing capabilities of PA applications"-Lavender Int. Consultancy – *API training course-module 2*-Houston-USA, 2011 (*not for distribution*)
29. OlympusNDT: "Advances in Phased Array Ultrasonic Technology Applications"-editors: N.Dubé and M. Moles, Waltham, USA, 2007, chapter 5.2
30. EN583-6: 2008: Non-destructive testing. Ultrasonic examination. Time-of-flight diffraction technique as a method for detection and sizing of discontinuities
31. DD CEN/TS 14751: 2004 Technical specification Welding - Use of time-of-flight diffraction technique (TOFD) for examination of welds.
32. ISO/DIS 10863: Draft for development: Welding — Use of time-of-flight diffraction technique (TOFD) for testing of welds
33. ASME CC2235-9: October 2005; Use of Ultrasonic Examination in Lieu of Radiography
34. ASTM E 2373-2004: Standard Practice-Use of TOFD Technique
35. ENV 583-6-2008: Non-destructive testing – Ultrasonic examination – Part 6: TOFD-technique as a method for detection and sizing of discontinuities
36. Ciorau,P., Gray, D., Daks, W.:" Phased Array Ultrasonic Technology Contribution to Engineering Critical Assessment (ECA) of Economizer Piping Welds"- *6th Int. Nucl. NDE Conf*-Budapest, 2007
37. Farley, J.M., Goujon, N.S., Sheperd, B.W.O.:"Critical Evaluation Of TOFD for Search Scanning"-*Proc. 16th WCNDT-paper 602*-Montreal, Sep.2004
38. Quimby, J.:"Practical Limitations of TOFD on Power Station Main Steam Pipework"-*Insight*, vol.48, no.9-Sep.2006, pp.556-563
39. Armitt, T.:"TOFD course for Olympus NDT"-Jan.2005
40. A Al-Ataby, W Al-Nuaimy and O Zahran:" Towards automatic flaw sizing using ultrasonic time-of-fight diffraction"- *Insight*, Vol 52 No 7 July 2010, p.366-371
41. J Charlesworth and J Temple:" Engineering applications ultrasonic time-of fight diffraction", RSP, 2nd edition, 2001
42. Silk, M. G.:"An evaluation of the performance of TOFD technique as a means of sizing flaws, with particular to the flaws with curved profiles:-*Insight*,vol.38, no.4, April 1996, pp.280-287.

Acknowledgements

The authors wish to thank the following organizations and people:

- OPG-IMS Management, Canada and Lavender Int. NDT Consultancy Services, UK for granting the publication of this paper
- OlympusNDT, Waltham-USA for allowing to use a figure from their book "Introduction to Phased Array Ultrasonic Technology Applications"

UT QUALIFICATION AND SITE FEEDBACK ON DISSIMILAR METAL WELDS OF WWER TYPE NPPS IN THE CZECH REPUBLIC

L. Horacek, I. Buldra, UJV Rez, Czech Republic
P. Mares, Centrum vyzkumu Rez, Czech Republic

INTRODUCTION

This paper is devoted to advanced UT implementation achievements and qualification activities on dissimilar metal welds (DMWs) in the Czech Republic. The paper contains a brief summary of recent advanced UT technology implementation based on ZIRCON UT phased array (PAUT) application with dual PAUT matrix search units and UT qualification achievements reached mainly for WWER 440 type Dukovany NPP with a focus on support of lifetime extension assessment and further Long Term Operation (LTO) of WWER type NPPs, partially for much younger WWER 1000 type Temelin NPP. The focus on DMWs and occurrence of specific degradation mechanisms in relation to extended lifetime assessment of appropriate components and piping systems with these welds has been initiated and supported by DMW SCC latest issues in the world (like 5 axial PWSCC at North Anna or circumferential SCC on WWER 440 type SG collector DMWs in Russia and Ukraine) and the State Office for Nuclear Safety (Czech Regulatory Body) requirements on provided License Renewal documentation related to the lifetime extension over 30 years of operation.

Due to the fact that welding technology, partially base metals and mainly buttering material sensitive to SCC degradation is the same for WWER 440 SG collector DMWs and the other WWER 440 and WWER 1000 DMWs around the world, there is no surprise that a high level attention has been devoted to the potential occurrence of SCC type degradation at those NPPs especially when these plants are operated relatively close to or over 30 years.

UT examinations analysed and performed during laboratory and qualification practical trials on the new test assembly have been completed from both austenitic and ferritic sides. Similarly examinations and CIVA simulations have been conducted for both realistic conditions (with and without weld crown). These different search units have been also analysed using CIVA simulations and conducting examinations on available test assemblies.

EXAMPLES OF RECENT UT QUALIFICATIONS OF DMWS

Description of cold and hot WWER 440 type SG collector DMWs at Dukovany NPP

Dissimilar metal welds at WWER type NPPs belong to the inspection areas of the highest concern in the last years. For WWER 440 type NPPs like Dukovany NPP the highest attention have been devoted to hot and cold steam generator dissimilar metal welds (DMWs, see Figure 1). Hot and cold steam generator (SG) dissimilar metal welds (two DMWs per SG, 12 DMWs per Unit, 48 DMWs at Dukovany NPP) were manufactured using the following materials:

Material of piping: 08Ch18N10T stainless steel (SS)
Material of nozzle: 22K carbon steel (CS)
Weld joint electrode: EA 400/10T.

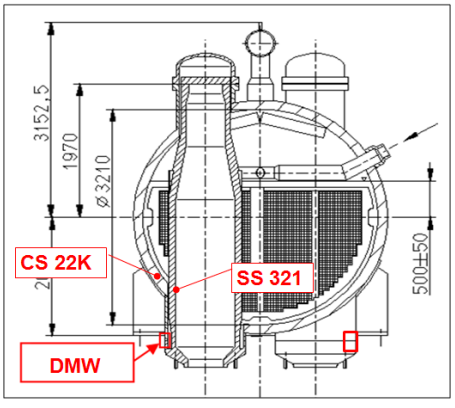

Figure 1: Simple drawing with cold and hot WWER 440 type SG collector DMW configuration

Pulse echo UT qualification of cold and hot WWER 440 type SG collector DMWs for Dukovany NPP

Mechanized UT qualification for pulse echo technique was performed in two phases. The first phase was completed in 1998 within PHARE project PH 1.02/94 as follows:

a) completed qualification trial including inspection procedure (IP), technical justification (TJ) and practical trials (PT) where representatives of PHARE project PH 1.02/94 consortium (JRC Petten) were in the role of the Qualification Body,

b) used simplified list of degradation mechanisms due to at that time worldwide unknown sensitivity of WWER type buttering material to SCC,

c) simple test block can be seen on Figure 2a) (degradation mechanism only general mechanical fatigue, low number of defects (4), full scale 1:1 test assembly segment, no specific location of defects except the weld and weld bevels).

2a) the test assembly from PHARE project 2b) test assembly for national qualification

Figure 2: Test assemblies for WWER 440 type SG collector DMW UT qualification

The second phase of the pulse echo UT qualification was completed in 2011 with the following changes to the first phase:

a) completed qualification of the same inspection procedure using the same equipment, manipulator and personnel,
b) elaborated technical justification and performed practical trials under the supervision of the Czech Qualification Body,
c) practical trials conducted on a new full scale 1:1 test assembly (see Figure 2b) with 20 defects (7 realistic fatigue crack simulations and 13 artificial defects including fabrication lack of fusion type defects, but no stress corrosion cracking type defects) located in different positions.

Defects in the new test assembly (see Table 1) are located in the weld, along weld bevels and some specific defects are positioned on different interfaces (ferrite material to the 1st buttering layer, 1st buttering layer to 2nd buttering layer and 2nd buttering layer to the weld).

The distribution of defects in the new test assembly meets the requirements based on the knowledge before 2011 (general degradation mechanism mechanical/thermal fatigue, no specific aggressive degradation mechanism like SCC/PWSCC, service induced defect initiated from the inner surface, the maximal height up to 1/3 of the SG collector wall).

Defect	Type	Length (mm)	Height (mm)	Location	Angle (°)
PG1	EDM-SE	10,0	3,0	F	0
PG2	EDM-SE	20,0	6,0	F	0
PG3	EDM-SE	15,0	5,0	BFL	15
PG4	EDM-SE	30,0	10,0	BFL	15
PG5	LOF	10,0	5,0	+WFL	10
PG6	EDM-SE	15,0	5,0	BLL	15
PG7	EDM-SE	30,0	10,0	BLL	15
PG8	EDM-SE	15,0	5,0	-WFL	15
PG9	EDM-SE	30,0	10,0	-WFL	15
PG10	FAT	15,0	5,0	-WFL	15
PG11	FAT	25,0	8,0	-WFL	15
PG12	FAT	30,0	10,0	-WFL	15
PG13	FAT	40,0	13,0	-WFL	15
PG14	LOF	10,0	5,0	-WFL	15
PG15	EDM-SE	15,0	5,0	+WFL	10
PG16	FAT	15,0	5,0	+WFL	10
PG17	EDM-SE	30,0	10,0	+WFL	10
PG18	FAT	30,0	10,0	+WFL	10
PG19	EDM-SE	45,0	15,0	+WFL	10
PG20	FAT	45,0	15,0	+WFL	10

Table 1: Defect distribution in the WWER 440 type SG collector DMWs test assembly for national qualification

Pulse echo UT examinations analysed and performed during laboratory and qualification practical trials on the new test assembly were completed from both austenitic and ferritic sides.

Similarly pulse echo CIVA simulations were conducted for both realistic conditions (with and without weld crown).

PAUT qualification of cold and hot WWER 440 type SG collector DMWs for Dukovany NPP

Mechanized UT qualification for PAUT technique started in 2012 as follows:

a) with PAUT inspection procedure also developed for dual search units (IMASONIC 1,5M32x2E64-15 with ZPA-ACC-W-DMW wedge and HQSonics 1,5 MHz, 64 elements (2rows of 32)) search unit with integrated wedge)
b) and new calibration blocks (based on EPRI PDI experience),
c) elaborated technical justification not yet completed for all dual probes and all defect types,
d) performed laboratory practical trials on new full scale 1:1 test assembly segment with 20 defects (7 realistic fatigue crack simulations and 13 artificial defects including fabrication lack of fusion type defects, but no stress corrosion cracking type defects) located in different positions.

To improve our knowledge on the new test assembly shape a laser scanning of the test assembly was performed to avoid potential impact of different types of uncertainties due to test assembly ovality, weld crown and the weld crown vicinity.

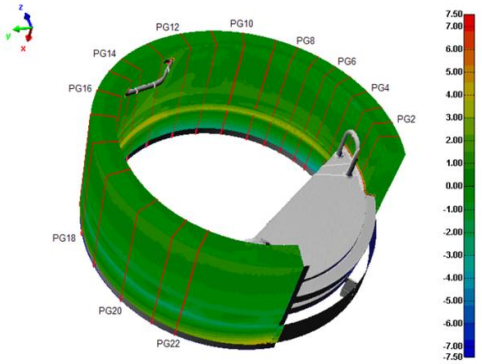

Figure 3: Laser scan image of the test assembly for WWER 440 type SG collector DMW UT qualification

PAUT examinations analysed and performed during laboratory and qualification practical trials on the new test assembly were completed from both austenitic and ferritic sides. Similarly PAUT CIVA simulations were conducted for both realistic conditions (with and without weld crown) and from both sides. All the different search units were also analysed using CIVA simulations and conducting examinations on available test assemblies.

Site feedback from SG collector DMWs ISI at Dukovany NPP

Circumferential stress corrosion cracks were detected and sized predominantly in the position along the interface of the buttering first layer to ferritic SG collector material by pulse echo traditional ultrasonic mechanized inspection and encoded phased array examination using either OMNISCAN or ZIRCON equipment with linear 16 elements search units and later with dual matrix phased array search units (see Figure 4, Figure 5).

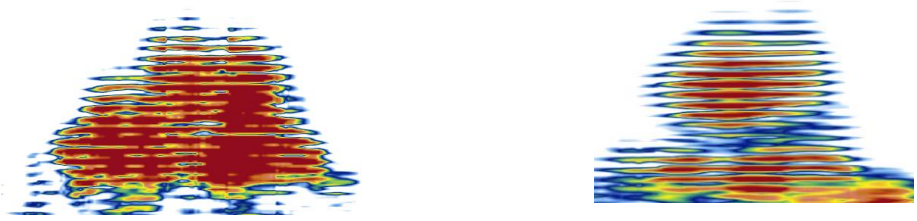

Imasonic PAUT dual probe HQSonics PAUT dual probe

Figure 4: Example 1 of SCC indication from WWER 440 type SG collector DMW before repair

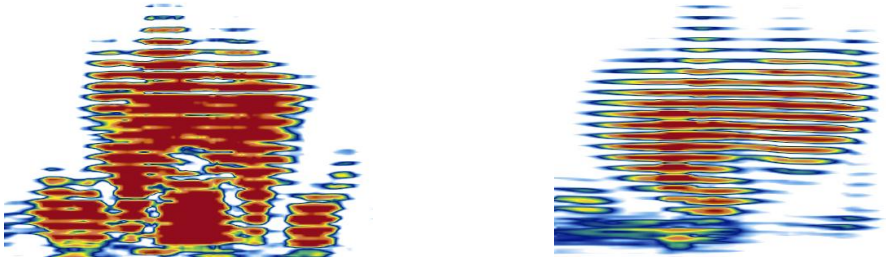

Imasonic PAUT dual probe HQSonics PAUT dual probe

Figure 5: Example 2 of SCC indication from WWER 440 type SG collector DMW before repair

Readiness to repairs of SG collector DMWs at Dukovany NPP

Readiness to repairs was influenced by the level of knowledge of degradation mechanisms and NDE issue root causes. Several factors like design failures, operational aspects and detailed knowledge of degradation mechanisms were of high importance. Very important role in root cause analysis was played by several operational aspects as strain loading up to app. 33% due to thermal expansion differences, non-standard corrosion medium (under corrosion deposits), corrosion medium in direct contact with the first layer of buttering sensitive to SCC and stress concentration factors on the crack tip.

The mentioned degradation mechanisms were identified, described and finally verified using also destructive examination results within the national Czech R&D project sponsored by CEZ.

Design failures, understood and considered only for the case of WWER 440 SG lifetime over 30 years, were caused mainly by the level of post welding heat treatment enabling carbon diffusion into the first layer of buttering and $M_{23}C_6$ on grain border and by applied non-stabilized steel with higher content of P and increased sensitivity to SCC

Due to the fact that welding technology, partially base metals and mainly buttering material sensitive to SCC degradation is the same for WWER 440 SG collector DMWs and the other WWER 440 and WWER 1000 DMWs around the world, there is no surprise that a high level attention has been devoted to the potential occurrence of SCC type degradation at those NPPs especially when these plants are operated relatively close to or over 30 years.

Implementation of Russian technology was conducted within the folowing phases:

1. Repair Technology was qualified in Czech Republic and implemented for Dukovany NPP by SKODA JS (known in the past as Skoda Nuclear Machinery)
2. Small lack of fusion (LOF) detected by UT in the weld root area of welding technology qualification test block
3. Challenge for CIVA simulation of LOF and comparison with real conventional and PAUT inspection results
4. Finally two SG hot collector DMWs repaired at Dukovany NPP at the end of 2012 (11/2012 – 12/2012) and in spring 2013 (04/2013). Repairs were performed within acceptable period of time of approx. 20 days

A degradation mechanism typical for defect initiation in this NDE issue is electrochemical corrosion with the defect propagation driven by anodic dissolution of 22K carbon steel at the interface of the 1st buttering layer to 22K carbon steel. Within the crack propagation the SCC was revealed as the dominant degradation mechanism (see Figure 5-7). The character of SCC is changing from small multiple cracks (see Figure 6) to one or several branched SCC (see Figure 5) propagated from the marginal defect.

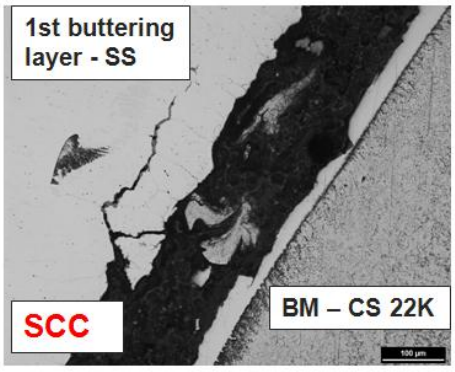

Figure 5: Branched SCC in the 1st layer of buttering at WWER 440 type SG collector DMW

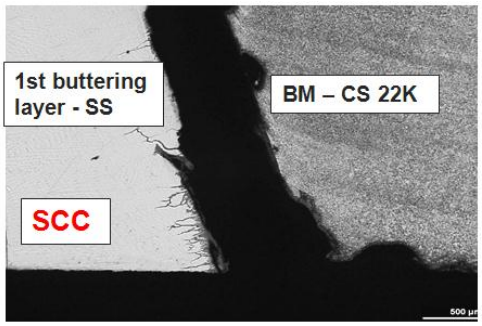

Figure 6: Very small SCC in the 1st layer of buttering propagated from the marginal crack

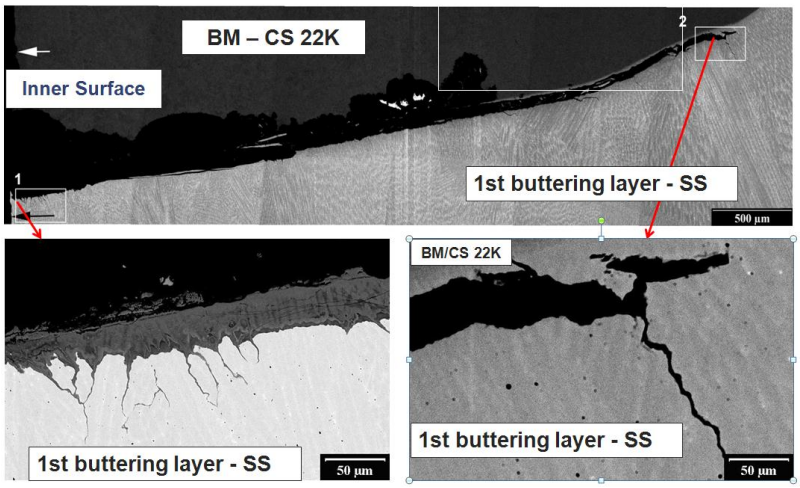

Figure 7: Other examples of SCC in the 1st layer of buttering propagated from the marginal crack

Near-far potential future candidates for SG collector repairs at Dukovany NPP will be determined based on Action plan of SG repair dependent on detected and sized corrosion type defect indications with SCC type degradation mechanism typical features.Typical determined features and parameters of SCC defect indications are a) inner surface breaking defect indication, b) location at or close to the interface carbon steel-the first layer of buttering and c) stress corrosion cracking spots at B-scans and defect indication echodynamic behaviour.

CONCLUSIONS

This paper is devoted to recent NDE issue related to WWER 440 type SG collector dissimilar welds..

In the paper is described and highlighted the whole UT qualification process both for conventional pulse echo UT and phased array UT techniques. The NDE issue leading to repairs of 2 hot SG collector dissimilar welds at Dukovany NPP is described from the point of degradation mechanisms identified, experimentally described and finally verified using also destructive examination results after the repairs within the national Czech R&D project sponsored by CEZ. From the point of lessons learnt there are summarized design failures and revealed operational aspects important for the initiation and propagation of revealed degradation mechanisms.

Potential near future candidates, if any, for SG collector repairs at Dukovany NPP will be determined based on Action plan of SG repair dependent on detected and sized corrosion type defect indications with SCC type degradation mechanism typical features within in-service inspections.

GENERIC IMAGE QUALITY QUANTIFICATION BASED ON ADAPTED ISO STANDARDS FOR VT SYSTEM QUALIFICATION

Y. Caulier, M. Taglione, A. Clay, R. Sancenot, AREVA, France

ABSTRACT

This paper addresses the image quality verification process for remote Visual Testing (VT) using closed circuit camera systems and recording media. VT, the oldest and most versatile NDE method, is applied to all components in the nuclear industry, from the reactor vessel and piping up to and including the concrete containment of the building itself. Even if VT is one of the most rapidly developing technologies of the nuclear NDE industry, the image quality measurement remains a subjective process, as it relies on the direct interpretation by the operator of images of reference test charts. For the resolution measurement e.g. the examiner assures that relevant flaws will be seen, by verifying that characters or lines of a specific size are depicted in the images. This is a simple and reliable method for a simple and reliable test.
Modern remote visual inspection technology is anything but simple. Nowadays automated delivery tooling, computerized video data recording and processing, integrated database storage and automated data output with real-time review and project status updates are used. Certainly given the amount of effort and resources which have been applied to the other aspects of obtaining the images, an objective method of video signal analysis would be not only reasonable to implement but would also speed the process and eliminate its subjective nature, thus lending additional credibility to the results.
The first part of this paper presents different algorithms dedicated to the automatic quantification of image quality developed according to ISO standards. These algorithms were specially adapted to the VT examination needs for different applications and systems (in air, under water, near or far field, endoscope examination…). The developed software application permits to quantify the noise, the resolution, the optoelectronic transfer function, the distortion, and the chromatic aberration of images acquired through the systems that have to be qualified.

1. INTRODUCTION

Over the past years, VT has been professionalized as an official NDT discipline through the COFREND certification process and its equivalent in the USA (the ASNT) and in Germany (the DGZfP). Remote VT has been included as technology has improved and is increasingly called upon for use by many industrial facilities. Different local and European VT standards have been set up over the years in order to define the general principle of VT, the equipment, and also the terminology. These NDT standards are updated with both the changes in technology and the changes in working practices.

VT is currently being relied upon to find flaws with a surface opening of ≥0.013mm (.0005") and to length size them to tolerances of ≤ 0.025mm (.001"). In France, VT is applied for the examination of the Pressurized Water Reactor (PWR) vessel's internals, such as the Bottom Mounted Instrumentation (BMI) weld, the nozzle inner radius, and the B-shell…[1] In the USA, the vast majority of the inspections are for Boiling Water Reactor (BWR) vessel/shroud annulus components and PWR vessel and internals components. The regulators of the nuclear industry, both in Europe and the US have reason to question the techniques applied to make these types of determinations and wonder about their repeatability and accuracy. Other NDE disciplines such as Ultrasonic Testing have implemented a Performance Demonstration Initiative (PDI) process to validate the technique and individuals utilizing it. Consideration is being given throughout the industry to implementing this performance demonstration process to VT as well to eliminate questionable practices and reduce the subjective error intrinsic to the exam. In fact some countries in Europe (Sweden and Switzerland) now require a PDI type qualification over and above the employer's certification. The US is currently studying this as well

[1] The pipes of the Chemical and Volume Control System (CVCS) and other piping connections are also concerned.

with funding from the NRC (Nuclear Regulation Commission) and support from EPRI (Electric Power Research Institute) and Pacific Northwest National Laboratory. It is only a matter of time before the framework for this type of qualification is determined and a program is enacted.
In general, the existing VT qualifications procedures have been defined according to the component being inspected, the client's recommendations, or also the equipment being used. In France the procedure often consists of verifying the color contrast and the lateral resolution by using appropriate test charts. This procedure has to be applied during the maintenance of VT system. In the USA, the VT check is done prior to and after a series of exams or periodically during a series of exams with the same camera/recording system. Any change of component requires a resolution check both with the old and new equipments. Other image quality aspects are however partially (geometrical distortion) or not (chromatic aberrations, noise) considered for the qualification of VT inspection systems. As VT images reflect the quality of the complete VT system plus the influence of the environment on the system, being able to quantify the quality of VT images on the basis of different relevant parameters would help the qualification of the complete systems.

This paper proposes a general procedure to quantify the image quality of VT systems. The objective of the development were not to create a new image quality software (different image quality evaluation software already exists[2]), but to develop a simple and dedicated application that can be easily used for nuclear VT examinations within the AREVA group. The main contribution consists of defining the image quality criteria reflecting the perturbations that might occur in remote VT systems and the specific algorithms permitting the description of these image characteristics. In order to setup a general image quality quantification procedure, following ISO standards were considered and adapted: the ISO14524 Optoelectronic Conversion Function [1], the ISO15739 Noise and Dynamic range [2], the ISO12233 Resolution [3], the ISO9039 geometrical distortion [4], and the ISO15795 chromatic aberration [5]. The defined algorithms were developed in order to be easily integrable in different working environments. Section 2 describes the five image quality quantification algorithms. The technical solution is presented in section 3. Application examples are provided in section 4. Section 5 concludes this paper.

2. DESCRIPTION OF THE IMAGE QUALITY QUANTIFICATION ALGORITHMS

2.1. Optoelectronic Conversion Function

The OECF (OptoElectronic Conversion Function) is the transfer function of digital sensors. Its determination is described in the ISO14524 standard. The OECF is not used directly as an image quality characteristic but is an essential input for other image quality algorithms (e.g. the noise or the spatial frequency response). The OECF of a camera depends on the scene luminance L [cd/m²], i.e. on the illuminance E [lux] (luminous flux per unit area), and the reflection properties (density D, a unit free parameter) of the surface. For an accurate OECF measurement, both values L and E must be determined. E should be constant over the complete measuring area, so that the variations of the transfer function will only depend of the variations of D. The illuminance value is measured with a photometer. Since for many applications, and especially for on site examinations, photometer measurements are impossible or quasi-impossible to realize, this value can alternativelybe estimated. Once, E known, the luminance is computed for a density D, $L = 10^D \cdot E / \pi$[3].

The OECF computation consists of selecting 9 test chart patches with different known densities D. Each patch mean gray value is computed over an area no smaller than 64 x 64 pixels, not including the edges of the patch, for each spectral band of the camera. The final OECF is the average of 9 OECF values computed for each of the 9 recordings. Figure 1 shows the considered test chart with the patches of densities {0.222, 0.384, 0.547, 0.710, 0.872, 1.035, 1.198, 1.360, 1.523}. The curve in the middle shows that the sensor has a linear OECF response (the values of D are linearly distributed). The illuminance E = 3.000 lx has been estimated.

[2] The IASLabTM software permits the evaluation of different digital devices outputs, such as scanners, printers or cameras. The Imatest software developed by Imatest LLC, permits the image quality evaluation according to different test charts.
[3] The standard recommends to compute the log luminance log10(L / L0), where L0 = 1 cd/m² is the unit luminance.

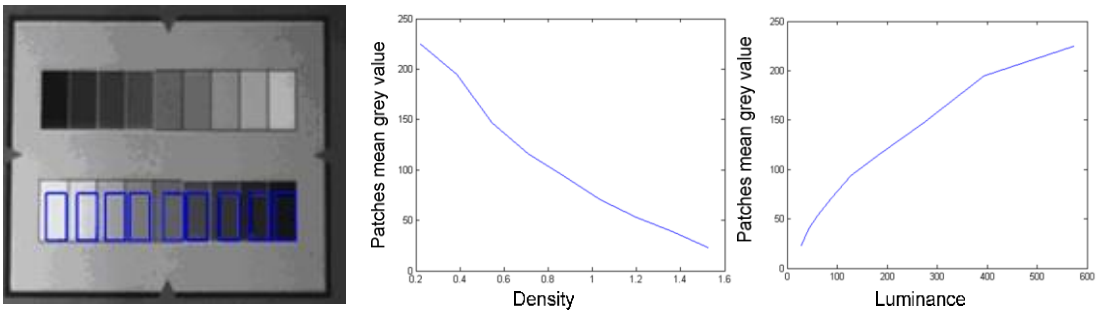

Figure 1: test chart (left), OECF curves (middle and right)

2.2. Noise

Digital image noise arises from basic physics, such as the photon nature of light or the thermal energy of heat. The computation of the electronic noise in a digital imaging system is based on the use of the same test chart as for the OECF computation (densities of 0.872 and 0.222 are used). The standard considers 3 noise types: the total noise σ_{tot}, resulting from all unwanted variations captured by a single exposure, which is decomposed into a fixed pattern σ_{fp} noise and a temporal σ_{temp} noise (both are not correlated). σ_{fp} refers to all unwanted variations which are consistent to every exposure, and σ_{temp} is the random noise due to sensor dark current, photon shot noise, analogue processing and quantization, which varies from one image to the next. The image is therefore characterized by the computation of 3 Signal to Noise Ratio (SNR) (Total SNR, Fixed Pattern SNR, and Temporal SNR), corresponding to the 3 above described noises:

$$SNR_{TOT} = \frac{L_{sat} \times R_x \times Inc_{Gain}}{\sigma_{tot}} \quad SNR_{FP} = \frac{L_{sat} \times R_x \times Inc_{Gain}}{\sigma_{fp}} \quad SNR_{TEMP} = \frac{L_{sat} \times R_x \times Inc_{Gain}}{\sigma_{temp}}$$

- R_x, R_y: reflectance values of the patches densities (e.g. $R_{0.18}$ = 18 % reflectance for a density of 0.9).
- L_{sat}: maximum unclipped level of the camera, (e.g. for an 8-bit camera, $L_{sat} = 2^8-2= 254$).
- Inc_{gain}: incremental gain (OECF first derivative at the point corresponding to patch of density 0.9).

Figure 2 shows the variations of the 3 noise types for different electronic gain values (200 to 700 [4] [5]).

Gain and illuminances	Test chart subimages	Gain and illuminance	Test chart subimages	
200 1.410 lx		500 340 lx		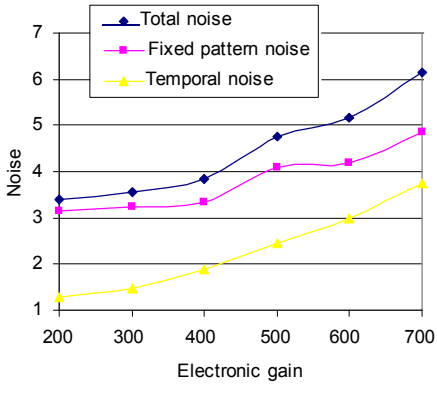
300 1.000 lx		600 250 lx		
400 640 lx		700 95 lx		

Figure 2: images for different gain and illuminance values (left), computed noises (right) (the illuminances were measured with a photometer)

[4] These values correspond to the gain value of the AVT_SmartView software.
[5] The illumination level was decreased so that the white test chart area is depicted with pixel values near the maximum 255 level. The test target was focused and the camera shutter was set to a high value in order to avoid flickering

2.3. Resolution

The resolution of digital images is an indicator of how far certain level of details can be visualized in the camera image. The "traditional" resolution measurements consists of determining the image resolution by observing an image having different bar patterns with different spatial frequencies (expressed in lp/mm or LW/PH). This subjective approach is the first method described by the ISO12233 standard, and is called the visual resolution[6]. This principle however provides a subjective indicator of the resolution (image sharpness), as it is strongly dependent on the observer. The ISO12233 standard proposes 2 further quantitative parameters for measuring the image resolution: the limiting resolution and the Spatial Frequency Response (SFR). These parameters are computed according to the different sub-areas of a specific test chart. Figure 3 shows 2 examples of resolution patterns (an USAF 1951 test chart and a sweep pattern, which is part of the test chart proposed by the ISO12333 standard) and the considered ISO1223 test chart with its different sub-areas.

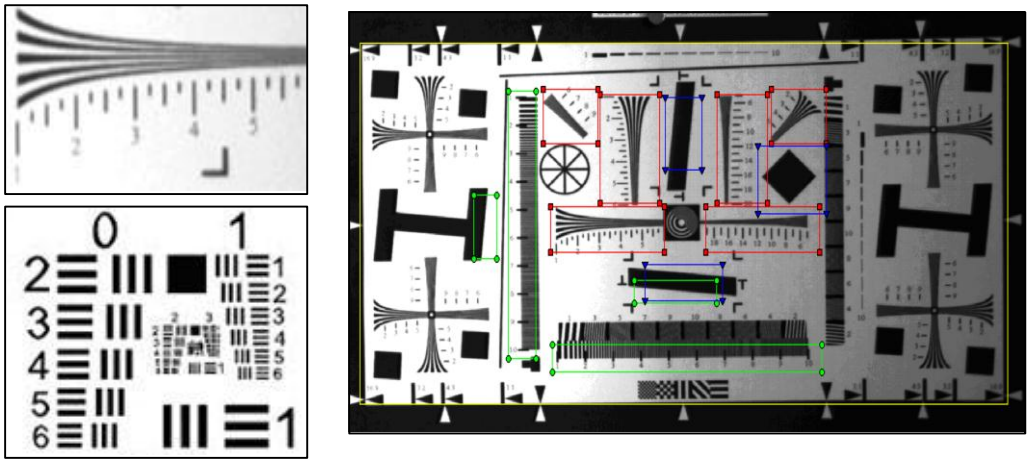

Figure 3: resolution charts examples: sweeps with fiducial marks (top left), USAF1951 (bottom left), and considered test chart for the resolution measurement (right)

2.3.1. Limiting resolution

The limiting resolution is the value in LW/PH of the portion of a black and white resolution wedge where the resolution response equals 5% of the reference response. The resolution response is determined with square wave sweeps having a logarithmic decreasing period (the sweeps include fiducial marks labeled from 1 to 10, corresponding to 100 to 1.000 LW/PH). The resolution response equals the difference of the maxima and the minima of the sweeps divided by their sum. The reference response equals the absolute value of two mean values of black white bars areas. Figure 4 shows the image of fiducial marks, the determination of the maxima and the minima position of the wedge, the resolution response (red decreasing curve) and 5 % the reference response (green horizontal line) (the vertical red line shows the value of the limiting resolution, here 495 LW/PH).

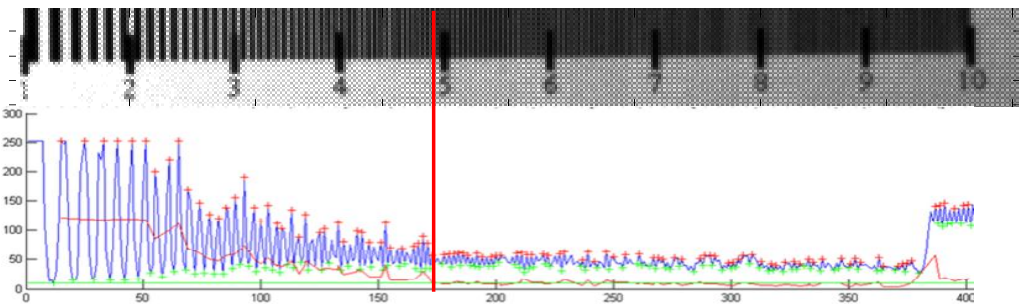

Figure 4: limiting resolution of approximately 495 LW/PH

[6] The image resolution corresponds to the bars frequencies defined by the observer as having "vanishing resolutions", i.e. where the pattern is not visibly distinct.

2.3.2. Spatial Frequency Response

The Spatial Frequency Response (SFR) of a camera is the quantitative evaluation of the way resolution evolves with respect to the spatial frequency of the pattern observed. The implemented SFR algorithm is the slanted edge method proposed in the ISO12233 standard and also described in [1]. The SFR computation procedure is illustrated in Figure 5.

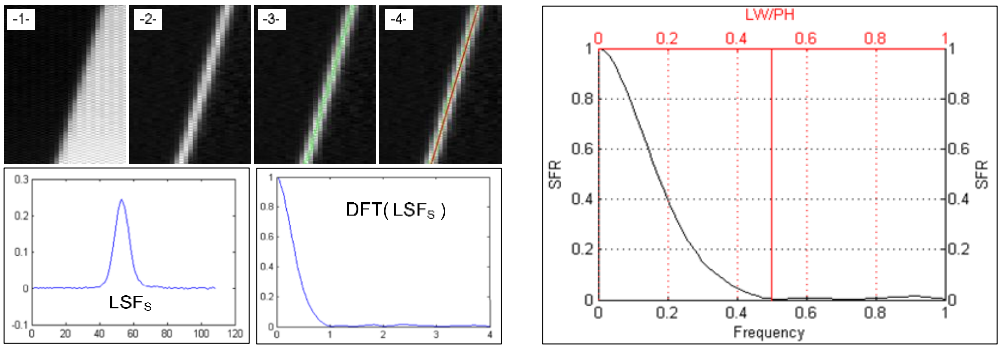

Figure 5 : SFR computation principle

The first step of the method consists of retrieving the Edge Line Function (ELF), by applying a 1D horizontal first derivative filter to the edge image, followed by a local interpolation (center of gravity algorithm). This permits to compute the sub-pixel positions of each centroid of the Edge Spread Functions (ESFs). The ELF is determined by fitting a line through the determined centroids. The second step consists of computing the super-sampled LSF by readjusting each line of the 'edge image' according to the distance to the ELF. The LSF is then multiplied by a Hamming window to reduce the effects of noise at the extremes of the window. The SFR corresponds to the normalized modulus of the Discrete Fourier Transform (DFT) of the super-sampled LSF. The SFR is expressed in the frequency domain with the sampling frequency *fe* and in line width per picture height [LW/PH] [7]. As, the use of a Hamming window permits to limitate the frequency band, the spreader the SFR response, the higher the image resolution. Figure 6 shows 3 SFR curves for the same image with reduction factors of 1:1, 1:2, and 1:3.

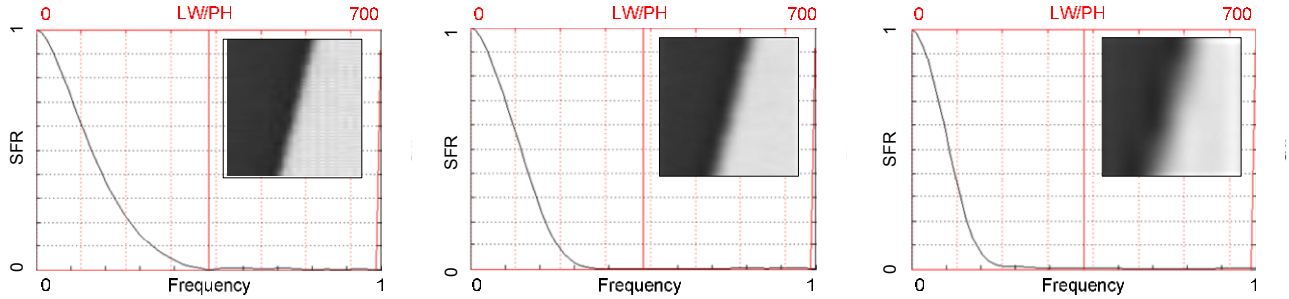

Figure 6: SFR and corresponding edge images examples for different resolutions (the figure shows the relation between the resolution and the area under the SRF curves)

2.4. Distortion

Image distortions arise when the light rays are deviated from their direction by the optics of the vision system. The distortion is the departure from the ideal geometry, and can be described by a position dependant vector with radial and tangential components. The ISO9039 standard which describes the distortion determination algorithm of optical systems deals only with the radial distortion. The distortion is carried out at 14 different horizontal and 14 different vertical reference image points[8] which are fixed pixel positions (they do not correspond to the reference target points).

[7]. The number of line width per picture height equals the number of black and white lines with equal width that can be resolved over the whole height of the image.

The algorithm automatically determines the reference target points (black dot centers) which are used for computing the radial distortion[9]. The reference distortion points used for computing the distortion values are the nearest black dot centers to the targets points. The distortion values are expressed as absolute ($Va = h' - hm$, in millimeter) and a relative ($Vr = 100 \cdot Va / hm$, in image size units) values (m is the system's lateral magnification, approximated by means of central image points, h is the position of the reference points). The final image distortion is expressed for the 14 horizontal and 14 vertical *Va* and *Vr* values computed at the target points. Figure 7 shows the reference grid with the reference image points (green 'o') situated on the horizontal and vertical central image lines, and the computed absolute distortion along the horizontal and vertical lines. For more clarity, only the vertical reference distortion lines (blue) used to measure the distortion of the reference points have been displayed.

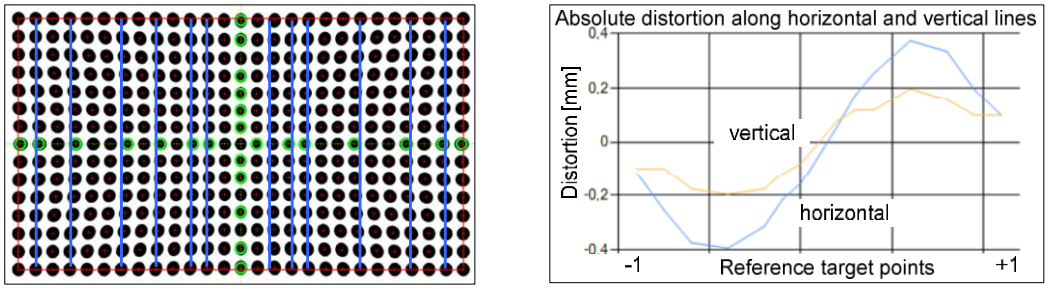

Figure 7: target image with the detected 28 reference target points (huge green 'o') and 14 reference lines (blue) (left), absolute distortion along horizontal and vertical lines (right)

The absolute distortion curves show high distortion values for the points situated at -0.5 and +0.5 *hmax* and lower distortion values for the extreme and central points. This can be also seen in the test chart image by comparing the distance between each green circle and the nearest vertical blue line. The ISO standard on which the distortion quantification algorithm is based does not recommend the computing of further features. However, as the sub-pixel positions of all the black dots are determined, other distortion characteristics could be retrieved if necessary (e.g. the tangential distortion).

2.5. Chromatic aberration

Chromatic aberrations are due to the wavelength dependence of the propagation direction of light rays. Two aberrations are distinguished: the lateral and the longitudinal, whether aberrations are perpendicular or parallel the optical axis. The chromatic aberrations of an optical system, described by the ISO15795 standard, are quantified by the variations of the image distances for different wavelengths or weighted spectral distributions[10]. The position and shape of the depicted Line Spread Function (LSF) for a given wavelength characterizes these light rays deviations synonymous of chromatic aberrations.

Four numbers are used to characterize the chromatic aberration, the Left Edge (*LE*) width, the Right Edge (*RE*) width (changes in the image plane of the LSF shape), the lateral chromatic aberration *T* (change in the image plane of the LSF position), and the longitudinal chromatic aberration *L* (variation along the optical axis of the LSF shape). These four numbers are computed with respect to a reference wavelength or a reference spectral distribution. *L* is computed with respect to a reference plane and for a defined focusing criterion. In the following only the computation of *LE*, *RE*, and *T* are explained.

[8] These points are situated at distances [-1 ; -0.85 ; -0.7 ; -0.5 ; -0.3 ; -0.2 ; -0.1 ; +0.1 ; +0.2 ; +0.3 ; +0.5 ; -0.7 ; -0.85. + 1] x *h'max*, where *h'max* is half the image width or image height if the 14 points are situated along the horizontal or vertical central lines.

[9] A morphological approach combined with an ellipse fitting algorithm permits to determine the sub-pixel dot centers.

[10] Single wavelength values for monochromatic or quasi monochromatic measurements and weighted spectral distributions for finite spectral bandwidth measurements (in the case of a white light and colour sensor e.g.).

The considered reference test chart permits the distortion measurement on 11 horizontal and 11 vertical image directions centered in the middle of the test chart active area[11]. The image height for each point is measured using the position of its LSF. The *LE*, *RE* and T values are retrieved from the ESF (Edge Spread Function), cumulated sum of the LSF. Both LSF and ESF are normalized to 1. The computations of *LE* and *RE* are based on areas above and under the ESF curve: *LE* and *RE* delimitates two equal areas in the intervals [0 : u_m] and [u_m: 0] (u_m is the sub-pixel position of the LSF).

$$LE = 2\int_{-\infty}^{u_m} ESF(u - u_m)du \qquad RE = 2\int_{u_m}^{+\infty} [1 - ESF(u - u_m)]du$$

The LSF, ESF, *RE*, *LE*, T values are computed for each wavelength or wavelength band. All measurements are taken versus a reference wavelength or waveband (for example, the green channel). Figure 8 shows a recorded test chart image (for clarity purposes, only the vertical reference points are depicted), an example of computed *RE*, *LE*, *T* parameters for a vertical line situated in a 20x13 ROI (Region Of Interest) of the test chart image (the red, green and blue components are depicted, a 26x26 lines grid test chart has been recorded with a 4096x3672 color CCD sensor).

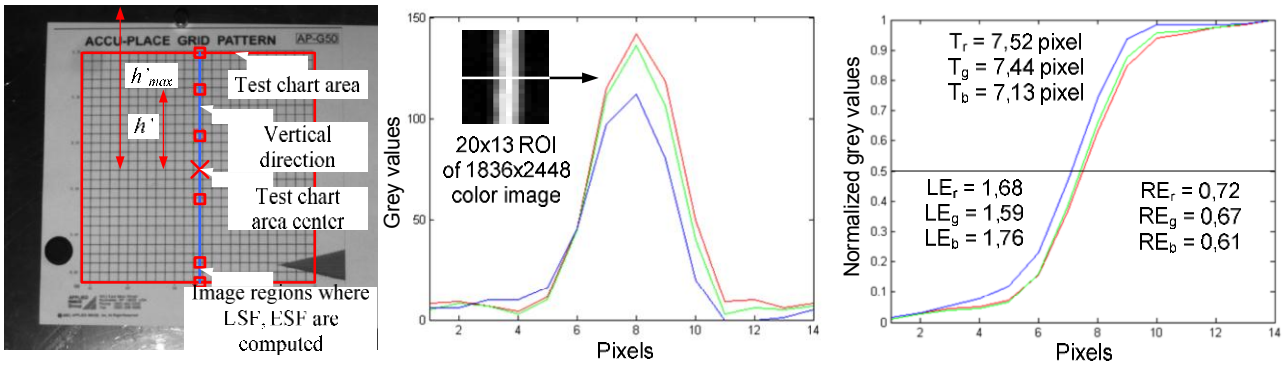

Figure 8: chromatic aberration test chart (25 horizontal and 25 vertical 1 mm distant lines)
LE, *RE* and *T* measurements for a vertical line recorded with a CCD color camera.
LSF (left) and ESF (right) (*LE* and *RE* correspond to the areas below and above the ESF curves)

The effect of chromatic aberration is clearly visible in the position of the cumulated sum functions (right graphic) whereas the raw line profiles (graphic in the middle) do not provide appropriate information. Indeed, the lines maxima are depicted on maximum 2 pixels, which is not enough to clearly define the maximum lateral position. The computed *T* values clearly show that the lateral deviations of the blue rays are high compared to the deviations of the red and of the green ones: T_b-T_g is three times more important than T_r-T_g. As the horizontal lateral resolution is 13 pixels / mm, this means that lateral chromatic aberrations of at least 30 µm (= T_b-T_r) will be observed in the images. Such deviations values might be non negligible in case of 2D measurements task for example.

3. TECHNICAL SOLUTION

In order to meet the requirements defined by the ISO standards, different recommendations have to be followed during the record of the reference test charts. These requirements concern the apparatus (arrangement and position of the different systems components such as the light source or the test chart), the sensor (focus, aperture…), the light source(s) (homogeneity, type…) and the environment (temperature, humidity…). One of the major and final purposes of these image quality quantification algorithms is the

[11] Considering that *h'* is the distance between the center of the image and a point on that image, and that h'_{max} is the half-image height on the dimension considered, the measurements is carried out for the 11 following values of *h'*: [-1 ; -0.85 ; -0.7 ; -0.5 ; -0.3 ; 0 ; +0.3 ; +0.5 ; -0.7 ; -0.85. + 1] x h'_{max}.

qualification of VT systems. However, as each system has its own specificities (components types, systems arrangement…) all the recommendations defined by the standards can not be fulfilled. This is the reason why, different level of importance for the requirements should be considered according to their impact on the image quality measurements.
This is e.g. the case of the light arrangement for the digital image noise measurement. The ISO15739 standard specifies that the angular distribution of influx radiation is at its maximum at 45° to the test chart normal, and is negligible at angles of less than 40° or more than 50° to the normal, at any point on the test chart. The purpose is here to have a light arrangement which provides a homogenous and bright lighting, but also to avoid the direct reflection of the light source in the sensor which would disturb the noise measurement. If these kinds of requirements can not be fulfilled for a specific system, their real impact on the measurement should be determined. In case of a high impact, an alternative recording method or data processing technique should be implemented.
Currently, the image quality quantification algorithms were developed as a dynamic linked library (dll) and implemented in a C++ application. This application permits the retrieval of the 5 different groups of image parameters previously described (OECF, noise, resolution, distortion, chromatic aberration). The interface permits to visualize the images of the tests charts and regions of interests, to load and change the parameters, and to visualize the algorithm outputs in terms of text and graphic.

4. APPLICATION EXAMPLES

4.1. Use of the developed application for other test charts

The following example shows the generic aspect of the developed technical solution, i.e. its ability to be used or adapted with slight improvements to existing VT visual check procedures[12]. A specific test chart is used for the preliminary visual check of VT examination systems developed by AREVA GmbH. This chart encompasses all the necessary features to compute different VT system characteristics, such as the color resolution, the spatial resolution, the digital noise and the geometric distortion. The test chart and the computed OECF graphic with the developed application are depicted in Figure 9.

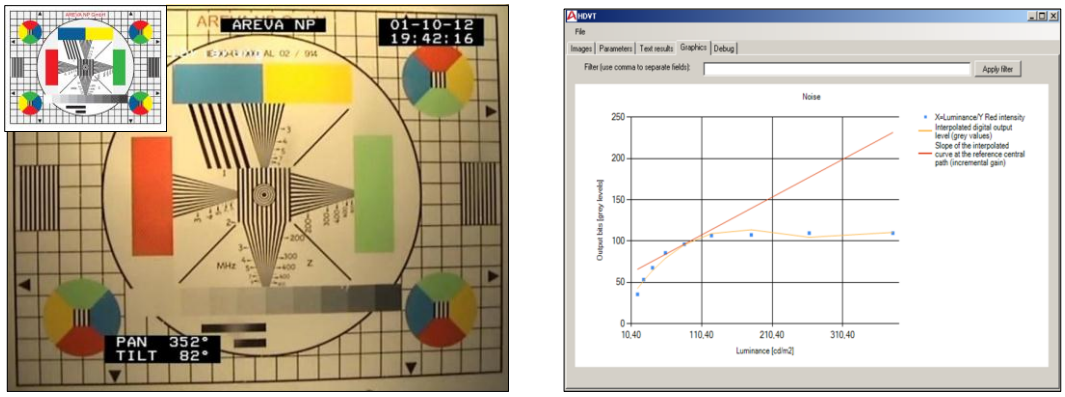

Figure 9: AREVA GmbH test chart for the visual check (left), computed OECF (right)

In the same manner, the developed image quality application can also be used to quantify the image noise and the image resolution. The computation of the optical distortion would necessitate slight changes of the developed application (in that case other features, such as the sub-pixel determination of the cruxes center should be implemented).

[12] The visual check is done according to the DIN 25435-4 standard in this example

4.2. Use of the developed framework for other applications

For AREVA Inc, the remote resolution measurement consists of demonstrating that characters are resolved according to the visual examination specifications. These specify that when the test chart is illuminated with a certain light intensity (expressed in lx) and placed at a certain distance from the camera, the lower case characters can be read. The operator records the same test chart at different distances. The resolution limit corresponds to the distance for which the lower case letters can not be distinguished[13]. Figure 10 shows the SFR for 2 images of the upper case letters recorded at 2 different distances (2 different resolutions 1:1 and 1:2) in case of the resolution test chart of AREVA Inc (this chart is used for the VT of US boilers and pressure vessels). The figure shows the relation between the distance and the resolution using the SFR, which permits to have an objective image quality value.

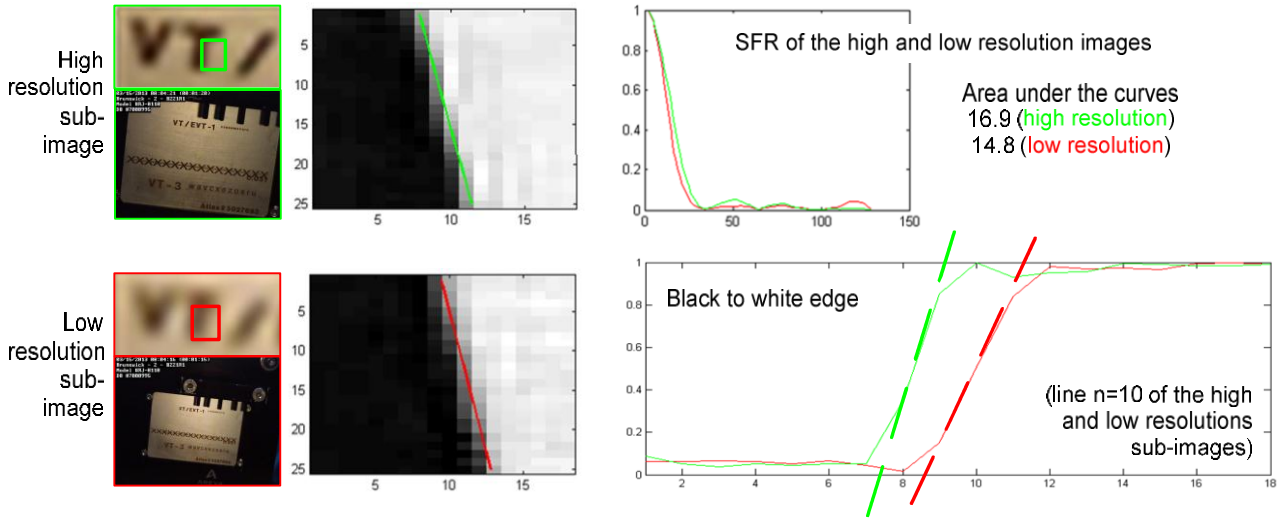

Figure 10: example of resolution measurement by means of the SFR on the test chart of AREVA Inc.

The developed application permits to compute other characteristic than the resolution. Figure 8 shows the computation of the chromatic aberration for a sub image of the AREVA Inc resolution test chart.

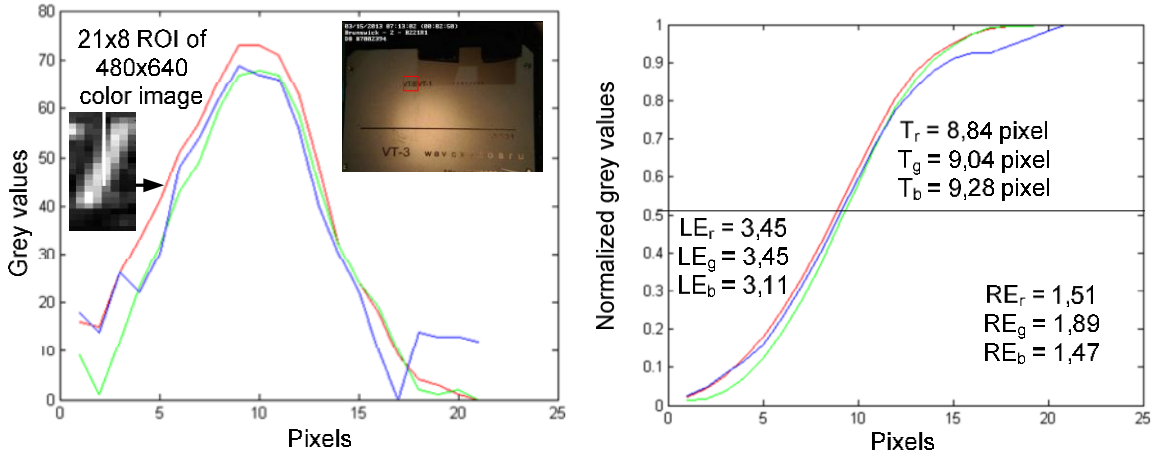

Figure 11: quantification of chromatic aberrations with the AREVA Inc. resolution test chart

[13] For France the procedure consists of verifying that it is possible to count the 3 vertical and 3 horizontal lines of a certain group - element couple of the USAF test chart.

4.3. Possible evolution of the developed algorithm

For AREVA France, specific qualification procedures have been defined for each VT examination of 900MW, 1.300MW, N4 reactors, and EPR vessels and nozzles. The qualification relies on the visual checking of the image quality and the size of the object field for different working distances and zoom values. The visual check concerns the resolution, the color and monochrome resolving powers, and the image geometrical distortions. The image quality verification is done by a qualified operator, who uses test charts reference recordings (in case of the colour check e.g.) or directly interprets the recorded test charts images (in case of the resolution check with the USAF test chart or a specific test chart), see Figure 12.

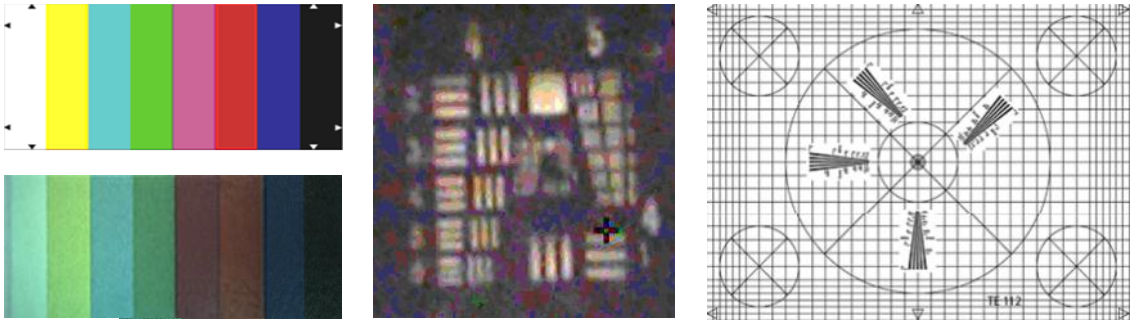

Figure 12: visual check test charts examples of AREVA France VT systems. Reference and recorded color test chart (left), recorded USAF 1951 test chart (middle) and specific ‘all in one’ test chart (right)

The image quality quantification tasks exemplified by Figure 12 could be easily integrated in the application.

5. CONCLUSION

This paper presented an application for the image quality quantification which can improve the qualification process of remote VT systems. Such an automatic quantification procedure is all the more important in case of diagnostics relative to surface defects characterization or structure dimensioning based on VT techniques.

These proposed image quality quantification approaches were defined according to the actual needs and applications within the AREVA group. The main contribution consisted in adapting the standards in order to define dedicated algorithms for image quality quantification and to integrate them in a standalone application. It has been shown how the developed methods permit to characterize the images of different test charts.

These methods can also take into consideration more specific needs. Paragraph 4 describes how the developed algorithms can be applied to quantify test chart images of AREVA France, AREVA Inc and AREVA GmbH in order to improve the actual qualification procedures. Next software developments could consist of integrating post-processing approaches to provide enhanced images to the operator: e.g. the image noise value would provide inputs for contrast enhancement approaches. Indeed, the noise value is directly related to the upper threshold of the noise reduction level to be applied to the image in order to increase the SNR and improve the image quality.

6. REFERENCES

[1] ISO14524, Photography - Electronic still-picture cameras - Methods for measuring OECFs. [2] ISO15739, Photography - Electronic still-picture imaging - Noise measurements.

[3] ISO12233, Photography - Electronic still-picture cameras – Resolution measurements.

[4] ISO9039, Optics and photonics - Quality evaluation of optical systems - Determination of distortion.

[5] ISO15795, Optics and optical instruments - Quality evaluation of optical systems - Assessing the image quality degradation due to chromatic aberrations.

[6] D.R. Williams, "Benchmarking of the ISO12233 slanted-edge spatial frequency response”. Proceeding of PICS, May 17-20, 1998.

INSPECTION QUALIFICATION II

QUALIFICATION OF INVESSEL VISUAL EXAMINATION FOR KERNKRAFTWERK LEIBSTADT (KKL) AND KERNKRAFTWERK (KKM) MÜHLEBERG PLANTS

J. Lindberg, EPRI, USA
R. Schwammberger, Kernkraftwerk Leibstadt, Switzerland
P. Graedel, BKW FMB Energie, Switzerland

BACKGROUND

In 2008, Swiss regulators implemented a requirement that all safety related inspections at nuclear power plants must be performed using qualified personnel and procedures. Prior to 2008, several inspection techniques were demonstrated on open mockups and personnel were not required to be qualified to perform data analysis. In 2009, a qualification project was started in support of the Kernkraftwerk Leibstadt AG (KKL) and Kernkraftwerk Mühleberg (KKM) In-Vessel Visual Inspection (IVVI) programs to detect stress corrosion cracking (SCC) using visual inspection techniques. To meet the regulation, KKL and KKM plant personnel initiated and coordinated a complex project to work with the Swiss qualification body, QSt; KKL and KKM's inspection vendor, GE-Hitachi; and the Electric Power Research Institute (EPRI) for qualification technical support.

The scope of this project was to develop and implement a qualification program as described by guideline HSK-B07[1], where the Swiss Federal Nuclear Safety Inspectorate, ENSI, requires all in-service inspection (ISI) to be performed by means of qualified inspection systems (procedure, equipment, and personnel). In compliance with ENSI, all IVVIs for detection of structurally significant cracking on reactor pressure vessel (RPV) internals shall be performed solely with qualified inspection systems, procedures, and personnel beginning with the 2011 outage. The 2011 outage time requirement was later revised to 2012.

QUALIFICATION REQUIREMENT AND SCOPE

The Swiss ENSI-B07 guideline requires all inservice inspection (ISI) to be perfromed by means of qualified inspection systems, which includes procedures, equipment and personnel. In Switzerland, every NDE qualification project is assessed by the Qualification Body (QB) consisting of representatives from the Swiss Association of Technical Inspection (SVTI/ASIT).

According to the qualification requirements, the qualification will ensure that the IVVI to be performed provide reliable and reproducible results that allows comparison with past and future inspections. The qualification process included "VT-1" visual examinations as referred in Swiss regulatory document, SVTI - Festlegung NE-14. Revision 6 [2]; and enhanced visual examination, EVT-1, as referred in the Boiling Water Reactor Vessel and Internals Project, BWRVIP-03, "Reactor Pressure Vessel and Internals Examination Guidelines", EPRI Report TR-105696, dated October 1995[3]. The overall scope of qualification included the following elements: the Invessel Visual Inspection (IVVI) procedures and related techniques, all remote visual examination equipment – underwater camera systems, and examination personnel – all Level II and Level III visual examiners.

The goal of qualifying IVVI is to detect flaws that have potential to affect public safety or the integrity of the component and are considered significant. IVVI should be focused on reliably detecting significant flaws rather than all possible flaws. Intergranular stress corrosion cracking (IGSCC) is considered the predominant damage mechanism in reactor internals (austenitic) components and this is the defect type selected for the qualification.

The qualification flaw was selected as a stress corrosion cracking (SCC) type defect with a crack opening dimension (COD) of 30 µm (microns) and a length of 25mm (0.984 inches). The 30 µm COD target was based on the median value for IGSCC taken from SKI report 2006:24[4], and remote visual examination testing results taken from a U.S. Nuclear Regulatory Commission report, NUREG 6943 [5]. The 25 mm long flaw was based on the minimum flaw length allowed per reactor internals flaw handbooks. The flaw detection capability for this target flaw and size were proven through parametric studies and verified via the successful qualification results.

TEST SPECIMEN DESIGN AND FABRICATION

Remote visual examination (RVT) test specimens had to be designed and fabricated to support the IVVI qualification project. Using recent research in RVT flaw fabrication, and their expertise in test specimen fabrication; EPRI designed and fabricated test specimens for parametric and qualification testing. In addition, they developed and issued the Technical Justification (TJ) for the KKL/KKM remote visual qualification test specimens, that was approved by QSt for the qualification program.

The test specimen fabrication process was a complex process that was implemented under ERPI's Test Specimen Fabrication Quality program; consisting of the following steps:

1. Design of flaws and test specimens; including qualification defect sizes, materials, surface finish/texture, color, and surface features, such as grinding marks, scratches, other anomalies.
2. Fabrication of the blank stainless steel and ceramic test specimens.
3. Laser micromachining of the surface of the test specimens to simulate SCC type flaws.
4. Addition of surface features, such as grinding marks, and scratches
5. Fingerprinting of the test specimens using metallurgical microscopy.
6. Completion of the test specimen fabrication documentation packages.
7. Development, issuance and approval of the Technical Justification for use of the test specimens for the KKL/KKM IVVI Qualification program.

The TJ identifies the essential parameters and shows that the test specimens have sound technical basis and are suitable for the planned qualification including parametric studies. The TJ validates that the test specimens, as designed, fabricated and described in TJ satisfy the procedure and personnel qualification based on a minimum targeted simulated SCC 0.98 inch (25 mm) in length and a crack opening dimension (COD) of 30 microns.

Justification was provided for the use of qualification specimens using flat plate fabricated from both 304 stainless steel and colored ceramic plates to represent both the original metallic and colored (oxidized surface) component conditions. The test specimens contained both weld crowns and a ground flush surface and were populated with non-flaw features such as tooling marks, grinding marks, and weld undercut.

The flaw production method used a laser micromachining process where light energy is used to machine narrow grooves in the surface of the material to simulate surface cracks with varying COD. The images in Figure 1 show that the laser machining technique is capable of simulating some characteristics associated with SCC.

a)

b)

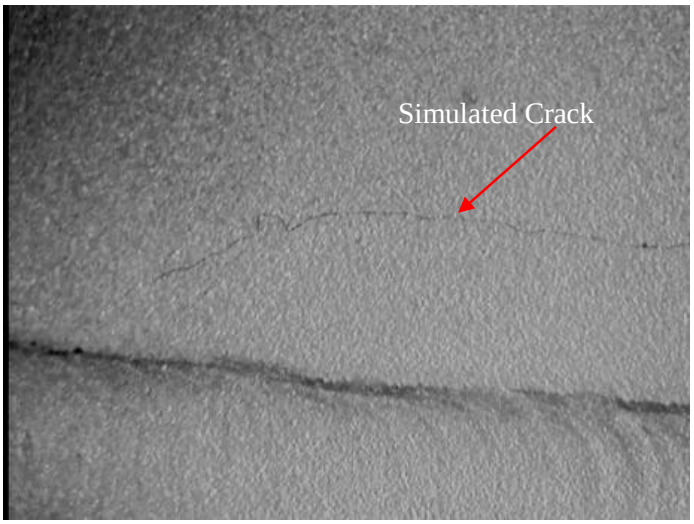

Figure 1 - Photographs of a Core Shroud Crack at KKM (a) and a Similar Simulated Crack on an EPRI Sample Viewed through Remote IVVI Inspection System with Sample Immersed in Water (b)

Additional discussion in the TJ addressed the conservative approach of specimen design as it relates to reactor component stress corrosion cracks. The purpose of this discussion was to document that the intent of specimen design was to provide a robust test of inspection capabilities. The methods used for the fabrication of test specimens that are described in detail in the TJ resulted in the production of specimens that have an appearance that closely simulates color, texture, surface features (weld crown, grinding marks, scratches, and weld undercut), and crack morphology of the actual components and SCC type flaws.

QUALFICATION PLAN

At the beginning of this qualification project it was recognized this project was a complex mission. There were several organizations and personnel with varying responsibilities, many first-of-a-kind and interrelated tasks, and a hard date for the successful completion of the qualification. A detailed project plan and schedule was prepared, reviewed, and approved by the project team. Because personnel and organizations were functioning separately and across the ocean; weekly telephone calls were implemented, detailed action item lists were maintained, and periodic face-to face meetings in Switzerland were held to drive progress and accountability to the project plan and schedule. The plan and schedule was discussed and revised on a frequent basis to update progress, address arising issues, and develop recovery plans, as needed. The main qualification program activities were as follows:

- Test specimen design, fabrication and fingerprinting – Lead by EPRI, Charlotte, NC
    - Development and issuance of test specimen technical justification – EPRI
    - Performed in parallel with most of the other key activities
- IVVI Procedural development and parametric studies – Lead by GE-Hitachi, Wilmington, NC
- Guided Practice to test procedure parameter and qualification methodology – GE-Hitachi , San Jose; QSt, KKL/KKM and EPRI personnel
- Procedure refinements, additional parametric studies – Lead by GE-Hitachi, Wilmington, NC
    - Development, review, and issuance of equipment and procedure technical justifications
- Finalize and issue IVVI procedure/techniques
    - Development, review, and issuance of final equipment and procedure technical justifications
- Finalize and issue IVVI Qualification methodology protocol – Lead by QSt, EPRI – technical support
- Implement qualifications – procedure and personnel – Performed at EPRI – Charlotte; Lead by QSt, EPRI – technical and qualification support, KKL/KKM support, GE-Hitachi

The qualification program took about two and a half years from beginning through the successful completion of the personnel qualification. The bulletized list of activities above oversimplifies the intricacies and challenges encountered in the implementation of the overall program. Each of the above activities was multi-faceted and interrelated, and required constant coordination. For example, test specimen fabrication activities were being performed in parallel with procedural development and refinement, parametric studies, preparation of technical justifications, and the development of the final qualification protocol. Periodically, test specimens were released to support parametric studies, prior to final approval of the test specimen technical justification. Also, there were challenges with resources. The inspection vendor encountered resource limitations during refueling outage seasons. While these interruptions were taken into account in the schedule; stopping and restarting vendor tasks caused schedule inefficiencies and apprehension with maintaining the schedule and goals. Ultimately, the teams' perseverance in meeting the schedule and achieving the goal resulted in success.

EXAMINATION TECHNIQUES

Standard distance based IVVI examination techniques were utilized during the first phase of the parametric studies to determine the effective limits for flaw detection. Surface illumination, lens-to-object distance and camera angle to the surface were significant factors to demonstrate repeatable examination results. The consequences of distance based examinations were realized when 3D models were developed based on the qualified distance. Many components had restricted access due to various configurations of piping and brackets.

During the 2nd phase of the parametric study, a "field-of-view" (FoV) examination technique was developed by GE-Hitachi. This technique allowed the use of camera's optical zoom to essentially duplicate the field-of-view obtained during the distance based calibration. With the use of the FoV technique, examiners were allowed to increase the lens-to-object distance up to 400 mm for improved access. The combination of the two techniques increases the examination coverage for many components that have configuration limitations.

QUALIFCATION METHODOLOGY

A critical element in the qualification process is the development and issuance of the qualification methodology or qualification protocol. In this case, the responsibility for the qualification protocol was with the qualification agency, QSt; with input from KKL/KKM and EPRI. Since the remote visual examination was a first-of-a-kind qualification for Switzerland there were a lot of technical challenges to address and resolve before a protocol document could be produced. Often, there were more questions and opinions than definitive answers. Questions like the use of live data versus recorded data for qualification; recording criteria, false call criteria, were discussed often and finally resolved. While certain aspects of the qualification process were well established, the options for implementing the actual qualification testing were flexible to some degree. The use of guided practice/trial qualification was an important activity in addressing many of the qualification implementation and protocol questions and challenges.

The guided practice was performed at GE-Hitachi's BWR test facility in San Jose, CA. The intent of this activity was to exercise the current version of the IVV procedure under simulated qualification test conditions, to assess readiness and procedure adequacy and evaluate the qualification testing methodology. The guided practice was very beneficial; as it was determined that additional parametric studies were needed to support the procedure technical justification, and aided in finalizing the qualification test protocol. The result was improved examination techniques and IVVI procedure; an implementable testing methodology, and finally an approved qualification protocol.

QUALIFICATION

Following the guided practice, it was decided to perform the procedure and personnel qualification testing at EPRI qualification test facilities in Charlotte, NC. EPRI had recently built a remote visual examination test tank and scanner, which was set-up in a light controlled and secure test area (See figure 2). QSt personnel had overall responsibility for conducting, monitoring, and grading the procedure and personnel qualification testing. EPRI provided technical support during the testing, and assisted in preparation and transfer of the test specimens in and out of the test area. KKL/KKM witnessed portions of the procedure and personnel testing.

The procedure qualification activity was performed in January and February 2012. This testing was performed in a blind manner, using live data; and exercised all examination techniques and camera systems. At the end of this testing, the IVVI procedure, with all techniques and camera systems, and four examination personnel were successfully qualified. Due to resource constraints to support spring outages, the personnel qualification testing started in late April 2012 and was completed by mid-May 2012. The personnel qualification was a more challenging task that the procedure qualification, because a total of 28 qualified visual examiners were needed to support the upcoming KKL/KKM IVVI workscopes. A two shift operation was established for the qualification. In addition, inspection vendor personnel (qualification candidates) were scheduled to complete procedure indoctrination training for two days prior to performing qualification testing. The personnel qualification testing was performed in a blind manner, using live data; and the candidate had to successfully demonstrate proficiency of 10 techniques from the procedure using both a color and black and white camera systems. Twenty eight examination personnel (Level II and III) were successfully qualified during personnel qualifications.

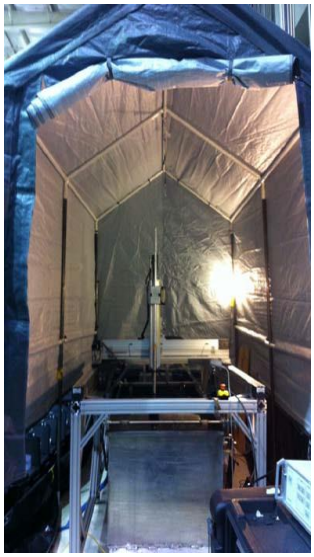

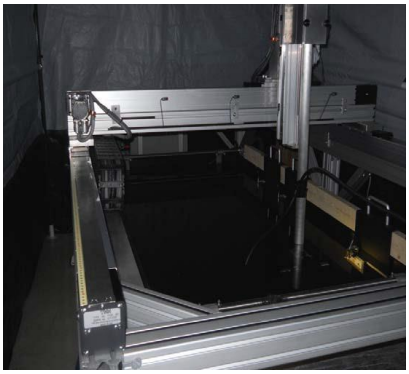

Figure 2 Photo (top left) shows remote visual examination test tank and scanner in secure test area; photo (bottom) shows close up of scanner with test specimen mounted on right side of scannner; photo (right) shows controlled area for examination personnel and test monitors

LESSONS LEARNED

This qualification was a challenging and complex task that resulted in the successful qualification of an IVVI procedure, three camera systems, and twenty eight remote visual examination personnel. The project took over two and half years to complete, and required a high level of management, coordination, technical support, and attention to detail. The following in a synopsis of key lessons learned that came out of this project:

- Do not underestimate the scope and complexity of qualifying remote visual examination
- Development of credible test samples with field representative surface color, texture, and realistic flaws (size, contrast etc) is complex and can be improved in the future
- Take your time with all involved parties to set ambitious, but realistic goals
- Do not rush the design of experiment for the Parametric study, because it may result in a lot of unnecessary work
- Camera handling with poles/ropes provides a lot of flexibility, but has its inherent limitations, which are difficult to simulate in a qualification
- Communication and teamwork is paramount to success; listen carefully to each other's deviating opinions before defending your own opinion

SUMMARY

This complex and challenging remote visual examination qualification program consisted of planning and implementing a multifaceted, multi-year plan that involved several global orgnaizations. The project included the simulataneous development of qualification acceptance criteria and test protocol; design, fabrication and technical justification of remote visual examination test specimens; and the performance of parametric studies and testing to develop and refine the examination procedure and determine capabilities of equipment. The culmination of the program was the implementation and successful qualification of examination procedure and associated techniques, equipment (3 camera systems), and 28 Level II and III visual examination personnel. More importanly, the qualfied procedure, equipment and personnel were succesfully implemented during KKL and KKM's 2012 outages with noted improved quality over previous examinations.

REFERENCES

[1] HSK-B07(ENSI-B07), „Sicherheitstechnisch klassierte Behälter und Rohrleitungen: Qualifizierung der zerstörungsfreien Prüfungen", September 2008

[2] Swiss regulatory document, SVTI - Festlegung NE-14. Revision 6, Dated January 01, 2005

[3] Boiling Water Reactor Vessel and Internals Project, BWRVIP-03, "Reactor Pressure Vessel and Internals Examination Guidelines", EPRI Report TR-105696, dated October 1995[2].

[4] Swedish Nuclear Power Inspectorate. Crack Characterization for In-Service Inspection Planning, SKI Report 2006:24, Stockholm, Sweden. May 2006.

[5] U.S. Nuclear Regulatory Commission. A Study of Remote Visual Methods to Detect Cracking in Reactor Components, Pacific Northwest National Laboratory. NUREG/CR-6943. Washington, D.C. 2004.

QUALIFICATION OF ULTRASONIC AND EDDY CURRENT TECHNIQUES TO EXAMINE THE CRDH (CONTROL ROD DRIVE HOUSING) OF A SWISS NPP

F. Fernández, P. Gómez, A. García, J. Sánchez
Tecnatom, Spain

ABSTRACT

Tecnatom have inspected in different ways the CRDH of some BWR vessels along the time. The different inspection techniques have depended on both the required examination volume and the postulated flaws. Also, considering the possible access to the component, several mechanical and data acquisition devices with different characteristics have been developed.

Tecnatom have been required by a Swiss NPP to develop and qualify an Inspection System to examine the CRDH of this plant. The techniques and equipment developed must meet the requirements of the Swiss Regulator Qualification Guideline B07 for the ISI and as a proactive action it must also meet the requirements of Code Case N-730.

To solve these inspections (detection and sizing of flaws), Tecnatom have developed an ultrasonic procedure (combining pulse-echo and TOFD techniques) and an eddy current procedure. Two new probe-holders have been manufactured, and several modifications have been made on the previous scanner and the data acquisition devices.

This paper describes the techniques developed and the equipment used for inspecting the CRDH.

INTRODUCTION

Tecnatom has been requested by a Swiss Nuclear Power Plant to carry out non-destructive testing on its Control Rod Drive Housings. The objective of these tests is to perform early detection and measurement (in depth and length) of the postulated imperfections, mainly intergranular stress corrosion cracking (IGSCC). The examinations are accomplished from the inside of the drive housing. Access to the component is from the lower part of the reactor vessel (BWR type).

Four different examination volumes, with different flaw morphologies and specifications, are to be considered in order to fulfil the qualification requirements.

Firstly, the examination volumes to be inspected in accordance with the in-service inspection (ISI) programme are the area adjacent to the J weld and the flange to pipe weld (see Figure 1 and Figure 2).

Examination volume 1. J-Groove according to ISI-programme	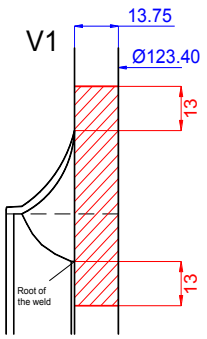
Flaw area. HAZ on the pipe side (parallel to coupling surface). OD connected. Skew: n.a. Tilt: 90° ± 10°	
Qualification flaw size (depth x length): 5.0mm x 20.0mm	

Figure 1. Examination volume (shaded areas) and flaw specification of V1

Examination volume 3. Flange to pipe according to ISI-programme	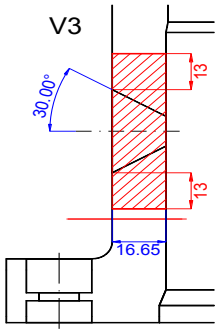
Flaw area. Axial and circumferential flaws. ID and OD connected. Skew: 0. Tilt: 0° ± 45°	
Qualification flaw size (depth x length): 2.0mm x 6.0mm	

Figure 2. Examination volume (shaded areas) and flaw specification of V3

According to Code Case N-730, the mechanical roll expansion technique may be used as a repair / replacement activity to eliminate leakage. Prior to and after roll expansion, the rolled region and the area of the housing adjacent to the J weld shall be examined (see Figure 3 and Figure 4).

Examination volume 2. Roll-repair according to Code Case N-730	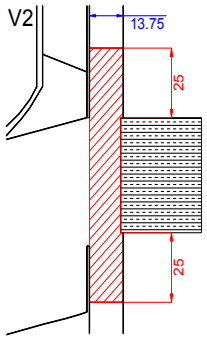
Flaw area. Axial and circumferential flaws. ID and OD connected . Skew: 0°. Tilt: 0° ± 10°	
Qualification flaw size (depth x length): 0.7mm x 4.2mm	

Figure 3. Examination volume (shaded areas) and flaw specification of V2

Examination volume 4. J-groove according to Code Case N-730	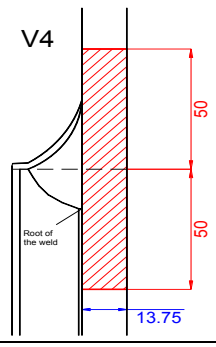
Flaw area. Axial and circumferential flaws. ID and OD connected. Skew: 0°. Tilt: 0° ± 10°	
Qualification flaw size (depth x length): 1.6mm x 10.0mm	

Figure 4. Examination volume (shaded areas) and flaw specification of V4

DEVELOPMENT OF TECHNIQUES

With a view to identifying the best combination of methods and techniques for examination of the CRDH areas, a test plan was drawn up with different ultrasonic and eddy current sensors. Three teams carried out the ultrasonic and eddy current techniques in parallel.

The first team performed the tasks required to cover the complete scope of the inspection (detection and measurement of flaws in the four examination volumes) using the ultrasonic method and pulse-echo technique. Ten different types of probes were evaluated and four were finally selected for performance of the following functions:

- Examination volume 1. Detection and measurement of flaws.
- Examination volumes 2, 3 and 4. Detection of all circumferential and axial defects open onto the outer diameter.
- Examination volume 3. Measurement in depth and length of flaws onto the outer diameter and measurement in depth only of circumferential flaws open onto the inner diameter. In this volume the presence of the weld means that the TOFD technique does not give good results in the measurement of these defects.

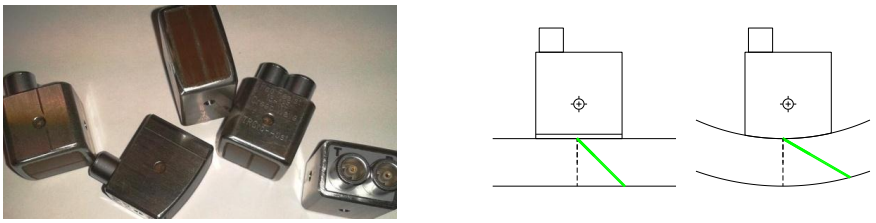

Figure 5. Ultrasonic probes. Pulse-echo technique.

The second team performed the tasks required to cover the complete scope of the inspection (detection and measurement of flaws in volumes 2, 3 and 4) using the ultrasonic method and the TOFD technique. Different models of TOFD probes were designed, with each new design enhancing the mechanical and acoustic characteristics of the previous model. Finally, three TOFD probes were selected for performance of the following functions:

- Examination volumes 2, 3 and 4. Measurement in depth and length of all the circumferential and axial flaws open onto the outer diameter, with the exception of the circumferential defects in volume 3, which were measured using the pulse-echo technique.
- Examination volumes 2, 3 and 4. Measurement in depth of all the circumferential and axial flaws open onto the inner diameter, once again with the exception of the circumferential defects in volume 3, which were measured using the pulse-echo technique.

Figure 6. Ultrasonic probes. TOFD technique

Finally, a third team performed the tasks required to develop the eddy current technique for the detection and measurement in length of flaws open onto the inner diameter of the housing. A plus-point type coil was selected to minimise lift-off and geometric variations, as well as to guarantee the detection of axial and circumferential defects. This technique was selected for performance of the following functions:

- Examination volumes 2, 3 and 4. Detection of all circumferential and axial flaws open onto the inner diameter.
- Measurement in length of the aforementioned flaws.

The techniques were verified on several test pieces with the same geometric characteristics, materials and manufacturing process as the actual CRDH's. These test pieces contain flaws representative of those postulated for each of the examination volumes.

Figure 7. Example of test pieces

MECHANICAL SCANNER AND PROBE-HOLDERS

The inspection is performed using the TEMIS-II mechanical equipment, developed by Tecnatom. This equipment is made up of a telescopic arm, on which are mounted two probe-holding modules. The reason for the mechanical equipment having two modules is the difference between the elevations of the examination volumes close to the J weld (V1, V2 and V4) and the flange-pipe weld (V3).

These probe-holding modules, upper and lower, are the supports on which the sensors are installed (ultrasonic and eddy current). The probe-holding modules are fitted with mechanisms that ensure the correct positioning of the sensors during the movement of the modules across the inner wall of the housing. In order to guarantee permanent coupling of the probes and coils, the modules are fitted with pneumatic devices that push the sensors against the wall of the housing.

The inspection is performed with a single insertion of the machine in the CRDH. All the ultrasonic and eddy current data necessary for the detection and measurement of the flaws are acquired in a single raster scan. Figure 8 shows a reconstruction of the TEMIS-II equipment with the arm deployed for performance of the inspection.

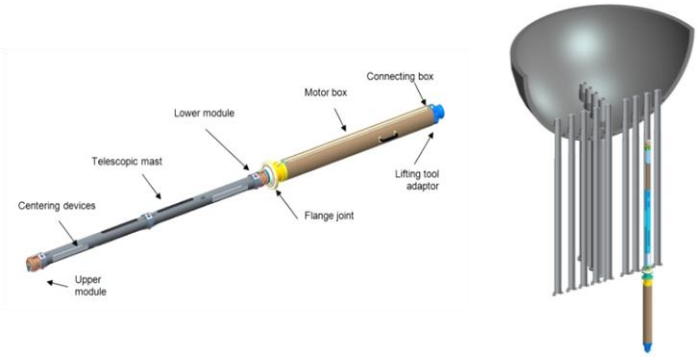

Figure 8. TEMIS-II inspection tool

INSPECTION SYSTEM

The ultrasonic data acquisition system is SUMIAD-F1 COMPACT. The emission and reception pulses are installed in two FPR-8 modules, connected to the SUMIAD-F1 COMPACT equipment by means of optical fibre. These two modules are located close to the probes in order to guarantee the quality of the ultrasonic signal. The eddy current data acquisition device is TEDDY+ A.

Figure 9. SUMIAD-F1 & TEDDY+ A

The ultrasonic data analysis software is InspectView. InspectView covers all the functionalities required to cover the inspection process: configuration of the inspection, calibration of the probes, acquisition of the ultrasonic data, and analysis of these data. This software is installed on a portable computer, which communicates with SUMIAD-F1 COMPACT via an Ethernet cable.

The eddy current data acquisition and analysis software is TEDDY-GEN. This software covers all the functions required by the inspection, such as configuration of the acquisition equipment, calibration of the coil and acquisition and analysis of the eddy current data.

The inspection system is described in Figure 10.

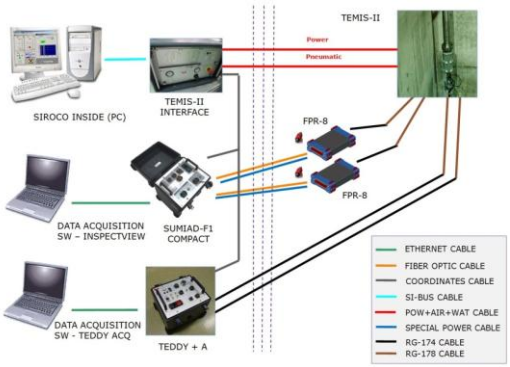

Figure 10. Scheme for connecting the sensors (UT & ET)

ULTRASONIC AND EDDY CURRENT TECHNIQUES

NDT TECHNIQUES

J-groove according to ISI-program (examination volume 1)

The flaws postulated in this examination volume are intergranular stress corrosion cracks (IGSCC) along the HAZ of the J-Groove weld initiated from the fluid connected side of the CRDH housing.

The detection of flaws in this examination volume is accomplished using the pulse-echo ultrasonic technique. The probe finally selected for the detection and measurement of these flaws is a bicrystal focussed 0° probe.

Table 1. Method and technique for examination volume 1. Upper probe-holder module

Volume	Connected to / orientation	Detection	Sizing	
			Length	Length
V1	-	UT (P-E)	UT (P-E)	UT (P-E)

Figure 11 shows the acquisition performed on one of the test pieces using the selected probe.

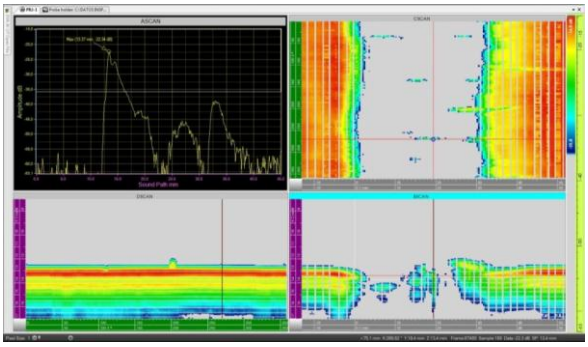

Figure 11. Example of UT acquisition on V1 test piece

Flange to pipe according to ISI-programme (examination volume 3)

The flaws mainly postulated in this examination volume are intergranular stress corrosion cracks (IGSCC) located along the heat affected zone of the weld. These flaws may have an inclination of ±45° due to the preparation of the weld edges.

The ultrasonic techniques that may be used in this examination volume are conditioned by the weld itself. Thus, certain circumferential flaws may be detected and measured only from one single side of the weld using the pulse-echo technique, while the detection and measurement of these same flaws using the TOFD technique has proven not to be possible.

The methods and techniques finally selected for the inspection of this examination volume are summarised in Table 2.

Table 2. Method and technique for examination volume 3. Lower probe-holder module

Volume	Connected to / orientation		Detection	Sizing	
				Height	Length
V3	OD	Circumferential	UT (P-E)	UT (P-E)	UT (P-E)
	OD	Axial	UT (P-E)	UT (TOFD)	UT (TOFD)
	ID	Circumferential	ET	UT (P-E)	ET
	ID	Axial	ET	UT (TOFD)	ET

By way of an example, the ultrasonic (Figure 12) and eddy current (Figure 13) data acquired from one of the test pieces corresponding to this examination volume have been represented.

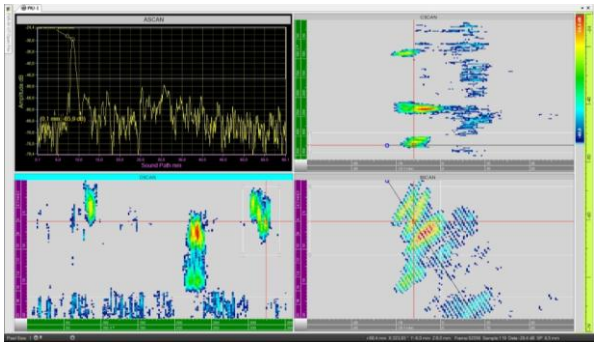

Figure 12. Example of UT acquisition on V3 test piece

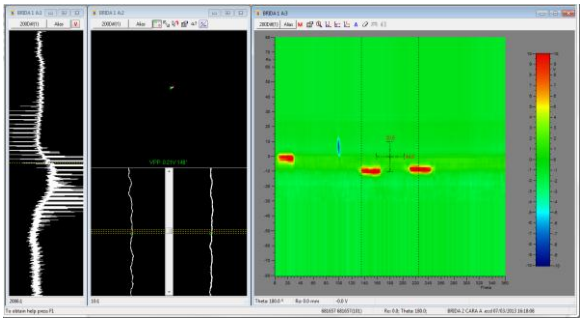

Figure 13. Example of ET acquisition on V3 test piece

Roll-repair and J-groove according to Code Case N-730 (examination volumes V2 and V4)

The flaws postulated in this examination volume are axial and circumferential cracks open onto the inner or outer diameter. The inclination of these flaws is ±10°.

The inspection techniques that may in principle be used in this examination volume are simple, since there is no weld and the inspection has to be performed only in the base material. The difficulty increases if consideration is given to the fact that the size of the qualification flaws in these examination volumes is very small. Furthermore, there are two geometric factors to be considered: the deformation of the surface of the housing due to the weld and the double step in the roll zone.

The methods and techniques finally selected for the inspection of this examination volume are summarized in Table 3.

Table 3. Method and technique for examination volumes 2 and 4. Upper probe-holder module

Volume	Connected to / orientation		Detection	Sizing	
				Height	Length
V4	OD	Circumferential	UT (P-E)	UT (TOFD)	UT (TOFD)
	OD	Axial	UT (P-E)	UT (TOFD)	UT (TOFD)
	ID	Circumferential	ET	UT (TOFD)	ET
	ID	Axial	ET	UT (TOFD)	ET
V2	OD	Circumferential	UT (P-E)	UT (TOFD)	UT (TOFD)
	OD	Axial	UT (P-E)	UT (TOFD)	UT (TOFD)
	ID	Circumferential	ET	UT (TOFD)	ET
	ID	Axial	ET	UT (TOFD)	ET

By way of an example, the ultrasonic data of an examination performed using the pulse-echo technique have been represented (Figure 14), along with those corresponding to an examination using the TOFD technique (Figure 15).

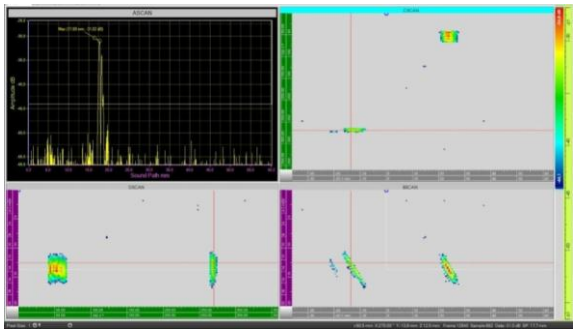

Figure 14. Example of UT acquisition on V4 test piece

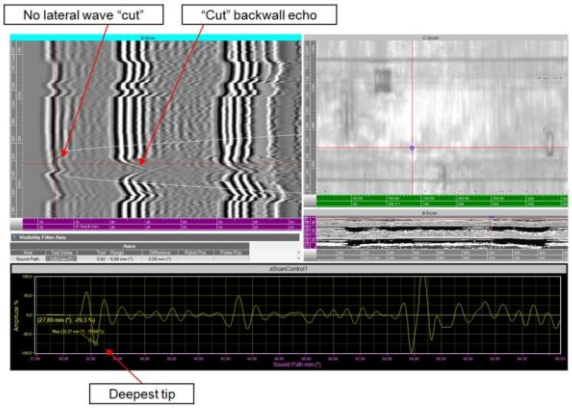

Figure 15. Example of UT acquisition on V2 test piece

QUALIFICATION

Before inspection, data acquisitions were performed on test pieces at the Tecnatom facilities with a view to qualifying the procedures, equipment and personnel. Test pieces containing known information on the flaws are used mainly to demonstrate the suitability of the procedures and equipment (inspection system). Other test pieces, in which information on the flaws is not revealed, are used to evaluate the capacities of the personnel (both data acquisition operators and data analysts).

The process of qualification was supervised by the Swiss qualification body (QSt), which is part of the Swiss Association for Technical Inspections (SVTI).

Both the ultrasonic and the eddy current procedures were finally qualified.

CONCLUSIONS

Tecnatom has developed an inspection system for the inspection of the CRDH's at a Swiss Nuclear Power Plant. In order to achieve this objective, an item of mechanical equipment has been modified, two new probe-holding modules have been manufactured and several improvements have been made to the data acquisition and analysis systems. Finally, the two procedures developed, both ultrasonic and eddy current procedures, have been qualified by the Swiss qualification body (QSt).

The inspection of the CRDH's at the nuclear power plant was carried out during the month of August 2013.

ACKNOWLEDGEMENTS

Tecnatom would like to thank its client the Swiss Nuclear Power Plant for which the work described in this paper was performed for its constant trust and support during qualification and inspection.

REFERENCES

- Case N-730. "Cases of ASME boiler and pressure vessel code". October 2006.
- ENSI-Guideline HSK-B07. Regulation for qualification equipment, rule of inspection and personnel for every NDE.

USE OF ADVANCED SIMULATION TOOLS: SOME EXAMPLES IN THE FRENCH QUALIFICATION PROCESS FOR ULTRASONIC APPLICATIONS

C. Hubert, S. Deydier, L. De Roumilly, EDF - CEIDRE, France
E. Lhuillier, B. Chassignole, EDF - R&D, France

ABSTRACT

The French regulations require EDF to qualify all NDE carried out on the Main Primary and Secondary circuits of PWR plants, before on-site implementation. Modelling is commonly used in the ultrasonic inspections qualification process: at the design stage, for feasibility studies, during the development phase, and at the end of the process. More specifically, for the feasibility and development phases, simulation tools enable the quantification of the impact of influential parameters arising from the component's geometry, material properties, probe and defects, and the reduction of the number of experimental trials and mock-ups. At the end of the qualification process, some performance illustrations can be carried out using modelling tools. With regard to ultrasonic applications, the calculations can be performed with semi-analytical tools (CIVA software) or finite element codes (ATHENA code). The aim of this paper is to set out some examples of the contribution of advanced ultrasonic simulations tools for the qualification process outcomes.

INTRODUCTION

The French regulations require EDF to qualify all NDE carried out on the Main Primary and Secondary circuits of PWR plants, before on-site implementation. The qualification process consists in a demonstration of the capability of an NDE to ensure that the performance meets the requirement of the NDE from the safety and customer's point of view in a reliable and repeatable manner. The performance and reliability demonstration of the NDT application is mainly based on engineering demonstrations, experimental tests on representative mock-ups with artificial or realistic flaws, feedback experience, and modelling simulations.
Modelling is more and more commonly used in the ultrasonic inspections qualification process at different conception stages. At the design stage, simulation tools help for the feasibility studies but also for the quantification of the impact of influential parameters arising from the component's geometry, material properties, probe and defects; they also help in the reduction of the number of experimental trials and mock-ups. At the end of the qualification process, some performance illustrations can be carried out using modelling tools. Finally, modelling tools help expert to understand inspection results and to validate examination diagnostics.
This paper presents examples of advanced simulations carried out at EDF on CIVA and ATHENA software products to provide technical justifications.

USE OF CIVA SIMULATION TOOLS IN QUALIFICATION PROCESS

The French qualification process consists in taking into account the influence of the component, the flaw, the technique, the environment and the operating in the demonstration of the detection of a critical defect. The use of simulation tools is thus helpful to draw the detection performance of an NDE for complex flaws which cannot be easily implemented in a mock-up because of technical difficulties and or its expensive cost, but also in case of lack of representative mock-ups.

This first paragraph presents two different examples of simulation use for UT manual inspection, using the CEA CIVA software [1], which is a semi-analytical calculation modelling tool mostly used in UT NDT development.

Simulation tool applied to complex flaw configuration detection

This first example presents a case of use of the simulation tool to bring technical justification and about the capability of a process to detect a crack localized in a complex crack network.

Context and description of the simulation configurations

The simulation tool CIVA was used to evaluate the detection performance of the UT process in case of flaws network, which can induce shadowing effect, possible decrease of the corner-echo amplitude and multiple reflections. The inspected component made of austenitic stainless steel type 316 L is indeed sensitive to the risk of in-service thermal fatigue cracks damage localized in bends (see figure 1) and which propagate as a network looking like crackling.

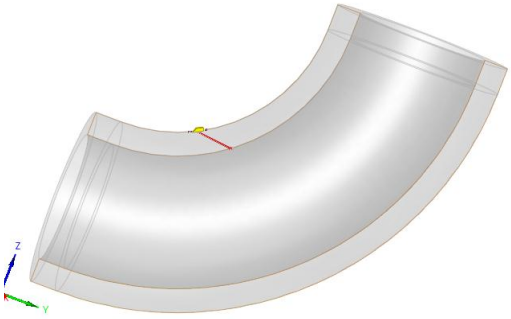

Figure 1: 56° SW inspection configuration

The In-Service Inspection (ISI) is performed with a manual contact examination technique using 2 MHz single element ultrasonic transducer generating inclined shear waves (SW). The flaw detection mechanism relies on the detection of a Shear Waves (SW) corner-echo reflection between the flaw and the inner pipe surface, thus the angle of SW for each transducer was designed to optimize the effect the angle attack of the beam on the flaw.

The simulation was used to determine the detection sensitivity of two types of flaws. The simulations of an inspection along and perpendicular to the flow propagation direction were respectively performed using a 56° SW and 37° SW transducers (see figure 1). The study was divided in two parts according to the considered flaw configuration (see figure 2):

- The flaw type A consists in a group of two plane defects with 3 mm high and 5 mm length dimensions used to evaluate a “simple” shadowing effect on detection sensitivity for the both examination configuration (CIVA shadowing functionality).
- The flaw type B is a complex defect consisting in a grid pattern with a square lattice (CIVA complex shape flaw functionality). Results for 3 mm high and 30 mm long dimensions considered as representative of a thermal crackling geometry are represented below. The use of such flaw aims to understand the contribution of the wave reflections on the corner of the defect in the detection sensitivity.

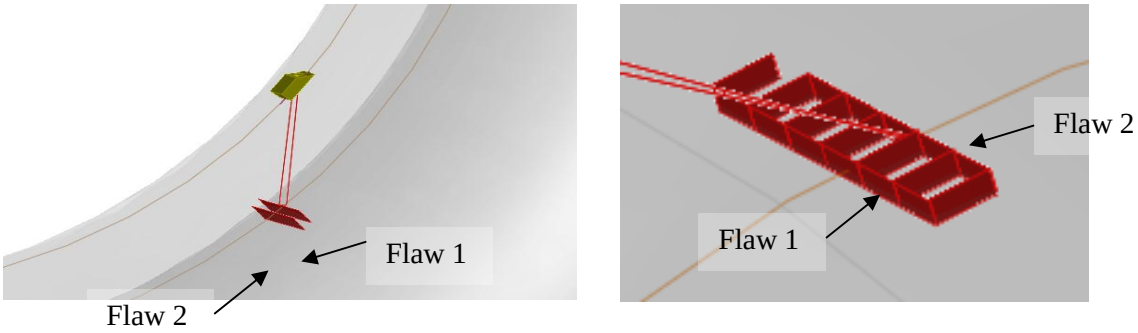

Figure 2: Defect configurations used for simulation: Type A - group a two successive plane flaws (left), Type B - grid pattern defect (right).

Results and conclusions

The results of the simulation for the first flaw configuration are presented in the table 1 and those for the second type in the table 2. The detection level threshold corresponds to the reference sensitivity corrected with the control gain determined for each configuration control. The results correspond to the amplitude detection (in dB) with respect to the detection level threshold to estimate the shadowing impact on the detection of a crack group of the same size.

Table 1: Amplitudes (dB) of the simulated SW echoes for the type A configuration flaw (simple shadowing effect) (Longitudinal and circumferential directions correspond to an inspection direction respectively parallel and perpendicular to the flow propagation direction).

Control direction	SW angle (°)	Flaw 1 (3x5 mm²)	Flaw 2 (3x5 mm²)
Longitudinal	56°	+6 dB	+4 dB
Circumferential	37°	+19 dB	+13 dB

All the flaw detection sensitivities are higher than the detection level threshold, with a minimum of +4 dB amplitude, and thus they would be all detected with the NDE process.

Table 2: Amplitudes (dB) of the simulated SW echoes for the type B configuration flaw (complex flaws geometry) (Longitudinal and circumferential directions correspond to an inspection direction respectively parallel and perpendicular to the flow propagation direction).

Control direction	SW angle (°)	Flaw 1 (3x30 mm²)	Flaw 2 (3x5 mm²)
Longitudinal	56°	+8 dB	+4 dB
Circumferential	37°	+23 dB	+14 dB

The results of the table 2 show that all flaws would be detected since all detection sensitivities are higher than the detection level threshold. Moreover, these results can be compared to those presented in the table 1 to illustrate the impact of the complex geometry of the flaw on the detection sensitivity: the flaw grid pattern effect seems to be negligible for a 3 mm high flaw.

The study has provided quantitative results on the influence of the flaws network geometry which have been used to substantiate the technical justifications.

Simulation tool applied to complex geometry component

This second example presents an other case of the use of the simulation tool to evaluate the performance of an NDE process in a component featuring complex geometry and attenuation. Representative mock-ups of simple line pipes exist and trials were performed. However, CIVA simulations were performed on a complex geometry instead of trials since no representative mock-up was available.

Context and description of the simulation configurations

The inspected component is a complex geometry pipe examined with a manual contact ultrasonic technique using 70° inclined SW corner echoes reflection principle. The evaluation of both effects (complex geometry and attenuation) was performed in two phases:

- Validation of the input data: Experimental tests performed during qualification trials on a simpler line pipe configuration mock-up were simulated and the corresponding detection sensitivities were compared to experimental ones in order to validate also the representativeness of simulation.
- Simulations on the complex geometry component were thus performed with an experimental validation.

Figure 3 illustrates the inspection techniques used in the simple pipe and in the complex component geometry. According to the component configuration, the SW angles are used to optimize the corner echo effect amplitude, then the 45° and 60° SW angle are retained in the simple pipe configuration while 60° and 70° SW angle are more adapted to complex pipe configuration. The inspection is performed using two different frequency ranges around 2.25 and 5 MHz.

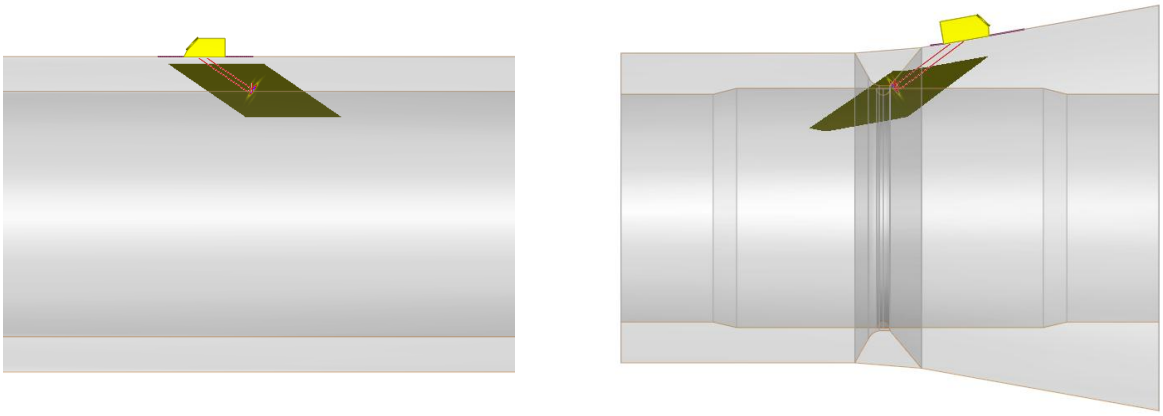

Figure 3: Simulated inspection for a simple pipe geometry (left) and for the complex one (right).

The piping component is made of 13 mm thick austenitic stainless steel type 316 L.

The acoustic attenuation was taken into account in the simulation, using a frequency filter model implemented in CIVA software:

$$\alpha(\omega) = \alpha_0 \left(\frac{\omega}{\omega_0} \right)^n \text{ with } \alpha_0 \text{ the attenuation coefficient for the central frequency } \omega_0 \quad (1)$$

The difficulty in using this functionality is to specify the relevant parameters n and α_0. The different coefficients of the expression (1) were determined for this study as following:

- Factor n=4; according to the ratio between the wave length and the medium grain size (60 µm) of the metal, the attenuation effect was considered to be mainly led by the Rayleigh scattering law [2].
- Attenuation coefficients α_0 was determined according to feedback experience and from the experimental tests performed on the simple pipe configuration:
  - α_0=0.025 dB/mm for 2.25 MHz central frequency,
  - α_0=0.075 dB/mm for 5 MHz central frequency.

Results and conclusions

The results of the simulation and the experimental trials for the simple pipe configuration are presented in the table 3. The results obtained for simulated SW amplitudes on the complex pipe geometry are presented in the table 4. The detection level threshold corresponds to the reference sensitivity corrected with the control gain determined for each configuration control. The results correspond to the amplitude detection (in dB) with respect to the detection level threshold.

Table 3: Amplitudes (dB) of the experimental and simulated SW echoes for the different inspection configurations of the simple pipe line geometry.

Frequency (MHz)	SW angle (°)	Experimental results (dB)	Simulation results (dB)
2.25	45°	+20 dB	+20 dB
	60°	+13 dB	+16 dB
5	45°	+20 dB	+21 dB
	60°	+14 dB	+15 dB

These results validate the representativeness of the simulation approach and the input data values used to model the detection sensitivity for the complex geometry line.

Table 4: Amplitudes (dB) of the simulated 70° SW echoes for the different inspection configurations of the complex pipe line geometry.

Frequency (MHz)	Attenuation coefficient α_0 (dB/mm)	SW angle (°)	Simulation results (dB)
2.25	0.025 dB/mm	70°	+17 dB
5	0.075 dB/mm	70°	+23 dB

The results of the table 4 show that the flaws would be detected with the NDE process since the simulated flaws amplitude is higher than the detection level for the different attenuation coefficient values. The detection amplitude level is higher for the 5 MHz inspection frequency than the 2.25 MHz one. The results are quite surprising since the attenuation effect is more important for high frequency than lower one, even if the reflectivity of the flaw is better at 5 MHz. As a conclusion, this result can be explained by the fact that attenuation effect is compensated by the reflectivity one.

USE OF SIMULATION AS AN EXPERTISE TOOL IN SUPPORT OF INSPECTION DATA ANALYSIS

Context and input data

Within the framework of the search for Under Cladding Defects (UCD) by UT method, simulations were performed in order to identify the possible origins of the appearance of an additional echo, besides the top and bottom diffraction echoes, called "3rd echo". The problem with this 3rd echo is bound to the fact that, if it is taken into account by the analyst, it may lead to the oversizing of the UCD during the analysis of the acquisitions, and thus lead to the conclusion that the height of the UCD has evolved since the previous inspection. Indeed this echo, which is rare and of very low amplitude, is roughly aligned with the top and bottom diffraction echoes and may be positioned at the depth which is twice the measured height between the two other echoes. 3D simulations were performed with CIVA software in order to analyze and recreate the conditions of the appearance of the 3rd echo with the aim of studying its possible artificial nature.
The nominal configuration characteristics are defined hereunder:

- Transducer

The search for UCD is performed by the means of UT focused immersed 2MHz transducers, which are designed in order to generate mainly 60° Pressure Waves (PW) inside the inspected components.

- Component

The inspected components are made of ferritic steel coated with a 7mm thick welded cladding, which elastic coefficients (with the assumption of a transverse isotropic symmetry, actual values are given in table 5) have been determined from ultrasonic velocity measurements on a 316L steel sample [6]. The PW (SW) velocity in ferritic steel is set to 5900 (3230) m/s. No attenuation is taken into account in the study.

- Under Cladding Defects

The UCD are modeled as 7mm high rectangular notches, perpendicular to the surface of the component with the top located at the cladding/ferritic steel interface.

Table 5: Elastic coefficient (in GPa) of the transverse isotropic cladding [6]

C_{11}	C_{33}	C_{13}	C_{55}
247	218	148	105

Study principle and Results

Starting from the nominal case, a sensitivity study is performed in order to identify parameter(s) which allow(s) recreating the 3rd echo and maximizing its amplitude.

- *Nominal case*

The comparison between a calculation performed with every propagation modes (Figure 4 left) and a calculation performed with the PW only (Figure 4 right) shows that the 3rd echo is only due to the propagation of the PW. This echo is not clearly separated from the bottom diffraction echo; its amplitude is around 13 dB lower than the amplitude of the bottom diffraction echo. When analyzing the simulation at

different time steps, one can observe that this 3rd echo comes from a very little part of the ultrasonic beam which propagates almost parallel to the surface of the component under the cladding, before the main 63° beam interacts with the bottom of the notch. Because of its propagation time, this additional echo is then automatically repositioned at a greater depth value than the bottom diffraction echo, in the continuity of the bottom diffraction one.
Starting from this case, sensitivity studies are performed in order to identify the parameters which may amplify the phenomenon. The most impacting are the followings ones.

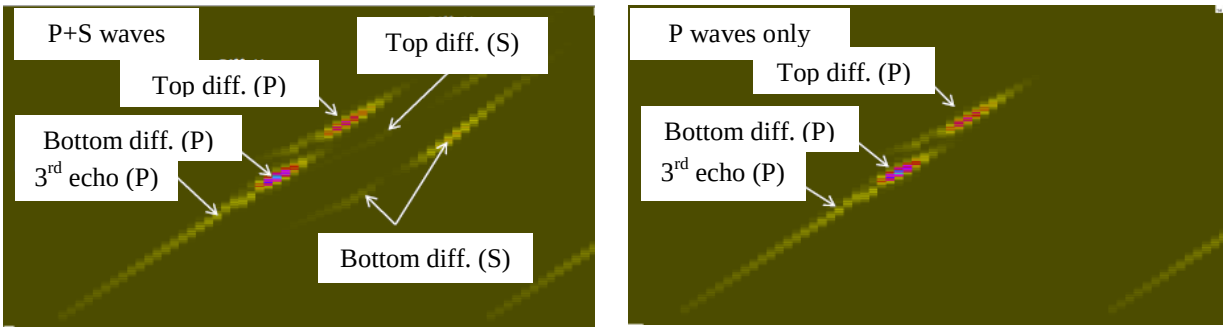

Figure 4: (left) simulated rough BScan with the nominal configuration and P+S waves;
(right) simulated rough BScan with the nominal configuration and P waves only

- *Use of a "step"*

After different simulation tests, the use of a "step" at the surface of the component is the most influential geometrical parameter which leads to separated 3rd echoes (see Figure 5). Moreover, it may recreate geometrical conditions which are expectable onsite and may induce the rise of 3rd echoes. The results show that the use of a "step" may lead to the separation of this echo, as well as an increase of its amplitude (in Figure 5, the amplitude of the 3rd echo is 6.5 dB lower than the bottom diffraction echo).

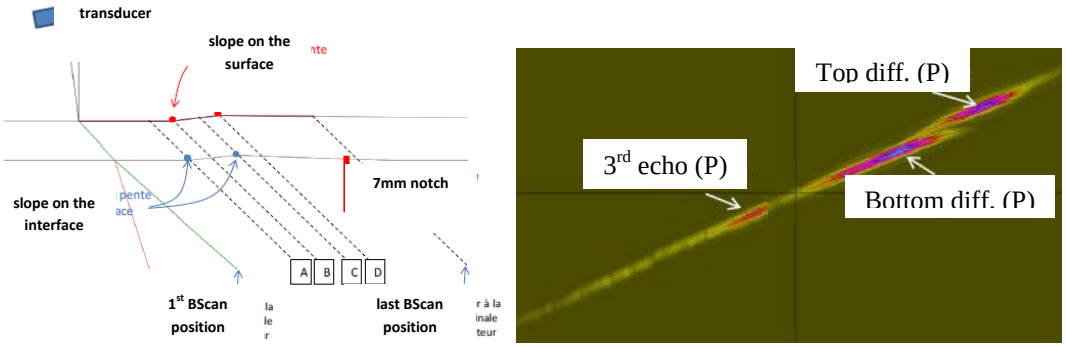

Figure 5: (left) use of a "step" at the surface of the component, [A B C D] being the 4 points of the step;
(right) PW B-Scan with a step (1mm high / 15mm long)

- *Height of the notch*

Starting from the step configuration, 3 notch heights are studied: 7mm, 10mm and 14mm. Figure 6 presents the relative amplitudes which are obtained with the simulation for the 3 height values. One can observe that the more the height is important, the more the 3rd echo is separate from the bottom diffraction echo and their amplitude gets close.

Notch height	Top echo	Bot. echo	3rd echo
7 mm	-0.2	0	-4.8
10 mm	0	-2,9	-8,1
14 mm	0	-6.8	-8.9

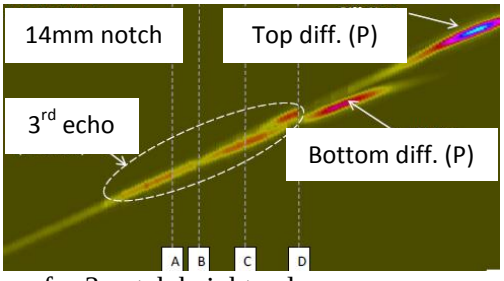

Figure 6: (left) amplitudes of the 3 echoes for 3 notch height values;
(right) PW BScan with a step (1mm high / 15mm long) and a 14mm height notch

Conclusion

The possible artificial nature of this echo was studied through different influential parameters, among which the presence of a step and the height of the notch have the greatest impact. Such results may be helpful for an examination diagnostic, if the artificial nature is clearly demonstrated.

USE OF ATHENA SIMULATION TOOLS IN ANISOTROPIC MATERIALS

This paragraph presents an example of the use of advanced EDF simulation software called ATHENA in NDT development.

Finite elements modelling

ATHENA2D is a finite element code for elastodynamic developed by EDF R&D (Electricité de France). The code is dedicated to the simulation of wave propagation in all kinds of elastic media and in particular, heterogeneous and anisotropic materials. One important feature of the code is the use of the fictitious domain method [3]. It relies on the combined use of a regular discretization of the calculation zone with a non-regular meshing of the defects. It allows combining the rapidity of regular meshes calculation with the possibility to model arbitrary shaped defects. Furthermore, ATHENA2D gives the possibility to use Perfectly Matched Layers (PML) to define the boundaries of the calculation domain. Reflections coming from the domain limits are then avoided. It thus enables to model virtually infinite components.

The ATHENA2D finite element (FE) code has no limitation for the description of complex materials such as heterogeneous and anisotropic structures. The code has been widely used by EDF to simulate the inspection of complex structures such as austenitic welds [4-5].

Context and description of the simulation configurations

The aim of the following simulations is to evaluate the effect of an anisotropic and attenuating cladding on the amplitude of a corner echo.

The inspected component is a 151 mm thick ferritic steel coated with a 8 mm thick austenitic stainless steel cladding in the inner surface. The goal of the inspection is to detect a 3 mm-high plane defect located under an austenitic cladding (see figure 7). The inspection was performed with a 2 MHz single element ultrasonic transducer generating shear waves (SW) with vertical position at 45° in the ferritic steel base metal. The flaw detection relies on the detection of a SW echo corresponding to the red ultrasonic path displayed in figure 7.

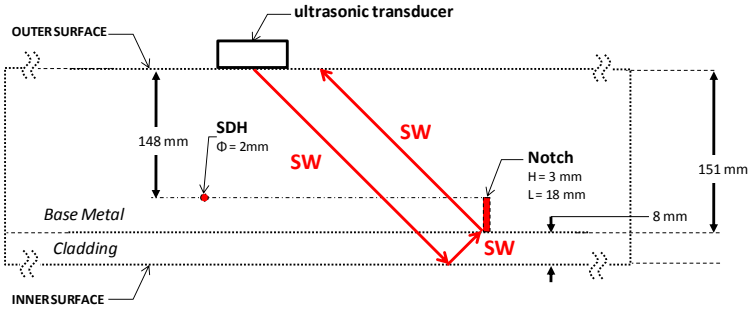

Figure 7: Inspection configuration, from the outer surface, of a 3 mm-high defect, located under the austenitic cladding.

The welded cladding is applied by Manual and Shielded Metal Arc Welding in horizontal vertical position. Figure 8.a displays a metallographic picture of the base metal and the cladding. After machining, the thickness of the cladding is 8 mm.

For the input of the ATHENA2D code, the mapping of the columnar orientation of the austenitic columnar grains has been obtained with the MINA code. In the configuration the main influent parameter of MINA is the tilt of the electrode during the welding process and it was set to 40° in the present case. The cladding is then described by a 2×2 mm² grid defining a set of anisotropic and homogenous domains with a given crystallographic orientation (figure 8.b).

Figure 8: a) Metallographic characterization of the cladding. b) Grain orientation mapping of the cladding obtained with the MINA code.

The elastic coefficients of the cladding (with the assumption of a transverse isotropic symmetry) have been determined from ultrasonic measurements velocity on a 316L steel sample [6]. The actual values are given in table 5. The SW velocity in ferritic steel was set to 3230 m/s. In the ATHENA2D calculations, the ultrasonic attenuation was taken into account. The data of the attenuation coefficient in the cladding have been extracted from a previous study. The attenuation, expressed as a function of the angle α between the propagation direction and the columnar grain axis, are given in Table 6.

Table 6: Attenuation coefficient of SW at 2 MHz as a function of the angle α between the direction of propagation of US waves and the columnar grain axis.

α (°)	0	10	35	45	60	80	85
Att (dB/mm)	0.1	0.12	0.52	0.72	0.54	0.16	0.11

Four different configurations were computed with the ATHENA2D code:

1) A Side Drilled Hole (SDH), located at the depth of the upper tip of the plane defect, i.e. 148 mm (see figure 7)
2) A 3 mm notch without cladding
3) A 3 mm notch with cladding and without attenuation (in the cladding)
4) A 3mm notch with cladding and with attenuation (in the cladding)

Results and conclusions

The B-scan corresponding to configuration 3) is displayed in figure 9. The amplitudes of the simulated SW echo for the different configurations are given in Table 7.

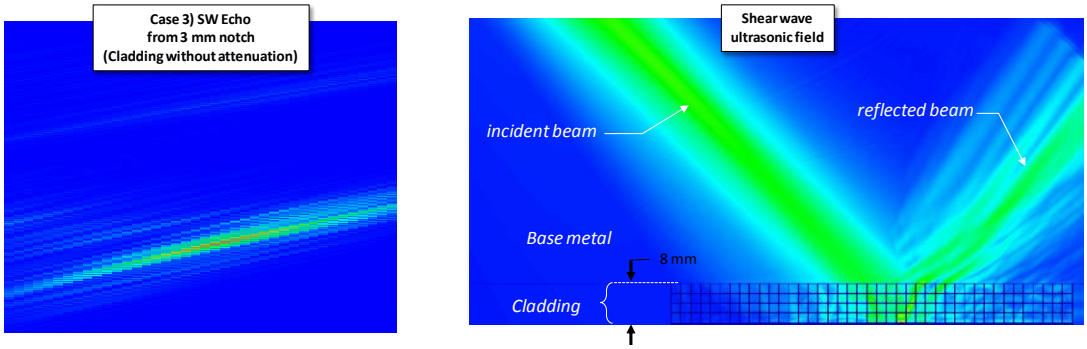

Figure 9: (left) Bscan of configuration 3) (see text) simulated with the ATHENA2D code, (right) ultrasonic field propagated by the SW45 transducer reflected by the cladding at the backwall.

One can see that the cladding has a very low influence on the amplitude of the SW corner echo. Indeed, the ATHENA2D simulations show that the amplitude of the SW echo in configuration 4 – with cladding and attenuation – is only 2.3 dB lower than its amplitude in configuration 2 – isotropic and homogeneous domain).

Table 7: Amplitudes (dB) of the simulated SW echo for the different configurations

Configuration	Amplitude (dB)
1) SDH Phi 2 mm	0 (ref.)
2) Plane defect 3mm without cladding	11.5
3) Plane defect 3 mm with cladding	11
4) Plane defect 3mm with cladding + attenuation	9.5

Several reasons can explain this phenomenon. Given that the mean grain orientation in the cladding is around 45°, the angle between the ultrasonic beam and the grain axis is ~0° or ~90° depending on the inspection direction. Those two situations give the same behavior of the ultrasonic shear wave and are favorable for the propagation of the beam. Indeed, in those cases the beam attenuation and deviation are minimal. The grain orientation map given as input of the ATHENA2D code is rather homogeneous. Thus the beam perturbations are very limited in the cladding. The picture of figure 9 shows a computation obtained with ATHENA2D of the reflected by at the backwall of the component. One can see that beam undergoes shallow perturbations and remain rather parallel after reflection on the inner surface of the component. Simulation results underline the very low influence of the cladding in the detection performances.

They are in good agreement with a other 3D CIVA simulations performed without attenuation.

The study has provided quantitative results on the influence of the cladding which have been used to substantiate the technical justifications.

CONCLUSIONS

Several examples of modeling applications were presented to illustrate our needs in simulation software, in case of complex flaws configuration, complex components geometries and also complex materials structure (cladding effect). However, simulations require upstream to assess the physical effect to be evaluated and to determine the relevant parameters to be taken into account, and downstream to validate hypothesis with experimental data and also though other simulation results comparison.

This paper illustrates the helpful contributions of simulation tools to understand and quantify physical effects due to component featuring complex geometry and attenuation, to evaluate the impact of multiple reflection and shadowing effect in case of complex flaws configuration or again in case of complex anisotropic structure cladding presence.

REFERENCES

1) S. Mahaut et al. An overview of ultrasonic beam propagation and flaw scattering models in the Civa software, Review of Progress in QNDE, Vol. 29 (AIP), pp. 2133-2140, 2010.
2) E. P. Papadakis Revised Grain-Scattering formulas and tables, Journal of the Acoustical Society of America, Vol. 37(4), pp. 703-710, 1965
3) Bécache, E., P. Joly, and C. Tsogka, An analysis of new mixed finite elements for the approximation of wave propagation problems. SIAM Journal on Numerical Analysis, 2000. 37(4): p. 1053-1084.
4) Chassignole, B., et al., Modelling the attenuation in the ATHENA finite elements code for the ultrasonic testing of austenitic stainless steel welds. Ultrasonics, 2009. 49(8): p. 653-658.
5) Chassignole, B., et al., Ultrasonic and structural characterization of anisotropic austenitic stainless steel welds: Towards a higher reliability in ultrasonic non-destructive testing. NDT & E International, 2010. 43(4): p. 273-282.
6) Bodian, P.-A., Propagation des ultrasons en milieu hétérogéne et anisotrope: Application à l'évaluation des propriétés d'élasticité et d'atténuation d'aciers moulés par centrifugation et de soudures en inconel, in INSA Lyon. 2011, Ecole Doctorale Matériaux de Lyon: Lyon. p. 165.

A PLENARY VIEW ON THE RELIABILITY OF NDE-SYSTEMS

C. Mueller, M. Bertovic, D. Kanzler, M. Skender, BAM, Germany
R. Holstein, DGZfP, Germany
J. Pitkanen, Posiva Oy, Finland

Abstract

The paper will give an overview of new methodologies for evaluating the reliability of NDE systems accurately, reliably and efficiently, in accordance with the specific requirements of industrial application and taking into account the very different nature of influencing factors. Using the Modular Reliability Model the three different main influencing elements, i.e. intrinsic capability (IC), application parameters (AP) and the human factors (HF), are, in the first instance, investigated separately. The intrinsic capability stands for the pure physical-technological process of the signal detection caused by the waves or the rays from a material defect in the presence of noise (caused by the material and the devices). This intrinsic capability is the upper bound of the possible reliability. Already when measuring this intrinsic capability for thick walled components the original one-parameter POD must be extended to a multi-parameter POD, where, in addition to the defect size, a number of additional physical parameters, such as the grain size distribution (or attenuation), defect depth, and angle or surface roughness, must be considered. For real life cycle assessments it is necessary to evaluate the signal response from real defects. The industrial application factors, e.g. coupling conditions, limited accessibility, heat and environmental vibrations, diminish the reliability. The amount of reduction can be determined quantitatively, if the underlying conditions are controlled. In case they are not controlled it is necessary to count for a fluctuation in the reliability in the field anyway. The third group of important influencing factors are the human factors, which do not only cover the individual performance capability of the inspectors but also the design of working place, the procedure, the teamwork quality, interaction with systems, the organization, and finally, the relationship between the companies involved in the inspection process and to which extend the responsible parties are aware of it. When comparing an "ideal inspection" with a "real inspection" it is worthwhile to look how the existing practices, rules and standards support reliable testing and where the "delta" is

Keywords: Qualification – Inspection, Reliability-Model, POD, Human Factor

DISSIMILAR METAL WELDS INSPECTION QUALIFICATION IN SPAIN

I. Real, S. Perez, Iberdrola Generacion, Spain
G. Bollini, Tecnatom, Spain
L. Francia, UNESA, Spain,
J. Julio Jimenez, CN Almaraz Trillo, Spain

Abstract

Dissimilar Metal Welds (DMW) Inspection is one of the most challenging activities carried out during a refuelling outage on a Nuclear Power Plant. It has also been one of the main goals for Qualification Activities all over the world. After a very brief introduction about the Spanish nuclear fleet particularities and the NDT Qualification Methodology, our paper will explain the way DMW inspection qualification has been faced in Spain: inspection scope, volume of interest, ultrasonic techniques used (both manual and automated UT from the outer surface and automated UT from the inner surface), mockups manufacturing process, to expand PDI-UT-10 scope to Spanish NPPs geometrical singularities, and main difficulties found and solved during the process.

Keywords: Qualification-Inspection

INSPECTION QUALIFICATION POD

APPLICATION OF "CIVA" SOFTWARE FOR MODELLING WWER-1000 REACTOR PRESSURE VESSEL UT WITH SK-187 SYSTEM FROM OUTER SURFACE

I. Kadenko, R. Iermolenko, A. Kadenko, N. Sakhno
Nondestructive Examination Training and Certification Facility, Ukraine

1. INTRODUCTION

Reactor pressure vessel (RPV) inspection is one of the most crucial issues to provide NPP safe operation especially beyond the unit designed life time. Applications of high-tech innovative equipment, efficient inspection methods and procedures as well as highly skilled staff are necessary to ensure NDE reliability and primary circuit structural integrity.

WWER-1000 units' design makes RPV in-service inspection (ISI) possible from outer surface. Therefore SK-187 inspection system was developed and supplied to WWER NPP units within last three decades. This system is dedicated for RPV outer surface visual and ultrasonic testing. Nowadays only two inspection systems SK-187 left in Ukraine. In addition there are three other qualified ISI systems at Ukraine NPPs for RPV examination from internal surface. For units under life time extension the Regulatory body of Ukraine requires to carry out internal as well outer surface ISI of RPV. Then the important topic raised how to beneficially cope with ISI results to finally optimize the utilization of both types of ISI systems.

In this paper we present WWER-1000 RPV UT modelling results with application of regular (conventional) piezoelectric transducers that comprise a scanning ultrasonic module of inspection system SK-187. The "CIVA" software version 9.1 was used and results of UT response modelling from artificial uncertainties embedded into RPV subsurface area were obtained.

Full scope model of WWER-1000 RPV bottom and cylindrical part with corresponding real dimensions and design features was developed. Echo-pulse mode of piezoelectric transducers with input angles 30º and 40º was used for UT modelling. Artificial flaws with different sizes, locations and directions were "implanted" into RPV base material. Distinctive feature of this work is modelling UT performance of RPV from outer surface (i.e. from base metal side). The results of modelling may be used to justify utilization of SK-187 system for specific examination areas where ISI systems from internal surface can not be considered as sufficient and reliable. Also the analysis of modelling results allows setting the limits for RPV outer surface UT application.

2. INSPECTION OBJECT

The examination area for modelling was VVER-1000 Reactor Pressure Vessel cylindrical part with welds Nos. 2-4 (Fig. 1). The RPV of VVER-1000 consists of base metal made of 15Kh2NMFA steel, and inner overlay manufactured of stainless steel 08Kh18N10T[1].

3. DESCRIPTION OF SK-187 SYSTEM FOR RPV INSPECTION FROM OUTER SURFACE

SK-187 system is applied for UT examination of RPV cylindrical part, including overlay bonding defects in cladding / base metal (weld) interface by means of acoustic block, moveable along RPV outer surface. SK-187 system consists of the following components:

- manipulator SK-187MYu;
- search unit, including acoustic block with UT transducers;
- UT instrument SK27.60;
- unit for data acquisition and processing;
- control unit;
- connecting cables;
- calibration specimens;
- couplant (water) supply system;
- mechanism for bottom examination.

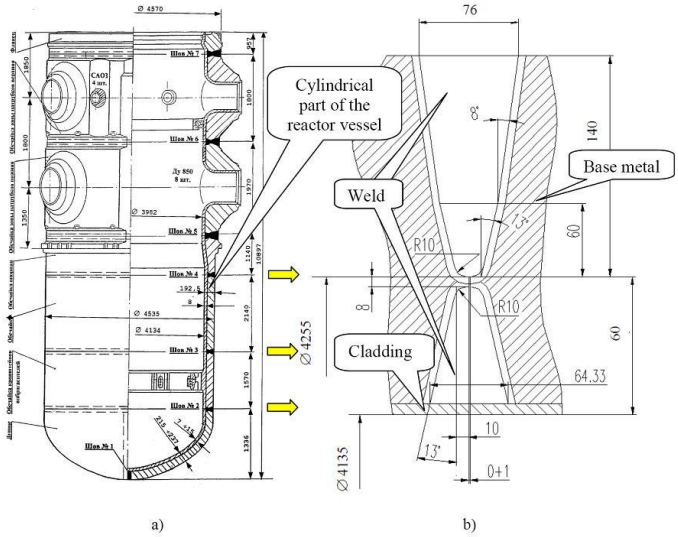

Figure 1 -a) WWER-1000 RPV; b) Welds Nos. 2-4 of WWER-1000 RPV; dimensions are in mm

UT of RPV base metal and welds is executed simultaneously in two planes: in a first plane of RPV generatrix and in a second perpendicular one. Wherein the shear wave angle beam transducers operated in echo-method, they move in two opposite directions within each of two planes. The following methods and transducers are selected to be utilized for UT with 1.25 MHz frequency:

- echo-method with application of angle beam transducers 40ET1,2 and 60ET1,2 (input angle of shear (transversal) wave (C_t) equals 40°); Straight Beam Contact Transducers, Dual Element 0SEL1,2 to detect bonding defects in cladding / base metal (weld) interface; and transducers 90ER1,2, operated in a surface wave mode;
- tandem method with 4 emitting transducers 60ET1,2 (shear wave input angle 60°, Nos. 1, 2 in vertical group and Nos. 11, 12 in a horizontal group) and receiving transducers 23EL1,2 (longitudinal wave (C_l) input angle 23°, Nos. 3-6 in vertical group and Nos. 13-16 in a horizontal group). Under this method shear wave converts into longitudinal one after reflection off the tip of a vertical flaw.

In SK-187 system for UT of RPV from outer surface the UT transducers with 30º и 40º wedges are designed as 2 wedges «1» (Fig. 2), separated with a screen «2». Both wedges are housed in a plastic holder «3» and can be moved relatively to holder with screw-nut «4». The nozzle «5» and sensor «6» are designed for couplant (water) supply and presence control [2].

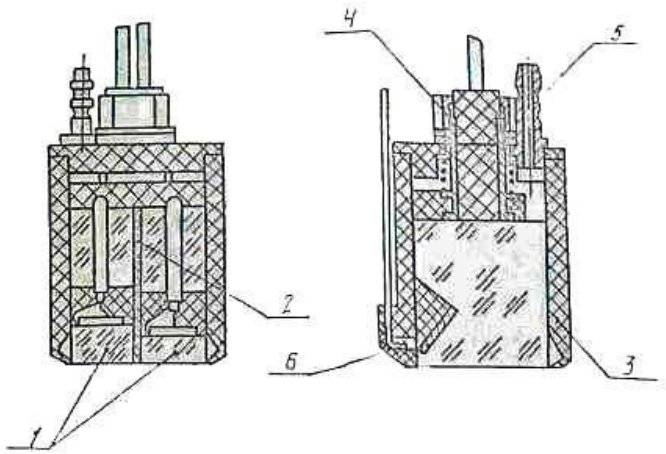

Figure 2 - UT search unit with 30º and 40º wedges: 1- search units (left - 40º and right - 30º wedges, correspondingly); 2 - screen; 3 – holder; 4 – screw-nut; 5- nozzle; 6 - couplant sensor

Let us note that a piezoelectric plate of both UT transducers generates longitudinal wave, travelling in wedge with 30º and 40º input angles and due to “Plexiglas - steel” interface these initial longitudinal waves are converted into shear and longitudinal waves (conversion mode occurs). Beyond the first critical angle (~ 27º) and taking into account Snell's Law equation, only the shear wave propagates into the RPV materials. For this reasons, in RPV only shear waves with 37º and 50º refraction angles are available for examination.

4. RPV UT MODELLING

UT modelling of WWER-1000 RPV cylindrical part with welds Nos. 2-4 was performed the CIVA software, version 9.1 [3]. In this software we have developed a model of RPV with welds Nos. 2-4 and geometry features (Fig.3).

The necessary acoustic characteristics of RPV metal for each of the elements of heterogenic structure model (base metal, overlay) were taken from [4 - 9]. Some of acoustic parameters were measured with real RPV specimens and manual UT instrument. The longitudinal and shear wave attenuation coefficients for base metal (steel), overlay metal (stainless steel) and weld metal are given in Table 1.

Table 1 - Acoustic properties of metal of WWER-1000 RPV cylindrical part and welds Nos. 2 - 4

Metal layer	Longitudinal wave attenuation coefficient, dB/mm	Shear wave attenuation coefficient, dB/mm	UT transducer frequency, MHz
Base metal	0.009	0.009	2.5
Weld	0.009	0.009	1.5
Overlay	0.063	0.074	1.5

Target detection flaw was considered as semi-elliptical crack in base metal with penetration into bonding layer between base metal and overlay.

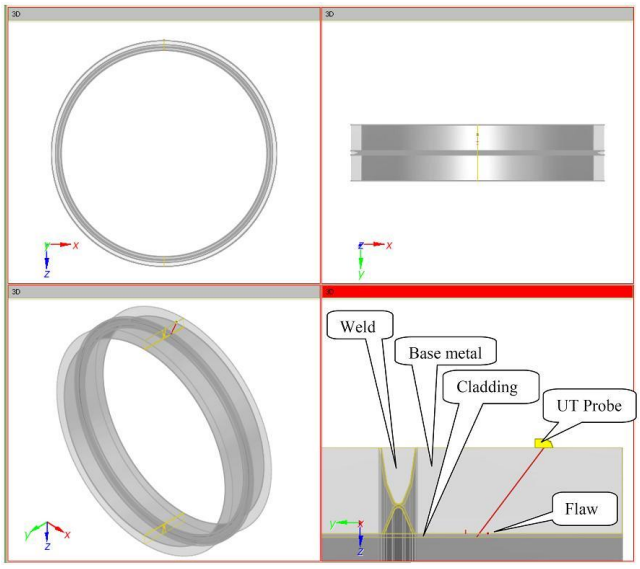

Figure 3 - WWER-1000 RPV and welds Nos.2-4 model in CIVA software

The sizes of such target defect were calculated in the EC sponsored project U1.05/08 T3 «Improvement of NDT Methodologies for In-Service Inspection (ISI) of NPP safety important components based on advanced modern approaches and improved international practices».

5. MODELLING SK-187 DETECTION CAPABILITIES FOR TARGET FLAWS

To determine a detection threshold for SK-187 system the signal to noise ratio must be calculated. With CIVA software it is possible to obtain the estimate of amplitude of the signal caused by flaw in a metal. In the same time it would be rather difficult to modelling noise in RPV. From our previous experience it is known, that the noise amplitude is comparable with signal amplitude caused by reflection of flat-bottomed hole with 2.2 mm diameter. That is why in our research we were using a noise level which is equivalent to signal amplitude of 2.2 mm flat-bottomed hole.
To study the detection capabilities of SK-187 system for semi-elliptical crack there were 2 cracks "implanted" in RPV model. Crack 1 was considered as semi-elliptical defect with 8.5 x 20 mm, positioned at 8 mm depth from overlay surface and athwart oriented to RPV internal surface. Crack 2 was modelled as 2.2 mm diameter flat-bottomed hole located at 10 mm depth from overlay surface and normally oriented to the direction of incident UT wave (Fig. 4). Results of modelling are given at Fig.5.

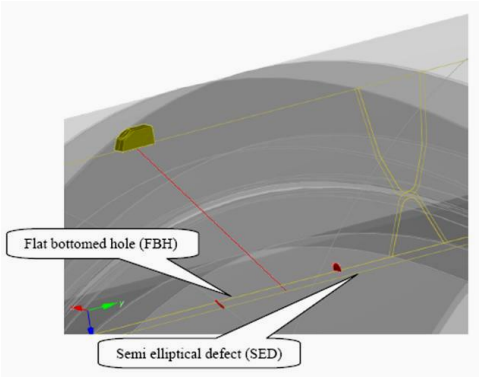

Figure 4 - Flaw locations in RPV welds Nos.2-4 model

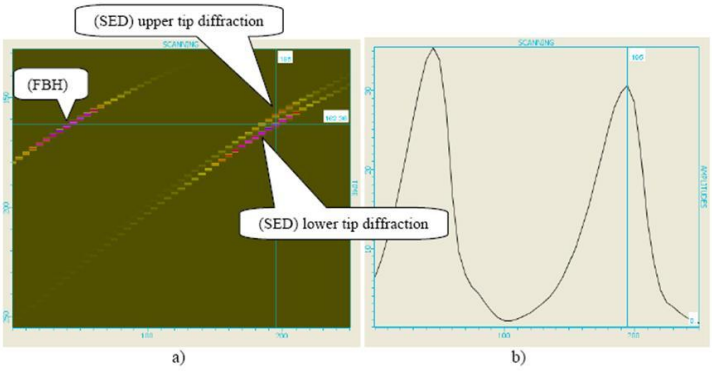

Figure 5 - Signal off cracks Nos.1 and 2: in representation: a) S-scan (side view); b) echo dynamics curve for UT transducer with 30º wedge

For amplitude representation a colour calibration scale was used (red colour - high signal amplitude, green colour - low signal amplitude). "Y" axis corresponds to «SCANNING» parameter in mm of UT transducer shift in axial direction perpendicular to weld orientation. The amplitude off flat-bottomed hole was determined as 36%, and off semi-elliptical crack – 33%. In other words, the signal to noise ratio equals and this semi-elliptical crack won't be detected with SK-187 system.

Taking into consideration our previous results [10] when we studied the signal amplitude off semi-elliptical under cladding crack dependence relative to "rotation", "tilt forward" and "lateral tilt", then one can assume a significant drop in signal amplitude off semi-elliptical 8.5 x 20 mm crack even for minor variation of rotation angle.

6. SIZING OF FLAWS DETECTED BY SK-187 SYSTEM

We also modelled cracks with dimensions, location and orientation presented in Table 2 and Figs.6 and 7. In Table 2 the results of UT modelling (30º wedge) are given. Signal amplitude was considered as a key parameter for this research.

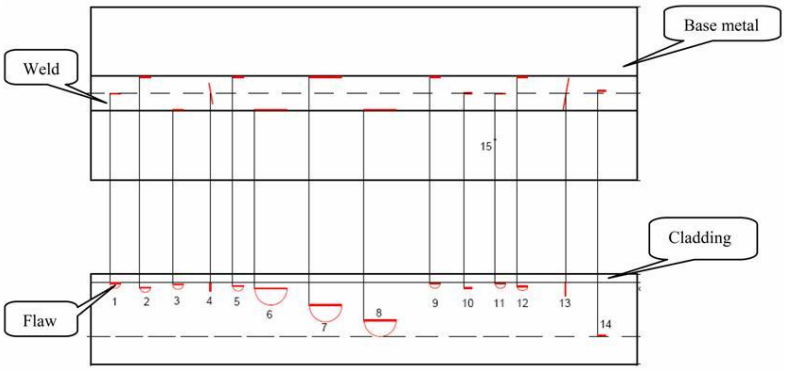

Figure 6 - Location and orientation of cracks in RPV cylindrical part

For each specific modelling we kept additionally as "implanted" 2.2 mm bottomed-flat hole. This bottomed-flat hole was positioned at 10 mm (ligament) and oriented athwart to the direction of incident shear wave. To keep a high modelling precision we used 5 mm scanning increment along RPV inner surface. When SK-187 is applied for RPV scanning, such increment is 10 mm [1]. Results of modelling for cracks Nos.1-3 from Table 2 and bottomed-flat hole are presented at Fig.7 and Table 2. The locations of cracks 1 through 14 from Table 2 are given in Fig.6.

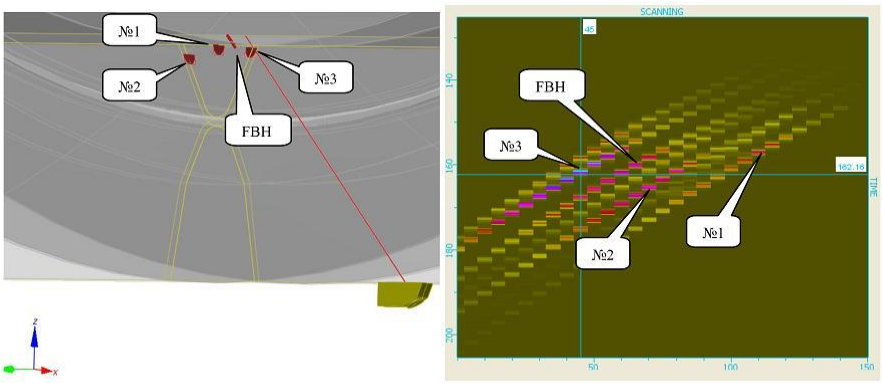

a) b)

Figure 7 - Results of modelling for cracks Nos.1-3 (Table 2): a) cracks Nos.1-3 and bottomed-flat hole in weld No. 4; b) S-scan (side view)

Table 2 - Possible crack parameters and modelling results for RPV and welds

Crack parameters								Results of modelling
No.	**Sketch**	**Height**	**Length**	**Ligament**	**Direction**	**Tilt angle (α), º**	**Skew angle (β), º**	**Signal to noise ratio**
1	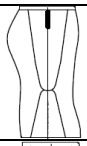	8	20	8	Transverse	0	0	1
2	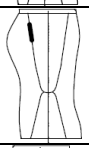	8	20	16	Longitudinal	13	0	0.68
3	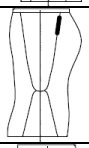	8	20	10	Longitudinal	-13	0	1.64
5	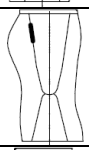	8	20	13	Longitudinal	13	0	0.5
6	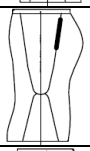	30	60	18	Longitudinal	-13	0	2.1
7	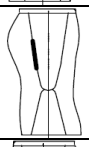	30	60	48	Longitudinal	13	0	1.65
8	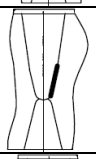	30	60	78	Longitudinal	-13	0	3.7
9	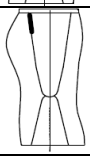	8	20	8	Longitudinal	13	0	0.49
10	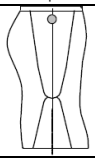	Ø3	15	16	Longitudinal	0	0	-
12	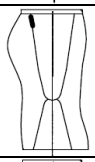	6	20	8	Longitudinal	13	0	0.48
14	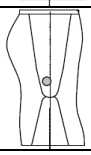	Ø3	15	103	Longitudinal	13	0	-

For sizing of semi-elliptical in-service crack with SK-187 system we modelled UT for cracks of different height with a/c ratios fixed. The results are given in Table 3.

Table 3 - Results of sizing for semi-elliptical cracks detected with SK-187 system

Height	Length	Signal to noise ratio
8	20	0,92
12	30	1,32
16	40	2.25

7. CONCLUSIONS

In this paper the modelling has been performed for cylindrical part of WWER-1000 RPV, namely welding Nos.2-4 with application of flaws "embedded" into welding joints. The following results are obtained:

- SK-187 system is not capable of detection of ISI defects with sizes 8 x 20 mm;
- SK-187 system can be used for detection of some quite large defects in RPV welds, presented in Table 2;
- SK-187 system can be used for reliable detection of ISI defects in base metal penetrating base-metal-overlay interface with sizes 16 x 40 mm and more.

8. REFERENCES

1) Procedure for automated UT SK187MYu.01.00.00.00.00.D1, Subsystem for RPV and bottom examination. – 2006. – 40 P., (in Russian).
2) Operational manual SK187MP 01.00.00.00.00.PE, Subsystem for WWER-1000 RPV examination,1993, 120 P., (in Russian).
3) Web-site: http://www-civa.cea.fr.
4) Klyuev V., "Nondestructive Examination and diagnostics, Guidance", Second issue, Moscow, Machinerybuilding, 2003, 656 P., (in Russian).
5) Ermolov I.N. and Lange Yu.V., "Ultrasonoc examination", Moscow, Mashinostroenine, 2004, 864 P., (in Russian).
6) Kretov E. F., "Ultrasonic defectoscopy in energy machinerybuilding", SPb, «Radioavionica» Ltd., 1995, (in Russian).
7) Lampman S.R. and Zorg T.B., ASM Handbook (Formerly ninth edition), Nondestructive Evaluation and Quality Control, Vol. 17, 1992, 795 P.
8) PNAE G-7-030-91. Unified procedures for examination of materials, welding joints and overlay of NPP equipment and pipes, (in Russian).
9) McIntire P., "Nondestructive testing handbook (second edition), Ultrasonic testing", V 7, 1991, P. 893.
10) Kadenko I., Kadenko A., Sakhno N. and Iermolenko R., "VVER RPV UT Result Modelling with "CIVA" Software Application", 8th Int. Conf. NDE in Relation to Structural Integrity for Nuclear and Pressurized Components, Berlin, Germany, 2010, JRC Scientific and Technical Reports, P. 388 – 400.

CANDU OWNER'S GROUP RISK-INFORMED INSERVICE INSPECTION PILOT STUDY

P. O'Regan, EPRI, USA, Paul Lafreniere, CANDU Owner's Group, Canada
M. Rezaie-Manesh, Ontario Power Generation, Canada,
S. Chesworth, Structural Integrity, USA

ABSTRACT

In 2009, the Canadian Nuclear Safety Commission (CNSC) prepared "Guidelines for Risk-Informed In-service Inspection for Piping," which provided guidance and acceptance criteria for licensees to develop an RI-ISI program as an alternate to the current CSA N285.4 and augmented programs for piping inspection. A project was initiated by the CANDU Owners Group (COG) to develop a best-fit RI-ISI methodology for the CANDU design and evaluate plant risk levels between current and RI-ISI inspection programs. The traditional EPRI RI-ISI methodology was selected as a starting point, and four plant systems were evaluated. Once the risk associated with each component was established, elements were selected for inspection based upon the sampling percentages of the EPRI RI-ISI methodology, and as a final check a comparison was made between plant risk under the current CSA N285.4 (and augmented) inspection program and under RI-ISI. The project was successfully concluded, and results confirmed that the EPRI RI-ISI methodology can be adapted to the CANDU design and the degradation mechanisms evaluated under RI-ISI are consistent with CANDU operating experience. The original CSA N285.4 basis for the CANDU Periodic Inspection Program (PIP) was validated, and potential improvements to the station inspection programs have been identified.

OVERVIEW OF CSA N285.4

CSA-N285.4 [1] defines requirements for the periodic inspection of pressure-retaining systems, components, and supports that form part of a CANDU nuclear power plant. Compliance with CSA N285.4 is required under a Power Reactor Operating License. CSA N285.4 provides certain criteria to specify the inspection requirements under the Periodic Inspection Program. System or portions of systems subject to inspection under CSA N285.4 include:

(a) Systems, and systems connected thereto, containing the fluid that, under normal conditions, directly transports heat from nuclear fuel, and other systems whose failure can result in a significant release of radioactive substances;
(b) Systems essential for the safe shutdown of the reactor and/or the safe cooling of the nuclear fuel in the event of a process system failure; and
(c) Systems and equipment whose failure or dislodgement could jeopardize the integrity of systems in Item (a) or (b), or both.

CSA N285.4 allows excluding systems (or portions of systems) from inspection when the subject piping:

(a) Has adequate barriers between fluid boundary and nuclear fuel,
(b) Has adequate barriers between fluid boundary and the outside atmosphere,
(c) Has acceptable level of dose release in the case of system failure and without operation of the containment system, or
(d) Is dormant and is subject to periodic testing or continuous pressure monitoring all the time.

Inspection categories in CSA N285.4 are determined based on failure size, fatigue usage and stress intensity. Inspection categories are A, B, C1 and C2, with category A being the highest and category C2 the lowest (no inspection required).

CSA N285.4 provides an implicit risk-related rationale for selection of inspection locations by:

(a) Selecting high risk areas (high inspection categories) with high failure consequence (failure size) and high failure potential (fatigue usage and stress intensity) for inspection;

(b) Minimizing inspection scope, effort and dose by reducing inspections in areas with low failure potential and low consequence; and

(c) Including provisions such as exempting systems or portions of systems from inspection if they are periodically tested or system pressure is continuously monitored.

CSA N285.4 sampling criteria differs from RI-ISI methodologies, where a percentage of welds from each risk category are selected.

OVERVIEW OF THE EPRI RI-ISI METHODOLOGY

The EPRI RI-ISI methodology [2] includes:

(a) Selection of RI-ISI program scope,

(b) Failure modes and effects analysis (FMEA) of pipe segments,

(c) Risk characterization of pipe elements,

(d) Selection of inspection locations and examination methods,

(e) An evaluation of risk impacts of inspection program changes, and

(f) Final RI-ISI program definition.

The FMEA process includes two independent evaluations. One evaluation addresses the consequences of pipe failures at each location. The second (completely independent) evaluation addresses the pipe failure potential based on degradation mechanism susceptibility.

The consequence analysis task focuses on the impact of a pipe-section failure (loss of pressure boundary integrity) on plant operation. This impact can be direct, indirect, or a combination of both, as follows:

(a) Direct impacts - A piping failure results in a diversion of flow and a loss of the train and/or system or an initiating event such as a loss of coolant accident (LOCA).

(b) Indirect impacts - A piping failure results in a flood, spray, or pipe whip, spatially affecting neighboring structures, systems, and components; a failure may also result in the depletion of a tank and loss of the systems supplied by the tank.

The consequence category is determined from the plant-specific PRA by calculating the conditional core damage probability (CCDP) and the conditional large early release probability (CLERP), as follows:

High = CCDP > 1E-4

Medium = 1E-6 < CCDP $\leq$ 1E-4

Low = CCDP $\leq$ 1E-6

For CLERP, the boundary values are one order of magnitude smaller.

The failure potential analysis task is to identify which degradation mechanisms are potentially operative in a piping segment within the selected system boundaries. Industry experience [3] has shown no correlation between original design stresses and failure probabilities. In most cases, failures resulted from the presence of an active degradation mechanism not identified in the design process and directly related to system operating conditions. The degradation mechanism procedure was developed to evaluate each system by comparing the actual piping design, system functions, and operating conditions to a set of material and environmental attributes. The failure potential category is determined using a predetermined set of degradation mechanisms and evaluation criteria based on these attributes.

Once the consequence evaluation and failure potential evaluation have been performed, each piping system is divided into segments based on pipe rupture potential and consequence. Each segment, including all elements within the segment, is then assigned to its appropriate risk category in the EPRI Risk Matrix (Fig. 1).

As shown in Fig. 1, the seven risk categories are combined into three risk regions for more robust and efficient utilization. For Risk Category 1, 2, or 3 (High Risk), the minimum number of inspection

elements should be 25% of the total number of elements in each risk category (rounded up to the next higher whole number). For Risk Category 4 or 5 (Medium Risk), the number of inspection elements should be 10% of the total number of elements in each risk category (rounded up to the higher whole number). Risk Category 6 and 7 (Low Risk) locations are not subject to NDE.

OVERVIEW OF THE CNSC DRAFT RI-ISI GUIDELINE

CNSC's viewpoint on the necessary guidelines to support development of a RI-ISI program is provided in [4]. Key points are summarized below, along with results of the assessment on whether the existing EPRI RI-ISI methodology [2] needed to be adapted or additional confirmatory analyses conducted in order to meet the guidelines.

Determine Scope of RI-ISI Program

A review process for piping exempt per CSA N285.4 was developed. CSA N285.4 has two means of classifying piping as exempt from inspection. The first has to do with defining the extent of the system that requires inspection. Piping remote from the nuclear fuel (i.e. beyond two equivalent barriers as defined in CSA N285.4) is exempt from inspection. The second means of identifying exempt piping is related to "failure size," with smaller failures having less importance than larger failures. Piping whose postulated failure size is small (per CSA N285.4) does not require inspection.

Per the review process, equivalent CCDP values were determined and used to generate Consequence Ranks for all exempt piping under CSA N285.4. Segments with a Low Consequence Rank did not receive a failure potential evaluation, since these segments would be categorized as Low Risk regardless of whether there was an active degradation mechanism. Segments with a Medium or High Consequence Rank were evaluated for failure potential, and risk ranking and element selection were also performed for these segments as necessary.

Assess Failure Consequence

The consequence analysis aims at evaluating the impacts of any events caused by failure of the pressure boundary on overall plant risk. The consequence evaluation consists of the following main steps:

(a) Determination of the plant impacts from piping failure, and
(b) Evaluation of failure consequence by using the probabilistic reliability analysis (PRA).

All considerations provided by the CNSC guidance document were consistent with the principles contained in the EPRI RI-ISI methodology. These include addressing a spectrum of break sizes, direct and indirect effects, automatic as well as manual isolation and recovery, and their impact on both core damage and large early release. PRA technical quality is also discussed in these sections, including the use of complementary analyses (e.g., quantitative, qualitative), as well as piping failures that are typically not modeled in the plant PRA.

Assess Failure Potential

Determining the failure potential of piping segments, either with a quantitative estimate or by categorization into groups, is based on an understanding of degradation mechanisms, operational characteristics, potential dynamic loads, flaw size, flaw distribution, inspection parameters, experience databases, etc. When using this approach, it is important that:

(a) The criteria used to decide whether or not a degradation mechanism could occur are conservatively set such that if the criteria are not met, one can confidently rule out the potential for that mechanism; and
(b) An in-depth review of plant service history and plant-specific experience is conducted due to the uniqueness of particular plant configurations, service conditions and maintenance practices that may influence the occurrence of a damage mechanism.

A CANDU-specific review of the EPRI RI-ISI degradation mechanism listing and evaluation criteria was conducted, and concluded that the existing set of degradation mechanisms and evaluation criteria are generally consistent with the CANDU experience.

Categorize Risk

In Section 6.4.5 of [4] it is discussed that the risk characterization and ranking process is performed by combining the information from the failure potential assessment and the failure consequence analysis. This characterization and ranking forms the basis of inspection groups and controls the proposed extent of inspection by non destructive examination (NDE). This is consistent with EPRI RI-ISI, and no change to the methodology was required.

Select Elements for Inspection

The CNSC document discusses various considerations that can be used (e.g., severity of suspected degradation) in developing a robust inspection population. These discussions are consistent with the EPRI RI-ISI methodology, as discussed in section 3.6.5 of [2]. Additionally, as part of the pilot study, an element selection meeting was conducted with knowledgeable site personnel to assure that inspection history, dose and access considerations were explicitly included in the element selection process.

Specify Inspection Requirements

In Section 6.4.7 of [4] it is discussed that for selected inspection locations, an inspection-for-cause process is performed to specify the examination methods, techniques, inspection volumes, inspection interval, acceptance standard, and evaluation standard used to identify and evaluate each credible mode of degradation. This is consistent with EPRI RI-ISI, and no change to the methodology was required.

Evaluate Risk Impact

In Section 6.4.8 of [4] it is discussed that a risk impact evaluation process is necessary to identify whether the changes from an existing ISI program to a RI-ISI program pose favorable changes in risk reduction, as determined by changes of core damage frequency (CDF) and/or large early release frequency (LERF). The purpose of the evaluation is to confirm that the proposed RI-ISI program does not adversely affect plant safety. This is consistent with EPRI RI-ISI, and no change to the methodology was required.

SCOPE OF SYSTEMS EVALUATED

The scope of this pilot application includes piping pressure boundary welds for the following four systems at Darlington Unit 2:

(a) Main and Auxiliary Primary Heat Transport (PHT), including all related subsystems (e.g., Pressure and Inventory Control, Shutdown Cooling)
(b) Emergency Coolant Injection (ECI)
(c) Main Steam, and
(d) Boiler Feed

The scope of application is limited to piping welds, consistent with the vast majority of RI-ISI applications conducted to date. The scope of the four systems:

(a) Includes both nuclear and non-nuclear systems,
(b) Includes both systems selected and exempted per CSA N285.4,
(c) Includes systems outside the scope of CSA N285.4,
(d) Includes systems where augmented inspection programs (e.g., FAC) exist ,
(e) Includes systems with significant impact on core damage frequency (i.e. systems considered to be risk significant in the PRA), and
(f) Provides an opportunity to compare the risk levels between the existing CSA N285.4 program, augmented inspection programs and the RI-ISI program.

The PHT, Main Steam and Boiler Feed systems are normally operating systems that experience high pressure and temperature operating conditions. The ECI system is normally in standby and experiences low pressure and temperature operating conditions. The PHT and ECI systems have piping located both inside and outside containment, while the Main Steam and Boiler Feed system piping is entirely outside containment. All systems are also both safety related and non-safety related with the exception of ECI, which is safety related only.

The scope currently inspected under the CSA N285.4 Periodic Inspection Program (PIP) include portions of the Main and Auxiliary Primary Heat Transport system and related subsystems (6 inch and larger) as well as portions of the Emergency Coolant Injection system (6 inch and larger). All other piping in the scope of this pilot application is excluded from inspection under the PIP per one or more of the criteria of CSA N285.4 (e.g., small pipe size, possesses adequate barriers). Such excluded piping is referred to in this evaluation as Non-PIP piping.

IMPLEMENTATION OF THE RI-ISI METHODOLOGY

Consequence Evaluation

The Darlington Unit 2 PRA was recently updated and was used for this evaluation. The Darlington PRA includes a comprehensive set of pressure boundary failures as initiating events, including failures in the PHT system, connections to the PHT system, and secondary system breaks in the Boiler Feed, Condensate, and Main Steam systems.

A somewhat unique aspect of the Darlington design is the open communication between multiple units outside containment. As a result, a large Main Steam or Boiler Feed system line break outside containment can have impacts on adjacent units. Specific initiating events were evaluated to assess CDF for these events and they were considered in this pilot study. Large secondary system breaks in the Main Steam and Boiler Feed system result in a High Consequence Rank. In contrast, for many LWR plants, these types of failures are assigned a Medium Consequence Rank.

The piping on top of the pressurizer was determined to have a Low Consequence Rank. Otherwise, breaks in the PHT system and connected piping prior to an isolation valve were determined to have a Medium Consequence Rank based on the fact that small LOCA breaks result in a Medium Consequence Rank. For the LWR fleet, especially the pressurized water reactor LWRs, these types of failures are typically assigned a High Consequence Rank. The lower ranking for the CANDU plant is due to the relatively high level of redundancy available to respond to these types of events (e.g., ECI).

While not an initiating event, some piping failures may degrade a plant's mitigating ability. The standby mitigating systems identified for evaluation in this pilot study (e.g., ECI) do not have significant separation; therefore a pressure boundary failure will typically fail the whole system. Also, as stated above, ECI is important in reducing the conditional consequence of PHT failures. As such, failure of this system has a large impact (High Consequence Rank) on the mitigative ability of the plant.

Potential Conservatisms in the Consequence Results

Piping outside containment in the ECI, Main Steam and Boiler Feed systems has been initially assigned a High Consequence Rank based on the current Darlington Unit 2 PRA. Potential conservatisms exist whose elimination could reduce the conditional core damage probability (CCDP) for these systems (or portions of these systems)

Failure Potential Evaluation

Consistent with the requirements of the EPRI RI-ISI methodology, the pilot study piping was evaluated for degradation mechanism susceptibility under normal operating conditions as well as all Level A (Normal) and Level B (Upset) plant transients. Level C (Emergency) and Level D (Faulted) events are outside the scope of the evaluation.

The degradation mechanisms evaluated, and the results of the failure potential evaluation for the in-scope systems, are summarized below.

Thermal Stratification, Cycling and Striping (TASCS)

For all systems within the pilot study scope (with the exception of portions of the PHT system), TASCS was shown to be not operative, primarily due to the lack of sources for hot/cold fluid mixing. This conclusion is also consistent with the conclusions of a preliminary COG evaluation of thermal fatigue in CANDU stations [5].

Thermal Transient (TT)

The PHT Main Circuit primarily encounters thermal shocks via the branch lines and branch connection welds from the reactor inlet and outlet header lines to other systems. ECI can only inject into the PHT following a significant PHT pressure-drop (i.e., under Emergency/Faulted conditions outside the scope of this evaluation).

The pressure and inventory control (P&IC) feed lines to the PHT Main Circuit can experience a thermal shock upon restoration of flow following a flow stoppage. However, any flow stoppage of reasonable duration will not result in a sufficient temperature differential to result in a Thermal Transient to the PHT.

When the shutdown cooling (SDC) subsystem of PHT is circulated by the HT pumps at the initiation of SDC operations, the SDC return lines and the region where they connect to the reactor outlet header balance lines experience a thermal shock, particularly during an abnormal cooldown (Upset) transient. However, plant service history shows that the SDC subsystem at Darlington 2 has been valved in once at a differential temperature of 110˚C, once at 50˚C, and several additional times at differential temperatures of 25˚C or less, none of which is as severe as any of the abnormal cooldown design transients. Based upon the relatively small temperature differentials and low number of cycles, the service history indicates that the SDC system and associated PHT lines are not susceptible to TT.

No other in-scope piping systems encounter thermal shocks during Normal and Upset plant transients.

Intergranular Stress Corrosion Cracking (IGSCC), Transgranular Stress Corrosion Cracking (TGSCC) and External Chloride Stress Corrosion Cracking (ECSCC)

None of the in-scope pilot study systems were identified as susceptible to IGSCC, TGSCC or ECSCC. For much of the piping this was due to the pipe material being carbon steel. There was, however, some piping made of austenitic stainless steel operating at elevated temperatures and with possible tensile stress. These piping systems were not susceptible to IGSCC or TGSCC due to being controlled for dissolved D_2, sulfate, fluoride, and chloride during normal operation and unit start-up. Also, with regard to ECSCC, no outside piping surface is exposed to wetting from concentrated chloride bearing environments (i.e., sea water, brackish water or brine) and any thermal insulation used over austenitic stainless steel is tested in accordance with ASTM C692 to establish that there is no SCC potential. This is comparable to the insulation chloride concentration limits specified in NRC Regulatory Guide 1.36 referenced in the EPRI methodology.

Pressurized Water Stress Corrosion Cracking (PWSCC)

Most in-scope piping systems were not susceptible to PWSCC due to their lack of Inconel piping (Alloy 600) or weld material (Alloy 82/182). At locations where Alloy 82/182 weld metal is present, there is no PWSCC concern since the normal operating temperature is too low for the mechanism to be active.

Microbiologically Influenced Corrosion (MIC)

Most of the piping in the pilot study scope was not susceptible to MIC since their full load operating temperature is too high for this mechanism to be active. In the case of the ECI system, many lines are typically stagnant at low (ambient) temperature and fluid sources are not treated with biocides. However, Appendix B of [6], which lists all locations inspected under the Darlington 2 Service Water Reliability Program, does not include any ECI System locations. Therefore, this system is not considered susceptible to MIC.

Pitting (PIT)
Most of the pilot study piping is not susceptible to PIT since it sees constant, high flow during normal operation. For other piping, control is provided for dissolved D_2, fluoride, and chloride during normal operation and unit start-up, and therefore the level of contaminants is maintained very low and PIT would not be active per the EPRI methodology.

Crevice Corrosion (CC)
Creviced locations associated with thermal sleeves do not exist in the in-scope piping. Therefore it is not susceptible to CC.

Erosion-Cavitation (E-C)
Throttled valves and flow orifices represent potential cavitation sources. For most locations within the in-scope piping, there are no throttled valves impacting system lines. Where throttled valves exist, even under the most conservative conditions, the maximum flow velocity is insufficient to represent an E-C concern.

Flow-Accelerated Corrosion (FAC)
The EPRI RI-ISI methodology points to the plant FAC program for identifying locations potentially susceptible to FAC. Most in-scope piping was identified as not susceptible to FAC under the plant FAC program, while other piping was considered susceptible to FAC but dispositioned (modeled in CHECWORKS). Since the plant FAC program identifies the inspection locations and the periodicity, FAC-susceptible welds are not identified in the weld list, since they do not factor into the Risk Ranking or element selection process.

Failure Potential Classification

Once the degradation mechanism(s) applicable to each piping segment were determined, segments were classified according to their pipe rupture potential as follows:

FAC = large potential (large leak)
Any other mechanism(s) = medium potential (small leak)
No mechanism = low potential (no leak)

Risk Ranking

Once the consequence evaluation and failure potential evaluation were completed, each piping system was divided into segments, with each segment including welds with a common pipe rupture potential and consequence. Each segment, including all elements within the segment, was then assigned to its appropriate risk category in the EPRI Risk Matrix (Fig. 1).

For the Non-PIP scope, results were determined for two cases. In the first case, the current PRA results were used as an input. In the second case, potential conservatisms in the PRA (previously discussed under the Consequence Evaluation) were removed, and alternate means were used for addressing the risk for other piping segments. The removal of these excess conservatisms resulted in reduced CCDP values for Non-PIP piping outside containment in the ECI, Main Steam and Boiler Feed systems, all of which was assigned a High Consequence Rank based on the current Darlington Unit 2 PRA.

Risk Impact Assessment

In the EPRI methodology, it must be shown that changes in plant risk due to changes in the number and locations of the inspections do not pose a significant adverse risk impact, as determined by changes in the CDF or LERF risk metrics. Large release frequency (LRF) was the risk metric used for this pilot study.

The COG RI-ISI pilot study showed that application of the RI-ISI methodology to the selected systems (PIP scope only) showed either a risk reduction or a very small increase in plant risk. Taking all systems together, the results showed a very small increase in plant risk consistent with the criteria

of [2] and [7]. In other words, the change in plant risk due to implementing the RI-ISI results for the PIP scope only meets regulatory acceptance criteria. It should also be noted that the inspection of any Non-PIP components would result in a reduction in plant risk, as these components do not currently require inspection under CSA N285.4.

In general, risk reduction possibilities are a function of having a sufficiently large number of High Consequence sites, High Failure Potential sites, or a combination thereof. There were no High Risk sites (i.e. Risk Category 1, 2, or 3) and only a limited number of Medium Risk sites (i.e. Risk Category 4 or 5) in the PIP scope. As such, there is a relatively small potential for significant risk reduction opportunities for this scope. This is primarily driven by the relative absence of postulated degradation mechanisms and the low consequence of failure of this piping.

Having a low number of welds identified as potentially susceptible to some type of degradation is consistent with light water reactor (LWR) experience. However, from a consequence of failure perspective, the LWR fleet typically has a number of welds with a high consequence of failure (e.g., CCDP > 1E-04) and therefore a relatively higher potential for risk reduction as compared to the results for the CANDU systems.

For the Non-PIP scope, three insights dominate the results. The first is that the majority of this piping is shown to be low risk and therefore risk reduction possibilities are remote. This is consistent with other RI-ISI applications performed in other countries and on other plant designs.

The second insight has to do with high energy piping penetrating the containment into the main turbine hall. This is both similar and different than some other plant designs. Many plants have high energy piping penetrating containment whose postulated failure may have the potential to fail multiple sets of equipment. In some instances this piping has been termed no break zone (NBZ) or break exclusion region (BER) piping, and specific programs (e.g., augmented inspection programs) have been defined for this piping. Additionally, for some of this piping, there is the potential to impact other units.

The third insight has to do with the ECI system. 410 welds were classified as Risk Category 4 (i.e., a high consequence of failure combined with a low failure potential). The ECI system is important in maintaining the PHT piping as Medium or Low Risk piping. That is, postulated PHT failures have a CCDP less than 1E-04 due to the high amount of redundancy (i.e., number of pumps) provided by the ECI system. However, from a pressure boundary perspective, failures at a number of locations within the ECI system will fail large portions of the ECI system due to the lack of separation and/or location isolation capability.

Table 1 provides the RI-ISI results for the PIP scope, as well as a comparison between the number of RI-ISI program selections required and those required under the existing CSA N285.4 program. The risk impact column of Table 1 shows the change in risk associated with moving from the current CSA N285.4 program to RI-ISI. Table 2 provides the RI-ISI results for the Non-PIP scope with conservatisms removed. Since there currently no CSA N285.4 selections required for the Non-PIP scope, including these RI-ISI selections would result in a risk reduction versus CSA N285.4.

SUMMARY AND CONCLUSIONS

This paper was developed in support of the CANDU Owners Group (COG) and documents the pilot study results of the application of the EPRI RI-ISI methodology to four systems at a CANDU reactor site (i.e., Darlington Unit 2).

The objective of this project was to evaluate the impact of CNSC's guidelines [4] to support development of a RI-ISI program for the CANDU design, and included the following:

(a) Selection of a CANDU best fit RI-ISI methodology,

(b) Implementation of the selected methodology on several systems at a CANDU reactor site,

(c) Performance of a change-in–risk assessment to compare and evaluate the risk levels between the RI-ISI program and the existing inspection program (e.g., CSA N285.4/augmented inspection, as applicable), and

(d) Exploration of overall risk reduction strategies (e.g., by moving existing inspections to other locations, adding inspections).

The results of this project show that the EPRI RI-ISI methodology can be adapted to the CANDU design, the adapted methodology can be applied to CANDU systems, and the results obtained are both reasonable and well-documented.

The pilot study also concluded that the systems selected for this pilot study provided a valid and comprehensive assessment of EPRI RI-ISI application for the CANDU design. This included evaluating both nuclear and non-nuclear systems, systems selected for inspection per CSA N285.4 as well as systems exempted or outside the scope of CSA N285.4, and systems where augmented inspection programs exist.

Since the pilot study assessed piping beyond the scope of the PIP, insights from these results can be used to further refine the inspection program and/or identify effective risk management strategies for this piping.

REFERENCES

1. Canadian Standards Association, "Periodic Inspection of CANDU Nuclear Power Plant Components," CAN/CSA-N295.4-05, 2005.
2. EPRI, "Revised Risk-Informed Inservice Inspection Procedure," TR-112657, Revision B-A, 1999.
3. American Society of Mechanical Engineers Boiler & Pressure Vessel Code, Section XI, Task Group on ISI Optimization, "Evaluation of Inservice Inspection Requirements for Class 1, Category B-J Pressure Retaining Welds in Piping," Report No. 92-01-01, 1995.
4. Canadian Nuclear Safety Commission, "Guidelines for Risk-informed Inservice Inspection of Piping, Draft Regulatory Document for Consultation," e-Doc #: 3313690, 2009.
5. Yetisir, M., "Thermal Fatigue in CANDU Stations," Document No. COG-07-4054, CANDU Owners Group, Inc. 2008.
6. Ng., W., "Service Water Reliability Program – Strategy Manual," Document No. NK38-MAN-72100-10001-R003, Ontario Power Generation, 2008.
7. Canadian Nuclear Safety Commission, "Deterministic and Probabilistic Criteria for Decision-making for Class 1 Nuclear Facilities," Regulatory Document No. RD-152, 2009.

FIG. 1
EPRI RISK MATRIX

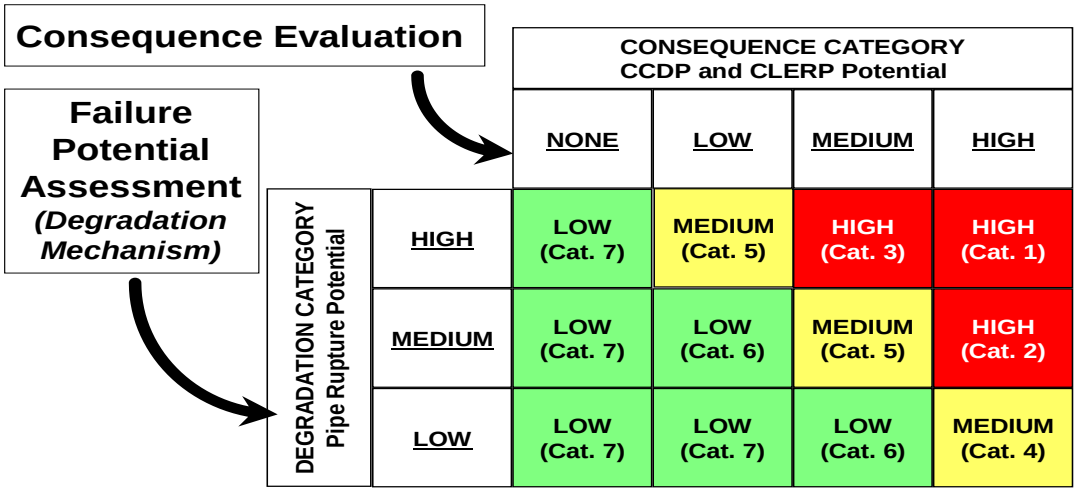

TABLE 1
RI-ISI RESULTS FOR PIP SCOPE

System	Risk Category	Degradation Mechanism	Number of Welds	RI-ISI Selections	PIP Selections	Risk Impact
PHT Main Circuit	5	TASCS	34	4	4	0.00E+00
	6	None	213	0	19	9.50E-12
PHT Rx Inlet/Outlet	6	None	28	0	6	3.00E-12
P&IC Bleed & Relief	7	None	47	0	5	2.50E-14
P&IC Pressurizer	5	TASCS	13	2	1	-1.00E-11
	6	None	4	0	0	0.00E+00
Shutdown Cooling	6	None	516	0	28	1.40E-11
Emergency Coolant Injection	6	None	143	0	6	3.00E-12
Total			998	6	69	1.95E-11

TABLE 2
RI-ISI RESULTS FOR NON-PIP SCOPE

System	Portion of System	Consequence	DM	Risk Category	Estimated Weld Count	RI-ISI Selections
PHT Main Circuit	Lines L23 through L26-D6	Medium	None	6		
	Bleed PHT to PV33 & 34, 35 & 36 (NC)	Medium	None	6		
	3/4 inch connections & connections to SDC	Medium	None	6		
PHT Autoclave	PHT to V1, V2, V7, V8 (NC)	Medium	None	6		
	Beyond 1st isolation valve	Low	NA	6 or 7		
P&IC Feed	PHT to NV23, NV24 (CV)	Medium	None	6		
	Upstream of 1st isolation valve	Low	NA	6 or 7		
P&IC Bleed	Bleed PHT to CV3, CV4 (FC, auto on ECI)	Medium	None	6		
	Downstream of 1st isolation valve	Low	NA	6 or 7		
Bleed Purification	PHT Bleed purification	Low	NA	6 or 7		
P&IC Pressurizer	Line L08-D2	Medium	None	5		
	Bleed & other connects to PZR bottom	Medium	None	6		
	Connection to top of PZR	Low	NA	6 or 7		
D2O Recovery	D2O Recovery	Medium	None	6		
Gland Seal	PHT Gland Seal Circuit	Low	NA	6 or 7		
D2O Leak Collection	PHT D2O Leakage Collection	Low	NA	6 or 7		
D2O Storage	PHT D2O Storage	Low	NA	6 or 7		
D2O Transfer	PHT D2O Transfer	Low	NA	6 or 7		
D2O Sampling	Sampling 3/4 inch and less tubing	Medium	None	6		
	Downstream of 1st isolation valve	Low	NA	6 or 7		
Main Steam	From SGs to Turbine Chest	High	None	4	62	7
	From SGs to Turbine Chest	Medium	None	6		
	Connections (smaller piping)	Low	NA	6 or 7		
Boiler Feed	Upstream of LCVs	High	None	4	77	8
	Upstream of LCVs	Medium	None	6		
	Downstream of LCVs	Low	NA	6 or 7		
	Upstream connections (smaller piping)	Low	NA	6 or 7		
ECI	Inside Containment from Pen to NVs	Medium	None	6		
	Outside Containment	High	None	4	123	13
	Outside Containment	Medium	None	6		
	Outside Containment pump suction	Medium	None	6		

NDE ERRORS ASSOCIATED WITH FLAW SIZING AND GROWTH ESTIMATES

L. Obrutsky, R. Lakhan, J. Lei, D. Horn
AECL, Canada

INTRODUCTION

Condition monitoring and operational assessments rely on Non-Destructive Examination (NDE) techniques and personnel to accurately size flaw indications found during steam generator inspections. However, several sources of error affect flaw sizing accuracy. Examples of these errors include data-analyst variability, probe guidance, calibration flaw depth, array probe coverage, tube wall thickness tolerance, flaw morphology, and technique sizing error. These errors propagate and interact, affecting the overall accuracy of flaw sizing and flaw growth estimates. Each of these errors needs to be identified and quantified individually.

A mathematical framework for the propagation of errors affecting eddy current flaw sizing estimates has been used to assess and understand the sensitivity of the overall uncertainty to each individual error [1]. This understanding may assist with technique improvement to effectively minimize the total uncertainty.

This mathematical framework was applied in two case studies. The first application assessed the uncertainties in sizing and estimating growth of tube-support fretting wear with bobbin probes in Alloy 800 tubing. The second application assessed uncertainties in sizing and growth of outside diameter (OD) pit-like indications in slightly-ferromagnetic Alloy 400 tubing with the X-Probe®. This paper discusses various sources of errors, gives examples of the methods used to assess some of these errors, and provides results from the error propagation method.

This error propagation method and sensitivity analysis can be applied to similar studies of other degradation modes, probes, or tubing to assist in identifying improvements in technique parameters that offer the greatest benefit in reducing overall error. By assisting in the reduction of overall errors associated with sizing and growth estimates, this model can help ensure that tube integrity is maintained.

SOURCES OF ERROR

The error sources that affect the accuracy of eddy current flaw measurements from steam generator tube inspections can be grouped into broad categories: (i) human factors associated with analysis techniques (including sizing and mixing algorithms), (ii) physical variations such as: flaw geometry, flaw environment, and tube variability and (iii) equipment factors. This intuitive grouping is shown in the first column of Figure 1, along with specific examples within each group. Some of these errors, their causes, and their possible effects on estimates of flaw size or growth, are discussed here.

X-Probe® is a registered trademark of Zetec Inc.

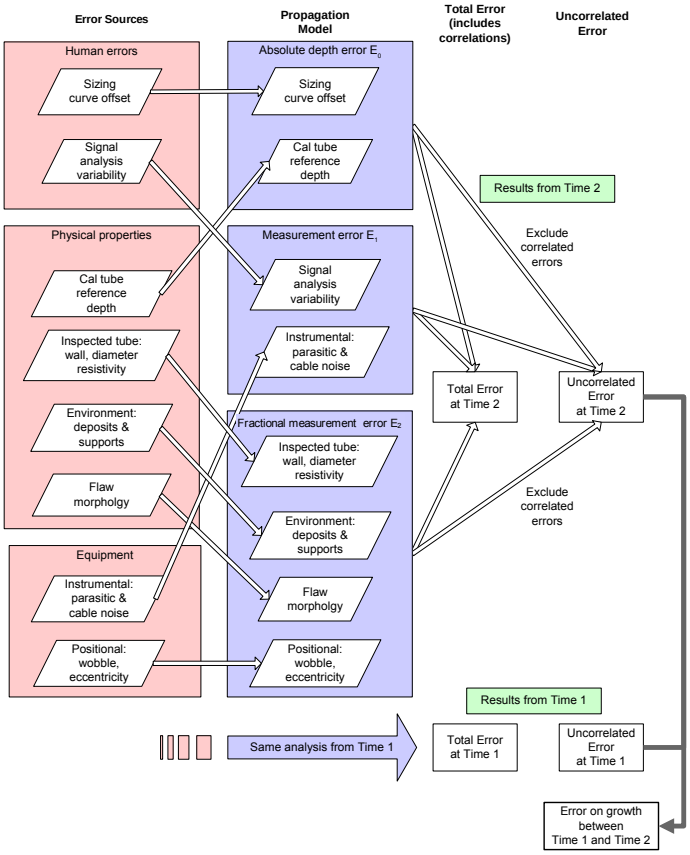

Figure 1 Framework for error propagation in the estimation of size differences.

Probe and Equipment Variability (Equipment Errors)

Errors caused by probe/instrument variability or by changes in the relative position between the probe and the tube wall, are introduced during the acquisition process. Probe/instrument variability can often be compensated for by the calibration process and, therefore, has little effect on flaw sizing or growth estimates. The EPRI Pressurized Water Reactor Steam Generator Examination Guidelines: Revision 7 [2] defines the tolerances regarding probe manufacturing specifications, and cable and equipment parameters, which are denoted as essential variables. Therefore, probe and instrument inconsistencies are limited by these guidelines.

Instrument electronic noise, also known as parasitic noise, diminishes the quality of the data and can decrease the accuracy of sizing tube degradation and flaw growth. The present work assumes a level of parasitic noise that is lower than other voltage error contributions.

Calibration processes assume that a given probe response is produced from a flaw of a defined geometry and depth. However, probe eccentricity affects the responses obtained from localized flaws since probe response decreases exponentially with distance [3]. Eccentricity in the calibration tube can affect the voltage normalization process before the analysis, and the shape of amplitude-based depth sizing curves. Probe eccentricity in in-service SG tubing is typically due to lift-off at geometrically distorted tube regions, such as the U-bend, and probe off-centring due to probe wear.

The following example illustrates the method used in our first case study to estimate probe eccentricity error caused by probe wear. The experimental work consisted of measuring the response of an off-centred bobbin probe to simulated flat wear scars for 36 rotational positions at 10° intervals. The probe was forced off-centre to the limit of acceptability based on the responses to three through-wall-holes (TWH) as prescribed in the inspection technique. Figure 2 shows the probe response versus depth measured at each rotational position. The plot illustrates the spread of probe responses due to probe eccentricity. The insets demonstrate schematically how the sinusoidal angle dependence results in the observed distribution peaked at its extreme values.

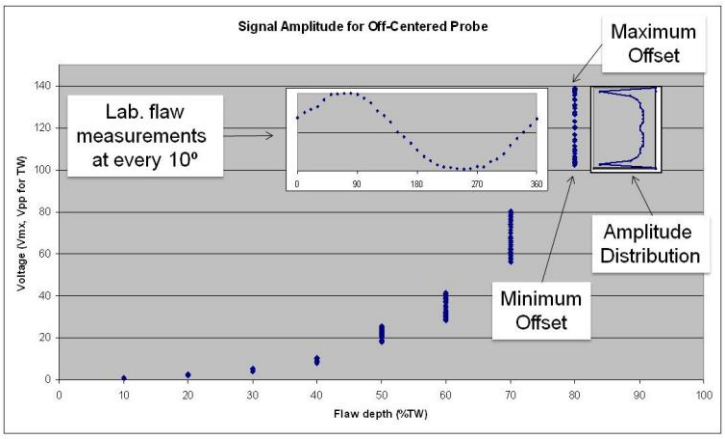

Figure 2 Probe eccentricity error.

One-half of the difference between the highest and lowest voltages of the distribution corresponds to the maximum (end-of-life) probe eccentricity error. This difference increases with flaw depth and can be expressed as an approximate linear function of flaw-signal amplitude for a centred probe, V_0, as follows:

$$\Delta V = aV_0, \text{ where } a=0.17 \text{ for this case}$$

Field data provided information of actual probe wear rate to estimate its effect in signal amplitude. Measurements of the three-TWH acceptability test from each set of calibration-tube runs were preformed over the course of probe life. These measurements showed a gradual evolution of the (maximum – minimum) voltage difference, which was expressed as a function of the number of tubes scanned between measurements. The sum of a series of narrower distributions for earlier stages of probe life to the end-of-life produces a centrally peaked distribution of the probe's life time. The calculated standard deviation in this case was 0.5, resulting in an eccentricity error estimate of $\Delta V = 0.085V_0$.

An additional source of error for array probes such as the X-Probe is coverage effects, given that the measured voltage from a flaw depends on the location of the flaw relative to the maximum sensing area of the detecting unit in the array. This variability affects the repeatability and accuracy of the absolute and comparative flaw size estimation.

The following example illustrates the estimation of coverage error performed in our second case study. Laboratory measurements of coverage effects on various depths of OD pits (10-50% through-wall (TW)) were taken with a centred probe, by rotating the probe in 2 degree increments. Similar to eccentricity, half the range of the measured voltage corresponds to the maximum probe coverage error for a given depth of pit. Based on these measured data the maximum difference in signal amplitude relative to the maximized response from a detecting unit (i.e., no coverage error) can be expressed as the approximate linear function: $\Delta V = 0.112V_0$.

The above 11% error in measured voltage represents the worst possible case in terms of maximum coverage error. To assess the magnitude of the average error contribution from coverage, the distribution of coverage errors was estimated. With maximum error normalized to 1, an average bias of -0.349 with a standard deviation of 0.391 was obtained using a normal distribution fit. Combining the functional dependence of maximum coverage error with this expected deviation, gives a coverage error estimate of: $\Delta V = 0.044V_0$.

Sideways motion of the probe (probe-wobble) as it navigates through a tube also introduces lift-off noise. Similarly, the distortions introduced by the pilger manufacturing process, are detected by ET probes. This variability mostly affects the horizontal component of the signals; it has little effect on vertical signal amplidue (V_{mx}) and is, therefore, more relevant for phase-based sizing or V_{pp} measurements.

Human Factors (Human Errors)

Signal analysis is a skill-based activity that relies on the interpretation of indications by different analysts during each outage. In the calibration process, small differences in set-up will result in different estimations of flaw size. Choices made by an analyst during the set up of multi-frequency mixes (for instance selection of the window width, balance point, support-plate signal, etc.) results in slightly different outcomes for the process channel, which may result in different estimations of flaw size.

Often, ET data analysis procedures require calibration curves to be built based on flaws from the calibration tube. This practice can lead to inconsistencies between calibration curves built by different analysts, and between measurements from successive outages. Each scan of a calibration tube yields slightly different signals due to probe eccentricity, circumferential location of the flaws in the calibration tube, lift-off due to probe-wobble, etc.

To estimate the human factors error, reported voltages and sizing estimates made by the three levels of data analysts (primary, secondary and resolution) during inspections were compared for a large number of indications. The pair-wise analysts reports variability (primary-secondary, resolution-primary, and resolution-secondary), expressed in terms of root mean square difference (RMSD) was found to be consistent across various sizing bins for all three analyst combinations.

Physical Variability in Tubes, Environment and Flaw Morphology (Physical Properties Errors)

Calibration tubes must have the same material specifications as in-service tubes. However, when the material used to fabricate calibration tubes is obtained from different batches and manufactured by different companies, the tolerance allowance for wall-thickness, material properties, and reference discontinuity sizes can result in differences in flaw depth estimation. One approach to assessing these errors is to use the manufacturing tolerances, but often the tolerances are found to be significantly larger than the actual variation, so estimates based on as-built variations should be used where available. Better yet, if the same calibration tube can be used for subsequent inspections, the effect on accuracy of growth estimates will be null.

Another factor is the environment in which the flaws are located. Inside magnetite deposits found in CANDU® steam generator tubes have a shielding effect on probe sensitivity. These deposits are not uniform along the tube and their thickness increases with time. Also, a deposit-removing process between inspections can have a significant effect on probe sensitivity.

When flaws are found at support-structure locations, their signals are distorted by the support-structure signal. Multi-frequency mix algorithms are used during analysis to minimize these distortions, but their application may still produce residual noise affecting the accuracy of flaw measurements. Furthermore, changes in support structures, such as degradation due to flow-assisted corrosion, change the residual noise associated with the mixing process and, thus, the environmental condition of a flaw indication.

External deposits in the sludge pile region or at support plates (either conductive, ferromagnetic, or a combination of both) can have a significant influence on the detectability of flaws. Background noise from deposits can also distort flaw signals and affect sizing accuracy. However, only changes to these deposits (increases between inspections or removal processes, such as chemical cleaning or water lancing) affect the accuracy of flaw growth estimates.

The type of flaw and its morphology play a fundamental role in flaw sizing capability. In both cases studied, it was the primary source of error. As indicated above, bobbin probe techniques often use calibration curves built from calibration tube flaws, such as those from the ASME standard or rectangular-shaped simulated frets. However, such flaws do not always reflect the expected physical characteristics of service-induced flaws. An improvement over this methodology is to use manufactured calibration curves, which are built based on pre-assigned values of signal amplitude correlated to flaw depth. These pre-assigned values are based on depth measurements from

CANDU® CANada Deuterium Uranium is a registered trademark of Atomic Energy of Canada Limited (AECL).

Ultrasonic Testing (UT) field inspections or a series of laboratory manufactured flaws with the expected geometry.

The resulting calibration curves might have a bias that varies with depth, often resulting from the algorithm used by the data analysis software to construct the curves. Furthermore, the sizing error likely changes with depth, increasing the error of estimated growth.

The following example illustrates the error caused by the sizing curve itself. The X-Probe ET-estimated depths for Alloy 400 pit-like indications with V_{mx} responses of less than 1.0 V were compared to UT-measured depths. This comparison resulted in a 6.4% TW root mean square error (RMSE), with an average bias of -3.0% TW. Assuming UT values to be true, the 6.4% TW RMSE can be taken as the total expected error, which includes sizing curve, eccentricity, and coverage, in addition to other error sources such as flaw morphology, tube geometry and property variations, magnetite deposits, (all sources of proportional voltage errors) and analyst variability (a source of absolute voltage error). The average bias is the error of the calibration curve.

The effect from flaw morphology is illustrated by the case study where an amplitude-based sizing technique was used to estimate depths of flat-bar fretting wear with bobbin probes. Although double-sided wear signals are typically much larger than those from single-sided wear, they are indistinguishable from single-sided wear with the bobbin probe and, therefore, the same sizing curve is used in both cases, introducing a large sizing error. To assess the effect of double-sided fretting wear in the baseline case study, it was assumed that two double-sided frets occurred per hundred flaws. If ten double-sided frets occured per hundred flaws, the contribution of this effect would be a larger: introducing 10 (instead of 2) cases into the combined error distribution. This increased occurrence of double-sided frets adds less than one percent to the calculated error.

Also, changes in tightness (i.e., crack-face conductivity) and circumferential extent of stress corrosion cracks and inter-granular cracking need to be taken into account in assessing the accuracy of depth and growth estimates.

STATISTICAL ERROR PROPAGATION

The groupings of the first column in Figure 1 reflect an intuitive categorization by topic. The errors introduced are, in fact, handled differently depending on how they contribute to depth sizing. The common rule of thumb for overall variance (magnitudes of additive error effects are summed in quadrature, while multiplicative effects contribute by their fractional errors summed in quadrature) is complicated by the fact that the measured quantity, typically a voltage or a phase, is manipulated further to obtain depth and then combined with absolute depth errors. The error contributions in the figure are, therefore, regrouped in the second column according to the following propagation model.

Analytical Expression for Depth and its Partial Derivative

Depth sizing depends on voltage measurements evaluated through calibration curves, which are typically constructed based on reference flaws. The expression $D_0 = f(V_0)$ converts the idealized voltage into a depth estimate. However, given all the sources of errors discussed earlier, the actual measured signal amplitude (V) may differ from voltage (V_0) and, therefore, the true depth, D, will be erroneously sized as

$$D_0 + \Delta D = f(V_0 + \Delta V) + E_0 .$$

where E_0 are additional errors not dependent on voltage that may contribute to the overall sizing.

For small voltage errors, the voltage dependence of the depth error, ΔD, is

$$\Delta D = \left.\frac{\partial f(V)}{\partial V}\right|_{V_0} \Delta V + E_0 .$$

In these case studies, specific tabulated sizing algorithms used by analysts were approximated by an analytical expression, and the sizing error, due to ΔV, was evaluated at V_0. Different expressions would be obtained for other sizing algorithms.

Propagation of Errors

The depth estimate from eddy current measurements can be considered in terms of deviations from perfectly executed, noise-free measurements of an idealized flaw with ideal equipment, processed through a perfect calibration algorithm.

Error components, E_k, can, like the voltage-independent error, E_0, contribute to depth error directly: $D_0 + \Delta D = f(V_0) + E_0$ or by way of the measured voltage: as a fixed value, as a fraction of the total voltage, or through a higher-order relationship. The general form is then

$\Delta D = E_0 + f(V) - D_0$ with $V = V_0 + E_1 + E_2 V_0 + E_3 V_0^{\,2} + \ldots$,

where each $E_{k>0}$ is the sum of all error components contributing to the voltage term of order (k-1).

Incorporation of the error parameters into the overall uncertainty, ΔD, makes use of partial derivatives with respect to E_k , which may, in turn, require application of the chain rule for differentiation, giving

$$\frac{\partial(\Delta D)}{\partial E_k} = \frac{\partial f(V)}{\partial V} \cdot \frac{\partial V}{\partial V_0} \cdot \frac{\partial V_0}{\partial E_k} \quad \text{for } k \neq 0, \text{ and } \frac{\partial(\Delta D)}{\partial E_k} = 1 \text{ for } k = 0.$$

The error propagation law [4] describes a transformation in which the row matrix of partial derivatives for each error component,

$$F = \left[\left(\frac{\partial(\Delta D)}{\partial E_k} \right)_1, \left(\frac{\partial(\Delta D)}{\partial E_k} \right)_2, \left(\frac{\partial(\Delta D)}{\partial E_k} \right)_3, \ldots \left(\frac{\partial(\Delta D)}{\partial E_k} \right)_n \right],$$

and its transpose, F^T, act on the variance-covariance matrix, C_X, to give the covariance of the output quantity, C_Y , by the relationship,

$C_Y = F C_X F^T$.

The error sources discussed here are linked to the analysis by the partial derivatives

$\frac{\partial(\Delta D)}{\partial E_k}$ for k= 0, 1, or 2,

depending on their position in the upper, middle, or lower grouping, respectively, in the second column of Figure 1. They form the variance-covariance matrix, of which the diagonal elements are the variances of each effect, $\sigma_i^{\,2}$. Off-diagonal elements are the covariances, σ_{ij} , but since the error sources discussed so far are uncorrelated, the $i \neq j$ elements are all zero. Matrix multiplication by F and its transpose will give the overall variance in sizing. Note that F depends on the mean V_{mx} for the specific flaw depth, which means that the calculated error will vary with depth.

ACCURACY OF DEPTH ESTIMATES

The calculations give the covariance of the output quantity, and the square root of this is the standard deviation, quoted here as the uncertainty. For the fretting-wear case, the sources of error, their analytical form, and the values assigned to each, give an overall uncertainty of just over 5% TW extent over the depth range studied, as shown in Figure 3.

Field data analysis from the same time period gave 4.8% RMSE relative to UT depth measurements for a small sample set of 10 flaws between 16% and 43% TW depth. This analysis provides an indication that the magnitudes of the main individual errors and their mathematical propagation, as calculated in the study, are reasonable.

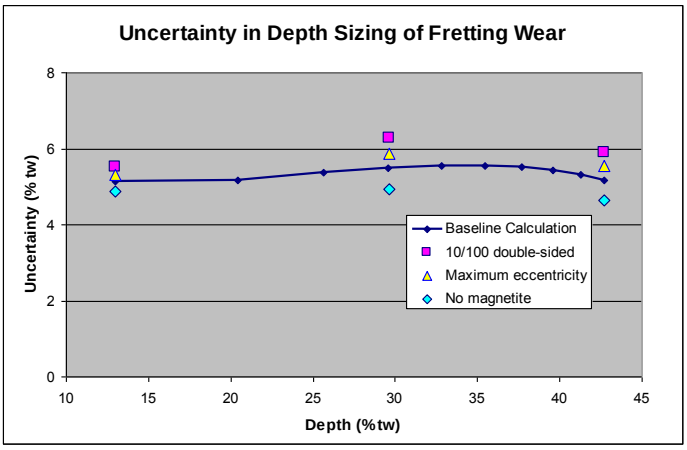

Figure 3 Calculated uncertainty in sizing for the case study of flat-bar fretting. Connected points represent the baseline calculation for the case study. Larger symbols show the sensitivity to various effects: more frequent double-sided wear, worst-case eccentricity, and absence of magnetite.

Accuracy of Growth Estimates from Signal-to-Signal Comparisons

Flaw growth rates, important in determining plugging criteria that optimize life management strategies, require comparison of successive depth measurements. A worst-case error for the difference measurement can be obtained by taking the square root of the sum of the squares of the two measurement errors. For the flat-bar fretting-wear case study, this calculation leads to a large error on a relatively small growth number, which results in a very large fractional error on the growth assessment.

If the objective is signal-to-signal comparison for growth assessment between Time 1 and Time 2, error components that are common between the two successive measurements may be excluded from the analysis. This is illustrated schematically in Figure 1, where error estimates at Time 1 and Time 2 are combined without their correlated components to obtain an error on the difference. Analyst variability, probe eccentricity, probe wobble, and magnetite thickness will continue to contribute independently to the errors, but other items, such as calibration curves and flaw morphology, may be correlated.

The covariance matrix for the error on the difference is built from the same error components as the one for error on the depth, but with each component appearing for both an initial and a final value. When the covariance matrix for the error on the difference is constructed, off-diagonal terms corresponding to correlated errors negate the contribution of those errors to the variance of the difference. The matrix elements occur twice along the diagonal and twice off diagonal. The first, second, seventh, and eighth rows represent the correlated quantities in the first measurement, and the eleventh, twelfth, seventeenth, and eighteenth rows represent the same quantities in the second measurement, providing zeroes in the off-diagonal elements. In this hypothetical example, two values corresponding to 20 and 35% TW depth are used for Time 1 and Time 2, respectively. The resulting through-wall depth error on the difference is calculated as 4.3% TW is relative to 15% TW growth (i.e., the growth estimate for this case is 15±4.3% TW). If the estimates had not been corrected for correlated errors, the results from the errors at those two depths, $\sqrt{(5.18\%)^2 + (5.55\%)^2} = 7.6\%$, would suggest the growth estimate was nearly twice as uncertain.

REALITY CHECK

A comparison of fretting-wear depth estimates from two successive inspections gives a data set for growth assessment. Only flaws deeper than 12% through-wall in the first inspection and unambiguously identified in the second are included in the comparison. The difference of the two data sets gives the distribution of growth estimates shown in Figure 4.

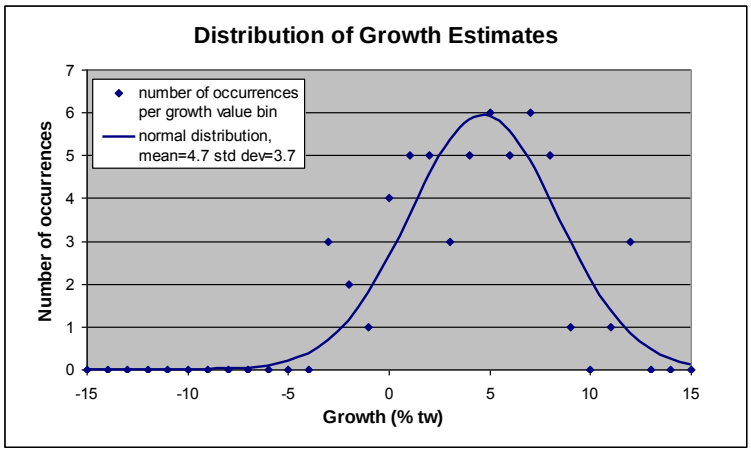

Figure 4 Distribution of growth estimates from the data of two successive inspections.

These growth values have a mean of 4.7% through-wall depth and a standard deviation of 3.7%. The standard deviation is close to the 4.3%, calculated as the error on the difference in this case study. The observed spread in growth estimates and the calculated accuracy for growth analysis are very similar, suggesting that the actual growth rates are consistent and that the observed spread is largely due to the estimation error. The small negative "tail" of the growth distribution, which extends to values that are physically impossible, but statistically expected for the estimation process (i.e., negative growth) provides an additional check on the calculation.

CONCLUSIONS

Error sources affecting eddy current sizing estimates were considered and analytical expressions developed for their effect on depth estimates. Two simple case studies in steam generators were used to model the analysis process. For each error source, the distribution of field data was assessed and propagated through the analytical expressions. The calculated magnitude of the sizing error in both cases was consistent with historical sizing accuracy from field data relative to depths from UT. In both cases, the largest error contributions came from the sizing curves and flaw morphology, with a smaller contribution from probe eccentricity and coverage in the case of the X-Probe.

The analysis of the error on growth estimates from signal-to-signal comparison gave values smaller than growth estimates. With the absolute and difference error equations, variance-covariance matrices, and partial derivatives established, additional calculations can be performed as needed. Changes in the identification of correlated effects, the magnitude of errors, and the analytical form of voltage response can be made easily. The calculated errors on growth can be used in reducing conservative estimates on plugging limits and the sensitivity analysis can be used to optimize inspection techniques.

REFERENCES

1) Horn D, Obrutsky L and Lakhan R, "NDE Errors and their Propagation in Sizing and Growth Estimates", 6th CNS International Steam Generator Conference, Toronto, Canada, 2009 November 8-11.

2) "EPRI Pressurized Water Reactor Steam Generator Examination Guidelines: Revision 7", EPRI 1013706, 2007 September.

3) Cecco V S, Van Drunen G and Sharp F L, "Eddy Current Manual", Volume 1, AECL-7523 Revision 1, 1981.

4) Arras K O, "An Introduction To Error Propagation: Derivation, Meaning and Examples of Equation $C_Y = F_X C_X F_X^T$", Technical Report Nº EPFL-ASL-TR-98-01 R3 of the Autonomous Systems Lab, Institute of Robotic Systems, Swiss Federal Institute of Technology, Lausanne, 1998 September.

POD CALCULATION ON A RADIOGRAPHIC WELD INSPECTION WITH CIVA 11 RT MODULE

D. Tisseur, M. Costin, CEA - LIST, France
S Fournier, C. Reece, EDF - CEIDRE, France
A. Schumm, EDF - R&D, France

ABSTRACT

The increasing use of simulation in Non-Destructive Testing (NDT) relies on its potential for optimization, qualification or demonstration of the performance of the techniques used. The CIVA [1-6] software platform, developed by CEA-LIST and partners, gathers simulation codes for three major NDT techniques: Ultrasonic testing (UT), Eddy Current testing (ET), Radiographic testing (RT). A new feature has recently been introduced in the CIVA 11 RT module: the Probability of Detection (POD) calculation. POD approaches are commonly used in the industry to determine a confidence level of the performance limits of a given NDT inspection. CIVA now offers POD calculations based on hundreds of different configurations in a few hours. RT inspection usually relies on visual interpretation of Radiographic films by NDT specialists. For automated POD calculations, CEA-LIST has developed two quantitative detection criteria based on a contrast to noise ratio in relation to the defect size. This paper presents an example of a POD calculation for a weld inspection of the secondary circuit of a nuclear power plant. In this case-study, the typical flaw is a thermal fatigue crack in the root of the weld with a circumferential orientation. Simulations taking into account the different weld geometries, the source and the crack positions in the weld have been conducted. POD calculations with CIVA allow comparing these simulations results with the two detection criteria. The results of this study show a good agreement with the EDF operational experience.
Keywords: Radiography, probability of detection, POD, CIVA, simulation, detectability criterion
PACS: 28.41.Ak

INTRODUCTION

NDE techniques are used mainly during inspection of nuclear components for maintenance operations.
For safety reasons, we need to know the performances of these NDE techniques. Simulation can be a powerful tool to evaluate the performances of NDE techniques. The NDE inspection performance depends on the influence several influential parameters, which needs to be quantified.
One way is to evaluate the performance of a NDE is the deterministic approach, which consists in adding the impact of these influential parameters algebraically in order to obtain the worst case performance of the NDR. Another is a probabilistic approach, such as Probability of Detection (POD) approaches that are commonly used in industry to determine a confidence level for a given NDT/NDE inspection. Since 2010, CIVA 10 [7-8] had developed a POD simulation tool for UT and ET techniques. This tool was introduced in CIVA 11 RT module. The aim is this study is to estimate, by a statistical approach, the influence of several parameters' variation range on a weld inspection. In a first part, we describe the NDE weld inspection with the influential parameters studied. Secondly, we present POD modelling in CIVA. And finally, we present the POD results of a RT inspection.

WELD INSPECTION AND INFLUENTIAL PARAMETERS

For this study, we have chosen a RT inspection on a homogenous ferritic steel weld. Double wall exposure/single wall viewing technique are used, with the source and the detector positioned on a diameter, such that the radiation is incident normal to the axis at the center of the region of interest. The pipe is about 400 mm diameter. The inspection is performed with an Ir^{192} gamma source. The source position could be shifted from its nominal weld axed position from +/- 15 mm. By convention, the source is shifted by -15 mm when the source is on the left side of the weld so opposite to the more thick part. As we can at figure 1 the inspection area is +/- 25 mm from the weld axis on the weld root. Each shot allows the inspection of an angular sector of 38.85°.

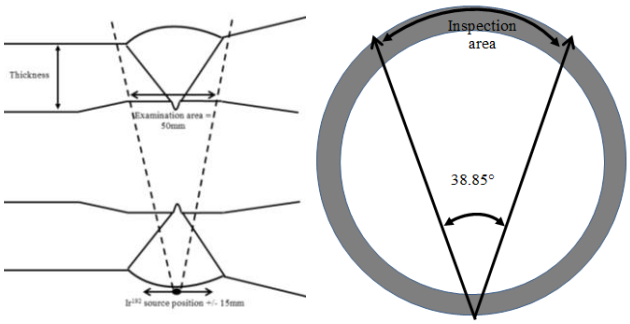

Figure 1: Experimental set up of the weld inspection.

Due to the angular sector and the pipe diameter, the POD simulation is divided into two parts:

- A first part with the source aligned on the detector (see figure 2 on the left)
- A second part with the source circumferentially misaligned (see figure 2 on the right)

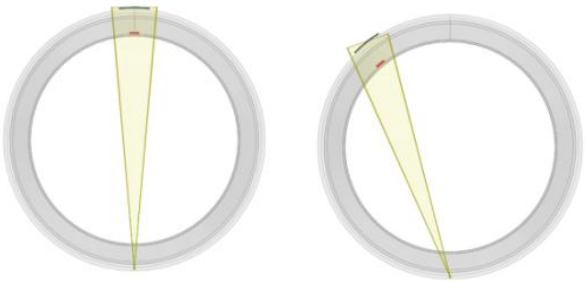

Figure 2: On the left, the source aligned on the detector. On the right, the source circumferentially misaligned

We consider 3 different welds thicknesses:

- Weld with maximum allowed thickness (24.1 mm)
- Weld with nominal thickness (21.4 mm)
- Weld with minimum allowed thickness (18.7 mm)

The typical flaw is a trapezoid shape defect as shown in the following figure.

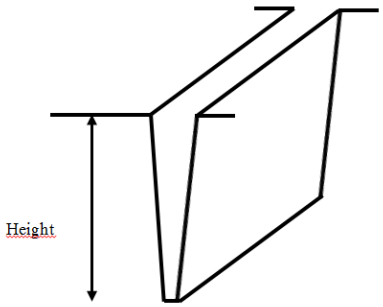

Figure 3: Typical flaw shape for the POD study

In this study, the main parameter is the flaw height. The aim is to determine the relation between defect height and probability of detection for this configuration.
The other influential parameters studied are:

- Gamma source positioning: - 15 mm, 0 mm, +15 mm
- Flaw positioning in the inspection area (uniform distribution from +/- 25 mm on the both sides of the weld axis)
- Weld geometries (maximum, nominal, minimum thickness)
- Inspection geometry (aligned, circumferentially misaligned)

POD MODELLING IN THE CIVA RT MODULE

POD curves are estimated in CIVA using the Maximum Likelihood Estimation methods recommended in the MIL-HDBK 1823A [11] for Hit-Miss and Signal Response data. The reader could find more details on ICNDE Yokohama proceedings [8].
The simulation-POD approach implemented in CIVA (see figure 4) follows the uncertainty propagation method which consists in:

- Defining a characteristic parameter for POD computation (typically the flaw size)
- Defining parameters to vary within the range of the studied procedure,
- Describing uncertainty distributions for each of the uncertain parameters,
- Launching computations corresponding to Monte-Carlo sampling of the uncertain parameters,
- Analyzing the resulting data set and compute POD curves.

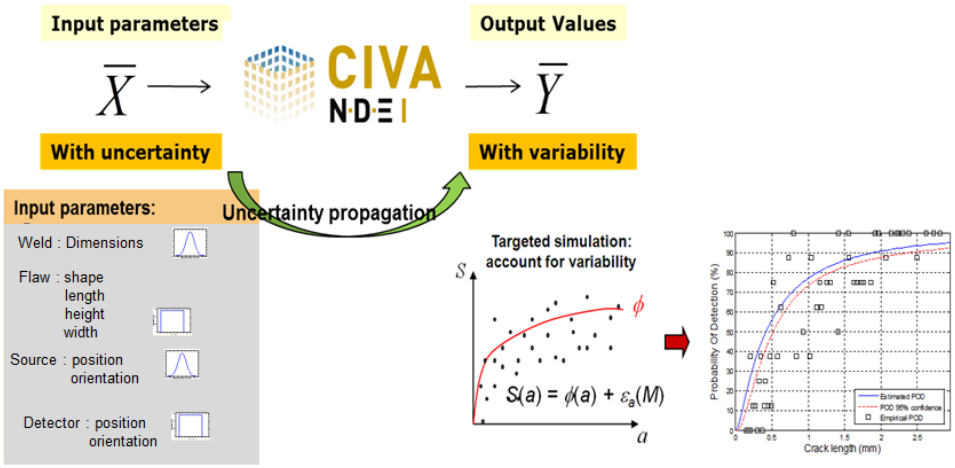

Figure 4: POD implementation on CIVA

For the radiographic technique, X/gamma ray film interpretation is based on human eye perception; thus there is no criterion of "universal" visibility / detectability. However, at least

one detectability criterion is required for an automatic POD study. In CIVA, several visibility criteria can be applied to POD calculations in order to establish quantitative comparisons and increase the reliability level of results. Detectability criteria are implemented in CIVA via a plug-in approach in order to easily cross results obtained with different detectability criteria on the same POD study.

Simple and classical contrast to noise ratio seems to be not sufficient to describe a detectability criterion**.** Two criteria are available in CIVA 11:

- A criterion based on the average contrast on a reference surface, named Ellipse criterion [9].
- A criterion based on the contrast to noise ratio balanced by the surface inspired by the Rose criterion [10], named Rose criterion.

POD curves are estimated using the Berens model. The conditions for the use of this model are:

- Linearity between characteristic parameter and detectability criterion
- Residuals present a normal distribution
- Standard deviation of residuals is independent of parameter characteristics

To comply with the Berens model, the Ellipse criterion response data must be fitted on a Log/Log scale. As we can see at figure 5, with Ellipse criterion signal response is linear with flaw height on linear/linear scale and log/log scale. But residuals distributions are more independent of characteristic parameter with a log/log scale representation.

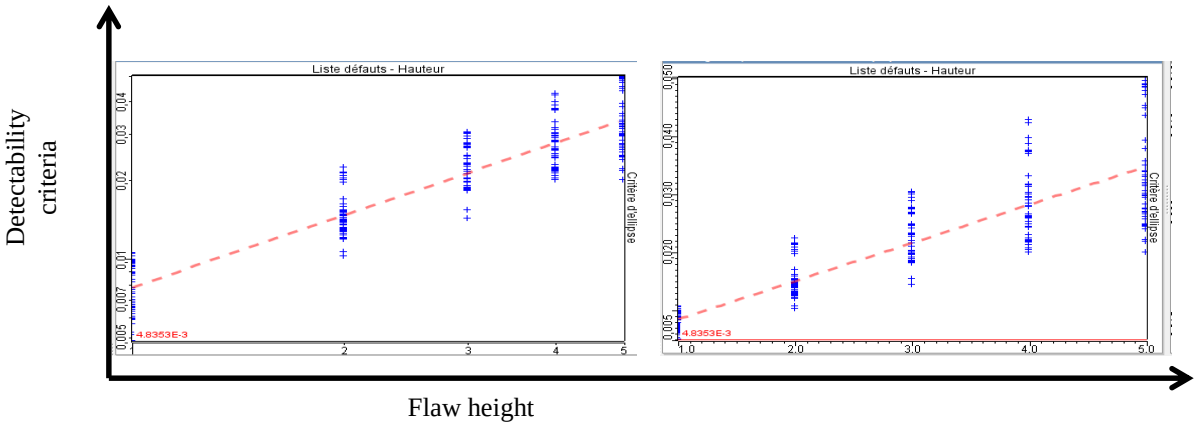

Figure 5: Ellipse criteria response data distribution with log/log (on the left) and linear/linear (on the right) scale representation

To comply with the Berens model, Rose criterion response data must be fitted on a linear/linear scale. As we can see at figure 6, with Rose criterion signal response is linear with flaw height on linear/linear scale and log/log scale. But residuals distributions are more independent of characteristic parameter with a linear/linear scale representation.

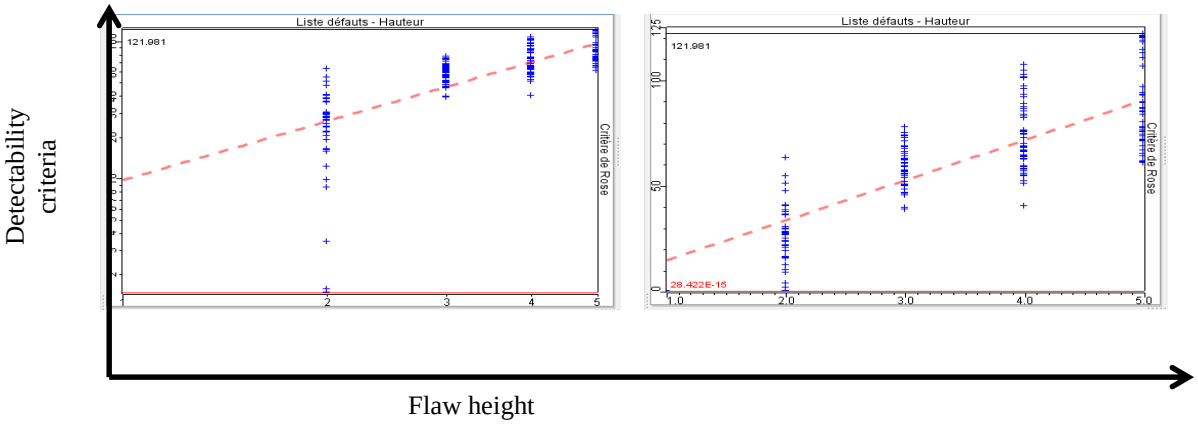

Figure 6: Rose criteria response data distribution with log/log (on the left) and linear/linear (on the right) scale representation

After describing POD modeling and detectability criteria, the following part presents results obtained on our study case.

POD RESULTS

In this POD study, we used the fusion approach of scattered and transmitted images respectively from Monte Carlo and analytical computations to simulate the final images [12]. The detector model developed by EDF [13] is based on the European standard EN 584-1 [14] and converts the incident dose into an optical density value. A decomposition of a volumetric source into several small source points allowed the simulation of the source blurring. Detector response has been estimated experimentally [15] and included in the model via a modulation transfer function approach.

For each POD study, we carried out 100 simulations for 6 different heights of defects (0.5 mm, 1.25 mm, 2 mm, 2.75 mm, 3.5 mm and 4.25 mm).

In the following results, we have extracted the a90/95 value. This value is the flaw height with 90% chances to be detected with a 95% reliability as presented in figure 7.

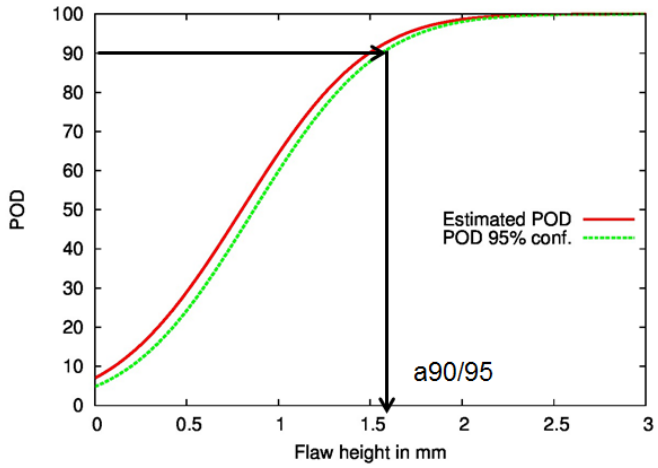

Figure 7: Example of POD curve and extraction of the a90/95 value.

Tables 1 and 2 summarize the results of the POD simulations.

Axed position	Weld max		Weld nominal		Weld min	
	a90/95 ROSE	a90/95 Ellipse	a90/95 ROSE	a90/95 Ellipse	a90/95 ROSE	a90/95 Ellipse
Axed	1.57	1.61	1.48	1.49	1.41	1.37
-15 mm	1.45	1.45	1.37	1.37	1.29	1.27
+ 15 mm	1.13	1.18	1.04	1.12	0.96	1.02

Table 1: POD results for aligned. a90/95 value is the flaw height with 90% chances to be detected with a 95% reliability

Circumferentially misaligned	Weld max		Weld nominal		Weld min	
	a90/95 ROSE	a90/95 Ellipse	a90/95 ROSE	a90/95 Ellipse	a90/95 ROSE	a90/95 Ellipse
Axed	1.77	1.57	1.55	1.35	1.47	1.27
-15 mm	1.48	1.06	1.44	0.99	1.39	0.92
+ 15 mm	1.39	1.35	1.29	1.29	1.31	1.24

Table 2: POD results for circumferentially misaligned position. a90/95 value is the flaw height with 90% chances to be detected with a 95% reliability

POD simulation curves provide in all cases a90/95 value lower than 2 mm. The POD module allows to compare the results of the extractions obtained with 2 criteria. Excepting the case with the circumferentially misaligned geometry with a source shifted of 15 mm, the a90/95 values computed with the Ellipse or Rose criteria are similar. In the case of this non-symmetric shape of the weld, the optical density image exhibits an important gradient. As ellipse criterion is more sensitive to image gradient than Rose criterion, the differences between Rose and Ellipse criteria results are the most important here.
The a90/95 values are higher than those for the case of the source shifted from -15 mm in comparison with the source shifted from + 15 mm. This is due to the non-symmetric shape of the weld. When the source is shifted from -15 mm the crossed thickness is more important (see figure 1). Rose criterion gives a better 90/95 value in the case of the aligned geometry compared to the misaligned case. But Ellipse criterion gives a better a90/95 value in the case of the circumferentially misaligned geometry. From an experimental point of view, the circumferentially misaligned geometry is the most penalizing geometry for detection, but Ellipse criterion is more sensitive to the optical density image gradient.

CONCLUSIONS AND PERSPECTIVES

This study presents an example of POD calculations with the new CIVA 11 RT Module for a weld inspection. POD simulations were performed with 2 criteria that can be easily compared each other. Results show a good agreement between the two criteria. As Ellipse criterion is quite sensitive to the optical density image gradient, POD results obtained with Ellipse criterion have to be interpreted with care. Work is under progress to improve the RT POD module in order to: - include directly source position and weld thickness as uncertain parameters,

- add new detectability criterion.

REFERENCES

1. http://www-civa.cea.fr
2. R. Fernandez, A. Schumm, J. Tabary, P. Hugonnard, “Simulation studies of radiographic inspections with CIVA”, in 17th WCNDT, Shanghai (2008).
3. J. Tabary, P. Hugonnard, A. Schumm, R. Fernandez “Simulation studies of radiographic inspections with Civa", in COFREND 2008
4. A. Schumm, O. Bremnes, B. Chassignole, "Numerical simulation of radiographic inspection: fast and realistic results even for thick components", in Proceedings of the 16th world conference of Non-Destructive Testing, Montreal (2004)
5. O. Bremnes, B. Chassignole, O. Dupond, A. Schumm, "Experimental And Simulation Studies Of Radiographic Inspections Of Pressure Vessel Reactors" in ECNDT London 2006
6. F. Mathy, C. Poidevin, G. Cattiaux, T. Sollier “Radiographic testing simulation with CIVA-RX – assessment on representative nuclear components”, in ECNDT Moscow 2010
7. C. Reboud, G. Pichenot, S. Paillard and F. Jenson,“Simulation and POD studies of riveted structures inspected using Eddy Current techniques”, Proceedings of the 14th International Workshop on Electromagnetic Nondestructive Evaluation, Dayton, 2009, Electromagnetic Nondestructive Evaluation (XII).
8. F. Jenson, E. Iakovleva and C. Reboud, "Evaluation of POD Curves Based on Simulation Results", 7th International Conference on NDE in Relation to Structural Integrity for Nuclear and Pressurized Components, 12-15 May 2009, Yokohama, Japan
9. A. Bonin, B. Lavayssière,“New Advances in the Development of MODERATO”, WCNDT 2000
10. Debbie Stokes, “Principles and Practice of Variable Pressure/Environmental Scanning Electron Microscopy (VP-ESEM)”, John Wiley & Sons, 2008.
11. MIL-HDBK-1823, “Department of Defense, Handbook: nondestructive evaluation NDE system, reliability assessment, 30 april 1999.
12. R. Guillemaud, J. Tabary, P. Hugonnard, F. Mathy, A. Koenig, A. Glière, "SINDBAD: a multipurpose and scalable X-Ray simulation tool for NDE and medical imaging", in PSIP 2003, Grenoble, France (2003).
13. A. Schumm, U. Zscherpel, “The EN584 standard for the classification of industrial radiography films and its use in radiographic modeling”, in Proceedings of the Sixth

International Conference on NDE in relation to structural integrity for nuclear and pressurized components (2007).
14. EN 584-1:2006, "Non-destructive testing – Industrial radiographic film – Part 1: Classification of film systems for industrial radiography", European standard for non-destructive evaluation
15. NF EN 13068-1:2000, “Radioscopic testing - Part 1: quantitative measurement of imaging properties.”, European standard for non-destructive testing.

OBSERVER POD FOR RADIOGRAPHIC TESTING

D. Kanzler, C. Müller, M. Bertovic, U. Ewert, BAM, Germany
J. Pitkänen Posiva Oy, Finland

The radiographic testing is an important non-destructive testing method, especially in industrial areas where people could be injured in case of failing of a component. There it is a mighty method to find volumetric defects. As bigger the penetrated length of the defect in the component is, as bigger is the radiographic contrast. The detectability of volumetric defects in its turn is not only depending on the contrast but also on the noise, the defect area and its shape. The currently applied POD approach uses mostly only the contrast and the noise as detection threshold. This does not reflect accurately the results of evaluations by human observers. A new approach is introduced, using the widely applied POD evaluation and additionally a detection threshold depending on the area of the defect.
The presentation shows the process of calculating the POD curves with simulated data by the modeling software aRTist and with artificial reference data. This approach was developed within a joint project with the company POSIVA, which is constructing a final depository for high active nuclear fuels in Finland. Radiographic testing is one of the NDT-methods they use to test the electron beam welds of the copper canisters. The copper canisters will be used in the depository as a corrosion barrier within the waste management concept.

Keywords: Reliability; Radiographic Testing; POD;

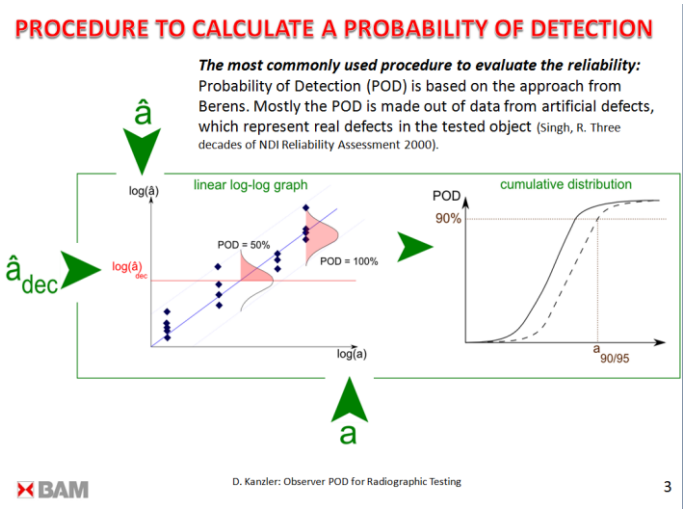

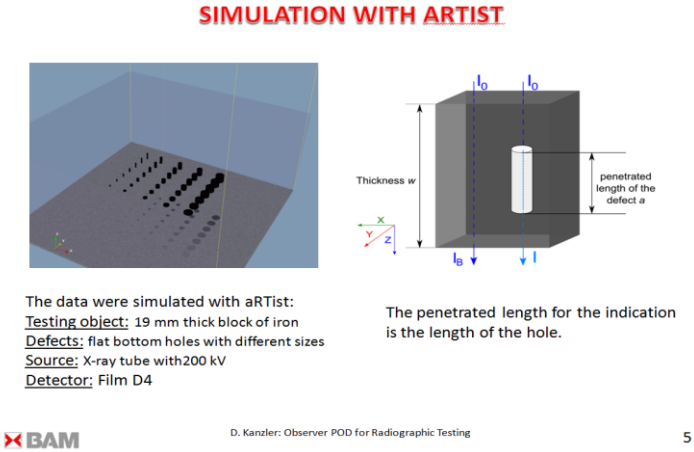

DETECTION THRESHOLDS (1)

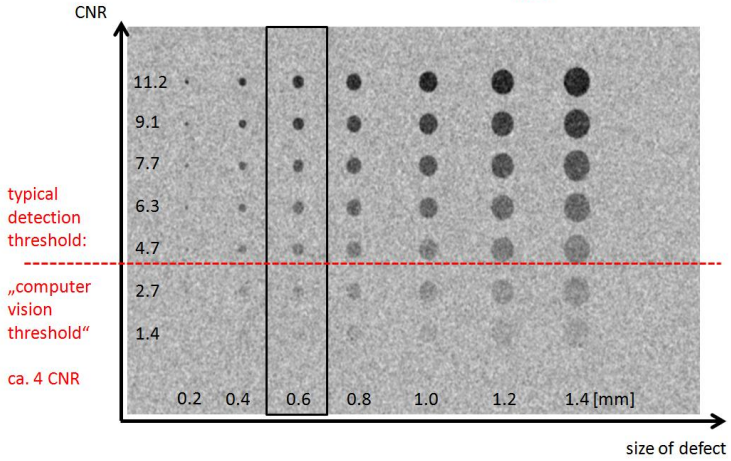

POD: RADIOGRAPHIC TESTING

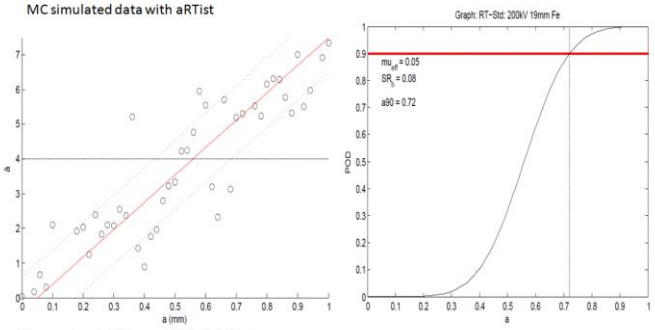

â = contrast of the artificial defects
a = penetrated length of the defect

DETECTION THRESHOLDS (2)

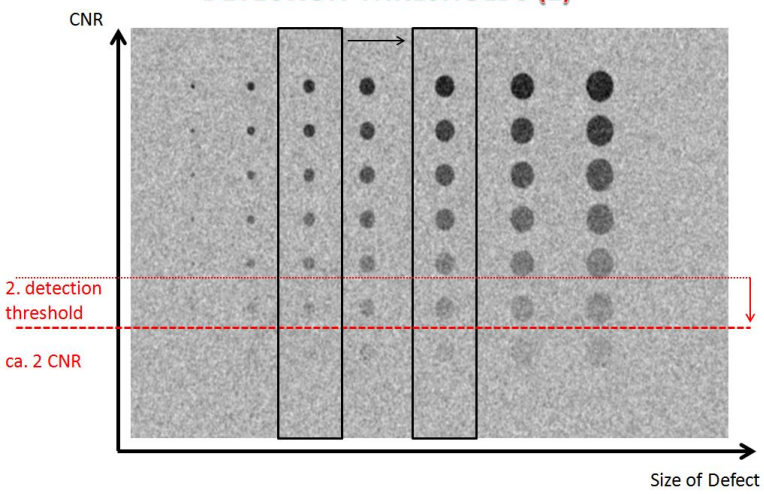

POD: RADIOGRAPHIC TESTING

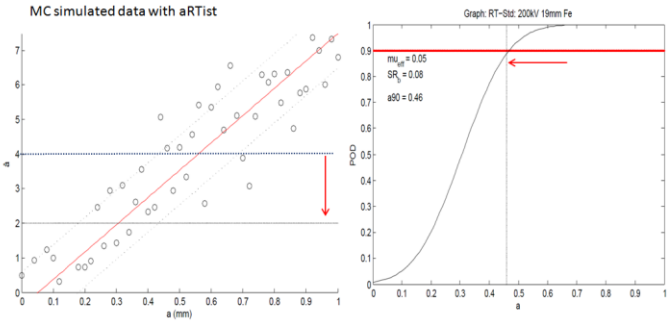

â = contrast of the artificial defects
a = penetrated length of the defect

DETECTION THRESHOLDS

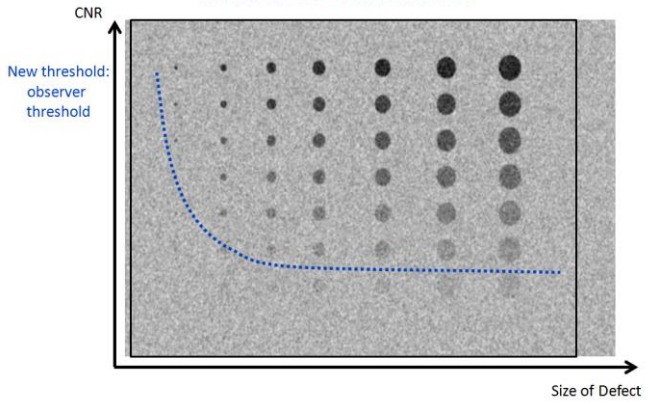

VERIFICATION THROUGH EXPERIMENTS

Experimental results for the detection threshold from evaluating 50 pictures per diameter.
The pictures were created by aRTist.

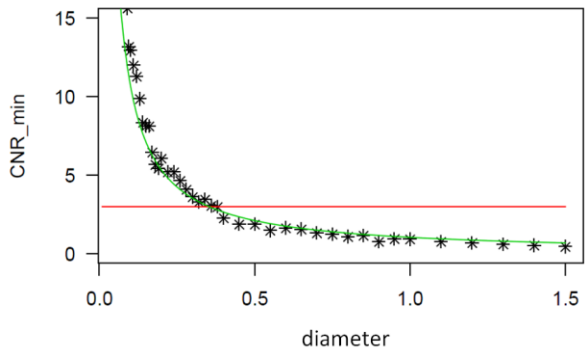

ROUND ROBIN EYE-TRACKER EXPERIMENTS

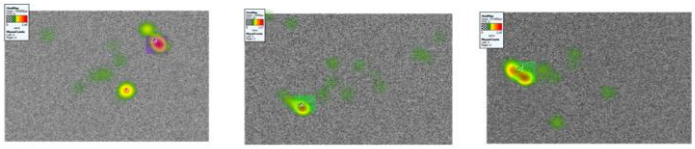

small diameter:
- Scattered searching pattern
- Difficulty in decision making
- Misinterpretation
- Not everyone found it

medium diameter:
-More concentrated searching pattern
-Fast identification/decision making

large diameter:
- Concentrated search
- Realizing of contours (fixations concentrated around the indication)

THEORY: DETECTION THRESHOLD FOR RT-POD

$$POD_{hole} = f(Th_{dec}, a_{RT})$$

$$Th_{dec} = f(diameter_{hole}, \hat{a})$$

$$CNR_{min} = \frac{PT \cdot SR_b^{image}}{diameter_{hole}}$$

Th_{dec}: Detection threshold
a_{RT}: penetrated length
$diameter_{hole}$: Diameter of the hole
CNR: $\hat{a}$
PT: Factor for the perception threshold (f.e. 10)
SR_b^{image}: basic spatial resolution in the image
CNR_{min}: minimal visible contrast noise ratio

Berens, A.P.: *NDE reliability data analysis. Metals Handbook (9th edn), Vol. 17, 1989, 689–701.*

Burgess, A. E.: The Rose model, revisited: Brigham and Women's Hospital and Harvard Medical School, Boston Massachusetts, Optical Society of America, 1999, 633-646.

Ewert, U.; Zscherpel, U.; Heyne, K.; Jechow, M. & Bavendiek, K.: *Image Quality in Digital Industrial Radiography* Material Evaluation Vol. 70, Nr. 8, 2012, 961-970.

DETECTION THRESHOLDS

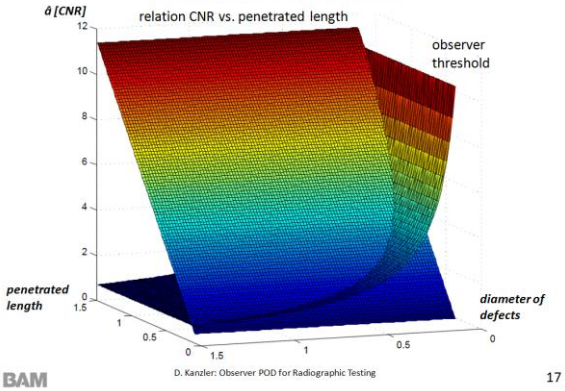

OBSERVER POD OF STEP HOLE IQI

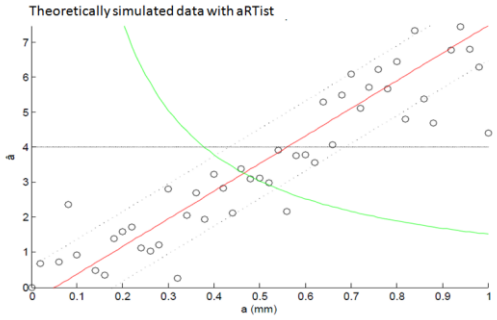

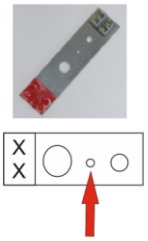

Step hole IQI for volumetric defects
ASTM E1025
EN ISO 19232-2
(EN 462-2)

â = CNR
a = penetrated length = Diameter

OBSERVER POD

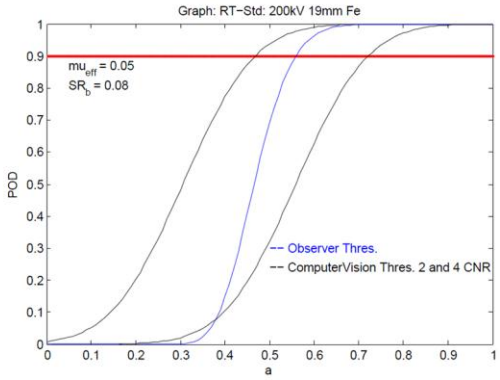

SUMMARY & CONCLUSION

- In addition to the CNR the size of the indication has influence on the probability of detection
- The observer threshold is using the dependency of the indication size to improve the POD (The POD will not be better but nearer to the real POD)
- With different experiments and approaches the observer threshold was verified.

Further experiments are planned to use the observer threshold for more complex geometries and for real defects.

A LEGACY OF PROBABILITY OF DETECTION (POD)

W. D. Rummel, D&W Enterprises, USA

ABSTRACT

The introduction of fracture mechanics was a revolution in engineering materials and structures design, life cycle management and risk analysis. Practical use of fracture mechanics requires integration of quantitative nondestructive evaluation (NDE) as a key element in design and service life management. The requirement for quantification of NDE was a revolution in NDE technology. In the United States of America, the National Aeronautics and Space Administration (NASA) "Space Shuttle" program incorporated fracture mechanics and damage tolerant design. I led a NASA program to assess and quantify crack detection capabilities for the NDE methods to be applied to Space Shuttle materials. The result was development of the Probability Of Detection (POD) as a rigorous metric for assessing crack detection capabilities.

Although rigorous POD assessment is useful and is specifically applicable in some applications, it is not practical in many applications. The legacy of POD is not in general applications, but in providing a framework and basis for many developments and assessments that support both a multitude of applications and practices for risk assessments in modern engineering structures and systems.

This paper describes some of the lessons learned and a suggested path forward for integration of NDE engineering into support and management of damage tolerance structures and systems. Key issues are in integration of materials science and engineering practices in NDE engineering; improvements in NDE system calibration; requirements for validation of NDE procedures; and emphasis personnel training and skills development for NDE craftsmen.

INTRODUCTION:

The development and application of damage tolerant/fracture mechanics technology was a milestone in improving structures design efficiencies, failure prevention, maintenance and risk analyses. One of the major requirements for implementation was quantification of the condition / damage state of materials, structures and systems on entry into service and throughout useful service life. Nondestructive evaluation (NDE) was the traditional method of condition assessment but results were rarely quantified. Quantified NDE was integrated as an essential element of damage tolerance. Although many applications of NDE had been validated in specific industries and service usage, most had been initially developed for purposes of process control and large margins were used to address risks. Increased design efficiencies and a multitude of new applications shifted focus to the capabilities of NDE. Myths, misconceptions, misunderstandings and false confidence in the capabilities of NDE had grown. Supporting data were required to take advantage of the benefits of implementing the advancements in damage tolerant design practices [DOD, 1974].

A pioneering program was initiated by the National Aeronautics and Space Administration (NASA) to support implementation of fracture mechanics technology on the Space Shuttle program [Rummel, 1974]. 2219 aluminum alloy had been selected as a primary material. Tightly closed fatigue cracks were selected as a potential damage mechanism. Two representative thicknesses were cut, with the grain rolling in both directions, to fabricate representative test panels.318 fatigue cracks were grown in random locations on both sides of 119 panels. The cracks had multiple aspect ratios and were distributed in size from 0.004 to 0.500 inches. Starter notches were removed by machining to produce representative surfaces finishes.

The test panels were then inspected by three different, skilled operators using production X-radiography, ultrasonic shear wave, eddy current, and high sensitivity fluorescent penetrant procedures. Detection results were recorded as "HIT / MISS" by panel number, and location on the panel.
All panels in the test set were then lightly etched to remove residual machining effects. Inspections of all panels were then repeated and documented (three operators, all NDE procedures). All panels in the test set were proof loaded to 70% of the nominal strengths. Inspections of all panels were then repeated and documented (three operators, all procedures). All cracks in all panels were then broken open, their size (length and depth) measured, and all data tabulated. The program sequence is shown schematically in Figure 1.

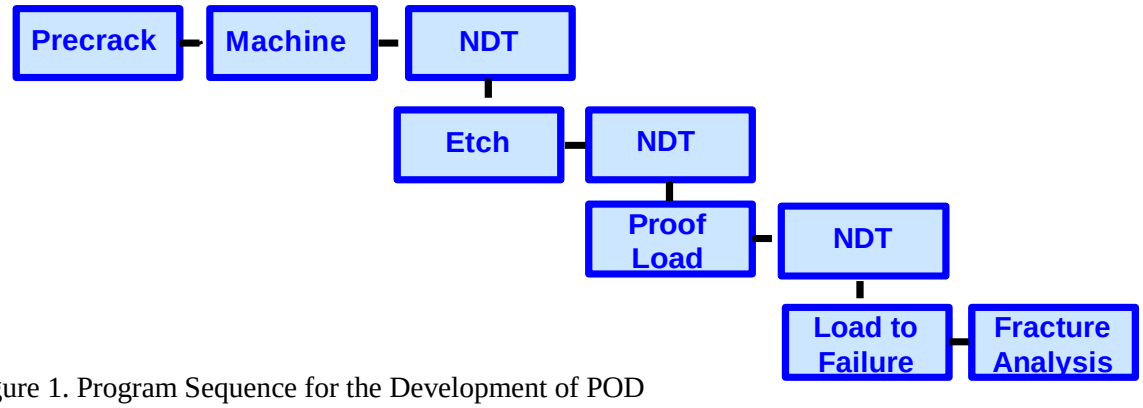

Figure 1. Program Sequence for the Development of POD

It was recognized that NDE procedures are the product of multiple variables and produces variable results. It was necessary to provide a quantitative output that could be used in fracture control analysis. The method that we selected was to order the data from the largest flaw in the data set to the smallest; combine the number of observations by counting down from the largest flaw to the smallest flaw in the sample group; do a point estimate calculation (hits divided by detection opportunities / binomial method); plot the calculated detection point at the largest size crack in the group; repeat the process for the next sample group and continue until the data were exhausted. The plotted result was a probability of detection (POD) curve as a function of flaw size. A lower 95% confidence was then calculated for each sample group data point using the methods described in MIL HDBK 5[DOD, 2003]. Visual examination of the various curves showed that the data were reasonably constant for larger flaws and each had an inflexion point at the 90% level and then rapidly decreased. The value selected to use for purposes of damage tolerance / fracture control analyses was the calculated lower 95% value at the location were the POD data plot passed through the 90% point. This descriptor was adopted by convention and is the 90/95 point that is referenced in the literature. An example plot from the original data is shown in Figure 2.

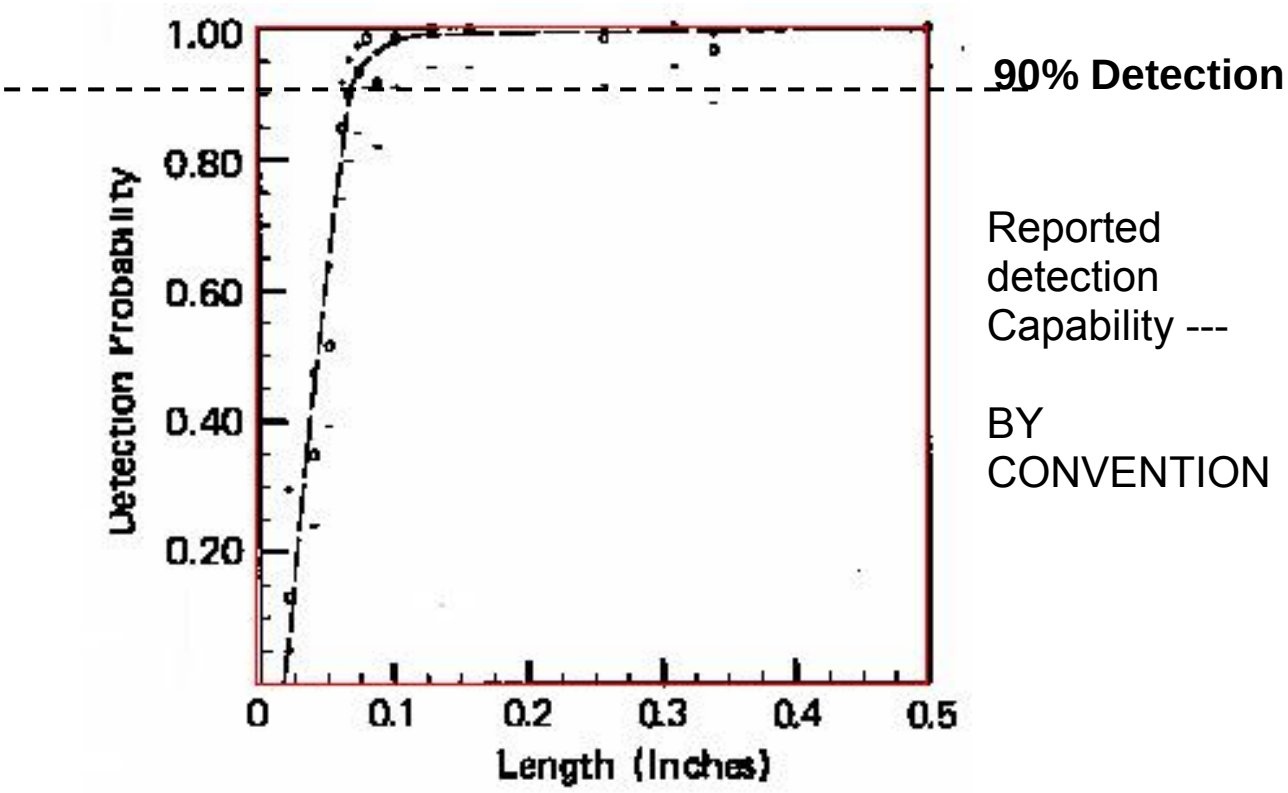

Figure 2. A POD PLOT FROM THE ORIGINAL NASA PROGRAM

This method is rigorous and provides a quantitative metric for the capability of the applied NDE procedure and test set. It is not a constant and varies with variations in test specimens, applied procedures and protocol. It is useful in the development and validation of procedures / NDE systems and in comparison of performance of different NDE methods. It is a measure of detection capabilities and is an essential element in NDE reliability assessments.

II. REACTION / POD RESPONSE

Advancements in damage tolerance and fracture control engineering methods and protocol have changed requirements for NDE applications in structures design, life-cycle maintenance requirements, and risk analyses. The need to quantify NDE capabilities in each damage tolerant structures application has changed requirements for NDE procedure development, validation and application. Note that change is resisted and threatens the status quo. Disclosure and publication of the original POD work generated multiple responses. The first responses were disbelief and attack. The work disproved many long held myths, beliefs, and misconceptions concerning NDE capabilities. Questions on many traditional and special purpose procedures were opened. The challenge was and is to understand the problem to be addressed and to integrate methods, technologies and skills that were outside of traditional NDE applications. The integrated elements have continued to emerge as “NDE Engineering”.

III. LESSONS LEARNED FROM POD DEVELOPMENT AND ASSESSMENTS

The legacy of POD was and is not a universally applicable method or procedure for determining the capability or reliability of an NDE procedure or procedure application, but is a framework and basis for many developments and assessments that support both a multitude of applications and practices for risk assessments in modern engineering structures and systems. Quantitative NDE is not required in all NDE applications. The major benefits of quantitative NDE are in quantifying "fitness for purpose", risk analysis, and quantified maintenance / revalidation of fitness for purpose of structures and systems (including retirement for cause). Figure 3 shows the role of quantitative NDE and engineering systems management.

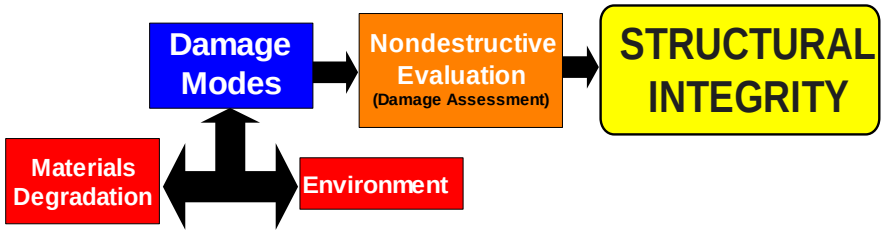

Figure 3. The Integrated Role of NDE in Structural Integrity

POD development provided a focus on parameters that constitute a useful and capable NDE procedure. Benefits have been in identifying and addressing those parameters and in challenging long held practices, beliefs, myths and expectations. A few of the findings include:

A. Understanding the problem and the requirements. Quantified design / fitness for purpose acceptance criteria are required. If quantitative NDE output is required, as a minimum, acceptance criteria must include:
   - Flaw type (damage condition)
   - Flaw size
   - Flaw location
   - Flaw origination
   - Nearest neighbor (combined conditions / indications)

B. The importance of selecting test objects / specimens that are representative of the population of objects / components that must be addressed by an NDE procedure. It is important to measure and document material properties of the specimens. Later the field test objects can be measured to validate the applicability of the procedure developed using "representative" specimens. Additional specimens, measurements and NDE engineering work may be required. [Caldwell, 2013].

C. The importance of "calibration" in development and application of NDE procedures. Indeed, many historical set-up / "calibration" procedures have been demonstrated to be inadequate for quantitative NDE applications. Multiple measurements over the range of expected flaw sizes and conditions are required. Note that a single point "calibration" is inadequate for quantitative NDE.

D. The importance of considering quantitative NDE as a multiple parameter measurement system is self evident in reviewing the initial and subsequent POD data and outputs.

- After an NDE measurement system has been "calibrated" and is stable, anomaly (defect) detection and discrimination, "accept / reject" (HIT/MISS) decisions may be based on an output / response signal that is above the (background) "noise" response. Note that "noise is NOT electronic noise, but is a combined (repeatable) low level response due to inherent properties of the test object material, shape, surface roughness, material grain structure, etc. Figure 4 and 5 show typical signal and noise response variances as a function of flaw size.

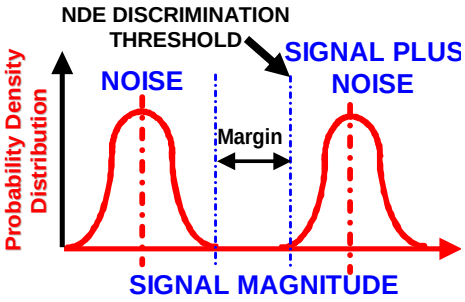

Figure 4. Clear Discrimination

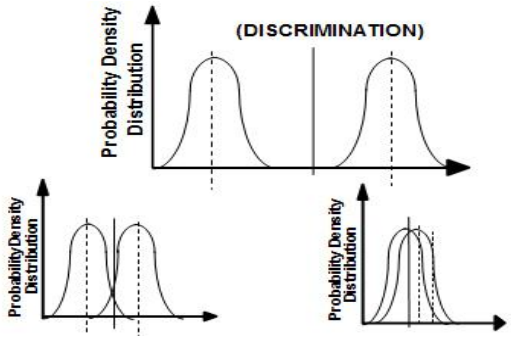

Figure 5. Reduced Discrimination at Smaller Flaw Sizes

The merger of two groups of normally distributed data may be described by a "log logistics" model was proposed for analysis of POD data by Berens [1997]. The form and requirements for use include:

- An increasing (near linear) signal response with increasing flaw size (below a saturation value)
- A near constant baseline noise
- Selection, application and documentation of a fixed NDE discrimination level

A typical data output form is shown schematically in Figure 6 and a POD result is shown in Figure 7. The a_{NDE} value is the value that is input to damage tolerance analyses.

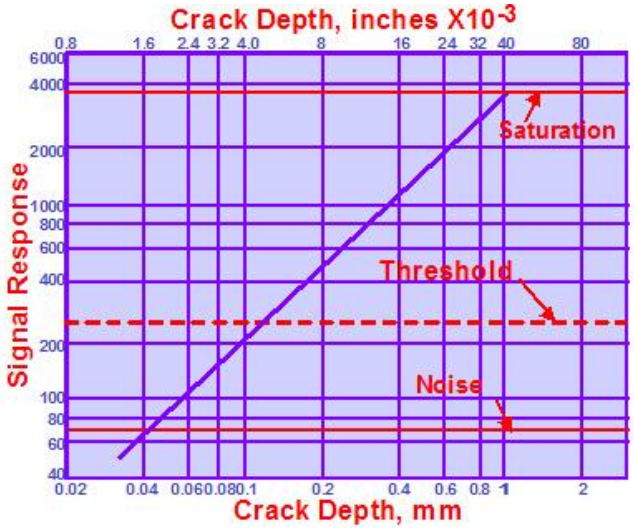

Figure 6. Data Form for the Berens Model

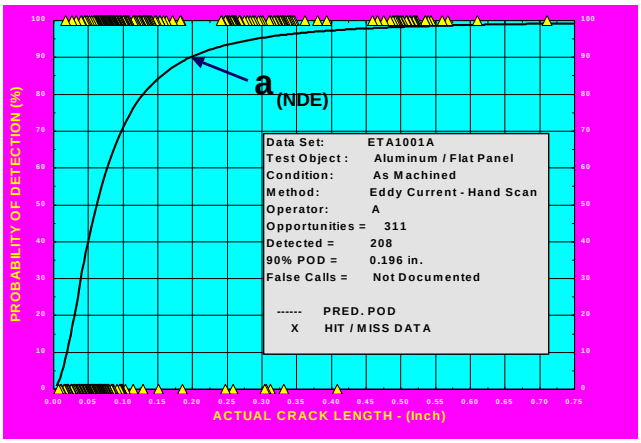

Figure 7 POD Output Using the Berens Model

The "Berens model" can be validated using the NASA data. The data includes visual image analysis and discrimination by energy field interrogations such as those used by eddy current and ultrasonic methods. The NASA signal data is characterized by the footprint of the interrogating field (probe) being large with

respect to the target / flaw size. Many NDE measurements and applications involve large target / flaw size with respect to the interrogating field. The output response may be near linear for smaller flaws, but may transition to a different form as the target flaw size increases. The Berens model has been widely used in NDE data analyses and has evolved as the basis for MIL STD 1823[DOD, 1999]. It is not applicable for analyses of all NDE data, but provides a useful template, protocol and constraints for NDE engineering and the development of procedures for many methods and applications. The Berens model spawned a large number of models and model types, including:

- Ray tracing
- Data analysis models
- Capability predictive models and
- Model assisted POD (Thompson)

The requirements, constraints and data form of models used in NDE procedures must be validated for each specific NDE procedure application [Aldrin, 2001; Thompson, 2008].

In the original NASA program application variables were identified as:

- ⟶ **Flaw (Artifact) Variables**
- ⟶ **Test Object Variables**
- **NDE Method Variables**
- **NDE Materials Variables**
- **NDE Equipment Variables**
- **NDE Procedure Variables**
- **NDE Process Variables**
- **Calibration Variables**
- **Acceptance Criteria / Decision Variables**
- **Human Factors**

Uncontrollable variables were identified as "flaw variables" and "test object" variables. The remainder were identified as "controllable variables." Traditional NDE focused on "human factors" and on "process control by quality assurance methods."Indeed, little attention had been given to development and validation of NDE procedures since the quantification had not been required and detection was assumed to be absolute or at the "calibration" level. Development of a new NDE procedure was usually based on previous experience or on used of a consensus procedure from one of the document selling organizations (SAE, ASME, AWS, ASTM, etc.). Consensus procedures can be useful starting points, but have rarely been validated.

Critical parameters to a reproducible and repeatable NDE procedure are:

- NDE measurement system
- Multiple point measurement system "calibration"
- Representative reference artifact (flaw) specimens
- Representative artifact signal response level and data form
- A stable and reproducible "noise" measurement level.
- A constant NDE acceptance threshold

Confidence level in the procedure application will vary with the number of artifact specimens in the data set and their representation of the population of artifacts to be detected. Important measurements that are critical to procedure development, validation and application include:

- Noise level (Assumed to be constant) measured range for both procedure validation and each application
- Signal level at target flaw / damage size and over the range of measurement requirements
- NDE threshold acceptance level
- Signal form (validation)
- Signal to noise level over the target range of measurements (validation)

Once a database has been established, measurement data may then be used to predict POD capabilities in similar applications – often referred to as the "Transfer Method"

Material properties of structures of the same design are not constant and variations are evident in NDE assessments. Limits to measured variations may be indicators of out of tolerance conditions are useful in assessing fitness for purpose. In like manner, NDE measurements may vary due to in-service loading, environmental conditions or unanticipated overload. Some adjustments to NDE measurement data and data form to accommodate predicted POD capabilities as a result of service conditions, stage in the service life cycle. For example, it is known that flaw signal response from a crack that has recently experienced and overload, will vary considerably from that measured at the time entry into service. This branch of NDE engineering has rarely been addressed and little data are available from field applications. [Corbly, 1969; Wooldridge, 1979 and 1980]. This accounts for some of the variations that have been observed in NDE measurements made during incremental maintenance assessments. NDE measurements may be the same, but the test object and target flaw responses will change and the results of NDE / flaw interactions will change. It is therefore obvious that POD is not a constant and adjustments to capability estimates are often required for in-service applications.

IV. SUMMARY

The legacy of probability of detection (POD) has been:

- To provide a metric and baseline framework for quantifying NDE capabilities.
- To challenge many long held assumptions, beliefs, myths, opinions and prior practices for NDE procedures applications
- To identify NDE applications as multi-parameter measurement procedures and critical parameters in procedures characterization
- To provide requirements for and protocol for linking design needs to NDE capabilities
- To provide data supporting analysis of risks, quantified inspection and maintenance scheduling and life-cycle fitness for purpose assessments

NDE engineering technology has developed as a special discipline that integrates a variety of science, mathematics, engineering skills and expertise. A substantial portion of that development has been directed to POD and NDE reliability. Integration of science, technology, and craftsman skills has identified a need for NDE engineering in each NDE application.

REFERENCES

1. Aldrin, J.C., "Overview of Mathematical Modeling in Nondestructive Evaluation (NDE)," R*eport NT-SP-O1-03,* Computational Tools, Gurnee, Illinois, November 2001.
2.Berens, A.P., "NDE Reliability Data Analysis, Nondestructive Evaluation and Quality Control, Quantitative Nondestructive Evaluation," *ASM Metals Data Book*, Vol. 17, 5th ed., ASM International, Materials Park, Ohio, December 1997, pp. 689–701.
3.Caldwell, Jeff, Michael Moles, Luke Robertson, Allan Hull and Anthony Sinclair, " Reference Discontinuities for Small Surface-breaking Cracks," *Materials Evaluation*, Vol. 71, No. 8, August 2013, pp. 929–935.
4.Corbly, D.M., P.F. Packman and H.S. Pearson, "The Accuracy and Precision of Ultrasonic Shear Wave Flaw Measurements as a Function of Stress on the Flaw," *Proceedings of the American Society for Nondestructive Testing Fall Conference*, October 1969.
5.DOD, *MIL-A-83444, USAF Damage Tolerant Design Handbook:Guidelines for the Analysis and Design of Damage Tolerant Aircraft Structures,* Department of Defense, Washington, D.C., 1974.

6.DOD, *MIL-HDBK-1823, Nondestructive Evaluation (NDE)System Reliability*, Department of Defense, Washington, D.C., 30 April 1999.
7.DOD, MIL-HDBK-5J, DEPARTMENT OF DEFENSE HANDBOOK: METALLIC MATERIALS AND ELEMENTS FOR AEROSPACE VEHICLE STRUCTURES (31 JAN 2003)
8.Rummel, W.D., P.H. Todd, Jr., R.A. Rathke and W.L. Castner, "The Detection of Fatigue Cracks by Nondestructive Test Methods," *Materials Evaluation*, Vol. 32, No. 10, October 1974, pp. 205–212.
9.Thompson, R.B., "A Unified Approach to the Model-assisted Determination of Probability of Detection," *Materials Evaluation*, Vol. 66, No. 6, June 2008, pp. 667–673.
10.Wooldridge, A.B., "The Effects of Compressive Stress on the Ultrasonic Response of Steel-steel Interfaces and Fatigue Cracks," *Report NW/SSD/RR/42/79*, Central Electricity Generating Board, London, United Kingdom, April 1979.
11.Wooldridge, A.B. and G. Steel, "The Influence of Crack Growth Conditions and Compressive Stress on the Ultrasonic Detection and Sizing of Fatigue Cracks," *Report NW/SSD/RR/45/80*, Central Electricity Generating Board, London, United Kingdom, April 1980.

OPTIMIZATION OF QUANTITATIVE DIGITAL RADIOGRAPHY FOR SIZING THE DEPTH OF CIRCUMFERENTIAL CRACKS IN BOILER WATERWALL TUBES: LATEST DEVELOPMENTS

S. Walker, EPRI, USA
B. Jackson, M. Cronin, H. Vaillancourt, Intertek AIM, USA
S. Paterson, PIKA Solutions, USA
R. Seals, R.I. Seals, Inc., USA

ABSTRACT

Efforts have continued in the development of a quantitative crack sizing technique for detection and characterization of circumferential thermal-fatigue cracks - a prevalent form of damage in fossil power plants that predominately occurs in water walls of coal-fired supercritical plants. This cracking most commonly initiates at the outside surface of the tubing on the fireside crown location and can be visually identified as tightly spaced parallel, horizontal cracks after the removal of coal ash deposits; however, current nondestructive evaluation technologies (e.g. ultrasonic, electromagnetic, potential drop, etc.) find it highly challenging to characterize the depth of the cracks due to their high density (more than 20 cracks per inch) and variable depths. This paper details the continual development of a quantitative digital radiography method (developed over the past 2-3 years) that can readily size the depths of these cracks. The accuracy of crack sizing has been improved through optimization of various radiographic parameters and the use of custom calibration blocks to calibrate the depth sizing locally in each radiographic image. Recent laboratory work has been able to size cracks with an error of as little as +0.003 inch (0.07 mm), and reliably to within 0.015-0.020 inch (0.38-0.51 mm). Field application is being performed in 2013 and the predicted crack depths are to be verified by destructive analysis.

INTRODUCTION

The research presented is part of a demonstration project initiated by EPRI to advance the current state-of-the art radiographic crack depth sizing technology. Advancements in radiographic equipment and transmitted X-ray intensity recording devices have begun to make the use of radiography as a quantitative tool for crack depth sizing a practical and competitive method. Accuracies equal to or better than traditional techniques are already achievable, as will be demonstrated. This paper is a continuation of the research first presented [1, 2, 3] and focuses on development of the knowledge gaps identified in initial stages of research. Topics covered are as follows:

- Introduction to the fundamental physics behind radiographic measurement of crack depth
- Summary of the methodology and data analysis developed to more efficiently process radiographic data from radiographs containing calibration blocks and unknown cracks
- Detailed study on optimization of calibration blocks for improved accuracy of crack depth sizing

Previous research has shown great potential for the use of quantitative digital radiographic testing (QDRT) for sizing of circumferential, thermal fatigue cracking in water wall tubes [1]. The term "X-ray" will be used throughout this paper for convenience and because all evaluations to date have been accomplished with X-ray generators; however, it is acknowledged that, with the proper choice of isotopes, gamma-ray radiography could be used.

The objective of this project was to demonstrate how digital radiography can be used to measure the depth of tube cracks. It is hoped that by refining the crack depth sizing methodology for this form of cracking, it can then be adapted to other forms of cracking in tubes and other components. Based on previous work, it appears that an achievable objective of this work will be to develop a technique that can be used with a variety of X-ray sources and image collection systems that can determine the depth of circumferential thermal fatigue cracks to within +/-5% of the tube wall thickness for cracks that have depths within the range of 10% to 80% of wall thickness.

CIRCUMFERENTIAL THERMAL FATIGUE CRACKS

A magnified image of a typical circumferential thermal fatigue crack is shown in Figure 1. Significant points to notice about the crack in relation to radiographic sizing are as follows:

- The cracks are oxide filled and round tipped – typically a vee-shape in cross section.
- These cracks have crack opening angles in the range of 12 degrees to 20 degrees.
- The crack tip (or near crack tip) opening width of these cracks is in the range of 0.0003 to 0.0005 inch (0.008 – 0.013mm).
- The cracks are often straight sided with only minor crack surface undulations.
- The cracking is most severe on the fireside crown surface of tubing (a surface that is very accessible, and enables placement of the imaging plate next to the crack surface).
- Cracks are orientated perpendicular to tube wall.
- There are usually many parallel cracks with spacing in the range of 15 to > 20 cracks per inch, making them challenging to image accurately by conventional techniques such as ultrasonic and potential drop.
- The oxide has much lower absorption than the low alloy, chromium-steel tube material.

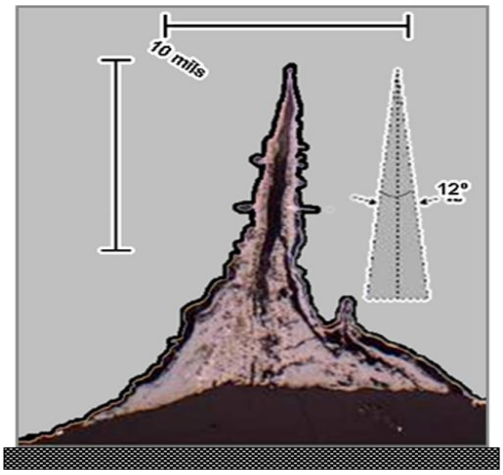

Figure 1
Example of Circumferential Thermal Fatigue Cracks.

FUNDAMENTALS OF DIGITAL RADIOGRAPHIC CRACK SIZING

Crack Contrast and Grey Levels

For notch or crack depth measurement, the local intensity of the remnant X-ray beam at crack indications can be compared to the remnant X-ray beam intensity at a location adjacent to the crack. The "crack contrast" is related to the differences in the X-ray beam intensity that is measured by X-ray film or other image collection systems. For X-ray imaging systems that have a logarithmic relationship between the incident beam intensity and the recorded "gray level", the crack contrast is related to the logarithm of the local beam intensities, as shown in Equation 1:

$$\text{Crack contrast} \sim \text{Log}\,(I_{\text{rem., next to crack}}) - \text{Log}\,(I_{\text{rem., crack tip}}) \qquad (1)$$

where,

$I_{\text{rem., next to crack}}$ = Intensity of the remnant X-ray beam after passing through the object at a location adjacent to the crack

$I_{\text{rem., crack tip}}$ = Intensity of the remnant X-ray beam after passing through the object at the crack tip

Figure 2 illustrates the graphical relationship between crack contrast and crack (or notch) depth. The shallower a crack, the lower the grey level contrast it provides on the X-ray film/detector. Thus, the contrast is caused by a difference in path length of X-rays going through the full wall thickness of a tube and then going through a reduced wall thickness in the area around a crack.
Figure 2 also illustrates the effect of accelerating voltage in the X-ray source. A lower accelerating voltage gives better crack contrast at shallower crack depths; however, a lower accelerating voltage gives less penetration capability compared to a higher voltage, making it less suited for heavier/thick walled tubes. For quantitative crack depth sizing to be successful, an optimization of accelerating voltage for each tube wall thickness must be established.
In order to translate the intensity of X-rays detected on an X-ray film or imaging plate, the concept of "grey levels" must be introduced. X-ray film provides a record of remnant X-ray intensity proportional to intensity and exposure time. Film is then scanned to produce a digital image, or a digital imaging plate may be used for the data capture.

Grey Level = Numerical Measure of Captured X-ray Intensity on Film

Numerical value is a function of pixel bit size. To put this into perspective, a 16-bit film scanner

is capable of detecting 65,536 shades of grey, where the human eye may only detect 64 shades of grey. This relationship may be used in depth sizing through the following simple relationship:

Crack Depth ~ Measured Grey Level – Background Grey Level

The results of the grey level analysis can be seen in Figure 3. In Figure 3, a cracked tube panel is shown with a lead mask around the cracks as a means of sharpening the image. The plot in the upper left of Figure 3 shows the output information plotted as grey level versus distance in order to show crack depths.

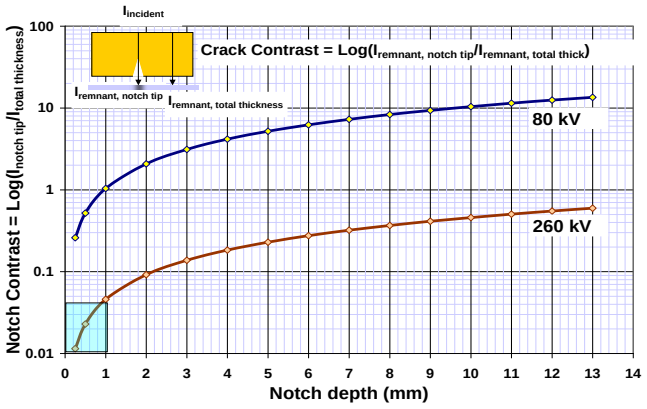

Figure 2
The Relationship between Crack (Or Notch) Contrast and Depth Sizing.

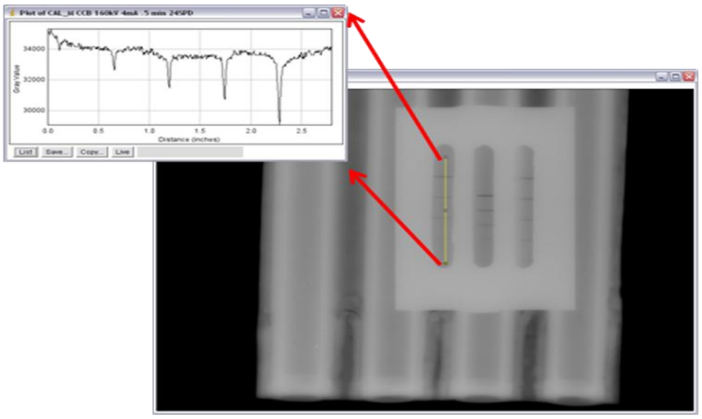

Figure 3
Grey Level Output from Cracked Tube Panel.

Geometric Considerations

The next most important phenomenon to consider when trying to perform quantitative measurements for a digital radiograph are the errors introduced by the geometry of the shot setup and interaction with the geometry of the tube panel. The following is a brief overview of the main points to consider [1]:

1. **Axial Offset:** When an X-ray beam is projected onto a flat surface, the amplitude of the diverging incident beam hitting the surface will become non-uniform since the distance from the X-ray source to the object is not constant. The X-ray beam intensity will be greatest at the location where the X-ray source is positioned directly perpendicular to the object being radiographed and will continually decrease at all points further away from this nearest distance point on the flat surface, as illustrated in Figure 4. Also, as the axial distance from the X-ray source increases, so does the angular distance that the X-rays must pass through the tube walls.
2. **Transverse Offset:** There is a more complex change in the metal path distance at different horizontal positions away from the X-ray beam perpendicular location. An example of the effective metal path thickness is illustrated in a ray diagram with the corresponding metal thickness measurements in Figure 5. The maxima on the metal thickness plots corresponds to the rays that are exactly tangential to the inside diameter of the tube. Note that the rays form a divergent source and are incident on the tube at slightly different angles. The increased effective metal thickness at non-perpendicular angles from the X-ray source results in a reduction in the X-ray intensity that is captured by radiographic film. This results in a non-linear background intensity (or "grey level"). This must be accounted for when performing quantitative crack depth measurements.
3. **Focal Point to Film Distance (FFD):** Both the angular offset and the distance from the source of the crack tip affect the detected intensity. The greater the offset, the more the X-rays pass through metal after passing through the crack. This extra distance through metal serves to further scatter the X-rays and results in a lower detected intensity at the film than would have otherwise been the case for X-rays passing through the crack alone. This leads to a maximum allowable axial offset for quantitative digital radiographic shot setups. As a rule of thumb, the maximum axial offset is 1/10 the FFD.

   These constraints lead to a defined area over which the radiographs may be taken in order to avoid distortion or artifacts on measured grey levels and calculated crack depths. The accurate fitting of a non-uniform background is essential to accurate crack depth sizing and has been one of the key points in the success of the recent work that is presented in this paper.

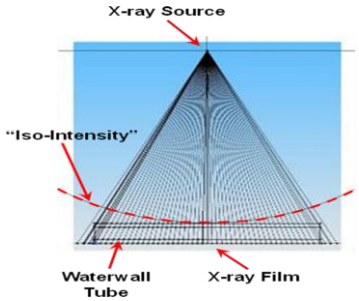

Figure 4
Geometrical Considerations for Radiographic Crack Depth Sizing – Axial Offset.

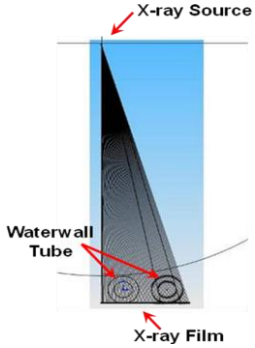

Figure 5 Geometrical Considerations for Radiographic Crack Depth Sizing – Transverse Offset.

Calibration Blocks

The main focus of the current research has been with optimization of a calibration block design that may be used in-situ to calibrate the crack tip grey level measured by taping the block to the tube wall during exposure to X-rays. This is accomplished by preparing a block with known notch depths in the surface produced by electro discharge machining (EDM). The image contrast developed from these known depths can then be used to prepare a grey level contrast versus crack depth plot from the measured notches in the tube. The concept is outlined in Figure 6. Images of the machined blocks – one set flat, and one set curved – are shown in Figure 6. Each of the notches has a 12º crack opening angle, is straight sided, and ends in a sharp notch tip at the base to simulate "ideal" circumferential thermal fatigue cracks of various depths. The blocks contain EDM notches in the range of 7 to 80% tube wall thickness (from 0.018 to 0.200 inch). The block thicknesses were made to be equivalent to two tube wall thicknesses minus the thickness of the membrane web above which they are placed and the calibration blocks were designed to mimic the metal path length the X-rays would travel through in the actual tube to be measured. A cracked panel with calibration blocks attached in the laboratory is shown in Figure 7.

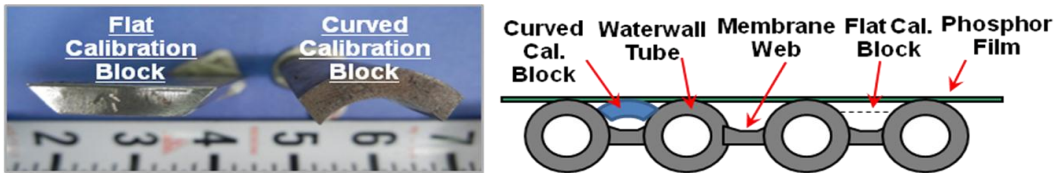

Figure 6
Schematic of Flat and Curved Calibration Blocks.

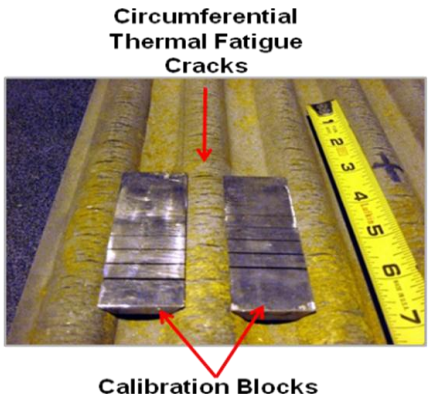

Figure 7
Photograph of Flat Calibration Blocks on Cracked Tubes

An image taken in-situ at a power plant is shown in Figure 8. This image clearly shows two of the calibration blocks between tubes, and the notches in the blocks. Cracking in this area is difficult to see due to the lightness of the radiographic image.

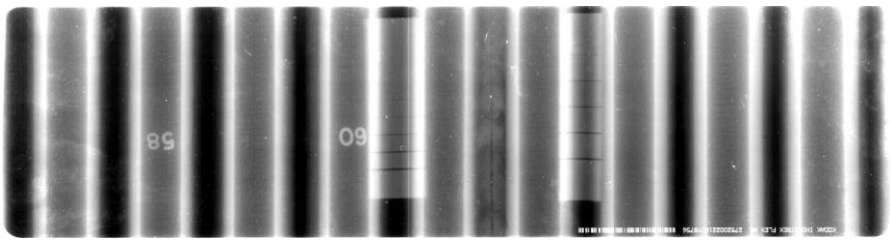

Figure 8
Radiographic Image of Calibration Blocks on Tube Panel In Power Plant

CONCLUSIONS

The following conclusions may be drawn from the results of the optimization experiments:

- The optimal calibration block thickness should closely match the metal path of the X-rays passing through the hot and cold side tube walls.
- Curved calibration blocks overall have a lower error than flat ones.
- All errors were on the side of overestimation of crack depth, making this a somewhat conservative technique for estimating damage.
- The use of lead masks in this set of experiments has shown to be of some benefit in increasing the sizing accuracy; however, when considering scale-up/field deployment of this technique, this may prove to be less practical. The experiments demonstrate what is possible, but further work is required to select the most practical parameters.
- It appears from the data that there may be a trend in crack depth sizing accuracy with the depth of the cracks that are being sized. From the data sets collected thus far, it appears that the curved calibration blocks are more consistently accurate with shallower cracks, but the variation in errors in sizing large cracks is greater than with the flat blocks. Use of the flat calibration blocks provides less accurate measurements than does the curved calibration blocks with shallow cracks (showing greater variation in accuracy) but less variability with deeper cracks. However, when results are averaged out over accelerating voltage and calibration block thickness, a different scenario is presented. In short, the authors do not believe that there is enough data to show a trend in this characteristic, and further experimental data sets should be collected to determine if there even is a trend and what that trend may be.
- Low kV X-ray tube exposures produce increased contrast with thickness and improved gray level contrast-based crack depth sizing.
- Calibration blocks with a thickness that produces slightly higher background dose values than at the tube crown locations provide somewhat more accurate depth sizing than thicker calibration blocks. This is understandable, because the notches present a larger percentage of thickness change.
- For shallow cracks, flaw depth sizing is enhanced by using curved rather than flat notched calibration blocks.
- **For a wide range of shot conditions and calibration blocks, crack depth sizing with an accuracy of -0.00 inch to +0.050 inch (-0.00 to +1.27 mm) was achieved.**

REFERENCES

1. Jackson B et al., “Quantitative Digital Radiographic Testing for Sizing the Depth of Circumferential Cracks in Waterwall Tubes”, EPRI Boiler Tube and HRSG Tube Failures and Inspections International Conference, Baltimore MD USA, April 19 – 21, 2010.
2. Paterson S et al., “Evaporator Tubing Circumferential Cracking in Supercritical Boiler”, EPRI Boiler Tube and HRSG Tube Failures and Inspections International Conference, Baltimore MD USA, April 19 – 21, 2010.
3. Jackson B et al., “The Optimization of Quantitative Digital Radiographic Testing for Sizing the Depth of Circumferential Cracks in Watewall Tubes: The Latest Developments”, International Conference on Advances in Condition and Remaining Life Assessment for Fossil Power Plants – Coal, Gas and HRSG, Hilton Head SC USA, October 17-19, 2012.

PIPING INSPECTION – EMBEDDED PIPES

BURIED PIPE INTERNAL DIAMETER INSPECTION TOOL

M. Sapia, P. Doverspike
GE Hitachi Nuclear Energy, USA

Abstract

This presentation will discuss the recently developed Surveyor Buried Pipe inspection robot. The robots have been used extensively in Europe where the technology has been refined to provide reliable travel long distances in the pipe. The topics of tool installation, pipe accessibility, and limits of travel will be discussed. The tool utilizes two different inspection heads: either an array of ultrasonic probes to detect and measure general wall loss; or an array of eddy current (electromagnetic) probes to also measure wall loss. The eddy current technique is unique in the industry because it performs the inspection using partial magnetic saturation. An overview of both NDE modalities will be provided. In addition to the discussion of tool specifications and capabilities, the presentation will also discuss field experience at nuclear plants where the tool has been deployed. Examples of reported indications as well as the subsequent follow-up to corroborate the findings will also be presented.

Keywords: Development in volumetric

THE INSPECTION OF VISUALLY INACCESSIBLE AREAS OF CONTAINMENT LINERS AND SHELLS UTILIZING ADVANCED NONDESTRUCTIVE EXAMINATION TECHNIQUES

B. P. Hohmann, T. C. Esselman, T. T. Taylor, Lucius Pitkin, USA
J. J. Wall, EPRI, USA

Abstract

This paper describes the results of a project on the inspection of visually inaccessible areas of containment liners and shells via advanced nondestructive inspection techniques. Full scale mockups that simulated shell and liner regions of interest in the containment of both a PWR and BWR were constructed. Inspections were performed with Synthetic Aperture Focused Transducer (SAFT) ultrasonic and Guided Wave inspection techniques. Inspections were performed on the mock-ups prior to the installation of flaws and prior to the placement of concrete. The effect of concrete being in close proximity to the liner and shell was determined. The capability to detect and size flaws with each inspection technique was evaluated. A discussion on the potential for these techniques to be utilized in commercial nuclear power plants is included.

1. Introduction

At a nuclear power plant, the containment building is of primary importance for safe operation. The primary containment and other safety related structures at a nuclear plant site must be capable of maintaining their design features for the operating life of the plant. Demonstrating the satisfactory condition of the containment building and other safety related structures is required for long-term operation of the plant, particularly when plant operation beyond 60 years is considered.

Operating experience from plants in the United States has shown that containment liners and shells are susceptible to both inner diameter (ID) and outer diameter (OD) corrosion [1]. Through-wall corrosion has been experienced at Brunswick Unit 2 (1999), North Anna 2 (1999), DC Cook 2 (2001), and Beaver Valley 1 (2009) [1]. Much of the corrosion from the OD has occurred because of foreign material that was left in the concrete during initial plant construction. The through-wall corrosion that occurred at Beaver Valley Unit 1 occurred at a location where a piece of wood was found embedded in the concrete and in contact with the liner [1, 3].At Brunswick 2, there were two locations that were ID initiated and one that was OD initiated. Some OD corrosion was also noted during concrete removal for steam generator (SG) and reactor vessel head replacement at Beaver Valley 1. It was determined that this corrosion likely occurred during exposure to the environment prior to the containment concrete being poured [2].This operating experience shows that PWR and BWR liners are susceptible to corrosion if foreign objects were left in the concrete when it was initially poured and if these foreign objects are in contact with the metallic liner. OD corrosion in a BWR drywell shell can also occur at regions where moisture can collect, like in the sand cushion region.

Many pressurized water reactors (PWRs) have liners and most of those liners have concrete poured inside of them to form a floor. ID corrosion can occur in at locations where there is an interface between the liner and the concrete. This location where the liner goes behind the concrete is a location of susceptibility to corrosion. Water seals are typically installed at this location and they have the potential to be damaged or degrade over time in service, resulting in water intrusion between the concrete and the liner. Liner corrosion in the region from the ID was noted at twenty three PWRs – all caused by coating failures or moisture barrier degradation [1]. This region is normally inaccessible for inspection. The drywell shells of boiling water reactors (BWRs) are also susceptible to ID and OD corrosion. Corrosion has been noted at Oyster Creek, Dresden, Hope Creek, and others [4, 5].

The OD areas in the sand cushion region and in the ID near concrete that has been poured are also susceptible to corrosion over time.

A feasibility study has been performed to gather data on nondestructive examination (NDE) techniques, including the use of state-of-the-art NDE equipment and systems that may be used to inspect containment building liners and shell systems in areas that are not visually accessible.

2. Mock-up Design and Construction

To demonstrate the adequacy of the respective inspection techniques described for inspection of inaccessible metallic liner and shell surfaces, a number of mock-ups were constructed. The mock-ups were designed to provide a full-scale, accurate representation of a PWR containment liner and a BWR drywell shell. Prior to construction, CAD drawings were prepared to provide a visual rendering of the fully fabricated assemblies. The PWR containment liner mock-ups were represented by two different mock-up constructions. One was for the transition of the external wall liner into the containment floor concrete. This is shown in Figure 1. A second mock-up was prepared for demonstrating a degradation screening process for a straight wall. The straight wall was meant to simulate an area where classical manual UT could be performed but would be too time consuming. This mock-up is shown in Figure 2. Once a location of potential degradation were noted in an accessible region with one of the proposed advanced NDE techniques, manual UT could be used to size the flaws or confirm their presence. The BWR drywell mock-up included the drywell shell adjacent to the sand cushion region. This is shown in Figure 3.

2.1 Mockup Design

The mock-up shown in Figure 1 is a replica of a typical liner design and includes liner plate butt welds, attachments, and surrounding concrete. The liner plate is 3/8 (0.375) inch (0.95 cm) thick along the wall and the curvature into the floor where it transitions to 1/4 (0.25) inch (0.64 cm) thickness. Testing of this mock-up was performed to demonstrate the extent of the coverage of the nondestructive inspection systems into the embedded liner and beyond the 90 degrees curvature where significant signal attenuation was anticipated due to contact with the steel embedment, welds, and concrete. There is currently no other non-destructive techniques commercially available to inspect the embedded portions of the liner. The mock-up was oriented in the field observed position with the containment wall concrete oriented vertically and the floor oriented horizontally. The potential effects of concrete bonding, concrete shrinkage, and deadweight on horizontal surfaces were then examined.

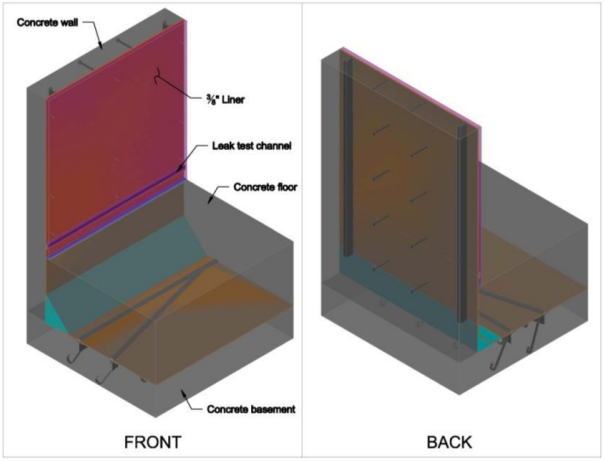

Figure 1: Rendering of Mock-Up of PWR Containment Wall Liner

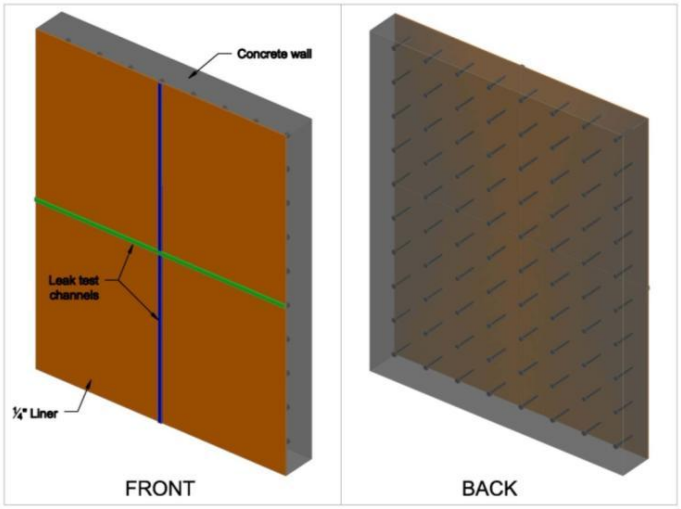

Figure 2: Rendering of Mock-Up of PWR Flat Wall Liner

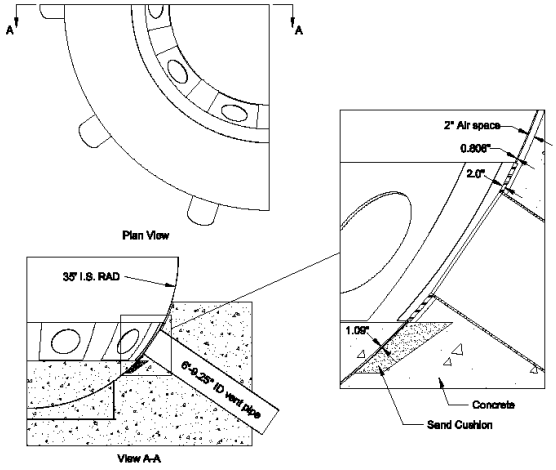

Figure 3: Rendering of Mock-Up of BWR Drywell Shell

The mock-up of the straight wall shown in Figure 2 represents a typical wall where the liner is exposed on one side and is backed by reinforced concrete on the other. The liner plate is 1/4 (0.25) inch (0.64 cm) thick. It contains butt welds and stud attachments on the concrete side. The value of nondestructively inspecting this mock-up was that it provided for the evaluation of an NDE system to scan a large surface area of the liner in a relatively short time.

The mock-up of the BWR drywell shell demonstrated the feasibility to inspect the area of a nuclear plant which is embedded in the concrete and adjacent to the sand cushion. The shell was 1 1/8 (1.125) inch (2.86 cm) thick, which closely represented the field observed shell wall thickness. This increased thickness necessitated a change in the inspection system parameters, most notably the use of a lower frequency range.

Testing of these mock-ups allowed for the investigation of multiple sizes and configurations of flaws. The ability to detect or not detect certain flaws was examined. The ability to accurately size flaws was also examined.

2.2 Mockup Construction

The steel shell and liner components for the three mock-ups were fabricated at a company specializing in the rolling of steel. The parts were delivered in pieces where all welding and final assembly was performed. Welding was performed in the laboratory where the mock-ups were to be assembled, as shown in Figure 4. Following assembly of the steel liner and shell components, the three mockups were inspected with the NDE techniques prior to any flaws being machined into them or concrete being poured, in order to gain a baseline reading for the advanced NDE techniques that were

selected for use. A detailed description of the test procedure is provided in Section 4.0 of this paper. The mockups were assigned the following nomenclature during testing: *BWR* for the BWR shell mockup, *A* for the PWR straight wall mock-up, and *G* for the PWR basemat mock-up. Figures 5 and 6 show the mockups prior to flaw insertion and concrete placement, while Figures 7 through 10 show the fully constructed mock-ups after flaw insertion and concrete placement. Flaws were placed on both the ID and OD sides.

Figure 4: Welding performed on mock-ups

(a) 

(b) 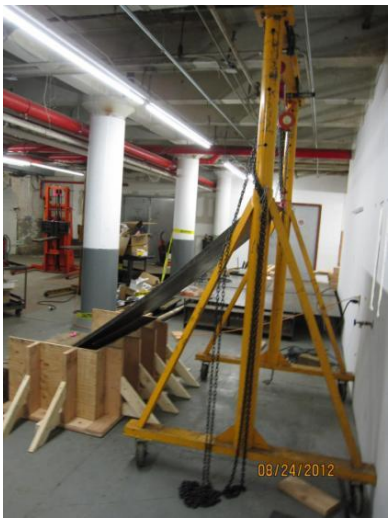

Figure 5: (a) Front and (b) side view of the BWR mock-up prior to concrete placement

Figure 6: The straight wall mock-up, *A*, lying with its OD side sticking up

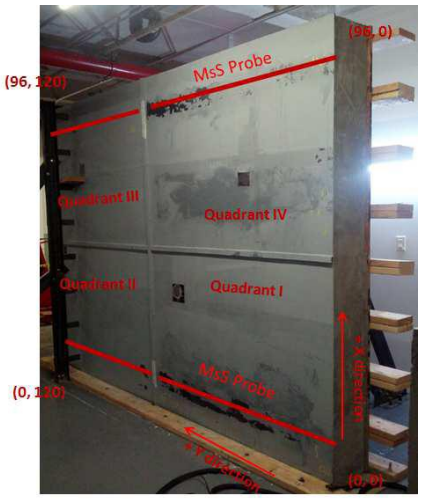

Figure 7: The PWR wall mock-up, *A*, in the upright position following placement of concrete. Orientation of the four mock-up quadrants, the mock-up coordinate system for flaw location, and location of the Magnetostrictive sensor (MsS) probe placement noted in red**.**

Figure 8: The PWR basemat mockup, *G*, following placement of concrete. The curved region of the liner can be seen.

(a)

(b)

Figure 9: (a) Front and (b) side views of the BWR shell mockup, labeled as *BWR*

Figure 10: Appearance of the three fully constructed mock-ups

3 Description of NDE Techniques

3.1 Guided Wave Inspection Technique

Guided waves (GW) are structure-borne elastic waves that propagate along the length of plate, guided by and confined within the inner or outer boundary of plate. This unique feature is a very capable tool for long-range plate inspection from a single probe location [6-7]. Since the wave is guided by the plate boundary, the boundary decides on the wave modes and propagating velocity. Figure 11 shows dispersion curves that plot wave velocities at different frequency propagating in 0.375-inch-thick (0.95 cm) plate. The plate has three wave modes: Symmetric Lamb wave (S), Asymmetric Lamb wave (A), and Shear-horizontal wave (SH). Except SH0 wave mode, the velocities of other wave modes vary with the wave frequency (dispersive). The velocity of the SHO-wave, however, is constant (that is, equal to the shear wave velocity of the plate material) independent of the frequency. The SHO wave is non-dispersive so that its wave form does not change as the wave propagates a long distance. Therefore, SHO wave mode is mostly used for the inspection of steel plate samples.

The Magnetostrictive sensor (MsS) generates and detects ultrasonic guided wave electromagnetically in the material being tested. For the generation of ultrasonic wave, the sensor relies on the Magnetostrictive (or Joule) effect; the manifestation of small change in the physical dimensions of ferromagnetic materials (on the order of several parts per million in carbon steel) caused by an externally applied magnetic field [6]. For wave detection, it relies on the inverse magnetostrictive (or Villari) effect. The change in the magnetic induction of ferromagnetic material is caused by mechanical stress (or strain). Since the probe relies on the magnetostrictive effects, it is called a magnetostrictive sensor (MsS).

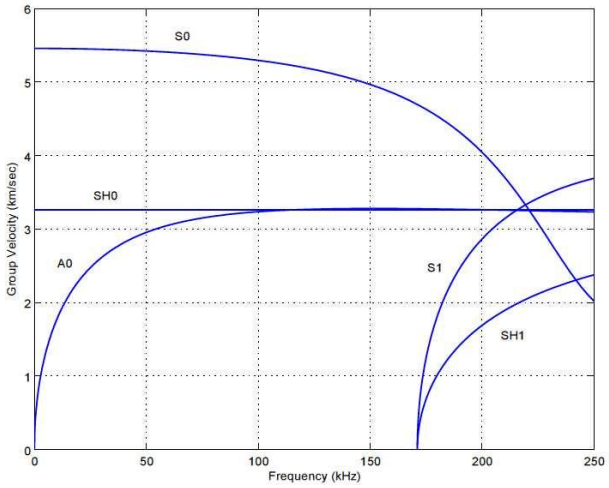

Figure 11: Dispersion curves of 0.375-inch-wall (0.95 cm) steel plate

3.2 SAFT Ultrasonic Inspection Technique

SAFT and T-SAFT stands for Synthetic Aperture Focusing Technique (SAFT) and tandem-SAFT (T-SAFT) inspection methodologies. "Synthetic aperture focusing" refers to a process in which the focal properties of a large aperture focused transducer are synthetically generated from data collected over a large area using a relatively small (compared to the inspection area) transducer with a divergent sound field [8]. The processing required to focus this collection of data has been called beam-forming, coherent summation, or synthetic aperture processing. The resultant image is a full-volume, high resolution, and high signal to noise ratio (SNR), focused characterization of the inspected area.
Utilizing the pulse-echo configuration for typical data collection, the transducer is positioned on the surface of the specimen, and radio frequency (RF) ultrasonic data is collected. As the transducer was scanned over the surface of the specimen, the A-scan records (RF waveform) are amplified, filtered, and digitized for each position of the transducer [8-10]. Each reflector produces a collection of echoes in the A-scan records. The unprocessed RF data sets were then post-processed using the SAFT algorithm, and invoking a variety of full beam angle values (between 1° and 12°) in an attempt to optimize the spatial averaging enhancement. A beam angle of 12° was used in this project. The SAFT system can be seen in Figure 12 performing a scan on one of the mock-ups.

If the reflector is an elementary single point reflector, then the collection of echoes will form a hyperbolic surface within the data-set volume. The shape of the hyperboloid is determined by the depth of the reflector in the specimen and the velocity of sound in the specimen. This relationship between echo location in the series of A-scans and the actual location of the reflectors within the specimen makes it possible to reconstruct a high-resolution, high SNR focused image from the acquired raw data.

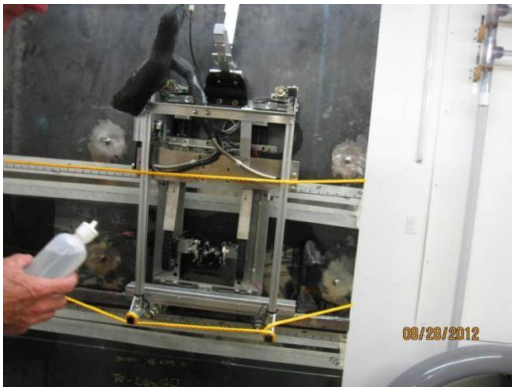

Figure 12: The SAFT system performing a scan on one of the mock-ups

4. Test Procedure

The feasibility study was conducted in three phases to enable the inspection of the mockups at the following fabrication intervals:

1) Inspection of the liner and shell components with welds and studs but prior to concrete being placed and with no flaws.
2) Inspection of the mockup liner and shell components following the introduction of flaws meant to simulate potential in-service degradation but prior to placement of concrete.
3) Inspection of the mockup liner and shell components with flaws and with concrete placed and cured.

The purpose of performing the inspections iteratively in the above described manner was to attempt to quantify the effect of signal attenuation in both the GW and SAFT methods as a result of both flaws and concrete.

4.1 Flaws Introduced into Mock-ups

Various types of flaws were introduced into all three of the mock-ups in order to simulate flaws typical of in-service degradation, such as pitting and corrosion, as well as flaws typically used in the evaluation of nondestructive systems, including flat bottom hole (FBH) flaws and cluster-type flaws of multiple FBHs in close proximity. The flaws and the number of flaws were selected to determine the feasibility and sensitivity of various inspection techniques. The flaws would have been different if they were to be used for qualification of inspectors. In all cases, a point of origin and coordinate system were selected for each mock-up, and the exact location of flaw placement was noted in order to compare with future inspections after concrete placement obscured visual observation of flaws. Flaws of varying depths and diameters were placed on both the ID and OD sides of the mock-ups, as shown in Figure 13, and a flaw map legend was developed to facilitate the quantification of each NDE technique with respect to flaw detection. A full description of the flaw map and inspection results is provided in reference [11].

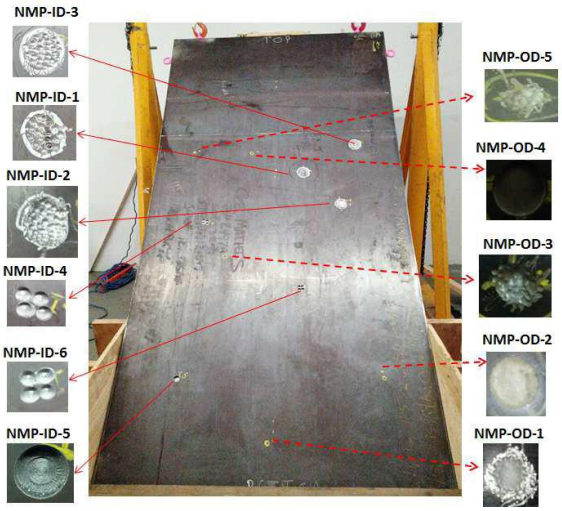

Figure 13: Various flaws inserted into both ID and OD side of the BWR mock-up

5. Results and Discussion

A full description of the flaws that were detected and that were not detected via the MsS guided wave and T-SAFT NDE systems is provided in Tables 1 through 4. The MsS guided wave and T-SAFT systems were selected because each one had unique advantages to flaw detection, and this can be seen by the fact that different types of flaws were detected by the different systems. In general, it was demonstrated that flaws or progressive degradation such as simulated corrosion could be detected with both the GW and SAFT techniques in visually inaccessible areas of the mock-ups. Simulated corrosion-type flaws, as small as 2 inches in diameter, were detected at a distance of several feet with the advanced NDE techniques.

It should be noted that the T-SAFT system used in this research was not optimized for the mock-ups under inspection. This system was borrowed from a prior inspection project performed by Pacific Northwest National Laboratory (PNNL), and the T-SAFT system parameters were not changed for this new inspection application. A redesign of the scanner as well as additional research into optimizing the detection and sizing capabilities of the T-SAFT system for this application would have been required, therefore it was decided to utilize the system as-is from the work performed at PNNL. As shown in Figure 14, the SAFT system obtained good signal to noise (SNR) ratio and flaw resolution for some flaw-types, while for others a high level of background noise was observed.

The MsS guided wave system was more effective than the SAFT system at overall flaw detection capability. This was due in part to the lack of optimization for the SAFT system. The SAFT system was somewhat better at sizing of the flaws, however neither system was able to size flaws with adequate precision. The SAFT inspection system was more suited to the thicker BWR shell mockup than the MsS guided wave system. This was due in part to the multiplexing capability of the ultrasonic transducer on the SAFT system, as well as the limited signal frequencies that could be used by the GW system on the thicker shell mock-up. In general, the presence of welds significantly attenuated the signals from both NDE techniques.
The presence of a liner thickness deviation at the weld location in the PWR basemat mock-up also significantly lowered flaw detection capability for both techniques.

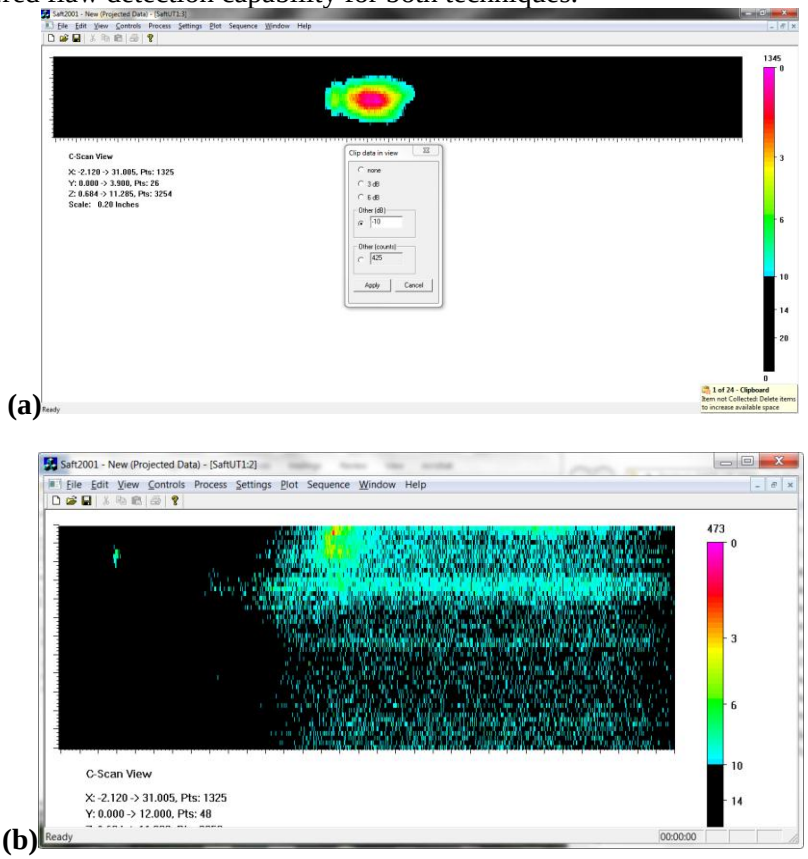

Figure 14: (a) good SNR and (b) higher background noise observed for flaw with SAFT

6. Conclusions

This research demonstrated that flaws or progressive degradation such as simulated corrosion could be detected with both the GW and SAFT techniques in visually inaccessible areas of the constructed nuclear containment mock-ups. Simulated corrosion-type flaws, as small as 2 inches in diameter, were detected at a distance of several feet with the advanced NDE techniques. The MsS guided wave system was more effective than the SAFT system at overall flaw detection capability. The SAFT system was somewhat better at sizing the flaws, however neither system was able to size flaws with adequate precision. The SAFT inspection system was more suited to the thicker BWR shell mockup than the

MsS guided wave system was. In general, the presence of welds significantly attenuated the signals from both NDE techniques.

The presence of a liner thickness deviation at the weld location in the PWR basemat mock-up also significantly lowered flaw detection capability for both techniques. With additional development of the SAFT equipment, it is believed that the GW inspection technique could be used as a screening technique for the presence of flaws, while the SAFT technique could be used as a follow-up NDE technique to confirm the presence of a flaw/defect and provide an approximate size and through-wall depth of the flaw.

Table 1: Inspection results for BWR shell mock-up

Flaw ID #	***Location ID /OD Coordinates Y, X, Z***	***Flaw Type and Trough Wall Depth***	***Guided Wave Pre-Concrete Detected (Yes/No)***	***Guided Wave After Concrete Detected (Yes/No)***	***T-SAFT System Pre-Concrete Detected (Yes/No)***	***T-SAFT System After Concrete Detected (Yes/No)***
BWR-ID-1	(-38, 18.75)	"Pitting" flaw; approx. 2in. diameter and 1/4 in. depth	Yes	Yes	Yes	No
BWR-ID-2	(-45.75, 11.5)	"Corrosion" type flaw; Scalloped flaw appearance 1.5 in. diameter and 1/4 in. depth	Yes	No	Yes	Yes
BWR-ID-3	(-31.5, 8.25)	"Pitting" flaw; approx. 2in. diameter and 1/8 in. depth	Yes	Yes	Yes	Yes
BWR-ID-4	(-49.25, 37)	"Cluster" flaw; four 0.5 in, diameter FBHs of 1/4 in. depth	Yes	Yes	No	No
BWR-ID-5	(-78.75, 38.5)	FBH; 1in. diameter and 1/4 in. depth	Yes	Yes	No	No
BWR-ID-6	(-63, 19.75)	"Cluster" flaw; four 0.5 in, diameter FBHs of 1/4 in. depth	Yes	Yes	No	No
BWR-OD-1	(-88, 24)	"Corrosion" type flaw; Scalloped flaw appearance 1 in. diameter and 1/4 in. depth	No	No	No	No
BWR-OD-2	(-78,8)	FBH; 1in. diameter and 1/4 in. depth	Yes	No	No	No
BWR-OD-3	(-57,32)	"Corrosion" type flaw; Scalloped flaw appearance 1 in. diameter and 1/4 in. depth	No	No	No	No
BWR-OD-4	(-33, 28)	FBH; 1in. diameter and 1/4 in. depth	Yes	Yes	Yes	Yes
BWR-OD-5	(-33, 40)	"Corrosion" type flaw; Scalloped flaw appearance 0.75 in. diameter and 1/8 in. depth	Yes	Yes	No	No

Table 2: Inspection results for PWR basemat mock-up

Flaw ID #	*Location ID /OD Coordinates Y, X, Z*	*Flaw Type and Trough Wall Depth*	*Guided Wave Pre-Concrete Detected (Yes/No)*	*Guided Wave After Concrete Detected (Yes/No)*	*T-SAFT System Pre-concrete Detected (Yes/No)*	*T-SAFT System After Concrete Detected (Yes/No)*
I1	47.75,47.5,36.5	2" dia. Pitted region, 0.125 deep	Yes	Yes	Yes	No
I2	39.5,45,19.75	2" dia. Pitted region, 0.1875 deep	Yes	Yes	Yes	Yes
I3	9.25,47.5,35	2" dia. Pitted region, 0.09375	Yes	Yes	Yes	No
I4	43.75,35.25,15.25	Scalloped region, 0.1875 deep	Yes	Yes	Yes	No
I5	24.25,30.75,14.5	FBH 1" dia., 0.1875 deep	No	No	No[1]	No[1]
I6	25,47.5,33.5	Scalloped 1" dia., 50 mils (very shallow)	Yes	Yes	No[1]	No[1]
I7	13,45.25,19.5	Scalloped 1" dia., 100 mils (shallow)	No	No	No[1]	No[1]
I8	30.5,12.5,14.5	FBH 2" dia., 0.09375 deep	Yes	Yes	No[1]	No[1]
I9	46,18.25,14.5	FBH 1" dia., 0.1875 deep	Yes	Yes	No[1]	No[1]
O1	12,8,14.5	FBH 1" dia., 0.125 deep	Yes	Yes	No[1]	No[1]
O2	31,47.5,75	scalloped region, 0.1875 deep	Yes	No	No[1]	No[1]
O3	13.5,47.5,75	scalloped region, 0.09375 deep	Yes	Yes	No[1]	No[1]
O4	46.25,47.5,90	2" dia. pitted region, 0.1875 deep	Yes	Yes	No[1]	No[1]

Note 1: The T-SAFT system was not able to see these flaws because the scanner was not designed to accommodate these types of flaws.

Table 3: Inspection results for PWR straight wall mock-up –ID side flaws

Quad.	*Flaw ID*	*Location Coordinates Y, X*	*Flaw Type and Through Wall Depth*	*Guided Wave Before Concrete Detected (Yes/No)*	*Guided Wave After Concrete Detected (Yes/No)*	*T-SAFT System Pre-concrete Detected (Yes/No)*	*T-SAFT System After Concrete Detected (Yes/No)*
1	A-ID-1	(34.25, 23.25)	Flaw Marked on Map but not put in Mockup	--	--	--	--
	A-ID-2	(20, 42)	Flaw Marked on Map but not put in Mockup	--	--	--	--
	A-ID-3	(36.5, 48)	"Pitting" flaw; approx. 3in. diameter and 1/16 in. depth	Yes	Yes	No[1]	No[1]
2	A-ID-4	(62.75, 36.75)	Flaw Marked on Map but not put in Mockup	--	--	--	--
	A-ID-5	(30.5, 88.75)	Flaw Marked on Map but not put in Mockup	--	--	--	--
	A-ID-6	45, 109.75	"Cluster" flaw; four 0,5 diameter FBHs, 1/8 inch deep	Yes	Yes	No[1]	No[1]
3	A-ID-7	(52, 63.5)	Flaw Marked on Map but not put in Mockup	--	--	--	--
	A-ID-8	(73, 95.5)	"Pitting" flaw; approximately 3 inches in diameter & 1/8 inch deep	Yes	Yes	No[1]	No[1]
4	A-ID-9	(71.25, 36.25)	Flaw Marked on Map but not put in Mockup	--	--	--	--
	A-ID-10	(91.25, 46.25)	Flaw Marked on Map but not put in Mockup	--	--	--	--

Note 1: The T-SAFT system was not able to see these flaws because the scanner was not designed to accommodate these types of flaws.

Table 4: Inspection results for PWR straight wall mock-up –OD side flaws

Quad.	*Flaw ID*	*Location Coordinates Y, X*	*Flaw Type and Through Wall Depth*	*Guided Wave Before Concrete Detected (Yes/No)*	*Guided Wave After Concrete Detected (Yes/No)*	*T-SAFT System Pre-concrete Detected (Yes/No)*	*T-SAFT System After Concrete Detected (Yes/No)*
1	A-OD-1	42.75, 11.25	Cluster – 4 ½ dia., 1/8 deep FBH	Yes	Yes	No[1]	No[2]
	A-OD-2	42.75, 13.75	1"dia., 1/8 deep FBH	Yes	Yes	No[1]	No[2]
	A-OD-3	27, 21.5	Corrosion 1" dia., 1/8 deep	Yes	Yes	No[1]	No[2]
	A-OD-4	30, 36	Cluster – 4 –½ dia., 1/16 deep FBH	Yes	Yes	No[1]	No[2]
	A-OD-5	43.5, 56	Pitting ~ 3"dia., max 1/8" deep	No	No	No[1]	No[2]
2	A-OD-6	24.25,78.5	Corrosion – 1" dia. Scalloped; through wall at center			No[1]	No[2]
	A-OD-7	44.5, 90	Corrosion 1" dia., 1/8 deep	Yes	Yes	No[1]	No[2]
	A-OD-8	36.25, 95.5	Corrosion 1" dia., 1/8 deep	No	No	No[1]	No[2]
	A-OD-9	24, 108	Cluster – 4 – ½ dia., 1/8 deep FBH	Yes	Yes	No[1]	Yes[3]
3	A-OD-10	72, 63	Cluster – 4 – ½ dia., 1/8 deep FBH	Yes	Yes	Yes	No[2]
	A-OD-11	51.5, 83	Corrosion 1" dia., 1/8 deep			No	No[2]
	A-OD-12	79.5, 104	Pitting ~ 3"dia., max 1/8" deep	Yes	Yes	Yes	Yes[3]
4	A-OD-13	66, 23.5	Pitting – 3" dia., localized pitting All were fabricated through wall	Yes	No	No[1]	Yes[3]
	A-OD-14	79.5, 45	Pitting ~ 3"dia., max 1/8" deep	Yes	Yes	No[1]	No[2]
	A-OD-15	72.5, 45	Cluster – 4 – ½ dia., 1/32" deep FBH			Yes	Yes[3]
	A-OD-16	72.5, 51	Cluster – 4 – ½ dia., 1/16" deep FBH	Yes	Yes	Yes	Yes[3]

Note 1: The T-SAFT system was not able to see these flaws because of a malfunction of the system. The send/receive transducers were not functioning properly.
Note 2: The T-SAFT system could not see the flaws because the signal to noise ratio was very poor.
Note 3: The T-SAFT system was able to see these flaws because the T-SAFT system inspected the Mockup from a different position.

7. References

[1] D. Dunn, A Pulvirenti, and M. Hiser, "Containment Liner Corrosion Operating Experience summary, Technical Letter Report, Revision 1", US Nuclear Regulatory Commission, Office of Nuclear regulation Research, August 2, 2011.

[2] First Energy, Beaver Valley Power Station Unit 1, Containment Liner Corrosion Report, CR 06-0122, February 20, 2006, ML091960488.

[3] NRC Letter from J. White to P. Sena, Beaver Valley Power Station, Unit 1, NRC Routine Inspection Report 05000334/2009006, July 6, 2009, ML091870328.

[4] US Nuclear Regulatory Commission License Renewal Interim Staff Guidance LR-ISG-2006-01, Plant Specific Aging Management Program for Inaccessible Areas of Boiling Water Reactor Mark I Steel Containment Drywell Shell, ML063210041.

[5] US Nuclear Regulatory Commission Information Notice 2011-15, "Steel ContainmentDegradation and Associated License Renewal Aging Management Issues", August 1, 2011.

[6] H.Kwun, NUREG/CR- 5724 Feasibility of Magnetostrictive Sensor Inspection of Containments, March1999

[7] J. Pei, M.I.Yousuf, F.L. Degertekin, B.V.Honein, and B.T. Khuri-Yakub, "Lamb Wave Tomography and its Application in Pipe Erosion/Corrosion Monitoring", Proceedings from 1995 IEEE Ultrasonics Symposium.

[8] A. F. Pardini, et.al., Annual Report: Remotely Operated NDE System for Inspection of Hanford's Waste Tank Knuckle Regions and Development of a Small Roving Annulus Inspection Vehicle T-SAFT Scanning Bridge for Savannah River Site Applications, PNNL-14072.

[9] V. Yu, Zaitsev1, P. Sas, M. Wevers; "Nonlinear modulation methods of structural damage detection based on dissipative nonlinear effects"; Proceedings of the International Conference on Noise and Vibration Engineering pages:233-242,International Conference on Noise and Vibration Engineering location: Leuven, Belgium Sep 13-15, 2000.

[10] H. F. Hu, W. J. Staszewski, N. Q. Hu, R. B. Jenal, and G. J. Qin; "Crack Detection Using Nonlinear Acoustics and Piezoceramic Transducers—Instantaneous Amplitude and Frequency Analysis", Smart Materials and Structures, Volume 19, Number 6, 2010.

[11] *Synthetic Aperture Focusing Technique and Guided Wave Examination of Containment Liners and Shells.* EPRI Technical Report No. 000000003002001720. Electric Power Research Institute. Palo Alto, CA. 2013.

Acknowledgement: This work was supported by the Electric Power Research Institute (EPRI) and the United States Department of Energy (DOE) through Idaho National Laboratory (INL).

INSPECTION TECHNIQUE FOR BWR CORE SPRAY THERMAL SLEEVE WELD

J.L. Fisher, G. Light, Jim Crane, Albert Parvin, Southwest Research Institute, USA
Yoshimasa Sugawara, Tokyo Electric Power Company, Japan

ABSTRACT

The core spray piping system in typical boiling water reactor (BWR) pressure vessels includes nozzles with thermal sleeves. Each sleeve consists of a carbon steel pipe welded to a stainless steel pipe [a dissimilar metal (DM) weld], which in turn is welded to a connecting head that feeds coolant to the remainder of the core spray system in the vessel. These welds are typically made in the fabrication shop, where they are machined flush to the pipe surfaces. The carbon steel pipe is welded at the field site to the carbon steel vessel nozzle. Usually, the outer surface of this carbon steel field weld is left in the as-welded condition. Stress corrosion cracking (SCC) has been found in other light-water reactor locations with DM welds and also with stainless steel-to-stainless steel welds. Access to the outer surface of the thermal sleeve for inspection could be achieved from the vessel interior, by inserting a probe into the annulus between the thermal sleeve and the nozzle. However, due largely to the limited access conditions, these welds are not generally inspected. In a series of projects with Tokyo Electric Power Company (TEPCO), SwRI developed a laboratory prototype system for this inspection problem. The system includes a thin, flexible probe delivery mechanism to insert probes into the annulus, a thin (7 mm thick) ultrasonic probe, and a video inspection system that could also be inserted into the annulus. The system was successfully demonstrated on a mockup with implanted SCC flaws.

INTRODUCTION

The core spray piping system used in boiling water reactor (BWR) pressure vessels is a key component of the plant operating and safety equipment. This system includes a thermal sleeve, which consists of a carbon steel pipe welded to a stainless steel pipe, which is in turn welded to a connecting head that feeds coolant to the sparger feeder pipes of the core spray system. These welds are typically made in the fabrication shop, where they are machined smooth to the pipe surfaces. The carbon steel pipe is welded at the site to the vessel nozzle. Usually the outer surface of this carbon steel field weld is left in the "as-welded" condition. Stress corrosion cracking (SCC) has been found in other BWR and pressurized water reactor (PWR) locations with dissimilar metal (DM) welds and also with stainless steel-to-stainless steel welds. However, due to very limited access conditions for the thermal sleeve DM and stainless-to-stainless metal welds, there is no known inspection system for these welds.

An investigation was conducted to develop a method that could be used to examine the DM and stainless-to-stainless steel welds for cracks extending 50 percent through wall and oriented either parallel or transverse to the weld.

GEOMETRY DETERMINATION AND ACCESS STUDY

A key step of the investigation was to define the range of geometries that effect the inspection and the accessibility. There are many different core spray thermal sleeve configurations, including different gaps between the nozzle bore and the thermal sleeve piping, different thermal sleeve pipe wall thicknesses, and different axial locations of the welds with respect to the inside surface of the BWR nozzle. Access to the metal welds in the core spray system was determined to be possible by reaching into the narrow annular gap formed by the bore of the core spray nozzle and the outside of the core spray thermal sleeve, or by scanning from the outside surface of the nozzle. Initial testing from the outside surface of the core spray sleeve was deemed not to be adequate. Therefore, the internal access as illustrated in Figure1 was investigated.

MOCKUP DESIGN

An annulus gap mockup was fabricated to simulate the dissimilar metal butt weld, carbon steel butt weld, and nozzle annulus for the purpose of assessing the NDE delivery methods and evaluating the viability of visually inspecting the nozzle annulus gap prior to ultrasonic testing (UT) probe inspection. The annulus gap mockup (illustrated in Figure 2) was constructed from 316 stainless steel and A508 forged carbon steel to match actual plant construction. The mockup was designed and constructed to have interchangeable annulus sleeves to allow for simulation of multiple annulus gap sizes and offsets. A total of three annulus sleeves representing annulus gaps of 8 mm, 15 mm, and 42 mm were constructed. These three sleeve geometries represent 81% (37 of 46) of all thermal sleeve gaps of TEPCO plants. The remaining nozzles are categorized as follows: 13% (6 of 46) with gaps below 7 mm (extremely challenging) and 7% (3 of 46) with gaps greater than 42 mm (not as challenging but requiring a different scanner approach). A series of internal and external EDM notches and external circumferentially-oriented implanted cracks to simulate SCC were placed in the DM weld and heat-affected zone.

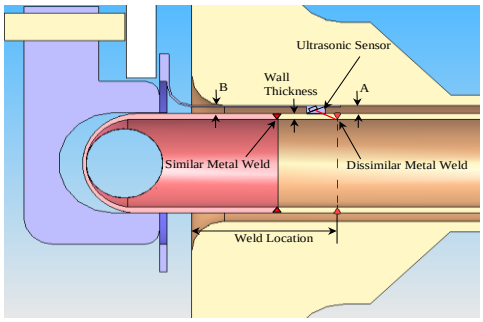

Figure 1. Illustration of access to the dissimilar and similar metal welds in the core spray system by (a) reaching into the narrow annular gap formed by the bore of the core spray nozzle and the outside of the core spray thermal sleeve.

The inspection plan is to first inspect the annulus with an articulating videoprobe to evaluate the condition of the annulus gap and also to detect signs of SCC that might be visible on the OD surface of the thermal sleeve. Visual inspection prior to UT probe insertion would also reduce the potential for damaging the probe delivery device. To test the videoprobe device, three visual indication marks, each approximately 1.5 mm x 5 mm, were placed on the outer diameter of the dissimilar metal weld. These marks represent through-wall cracks.

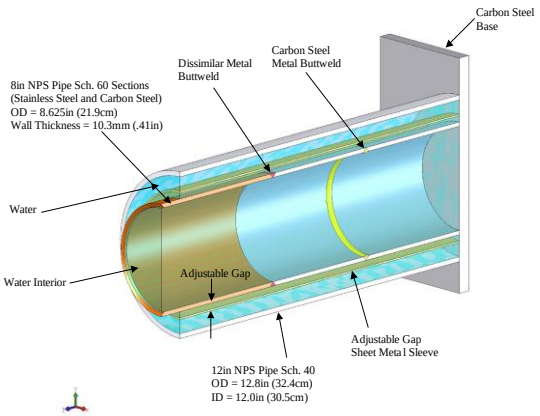

Figure 2. Thermal sleeve geometry mockup. The mockup can be oriented vertically and filled with water to simulate inspection conditions.

SYSTEM CONCEPT

This inspection system requires access to the interior of the vessel and use of the refueling crane for delivery. The inspection system concept design places a low profile conventional bulk wave transducer inside the annular gap of the core spray nozzle, as illustrated in Figure 3. The transducer is designed to scan the surface close to the weld of interest, which increases its ability to detect and characterize a defect. In addition, the interior scanning unit would include visual capabilities to allow the operator to see the physical condition of the annular gap and DM weld prior to inspection with the ultrasonic sensor.

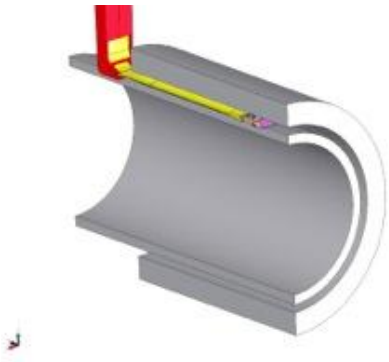

Figure 3. Illustration of a low profile bulk wave transducer inside the annular gap of the nozzle

The scanning concept consists of 5 major subsystems. The subsystems are described below. It should be noted that in these descriptions, the designations axial, radial, and circumferential are with respect to the core spray nozzle.

(1) Probe subsystem. There are 2 different probe systems: (1) UT probe subsystem and (2) Video testing (VT) probe subsystem. The UT probe subsystem consists of a flexible support member to which the UT sensor is attached. The flexible support member is used to transport the UT sensor into the annular gap and provide good contact between the UT transducer and thermal sleeve. The VT probe system is designed to support and transport a video capture device into the annular gap. The UT probe subsystem is shown in Figure 4. It includes a 45-degree, 0.375-in diameter transducer. The VT probe subsystem model is shown in Figure 5. It has a CCD imager camera with a resolution of 500 x 582 pixels. Lighting is provided by 2 LEDs mounted on either side of the camera.

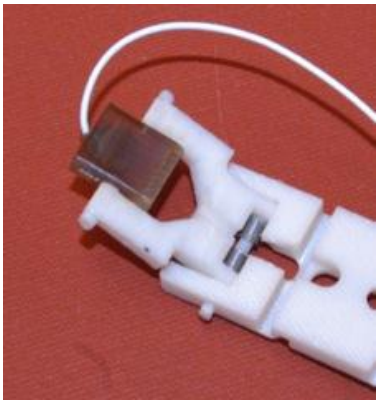

Figure 4. UT probe subsystem, with a breadboard track. The probe and track are only approximately 5 mm tall, to fit in a 7 mm gap

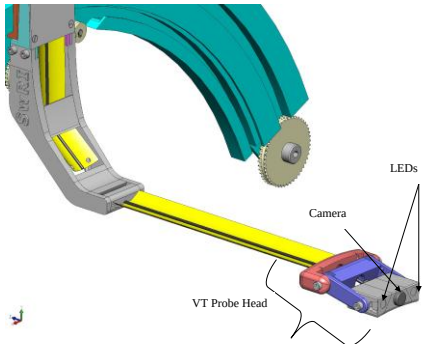

Figure 5. VT Probe subsystem, showing camera and LEDs for lighting. The manufactured subsystem could also fit into a 7 mm gap.

(2) Sensor Delivery Transport (SDT) subsystem. The SDT subsystem is designed to deliver the probe subsystem into the annular gap. It includes axial and circumferential drive motions. The design concept uses 2 SDT subsystems, oriented 180° apart circumferentially. A semi-rigid single bend retractable prototype device was developed and integrated with the rest of the system. It consists of a thin concave sheet of material (main body) placed in a guide track to assist in directing and making the probe main body rigid. The guide track has a drive assembly attached, which extends and retracts the main body into and out of the annulus. The main body and guide track are shown in Figure 6. The drive assembly consists of a belt drive that is driven by micro servo motors. An optical encoder was used to obtain the position of the probe main body. A rigid interchangeable pre-shaped guide was used to direct the probe's main body into and out of the annular gap of the annular gap mockup.

(3) Circumferential Scanning (CS) subsystem. The CS subsystem is designed to adjust the position of the SDT to match the diameter of the core spray nozzle thermal sleeve. The CS subsystem will be used to revolve the SDT subsystem 180° around the circumference of the nozzle during inspection, since each SDT subsystem can only inspect approximately 180° without this motion. In addition, as described later, it will provide radial motion of the SDT subsystem that will be used as part of the SDT insertion process. The CS subsystem is shown in Figure 6.

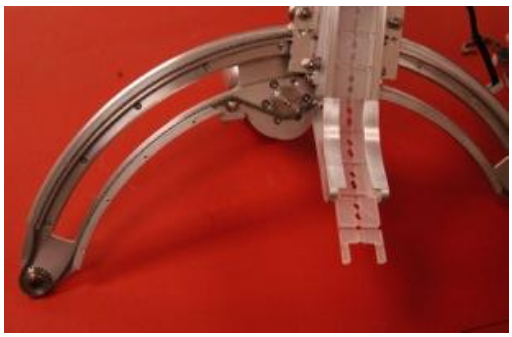

Figure 6. Circumferential Scanning subsystem with Sensor Delivery Transport subsystem attached.

(4) Positioning subsystem (PS). The positioning subsystem will align the CS subsystem with the core spray nozzle thermal sleeve, in order to deliver the sensor into the annular gap. The PS subsystem would attach to the sparger feeder pipe with a specialized clamping mechanism to provide registration of the entire system with respect to the vertical location of the nozzle once in place, suction cups also located on the PS will deploy against the wall to secure the device and minimize any possible load on the feeder pipes. Also, a centering, clamping mechanism will concentrically locate the system with the core spray nozzle, by clamping on the nozzle header. Once the PS subsystem is engaged, the CS subsystem will be engaged to deliver the SDT probe. A solid model of the PS is shown in Figure 7.

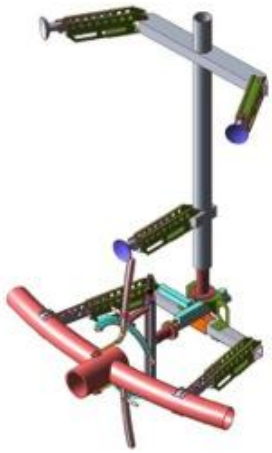

Figure 7. PS subsystem shown with clamp mechanism to provide registration to the feeder pipe, suction cups to maintain position on the vessel wall. The CS and SDT subsystems are also shown.

(5) Transport subsystem. The transport subsystem is designed to deliver the overall unit to the core spray thermal sleeve, and will utilize the refueling crane. This subsystem was not prototyped.

For a better understanding of the interior scanner system, Figure 8 identifies the five major interior scanner subsystems.

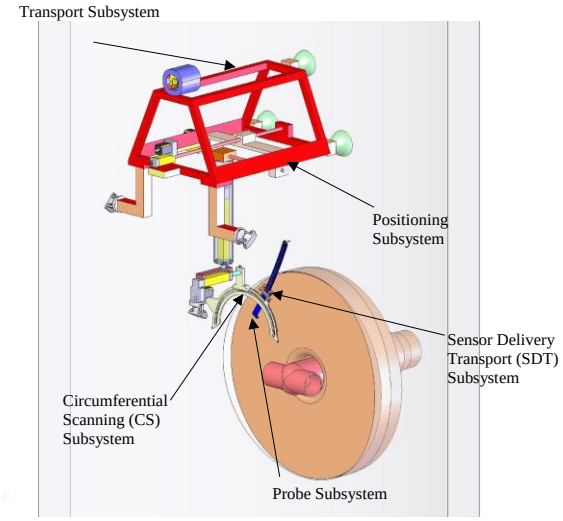

Figure 8. Interior scanning system concept showing the 5 major subsystems

The completed portions of the system that were manufactured (probe subsystem, SDT, CS) are shown in Figure 9.

Figure 9. Assembled system components, mounted on the thermal sleeve mockup

UT INSPECTION RESULTS

Table 1 provides a summary of the flaws in the thermal sleeve mockup, as measured. All of these flaws were located in the outer surface of the mockup.

Table 1. Summary of the flaws in the mockup

Flaw	Type	Orientation	Flaw Location	Length (mm)	Depth (mm)	Width (mm)	Distance From Weld C/L	Degree Location	mm Location
S1	SCC*	CIRC	WELD C/L	25	4.4	N/A	N/A	23°	750
S2	SCC	CIRC	WELD C/L	51	4.4	N/A	N/A	75°	634
S3	SCC	CIRC	S/S	51	4.4	N/A	13	137°	496
S4	SCC	CIRC	C/S	51	4.4	N/A	13	200°	356
C1	EDM NOTCH	CIRC	C/S	26	7.9	0.5	25	246°	254
C2	EDM NOTCH	CIRC	WELD C/L	26	7.9	0.4	N/A	280°	178
C3	EDM NOTCH	CIRC	S/S	25	7.9	0.4	25	314°	102

As expected, the SCC crack response was much lower (by approximately 6 dB) than the EDM notch response, and detection through the stainless steel side of the weld was more difficult than detection through the carbon steel side. For the nozzles investigated, it should be possible to inspect from both sides of the weld. All EDM notches were easily detected. An example of a crack response is shown in Figure 10.

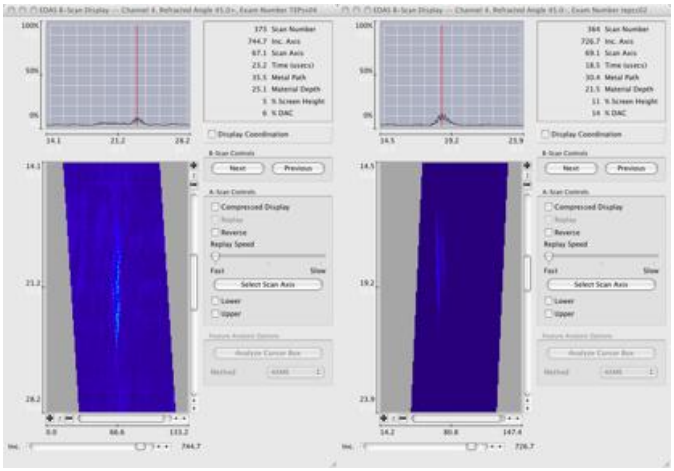

Figure 10. Left - Crack S1 detected from carbon steel side of the weld. Right - Crack S1 detected from stainless steel side of the weld.

VT INSPECTION RESULTS

The VT probe subsystem was scanned over a portion of the exterior mockup, in the region of flaw C3. Figure 11 and Figure 12 show images of this region. In Figure 11, the flaw is visible; in Figure 12 the label “C3” is clearly visible.

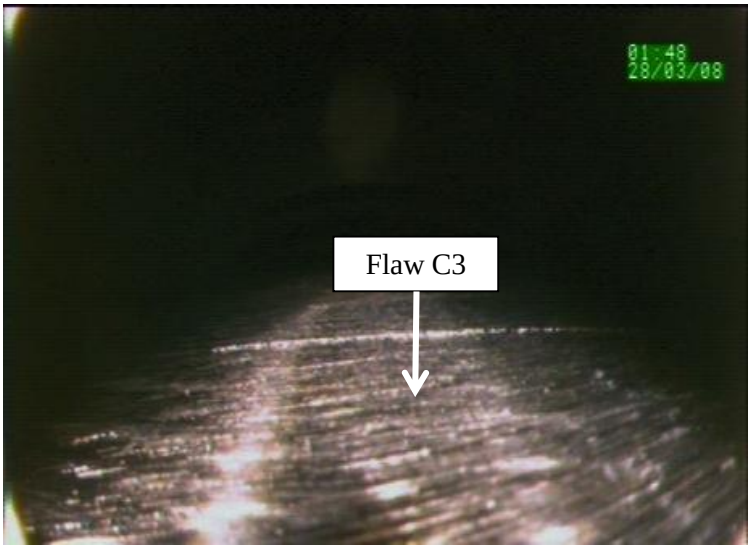

Figure 11. VT probe in the region of Flaw C3, which is visible in the image

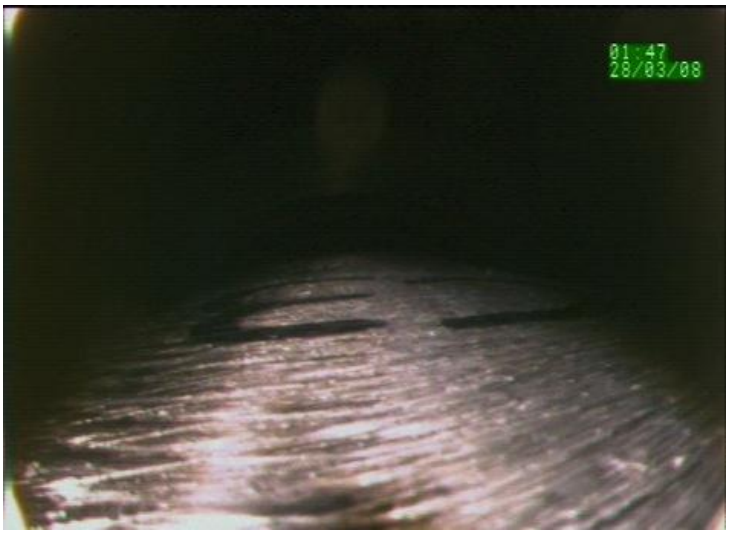

Figure 12. VT probe moved slightly away from Flaw C3. The label C3 is clearly visible in the image

CONCLUSIONS

Based upon the testing conducted, the following conclusions were reached.

(1) A new prototype interior scanner consisting of the UT probe subsystem, VT probe subsystem, Sensor Delivery Transport subsystem, and Circumferential Scanner subsystem, was designed and manufactured. The experimental results indicate that the concepts developed in these projects can be applied to inspection of the dissimilar and similar metal welds in typical BWR core spray thermal sleeves.

(2) The UT and VT probe subsystems successfully handle annulus gaps of approximately 7 mm to 22 mm.

(3) All implanted crack defects were detected. In order to ensure high reliability of crack detection, the dissimilar metal weld should be inspected from both the carbon steel side and the stainless steel side

ACKNOWLEDGEMENTS

This work was sponsored by the Tokyo Electric Power Company.

TESTING OF BURIED PIPES BY SLOFEC™ TECHNIQUE IN COMBINATION WITH A MOTOR-DRIVEN CRAWLER SYSTEM

W. Kelb, KontrollTechnik, Germany

Introduction

In 2001 Kontrolltechnik applied the SLOFEC® - technique for the inspection of storage tankfloors and above ground pipes for the first time. In the meantime scanners, inspection procedures and signal evaluation have undergone several improvements to meet client requirements and to expand the area of applications. In this sense development of the SLOFEC® - technique for the inspection of buried pipes is a continuous improvement process.

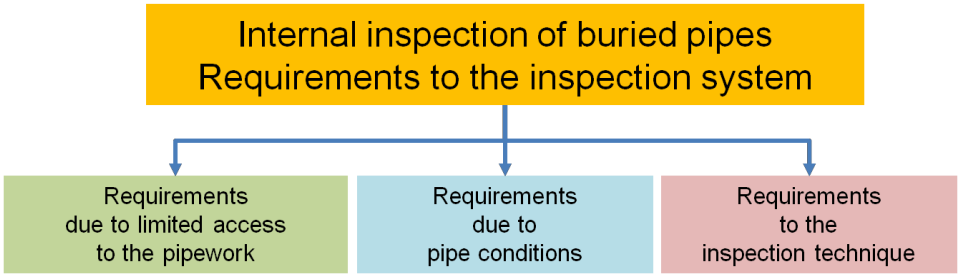

Nuclear plants have a large number of buried pipes for cooling and process water supply and disposal. Due to the age of those pipes, the demand for inspection of such pipework is rising. These pipeworks generally were not designed with piggability in mind. Inspection systems therefore have to fulfill multifarious requirements to be applicable to the inspection of non-piggable pipes. The requirements can be classified as follows:

Accessibility requirements to the inspection tool are:

- In many cases pipelines are not foreseen to be piggable, meaning that launching/receiving stations are nonexistent. Therefore for insertion of the tool only a short pipe section or an armature can be removed or the tool has to be inserted through a dome.

- In many cases access into the pipe is possible only from one end. The tool must allow bi-directional movement. Therefore the inspection tool must be connectable to a crawler system.

Fig. 1: Examples for tool installation situations for testing of buried pipes

Requirements to the inspection tool due to pipe conditions are:

- Most of the pipes have short bends with radiuses down to 1.0 x D. The inspection tool must be able to pass such bends.
- Pipes can be coated on the inner surface by rubber, GRP or concrete. Testing through coatings shall be possible.
- Comprehensive cleaning prior to the inspection is not possible. The surface can be covered by residue from product, debris, scaling, etc… Testing shall also be possible if rest of product, scale or debris remain in the pipe.

Fig. 2: Examples for conditions of pipes

Requirements to the testing technique are:

- In many cases the use of foreign products or the use of any liquid is unwanted or even not allowed. Additionally, the use and feeding of coupling media can be difficult. For that reasons inspection techniques working without coupling media are preferred.
- The testing technique shall reliably identify signals from defects and discriminate those from noise signals e.g. generated by grinded-off transport eyes, external pipe supports, ground anchors etc…
- The testing technique shall evaluate the depths and dimensions of wall thickness reductions with a defined accuracy.
- The testing technique shall reliably determine and document the position of defects in axial and circumferential directions.

Fig. 3:Re-examination of the defect depth detected by the SLOFEC® - technique

The Inspection Tools

Kontrolltechnik has developed three types of inspection tools for the inspection of non- piggable buried pipes, meeting the above stated requirements.
By the modular design, each inspection tool can be configured according to the situation on site.

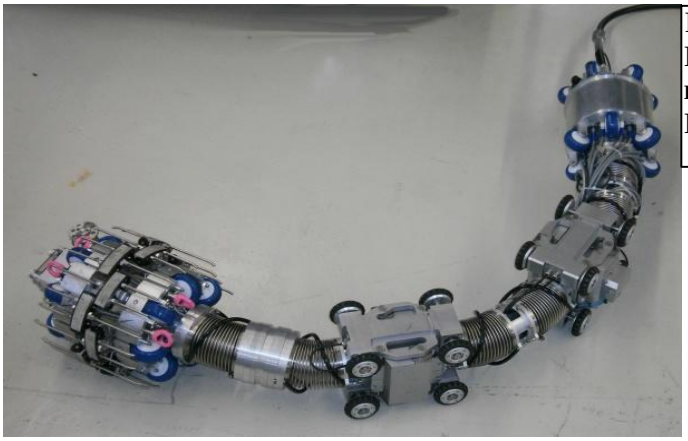

Fig. 4
Internal Pipe Scanner Type PLM with a motor-driven crawler system from Inspector Systems

Fig. 5
Internal Pipe Scanner Type PLS with a motor-driven crawler system from Inspector Systems

Fig. 6
Internal Pipe Scanner Type Pegasus during the testing of a drinking water pipe

The design features of the SLOFEC™ pipe inspection tools are as follows:

- The SLOFEC™ pipe inspection tool consists of single modules, which are connected by flexible joints. Each module is minimized in length allowing the tool to pass narrow bends down to 1.5 x D.
- The modules of the tools can be assembled on site if necessary. Even if due to limited access only modules or parts of the tool can be inserted in the pipe in many cases the assembly inside the pipe is possible.
- Each SLOFEC™ pipe inspection tool can be moved bi-directionally using a crawler system or can be pulled through the pipe by means of a winch.
- The SLOFEC™ pipe inspection tool type PLS has retractable centering devices and a retractable sensor head to pass sections with a reduced diameter.
- All inspection tools are equipped with inspection cameras and illumination for parallel video inspection.

SLOFEC® Internal Pipe Scanner Type PLM

The SLOFEC® Internal Pipe Scanner Type PLM is designed as a drive-through unit either connected to a crawler system or pulled by a winch. The sensors are spring loaded and arranged between the poles of the magnetization unit. The complete sensor head is guided on wheels for low friction and bi-directional operation.

Advantages of the PLM Type

- applicable to relative small pipe diameter
- reaches a relative high inspection speed

Disadvantages of the PLM Type

- the net weight of the scanner increases due to the necessary magnetization field strength disproportionate to an increase of the pipe diameter. In consequence, this concept is practically not applicable to pipes with larger diameters.
- due to the limited number of sensor channels, the resolution decreases with increasing pipe diameter

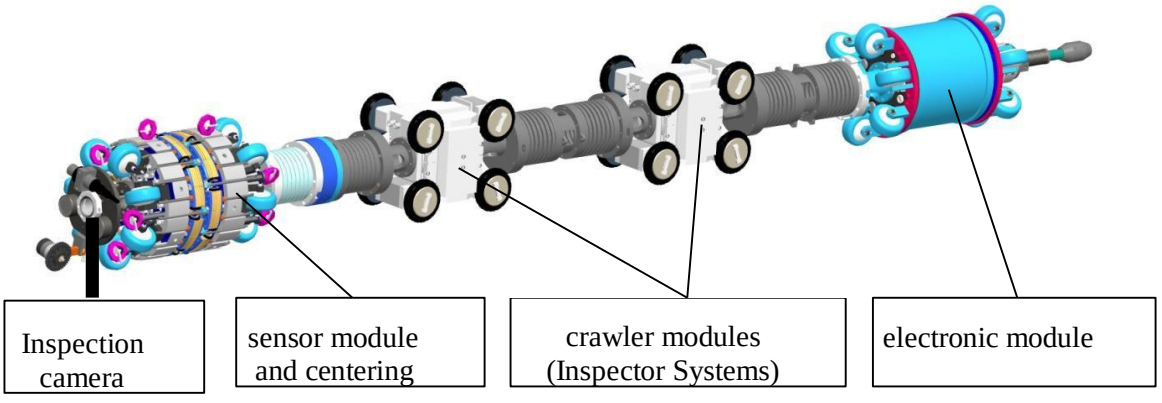

Technical Data :

Diameter range	:	10“ – 18“
max. wall thickness	:	16 mm (depending on the coating thickness and the detection limit)
max. coating thickness	:	10 mm
smallest passable radius	:	1,5 x pipe diameter (for 10“ – 2,5 x pipe diameter)
max. inspection length	:	300 m
max. inspection speed	:	6 m/min
drive systems	:	electr. crawler / pulling winch

SLOFEC™- Internal-Pipe-Scanner Type PLS

The SLOFEC™ Internal Pipe Scanner Type PLS is a scanner unit with a rotating sensor head. The scanner unit is designed to be connected either to a crawler system or pulled by a winch. For data acquisition the scanner will be positioned by the crawler or winch in axial direction. In position, the sensor head will be pressed in radial direction against the pipe wall by means of pneumatic or hydraulic cylinders and moved in circumferential directio n. After completion of a complete circumferential scan, the sensor heads will be retracted and the complete pipe testing unit will be moved by one sensor head width in axial direction. In this position, the data acquisition procedure will be started again. The scanning procedure is fully automated to reach reasonable inspection velocities. The complete sensor head is guided on wheels for low friction and bi-directional operation. The centering devices can be expanded and folded to pass sections with reduced diameter.

Advantages of the PLS Type

- the net weight of the scanner compared to the PLM type is drastically reduced.
- it has a higher resolution than the PLM type. The resolution is independent of the pipe diameter.
- the centering is variable in diameter and can compensate pipe diameter changes in both directions.
- dead zones on either side of butt welds and pipe collars are minimized.
- pipe sections with heavy debris or contamination can be passed without the need to doze the debris in front of the scanner.

Disadvantages of the PLS Type

- inspection speed is lower than for the PLM type tools

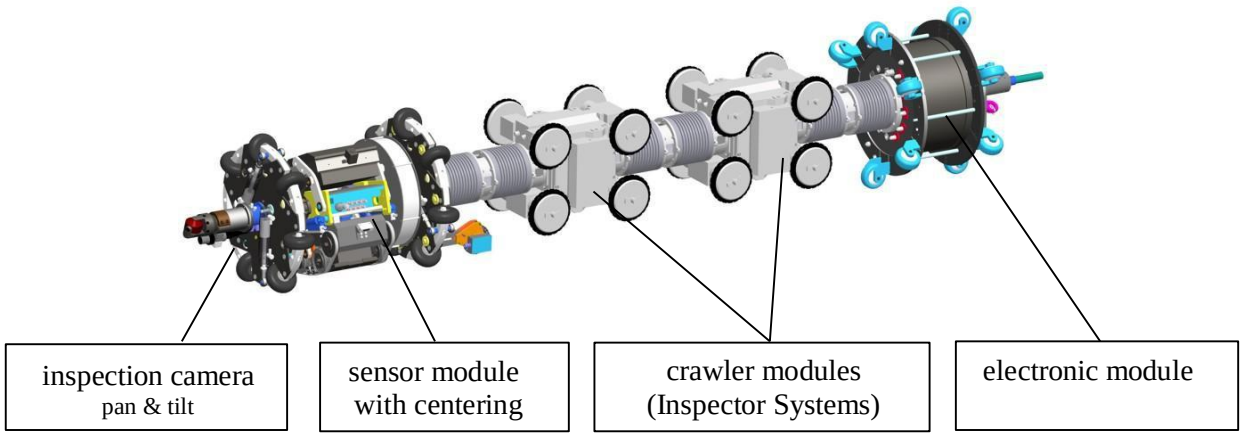

Technical Data :

Diameter range	:	≥ 20“ – 30“ (planned up to 48“)
max. wall thickness	:	19 mm (depending on the coating thickness and the detection limit)
max. coating thickness	:	10 mm
smallest passable radius	:	1,5 x pipe diameter
max. inspection length	:	300 m
max. inspection speed	:	0,2 m/min
drive systems	:	electr. crawler / pulling winch

SLOFEC^{TM} Internal Pipe Scanner Type Pegasus

The SLOFEC^{TM} Internal Pipe Scanner Type Pegasus is a scanner unit with a rotating sensor head. The scanner unit is designed for the inspection of big diameter pipes were a crawler system cannot be applied. With the Pegasus unit inspections with pipe diameters of up to 2m were realized. The unit can either be pulled by a winch or moved manually in humanly accessible pipes. The main advantage of the unit is that it can be completely assembled inside the pipe, allowing a high flexibility for the inspection of pipes, which are accessible
only through a dome.

Advantages of the Pegasus Type

- low net weight of the scanner
- has a higher resolution than the PLM type. The resolution is independent of the pipe diameter
- fast adaption to different pipe diameter
- the centering is variable in diameter and can compensate pipe diameter changes in both directions.
- dead zones on either side of butt welds, pipe collars are minimized.
- Pipe sections with heavy debris or contamination can be passed without the need to doze the debris in front of the scanner
- Installation through manholes is possible

Disadvantages of the Pegasus Type

- the inspection speed is lower than for the PLM type tools
- the scanner cannot be operated in combination with the crawler system

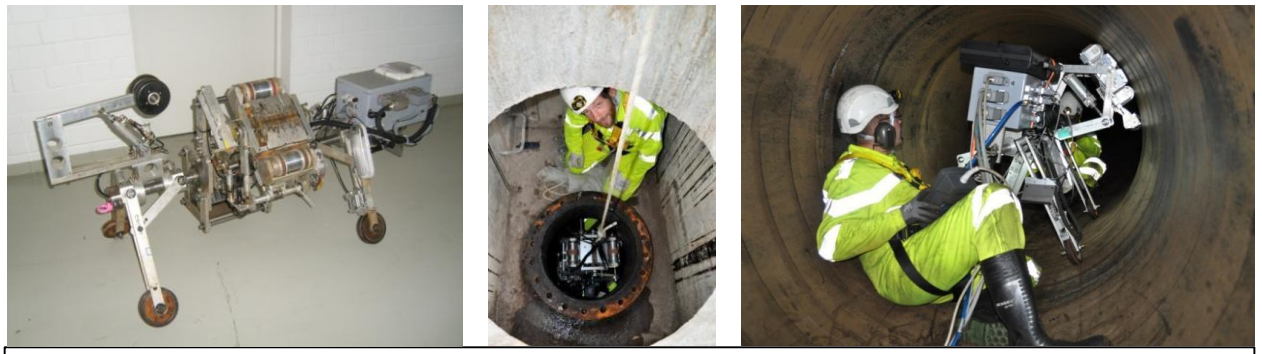

Fig. 7 SLOFEC®-Internal-Pipe-Scanner Type Pegasus, Installation of the scanner through a manhole, operation of the scanner during inspection of a drinking water pipe with manual feeding

Technical Data :

Diameter range	:	≥ 30“ (realized up to 3 m pipe diameter)
max. wall thickness	:	19 mm (depends on the coating thickness and the detection limit)
max. coating thickness	:	10 mm
smallest passable radius	:	5 x pipe diameter
max. inspection length	:	300 m
max. inspection speed	:	0,2 m/min
drive systems	:	pulling winch / manual

The SLOFEC® - Technique

The SLOFEC® inspection system is based on the eddy current method with superimposed DC- magnetization.

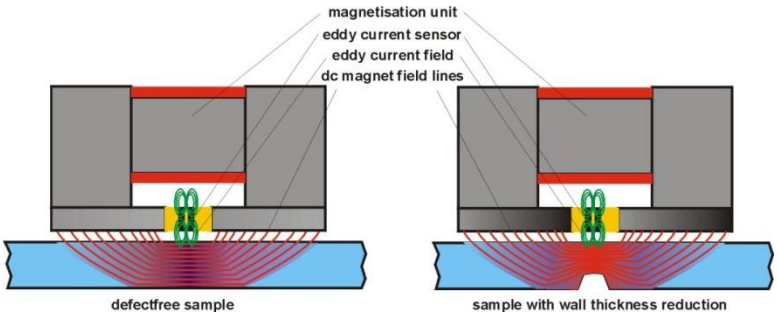

Fig. 8:field distribution in a defect- free sample

Fig. 9:field distribution in a sample with wall thickness reduction

Figure 8 shows schematically the working principle of the SLOFEC™ technique at a defect- free sample. A magnetic yoke containing a permanent or electro-magnet is used to generate a strong magnetic field in the material to be tested. The magnetic DC field has an effect to the material properties of the test sample. In a defect-free sample the magnetic field leads to a homogenization of the material properties.
Between the poles of the yoke an eddy current sensor is located. This sensor also generates a small alternating magnetic field in the material under test, super-imposed to the magnetic field of the yoke. The eddy current field is sensitive to changes of the material properties of the test sample. In a defect free sample the DC magnetization and therefore the material properties do not change. As a result the eddy current signal remains unchanged.
Figure 9 shows the field distribution at a sample with a wall thickness reduction. A reduction of the wall thickness, e.g. by a corrosion pit will result in a concentration of the magnetic fields in the remaining wall, resulting in an increased magnetic field strength above and around the defect. This results in a change of the material properties at this location. This local change of the material properties will be detected by the eddy current sensor.
The eddy current signal amplitude of the defect indication is a measure for the volume of metal loss.

Figure 10 and 11 show the typical SLOFEC® signal responses at the example of 40% deep flat bottom holes placed at the inner and outer surface of the pipe. Characteristic is the phase difference of signals from external and internal defects.

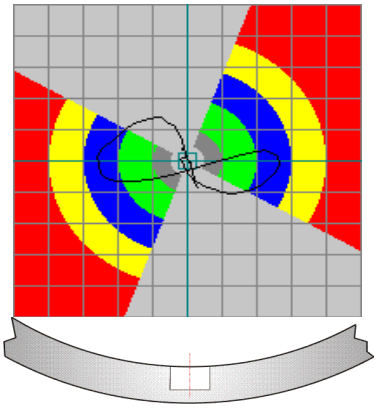

Fig. 10 S i g n a l response from a flat bottom hole at the inner surface of the pipe

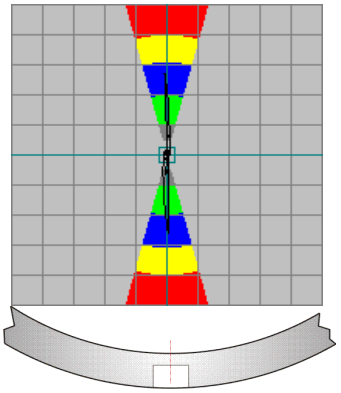

Fig. 11 S i g n a l response from a flat bottom hole at the outer surface of the pipe

Influence parameter and signal analysis

The signal response of the SLOFEC® – technique depends on several influence parameters as shown in figure 12.

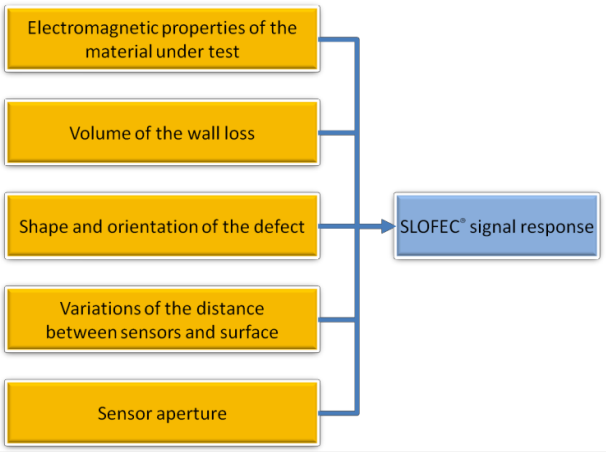

Fig. 12 Influence parameters to SLOFEC® signal response

Like all other electromagnetic testing techniques, SLOFEC® is a comparative technique, meaning that the signal response from a defect will be compared to signal responses from known defects and evaluated accordingly.
In other applications like e.g. SLOFEC® tankfloor testing, follow-up tests e.g. by ultrasonic testing can be performed to confirm the evaluated depths. In the field of buried pipe inspection due to the limited access to the pipe, follow-up tests are not possible or are time and costs intensive. Therefore more comprehensive data analyzing procedures under consideration of the influent parameters have to be applied than it would be necessary for other applications.
The defect volume has essential influence on the SLOFEC® signal response and is therefore a major influence factor. Following the SLOFEC® depth evaluation procedure under consideration of the defect volume is shown.
The defect depth evaluation will be performed using so-called amplitude – defect depth calibration curves, showing the relation between defect depth and signal amplitude. For generation of the amplitude – defect depth calibration curves flat bottom holes and half-round shaped holes with known depths are used. Unique amplitude – defect depth calibration curves can be generated for different hole diameters (see figure 13). Several of these calibration curves are stored in the data analysis software.

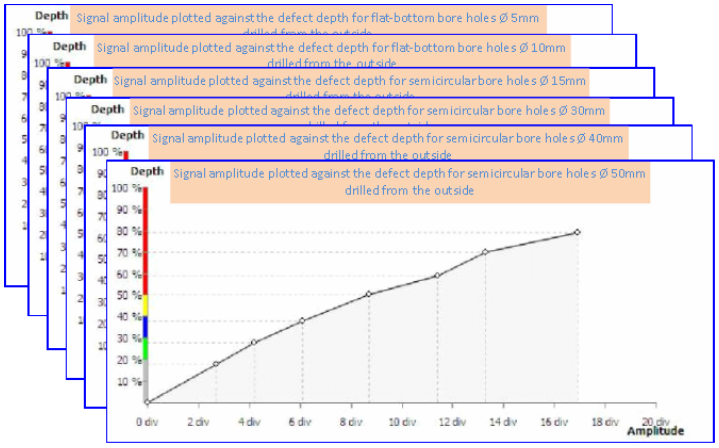

Fig. 13 amplitude – defect depth calibration curves for flat bottom and half-round holes at the outer surface of the pipe

The signal analysis software evaluates besides the signal amplitude and signal phase also the distance between the amplitude maxima, which is proportional to the diameter of the defect (figure 14). The signal phase determines, if the signal is generated by an internal or external defect.

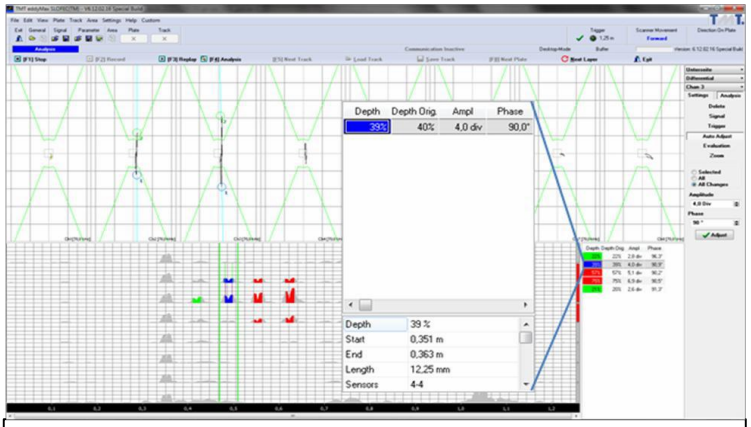

Fig. 14 Evaluation of the amplitude maxima distance

All of the amplitude – defect depth calibration curves represent a plane as shown in figure 15.
Using the values of the signal amplitude and the distance of the amplitude maxima a point in the plane will be determined, which is used for the depth evaluation. Points between two calibration curves are calculated by interpolation.

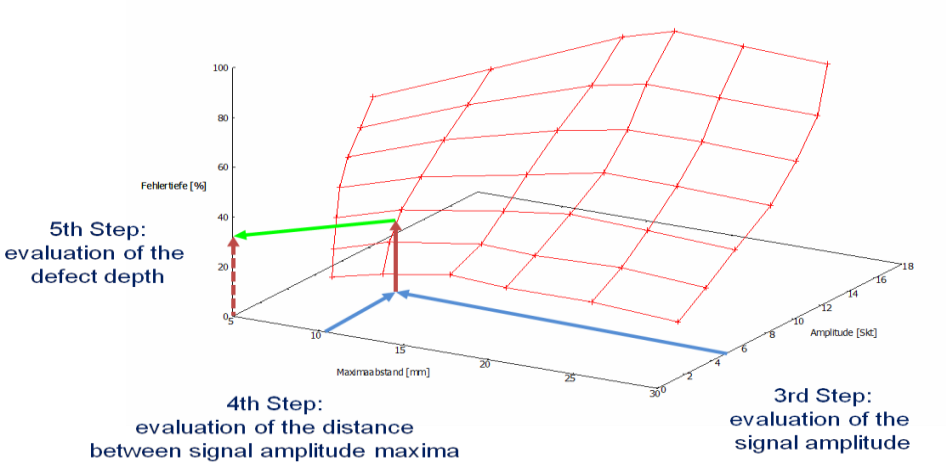

Fig. 15 Evaluation of the defect depth under consideration of the defect volume

By application of the above described and additional measures a satisfying accuracy in defect depth determination even for a large spectrum of different defects is achieved. Figure 16 shows the result of a blind test with more than 60 defects with different dimensions and forms. The tolerance of ±20% in defect depth determination corresponds to the accuracy of intelligent pigs.

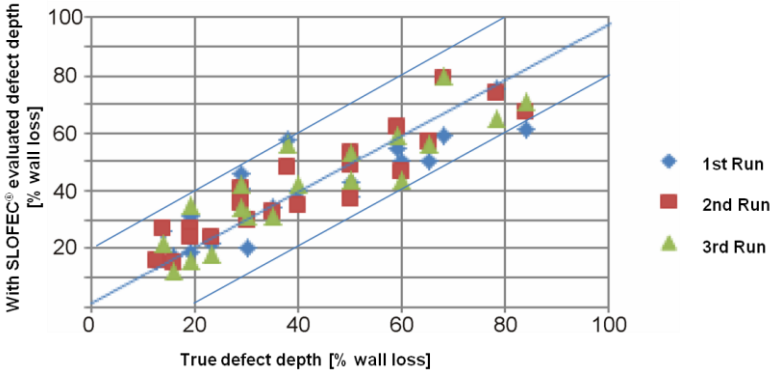

Fig. 16 Accuracy in defect depth determination (result of a blind test)

Detection limit for various types of defects

The detection limit for particular defects depend on the magnetization field strength the tool can generate, the orientation of the magnetic field relative to the defect, the distance of the sensors to the surface and the condition of the pipe surface. Figure 17 gives a general overview about the detection limit for the SLOFEC® internal pipe scanner type PLS and type Pegasus. Due to the fact that for both scanner types the magnetic field is oriented in circumferential direction of the pipe, all defects with an extent in axial direction have a good detectability. Such defects are slots and notches with axial orientation as well as pitting and trough shaped wall thickness reductions. With an increasing ratio between circumferential length to axial width the detection limit will decrease. The same is valid for big planar defects with small gradients. The detection limit for planar defects decreases with increasing areal extent and decreasing gradient.

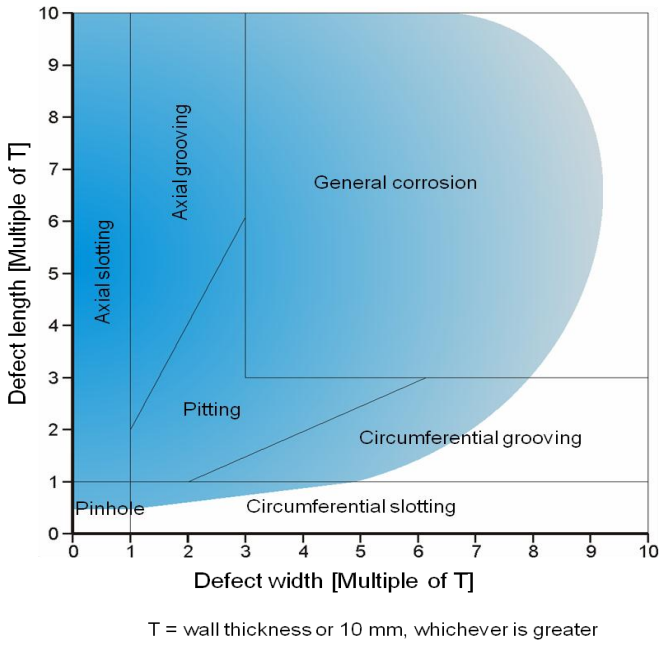

T = wall thickness or 10 mm, whichever is greater

Fig. 17 detection limit for various types of defects for the SLOFEC® Internal Pipe Scanner Type PLS and Type Pegasus

The SLOFEC® internal pipe scanner type PLM has qualitative the same detection limit to various defect types. However due to the orientation of magnetic field lines in axial direction of the pipe for the PLM types, the detection limit for defects with circumferential orientation is higher and the detection limit for defects with axial orientation lower.

SLOFEC® - data acquisition and result documentation

During the SLOFEC® data acquisition the signals of all sensor channels are displayed online. By this function the operator can overview the signal data quality and repeat the data acquisition if necessary. Figures 18 and 19 show the typical signal data of all 8 sensor channels of the PLS type scanner for one turn of the sensor head. Directly after completion
of the data acquisition the software analyses the data and shows the operator the results.
The operator can now confirm, delete, edit the result data or select from the chart display sections to be analyzed. For documentation the raw signal data as well as the result data will be stored.
Figure 18 shows the screen of the data acquisition software for a pipe section without wall thickness reductions. Only signals caused by surface roughness and lift-off of the sensor head can be seen.

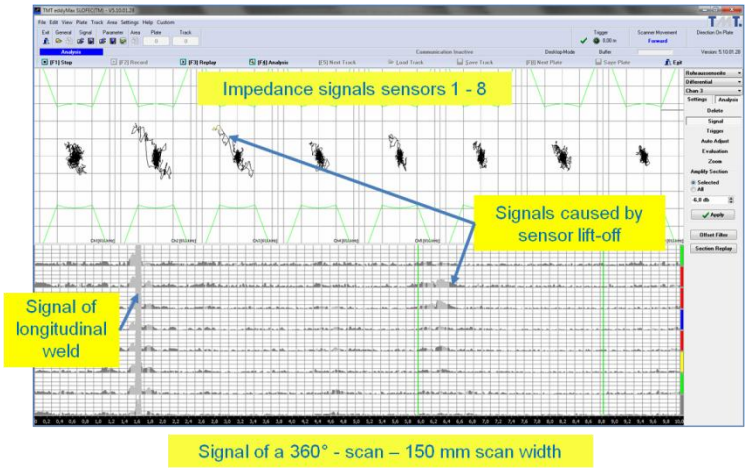

Fig. 18 screen of the SLOFEC® data acquisition software for a pipe section without wall thickness reductions

Figure 19 shows the screen of the data acquisition software for a pipe section with three typical indications caused by pitting shaped defects. The big, red colored indication was caused by a 100% deep through the wall pit and both small, green colored indications were caused by 20% deep pits.

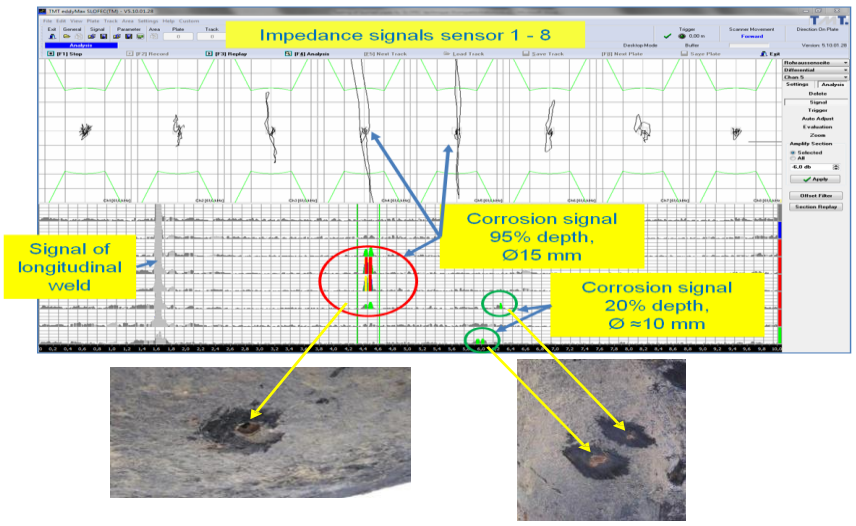

Fig. 19 screen of the SLOFEC® data acquisition software for a pipe section with indications from a 100% deep pit and two 20% deep pits at the outer surface of the pipe

After confirmation by the operator the evaluated defect depths are converted into an easy to read colored C-Scan with defined colors representing defect depths.
Besides the inspection report, the documentation consists of a colored „Pipe-Scan-Report“ for each tested pipe section (see figure 20) and an indication list (see figure 21).
The Pipe-Scan-Report shows a schematic picture of the pipe consisting of single pipe sections. For each tested pipe section the inspection result in colored C-scan mode is shown. Wall thickness reductions are displayed in different colors according to the evaluated depths and the colors defined in the color palette.
The indication list contains for each evaluated defect its depth, position and classification as internal or external defect.

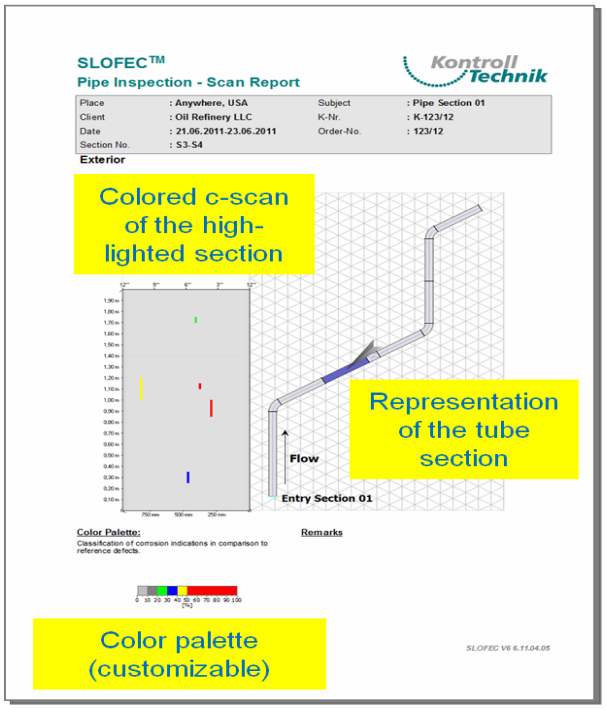

Fig. 20: Example of a Pipe-Scan- Report

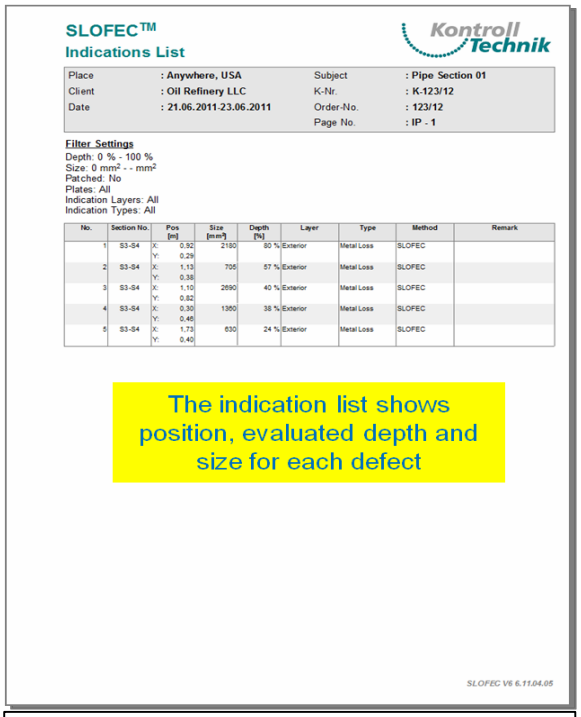

Fig. 21: Example of an indication list

NONDESTRUCTIVE EVALUATION OF WALL THINNING OF CARBON STEEL USING PULSED EDDY CURRENT TECHNIQUE

D.G. Park, M.B. Kishorea, K.H. Kim, D.H. Lee
Korea Atomic Energy Research Institute, South Korea
M.B. Kishore, C.G Kim, Chungnam National University, South Korea

ABSTRACT

Local wall thinning is a point of concern in almost all steel structures such as pipe lines covered with a thermal insulator made up of materials with low thermal conductivity (fiberglass or mineral wool); hence, Non Destructive Technique (NDT) methods that are capable of detecting the wall thinning and defects without removing the insulation are necessary. In this study we developed a Pulsed Eddy Current (PEC) system to detect the wall thinning of Ferro magnetic steel pipes covered with fiber glass thermal insulator and shielded with Aluminum plate. The developed system is capable of detecting the wall thickness change through an insulation of thickness 10cm and 0.4mm Aluminum shielding. In order to confirm the thickness change due to wall thinning, two different sensors, a hall sensor and coil sensor were used as a detecting element. In both cases, the results show a very good change corresponding to the thickness change of the test specimen. During these experiments a ferro magnetic steel tube of diameter 210mm and a length of 620mm, which is covered with insulator of 95mm thickness was used. To simulate the wall thinning, the thickness of the tube is changed for a specified length such as 2.5mm, 5mm and 8 mm from the inner surface of the tube. A 0.4mm thick Aluminum plate was covered on the Test specimen to simulate the shielding of the insulated pipelines. For both hall sensor and coil detection methods fast Fourier transform (FFT) was calculated using window approach and the results for the test specimen without Aluminum shielding were summarized which shows a clear identification of thickness change in the test specimen by comparing the magnitude spectra.

INTRODUCTION

The pipelines of power plants and heat exchangers are covered with a thermal insulator to decrease the heat loss. During long-term services, corrosion might occur on the outer side of the pipe as corrosion under insulation (CUI), or on the inner side of a pipe as flow accelerated corrosion (FAC) and develops into wall thinning of the pipelines is a real threat for the reliability of carbon steel equipment, which may finally result in a catastrophic failure. Therefore, local wall thinning is a point of concern in almost all steel structures. Usually, thermal insulators used for the purpose of covering the pipelines is made up of materials with low thermal conductivity (fiberglass or mineral wool); hence, NDT methods that are capable of detecting the wall thinning and defects without removing the insulation or through this insulation are necessary.

The PEC technique offers an alternative to these conventional techniques due to its potential advantages, such as less susceptible to interference, less power consumption because of using short pulses which are more desirable specification in the development of portable instruments. The conventional ECT which operates with a single frequency sinusoidal excitation has gained wide acceptance in the field of NDT [1]; yet, this technique suffers from a limitation, i.e., penetration depth or skin depth. The skin depth equation is given by $\delta = \sqrt{1/\pi\mu\sigma f}$, where μ is the permeability, σ is the conductivity and f is the frequency of excitation, and the penetration depth δ depends on excitation frequency f [2]. In contrast to the traditional ECT, the PEC employs a nonsinusoidal excitation, such as a pulse or square wave, instead of a single frequency sinusoidal excitation. Because the Fourier transform of a pulse contains multiple frequency components [3, 4], a rectangular pulse can provide the

depth profile of a material under test [5, 6]. The usage of short current pulse excitation reduces the power consumption, which is the most desired specification in the development of portable instruments. Due to the potential advantages of the PEC, prevalent investigations on this technique have been conducted, such as detection of wall thinning and corrosion in aircraft multilayer structures [7, 8].

Pulsed eddy current nondestructive testing is widely used for the characterization of deep flows in ferromagnetic materials and the characterization of the electromagnetic properties as well as the thickness of metallic plates. PEC techniques use pulsed excitation that is characterized by the richness of frequency contents. This is thought to be potential in bringing up information about the testing condition. In contrast to conventional, multi-frequency or broadband eddy current techniques, where a single, multiple, or a broadband frequency sinusoidal field excitation is used. The (PEC) technique offers its potential advantages such as less susceptibility to interference and less power consumption owing to the use of short pulses, which are more desirable specifications in the development of portable instruments. In case of Ferro magnetic materials, when the probe is in close proximity to the sample the reactance of the coil increases instead of decreasing. A Ferro magnetic material whose permeability is higher will concentrates the primary flux into the sample and overshadows the detected eddy current fields. The developed PEC system is optimized for the detection of thickness change as well as surface crack detection on the Ferro magnetic samples. A Lab VIEW based program is used to record the data and to analyze the recorded data. We conducted two different experiments simultaneously to maintain the same experimental conditions and both results were summarized for the thickness variations of the tested sample

SYSTEM DESIGNING

The PEC system consists of a pulse amplifier, a probe with a driving coil and a magnetic field detecting sensor, a sensitive PEC differential amplifier with variable gain to amplify the output voltage from the magnetic field detection sensor, a A/D converter, and a computer with signal processing software. A schematic of the PEC system is shown in Fig 1(a). From this figure it is clear that the pulse amplifier drives the excitation coil and the sensor electronic reads the output from magnetic sensor used in probe and conditions the detected signal, the proper conditioned signal is recorded in computer using some software application. The PEC probe characteristics are determined by a combination of measuring environments and a PEC probe consisting of an exciting coil and a field detection sensor. The excitation coil is made by wounding a copper wire of 1mm diameter on a bobbin; a commercially available hall sensor with proper connections was placed in the middle of the excited coil to detect the response from eddy currents. Another coil made up of a copper wire with diameter 0.8mm is wound over the exciting coil as shown in the Fig 1(b), this coil can be used as another field detection sensor. The two sensors are used simultaneously to detect the eddy currents.

A real-time LabVIEW program was developed for the data acquisition and for scanning the probe on the insulated and shielded sample. The scanning and analyzed results were displayed on the computer monitor.

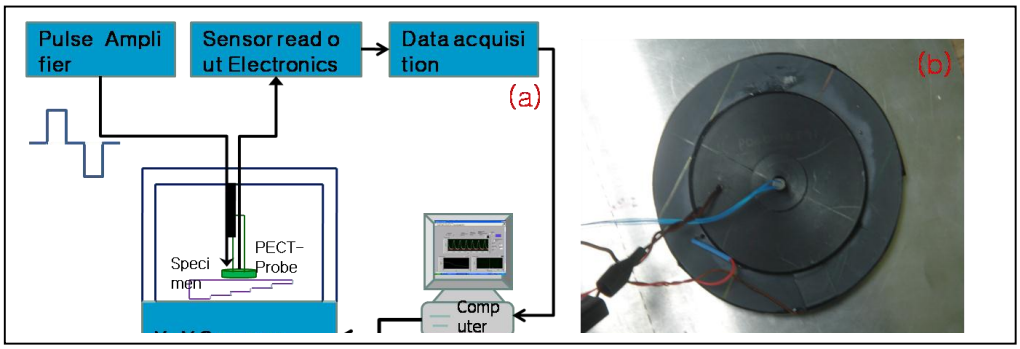

Fig 1.a) Schematic diagram of PEC system b) Probe with both hall sensor and coil as the field detecting sensors

EXPERIMENTAL SETUP

To simulate the wall thinning of a steel pipe, a mock-up of a wall thinned pipe with various thickness regions 2.5mm, 5mm and 8mm respectively was fabricated. A 95mm thick insulator with galvanized cladding of 0.4 mm thickness covers the pipeline to simulate real time environment as shown in the Fig 2(b). The test specimen also consists of three similar cracks of 5mm width, 1mm depth on 2.5mm thick region and same quantity of 5mm width, 2mm deeper cracks on 5mm thick region. Fig 2(c) clearly depicts the inner cross section of the tube covered with insulation and shielded with Aluminum plate, three similar cracks also can be observed on 2.5mm and 5mm thick regions.

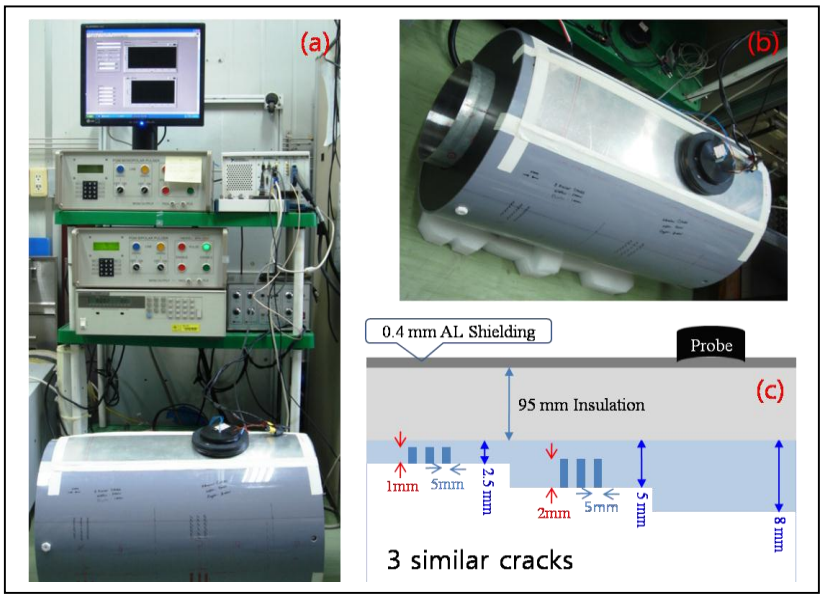

Fig 2.a) Experimental Setup of PEC system b) Test Specimen c) Inner Cross sectional view of the test specimen

A bipolar rectangular current pulse generated from Pulse Amplifier was used to excite the driving coil and the detected sensor output is fed to the PEC amplifier for signal conditioning and then connected to a computer through DAQ equipment as shown in the Fig 2(a). While placing the probe great care was taken to avoid the cracked region not to come under the probe area in order to avoid the ambiguity in the results of thickness change. The probe was scanned along the different thickness step of pipe, and the excited pulse is repeated for five times and the average of the response is recorded as the resultant detected pulse corresponding to a thickness of the test sample which leads to reduce the percentage of error as less as possible. After finishing the measurement, the probe is moved to 5 mm thick region of the sample and repeated the same process to record the detected signal corresponding to 5mm thickness. Finally, the probe is moved to 8mm thickness region and its corresponding detected pulse is recorded in same fashion. All the data recording process has been developed in LabVIEW environment also the data analysis and processing can be done by using this program. Once after completing the data recording process all the data is analyzed and displayed on the computer. Also FFT can be calculated for the analyzed data and displayed on the computer monitor. The system applied in the mock-up can distinguish a wall thickness of 2.5, 5, and 8 mm under 95 mm insulation covered with 0.4 mm of stainless cladding.

RESULTS AND ANALYSIS

When a high-level current is applied to the exciting coil, the coil makes a static magnetic field (primary magnetic field) in the sample; when there is a sudden transition in the exciting current, eddy currents are induced in the sample; the time-varying magnetic fields (secondary magnetic field) generated by the decaying eddy currents are captured by the Hall-sensor as a voltage signal. The strength and duration of an induced pulse signal resembles the average wall thickness that can be measured. The duration of the eddy currents will have an effect on the transition period of the detected pulse. Form the Fig 3(a) it is clearly observed that the transition time gradually increases as the thickness of the sample increases during the rising of the detected pulse. In other words the rising edge of the detected pulse is delayed more as the thickness of the sample increases, during its falling edge the delay is decreasing as the thickness increases also the magnitude of the detected pulse gradually decreases with increasing sample thickness. When the insulation over the test specimen is covered with 0.4mm Aluminum plate, same phenomenon is observed i.e. the transition period gradually increases as the thickness of the sample increases during the rising of the detected pulse, also the magnitude of the detected pulse gradually decreases with increasing sample thickness in the detected pulse. The detected pulse is further reduced compared to the previous case i.e. without aluminum plate on the insulation as shown in Fig 3(b). The slope of rising pulse in the Al shielded one increased compared to that of unshielded one, which is attributed to the damping of the eddy current by Al shield.

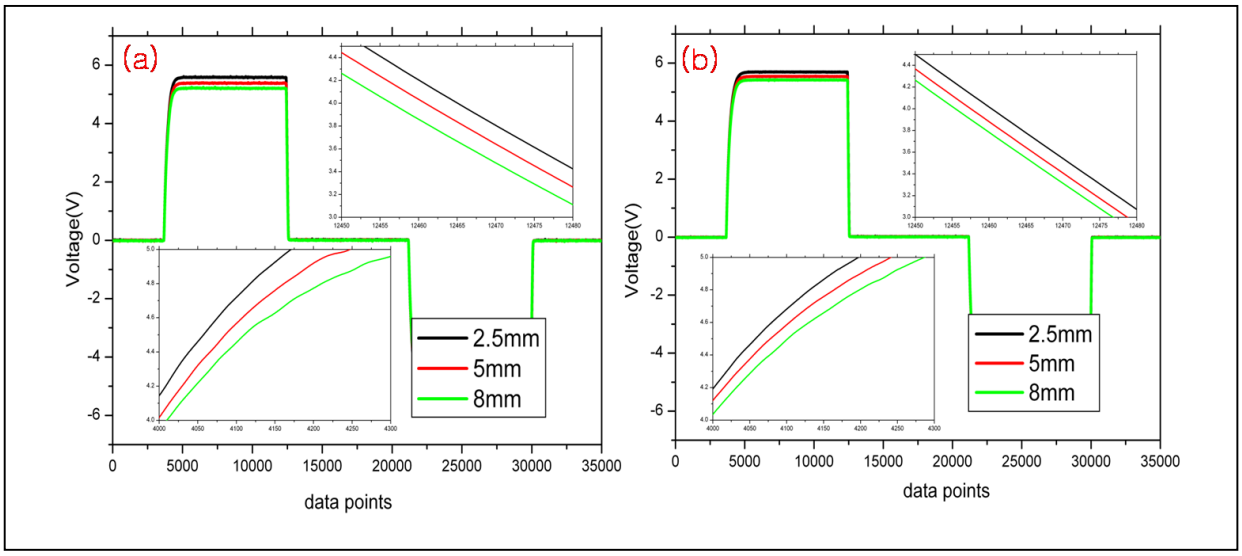

Fig 3.a) Hall Sensor output with 95mm Insulation and not Aluminum shielding b) Hall Sensor output when the sample insulated with 95mm Insulation and shielded with 0.4mm Aluminum plate

To confirm the Hall sensor results, the coil sensor results are also analyzed which concludes the same as that of hall sensor detection method. Since both the experiments are conducted in a single instant all the experimental conditions are exactly same as the prior experiment which is clearly shown in Fig 4(a). From this figure it is clear that the peak of the sensing signal gradually increases as the thickness of the tube decreases, it is observed that the decaying of the eddy currents increases as the thickness decreases which is a clear identification of the change in the sample thickness. When the insulation on the sample is shielded with Aluminium plate the magnitude of the detected pulse considerably decreases since the penetration of the excited magnetic fields are limited by the aluminium shielding.

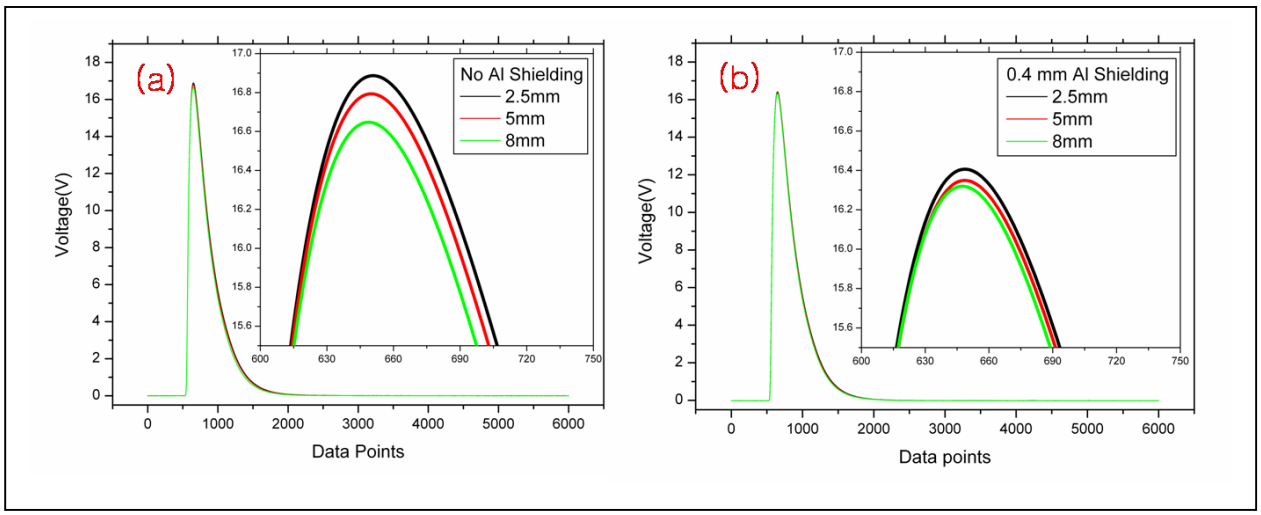

Fig 4.a) Coil Sensor output with 95mm Insulation and not Aluminum shielding b) Coil Sensor output when the sample insulated with 95mm Insulation and shielded with 0.4mm Aluminum plate

Fig 5(a) and 5(b) shows the frequency spectrum of the detected pulse from hall sensor and coil respectively measured without Aluminium shielding. The frequency spectrum clearly states that the energy of the detected pulse from a lower thickness region is higher than that of the higher thickness region. The frequency spectrum of the detected pulse from Hall sensor shifted to lower frequency region compared to that from coil sensor. The eddy currents decays at a faster rate as the thickness increases, which means that the energy of the detected pulse for higher thickness region is small compared to that of lower thickness regions. Therefore, we can discriminate the thickness of the test specimen from this frequency spectrum of induced pulse signal.

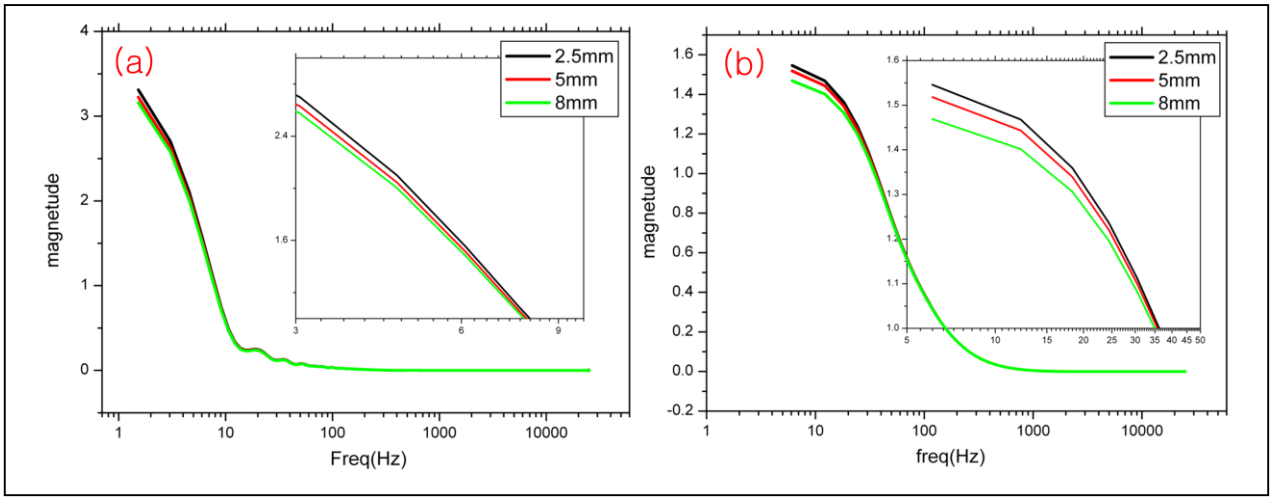

Fig 5.a) FFT of Hall Sensor output with 95mm Insulation b) FFT of Coil output when the sample insulated with 95mm Insulation

CONCLUSION

The PEC technique which detects the wall thinning of pipelines covered with thick insulation was developed using a Hall sensor and coil sensor. The probe performance was tested using the wall thinning pipe covered with 95 mm insulation covered with 0.4 mm of stainless cladding**.** The results obtained from Hall-sensor show better resolution than that of coil sensor. The detected pulse is further reduced compared without aluminum plate on the insulation. The slope of rising pulse in the Al shielded one increased compared to that of unshielded one, which is attributed to the damping of the

eddy current by Al shield. The frequency spectrum of the detected pulse from Hall sensor shifted to lower frequency region compared to that from coil sensor. The eddy currents decays at a faster rate as the thickness increases, which means that the energy of the detected pulse for higher thickness region is small compared to that of lower thickness regions. We can discriminate the thickness of the test specimen from this frequency spectrum of induced pulse signal.

REFERENCES

[1] N. Nair, V. Melapudi, J. Hector, X. Liu, Y. Deng, Z. Zang, L. Udpa, J. M. Thomas and S. Udpa, A GMR based eddy current system for NDE of aircraft structures, IEEE Trans. Magn. 42, 3312 (2006).

[2] R. Griberg, L. Udpa, A. Savin, R. Steigmann, V. Palihovic and S. S. Udpa, "2D eddy current sensor array", NDT&E Int. 39, 264 (2006).

[3] A. Sophian, G. Y.Tian, D.Taylor, J. Rudlin, A feature extraction technique based on the principal component analysis for pulsed eddy current NDT, NDT & E int., Vol. 36, 37, (2003).

[4] Zhang Gang, Zhao Liang, Research on thickness of metallic layers from pulsed eddy current nondestructive measurements, Transducer and Microsystems Technologies, 25(4), 35 (2006).

[5] C. J. Renken. The use of personal computer to extract information from Pulsed eddy currents, Materials Evaluation, 59(3), 356 (2001).

[6] J. Blitz, Electrical and magnetic Methods of nondestructive testing, Chapman & Hall (London). 1997.

[7] M. A. Robers, R. S. Scottini, Proc. of 8th ECNDT conf, ndt.net, 7(10), Barcelona, June (2002).

[8] R. A. Smith, G.R. Hugo, Transient Eddy-current NDE for aging aircraft capabilities and limitations, Insight, 43(1), 14 (2001).

PIPING INSPECTION I

APPLICATIONS OF NEW-GENERATION PORTABLE PHASED ARRAY SYSTEMS FOR TRULY EFFICIENT INSPECTIONS

P. Tremblay, L. Enenkel
ZETEC NDT Solutions, Canada

INTRODUCTION

The first generation of portable phased array UT (PA UT) systems has hit the market in the early 2000's. The massive adoption of these devices has been a game-changer for ultrasonic inspections of critical components in oil & gas, aerospace, heavy industry and power generation plants.

Taking advantage of the last ten years of improvements of digital electronics and leveraging on lessons learned from field experience, manufacturers have recently developed systems which offer much more power and performance. For example, users of these systems can now benefit from larger data file size, better amplitude resolution, faster data acquisition rate and advanced on-board data analysis. This opens brand-new possibilities to the non-destructive testing industry for the application of portable PA UT systems.

This paper will show how enhanced computing power and hardware performance of new-generation portable PA UT systems (see **Error! Reference source not found.**) allow more powerful on-board software. Various practical examples will be presented to illustrate how this translates into more efficiency in preparation, acquisition, analysis & reporting of a PA UT inspection.

Figure 1: New-Generation Portable PA UT System

PREPARATION

Any good UT inspection starts with an adequate preparation. Starting from the geometry and material of the component to be inspected (see
F igure 2), the right insonification strategy needs to be established, leading to the inspection method, (conventional UT, TOFD, PA UT or any combination), acoustic beam parameters, probes & wedges to be used, and positioning of the search units to adequately cover the volume of interest. This initial process is usually called scan planning.

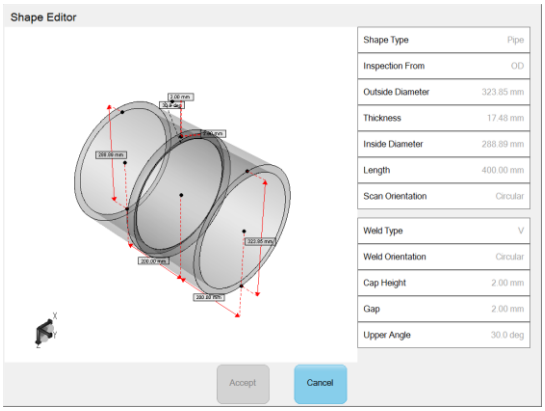

F igure 2: On-board Specimen Editor

The graphic processing power of new generation portable PA systems allows on-board creation of a 3D representation of the inspected part, including weld profile, for mostly flat or cylindrical geometries. This greatly facilitates the creation of an adequate scan plan. Indeed, with the visual feedback provided by the on-board focal law calculator, the optimization of the inspection angles and search unit positioning can be done by simply sliding the representation of the search unit on the representation of the inspected part (see Figure 3). Also, for multi-channel (or multi-group) setups, coverage assessment can be visualized, even when using different inspection methods simultaneously (see Figure 4).

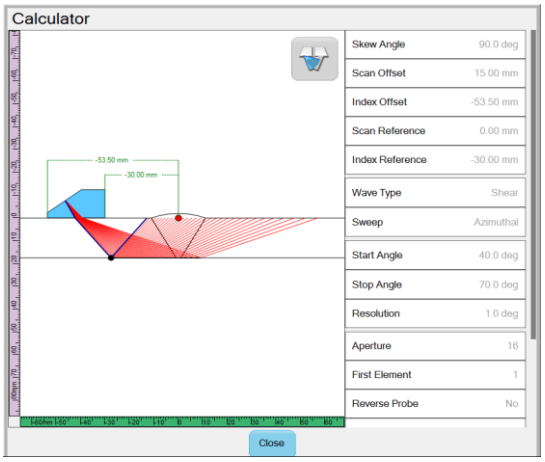

Figure 3: On-board Phased Array Calculator – Single Channel

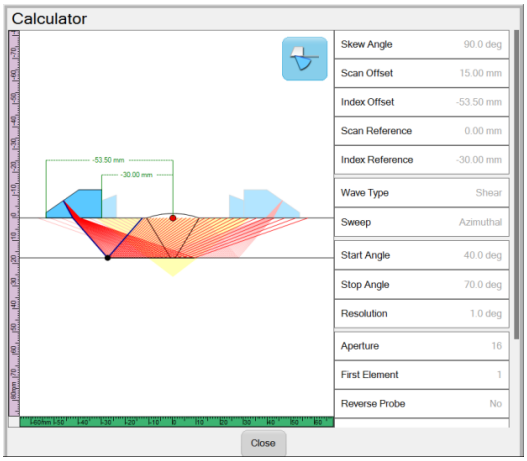

Figure 4: On-board Phased Array Calculator – Multiple Channels

For non-experts, setting up a TOFD channel on a first-generation portable PA system can be quite complicated. First, you need to manually determine the angle and the probe-center separation (PCS) required to get adequate crossing point of the transmitter and receiver beams. Then, depending of probe frequency, probe diameter, wedge angle and material velocity, you need to make sure the divergence of the acoustic beam will provide adequate coverage of the volume of interest. Finally, you need to manually set the timebase start and range to record the signal from the lateral wave to the first mode conversion, as required by many codes. And this process obviously becomes more tedious when the inspection is performed on a more challenging configuration such as a longitudinal seam weld.

The visual feedback provided by new-generation portable PA systems makes TOFD channel creation easy (see Figure 5). By setting the required depth of the crossing point of the transmitter and receiver beams, the PCS is automatically calculated. Moreover, to facilitate the positioning of the probes and wedges on the scanning device, the front-wedge separation is also provided. The beam divergence (at -3, -6, -12 or -20 dB) of the TOFD configuration is calculated and displayed to adequately evaluate the coverage of the volume of interest. The theoretical values of timebase start and range are automatically applied, simplifying even more the TOFD setup creation.

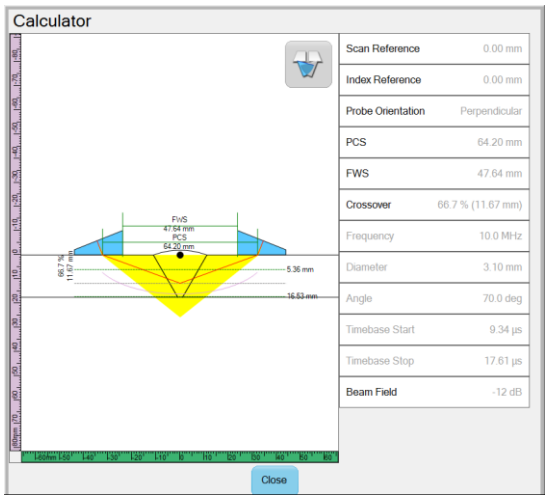

Figure 5: On-board TOFD Calculator

ACQUISITION

Data acquisition is often delegated to a less experienced operator. It is therefore primordial that the acquisition unit makes that process as smooth and easy as possible. The high performance of new-generation portable PA systems can help mitigating the risk of costly rescans by providing more visual support for the interpretation of PA UT data, by allowing a faster acquisition speed and by offering a better management of sensitivity levels.

Even though the interpretation of the PA UT data is usually the responsibility of the data analyst, the operator in charge of acquisition needs to validate the quality of the signals he is acquiring. Therefore, he needs to have a basic understanding of the signal he sees on the screen while scanning. In addition to the typical A-, B-, C-, D- and S-Scan views, new-generation portable PA systems offer volume-corrected on-line merged views (see Figure 6). By displaying information from all the UT beams of one channel in a single Side (B), Top (C) of End (D) view, data interpretation during acquisition is greatly facilitated.

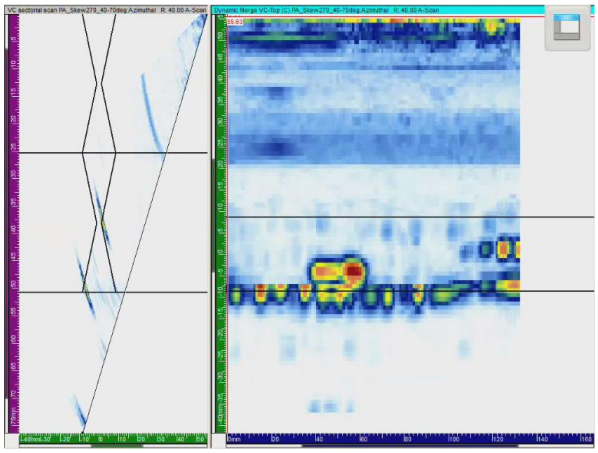

Figure 6: Volume-Corrected On-Line Merged Top View (right)

For any ultrasonic setup, the maximum pulse repetition frequency (PRF) is limited either by the acoustic properties (sound velocity, time base range, number of acoustic beams, etc.) or by the maximum data recording rate of the hardware. Of course, it is impossible to modify the physics of sound. However, the improvements of computing capabilities have allowed new-generation systems to write data faster in memory: 10 MB/s compared to 6.1 MB/s for first-generation systems. For setups with relatively small time base range, these improved performances directly reflect on the maximum PRF and allow typically 65% faster data acquisition.

New-generation portable PA systems allow efficient acquisition of data encoded on up to 16 bits. The high amplitude resolution provided by 16-bit data allows the efficient use of software gain. This tool can be seen as a zooming function on the amplitude scale. It allows applying or removing gain by a simple software process either on-line or in post-acquisition data analysis. A common practice for weld inspection using first-generation portable PA systems involves performing two scans: one with high gain to allow easy detection, and another with lower gain to avoid saturation for amplitude-drop sizing. With the efficient use of software gain provided by the 16-bit data resolution of new-generation portable PA systems, only one scan is required for detection and sizing. Figure 7 shows detection of a planar (lack of side-wall fusion) and volumetric (cluster porosity) indication in a single data file. During acquisition, the hardware gain level was low enough to avoid saturation of the specular reflexion of the planar indication. Still, by using software gain, the volumetric indication is clearly detected.

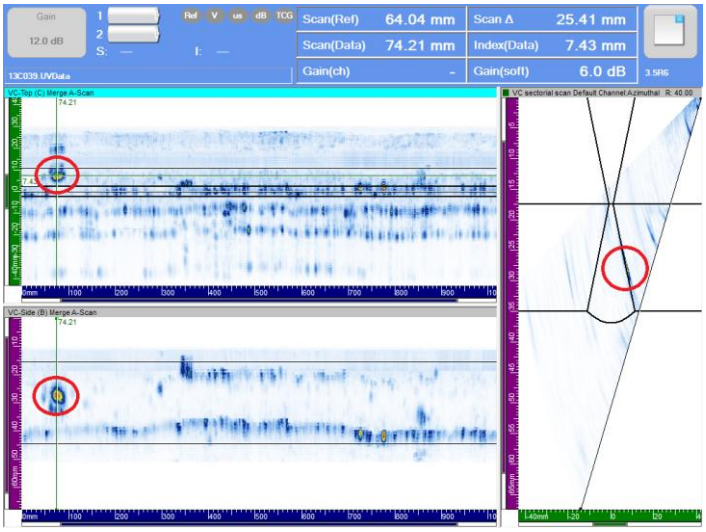

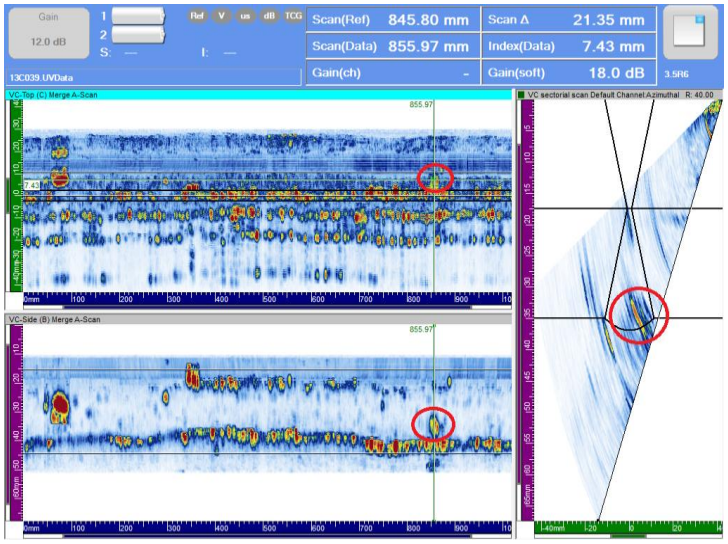

Figure 7: Efficient use of software gain on planar (above) and volumetric (below) indications

Data storage media have also significantly evolved in the last few years. The solid-state drives (SSD) in particular are now a great option for portable PA systems. Since these drives do not have any mobile parts, they prove to be very rugged yet provide large data storage capacity and fast read/write access. We now find portable PA systems equipped with 120 GB SSD, allowing for convenient data management. This also allows for acquiring larger data files. While first-generation PA systems were usually limited to 160 or 300 MB, new systems can acquire files up to 700 MB and still offer convenient on-board data analysis capabilities.

ANALYSIS

New-generation portable PA systems are now equipped with high-performance yet low-consumption processors and high-resolution multi-touch diplays. This improved computing power and user interface allow performing on portable PA systems analysis operations which could only be made on advanced analysis software before.

Every experienced data analyst has his own preferences for data analysis display layouts. The lack of customizability of the display layout on first-generation portable PA systems made data analysis tedious to perform on-board. New-generation portable PA systems offer the same level of customization of the display layout as advanced PC-based analysis software. Data analysts can create, save and load custom layouts with no limitation, other than the size of the screen, on the number of channels (or groups) displayed.

High-performance processors and extended RAM memory of new-generation portable PA systems now allow performing on-board volumetric merge. This operation could only be made on advanced analysis software before. Data merging combines in a single group data coming from multiple acoustic beams, which greatly facilitates the interpretation of PA UT data (see Figure 8).

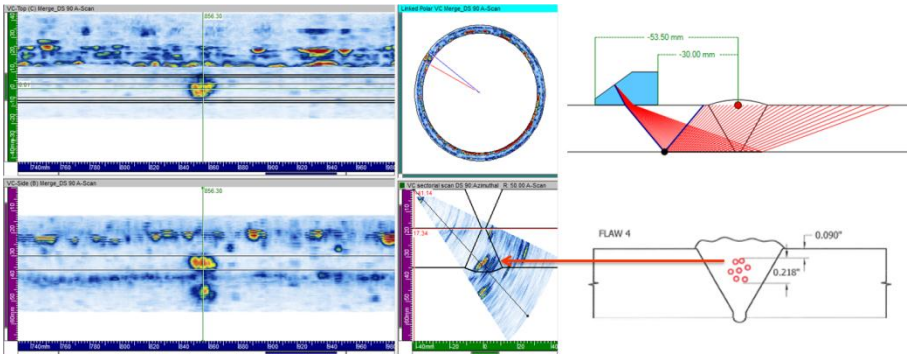

Figure 8: Volumetric Merge on Cluster Porosity

REPORTING

For most customers, the reports are usually what they are paying inspection vendors for. Even though this is not the most value-added part of the inspection process, reporting is nonetheless a key task as reports are the reflection of the professionalism of the inspection vendors.

As they are based on up-to-date operating sytems, new-generation portable PA systems can generate ready-to-print customizable PDF reports. The data analyst can select the information he wants to display in the report, from hardware settings, scan plan to indication information, and can add a list of custom fields (see Figure 9). By providing a meaningful report by the click of a button, new-generation portable PA systems help keeping the post-inspection paperwork to the bare minimum.

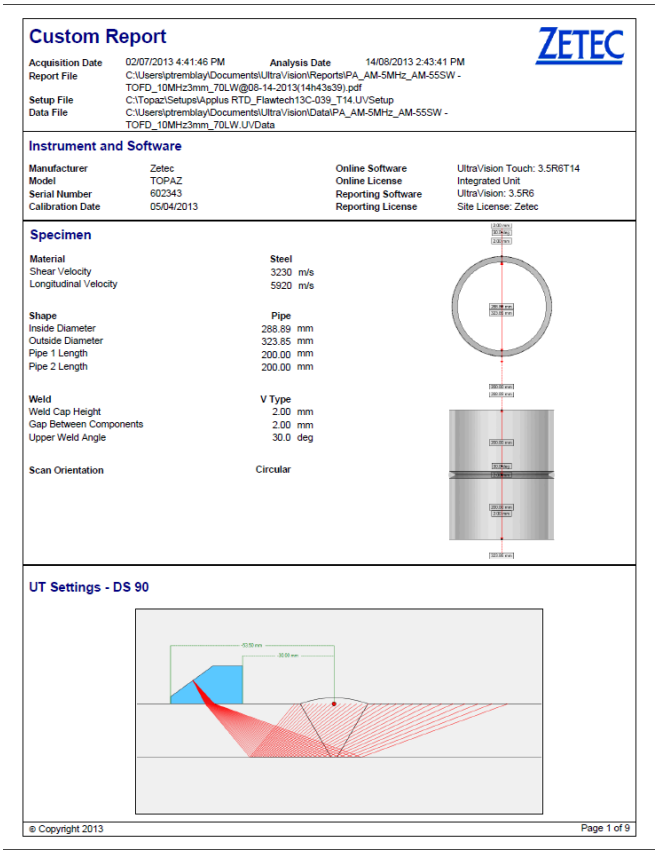

Figure 9: Custom Inspection Report

SOFTWARE COMPATIBILITY

Since the performance of the on-board processors and operating system of new-generation portable PA systems are similar to those of a standard PC, their on-board UT software is using exactly the same engine as advanced PC-based UT software suite, but with an adapted user interface. Therefore, this provides full compatibility for setup files and data files.

Even though new-generation portable PA systems have been designed to work in full autonomy, setups can be created using advanced PC-based software, with all the extra features it has to offer. For example, when the use of more complex probe configurations is required (2D matrix, annular or custom arrays), setup creation can be done on the PC-based software and then loaded into the systems through a USB memory stick. As the setup file format is the same for both platforms, the operation is seamless. This allows more flexibility to tackle the most challenging applications.

The same concept also applies to data files. When more advanced analysis features – such as 3D visualization of UT data – is required, or just for more comfort provided by larger PC monitors, data files can be transferred to the PC-based software. As the data file format is the same for both platforms, the operation does not require the use of converter.

In addition, it is also possible to perform data acquisition by remotely driving new-generation portable PA systems by PC-based software through Ethernet connection. Since data are saved on the PC's hard disk, the maximum data file size then becomes 20 GB instead of 700 MB.

CONCLUSIONS

From the work presented in this paper, the following conclusions can be drawn:

1. The enhanced computing power of new-generation portable PA systems allow improved efficiency for:
    i. Setup preparation by providing visual feedback of focal laws and TOFD configuration;
    ii. Data acquisition by providing more visual support for the interpretation of PA UT data, by allowing a faster acquisition speed and by offering a better management of sensitivity levels;
    iii. Data analysis by allowing creation of custom display layouts and by offering on-board volumetric merge;
    iv. Reporting by generating ready-to-print customizable PDF reports.
2. Even though new-generation portable PA systems have been designed to work in full autonomy, they still provide full compatibility with advanced PC-based UT software allowing more flexibility to tackle the most challenging applications.

PORTABLE PIPING THICKNESS MEASUREMENT SYSTEM

J.L. Fisher, K. Bartels, A. Schaefer
Southwest Research Institute, USA
E. Shiina, T. Shimomura, T. Hamano, IHI, Japan

ABSTRACT

At the present time, many piping system components, especially elbows, are periodically examined for wall thinning due to flow-accelerated corrosion or erosion corrosion damage. The general approach to monitor the component is to periodically make a thickness map of the critical areas. The first step is to mark a grid on the component, then make thickness readings using a 0-degree ultrasonic transducer at grid intersection points, and then manually record the location and measured thickness. Sequential thickness maps are compared to determine the wastage rate. This measurement approach can be accomplished with relatively little training and with equipment that is low cost and lightweight, but measurement position repeatability is difficult to maintain, and the cost and time for the exam increase greatly if it is desired to perform an exam with high spatial resolution. The newly developed piping Thickness Measurement System (TMS) is a hybrid approach to thickness measurement, by maintaining the manual probe motion but acquiring the probe position and waveform using a manual scanner, UT instrument, and a computer. The manual scanner is a lightweight spine that attaches to the pipe by suction cups or magnetic clamps. Two string position encoders are attached to each end of the spine; the strings are in turn attached to the probe. The computerized data acquisition system calculates the probe location from the 2-dimensional input from the position encoders and a 3-dimensional model of the pipe, using known pipe elbow parameters, including pipe diameter and bend radius. The only position information that has to be manually entered into the system is the location of the scanner and its orientation (pointing upstream or downstream) on the pipe, and the desired exam region. A thickness map is made by acquiring data with the scanner at multiple positions on the pipe, and then combining the resultant data.

INTRODUCTION

Flow-accelerated or flow-assisted corrosion (FAC) and erosion corrosion cause gradual wall thinning in piping systems; if left unchecked, the thinning can lead to dangerous ruptures. The areas that are most susceptible to this type of wall thinning are in regions of changing geometry of the piping system, e.g., elbows, tees, and reducers. Mechanized scanning systems for these regions tend to be heavy, difficult to set up, and expensive. At the present time, inspections in the critical regions, such as elbows, are typically made using manual techniques in the following way. The operator uses a tape measure and marker to lay out a grid on the part and uses manual ultrasonic test equipment to measure the wall thickness at grid intersection points. The data is then manually recorded. These grid intersection points may be separated by as much 100 mm. It would be desirable to have a system to facilitate data collection using a much finer grid spacing, on the order of 2 mm, especially in regions where there is some evidence or suspicion of wall thinning. To meet this requirement, SwRI developed a new inspection system that integrated an easy to use scanner and the SwRI EDAS® data acquisition and analysis system (as described in the following sections). This new system would primarily be used on carbon steel pipes with elbow or tee geometries, with diameters of 150 - 660 mm, and with wall thicknesses of 10 – 40 mm.

SCANNER DESIGN

The scanner chosen for the system is a commercially available product, the NDT Systems StringScan-II device, shown in unmodified form in Figure 1. It consists primarily of a spine with string encoders at each end, a probe base in the center of the spine, and suction cups (shown) or magnetic bases to attach it to the inspection surface. The encoder strings are attached to a probe holder by rings that maintain the string orientation so that they are always directed toward the central axis of the probe.

The original system is designed to inspect relatively flat structures, such as aircraft wings. For the piping inspection requirement, the scanner was modified by adding hinged support brackets to allow the suction cups or magnetic bases to swivel to match the surface orientation of pipes as small as 150 mm in diameter and to help orient the spine parallel to the circumference of the pipe surface. It was also modified by adding an alignment hole near the probe mount, to define the "zero" position of the scanner. In order to use position data from this 2D scanner to determine the probe location on the surface of a pipe elbow, it is necessary to convert the 2 encoded string lengths into a position on the surface of a 3-dimensional object. The methodology is described in the following section.

Figure 1. StingScan-II scanner as supplied by NDT Systems

POSITION ALGORITHM

The pipe elbow is modeled as a section of a torus. The torus is defined in 3-space (x, y, z) in terms of the two angular parameters u and v.

$$\begin{aligned} x(u,v) &= (R + r\cos v)\cos u \\ y(u,v) &= (R + r\cos v)\sin u \qquad 0 \le u < 2\pi,\ 0 \le v < 2\pi \\ z(u,v) &= r\sin v \end{aligned} \tag{1}$$

A 90-degree elbow is created by restricting u to $0 \le u \le \pi/2$. Figure 2 shows a complete torus with R=1 and r = 0.5. The blue circle on the surface of the torus is traced by varying u from 0 to 2π and letting $v=\pi/2$. Therefore, the blue circle is a circle with radius R (R= 1 in this example). The red circle is traced by varying v from 0 to 2π and letting u=0. The red circle, therefore, has a radius of r (r= 0.5 in this example). The string scanner has two string encoders with the strings attached near the top of the UT probe. It is assumed that the strings intersect at the central axis of the probe. The encoders report the lengths (s_1,s_2) that the strings are withdrawn from the encoder. Figure 3 shows the model of the string scanner on a 90° elbow. The 90° section of pipe is drawn in black; it is a section of a torus with R = 48cm, and r = 16cm. The strings of the string scanner are shown in green; in this case s_1=40 cm and s_2=45 cm. Once fixed in length, the strings trace out a circle in 3-space that intersects the pipe elbow. Finding the (u, v) position of the probe on the pipe involves finding the intersection of this circle and the surface of the elbow. As seen in Figure 3, the circle intersects the pipe elbow in two locations and the mathematical torus in four locations. Depending on the lengths of the strings, the circle may intersect the torus at 0, 1, 2, 3, or 4 points. The model chooses the solution that places the probe on the pipe (black) section of the torus such that the probe is on the outside surface of the pipe. If no intersection point is found, the model reports an error that the string lengths are too short to reach the pipe.

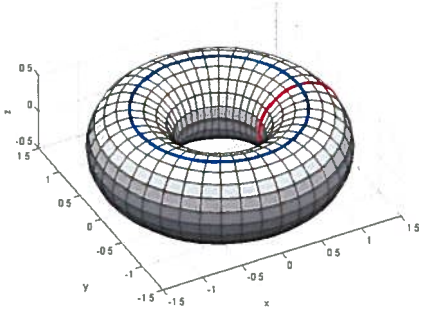

Figure 2. Torus as defined in Equation 1 with R=1 and r = 0.5

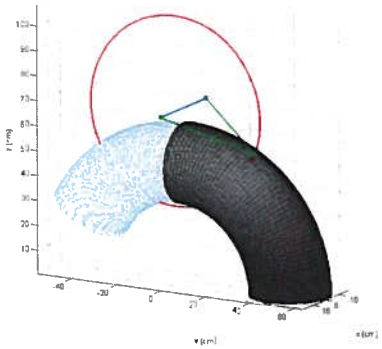

Figure 3. Model of string scanner on a 90° elbow (black). The blue section shows a mathematical extension of the elbow's torus that is not part of the model pipe section.

The model was made flexible so that any section of the torus can represent the pipe and so that the scanner can be placed anywhere on the pipe, because multiple positions of the scanner are required in order to inspect 100 percent of the pipe surface. Figure 4 shows the model of the system with the string scanner centered at location $(u, v) = (\pi/4, \pi/4)$ radians = (45°, 45°). In this case, the string lengths were $(s_1, s_2) = (30, 30)$ cm. The model also allows for the string scanner to be placed on the straight pipe section that the elbow is typically welded to. This position is often convenient for mounting of the scanner. This placement is shown in Figure 5. Here, the straight section of pipe is shown in red. In this example, the scanner is centered 6 cm from the end of the straight section and 45° offset in the u direction.

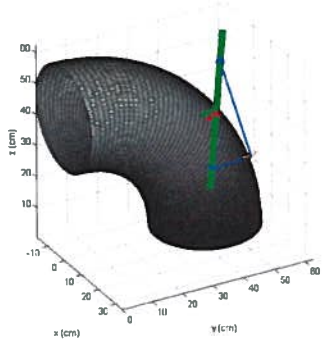

Figure 4. The model allows the string scanner to be placed anywhere on the elbow. "x" represents the location of the probe.

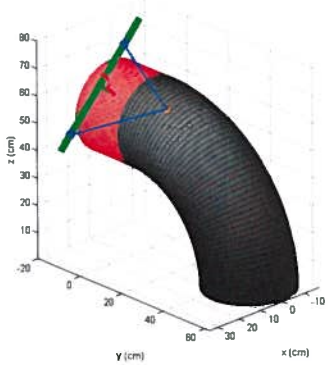

Figure 5. The model allows the string scanner to be placed on the straight section of pipe entering the elbow. "x" represents the location of the probe.

INSPECTION OPERATION

An inspection of an elbow requires multiple placements of the scanner. Each placement is measured by the position of the scanner origin (the position on the surface of the alignment hole) relative to the elbow origin, defined as the intersection of the elbow with the straight section of pipe, at the elbow extrados (the circumferential location with the greatest bend radius of the elbow). Two different placements are shown in Figure 6 and Figure 7. Additional spatial parameters that must be defined for each placement include pipe diameter, bend radius (at the pipe center), exam extent in the circumferential direction, exam extent in the axial direction, data collection interval along each axis, tolerance (required accuracy of probe position with respect to desired data acquisition locations), and direction of the string extension (either upstream or downstream with respect to product flow). In addition, the ultrasonic parameters are defined in a calibration program. These parameters include gate start and gate stop in mm (after a time/distance calibration is performed), gain, time-controlled gain (TCG) settings if needed, and the portion of the waveform within the time gate that is displayed by default. This display region can be configured to include the pipe backwall as the largest reflector; then the color scale can be used to display the time of the peak reflector; in this way, a color map of the wall thickness is produced. Figure 6 shows a display of the acquisition screen color map. The initial color of this screen is red, used to indicate either a very thin wall or missing data. As data is acquired at the desired locations, the map is filled in. In the example shown in Figure 6, the portions of the display shown in red have not yet been scanned.

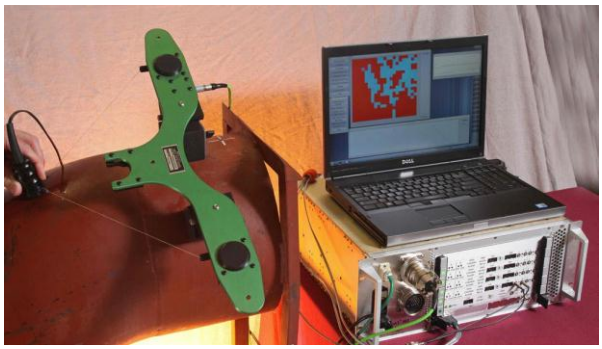

Figure 6. System shown mounted on an elbow mockup, along with the data acquisiton computer and instrumention (right)

Figure 7. Scanner moved to different position on elbow for additional coverage

CONCLUSION

A new prototype system for high resolution inspection of wall thickness of piping elbows has been developed. The system uses a lightweight, low cost, 2D string scanner and a model of the pipe to accurately encode the position of the probe used for thickness measurements. The system produces color maps of the thickness that can be used to quickly judge the wall thickness.

ACKNOWLEDGEMENT

This work was supported in part by IHI Corporation.

ADVANCED NDE SYSTEMS FOR IN-SERVICE INSPECTIONS NEW SCANNERS COMBINED WITH ADAPTED UT PHASED ARRAY

F. Wolfsgruber, G.Guse, F.Mohr, AREVA, Germany

ABSTRACT

Some risk based inspection programs or/or life extension programs demand tracking of defect growth . This can only be calculated, if both the initial and the subsequent defect boundaries are well known with high accuracy. Baseline inspection and final measurements must be compared, therefore both datasets should be collected in the same way and with the same quality. In many cases, particularly outside Germany, data from a high-quality automated baseline inspection are not available because the local code did not demand it in the past. Only automated systems can deliver the accuracy needed to accurately assess flaw growth rate.
The most accurate inspection results can be achieved with a complete tool-box including high precision scanners, quality inspection transducers producing good data over a sufficiently small beam area plus high-quality flexible analysis software capable of displaying any indications in an understandable and comparable way. For complex shapes, modeling programs are also frequently beneficial to understand the UT wave propagation and aid in analysis of the results. All of these building blocks exist from several different inspection vendors. In an ideal inspection world and frequently even in order for the inspections to be practical, all these features must work seamlessly together to allow for efficient component inspection. AREVA NDE-Solutions is a front runner in creating advanced inspection systems and approaches the ideal inspection world by realizing all of these building blocks into a seamlessly integrated working system to efficiently master the most demanding inspection challenges. In this paper, the most recent steps in this integration are presented. Starting with the modeling tool for high complex geometries (iMaV), coupled with the presentation from robotic based multi axis scanners (light weight scanner), the integration tasks continues with specific task adapted sensors (Phased Arrays), plus high-end analysis software including advanced tools like 3D-SAFT, TOFD and Tomography. This paper shows typical applications were these pieces of the tool-box are combined to yield efficient, high quality inspections to fully address the safety concerns of critical components to be inspected.

INTRODUCTION

Some risk based inspection programs or life extension programs demand tracking of defect growth rate. This can only be calculated, if both the initial and the subsequent defect boundaries are well known with high accuracy. Baseline inspection and final measurements must be comparable; therefore both datasets should be collected in the same way and with the same quality. In many cases, particularly outside Germany, data from a high-quality automated baseline inspection are not available, because the local code did not demand it in the past. Only automated systems can deliver the accuracy which is needed to accurately calculate flaw growth rates.

The most accurate inspection results can be achieved with a complete and integrated tool-box including high precision scanners, quality inspection transducers producing good data over a sufficiently small beam area plus high-quality flexible analysis software capable of displaying any indications in an understandable and comparable way. For complex shapes, modeling programs are also frequently beneficial to understand the UT wave propagation and aid in analysis of the results. All of these building blocks exist from several inspection vendors. In an ideal inspection world and frequently even in order for

the inspections to be practical, all these features must work seamlessly together to allow for efficient component inspection.
AREVA NDE-Solutions is a front runner in creating advanced inspection systems and approaches the ideal inspection world by realizing all of these building blocks into a seamlessly integrated working system to efficiently master the most demanding inspection challenges. In-house competences and knowledge regarding all segments of the inspection chain allows efficient adaptation of existing approaches to new challenges resulting in high success rates for the required inspection qualifications and acceptance tests.

BACKGROUND

AREVA NDE-Solutions as an NDE service provider has historically specialized in mechanized non-destructive testing (NDT) systems for the nuclear industry. Many of the applications were developed for extreme conditions, like underwater and for operations at elevated temperatures. Complex component geometries and the requirements from many different country specific codes demand very high precision scanning tools, software tools to explain the inspection physics and display the results in a simple and understandable way to non- specialist regulatory authorities and managers. The developments in the robotics and in the computer technology allow more advanced solutions and open new possibilities to achieve high quality results with reduced inspection times, with higher workload throughput, and at reduced per-piece inspection costs. This development is not only relevant for NDT-services in the nuclear field, it also influences service activities in other industries as well as the design of NDE-Systems for complex NDE inspection scopes tailored for the aircraft industry, or steel industry. The greatest differences between portable service Inspection systems and permanently installed industrial system applications is the service system demand for flexibility to be shipped easily, and therefore be small in size and weight and be able to readily mount to arbitrarily diverse parts. In contrast, factory installations can be permanently mounted into an optimized inspection cell and the inspection targets can be delivered and position registered within the inspection cell.

Figure 1 Standard UT probes

Historically, most items in the inspection tool-box were developed separately. The goal was to optimize each specific tool with little consideration for the overall inspection target. UT-probes were designed and fabricated for optimized UT-echos with little consideration for geometry fittup and cable management.. Good electronic and ergonomic features were important for the UT-instrument. Acquisition, robot control, analysis, display, and modeling software were developed separately with little focus on integration. Scanners and robots were designed to be able to fulfill the scanning parameters frequently with little consideration for transducer gimbaling or flexibility to adapt

Figure 2: UT-Equipment for manual inspection

to off-design components. .More advanced systems were based on cobbled together manual inspection systems. For example: pipeline inspection standard UT probes for manual inspections (Figure 1) coupled with a standard UT-instrument (Figure 2) were combined with a line scanner for an early integrated automated pipe scanner. The documentation was done by printouts of screen dumps with the manual comments. On complex geometries the inspector had to think 3- dimensionally to understand the signals on the screen. The differentiation between geometrical and real indication was done manual by geometrical reconstruction. This was not necessarily intuitive and required highly skilled analysts to consistently make the correct analysis calls.

PROCESS EVOLUTION

As inspection systems got more complex and more difficult to understand, the interfaces between the different development teams became more important. In more recent years, additional requirements from qualification performance and acceptance procedures have become more important. As more people get involved, more and more detailed interface specifications are demanded. The development process became more formal with stage-gates and decisions that must be documented and explained to customers as well as vendor management. All this influences the workload and finally the cost for new applications and development processes.
To improve efficiency, development time, and costs, modeling has become more important. Simulations not only allow selection of optimum tools without committing to specific hardware then iteratively optimizing the chosen hardware configuration, but also simulations aid in component integration at an early development stage.
By using the available development tools, the process for designing or adapting a new NDE-solution changed significantly. The ideal process starts with the CAD-file of the component to be inspected. The inspection target (form, size, orientation of expected defect) must be defined and integrated in the CAD file. Material characterization and surface conditions must also be added. In a next step, the sound path is calculated under the criteria of optimized conditions for striking the defect. The scanner is then adapted into the model allowing definition of possible scan paths.
Then the probe is designed based on simulated sound fields, focus points and the previously developed sound-path model coupled with the known capabilities of the planned UT-equipment These steps must be completed before the first hardware is touched. Tests and commissioning are still needed but minimized by continuous crosschecks and comparison with the model results. This comparison is ideally based on visual comparison of the CAD and UT model with corresponding similarly displayed test results.

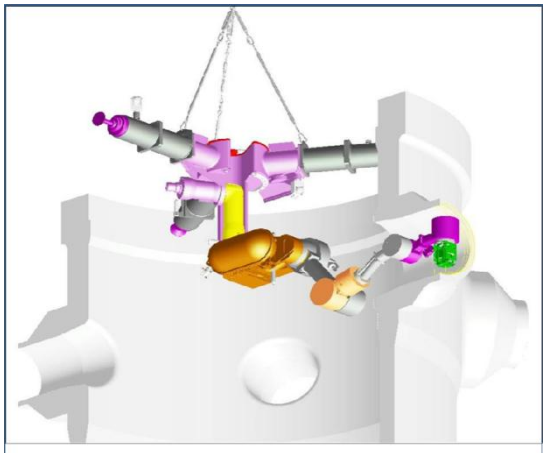

Figure 3: AREVA TWS underwater reactor vessel examination 7 axis robot

EXAMPLES

Reactor Vessel Inspection

Vessel inspection in nuclear power plants is typically on the outage critical path. The on-vessel inspection time is one of the limiting factors before the plant can go back on-line therefore minimizing this inspection time is important and valuable. Minimizing this time means that the inspection system (probes, equipment, scanner) should be able to cover as much as possible with as few tool- changes as possible.

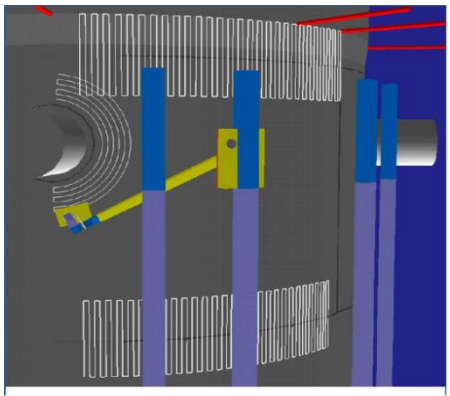

Figure 4: AREVA SWR OD reactor vessel examination 6 axis robot

AREVA NDE Solutions has developed and qualified vessel inspection techniques by using a modeling approach. In PWRs the inspection is done from inside where in BWRs, the inspection is mostly from outside. The 2 most complex inspection areas are the dissimilar nozzle-pipe-safe-end welds, and the nozzle-to-shell weld For these areas, the inspection targets were defined by the code and simulated in the modeling program.

To cover all the requested angles without too many tool changes, phased array (PA) UT probes were chosen. To operate these PA probes with their high data throughput within the shortest time, the UT System SAPHIR was adapted to the robotic delivery and for the target inspection. The solution for the scanner showed that industrial robots are not wellsuited for these applications. PWR inspections must be performed under water for at least the lower part of the vessel since this region must remain underwater due to high radiation levels in the core-belt area. The PWR vessel examination robot must therefore be water resistant. (Figure 3) For the BWR, the limitation to the robot design was the narrow gap between the vessel wall and the thermal shielding. (Figure 4). Both robot configurations can perform the vessel scanning in circumferential and axial directions including inspection of the vessel to nozzle weld and the area of the inner radius. This nozzle inspection is a complex 3- dimensional inspection task that depends on the specific design geometry and therefore is very hard to standardize. The first step in the process is to incorporate the CAD design file of the component into the UT modeling program. The 2nd step is the target definition in the component model. The 3rd step is the sound path calculation (Figure 5), based on the defect position and the available scanning surface. The 4th step is the probe design, based on the previously determined beam parameters from the model. The sound field (Figure 6) and the requested functions of the UT probe combined with the limitations to probe housing size and scanning limitations influence the final design. In parallel to these steps the scanner was designed.

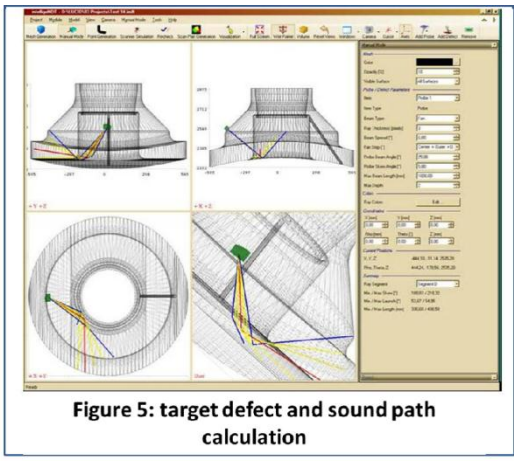

Figure 5: target defect and sound path calculation

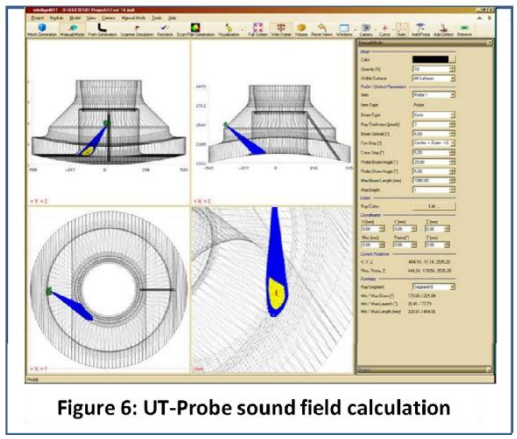

Figure 6: UT-Probe sound field calculation

The scanner must accommodate the maximal number of probes and allow delivery of the probes to the target inspection surfaces to achieve the desired volumetric coverage (Figure 7). Based on all this calculations the final NDE inspection system was designed and built.

The final inspection system was qualified according local codes in USA, Switzerland, Finland and Germany. This general approach has been used on site in different nuclear power plants (Figure 8, and 9)

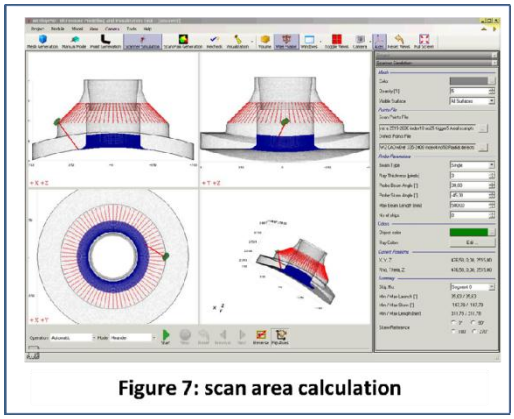

Figure 7: scan area calculation

Figure 8: Vessel UT inspection from o.D on site

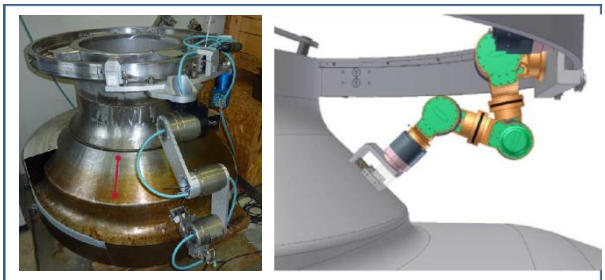

Figure 9: Nozzle UT inspection with 4 axis robot from o.D

NDE systems for railway wheels

Another application developed according the same development principles focused on high speed train wheels. If wheels of trains fail, people can be hurt or even killed. Consequently, regulations have been put in place requiring rail wheels and axels to be periodically inspected. Critical inspection criteria to minimize the costs were to allow the inspection to take place during the regular maintenance on the mounted wheels. The available space under the train is very limited due to housing and brakes (Figure 10). The challenge was to develop a inspection system which can perform a full volume inspection by turning the wheel only once. The probe arrangement had to fit under the train and s cover a wide variation of different wheel geometries. The system must also be able to perform a very high-sensitivity detection of small defects, and have the ability to distinguish geometrical reflections from real flaws.

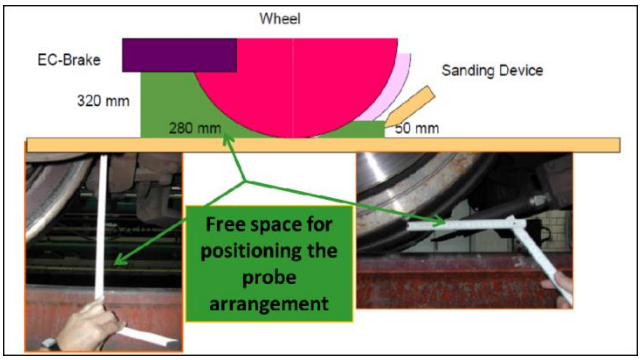

Figure 10: Limited acces for wheel inspection

To solve this challenge, simulations with numerous different wheel geometries and inspection targets were modeled.

Probes were also modeled for functionality, dimensions and orientation to optimize the probe arrangement (Figure 11 and 12). Not only the height, but also the length of the full probe system were essential parameters to bring the solution to success. The final solution was a combination of different NDE technologies (UT and ET) and was built up out of standard sensors plus UT phased array sensors (Figure 13).

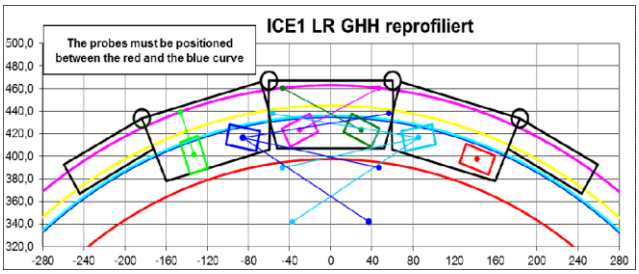

Figure 11: probe arrangement calculation

The simulation modeled the sequence of firing the UT transducers and aided in optimizing the overall time to inspect the wheel areas of interest. This was a complex transducer firing sequence requiring customized programming of the SAPHIR UT instrument. The AREVA NDE Solutions UT equipment fulfills all the requested functions. The SAPHIR UT-system also provided all needed software tools to discriminate real defects from geometrical indications (Figure 14).

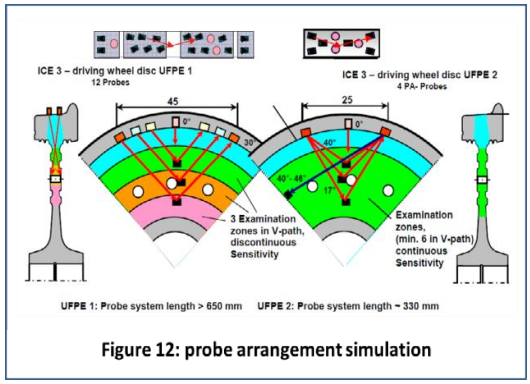

Figure 12: probe arrangement simulation

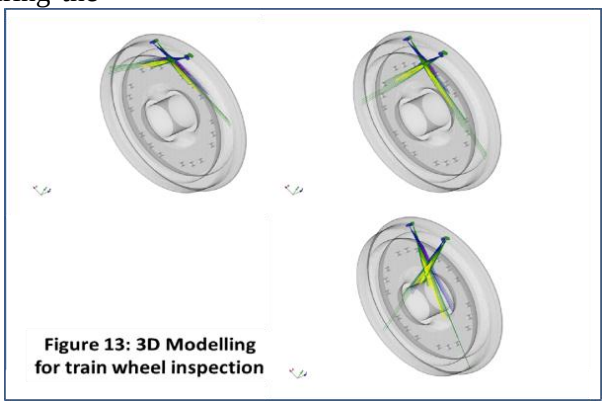
Figure 13: 3D Modelling for train wheel inspection

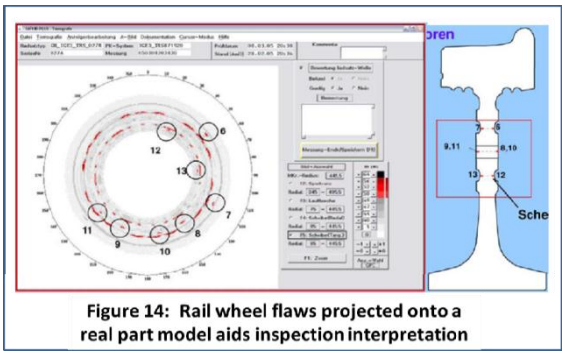
Figure 14: Rail wheel flaws projected onto a real part model aids inspection interpretation

The presentation of the inspection results must be projected onto the real geometries and must provide all needed values for a qualified operator to analyze the data in a short time. After freezing the design, probes were manufactured in house and the arrangement was setup and tested. The test results were compared with the model data and small modifications were integrated. Parallel to the test, the final manipulator system was designed and a 3-D Model was generated for

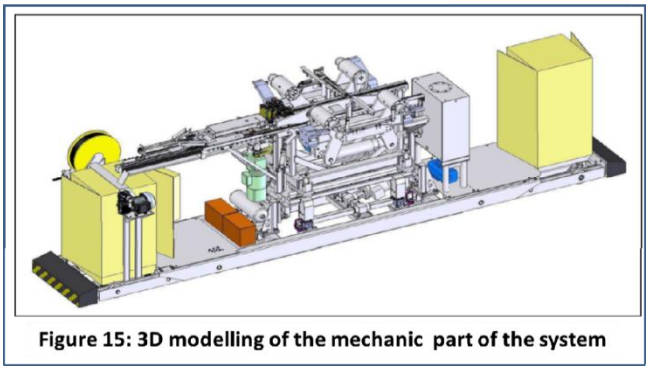
Figure 15: 3D modelling of the mechanic part of the system

checking collision points (Figure 15). Before going on site, a pre acceptance test was performed with the full system during the pre-commissioning phase allowing system adjustments to be made away from the confusion train inspection facility. The final installation was successful with great customer satisfaction (Figure 16)

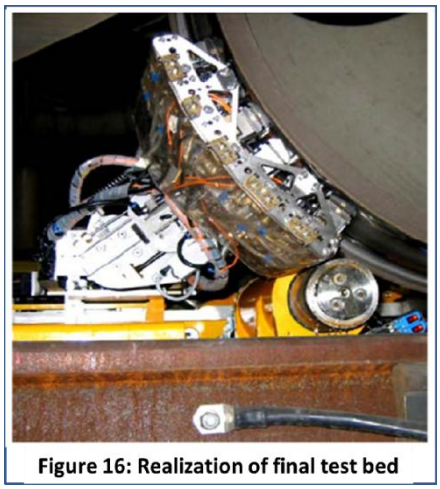

Figure 16: Realization of final test bed

NDE for aviation systems

A last example demonstrates that the development principle must be as flexible as possible. NDE technologies are not only developed for steel inspections. New materials, like composites for aircraft, sometimes demand even more inspections than steel components within nuclear power plants. This is partially due to continued focus on optimizing strength to weight ratios and the economic interest to make the airplane with as little material as possible. In addition, engineers have less experience with composites and are aware that fabrication techniques are subject to flaws that can weaken the structures. Inspections can detect these flaws before they become a safety issue. Composites are manufactured in numerous configurations (Figure 17) and these various forms and shapes demand customized inspection systems. The specific complexity of composite parts creates new challenges for the NDE technology. The inspection pieces have all kind of shapes, sizes and soft structures, with stringers and a lot of corners. A high percentage of coverage is requested by the different customer. The finally chosen NDE-method must also be sensitive to very small defects. The challenge is high sound attenuation and the limited inspection times (due to the manufacturing process). This opens a lot of new questions for the NDE applications. To test and to qualify new NDE technologies, test samples with artificial defects are needed. They have to be well defined and manufactured by the customers (Figure 18). Before tests can be done on the test samples the development procedure starts again. The inspection

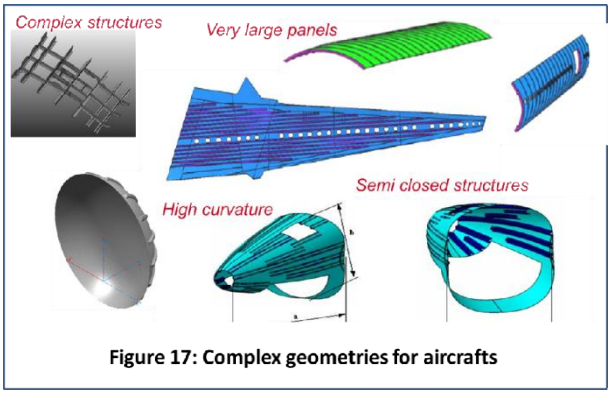

Figure 17: Complex geometries for aircrafts

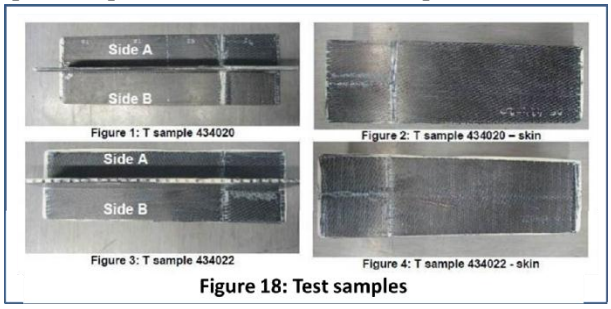

Figure 18: Test samples

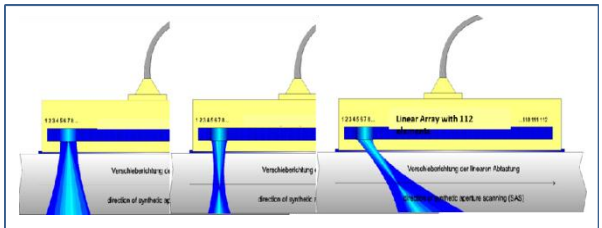

Figure 19: simulation of probe function

technique is designed by modeling and simulation. Standard computer modeling like CIVA as well as customized internally developed modeling tools are used to optimize the technique and the UT probes (Figure 19).

Due to the requirement of small inspection targets on the one hand and high through-put demands on the other, a large number of parallel conventional probes or even multiple phased array transducers are used. The phased arrays have the additional benefit to combine a larger scanning path with the multi angle function in a single housing and therefore a reduced probe arrangement. The final probe is designed for long life and optimized size, weight and handling for fitting to the inspection machine. First tests with new customized probes, on the test samples, give initial feedback of the real function of the designed technique(Figure20)

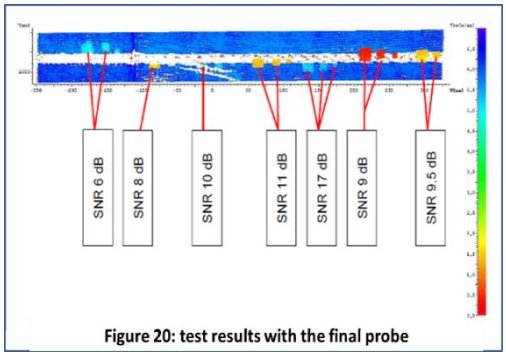

Figure 20: test results with the final probe

Flat pieces are relatively easy to inspect but corners with both convex and concave radii of curvature create the real challenges for developers of optimized NDE techniques and systems (Figure 21). For this task limited access is one limitation. The coupling and the right angle of incidence at each area of the radius is another restriction. Again modeling and simulation provide the needed data for developing successful techniques (Figure 22).

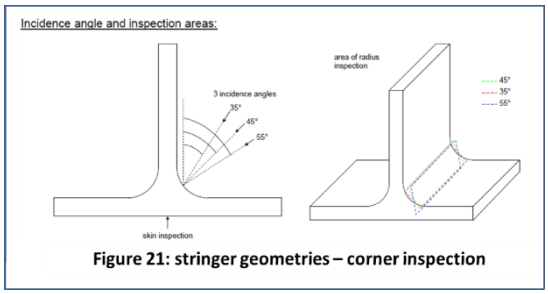

Figure 21: stringer geometries – corner inspection

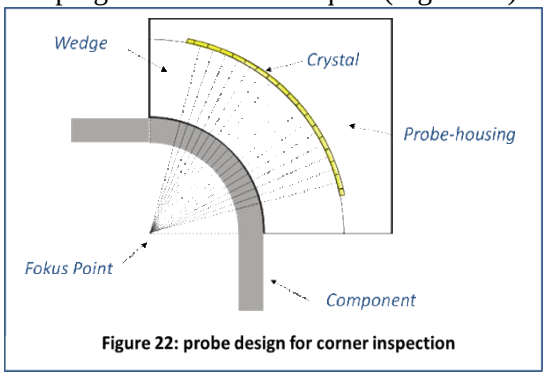

Figure 22: probe design for corner inspection

Based on this model, a first prototype UT Probe was developed and tested (Figure 23).

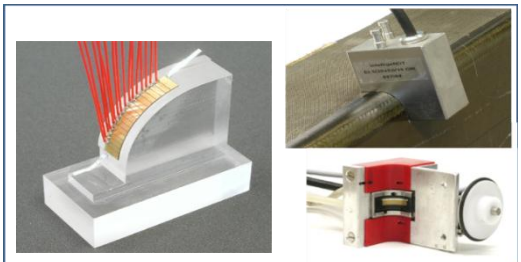
Figure 23: probe realization

For this application again specific features of the UT equipment and analysis software are required. Having "in-house" expertise as within AREVA NDE Solutions, design interfaces are managed smoothly to optimize customization of transducers, software, robotics, and electronics. "The SAPHIR quantum" (Figure 24) is the latest generation of the UT equipment from AREVA and shows great flexibility to be adaptable in many applications. The system offers fully parallel firing and receiving of 32 to 256 channels or more with a

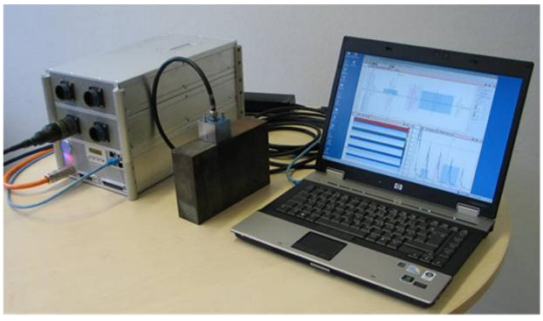
Figure 24: inhouse UT system SAPHIR*quantum*

wide dynamic range and very high voltage pulse. The corresponding analysis software is focused on the need of the operator. A wide variety of analysis tools ranging from an essentially infinite choice of focal laws to availability of advanced signal enhancement techniques like SAFT and integration with modeling software support the most sophisticated signal analysis strategies. Results can then be projected onto 3-D representations of the parts to enhance data interpretation and explaining the results to non-UT- specialists.
The right combination of all this customized features, together with the most precise inspection technology, results in a well efficient inspection system for complex geometries (Figure 25).

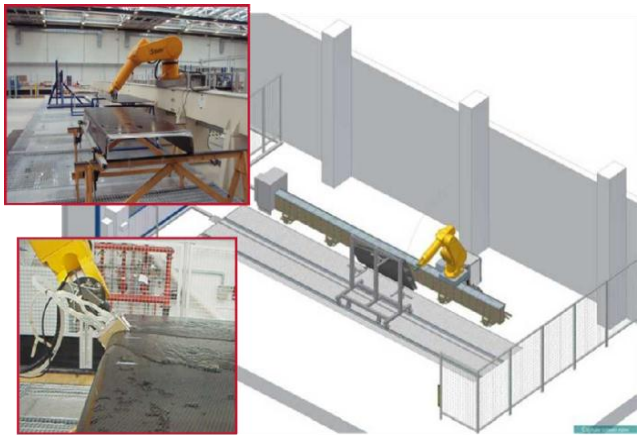

Figure 25: full test bed design and realization for complex geometries

Summary

The presented examples of creating best technical solutions for complex inspection tasks in a areas of the producing industry, demonstrate that the success starts with a well established development process. Modeling and simulations a key process steps which guaranties faster development time, less development cost and most important for the quality higher accuracy in the test results. AREVA NDE Solutions with his high level in-house competences, is able to deliver customized test applications worldwide, with great customer satisfaction.

VOLUMETRIC INSPECTION OF WELDS USING THE TOTAL FOCUS METHOD

R.L. Ten Grotenhuis, C.M. Moes, A. Hong, A. Sakuta
Ontario Power Generation, Canada

ABSTRACT

Ontario Power Generation (OPG) has successfully combined the Full Matrix Capture (FMC) data acquisition technique with a proprietary version of the Total Focus Method (TFM) as an automated NDE analysis platform. The integrated system was initially developed to address the inspection of compound fitting joints for localized Flow Assisted Corrosion (FAC) damage. The system has been successfully deployed on a number of inspection campaigns and has confirmed FAC damage in the weld region. In addition to the FAC damage, minor volumetric discontinuities were also identified in the welds.

It was apparent from the outset of the development; the analysis technique could be extended to perform full volumetric inspection inclusive of crack detection. The principal benefit of this approach is that two separate inspections, localized FAC and weld cracking, could be conducted simultaneously. This strategy has the potential to significantly save critical inspection time while reducing radiation exposure to inspection personnel.

This paper describes the extension of the current technology to the problem of crack detection. Results are provided for both the controlled EDM notch series as well as implanted defects in fitting welds.

Keywords: Total Focus Method, Volumetric Inspection, Arbitrary Geometry

INTRODUCTION

Over the course of several decades of operation of CANDU reactors, OPG had discovered Flow Assisted Corrosion (FAC) as a degradation mechanism in Primary Heat Transport piping of its units. It was also determined there were two aspects to the FAC damage, one of wide spread gradual thinning in the outlet feeder pipes, the other highly localized thinning associated with the weld root of fitting to fitting and fitting to Grayloc configurations, see Figure 1.

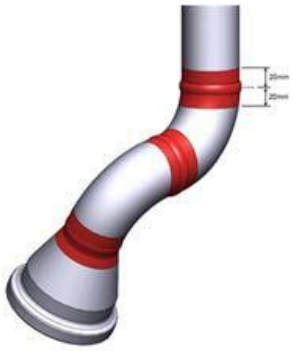

Figure 1 Inspection zones on feeder pipes.

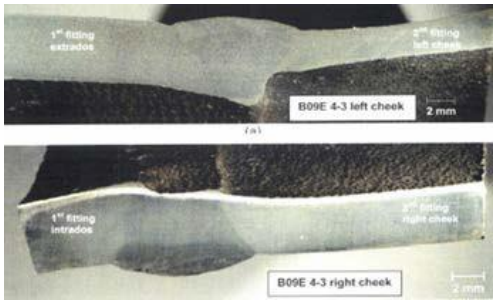

Figure 2 FAC damage under welds in ex-service feeders.

An inspection system was developed by the Inspection & Maintenance Services Division of OPG employing a combination of FMC data acquisition and TFM analysis for the examination of fitting-to-fitting welds at its CANDU stations, see References [1] and [2]. The purpose of the system is to examine the weld and material immediately adjacent for localized FAC associated with the weld root. The system is capable of defining the exterior surface of an arbitrary geometry and imaging the material volume beyond the surface (Figure 3), rendering both exterior and interior surfaces in true 3D, see Figure 4. The system has been successfully deployed several times since its first use in 2010.

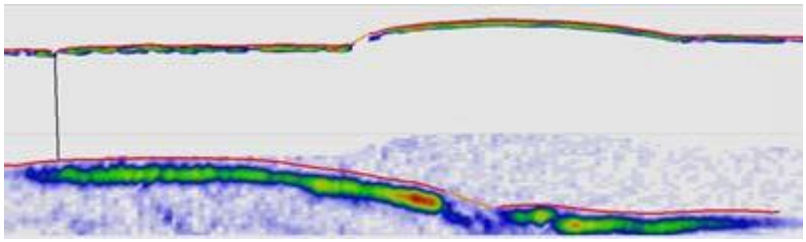

Figure 3 Typical results obtained for cross section through weld.

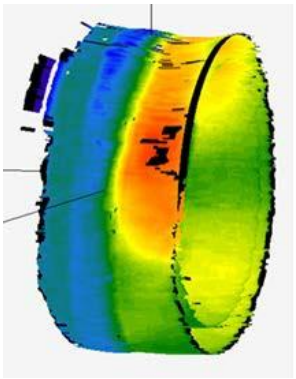

Figure 4 3D result for fitting to fitting weld.

Results obtained from inspection campaigns have highlighted what are believed to be fabrication defects in the weld volume that are acceptable per ASME Section III rules see Figure 5. The capability to identify isolated discontinuities was beyond the scope of the original tool design. Observation of these inclusions posed an interesting question of whether the system could be enhanced as to provide a more complete inspection solution.

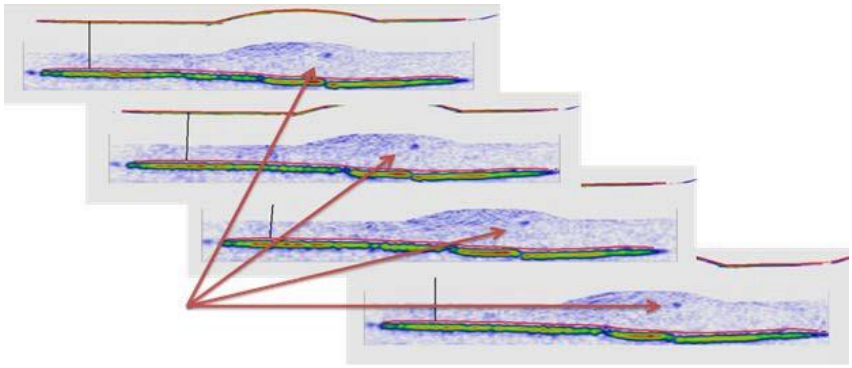

Figure 5 Weld inclusion identified in multiple adjacent frames.

FMC DATA SET

The FMC data acquisition method has been described in References [4] and [5]. FMC is defined by the process in whereby one element in the array transmits and all elements receive, the next element transmits, again all elements receive. The process continues until every element in the array has transmitted thus forming an N-by-N data structure of A scans where N is the number of elements in the array. For the case of a 128 element linear array, up to 16,384 A scans are acquired. FMC is widely regarded as being the most complete data record possible for a given transducer placed at a specific orientation with respect to the inspection volume. However, it is also recognized the extent of the data record is achieved at the expense of both inspection speed and data file size.

TOTAL FOCUS METHOD

A description of the TFM algorithm is well articulated in the work by Holmes et al see reference [3]. The efforts described herein are based upon this work. The TFM beam former is implemented in the following manner. The flight times from each element in the array to each point in the search grid are calculated and stored. The flight time for a transmit-receive pair to a specific point determines the time index from which the signal value is retrieved from the A scan. The signal value for the point in consideration is the sum of all pertinent transmit-receive pairs capable of interaction with the point. The individual signal contributions will constructively interfere where a valid surface exists. If no valid surface exists, the signals destructively interfere resulting in a low-level residual background. An edge detector is applied to generate the coordinates of the exterior surface once the surface is imaged. Note the TFM algorithm employs the analytic representation of the FMC time domain matrix to achieve effective cancellation.

The interior volume of the inspection zone is imaged via the same strategy with the added complication of determining the correct flight time to the points of the search grid. The appropriate path is determined by evaluating all flight paths through the interface, applying the Fermat principle to select the minimum flight time. Once the interior surface is imaged, edge detection methods are again applied

to define the coordinates of the interior surface. Outputs of the process are the image of the exterior surface, image of the interior volume including the interior surface, edge detected coordinates (profiles) of both exterior and interior surfaces.

CODE DEVELOPMENT

The OPG development team has taken a stepwise approach to the goal of imaging and identifying both mid wall and surface breaking discontinuities. Given the evidence that mid wall discontinuities are currently being imaged, the team focused efforts to imaging interior surface breaking discontinuities. The OPG version of the TFM algorithm described above was the appropriate starting point for developing an extension that would be able to image interior surface breaking discontinuities. All work was performed using the Matlab 2012 development environment.

General Derivation

Consider the configuration presented in Figure 6 where S_E and S_I represent the exterior and interior surfaces of an arbitrary geometry. A linear array transducer is located above the inspection zone.

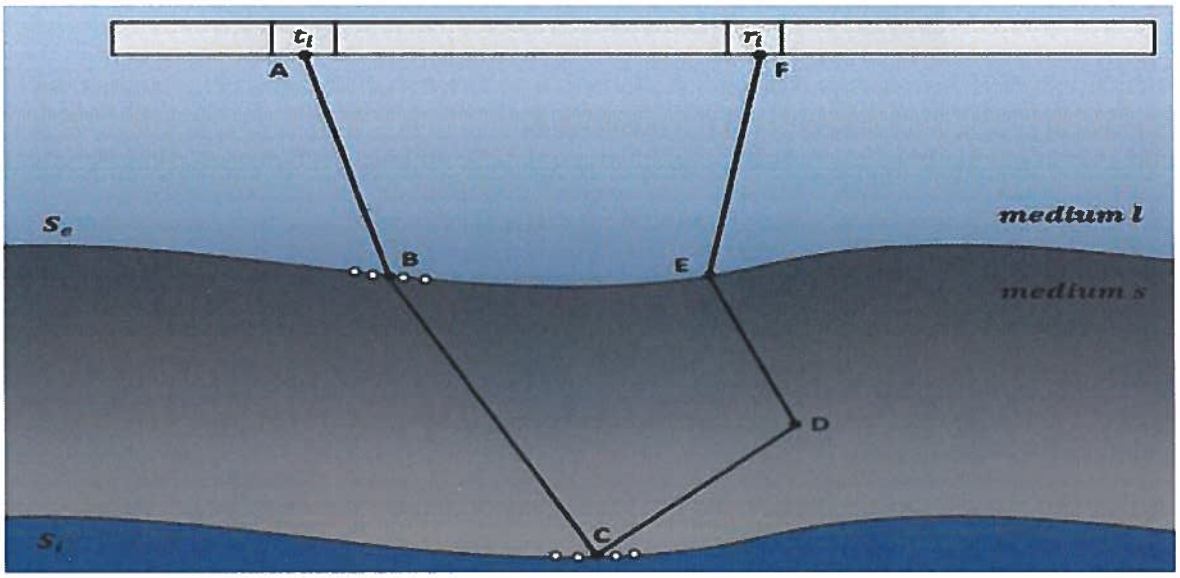

Figure 6 Path combinations involving single reflection from interior surface.

With reference to the figure, the total flight time from transmitter i to receiver j involving a single reflection from the inside surface can be expressed as:

$$t_{i,j} = \sum_{B,E \in S_E,\ C \in S_I} \frac{\overrightarrow{AB}}{V_l} + \frac{\overrightarrow{BC}}{V_{S_m}} + \frac{\overrightarrow{CD}}{V_{S_m}} + \frac{\overrightarrow{DE}}{V_{S_m}} + \frac{\overrightarrow{EF}}{V_l}$$

Where:

V_l is the velocity of sound in the coupling media (water) corrected for temperature variation,

V_{S_m} is the velocity of sound in carbon steel for mode m under consideration,

B, E are points on surface S_E, and C on surface S_I.

Note the case of a direct reflection from the subject point itself has already been addressed in the work performed to address the interior surface for the L-L wave mode. The other combinations of L-S, S-L and S-S may be addressed separately.

The case of a second reflection from the interior surface would add a 6th component to the summation. The segments $\overrightarrow{BC}, \overrightarrow{CD}$ and $\overrightarrow{DE}$ must be evaluated in L wave and S wave modes. Thus for $t_i r_j$ at point D, there will be a set of discrete contributions corresponding to the possible wave mode combinations such that $t_{i,j} \in T_{i,j}$. Possible combinations are listed in the following table:

Table 1 Possible wave mode combinations for sound paths

Leg	Mode							
$\overrightarrow{BC}$	L	L	L	L	S	S	S	S
$\overrightarrow{CD}$	L	S	L	S	L	S	L	S
$\overrightarrow{DE}$	L	L	S	S	L	L	S	S

The intensity value of the image at point D is expressed as:

$$I_D = \sum_{i,j}^{n} U(T_{i,j})$$

where I_D is the intensity map value, $U(T_{i,j})$ is the analytic waveform vectors for the set of $T_{i,j}$ and n is the number of elements in the array. The intensity is calculated for all defined search points bounded within the exterior and interior surface.

Additional Considerations

We must remain cognisant of the implications of the process upon the FMC dataset presented for analysis. The process must be robust with respect to the characteristics of the dataset. These characteristics include; dynamic range, phase inversion and mode conversion phenomena, process error and conditional summation.

The FMC dataset contains all possible signals; interface, interior reflection, diffraction, corner traps and mode conversions see Figure 7. With respect to the interface, the interior reflection is typically -19 dB, corner trap signals are typically -32 dB and diffracted responses are typically -36 dB. This dynamic range poses a challenge to effective summation. Within the code developed, we have adopted a sequential strategy where once a surface has been imaged and identified, the signals associated with that surface are removed via autocorrelation and template subtraction. The effects of signal suppression are presented in Figure 10, Figure 11 and Figure 12. This approach yields satisfactory results however may be revisited in future enhancement efforts.

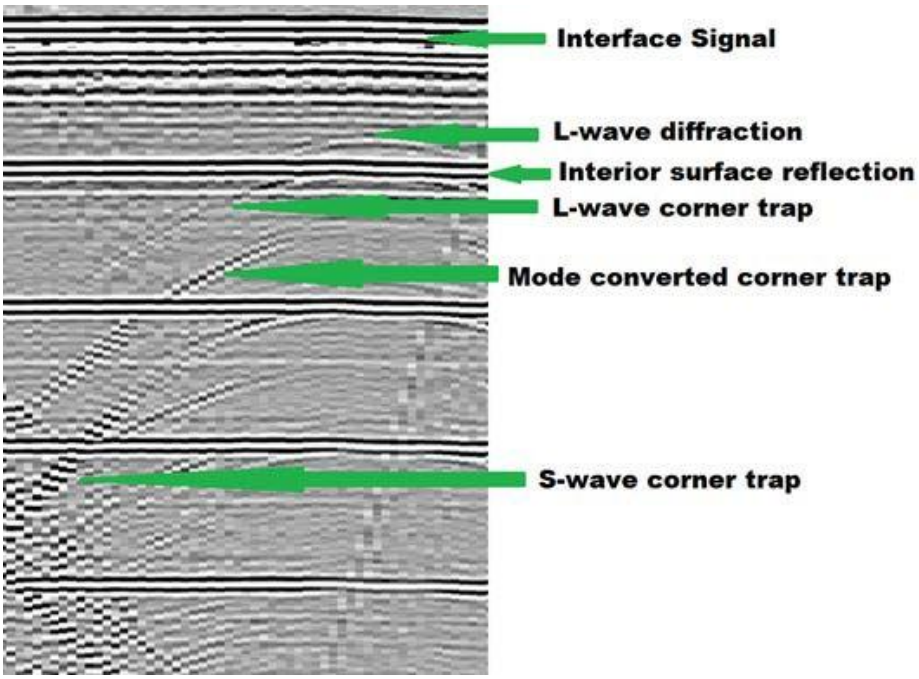

Figure 7 Signals of interest in a section the FMC main diagonal.

Phase inversion phenomenon is invariably observed in the FMC dataset. If phase inversion is not addressed prior to summation, the result will be attenuation of the artefact in the final intensity map. Phase inversion is accommodated by tracking the number of reflections in a path and inverting the analytic signal as appropriate; see Figure 8 and Figure 9. Mode conversion on the other hand is problematic to address. The use of multiple wave modes in the intensity map summation results in phase error. The magnitude of the phase error is proportional to the ratio of transit time in the shear mode with respect to the overall transit time. The phase error can result in blurring and attenuation of artefacts in the intensity map. Frequency domain techniques may be a means to address mode conversion however has not yet been investigated at this time.

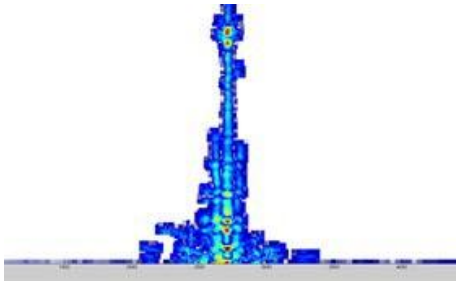

Figure 8 8 mm EDM notch without phase inversion compensation.

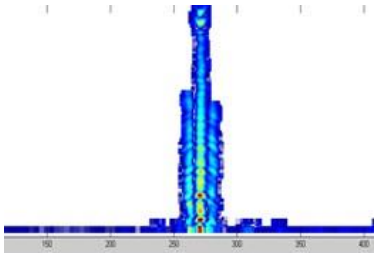

Figure 9 8 mm EDM notch with phase inversion compensation.

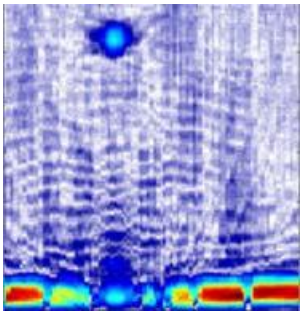

Figure 10 L-L wave, no suppression.

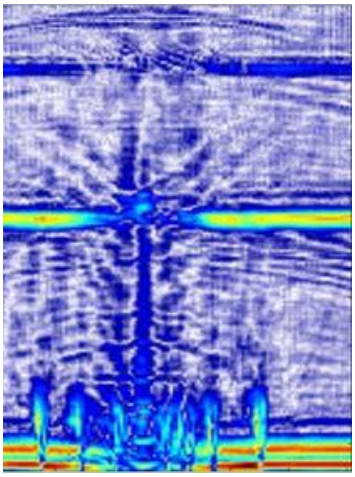

Figure 11 L-L, L-L-L wave, no suppression

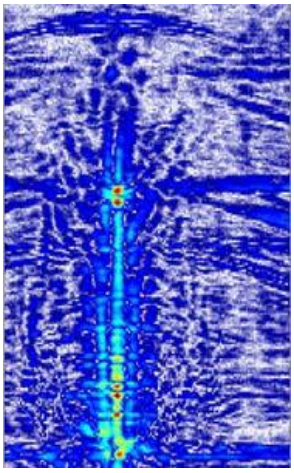

Figure 12 All modes with signal suppression.

Given the sequential method of determining the location of the interface, internal and discontinuity surfaces it is easily appreciated how the errors in one surface propagate when determining the next surface. Tests of the algorithm demonstrate that errors in the interior surface location of 0.05 mm have a discernible effect on the formation of the discontinuity image. With an error of 0.1 mm the image of the discontinuity is greatly attenuated. A similar effect is observed with errors in the longitudinal and shear wave velocities. Errors in the shear wave velocity as low as +/ 0.4% appreciably degrade the intensity map image. The same effect was observed with errors in the longitudinal velocity of +/-0.3%. It is anticipated other error sources such as couplant velocity and transducer delay variation will have a similar effect. The magnitude of these error sources has not been measured.

The motivation for conditional summation is to account for the direction, with respect to the artefact, from which the intensity map is formed. Consider a vertical planar discontinuity. Paths on the right side of the artefact will form an image to the left, conversely paths on the left form an image to the right. As the width of the discontinuity increases, the individual images will merge and modulate each other, see Figure 13. In the current version of the imaging code this problem has been addressed by forming the intensity maps independently. Where an image is formed at the same coordinates, a cross correlation is applied and the resultant image plotted see Figure 14 and Figure 15.

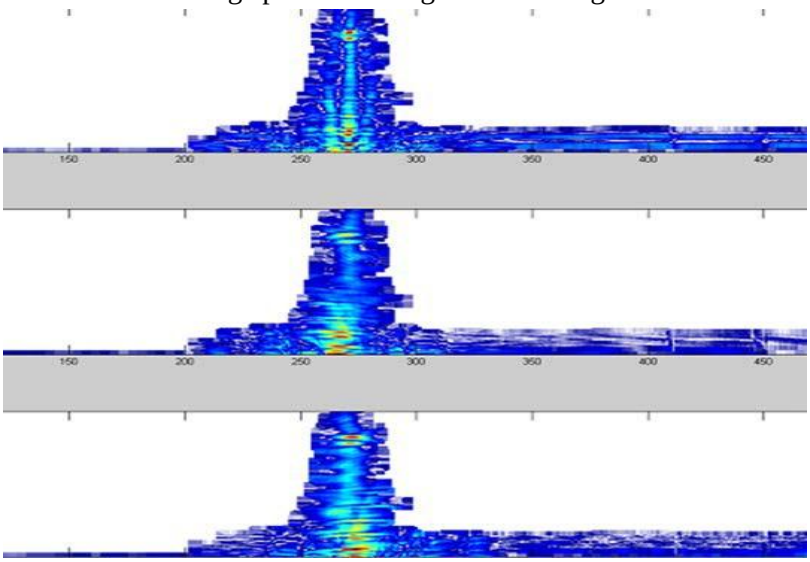

Figure 13 Summation of array elements from left (lower), right (mid) with conditional summation (top). Note the cancellation of the image at top.

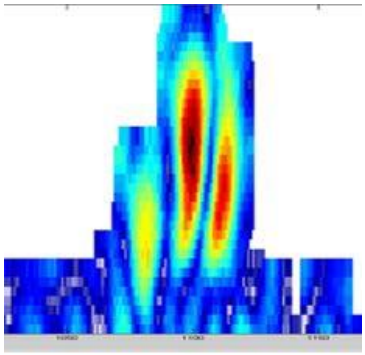

Figure 14 Conditional summation of image contributions for 1 mm high EDM notch.

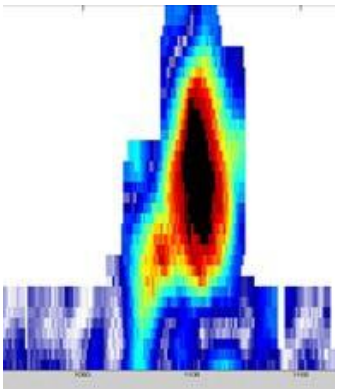

Figure 15 Cross correlation of image contributions for 1mm high EDM notch.

RESULTS

The results presented are the composite images for a step wedge with an angled entry surface. The 1 mm EDM notch has been imaged separately and merged with the existing image for the step block.

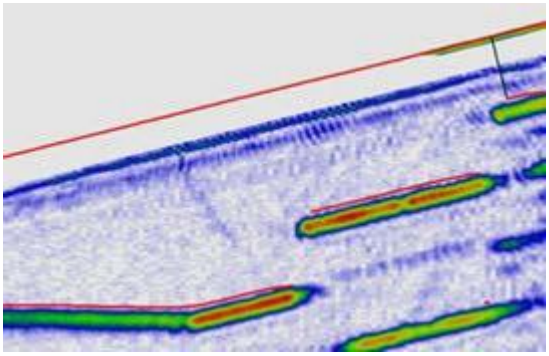

Figure 16 Step wedge without notch image.

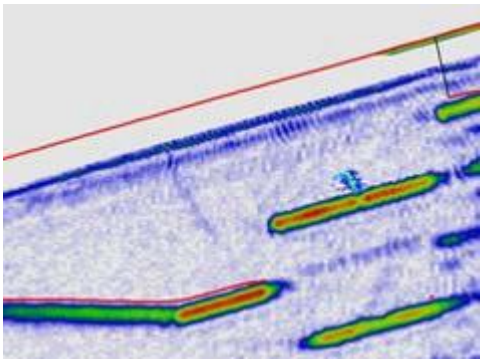

Figure 17 Step wedge merged with 1mm EDM notch image.

The code modification was tested on two separate weld samples. The images for these samples have been formed based on coordinate matching rather than superimposing pixels. The results for the implanted flaws are presented in Figure 18 for the sample containing a crack superimposed over an excess root penetration geometry. The crack is imaged however the excess penetration is only partially apparent.

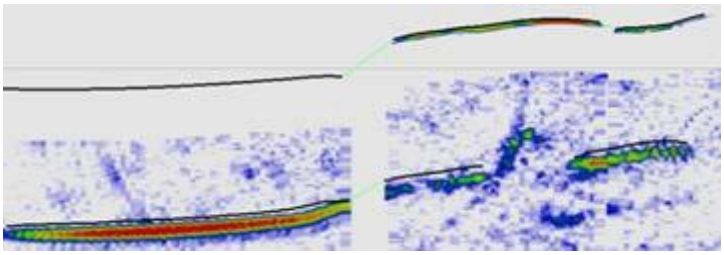

Figure 18 Crack and excess penetration at weld root

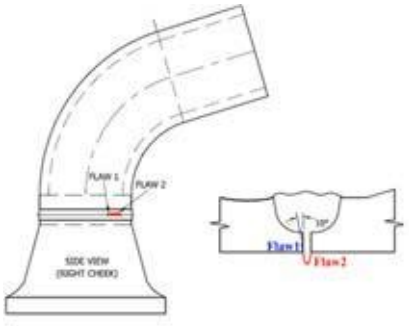

Figure 19 Sketch of weld sample.

The results for the second sample are found in Figure 20 and Figure 21. The Heat Affected Zone (HAZ) crack has been successfully imaged in both frames.

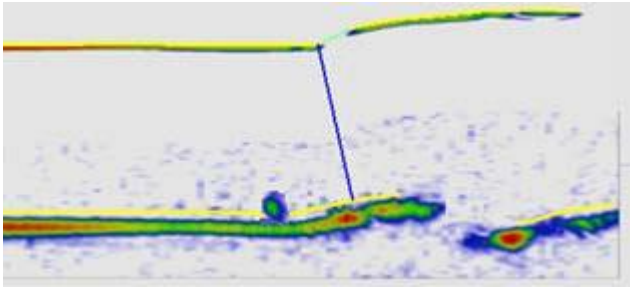

Figure 20 HAZ crack identified adjacent weld.

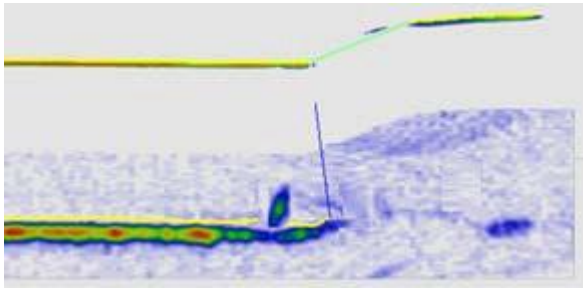

Figure 21 HAZ crack identified adjacent weld.

CONCLUSIONS

A novel method for imaging discontinuities in the volume of an inspection sample has been demonstrated. The method is an extension of the TFM beam former developed by OPG for arbitrary geometries. Several characteristics of the waveforms in the FMC dataset had to be addressed in order to yield robust performance. The technique has been successfully applied to conventional geometries to image surface breaking defects as small as 1 mm vertical extent in flat and inclined surfaces. The method has been applied to weld samples containing implanted weld discontinuities and has successfully imaged the defects. Further work to refine the underlying techniques is recommended.

REFERENCES

[1] T e n Grotenhuis R, Hong A and Sakuta A, "Inspection of complex geometries using the full matrix capture (FMC) method", 9th Int Conf on NDE in Relation to Structural Integrity for Nuclear and Pressurized Components, Seattle WA, USA, 2012.

[2] T e n Grotenhuis R and Hong A, "Imaging the weld volume via the total focus method", 9th Int Conf on NDE in Relation to Structural Integrity for Nuclear and Pressurized Components, Seattle WA, USA, 2012.

[3] Holmes C, Drinkwater B and Wilcox P, "Post-processing of the full matrix of ultrasonic transmit-receive array data for non-destructive evaluation", NDT & E Int, 2005 38(8), 701-711.

[4] Hunter A J, Drinkwater B W and Wilcox P D, "The wavenumber algorithm for full-matrix imaging using an ultrasonic array", IEEE Trans. On Ultrasonics, Ferroelectrics and Frequency Control, 2008 55(11), 2450-2462.

[5] Long R, Russell J, Cawley P and Habgood N, "Ultrasonic phased array inspection of flaws on weld fusion faces using full matrix capture", 35th Annual Review of Progress in Quantitative NDE, Chicago, USA, 2008.

RECONSTRUCTION OF PHASED ARRAY TECHNIQUES FROM THE FULL MATRIX CAPTURE DATA SET

R.L. Ten Grotenhuis, J.X. Zhang, A Sakuta, A. Hong
Ontario Power Generation, Canada

The Full Matrix Capture (FMC) ultrasonic data acquisition method is a powerful technique. Combining Total Focus Method (TFM) analysis and FMC can provide results beyond the capabilities of standard UT inspection methods. Moreover, the FMC data set can be analyzed by a range of algorithms to obtain different beam forming results. This paper discusses the development and implementation of Phased Array methods reconstructed from FMC data sets. Results are provided for a sample series of Electro Discharge Machining (EDM) notches in both conventional weld geometries and fitting to bend welds (arbitrary surfaces).
Keywords: Phased Array, Full Matrix Capture, Reconstruction

Introduction

The FMC ultrasonic data acquisition technique generates the complete data set that may be obtained for a given array transducer with a specified orientation over an inspection surface [1]. FMC data sets can be analyzed using a number of post processing beam forming techniques such as Wavenumber Method [2], Back Propagation Technique and the Total Focus Method (TFM) [3][4].
When FMC is combined with TFM the result is a very powerful method for imaging the weld volume of complex inspection geometries [5].

In addition to the above beam formers, other conventional UT techniques may be reconstructed during the process of offline analysis. For example Phased Array techniques may be derived from the conventional time domain signal [6]. This approach emulates dynamic surface adaptation phased array techniques. The Phased Array result may be further enhanced via substitution of the time domain signal with the analytic signal series when performing element summation.

Reconstruction of Phased Array addresses several specific requirements. Firstly this process establishes a relationship between Phased Array and the FMC data set. It also serves as a useful platform to progress users from the familiar Phased Array representation to the output of other beamforming methods. It offers the user the ability to isolate and examine regions of interest within a defined range of angles. This is helpful when testing for weld discontinuities with specific orientations. Finally it provides the possibility to derive a code compliant inspection on an otherwise intractable geometry.

Background and PA reconstruction requirements

The Inspection and Maintenance Services Division of Ontario Power Generation developed and implemented an inspection system combining the FMC data acquisition technique with the TFM beam former. The combination of the two technologies was called the Matrix Inspection Technique (MIT) [5]. The system was developed to address the inspection of complex geometries for Flow Assisted Corrosion (FAC) damage (see Figure 1 and Figure 2). The inspection geometries under consideration are: fitting to Grayloc, fitting to fitting and fitting to pipe welds.

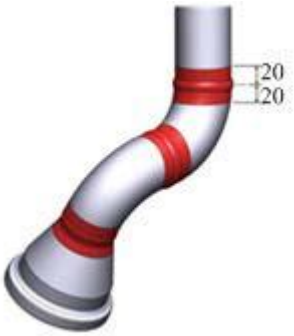

Figure 1: Typical inspection zones in CANDU feeder pipes.

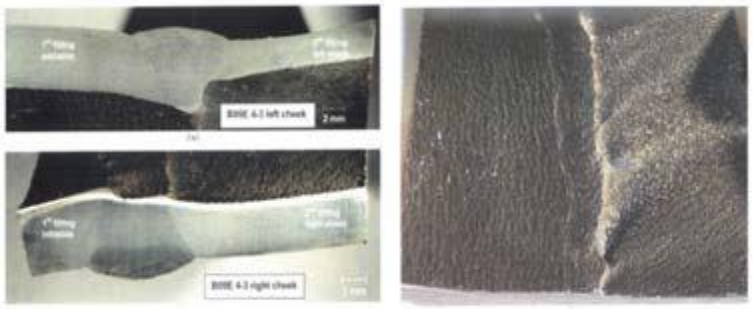

Figure 2: Localized FAC identified in ex-service feeder pipes.

The MIT system has been deployed on several inspection campaigns following the completion of its development in 2010. The results obtained significantly exceeded the ability of the previous UT inspection methods. The system is capable of resolving the exterior and interior profiles of the region inspected. Figure 3 shows the MIT intensity map of a weld cross section congruent with ex-service fitting-to-fitting sample (Figure 4). In the intensity map, both the outer surface (the upper curve in Figure 3) and the root are detected accurately.

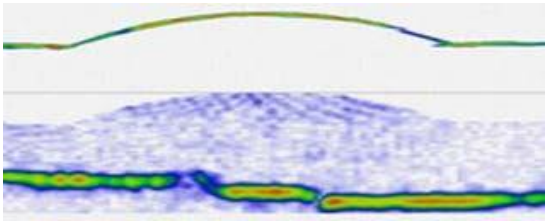

Figure 3: Intensity map of weld cross sections.

Figure 4: Weld cross sections (Congruent with ex-service fitting to fitting samples).

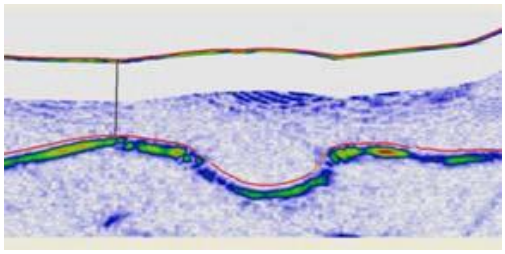

Figure 5: Lab specimen - abrupt cross section changes through weld region.

Figure 5 shows the intensity map of abrupt X-Section changes through the weld region. The inner surface (the lower curve) is detected successfully.

Figure 6: (L) Inspection sample.
(R) 3D reconstruction of inspection sample.

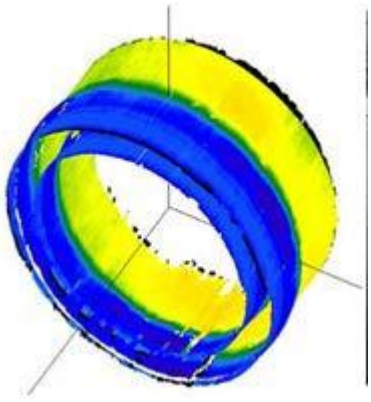

Figure 7: 3D rendering of inspection sample.

When the individual surface profiles are assembled, a 3D rendering of the inspection configuration is produced (see Figure 6(R) and Figure 7). The precision and coverage of the MIT system is such that photo realistic results of the inspection geometry are obtained.

Following the development of the MIT inspection system, the addition of other beam former methods was initiated, specifically phased array beam formers. The re-construction of phased array techniques is motivated by the desire to access several perceived benefits:

- Managing the transition from traditional phased array inspection methods to other beam formers, both from the perspective of personnel training and inspection technology continuity
- Pursue the potential of obtaining a code compliant inspection on complex surfaces
- Provide additional supporting evidence for Inspection Qualification of the MIT system

FMC data set

The Full Matrix Capture data acquisition strategy is implemented on a linear array transducer by transmitting on one element and receiving on all elements in the array. The next element then transmits and again, all elements in the array receive. The process is repeated until every element in the array has transmitted with all receiving, resulting in a 128 by 128 data matrix, see Figure 8.

The FMC data acquisition process does not introduce focal laws, i.e., no separate transmission or reception delays. A key attribute of FMC is that all phase relationships between transmitter and receiver are retained. This feature permits the post-acquisition application of a range of beam forming analysis strategies. Via the FMC method all waveforms are recorded regardless of mode, source or path. This is an essential attribute when inspecting complex or rapidly varying geometries.

The fundamental limitation of an FMC based inspection is the ability to deliver sound into, and receive sound back from the inspection volume. The FMC data collection process does yield exceptionally large data files and is consequently slower compared to other data acquisition methods. One proposed solution to address the file size and data collection speed is to perform half matrix capture. This strategy takes advantage of the symmetrical property of the matrix about the main diagonal, that is: $t_i\, r_j = t_j\, r_i$. Beam formers that are not sensitive to phase can utilize this approach however in practice we find that $t_i\, r_j \cong t_j\, r_i$. Slight variations exist from element to element, and channel to channel, in addition to noise contributions that are in turn manifested in beam forming strategies sensitive to signal phase.

Phased Array Beam Formers

UT phased array inspection technology is both well understood and widely adopted by the NDE community. Simply described; phased array is realized by applying the appropriate time delays to achieve superposition of individual wave sources for the transmission of a UT wave front in a specific direction to a predetermined location in the inspection volume. Typically the same delays are used for reception of the returned response from the same location in the inspection volume. The individual element contributions are then summed into a single A scan representation for the focal law in under consideration. The A scans from multiple focal laws are plotted together in a common representation; for example, a sectorial scan.

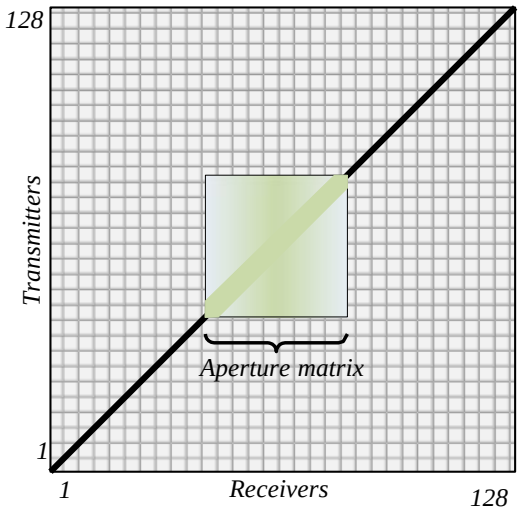

Figure 8: FMC data set.

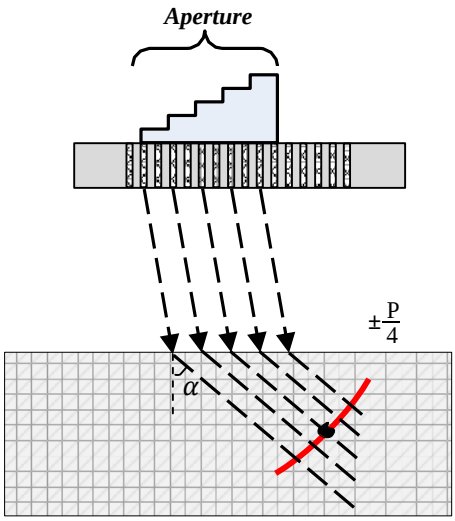

Figure 9: Focal Laws.

Given a linear array operating in the FMC data collection mode, we may define a sub aperture denoted as the aperture matrix (Figure 8). Phased array focal laws can be implemented on the aperture matrix by applying appropriate delays to the individual A scan members and then performing summation see Figure 9. Note that it is necessary to up sample the constituent A scan signals to a higher effective digitization rate such that the appropriate delay may be applied. The principal contributors to the resultant A scan are found along the main diagonal and the adjacent parallel diagonals of the aperture matrix. The extent of offset distance from the main diagonal is a function of a number of parameters. The main parameters include; element pitch, frequency, velocity, required steering angle and scattering function of the target reflector. The reader will recognize the same parameters are key inputs to the calculation of focal laws and hence intuitively appreciate that a linkage between the FMC data array and phased array exists.

Recall that in the time domain, signals will constructively interfere within a window of +/- P/4 where P is the nominal period of the wave pulse. Should the individual waves superimpose in a time increment greater than P/4, destructive interference predominates. Given a transducer with a centre frequency of 7.8 MHz, a pitch of 0.27 mm, the interval over which constructive interference occurs is approximately 65 ns. As an illustrative example, a focal law has been applied to create a longitudinal refracted wave in steel of 50 degrees. Isochronal arcs have been plotted for the centre element of the aperture as well as a series of adjacent transmit-receive combinations at an arbitrary distance in the inspection volume, (see Figure 9). The extent over which the members of the adjacent diagonals of the aperture matrix interact is apparent. Further work will derive the empirical formula describing focal law characteristics expressed in terms of the FMC data array.

The application of focussing delays has the effect of incorporating elements further away from the main diagonal. Introduction of these elements into the A scan summation restricts the inspection volume in which constructive and destructive interference occurs thus enhancing resolution and signal to noise ratio (SNR) within this region (Figure 10). Beyond this volume, the resolution and SNR begin to deteriorate. These areas can be addressed by re-calculating the delays and performing the summation again. In this manner several focal regions can be defined and the results merged into one plot. This feature essentially emulates the dynamic depth focussing capability in conventional phased array systems. Performing focussing on the post-acquisition FMC data set permits the user to define an arbitrary series of focal regions, such as the fusion line along a weld preparation for example.

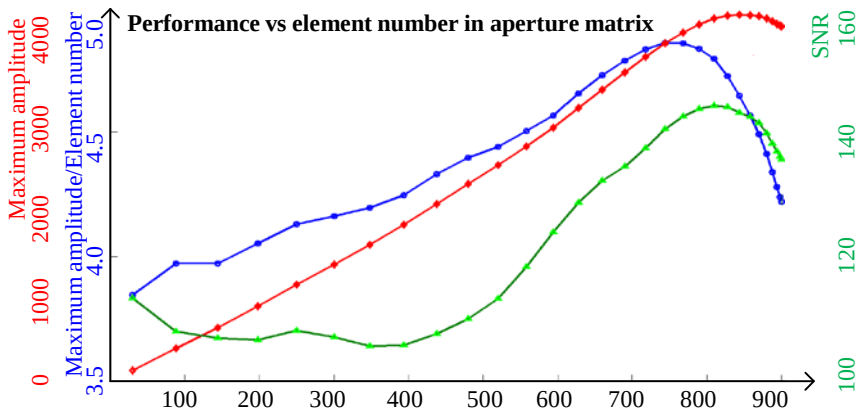

Figure 10: Performance vs the number of elements in summation for a SDH reflector.

The scattering function of the target reflector is also influential in defining the region in the aperture matrix from which the contributions are obtained. Volumetric reflectors such as slag and porosity will reflect across a wider range of angles. This stands in contrast to smooth planar reflectors e.g., side wall lack of fusion that return sound in a narrower range to fewer elements.

Implementation

During the development portion of this effort, the code was written using MATLAB 2012 development tools. MATLAB is a powerful, well-established package that permits rapid development of code. However the plotting capabilities in MATLAB provided a limited range of avenues in which the user can effectively interact with the output. The plots presented in the next section are based on the MATLAB version of phased array software. Following the initial development of phased array capability, the next step in the effort will be to convert the MATLAB code into equivalent C# code for implementation within the OPG Neovision® software. A user interface feature will be created along with the conventional A, B, D and sectorial scan representations. A variety of tools will also be provided to expand the user's ability to interact with the phased array results. The initial development efforts were directed at obtaining phased array sectorial scans from rudimentary geometries such as linear surfaces with side drilled hole (SDH) targets. The rationale behind this approach was to establish the correct methodology on a commonly used and easily verified geometry then progress to successively more complicated configurations.

Experiments with flat surface

- *IOW block (side drilled holes)*

Figure 11 and Figure 12 depict an immersion L-wave sectorial scan on an IOW block applying a twenty element aperture in a B scan fashion. The results obtained were confirmed with an equivalent set-up using a conventional phased array instrument. The main diagonal image of the FMC data set for this scan is found in Figure 13.

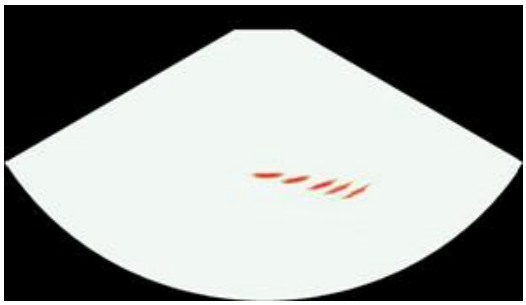

Figure 11: L-wave sectorial scan of SDH series in IOW block. IOW block.

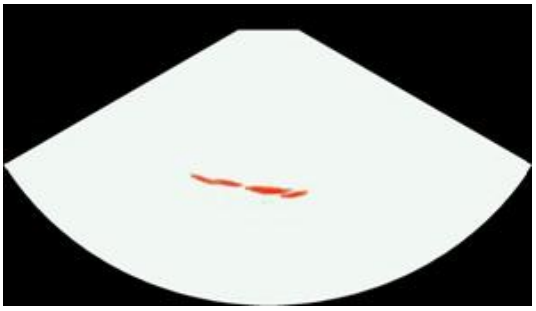

Figure 12: L-wave sectorial scan of SDH series in

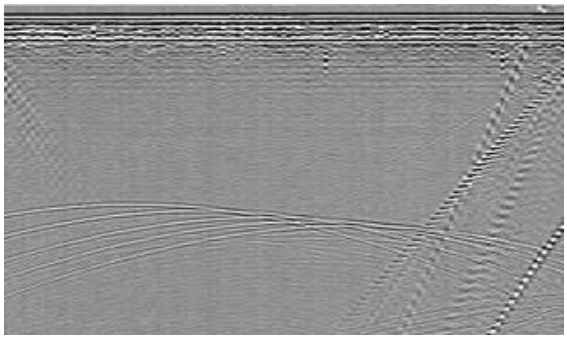

Figure 13: Main diagonal in FMC data set of IOW block. EDM notch in 5mm specimen. (Notch at the position of element 71)

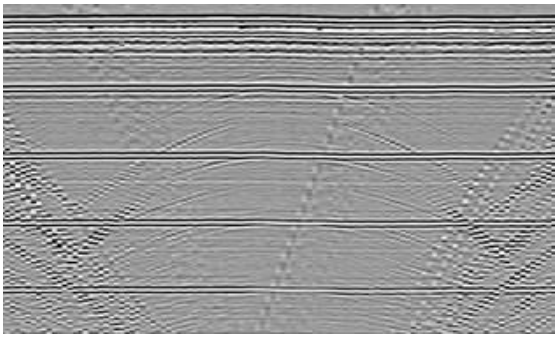

Figure 14: Main diagonal in FMC data set of 1mm

- *1mm EDM notch in 5mm specimen*

To test performance with planar reflectors, a 1mm EDM notch in a 5mm specimen was introduced in another experiment. The main diagonal for this FMC data set is shown in Figure 14

Figure 15 and Figure 16 are the results from L-wave and S-wave respectively. The notch can be observed from both sides so both L-wave result and S-wave result are symmetric to the notch position.

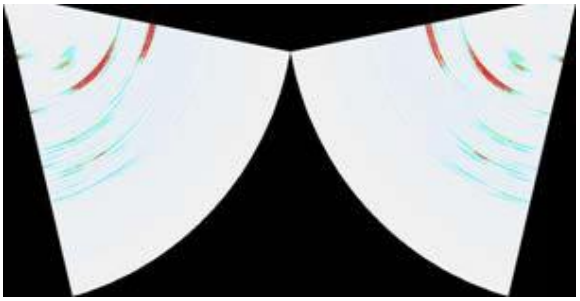

Figure 15: Lwave result from both sides. (L) Mid of aperture is element 47. (R) Mid of aperture is element 95.

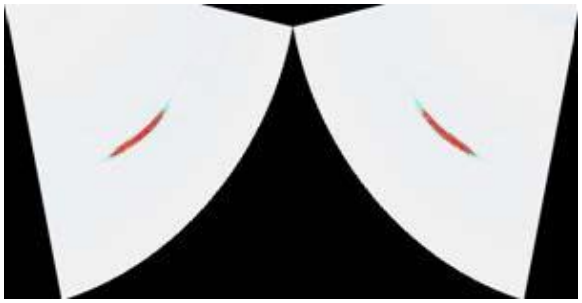

Figure 16: S-wave result from both sides. (L) Mid of aperture is element 33. (R) Mid of aperture is element 109.

- *1mm EDM notch in 5mm specimen*

Following examination of the flat surface parallel to the transducer, an angled step wedge with 1mm notch was tested. The surface of the step wedge has a 15 degree angle to the transducer (its FMC main diagonal data are shown in Figure 17). Because of the angle between the sample surface and the transducer, the notch can be seen only from one side (the red rectangle in Figure 17). Its S-wave result is shown in Figure 18.

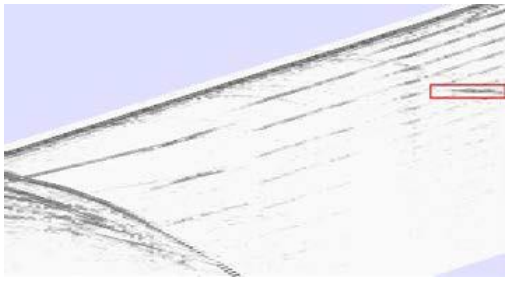

Figure 17: FMC main diagonal data for an angled step wedge with 1mm notch.

Figure 18: Result of S-wave.

Experiments with arbitrary surface

The approach adopted when addressing surfaces that are not accurately represented by a linear geometry is a hybrid of TFM and phased array. In this method, the Canny edge detector is applied to the TFM image to derive the coordinates of the interface surface. The user provides additional input parameters such as the index point on the interface, desired aperture, range of angles to plot, and focal point, if any. The appropriate delays are calculated through the interface solving the beam paths back to the individual elements at the transducer using the Fermat principle. The method has been tested on a limited range of convex and concave geometries however the results have yet to be verified against the equivalent implementation on conventional phased array instrumentation. This approach is adequate for the first half skip however may be sensitive to variations of the interior surface on the reflected second half skip.

- *Arbitrary Geometries 1 – Heat Affected Zone (HAZ) crack in feeder pipe*

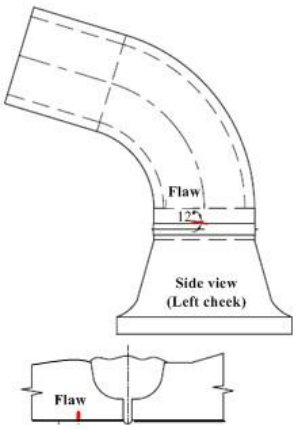

Figure 19: HAZ crack design.

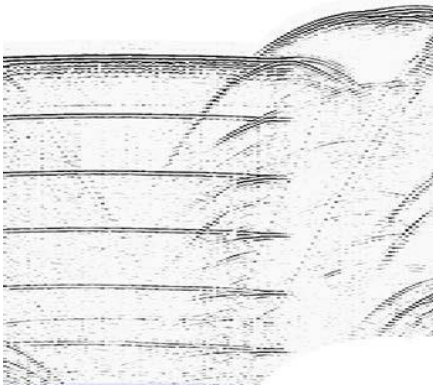

Figure 20: FMC main diagonal for HAZ crack.

Because of the complication of the feeder pipe geometry and position of transducer, the distance and the angle between the transducer and specimen's surface cannot be pre-determined. The only solution is to treat the specimen's outer surface as an arbitrary curve. The design of specimen is shown in Figure 19 and its main diagonal data are shown in Figure 20. The crack is detected using S-wave (Figure 22).

Figure 21: S-wave result for region containing a HAZ crack.

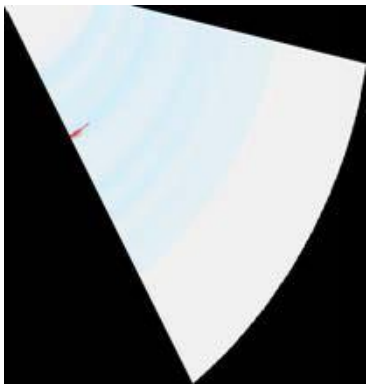

Figure 22: S-wave result for region adjacent to HAZ crack.

As depicted in Figure 19, the crack has a limited circumferential extent along the weld HAZ. To further verify the accuracy of the inspection, the region adjacent the HAZ crack was evaluated. The indication noted in Figure 21 is absent in Figure 22.

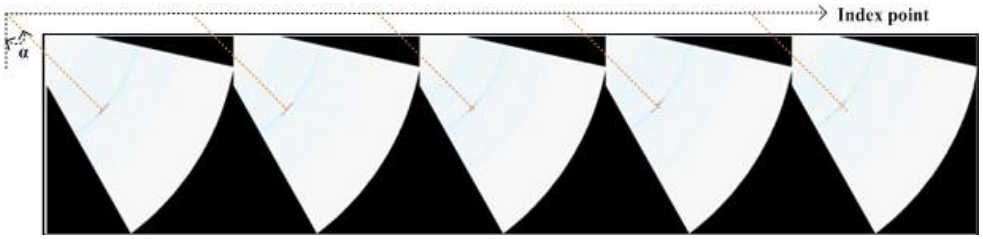

Figure 23: Flaw sample 005 result for different index points.

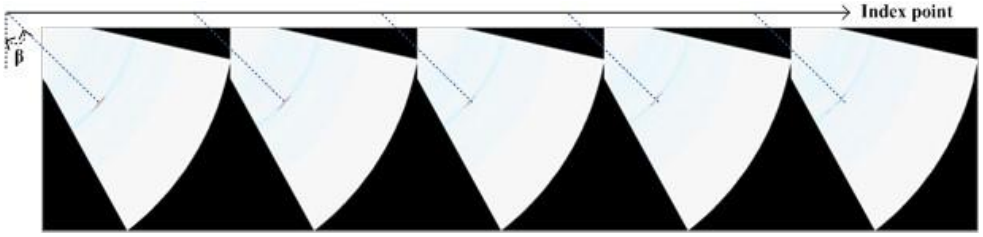

Figure 24: Flaw sample 005 result for different index points.

Another experiment was to generate a series of sectorial scans for the crack at discrete circumferential intervals (frames). These multiple frames were tested with the same series of aperture positions (with all the other parameters remaining constant). The crack is observed in this series of frames. In a single frame, when the index point moves right along the surface, the crack position moves accordingly (closer to its index point). These experiments confirmed the validity of the algorithm for phased array beam forming.

- *Arbitrary Geometries 2 – Crack & excess pen. at root*

In this experiment, the crack (flaw 1 in Figure 25) is at the same position as the flaw 2 at the weld root. Its main diagonal FMC data are shown in Figure 26.

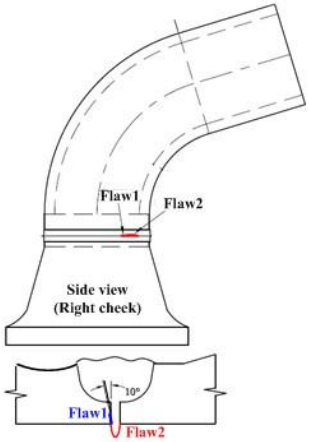

Figure 25: Crack & excess pen., at weld root.

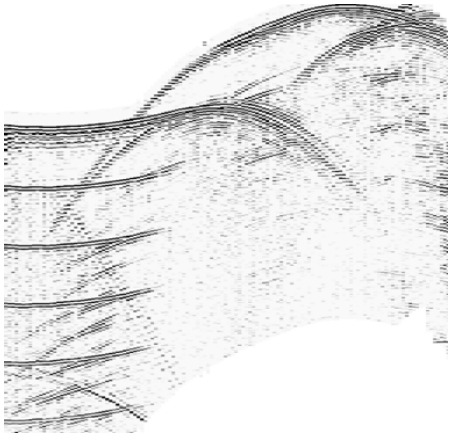

Figure 26: FMC main diagonal for crack & excess pen at weld root.

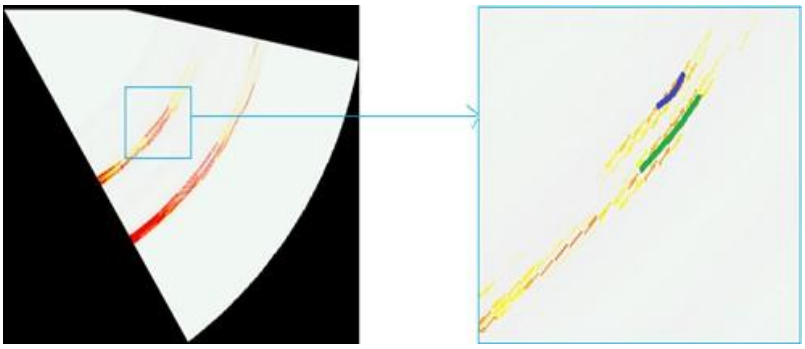

Figure 27: S-wave result for crack & excess pen. at weld root. (L) Sectorial scan. (R) Enlarged area of interest.

The left image in Figure 27 is the sectorial result. The right image in Figure 27 is the enlarged part to illustrate the 2 flaws clearly. The results of this experiment are also verified through multiple frames and multiple aperture positions in a single frame.

Conclusions

This paper presents a method to reconstruct phased array techniques from the FMC data set as a post acquisition beam forming process. The ability to re-construct phased array techniques from the FMC data set post acquisition has been demonstrated with both simple geometric samples and arbitrary surface samples. The method is verified through with a variety of samples containing manufactured discontinuities.

By successful reconstruction of Phased Array, a relationship between Phased Array and the FMC data set is established. The technique can serve as a useful platform to progress users from the familiar Phased Array representation to the output of other beam forming methods.

References

[1] Tremblay P and Richard D, "Development and validation of a full matrix capture solution", 9th Int Conf NDE, Seattle WA, USA, 2012.

[2] Hunter A J, Drinkwater B W and Wilcox P D, "The wavenumber algorithm for full-matrix imaging using an ultrasonic array", IEEE Trans. On Ultrasonics, Ferroelectrics and Frequency Control, 2008, 55(11), 2450-2462.

[3] Ten Grotenhuis R and Hong A, "Imaging the weld volume via the total focus method", 9th Int Conf on NDE in Relation to Structural Integrity for Nuclear and Pressurized Components, Seattle WA, USA, 2012. [4]Long R, Russell J, Cawley P and Habgood N, "Ultrasonic phased array inspection of flaws on weld fusion faces using full matrix capture", 35th Annual Review of Progress in Quantitative NDE, Chicago, USA, 2008.

[5] Ten Grotenhuis R, Hong A and Sakuta A, "Inspection of complex geometries using the full matrix capture (FMC) method", 4th Int CANDU In-service Inspection and NDT, Toronto, CA, 2012.

[6] Holmes C, Drinkwater B and Wilcox P, "Post-processing of the full matrix of ultrasonic transmit- receive array data for non-destructive evaluation", NDT & E Int, 2005 38(8), 701-711.

PIPING INSPECTION - WELDING

SAFETY RELATED SERVICE WATER PIPING ASSESSMENT FOR NUCLEAR POWER STATIONS

R. Royer, K. Rach, A. Crompton, D. Keene
Structural Integrity Associates, USA

Safety related service water (SW) piping systems in nuclear power plants are critical to plant operability and safety as their primary purpose is to provide cooling capability to essential equipment and components in the event of an accident. Recent trends in the industry indicate that one of the dominant degradation mechanisms for these systems is internal corrosion. Typical SW systems can be prone to internal corrosion degradation depending on the quality of the water being run through them, the water treatment regime, and if the lines contain stagnant water for prolonged periods of time. As such, periodic assessments to determine the condition of these lines are required to assure safe plant operability. Once it has been decided to perform an assessment of the system, it is then necessary to select an appropriate assessment strategy including selecting the appropriate inspection technologies, determining how to manage the data collected, and what actions are to be taking in the event that degradation is found during the examinations. Presented herein will be an inspection strategy, utilizing advanced ultrasonic technologies, developed and recently executed in a nuclear power plant setting for performing a comprehensive assessment of ~5,000 ft. of SW piping, including complex geometries. Also presented will be the engineering analysis and pre-inspection planning incorporated to effectively disposition and remediate degraded areas without forcing a plant shut down and the database management approach used for organizing the large amounts of inspection data acquired.

INSPECTION TECHNOLOGY SELECTION

Many different technologies and strategies can be employed to assess the condition of piping systems including ultrasonic testing (UT), radiography, visual inspections, ultrasonic guided wave testing (GWT), and others. Most of these techniques offer only a localized inspection capability and require direct access to the pipe to perform the inspection. When considering most SW systems contain thousands of feet of piping which requires insulation removal and scaffolding to be built for direct access, it is clear that performing a comprehensive assessment of the entire system with localized inspection technologies is impractical. GWT, alternatively, provides a cost effective means to screen long sections of the piping system from only one access point in order to identify areas of potential degradation where conventional inspection approaches, such as UT, can be focused to provide quantitative data of the remaining wall thickness of the pipe [1].

PLANNING FOR DEGRADATION DETECTION AND REMEDIATION

There are two approaches that can be taken for any comprehensive system evaluation. One approach is a well thought out plan with evaluation criteria already established prior to starting any inspections and methodologies to disposition the inspection findings. The other approach is the post inspection evaluation methodology, or the "cross your fingers" and hope methodology. This article will focus on the recommended comprehensive pre-inspection evaluation methodology.

No Pre-Inspection Methodology

This approach typically begins with the selection of a number of inspection locations for detailed examination. Plant engineering usually has limited input at this point in the process, with that input being guidance on inspection locations and gathering of system design basis documents. The minimum allowable wall thickness, t_{min}, is either pulled from design basis documents or calculated in accordance with the Code of Construction. For Class III and B31.1 components, such as the SW system, the Code of Construction does not consider local thinning in piping. Therefore, the calculated t_{min} value is not limited in the axial or circumferential extent. This makes applying this limit relatively straightforward. Any indication with wall thickness greater than t_{min} is acceptable for continued operation. In practice, an indication is considered acceptable when wall thickness exceeds t_{min} plus some allowance for future wall loss.

For certain systems, this approach has significant financial advantages. Systems with no active degradation method are not expected to challenge the structural integrity of the piping, making pre-inspection evaluations of limited value. For systems in which the anticipated flaw type is highly variable, the likelihood that pre-inspection evaluations bound discovered indications is low. The disadvantage of this approach is that it has the potential to force an unplanned outage. This can happen in a number of ways. In some situations, the design basis stress report may have used a limiting location to bound large portions of the system or assumed unrealistically high loading. Although conservative, this can unnecessarily restrict the allowable flaw size for the entire system. It is unlikely that a design basis stress report could be recreated; eliminating the overly conservative aspects, in the time frame of a typical limiting condition for operation (LCO). Another situation that could cause a LCO to expire is if the number of indications exceeds engineering's ability to process them. Both of the above scenarios have the potential to cycle the plant into and out of a LCO.

PRE INSPECTION PLANNING

Planning requires an integrated approach with all the appropriate stakeholders at the site and includes operations, design engineering, systems engineering, NDE personnel, along with the maintenance teams to repair any areas that require repair in a timely fashion and prevent an unnecessary plant shutdown. This article will concentrate on the interaction between the engineering and NDE personnel.

The planning for this integrated approach must start well in advance of the actual inspection activities. In order to increase the efficiency of the inspections the engineering teams need to understand the inspection methodology and the NDE personnel need to know how to apply the engineering evaluations. Some level of pre-inspection engineering evaluations is recommended prior to inspection activities. For safety related piping, these evaluations are considered critical. The purpose of the evaluations is threefold:

1. Establish flaw tolerance of piping
2. Determination of inspection technique
3. Rapid disposition

The first purpose, establishing the flaw tolerance of the piping, reveals the margin between the design basis stresses and the ASME Code allowable stresses. This can identify situations in which the design basis stress report may be overly conservative, which can unnecessarily restrict the allowable flaw size. By establishing the margin prior to receiving inspection results, actions can be taken to reduce overly restrictive assumptions and increase margin without the added pressure of being in a LCO. Once the flaw tolerance of the piping is established, the second purpose of the pre-inspection evaluations is to determine the appropriate inspection technique and sensitivity requirements. The final purpose of the pre-inspection evaluations is the compilation of a group of flaw parameters for which the safety margins in the ASME Code are met. This is commonly referred to as a flaw handbook.

Example

A project was recently completed at a commercial nuclear power plant to comprehensively assess the condition of the essential service water (ESW) system. An extensive pre-project planning phase was conducted by a multi-disciplined team of NDE specialists, engineers, and project managers in order to select the proper inspection technologies to meet the plant's objectives, determine the proper dispositioning and remediation actions to be taken if and when degradation was found, and develop a plan for organizing and managing the large amounts of inspection data created. The goal of the assessment was to perform a comprehensive evaluation of the system, not just local inspection of select areas.

Based on the plant's objectives, GWT was selected as a key driver of the inspection phase of the project in order to screen long lengths of piping to intelligently select areas of interest for prove up using conventional ultrasonic testing (UT). The use of GWT allowed the plant to screen long sections of pipe, including inaccessible regions such as wall and floor penetrations, from areas which were easily accessible. This approach resulted in tremendous cost savings by not having to remove insulation in areas other than the areas where the GWT was performed or where areas of interest were identified for prove up. Further, test locations could be selected to minimize the amount of scaffolding required to access the piping. Piping geometries which were not suitable for GWT, such as short

lengths of pipe, elbows, tee-pieces, etc., were 100% screened with conventional UT and select welds throughout the system were inspected using Phased Array UT.

The assessments identified multiple areas of internal wall thinning from under deposit corrosion and pitting which violated the minimum allowable wall thickness criteria identified in design basis documents. The plant established administrative limits (t_{admin}) which provided additional margin above the t_{min} requirements to account for ESW system configuration and the potential for degradation. The t_{admin} limits provided allowed the station to disposition flaws well above the t_{min} limits. Individual flaw evaluations and Code Case N-513 for class 3 piping was invoked resulting in repair or replacement of piping throughout the plant. Because the flaw evaluations and code case calculations were conducted prior to the inspections, the plant could continue to operate and conduct repair activities while on-line and defer replacements until the next refueling outage. In the event that a wall thickness was detected less than t_{min}, a typical approach to dispositioning the flaw would be to first size the flaw and then grid out the entire circumference of the pipe at the flaw location to gather thickness measurements to be used as inputs into the calculations. Figure 1 shows a typical sizing and banding pattern for dispositioning an internal flaw. Figure 2 shows a typical repair encapsulation applied to maintain structural integrity of a flawed region. Figure 3 shows a photograph of the internal degradation from a section of pipe which was cut out and replaced.

A total of 5,000+ ft. of pipe was examined resulting in the replacement of ~180 ft. of piping to date and numerous repairs throughout the system. Since the inspections began no leaks have occurred over the inspected piping. In order to manage the massive amounts of GWT and UT inspection data collected during the assessment, the entire ESW system was digitized and all of the inspection data was stored in the digitized BPWorks/MapPro View database. By doing so, the plant has been able to easily review the assessment findings and identify and monitor areas where wall thinning was detected but didn't violate t_{admin} or t_{min} limits. From this information, a replacement strategy has been formulated prioritized primarily by the inspection data. A sample digitized piping system showing areas of GWT inspection coverage is illustrated in Figure 4. An example piping segment showing the locations where indications were detected during the GWT inspections is illustrated in Figure 5.

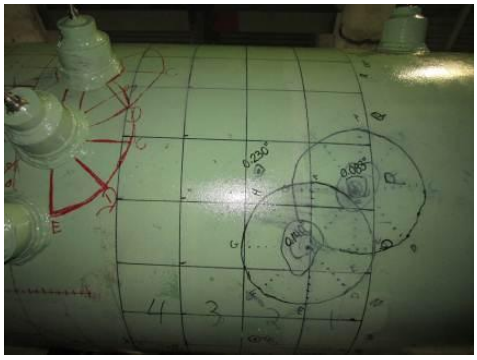

Figure 1. Photograph showing the sizing of flaws and full circumferential grid for flaw dispositioning.

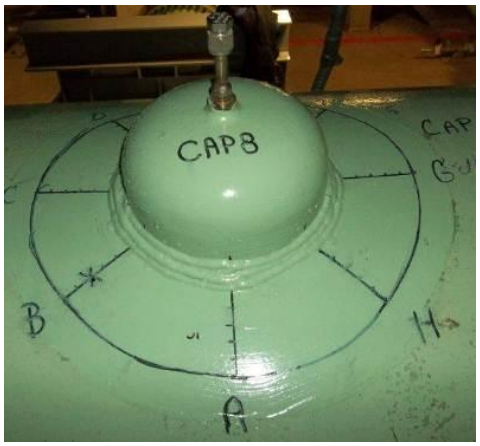

Figure 2. Photograph showing a typical encapsulation repair.

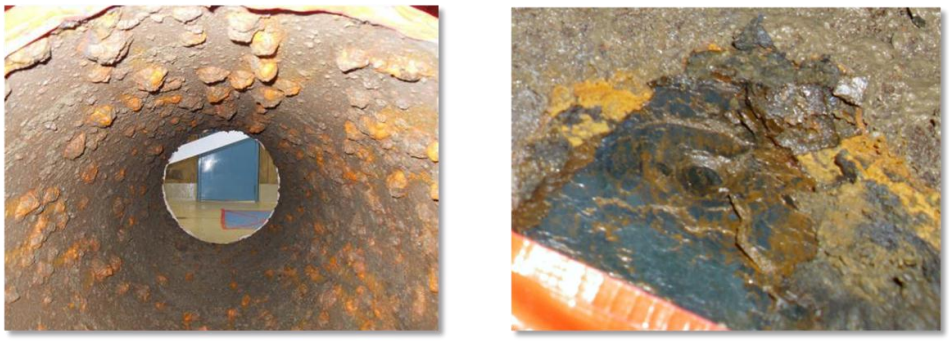

Figure 3. (Left) Photograph showing internal build-up on a section of piping replaced. (Right) Close-up photo of an internal pit.

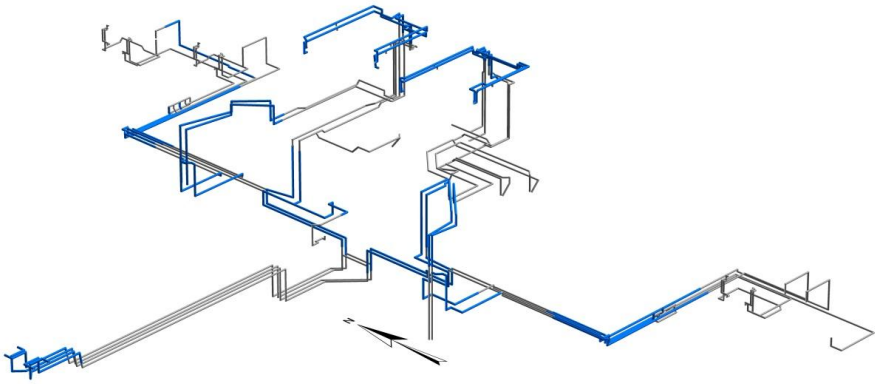

Figure 4. A sample digitized piping system showing areas of GWT inspection coverage (shaded in blue).

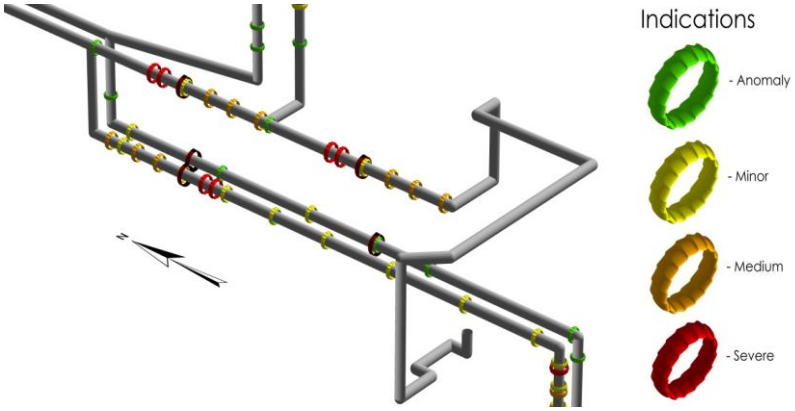

Figure 5. An example piping segment showing the locations where indications were detected during the GWT inspections. Detected indications were classified as a severe concern, medium concern, minor concern, or anomaly based on the response characteristics.

Summary

Described in this paper is a comprehensive approach to assessing the condition of a SW system; something which is not simple given such systems can have thousands of feet of piping which bends and wraps itself throughout the plant and creates challenges for inspection due to many regions which are not accessible or very difficult to access. Key to the success of such an assessment is the pre-project planning and coordination to review the objectives, select the appropriate inspection technologies, determine how flaws will be dispositioned while remaining on-line, and how the large amounts of data will be captured and managed. This approach was successfully applied at a commercial nuclear power plant to assess the SW piping system where areas of piping degradation were detected, dispositioned, and remediated without affecting plant operations. The plant realized significant costs savings from the use of GWT vs. manual scanning of the piping and much more from proper planning of the assessments allowing the plant to continue operations and not shut down when degraded areas were detected that violated code of constructions limits.

1) J. L. Rose. *Ultrasonic Waves in Solid Media.* Cambridge University Press, New York, 1999.

SIMULATION OF ULTRASONIC INSPECTION OF DISSIMILAR METAL WELDS USING RAY-BASED APPROACHES

H. Lourme, A. Gardahaut, K. Jezzine,F. Jenson, CEA - LIST, France
G. Cattiaux, T. Sollier, IRSN, France

ABSTRACT

Dissimilar metal welds (DMWs) of the primary loop of French nuclear power plants exhibit complex anisotropic and inhomogeneous material properties. Ultrasonic inspections of such materials are limited due to beam attenuation, skewing and splitting. Accurate numerical simulation tools are useful to optimize Ultrasonic Non Destructive Testing, and develop new signal processing and data reconstruction techniques dedicated to inspection of DMWs. In the past years, several approaches were addressed, either relying on numerical algorithms (finite elements, finite difference-time difference) or semi-analytical techniques (ray-based approaches). This paper presents two ray-based approaches applied to the simulation of DMW inspection. Firstly, the weld material properties are described as a set of anisotropic homogeneous domains. Rays travel in straight lines between two interfaces and reflection coefficients are taken into account as the ray moves from one domain to the next. In the second approach, which is an improved version of the first approach, a smooth description of the grains orientation is considered. Such descriptions may come from a functional form which links the grains orientation to a set of parameters that must be fixed for the considered weld. Alternatively, grains orientation is obtained through an image processing technique applied to metallographic pictures of the weld. Ray propagation is then computed using a dynamic ray tracing algorithm. Here, both approaches are applied to DMWs similar to those found in French nuclear power plants. Simulation results are discussed and compared to finite elements and experimental results.

INTRODUCTION

In the nuclear industry, Ultrasonic Non Destructive Testing (NDT) techniques are used to control welded joints of the primary circuit of Pressurized Water Reactor (PWR). Those techniques allow the detection, the localization and the characterization of defects located inside or in the vicinity of bimetallic welds. However, the interpretation of on-site inspections of dissimilar welds is particularly difficult due to their internal structures. Indeed, the anisotropic and inhomogeneous polycrystalline structure of the weld implies some disturbances of the beam, such as splitting and skewing [1]. Then, the simulation of ultrasonic inspection can be a powerful tool to understand these phenomena.

Various models have been developed to simulate the ultrasonic propagation such as finite element models [2][3] or ray-tracing models [4]. In the CIVA software [5], a semi-analytical propagation model, based on Dynamic Ray Tracing model (DRT), which evaluate the ray trajectories and the travel-time and compute the amplitude of a ray tube during the propagation, has been implemented. This model has been applied on a weld described as a set of several homogeneous domains with a constant crystallographic orientation [6]. In this paper, we present a generalization of this model that takes into account a continuously varying description of the grain orientation in the weld. The validation of this model is performed with comparisons with finite element model and with experiments.

PRESENTATION OF THE MODELS

A bimetallic weld located in the primary circuit of nuclear power plants is composed of Inconel or stainless steel and joined ferritic steel and stainless steel. Its metallurgical structure (which depends on many parameters such as the grade of steel, the diameter of the electrode, the velocity and the process of the welding) is inhomogeneous and strongly anisotropic (cf. Figure 1a).

To simulate this kind of welds in the CIVA platform, the current model is based on the DRT model applied to homogeneous media. This model consists in the resolution of two systems of differential equations: the first, named axial ray system, enables the evaluation of the ray trajectory and the associated time of flight and the second, the paraxial ray system, enables the estimation of the amplitude associated to an elementary tube of rays. In the current model, the weld needs to be described as a set of several homogeneous domains with a given crystallographic orientation (cf. Figure 1b). The ray propagates then along a constant direction of energy and the transmitted and refracted coefficients are evaluated at each interface (Figure 2a). For that, the geometry of the weld, the elasticity constants, the attenuation of the welding materials and the crystallographic orientation of the grain are required.

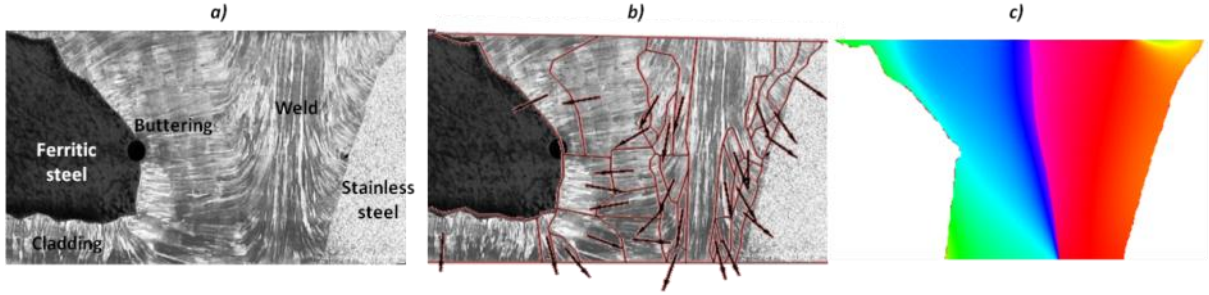

Figure 1: a) Macrograph of the DMW, b) piecewise description and c) continuously varying description obtained by applying an image processing technique on the macrograph.

This model gives satisfying results while the domains have greater dimensions than the wavelength. Nevertheless if the contrast of impedance between two neighboring media is big, the limits of the model are reached. Furthermore, the division of the weld in homogeneous domains is not always easy and can imply numerical artifacts or unrealistic mode conversions. Thus the DRT model must evolve to be applied on continuous descriptions of the crystallographic orientation in order to limit these problems. In this extension of the model, the position and the energy velocity are evaluated at each step of time. Consequently, the ray does not propagate in straight line anymore but in curved line (Figure 2b). Description such as slowly continuously varying cartography of the orientation can be obtained either with an analytical law [4] or thanks to an image processing technique as illustrated in Figure 1c) [7].

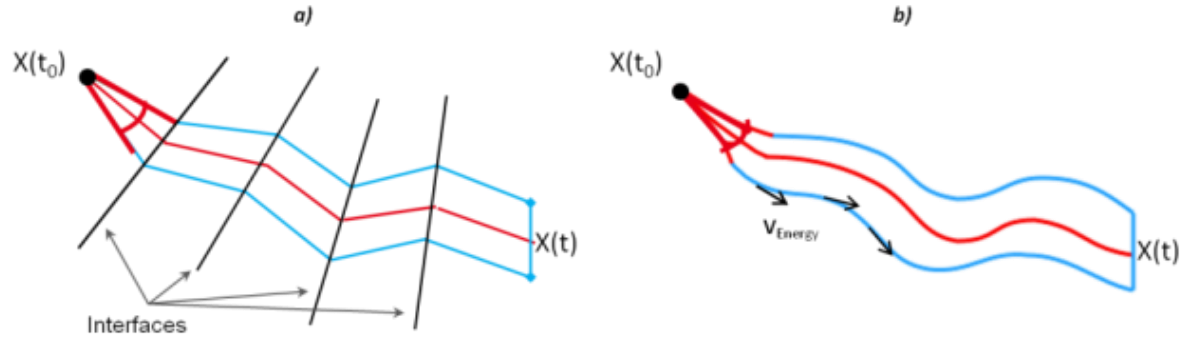

Figure 2: Principle of the Dynamic Ray Tracing model for a) piecewise description and b) smooth description.

NUMERICAL VALIDATION

Comparison with piecewise description

The first validation of the improved model consists in comparison with the current model. For that, two piecewise descriptions, a description in 7 homogeneous domains and a description in 23 homogeneous domains, are used.

The improved DRT model has been applied on a V-shaped weld on which the crystallographic orientation is described by a closed-form expression proposed by Ogilvy [4]:

$$\theta = f(x) = \begin{cases} \tan^{-1}\left(\dfrac{T(D + z * \tan\alpha)}{x^{\eta}}\right) & \text{for } x > 0 \\ {}^{\pi}/_{2} & \text{for } x = 0 \\ -\tan^{-1}\left(\dfrac{T(D + z * \tan\alpha)}{(-x)^{\eta}}\right) & \text{for } x < 0 \end{cases}$$

Parameters D and α describe the geometry of the weld when T and η express the evolution of the orientation of the grains. In this example, the following values have been chosen: D = 2 mm, α = 21.8°, T = 1 and η = 1. The different descriptions are given in Figure 3.

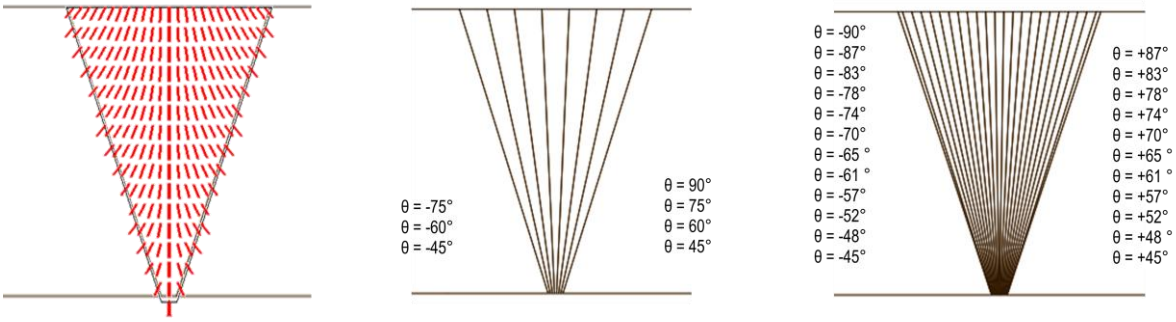

Figure 3: Different descriptions for the validation: from left to right, smooth description, 7 domains description and 23 domains description.

First, the ray trajectories have been compared in order to validate the resolution of the axial ray system.

Figure 4 represents the ray trajectories evaluated for the different descriptions. The trajectories of a ray evaluated with the dynamic ray tracing model are identical to those obtained by the piecewise description. However more is the number of domains, more the ray trajectories converges. Indeed in the description in 7 domains, the trajectories are more rectilinear and a little difference between the impacts of the rays can be observed.

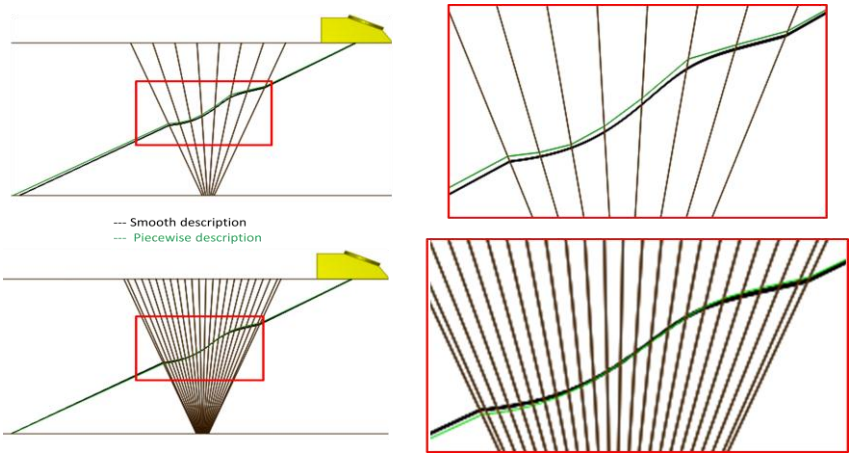

Figure 4: Comparison of ray trajectories between smooth description and piecewise description: on the top, description in 7 domains and on the bottom, description in 23 domains.

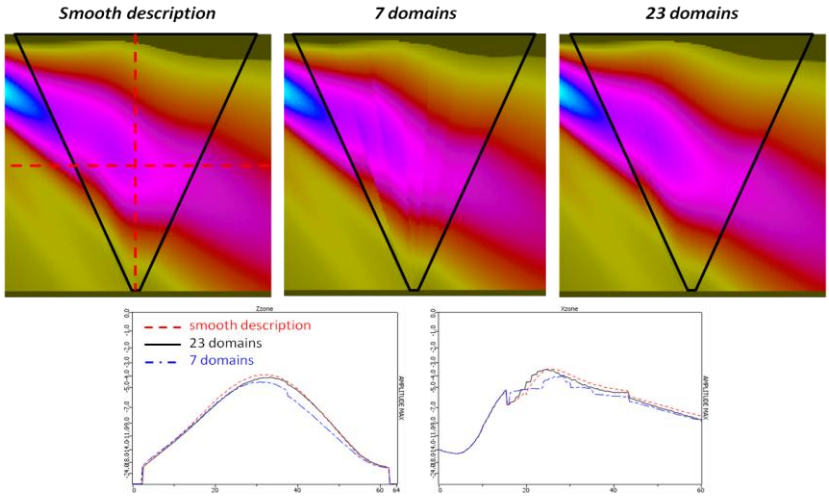

Figure 5: Representation of the maximum amplitude of the velocity modulus for a weld described by a closed-form and comparison of the results obtained with a description in homogeneous domains.

The axial ray system has been validated through the comparison of the ray trajectories. The next step consists in the evaluation of the ray amplitudes. To this aim, we have compared the ultrasonic wave field computed with the smooth and the piecewise descriptions. The comparison of the maximum particle velocity is given in Figure 5 for the different descriptions. A good agreement is obtained between smooth descriptions and the description in 23 domains. On the other hand, with the description in 7 domains, the interfaces of each domain are more visible on the beam. Furthermore, the comparison of echodynamics, which are the maximum of the particular velocity modulus on a line, shows that results for 7 domains are not as good as for 23 domains. Indeed, discrepancies of 1.5 dB are observed and the echodynamics are disturbed.

Comparison with Finite Element model

Now that the convergence between the piecewise and the smooth descriptions has been validated on a simple description of weld, the aim is to apply the DRT model to a more realistic description of the crystallographic orientation. The smooth description of realistic dissimilar metal weld presented in Figure 1c) is thus studied. This description is obtained by an image processing of the macrographs, the steps of this process being presented in [7]. The maximum particle velocity evaluated with the DRT model is then compared with those obtained with the hybrid code CIVA-ATHENA. In this code, a computation area is defined. Out of this area, a semi-analytical model is used for the computation of incident beam whereas in this area finite element (FE) model is used [8]. The simulation has been done in 2D with an immersion probe with a 12.7 mm diameter emitting longitudinal waves at 60° at 2 MHz. Results are shown in Figure 6:

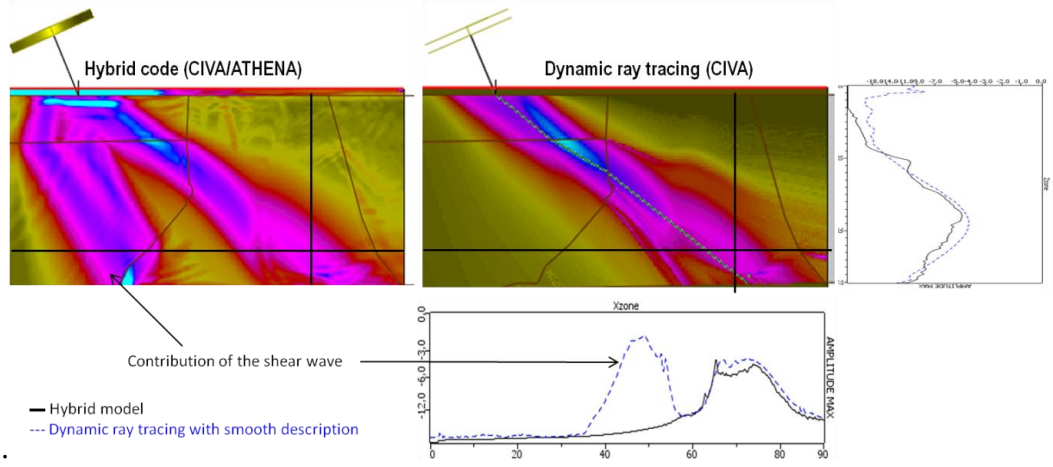

Figure 6: Representation of the maximum amplitude of the velocity modulus for a weld described by an image processing of the macrograph and comparison of the results obtained with a 2D hybrid code and a DRT model in 2D.

The comparison of the longitudinal wave field evaluated with both models presents a very good agreement. Nevertheless, some differences are observed since the simulation with the DRT model has been made only for the direct longitudinal wave while the hybrid code takes into account all the physical phenomenon such as the shear waves, the reflections and the mode conversions. The beam of greater intensity on the echodynamics evaluated with the hybrid model corresponds to the shear wave. Furthermore, on the ultrasonic wave field evaluated with the DRT model, the beam seems to split in three beams: the main beam similar to those obtained by the hybrid model, one caused by the junction of weld and cladding interfaces and another one caused by the modification of the bevel slope. The latter are numerical artifacts caused by non smooth interfaces which are not well taken into account in the ray theory. Non smooth interfaces are interfaces for which the normal at the interface is non continuous.

EXPERIMENTAL VALIDATION

Comparison with transmitted beam measurement

Since it is not possible to perform 3D computation with the hybrid code CIVA/ATHENA, experimental validations have been performed on a mock-up of the weld used for the numerical validations in order to validate the 3D model. The acquisition has been realized with a L60° wedge probe with 12.7 mm diameter at 2 MHz fixed on the weld. The receiver is a 0.2 mm needle hydrophone which can be moved to do a 2D scanning in order to measure the transmitted beam. The experimental setup is shown in
Figure 7.

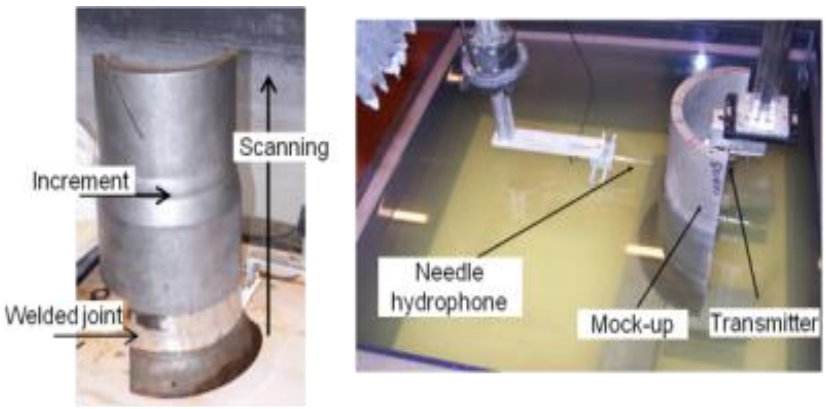

Figure 7: Experimental setup of transmitted beam measurement.

This configuration has been reproduced in simulation in order to compare experimental and simulated beam of the ultrasonic longitudinal wave. Results are shown in Figure 8 and Figure 9 for the transmitter above the weld and above the cladding respectively. On the left of these figures, are presented the maximal amplitude of the transmitted beam for each position of the receiver. On the right, are given the echodynamics which corresponds to the amplitude on the red lines on the transmitted beam: the curves on the top corresponding to the vertical ones and on the bottom to the horizontal ones. The amplitudes have been normalized and only the dimensions are compared.

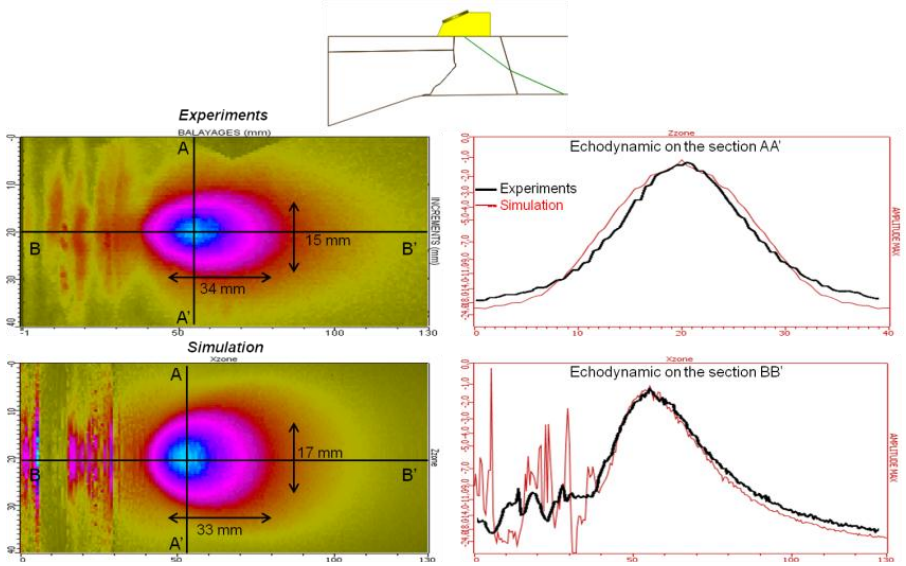

Figure 8: Comparison of the experimental and 3D computed transmitted wave field of the longitudinal wave with the probe above the weld.

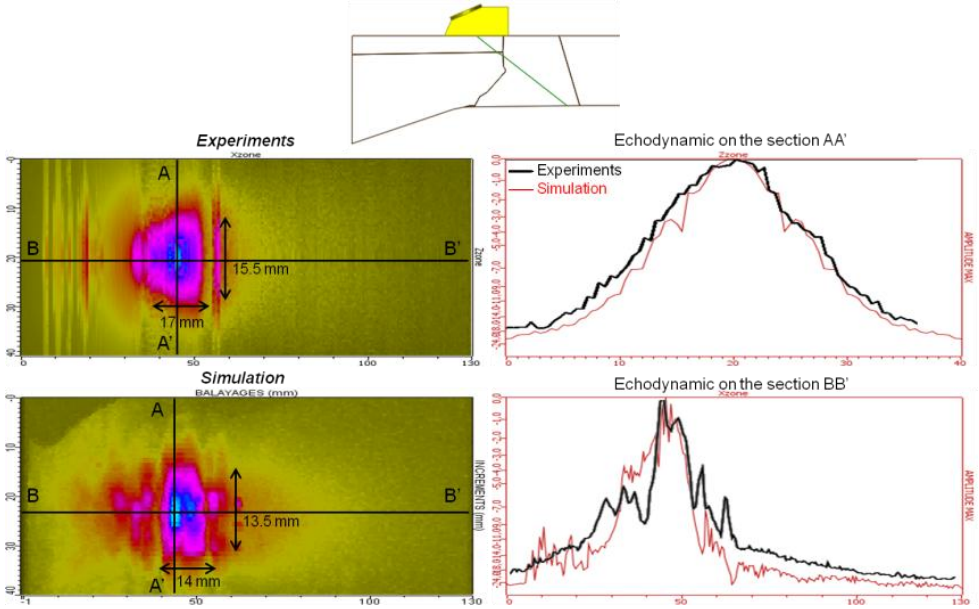

Figure 9: Comparison of the experimental and 3D computed transmitted wave field of the longitudinal wave with the probe above the cladding.

The experimental and simulated results present a good agreement as shown in the representation of the wave field and on the superposition of the echodynamics. Furthermore, the dimensions of the longitudinal focal spot at -6 dB are well evaluated with the DRT model. However, some numerical problems are shown in the simulated wave field. In Figure 8, the important contributions on the left of the picture are numerical artifacts due to the interface. Indeed, they come from the discontinuity of the normal at the interface between the weld and the buttering. Furthermore, the echodynamics in Figure 9 are disturbed which corresponds to a chaotic behavior of the rays [9], resulting in an inaccurate wave field computation. In order to overcome this problem, a work can be made to smooth the description thanks to the minimization of the Sobolev norm of the slowness [10] or on the model by solving the problem of caustics with the Maslov method [11].

CONCLUSION

This paper has presented the improvements made in CIVA platform to simulate the ultrasonic propagation in anisotropic and inhomogeneous media, such as welds. A dynamic ray tracing model, usually applied in geophysics, has been developed. First, this model has been validated for a V-butt weld whose crystallographic orientation has been described by a closed-form expression. The ray trajectories and the longitudinal ultrasonic beam have been successfully compared to a piecewise description. Then the model has been applied on a smooth cartography of the crystallographic orientation and compared with results obtained with a hybrid code. The 2D simulations of the ultrasonic longitudinal wave field realized with both models have shown very good agreement. Lastly, 3D simulations have been successfully compared to experimental results.

In comparison with the current model in CIVA, the DRT model enables to obtain better results with a more realistic description. Nevertheless, some additional improvements are expected. First, the shear waves have to be taken into account to fully validate the DRT model. Secondly, numerical problems such as the chaotic behavior of the rays must be solved. In order to improve the computation time and the numerical precision, the order of the underlying iterative numerical scheme is planned to be increased by using the common fourth-order Runge-Kutta method. Then, the model will be applied to other mocks-up of bimetallic and austenitic welds described with a continuously varying crystallographic orientation.

REFERENCES

[1] B. Chassignole, O. Dupond, L. Doudet, V. Duwig, N. Etchegaray, "Ultrasonic examination of austenitic weld: illustration of the disturbances of the ultrasonic beam", in Review of Progress in Quantitative Nondestructive Evaluation, edited by D. O. Thompson and D. E. Chimenti, 2009, vol. 28, 1886-1893

[2] A. Apfel, J. Moysan, G. Corneloup, T. Fouquet, B. Chassignole, Coupling an ultrasonic propagation code with a model of the heterogeneity of multipass welds to simulate ultrasonic testing, 2005, Ultrasonics 43, 447-456

[3] B. Chassignole, V. Duwig, M.-A. Ploix, P. Guy, R. El Guerjouma, "Modelling the attenuation in the ATHENA finite elements code for the ultrasonic testing of austenitic stainless steel welds", 2009, Ultrasonics 49, 653-658

[4] J. A. Ogilvy, "Computerized ultrasonic ray tracing in austenitic steel", NDT International, 1985, 18 (2), 67-77

[5] CIVA software platform for simulating NDT techniques (UT, EC, RT) (2013), URL http://www-civa.cea.fr

[6] A. Lhémery, P. Calmon, I. Lecoeur-Taïbi, R. Raillon, L. Paradis, "Modeling tools for ultrasonic inspection of welds", NDT&E international, 2000, 33, 499-513

[7] A. Gardahaut, K. Jezzine, D. Cassereau, "Paraxial Ray-Tracing Approach for the Simulation of Ultrasonic Inspection of Welds", in Review of Progress in Quantitative Nondestructive Evaluation, edited by D. O. Thompson and D. E. Chimenti, 2013, to be published

[8] S. Mahaut, N. Leymarie, C. Poidevin, T. Fouquet, O. Dupond, "Study of Complex Ultrasonic NDT Cases Using Hybrid Simulation Method and Experimental Validations", Insight - Non-Destructive Testing and Condition Monitoring, 2011, 53(12), 664-667

[9] H. Keers, F. A. Dahlen, G. Nolet, "Chaotic ray behaviour in regional seismology", Geophys. J. Int., 1997, 131, 361-380

[10] K. Žácek, "Smoothing the marmousi model", Pure appl. geophys., 2002, 159, 1507-1526

[11] L. Klimeš, "Ray-centered coordinate systems in anisotropic media", Stud. Geophys. Geod., 1984, 28, 237-247

ULTRASONIC IMAGING AND SIZING OF STRESS CORROSION CRACKS IN WELDED AUSTENITIC COMPONENTS USING THE SYNTHETIC APERTURE FOCUSING TECHNIQUE

H. Rieder, A. Dillhöfer, M. Spies,
Fraunhofer-Institut Für Techno-Und Wirtschaftsmathematik Itwm, Germany
S. Dugan, MPA, Universität Stuttgart, Germany

Abstract

The detection and evaluation of intergranular stress corrosion cracks (IGSCC) using ultrasonic testing is aggravated due to the crack properties. Their complex branched geometry dramatically influences the defect signals, thus amplitude-based sizing techniques may fail. In this contribution we report on examinations on specimens with artificially grown IGSCCs, where we have applied conventional techniques using angle beam inspection. The defect sizing has been performed on the basis of reconstructions using the Synthetic Aperture Focusing Technique (SAFT), where we have evaluated the mirror angle and crack tip signals. Results of dye penetrant testing and radiography are shown for comparison.

1. Introduction

The occurrence of service-induced damages in dissimilar welds in various foreign nuclear power plants has stimulated respective investigations in Germany [1,2]. In dissimilar welds, the problem of crack initiation and growth by intergranular stress corrosion cracking (IGSCC) mainly affects the nickel-based weld material. For Cr-Ni-steels, not only the weld itself is susceptible to IGSCC, but also the heat-affected zone (HAZ). The detection and evaluation of such cracks using ultrasonic testing is aggravated due to the crack properties. The complex branched geometry of IGSC cracks dramatically influences the defect signals, thus amplitude-based sizing techniques may fail. Simulations for optically measured, real rough crack surfaces have shown that the initially specularly reflected beam field becomes more and more diffuse as the crack face is increasingly branched. Correspondingly, the reliability of the ultrasonic sizing technique is decreasing. We have examined a set of austenitic base metal specimens with artificially grown IGSCCs, where the Synthetic Aperture Focusing Technique (SAFT) [3,4] has lead to an improvement of the signal-to-noise ratio, especially for the crack tip signals. Here, we also report on examinations on welded specimens, where we have applied conventional techniques using angle beam inspection. The defect sizing has been performed on the basis of SAFT-reconstructions, where we have evaluated the mirror angle and crack tip signals. Results of dye penetrant testing and radiography were at hand for comparison. The advantages of SAFT particularly for the enhancement of the tip signals as well as further improvements based on a combination of several inspection modes will be discussed.

2. Geometry of Intergranular Stress Corrosion Cracks

The geometry and the structure of surfaces of intergranular stress corrosion cracks are different from those of artificial flaws like notches as well as those of fatigue cracks. While notches and fatigue cracks display a very smooth crack surface which is perpendicularly oriented with respect to the component surface, stress corrosion cracks are oriented along the grain boundaries. In many cases, they have a branched geometry displaying a rough, irregular crack surface. Figure 1 shows a comparison of a fatigue crack and an intergranular stress corrosion crack in an austenitic base metal. IGSCCs in the HAZ of welds often show first an unbranched appearance e.g. along the melt line and then begin to branch at a certain depth; a respective example is shown in Fig. 1, right.

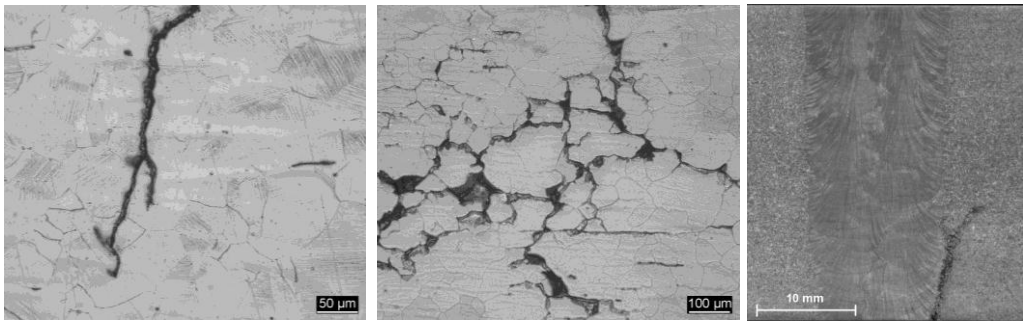

Figure 1 Etched macrographs of fatigue crack (left), intergranular stress corrosion crack in austenitic base material (middle) and in the HAZ of an austenitic weld (right).

3. Scattering of Ultrasonic Waves at Rough Surfaces

The effect of branched cracks on the scattering/reflection of ultrasound can be illustrated using a basic modeling approach for rough surfaces. In [5], the analysis of the ultrasonic field scattered at a rough crack has been performed by evaluating a representation derived by Ogilvy [6]. Using Kirchhoff's approximation and assuming plane wave incidence on the crack, the scattered scalar wave field can described by an integral representation for the far-field. To perform its evaluation, information about the scattering crack surface, i.e. its coordinates and its normal vector(s) have to be used. In the approach applied in [5], the scattering surface is made up by a large number of triangular sub-surfaces, whose node points and surface normal vectors have been determined with a high-end optical system based on the principle of triangulation [7]. Projected fringe patterns are observed with two cameras (Fig. 2) and the three-dimensional coordinates for each camera pixel are calculated with high precision. At the end of the subsequent data processing, the facet normal vectors and the vertices of the sub-surfaces are available and used for the calculation of the triangle areas as the various parts of the scattering crack surface. Figure 2 also shows the exemplarily examined specimen which is a fragment of a ferritic circumferential weld, where sudden rupture occurred during a pre-service pressure test; the crack surface exhibits a remarkably rough topology.

Three areas of different degrees of roughness - smooth, medium and strong (Fig. 3) - have been identified from the measured data and used for the evaluations. For each of the recorded profiles, calculations have been performed assuming plane wave incidence onto a circular crack of 2 mm diameter. Figure 4 shows the scattered radiation patterns for the wavelength-to-crack diameter ratios $\lambda/D = 1$ and $\lambda/D = 1/6$, respectively, referring to two different inspection frequencies. For the lower frequency, the radiation lobes are similar to the specular field patterns scattered at smooth cracks. At the higher frequency, the scattered radiation patterns appear considerably diffuse, indicating deteriorated ultrasonic detection capabilities.

Figure 2. Left: ATOS II SO optical system as shown on the ‘gom’ website [7]; right: fringe projection on the examined ferritic weld specimen.

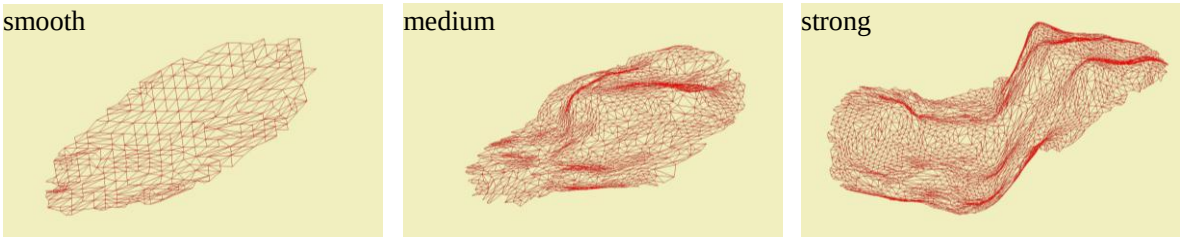

Figure 3. Optically measured crack surfaces of the examined specimen in projected views. The three selected profiles exhibit smooth, medium and strong roughness. The latter is characterized by roughness values of R_a = 0.16 µm and R_{max} = 0.54 µm [5].

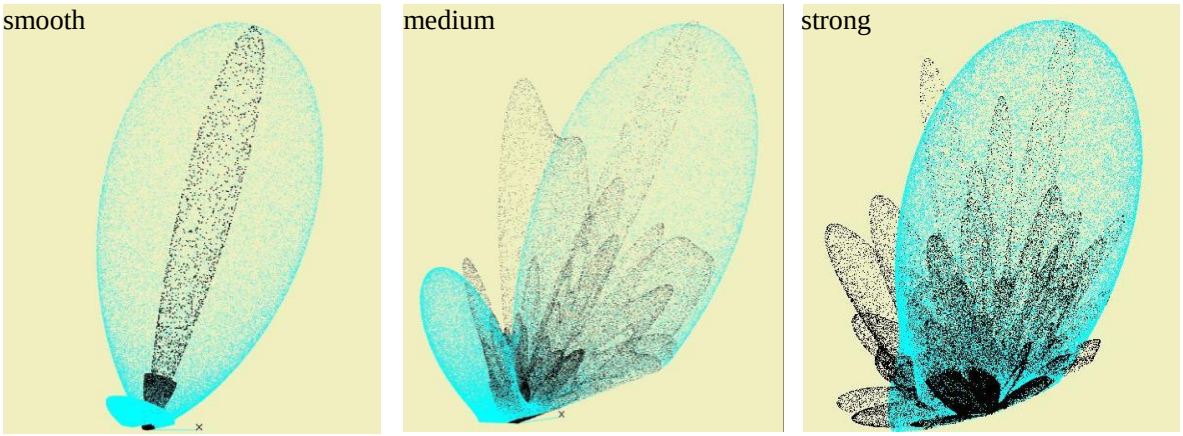

Figure 4. Three-dimensional point cloud representation of the ultrasonic field scattered at the model crack with smooth, medium and strong roughness (low frequency: blue, high frequency: black) [5].

4. Inspection Techniques and the Applied SAFT Algorithm

Efficient ultrasonic inspection of welds relies on various techniques which are based on the angle beam incidence of longitudinal and transverse waves from both sides of the weld. Here, besides operation in transmit-receive or impulse-echo mode a combination of both is also possible [8]. The use of 3D-SAFT has been proven to be most beneficial with respect to the improvement of the signal-to-noise ratio (SNR) [9]. This is particularly useful in view of the enhancement of the crack-tip signals which are in many cases buried within the (grain) noise signals. In addition, IGSCCs often are more blunted than (straight) fatigue cracks, which also causes a weakening of the crack-tip signals. Thus, SAFT imaging of the crack-tip signals and the mirror-angle reflections is required to reliably determine the crack depth and to perform the sizing of the cracks.

The principle of the Synthetic Aperture Focusing Technique SAFT is based on the division of the evaluation volume (in 3D) or the evaluation plane (in 2D) into voxels or pixels, respectively, and on the addition and storage of the recorded, spatially dependent signal amplitudes in the respective voxels (or pixels) according to the times-of-flight and the probe divergence angle. The amplification of the defect signals (signals of the reflectors) is due to coherent superposition, while the noise signals are diminished by incoherent superposition. The nominal incidence angle, the beam divergence angle, the probe's index point and the exact probe position on the wedge as well as the voxel (pixel) size influence the achievable accuracy of the SAFT reconstruction. To optimize the efficiency of the SAFT reconstruction we apply

- acquisition and digitization of the RF-A-scans via line scans in 2D or via meander- or comb-like scans in 3D,
- virtual extension of the transducer aperture via equidistant scanning with probe position distances and line-to-line distances equal to one third of a wavelength,
- selection of small volume elements (voxels) to enhance the resolution,
- selection of ultrasonic sensors with small diameters to enhance the lateral resolution and with large beam divergence to improve the SNR.

We have performed the measurements using an inspection system which consists of a two-channel electronic unit for ultrasound generation, a standard data acquisition module, an intelligent scanner control unit, a three-axes manipulator with flexible sensor holdings and of an industrial PC [10].

5. Results for IGSCC Austenitic Base Material Specimens

We have performed conventional angle beam inspection with shear waves at 45° incidence in order to detect intergranular stress corrosion cracks in several base metal specimens, prepared by MPA University of Stuttgart [11]. The average depths range from 2.5 mm to about 16 mm. For comparison, two specimens with several notches extending over the whole sample width were also available. In Table 1, the specimen dimensions and the crack characteristics are listed. The crack depths had been determined using X-ray radiography and dye penetrant inspection at both sides of the specimens.

The inspections have been performed using 2.25 MHz and 3.5 MHz standard probes with appropriate wedges to generate shear waves at 45° incidence. The specimens were scanned in two directions (+45°, -45°) and the recorded RF-data were then processed using the SAFT-algorithm. To illustrate the performance of 3D-SAFT in terms of crack depth determination, we have first examined Specimens P22 and P27, which contain artificial flaws (EDM notches). Figure 5 shows the reconstruction results for the 2 mm and the 10 mm notches. The sizing can be efficiently performed by evaluating the mirror angle and the crack tip signals. In the following, we representatively focus on the results obtained Specimen P35. Figure 6 shows the results of the SAFT-reconstruction of the +45° and -45° inspection datasets.

The SAFT-B-Scan images show the reconstructed indications as projections over the sample width. The crack depths determined using the mirror angle reflections and the various tip reflection signals are ranging from about 13 mm to 16 mm. These values show excellent agreement with the values determined by dye-penetrant and X-ray inspection (Table 1). Looking at the superposition of the +45°- and -45°-reconstruction results [8], we see a remarkable agreement of the reconstructed branching crack geometry in comparison with the two reference inspection methods, as illustrated in Figure 7. Similarly good results have been obtained for Specimen P36, where similar images of the actual crack geometry had also been determined using dye penetrant and x-ray inspection.

	Size			Reflector					
Specimen	Length [mm]	Width [mm]	Thickness [mm]	Type of defect	Depth				
					left [mm]	right [mm]	Average [mm]	Tolerance [mm]	y-position [mm]
P29	360	44	32	crack	5/6	8/5	6	+/- 2	170
P30	360	44	32	crack	6/7	5/5	5.75	+/- 1.25	179
P35	350	40	32	crack	19	13	16	+/- 3	172
P36	320	40	32	crack	9/10	12/10	10.25	+/- 1.75	151
P37	319	40	32	crack	17	10	13.5	+/- 3.5	150
P38	326	46	32	crack	1.5	3.5	2.5	+/- 1	154
P39	326	41	32	crack	4	3	3.5	+/- 0.5	155
P22	355	38	32	notch	.....	.....	2	.....	230
P22	355	38	32	notch	10	10	10	.....	125
P27	354	36	32	notch	2	3	4	.....	229
P27	354	36	32	notch	4	5	6	.....	125

Table 1. Characteristics of the examined specimens and reflectors. The depths of the cracks have been determined by dye penetrant testing at both sides of the specimens.

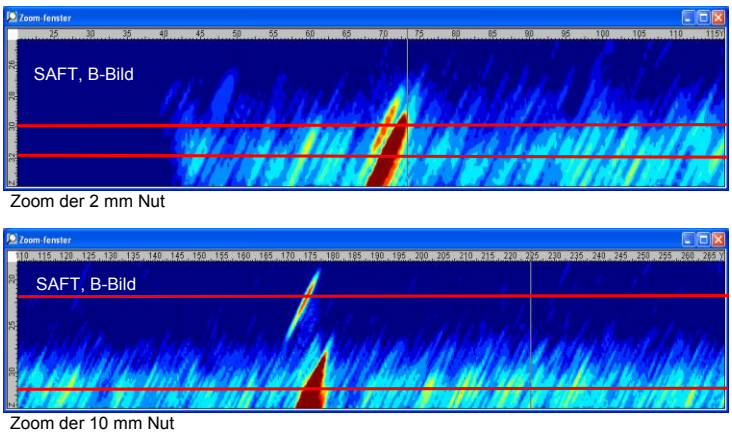

Figure 5. SAFT-B-Scan image for Specimen P22: evaluation of the 2 mm and the 10 mm notches on the basis of the reconstructed crack tip and mirror angle signals.

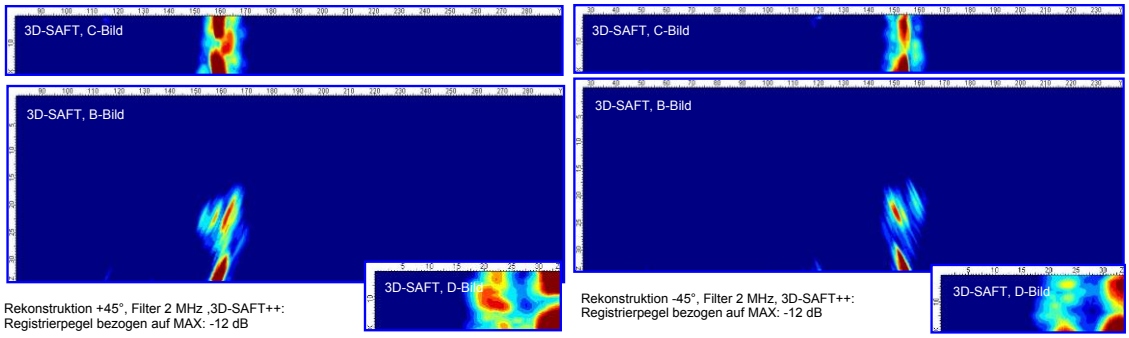

Figure 6. 3D-SAFT reconstruction for Specimen P35 for +45 ° (top) and -45 ° (bottom) angle beam inspection. The RF-datasets were preprocessed using a 2 MHz filter; when using a 4 MHz filter, no significant differences arise.

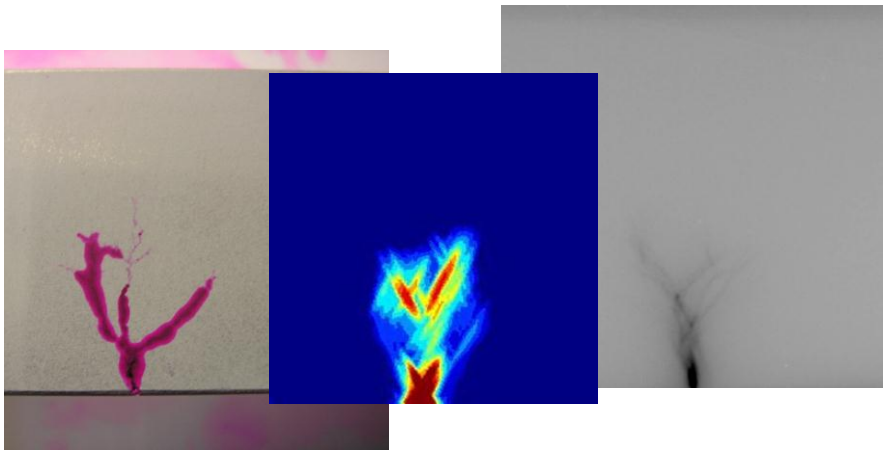

Figure 7. Comparison of crack imaging by means of dye penetration (left), ultrasound and SAFT (center) and x-ray (right) for sample P35 (the scaling is not exactly identical).

Table 2 shows a comparison of the crack depths and notch depths obtained for all specimens determined by ultrasonic and by dye penetrant/X-ray inspection. A relevant discrepancy has only resulted for Specimen P37, which should be considered again in detail. The cracks with depths of less than 5 mm (Specimens P38 and P39) could not be sized, since the crack tip reconstructed signals could not be separated from the mirror angle reflection signal. For IGSC cracks with such complex geometry, the successful sizing of the crack in Specimen P30 shows that a crack depth of 5 mm can be considered as the lower resolution limit of the applied inspection approach. For smaller crack depths, the crack can still be detected by the mirror angle indication but sizing is not possible.

Specimen	Crack length	Crack length SAFT
P22	2/10 mm	2/10 mm
P27	2/4 mm	2/4.5 mm
P29	5-8 mm	5.5-7.5 mm
P30	5-7 mm	5-6 mm
P35	13-19 mm	13-16 mm
P36	9-12 mm	10-13 mm
P37	10-17 mm	8-10 mm
P38	1.5-3.5 mm	- mm
P39	3-4 mm	- mm

Table 2. Comparison of the crack depths determined by ultrasonic inspection and SAFT processing with the results of dye penetrant and x-ray inspection.

6. Results for IGSCC Austenitic Weld Specimens

We have performed further investigations on a set of welded specimens with artificially generated cracks. The specimens were also manufactured by the MPA University of Stuttgart, focusing on the production of realistic flaws. In order to obtain several specimens with comparable welds but different crack geometries, stainless steel plates were butt-welded, the welds being performed as wide-gap or narrow-gap U-groove welds or asymmetric U-groove welds. Crack growth was initiated by a corrosive liquid, which was placed over a starter notch located in the weld root. A three-point bending load was applied. In all test specimens, the IGSCC have grown along the weld seam in the HAZ. The final crack geometry and depths were documented by etched macrographs of the two side surfaces, by dye penetrant and x-ray inspection.

In the following, we focus on a representative example of the inspection results. Figure 8 shows a schematic sketch of Specimen P15 and a macrograph of the weld and the IGSCC in the HAZ. In the case of +45°-inspection, the ultrasonic wave travels only through the base metal before interacting with the crack. Thus, ultrasound propagation is not affected by the inhomogeneous, anisotropic weld and good results for crack detection and crack depth sizing are obtained. In this way, the crack depth could be determined from the ultrasonic signals reflected at the crack branches for most of the examined specimens. The crack tip signals near an austenitic weld are usually too weak to be distinguished from the ultrasonic noise which arises from the interaction of the ultrasonic wave with the grain structure of the weld. For Specimen P15, Figure 9 shows the +45°-scan through the base metal resulting from the standard B-Scan technique, where the mirror angle signal and a reflection at an upper crack branch can be recognized (1 MHz dual element probe, from [12]). In Figure 10, we display the standard B-Scan image and the superimposed 3D-SAFT reconstruction images for the inspection from both sides of the weld (+45°/-45°, 3.5 MHz).

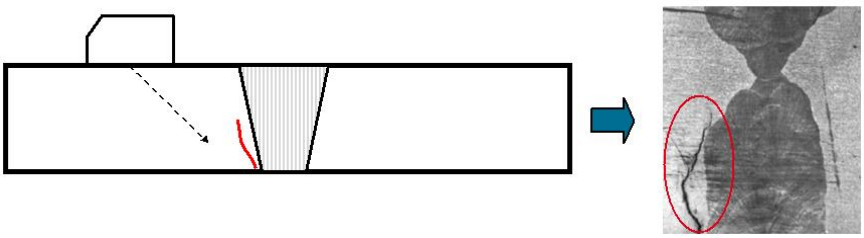

Figure 8. Schematic sketch and micrograph of the IGSCC near the weld – Specimen P15.

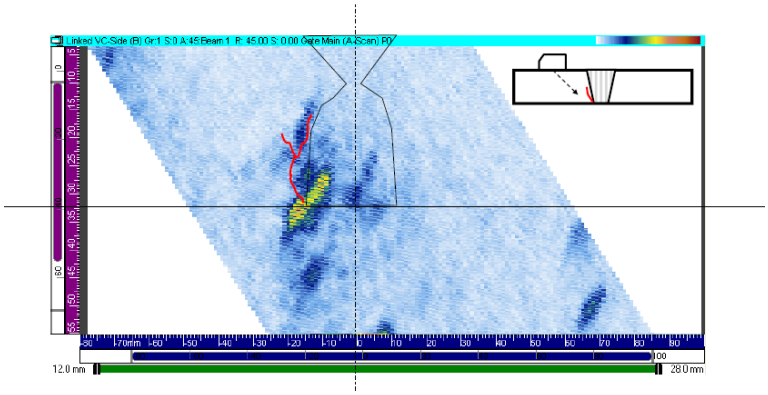

Figure 9. B-Scan image of the raw 45°-data - Specimen P15.

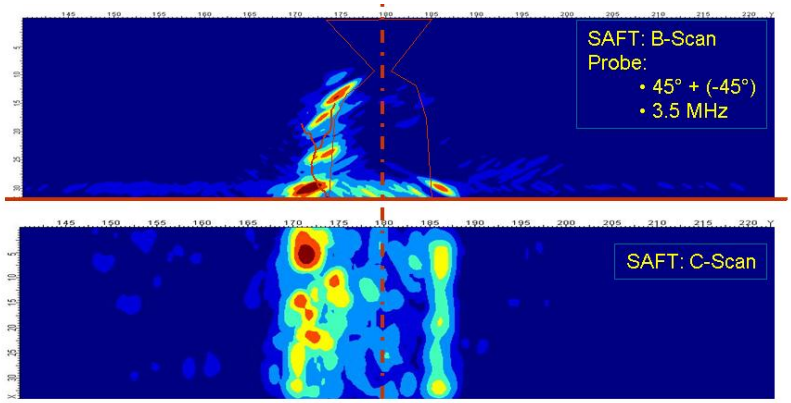

Figure 10. 3D-SAFT reconstruction – superposition of the +45°- and -45°-results - Specimen P15.

Here, the different parts of the crack are more clearly visible. In the +45°-scans, the ultrasonic wave travels only through the base material before interacting with the crack. In the -45°-inspection, the ultrasonic wave travels through the weld and is highly attenuated, thus not contributing at all to the visibility of the crack. The corresponding C-Scan image shows a variation of the ultrasonic signals along the x-direction parallel to the weld seam, indicating that the shape and orientation of the crack branches vary along the crack as well.

6. Summary

We have carried out inspections using conventional ultrasonic techniques to detect IGSC cracks in austenitic base material and in welded specimens in order to image the shape of the cracks and to determine the crack depths. A significant improvement results from the post-processing of ultrasonic RF-datasets using the SAFT-algorithm. We have shown that the 3D-SAFT imaging allows a further evaluation of the ultrasonic data and the reliable determination of the crack length. This is mainly due to the improvement of the signal-to-noise ratio, especially for the various crack tip signals characterizing the IGSCCs. The results show an excellent agreement of the SAFT-reconstructed and the actual crack sizes. We have also illustrated that calculations based on appropriate models provide useful information for interpreting the physical background of scattering at rough surfaces. Respective models should be used for the optimization of such complex test situations. This holds especially for inspection situations where the ultrasonic waves have to travel through the weld before interacting with the defects. As our results have also shown, further research has to be performed in this field.

References

[1] Damages in Dissimilar Welds of Pressure Vessel Nozzles at the Nuclear Power Plants Virgil C. Summer (USA) and Ringhals 4 (Sweden) Detected in Autumn 2000 (in German). GRS-Weiterleitungsnachricht WLN 2001/05, Gesellschaft für Anlagen- und Reaktorsicherheit (GRS) mbH, Cologne, Germany (2001)

[2] S.R. Doctor, Nuclear Power Plant NDE Challenges – Past, Present and Future, in: Review of Progress in QNDE, Vol. 26, AIP Conference Proceedings CP894, 17-31 (2007)

[3] S.R. Doctor, G.J. Schuster, L.D. Reid, T.E. Hall, Real-Time 3D SAFT UT System Evaluation and Validation, Report Pacific Northwest National Laboratory, USA, NUREG/CR-6344 PNNL-10571 (1996)

[4] V. Schmitz, Nondestructive Acoustic Imaging Techniques, in Imaging of Complex Media with Acoustic and Seismic Waves, Topics Appl. Phys. 84, edited by M. Fink et al., Springer, Berlin (2002), 167-190

[5] M. Spies, W. Satzger, J. Bamberg, Evaluation of Ultrasonic Scattering at LCF Cracks Including Optically Measured, Real Roughness Profiles, in: Review of Progress in QNDE, Vol. 26, AIP Conference Proceedings CP894, 1823-1830 (2007)

[6] J.A. Ogilvy, Theory of Wave Scattering From Random Rough Surfaces, Adam Hilger, Bristol, Philadelphia and New York (1991)

[7] 'gom Optical Measuring Techniques' Website: http://www.gom.com

[8] H. Rieder et al., SAFT- and TOFD-Evaluation for the Ultrasonic Weld Inspection of Longitudinally Welded Large Diameter Pipes (in German), DGZfP-Proceedings BB122–CD, Jahrestagung 2010, DGZfP, Berlin, Germany (2010), Mi.2.A.1

[9] M. Spies, H. Rieder, Synthetic Aperture Focusing of Ultrasonic Inspection Data to Enhance the Probability of Detection of Defects in Strongly Attenuating Materials, NDT&E International, Vol. 43, No. 5 (2010), 425-431

[10] H. Rieder, A. Dillhöfer, M. Spies, MMC-USIS – Development of a Compact LAN-Based Inspection System for Automated Ultrasonic Testing, SAFT-Evaluation and 3D-Visualization (in German), DGZfP-Proceedings BB122–CD, Jahrestagung 2010, DGZfP, Berlin, Germany (2010), P46

[11] S. Dugan, S. Wagner, S. Zickler, Manufacturing of Test Specimens with Realistic Defects for Ultrasonic Testing (in German), DGZfP-Proceedings BB122–CD, Jahrestagung 2010, DGZfP, Berlin (2010), Di.2.B.3

[12] S. Dugan, S. Wagner, Ultrasonic Inspection of Austenitic Stainless Steel Welds with Artificially Produced Stress Corrosion Cracks, to be published in: Review of Progress in QNDE, Vol. 33, AIP Conference Proceedings

DEVELOPMENT AND QUALIFICATION OF A PROCEDURE FOR THE MECHANIZED ULTRASONIC EXAMINATION OF STRUCTURAL WELD OVERLAYS.

V. Chardome, M. Plateau, V. Van Brabant, J. Cermak
Vinçotte, Belgium

Abstract

For the project of applying a structural weld overlay on the dissimilar metal welds of the pressurizer safety, discharge and spray nozzles in the Belgian nuclear power plants, Vinçotte was requested the development and qualification of a procedure for the mechanized ultrasonic examination of such welds. The overlay weld material and the upper portion of the underlying dissimilar metal weld are to be ultrasonically examined. Dedicated phased array probes were developed to provide the required detection and sizing capabilities. A specific procedure was developed and tested on various welded mockups. This paper details the work and the results during the development and qualification phases of this project.

Introduction

The ultrasonic examination of dissimilar metal welds is always a challenge. Adding a structural weld overlay (SWOL) increases the challenge considerably. It is commonly known that the ultrasonic examination of austenitic and dissimilar metal welds requires specific ultrasonic probes designed. Due to the coarse grain structure of the weld material, the frequency of the transducers to use is typically found between 1 and 4 MHz. Among others, typical characteristics are wave type, high damping and high sensitivity of the probe elements. Using the experience with similar welds, a procedure was developed for the mechanized ultrasonic examination of a SWOL on the 4” and 6” nozzles on top of a pressurizer (figure 1a and 1b).

Figure 1a: typical nozzle layout on a pressurizer

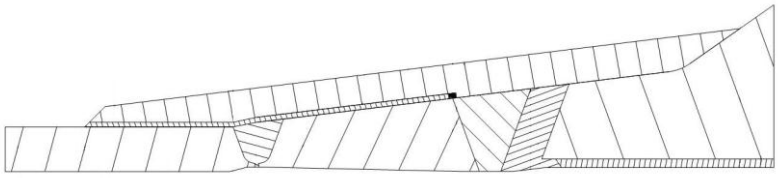

Figure 1b: typical pipe to pressurizer weld configuration with SWOL

Volume to examine

Full scale welded mockups were provided for the development of the entire ultrasonic acquisition system. The thickness is 20/30 mm (DM weld) plus ca 17 mm of weld overlay. The examination volume is given by the Code Case N-740-2 as SWOL acceptance volume and PSI / ISI volume, illustrated by figures 2a and 2b.

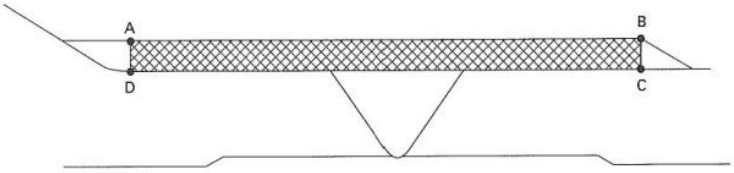

Figure 2a: SWOL acceptance volume

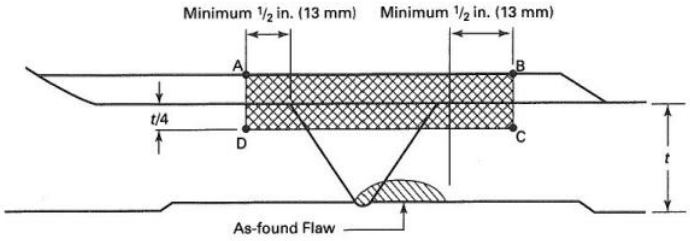

Figure 2b: PSI & ISI volume

Based on the Vinçottes experience with this kind of materials, the use of dual matrix phased array (TRL PA) probes was obvious. A transmitter / receiver configuration was to be defined and tested for this specific weld configuration.

Surface conditions

The proposed footprints of the TRLPA probes are 34x34 mm and thus the surface conditions were to be evaluated. This was done by scanning the entire mockup with a 3D laser scanning system. The digitised surface (figure 3) could then easily be compared with the theoretical surface. Surface condition studies performed in the past showed clearly that the surface conditions (waviness) may affect the forming of the ultrasonic beam.

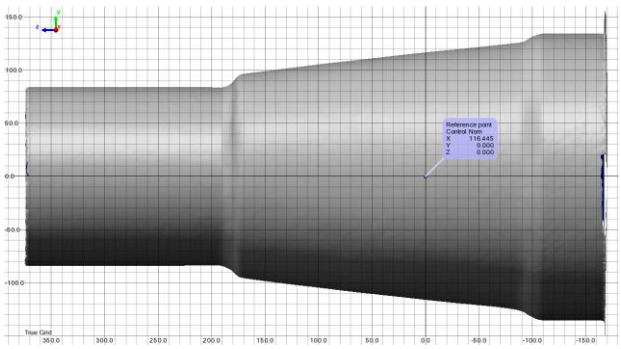

Figure 3: SWOL digitised surface

During lab tests it became clear that a 3D laser scanning of the SWOL surface on site would be very difficult or even impossible (dose consuming and geometrical restrictions). Therefore a simple device was made, allowing a quick evaluation of the surface condition necessary for the ultrasonic examination (figure 4).

Figure 4: waviness evaluation tool

Probe development

Dual matrix phased array probes of 1 up to 4 MHz in a transmitter/receiver layout were selected as base for the examination of the SWOL. These TRLPA probes were first tested by simulation. This allowed to define wedge angles, UT examination angles, focal depths and other parameters typical for these TRLPA probes (figures 5a & 5b).

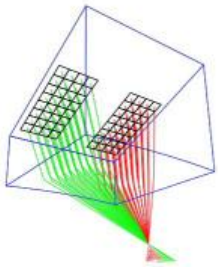

Figure 5a: beam forming

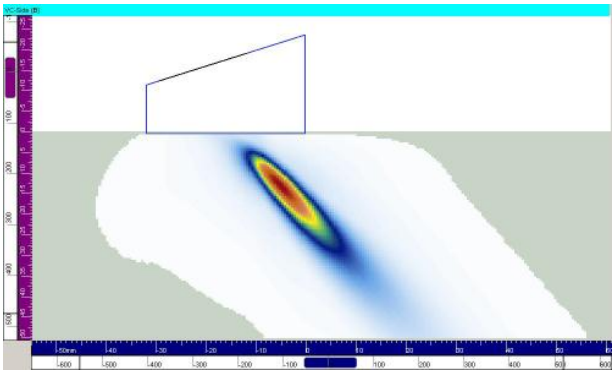

Figure 5b: beam simulation

Pre-selected angles and focal laws were tested on side drilled holes (SDH) in the mockup. Each angle/focal law was characterized to determine angle, probe delay and exit point. For each selected angle a DAC was established on the SDH in the mockup (figure 6).

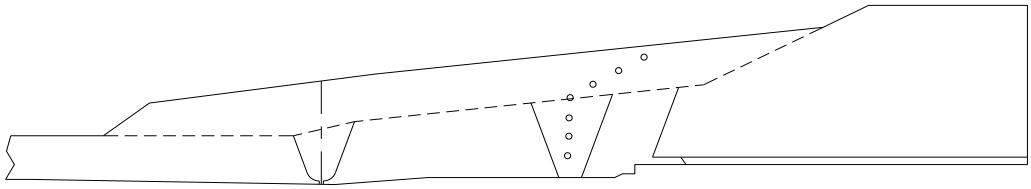

Figure 6: SDH in mockup

Qualification

The procedure qualification is based on a performance demonstration (ASME based) with a technical justification (ENIQ based). The qualification flaws are sharp edge notches with their respective tips at various depths with different orientations, parallel and transverse to the weld center line (figure 7). Additionally, some flat bottom holes (FBH) were added with orientation such to simulate vertical and horizontal oriented lack of fusion.

Figure 7: Qualification reflectors in mockup

The detection phase demonstrated that the applied ultrasonic techniques show the observed signals on the qualification reflectors (flaw tips) with an average signal to noise ratio exceeding 6 dB (i.e. all reflectors were clearly detected).

Through wall sizing

The through wall capability was evaluated by two different methods: simulation (figure 8) and practical demonstration.

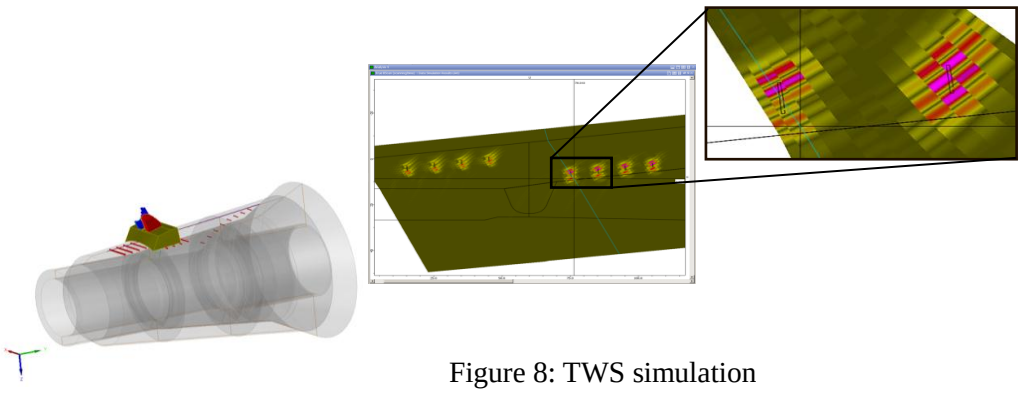

Figure 8: TWS simulation

For the practical demonstration, a portion of the mockup was used to insert subsurface planar flaws at a specific depth (SWOL thickness, ca 17 mm). To enable the smallest possible width of the subsurface flaws, a pilot hole needed to be made (dia. 0.6 mm). This made possible to insert a small (dia. 0.2 mm) EDM wire for the manufacturing of the subsurface flaws (figure 9). Flaw heights are from 1.4 to 2.8 mm.

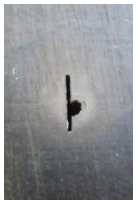

Figure 9: zoom on subsurface planar flaw

The result of the simulation and the practical demonstrations (figure 10) showed consistency about the sizing by tip diffraction (ability to resolve tip and bottom signal). This was demonstrated to be $h \geq 1.8$ mm.

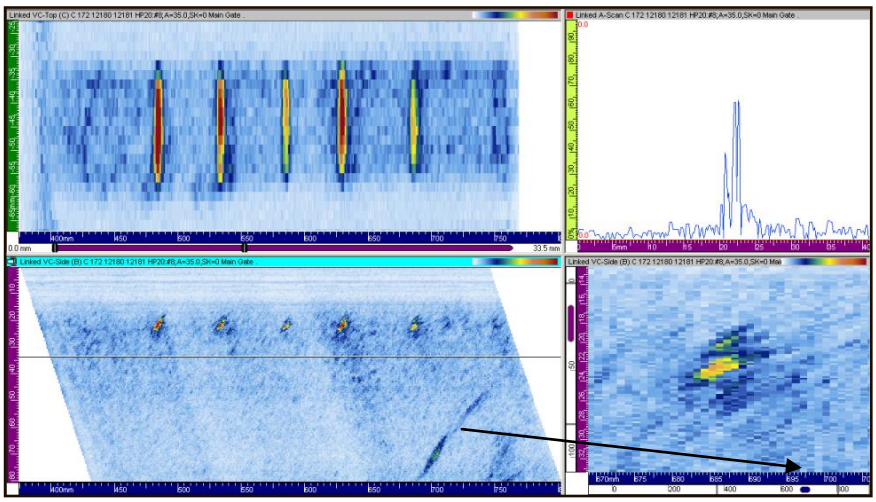

Figure 10: TWS UT data

Acquisition system

Running a TRL phased array matrix probe required a phased array system capable of handling 2 x 32 elements in a pulser/receiver configuration. An Omniscan 32/128 PR system was chosen to control the proposed phased array probes with dedicated wiring. The UT acquisitions are performed by a PC through a network cable (up to 100 m distance to the weld). The mechanical system is based on Vinçottes PIMMS2000 scanning system (figure 11).

Figure 11:
TRLPA probe on PIMMS2000 scanner

Procedure development

Based on all the above, a procedure was written, describing the probes (angles, focal depths), the acquisition system, the evaluation and analysis rules. For flaws that could not be sized in height by tip diffraction, an amplitude evaluation was foreseen based on the DAC established on the SDH in the mockup.

Conclusion

A procedure was developed for the mechanized ultrasonic examination of full structural dissimilar metal weld overlays. This procedure was demonstrated on a real as welded mockup with artificial flaws. This procedure is intended to be applied on the SWOL at the Tihange 2, Doel 3 and Doel 4 nuclear power plants during their next outages.

DISSIMILAR METAL WELD EXAMINATION ASSESSMENT PROCESS

P. Sullivan, J. Hayden, C. McDonald
Structural Integrity Associates, USA

ABSTRACT

Dissimilar metal welds (DM welds) in nuclear power plants are critical to plant operability, safety and historically have been examined by ultrasonic techniques that have been qualified in accordance with ASME Section XI, Appendix VIII. In pressurized water reactor (PWR) plants, primary water stress corrosion cracking (PWSCC) has emerged as an active flaw mechanism that challenges the integrity of reactor coolant system DM welds. Recent industry operating experience (OE) at a US nuclear facility, resulted from the missed detection of several presumed to be PWSCC flaws that exposed a number of shortcomings associated with the processes involved with the examination of dissimilar metal (DM) welds, which includes the design and evaluation of ultrasonic techniques through the required demonstration of technique capabilities through field implementation. Presented herein will be the description of a DM weld assessment program that provides specific recommendations for technique modifications that will optimize the robustness and placement of the sound field which will enhance flaw detection capability and increase examination coverage. The recommendations will describe the specific probe that must be modified to achieve the stated optimization goals. Modeling will visualize both the formerly applied and new, optimized sound fields. Also presented is how the DM weld assessment program provides utilities a way to fully address the heightened regulatory focus and imminent requirements associated with: Augmented DM weld examination programmatic requirements being formed in the response to the U.S. nuclear industry OE from Spring 2012, ASME XI Code Case N-770-1 and the NRC modification thereto, requiring expanded coverage of the PWSCC-susceptible material of DM welds, and the NRC involvement in evaluating the effectiveness of currently-applied UT techniques for critical DM welds.

OVERVIEW

The emergence of primary water stress corrosion cracking (PWSCC) has posed challenges to the integrity of the PWR reactor coolant pressure boundary is a strong influence for the development of this process. PWSCC is the initiation and propagation of intergranular cracks caused when any of the three controlling factors are sufficiently severe: material susceptibility, tensile stress and corrosive environment. Figure 1 below depicts this relationship.

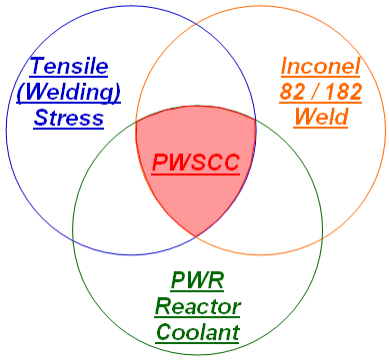

Figure 1: PWSCC Influential Factors

Moreover, several U.S. nuclear power industry events relating to the ultrasonic examination of dissimilar metal (DM) welds provide additional incentive for this work:

First, the U.S. NRC has modified N-770-1 to focus on attaining coverage of 100% of the PWSCC-susceptible material (i.e. Inconel 82 / 182 weld-deposited materials) for both axially and circumferentially oriented flaws. This is because PWSCC flaws initiate and grow in Inconel 82 / 182 materials, but the flaw's growth stops when it reaches the base material interface. Prior EPRI / MRP 139 examination requirements limited the 100% coverage requirement to scanning for circumferentially oriented flaws only, and coverage was defined as the entire ASME Section XI defined volume. See Figure 2 below for definition of the subject examination volumes.

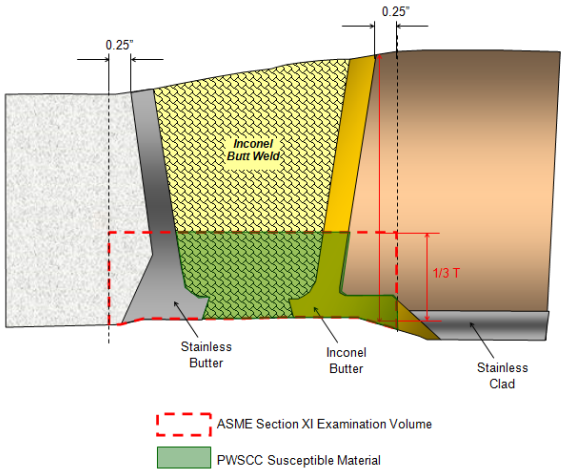

Figure 2: Examination Volumes

Second, in the spring of 2012 at a U.S. nuclear plant, an examination of a steam generator inlet nozzle-to-safe end DM weld failed to detect several significant inside surface-connected PWSCC flaws. During the root cause investigations, which were conducted by the plant owner and by EPRI, a number of deficient practices were identified that led to the failed examinations. Chief among those causes is the lack of preemptive sound field modeling and search unit optimization. The specific weld configuration and tandem probe sound field simulation are shown below in Figure 3.

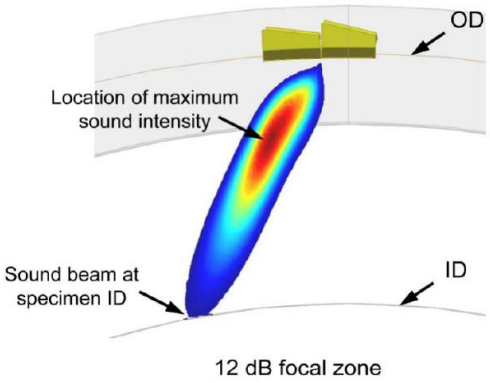

Figure 3: Tandem Probe Simulation

It is therefore a logical assumption that numerous other situations exist where the ultrasonic examination of nuclear components is being conducted using techniques that are qualified by an accepted program, but have not been optimized. It is entirely plausible that the ultrasonic techniques are unknowingly being employed at or very near their limit of practical effectiveness.

EVALUATION OF THE DW WELD CONFIGURATION

This comprehensive program is based on expert analyses of industry related Codes, Standards and regulatory documents as related to the examination of DM welds in operating nuclear power plants. This detailed program is developed by methodically evaluating DM weld geometry and dimensions, material properties and physical constants, crystalline structure and grain alignments, welding processes and repair history, and finally, probe array parameters, which result in CIVA sound field and flaw interaction simulation models. We also evaluate and confirm the applicability of the examination procedure to the Appendix VIII qualification document. Lastly, we verify whether a full-scale, material-faithful, site-specific mockup must be fabricated. This process is conducted independently of any prior determinations, evaluations or examinations that may have been conducted in the past.

At the center of this process is the application of CIVA ultrasonic simulation software. CIVA is an expertise software platform designed by CEA, the French Alternative Energies and Atomic Energy Commission, similar to the NRC in the U.S. CIVA software has been in existence for over 15 years, and is currently being used in the U.S. nuclear industry by Structural Integrity Associates, the U.S.NRC, through their NDE contractor Pacific Northwest National Laboratory and the Electric Power Research Institute. The primary applications of CIVA include the simulation of ultrasonic energy fields and the prediction of interaction between those ultrasonic energy fields and potential flaws within the examined components.

CIVA MODEL-BASED EVALUATION OF CURRENTLY APPLIED TECHNIQUE

The purpose of this process is to evaluate the effectiveness of currently applied examination techniques. This is accomplished through the determination of specific metallurgical and acoustic properties of the component base and weld materials and the critical probe parameters.

Reliable and detailed knowledge of the material under examination - and their properties - is crucial to the process. This is why this process requires input from subject matter experts in the fields of material science, welding engineering and nuclear ultrasonic examination. An interdisciplinary team of experts provides specific detailed information regarding the metallurgical and physical characteristics of the base materials and anisotropic elements of each DM weld being evaluated. The influential features of the ultrasonic search units are also completely identified, evaluated and quantified before being incorporated into our process.

A full-scale 3-D SolidWorks model must be generated for each component. The input for which may be design drawings, in-plant visual, contour and thickness information, or some combination thereof. In cases where access to the component exists, or for planned evaluations of complex components with challenging contours, high-resolution surface data are captured using 3-D laser profilometry. Details form weld joint design drawings, visual features and measured thickness are then combined to generate full-scale, material-faithful SolidWorks models, which are then exported to CIVA for further simulations. See Figure 4 below.

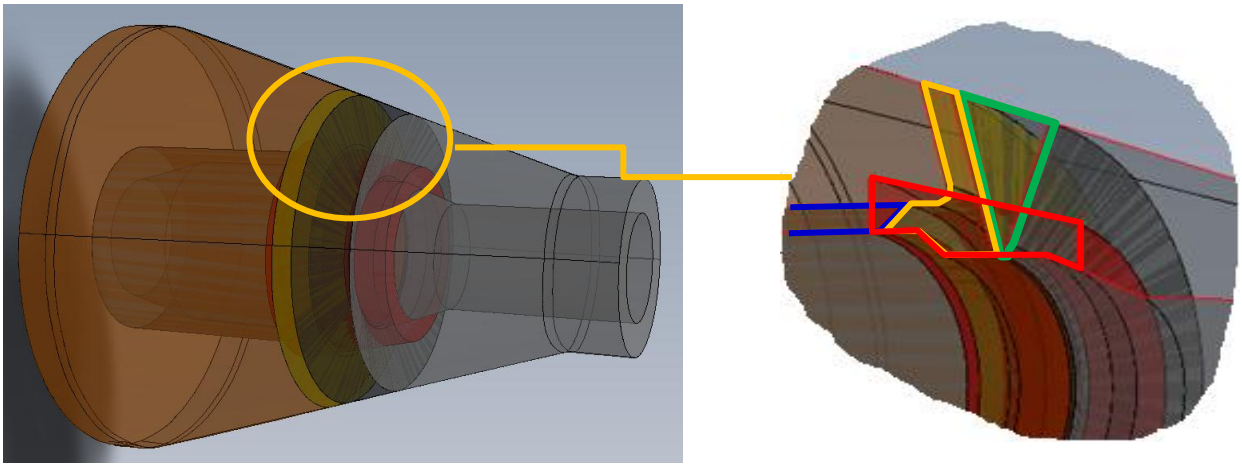

Cut-Out Revealing Internal Cross-Section Detail of:

- Buttering
- Butt Weld

} PWSCC Susceptible Materials

- ID Cladding
- Code-required volume

Figure 4: Example of 3-D SolidWorks Model of DM Weld

The final modeled configuration of the component is then reviewed for accuracy of dimensions and material boundaries and is them imported into CIVA for further development based on the physical and mechanical properties of each constituent material, as determined by the team of materials and welding experts. See Figure 5 below.

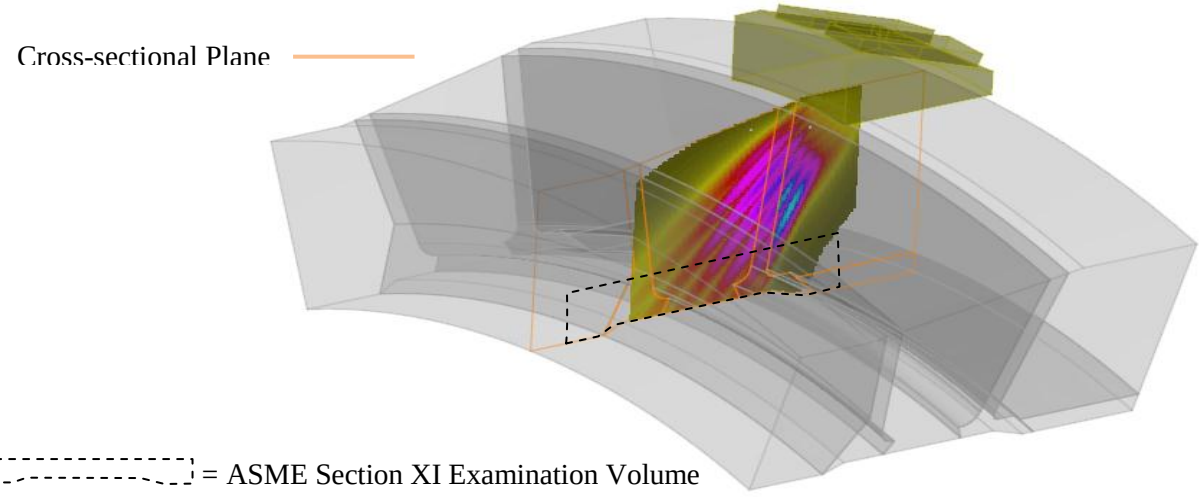

Figure 5: Example of 3-D CIVA Model of Reactor Coolant System DM Weld

The calculated sound paths to insonify the required examination volume in both axial and circumferential scanning directions are also factored into the evaluation of the CIVA simulated sound fields. Lastly, we calculate the currently achieved examination coverage, with specific emphasis on Code Case N-770-1 examination coverage requirements. A rigorous procedure directs the performance of each phase of the process, which requires independent expert peer review and verification that correct inputs have been made into the CIVA software.

CIVA MODEL-BASED SPECIFIC TECHNIQUE OPTIMIZATION

When warranted by the outcome of the above evaluation, using CIVA, adjustments will be made to probe parameters which will optimize the robustness and placement of the sound field, enhancing flaw detection capability and increase, to the maximum extent possible, examination coverage the required volume. The focus is placed on the material volume susceptible to the active flaw mechanism for the component. The recommendations will specify probe and / or focal law parameters that must be modified to achieve the stated technique optimization goals.

The images of the resultant sound fields, simulated by a CIVA model of the currently-used and the optimized sound fields will be provided to document this comparison. Examples of CIVA simulations of sound fields are shown below, depicting the sound field generated by an actual probe that was applied for the examination of a reactor coolant pump DM weld. The most intense and efficient part of the sound field (imaged using the light blue color) is formed well above the examination volume of the component, as shown in Figure 6 below. Additionally, the sound field becomes attenuated is it enters the buttering and butt weld materials, as is evident from the image below.

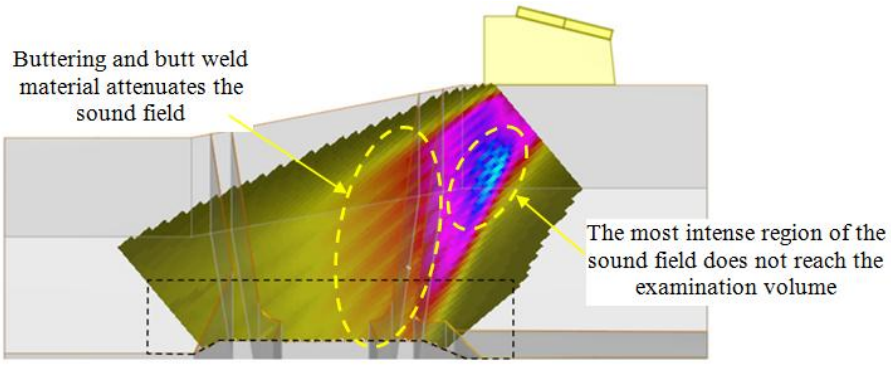

Figure 6: Currently Used Phased Array Probe (1.5 MHz)

The example shown below depicts the sound field generated by a recommended probe for the examination of the same reactor coolant pump DM weld. The most intense, efficient part of the sound field (imaged using the light blue color) is formed within the inside surface of the component, as shown in Figure 7 below. Additionally, as the sound field is much less attenuated is it enters the buttering and butt weld materials, as shown in the image below.

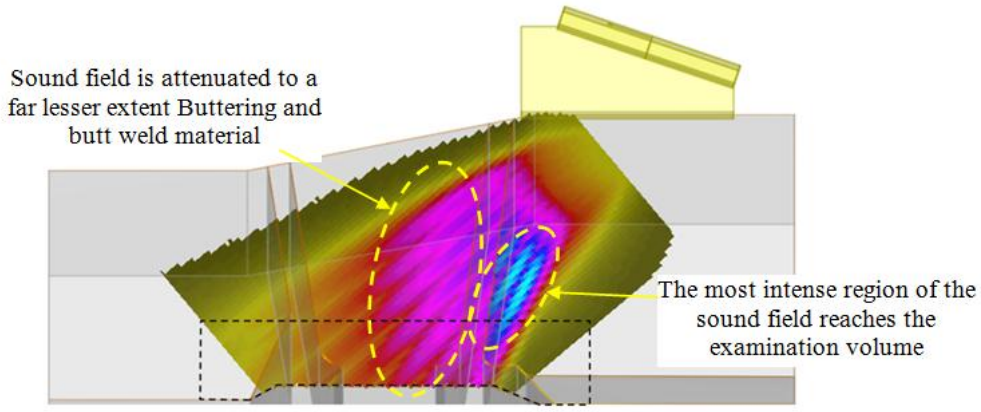

Figure 7: Recommended Phased Array Probe (1.0 MHz) with Larger Aperture

CIVA / 3-D Model EXAMINATION COVERAGE ASSESSMENT

Unlike examination coverage estimates based on two-dimensional cross-sectional sketches, this process employs full-scale volumetric 3-D SolidWorks models. This enables the precise volumetric sound field projections that can be based on both the traditional central axis method and on the more realistic boundaries of the modeled sound field at empirically established and technically defensible limits.

Using the traditional central axis coverage technique, the central axis of the examination angle beam paths are simply projected from the sound exit point of the probe on a straight line path without accounting for the metallurgical conditions or attenuative effects present within the material. This approach can lead to wrongly overstating the extent of examination coverage. See Figure 8 below.

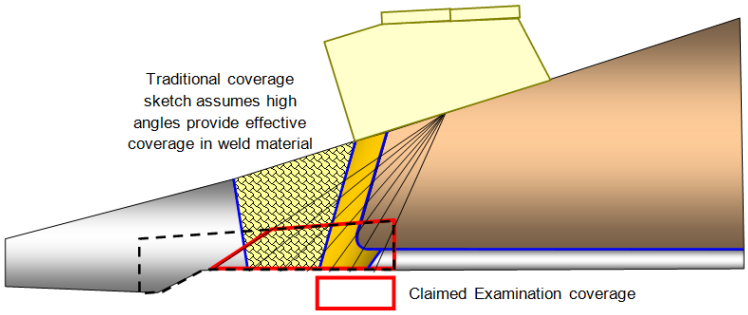

Figure 8: Traditional (Central Axis) Method of Defining Examination Coverage

Using the volumetric 3-D SolidWorks modeled coverage technique, a CIVA simulated sound field is imaged in the model, completely accounting for the probe coupling, metallurgical conditions and attenuative effects present within the material. This approach provides a technically-defensible basis for estimating the extent of examination coverage. See Figure 9 below.

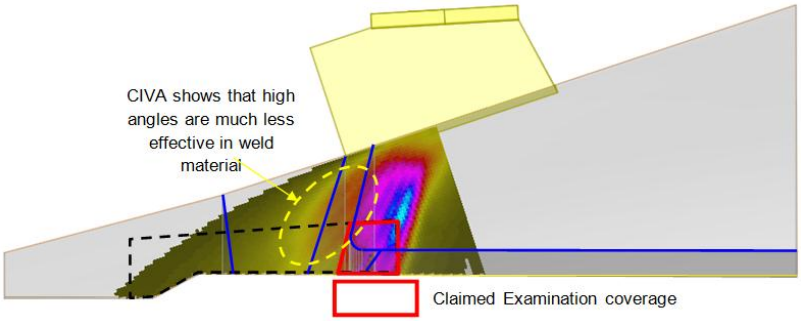

Figure 9: CIVA Simulation Method of Defining Examination Coverage

Examination coverage calculations using both the central axis and 3-D modeled techniques should be generated and presented to the client.

DOCUMENTATION

Comprehensive and detailed documentation will be provided to our client that includes all of the influential information that was evaluated, along with a sound technical justification for SI's recommendations for the optimization ultrasonic examination of components.

APPLICABILITY

The DM weld Assessment Program results in a thorough understanding of the design, physical and macro-structure characteristics of the DM weld being examined, along with a knowledge of specific and optimal matrix array probe parameters which will enable the generation of the most well-suited sound field. These assessments and recommendations are capable of evaluating and optimizing the effectiveness of the examination techniques applied by any ISI vendor, for plants located anywhere in the world, and may be applied for both conventional (fixed angle) and phased array ultrasonic techniques.

REFERENCES

1. American Society of Mechanical Engineers, Boiler and Pressure Vessel Code, Section XI, *Inservice Inspection of Nuclear Power Plant Components*, 2007 Edition with Addenda through 2008
2. American Society of Mechanical Engineers, Boiler and Pressure Vessel Code Case N-770-1, *Alternative Examination Requirements and Acceptance Standards for Class 1 PWR Piping and Vessel Nozzle Butt Welds…*, 12/25/2009
3. *Material Reliability Program: Primary System Piping Butt Weld Inspection and Evaluation Guideline* (MRP-139, Revision 1) December 2008

NEW PLANT CHALLENGE – PRE-SERVICE VOLUMETRIC EXAMINATION OF A HEAVY-WALL DISSIMILAR METAL WELD INVOLVING A CAST STAINLESS STEEL BASE MATERIAL

R. D. Rishel and J. Monaco
WesDyne International, USA

INSPECTION REQUIREMENT

A new plant has a unique component-to-component weld configuration, as shown in Figure 1, that results in a dissimilar metal weld between a stainless steel clad low alloy ferritic steel steam generator and a statically cast stainless steel reactor coolant pump. This weld is approximately 140mm (5.5") thick with a defined ASME Section XI pre-service and in-service inspection volume consisting of the inner one-third of the thickness including the weld, the buttering, and 6mm (0.25") of adjacent base material. This inspection volume is specified in ASME Code Case N-799 [1]. An ASME Section XI pre-service inspection solution is required for this weld.

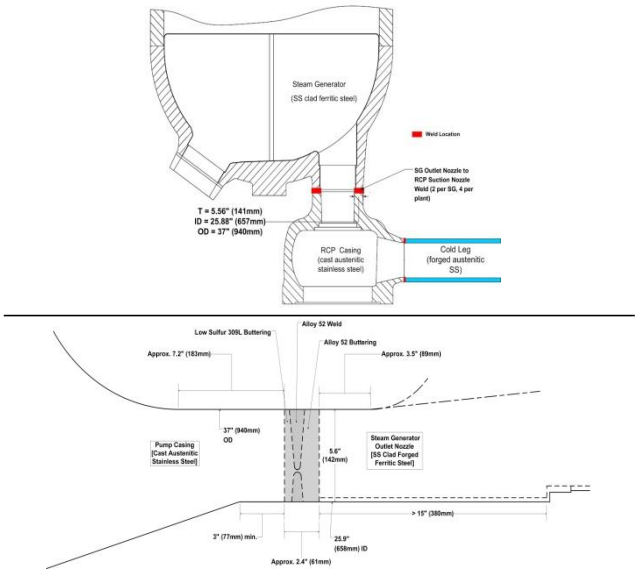

Figure 1: Steam Generator to Reactor Coolant Pump Casing Weld Configuration

INSPECTION SOLUTION

Reliable inspection of the required inspection volume from the outer diameter (OD) surface is challenged by the highly attenuative, heavy-walled cast stainless steel material, and the tapered outer diameter surface on the steam generator side of the weld. An inspection constraint on the inner diameter (ID) surface includes a taper on the pump side of the weld. Other inspection challenges include the multiple material types, interfaces and grain structures.

To accommodate these inspection constraints, an ID surface applied inspection approach, involving ultrasonic (UT) and supplemental eddy current (ET) methods, is being pursued.

For the weld and buttering material, and the stainless steel clad low alloy ferritic steel side of the weld, the ultrasonic inspection system must comply with ASME Section XI, Appendix VIII [2]. Appendix VIII requires performance demonstration of the UT equipment, procedure and

personnel. For the inspection volume associated with the cast stainless steel (SS) side of the weld, ASME Section XI, Appendix VIII has no UT system performance demonstration requirements. As such for the UT inspection system applied on the cast SS side of the weld, we have adopted the ASME Section V, Article 14 intermediate rigor process for examination system qualification. We have also chosen to have the supplemental ET inspection system satisfy ASME Section V, Article 14 intermediate rigor requirements.

Therefore the combined UT/ET approach uses an existing EPRI/PDI qualified WesDyne UT procedure for reactor vessel nozzle piping welds, where the materials of fabrication are similar, and an existing ENIQ-based qualified WesDyne ET procedure for the same type welds. This combined UT/ET system is intended to detect, length size and depth size service-induced flaws initiating in the inspection volume.

The UT inspections from the ferritic steel side of the weld require blind performance demonstrations of the procedure and personnel in accordance with ASME Section XI, Appendix VIII and the EPRI/PDI program since the existing qualified procedure is valid only to a weld thickness of 76mm (3”). The UT inspections from the cast SS side of the weld require non-blind or blind procedure demonstrations and blind personnel demonstrations to comply with ASME Section V, Article14.The supplemental ET inspections require similar performance demonstrations as required for the cast SS UT system. Such demonstrations necessitate the fabrication of representative flawed test specimens.

The solution required that the existing inspection procedures be adapted to satisfy the specific weld configuration, and that a technical justification be prepared to address those inspections from the cast SS side of the weld.

PROGRESS ON THE INSPECTION SOLUTION

For the technical justification associated with the cast SS inspection, it was established that the most plausible damage mechanism is thermal fatigue. A deterministic fracture mechanics analysis determined the allowable flaw sizes were on the order of 38%T, where T is the weld thickness, for axial cracks and 28%T for circumferential cracks. These crack depths assumed a length to depth ratio of 10:1. Smaller length to depth ratios yielded larger allowable flaw sizes. As such target qualification flaw sizes for the case SS material were defined to be 25%T for axial cracks with length to depth aspect ratios of 2:1 to 4:1, and 19%T for circumferential cracks with length to depth aspect ratios of 4:1 to 10:1.

It is noted that the qualification flaw sizes for inspections of the weld, buttering and adjacent ferritic steel base material from the ferritic steel side of the weld are those ≥ 10%T as defined in ASME Section XI, Appendix VIII.

For the cast SS material inspection, it was established that the flaw detection rate be ≥ 80% with a false call rate of < 20%, and the flaw length sizing errors to be ≤ 19mm (0.75”) Root Mean Squared (RMS) for the UT process and ≤ 13mm (0.5”) RMS for the ET process. The target flaw depth sizing error was established to be ≤ 6.4mm (0.25”) RMS.

For the inspections of the weld, buttering and adjacent ferritic steel base material from the ferritic side of the weld, the detection and false call rates and the UT flaw length sizing error are the same as above. The UT flaw depth sizing error is ≤ 3.2mm (0.125”) RMS. These criteria are defined in ASME Section XI, Appendix VIII.

To understand the impact of attenuation and localized ultrasonic velocity changes for beams in the axial direction, a series of eleven 2.4mm (0.093”) diameter circumferentially oriented side-drilled holes were placed in an existing weld coupon, which fully represented the weld, buttering, and base materials and the weld thickness. These holes were placed at a depth range of 6.4mm (0.25”) to 127mm (5”) and are located on the centerline of the weld.

Tests using the UT probes intended for this weld indicated that there was a beam angle drop ranging from 1.5° to 8.5° for inspections from the cast SS side of the weld which results in a lesser accuracy in locating reflectors in depth below the surface. In addition, the focal depth range for the medium and long range focus process was effectively shortened due to attenuation losses. Two full weldment test specimens containing ID surface-connected planar flaws and lack of fusion flaws in the weld and buttering, and ID surface-connected planar flaws in the cast SS material have been fabricated for the demonstration processes. One test specimen represents an open sample for the ASME Section V, Article 14 UT and supplemental ET procedure qualifications. The other test specimen represents a blind sample for the ASME Section XI, Appendix VIII UT procedure and UT personnel performance demonstrations, and for the ASME Section V, Article 14 UT personnel qualifications. Figure 2 shows the open and blind test specimens.

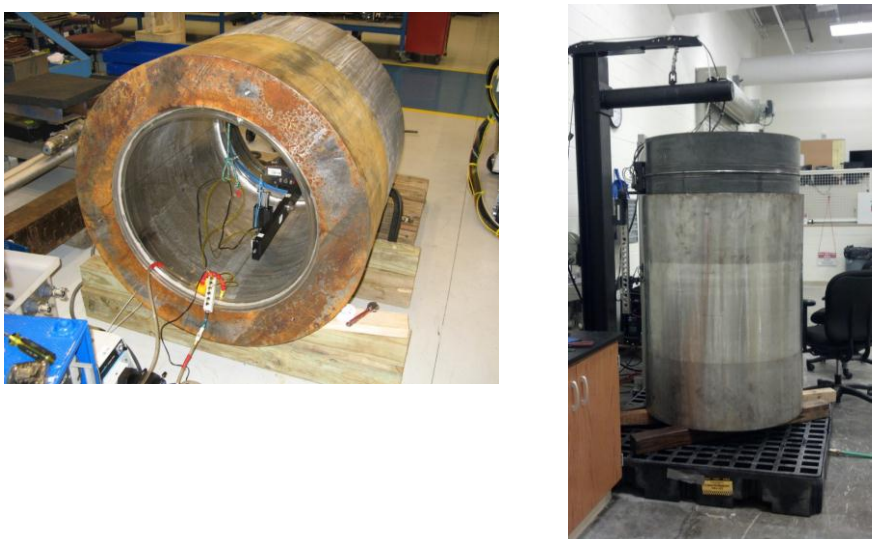

Figure 2: Fabricated Test Specimens (Left – Open Sample; Right – Blind Sample)

The open test specimen contains flaws in the weld and buttering material and in the cast SS material. The weld contains both ID surface-connected thermal fatigue cracks and embedded lack of fusion. The implanted weld flaws consist of: five (5) circumferential cracks ranging in depth from 12% T to 93%T with length to depth aspect ratios from 1.42:1 to 2:1; three (3) axial cracks ranging in depth from 13%T to 70%T with length to depth aspect ratios from 1.65:1 to 4:1; and five (5) lack of fusion flaws ranging in through-wall depth from 4.5%T to 7.2% and located within the inner 1/3T of the weld. The cast SS material includes ID surface-connected thermal fatigue cracks with compressed EDM notch tips, and compressed EDM notches. The cast SS material flaw matrix consists of four (4) circumferential flaws ranging in depth from 22%T to 63%T with length to depth aspect ratios from 1.96:1 to 4.8:1, and four (4) axial flaws ranging in depth from 25%T to 75%T with length to depth ratios from 0.5:1 to 1.3:1.

The design, fabrication oversight, and quality control of the test specimens were performed by EPRI, and the test specimens were fabricated by Sonaspection (flaw block vendor) and Westinghouse PCI (narrow groove welding vendor). EPRI maintains control of the blind test specimen; as such details of the flaws in terms of type, number, location, orientation, and sizes are unknown to WesDyne. However the blind test specimen does contain two identical dissimilar metal welds in order to ensure sufficient grading units for the blind demonstrations.

A custom-built scanner, as shown in Figure 3, was designed and fabricated to deliver the UT and ET probes. This scanner is of a quick interlock design that requires no tools for installation. It is comprised of a mast assembly and a scanner assembly that fit individually

through a steam generator channel head manway. It contains 2 encoded axes that are center-mounted, and drives two sled assemblies that are located 180° apart. Each sled carries four UT and/or ET probes.

Figure 3: Custom-Built Scanner in Mock-Up

The UT process is based on multiple angle transmit-receive (TRL) focused probes ranging in test frequency from 1 MHz to 2 MHz. For circumferential flaw detection within the inspection volume, the UT probes consist of a short focus 70° beam, and short and medium focus 45° beams. For axial flaw detection within the inspection volume, the UT probes consists of a short focus 70° beam, a short focus 45° beam and a medium focus 37° beam. For circumferential flaw sizing throughout the weld thickness, the detection probes are complimented with a short focus 60° beam, a long focus 45° beam and a medium focus 37° beam. For axial flaw sizing throughout the weld thickness, the detection probes are complimented with a short focus 60° beam, and a long focus 45° beam. The WesDyne 16 channel PARAGON™ UT system is used for data acquisition and analysis.

Figure 4 shows the C-scan images of the short focus 70°, axial beam probes scanned over the weld, buttering and adjacent base materials in two directions. All 5 circumferential cracks are detected from both directions. Four of the 5 lack of fusion flaws were detected from either one or both sides of the weld. The remaining lack of fusion flaw is beyond the focal range of the probe type. This remaining flaw was detected with the short focus 45° axial beam probe in two directions.

Figure 5 shows the C-scan images of the short focus 70°, axial beam probes scanned over the cast SS material in two directions. All 4 circumferential cracks are detected from both directions. The images also show the detection of flaws in the weld.

Figure 6 shows the C-scan images of the short focus 70°, circumferential beam probes scanned over the weld, buttering and adjacent base materials in two directions. All 3 axial cracks are detected from both directions.

Figure 7 shows the C-scan images of the short focus 70°, circumferential beam probes scanned over the cast SS material in two directions. All 4 axial cracks are detected from both directions.

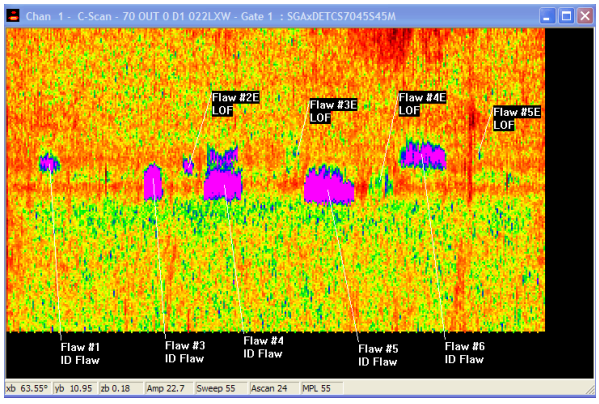

70° toward cast SS material

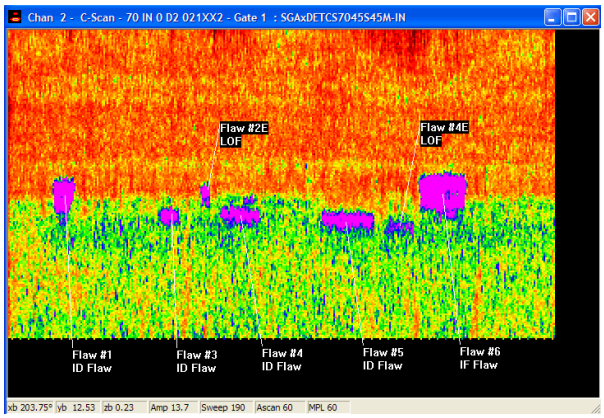

70° toward ferritic steel material

Figure 4: C-Scans of Short Focus 70° TRL Axial Beam Probes When Scanning Weld, Buttering and Adjacent Base Materials in Two Directions

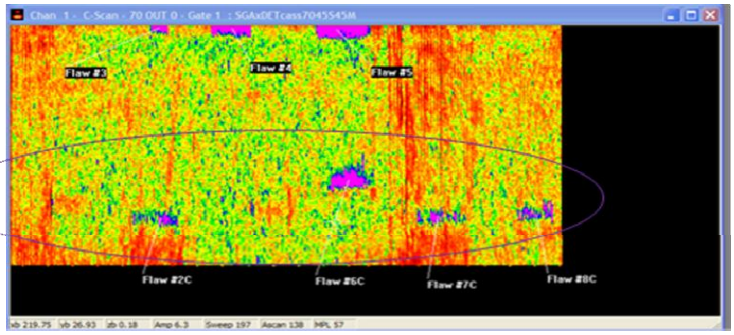

70° toward cast SS material end of block

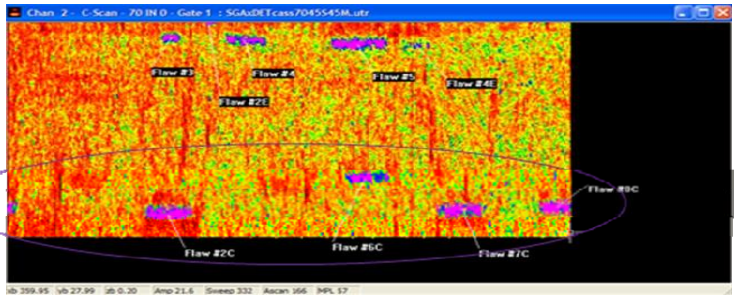

70° toward ferritic steel material end of block

Figure 5: C-Scans of Short Focus 70° TRL Axial Beam Probes When Scanning Cast SS Flaws

in Two Directions

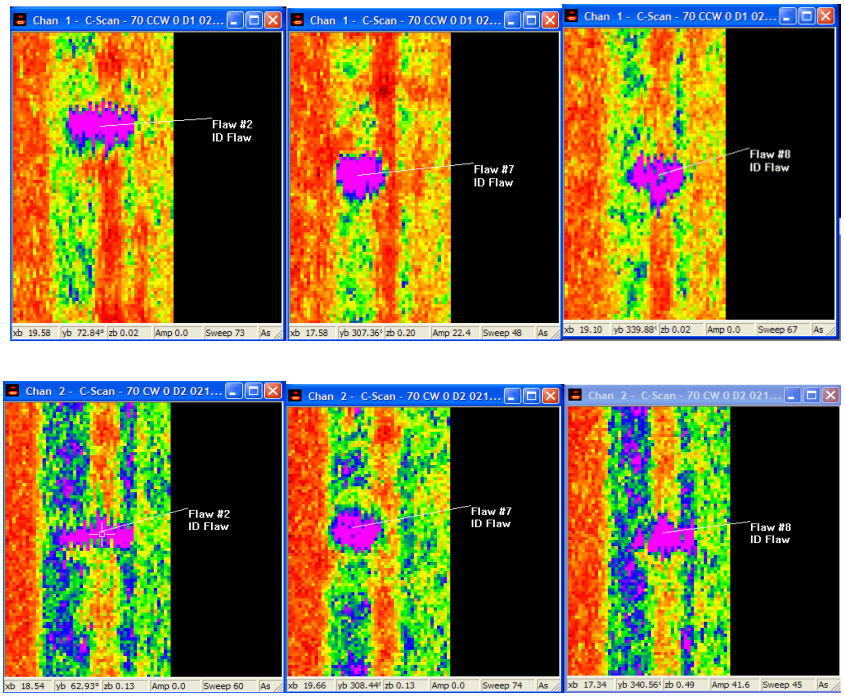

70°counter-clockwise

70° clockwise

Figure 6: C-Scans of Short Focus 70° TRL Circumferential Beam Probes When Scanning Weld, Buttering and Adjacent Base Materials in Two Directions

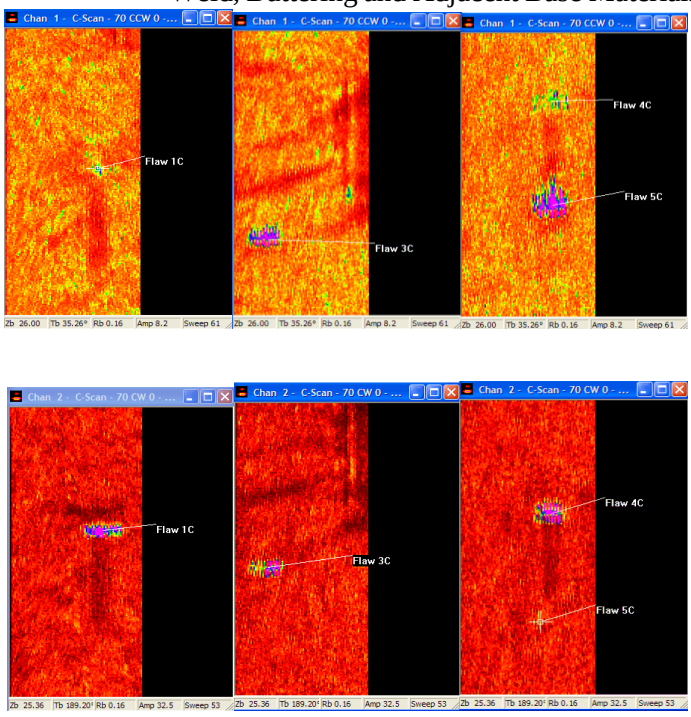

70° counter- clockwise

70° clockwise

Figure 7: C-Scans of Short Focus 70° TRL Circumferential Beam Probes When Scanning Cast SS Material in Two Directions

Thus with the UT process, all flaws within the inspection volume are detectable. The flaw

length sizing results, which by procedure are addressed with the short focus 45° probe, yielded a RMS error of less than 8.6mm (0.34") on both the weld and cast SS flaws which meets the target of ≤ 19mm (0.75") RMS. Flaw depth sizing using multiple probes for the weld flaws resulted in a RMS error of approximately 6.4mm (0.25") with one UT operator indicating that the target value of ≤ 3.2mm (0.125") RMS may be a challenge. Flaw depth sizing using multiple probes for the flaws in the cast SS material was not considered practical using only ID surface applied examinations; attenuation limited significant ultrasound penetration into the cast SS beyond approximately mid-wall (50%T).

The supplemental ET process includes Zetec +-Point® surface riding probes operated in driver-pickup mode. Each of the two probes are skewed 45° with respect to the coil winding in order to enhance detection of both axial and circumferential ID surface connected flaws. The inspection frequencies include 100 kHz, 250 kHz and 500 kHz, with the 250 kHz frequency used for flaw detection and length sizing. The WesDyne 4 channel PARAGON™ ET system is used for data acquisition and analysis. This system is used in parallel with the UT process.

Figure 8 shows a C-scan of the axial ET scans of the weld, buttering and adjacent base materials. All 5 circumferential cracks were detected. It is noted that the 3 axial cracks are also observed given the capability of the skewed ET probes to detect cracks oriented two directions. Conversely, the C-scan of the circumferential ET scans of the weld, buttering and adjacent base materials shows the 3 axial cracks, and also detected the 5 circumferential cracks.

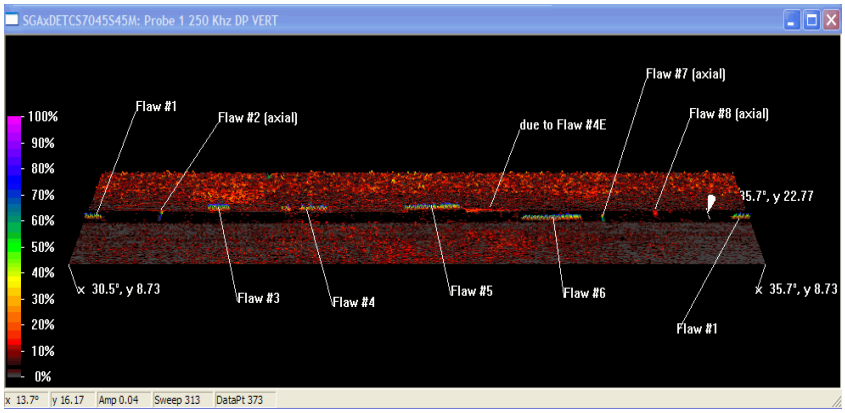

Figure 8: C-Scan of Axial ET Scans of Weld, Buttering and Adjacent Base Materials (250 kHz)

Figure 9 shows a C-scan of the axial ET scans of the flaws in the cast SS material. All 4 circumferential cracks are detected and all 4 axial cracks are also observed (not indicated ono the figure). It is noted that the lower amplitude responses on one side of most of the flaws are from weld material associated with the flaw implantation process, i.e. not cast SS. Also flaws in the weld are observed in the lower part of the image.

With the ET process, all the ID surface-connected flaws are easily detectable. Flaw length sizing has yielded a RMS error of 2.8mm (0.11") for flaws in the weld and 12.4mm (0.49") for flaws in the cast SS material. These results are within the RMS target of ≤ 13mm (0.5").

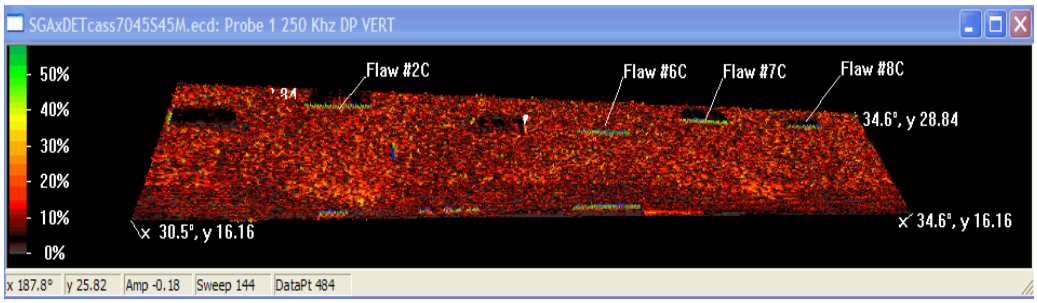

Figure 9: C-Scan of Axial ET Scans of Cast SS Material (250 kHz)

FUTURE PLANS

This work is still ongoing. In Fall 2013, it is intended to conduct OD surface scans using both conventional and phased array UT techniques to supplement flaw depth sizing on flaws in the cast SS material and if necessary, on flaws in the weld. Such scans are intended to focus on the outer 50%T of the material.

In the 1st quarter of 2014, the UT process will undergo formal performance demonstrations using EPRI/PDI as the administrator. These demonstrations are to include: open procedure demonstration on the open test specimen for the cast SS flaws to satisfy ASME Section V, Article 14; blind procedure and personnel demonstrations on the blind test specimen welds to extend the current ASME Section XI, Appendix VIII qualified procedure to a greater weld thickness; and blind personnel demonstration on the blind test specimen cast SS material flaws. The non-blind procedure demonstration on the open test specimen is intended on establishing the flaw depth sizing capabilities for the personnel demonstrations.

The ET process will undergo performance demonstrations (non-blind – procedure, blind – personnel) internally within WesDyne following an established protocol.

REFERENCES

[1] American Society of Mechanical Engineers, *Case N-799: Dissimilar Metal Welds Joining Vessel Nozzles to Components, Section XI, Division 1*, December 20, 2010.

[2] American Society of Mechanical Engineers, *Section XI: Rules for Inservice Inspection of Nuclear Power Plant Components* including *Appendix VIII: Performance Demonstration for Ultrasonic Examination Systems*, 2007 Edition with the 2008 Addenda.

STEAM GENERATOR PRIMARY I

FORERUNNER – EFFICIENT AND SMART SOLUTION FOR SG INSPECTION

P. Mateljak, D. Liebl, Z.Č. Cvjetičanin
INETEC, Croatia

ABSTRACT

The steam generator (SG) is a critical component in nuclear power plants (NPP) with the largest surface area in the primary reactor coolant system, and its integrity is essential for avoiding possible radioactivity release to the environment. SG tube walls are susceptible to aging, i.e., various degradation mechanisms take place in its structural material, such as volumetric material loss due to fretting wear, stress corrosion cracking (SCC), pitting corrosion, flaw accelerated corrosion, intergranular attack (IGA) etc.

New more strict regulatory requirements request plant management to assure the safety of the public and the environment, as well as better SG life management strategies. Therefore, those requirements forced specialized inspection companies to develop advanced probe technologies, more reliable instruments and robotics, and improve training and knowledge of personnel involved in the inspection process.

Thanks to intensive evolution of electronics and computers in the last decade, inspection systems have evolved to a much higher level of automation, efficiency and reliability. Tools based on the eddy current examination techniques were subject to continuous development - from a simple detection tools to advanced diagnostic tools that provide input for decision making based on the integrity assessment.

Forerunner is a part of INETEC's inspection system for PWR plants, primarily used for quick and accurate positioning of the tube guide on the SG tube sheet, and efficient performance SG tube walls inspection. It is a light mobile robot, adjustable for different tube sheet configurations and inner tube diameters. Integrated electronics based on the EtherCAT technology increases the speed of operation and simplifies the cable management. Using the strongest grippers currently available at the market, the FORERUNNER is a reliable and robust system, highly automated with a machine vision, and built-in smart algorithms for optimal movement.

Forerunner is controlled by PC-based software, which is synchronized with INETEC EddyOne software package. The complete scope of inspection activities, the planning, examination, data analysis and final report, became a highly automated process, which makes the inspection much easier and more reliable.

1 INTRODUCTION

Steam generators are heat exchangers used to convert water into steam from heat produced in a nuclear reactor core. They are used in pressurized water reactors between the primary and secondary coolant loops. These loops have an important safety role because they constitute one of the primary barriers between the radioactive and non-radioactive sides of the plant as the primary coolant becomes radioactive from its exposure to the core. For this reason, the integrity of the tubing is essential in minimizing the leakage of water between the two sides of the plant. Steam generator tubes are susceptible to several degradation mechanisms like outer diameter stress-corrosion cracking (ODSCC), either circumferential or axial or intergranular attack (IGA) which can result with cracking. Crack defects can also be initiated from primary side in form of primary water stress corrosion cracking (PWSCC). An other common degradation form is volumetric loss of tube material due to wear, wastage, pitting corrosion and impingement. There is a potential that, if a tube bursts while a plant is operating, contaminated steam could escape directly to the secondary cooling loop.

Thus during scheduled maintenance outages or shutdowns, some or all of the steam generator tubes are inspected by eddy current testing (ECT).

Recently, INETEC has developed a new generation of the PWR steam generator inspection system, using modern technologies and great experience from the previous inspections. New inspection system consists of three sub-systems: manipulator, probe pusher with ECT instrument and advanced software solution for PWR steam generators inspection. All of the features of the new system will be described in detail in the paper.

2 PWR STEAM GENERATOR INSPECTION SYSTEM

INETEC's new system for PWR steam generator inspection has been designed as modular system with a light mobile robot called Forerunner. Its role is to position the guide tube at the exact coordinates in the tube sheet according to the inspection plan. In order to perform the data acquisition and obtain all inspection requirements, the Forerunner is linked with other devices in the system.

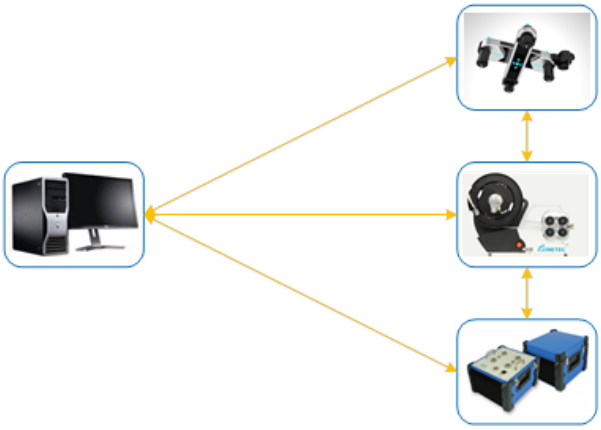

Figure 1: SG inspection system components

Usher is a probe pusher used for testing the integrity of the pipes wall by the eddy current method. It is primarily developed for the testing of steam generators in nuclear power plants, but it can also be used for testing other heat exchangers on the balance-of-plant side of the nuclear power plant. It is a link between the Forerunner and the ECT instrument. In the case of manual positioning of the probe Usher can work as a standalone device. These two devices are connected via communication link with operator's workstation where control software is installed. Operator performs inspection process with EddyOne software package that consists of several modules that will be presented later.

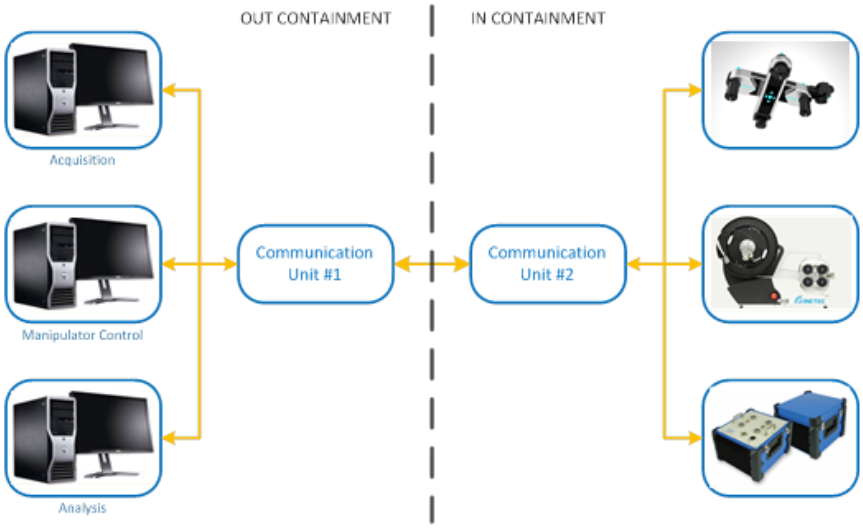

Figure 2: SG inspection system layout

On the site, equipment is set on two locations as shown in Figure 2. Manipulators and ECT instruments are installed in reactor building. Pressurized air and 110/220VAC power supply are required on site to perform the inspection. On the other hand, workstations with EddyOne software installed are located in operator's room. In order to connect these two locations and exchange audio, video and control data, special communication system is designed. With only one optical fiber all data are transferred to central control system.

2.1 Forerunner

Figure 3: Forerunner

Forerunner is a polyvalent device designed to perform different tasks in steam generators with the aim of positioning, movement and working with a variety of tools. Primarily, Forerunner works with probes for NDT testing, but it can also carry plugging tool in order to do corrective operations. Moving is achieved by translating the main axis and sticking fingers (grippers) in the tubes of the steam generator tube sheet. The device has a capability for spider-like movements in all working positions on horizontal, or vertical tubesheets, and easy adaptation to different parameters of heat exchangers.

Forerunner is designed as finger-walker and it has two pairs of fingers to hold the manipulator in contact with the tubesheet. The manipulator has five degrees of freedom, two for moving across the tubesheet and three degrees of freedom for tool positioning. In that way, the manipulator can reach and perform inspection of all tubes in the tubesheet, which means there are no exclusion zones.

As it is shown in Figure 3, Forerunner has three main parts: control system unit, main axes unit and auxiliary axes unit. Control system unit is consists of motion control electronics and actuators that are used to generate forces needed for manipulator movement. Main axes unit perform manipulator movement and positioning on the tube sheet according the inspection plan. In order to assure independent position verification, Machine Vision is integrated in the system. Auxiliary axes are in charge of accurate positioning of various tools that can be used during inspection. The great advantage of employment of the auxiliary axes is high speed of inspection because Forerunner's main axes remain idle with grippers (A, B, C and D) locked while the auxiliary axes can inspect up to 72 tubes before the next movement of the manipulator.

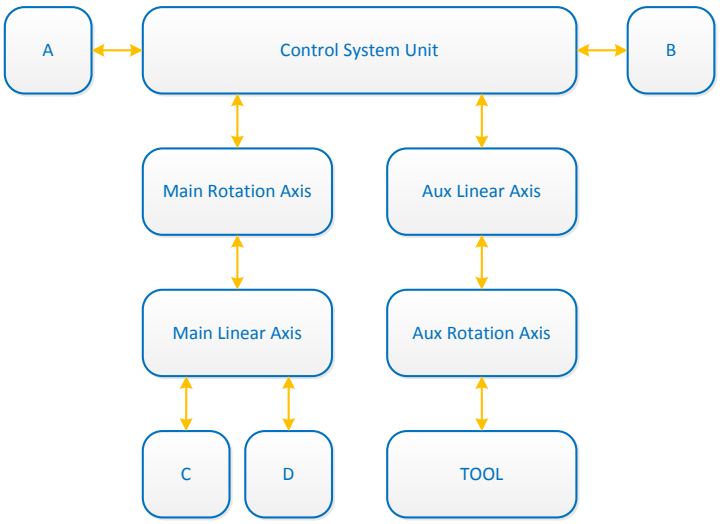

Figure 4: Forerunner block scheme

2.2 Performances and features

Forerunner requires 110/220 V AC power supply. However, the operating voltage is 48 V DC for motors and 24 V DC for sensors and control electronics. It means that Forerunner is low-voltage device that can be used in areas with high humidity without any harm. Motion control system can reach linear speed up to 95 mm/s and over 45 degrees per second during rotation. In addition, the maximal force that can be achieved in motion is over 550 N, which means that Forerunner can easily operate on vertical tubesheets.

During motion, Forerunner uses grippers to keep the contact with tubesheet. Forerunner's grippers are specially designed to withstand all forces that can occur during inspection with dual probe pusher system. Each gripper is pneumatically actuated with total force up to 1700 N. Also, it has specially designed mechanical locking system that is used while gripper is in the tube. With this mechanical system, Forerunner can be locked in the steam generator tubesheet as long as needed even in case of loss of pressurized air or power supply. To unlock the gripper air supply should be present and all safety requirements have to be met which is controlled by fail-safe logic. Additional function that is used in the grippers operation is active self-leveling, which is used to maintain the permanent contact of all grippers with the tubesheet. It is done by monitoring the tubesheet contact sensors on every pair of grippers and performing self-leveling function in case of lost contact. Self-leveling function uses a pair of grippers that are in contact with the tubesheet to pull the manipulator to the tubesheet while contact sensors on grippers that lost contact are activated.

From safety side of view, there is one more subject that has to be resolved when working with finger-walker type of manipulator in the steam generator. It is extremely important to keep the manipulator on the tubesheet without any damage caused to any tube. Forerunner's grippers are currently the strongest grippers on the market. However, they do not make any damage to the steam generator tubes because of large contact surface and carefully chosen materials that are used as finger coating. For that purpose, numerous experiments were carried out, all with satisfactory results.

In order to test contact with inner surface of tube and determine possible damage to tube, INETEC has made a tubing model and a procedure to load fingers on tubing. When all test phases have been performed, INETEC made eddy current examination of the tubing. Grippers testing model is presented in Figure 1.

Figure 5: Grippers testing model

Tubes are inspected by bobbin coil and rotating probe technique in accordance with INETEC procedure for in-service inspection of vertical steam generators tubes by using multi-frequency eddy current examination techniques.

Tubes are recorded 5 times after 5 phases of load per procedure. After the latest phase, bobbin technique and rotating probe technique did not find any damage that could be detected by performed inspection technique. Visual examination has detected areas on the tube inside diameter surface, spread in axial direction, and which disappeared after cleaning process made by dry textile.

On tube No. 3 (where severe load was made per procedure) pancake coil detected signal initiated from inside tube diameter, axially oriented, with small volume that did not allow any sizing procedure. It has to be added that pancake coil is very sensitive to changes in geometry. Cross wound coil did not find any response on this particular location, what indicates that there is neglected change in geometry. Further, visual examination detected small change in tube surface color, spread in axial direction which did not disappear by using cleaning process with dry textile. By using magnifying glass, no damage was detected. Also, a needle with curved end was used; no change on inside diameter surface of tube was detected as well. Therefore, it might be concluded that EC examination did not find any damage in the tubes on the model, which were loaded per defined procedure.

2.3 Control system

Forerunner control system is designed as 3-level control system with precisely defined functions. Low level is in charge of motion control for particular degree of freedom, and it monitors all sensor activity. Middle level is used to synchronize independent motions of each degree of freedom in a way that is needed to carry out planned trajectory. High level control system is link between operator and the manipulator. It can plan the movement trajectory according the inspection plan, monitor all activities that have been performed, and run the diagnostics algorithm in case of any unplanned situation. General schematics of Forerunner control system is given in Figure 6.

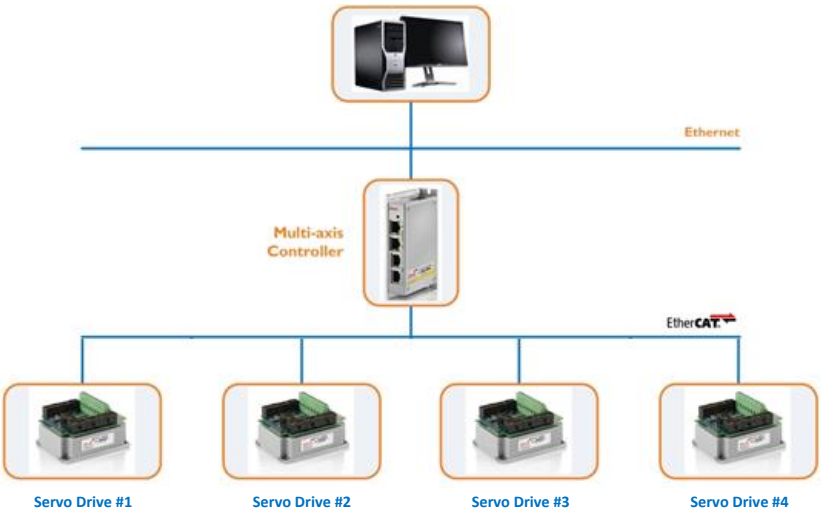

Figure 6: Forerunner control system

This control system is able to manage the whole inspection process automatically after it has all information about the steam generator to be inspected (e.g. SG type, tubesheet scheme, plugged tubes …) and scope of inspection. It has to be emphasized, that trajectory planning algorithm is based on optimal control using several criteria. Criteria that can be used in trajectory planning include, but are not limited to estimated inspection time, inspection plan, position of installed plugs in specific steam generator, presence of other Forerunner or any other device that is used in inspection, and any other constraint.

2.4 Usher

Usher is used to push the cable shaped probe inside the tube with controlled speed and position. Combining the years of experience from the field and the modern technology, numerous new features are built in the Usher, which makes this device fast, reliable and easy to operate with. The all-in-one design means that the control electronics are integrated inside the device increasing the speed, simplifying cable management and reducing the noise of the measuring signal. A single Ethernet connection from the host acquisition computer provides all of the control communication. Usher architecture supports simultaneous usage of multiple devices through a common interface. This option is used to reduce the inspection time.

Like Forerunner, Usher is also based on the 3- level control system: the first level consists of servo drives and input/output unit, in the second level is the main controller, and in the third level is PC application directly controlled by the operator. Most operations are carried out in the first and second level, which makes the Usher highly automated device.

Figure 7: Usher

As it is shown in Figure 7, the Usher can be easily disassembled by the clip-on connection into two main parts: pusher drive unit and controller unit. This is useful during manipulation when the mass is equally distributed in the both hands. Usher can work even in disassembled mode, when additional conduit and extension cable should be inserted between separated units. This mode is used in the narrow space when only pusher drive unit is close to the tube sheet while the probe could be exchanged at up to 10 m remote location.

The pusher drive unit consists of a drive mechanism, driving wheels and the housing with all electrical and pneumatic components. For the practical reasons air supply and two connectors for sensing coils are placed in the front of the unit below the drive mechanism. Driving wheels are pushed by two pneumatic cylinders against the probe ensuring the traction force. Contact pressure between the wheels and the probe is regulated according to the working conditions. The wheels are driven by a special torque motor whose dimensions and a power/weight ratio are the most convenient to this application. Probe speed inside the tube can be set in the range within 0.5 mm/s to 2.6 m/s, while the pushing force can be set in range between 100 N and 1000 N. The exact location of the probe inside the tube is measured by the linear encoder. Comparing the data from the linear encoder and the motor encoder wheel slippage can be detected. In that case Anti Slipping Control (ASC) progressively increases the wheels pressure to a maximum value. If the slippage is still present, control system will give up on pushing and notify the operator. This function assures optimal pushing force during inspection and increases the probe lifetime.

Controller unit consists of take up reel and housing for the main control unit. The reel is also driven by torque motor controlled with algorithm that controls the torque and the winding speed according to operating conditions. On the reel there is a slip ring that is used to transmit the signal from the probe to the instrument next to the device. Special instruments that are embedded into the take up reel digitize signals before passing through the slip ring and thus further reduce the measuring noise. Usher supports many different types of instruments including these one.

Interaction with Eddy Current instrument includes exchange probe position data and start/stop signals. Remote control features include remotely operated emergency stop that can be arranged to stop all devices if more than one Usher is used in inspection. On the other hand, there is possibility to use remote control accessories in order to operate each device.

Due to harsh work conditions in the high radiation zone in nuclear power plants, where operators wear special suits and multiple layers of protective gloves, special attention is paid to safety and ergonomics issues. The emergency stop button is placed at an easily accessible location with optional remote button near the operator. The entire device is powered with low voltage (48 V DC) in order to reduce the possibility of electric shock. Front-wheel drive can be set up with protective cover which minimizes the possibility of injury from mechanical parts.

From the ergonomic point of view the Usher is suitable for handling particularly due to significantly less weight than other similar devices. All surfaces are very smooth with no pockets in which radioactive dust might be deposited. Because of its shape and IP protection level Usher is very suitable for decontamination after usage.

2.5 EddyOne

EddyOne Software Package is a complete solution for eddy current inspection of nuclear power plant components. EddyOne software package is consisted of: Inspection Management, Manipulator Control, Acquisition and Analysis. Inspection Management is a central database for modeling of the steam generator (tubesheet, landmarks…), inspection planning and progress tracking. After the inspection it's used for interpretation of results and generating of the required reports.

INETEC's manipulators are driven using the Manipulator control software. It is used to control the manipulators and track their status. It supports the automatic acquisition mode where the predefined inspection plan is used to automatically perform the inspection. The Acquisition software is used to record the eddy current data and track the inspection procedure, while Analysis software is used for offline analysis of the recorded data.

Automatic analysis further simplifies the analysis procedure by reducing time and costs required for data analysis. All the software is available in multiple languages and can be customized according to the user's needs.

3 CONCLUSION

In order to reduce outage time of nuclear power plant, development of new inspection systems is needed. They have to provide faster inspection, be compact for easier installation and be able to bring more information about steam generator condition. All these requirements have to be met to perform better structural integrity assessment and fulfill ALARA recommendations at the same time.

New generation of INETEC's steam generator inspection system is designed to satisfy all regulatory requirements and give the best inspection results at the same time. This system has been designed as modular system with a light mobile robot called Forerunner. Its role is to position the guide tube at the exact coordinates in the tube sheet according to the inspection plan. In order to perform data acquisition and obtain all inspection requirements, the Forerunner is linked with other devices in the system, primarily probe pusher and ECT instrument. All inspection data are collected and managed by EddyOne software package that is a complete solution for eddy current inspection of nuclear power plant components.

REFERENCES

1) Nuclear Energy Institute, "Steam Generator Program Guidelines", NEI 97-06 [Rev1], January 2001.
2) S. Galošić, M. Vavrouš, "INETEC SG Inspection and Repair System", SMiRT 21, New Delhi, India 9.11.2011.
3) A. Bakić, "PWR Steam Generator Inspection System", Workshop on advanced NDE applications, China Nuclear Operation Technology Corporation, Wuhan, China
4) A.Bakić, P.Mateljak, D.Rohde, "Advanced System for VVER Steam Generator Inspection", 8 ISTC Safety Assurance of NPP with VVER OKB GIDROPRESS, Podolsk, Russia
5) M. Vavrouš, „Advanced system for VVER SG tubing inspection", The III International Forum of Nuclear Industry Suppliers ATOMEX 2011, December 6–8, 2011, Moscow

HISTORICAL COMPARISION OF STEAM GENERATOR TUBING EDDY CURRENT DATA CONCURRENT WITH VESSEL INSPECTIONS

T. O'Dell, T. Woller, N. Larsen, ZETEC, USA

ABSTRACT

Traditionally eddy current data acquired from nuclear power plant primary loop steam generator tubing during an inspection is compared with historical data to understand change in signals. This historical comparison process has been a manual effort requiring the analysis to independently recall both sets of data and compare results. Due to the effort required to manually compare, this action could only be partially performed on the data.

A new technology has been developed where two independent data files acquired at different times on the same steam generator tube can be automatically compared. This technology solves the equation of slewing and correlating the data to align the signals for comparison. Rather than compare only current signals of interest to history, this developed technology detects change between multiple files sets to create a more comprehensive analysis and leverages an automated analysis framework to provide the results in a timely fashion.

INTRODUCTION

A new technology has been developed whereby the two or more independent data files are aligned, correlated, and subtracted to create a "delta" process channel for detection of change. This delta channel can be used as a standalone indicator of change for a manual process or integrated into an auto analysis software system. RevospECT® analysis software by Zetec inc.® incorporates an automated historical data comparison tool called HDC™ that automatically performs the correction of data slewing, alignment of signals, and subtraction to create a delta channel of change. RevospECT performs this comparison for two sets of historical data files against the current data file to provide two independent delta channels to be used in the analysis process. The processing of the comparison and creation of the delta occurs on the entire available data so the resulting delta channel can be interrogated as a comprehensive analysis of change for the entire available data set. This is an important distinction as with growing use of automated analysis systems, the automatic evaluation of change on all of the acquired data is valuable to the overall analysis process.

FUNDEMENTAL OF HISTORICAL COMPARISIONDETECTING REGIONS OF INTERST

The defined goal of historical comparison of data files is to create an output that represents change. The implementation of this goal is to create a change or delta channel that represents all change between the entire two data files rather than rely on comparisons of specific indications detected during the traditional analysis process. This adds defense in depth to the analysis. This delta channel is analogous to an eddy current process channel therefore can be used within the analysis process. A delta signal process channel can be utilized as a detection channel for change, a confirming channel to traditional eddy current analysis, and historical reference to support the resolution process of the traditional eddy current analysis.

The creation of the delta signal process channel is broken down into four distinct phases, segmentation of the tube file into regions of interest, coarse alignment of data files by regions of interest, correlation of signals within each region of interest, and subtraction of data files to create the delta signal process channel. The final process channel is a subtraction of the two aligned and correlated data files. The delta signal process channel is created for each frequency in the data file and applies to mix process channels as well.

Typically the historical comparison against the current data file is performed on the prior inspection data and the baseline inspection data.

This creates two distinct delta signal process channels that are simultaneously available for the analysis process to use. These delta signal process channels provide a good description of signal morphology with respect to change.
In the implementation of HDC in RevospECT, HDC can be performed on all bobbin data and across all bobbin data frequencies within the data file. RevospECT utilizes a unique method of applying the current analysis calibration setup across the history data files so measurement can be taken from each historical data file and compared to measurements taken in the current data file simplifying the analysis process and providing accuracy to the results. RevospECT HDC can accommodate significant variations in probe speed, direction of inspection, and situations of partial historical data files.

Region of interest segmentation
Regions of interest are the individual sections of the tube that are defined by either the individual free span sections or each of the tube structure types that exist within the tube. The tube structures are detected within the eddy current data by a series of algorithms developed to detect and define the structure locations and extents.

Alignment of regions of interest
The alignment of the regions of interest utilizes an algorithm to process the edges of the historical data file to the current data file. This is the primary alignment of the data files where the edge of each region of interest in the historical data is matched to the region of interest edges in the current data file. Each region of interest receives a label corresponding to the define landmark table for the steam generator vessel.

Correlation of signals by region of interest
Each of the regions of interest is subject to further processing by several incremental correlation algorithms that crawl through the data and align the entire region of interest with respect to the signal signature. Once the tube files are segmented, aligned, and correlated, it is possible to process the subtraction of the data files to produce a delta signal process channel.

Subtraction of data files
Once the data files are segmented, aligned, and correlated, the processing of the data by subtraction produces a delta signal change channel similar to Figure 1 below. The nature of the delta signal change channel does not lend itself to conventional eddy current data analysis therefore can only be used as a marker for change. This change channel provides detection of change and data points for evaluation using standard eddy current analysis methods on the current and historical data files used to create the delta channel. An individual delta channel may be generated for each frequency used in the current and history data files so an evaluation of change can be considered for each frequency

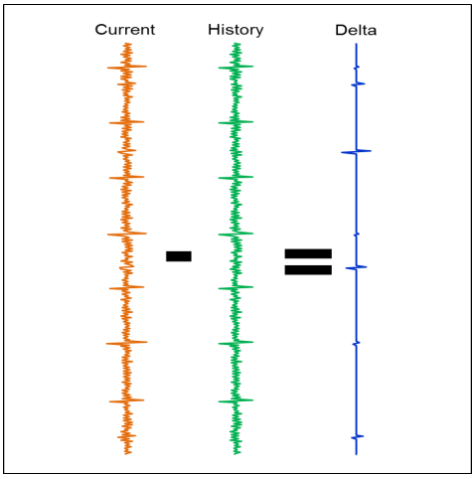

Figure 1 Subtraction of signals

UTILIZING THE RESULTS OF CHANGE

Implementation of HDC within a capable software package such as RevospECT provides the ability to process change analysis on a large amount of data. In the example of Figure **2**, tube to tube wear is apparent on the low frequency absolute channel for the history and current data files indicating the wear occurred following initial operation of the power plant. The delta signal for this wear is significant and simple to capture with an auto analyzer detector.

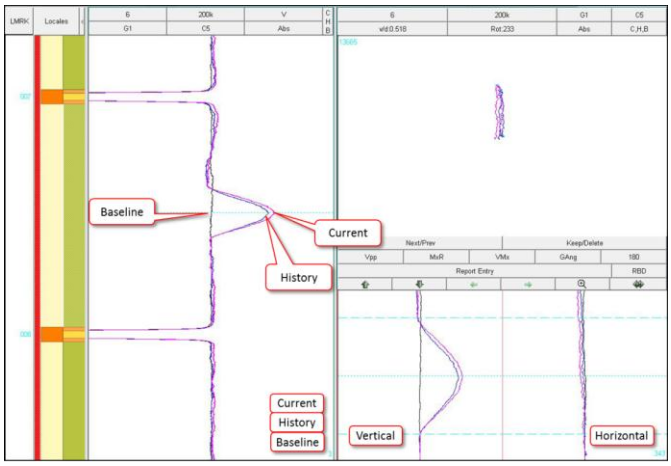

Figure 2 Tube to Tube Wear

Another example is an MBM signal which is characterized by the low frequency channel and occurs across the baseline, history, and current inspection data. In Figure **3**, a MBM signal is clearly visible three inspections with little of now change. In steam generator with a significant quantity of MBM indications, the automation of historical comparison can greatly improve the process of addressing all MBM indications for change while improving the accuracy of MBM change analysis.

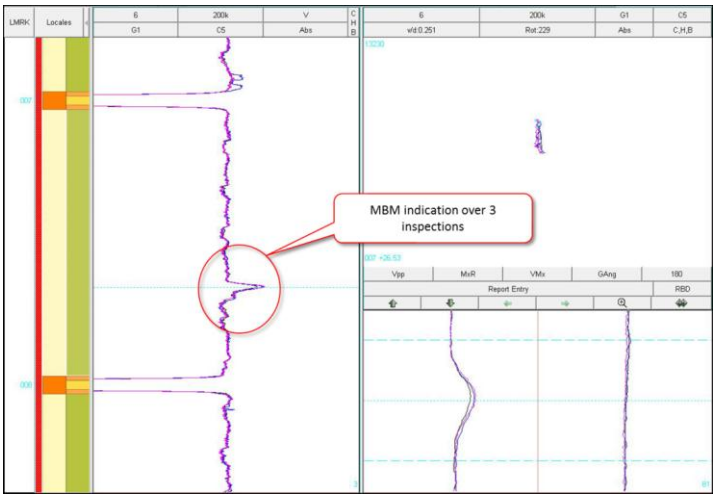

Figure 3 MBM Signal

An example of the comparison of data with no change is provided in Figure **4**. This example shows on the 6th support of the 750kHz channel, the delta signal has no significant change. While both the history and current data do have a significant response from the support plate, the current/history overlay shows the remarkable correlation of the signals between the two data sets even though some distortions in the support signal.

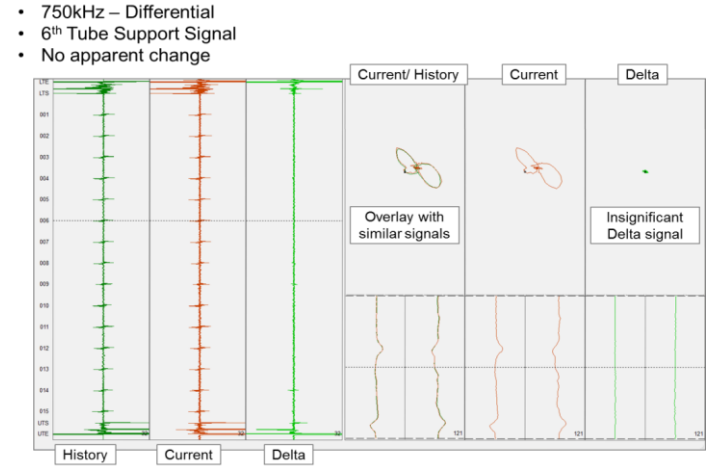

Figure 4 Normal structure with no wear

An example of the comparison of data with change is provided in Figure 5. This example shows on the 14th support of the 750kHz channel, the delta signal has significant change as a result of a wear indication. The current/history overlay shows the distortion of the current support signal in comparison to the historical signal. The resulting delta change channel provides a significant signal for detection.

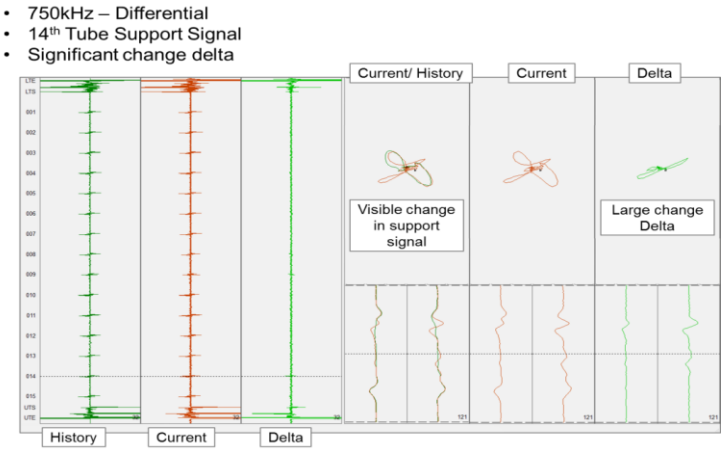

Figure 5 Structure with wear indication of change on primary channel

An example of the comparison of data with change is provided in Figure 6. This example shows on the 14th support again but using the 750/200kHz structure suppression mix channel, the delta signal has significant change as a result of a wear indication. The current/history overlay shows the significance of the wear signal over a cleanly mixed support structure. The resulting delta change channel provides a significant signal for detection.

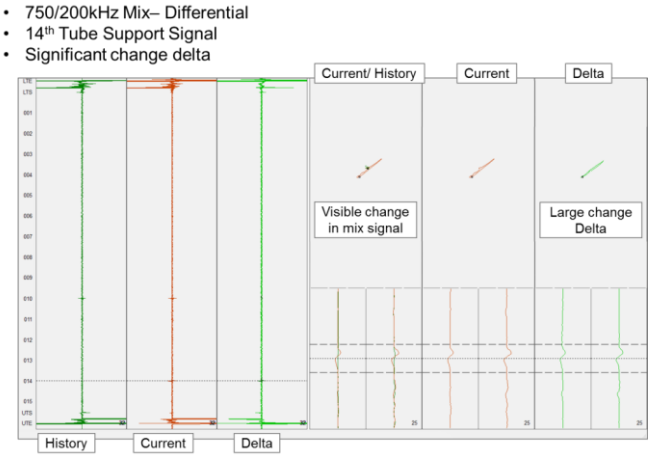

Figure 6 Structure with wear indication of change on suppression mix channel

An example of the comparison of data with change is provided in Figure 7. This example shows on the 10th support again using the 750/200kHz structure suppression mix channel, the delta signal has insignificant change as a result of no change although both the history and current data files display a wear indication. The historical comparison of the signals indication no growth in the wear indication.

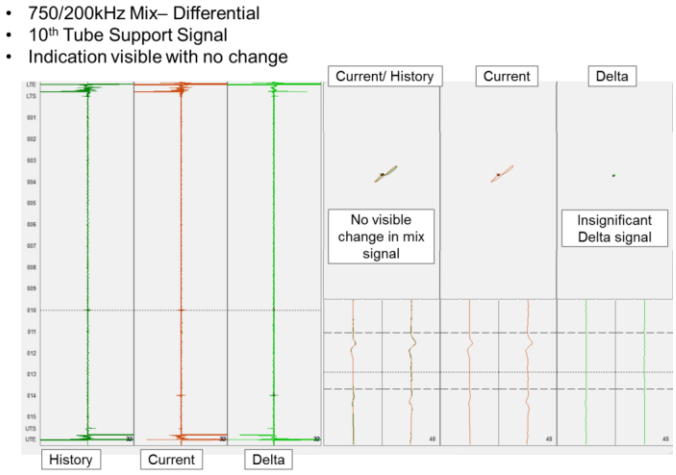

Figure 7 Structure with wear indication showing no change on suppression mix channel

SUMMARY

Automated historical change analysis provides additional integrity to the analysis process. Incorporated in an auto analysis such as RevospECT it has the capability to evaluate change in situations of difficult data either from tubing noise or a large population of reportable damage within the tubing. Utilizing the automation of the historical comparison and evaluating the change on the entire dataset available provides defense in depth to the analysis process. This has a positive effect on inspection accuracy, operational assessment and outage schedules.

AIDA – THE EDDY CURRENT ANALYSIS SOFTWARE

F. Sauriat, AREVA, France
R. Vojvodic, B. Everett, AREVA, USA

BACKGROUND OF EDDY CURRENT ANALYSIS SOFTWARE

A wide variety of eddy current software programs are in use for non-destructive examinations today. The degrees of sophistication and performance of these software applications vary, and typically increase with the complexity and requirements of the particular non-destructive examination. Basic examinations of a few components using single coil-pairs in impedance modes may be performed with simple software programs that show Lissajous and strip chart displays. These programs are used in a range of portable tests to determine a "good" or "not good" result for a particular measurement and in straightforward remote examinations. As components become more intricate or contain more parts to examine, the eddy current software must have capabilities to store and retrieve an extensive set of results, typically in the form of calls (or report entries) in a database. As the degradation and component conditions to be reported become more multifaceted, the eddy current software must provide a way to enter different condition descriptions for manual analysis examinations. For automated analysis examinations, the eddy current software must be able to not only detect indications of interest, but also differentiate between reportable indications and correctly denote and annotate their report entries. For examinations of safety-critical components, eddy current software programs must meet industry standards and requirements with increasing rigor.

For an examination that is both complex and critical, such as a steam generator inspection, there are a small number of eddy current software programs available. Most of these applications are produced by either NDE vendors that sell software and hardware products or by inspection service companies that create and use their own examination software. In the case of steam generator examinations, many of the utility customers require or desire specific functionality and results, and eddy current software with custom features are best suited to meet these utility-specific or regional-specific needs. In a time period of fiscal conservatism, the relatively small number of users for a sophisticated software product creates an economic challenge for software vendors. As a result, inspection service companies have found benefit in designing their own eddy current software products to best meet their customers' inspection needs. Additional eddy current software capabilities have been developed or supplemented by the academic community. Universities have been used to research specific eddy current software applications and advancements. As with any research, these academic research projects produce various degrees of success and usefulness for applications in field examinations.

AREVA has extensive experience providing eddy current examination services to customers worldwide. Headquartered in Paris, France, AREVA has three major NDE Solutions divisions in France, the United States, and Germany. To meet a variety of utility inspection needs around the world, AREVA has used both vendor produced software products as well as AREVA's own in-house developed eddy current software. To provide optimum inspection capability, AREVA has made significant investment in increasing the capability of AIDA, AREVA's eddy current analysis program, incorporating best practices from multiple customers and more than 30 years of inspection experience. Such development is achieving AREVA's goal to make AIDA the eddy current analysis software of choice in the NDE industry. This paper discusses AIDA, the eddy current analysis software, summarizes its capabilities and highlights its recent breakthrough developments.

INTRODUCTION TO AIDA, THE EDDY CURRENT ANAYSIS SOFTWARE

Development for the AIDA eddy current analysis software program began in the early 1990s, as a program to automate the analysis of bobbin data for examinations of EDF steam generators. Today, after over 20 years of continuous improvements, AREVA has multiple versions of AIDA that serve both commercial and noncommercial customers and serve utilities in eddy current examinations around the world. In the past 10 years, an AIDA version adapted for the US market has served at 24 sites and 34 units through 76 deployments, and is now AREVA's analysis software of choice for eddy current examinations. In 2011, AREVA announced plans to improve manual analysis and add capabilities for analysis of rotating and array data, and has since developed an economical analysis interface for all major SG eddy current techniques. AIDA is now a part of AREVA's complete eddy current examination system, which includes acquisition, analysis, data management and component integrity and engineering assessments.

AREVA uses both its own acquisition software, ARIA, as well as other vendor acquisition software programs to acquire eddy current data. In a sense, the best data analysis begins with the best data acquisition, as good analysis requires the data to be acquired with high quality – having low noise, complete extents, and accurate documentation of examination technique and component information within the data record.

The detection, analysis and reporting of indications is the main purpose of AIDA, and aspects of this analysis are discussed in depth throughout this paper. AIDA uses resolution processes with automated logic-based assessments and history comparisons to review analysis results. This ensures correct analysis reports are fed into AREVA's data management databases. These databases are used to control and verify examination scopes of multiple techniques, such as bobbin probes, rotating probes and array probes.

Although AIDA's primary purpose is to detect and report degradation, AIDA does much more. A number of complementary functions and features are performed by AIDA to assess component integrity, such as AVB mapping and evaluation, deposit mapping, tube identity verification, and noise measurement. The advanced AIDA platform interacts with engineering applications to efficiently provide these test results, organized in manners needed for the component assessments. AREVA's component integrity group draws results from the eddy current exam to perform engineering assessments and to monitor and trend component conditions.

As AREVA's eddy current software programs and engineering processes become more automated, the traditional process steps of acquisition, analysis and data management become less distinct and more integrated. Through the automation and combination of intricate processes, AREVA is composing an advanced platform of AIDA and its associated eddy current programs to dramatically increase examination capabilities and performance. With minimal human interaction, data may be automatically acquired, calibrated, verified, and analyzed with the examination results archived in databases. At the present pace of improvements, this analysis and reporting will happen in near real-time with data acquisition.

Examination Components

The main component examined with eddy current techniques by AREVA is the tubing of steam generators in nuclear power plants and systems. A steam generator tubing exam is perhaps the most complex of eddy current examinations performed, as these inspections involve a large number of tubes, a wide variety of generator designs, a complex set of damage mechanisms and reportable conditions, and rigorous set of regulatory requirements and guidelines. AREVA began development of the AIDA eddy current analysis software specifically for these complex examinations of steam generator tubing. AREVA has extensive steam generator examination experience and has used AIDA to examine all of the major types of nuclear steam generators in use today. Steam generators with a variety of designs and tubing sizes, made by all major manufacturers, and containing a wide range of damage and special interest conditions have been successfully inspected. AREVA has yet to find a steam generator design that AIDA can not analyze.

In addition to steam generator tubing exams, AREVA performs a number of specialty eddy current examinations on other balance of plant components, such as pressurizer tubes, thimble tubes, and welds.

Reactor vessel inlet pipe welds, safety systems piping welds, control rod penetration welds in reactor closure heads, and bottom mounted nozzle welds in the reactor floor are all examples of welds inspected by AREVA with a variety of eddy current techniques, including newly developed array probes developed specifically for the weld to be inspected. Due to the small quantity and specialized nature of these specialty exams, AREVA has previously employed the acquisition and analysis software of the probe vendors. AREVA is now preparing the AIDA software to also have the capability to analyze the data from these specialty weld and balance of plant exams. When ready, AIDA will be able to offer the same leading edge analysis technology developed for complex steam generator tubing inspections to other eddy current examinations.

Examination Techniques

For steam generator examinations, there are three main eddy current techniques: bobbin, rotating probes, and array probes. The bobbin exam is the exam of record for most steam generator examinations, and the rotating and array techniques are used as supplemental or alternate exams to provide additional information about degradation type, characteristics and size. AIDA has been improved to allow the analyst to either manually analyze or automatically analyze all three techniques. Further, the AIDA resolution process has been developed to compare the results of the various examinations to assess the degradation or condition of the component examined.

AIDA'S ANALYSIS METHODS AND CAPBILITIES

Manual Analysis

Even in an environment of increased auto-analysis, the need for manual analysis remains. A software that delivers efficient, robust manual analysis functionality is still both desired and required. During manual analysis, the analyst must view many aspects of the data acquired, viewing multiple data channels in various views to determine the condition of the component. Often, in a production environment for an examination of many components, such as the thousands of tubes in a steam generator, the analyst must perform a series of repetitive tasks.

AIDA has been designed using the best practices of the industry and ergonomic considerations to provide a way for analysts to view the data as necessary, with a minimal amount of effort. Various layouts have been designed for each examination type. User-friendly operation using human factors and ergonomics include the following considerations. The number of mouse motions, clicks and keyboard strokes have been minimized. Controls and buttons are organized and placed with the analysis process in mind. Better graphical processes provide increased manual speed capability. Reducing fatigue leads to reduced errors and better analysis results. The buttons and controls are intuitive for both novice and experienced analysts, so there is minimal (or no) software training required for experienced analysts. This allows AIDA to be easily adapted by secondary vendors worldwide. The key goal AIDA meets is that it allows analysts to focus on the data, without the distraction of thinking about how to operate the software.

Automated Analysis

Automated analysis is the use of a computer algorithm to detect, analyze and report indications. The advantages of automated analysis are clear. As with any automated process that replaces a manual process, automated analysis has the benefits of producing objective, consistent and fast results. The reliability of objective exam results without human error and the financial benefits of faster analysis results have lured research efforts since before AIDA even existed. The concerns for automated analysis are also typical of the concerns for any automated intelligence, in particular, how does one compensate for uncertainty? For the field of NDE, examinations are performed to eliminate uncertainty. How does one ensure there are no programming errors that would result in a miss of a significant indication? How does one ensure the detection of all degradation types, particularly flaw responses that are not well described or are in regions of signal noise and uncertainty. The varying conditions of steam generators and the variety of signals in these examinations have proven to be a challenge to automated analysis algorithms for decades. AREVA has met these challenges, first with developments and advancements in traditional automated analysis techniques, followed by recent breakthroughs in the discoveries of advanced automated analysis algorithms.

Preparation

AIDA's automated routines are prepared for each examination using industry experience databases and site-specific historical data. Such preparation ensures that both expected and unexpected damage mechanisms will be detected. Both industry performance tests and site specific tests are used to demonstrate and qualify AIDA for examinations. In the entire history of using AIDA as an automated analysis tool, AIDA has never missed an indication on a site specific test, providing perfect site qualification testing results.

Locating

One element to AIDA's automated success is landmarking and locating. In a steam generator exam, there are several tubing regions divided by the support structures of the steam generator, namely the tube sheets at each end of the tubing and the tube support plates in between that provide structural stability for the tubing. Various damage mechanisms occur as a relation to location and the associated structures, such as wear at supports, pitting in tubesheet sludge piles, and stress corrosion cracking at regions of tube diameter expansions. AIDA has multiple processes to locate structures in any generator type and then verify their location, to ensure proper analysis. Although steam generators have a set number of support structures, how they intersect a specific tube may be different for each of thousands of tubes in the steam generator? For this reason, AIDA has begun to use tube by tube landmark tables, which are large databases that store the description of the support locations for each individual tube.

Detection, Analysis, and Reporting

AIDA allows the user to control and customize each aspect of the analysis process: detection, analysis, and reporting. Although the word "analysis" is generically used to describe all three of these steps, there are key differences that should be noted, particularly when comparing the AIDA service to other analysis products.

In the detection step, AIDA detects signals of interest that may or may not be degradation. The very basic of methods for detection is to use a series of phase and voltage measurements from various frequencies and frequency mixes in a set of parameter-specified if-then logic-based determinations to identify potential signals of interest. Such logic-based assessments are a beginning step to mimic the thought processes of a human analyst. Many signals can be identified during this detection step, both degradation that should be reported as wells as overcalls (or false positive calls) that should not be reported. Many eddy current products have such routines, which are more accurately called data screening routines, as the data screening (or detection) process screens out possible degradation along with many other similar signals, in a similar way that panning for gold can screen out small amounts of gold in a pile of sand or rocks.

The analysis routines are what differentiate the degradation and other signals of interest from those signals that need not be considered for reporting, like picking specks of gold out from the rubble. Industry tests such as EPRI's Automated Analysis Performance Demonstration Database (AAPDD) tests, measure both detection (how many truth calls were reported) and analysis capability (how few overcalls were reported). In both the bobbin and the array AAPDD tests, AIDA has scored well in both categories. In the recent AAPDD array test, AIDA detected 100% of the degradation (perfect detection capability, that exceeds human analyst performance) and average only 0.58 overcalls per tube (excellent analysis capability, that is similar to human analyst performance).

After analyzing all detected signals to identify the relevant indications, the abilities to adjust reporting criteria and control what is reported are essential to meeting customer expectations for an inspection. Each of AREVA's dozens of customers have unique requirements and desires for each of hundreds of steam generators, based on regional regulations that are required by law as well as traditional practices that need to be maintained to avoid inspection transients. AIDA's reporting requirements ensure that the degradation level that needs to be reported is reported, without reporting indications below a specified threshold of interest. AIDA can create multiple reports simultaneously from the same sets of data records, to provide results and information for different types of exams and exam scopes. In addition to reporting degradation, AIDA provides reporting capability for tube ID verification, AVB mapping, noise reporting, sludge, denting, deposit mapping, landmark verification, and more.

Convenient Automated Features

Often after the detection, analysis and reporting of indications, there are manual operations that an analyst performs on a reported degradation responses. Some of these manual steps can be subjective and/or time consuming, such as measuring an extent, or measuring several depths along an extent.

New features in development for the AIDA analysis software include automated routines that measure flaw extents and boundaries, and automated routines to perform line-by-line sizing. The extents of flaws in tubing have traditionally been measured as lengths in two axes: a circumferential extent and an axial extent. AIDA has a prototype routine which will outline a flaw boundary, providing detailed shape information, as well as the traditional axial and circumferential lengths. An example of an automatically detected flaw boundary is shown in Figure 1.

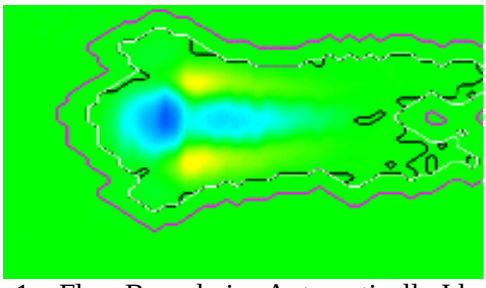

Figure 1 – Flaw Boundaries Automatically Identified

Once a flaw extent is determined, either manually or automatically, a measurement can be made across each data point along the flaw's extent using the Lissajous in the opposite direction of the extent. This incremental sizing (called line by line sizing) can be performed consistently and quickly through automation. As with any automated call parameters, the extents and start and stop locations of an automated call may be manually adjusted in the database report entries.

An Important Technical Advancement

AREVA has recently developed three new algorithms to detect degradation signals. Each of the three algorithms is documented and proven to be an independent and separate method with different operations and results. These processes are easy to configure for a wide variety of examinations. The new algorithms are not like the traditional rule based analysis methods, but are advanced mathematical signal processing concepts, which are applied for the first time in ET SG exams. AREVA is seeking patent protection for these first-of-a kind applications.

The new algorithms represent a breakthrough ability in the field of automated analysis. Traditionally, automated routines have had difficulty detecting small indications and have had difficulty detecting degradation in regions of signal noise. As a result, small indications may go undetected, or if thresholds are set to call small indications, a large number (hundreds or even thousands) of overcalls may be made. Since automated reports are manually reviewed to eliminate the false calls and keep the real degradation signals, a large number of overcalls burdens the analysis process. AREVA's advanced algorithms have the ability to detect small degradation responses, and to detect indications in areas of noise without making overcalls (false positive calls). In a sense, the new algorithms both detect and analyze degradation, by simply not detecting noise signals. Recall that in previously discussed definitions, detection was considered to be the finding of a potential signal of interest and that analysis was the characterizing that signal.

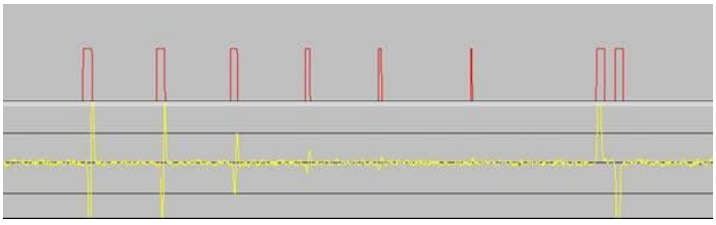

Figure 2 – Advanced Algorithm Detects And Reports Small Degradation Without Reporting Noise

An example of one of the advanced algorithms is shown in Figure 2. At the bottom of the figure is a stream of eddy current data that contains several degradation responses of varying amplitudes. In the top of the figure are the resulting detections of one of the advanced analysis processes.

One may notice that the sixth degradation response is barely noticeable, and this small noise-like response would not likely be called by a human analyst, unless the analyst knew the degradation was there and was instructed to call the signal. The small signal is not a noise response; it is a response from actual (very shallow) degradation. Also note that the advanced analysis process did not produce any false positive calls from this data. These results show that the advanced analysis process meets or exceeds the detection, analysis and reporting abilities of an experienced human analyst.

CONSIDERATIONS REGARDING AUTOMATION AND EXAMINATION PERFORMANCE

There are some discussions in the industry regarding the performance and reliability of automated analysis. Does automation produce a high enough probability of detection? How can unknown conditions be programmed for detection or evaluation? Should every call made by an automated system be manually reviewed? How can the detection and analysis performance of automated analysis systems be objectively compared? AREVA has developed AIDA to address these issues and concerns as follows.

Probability of Detection

For some manual examinations, two independent parties (or groups) of analysts are required to analyze the data, essentially analyzing the data twice. The results of the two analysis groups are reviewed by a third group of analysts called resolution analysts. These resolution analysts are also divided into two groups, and each resolution group reviews indications of potential degradation that are deleted. For US examinations, a fifth independent analyst further reviews the data. The two-party, multi-review process is designed to increase the probability of detecting (and reporting) degradation. With the advent of automated analysis, manually edited reports of automated analysis calls have taken the place of either one or both analysis parties.

AREVA has designed AIDA to be able to perform either a manual analysis or an automated analysis. With the invention of the independent analysis algorithms, the AIDA software can perform separate automated analyses for an examination. With these options, utilities may choose the level of manual analysis or automation desired to ensure a required probability of detection. AIDA could be used for dual manual analysis, single manual and single automated analysis, dual automated analysis, or any combination of these choice in addition to a third non-AIDA analysis. Using AIDA's recent EPRI AAPDD test results of 100% detection of array data indications along with other site-specific test results allows AIDA to offer a high probability of detection with or without the addition of a manual analysis party.

What should be required for overcalls (false positive calls)

AREVA eddy current analysis processes have always required that human analysts review every call made by an automated eddy current system, and to determine the relevance of the call - whether the call should be kept or deleted. The more overcalls that an automated system makes, the greater the chance of human error occurring when keeping or deleted the indications. If overcalls are not reviewed (or more precisely, if some calls are disregarded and not manually reviewed to determine if they are overcalls), then there is a risk of not reviewing and reporting a critically important degradation response. Disregarding a set of automated calls, perhaps based upon some voltage threshold, in essence leaves part of the data un-analyzed - and not just any part of the data, but a portion of the data that is more likely to contain a significant indication than nominal tubing (since there is an indication there to begin with).

With traditional AIDA auto-analysis methods, few overcalls occur. The range of overcalls per tube that has occurred in past inspections is 0.1 to 4.0, depending upon tubing and data conditions. A typical overcall rate for present day examinations of replacement generators is 0.5 calls per tube. With the incorporation of AREVA's advanced auto-analysis algorithms, these overcall rates may be further reduced. By having an automated analysis software with such a high analysis ability, AREVA can continue to manually review every analysis result, either with a review analyst or a resolution analyst, and leave no portion of data unanalyzed.

Detecting the Unknown

A final concern about automated software is its ability to detect a condition for which it has not been programmed. How well can automated analysis detect degradation in unexpected and unusual responses? The answer to detecting unexpected condition lies in comparing present data with past data, such as either the previous outage data or the baseline data. AREVA has developed a method of mixing the historical data with the present data to show regions of change. This change can then be assessed to determine if degradation or a condition that needs investigation is present. This application of a graphical historical comparison can "let you know what you don't know", and identify potentially new degradation responses.

CONCLUSION

Many parts of an analysis software program must function well and work together effectively in order to perform successful eddy current examinations. AREVA has developed the AIDA analysis software to perform multiple analysis functions, and interface with both acquisition and reporting systems. Extensive and comprehensive manual controls to operate highly customizable automation processes allow AIDA to produce accurate results in desirable formats, meeting both customer requirements and desires. AREVA's significant investment in continuous improvements and in research of new mathematical signal processing methods have produced a world-class eddy current analysis software, with unique and advanced capabilities and functions designed to exceed industry standards.

Additional Information

Please contact AREVA for more information about AIDA, the eddy current analysis software, and how utilities benefit from this inspection service. In Europe, ASIA or Africa, please contact Joel Martens in AREVA's Rungis, France office, at 33-01-49-78-4084 or joel.martens@areva.com. For those in the Americas or Australia, please contact Ratko Vojvodic in AREVA's Lynchburg, VA, USA office, at 434-832-4081 or ratko.vojvodic@areva.com. Thank you for your interest in AIDA eddy current analysis.

STEAM GENERATOR AVB GAP MEASUREMENT BY UT AND ET

S.W. Glass, M. Boudreaux, R. Vojvodic, J. Wyatt, AREVA, USA

ABSTRACT

Flow induced vibration wear has been detected in nuclear power plant steam generator tubes at the location of the anti-vibration bars (AVBs) and at tube midspans. In extreme cases, this can lead to a primary coolant leak and compromise plant operability (Figure 1). Excessive vibration can be caused by a number of factors - one of which is the uncontrolled gap between the tubes and the AVBs. Since there is no direct access to this area of the steam generator AREVA developed two non-destructive-examination (NDE) techniques to measure this gap. One technique is based on the eddy current (ET) method, which is a standard NDE inspection method for SG tubing, and the other is an ultrasonic (UT) method, known to provide very high accuracy distance measurement. Surface riding ET is used to rapidly measure a large number of AVB gaps and immersion UT is compared on a sample of these measurements to validate the ET calibration. The measurements derived from these inspections allow AREVA engineers to assess the condition of the SGs, validate models of the SGs operation and justify remediation actions necessary to arrest or limit further vibration related wear and continued operation of the plant. This paper explains the development and qualification of the techniques and discusses typical site implementation.

INTRODUCTION

Replacement steam generators are frequently designed to support higher megawatt power uprates. This is also true for older steam generators that have had design modification to increase plant power. Since the higher power generators must fit generally within the same space of the older generators**,** this typically implies higher steam flows and in some cases, higher primary flows. In some cases, tube to tube and tube to AVB wear has been detected by eddy current inspections. In extreme cases, the wear can lead to a through-wall leak that can compromise the safety of the plant.

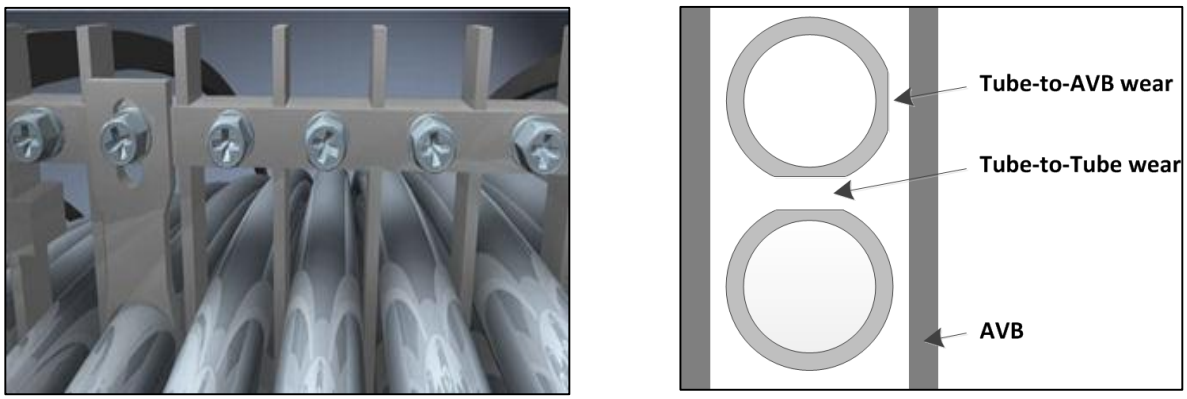

Figure 1: AVBs are placed at strategic locations within the SG - particularly in the U-bend area above the tube support plates (left). Excessive vibration can lead to tube wear against the AVBs and against other tubes (right).

The primary suspected wear cause is Fluid Elastic Instability (FEI) initiated and promoted by several factors including (Ref 1,2, & 3):

- High concentration of steam with fewer and smaller water droplets available to dampen vibration in localized area of tube bundle
- Gaps between the tube and AVB not within design specification resulting in
  - High vibration due to lack of tube restraint at AVB
  - Ineffective AVB "contact force" to stop motion
- Too perfect manufacturing practice resulting in a lack of any side preload between the tubes and their supports

To aid in analysis of these issues and to design and verify mitigation measures for steam generators with pre-mature wear indications, it was desirable to measure the gaps between the tubes and the SG's AVBs. This region of the generator is not readily accessible from the secondary side. Hand-hole openings are available or can be cut to access the periphery tubes but this only provides a limited view of the tube-AVB spacing. The only practical approach for large-scale measurement of these areas is by remotely measuring the gap from inside the SG tube. This same approach is used for the primary inspection of the tubes for cracks, wear, and other degradation and a significant amount of technology has been developed for rapidly inspecting these tubes in compliance with code and regulatory guidelines. An expansion of traditional eddy current and ultrasonic methods to address this gap measurement is a natural approach for this challenge.

BOBBIN EDDY CURRENT

Bobbin eddy current inspections are the most common form of tube inspection. With AREVA's AIDA automated analysis package, the location of AVBs can be mapped automatically (Figure 2). The presence or absence of the AVBs are detected by a change in the low frequency eddy current response. When there is additional conductive material closer to the tube, there is a larger eddy current response. When the AVBs are further away or as in some cases that have been observed, the AVBs have been dislodged or eroded away, the voltage response is significantly reduced or nonexistent. Moreover, if the AVBs are skewed with respect to the tube, this can be detected by the bobbin coil (Figure 3). The bobbin probe however presents an aggregate response to AVBs on either side of the tube. It is not readily possible to separate the signal from each AB. If the tube wall is thinned from wear, this type of signal also influences the AVB signal and cannot be separated.

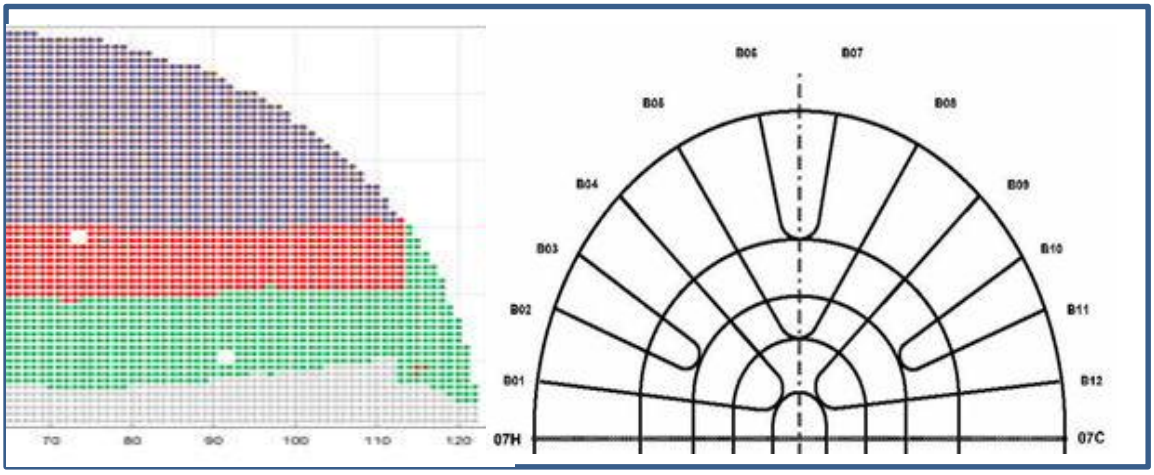

Figure 2: AVB locations can be automatically registered with AREVA's AIDA software from the bobbin eddy current data as part of a normal inspection.

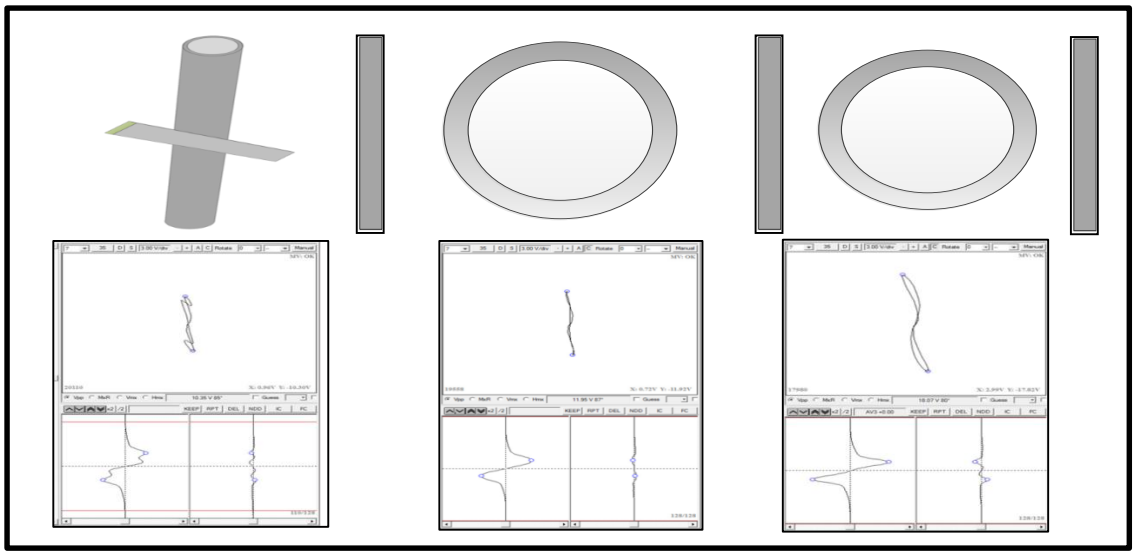

Figure 3: Bobbin probe AVB response- Misalignment (left) = reduced voltage plus distortion; wider gap (center) = reduced voltage, tighter gap (right) = increased voltage

ROTATING AND ARRAY PROBE TECHNOLOGY

A single pancake coil or a pair of pancake transmit/receive coils have a similar response to the presence of metal as the bobbin probe but in a more local sense. The rotating probes are inserted into the tube then pulled while rotating to produce a helical scan of the area of interest. The presence of metallic AVBs produces a measurable local voltage response. The response to each AVB is measured separately. Thus the terrain plot of the rotating probe response can be evaluated for the distance between the tube wall and the AVB on each side of the tube separately (Figure 4).

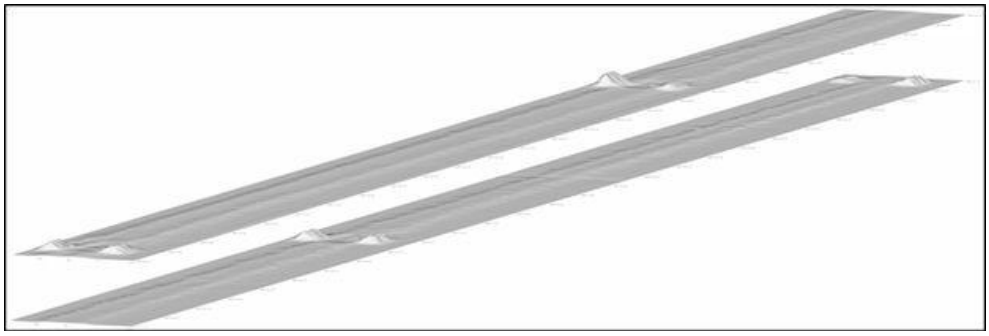

Figure 4: Rotating and array probes measure the local combined signals from AVB proximity and tube wear.

An array probe produces essentially the same response except that instead of one coil or a single pair of coils, the array probes have 36 or more coils arranged around the circumference of the probe. These coils typically are slightly further away from the tube ID wall and they are calibrated as a group. This may explain why the array probe is capable to quantify the gap with the threshold of 0.004" (0.01mm) and the resolution of 0.002" (0.05mm) while the RPC is capable to quantify the gap with the threshold of 0.002" (0.05mm) and the resolution of 0.001" (0.025mm). The array pull speeds however are up to 1m/second or more compared to a few mm/second for the rotating probes. Array probes can achieve inspection rates of 15-35 tubes per hour per probe compared with the MPRC rate of 4-10 tubes/hour per probe. In some cases, two or more probes can be placed in play within a single generator to accelerate the overall inspection speed.

Both the rotating and the array probes however are similarly sensitive to the aggregate effect of wear and the presence of the AVBs. Simplistically speaking, it is difficult to separate signals from the loss of metal associated with tube wear from the addition of conductive metal close to the coils associated with the close proximity of the AVBs. The calibration curve for AVB gap is substantially different as a function of the % tube wear (Figure 5).The tube material however is closer to the sensing coils than the AVBs. By taking advantage of the reduced skin-depth or penetration depth with higher frequencies compared to extended penetration depths for lower frequencies, higher frequencies can be used to quantify wear independent of the distance from the AVBs then this information can be used to calibrate and adjust the response to AVBs primarily relying on the lower frequencies. A family of curves was created and a computer routine was used to aid the analysts to determine the best AVB gap estimate on a production basis (Figure 6).

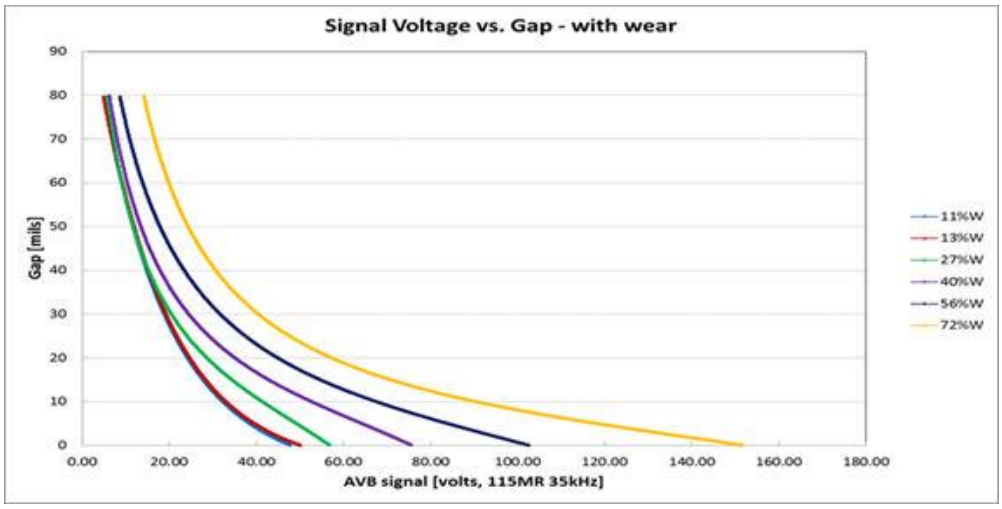

Figure 5: MRPC Response to AVB in the presence of various %TW wear

Independently from the AVB gap measurement challenges, the array and MRP technology has been instrumental to describe and characterize the nature of the tube wear. Automated computer displays have been created to capture the detailed tube analysis to show exactly how the wear is manifested with both transverse tube and axial tube cross sections (Figure 7). The wear can clearly be identified to be opposingly aligned as one would expect for tube to tube wear associated with excessive vibration and tube contact. Understanding the wear locations and patterns is essential to designing and implementing repair and mitigation processes.

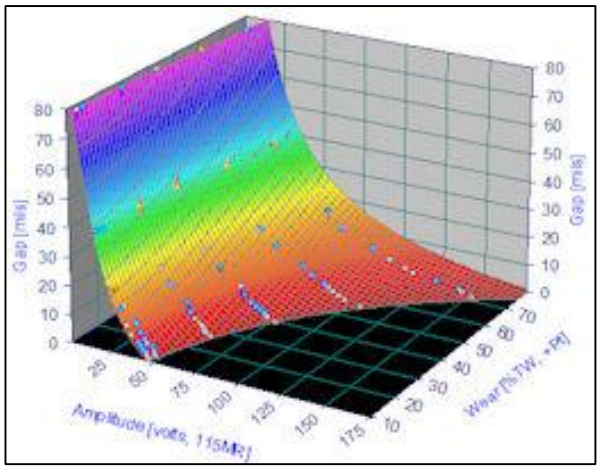

Figure 6: MRPC family of curves created to aid in AVB gap considering wear

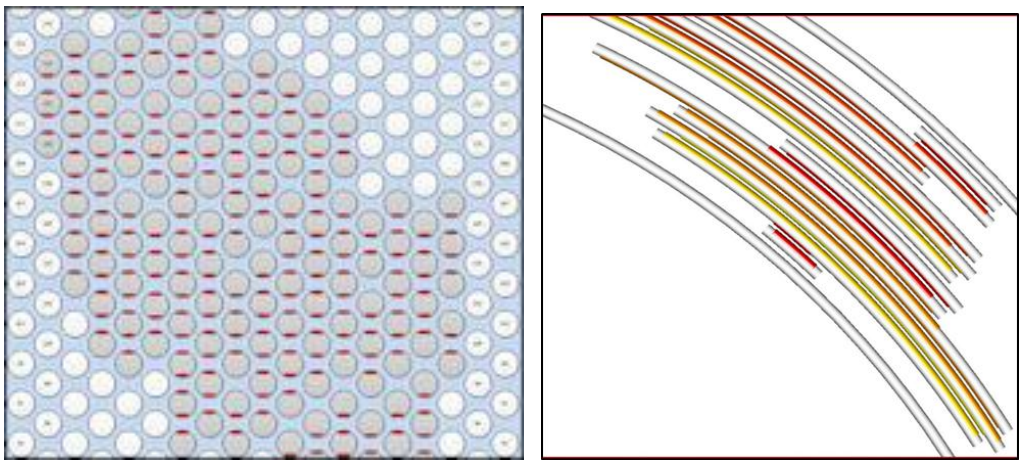

Figure 7: Wear detected - orientation shown on left, color proportional amplitude on right. Note opposing face wear locations

ULTRASONIC GAP MEASUREMENT

Both ET array and MRPC technology have good accuracy but they require precise calibration and can be sensitive to subtle changes in the metallurgy of the tube and the AVB. Ultrasound is relatively insensitive to such metallurgical influences. The ability of ultrasound to penetrate through the tube wall and through the water-filled secondary side of the tube to the AVB and then reflect back from the AVB surface (or adjacent tube surface) through the secondary side water, through the tube wall and ultimately be received by the UT probe was tested. Although there was clearly a signal, analyzing the raw signal reflection to determine the distance between the tube and AVB proved to be difficult or impossible. The natural ringing and noise from the tube was the same order of magnitude or greater than the reflected signal from the AVB. To overcome this problem, software was developed to average the local tube wall noise and subtract it from the signal at each circumferential location around the tube. This enabled even more precise measurement of the AVB gap (Figure 8). This patent pending approach works well as long as there is no tube wear. AREVA NDE Solutions personnel are working to adjust this approach to also work in the presence of wear.

Based on this method, a field deployable UT system was developed (Figure 9). The measurement sequence first requires the secondary side to be filled with water. The UT probe is deployed much like an eddy current probe using a robotic SG bowl-mounted manipulator to align a snorkel with the tube to be inspected. A probe-driver then inserts the UT probe into the tube to the elevation to be inspected. The annulus between the probes fore and aft water seals is filled with water then the probe is rotated and translated through the region of interest generating a helical scan of the AVB region. Inspection speeds are only a few mm/second making the overall production rate only a few tube/hour.

Advantages of the UT examination approach include:

- Low measurement error (<± 0.5mills, 0.013mm)
- Independent of specific tube metallurgical parameters simplifying calibration

Disadvantages for UT measurement include:

- Slow inspection speeds compared to all eddy current methods.
- Need to flood the secondary side of the SG at least to the elevation of the highest AVB gap to be tested.
- Water must also be supplied to the primary side of the tube. This is managed within the UT-360 probe delivery system.
- The current method does not work in the presence of wear. Work is ongoing to improve the technique to work in the presence of wear but this approach is not yet available.

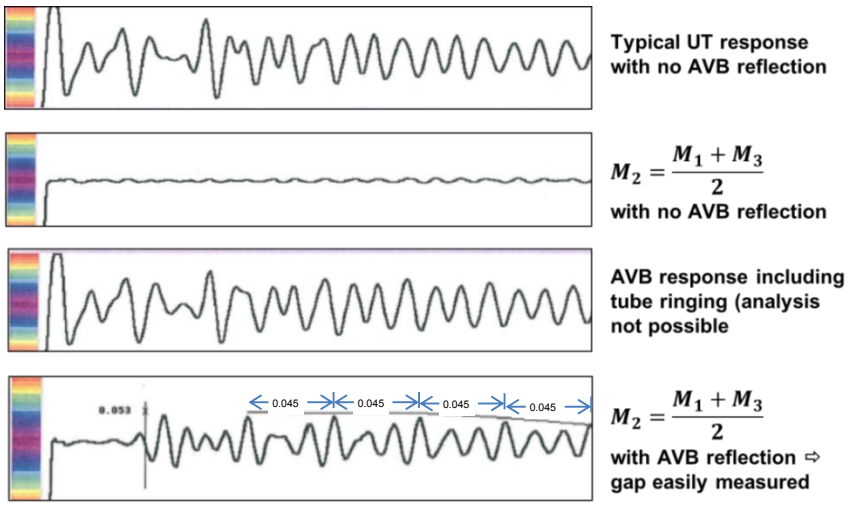

Figure 8: Signal processing algorithm making UT indication from AVB analyzable

Figure 9: UT probe to measure AVB gap in straight tube and u-bends. Note water seals on either end of the probe.

FIELD EXPERIENCE

Since developing these techniques, they have been deployed to 3 sites and measurements have been made on several thousand AVBs. This is not an experimental method. Rather it is a fully qualified field hardened inspection method that can be readily deployed as an extension of traditional inspection technologies.

CONCLUSIONS

Conventional axial bobbin probes are not capable to quantify AVB gaps due to the inability to separate the influence of two AVBs on the signal response. Array probes are capable to quantify the AVB gaps with the threshold of < 0.004" (0.01mm) and the resolution of 0.002" (0.05mm) with relatively short inspection times (15-35 tubes/hour with a single probe). RPC is capable to quantify the gap with the threshold of 0.002" (0.05mm) and the resolution of 0.001" (0.025mm) with or without the presence of wear with longer inspection times (4-10 tubes/hour with a single probe). UT is capable to quantify the gap with the threshold and resolution of 0.0005" (0.012mm) but with no wear and still longer inspection times (~1 tube/hour for 6 AVBs only). These approaches are fully qualified and have been deployed several times for inspection of thousands of AVBs.

REFERENCES

1. Southern California Edison Unit 2 return to service report, Sept 25, 2012
2. Dyke, John M; The Role of Two Phase Coolant in Moderating Fretting in Nuclear Steam Generators, ICON 12, April 23, 2003
3. Au-Yank, M.K., "Flow Induced Vibration in Power and Process Plant Components, ASME Press, New York, 2001

A REVIEW OF REAL TIME VISUALIZATION OF EDDY CURRENTS IN A SMALL BORE-PIPING SYSTEM USING SOLID-STATE HALL SENSOR ARRAYS

J. Lee, C. S. Angani, J. Kim, M. Le, Chosun University, South Korea
Hwa Sik Do, KEPCO, South Korea

ABSTRACT

Small-bore piping system is a significant part in heat exchangers in nuclear power plants (NPPs) such as steam generators (SGs), in which the pressure and temperature are very high. These conditions encourage the initiation and rapid propagation of cracks which degrades the pipeline and threaten the integrity of the system. Over the decades, different NDE systems and probes have been developed and improved to apply in the SGs assessment such as a bobbin probes, motorized rotating pancake coils, X-probes and magnetic cameras for the real time inspection of cracks. The magnetic cameras consist of the arrays of solid state magnetic field sensors. There are different kinds of sensor arrays developed and classified based on the arrangement of sensor arrays for different applications, such as linearly integrated Hall sensors array (LIHaS), area type integrated Hall sensors array (AIHaS), bobbin-type integrated Hall sensor array (BIHaS) and a cylinder type integrated Hall sensor array (CIHaS). In this study a review has been given on development of bobbin type magnetic cameras for the assessment of defects in SGs. Employment of Hall sensor arrays provides a large area of inspection with high spatial resolution. The advantage of high spatial resolution of sensor makes an ease and reliability of evaluation of a crack. The proposed magnetic sensor arrays are used to detect the inner-diameter (ID), outer-diameter (OD) and circumferential stress corrosion cracks in small bore pipelines. Two kinds of specimens, copper and titanium alloy were prepared to verify the effectiveness of the magnetic camera. The images of distorted magnetic fields due to stress corrosion cracks are successfully detected and estimated the crack volume. Results show that the proposed technique can be the potential tool for NDT inspection of SGs in NPPs.

INTRODUCTION

Pipeline structures play a key role in large industrial structures like power plants, petrochemical plants, petroleum refineries and natural-gas processing plants [1]. For example the small bore piping system used as heat exchangers in NPPs. The SGs are the most critical components of the NPP and they are operates at extremely harsh conditions such as high temperature and pressures, which are tend to flow accelerated corrosion (FAC), stress corrosion cracking (SCC) [2]. As a result crack could be initiated, and it may cause the catastrophic failure or emergency shutdown of the plant. Hence, in order to determine the reliability and economic feasibility of a structure, NDT is an effective technology for detecting and evaluating the extent of damages in the structure. Thus, the rapid and accurate inspection of cracks or defects in the pipelines is necessary to prevent the failures.

The SGs are normally manufactured using austenitic nickel-chromium based super alloys and non-ferromagnetic titanium alloys. Generally, 2 to 4 sets of SG tubes were installed in NPPs, each set consists of 3,000 to 16,000 tubes, and SGs are about 20mm in diameter and 21m in length [3, 4]. During several decades, the eddy current testing (ECT) has been reliably applied in the field of NDT, bobbin probes have been the industry standard for general inspection of SGs and heat exchanger tubes [5, 6]. The bobbin probes are reliable and can be used to quantify volumetric flaws such as fretting wear and pitting corrosion, conversely, they are unsuitable for detecting circumferential cracks [7]. Moreover, ECT requires high inspection skills to analyze and evaluate the data [8, 9]. The small

diameter and long length of SGs makes complications in designing the inspection probe, limitation of spatial resolution due to size of coil, and takes high costs. However, different kinds of probes based on different ECT techniques, such as multi frequency ECT, remote field ECT have been developed to obtain 2-D images [10, 11]. Further, motorized rotating pancake coil (MRPC) probes were used with high spiral rotation to obtain 2-D images in SG, but MRPC are 80 to 120 times slower than ECT using bobbin coil [12, 13]. The ever increasing needs of electricity production and the economic globalization required shorter and more cost effective inspection methods, which can reduce the inspection frequency.

To overcome the a foretold difficulties different probes which use solid sate magnetic field sensors were developed in the NDT technology [14-16]. Recently J. Lee at al., proposed more advanced sensors array technology for the real time NDT, such as the linearly integrates Hall sensor (LIHaS), area type integrates Hall sensor (AIHaS), bobbin-type integrated Hall sensor (BIHaS) and cylinder-type integrated Hall sensor arrays (CIHaS) [17-19]. The magnetic camera can be employed in magnetic flux leakage testing (MFLT) and eddy current testing (ECT) methods. In CIHaS solid-state Hall sensor arrays are mounted as bobbin coil probe for easy inspection of pipelines. It has the advantages of high spatial resolution, high speed of imaging so that the crack could be real-time inspected and it has no moving parts as in MRPC in order to get image of a crack. A copper coil has been wound around the sensor array; this coil act like an excitation coil for sensor arrays such as in the conventional ECT. This manuscript reviews the bobbin-type magnetic camera as an NDT system to inspect and evaluate the defects in pipeline structures.

DESIGN OF MAGNETIC CAMERA NDE SYSTEM

The magnetic camera consists of the arrays of solid state magnetic field sensors, such as Hall sensors. The magnetic cameras are classified based on the arrangement of sensor arrays, such as linear arrangement i.e., sensors arrayed in a single line for a LIHaS [20, 21]. The sensors are arranged in multiple rows and columns i.e., like a matrix for a AIHaS [22, 23], In BIHaS the sensors are integrated in a line on a cylinder shape flexible printed circuit board (PCB) and for a CIHaS arrayed as a matrix on a cylinder PCB [24]. Subsequently, the sensors with connecting wires are molded by using anti-shock insulation resin.

The magnetic camera consists of magnetic source, a signal processing unit, a high speed switching circuit, linear guide motor scanner, a PC with real time scanning control and data processing imaging software. The magnetic source can be excited either by DC current to induce the magnetic flux leakage or AC current to induce the eddy currents into the test specimen. Different types of magnetizers have been used for different kinds of magnetic cameras, such as a yoke-type magnetizer used for LIHaS and bobbin type excitation coil which is wounded around the CIHaS. According to Faraday's law of electromagnetic induction the eddy currents will be induced in the electrically conducting test specimen when we bring it proximity to an excitation coil which is excited with alternating magnetic field. The induced eddy currents will be distorted if there is a change in the electrical conductivity or the existence of cracks in the test material. The distribution of perturbed magnetic fields detected and transformed into voltage signals by sensor arrays. Each Hall element includes two power pins and two output pins. The voltage difference between the two output pins, i.e., the Hall voltage, which is proportional to the intensity of the vertical (tangential) direction of the magnetic field, is measured by using a differential type op-amp. The output signals of the sensors from the probe are given to the signal processing unit. This unit consists of amplifiers (AMPs), high-pass-filters (HFPs) and root-mean-square (RMS) circuits. The analog voltage signals which are proportional to the perturbed magnetic fields due to the defects are digitized by using analog to digital (A/D) converters and supplied to the computer to store, process and display the images of scanning area.

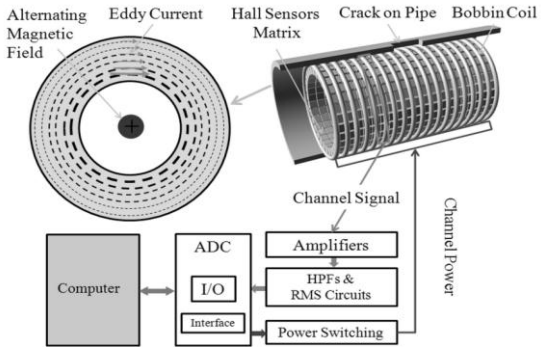

Figure 1. Schematic of the magnetic camera NDE system.

The CIHaS has been developed to inspect the small bore piping system, for example a 1024 InSb Hall sensor elements arrayed (32×32 matrix) with spatial resolution of 0.78 mm on a cylinder shape PCB like a bobbin as show in Fig.2 (a). Diameter and length of the bobbin are 15mm, 25mm respectively. The sensor matrix covers the large area of test specimen to measure the magnetic field distribution with a high resolution. The covered area of the Hall sensor matrix (measurement area) has a curvature angle of 202° on the bobbin, thus the sensing area of magnetic camera is 25 mm × 202°. A 0.25 mm thick copper wire of 120 turns (i.e., excitation coil) is wound around the sensor array to induce eddy currents in to the test specimen. There are two operating modes for a CIHaS, one is linear-scan imaging mode and the other is the area-scan mode. Usually the CIHaS is operated using 32 power lines and 32 output signal lines, which are controlled by a switching circuit. By using this circuit we can switch the power lines of sensors to activate a specific column in the matrix (usually the center column) or the complete matrix of sensors in CIHaS. When a column of 32 sensors in the matrix is activated then the CIHaS works in linear scan mode, in this mode, the magnetic camera acts as a BIHaS. In order to get 2-D images of distributed magnetic filed in the test object, the BIHaS need to scan axially inside a tube specimen, and hence continuous eddy current images can be obtained in the linear scanning mode. Another mode of CIHaS is area scan mode; in this mode all the sensor elements in the matrix have been activated by switching the power lines in a sequential order using a high speed switching circuit. The speed of power switching in the area scan mode is 30 ms, hence the frame speed is 1 fps, thus area-type distribution of the magnetic field can be measured by placing the magnetic camera on a stationary position and we could able to get 2-D images. First the probe is operated in linear scan mode, if there is any defect is detected, than in order to get more detailed information around the crack, area-type imaging can be used depending on the test requirements. The CIHaS is fixed to a linear guide motor scanner and scanning has been performed as shown in Fig. 2 (b). The experiments were performed with magnetic camera on two types of standard test specimens (tubes) made by copper and titanium alloys with different kinds of well defined defeats.

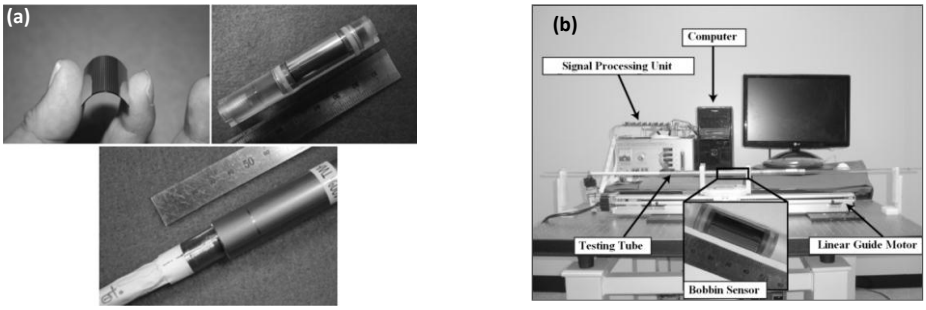

Figure 2. Photographs of (a) CIHaS magnetic camera sensor array, (b) experimental setup.

Experimental Results

Testing of Copper Alloy Pipe

To test the utility of magnetic camera, a standard small bore pipe specimen (ASME/ID PIT CAL. STD for YG12) made of copper alloy (Cu 90%, Ni 10%) has been used [19]. Thickness, inner diameter and length of the specimen are 1.27 mm, 16.56 mm and 500 mm respectively. Several artificial defects of different types and sizes were introduced in to the specimen, such as through holes, inner diameter (ID), outer diameter (OD) and circumferential-type defects in order to simulate the inner-diameter stress corrosion cracks (IDSCCs) and outer-diameter stress corrosion cracks (ODSCCs) respectively. Table I gives the details of defects, here C and CF represent circular hole-type and circumferential-type, ID and OD represent inner-diameter and outer-diameter, and T and ST represent through-hole and stepped through-hole respectively. The volumes of the cracks were calculated by a 3D design tool using the parameters like diameter and the depth of the crack.

TABLE-I

No.	Shape	Width [mm]	Depth [mm]	Volume [mm^3]	No.	Shape	Width [mm]	Depth [mm]	Volume [mm^3]
1	C-ID	3.0	0.30	2.12	7	C-T	1.0	1.27	1.07
2	C-ID	3.0	0.60	4.24	8	C-ST	2.0/1.0	1.27	2.76
3	C-ID	3.0	0.90	6.36	9	C-OD	2.5	0.81	3.98
4	C-T	3.0	1.27	9.60	10	C-OD	4.5	0.38	6.04
5	C-OD	3.0	1.01	7.14	11	CF-OD	3.0	0.22	17.72
6	C-OD	3.0	0.65	4.60	12	CF-ID	1.0	0.22	4.58

Table I. The demotions of the defects which are introduced in copper alloy pipe.

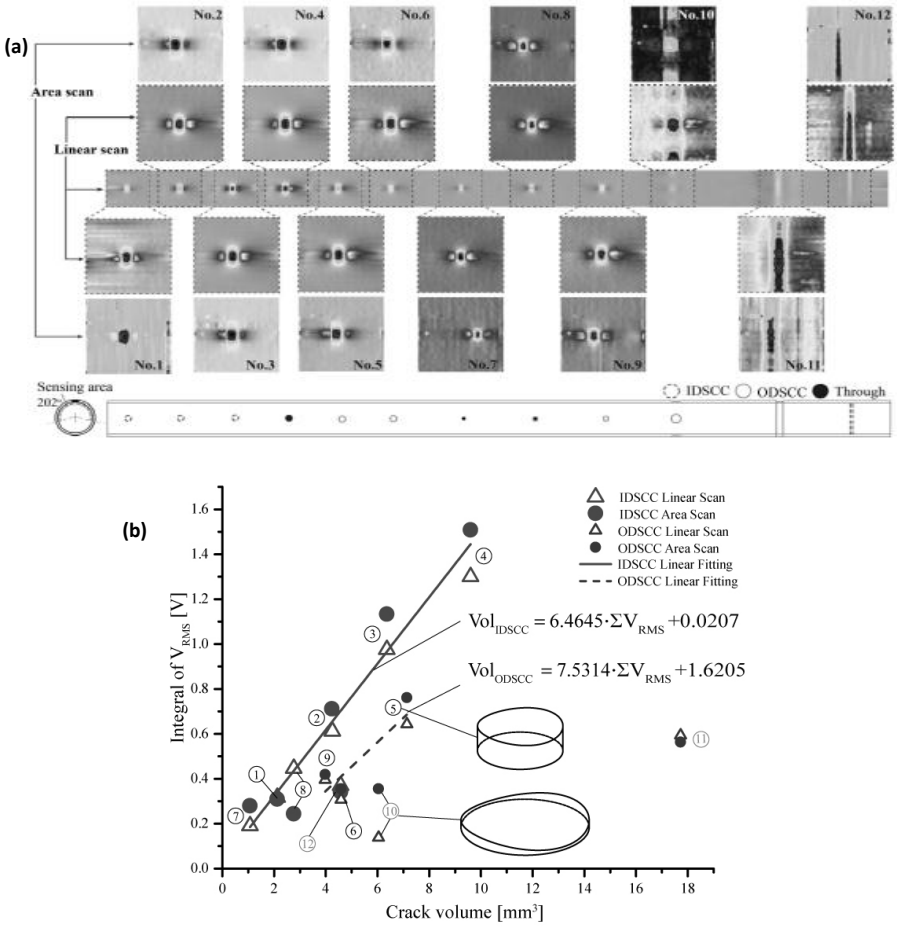

Figure 3(a) Experimental results of line-scan and area-scan images of the IDSCC and ODSCC (b) relationship between integral of ΔV_{RMS} and crack volume.

During the experiment the solid state bobbin type sensor array is inserted in to a small-bore pipe line, an alternating current of 450 mA with a frequency of 5 kHz is supplied to the excitation bobbin coil. As the outputs of the Hall sensors connected to the differential type op-amps, the Hall voltage signals which are proportional to the induced eddy currents from the sensor array are detected. Since the excitation coil is driven by an alternating current to induce the eddy currents in to the test specimen, so the resulting Hall voltages are also alternating voltage signals, hence the root-mean-square (RMS) circuits are used to extract V_{RMS} signals i.e., DC signals from the sensors [25, 26]. The data is analyzed by calculating $\Delta V_{RMS}(\theta, z)$ which is the difference between $V_{RMS}(i, j+1)$ and the neighbor $V_{RMS}(i, j)$ by using equation (1), Therefore, $\Delta V_{RMS}(\theta, j)$ expresses the difference of two V_{RMS} points in two positions in the axial direction.

$$\Delta V_{RMS}(\theta, z) = V_{RMS}(i, j+1) + V_{RMS}(i, j) \quad (1)$$

Where, i and j are the points in angular and axial direction of detected data. Fig.3 (a) shows the experimental image results of OD as well as ID defects in linear scan and area scan modes, which are processed by using equation (1). The images of the cracks generated by the two modes (linear and area scans) exhibit a good similarity; it suggests that the magnetic camera can be used in any of two modes. In addition, as shown in box No. 10 in Fig. 3 (a), though there are 4 ODSCCs, only 3 cracks are visualized, this is because the measuring region of the sensor array has an angle of 202°. Furthermore, circumferential ODSCCs and IDSCCs are also detected, as shown in boxes No. 11 and No. 12, respectively.

$$\Sigma V_{RMS} = \sum_{i=1}^{n}\sum_{j=1}^{m}\left|\Delta V_{RMS}(i.j)\right| \quad (2)$$

An algorithm has been proposed which obtains a relation between the integral of $\Delta V_{RMS}(i, j)$ and the crack volume. The spatial integration ΣV_{RMS} of $\Delta V_{RMS}(i, j)$ is expressed by equation (2). To calculate the ΣV_{RMS}, a certain areas of the image (the defect region) is considered which is a matrix having the size of $m \times n$. The relation between ΣV_{RMS} and crack volume has been given in Fig. 3 (b), large and small symbols in the graph are IDSCC and ODSCC respectively. In addition, open and filled symbols represent ΣV_{RMS} in the linear scanning mode and area scanning mode respectively. As shown in the Fig. 3 (b), ΣV_{RMS} is little larger in the linear scanning mode than in the area scanning mode. Moreover, the ΣV_{RMS} of IDSCCs is larger than that of ODSCCs. The relationship between the ΣV_{RMS} and the crack volume is well fitted with linear curve. However, the data of circumferential cracks No. 11 and No. 12, lie outside of the linear relationship since the crack shape is different and also the eddy currents are minimized because as the induced currents are circumferentially oriented, and these induced currents obstruct the diffusion of magnetic flux through the pipe wall and also as the both the crack and induced currents are in same direction hence the perturbation of eddy currents is minimum. Finally, the data point for box No.10 also resides outside of the linear relationship, this is because the depth of ODSCC is small compared with its width; hence, the crack volume deviates from that of other cracks.

Testing of Titanium Alloy Pipe

After a successful testing of a copper alloy pipe, the magnetic camera is considered to test another important alloy material which is used for SGs, for this purpose a tube specimen was prepared in accordance with ASME SB338 GR2 standard [24, 27] by titanium alloy with inner diameter of 17.28 mm and wall thickness of 0.86 mm. Several artificial defects were introduced in a small bore test pipe, in table-II the parameters of outer diameter stress corrosion cracks (ODSCCs) of different widths and depths are given, where C and CF are circular hole-type and circumferential-type respectively. The hole-type ODSCCs have diameters ranging from 1 to 4.6 mm, and depth between 0.335mm to 0.86mm (through-hole). The width and depth of the ODSCC circumferential defect are 3 mm and 0.163mm, respectively.

No.	Shape	Depth [mm]	Width [mm]	Volume [mm^3]
1	C	0.860	1.0	0.68
2	C	0.697	1.8	1.77
3	C	0.499	2.7	2.86
4	C	0.335	4.6	5.57
5	C	0.155	4.6	2.57
6	CF	0.163	3.0	17.09

Table II. The demotions of the defects which are introduced in titanium alloy pipe.

Solid state bobbin type sensor array is inserted in to a small bore pipe system, an alternating current is supplied to the excitation coil and the resultant V_{RMS} signals from the sensor array are detected. The ΔV_{RMS} (θ, z) is calculated by using equation (1). Fig. 4 shows the ΔV_{RMS} (θ, z) experimental result images of different ODSCCs. Note from the figure that the ΔV_{RMS} image is clearer for the hole with the largest depth (image No.1), this is because of higher perturbed eddy currents. For defects having same width but different depths, the distribution of ΔV_{RMS} become small for the smaller depth defects, as shown in the images No.4 and No.5, since, the eddy current perturbation is less if the depth of the defect from the surface is less. As shown in image No.6, the circumferential defects are also detected and magnetic field distribution is visualized.

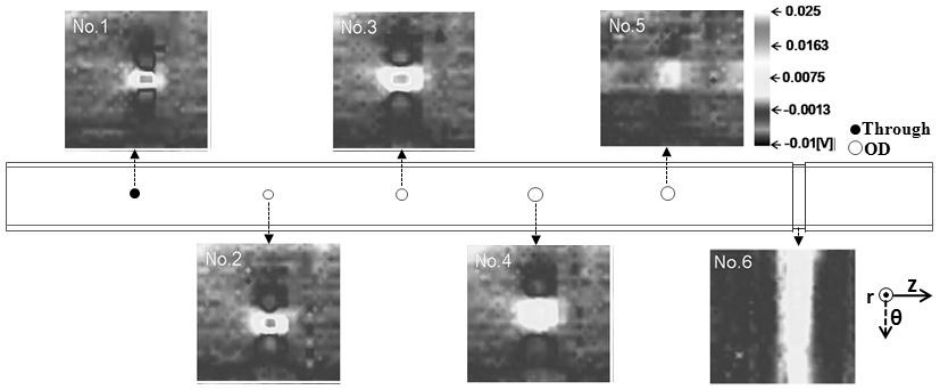

Figure 4. Experimental results of the titanium alloy pipe.

To evaluate the volume of the ODSCC, the absolute integration of the magnetic image ΣV_{RMS} has been calculated by using (2). Though there are 32 x 32 Hall sensors matrix is used to measure ΔV_{RMS} (i, j), but 27 x 30 sensors of matrix are used for the ΣV_{RMS} calculation. Fig.5 shows the volume of ODSCC versus ΣV_{RMS}, and a relation has been obtained between these two parameters as given in (3). By using this equation, volume of the defect can be estimated when we know the absolute integral of an image which is obtained from a defect.

$$Vol = 2.67 \cdot (\Sigma V_{RMS})^{5.402} \qquad (3)$$

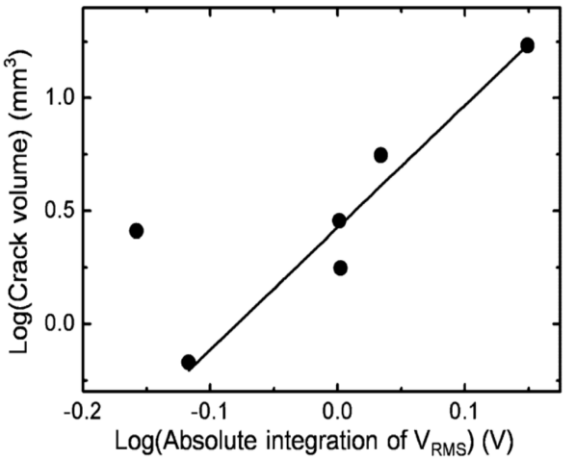

Figure 5. Relationship between ΣV_{RMS} and volume of ODSCC.

SUMMARY

The paper presented a review on the development of bobbin type magnetic camera and its application for the NDT of small bore pipeline structures. The magnetic camera consists of array of solid state magnetic field sensors, and these magnetic cameras are classified based on the arrangement of the sensor arrays. Cylinder type integrated Hall sensor array (CIHaS) is one among them in which Hall sensors are arrayed on circumference of a cylinder like a bobbin probe. The CIHaS can be used in two modes, one is linear scan mode and other is area scan mode, in linear scan mode the CIHaS is acts as bobbin-type integrated Hall sensor array (BIHaS). In order to test the defect detection ability of the bobbin type magnetic camera, two kinds of standard small bore pipe specimens of copper and titanium alloys were prepared with different kinds of artificial ID and OD defects. The experiments were performed in linear scanning mode and area type scanning modes of magnetic camera, both the modes shows a good similarity. Results show the good experimental evidence of the detection capability of the developed bobbin type magnetic camera. ID and OD stress corrosion cracks and also circumferential defects were successfully visualized by using the magnetic camera; an algorithm was proposed and used to estimate the volume of the defects. Results show that the bobbin type magnetic camera can be a potential tool for the NDT of pipeline structures.

ACKNOWLEDGEMENT

This work was supported by the NRF (National Research Foundation of Korea) (2013043688) and by the IT/SW Creative Research Program by the NIPA (National IT Industry Promotion Agency) (NIPA-2013-H0502-13-1008) under the supervisation of MSIP (Ministry of Science, ICT & Future Planning), Korea.

References

1) Nondestructive Testing for Plant Life Assessment, IAEA, ISSN 1018–5518, Vienna, 2005.
2) Stephen M. Bruemmer, “Microstructural and microchemical mechanisms controlling intergranu- lar stress corrosion cracking in light-water-reactor systems”, J of Nuclr. Mat., 1994 216 348-63.
3) Obrutsky L, Renaud R, Lakhan R. “Steam generator inspections: faster, cheaper and better, are we there yet ?” , IV Conferencia Panamericana de END, 2007 1-17.
4) Duck-Gun Park, Kwon-Sang Ryu and Derac Son, Detection of Magnetic Phase in the Steam Generator Tubes of NPP, Steam Generator Systems: Operational Reliability and Efficiency, Dr. Valentin Uchanin (Ed.). 2011, Chapter.9, 165-183.
5) Uchanin V, Najda V, “The development of eddy current technique for WWER steam generators inspection”, Croatia: In Tech, 2011 145-64.
6) Joubert P Y, Le Bihan Y, Placko D, “Localization of defects in steam generator tubes using a multi-coil eddy current probe dedicated to high speed inspection”, NDT & E International, 2002 35 53-59.

7) Obrutsky L, Lepine B, Lu J, Cassidy R and Carter J, “Eddy current technology for heat exchanger and steam generator tube inspection”, 16th World Conference on NDT-2004, Montreal, Canada, 2004.
8) H. M. Sadek, “NDE technologies for the examination of heat exchangersand boiler tubes-Principl es, advantages and limitations,” *Insight, ,* 2006 48(3) 181-183.
9) A. S. Birring, “Selection of NDT techniques for inspection of heat exchangertubing,” presented at the ASNT Int. Conf. Petroleum Ind. Inspection,Houston, TX, Jun. 1999.
10) Joubert P Y, Vourc’h E, Thomas V, “Experimental validation of an eddy current probe dedicated to the multi-frequency imaging of bore holes”, Sensors and Actuators A: Physical 2012 185 132-138.
11) Yushi Sun and Ouyang T, “Applications of flat geometry remote field eddy current techniques in aircraft nondestructive inspection”, 16th WCNDT 2004, NDT.net, Montreal, Canada, 2004.
12) H. Schepens, M. Pigeon, B. Benoist, J. Reuchet, D. Boulanger, “Rotating Excitation Probe for Inspecting PWR SG Tubes”, Rev Progs in Quanti Nondest Eval., 1998 17A 299-306.
13) Yoo J Y, Song S J, Jung H J, Yu H J, Choi Y H, Kang S C, Lee D H, “Prediction of motorized rotating pancake coil probe signals simulated by numerical analysis in SG tubes ”, Key Engg Mat., 2006 326-328 493-496.
14) Gwan Soo Park and Eun Sik Park, “Improvement of the Sensor System in Magnetic Flux Leakage-Type Nondestructive Testing (NDT)”, IEEE Trans. Magn., 2002 38 1277-1280.
15) Sharatchandra W, Rao B P C, Vaidyanathan S, Jayakumar T and Baldev Raj, “Detection of leakage magnetic flux from near-side and far-side defects in carbon steel plates using a giant magneto- resistive sensor”, Meas. Sci. Technol 2008 19 015702 (8pp).
16) Allweins K, von Kreutzbruck M, and Gierelt G, “Defect detection in aluminum laser welds using an anisotropic magneto-resistive sensor array”, J. Appl. Phys., 2005 97 10Q102.
17) Jungmin Kim, Myoungki Choi, Jinyi Lee, “Empolying magnetic sensor array for inspecting cracks in a pipeline”, Sensors Applications Symposium (SAS), San Antonio, TX, IEEE , 2011.
18) Jiseong Hwang, Jungmin Kim, Jinyi Lee, “Magnetic images of surface crack on heated specim-en using an area-type magnetic camera with high spatial resolution”, I2MTC 2009, International Instrumentation and Measurement Technology Conference, Singapore, 2009.
19) Jongwoo Jun, Jinyi Lee, Jungmin Kim, Minhhuy Le, and Sehoon Lee, “Eddy current imager based on bobbin-type hall sensor arrays for nondestructive evaluation in small-bore piping system”, Rev Prog Quant Nondest Eval., 2012 32 502-509.
20) Jun J, Choi M, Lee J, “Nondestructive Evaluation of Austenitic Stainless Steel Using CIC-MFL and LIHaS”, IEEE Trans. Magn. 2011 47(10) 3959-3962.
21) Jun J, Choi M, Lee J, Seo J, Shin K, “Nondestructive testing of express train wheel using the linearly integrated Hall sensors array on a curved surface”, NDT & E Int. 2011 44 449-455.
22) Lee J, Choi M, Jun J, Kwon S, Kim J H, Kim J, Le M, “Nondestructive Testing of Train Wheels Using Vertical Magnetization and Differential-Type Hall-Sensor Array”, IEEE Trans. Instrum Meas., 2012 61(9) 2346-2353.
23) Jun J, Park Y, Lee J, “Real Time Visualization Of Alternating Magnetic Fields Using 2-Dimensional Integrated Hall Sensor Array”, J of Electrical Engg., 2010 61(7) 32-35.
24) Lee J, Jun J, Kim J, Choi H, Le M, “Bobbin-type solid-state hall sensor array with high spatial resolution for cracks inspection in small-bore piping systems”, IEEE Trans. Magn., 2012 48(11) 3704-3707.
25) Jun J W, Hwang J S, Kim K J, Ogawa K and Lee J Y, “Development of signal processing circuit of magnetic camera for NDT of a paramagnetic material”, Key engg. Mat, 2007 353 2379-2382.
26) Jun J W, lee J Y, “Nondestructive evaluation of crack on austenitic stainless steel using sheet type induced current and Hall sensor array”, J of Mech Sci and Tech, 2008 22 1684-1691.
27) ASME Standard, “ASME SECTION II B SB-338-2009 SB-338 Specification for Seamless and Welded Titanium and Titanium Alloy Tubes for Condensers and Heat Exchangers”.

STEAM GENERATOR PRIMARY II

NDE OF SLEEVES AND SLEEVED TUBES

R. Bienentreu, E. Lecour, F. Lesage, J.L. Renaud
Westinghouse Electric Company

Abstract

Sleeving Technique was developed and qualified more than 15 years ago by Westinghouse for the repair of steam generator (SG) tubes of pressurized water reactors of a Nuclear Steam Supply System. The affected tubes with ET indications can be fixed by this repair method. It can effectively substitute the repair method of sealing SG tubes by plugging, as far as the recorded indications do not reach or exceed the plugging criteria limit as laid down in the relevant Guidelines. The working method consists of installing a narrow tube called PLUSS sleeve which spans the defective section of the SG tube. The expression PLUSS stands for mechanical PLUG replacing Sleeve which also stabilizes the SG tube.

The sleeve/SG tube assemblies are controlled by Eddy current testing (ECT). ECT is used to check the proper installation of the sleeve and lateron to inspect the sleeved SG tube in the course of the plant operation.

- EC testing for process verification (NDT) and for baseline inspection are performed just after the installation of the sleeves. The objective is to establish baseline data and initial installation acceptance data on the primary pressure boundary of the sleeve/SG tube assembly: The minimum distance between the sets of 3 expansions and the distance between the top of the tubesheet and the first expansion are verified,
- In-service inspection (ISI) of the sleeved tubes (NDE) is done as part of the periodic inspection program of the steam generator tubing (same inspection interval),

The Plus-Point coil set with motorized rotating unit (MRPC) is used as inspection coil. This type of coil consists in two surfaces riding coils which are perpendicular. The coils are put on the detachable holder that is spring loaded to maintain constant contact with the sleeve inner surface.

The paper will discuss in detail following items:

- Technical Background,
- Implementation of the inspection,
- NDE capabilities and performances,
- Lessons Learned on site jobs.

A RETROSPECTIVE – 10 YEARS OF INTELLIGENT ECT SYSTEM EXPERIENCE

T. Hasebe, T. Shichida, N. Kawase, T. Matsuura, K. Kawata, M. Kurokawa
Mitsubishi Heavy Industries, Japan,
J. Siegel, SOLNEX, USA

Abstract

With its array of specialized coils, the Intelligent Eddy Current Testing (ECT) probe (I-Probe) represents a highly reliable and efficient and comprehensive approach to Steam Generator (SG) tube inspection. As the unique design of the probe evolved, the analysis software had to become more sophisticated. Ultimately, the software that was developed to complete the system, and enable the practicality and efficiency of the technique, is known as the Mitsubishi Intelligent Data Analysis Software (MIDAS). Since its official application in Japan started in 2003, the tightly integrated Intelligent ECT System (IES) is now considered to be a mature and trusted "one-pass" solution.

This year, 2013, marks the 10th anniversary of the official application of the IES technology in Japan. We now have a decade of experience inspecting 100% the SG tubes, full length, in all thermally treated Inconel 600 (TT600) and some TT690 SGs in Japan. Some inside surface axial and circumferential cracks located at the Tube-Sheet (TS) region were detected and some of them were plugged with TT600 SGs. As a result, there have been no instances of tube leakage or requirement for any unscheduled plant shutdowns due to missed defects in Japan.

In this report, we will discuss the wide variety of tube degradation for which the IES technology has proven effective during actual ISIs. We will explain how the IES technology is a highly reliable, efficient tool and well suited to consistently detect all known SG degradation phenomenon. Finally, we will discuss how the MIDAS system has managed to overcome the challenges of managing the massive amounts of data produced by the I-Probe, and we detail how the semi-automated design of its data analysis functionality provides more efficiency, less opportunity for human error, and a "defense in depth" approach to results reliability. Additionally, we will show how the IES technology is useful to monitor secondary side Tube Support Plate (TSP) blockage caused by deposits.

The techniques which combine the highest quality and practicality should be applied to ensuring the safe and economical operation of the nuclear power plant SGs, and replacing from the sampling approach by bobbin and rotating probe (MRPC) to the one pass approach by IES would be a solution. We believe that using the one pass array will not only provide a better quality inspection, but it will ultimately prove to be the most reliable and cost efficient for the plant owners.

Features of Intelligent ECT system

Intelligent ECT shown in Figure 1 is a kind of array ECT probe for PWR(Pressurized Water Reactor) SG tube inspection aiming to actualize both fast inspection (up to 1000mm/s) and detectability equivalent to conventional MRPC probe as shown in Figure 2. Localized sensing area, driver-pickup coil configuration and built-in liftoff cancellation mechanism against both parallel and tilted liftoff enhances the detectability. Figure 3 shows numerical analysis of the distribution of eddy current. Off-axis excitation enables the detection of both axial and circumferential defects at the same time. As both axial and circumferential defects appear on the same channel and analysts can check both at the same time, it is useful for efficient analysis.

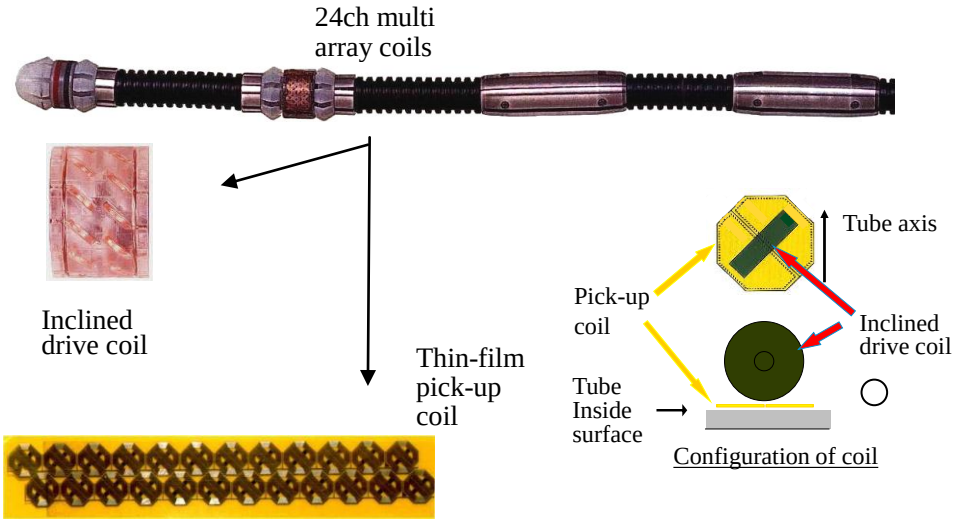

Figure 1 Appearance of Intelligent ECT Probe

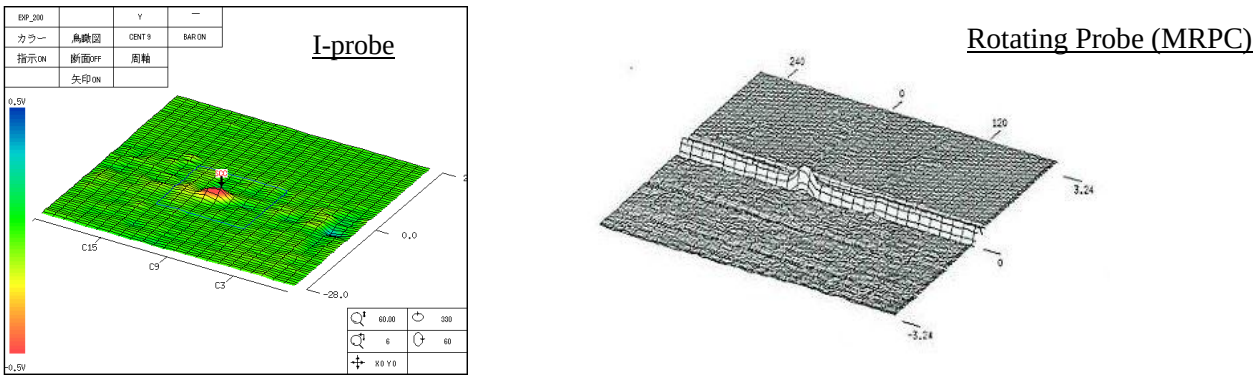

Figure 2 Signal comparisons between Intelligent ECT and MRPC probe
(Circumferential ODSCC (Outside Diameter Stress Corrosion Crack) at Expansion Transition)

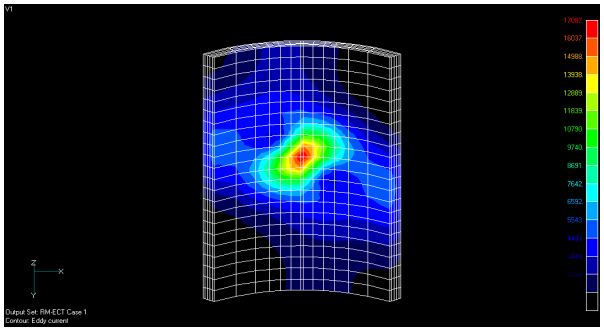

Figure 3 Numerical analysis of the distribution of eddy current

Figure 4 shows the analysis flow of MHI Intelligent Data Analysis Software (MIDAS). This software has a unique collaboration feature between computational automatic processing and skilled human analysts. During preparation stage prior to inspection, preadjustments, such as multi frequency mixing condition, landmark information, is executed by a software administrator. The validity is confirmed using test data including previous outage data. After that, automatic processing is executed. There is a unique signal segmentation process called "Auto Extraction", which extracts all free span regions with amplitude change and structure regions such as TSP or TS, where the potential of defects is comparatively high. Free span region which has no amplitude is not segmented to reduce the analyst load by reviewing such regions. On the other hand, "Auto analysis" is designed to pick up all indications candidates conservatively on the premise of analysis by human experts.

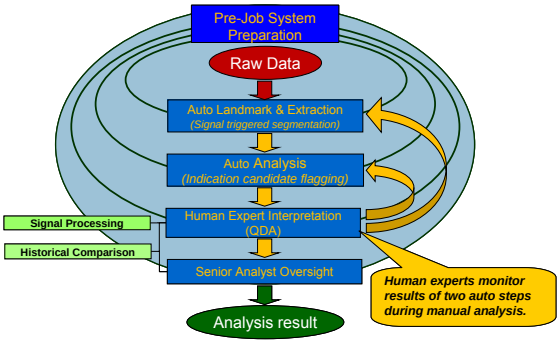

Figure 4 Analysis flow of MHI Intelligent Data Analysis Software

As the result of auto processing, experts can focus on significant signals and can use the capability and experience of analysis effectively. Fatigue and habituation effect may be important potential causes of incorrect analysis in general. Inappropriate threshold of auto classification of signal may be also another important cause.

Our analysis approach is an effective and efficient answer to reduce such concerns. Although data size is 10 times than conventional probe, analysis time is basically same as conventional one.

History of Intelligent ECT system

The trigger of the development of Intelligent ECT system was the Mihama-2 tube rapture, which was the first time when Emergency Core Cooling System (ECCS) activated in Japan. There were many lessons learned from this event and one of them was a request of development of better inspection technology. It had taken 7 years to establish a concept of new array probe and confirm its capability since 1992. Furthermore, subsequent improvement of 4 years was necessary to make the technology into a practical level for field use, such as improvements of production quality and durability, development of small U-bend probe, analysis software enhancement for handling large amount of data, and improvement of signal processing and auto processing. The outcome was qualified by independent qualification committee in summer of 2003 and official application to TT600 SGs started in winter of 2003. At that time, Japanese utilities selected “One-Pass” solution by Intelligent ECT system, which means that full length of all tubes including small U-bend region were inspected by only Intelligent ECT probe.

Figure 5 shows the cumulative number of examined tubes by IES in these ten years in Japan. Although the targets at the beginning were all TT600 SGs, nowadays some TT690 SGs are also inspected by IES. There is no tube leakage since first application of IES in 2003. It should be noted that all inspection regions were full length and total inspected length has become over 8000 km. Also IES’s effectiveness is fully proven around the world as shown in Table 1.

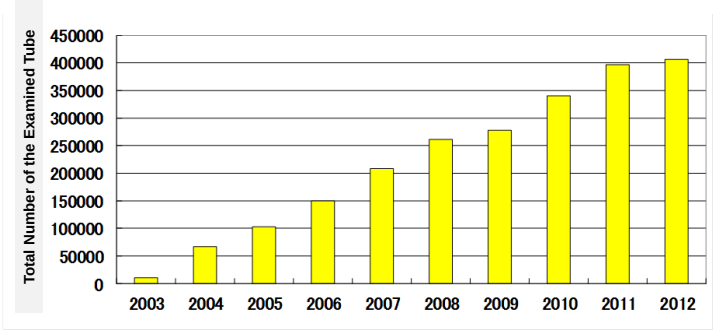

Figure 5 Cumulative numbers of examined tubes in Japan

Table 1 Worldwide experience of IES

Date	Plant	SG Model	Tube Dia.
Feb. 2002	Prairie Island Unit-2	WH 51	7/8 in.
Apr. 2002	Palo Verde Unit-2	CE System 80	3/4 in.
Apr. 2002	Sequoyah Unit-2	WH 51	7/8 in.
Jun. 2002	San Onofre Unit-2	CE 3410	3/4 in.
Oct. 2002	Palo Verde Unit-1	CE System80	3/4 in.
Oct. 2002	Arkansas Unit-1	B&W OTSG	5/8 in.
Jan. 2003	Comanche Peak Unit-1	WH D4-2	3/4 in.
Feb. 2003	Diablo Canyon Unit-2	WH 51	7/8 in.
Sep. 2003	Watts Bar Unit-1	WH D3	3/4 in.
Oct. 2003	Sequoyah Unit-2	WH 51	7/8 in.
Apr. 2004	Callaway	WH F	7/8 in.
Nov. 2004	Manshan Unit-1	WH F	11/16 in.
Apr. 2005	Manshan Unit-2	WH F	11/16 in.
Nov. 2005	OPPD Fort Calhoun RSG	MHI-49TT1	3/4 in.
Feb. 2006	Manshan Unit-1/2	WH F	11/16 in.
Nov. 2008	Oconee Unit-2	ROTSG	5/8 in.
Mar. 2009	Catawba Unit-2	WH D5	3/4 in.
Jun. 2010	Watts Bar Unit-2	WH D3	3/4 in.
Feb. 2010	Manshan Unit-1	WH F	11/16 in.
Nov. 2011	Chinon Unit-2	WH 51	7/8 in.

In these 10 years, 37 tubes with Primary Water Stress Corrosion Crack (PWSCC) in TS were found and plugged as shown in Table 2. Figure 6 shows a PWSCC signal founded near tube edge. As it was circumferential crack, this was one of the most effective cases of Intelligent ECT. Some of the degradation tubes were pulled and investigated its profile and it was proven that the result of IES inspection was collect.

Table 2 PWSCC in TS Experience of IES

Plant	# of SGs	Outage #	# of plugged tubes for PWSCC	Axial / Circ.
Plant A	2	#15	1	Circ.
Plant B	3	#21	1	Axial
Plant C	3	#18	1	Axial
		#19	1	Axial
		#20	2	Axial
Plant D*	3	#16	5	Axial
		#17	13	Axial
		#18	13	Axial

*The SGs of Plant D ware already replaced to TT690 SGs.

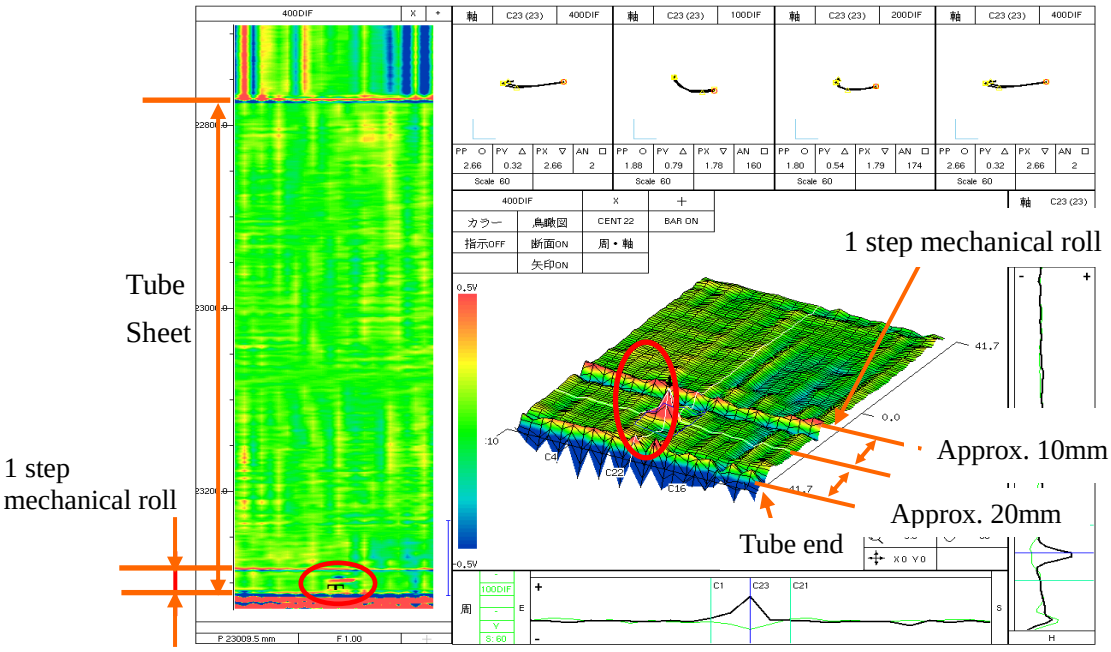

Figure 6 PWSCC signal in TS

Value of Intelligent ECT system

Various degradation modes are still observed at TT600 SGs in worldwide shown on Table 3. Even if TT690 SGs, there are wears caused by loose parts or unintended vibration. As some of them are very localized or circumferential, usage of MRPC or array ECT is better. However, as these damage modes are distributed whole tube, it is difficult for MRPC probe to cover them. As Intelligent ECT can cover all these damage modes and have a fast inspection speed, it can actualize “One-pass” solution and can contribute to raise the reliability of whole tube, whereas combination of conventional bobbin and MRPC sometimes causes complicated planning.

Table 3 degradation modes of SG observed in worldwide

Tube location	Damage mode
(A) Tube Sheet	Axial/Circ. PWSCC
(B) Top of Tube Sheet	Loose Parts Wear
(C) Tube Support Plate	TSP Wear Circ. Fatigue Crack
(D) Free Span	Tube to Tube Wear ODSCC on DENT/MBM
(E) AVB	AVB Wear
(F) U-bend	PWSCC

Figure 7 shows an example of cost comparison. The inspection of whole hot TS region including 100mm from top of TS is presumed to target cracks of whole TS and loose parts wear. As this figure shows, Intelligent ECT inspection is advantageous to MRPC inspection. Moreover, it is assumed that the wider the inspection scope becomes, the better efficiency becomes. The reasons are better probe life by non-surface riding comparing to MRPC, efficient usage of analysis resource due to the collaborative approach of human and auto and eliminating probe exchange by "One-pass" solution.

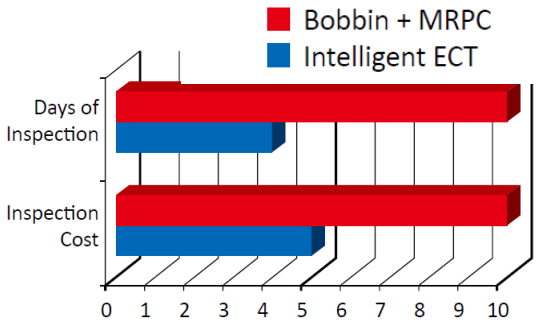

- ✓ (2) Steam Generators
- ✓ # of Tubes: 10,000 (2 X 5,000 tubes/SG)
- ✓ Scan Distance: 26"
- ✓ # of Shifts /Day: 2, Hours /Shift: 12
- ✓ # of Guide Tubes(GTs) / 2 SGs: MRPC=2 vs. I-Probe =4

Figure 7 Example of cost comparison (HOT TS Inspection)

Intelligent ECT also offers the monitoring technique of secondary side TSP flow slot blockage as an extra value of "One-Pass" solution. Figure 8 shows an example of the evaluation. Total tendency or unevenness of the clogging distribution in all TSPs can be automatically evaluated and visualized. As the data of "One-pass" solution by Intelligent ECT can be utilized as is, additional inspection is not necessary. This extra value enables preventing operational issues such as water level oscillations that could leads to depression of SG performance.

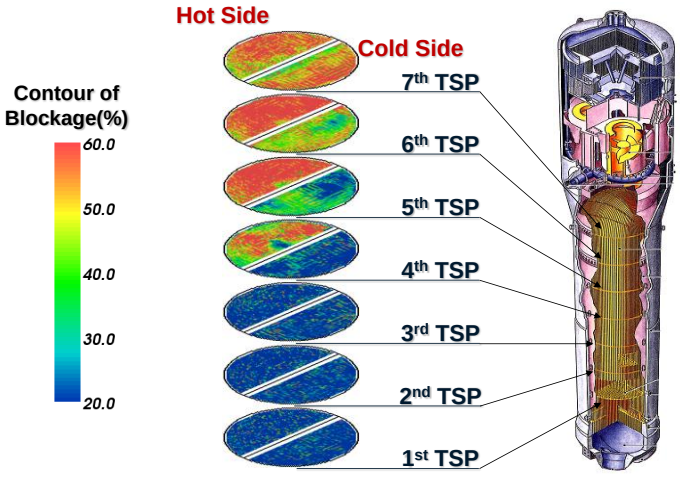

Figure 8 Example of evaluation of TSP Flow Slot Blockage by Intelligent ECT

Conclusion

As the 10th anniversary of IES, its history was looked back. The unique design of I-probe and the analysis software are based on our own concept and the philosophy. IES's long history of the development was triggered by Mihama-2 tube rapture. After the first official application in 2003, it has inspected more than 400,000 full length tubes and contributed to maintain high integrity of Japanese SGs about 10 years. As this paper shows, Intelligent ECT is a mature solution to actualize comprehensive inspection by "One-pass" approach and assure the increase of reliability and efficiency on a practical level.

Reference

1) M. Kurokawa, et al., "Development of New Eddy Current Testing Probe", Proceedings of the 14th International Conference on NDE in the Nuclear and Pressured Vessel Industries, Stockholm, 1996, pp.113-119
2) M. Kurokawa, et al., "Eddy-current Flaw Detector Probe", US Patent. No. 6501267, 1999
3) M. Kurokawa, et al., "Recent Improvements of Intelligent ECT System", 20th Annual EPRI SG NDE workshop, Orland, 2001
4) Y. Asada, K. Tokuhisa, M. Takatsugu, "The Degradation Experience of Steam Generator Tubing in Tamari Unit 1", Proceedings of the 7th International Conference on NDE in Relation to Structure Integrity for Nuclear and Pressured Components, Yokohama, 2009, pp.964-970
5) J. Siegel, M. Takatsugu, et al., "The Value of The MHI Intelligent Array System for SG Inspection", Proceedings of the 9th International Conference on NDE in Relation to Structure Integrity for Nuclear and Pressured Components, Seattle, 2012, pp.352-359
6) M. Michihashi, et al., "TSP Flow Slot Blockage Monitoring by Intelligent ECT", 31th Annual EPRI SG NDE workshop, Brethon Woods, 2012

ARRAY PROBE EVALUATION BY WESTINGHOUSE

D. Stepnick, Westinghouse Electric Company, USA

BACKGROUND

The US nuclear industry experienced a number of unplanned and/or forced outages in the 1980's. Several of these outages were caused by primary to secondary leakage from degraded steam generator tubes. As a result, the industry recognized the need for more sensitive inspection techniques facilitating the early detection of a variety of tube degradation mechanisms.
At the time, there were very few options available relative to ECT probes. The bobbin probe was the standard means to acquire tube end to tube end data. It allowed high test speeds but had less test sensitivity at various locations (i.e. supports, tube sheet, loose parts, etc). Rotating probes were also available but were mainly used for support and tube sheet inspections. They had high test sensitivity but low test speeds. Therefore, the goal was to develop a probe that offered high test sensitivity as well as high test speeds.

Array probes have been in development and various degrees of use for more than 30 years. A few examples of the evolution of these probes are listed below.

- 1980's - 8 Coil Array Probe & 8 x 1 Array Probe
  - Originally designed for dent profilometry
  - Circumferential cracks @ Top of Tubesheet
- 1990's - Cecco
  - Defect detection (circumferential cracks @ tube support plates)
- 2000's – X-Probe & Intelligent Probe
  - With or without a bobbin probe
  - Multiple coil designs
  - Qualification of multiple degradation mechanisms

Based on both field experience and the extensive testing performed by the industry, some clear advantages of the array probe can be found.

- Increased test speeds vs. RPC
  - Up to 30"/sec
- Detection & characterization of Axial, Circumferential and Volumetric Flaws
- Improved POD over bobbin probes
- Single pass inspection (with bobbin probe)
  - Zero to minimal Rotating Probe usage
  - Zero to minimal re-inspection requirements
- Improved wear sizing
- Tube end to tube end data for historical reviews

Example of Increased Sensitivity
Array vs. Bobbin in Detecting Axial ODSCC @ Supports

2009 Bobbin 2009 X-Probe

Similarly, some disadvantages of using an array probe have been determined.

- Decreased test speeds vs. Bobbin
- Large volume of data (~30mb/tube)
  - One solution may be to parse the data to concentrate on areas of interest
- Analyst support requirements (quantity & training)
  - Auto analysis programs are available which reduces the analyst burden
- High probe costs
  - Early procurement & volume discounts could reduce costs
- Probe durability (bobbin coils)
  - Recent design changes have resolved this issue
- Limited qualifications (Axial & circ cracks at dings & dents)
  - Qualify new degradation mechanisms, as required, or
  - In the US, use “extended application” per EPRI tube integrity guidelines

In the US, utilities have elected to deploy array technology, mainly the X-Probe, for a variety of different reasons over the past few years. They can be placed into three separate categories.

- In Replacement Steam Generators, an unexpected indication could eliminate planned skipped inspection outages
  - Tube End to Tube End baseline data for a historical review may be used to verify that the indication existed from manufacturing
- In Replacement Steam Generators, a leaker outage caused by loose parts damage may be the most significant concern
  - Array probes provide enhanced detection vs. Bobbin probes
- In Original Steam Generators, large Special Interest programs
  - Higher speeds vs. RPC
  - Enhanced detection @ various supports

RECENT WESTINGHOUSE X-PROBE EXPERIENCE IN THE US

Plant 1 was interested in obtaining baseline data for potential historical review. It should be noted that this was their 2nd In Service Inspection (ISI) after steam generator replacement, but probe cost & probe life issues precluded prior use of an array probe.

- General Information
  - 2 Loop Westinghouse Pressurized Water Reactor
  - BWI 56/19 Replacement Steam Generators
  - .75" x .043" I690 Thermally Treated tubing – 4,868 tubes/SG
- Existing & Potential Degradation
  - Wear
  - Loose parts damage
- Inspection Scope
  - X-Probe
    - HL & CL Straight Section – Rows 1 thru 7 (approximately 800 tests/SG)
    - Full Length – Rows 8 & higher (approximately 4100 tests/SG)
  - Bobbin Probe
    - Hot Leg Candy Cane – Rows 1 thru 7 (approximately 800 tests/SG)
  - Rotating Probe
    - HL & CL Straight Section SI – (approximately 25 tests/SG)
    - HL & CL U-Bend SI – (approximately 5 tests/SG)
- Outage Performance
  - 144 hour ECT window
  - 2 PEGASYS robots (1 per SG, shared between HL & CL) with dual guide tubes
  - RevospECT single pass analysis
  - Probe usage
    - 10 X-Probes used @ 28"/sec (711 mm/sec)
    - 4 Bobbin probes used @ 40"/sec (1016 mm/sec)
    - 4 RPC probes used @ .5"/sec (12.7 mm/sec)
- Outage Summary
  - Westinghouse/Zetec/Utility team successfully completed the SG inspection scope within the scheduled window
  - Cost neutral when compared to "traditional" standards
    - X-probe vs. Bobbin/RPC
- Results:
  - Utility has tube end to tube end baseline date for historical review

Plant 2 has a history of loose parts & loose parts damage at the top of the tube sheet. They originally planned on an extensive RPC program

- General Information
  - 4 Loop Westinghouse Pressurized Water Reactor
  - BWI CFR-80 Replacement Steam Generators
  - .688" x .040" I690 Thermally Treated tubing – 6,633 tubes/SG
- Existing & Potential Degradation
  - Loose parts & loose parts damage
- Inspection Scope
  - Bobbin Probe
    - 100% full length - (approximately 6,600 tests/SG)
  - Rotating Probe

        - No scheduled tests
    - X-Probe
        - HL & CL - Tube End to 1st Tube Support Plate – (approximately 1,725 tests/SG plenum or 14,000 total tests)
        - Special Interests – (approximately 400 tests/SG)
- Outage Performance
    - 168 hour ECT window
    - 4 PEGASYS robots (1 per SG, shared between HL & CL) with dual guide tubes
    - Westinghouse Auto/Auto analysis programs
    - Enhanced ADS – "rule-based" program
    - Real Time Auto Analysis (RTAA) – "noise-based" program
    - Probe usage
        - 6 X-Probes (with bobbin) used @ 28"/sec (711 mm/sec)
        - 2 X-Probes (w/out bobbin for low rows) used @ 28"/sec (711 mm/sec)
        - 39 Bobbin probes used @ 40"/sec (1016 mm/sec)
- Outage Summary
    - SG inspection scope successfully completed 24 hours faster than planned
    - X-probe speed vs. RPC speed
    - More economical solution
    - X-probe cost and extended life vs. RPC cost and life
- Results:
    - Utility received a more sensitive test (X-probe) for loose parts detection

Plant 3 has their original steam generators, with a variety of existing degradation mechanisms and therefore an extensive RPC program planned

- General Information
    - 4 Loop Westinghouse Pressurized Water Reactor
    - Westinghouse D4 Original Steam Generators
    - .75" x .043" I600 Thermally Treated tubing – 4,578 tubes/SG
- Existing & Potential Degradation
    - Tube End (TE) PWSCC – Hot and Cold Leg
    - Tube Sheet, BLG/OXP PWSCC
    - Top of Tube Sheet (TTS) ODSCC and Loose Parts/Wear
    - 18th Baffle Loose Parts/Wear
    - AVB and TSP Wear
    - PWSCC/ODSCC at Dings
    - ODSCC at TSP Locations
    - PWSCC/ODSCC at Expanded Baffles
- Inspection Program
    - Bobbin
        - 100% Straight length of rows 1-5
        - 100% Full length of rows 6 and above
    - X-probe
        - 100% inspection of row 1 U-Bends
        - 35% inspection of rows 2-5 U-Bends
        - 20% inspection of row 10 U-Bends
        - 100% inspection of the hot leg tube sheet (TEH-TSH+3)
        - 2 rows periphery inspection of the cold leg (TEC-TSP1)
        - 50% inspection of existing dents and dings
        - ~400 Special interest inspection
- Outage Performance

    - 204 hour ECT window
    - 4 PEGASYS robots (1 per SG, shared between HL & CL) with dual guide tubes
    - Westinghouse Manual/Auto analysis programs
    - ANSER manual analysis program
    - EADS automated analysis program
    - Probe usage
        - 10 X-Probes (with bobbin) used @ 22”/sec (559 mm/sec)
        - 4 X-Probes (w/out bobbin for low rows) used @ 22”/sec (559 mm/sec)
        - 36 Bobbin probes used @ 40”/sec (1016 mm/sec)
- Outage Summary
    - SG inspection scope successfully completed 36 hours faster than planned
        - X-probe speed vs. RPC speed
    - More economical solution
        - X-probe cost and extended life vs. RPC cost and life
- Results:
    - Utility received a more sensitive test (X-probe) for both Special Interest and Loose Parts detection

SUMMARY

In summary, there are many different applications and approaches to consider when using the X-Probe for the inspection of Steam Generator tubes. Depending on your inspection scope, the X-Probe can provide an economical and time saving solution

SINGLE PASS ANALYSIS USING DUAL SENSOR TECHNQUES AND AUTOMATED ANALYSIS METHODS

Nicholas Cardillo, ZETEC, USA

BACKGROUND

A single pass inspection is the ability to fulfill the inspection requirements for a tube by inspecting a tube only once and using multiple, independent, complimentary techniques to analyze the data in a single pass. This requires a single pass probe and automated single pass analysis software to analyze the data which is complex in nature. True single pass inspections have only recently occurred and are still in their infancy. Advancements in probe technology and software algorithms alongside the evolution of analysis processes now makes single pass inspections a reality.

Probe technology began with the simple bobbin probe which is fast but has low resolution. Later motorized rotating coil designs emerged which have excellent resolution capabilities but the inspection time is very slow. In the late 1990's and early 2000's probe and instrument technologies advanced to the point where array probes could be economically manufactured and practically applied. The array probe has the speed benefits of the bobbin probe and the resolution of the rotating probe.

Analysis of the resulting inspection data began by using a single party to review the inspection results. Soon afterward, it became apparent that data review redundancy was needed due to various human performance issues. Dual party analysis consisting of separate primary and secondary teams followed by a resolution analysis process to compare the two sets of results became the norm. The resolution process evolved into having multiple pass resolution processes involving independent QDA's (Qualified Data Analyst) and other specialized analyst roles. The manual review analysis burden is large which is resource intensive and time consuming.

To lessen some of this burden and to mitigate human performance issues, auto analysis software was developed starting with rudimentary versions in the late 1980's. These early tools were developed into true computerized data screening software which evolved through the 1990's and 2000's. The screening software was just that – data screening to point out potential signals of interest for the human analysts to disposition. The screening software did not "analyze" the data and make the final call. Significant advancements in signal processing and raw processing power of computers along with advanced algorithms allowed for software to be developed which can detect, extract, measure, and classify signals thus analyzing the data and making a final call without human influence.

SINGLE PASS PROBES

The general inspection workhorse for the evaluation of steam generator tubing is still the bobbin probe. This probe gives fast and accurate results for the detection of volumetric and axially oriented flaw types. Other types of probes such as the X-Probe or motorized rotating probe coil designs (ex. MRPC®) provide further characterization of the signals as well as detection of flaws in the circumferential flaw plane.The combination X-Probe is an example of a single pass probe which incorporates array coils and bobbin coils in a single probe. This probe can record data at typical bobbin probes speeds (1 meter/sec) but has the data resolution comparable to slower (10.2mm/sec) rotating probes. Because the probe contains both array and bobbin coils, dual and independent techniques can be used. This allows for a tube to be inspected only once hence the single pass probe concept is realized. The typical application of single pass probes is that the bobbin data is analyzed to satisfy the base bobbin scope requirements. Then any bobbin signals that need further characterization or other pre-defined special interest exams are analyzed from the array data. If a single pass probe is not used then the tube would have to be inspected again with a rotating coil exam at very slow speeds.

THE NEED FOR AUTOMATION

To take advantage of the all of the capabilities of the single pass probe in an efficient manner, automated analysis software must be employed. Also there are challenges in using a single pass probe that only automated analysis software can overcome.

Data Density

The array portion of the probe generates much more data than rotating probes. This data consists of sometimes hundreds of individual channels and the data itself is complex in nature. This presents some challenges:

1. The volume of data is typically too time consuming to analyze by manual analysis.
2. The size of the data files is quite large making it challenging to transfer the data remotely between analysis parties.

Human Performance Variability

As mentioned, the manual analysis process consists of two party production analysis followed by a multiple pass resolution processes. This analysis redundancy and extensive multiple review process is to account for human performance variability in order to achieve consistent and accurate final results. Even with all of these layers there are numerous examples of inconsistencies based upon human subjectivity. In regards to array data analysis, because of the volume of data these additional human performance factors come into play:

1. Loss of focus: Humans can focus on a small single area at any moment. Because of the volume of data with the array, manual analysis can miss signals of interest.
2. Attention to detail: Manual analysis of array data is very time consuming. Often there are schedule pressures and pressure to keep pace with the acquisition team. This can lead to steps being missed and other analysis methods being overlooked.
3. Lack of consistency: Array data analysis is relatively new and often analysts are not familiar with the data. Some apply the same criteria they would use for bobbin or rotating probes and others do not. This unfamiliarity has resulted in misclassification of signals from steam generator to steam generator and even outage to outage at a particular steam generator. The problem is that these signals are now part of the history for the steam generator.
4. Complacency: Manually analyzing thousands of tubes collected with complex array data for 12 hours a day for 72 hours a week can cause the manual analyst to fatigue which can result in complacent behaviors.

Probe Costs

Single pass probes typically cost more than bobbin and rotating probes. To make them economical to be used for an inspection, it had to be demonstrated that they can be used efficiently to reduce the time of the inspection and yield results that provided more accurate answers than from bobbin probes.

SINGLE PASS AUTOMATED ANALYSIS SOFTWARE

To solve the challenges presented by the single pass probe and to mitigate human performance variability, Zetec developed single pass automated analysis software called RevospECT®. RevospECT® uses multiple, independent, and complimentary methods to analyze bobbin, MRPC®, and array data. In a later section a general overview of the process flow will be described. One of the key benefits of the software is its ability to auto analyze both the array and bobbin data of a single pass probe simultaneously and compare the results from each to come to a final answer or result of a signal of interest. The methodology of comparing the results from two different and independent probe types simultaneously provides for more reliable and accurate inspection results. Flaws can be better characterized when looking at both sets of data.

Consider a three contact broached tube support plate with wear at two of the three contact points in the same axial location. The bobbin probe would detect the wear signal but, due to its design, it will average both signals into one combined signal with a conservative depth estimate.

The high resolution of the X-Probe data would yield two distinct wear signals that can be individually sized which gives a more accurate depth of both indications. This type of analysis would prevent tubes from being removed from service unnecessarily due to the conservative nature of the bobbin probe analysis.

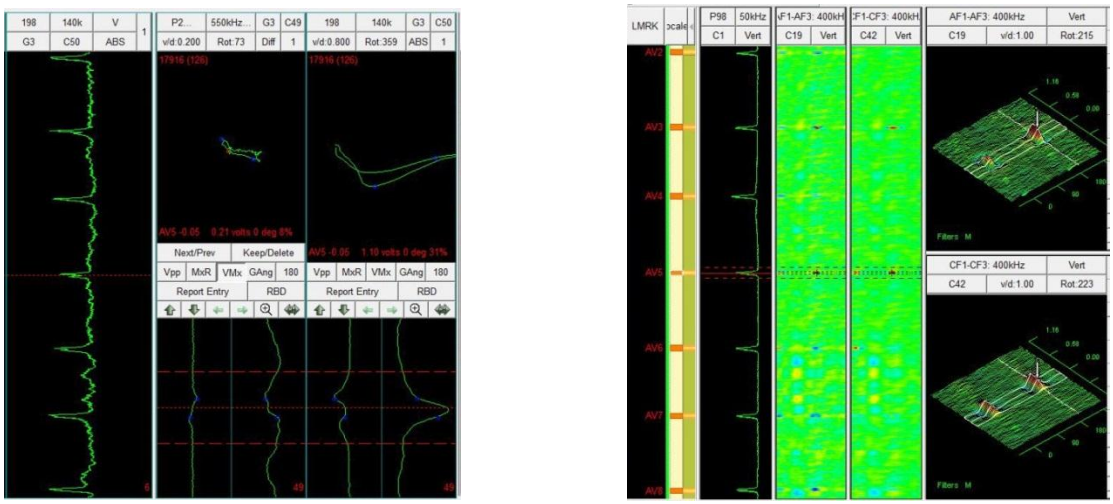

Figure 1 Bobbin data (left) showing only one wear indication compared with X-Probe data (right) showing two distinct wear indications

Likewise an indication at a support structure reported by the bobbin probe will only give the volume of the flaw and not the origination type. A wear signal and ODSCC could appear similar to the bobbin coil where the X-Probe would be able to distinguish the difference and complement the bobbin reporting of the flaw. The X-Probe will also be able to discern whether the indication is at the structure contact point or in the non-contact area, indicative of loose part wear vs. land contact wear. These responses can also be automated and a final decision made within the automated analysis software as the tube is analyzed. There may be no need for further inspections of the degradation site when a combination probe is utilized.

Indications in the freespan can also benefit from dual and complementary techniques. Wear marks from tube buffing or from tube-tube contact can be easily detected with the bobbin probe, however if multiple scars are adjacent to each other, the depth sizing will be conservative and may result in tube plugging unnecessarily. The X-Probe results will quickly show the proper results where multiple indications occur in the same axial plane.

At times bobbin signals can be difficult to discern and the decision to call a signal a flaw varies from analyst to analyst and can be a subjective opinion based on experience. The following figure shows a bobbin signal which was called in history as a wear signal but the X-Probe does not provide a corresponding confirmation. RevospECT® analyzes both sets of data and compares the historical calls. Depending on the criteria, RevospECT® can take these questionable historical calls and now downgrade them if so desired.

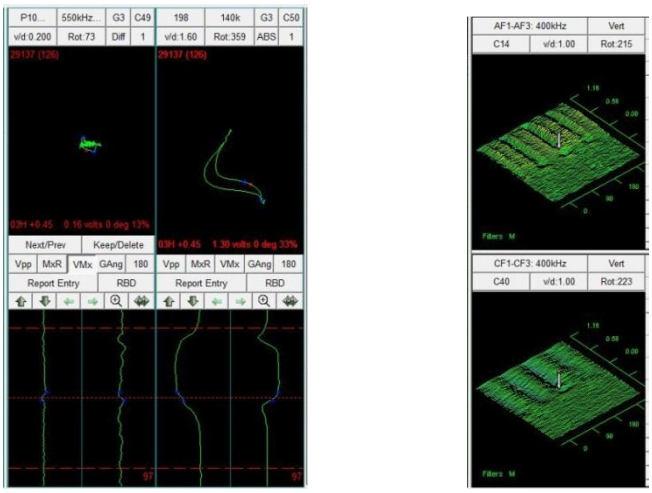

Figure 2 Bobbin data (left) with a questionable historical call and the X-Probe data (right) showing no confirmation

There are at times where the bobbin data may not have the resolution capabilities to detect small flaws in the presence of larger tube support plate structures. The following figure shows an example of a small wear signal in the middle of the tube support plate. In the bobbin data, the influence of the tube support plate, even in the mix, makes it nearly impossible to discern the small wear indication. The high resolution capabilities of the X-Probe allows for this small wear signal to be easily detected and classified.

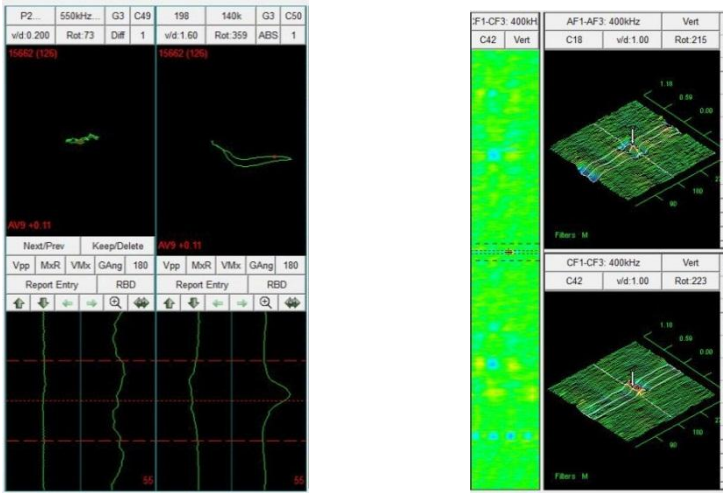

Figure 3 Bobbin data (left) showing no wear indications and the X-Probe data (right) showing a small wear indication in the middle of the tube support plate structure

In the United States, there is large effort to detect foreign materials or loose parts in the steam generator. Traditionally the bobbin probe has been used to detect loose parts but its detection capabilities are limited to larger loose parts that were contacting or in very close proximity to the tube and some distance from a structure. Also depending on the sludge conditions in the steam generator, it is difficult to discern loose parts from sludge deposits. The X-Probe now is widely used for loose part detection and there are numerous examples of array detected loose parts without corresponding bobbin detection. These array detected loose parts are then confirmed by FOSAR or other similar visual examinations. The following figure shows and example of a loose part detected by the X-Probe that is not detected by bobbin.

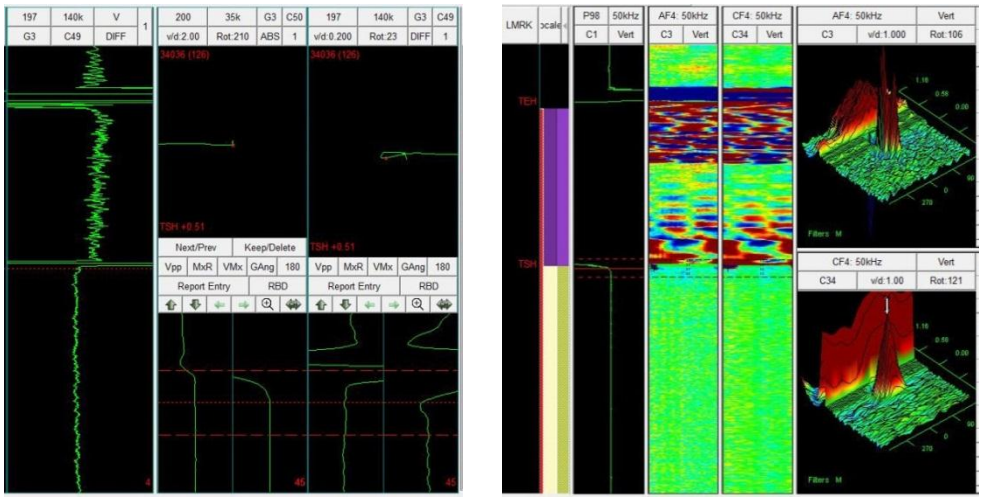

Figure 4 Bobbin data (right) showing no loose part being detected and the X-Probe data (right) clearly showing the loose part

REVOSPECT® PROCESS FLOW

RevospECT®'s single pass analysis configuration is done before the inspection and consists of many detailed sub-configurations including:

1. Channel aliases
2. Locales
3. Analyzers
4. Map analyzers to locales
5. Input historical data
6. Historical Data Comparison configuration

Once the configuration is complete, it is locked for editing and revision controlled.

Analyzers contain two components: "detectors" and "classifiers". Detectors use a variety of methods to detect and then extract the signals of interest. In a given configuration multiple (limited only by processing speed) detectors can be configured. Multiple detection modes are available based on a variety of unique algorithms. These detectors can be independent or combined with other detectors. Classifiers then take the detected signals of interest and measures, discriminates, and applies reporting codes to the signal according to specific criteria. There can be multiple classification rules and multiple test conditions. Single or multiple channels can be applied to classifiers and classifiers can also be independent or combined with other classifiers. Relationship rules are created to assign specific detectors and classifiers to regions of interest or "locales" such as freespan areas or support locations. Detector and classifier sets can be assigned to multiple locales at various levels of detail. The following figure is an example of the relationship rules of analyzers to locales.

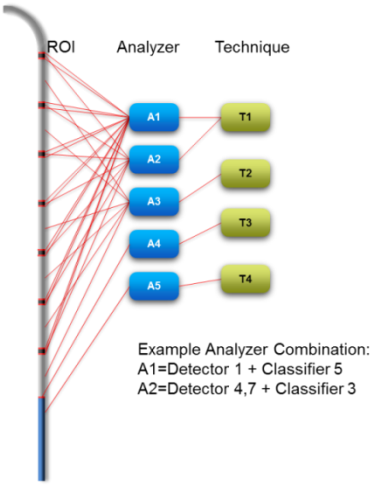

Figure 5 Analyzer to ROI mapping

Once the signals are classified, the process flows into the "Final Acceptance" portion of RevospECT®. Final Acceptance uses proprietary algorithms to perform the following functions:

1. Comparison analysis of the bobbin and array data
2. Historical comparison
3. Overlap resolution: Determining correct calls to report based on historical calls and/or preferred technique or configured methods
4. Uses information from noise analyzers to measure confidence level with the local signal to noise ratio
5. Merging multiple calls
6. Flaw ambient noise measurements
7. Perform resolution decision making processes

From all of these functions, each signal of interest is dispositioned and a final result is produced. The details of these functions and how they all work with each other minimize false positive calls. The following figure is an example single pass flow chart that Final Acceptance can use to properly disposition bobbin and array data collected simultaneously with a single pass probe.

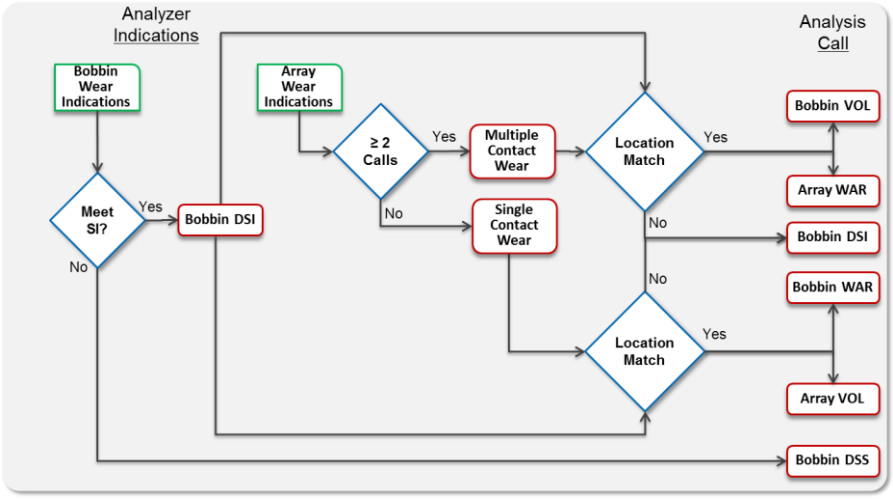

Figure 6 Single pass flowchart used by Final Acceptance

PRACTICAL APPLICATION

The single pass methodology of using a single pass probe married with single pass automated analysis software has been used for inspections since 2010. The Prairie Island Unit 1 steam generator inspection in November 2012 is an example of how the array and bobbin were simultaneously analyzed and compared to reach a final answer. This unit contains two Framatome Model 5619 steam generators with 4868 Inconel 690TT tubes. The tube dimensions are 19.05 mm OD by 1.09 mm wall thickness. The steam generators were installed in 2004 with mechanical wear at the AVB's and tube support plate structures being the only active damage mechanism. Loose parts are a concern as well.

Inspection Overview

In previous inspections 100% full length examinations of the tubes were performed with the bobbin probe. Select tubes were then re-inspected using MRPC® based on bobbin signals of interest that needed further characterization. For this inspection, row 8 and above were tested full length with the X-Probe. For rows 7 and below, the X-Probe was used to test the straight section of the tubes and the bobbin probe was used to test the u-bends. MRPC® was used for 56 tests as a "technology bridge" to demonstrate that the X-Probe had correctly identified all indications. The array data was to be used in lieu of MRPC® for all special interest exams and the bobbin and array data would be analyzed simultaneously with RevospECT® for the final coding of a signal. The array and bobbin techniques are considered independent therefore justification could be made that the analysis could be made in a single pass.

The inspection finished ahead of schedule and fewer probes were used compared to previous inspections. The results of the data showed that the array results were comparable to MRPC® and provided more accurate results as compared to using just the bobbin probe. The loose part detectability of the X-Probe, as compared to the bobbin probe, was better than expected. In one steam generator, the X-Probe provided 21 indications of loose parts and 18 of these were confirmed with FOSAR. The bobbin probe only provided 1 of these 21 indications.

INSPECTION ECONOMICS

This single pass methodology had a significant positive impact of the inspection economics to the utility. There was a 30% reduction in the number of probes that were used. A total of 12 X-Probes were used to inspect both steam generators. There was a significant decrease in the required trips to the high radiation area to change probes. This was due in part to less probes being used but also due to the fact that less probe changes were performed because there was not a need to switch between bobbin and MRPC® probes as with previous inspections. Every trip to the high radiation area requires a person to change into expensive contamination protection clothing. These trips also cause downtime for the inspection and increases personnel radiation dose. The reduction in trips to the high radiation area resulted in a 50% reduction in radioactive waste (probe and protective clothing), and an 18% reduction in personnel dose exposure. The use of RevospECT® and using the single pass analysis model reduced staffing costs by 50%. This accounts for the physical people used for the inspection but also the administrative costs (badging, travel, etc.) associated for these resources. In all, the inspection schedule was reduced by 16% using this single pass inspection methodology.

CONCLUSION

Single pass probes married with single pass automated software has demonstrated how to improve the quality and economics of a steam generators inspection. Analyzing both the array and bobbin data simultaneously better characterizes the signals of interest and provides a more accurate final answer. This model reduces human performance variability and ensures consistent results.

The nuclear industry is facing challenges from competitive alternate resources. There is a strong push in keeping nuclear energy an economically viable option. Inspection accuracy and economics for a nuclear power plant plays a large part into the financial health of plant. Using the single pass model has demonstrated how inspection economic factors such as radioactive waste, radiation exposure, staffing, probes, and schedule can all be reduced.

REFERENCES

1) William Ziegenhagen, “Industry Events and Probe technology Improvements”, EPRI Steam Generator Workshop, Park City, Utah, 2013
2) Kevin Newell, “Automatic Analysis using Dual Test Techniques”, EPRI Steam Generator Workshop, Park City, Utah, 2013
3) Troy Woller, “Enabling Broad Spectrum Analysis”, EPRI Steam Generator Workshop, National Harbor, Maryland, 2009

ACKNOWLEDGMENTS

Troy Woller, Zetec
Tom Bipes, Zetec

ARRAY PROBE IMPLEMENTATION (SMX) ON EDF STEAM GENERATOR TUBES

Q. Mistral EDF - CEIDRE, France
T. Charret, J.Martens AREVA, France

Abstract

In 2009 EDF decided to implement an array probe for in-service inspection of some French steam generator tubes. AREVA NDE Solutions/Intercontrôle, in collaboration with EDF and Zetec, developed the operating conditions for the deployment on site of a combined Bobbin/Array probe called "SAX/SMX". The technique is quite similar to the method developed by AREVA NDE Solutions (USA) that has been used for several years. This inspection has now been adapted to French NPP steam generators.
The standard bobbin coil probe required for EDF tube examination is included within the SAX/SMX probe. The industrialization process includes an automated acquisition cycle, on line calibration setup and advanced data quality verifications plus both manual and auto analysis. This paper discusses the system qualification and how these advanced features benefit the overall steam generator inspection program.

Introduction

The usual EDF inspection plan for steam generator (SG) tubes of a nuclear power plant (NPP) includes the inspection of all steam generators (SG) with axial probes (SAX) and rotating probes. Axial probes can be seen as screening devices, and rotating probes inspections are triggered by indications flagged by the axial probe. The test plan is completed by inspection with rotating probes of specific zones where a known risk has been identified. This is the case of expansion transition (ZTD) at the top of tube sheet (TTS) where residual stress is known to induce stress corrosion cracking in Inconel 600. This inspection plan is compliant with usual ageing of the tubes. However, the material chosen for some SG is known to be sensitive to corrosion (inter granular attack) and stress corrosion cracking (SCC). The main propagation mechanism for cracks favors longitudinal cracks for which the axial probe is well adapted. Circumferential cracking is a rarely observed degradation. The defect depth to be detected is rather small (usually 40% wall) and is particularly hard to detect with axial probes (EDF, 2010).
In the case where circumferential cracking is suspected, rotating probe inspections must be performed. The usual inspection speed for rotating probes is several millimeters per second where axial probes speeds range from 1 to 3 meters per second. The rotating probe's low speed and, in some case limited life span, means that rotating probes can only cover limited zones. In addition, operating the rotating probe is a complex and timely task. Each part of the tube length needs a dedicated probe for the inspection thereby adding more complexity to the inspection plan.
In 2010, EDF investigated the international experience for circumferential crack detection. The survey identified array probes as candidates to cover the target inspection. Array sensors enable inspection of the tube full length, with the promise of better detection rates versus SAX, particularly for circumferential cracking.
EDF set up a rigorous plan to qualify processes and make them available as a practical inspection technology. Two majors constraints where set:

1) Maximize the speed of the probe
2) Adapt the standard EDF axial sensor to the probe
3) The defects EDF is interested in are very general: array technology is assumed to be a screening device, with a specific focus on circumferential crack detection.

The plan included experimentation on four sites to progressively acquire knowledge and competences and to be able to specify such inspections. The test plan started in 2011 at Chinon B2 with the inspection of 50 tubes.

This test was performed relying on US experience with standard array probes for both acquisition and analysis. In the summer of 2012, a French style axial sensor (SAX) was added to the array probe and 100 tubes (with small radii included) where inspected at Paluel 2. Because the SAX sensor differs from the US bobbin since it incorporates a saturation coil instead of a magnet; a special development had to be performed. The acquisition process was a mixture of US procedures and the French procedures. During the autumn of 2013 and summer of 2014, EDF plans to inspect 25 % of the tubes in 5 SGs at two plants. The main goal is to have a fluid acquisition/analysis industrial process. That process includes the formal tests to qualify the combined SAX sensor as well as validating the array sensors: array sensor even though the array sensor won't be qualified according to the French Order required inspection.
To minimize inspection time, the new array probe must include a qualified French style axial sensor. This has some impact on each inspection procedure in order to have an overall coherent process. For example, a reference tube must be on line with automated signal normalization and signals quality checks. EDF also perform the role of independent quality analysis (IQA) in the US procedures which means that acquisition and results have to be pushed "live" to EDF offices for second level analysis of signals. These constraints were considered in conjunction with EPRI experience and the EPRI guidelines (EPRI, 2007)(EPRI, 2002) were followed as closely as possible. The second constraint was related to the performances: EDF sought to increase the overall detection probability for circumferential cracking along the whole tube, even though field experience does not back up that case. This means that the complete length of the tube must be analyzed. As a temporary solution, delayed manual analysis will be performed but the quantity of data, and thus the time spent to analyze data is significant. EDF has asked to test screening software that would allow the analyst to focus only on suspicious indications.

Examination extent
The examination is carried out on the full length of all SG tubes, including the tube sheet, the straight parts and the U Bend except in the low-row tight u-bend areas where only partial tube lengths are examined from each side. The "Candy cane" cycle allows controlling one leg of the tube plus the U Bend and extending beyond to the highest Tube Support Plate (TSP) of opposite leg. If it is necessary to cover all the tube, then two candy cane cycles are necessary from both legs, on the same tube.
Depending on the length of the tubes, 2 different acquisition cycles could be performed, both in a fully automatic mode using AREVA NDE Solution's Acquisition Supervisor:

- Tube rows ≥ 10 (Figure 1):
    - The inspection is performed on the total length of the tube, with saturation current enabled only on the pull,
    - The inspection is performed with a combine SAX /SMX probe.
    - Push & Pull data are recorded

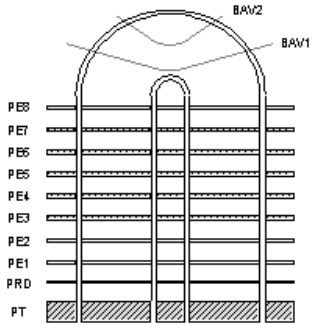

Figure 1: full tube length examination

- Tubes of row < 10 : (Figure 2)
    - The control is performed to minimum 20 mm beyond the opposite highest TSP leg,
    - The control is performed with a single SMX probe,
    - If required, 2 candy cane cycles can be realized to cover the completeness of the tube.

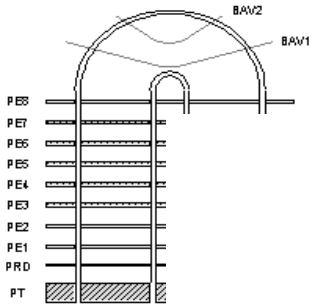

Figure 2: Candy Cane examination

The reference tube is positioned in-line and recorded on each acquisition cycle to calibrate the data and allow data quality verification.
The maximum speed of the probe is 1m/s and is adjusted in order to obtain an accurate sampling rate of 2 points/mm.
The data are recorded in a free specific format in accordance with EPRI guidelines. Both the acquisition software and data format will be EDF qualified in the beginning of 2014.

Probes
Two types of external diameter 7/8 " probes have been developed by the company Zetec:

- The SAX / SMX probe (Figure 3) is a combined probe including 2 sensors:
  - An SMX array sensor containing two rings of 19 coils with a diameter 18,3mm,
  - An SAX axial sensor containing 2 windings for measurement and one winding for elimination of the magnetic permeability indications (saturation current),
  - The SAX / SMX Probe is used in the tube rows ≥ 10

Figure 3.SAX/SMX Combined SAX and X-probe sensors used at PAL2 inspection.

- The SMX probe (Figure 4) consists of :
  - A single array sensor SMX containing two rings of 19 coils, external diameter 18,0mm,
  - The SAX / SMX Probe is used in the tubes of row ≤ 9

Figure 4.SAX low row array probe used for tube inspection (no axial probe incorporated).

Both array and SAX sensors of each probe are rigorously checked in the laboratory following EPRI guidelines and according additional EDF requirements to meet French standards.

Reference tube
The reference tube, acquired during each acquisition cycle is identical to the reference SAX tube used within the framework of the SAX examinations. It consists of several artificial defects as shown in figure 5.

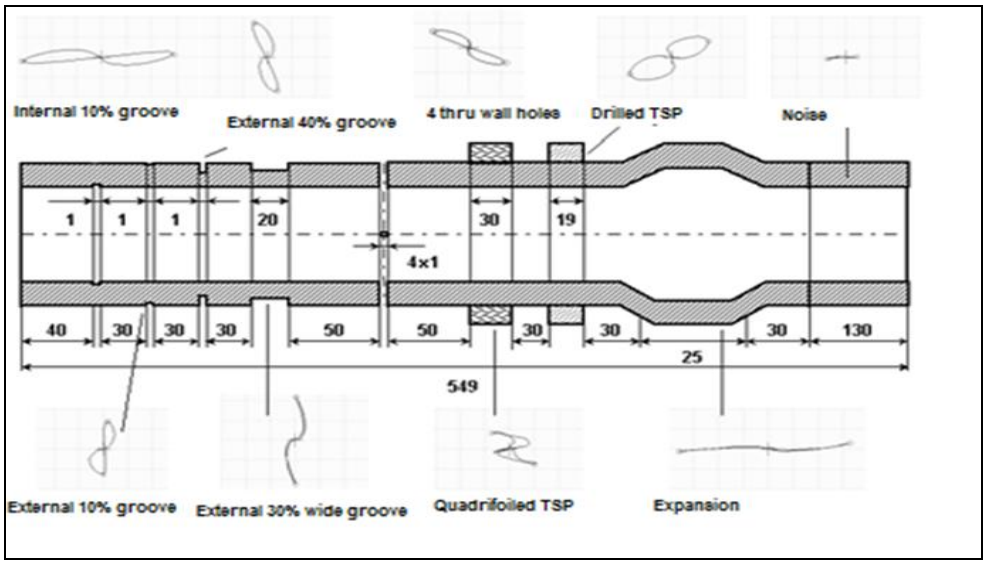

Figure 5: .Schematic of EDF standard for axial probe: insert eddy current Lissajous show expected signals from the axial probe. The same standard is used for array signal's normalization and quality checks. Dimensions are given in millimeters.

Data processing

All the successive steps of the data processing are automatically performed by the Aida Array software, which has been qualified by EPRI for automatic array analysis and will be qualified for EDF in the beginning of 2014.

Calibration

Calibration of ECT channels is made on SAX reference tube using an OD groove (GLE30) for the amplitude setting and Expansion (VD) for the phase setting (Figure 6).

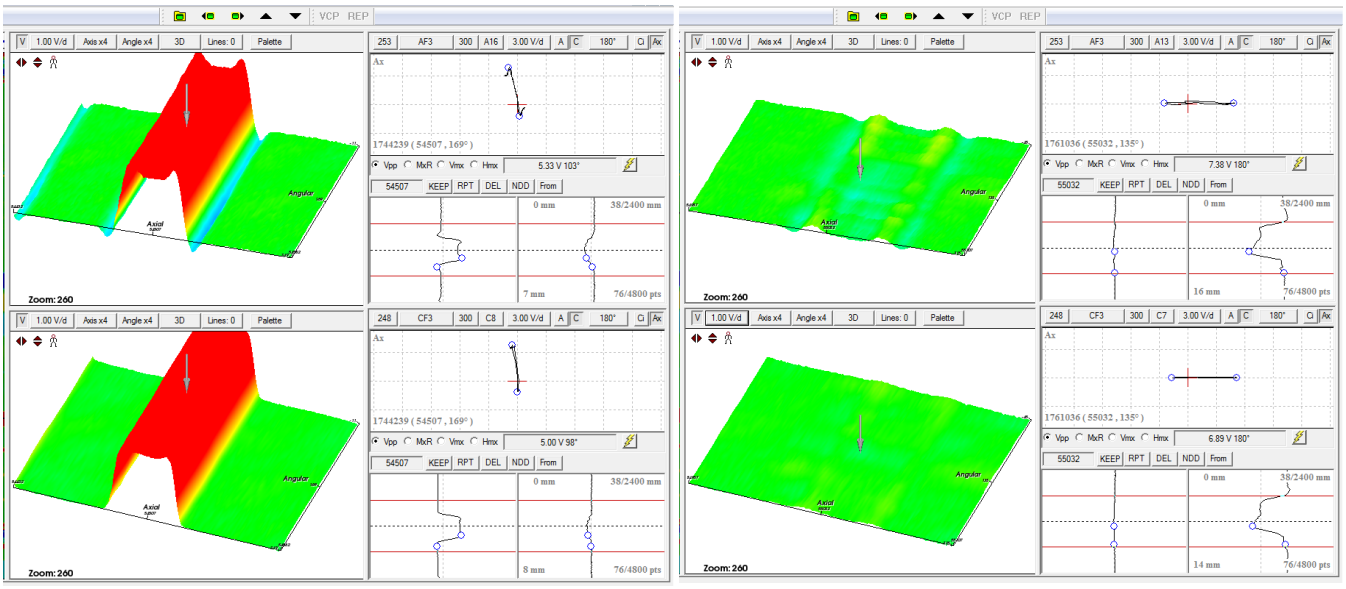

Figure 6.Two AIDA array screen capture showing on the left, 300 kHz signals of the 30% outer diameter groove, on the right expansion signals. AIDA array displays 3D, Lissajous and temporal signals of both circumferential (bottom) and axial signals (top).

Quality check
The quality check of the acquired and stored data is performed on every acquisition. The Quality Check (CQ) consists of several tests with acceptance criteria which can reject automatically the acquisition if not OK.
AIDA Array software prints an assessment sheet recapitulating all the tests, as well as the performed measurements.
Data analysis
At this stage of array probe implementation on French SG tubes, Analysis will be performed manually applying guide lines based on axial or circumferential channel scrolling.
Automatic algorithms developed for EPRI qualification will be applied in parallel with manually analysis before formal implementation for EDF.
Data format
An important requirement was for the file format: to be readable for years to come, so EDF has stipulated the EPRI open format (EPRI, 2008). Intercontrôle modified some fields to cope with on line reference sample and add "vendors" fields to store information for normalization of data quality checks as required by EDF. This format is being used within the AREVA US file format for array inspections.

Conclusion

The first goal of this work, i.e. having a combined array and SAX probe ready for inspection will be achieved. At this stage, EDF is satisfied with the acquisition and analysis near-term compromises because a limited number of SGs are targeted to be inspected this way. A supplemental industrial test plan on 900 MW and 1300 MW SG will be performed in the coming years. This test plan will incorporate the decommissioned SG (Sherlock program) programmed in 2014/2015.
For the future, array technology can offer opportunities for many defects. Some prospective work is in progress (EPRI guidelines Annex I seems to be an interesting starting point). EDF also notes that array technology is demanding for hardware and software. Low rows examinations where one-shot full tube inspections are not possible, is an example.
EDF will explore these possibilities and determine if performances are sufficient. The compromise between fully qualified slower rotating probe inspections versus full-tube array technology is being evaluated. The expectation is for the process price to decrease coupled with an increase of the overall inspection speed by running the axial technology in parallel with conventional axial probes. The analysis part of the process should not be forgotten as the quantity of data generated by array technology is tremendous. Full manual analysis will lead to prohibitive and cumbersome work schedules. Only the help of automations (detection of RAS tubes or zones, automated analysis …) and correct measurements tools (surface, volume, multi frequency measurements…) will enable inspection generalization to other SGs.

References

1. **EDF. 2010.**Circumferential ODSCC at drilled TSPs Bugey 3 experience. Vail : 29th EPRI SG-NDE Workshop, 2010.
2. **ENIQ. 2007.**European methodology for qualification of non-destructive testing. 2007. EUR 22906 EN.
3. **EPRI. 2002.**Eddy current Data Quality Parameters for inspection of Steam Generator Tubes : Vol 4. array probes. Palo Alto : s.n., 2002. 1007314.
4. **2008.**Standardized file format. Charlotte : s.n., 2008.
5..**2007.**Steam Generator Management Program:Pressurized Water Reactor Steam GeneratorExamination Guidelines, Revision 7. Paol Alto : s.n., 2007. 1013706.

STEAM GENERATOR

TSP BLOCKAGE OF STEAM GENERATOR MONITORING METHOD BY INTELLIGENT ECT

T.Hasebe, Y. Kohashi, T.Shichida, N.Kawase, T.Matusura, K.Kawata
Mitsubishi Heavy Industries, Japan

Abstract

Array ECT (Eddy Current Test) probe called Intelligent ECT probe (I-Probe) has a capability to inspect tubes more accurately than bobbin ECT probes.

I-Probe provides “One-Pass” solution by combination with Mitsubishi Intelligent Data Analysis System (MIDAS). It has been applied as full length official inspection in Japan since 2003, and we have much field experience to date. I-Probe can increase reliability of Steam Generator (SG) maintenance.

On the other hand, a phenomenon in SG secondary side is known that scale deposits clog flow holes of quatrefoil type tube support plate. Water level oscillation of secondary side caused by excessive blockage of scale deposits may become one of the unintended trouble possibilities. Periodical monitoring of blockage condition and applying countermeasures like secondary side cleaning are important. However, there was not a monitoring method of blockage condition using data of Intelligent ECT. Therefore, the new method has been developed to evaluate blockage condition using I-Probe data. The software was also developed and it evaluates all flow holes in SG automatically and visualize the evaluation results. This new method may contribute increase of reliability of SG maintenance, because the new method makes possible to monitor whole SG.

Background

SG in Pressurized Water Reactor has several thousand tubes. These tubes are supported by Tube Support Plates (TSP). TSPs have a quatrefoil type flow hole shown in Figure 1 which is designed to avoid condensation of environmental impurity in secondary coolant between a tube and a TSP. However, the flow holes still could be clogged by scale deposits during the plant operation. There is a possibility that this phenomenon in SG secondary side may cause water level oscillation of secondary side and power reduction. Area ratio which be clogged scale deposits is defined as blockage ratio. To reduce the blockage ratio, it is necessary to apply some kind of cleaning technology, such as mechanical cleaning by water jet or chemical cleaning. Therefore, periodical monitoring of blockage condition and applying appropriate countermeasures at appropriate timing are important.

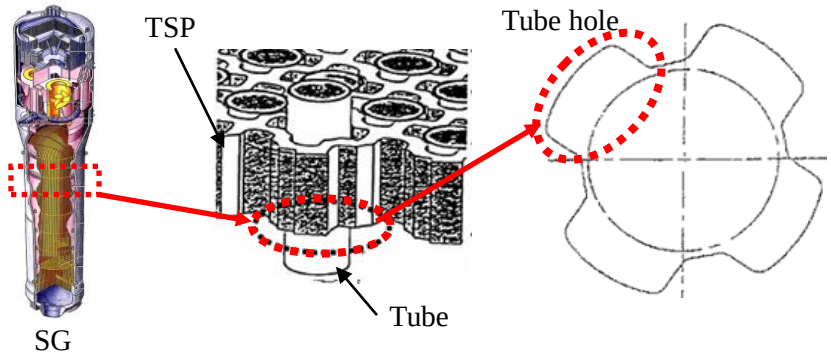

Figure 1 Tube support plate and flow holes

Table 1 shows typical monitoring method of TSP blockage. As each method has advantage and disadvantage, it is common that the combination of both methods is applied. Generally, ECT method is used for comprehensive monitoring and is applied with high frequency. On the other hand, visual method is used for confirmation of ECT result and detail understanding, and is applied with low frequency. Figure 2 shows an example of visual monitoring. The detail of the distribution of deposits can be seen clearly.

Table 1 Monitoring method of TSP Blockage

Method	Advantage	Disadvantage
Visual monitoring	● Can confirm detail feature of scale deposits	● Accessible area is limited by limitation of mechanical access ● Data acquisition speed is comparatively slow
ECT	● Accessible area is unlimited ● Data acquisition speed is comparatively fast ● No need for additional acquisition in case of using defect inspection data	● Indirect evaluation

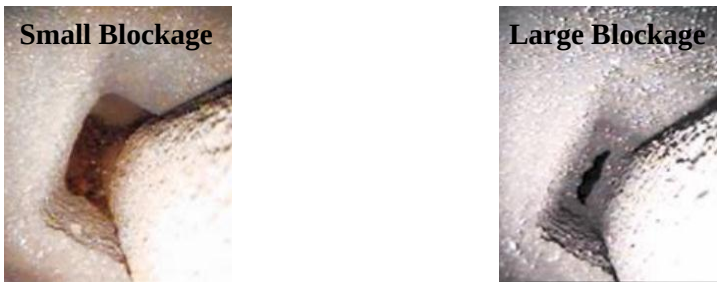

Figure 2 Example of Visual monitoring

ECT inspection is applied periodically for integrity of SG tubing. Conventional method was a combination of high speed bobbin probe and high detectability rotating probe complementing the disadvantage of each as shown in Table 2. In these days, array ECT probes for SG tubing which have advantages of both bobbin probe and rotating probe have already developed. I-Probe is a kind of array ECT probe for SG tubing and is applied to all old type SG tubes made of alloy 600 in Japan in full scale, which means full length of all tubes are inspected with only I-Probe. As the result, we could get simple solution called “One-Pass” solution, avoiding complicated inspection planning and getting full cover by high detectability coil. Field use in full scale has already 10 years history and shows the maturity. However, as the method of TSP blockage evaluation using I-Probe data didn’t exist, we still needed to handle bobbin data. That is a reason we developed the new evaluation method of TSP blockage using I-Probe data.

Table 2 ECT inspection for tube integrity

	Probe	**Detectability**	**Inspection Speed**	**Blockage Monitoring Method**
Conventional Inspection	Bobbin ECT Probe	Middle	Fast	Established
	Rotating ECT Probe	High	Slow	
“One-Pass” Inspection	Intelligent ECT Probe	High	Fast	**Our Target** Newly developed

Blockage monitoring method with I-Probe

I-Probe is an array probe with 24 coil elements (12 coils x 2 rings). Figure 3 shows appearance of I-Probe and Table 3 shows the features. Localized sensing area, drive-pickup coil configuration and built-in liftoff cancellation mechanism against both parallel and tilted liftoff enhances the detectability. Off-axis excitation enables the detection of both axial and circumferential defects at the same time. Non-surface riding assures better probe life than contact ECT probe like rotating probe. Figure 4 shows an example of I-Probe signal at tube expansion region. I-Probe has an equally detectability as rotating probe.

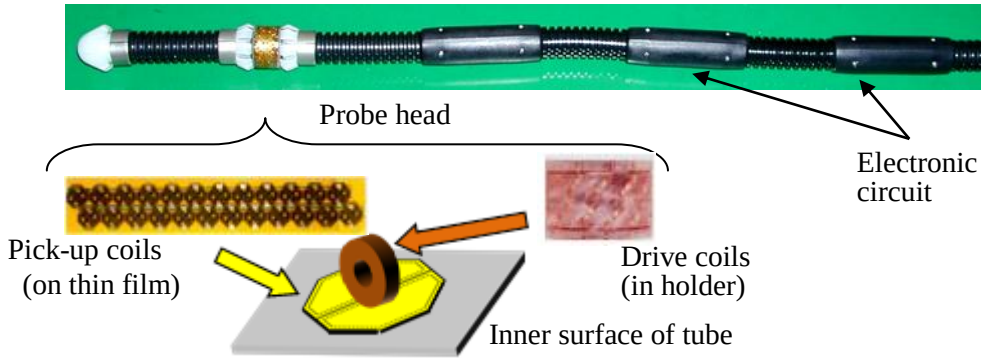

Figure 3 Intelligent ECT probe

Table 3 Features of I-Probe

Item	Description
Probe type	Mutual induction / Self-comparison type
Pick-up coil	Thin film coil
Drive	Off-axis excitation
Sensor layout	24 sensors in a circumferential direction (12 coils x 2 rings)
Contact / Non-contact	Non-contact

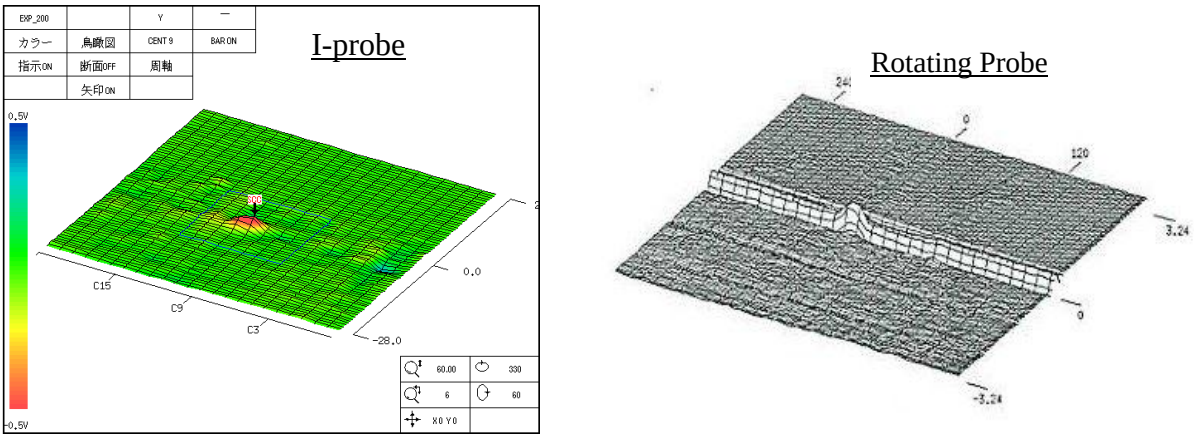

Figure 4 Signal examples of I-Probe

Figure 5 shows an example of scale deposits signal of I-Probe at TSP. Vertical direction of C-scan corresponds to axial direction of the tube and horizontal direction corresponds to circumferential direction of a tube. Color of C-scan corresponds to signal amplitude of ECT data and the region of high amplitude is shown redly. 4 blurred axial regions of C-scan correspond to 4 flow holes of TSP. Scale signal is shown as high amplitude area at the bottom side of TSP. Figure 6 shows the comparison of ECT signal and image of visual monitoring of both small and large blockage. As this figure shows, there is a correlation between blockage ratio and ECT signal amplitude. Our new technique focuses attention on this amplitude.

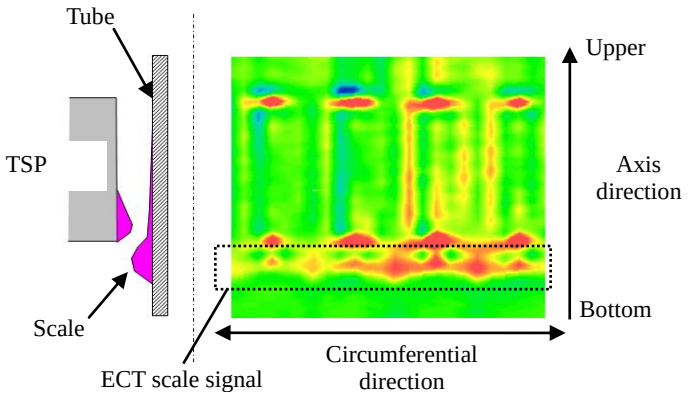

Figure 5 Explanation of scale deposit signal of I-Probe at TSP

Item	Small Blockage	Large Blockage
Image of Visual monitoring		
C-Scan of Intelligent ECT	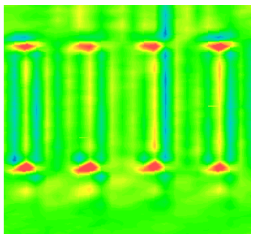	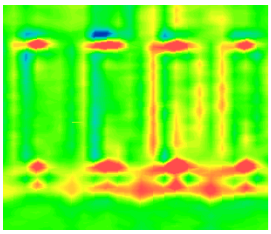

Figure 6 Example of blockage signal

Figure 7 shows flow diagram of blockage evaluation. Left side of this figure shows the inspection of defects for the tube integrity. Right side shows the flow of newly developed blockage evaluation. As this flow shows, acquisition data for tube integrity is also used for blockage monitoring as is. Newly developed software can evaluate all TSP signals of all tubes automatically and can visualize to blockage map and average blockage ratio.

Figure 8 shows an example of blockage color map that displays all TSPs from 1st TSP to 7th TSP. Left side of color map shows HOT side, and right side shows COLD side. As this figure shows, this color map makes intuitive understanding possible about the difference of blockage ratio between TSPs or unevenness of the blockage distribution within a TSP.

Trial of Blockage Evaluation

We confirmed new evaluation method using field data where typical 2 different cleaning methods were applied.

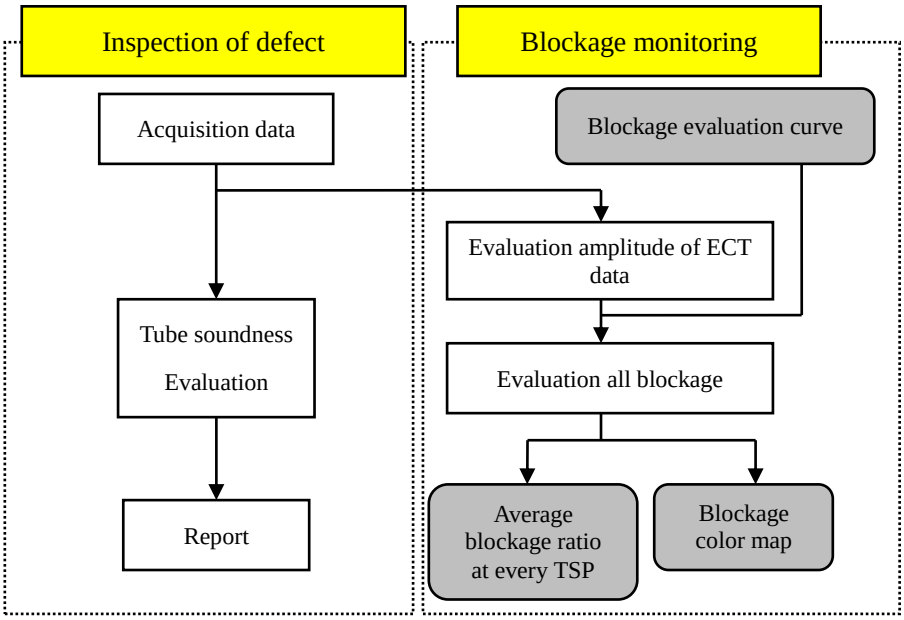

Figure 7 Flow diagram of blockage evaluation

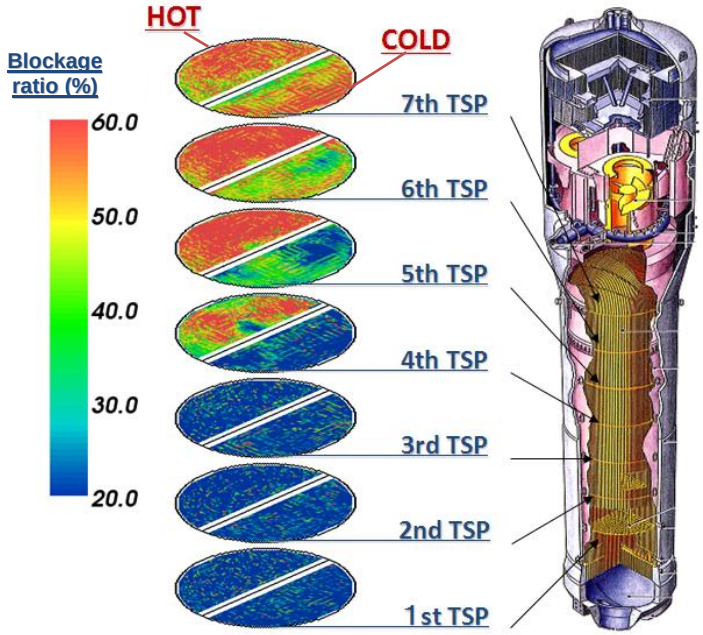

Figure 8 Blockage color map

Figure 9 shows blockage color map in case of mechanical cleaning. The letter "N" in this figure means outage number. A mechanical cleaning is usually applied to half area of 3 upper TSPs. Figure 9(a) shows color map after first cleaning, and Figure 9(b) shows color map after second cleaning. It is confirmed that the non-red area of upper 3 TSPs on Figure 9(a) corresponds to the fact of half cleaning. It is also confirmed that 3 red linear areas of 3 upper TSPs corresponds to inaccessible area of mechanical cleaning. From these results, it seems that these color maps can visualize the distribution of blockage appropriately.

Figure 10 shows blockage color map in case of chemical cleaning. The letter "N" in this figure means outage number.

Chemical cleaning was applied every outage after “N+1”. It increase blockage with the plant operation from “N” to “N+1”, because an operation from “N” to “N+1” proceeds clogging in flow holes without applying chemical cleaning. Especially in upper TSPs, the blockage ratio was increased a lot. After “N+1”, whole blockages are decreasing by chemical cleaning. It seems that these color maps can visualize the historical transition of blockage.

Figure 11 shows historical transition of blockage ratio in case of chemical cleaning. It is also confirmed that average blockage ratio decreases in proportion to the number of cleaning.

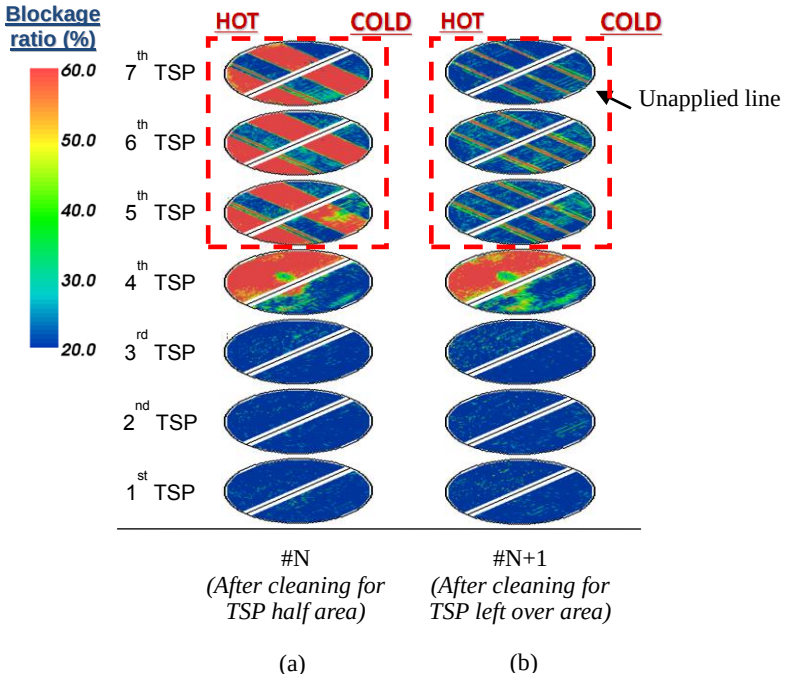

Figure 9 Historical change of blockage color map by mechanical cleaning

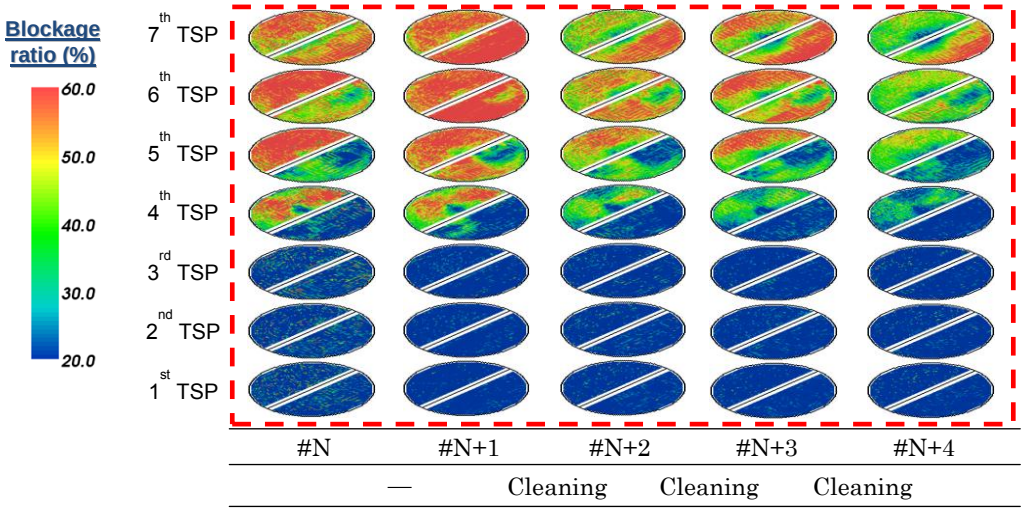

Figure 10 Historical transition of blockage color map by chemical cleaning

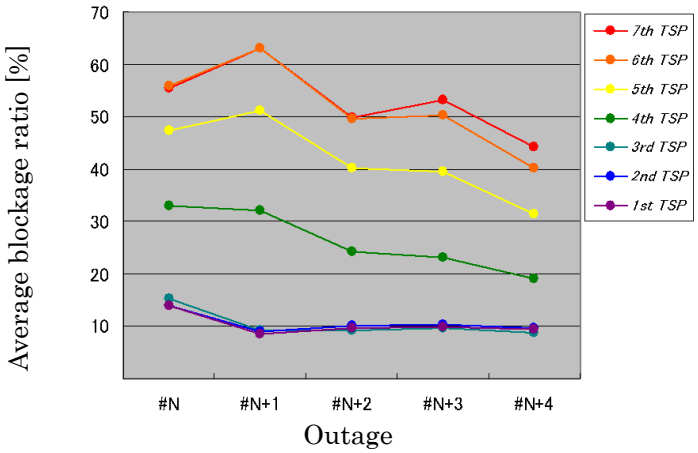

Figure11 Historical transition of blockage ratio by chemical cleaning

Conclusion

We developed the method for the blockage evaluation with array type ECT probe. The method enables blockage evaluation automatically. It is confirmed that the color map is useful to visualize distribution and historical transition of blockage condition. The historical comparison of average ratio can shows transition of blockage ratio.

Reference

1) Y. Asada, K. Tokuhisa, M. Takatsugu, “The Degradation Experience of Steam Generator Tubing in Tomari Unit 1”, Proceedings of the 7th International Conference on NDE in Relation to Structure Integrity for Nuclear and Pressured Components, Yokohama, 2009, pp.964-970

2) J. Siegel, M. Takatsugu, et al., “The Value of The MHI Intelligent Array System for SG Inspection”, Proceedings of the 9th International Conference on NDE in Relation to Structure Integrity for Nuclear and Pressured Components, Seattle, 2012, pp.352-359

PROBE BASED ON A GIANT-MAGNETO-RESISTANCE (GMR) SENSOR FOR THE THICKNESS MEASUREMENT OF MAGNETIC DEPOSIT ON STEAM GENERATOR TUBES

S. Paillard, B. Marchand, J. M. Decitre, CEA Tech, France
M. El Guedri, EDF - STEP, France

Abstract

Eddy current (EC) inspection of Steam Generator (SG) tubes is an important aspect of the safety of the nuclear plants. In particular, gradual deposit of ferromagnetic material on the free-span area creates an additional weight which has to be evaluated. In this context, EDF and CEA start a collaborative work to explore the potentialities of new technologies for industrial non-destructive testing method, used for the tube inspection, by developing a probe based on a Giant-Magneto-Resistance (GMR) sensor. EC probes used in Non Destructive Testing (NDT) are mainly based on winding coils. This technology has shown good efficiency and gave good results in several applications. Nonetheless, winding coils lose sensitivity when frequency decreases. Thus, detection and moreover thickness measurement of magnetic deposit, which requires low frequency use, is hardly achievable.

To bring solution and to improve non-destructive techniques, new technologies have been investigated at CEA LIST: magnetic sensor GMR. In the aim of thickness measurement of magnetic deposit, a probe based on a GMR sensor, optimized using the NDT platform CIVA, has been specially designed for this need. A comparison with an axial probe used in industrial NDT is lead, and experimental results are given on SG tubes mock-up with several thickness of magnetic deposit.

Keywords: Application areas of NDT (RPV-SG-Internals and primary circuit-Other component)

TUBE SUPPORT PLATE CLOGGING AND SECONDARY SIDE DEPOSIT: PERFORMANCE EVALUATION USING SIMULATION AND SITE RESULTS

N. Le Lostec, Y. Kernin, C. Ferré, J.l Martens, AREVA, France
D. Dumay, EDF - CEIDRE, France

ABSTRACT

Because of tube support plate (TSP) flow hole clogging by corrosion products, the secondary fluid flow through the steam generator can differ (in velocity, pressure, flow rate) from the design basis. Deposits on the freespan of the tubes (length between TSPs) may have similar effects. These differences have a significant effect on the safety and performance of the steam generator [1]. For example, at Cruas Nuclear Power Plant (NPP), the combination of specific features of these steam generators (no tubes in the central area of the tube bundle and no anti vibration rod support for some tubes in this region) and clogging of TSP holes led to an increase in flow velocity which produced excessive vibration and subsequently circumferential fatigue cracking of tubes.

Three techniques are used for deposit estimation: eddy current testing, magnetic flux leakage testing and visual examinations. Here we propose a simulation-based performance evaluation of eddy current and magnetic flux leakage techniques for the measurement of TSP clogging and secondary side deposits. The software used for numerical simulation is Flux3D developed by Cedrat [2]. Simulation results in different configurations are compared to those of measurements on mock-ups. Probes, analysis method and analysis software are proposed for automated evaluation of TSP clogging and secondary side deposits from on-site measurement results.

INTRODUCTION

Tube support plate clogging and tube secondary side deposition [1]

Corrosion products in the secondary loop of nuclear power plants form deposits inside the steam generators. In particular, deposits have been observed on the tubes and inside tube support plate holes; see Figure 1 and Figure 2. Note the nature of clogging in Figure 2 is asymmetrical for the top and bottom of the TSP. This observation is essential to the clogging assessment approach.

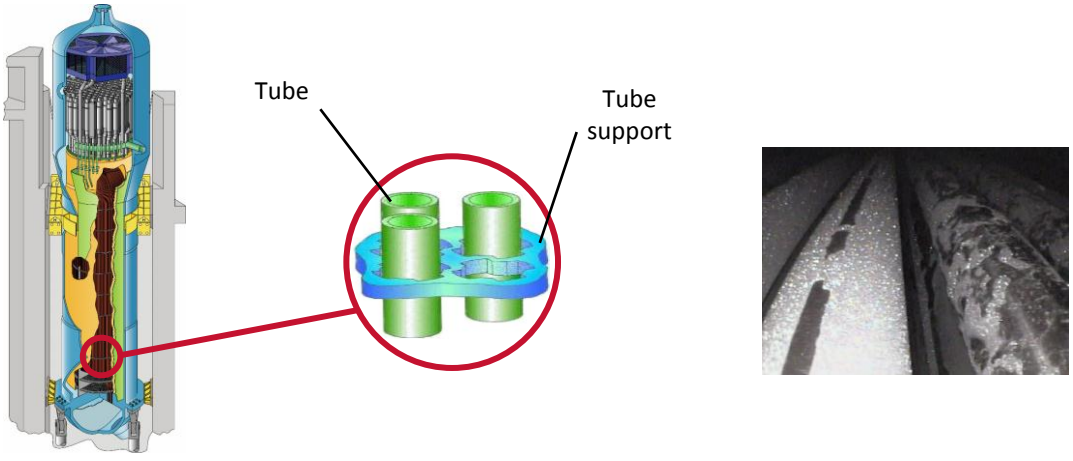

Figure 1 - Left: steam generator cut away. Right: steam generator tube secondary side deposit

Clogging of tube support plate broached holes can induce a velocity increase of the fluid flow. In the case of the tube not being supported by anti vibration bars, excessive vibration and stress on the tube due to fluid structure coupling can occur. These tubes are subject to high cycle fatigue and are likely to develop fatigue cracking.

On a larger scale, clogging affects how the tube support plates and tie-rods are subjected to loads from the water-steam flow and local loads can be greater than the design loads. Higher than anticipated stresses can also result from accident or off-design situations, in which the supplementary stresses due to clogging might be a risk factor for safety. Steam generator operational efficiency is also affected by clogging and deposits as noted below:

- deposit on the tubes reduces the heat exchange between primary and secondary sides,
- circulation ratio, an index of the mixing inside the steam generator, is decreased,
- the amount of water available for cooling in the secondary part of the steam generator can be decreased, which reduces the safety margin, in particular there is a risk of water level oscillation for rapid power transients.

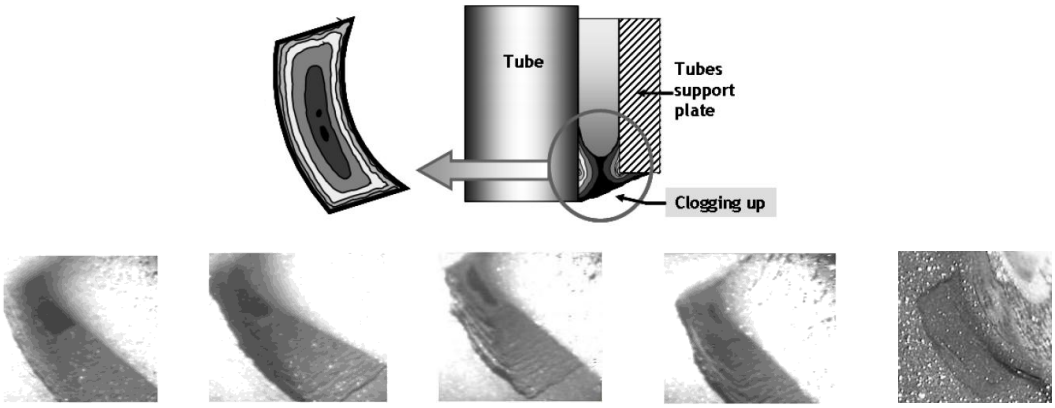

Figure 2 - Top: Tube support plate clogging sketch. Bottom: hole diaphragm clogging, from very small clogging to complete obstruction

Moreover the eddy current examination of steam generator tubes is disturbed by deposits on their external or secondary side, therefore possible defect detection performance might be affected.

For all these reasons NDE techniques are required to monitor the scale and progression of clogging and deposits to take actions such as chemical cleaning. NDE techniques for clogging and deposit estimation also serve the purposes of cleaning efficiency checking.

Industrial solution: probe and software for estimation of clogging % occlusion and deposit

AREVA NDE Solutions has developed a specific combined probe in the frame of these requirements. It consists in an eddy current axial sensor (SAX bobbin probe) dedicated to the measurement of free span deposit as well as the usual tube examination, associated to a FLIP sensor (flux leakage technique based) for tube support plate clogging estimation [3]. The probe measurements are exploited using Aida G3, an AREVA signal processing and visualization software. It performs an automated analysis using transfer function between signal and clogging/deposit and delivers graphical representation of clogging/deposit maps on steam generator 2D/3D views (See Figure 3).

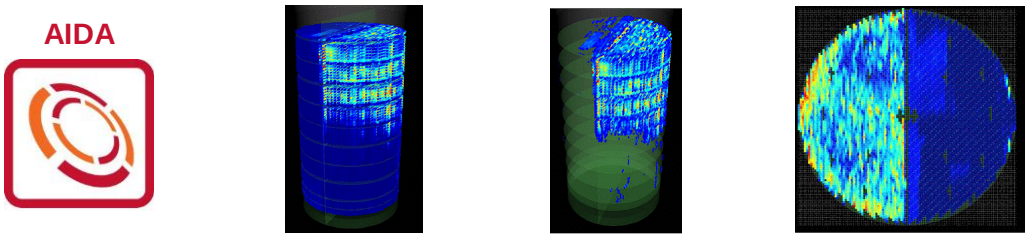

Figure 3 - Left: Aida G3 software logo. Right: 3D and 2D samples of clogging/deposit mapping from probe measurement onto steam generator geometry

A performance evaluation of the industrial solution is in progress in collaboration between EDF and AREVA, involving mock-up measurements, numerical modelling and simulation and site results. This is the work presented in this paper.

SECONDARY SIDE DEPOSIT

Technical approach

The performance evaluation for the secondary side deposit examination focuses on the probe response to deposits of varying characteristics. These characteristics are deposit thickness and mass percentage of magnetite (Fe_3O_4). Magnetite is representative of actual deposits but the electromagnetic properties (electrical conductivity and magnetic permeability) of deposits in steam generators are not known.

Two references tubes have been manufactured:

- one tube with deposits of different thickness values, with same composition,
- one tube with deposits of same thickness but with different magnetite mass percentage values,

The deposit is homogeneous along the tube axial direction. In the orthoradial direction the deposit is either homogeneous or only present on half the tube perimeter.

A theoretical formulation of the magnetic permeability of the deposit, function of the magnetite composition% occlusion is also challenged.

The axial probe numerical model and the theoretical formulation for magnetic permeability are to be validated by comparison of numerical finite element simulation results to experimental measurements. Using the validated numerical model and formulation, the performance of the probe will be evaluated doing a numerical parametric study in order to quantify the influence of parameters such as:

- deposit materiel electrical resistivity,
- tube material,
- deposit configuration,
- deposit density and composition.

Finally the transfer functions obtained by modelling and simulation will be used for estimation of deposit from onsite signals.

Model validation

Finite element modelling and simulation are done using Flux3D software. The geometry of the numerical model is represented in Figure 4. Only half of the tube, probe and deposit are modelled and the deposit is divided in two parts to be able to have deposit on only the half of the tube circumference when the symmetry condition is applied.

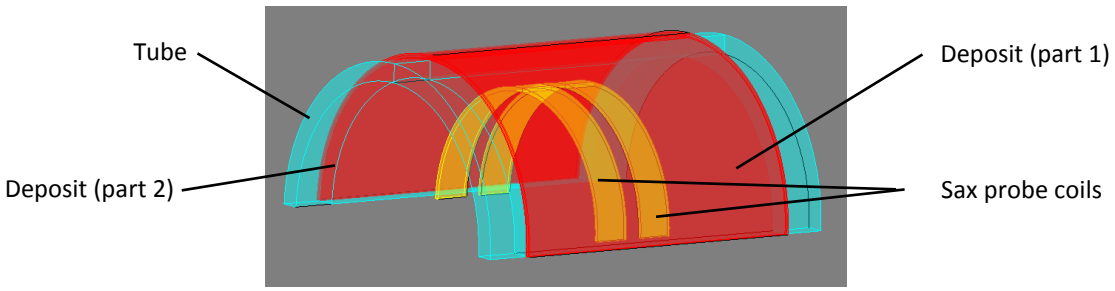

Figure 4 - SAX bobbin probe and tube with deposit numerical model

Simulated signals are compared to measured signals in two cases:

- variable deposit thickness with fixed magnetic relative permeability (magnetite 50% of mass , μ_r=1.08) see Figure 5,
- variable deposit magnetic permeability with fixed thickness (0.23mm), see **Figure 6**.

We observe that the agreement between the simulated and measured signal is quite good, with maximum errors of 12.5% for signal with variable magnetic permeability and 5% for signals with variable thickness. Therefore we can consider that the numerical model and the theoretical formulation for the computation of magnetic permeability are validated.

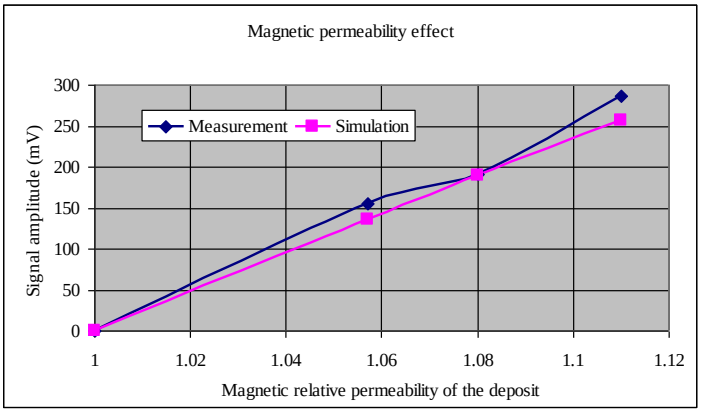

Figure 5 - Effect of the magnetic permeability of the deposit material on the axial probe signal

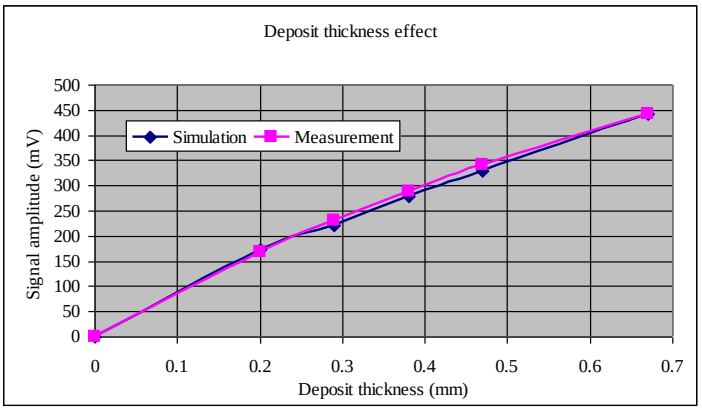

Figure 6 - Effect of the thickness of the deposit on the axial probe signal

Parametric study

From the validated numerical model of the probe and tube with deposits, the previously described parametric study leads to the following conclusions:

- There is no influence from the electrical resistivity of the deposit material above $10^{-4}\Omega.m$, as can be seen on Figure 7,
- There is nearly negligible effect of the tube material, with a signal difference smaller than 1.5% between the signal obtained with Inconel 600 and Inconel 690, considering a deposit thickness varying between 0 and 0.67mm, see Figure 8,
- There is a significant effect of the deposit geometry on the probe signal for constant mean deposit thickness. Two geometries have been modelled: 360° deposit and 180° deposit and signals are compared for the same value of mean deposit thickness (see Figure 9). With 180° homogeneous deposit instead of 360° the deposit thickness is under estimated by around 23% for a maximum thickness of 0.67mm,
- The theoretical formulation of the magnetic relative permeability from the magnetite mass rate in the deposit gives the following values: 1.37 to 1.41 for 88 to 95% magnetite mass percentage.

It must be noted that we have considered no copper in the deposit material. However the presence of copper as well as metal oxides can have an important effect on the signal (in particular the electrical conductivity of the deposit material is changed). Therefore it will be necessary to complete the present results with dedicated experiments and modelling, which includes the manufacturing of specific mock ups with representative deposit material.

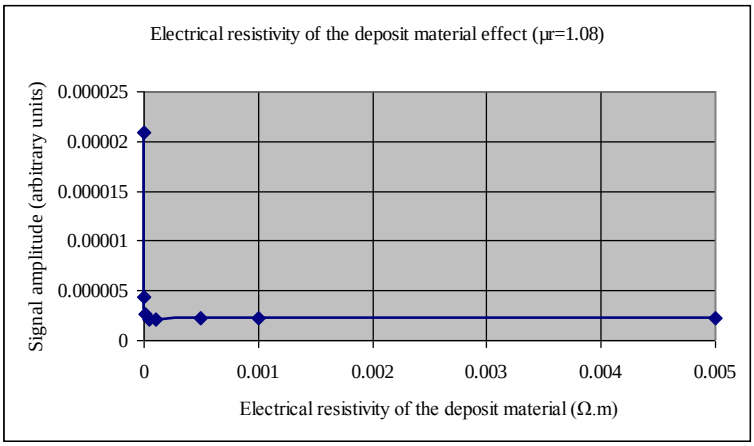

Figure 7 - Influence of electrical resistivity of the deposit material on the axial probe signal

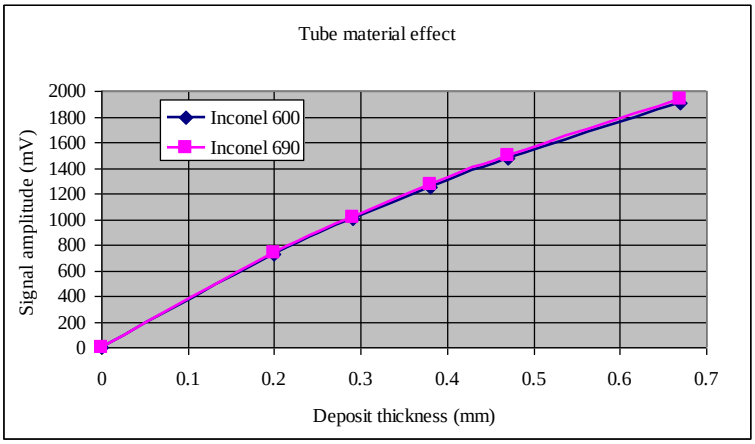

Figure 8 - Influence of tube material on the axial probe signal

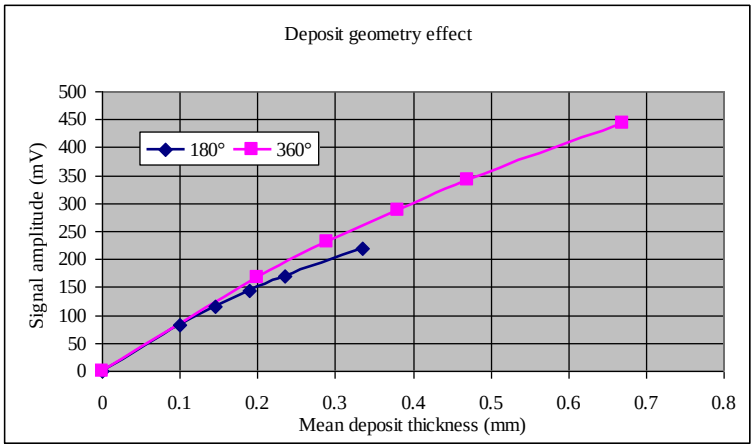

Figure 9 - Deposit geometry effect on the axial probe signal

On-site implementation

Since 2009, the analysis of three EDF steam generator's secondary side have been performed and three more are planned. The tube sizes of the different steam generators concerned are 3/4 and 7/8" and 25 to 50% of the tube bundle has been examined. From the probe signals, Aida G3 software has been used to evaluate the deposit material mass inside the steam generator secondary side. These estimation results are compared to those of EDF reference (mass balance method), see
Table **1**. We observe a good correlation between the masses estimated by the two methods.

	SG1	SG2	SG3
AREVA deposit mapping Estimated deposit material mass (kg)	1104	733	513
EDF reference (kg)	1250	1000 (±30%)	500 (±40%)

Table 1 - Comparison of deposit mass estimate by probe measurement to EDF reference values

TUBE SUPPORT PLATE CLOGGING

Technical approach

A performance evaluation of the two probes, the SAX eddy current bobbin probe and the FLIP flux leakage probe, has been started using finite element software Flux3D. The study is realized under AREVA – EDF collaboration and its program is as follows:

- Step 1 - validation of SAX and FLIP probe numerical models: to perform this validation, Flux3D is used to compute simulated signals corresponding to examination of EDF mock-ups for clogging of tube support plate. The simulated signals are then compared to experimentally measured signals in the same configuration. The clogging of the mock-ups is a homogeneous diaphragm shaped clogging with occlusions of 0-25-50-75-100%, identical in all four holes. It is located at the bottom of the tube support plate holes and its height is 3mm, close to the actual clogging height. Sketches of the mock-up clogging are represented in Figure 10. This kind of clogging is representative of the actual clogging that as been observed during visual examination of steam generators. Mock-ups are made of Inconel 600 for the tube, 410 Stainless Steel-Z10C13 for the tube support plate and a magnetite-glue mix for the clogging material with 95% in mass magnetite and 5g/cm^3 density. These materials are representative of the actual steam generator materials. The geometry is of the 68/19 steam generator type with 3/4" tube diameter.
- Step 2 - evaluate the influence of model parameters on real deposit and clogging configurations using finite element simulation with the previously validated probe models. The clogging and deposit shapes are defined by variable geometric and material parameters. Then a parametric study is realized to evaluate and quantify the influence of each parameter: different sets of parameter values are introduced in the numerical model and related features are extracted from the simulated signals. This parameter-feature mapping can then be used to evaluate the parameter values from onsite measurements.
- Step 3 - predict signals from the defined clogging and deposit configurations, that is to say from representative sets of value of the different parameters.

Considering the results obtained at these different steps, the performances of SAX and FLIP probes for clogging examination will be compared.

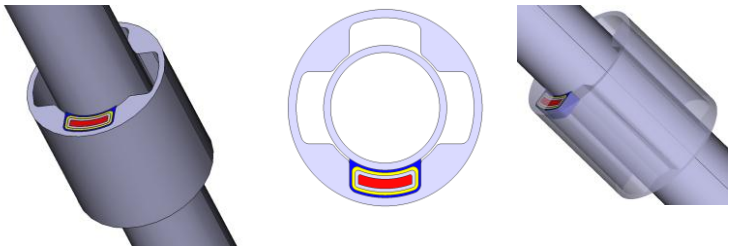

Figure 10 - Clogging configuration of the mock-up numerical models.

The tube is centered in the support plate. The plate diameter has been reduced with no effect on the results. Blue, yellow, grey and red clogging volumes correspond to the different clogging occlusion values (blue: 25%, + yellow: 50%, +grey: 75%, +red: 100%). Here clogging is drawn only in one hole but it is present in all four holes.

The current state of advancement is step 1 - validation of the FLIP probe model, is detailed in the next paragraph.

FLIP probe model validation

The numerical model of the mock-ups used for the FLIP probe validation does not include the tube because the tube's relative magnetic permeability is very close to one therefore the magnetic field is not influenced by the tube. Moreover, thanks to symmetry, only one eighth of the geometry is modelled. Images of the tube support plate and clogging volumes are presented in Figure 11.

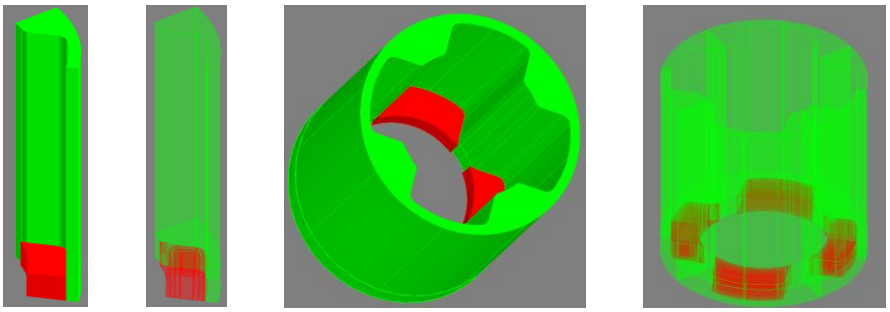

(a) (b) (c) (d)

Figure 11 - Flux3D numerical model of the mock-up, in red the cloggin volumes, in green the tube support plate. (a) and (b), 1/8th of the actual geometry used for the computation, (c) and (d) full geometry when the symmetry conditions are applied

The magnetic permeability of the mock-up materials (tube support plate material and clogging material) are not known therefore the model validation is two-fold:

1. establish that the simulated signal is similar to the experimentally measured signal,
2. find the values of tube support plate and clogging material's magnetic permeabilities that make the simulated and experimental signals fit.

The best fit of simulated and measured signals are shown in Figure 12 for clogging occlusion values of 25-50-75-100%. The agreement between the signals is excellent then the numerical model of FLIP probe is validated. The corresponding relative magnetic permeabilities are in the range 2.5-2.75 for the clogging material and between 700 and 1000 for the tube support plate material. This last range of values is the one found in the literature (matweb.com) for the material (410 Stainless Steel – Z10C13), and we observe that within this range the permeability value has very little effect (≤1%) on the simulated signal.

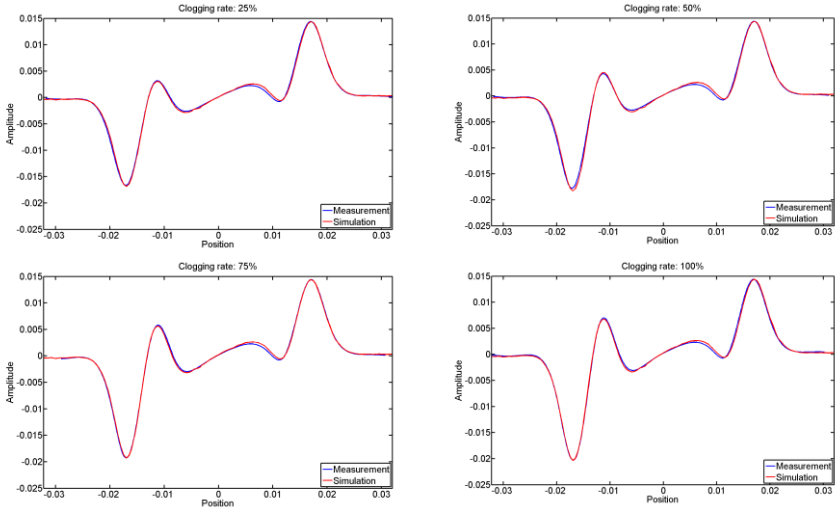

Figure 12 – Best fit of measurement and simulated signals for clogging % occlusions 25-50-75-100%

Transfer function

From signals obtained on configurations with known clogging % occlusions and material properties, a transfer function between the clogging % occlusion and one specific feature of the signal can be defined. This feature is the amplitude ratio of the clogged side signal to the un-clogged side signal. The amplitudes and support plate segments are shown in Figure 13. The transfer function is used to estimate the clogging % occlusion from experimental signal where the amplitude ratio of the measured signal is computed and the corresponding clogging % occlusion is read by applying the transfer function. The transfer function is either obtained with experimental measurements on the clogging mock-up, as shown in Figure 14, or using simulation result.

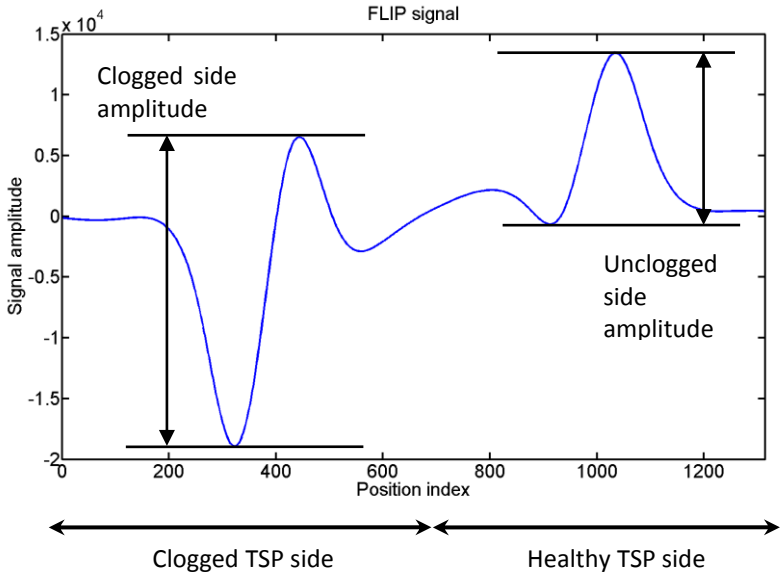

Figure 13 - FLIP signal from clogged and unclogged TSP sides

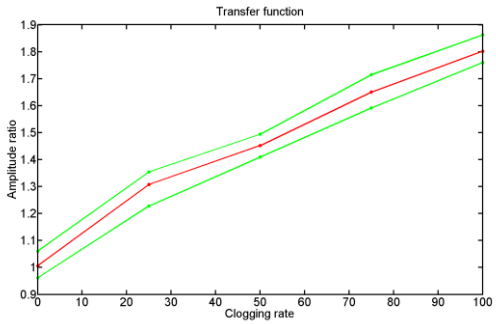

Figure 14 - Transfer function obtained with the EDF clogging mock-up. In red the mean transfer function, in green the maximum and minimum transfer functions for the different acquisitions

CONCLUSION

We have presented here the challenges of modelling and estimating secondary side deposits on tubes and clogging of the tube support plate inside nuclear power plant steam generators. The industrial solution developed by AREVA NDE Solutions and applied in the field with the collaboration of EDF Ceidre has been introduced and the current state of its performance evaluation shown.

This performance evaluation relies on comparison of mock-up experimental results to those obtained using finite element numerical modelling and simulation. This allowed validation of the numerical models and software package. Using this validated models the influent parameters are identified by relevant simulation and the results are used to fine tune transfer functions.

These updated transfer functions will ultimately be introduced in the Aida G3 processing and visualization software to evaluate and display the deposit and clogging state of the examined steam generator.

The comparison of results obtained by the industrial solution for deposit estimation to actual measurement of deposit mass inside steam generators gave very positive results

REFERENCES

1) Bodineau H and Sollier T, "Tube support plate clogging of french PWR steam generators", Eurosafe Forum, Paris, 3-4 November, 2008

2) http://www.cedrat.com/

3) Piriou, Marc. Glass, S.W., Steam Generator Secondary Side Deposit NDE Method for Support Plate Clogging; The 24th KAIF/KNS Annual Conference; March 2009, Seoul, Korea.

UTILIZING NDE INFORMATION TO SUPPORT LONG TERM STEAM GENERATOR DEPOSIT MANAGEMENT STRATEGIES

J. C. Le Querre, Westinghouse, France
S. Wozniak, Westinghouse, USA

Abstract

Scale buildup within steam generators can have detrimental effects. Scale can buildup either on the free span tube surface or for plants with broach tube support plate (TSP) designs, within the flow regions of the broached TSPs. A strategic approach to SG deposit management can limit negative consequences of SG performance degradation. This requires a good understanding of current conditions, including:

- Spatial distribution of deposits
- Quantification of the deposits (amount of magnetite)

Two methods for detecting and monitoring the scale buidup within these regions will be discussed – Scale Profiling and Quatrefoil/Trefoil Blockage Assessment.

Scale Profiling uses low frequency eddy current data to estimate deposit inventory in each steam generator. From this data, visualizations created provide the intensity, extent, locations and distribution patterns of secondary side deposits within the steam generator. For steam generators utilizing the quatrefoil/trefoil design tube support plates, the broached TSP flow regions can become blocked by scale deposits. Based on plant experience, blockage of the broached TSP flow holes decreases the flow area and results in increased pressure drop across the tube support plate. Plus-point or RPC data collected within the TSP region is converted to visualizations and provides information about the amount of scale blockage as well as location and extent. This information can be correlated with thermal and hydraulic data to determine the relationship of TSP blockage to steam generator flow oscillations.

Examples of both methods will be presented with the last additional capabilities that have been developed to assess steam generator deposits and showing how this information are being used by utilities to support long term steam generator deposit management strategies.

Keywords: Application areas of NDT (RPV – SG - Internals and primary circuit - Other component)

STEAM GENERATOR SECONDARY SIDE TELEVISUAL INSPECTIONS

E. Lecour, G. Gaillard, J.L. Renaud, Westinghouse Electric Company, France

Abstract

Purpose of televisual inspection on Steam Generator Secondary Side is the following:

- Collect as much data as possible to estimate the quatrefoils blockage and tube deposits,
- Estimate the spatial distribution all along the TS of the blockage,
- Collect as much information as possible about cleanliness,
- Detect foreign objects.

Westinghouse developed tools to inspect following parts of the Steam Generators:

- Upper and middle support plate for in-bundle blockage evaluation,
- Tubesheet and flow distribution baffle for in-bundle, peripheral and central-lane inspection,

All these equipments are remote operated and inspection phases are automated.
The paper will present the performance evaluation, qualification approach, and lessons learned from site jobs.

Overview

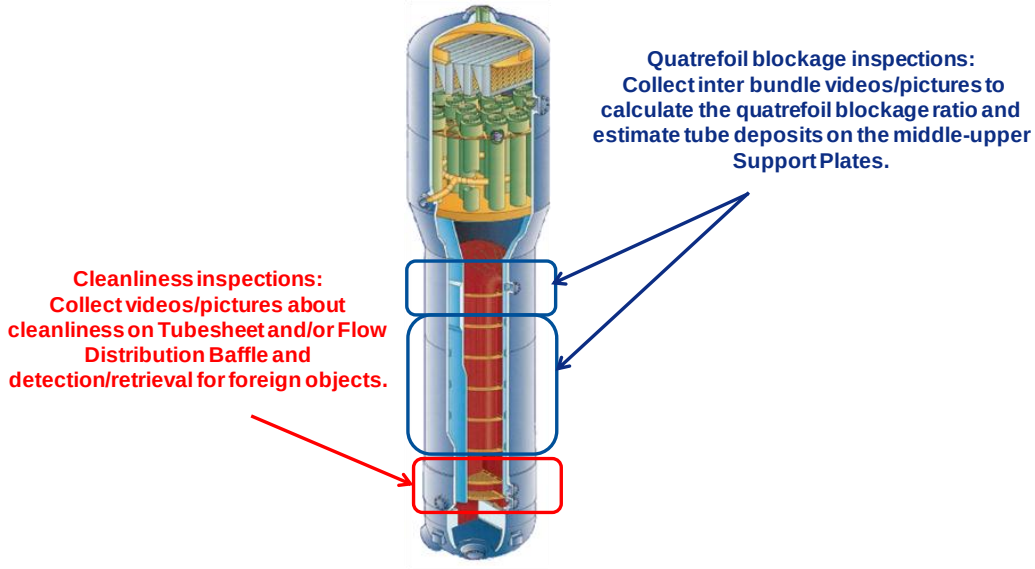

Quatrefoil blockage inspections: upper plate

Tool:

Remote operated and automated for inspection phase tool operating under-water using camera hole access.

Performance:

- Qualification for French Market: 2007 (1300 MW) & 2009 (47/22 SG),
- Interventions on site : 14,
- 4 hours each full bundle (included set-up and tear-down on SG),
- Hight quality pictures/videos,
- Low integrated dose.

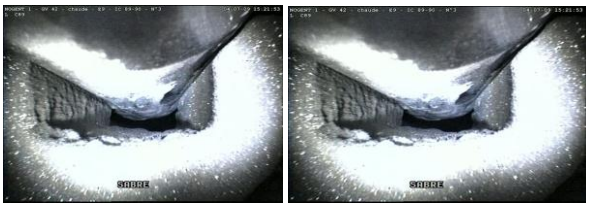

Tube deposit Quaterfoil blockage

Quatrefoil blockage inspections: upper plate

Equipment is made of multiple parts assembled to make a flexible chain in
which the inspection camera (sword) is delivered.The system is operating underwater

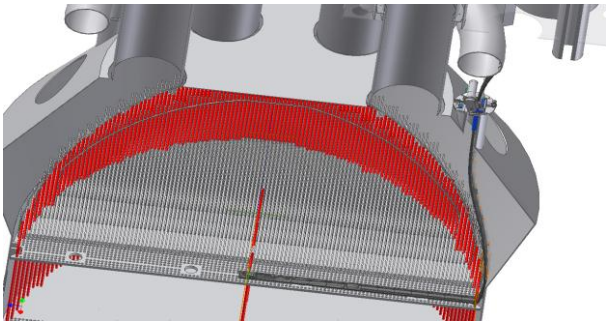

Sword

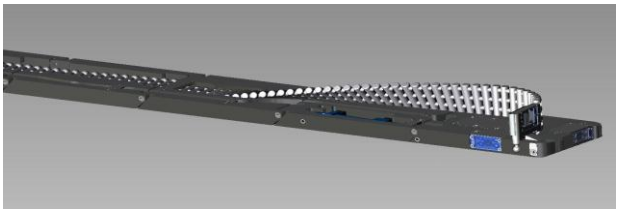

2 SG Mock up including :

- Wrapper with Swirl vane geometry, camera hole
- Decks
- Upper TSP and quaterfoils (in water conditions)
- Tube bundle

Quatrefoil blockage inspections: middle plate

Tool: Remote operated and automated for inspection phase tool using lateral eye hole access (minimum diameter = 38 mm) with inspection sword.

-Guide Movements (rotation and translation) in the central lane,
-Sword Movements (translation) inter-bundle

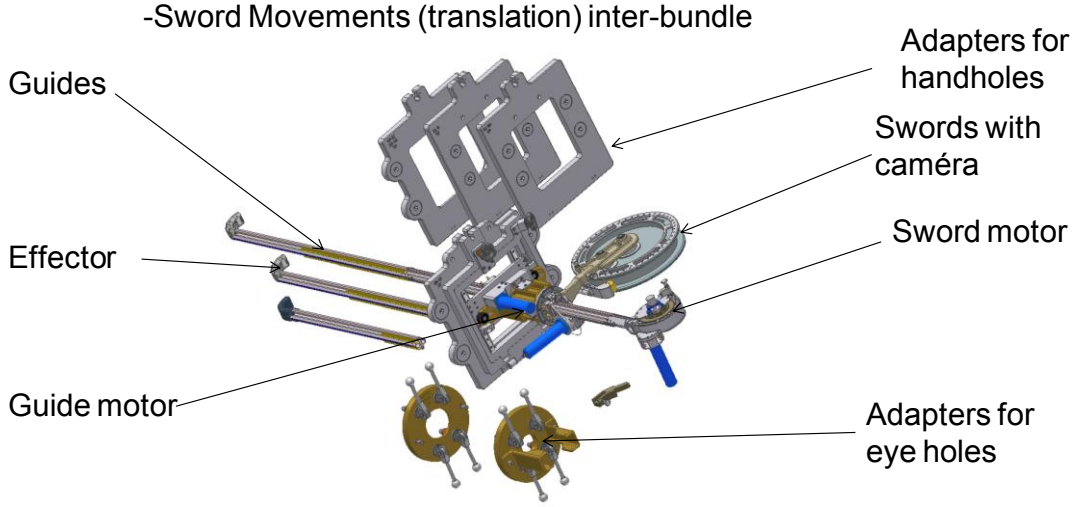

Fixed on hand-holes or eye-holes (Ømini 38 mm)

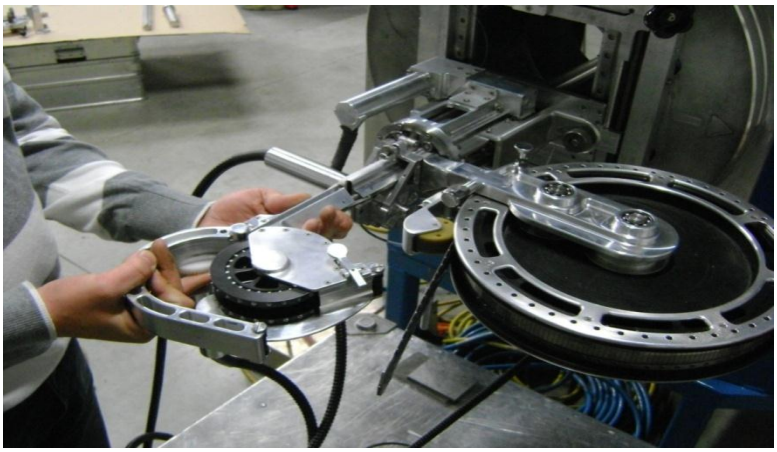

Performance:
Qualification for French Market: 2011,
Interventions on site : 6,
Bottom view plate = 1h30 each full bundle (included set-up and tear-down on SG),
Top view plate = 2h00 each full bundle (included set-up and tear-down on SG),
Hight quality pictures/videos.

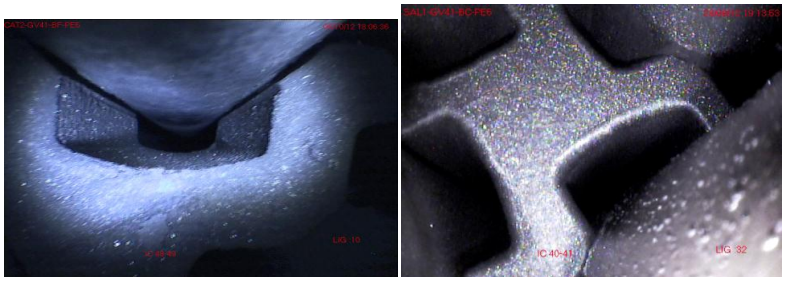

Top view Bottom view

2 types of sword according to the angle view

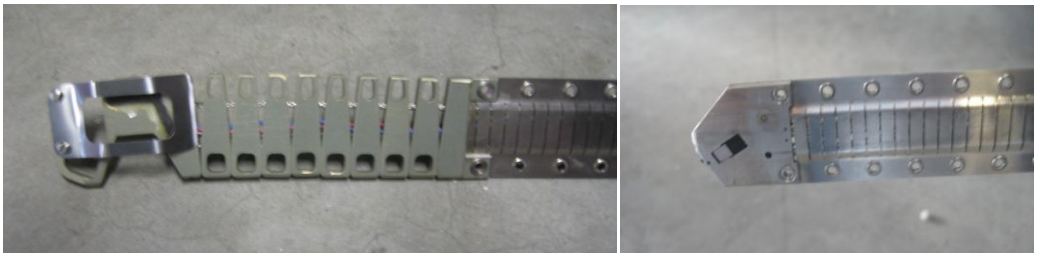

Articulated probe, 90°(Perpendicular to the plate) Probe at 30°

Quatrefoil blockage inspections: analysis

- Inspection are performed on bundle samples,
- Pictures are analysed to define blockage ratio for each inspected quatrefoils,
- Base on these results, an average blockage ratio is defined for each half a plate.

-> This data allows EDF to follow the quatrefoil blockage progress for each plate and implement maintenance plan according to these results.

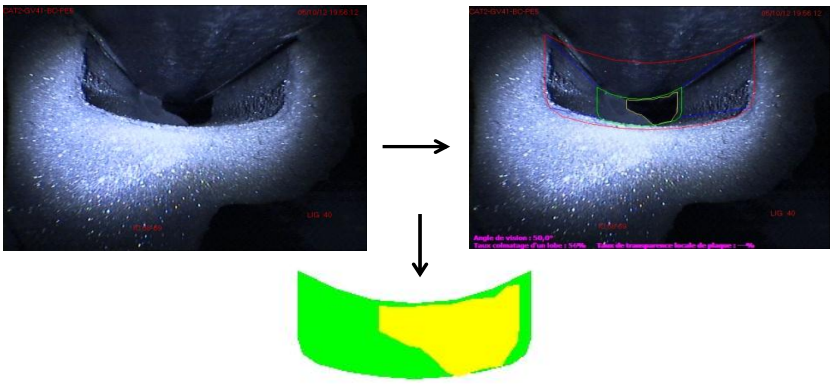

Cleanliness inspections: inter-bundle

Tool:

Same tool as middle plate inspection using handhole/eyehole access and specific inspection sword. Could operate on tubesheet and flow distribution baffle

Performance:

- Qualification for French Market: 2012,
- Interventions on site : 6,
- Bottom view plate = 1h30 each full bundle (included set-up and tear-down on SG),
- Hight quality pictures/videos,
- Allowing the caraterisation of foreign object or tube indications.

Same remote controllled video probe as middle plate inspection with 0° sword.

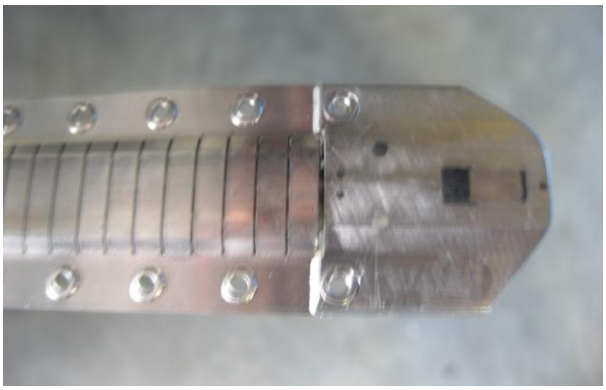

Some pictures :

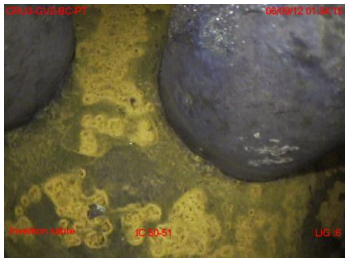

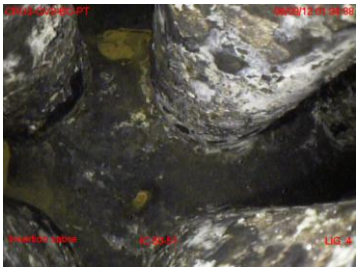

Cleanliness inspections: annulus inspection

Tool:

Remote operated magnetic car moving on the wrapper with inspection camera using handhole access. Only tubesheet is inspected.

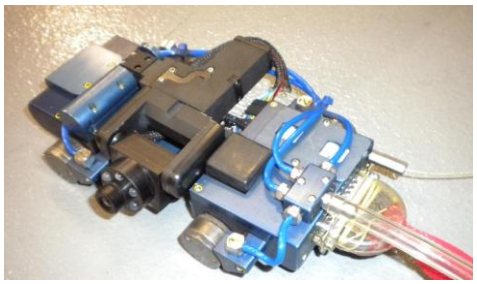

Performance:

- Qualification for French Market: 2011; 10 operations each year
- Tubesheet inspection= 8h00 (included set-up and tear-down on SG),
- From tubesheet to flow distribution baffle inspection= 16h00 (included set-up and tear-down on SG),
- Hight quality pictures/videos,
- Could permit to detect and caracterize foreign object or to perform visual assistance during object retrieval activities.

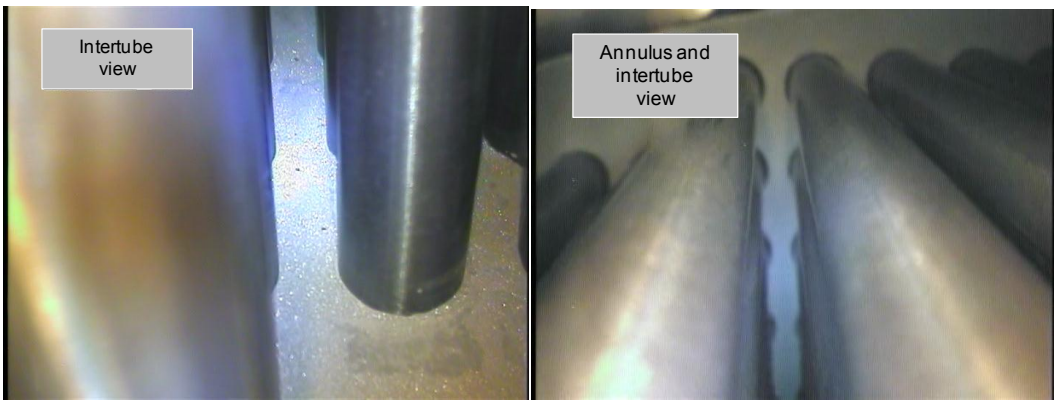

Cleanliness inspections: Central lane inspection

Tool:

Manual perch camera using handhole/eye hole.

Performance:

- Qualification for French Market: 2011,
- Inspection on site : 10,
- Full central lane inspection on tubesheet = 1 hour (included set-up and tear-down on SG),
- Full central lane inspection on flow distribution baffle = 0,5 hour (included set-up and tear-down on SG),
- Hight quality pictures/videos,
- Allowing detection and caracterization of foreign object.

SIZING OF MAGNETITE PILE ON STEAM GENERATOR TUBING WITH TWO-PROBE EDDY CURRENT TECHNIQUE

J. Tarja, L. Kari, VTT Technical Research Centre of Finland

ABSTRACT

During in-service inspection the steam generator tubes are generally inspected using single probe eddy current techniques. Magnetite deposit built up on the outer surface of the tubes can be detected with the applied techniques. As deposits grow thicker they tend to split as flakes from the surface of the tubes. These flakes often build magnetite piles between the tubes. The piles restrict free flow of secondary water. Under magnetite piles the conditions are also favourable for corrosion induced defect initiation and growth on the outer surface of the steam generator tubing. The height of the magnetite piles cannot be sized properly with the standard single probe techniques.

In this study experiments were conducted to size the height of the magnetite piles. For this purpose a small simple steam generator mock-up with parallel tubes was constructed. Flake piles of magnetite deposits were heaped up between the tubes. A developed two probe technique was used. In this technique two eddy current probes are pulled simultaneously through two neighbouring tubes. The probes were axially aligned.

The test showed that the pile of the magnetite can be located and its height can be estimated with two-probe technique. The results of the experiments are presented.

INTRODUCTION

Eddy current method is the main method in the in-service inspections of the steam generator (SG) tubing. The method has high inspection speed and it is sensitive to both inner surface and outer surface defects. The applied inspection techniques are based on the use of bobbing probes. The main purpose of the eddy current inspections of steam generators is to detect and to characterize the possible degradation of the steam generator tubes. The applied techniques are sufficiently reliable and give repeatable results in detecting and in sizing volumetric defects and axial cracks in the tubing.

During operation of the VVER-440 pressurized water reactor (PWR) magnetite deposits precipitate on the outer surfaces of the steam generator tubing. After deposits have grown thick enough, the deposits peel as flakes from the surface of the tubes. These magnetite flakes can form magnetite piles between the tubes.

The magnetite deposits and magnetite piles can be detected in standard eddy current inspections when absolute technique and low inspection frequency e.g. 25 kHz are used. However the detected magnetite indications are not generally used to quantify the thickness of the magnetite deposits or extension of magnetite piles.

This study is a part of the NDE project in the Finnish Research Programme on Nuclear Power Plant Safety SAFIR 2014. The goal of the study is to develop a method applicable to locate and to map the magnetite piles within the steam generator tubing or the magnetite piles extending from the bottom of the steam generator shell up to the steam generator tubing.

In this study the results of the laboratory measurements of the height and thickness of the magnetite piles are given. The measurements were conducted using eddy current method and standard bobbin probes. The results of absolute eddy current techniques in sizing the height and thickness of magnetite piles within the SG tube bundle are given. Four different eddy current frequencies were used.

MAGNETITE ON STEAM GENERATOR TUBING

Walls of the steam generator tubes are part of the pressure boundary of the primary water circuit of the PWR. Deterioration of SG tubing can shorten the lifetime of the reactor. For this reason the integrity of the SG tubes is important and it is imperative to conduct careful, regular well-planned inspections.

One of the concerns in the field of steam generator tubing is magnetite deposits accumulating on the secondary side of the tube. Material of the deposits (or sludge) is ferromagnetic and is mainly composed of magnetite. The iron oxide particles in the secondary water circuit form magnetite layers on the SG tubes. When deposit is thick enough, magnetite layers i.e. deposits peel from the surfaces of the tubes as flakes. The magnetite flakes build up magnetite piles when falling on the tubes, tube support plates or on the bottom of the horizontal steam generator or on tube sheet and on tube support plates of the vertical steam generators.

The piles restrict free flow of secondary water and thus decrease the heat transfer of the SG tubes. Under magnetite piles the conditions are also favourable for corrosion induced defect initiation and growth on the outer surface of the steam generator tubing. In spite of this the magnetite indications detected in in-service-inspections are not usually analysed or reported in details. In this study an eddy current technique has been developed to detect, to locate and to size the extension of the magnetite piles within the SG tubing.

DETECTION OF MAGNETITE PILES

Magnetite piles can build up a complex geometry that generates high amplitude indications. In laboratory scale, several mock-up structures have been used for detection of magnetite piles [1–3].

There have been successful set-ups to measure the thickness of the magnetite deposit on the surface of the tube [2, 3]. In these set-ups the circumferentially symmetric magnetite layer extended around the tube. The thickness of the magnetite was constant at each cross-section and it was changing in axial direction. The amplitude of the eddy current signal correlated well with the thickness of the magnetite deposit. The respective graph of this data (the amplitude versus deposit thickness) can be used as a reference graph when analysing actual inspection results, only if the magnetite layer on the outer surface of the tube is remaining constant.

The preceding studies [4] have proven that it was possible to measure the magnetite thickness up to 10 mm thickness, when the frequency was 10 kHz and up to 8 mm when the frequency was 25 kHz. A single bobbin probe and absolute technique were applied in the measurement. The described techniques apply only when the height of the pile of the magnetite deposit is constant. If the deposit pile height is not constant in each test, the maximum or minimum thickness of the deposit between the two tubes cannot be judged from the data.

Arora et.al. [5] have used a two probe method that they call “tube-to-tube” measurement to detect wall loss and grooves on heat exchanger tubes and later Shatat et.al. [6] have also used the same method when inspecting finned tubes.

EXPERIMENTAL METHODS

The work presented in this article has been conducted in the NDT-research laboratory at VTT. The purpose of the conducted experiments was to study the effect of the magnetite piles on the eddy current signal of the bobbing probe. To be able to detect the magnetite deposits on the outer surface of the tube, the eddy current frequency has to be low enough to be able to penetrate the tube wall. To be able to detect and to measure the existence of the magnetite piles between the tubes, the magnetic field generated by eddy currents has to extend further into the magnetite pile.

The experiments were conducted using two similar bobbin probes, one transmitting and another receiving, in the adjacent parallel tubes. The applied eddy current frequencies were 12.5, 50, 100 and 200 kHz. The diameter of the applied probes was 12 mm. The fill factor of the probes was 0.85. The eddy current equipment Zetec MS5800 and Magnify 2.0R3 software were used. The applied parameters are shown in Table 1. Absolute technique was used.

A simple mock-up of the horizontal steam generator tubing was used in the experiments (Fig. 1). The horizontal free span between tubes in VVER-440 type horizontal steam generator and in the mock up is 14 mm. The material of the tubes in the mock-up was Ti-stabilized austenitic steel AISI 316 Ti. The outer diameter of the tubes was 16 mm and wall thickness 1.5 mm. The magnetite material i.e. the flakes were from the steam generator nuclear power plant.

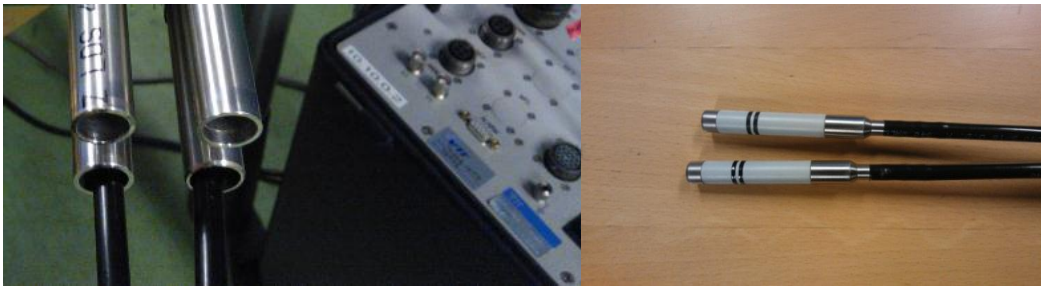

Figure 1. On the left there are the ends of the tubes in the mock-up simulating the SG tubing. On the right there are the eddy current probes used in the measurements.

Table 1. The applied parameters in eddy current tests.

Test	Description	Probe diam	Freq.	Gain/ Voltage	Comments
A	Magnetite detection, probes in adjacent tubes, absolute technique	12 mm	12,5, 50, 100 and 200 kHz	60 dB 3 V	The height of the magnetite pile was increased: from 10 mm under the lower tubes up to the level where second row was fully covered with magnetite.
B	Magnetite detection, probes in adjacent tubes absolute technique	12 mm	12,5, 50, 100 and 200 kHz	60 dB 3 V	The transmitting probe was in the tube submerged into magnetite pile, receiving probe was in the adjacent free tube outside magnetite pile. The thickness of magnetite layer between the tubes was increased up to 14 mm (flakes, 1, 1.8, 3.4, 4.1, 4.9, 5.8, 7.1, 8.6, 11 and 14 mm)

In the test series A and B the transmitting probe and receiving probe were in the two lowest tubes of the mock-up. In the first measurement of test series A the height of the magnetite pile was increased in steps. First the magnetite pile was below the lower tubes. The free distance between the lower tubes and the pile was 10 mm. In the second measurement the free distance between the lower tubes and the pile was 7 mm. In the third measurement the magnetite pile touched the lower surface of the lower tubes. In the fourth measurement the lower tubes were covered by magnetite. The upper surface of the pile was on the same level than the upper surface of the lower tubes. In the last measurement surface of the pile was on the same level than the upper surface of the tubes in the next tube row. The level of the magnetite in the last measurement is shown in Figure 2a.

In the test series B the width of the magnetite pile was increased in the horizontal direction. The height of the pile was kept constant through all the measurements in the vertical direction. The pile extended to the upper surface of the tubes of the row two as shown in Figure 2.The thickness of the pile was controlled by a plastic plate (Fig 2b). One of the tubes was embedded in the magnetite pile. The transmitting coil was in this tube. The other tube was free of magnetite. The indication due to magnetite pile was studied. Thickness of the magnetite layer between these two tubes was changed from 1 to 11 mm (steps: 1, 1.8, 3.4, 4.1, 4.9, 5.8, 7.1, 8.6, and 11 mm). In one additional measurement there was one layer of magnetite flakes on the surface of the tube with driving probe. The flakes were attached to the tube surface with a plastic tape.

In another additional measurement both of the tubes were completely submerged into magnetite pile. In that case the thickness of the magnetic pile between the tubes was 14 mm (equal to the distance of the outer surfaces of the tubes).

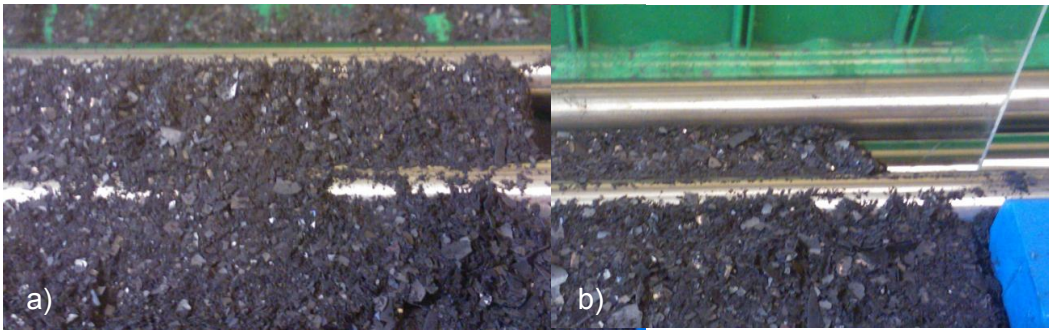

Figure 2. a) Test series A: The level of the magnetite in the last measurement. The magnetite pile extended up to the upper surface of the tubes in upper row. b) Test series B: The lower tube with transmitting probe was embedded into the magnetite pile. The lower tube with receiver probe was free of magnetite piles and deposits. The thickness of the pile in horizontal direction between the tubes was controlled by the acrylic plastic plate.

RESULTS

The results of the conducted tests show that the sensitivity in magnetite detection was greater when the lower eddy current frequency was used. With both 12.5 kHz and 50 kHz frequencies the changes in the amplitude of the magnetite indication was high enough to be able to measure the height of magnetite pile in the bottom of the mock-up.

The results of test series A are given in Figure 3. The amplitude of the eddy current indication due to the magnetic pile is given as a function of the distance between the upper surface of magnetite pile and the lower surface of the lower tubes in the mock up. The amplitude of the eddy current indication was nearly zero when the free distance between the tubes and the magnetite pile was 10 mm. When the free distance was 7 mm, the existence of the pile can already be detected. When the pile was touching the lower surface of the tubes i.e. the distance between the pile and the lower surface of the tubes was 0 mm, the amplitude was ranging from 0.1 to 0.34 V depending the applied eddy current frequency. The amplitudes of the indications due to magnetite pile were increasing when the height of the pile was growing.

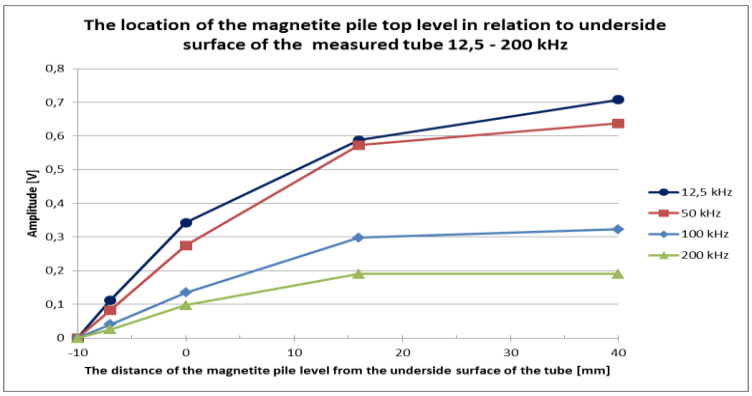

Figure 3.Test series A: The amplitude of the eddy current indication versus the distance of the upper level or the pile from the lower surface of the tubes that the probes were in.

The results of test series B are given in Figure 4. The amplitude of the magnetite indication is given as a function of the thickness of the magnetite layer between two tubes. The thickness of the magnetite was controlled by plastic plates. The trend of the curve is rising. However, the slope of the amplitude versus thickness graph is decreasing strongly when he the thickness of the magnetite layer is exceeding 1 mm.
The saturation effect was stronger when higher frequencies (100 kHz and 200 kHz) were used.

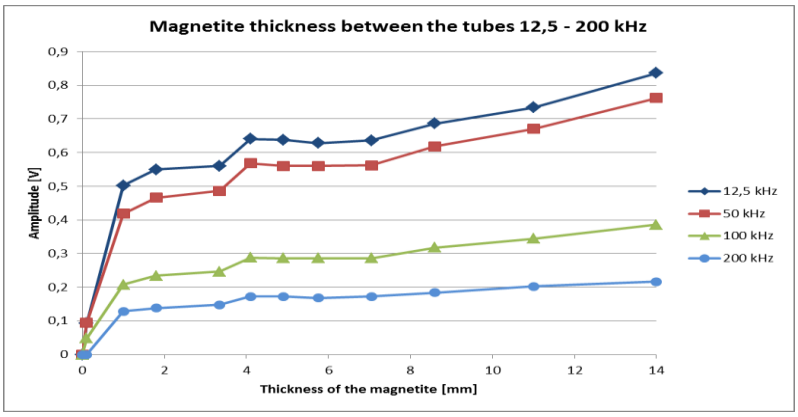

Figure 4. Test series B: The amplitude of the eddy current indication as a function of the thickness of the magnetite layer between the two adjacent tubes that the transmitting and receiving bobbin probes were located.

Discussion

Figure 3 shows that sections of the tube pairs embedded into the magnetite pile can be easily detected with the presented two-probe technique. With this technique it is possible to map the areas where magnetite piles fill the volume between the steam generator tubes.

Figure 4 shows that it is not possible to measure the thickness of the magnetite layer between nearby tubes reliably with the applied technique when the thickness of the layer is considerably more than 1 mm even if the height of the pile were constant.

The test series B was carried out with a set-up, where the transmitting probe was always in the tube that was surrounded with magnetite and the receiving probe was in the tube with no magnetite around respectively. Some tests were conducted with vice versa set-up that the receiving probe was in the tube covered with magnetite. There was no significant difference in the amplitudes of the magnetite indications whether the probe in the tube, covered with magnetite, was transmitting or receiving. This property helps when the technique is used to map the areas where the magnetite piles have grown into the tubing of the steam generator. In test series A and B the best sensitivity was achieved, when the eddy current frequency was quite low, 12.5 or 50 kHz.

When the two-probe technique is used it is very important that the transmitter and receiver probes locate exactly parallel in the same cross-section perpendicular to the axis of the two tubes. Any deviation from the proper location will generate indication which have same phase angle than the magnetite indication (Fig. 5).

With the applied probe configuration it is not possible to distinguish whether the indication is due a magnetite pile or due to the location error of the transmitter and receiver probes. The proper probe location has to be assured with push puller or with more developed probes or probe configuration possibly combined with intelligent push pullers.

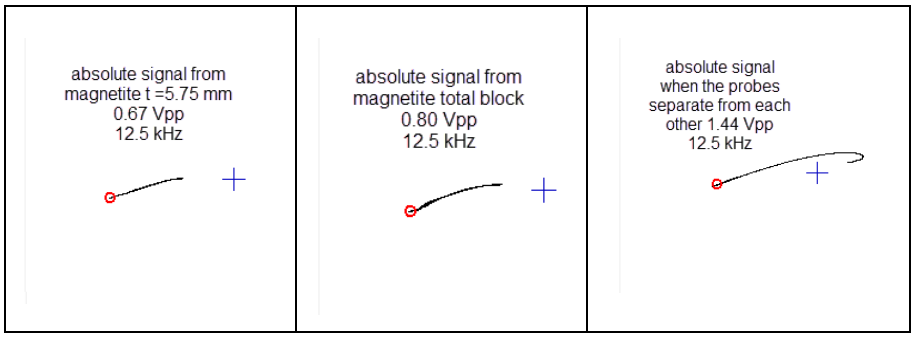

Figure 5. Impedance plane presentations of the eddy current indications illustrate that it is impossible to judge from the eddy current indication if there is a magnetite indication or if the probes have lost their proper location. The red dot implicates the impedance of the probe when the probes are in proper location in respect to each other in the adjacent parallel tubes and no magnetite is present.

Conclusion

In this work the aim was to develop and test a technique capable to map a magnetite pile within the tube bundle of the mock-up simulating SG tubing. The measurements were conducted using eddy current method and standard bobbin probes. Transmitting and receiving probes were located in the separate adjacent tubes. Four different frequencies and absolute technique were used.

The results of the tests showed that the extension of a magnetite pile can be mapped with the two-probe eddy current technique used in this study.

REFERENCES

1. Son, D., Jung, W., Park, D.G. & Ryu, K.S. *Magnetic Sensor for the Defect Detection of Steam Generator Tube With Outside Ferrite Sludge*. IEEE Transactions on Magnetics 2009, Vol. 45, No. 6, pp. 2724-2726.
2. Kim, M., Yim, C., Um, K., Kim, J., Kim, C. & Lee, S. *Development of Scaled Deposit Measurement Technologies for Steam Generator Tubing*. Singapore International NDT Conference & Exhibition. 4th April. 2011.
3. Piriou, M. & Glass, S.W. *Steam Generator Secondary Side Deposit – NDE Method for Support Plate Clogging*. 7th International Conference on NDE in Relation to Structural Integrity for Nuclear and Pressurized Components. Yokohama, Japan, 12th-15th May. 2009.
4. Jäppinen, T., Lahdenperä, K. & Ala-Kleme, S. *Locating Magnetite on the Steam Generator Tubes with Eddy Current*. WCNDT. Durban, South Africa, 16th-20th April. 2012.
5. Arora, Y., Atherton, D.L. & Shatat, A.A. *The Tube to Tube Through Transmission Technique for Inspecting Finned Heat Exchanger Tubes*. Journal of Nondestructive Evaluation 1998, Vol. 17, No. 4, pp. 191-197.
6. Shatat, A. & Atherton, D. *The tube-to-tube through transmission eddy current technique*. Materials Evaluation 1998, Vol. 56, No. 1, pp. 90-93.

FROM CONCEPT TO REALITY: PERFORMANCE OF STEAM GENERATOR INLET/OUTLET NOZZLE DISSIMILAR METAL WELD EXAMINATIONS FROM THE INSIDE SURFACE

W. A. Jensen, NextEra Energy, USA
C. M. Barrera, S. Todd, R. Villagomez, IHI Southwest Technologies, USA

Due to recent issues concerning primary water stress corrosion cracking (PWSCC) in dissimilar metal (DM) welds in pressurized water reactors, the American Society of Mechanical Engineers issued Code Case N-770-1 "Alternative Requirements and Acceptance Standards for Class 1 PWR Piping and Vessel Nozzle Butt Welds Fabricated with UNS N06082 or UNS W86182 Weld Filler Material With or Without Application of Listed Mitigation Activities." In addition, the United States Nuclear Regulatory Commission (U.S. NRC) issued regulations on June 21, 2011 through Title 10 of the United States Code of Federal Regulation (10 CFR) 50.55a (g) (6) (ii) (F) (1) through (10) that required licensees to complete baseline examinations of any butt welds that rely on Alloy 82/182 for structural integrity by the end of the first refueling outage that started after January 20, 2012.

At the time of the issuance, the only approved method for performing examinations of Steam Generator Nozzle DM welds was ultrasonic examinations using procedures demonstrated in accordance with Appendix VIII, Supplement 10, of ASME Section XI from the outside surface (OD). Examinations from the inside surface (ID) were already well established for examination of the butt welds at the reactor pressure vessel (RPV) inlet/outlet nozzle to reactor coolant piping welds, but had not been for the corresponding steam generator (S/G) inlet/outlet nozzle to reactor coolant piping welds.

In the case of the S/G nozzle DM welds, an ID examination has the advantages of using a previously qualified technique, launching the ultrasonic sound beam from the side susceptible to PWSCC, and avoiding potential problems with geometry or material conditions on the exterior surface. In particular, Westinghouse plants have either static or centrifugally cast elbows welded to the nozzle and/or safe- ends, which would make examination from that side of the outer surface difficult.

Therefore NextEra Energy and IHI Southwest Technologies teamed up to develop a new tool that allows application of an ultrasonic examination that was previously qualified for examination of the welds at the RPV nozzle to meet the requirements of examination of the welds at the S/G nozzle DM weld from the nozzle interior. The project to design, fabricate, and successfully deploy an ID tool for S/G nozzle DM weld examinations are described in detail in this paper.

BACKGROUND

ASME Section XI (Rules for Inservice Inspection of Nuclear Power Plant Components) requires that the Steam Generator (S/G) welds and interior components be examined on a periodic basis. Due to recent issues concerning primary water stress corrosion cracking (PWSCC) in dissimilar metal (DM) welds in pressurized water reactors, the American Society of Mechanical Engineers issued Code Case N-770-1 "Alternative Requirements and Acceptance Standards for Class 1 PWR Piping and Vessel Nozzle Butt Welds Fabricated with UNS N06082 or UNS W86182 Weld Filler Material With or Without Application of Listed Mitigation Activities." In addition, the United States Nuclear Regulatory Commission (U.S. NRC) issued regulations on June 21, 2011 through Title 10 of the United States Code of Federal Regulation (10 CFR) 50.55a (g) (6) (ii) (F) (1) through (10) that required licensees to complete baseline examinations of any butt welds that rely on Alloy 82/182 for structural integrity by the end of the first refueling outage that started after January 20, 2012.

At the time of the issuance, the only approved method for performing examinations of Steam Generator Nozzle DM welds were ultrasonic examinations using procedures demonstrated in accordance with Appendix VIII, Supplement 10, of ASME Section XI from the outside surface (OD). Examinations from the inside surface (ID) were already well established for examination of the butt welds at the reactor pressure vessel (RPV) inlet/outlet nozzle to reactor coolant piping welds, but had not been for the corresponding steam generator (S/G) inlet/outlet nozzle to reactor coolant piping welds.

In the case of the S/G nozzle DM welds, an ID examination has the advantages of using a previously qualified technique, launching the ultrasonic sound beam from the side susceptible to PWSCC, and avoiding potential problems with geometry or material conditions on the exterior surface. In particular, Westinghouse plants have either static or centrifugally cast elbows welded to the nozzle and/or safe- ends, which would make examination from that side of the outer surface difficult.

POINT BEACH SPECIFICS

Point Beach Nuclear Plant (PBNP) is located approximately 30 miles southeast of Green Bay, Wisconsin and has been owned and operated by NextEra Energy Resources since September, 2007. PBNP consists of two (2) Units, both Westinghouse-designed, two-loop PWR's with 34-inch [86.36 cm] Outlet, and 32-inch [81.28 cm] Inlet Nozzles. Both units were designed and built in the mid- to late 1960's and were some of the earliest PWR's in the United States to commence commercial operation. PBNP Unit 2 has four (4) Alloy 82/182 (UNS N06082 / W86182) welds which have an Alloy 52/152 (UNS N06052 / W86152) inlay, and therefore were initially believed to fall into Code Case N-770-1 Category "G". Category G welds are considered to have a low probability of experiencing PWSCC because they are made of PWSCC-resistant materials or have been inlayed or clad, with PWSCC-resistant materials assuring that no susceptible material comprises the wetted surface. For PBNP Unit 2, these welds are located on the Safe-End to Inlet Nozzle and Outlet Nozzle to Safe-End locations for each Steam Generator (Figure 1). The configuration of this weld is similar to Performance Demonstration Initiative (PDI) Sample series 712/X (Figure 2). At the time of the issuance of the PBNP Unit 2 bid specification, there were no qualified procedures, techniques, or personnel available to perform UT on this type of a weld configuration from the ID. However, since these welds were considered to very similar to the RPV nozzle to safe-end configurations, the idea of performing the ID UT with RPV butt-weld techniques was born.

PBNP Unit 2 commenced commercial operation on October 1, 1972. Due to tube plugging / degradation issues in the 1990's, the original Westinghouse Model 44 Steam Generators (S/G's) were replaced in 1997 with Westinghouse Model Δ47 S/G's, which are functionally the same as the original S/G's. The S/G's are 127.8 inches [324.6 cm] diameter (lower region) with a 2.61 inch [6.63 cm] shell thickness (lower region). The S/G inlet and outlet nozzles are SA-508 CL 3, clad with stainless steel (309L). The nozzles ends are buttered with Inconel 82/182 and then welded to an SA-336CL1 (F316L) forged safe-end. The attachment weld is Inconel 82. The surface of the nozzle to safe-end weld is clad with Inconel 52/152 (in-lay) and machined smooth. The S/Gs sit on elevated platforms which are approximately 20 feet [6.09 meters] above the steam generator cubicle concrete floor (10 ft. [3.04 meters] platform).

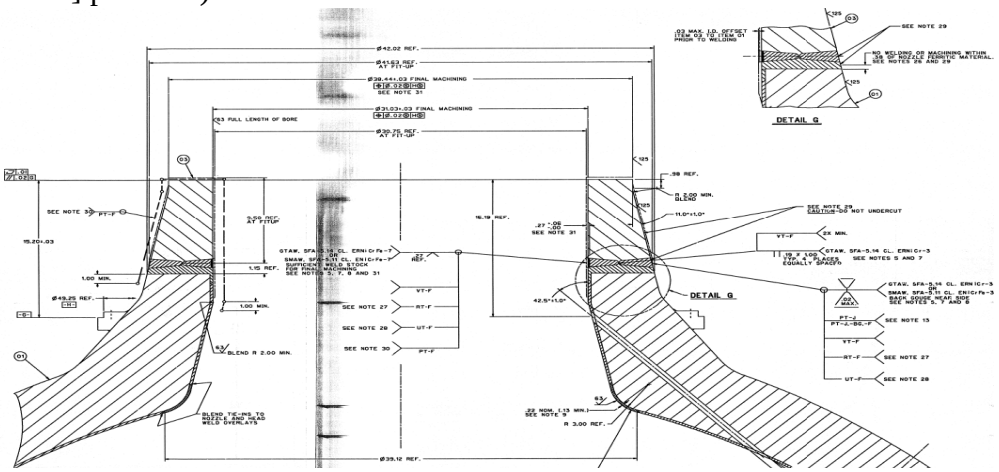

Figure 1
Point Beach Unit 2 S/G Inlet/Outlet Nozzle Configuration

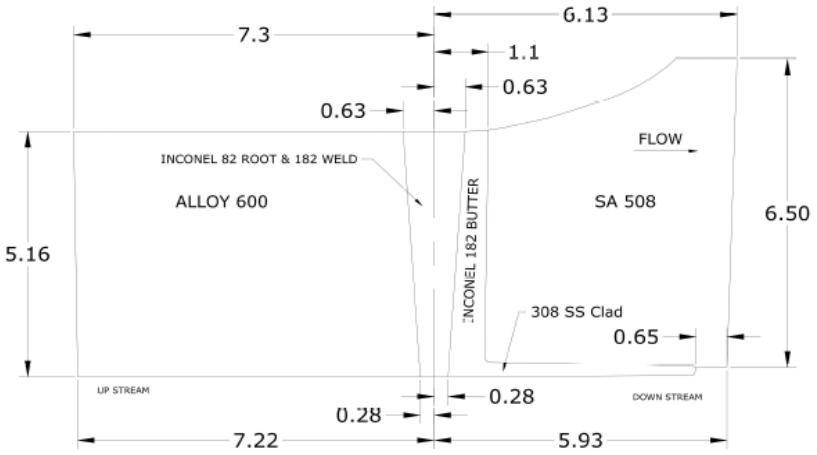

Figure 2
PDI Sample Series 712/X Configuration

PBNP is currently in its 5th 10-Year In-service Inspection Interval and is committed to the 2007 Edition through the 2008 Addenda of the American Society of Mechanical Engineers Boiler and Pressure Vessel Code, Section XI, "Rules for In-service Inspection of Nuclear Power Plant Components." PBNP has been granted a 20-year extension to its original operating license with the period of extended operation for commencing on midnight March 8, 2013. PBNP's 5th Inspection Interval for both Units ends on August 1, 2022.

SELECTION OF AN EXAMINATION VENDOR

Due to the Nuclear Regulatory Commission ruling in June, 2011, the Engineering Programs Group at PBNP sought out competitive bids from three (3) vendors capable of performing 10-Year RPV examinations, as it was believed that an expansion of a current RPV qualification through PDI would be most expeditious. The bid request went out in the Fall of 2011, with a required implementation date of Fall 2012 (U2R32). It was recognized at the time of issuance that PBNP was asking a great deal out of all three vendors, but especially the successful bidder. Due to the short turn-around time involved (less than one year from contract award to onsite implementation), PBNP was willing to fund the development and PDI procedure expansion for the successful bidder.

Due to various reasons, one of the requested bidders submitted a "no bid", and a second bidder submitted a proposal to study the problem further. Based upon the short timeframe, PBNP chose the only vendor who supplied a proposal meeting the intent of the RFP – IHI Southwest Technologies (IHI) of San Antonio Texas. The contract was issued in February, 2012 (less than 10 months before the onsite work), and IHI immediately commenced design work on the tooling, as well as communications with the Electric Power Research Institute (EPRI) to schedule time at the PDI testing facility to perform a procedure expansion. Shortly after the contract was issued, PBNP and IHI personnel also met face- to-face with PDI personnel in an attempt to chart a roadmap to success for IHI's procedure expansion demonstration.

EXAMINATION EQUIPMENT SPECIFICS

IHI developed a collapsible examination tool, named the Steam Generator Nozzle Examination Tool (SG-NExT™), which would be manually inserted into the S/G manway and then hoisted into the nozzle via a rope / pulley system. The placement system for the SG-NExT™ was rather "low tech", however, both IHI and NextEra felt that equipment simplicity would minimize the chances of failure and, if issues arose, speed any repairs.

Long handled poles were first used to install both mechanically and pneumatically operated pins into the end of an S/G tube at the tube sheet and on the nozzle dam ring. These pins supported pulleys (tube sheet) and a guide pin (nozzle dam ring) which were used to raise the SG-NExT™ into the S/G bowl and then lower it into position on the nozzle dam ring. The SG-NExT™ was then pneumatically clamped on the ring for rigidity.

The three (3) support legs and search unit module arms were collapsed and oriented in a manner which allowed insertion and retrieval through the S/G manway. These same legs and arms were then expanded when lowered onto the nozzle dam ring. Existing holes on the ring were used for registration and clamping the SG-NExT™ into place.

Figure 3
SG-NExT – Expanded for Examination

The SG-NExT™ has two (2) axes of motion, axial and circumferential (X and Y), and was designed primarily to support circumferential scanning and axial incrementing. The SG-NExT™ used four (4) PA-UT probes and 2 ET probes, sufficient to conduct the entire weld examination without requiring removal / reinsertion of the tool. A remote camera system was included to monitor the SG-NExT™ during and after installation process, perform the nozzle inner radius examination, and monitor removal after completion of the examinations.

IHI used the Zetec Tomoscan III/PA 32/128 phased array (PA) system (T-III) for UT data acquisition and analysis, and the Zetec MultiScan MS 5800 eddy current (ET) system for ET data acquisition and analysis. The T-III equipment and procedures had been fully demonstrated through ASME Section XI, Appendix VIII, as implemented by the Performance Demonstration Initiative (PDI). All data was collected inside containment, verified by certified personnel, and then transmitted via Ethernet cable to the certified Level II or Level III data analyst in a trailer outside containment to minimize radiation exposure.

The PA-UT techniques allow the collection of multiple examination angles generated by a single probe to improve both detection capability and examination efficiency. Examinations were performed in 4 directions in order to detect possible flaws both parallel and transverse to the weld using a beam angle range from 60-88 degrees. The 1.5 MHz PA probes and beam angle range were selected specifically for ID application to allow efficient detection in the inner 1/3T of the weld.

The ET technique was developed and demonstrated specifically for this examination in order to detect surface flaws and discriminate between surface and sub-surface flaw in DM welds. Two ET excitation frequencies (30 kHz and 80 kHz) were utilized for this examination. The higher frequency was chosen for its shallow penetration depth and high sensitivity to surface flaws, while the lower frequency complemented that by having a greater penetration and higher sensitivity to sub-surface flaws.

IHI had a mock-up fabricated which replicated the materials and weld configuration and had a number of flaws of various sizes / lengths placed into it at various angles in order to demonstrate the capabilities of the procedure in accordance with Appendix IV of Section XI.

The EVT-1 examination was performed utilizing an RJ Electronics color pan-tilt-zoom (PTZ) camera. This camera was mounted on a bracket mechanically clamped to the S/G Tubesheet and was also utilized as the overview camera for installation / removal of the SG-NExT™. Video quality was demonstrated prior to and upon completion of the examination via viewing of the 0.001 inch diameter wire mounted on a character card which was inserted with a long handled pole.

The viewing monitor was then "calibrated" by setting the zoom to the optimum quality with the 1-mil wire in view and then measuring the size of one of the nozzle dam ring holes. This measurement was recorded and could be used both to ensure that the camera was back at the correct zoom if the examiner moved the zoom in or out for some reason or to "size" any indication that might be recorded.

PLANNING

Due to the impact on the schedule of the refueling outage, this examination received an extremely high level of attention from management both at the site, and the NextEra corporate offices. Due to their familiarity with both ASME Section XI and the overall job scope, the PBNP NDE Level III and In- service Inspection Coordinator were chosen as the Day Shift Lead and Night Shift Lead, respectively.

Personnel from Operations, Maintenance, Radiation Protection, Nuclear Supply Chain, and Production Planning (Outage Scheduling), as well as several personnel from Engineering Programs were engaged in the planning process. These groups were recognized as playing an integral part of the overall success of the examination.

An initial kick-off meeting was held at IHI's offices in San Antonio, Texas in early March, 2012 which was followed the next week with a meeting at the Electric Power Research Institute's (EPRI) NDE Center in Charlotte, North Carolina to lay-out the PDI qualification activities that would be required on an expedited basis.

The PBNP S/G mock-up which is used for ET and nozzle dam just-in-time-training (JITT) was shipped to IHI in

March, 2012 to assist with tooling development and training. This was a valuable tool for the design engineers, most of whom had never seen an S/G manway / bowl up-close.

IHI made several minor modifications to the S/G mock-up in order to optimize it for their purposes – this included insertion of several tubes into the sheet metal "tube sheet" on top of the mock-up and adding a nozzle extension to the nozzle to allow the SG-NExT™ to be fully exercised in both the X and Y direction. In addition to the PBNP S/G mock-up, IHI utilized a large nozzle DM weld mock-up to test the couplant delivery system & detection capabilities of both the PA UT and ET systems as mounted on the SG-NExT™.

Since no vendors had successfully demonstrated the capability to meet the through-wall sizing acceptance criteria of Appendix VIII, Supplements 2, 3, and 10 [0.125 inch (3.175 mm)] root mean square (RMS), a request for relief (RR) from the requirements of the U.S. Code of Federal Regulations (CFR) governing in service inspection [10 CFR 50.55a(g)(4)] would have to be submitted if PBNP wanted to utilize the PA UT from the ID for sizing any flaws. Because of the compressed timeframe, PBNP chose to utilize a contingency of having an outside diameter (OD) capability as the back-up for flaw sizing. Two contingency items were implemented: (1) PBNP's manual ISI vendor was contracted to have equipment in place at their home office capable of being shipped overnight; and (2) the DM weld mock-up from North Anna Nuclear Power Station (NAPS) was borrowed and would be staged on site during the outage so the OD equipment could be site demonstrated to the Authorized Nuclear In- service Inspector (ANII) as necessary. It was determined that the NAPS replacement S/G nozzle configuration (thickness, taper, etc.) was within the bounding tolerance of the PDI procedures, therefore minimal preparation would be required to implement this contingency.

In early July, 2012 a tooling demonstration / challenge meeting was held at IHI to provide PBNP personnel the opportunity to view and critique the "final" design of the SG-NExT™. Based upon the demonstration results, minor modifications were made to the tooling prior to shipment to site in October.

In parallel with the equipment activities, IHI had been preparing changes to their previously qualified ID procedure for the examination of RPV DM welds in order to demonstrate the capability of the probes to detect flaws using "flooding" of the search unit for coupling rather than complete submergence. These activities took place in June and July of 2012, with final approval from EPRI/PDI in August.

Just prior to commencement of U2R32, a final hurdle was placed in front of the NextEra / IHI team. Personnel from Operations had reviewed the examination plan's use of deionized water taken from a connection inside containment and pumped through the end-effectors for couplant and raised the concern of dilution of the reactor coolant system (RCS) inventory.

During the PDI demonstrations, PBNP had requested that IHI obtain flow-rate information on the flooding system, and that had been presented to PBNP Operations for review.

Based on the approximately 2 gallons per minute (GPM) flow rate of the flooding system and the approximately 8 hour per nozzle examination time, Operations personnel determined that a sizable "slug" of non-borated would reside within the RCS which could not be properly mixed prior to commencement of refueling activities. This would increase the risk of a reactivity event during refueling. At this point Operations informed Engineering Programs that only borated water could be utilized for couplant.

EXECUTION

In October 2012, U2R32 commenced. The original plan showed the IHI equipment being staged onto the "A" S/G manway platform on the 8th of November and the examination commencing the following day, with the "B" S/G running essentially in parallel. Due to other issues at the plant, the actual commencement of examinations occurred early on the morning of the 14th of November. The visual examinations of the "A" and "B" Hot Leg inner radii were completed prior to the start of the day shift that day.

Unfortunately, there were equipment issues which caused a delay in the commencement of the UT activities in the "B" S/G, and by approximately 1700 on the 15th, the Outage Control Center (OCC) made the decision to have IHI pull their equipment out of the "B" S/G to make way for the S/G Eddy Current (ET) examinations.

While the "B" S/G troubleshooting had been ongoing, the "A" S/G examination was continuing, albeit slowly. At approximately 1800 on the 14th, the examination of the "A" Hot Leg had completed, and the equipment was de-mobilized off the platform to make way for the S/G ET equipment.

After the equipment had been secured, IHI and PBNP personnel met to perform a critique of the execution thus far.

It was determined that there were several weak spots which had not been properly accounted for during the original work planning & staffing:

- Two people for manipulation of equipment was insufficient.
- The mock-up contained a Cold Leg configuration, and the installation on the Hot Leg was far more limiting due to the angles / obstructions on that side of the platform.
- The radiation shield door and insulation package were not accurately modeled. Both limited tooling manipulation.
- An hour was lost due to individuals having to return to the RP station to have their set-points "bumped up". RP initially mandated that only two (2) personnel could have bumped up alarms at one time.
- Technical difficulties with the headset radios used to communicate with RP caused delays & an increase in exposure.
- The S/G bowl during camera installation was much darker than anticipated.

Since the S/G ET crew was scheduled to perform 100% of the Hot and Cold Leg tubes on both generators, PBNP and IHI personnel utilized the "down time" to their advantage. In addition to addressing the items listed above, as well as others, personnel went back out to the S/G mockup for additional training on body positioning and practicing on placement of the monitoring camera.

At 1200 on November 17, 2012 IHI took ownership of the "B" S/G platform from RP. Examinations of the "B" Inlet Nozzle commenced at approximately 1400, followed by the Outlet Nozzle 20 hours later.

The total duration on the "B" S/G was approximately 30 hours. On the morning of November 18th, the SG-NExT was placed into the "A" Outlet Nozzle to perform that examination. The total time for set-up, examination, and tear-down on the "A" Outlet Nozzle was 13 hours, a marked improvement over the "B" S/G.

After completion of examinations, one piece of foreign material (FM) was required to be retrieved, using remote tooling provided by the site. The FM event occurred due to a previously unrecognized single-point vulnerability failure. IHI immediately captured this issue in the project lessons-learned file for re-design after the outage. The FM retrieval equipment was de-mobilized off the "A" manway platform and it was turned back over to the station by 0200 on the 19th of November.

The examination data (both UT and ET) were excellent, with the weld and "inlay" regions clearly discernible (See Figure 4). No indications of cracking, inclusions, or any other defects were detected.

Total exposure for the work was just over 5,000 mR (0.050 sv) expended with over 750-person hours logged in the RCA. There was also a minor heat-stress event and a minor personnel contamination event, as well as the FM event discussed above.

Figure 4
Examination Results (Typical)
ID-11 SG B Safe-End to Inlet Nozzle (Away Towards)

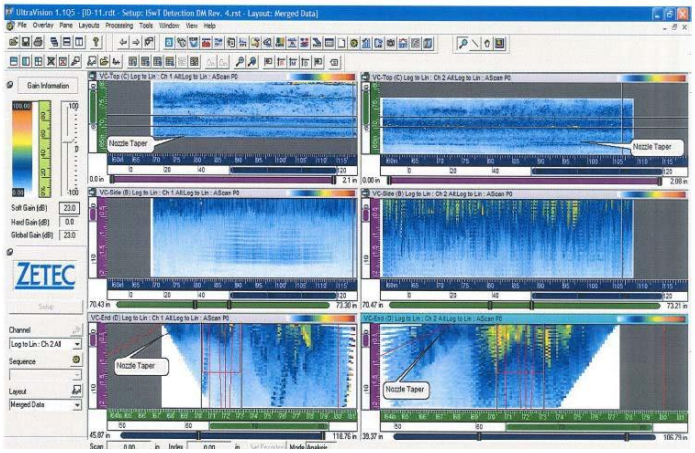

CONCLUSIONS / LESSONS LEARNED

The examination of the PBNP Unit 2 S/G DM welds from the ID was a first-of-a-kind event in the U.S. which was conceived and implemented in approximately 12 months. The pace of this project is never recommended, however it was successful for a number of reasons, mostly due to the dedication and hard work of both NextEra Energy and IHI personnel working as a team. Based on the experiences over the past three years, the following items should be considered when planning for such an activity:

1. The bid specification should clearly state all site requirements and how the bidder will address them, including any procedure review/revisions, training, demonstrations, or meetings that should be considered as basic "in-scope" work. In addition, the bids should clearly have any site support requirements identified as well as the site's expectations for Foreign Material controls, Security/Badging requirements, and any penalties that would be imposed upon the vendor for violation of those requirements.

2. The use of the High Impact Team concept that includes various work groups on site as well as the examination vendor is an excellent method to ensure that neither the implementing organization (Engineering Programs at PBNP) nor the vendor are complacent with their planning and preparation.

3. The vendor should be considered a team member and not treated as someone who will just show up, do a job, and leave. Communication to vendor personnel by the site should occur frequently and they should understand how important their job is to the overall success of the outage, as well as the future of the plant.

4. A clear communication plan for both vendor-to-site contact communication as well as project- to-outage control center communications. This helps keep rumors to a minimum and helps keep personnel in the field from being distracted by non-project personnel wanting status updates.

5. Site project personnel should become intimately familiar with the equipment, procedures, and processes so that when challenges arise, they can understand some of the bases for recommendations that may come from the vendor.

6. Radiation dose rates and time to install equipment should be carefully reviewed and previous rates should be looked at skeptically. During the planning phase, the exposure rates provided by RP were combined with the installation times provided by IHI to come up with a dose estimate.

Due to the higher dose rates encountered on the platform, as well as the extreme congestion of the platform areas, 75% of the original exposure estimate was expended during the set-up phase alone. In addition, the average platform dose rate was >150 mR/hr (0.0015 sv/hr), which was 1.5 to 2 times the estimate provided by RP prior to the outage.

7. During equipment fabrication, an individual outside of the design / fabrication team should review the entire process to look for possible single-point vulnerabilities.

8. The mock-up training should consider the possibility of additional limitations such as support beams, ladders, and temporarily installed equipment in the same area where the tooling installation personnel will be working. In the case of the PBNP work, there was not an outage prior to the work that walk downs and careful measurements could be taken to include these limitations during the training.

THANKS

The authors would like to thank the following individuals and or groups for their support during this evolution:

NextEra Energy - Point Beach Nuclear Plant:

Messrs. Charles Trezise, Bryan Woyak, and Roger Bardo

IHI Southwest Technologies

Messrs. Carlos M. Barrera, Jesse R. Delgado, Hector Diaz, Joel G. Godwin, and Ramon Villagomez.

REFERENCES

1) American Society of Mechanical Engineers (ASME) Boiler and Pressure Vessel Code, Section XI, Division 1, "Rules for In-service Inspection of Nuclear Power Plant Components, 2007 Edition through 2008 Addenda," ASME, New York, New York, 2008 as modified by 10 CFR 50.55a, dated June 21, 2011.
2) ASME Code Case N-770-1, "Alternative Examination Requirements and Acceptance Standards for Class 1 PWR Piping and Vessel Nozzle Butt Welds Fabricated with USN N06080 or UNS W86182 Weld Filler Material With or Without Application of Listed Mitigation Activities, Section XI, Division 1", ASME, December 25, 2009.
3) ASME Code Case N-619, "Alternative Requirements for Nozzle Inner Radius Inspections for Class 1 Pressurizer and Steam Generator Nozzles, Section XI, Division 1", ASME, February 15, 1999.
4) Electric Power Research Institute (EPRI) letter from Carl Latiolais to William A. Jensen, "Summary of IHI Southwest Technologies Supplements 2 & 10 Depth Sizing Results Obtained from the Inside Surface," EPRI, Charlotte, North Carolina, February 25, 2008.
5) IHI Southwest Technologies, "Exam Plan – Automated Ultrasonic Examination of the Steam Generator Inlet and Outlet Nozzle Dissimilar Metal Welds and Nozzle Inner Radius," San Antonio, Texas, September, 2012.
6) IHI Southwest Technologies, "Final Report – Automated Ultrasonic Examination of the Steam Generator Inlet and Outlet Nozzle Dissimilar Metal Welds and Nozzle Inner Radius at Point Beach Nuclear Plant Unit 2," San Antonio, Texas, November, 2012.

INSPECTION QUALIFICATION III

QUALIFICATION OF END OF MANUFACTURING NON DESTRUCTIVE EXAMINATION FOR HIGH INTEGRITY COMPONENTS

JL Gobert, F Lasserre, M Jambon, JM Crauland
AREVA, France

ABSTRACT

In the frame of the construction of an EPR™ for the UK, a demonstration of avoidance of fracture for High Integrity Components (components for which a gross failure can be discounted) forming the main primary and secondary circuits is required. The purpose of this demonstration is to show that the likelihood of failure of these components is so low that it can be discounted.
This demonstration is based on:

- Fracture mechanic analysis,
- Fracture toughness measurement,
- Implementation of a qualified non destructive examination at the end of manufacturing.

The target defect size is determined by fracture mechanic analysis and the objective of the qualification of the end of manufacturing examination is to demonstrate that the components enter in service without defect of structural concern.
The qualification process is based on ENIQ [1] (European Network for inspection and qualification) principle but is adapted to manufacturing process especially regarding the type of defects to be detected.

The present paper gives an overview of the qualification process set up for non destructive examination of welds of HIC components and applied by AREVA for the manufacturing of these components for the construction of an EPR™ in UK.
A practical example implemented for the qualification of UT examination of the steam generator welds for secondary part is also presented.

INTRODUCTION

In the frame of the construction of an EPR™ the United Kingdom nuclear regulation required a multi-legged safety case to be produced to support arguments made regarding the structural integrity of High Integrity Components (HIC component for which a gross failure can be discounted). As a part of the achievement of the integrity leg for the structural integrity safety case it is required to demonstrate that these components are free from significant defects at the end of manufacturing process. This is carried out through the use of suitable redundant and diverse inspections during manufacture, complemented by the use of a qualified inspection at the END of manufacturing to detect defects of structural concern with high reliability.

The high Integrity Components are the components of the main primary and secondary circuits:

- Reactor Pressure Vessel
- Steam Generator
- Pressurizer
- Main Coolant Line
- Reactor Coolant Pump
- Main Steam Lines

The requirements for qualification are concentrated on the welds that are the most sensitive area of these components.
The qualified examination is the examination carried out after final post weld heat treatment if any and is mainly ultrasonic examination.

The present paper gives an overview of the qualification process set up for non destructive examination of these welds and applied by AREVA and a practical example implemented for the qualification of UT examination of the steam generator welds for secondary part is also presented.

QUALIFICATION PROCESS

The principle of the qualification process is based on European Network Inspection and Qualification (ENIQ) methodology [1]. This methodology written for the qualification of in service inspection has been adapted to manufacturing inspection

Different stakeholders from the customer and the manufacturer are involved in collaborative work for the qualification process and also an independent third party, the Qualification Body (QB) according to ENIQ. The Qualification Body has in charge to establish the qualification procedures.
A simplified flowchart of the qualification process is described in Fig 1 and the main phases of this process are described below.

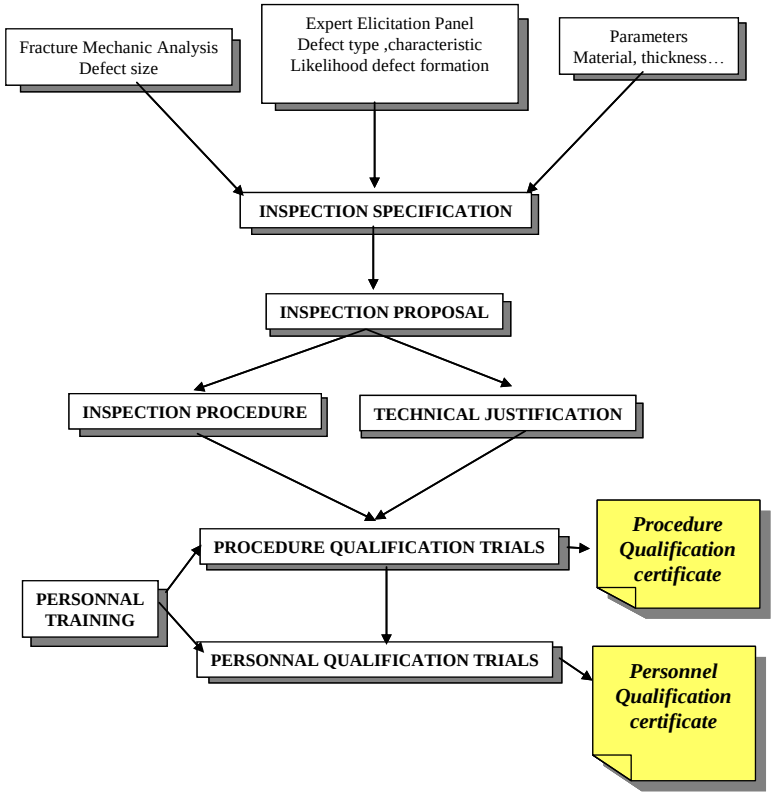

Fig 1 qualification flowchart

Inputs data for qualification

Target defect size
The size of the defect that can induce a gross failure at the end of life of the component is established by means of fracture mechanic calculations for planar defects oriented perpendicular to the surface of the component. A margin of 2 is applied to the calculated size in order to establish the Qualified Examination Defect Size that is the target defect size to be detected by the qualified non destructive examination.

Type and characteristic of the defects that can occur.
The examination concern the manufacturing welds and it is necessary to establish the type of defect that can occur and to determine their characteristics as the orientation (tilt and skew) and the main aspect (rough or smooth).
In order to establish these parameters an Expert Elicitation Panel (EEP) has been implemented with experts in metallurgy, welding and non destructive examination.
The lists and characteristic of the defects that can occur have been established by the experts. They have taken into account, the analysis of the materials, the manufacturing and welding process involved for each welds and their knowledge of similar manufacturing and welding processes. A likelihood of defects formation has also been established:

- Conceivable – Likely: These are defects which can occur in normal manufacture when all the specified controls are apparently in operation.
- Conceivable – Unlikely: These are defects which could occur in normal manufacture if a single essential control was not effectively applied.
- Conceivable – Highly Unlikely: These are defects which could occur if a series of redundant and diverse controls were not properly applied. This category may also cover other orientations of defect types that are themselves "conceivable – unlikely".
- Inconceivable - These are defects which, even with gross lapses in the manufacturing controls, cannot be conceived to be present.

Grouping of the welds
In order to limit the number of qualifications, many welds may be grouped in a same qualification group if, the material, the thickness of the component, the welding process and the previous input data as target defect size type and characteristic, are the same or very similar even with two different components. In this case it is likely that the non destructive examination implemented can be the same and a single qualification can be carried out for all the welds of this group.
For the HIC components of the EPR™ 13 different qualification groups have been identified.
Inspection specification
The inspection specification is the entry point for the qualification process so a key document. This document written by the customer summarise all the input data for the qualification of a weld or a group of welds and defines

- The Target defect size
- The type of defects and their characteristic tilt and skew
- The requirements for the qualification

For the qualification of the examination of the HIC components welds the requirements have been defined on the detection and characterisation (planar or volumetric) of conceivable likely or unlikely defects. For conceivable highly unlikely defects an assessment of the capability only is foreseen.

Inspection proposal

The first answer of AREVA is to propose a NDT technique, which is in line with the requirements and can be able to detect the target defects, and to describe the process intended to be implemented for the justification of the capability of the NDT technique used to detect the required defects. The intend of this document is to avoid the development of techniques or justifications that do not correspond to the customer or Qualification Body objectives.

It has to be noted that even if the redundant diverse and complementary examination carried out at different stages of the manufacturing are able to detect the defects the NDT qualification is only based on the examination carried out at the end of manufacturing. Therefore a simple examination based on the code requirements only, which are based on the complementarities of the different examinations during manufacturing, is not sufficient to satisfy the requirements of the inspection specification.

Technical justification

The purpose of the technical justification (TJ) is to present the analysis and justification of how and why the intended examination will be capable of achieving the aims of the inspection specification. This justification is performed with the assessment of the influential parameters and the justification that these parameters are taken into account in the qualification process and in the examination procedure if necessary.

This justification include

- An analysis of the influential parameters
- Physical reasoning and logical argument
- Results obtained with modelling software
- Justifications with existing results
- Results on practical trials with need of mock-up if necessary

The technical justification is assessed by the customer and by the QB

Inspection procedure

The inspection procedure is developed in parallel with the TJ and take into account the parameters analyzed by the TJ.

The inspection procedure is assessed by the customer and by the QB

Qualification of the procedure

The qualification of the procedure is carried out with practical trials on an "open test" mock-up.

The defect embedded on this mock-up must be representative of the manufacturing defects defined in the inspection specification according to the EEP process.

The material and welding process shall be similar for ferritc weld and identical for austenitic welds or dissimilar metal welds.

The Qualification Body is in charge of the procurement of the mock-up and for a group the mock-up is designed taken into account the geometry of the welds the access restrictions and the worst case defect according to the TJ analysis

Training of the personnel

Qualified examinations require generally more complex operations than current examinations carried out by the operators and specific requirements and new techniques can be used. The operators need to be experimented on the examination of this type of components, they shall have a perfect knowledge of the procedure and they shall be able to implement correctly this procedure with the respect of all essential parameters .A theoretical and practical training are therefore necessary . After the training the operators shall be qualified according to theoretical and practical exams

Personnel qualification

After the training the operators shall be qualified according to theoretical and practical exams

The personnel qualification is validated by the Qualification Body according to a justification of the personnel experience and after theoretical exam and practical exam on a "blind test" mock-up. This mock –up is designed by the QB which is the only one who has the knowledge of the defects embedded in the mock-up.

QUALIFICATION OF THE EXAMINATION OF STEAM GENERATOR WELDS

The main welds of the Steam Generator for which the end of manufacturing NDT shall be qualified are shown in Fig 2.

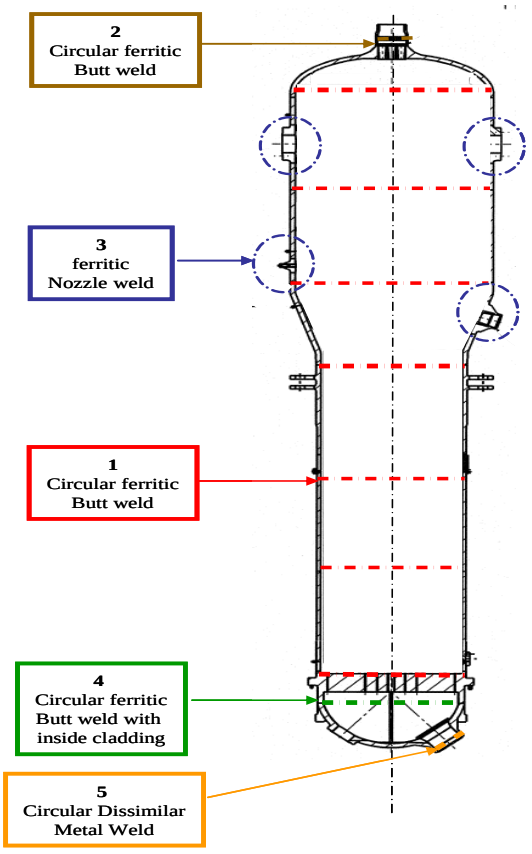

Fig 2 main welds of Steam Generator

According to the different input data five different groups of welds have been defined
In the secondary part of the Steam Generator

- **1** Main circular ferritic welds of the SG shells (7 welds)
- **2** Circular ferritic weld of the outlet steam tubulure (1 weld)
- **3** Nozzle ferritic welds on the shells (4 welds)

On the primary part of the Steam Generator

- **4** Circular ferritic weld with inside austenitic cladding between the tube sheet and the primary head (1 weld can be grouped with similar welds on other components)
- **5** Circular Dissimilar Metal Weld (inconel) between the primary head and the safe end (2 welds can be grouped with other similar welds on other components).

First development of the qualification process for the main circular ferritic welds of the SG shells

Input data
Material: 20 MND5
Thickness: 98mm to 131 mm Diameter: 3799 mm to 5165mm
Welding process: Submerged Arc Welding Narrow gap weld as shown in Fig 3.After welding the root pas is machined and the weld is internally and externally ground flush

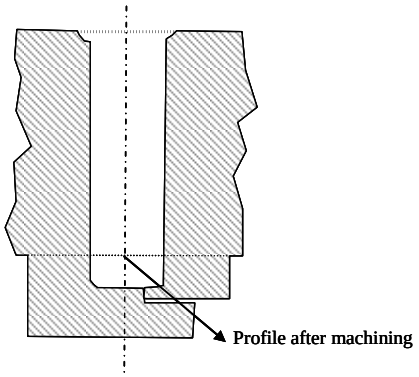

Fig 3 Steam Generator Narrow Gap Weld

A first fracture mechanic analysis has establish the Qualification Examination Defect Size :
10 mm trough wall extend x 60 mm length.
According to the robust manufacturing and welding processes the Expert Elicitation Panels does not identified any planar defect as being conceivable likely only planar defect as lack of fusion or hydrogen cracking have been identified as conceivable unlikely. The other types of defects have been classified conceivable highly unlikely or inconceivable.
The main requirement for the qualification of the inspection procedure is finally a high reliable detection and characterisation of longitudinal planar defect rough or smooth with sizes 10mm x 60mm or greater every where in the weld or in the heat affected area..
According to the type of bevels and welds, these defects are oriented parallel to the weld axis and near vertical. Therefore the possible variation of tilt and skew has been limited to 5°
An assessment of the NDT examination without qualification criteria shall be also carried out for highly unlikely longitudinal and transverse defects with greater tilt and skew up to 20°
Inspection proposal
The inspection proposed is an ultrasonic examination with 0° compression wave and angle beam shear waves
According to the current practice the examination is a manual examination that can be carried out from each side of the weld and from the outside and inside surfaces.
In order to increase the detection capability and reliability three different angles will be used 45°-60°-70°.
Due to the orientation of the defects, near vertical, the detection is difficult when they are smooth and not near the surfaces (no corner effect) therefore a tandem technique will be also implemented for the detection of such defects.
A synthesis of the UT examination is given in Fig 4 and 5

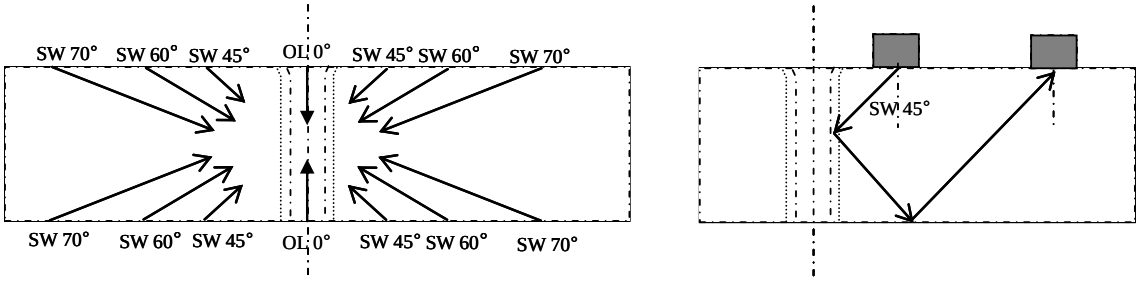

Fig 4 detection of longitudinal defects with 0° compression waves, angle beam shear waves and tandem

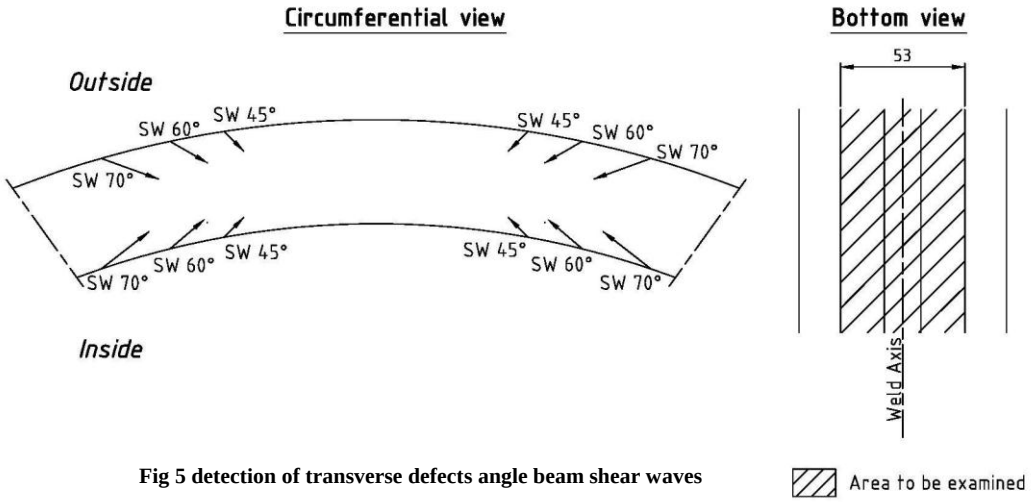

Fig 5 detection of transverse defects angle beam shear waves

The development of the procedure and the technical justifications are in progress and in parallel automated Phased Array and TOFD UT techniques are is also developed to be used with the same qualification objectives

CONCLUSIONS

Even if the ENIQ rules are used as a reference, the definition and the implementation of a qualification process for the end of manufacturing need an intensive collaborative work between the different stakeholders involved in the process, as the customer, the manufacturer, the qualification body ,because it does not exist defined rules that described such a process .Therefore the qualification process rules must be discussed defined and agreed between the different stakeholders. In the case of the UK EPR™ the specific objectives of the safety case demonstration have been taken into account.
The qualification of NDT examination is currently used for the preservice and in-service inspection but rarely for the manufacturing inspection and in this case the scope of qualification regarding the type and localisation of defects to be detected and area to be examined is more extended
Some assumptions may be necessary to implement the process. For example it is not possible to have the final results of the fracture mechanic analysis of all the welds at the beginning of the process and a first calculation with conservative hypothesis may be use.
In the case of the qualification process developed for the UK EPR™ the qualification of NDT for the safety case demonstration is based only on the last end of manufacturing examination after post weld heat treatment. Therefore an examination after post weld heat treatment based only on the code requirements is not sufficient to assume a high reliable detection of the defects as required by the qualification criteria.

REFERENCE

1) European methodology for qualification of non destructive testing ENIQ report N° 31

QUALIFICATION OF THE ULTRASONIC INSPECTIONS OF VACUUM VESSEL WELDS OF THE ITER REACTOR

F. Fernández, A. García, M.C. Pérez, R. Martinez-Oña Tecnatom, Spain,
G. Pirola, Ansaldo Nucleare, Italy
A. Dans, A. Bayón, F4E, Spain

ABSTRACT

The ultrasonic inspection of ITER Vacuum Vessel welds is a challenge, due to the complex geometry of this component and the anisotropy of the austenitic weld material. This inspection could require the combination of several ultrasonic techniques.

To detect and characterise defects in these materials, Tecnatom is developing a main ultrasonic inspection technique based on phased array probes. Additionally, other inspection techniques are used, which works with emitter – receiver conventional probes. The purpose of these last techniques is to complement the examinations performed with phased array probes in the detection and characterisation of specific defects.

The seven sectors of the ITER Vacuum Vessel, which are being manufactured by an Italian Consortium led by Ansaldo Nucleare and including Mangiarotti and Walter Tosto as manufacturing partners, will have available a set of several ultrasonic techniques to guarantee the fulfilment of the RCC-MR Code edition 2007 requirements.

The qualification of these inspection techniques is being supervised by the European Domestic Agency Fusion for Energy that is the responsible of managing the production of the Vacuum Vessel.

INTRODUCTION

The vacuum vessel is an austenitic steel component that houses the fusion reaction. The plasma particles revolve inside a toroidal inner chamber with a D-shaped cross-section. Both the design and manufacturing of the vacuum vessel and the corresponding examinations are in accordance with the requirements of the 2007 edition of the RCC-MR Code.

This Code requires that a radiographic examination be performed on all category 1 and 2 welds of the vacuum vessel. Given the geometric characteristics and the construction sequence of the vacuum vessel, certain of these welds are accessible only from one surface. These characteristics mean that it is not possible to perform the volumetric examination of these welds (represented in Figure 1) using radiographic techniques.

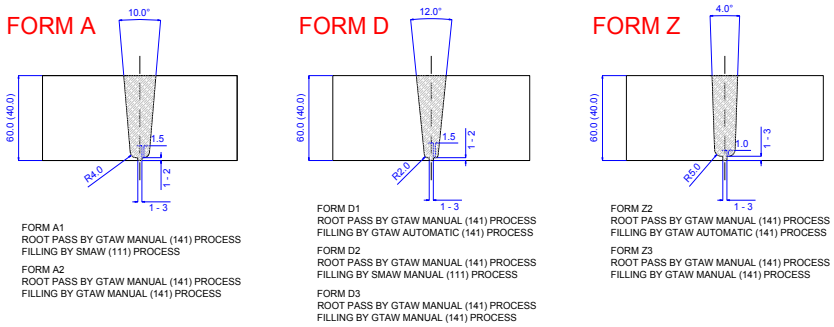

Figure 1. Welds to be inspected ultrasonically

The alternative is using ultrasonic techniques, when it is demonstrated that radiographic techniques cannot be developed. This alternative of carrying out the volumetric inspection using ultrasonic techniques entails the following difficulties, among others:

- The welds are manufactured using austenitic stainless steel and several different welding processes (automatic and manual). The habitual thickness of the welds is 60mm. Despite the highly demanding quality requirements applicable to the materials and welding procedures, the inspection of austenitic welds is always a challenge because of the anisotropy of the materials.
- In certain welds, the accessible surface (i.e., the surface to which the probe is coupled) on either side of the weld is limited. This situation is due to the complexity of the geometry of the vacuum vessel. In order to guarantee the ultrasonic inspection of all the welds, the probes and examination techniques have been designed such that the coupling surface required on either side of the weld is as small as possible. In this respect, certain changes have been made to the design of the vacuum vessel in order to guarantee this minimum accessible surface on all the welds.
- The probe coupling surface is curved in shape. Given the toroidal shape of the vacuum vessel, there are welds with concave and convex coupling surfaces both in the direction of the weld and in the direction perpendicular to the weld. Although in most cases these curves are negligible for the ultrasonic inspection, given the large dimensions of the vacuum vessel, this is not always the case.
- The weld centreline may be straight, curved or circular. In order to ensure inspection of all the welds with maximum guarantees, all the examinations performed "in situ" (i.e., on the actual component) will be carried out using a semi-automatic device that allows the position of the probe to be coded. For each examination performed on each of the welds, a data file will be generated containing the complete ultrasonic signal of each of the probes, along with the positions (coordinates) at which the probe acquired the ultrasonic data.
- The RCC-MR Code requires each of the defects detected to be characterised, establishing whether these defects are planar or volumetric. All planar defects (cracks and lack of fusion) are unacceptable, regardless of their size and position.

In view of the difficulties described above, the European Fusion for Energy Agency, which is responsible for managing the manufacturing of seven sectors of the vacuum vessel, requires the qualification of the ultrasonic volumetric inspections of welds accessible from a single surface. Tecnatom is responsible for such qualification.

DEFECTOLOGY

Postulated defects in the weld are classified as planar or volumetric. The essential variables of defects currently considered are: size (length and through wall extension), position (base metal, weld metal or weld interface), location along the thickness (scanning surface breaking, embedded, or opposite to scanning surface breaking), orientation (perpendicular or parallel to the weld), skew, and nature (planar or volumetric). A relation of the defects that have been postulated is given in Table 1.

To develop and assess the capability of the ultrasonic techniques they must be also considered the imperfections in the root area and the disturbing factors (see Table 1).

Table 1. Postulated defect. Weld imperfections and disturbing factors

Weld defects	
Slag inclusion (for SMAW)	Volumetric
Tungsten inclusion (for GTAW)	Volumetric
Porosity and gas pore	Volumetric
Crack	Planar
Hot crack	Planar
Lack of fusion	Planar
Undercut	Planar
Weld imperfections in the root area	
Lack of root penetration	--
Root concavity	--
Excessive penetration	--
Shrinkage groove	--
Disturbing factors	
Weld node	--
Weld repair	--
Misalignment	--

INSPECTION TECHNIQUES. PHASED ARRAY PROBE

Taking into account all the ultrasonic examination requirements indicated above, the basic ultrasonic technique proposed is the pulse-echo technique, using a phased array probe performing the inspection in the two directions (perpendicular and parallel to the weld) and in the four possible orientations (Y+, Y-, X+ and X-). This probe is of the dual type (i.e., with the emitting and receiving stages separate) and is mounted on an angle wedge. The advantage of using a phased array probe is that this type of probes allows scanning movements to be minimised (this being adequate in view of the small space available on either side of the weld), and also allows ultrasonic beams with different angles and with both types of wave (longitudinal and transversal) to be refracted in a single examination.

With dual probes, the maximum sensitivity occurs in the zone in which the ultrasonic beams of the emitter and receiver stages cross. The advantage of this design is that it improves the signal-noise ratio of the ultrasonic signal in the crossover zone.

The focal laws are calculated for steering of the inspection volume with refracted beams varying within a given range of angles. A first set of ultrasonic beams covers the upper third of the inspection volume with longitudinal waves; a second set covers the intermediate area and lower third with longitudinal waves; and a third covers the lower third with transverse waves. In this way, a dual array probe replaces an entire series of conventional probes, allowing inspection times to be reduced.

In order to detect defects parallel to the weld, the probe is displaced along either side of this weld (see Figure 2). To detect defects perpendicular to the weld, the probe is passed along the weld in the two possible orientations (X+ and X-) (see Figure 3).

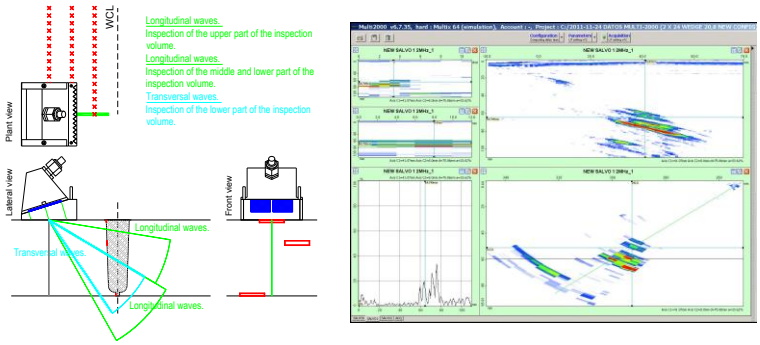

Figure 2. Scanning for detection of defects parallel to the weld

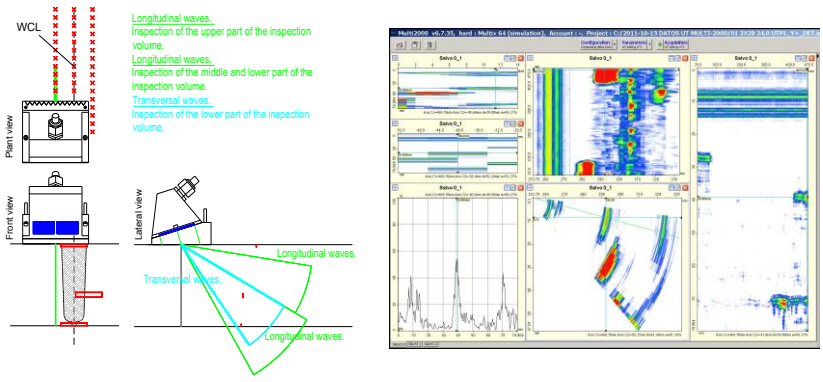

Figure 3. Scanning for detection of defects perpendicular to the weld

OTHER TECHNIQUES. CONVENTIONAL PROBES

As a complement to the phased array probe technique described above, other inspection techniques using conventional probes are being developed. The purpose of these techniques is to complement the examinations performed using phased array probes for the detection and characterisation of certain specific cases. These probes are as follows:

- Creep wave probes with the pulse-echo technique for the detection of defects open to the scan surface, both perpendicular and parallel to the weld. Although phased array probes detect these defects, the use of creep wave probes notably improves the signal-noise ratio with which they are detected. Consequently, it has been proposed that the inspection of all the vacuum vessel welds include an examination with these probes in the four directions (Y+, Y-, X+ and X-, see Figure 4 and Figure 5).

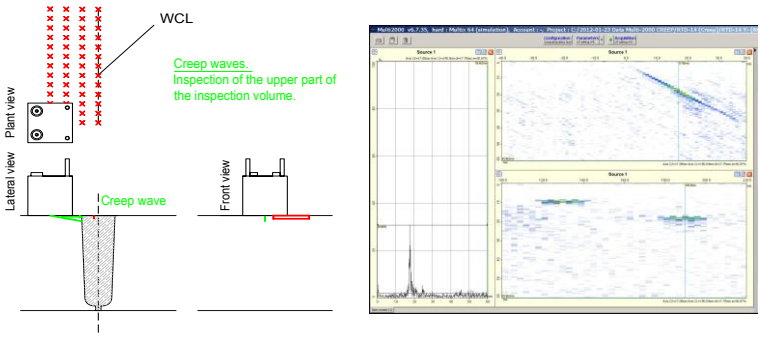

Figure 4. Scanning for detection of defects open to the inspection surface

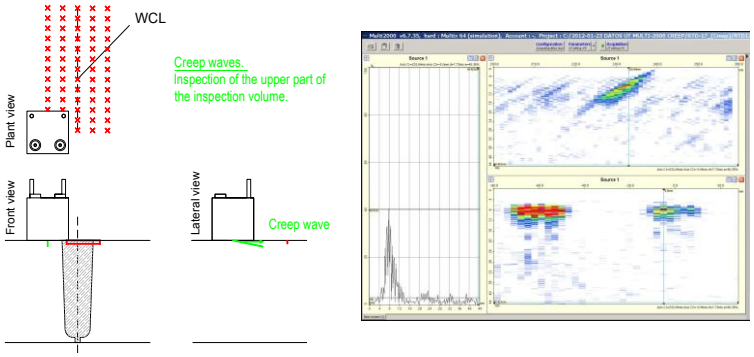

Figure 5. Scanning for detection of defects open to the inspection surface

- Low frequency probes with pulse-echo technique for the detection of defects perpendicular to the weld and open onto the surface opposing that used for the inspection. The detection of these defects may be performed with phased array probes by positioning the probe on the base material and orienting the position of the probe with respect to the weld centreline. However, the detection of these defects by positioning the probe just above the centreline of the weld (i.e., with the ultrasonic signal always travelling through the weld) is possible only with this type of probes (see Figure 6).

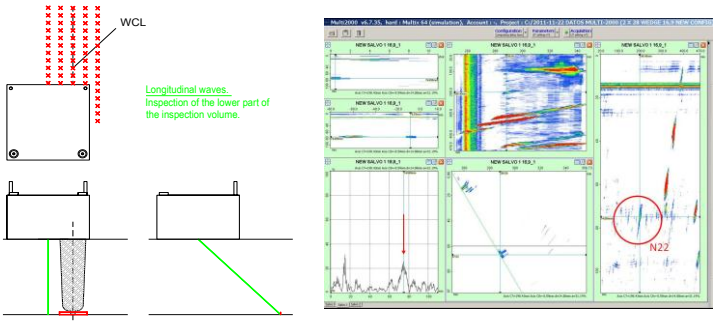

Figure 6. Scanning for detection of defects open to the opposite surface

- Focussed probes with the pulse-echo technique for the characterisation of defects (through the search for diffraction signals). With phased array probes it is possible to observe the diffraction signals of planar defects. The signal-noise ratio of these diffraction signals may be improved in different ways. For example, the signal may be improved by using matrix phased array probes or root angled wedges. However, the simplest way to improve this signal-noise ratio is by using conventional probes focussed at different depths (see Figure 7).

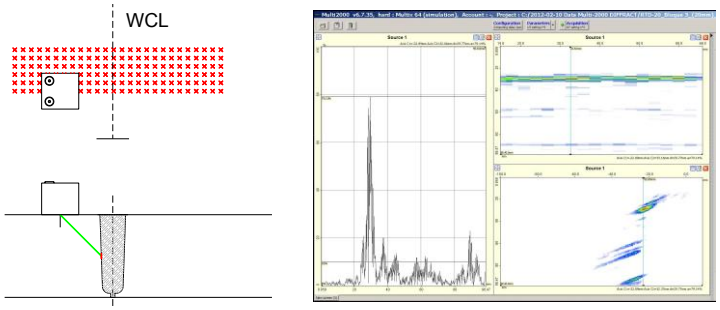

Figure 7. Scanning for characterization of defects (focused probes)

- Shear wave probes with the tandem technique. The objective of this technique is to confirm that defects characterised as being planar (due to possible diffraction signals having been observed) are in fact planar. The criterion postulated for use with this technique is to consider the amplitude of the signal reflected by a planar defect to be greater than the amplitude of the signal reflected by a volumetric defect. The range of thicknesses in which this technique may be applied is approximately between 0mm and 40mm (see Figure 8).

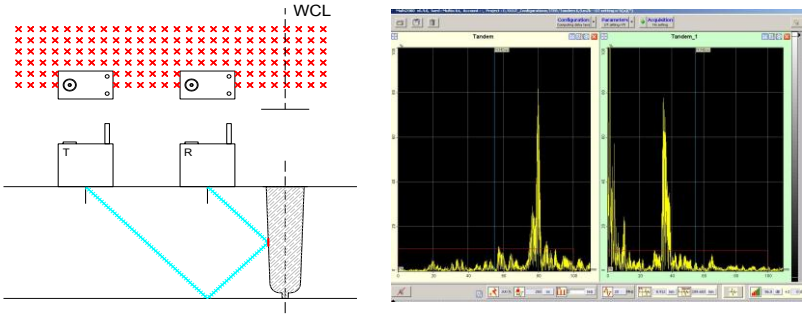

Figure 8. Scanning for characterization of defects (tandem probes)

- LLT probes with the auto or round trip tandem technique. The objective of this technique is the same as for the tandem technique. The range of thicknesses in which this technique may be applied is approximately between 30mm and 60mm (see Figure 9).

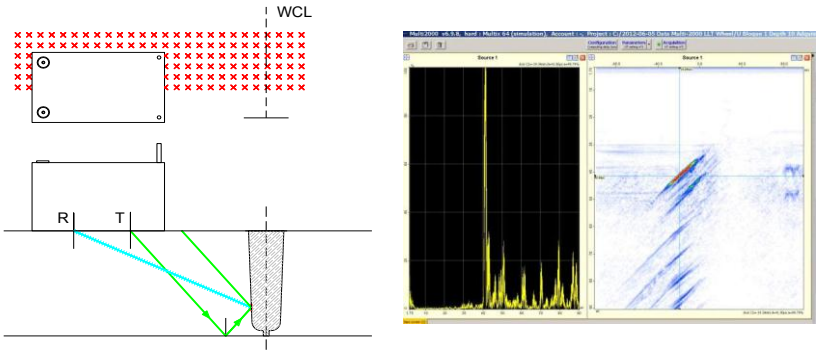

Figure 9. Scanning for characterization of defects (LLT probes)

CONCLUSIONS

The volumetric examination of certain vacuum vessel welds may be performed using ultrasonic techniques from one only of its surfaces. In this case, the difficulties due to the limited space available for performance of the examinations, the complexity of the geometry of the vacuum vessel and the stringent requirements of the RCC-MR Code are to be added to the habitual difficulties involved in inspecting austenitic welds.

In view of all these difficulties, the European Fusion for Energy Agency requires the qualification of the volumetric ultrasonic inspections of the vacuum vessel welds accessible from a single surface. Tecnatom is responsible for this qualification.

It has been proposed that the basic ultrasonic inspection of the vacuum vessel welds be performed using the pulse-echo technique with phased array probes. This basic inspection will be complemented with other techniques and probes to detect and characterise specific defects.

REFERENCES

1. RCC-MR, Design and Construction Rules for Mechanical Components of Nuclear Installations, Section 3: Examination Methods and Section 4: Welding. Edition 2007.
2. CEN/TR 14748:2004, Non-destructive testing – Methodology for qualification of non-destructive tests.

SPANISH METHODOLOGY FOR STEAM GENERATOR INSPECTION QUALIFICATION

A.G. Bueno, Tecnatom, Spain
L. Francia, UNESA, A.E. Industria Electrica, Spain
J. J. Jimenez, Almaraz, Trillo NPPs, Spain
J. Torrens, Asco, Vandellos NPPs, Spain

The purpose of this paper is to provide pertinent information related to the Spanish Methodology for the Qualification of the Steam Generator Tubing Inspection.

The Spanish Nuclear Power Plants have their own In Service Inspection (ISI) program which is ruled according to the Section XI of ASME Code. Apart from this, the Spanish Methodology UNESA CEX-120 for the Qualification of ISI Non Destructive Examination (NDE) methods, based on the ENIQ methodology was agreed by the Spanish Nuclear Utilities and approved by the Spanish Nuclear Regulatory Authority.

In particular this paper is related to the qualification process that applies to the Steam Generators (SGs) tubes eddy current inspections.

In Spain there are 6 PWR nuclear power plant units and the SG model, manufacturer and tubing are the following:

- Almaraz 1&2 and Asco 1&2, 3 SG/unit, with Siemens/Framatome design, model 61W/D3 SGs, and 3/4" x 0.043" Incoloy 800 modified tubing. These SGs replaced the original ones in the past. There are a total of 12 SGs of this model containing 61.560 tubes.
- Trillo with 3 KWU design, model 54GT SGs, and 6.93/8" x 0.048" Incoloy 800 modified tubing and a total of 12.258 tubes between the 3 SGs.
- Vandellos II with 3 Westinghouse design, model "F" SGs, and 11/16" x 0.040" Inconel 600 TT tubing and a total of 16.878 tubes between the 3 SGs.

According to the methodology three different types of defects were considered for each type of the above SG model:

SPECIFIC: Defect that has been detected in a component of the plant in a given zone, its characteristics are known and a practical demonstration is required in order to get an optimized procedure for detection and sizing of the defect. The practical demonstration was performed on flawed test specimen that reproduces the affected area and specific defects, and then, a Technical Justification was performed in order to complete the results obtained in Practical Demonstration.

POSTULATED: It is a defect that is assumed to exist based on design characteristics or applicable operating experiences in identical component in other plant. The characteristics of the defect are based on technical study. A Technical Justification was considered the most suitable qualification element to qualify inspection systems for these defects; however when the Technical Justification could not justify all essential variables and ISI objectives, practical demonstration on test specimens were required.

INDETERMINATE: They are non-existing reported defects, they are not industry experience and the inspection is based on ASME Code or others applicable requirements. A simplified Technical Justification was performed and the calibrations were made on the specified calibration blocks that were included in the Technical Justification.

Based on the above, the types of defects that were considered for each type of the three SG existing models were as follows:

Plant	SG Model	Type of Defect	
		SPECIFIC	**POSTULATED**
Almaraz 1 & 2 Asco 1 & 2	61W/D3	Wear at AVB	None
		Wear tube support grid	
		Loose part wear	
		Circumferential SCC	
Trillo 1	54GT	Wear at AVB	None
		Wear tube support grid	
		Loose part wear	
		Structural wear	
Vandellos 2	F	Wear at original AVB	PW SCC OD SCC
		Wear at new AVB	
		Coincident AVB wear	
		Loose part wear	

The postulate defects for the model F SG that were considered are: PWSCC and ODSCC circumferential and axial at Top Tube Sheet. Other recent postulate defect related to axial PWSCC at the smallest radius U-bend is in progress to be qualified.

On the other hand and applicable for all types of SGs, the qualification program for loose part wear in the vicinity of any structural part of the SG, such as the top of tube sheet, the flow distribution baffle, supports plates or support grids is in progress to be qualified.

The overall qualification program has been carried out as follows:

Specification of ISI objectives
Reports of Qualification Objectives
Development of Procedures
Technical Justifications
Specification & Fabrication of mock-ups
Practical Demonstrations
Final Qualification Report.

In the case of model 61W/D3 model SGs the locations of the specific defects are the following:

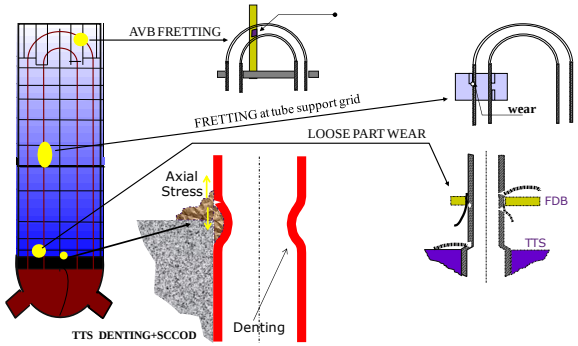

The locations of the specific defects in the 54GT model SGs are the following:

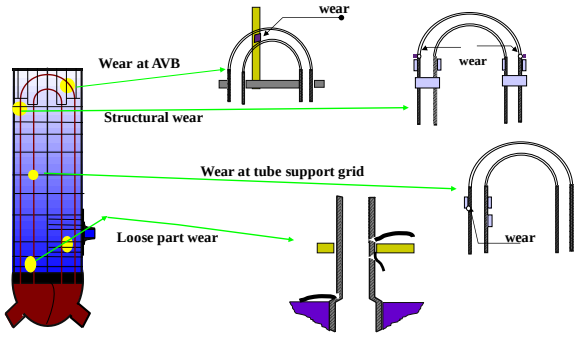

In the case of model F SGs the locations of the specific defects are the following:

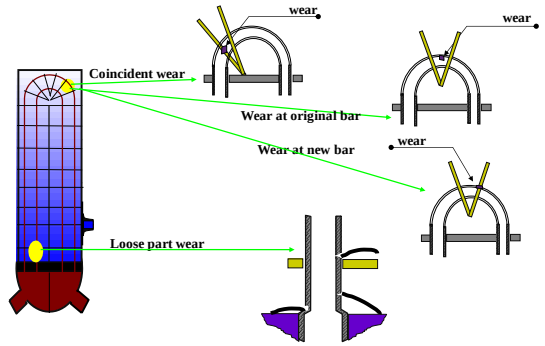

The Qualification Objectives for the specific and postulate defects were the following:

Specific Defects:

Fretting at AVB or support plate or support grid

Loose part wear

Circumferential (Only present at model “61W/D3” SG)

Any orientation and length

PoD ≥ 80% (Confidence Level ≥ 90%)

PoD = 100% if depth ≥ 40% (maximum allowable depth)

False calls ≤ 30% (Confidence Level ≥ 90%)

RMSE sizing error < 20% (wall thickness)

Postulate Defects: (Only for model “F” SG)

PW SCC risk based in crack length (not depth)

OD SCC 40% (maximum allowable depth)

After finishing the qualification program, the gathered results with regard the Probability of Detection and Root Mean Square Error for each type of defect and SG model were as follows:

SG "61W/D3"		
Type of Defect	**PoD** (%)	**RMSE** (%)
Wear at AVB	89.6	3.38
Wear tube support grid	82.7	7.51
Loose part wear	89.6	6.02
Circumferential SCC	87.3	9.45º

SG "54GT"		
Type of Defect	**PoD** (%)	**RMSE** (%)
Wear at AVB	89.6	2.33
Wear tube support grid	89.6	5.49
Loose part wear	94.7	8.17
Structural wear	82.7	11.39

SG "F"		
Type of Defect	**PoD** (%)	**RMSE** (%)
Wear at original AVB	89.6	1.85
Wear at new AVB	89.6	1.98
Coincident AVB wear	89.6	1.66
Loose part wear	92.6	14.03

RED DYE PENETRANT TESTING QUALIFICATION FOR THE IN-SERVICE INSPECTION OF FRENCH NUCLEAR POWER PLANT COMPONENTS – OVERVIEW OF CURRENT PRACTICES

C. Caperaa, Y. Forestier, L. Quemard, EDF - CEIDRE, France
M. P. Leyris, EDF - CNEPE, France

Non-destructive examination (NDE) techniques applied to components of the main primary and main secondary loops of Pressurized Water Reactors (PWR) in EDF-operated Nuclear Power Plants (NPP) have to go through a formal qualification process, following the RSE-M code methodology. The conformity of the NDE is assessed by a second-party accredited qualification body.

This paper gives an overview on the methodology chosen by EDF/CEIDRE in order to successfully qualify a "specific" red dye penetrant testing (PT) procedure, which will ultimately be used during In-Service Inspections (ISI) for crack detection. Two cases of "specific" qualifications (one automated and one manual NDE) for EDF NPP components are described below as examples of red dye PT qualifications. Theoretical and experimental examples are given to illustrate the different types of justification that have been used recently.

Keywords:
PT, coloured dye, steam generator, steam relief valve, fatigue crack, SCC, qualification, influential parameters, surface wettability, defect width, hygrometry ratio, mockup

OBJECTIVE AND PRINCIPLE OF A "SPECIFIC" QUALIFICATION

A "specific" qualification relates to the case where a real defect has been found in a specified area of the component. This defect:

- relates to a damage mechanism that has been identified,
- is generic for a given type of component,
- has well-known characteristics (size, position, propagation path), obtained e.g. through (destructive) metallurgical examinations,
- has potential consequences on the safety of the nuclear power plant (generally, the plant operator also carries out structural integrity studies in parallel with the NDE development).

The main objective of a "specific" qualification is to demonstrate the ability of the NDE technique, implemented by personnel with a specified skill level, to detect indications corresponding to the targeted defect in the concerned area of the component. A "specific" qualification can be considered as a sum of technical and practical justifications (e.g. physical reasoning, tests on mockups…). In the case of both PT applications described in this paper, the performance demonstration was based on a notch, contained in the targeted defect. It has a well-defined geometry in terms of shape, orientation and size (length, depth, minimal and maximal width), as shown in Fig.1.

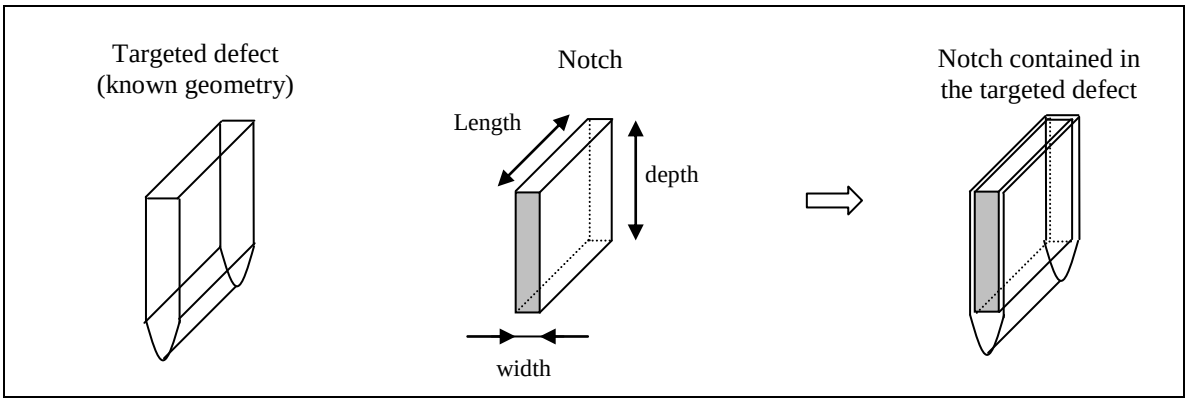

Figure 1: Representation of the principle of the reference notch contained in the targeted defect

"SPECIFIC" QUALIFICATIONS OF RED DYE PT FOR FRENCH NUCLEAR POWER PLANTS COMPONENTS

Two examples of "specific" situations (where a real defect was found and subsequently characterised) for components operated by EDF are described in this paper, as examples of red dye PT qualification.

Case No.1 is a NDE of the partition stub / partition plate area in steam generator water boxes. The objective of this automated red dye PT is to detect stress corrosion cracks (SCC) parallel to the weld. The base metal is Inconel 600 or 690, the filler metal Inconel 182 or 152. Table 1, Figures 2 to 4, illustrates this case.

Case No.2 deals with thermal fatigue cracks propagating in the hard-coated surface of main steam relief valves. In this case, manual red dye PT is performed. The description of these valves (taken from different reactor series) is presented in Table 1, Figures 5 to 7.

In both cases, the PT product family designation is II-A-d, level 2 sensitivity, according to [1].

Case No.1: Stress corrosion cracking from weld in the area partition stub / partition plate from bottom end cover of steam generator	*Case No.2: Thermal fatigue cracking in the hard-coated surface of main steam relief valves*
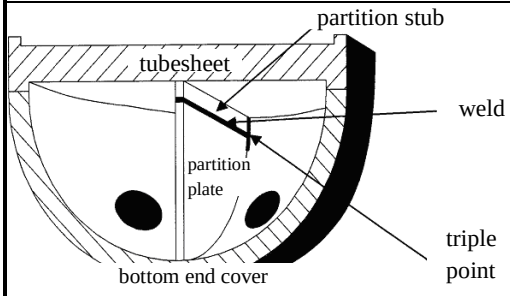 Figure 2 : Representation of the partition stub / partition plate welded joint	 Figure 5 : Photograph of a main steam relief valve body
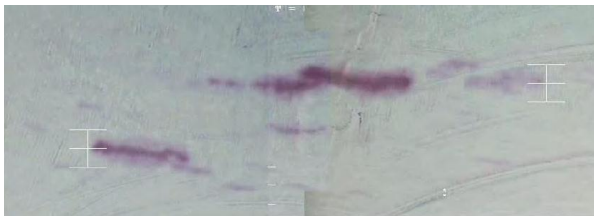 Figure 3 : Example of automated in-service inspection – detection of a SCC crack (group indication 30 mm long)	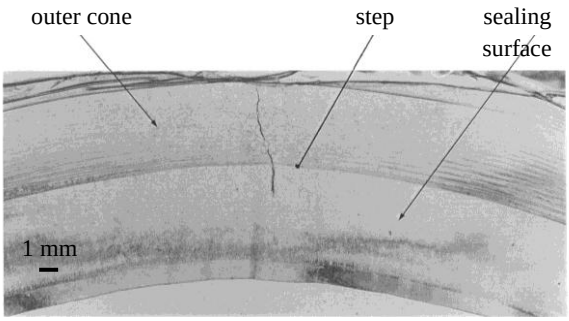 Figure 6 : Example of macroscopic aspect for thermal fatigue cracks
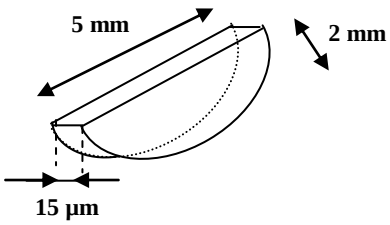 Figure 4 : Associated semi-elliptic notch (perpendicular to the surface)	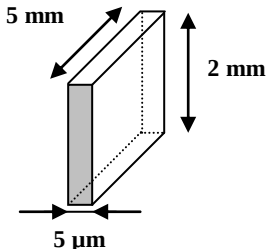 Figure 7 : Associated rectangular notch for Stellite 25 and Inconel 82 hard-coated surface (perpendicular to the surface)

Table 1: Two examples of "specific" situations for component operated by EDF related to red dye PT qualification

TECHNICAL JUSTIFICATIONS examples FOR A “SPECIFIC” QUALIFICATION

General principles

The purpose of the Technical Justifications is to establish the performances associated with the NDE application:

1. Sensitivity i.e. ensuring detection of the targeted defect
2. Zone coverage of the concerned area of the component
3. Localisation and sizing of indications

As a rule, “Technical Justifications” may involve physical reasoning, experimental results (mockup trials, laboratory tests), numerical simulations, ISI feedback or a combination of these options. In the case of red dye PT qualifications, this part of the qualification process aims at studying the influential parameters related to the component, the notch characteristics (associated to the targeted defect), the red dye PT technique and the environment, as shown in Table 2.

Component	✓ Surface finishing and preliminary state ✓ Type of material and wettability ✓ Surface orientation ✓ Shadowed areas ✓ Surface temperature
Notch	✓ Profile (rectangular, semi-elliptic, trapezoidal) ✓ Minimal and maximal width ✓ Orientation with regard to the surface (propagation path) ✓ Available defect volume for penetrant retention ✓ Number of open defects sides (for example, surface-breaking or through-wall crack)
Technique	✓ Method for surface preparation ✓ Type of product family ✓ Method for penetrant application and dwell time ✓ Method for excess penetrant removal ✓ Method for developer application and development time ✓ Observation conditions (direct or remote display) ✓ In the case of an automated NDT, manipulator positioning accuracy
Environment	✓ Room temperature ✓ Hygrometry ratio

Table 2: First-order influential parameters in a “specific” qualification for red dye PT

Example No.1: « maximal width of the notch » justification

A maximal detectable width of the notch has to be considered because a very wide surface-breaking crack may not be detected due to:

- Over-washing of the penetrant removal during the “excess penetrant removal” step,
- Lower capillary attraction during “development” step (the smaller the width, the higher the capillary rise force).

For Case No. 1, an experimental trial was performed with a trapezoidal notch 5 mm long, 2 mm deep and 490 µm wide, embedded into an Inconel 600 mockup. It was found that the selected level 2-sensitivity PT product family allows detection of this notch. With a conservative approach, in the case of Inconel 600, a 400 µm upper limit was adopted in terms of surface-breaking defect width.

Furthermore, the technical justification for maximal detectable width in other materials than Inconel 600 was addressed in the “type of material and wettability” study (example 2 below).

Example No. 2: « type of material and wettability» justification

Sensitivity of red dye PT highly depends on the ability of the penetrant product to spread out evenly on the examined surface and to seep into the discontinuities during the dwelling phase. Surface wettability is the physical property involved. Considering the (penetrant product, material) couple, two situations may be encountered: partial or total wetting, as described in Figure 8.

Young's equation uses the surface tension between the three phases: solid, liquid and gas. The contact angle of a liquid droplet on a solid surface is related to all three surface energies γ_{LG}, γ_{SG} and γ_{SL}, as shown in Figure 9.

Based on these physical properties, the surface energy of different steels and nickel-based alloys was measured for both specific qualification cases. For case No.2, quantitative characterisations of surface wettability were performed in order to compare the real component materials (Stellite 25 and Inconel 82) to mockups with an embedded reference notch (nickel-chromium reference testblock, cf. [2]). The surface energies of these three materials were measured by Laboratoire Dubois (Switzerland) using the Owens-Wendt method. It was shown that nickel-chromium has the lowest surface energy of all three materials and thus, lower wetting properties than Stellite 25 and Inconel 82. Using this ranking information, it was concluded that if the reference notch embedded in a nickel-chromium reference testblock is associated with a PT indication, then the same reference notch would also be seen on a Stellite 25 or Inconel 82 surface (see also : example 5).

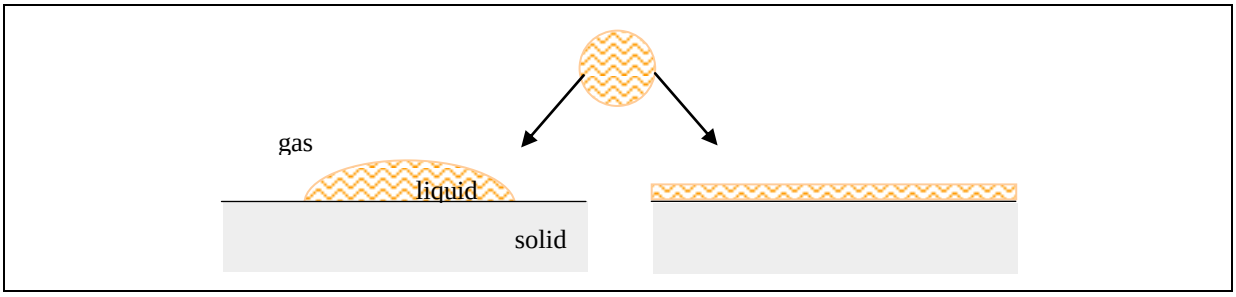

Figure 8: Partial wetting (left) and total wetting (right) of a liquid droplet set on a solid surface

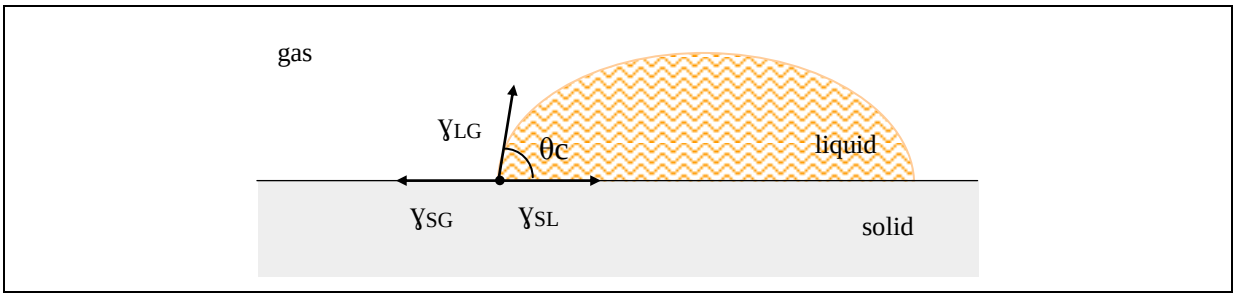

Figure 9: Contact angle of a liquid droplet wetted to a solid surface

Example No. 3: « hygrometry ratio » justification

The hygrometry ratio in the surrounding environment, associated with the temperature of the component and of the PT products, have a combined influence on the sensitivity of the NDE. First of all, two potentially tricky situations were identified:

Situation 1: High hygrometry ratios (85 à 100 % RH) and low temperatures (< 15°C). In this situation, PT classical systems could not be qualified without experimental data, because:

- The presence of condensation on the surface may interfere with penetrant seepage into the defect,
- Penetrant viscosity increases at lower temperatures, making penetrant seepage slower,
- Developer drying time is longer.

Situation 2: Low hygrometry ratios (< 20 % RH) and high temperatures (> 45°C). In this situation, PT sensitivity may also be reduced because of:

- Penetrant degradation,
- Penetrant drying on the surface of the component, making excess penetrant removal more difficult,
- Penetrant drying into the defect (blockage)
- Penetrant capillary retention decrease (penetrant drawing out prematurely)

Laboratory tests were performed in a climatic enclosure with 30 µm and 50 µm test cut-outs from type 1 reference blocks [2].

Based on the preceding discussion, the objective was to verify whether sensitivity level 2 from the selected product family was maintained in the hygrometry ratio/temperature combinations defined in Table 3.

		Climatic enclosure relative hygrometry ratio (% RH)		
		90%	50%	20%
Climatic enclosure temperature (°C)	Room temperature (≈ 22 °C)	Test No. 1	Test No. 2	Test No. 3
	10°C	Test No. 4	Not evaluated	Not evaluated
	45°C	Not evaluated	Not evaluated	Test No. 5

Table 3: Combined hygrometry ratio-temperature experimental design

Results of the evaluation of the percentage of discontinuities found from the type 1 reference block confirmed that level 2 sensitivity was maintained for every test. The sensitivity performance of the PT procedure is then considered as valid for:

- Hygrometry ratios between 20% and 90% RH,
- Temperatures between 10°C and 45°C.

During the tests, it also appeared that for 90% RH and above, condensation droplets tended to form on the testblocks' surface. These droplets would reappear immediately after wiping the surface with a clean, dry and lint-free cloth. This observation was used in the ISI manual PT procedure, as a practical and fast way of checking the acceptable humidity rates:

"After wiping, no condensation droplet should be found within the first 30 seconds. Otherwise, the actual hygrometry ratio has to be measured accurately and the value should be lower than 90%".

Example No. 4: « method for products application » justification

For qualification case No.1, an automated NDE is performed using the ICAR3G manipulator; the development and in-service inspection are performed by Westinghouse Electric France (WEF).
The penetrant and developer products are applied with tools carrying an atomising nozzle moving horizontally (Figure 10).

First, geometrical calculations were made for each type of steam generator to verify zone coverage in the vertical and horizontal directions. The PT products must be applied to a surface larger than the required examination surface of the partition stub/partition plate; figure 11 gives an example of such calculations.

These theoretical considerations were then confirmed during the PT qualification trials for each new type of steam generator before the actual inspections took place. These trials include verifications for both sensitivity and zone coverage.

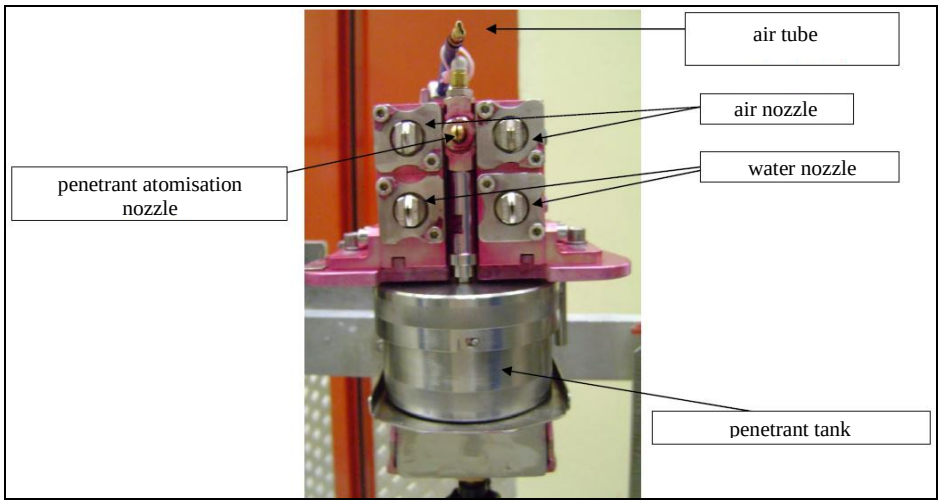

Figure 10: ICAR3G manipulator - penetrant tool

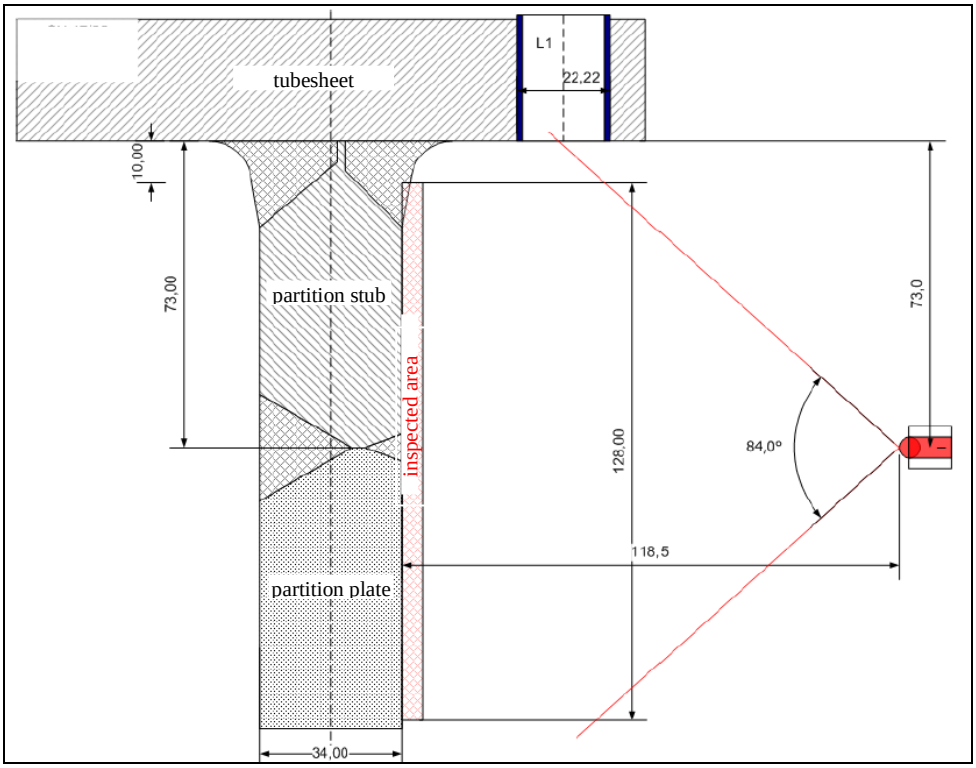

Figure 11: ICAR3G manipulator – Zone coverage calculation for penetrant product application

EXPERIMENTAL JUSTIFICATIONS FOR A "SPECIFIC" PT QUALIFICATION

General principles

Using a practical approach for technical justifications is one way of demonstrating the ability of the NDE technique to retain the required performances in operational conditions representative of the ISI of a NPP component. As a consequence, in addition to the procedure contents, the NDE equipment (possibly including a manipulator) and the global environment (radiation, accessibility conditions…) must also be taken into account. Influential parameters of the real ISI that are not consistently reproduced during the trials will have to be justified by means of additional analysis. Experimental justifications are generally based on trials on mockups (open or blind testblocks).

Example No. 5: Practical Justifications for Case No. 2

For qualification case No. 2, thermal fatigue cracks were the targeted defect. Practical trials were performed using a real-size mockup of a main steam relief valve. The objective of the first trial was to check the correct application of testing products on the examined area. Figure 12 (left) shows that penetrant application is satisfactory. The second trial was a sensitivity demonstration (detection of the targeted defect using a level 2-sensitivity system). A nickel-chromium mockup (15 mm long and 5 mm wide), containing a reference crack, was positioned upon the examination area of the valve. Figure 12 (right) illustrates that the mockup crack did create a penetrant indication as expected.

Finally, technical justifications were added in order to compare the characteristics of the mockup crack and of those of the reference rectangular notch for the main steam relief valve (see Table 4).

Figure 12: PT trial on main steam relief valve (left) adding nickel-chromium mockup embedding a reference crack (right)

		Main steam relief valve	Nickel-chromium mockup	Worst case configuration for PT sensitivity of detection
Material	**Wettability**	Inconel 82 and Stellite 25 presents higher wettability than nickel-chromium		Nickel-chromium mockup
	Roughness	Ra < 3,2 µm		No difference
Reference crack/notch	**Shape**	Parallelepiped		No difference
	Orientation	Perpendicular with regard to the surface		No difference
	Length	5 mm	5,03 mm	No difference
	Width	5 µm	4 µm	Nickel-chromium mockup
	Depth	2 mm	30 µm	Nickel-chromium mockup
	Type of reservoir	Reservoir opened on 1 or 2 sides	Reservoir opened on top + 2 lateral sides	Nickel-chromium mockup

Table 4: Characteristics comparison between main steam relief valve and nickel-chromium mockup

Therefore, Table 4 establishes that the reference notch for the main steam relief valve should always be easier to detect than the nickel-chromium mockup crack with red dye PT. The reasons for this are:

- Higher material wettability for Stellite/Inconel than nickel-chromium,
- Higher defect volume (width, depth) available for penetrant retention,
- Same number (or fewer) sides of the defect are surface-breaking,

All of these parameters are more favorable with regard to PT sensitivity.

As a conclusion, in Case No. 2, the practical trials with added technical justifications demonstrated the PT procedure's ability to detect the targeted defect in main stream relief valves.

CONCLUSIONS

Two examples of EDF's approach for "specific" qualification of manual or automated red dye penetrant testing were presented in this paper. As a rule, a mixture of technical and practical justifications is a good compromise.

This illustrates the fact that it is compulsory to understand the physical principles associated with penetrant testing, and subsequently to analyze individually the influential parameters that may influence the overall performances of the ISI.

The main advantage of this kind of demonstration is that it allows for the use of a very limited number of mocks-ups, with simple reference defects, cutting down fabrication time and costs.

REFERENCES

1) ISO 3452-1: Non-destructive testing - Penetrant testing - Part 1: general principles
2) ISO 3452-3: Non-destructive testing - Penetrant testing - Part 3: reference test blocks
3) Cahiers de la COFREND – manuel de ressuage

QUALIFICATION AND IMPLEMENTATION OF A NDT BASED ON PHASED ARRAY FOR THE ON-SITE INSPECTION OF BOILER TUBES OF COAL FIRED POWER PLANTS

F. Deneuville, A. Ayoub, Vallourec, France
P. Cornaton, J. Delemontez, A. Pawlak, EDF, France

ABSTRACT

EDF (Électricité De France) as a major electricity supplier has high expectations of its power plants availability and reliability. Facing an unusual number of boiler tubes failures in one of its coal fired power plants, EDF decided to perform a non destructive examination of the waterwall panels. The failures were located fireside with a wide scattering.

First, EDF organized a qualification stage to compare different available technologies and suppliers. Taking into account tubes dimension, corrosion scale and defects shape. V&M (Vallourec & Mannesmann a company of the Vallourec group) have participated to this approach by developing an ultrasonic testing solution based on Phased Array technology. Through numerical simulations, lab tests and blind tests on artificial notches and field samples, V&M demonstrated the efficiency of the proposed solution, which was finally qualified by EDF according their specifications based on a deterministic and pragmatic approach for such on-site inspection demands.

Following the qualification announcement, an inspection campaign was done in the concerned coal fired power plant. During the on-site control, V&M inspected an important amount of tubes to make a detailed mapping of the tubes condition assessment. Tubes with ultrasonic indications over the detection criteria have been replaced and analyzed in lab.

This paper provides the main results of the qualification phase and the achievements of the field examinations. It shows the benefits of the qualification to achieve the aims of the NDE and offers an overview of how a well known inspection technology used in tubes manufacturing process can be adapted in an innovative way and used for the assessment of 35 year old tubes in a power plant.

LA MAXE POWERPLANT

Waterwall failures

The EDF power plant of La Maxe, near to Metz in east of France, is a coal power-plant running two boilers of 250MW each. The boiler n°2 was facing leakages on water-wall tubes. These failures were due to longitudinal cracks on inner wall at fireside, initiated from hydrogen and creeping damages. To identify the defected zones and decide about the preventive maintenance actions to launch, the power plant was searching a relevant non-destructive examination technique able to detect such inner defects and capable to inspect a wide part of the boiler concerned by the leaking in the timeframe of the annual outage.

The tubes to be inspected are seamless tubes in carbon steel, with dimensions of 51 mm × 5.6 mm (outside diameter × wall thickness). The minimal defect to be detected has been fixed by EDF technical teams at the following dimensions: 10 mm in length, 1 mm in depth (i.e. height from the inner surface).

Before the work in partnership with V&M (Vallourec & Mannesmann, a company of the Vallourec group), two standard available techniques were tried by EDF: radiography and eddy current. The radiography was able to detect defects higher than 1 mm in depth, but 1 mm depth defects are more difficult to sort reliably on the radiograph because they are in the shadowing area close to the inner surface. In addition, the radiography examinations on site involve a lot of safety constraints: usually these inspections are done during the night shift with restrictive access to the power-plant to other persons. At last, the time of inspections required by the radiography permit to inspect only small surfaces of the water-wall panel during the time allowed by the unit outage.

The low frequency eddy current method tested by EDF was more adapted for inspecting a large zone in the boiler. However this technique has shown many false alarms during first tests, in fact the indications found by this technique didn't show any defect after sample remove and analysis. In addition, on such tubes, the minimal defect detected by this technique is finally out of the specifications.

Therefore, EDF objective was to qualify non destructive techniques able to detect and classify the inner cracks present in La Maxe water-wall tubes with the smallest defect to be detected of 10mm length and 1 mm depth. The deadlines were very short due to fixed summer power plant maintenance in June 2012.

Vallourec proposed solution

Based on the type of defect, the material of the tubes and their surface conditions, Vallourec has proposed, based on its own experience of the inspection of the tubes produced by the group, to develop and use a specific Ultrasonic Phased Array solution approved from EDF.

This technology used in tubes manufacturing process from more than 10 years now is well mastered by Vallourec NDT experts. It is suitable for detection of thin inner cracks in a large range of material and tube thickness, and it offers the possibility to do a large and fast angular covering of the fireside thanks to electronic scanning along the Phased Array probe.

The technology used in production with encircling probe was declined to be used on site. A semi encircling Phased Array probe was used to cover a large circumferential part of the fireside of the tubes. The probe is connected to a hand-held Phased Array electronic. The acoustic coupling between the probe and the steel is done by using non corrosive ultrasonic gel.

Figure 1: ultrasonic phased-array equipment for testing of tube in production line

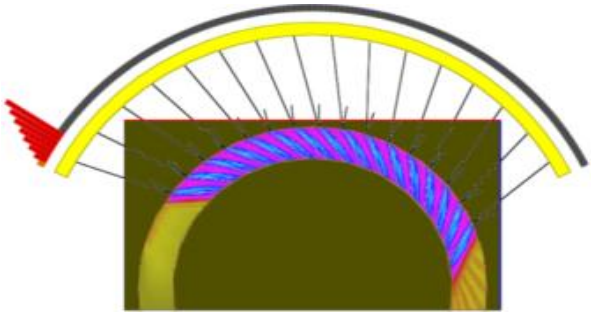

Figure 2: principle of the inspection technique illustrating under CIVA simulation software

To validate the efficiency of the ultrasonic Phased-array technique, EDF requested a qualification phase in order to define:

- NDE and industrial performances of the proposed solution
- Best parameters for the design
- Study of critical influent factors and their variation range
- Inspection procedure

The qualification phase was driven by EDF technical teams of EDF-CIT, Paris (Thermal Engineering Centre), in link with EDF-DTG, Grenoble (General Technical Direction) and the maintenance team of the La Maxe production unit. For Vallourec, the actors of the development and the qualification of the ultrasonic phased-array solution were the Vallourec Research Center (VRA), Aulnoye-Aymeries, and the powergen division of V&M France, Boulogne-Billancourt.

QUALIFICATION PHASE

The main steps of the qualification process were the following:

- Listing and selecting the influent factors on the NDE performances ;
- Theoretical analysis on the impact of the influent factors by numerical simulations and technical justifications ;
- Practical trials to assess the performance (mainly sensitivity, consistency and repeatability) of the NDE, divided into:
    - Open and blind tests in lab on samples with artificial defects
    - Trials on site on a mock-up and on natural defects
- Documentation of the results in a qualification report and proposal of an inspection procedure in accordance with the results and the conclusions from the qualification.

The qualification process was done in accordance with the recommendation of the EN 14748 standard: “Methodology for qualification of non-destructive tests”.

Theoretical analysis

Vallourec proposed an analysis of the main influencing parameters related to

- The technique and the tool (coverage, speed, guiding…)
- The tubes (wall thickness, surface condition...)
- The defects (depth, localisation...)

From this analysis, the following testing matrix was agreed between Vallourec and EDF:

	Numerical simulation	Technical justification	Practical trials
Detection sensitivity	✓		✓
Circumferential coverage	✓		✓
Uncontrolled parts		✓	✓
Coupling verification		✓	✓
Length measurements	✓		✓
Guiding influence	✓		✓
Repeatability and Reproducibility			✓
Wall thickness influence	✓		✓
Speed influence		✓	✓

According to this matrix, each important parameter is covered by at minimum a practical test. In addition of the results of practical tests, some theoretical analyses have been done by numerical simulations on a major part of the parameters, the parameters for which the numerical simulation was feasible and relevant.

In this paper, we describe first the main results of the numerical simulations done in this qualification process, and then some examples of the results obtained during the practical trials in lab.

Numerical simulations

Detection sensitivity

Defects of different depths have been first simulated under CIVA platform. Main result was that a defect of 0.5mm depth is detected with a signal at -3dB compared to a 1mm depth notch, which validate the detection capability of the method.

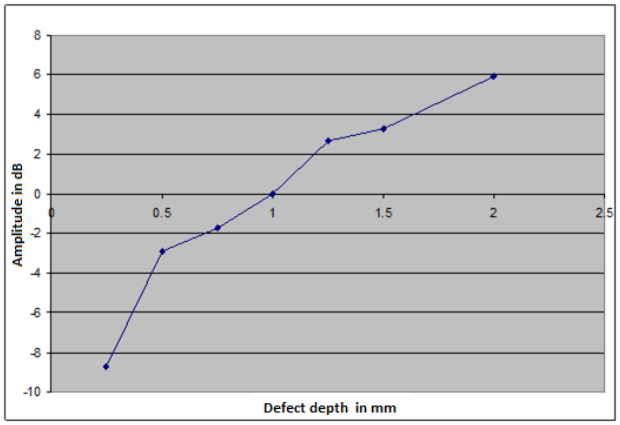

Figure 3: ultrasonic responses for different defect depths according CIVA simulation

Circumferential coverage

The circumferential coverage limits was checked by simulating defects placed at different angles around the circumference. It has been shown that the parameters of the ultrasonic system permits to cover a sufficient part of the tubes at the fireside.

To obtain this performance, a particular study was done to find the best setting of the probe command: number of element per aperture and pitch between apertures. The following figure illustrates the overlay between two consecutive aperture set on the Phased array probe. The sensitivity to a defect whatever its circumferential position (angle) remains always in a range smaller than 1.5 dB.

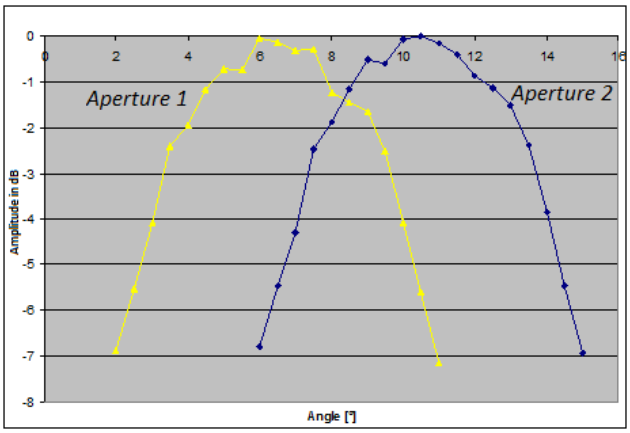

Figure 4: ultrasonic responses for different circumferential positions (angle) between two consecutive apertures of the phased-array probe

Wall thickness influence

After having evaluated theoretically the performance of the ultrasonic solution proposed, numerical simulations were then focussed on the impact of the main influent variations occurring on the products to be inspected and during the NDE process.

First factor studied is the potential variations of the wall thickness of the tubes. Indeed as the tubes have run since many years, we can be faced to different wall thickness of the tubes due to inner erosion phenomena. Different wall thicknesses were simulated under CIVA software. The results, illustrated on the Figure 5, show that this factor does not influence critically the NDE performance: less than 1 dB for 1.6 mm of wall-thickness reduction.

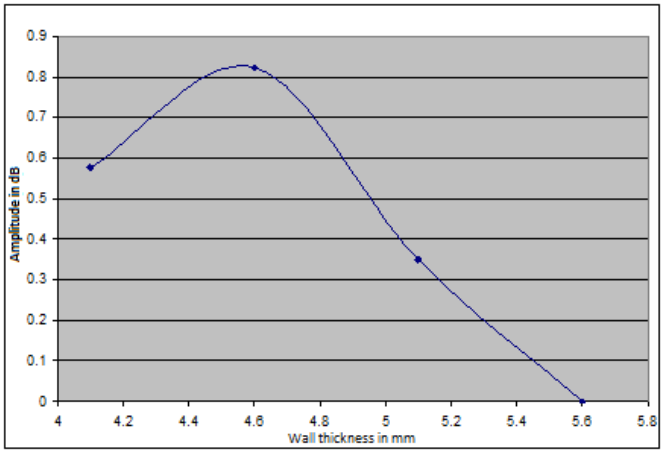

Figure 5: Ultrasonic responses for different tube wall thickness

Guiding influence

For assessing the influence of the guiding tolerance which will impact the NDE process on site, two different variations were simulated under CIVA: the height between the sensor and the tube and the tilt of the probe relative to the tube (See Figure 6).

Figure 6: simulation with a tilt of the phased-array probe
relative to the tube (drawing not to scale)

According to simulation results, the variations of these guiding parameters in their estimated variation ranges induce some reasonable variations on the ultrasonic responses. It have been so demonstrated that the detection of the defects remains feasible under the on-site guiding conditions limits.

Practical trials

To verify and complete the theoretical study, EDF has prepared “Open” and “Blind” tests on some selected samples containing different kinds of artificial notches made by Electro-Discharge Machining (“EDM”). The samples are of the same dimensions and surface conditions than the tubes to be inspected in the power-plant.

Trials on reference samples from EDF

The first tests were made on a sample with machined inner and outer surfaces and showed promising results. Therefore, EDF provided samples with same surface conditions than in La Maxe powerplant and with longitudinal inner notches of different shapes, depths, lengths and positions. For one of the samples, Vallourec received from EDF the detailed schematic with notches properties and localisation made (“open” tests). For another sample, Vallourec had to make the tests under EDF supervision without any information about the notches present in the samples (“blind” tests).

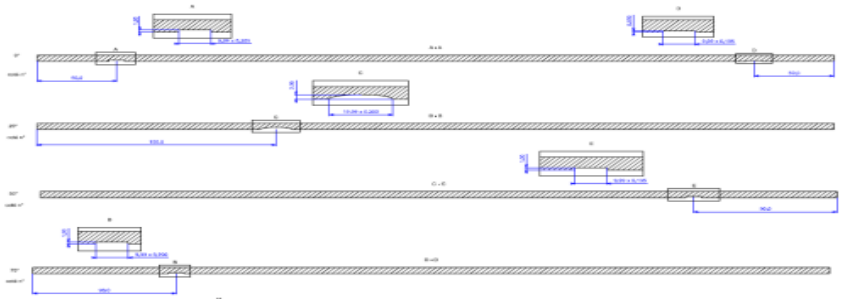

Figure 7: Schematic of one of the EDF samples

Figure 8: Photography of an EDM notch

Vallourec demonstrated the ability of the ultrasonic Phased-Array technology to detect the different notches during both the open and the blind tests. Results of the tests on one of the sample are reported hereafter, with the ultrasonic cartography (C-scans) and the detailed results on the different notches (maximal amplitude of the ultrasonic response and signal to noise ratio SNR on each notch).

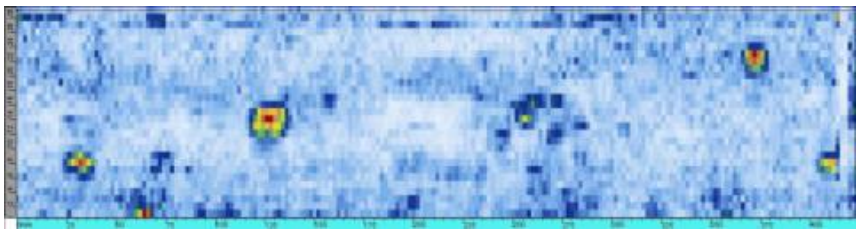

Figure 9: Ultrasonic cartography

Shape of the notch	*Length (mm)*	*Depth (mm)*	*Angular position*	Maximal amplitude	SNR
Rectangular	*10*	*1*	*0°*	**0 dB**	**>15 dB**
Semi-elliptical	*20*	*2*	*~20°*	**+0,9 dB**	**>15 dB**
Rectangular	*10*	*1*	*~50°*	**-1,4 dB**	**>15 dB**
Rectangular	*10*	*0,5*	*0°*	**-3,4 dB**	**>15 dB**

Table 1: Ultrasonic results on some EDM notches

In addition some repeatability tests has been done on the samples, showing a spread on 10 runs lower than 4 dB, which corresponds to a very good repeatability performance for a semi-manual ultrasonic inspection process. The detection threshold fixed in the procedure has been chosen in relation to the previous results in order to secure the level of probability of detection of the NDE.

Measure n°	Ultrasonic amplitude (% FSH)
1	66.1
2	57.9
3	78.2
4	73.9
5	64.9
6	84.5
7	69.6
8	54
9	68
10	78.2
Mean	**69.53**
Std deviation	**8.98**
Max	**84.50**
Min	**54.00**
Range (Max-Min) in dB	***3.89***

Table 2: Results of repeatability tests on a 0.5 mm depth notch

Tests on a "mockup" waterwall

In order to complete the qualification, some other trials have been done under conditions close to the field inspection conditions into the boiler.

For that, EDF prepared a "mockup" water-wall panel (see Figure 10) composed of few tubes taken from the boiler. The test was used to assess the efficiency of the proposed ultrasonic NDE in field conditions. It has permitted to demonstrate the inspection speed performance and to check the reliability of the methods which have produced no false calls during this testing on undamaged tubes.

Validation on samples with natural defects

Lastly some tests have been done on the few samples with natural defects which were available during the qualification phase. Tests have been made on different tube samples previously removed from the boiler. Natural defects were found by the phased array technology and confirmed after micrographic investigations.

Figure 10: Tests in field conditions on a mockup prepared by EDF

As a conclusion of the qualification phase, the ultrasonic Phased array technology proposed by Vallourec has shown very good results for the detection of the inner cracks on water-wall tubes. The performances of this method were agreed by EDF technical team, who have consequently pronounced the qualification of this method for this application.

ONSITE CONTROL PHASE

Once the qualification of the NDE techniques pronounced, Vallourec were solicited by EDF La Maxe power-plant for making an inspection campaign on water-wall tubes during the outage of the boiler in summer 2012.

Preparation

On one hand, EDF La Maxe powerplant prepared the inspection campaign by: installing scaffolding inside the boiler, cleaning the tubes by high pressure water to remove ash deposit, and plotting the tubes numbers and levels. On the other hand, Vallourec organised an extensive training program for the participants related to safety requirements, and also some internal training of inspectors to the use of the developed ultrasonic tool. All the needed material for the inspection was also prepared on a short period.

Onsite control

Vallourec team was composed of 12 participants working in 2 shifts (morning and afternoon). The NDT experts and inspectors worked during two weeks at the different scaffolding levels to inspect more than 8000m tubes. The NDT experts from EDF were in charge to validate the respect of the use of the qualified tool and of the associated examination procedure.

Figure 11: Scaffolding in the boiler unit

Figure 12: Inspection by Vallourec inspectors

Found defects were classified depending on their ultrasonic maximum amplitude, by comparison with amplitudes of notches of different depths. Tubes with defects have been marked during the examination and EDF informed so that the power plant maintenance management team was able to take rapid decisions before re-starting the boiler. They decided to cut and replace 10 tubes with the highest signal amplitudes.

In addition to the marking on site, a detailed inspection report was also delivered to EDF La Maxe power plant. In this report, inspection results were presented for each panel under a recapitulative table and a mapping with the defect locations reconstructed from the ultrasonic data records. On defective zones, cartographies (or C-scans) of the ultrasonic response in the corresponding zones were also delivered, in order to offer more information on the cracks distribution along the length and the circumference of the tubes. The detailed information allows La Maxe power plant to make targeted replacements on the next boiler outages.

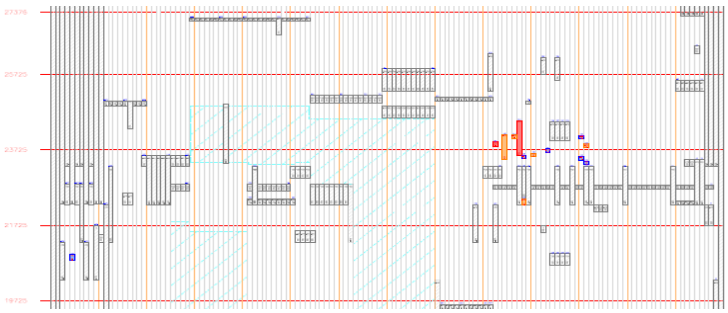

Figure 13: Example of mapping of the boiler with the inspection results

Removed tubes

On the removed tubes, 4 samples were analyzed by Vallourec through micrographic examinations. On all the samples cut, the presence of longitudinal defects has been confirmed. An example of such confirmation is shown in the following figures. Moreover the results showed a good correlation between ultrasonic signals and defect depth confirming the classification delivered to EDF.

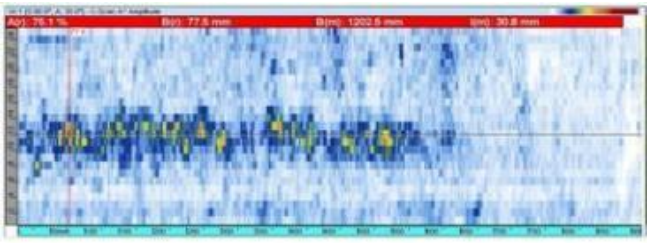

Figure 14: Ultrasonic cartography of a defected zone

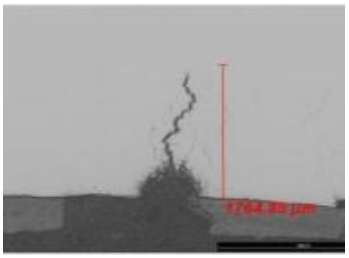

Figure 15: Defect on a removed tube

Mutual partnership

This project was an opportunity to work on a mutual partnership between Vallourec and EDF. The EDF CIT (Thermal Engineering Centre) helped to coordinate the different tests and assessed the speed inspection. La Maxe team accepted to open the doors for the qualification and the on-site control to Vallourec participants and to prepare the easiest working conditions. The numerous exchanges between the NDT experts from EDF DTG (General Technical Direction) in Grenoble and Vallourec Research Center in Aulnoye-Aymeries were beneficial for both parties.

EFFECT OF THE DIFFERENT ARTIFICIAL FLAW TYPE IN QUALIFICATION PURPOSES FROM THE POINT OF VIEW OF THE INSPECTION COMPANY

M. Vavrous, K. Markulin, INETEC, Croatia
M. Kemppainen, I. Virkkunen, K. Miettinen, Trueflaw, Finland
R. Paussu, J. Pirinen, Fortum Power and Heat Oy, Finland

ABSTRACT

A comprehensive in-service inspection programme of the primary circuit components assures their safe and reliable operation with resultant benefit to the overall nuclear safety. Qualification of in-service inspection of nuclear power plant primary components is a powerful tool which provides confidence that a given in-service inspection is fit for its purpose.
Through the process of qualification the estimate of the defect detection and sizing capabilities including defect characterization is provided. For that purpose, representative specimens with different type of defects are manufactured in order to make sure that in-service inspection will have capabilities to successfully address potential degradation and deterioration of primary circuit components.

Moreover, in order to reliably simulate real inspection conditions, qualification specimens need to fully correspond to the intended areas of control, they need to be made of the same or similar material from which the subject component is made of and finally need to have the same constructional elements including the welded joints. Implementation of the defects in such specimens is of great importance and could affect the chemical composition, structure, physical and mechanical properties which later on affect the inspection system capabilities to locate, characterize, size, evaluate and adjudge defect types and detectable defect sizes with previously identified accuracy.

This article will introduce defects manufactured in three different ways to be used in qualification purposes and their comparison from the view point of the inspection company, i.e. detectability and sizing capability including advantages and disadvantages of the different defect types will be presented and analyzed coupled with experience from the actual specimens.

INTRODUCTION

In nuclear industry periodical maintenance through application of non-destructive testing is essential activity for ensuring the safe and reliable operation of plant components and nuclear power plant as a whole unit. Maintenance activities as in-service inspections and non-destructive testing performed during outages are important to efficiency of outage and entire operation of the plant.

Constant demand is that maintenance and in-service inspections is performed in more efficient manner with less expense of time. In order to keep high level of quality of in-service inspection and high level of reliability of non-destructive testing, one of the tools used are qualification proceedings.

Through qualification process, validation is performed if selected in-service inspection with related non-destructive testing methods has sufficient capabilities to meet requirements defined with applicable standards and codes.
Within qualification process, practical trials are key segment to verify inspection capability. To make practical trials worthwhile, used qualification samples must be representative. Representative covers similarity to inspected component and defects that will realistically represent types of degradation that exists on actual component in real operating conditions. Methods of creating, manufacturing or implementing the artificial defects that will be used for qualification and assessment of inspection is critical because on success of selection and implementation of defects success of qualification will be affected.

DEFECTS FOR QUALIFICATION

Nowadays, number of different flaw manufacturing techniques are available to the flawed test pieces needed for qualification. Over the years, more techniques have become available and each technique has developed. At the same time, both the inspection techniques and qualification practices have developed. This has resulted in increase of the quality of the test flaws and test pieces.

At first, most samples contained mechanically machined flaws, i.e. flat bottom holes, saw cuts and later EDM (electro-discharge machined) notches. These can be easily manufactured to tight tolerances. However, as NDE methods and requirements developed, it soon became apparent that their representativeness was not good enough for service induced cracks. The techniques were developed to decrease the opening to minimum and to introduce surface roughness and out-of-plane surface forms. EDM notches are widely used, e.g., for signal calibration due to their very high repeatability and cost effectiveness. EDM notches are sometimes the only flaw production technology applicable. Also, the EDM notches do not cause any changes in surrounding microstructures that might affect the inspection.

To offer better representativeness, various welded flaw simulations have been developed. These are manufactured, in simple terms, by either implanting an existing crack by welding to the test piece, or by inducing cracking of the weld by carefully chosen weld parameters. The welded in flaws offer better simulation of the tortuous crack paths of real service-induced cracks. They can be manufactured with low cost, especially during test block manufacturing. In particular, for large cracks they offer good compromise between representativeness and cost.

Finally, to offer even better representativeness and to avoid microstructural alterations that might affect the inspection, new techniques have been developed. These employ a true damage mechanism, which is accelerated and controlled to allow artificial production of service induced flaws. These cracks offer very good representativeness for wide range of service induced cracks and NDT techniques. They also do not cause microstructural alterations, because there's no welding involved. Especially, the delicate crack tips are retained and crack opening is typically much smaller than it is for other techniques.

Figure 1 shows the development of different flaw manufacturing techniques on time scale. In many cases, a combination of different flaw manufacturing types is used for a given qualification project.

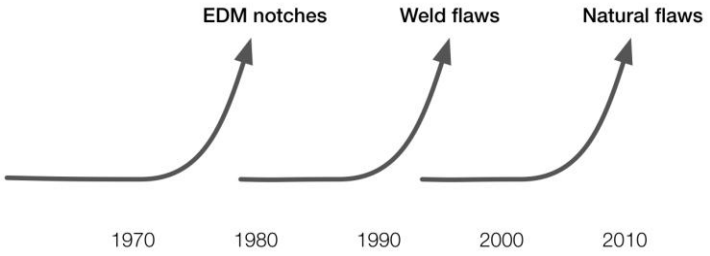

Figure 1. Development of flaw manufacturing techniques for NDE training and qualification.

DESCRIPTION OF SAMPLES WITH DEFECTS

For present study, four different samples were selected, each containing different artificial flaws. The first three (designated YC033, YC035 and YC036), the representative component was control rod drive housing. For the fourth sample (designated YC015), the representative component was reactor pressure vessel and, in particular, the inner cladding for the RPV wall. The different samples are shown in Figures 2 and 3. Example surface images for thermal fatigue flaw type is shown in Figure 4.

YC033 (pipe / flange)

Test block is a cut off from a real control rod housing. This is the worst case considering flaw manufacturing population. There is very limited access to inside surface of weld.

Grinding of openings and seeing inside was not so easy. Welding of solidification crack was possible only by welding using mirror. Tiny hands of lady welder made it possible to get inside and see the mirror while welding and feeding filler metal. The test blocks contains solidification cracks and EDM notches. Due to the manufacturing difficulties, the quality of the solidification cracks is questionable.

YC035 (small pipe / reducer)

Test block is a cut off from real control rod housing. The test block contains thermal fatigue cracks and EDM notches.

YC036 (small pipe / flange)

Test block is a cut off from real control rod housing. The test block contains solidification cracks and EDM notches.

Figure 2. Test pieces YC033, YC035 and YC036, which represent various inspection targets in the control rod drive housing.

Figure 3. Test pieces YC015 and YC030, which represent the reactor pressure vessel cladding area.

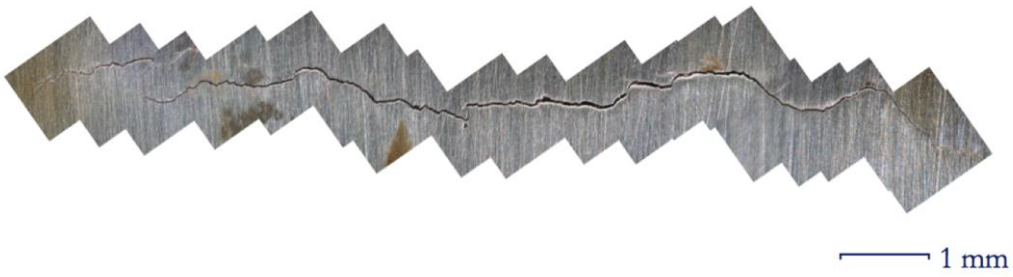

Figure 4. Example thermal fatigue flaw surface image found in one of the test pieces.

INSPECTION COMPANY ASSESSMENT

A pulse-echo and phased-array probes with nominal frequencies ranging from 1 to 4 MHz were used for nondestructive testing of defects manufactured for qualification of automated examination of different nuclear power plant primary components. Nondestructively tested qualification specimens were typically made of austenitic titanium stabilized stainless steel, designated by 08X18H10T similar to AISI 321 or W 1.4541, or 22K material (carbon steel), or low alloyed chrome-molybdenum vanadium steel of grade 12X2MΦA or 15X2MΦA. Consequently pulse-echo and phased-array probes were designed for examination of these materials.

The available specimens had the range of different defect values and length dimensions provided the good source for determination of the detection and measurement accuracy, with the great number of defects manufactured in three different ways which is sufficient for extensive analysis. The following observations have been drawn after extensive ultrasonic data analysis of numerous specimens.

As the material surrounding the EDM notch is left in the original state and the width of EDM notch is usually much greater than the width of true crack, an ultrasonic echoes from such geometric reflectors provides clear tip signals without noise that may affect the depth sizing and consequently result in the easiest detectability and sizing capability of NDE procedure when compared to the other defect types used for qualification purposes. Figure 5 shows the ultrasonic response from such geometric reflector of nominal depth 5 mm located on opposite surface to the scanning one. A clear tips signals are typical for such reflectors and represent 1 - upper tip response seen as OD surface reflection, 2 - corner trap response and 3 – upper tip response seen directly.

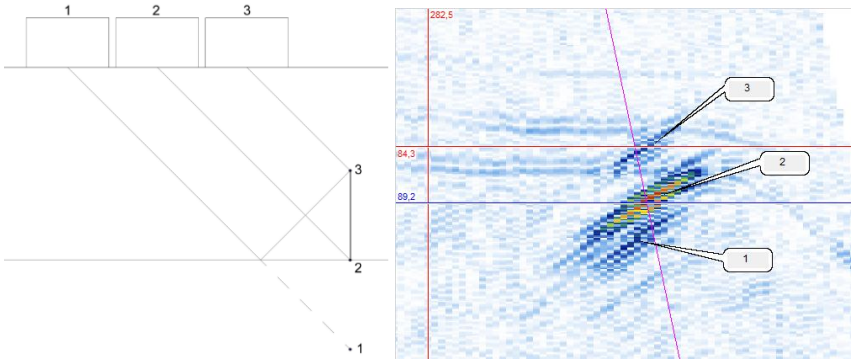

Figure 5. Typical ultrasonic echo from the EDM notch

However, because ultrasonic echo received from EDM notch is not well correlated with the echo received from true crack, its use in evaluation of inspection system capabilities in true crack detection and length and depth sizing is questionable. The reason for that lay in the fact that the ultrasonic echoes received from true cracks which have rough surfaces tightly closed or irregular surfaces with extremely sharp edges with specific crack profile cannot be well compared to smoothly machined EDM notch profile having constant width and depth dimensions.

On the other hand, the constant width and depth dimensions is the main advantage of this type of reflectors as it result in constant and repeatable ultrasonic echo along EDM notch length. This advantage is very useful in calibration and calibration verification of ultrasonic testing systems. Further advantage of using the EDM notches, which are standardized across the industry, is the easier comparison of the results of qualifications and later on inspections performed at different sites.

Echoes from in-situ produced thermal fatigue cracks reflectors also provides very clear tip signals without surplus noise, as shown in Figure 6, and as a result detection probability and sizing ability is very similar to one achieved in ultrasonic examination of EDM notches. In opposite to EDM notches profile, the in-situ produced thermal fatigue cracks, as well as welded solidification cracks, have profile which is not constant in depth and width along each defect length, so the ultrasonic echoes received from such defects, especially in application of automated examinations are more comparable to echoes received from true cracks, so inspection company realize these as crack like flaws.

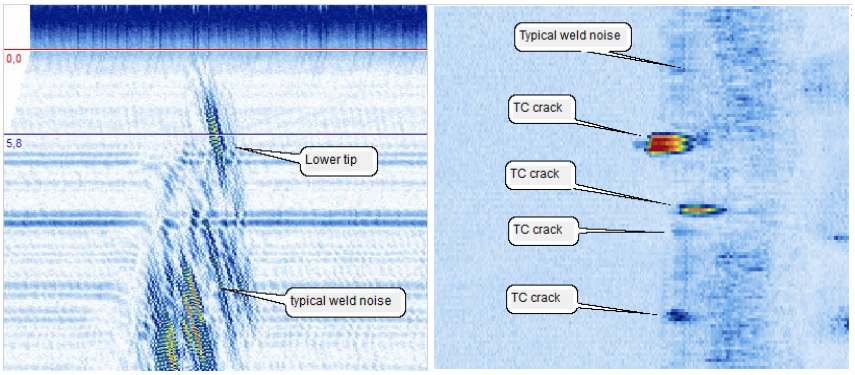

Figure 6. Typical ultrasonic echo from the in-situ produced thermal fatigue cracks, side and top view

Because an automated ultrasonic examination has to be performed with qualified scan pattern parameters, for example scan, index, or overlap, these are subject to qualification. An index resolution is parameter highly affected by the defect profile and critical defect length previously specified by the plant owner. From the index dimension, a total length of defect is determined by observing and counting sweeps having proper, discernible echo-dynamic signal as seen on Figure 7.

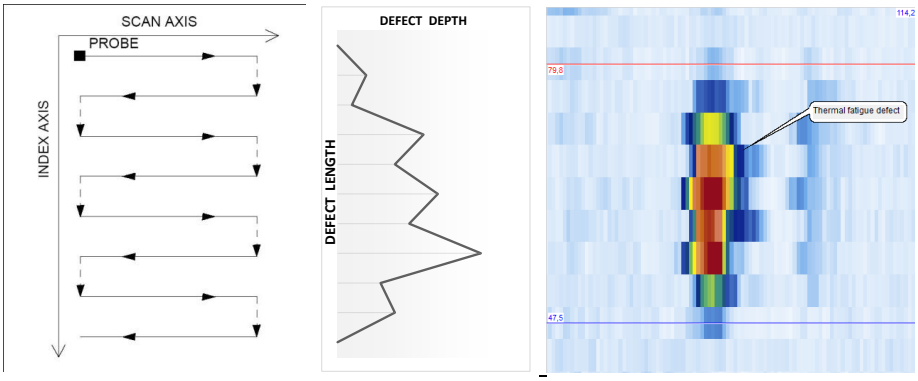

Figure 7. Bidirectional scan, example defect depth profile and thermal fatigue defect top view

The index dimension is closely correlated to the root-mean-square (RMS) value of depth sizing errors from ultrasonic data. As index dimension increases, defect depth estimation decreases, as well as RMS value of depth sizing errors increases because of defect depth changes along the defect length. In order to estimate defect depth with previously identified accuracy, inspection company NDE procedure has to take above in account during the procedure qualification if the EDM notch is only defect type available. Clearly, this is very important advantage of both the in-situ produced thermal fatigue cracks and welded solidification cracks over the EDM notches when used for qualification and assessment of inspection.

Regardless the shapes of the in-situ produced thermal fatigue cracks and welded solidification cracks are crack like, though ultrasonic echoes are not exactly the same to echoes from true cracks. Echoes from welded solidification cracks are pretty noisy, shown in Figure 8, most probably because of the way they are manufactured, by either implanting an existing crack by welding to the test piece, or by inducing cracking of the weld by carefully chosen weld parameters. This surplus noise requires additional efforts for inspection company to distinguish tips from unwanted noise and, as a result do not accurately represent types of degradation that exists on actual component in real operating conditions.

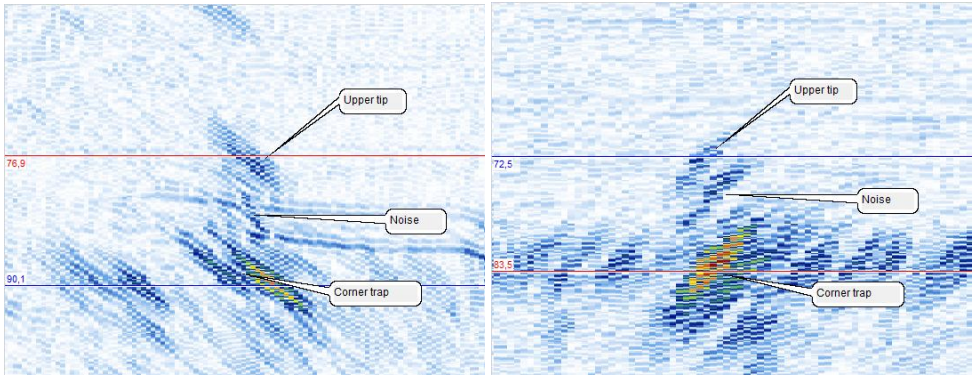

Figure 8. Typical ultrasonic echo from the welded solidification cracks

Examples of surplus noise can be seen on aid piece flaws where used method of creation of flaws is solidification combined with use of aid piece. This way flaws simulating lack of fusion or thermal fatigue cracking can be achieved. In case that aid piece flaw is simulating lack of fusion defects, aid piece is tack welded against straight surface tightly and pressed tightly surface to surface. Aid piece ends are welded carefully and also the rest of opening. Figure 9 presents response from aid piece lack of fusion flaw.

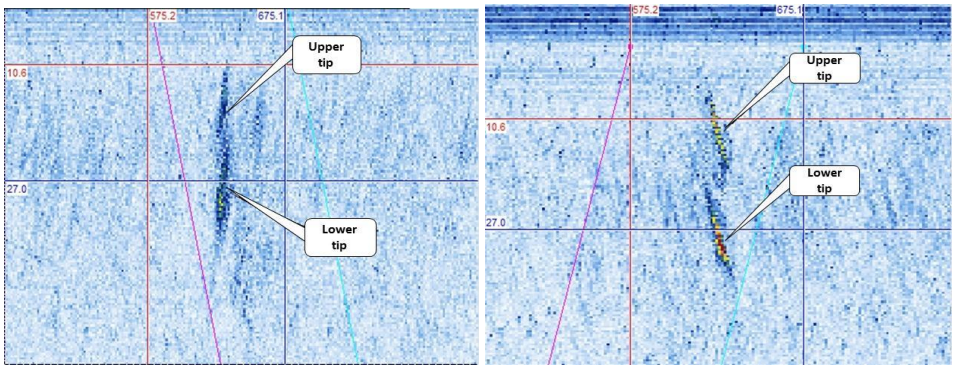

Figure 9. Typical ultrasonic echo from flaws produced by aid piece simulating lack of fusion defect

Lower and upper tip are present and seen without noise from the side of straight cut surface. The other direction response has higher level of noise due to implanting welding.
Alternatively, similar response is received when aid piece is used for creating a flaw that simulates thermal fatigue cracking. Similar approach to produce fatigue crack into straight cut surface by welding and bending aid piece weld produces crack which is fixed tightly face to face and welded into opening. Figure 10 presents response from aid piece thermal fatigue flaw.

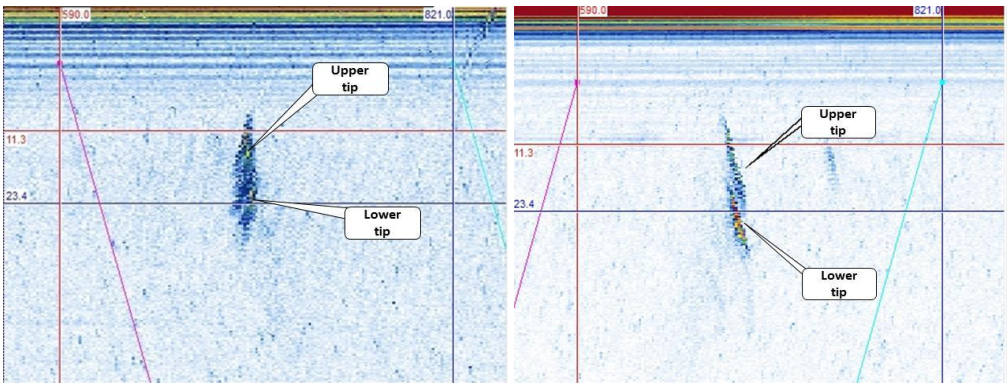

Figure 10. Typical ultrasonic echo from flaw produced by aid piece simulating thermal fatigue defect

Response from such crack is noisier but it includes the tortuous crack path and crack opening can be controlled by manipulation. The noise is low while scanning from straight cut side and higher from the side of opening welding.

The in-situ produced thermal fatigue cracks have been in great extent detected with no material noise similar to one seen at welded solidification cracks and/or other changes visible which could affect the inspection system sizing capabilities and requires additional precautions to be taken during the analysis in order not to miss or misinterpret the defect.

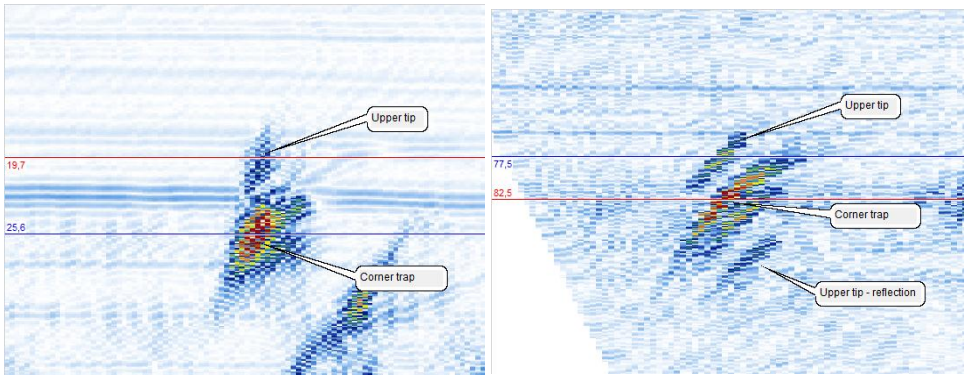

Figure 11. Comparison of ultrasonic echo from the in-situ produced thermal fatigue cracks with the EDM notch

An additional challenge that Inspection Company has to deal with was in certain number of defects a detection of crack tips which found to be hardly detectable, thus when examination was performed with phased array probes, detection and sizing were found to be more efficient.

On the other hand, the approach to qualification which assures more challenging conditions than real operating conditions are welcome and will make sure that in-service inspection will have capabilities to successfully address all potential degradation and deterioration of primary circuit components.

CONCLUSIONS

Based on achieved results through experimental testing and qualification proceedings characteristically responses for each flaw type used during qualifications were obtained. For each artificial flaw group there is an area of application within qualification sample. Certain flaw types like EDM notch can provide solution due to it's repeatability and ease of manufacturing while flaws made by complex techniques like thermal fatigue provide flaws that are more representative of actual existing degradations from the standpoint of flaws size and crack tips, or can provide a challenge for inspection applications due to difficulty to adequately detect and size such flaws.

Selection of adequate flaw types within test sample is crucial step and overall success of test sample will depend on it. Component that test sample is simulating also plays a role in selection and manufacture of defects.

Qualification as a verification process to assess capability of selected inspection techniques is highly defendant on the tests sample and flaws within it, and only if all aspects of artificial flaws, both from component and degradation side and inspection technique side are taken into account will the test sample be successfully prepared and consequently, qualification will be successful and reflect problems and challenges that can occur during actual application of in-service inspection in real conditions.

REFERENCES

1) FNS-262714 LO1-K854-963-50, "INPUT INFORMATION: Reactor pressure vessel", O. Hietanen, R. Korhonen, A. Neuvonen, J. Pirinen, 25 June 2009
2) FNS-280989 LO1-K854-963-60, "INPUT INFORMATION: CRD Protection Pipe", A. Neuvonen, J. Pirinen, 13 April 2010
3) YVL GUIDE YVL 3.8, „NUCLEAR POWER PLANT PRESSURE EQUIPMENT: In-service inspection with non-destructive testing methods", 3rd edition, STUK - Radiation and Nuclear Safety Authority, Finland, 22 September 2003
4) Technical Justification for the Loviisa Power Plant Control Rod Drive Protection Pipe Examination, M. Vavrous, K. Markulin, June 20, 2012
5) Technical Justification for the Loviisa Power Plant Reactor Pressure Vessel Examination, M. Vavrous, A. Matoković, June 20, 2012

INSPECTION QUALIFICATION IV

NEEDS FOR MASSIVE MOCK UPS AND CHALLENGES IN MANUFACTURING OF THEM FOR QUALIFICATION PURPOSES

J. Pirinen, R. Paussu, V. Nikula Fortum Power and Heat Oy, Finland
I. Virkkunen, M. Kemppainen, K. Miettinen, Trueflaw, Finland

ABSTRACT

Fortum operates two VVER-440 nuclear power plants units in Loviisa, Finland. The main focus of the in service inspections of the primary circulation components are in ensuring the reliable and safe operation of the both units. These components are reactor pressure vessel, pressurizer, and steam generators including piping, valves and pumps linked to them. The in-service inspections of components are closely following ASME Section XI requirements. Inspection objects of the components are qualified according to Finnish qualification rules, closely following ENIQ recommended practices. Over the years, Fortum has gathered experience on inspection qualifications and on fabrication of own mock ups and defects.

Primary components have significant safety importance. The importance of the integrity of the primary components is the main reason to invest in the development of qualification. This includes development of the manufacturing techniques, purchasing relevant material for the mock ups and finally improving the qualification of the inspection system. Also the fact that main components are effectively not replaceable has to be considered when evaluating the needs for massive mock ups.

Massive mock ups are needed for the above mentioned components. It has been said, that the qualification of the inspection system will be as good as the used test blocks. The goodness or effectiveness can be estimate with several parameters. Probable the most significant factor is the authenticity of the mock up and more precisely the geometry and the materials of the test block. As known the main goal in qualification is to perform the capability of the selected inspection system (includes used manipulator, probes, data etc.) and that the inspection system fulfills requirements set up for the inspection.

Main focus in this paper is in the challenges in manufacturing massive mock ups, both in general and with respect to two different cases with similar challenges. Also reasons for use of the mock ups have been discussed. To have more practical view of the challenges, these are presented via two on-going cases.

Challenges in manufacturing of the massive mock up consist mainly from the way to handle the test pieces; is the mock up transportable to work shop. Is it needed to move the flaw manufacturing systems to the mock up. Preparing defects to emergency cooling nozzle inner radius in full-scale reactor pressure vessel and bottom head of the pressurizer for qualification purposes will be presented as example cases.

INTRODUCTION

Fortum operates two VVER-440 nuclear power plants units in Loviisa, Finland. The main focus of the in service inspections of the primary circulation components are in ensuring the reliable and safe operation of the both units. These components are reactor pressure vessel, pressurizer, and steam generators including piping, valves and pumps linked to them. Also these primary components have significant safety importance. The in-service inspections of components are closely following ASME Section XI requirements. Inspection objects of the components are qualified according to Finnish qualification rules, closely following ENIQ recommended practices. Over the years, Fortum has gathered experience on inspection qualifications and on fabrication with subcontractors of own mock ups and defects. Tight cooperation with Finnish companies Mekelex (EDM machining) and Trueflaw Ltd (thermal fatigue cracks) has started already early in their starting history and the cooperation still continues and develops.

The importance of the integrity of the primary components is the main reason to invest in the development of qualification. This includes development of the manufacturing techniques, purchasing relevant material for the mock ups and finally improving the qualification of the inspection system. Also the fact that main components are effectively not replaceable has to be considered when evaluating the needs for massive mock ups.

The main goal in qualification process is to verify the capability of the selected inspection system (includes used manipulator, probes, data etc.) and personnel to do inspections with qualified inspection procedure. During the qualification process, the inspection vendor selects techniques for inspection and also justifies selections in technical justification. Selections shall fulfill the requirements presented in the input information. Functionality of the selected inspection system is performed in open trials and witnessed by the qualification body Capability of the Inspection personnel to do data analyzing is performed with blind trial. In Blind trials the data is collected with selected inspection system. Blind-trials are also witnessed by the qualification body.

WHY MASSIVE MOCK-UPS ARE NEEDED

In Loviisa power plant cases the principle to use as authentic and representative mock-ups as possible, has been followed as often as possible. The geometry, size and materials of the mock-up should be as close to real situation as possible. In minimum, in the open trials have used at least geometrically as representative mock-ups as possible. Massive mock-ups for qualification process are usually needed in the cases where inspection objects are in the massive components like pressurizer, reactor pressure vessel etc.

Modeling is seen also as a potential option. The number of the flaws for qualification can be increased with modeling, but it does not replace the need to use mock-ups. The inspection performance especially in the open trials is needed to verify the inspection system in operation. Performing the actual sound paths is also one of the advantages while using the full scale massive mock-ups. Also, manipulator design results and further development needs can be discovered in testing due to the representative inspection conditions.

The goodness or effectiveness of the qualification process can be estimate with several parameters. Probably the most significant factor is the authenticity of the mock up and more precisely the geometry and the materials of the test block. The lack of representative materials is generally the reason that massive test blocks are not used. Years ago Fortum was able to purchase authentic full scale primary components which have been used for qualification purposes in resent year. These components include steam-generator, reactor pressure vessel, reactor pressure vessel head and all the internals.

The largest mock-up project up to date was the manufacturing of the collector nozzle to steam generator (dissimilar metal weld). Other large mock-ups were manufactured even before to main circulation pipe inspection qualification purposes. In these components more authentic materials were used. In contrast e.g. to the bottom head mock-up of pressurizer where western type of materials were used.

Fortum has been able to use authentic mock-ups for qualification in those cases. Materials and geometry could not be closer to real situation. After decision to use the massive mock-ups in qualification purposes manufacturing activities were started. For first massive mock up case was selected the qualification of the emergency cooling nozzle inner radius (TH-NIR). Before the manufacturing of the flaws to the reactor pressure vessel (RPV) TH-NIR, all manufacturing systems had to be redesigned to be movable.

In the first phase the manufacturing started with pressurizer bottom head which was assumed to be simpler than the full scale reactor pressure vessel. Bottom head of the pressurizer was seen as an excellent place for training and testing of the defect manufacturing systems. In addition, the development work of the defects manufacturing systems would not be needed during the defect manufacturing for TH nozzle inner radius. In that second phase the target was to use advanced manufacturing method without time consuming development work.

Needed practical training was one of the reasons to manufacture the full scale mock-up for qualification of the pressurizer bottom head inspections. In that case the manufacturing had to start by purchasing the bottom head of the pressurizer.

INSPECTION OBJECTS TO BE QUALIFIED

Example cases of this paper are related to the qualification of the inspection objects in pressurizer bottom head and emergency cooling nozzle in reactor pressure vessel. Both of these components inspection objects will be externally inspected with ultrasonic examination with long sound path.

In bottom head mock-up consists several inspection objects where to manufacture the defects. The most critical inspection object of the bottom head of the pressurizer is the inner radius of surge line nozzle, corrosion sleeve and its fixing weld in addition to dissimilar weld of nozzle. Also fixing welds of thermal sleeve holders that are located near the critical inner radius area are important.

In the rector pressure vessel there are four emergency cooling nozzles where to manufacture defects and one inspection object in each nozzle in proportion to the pressurizer inspection objects. Inspection objects are presented in through to Figure 3.

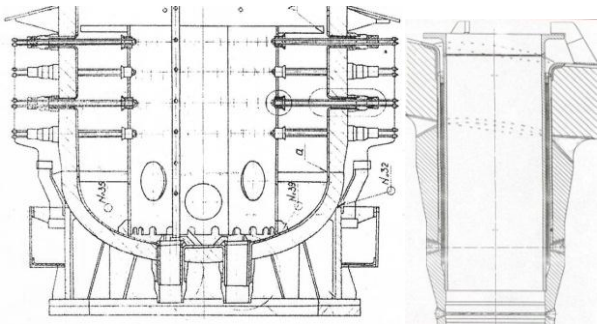

Figure 1. Bottom head of the pressurizer on left and example from the nozzles on right

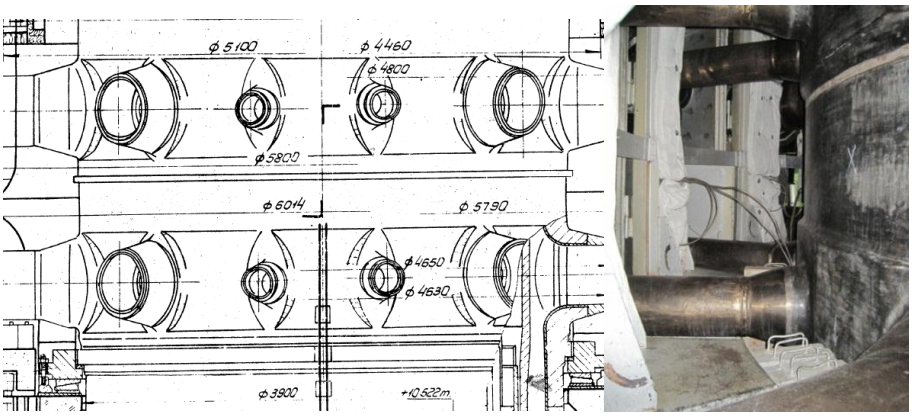

Figure 2. Front view from the reactor, TH-NIR in the middle on the left side and challenging inspection environment on right

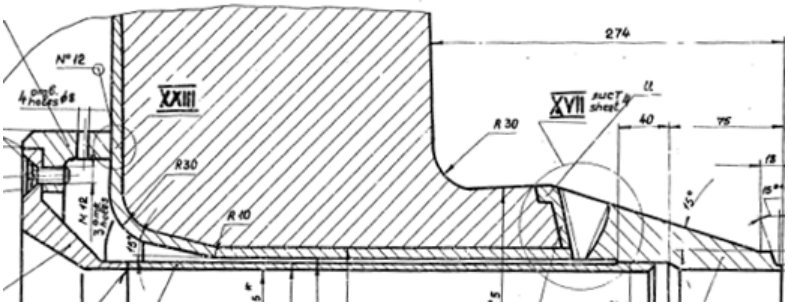

Figure 3. Crossection from the emergency cooling nozzle, inspection object is nozzle inner radius (TH-NIR)

REQUIREMENTS FOR THE MOCK-UPS

Any special requirements as compared to "smaller" mock ups were not placed. Test block design and selection of flaw types to be manufactured are performed by the utility based on the input data for qualification of the inspections. ASME XI principles have been applied in designing of the mock-ups. Same artificial defect types have been used to massive-mocks up as to other mock-ups. Detection targets and critical flaw sizes have also guided the selection of flaw fabrication methods. Used artificial defect types are thermal fatigue cracks, electro discharge machining EDM notches, solidification cracks and implantation defects. As the different types of defects have their advantages and disadvantages in detection and sizing, whole arsenal of manufacturing methods was desirable.

The amount of the defects is mostly limited due ASME requirements of the grading unit, which should be at least 75mm. Current requirement has been followed in designing of the defect population. Also requirements presented in the input information for the qualification have been followed. These requirements are, among the other things, the detection target, specific and postulated defect types and assumed locations of them.

SPECIAL CHARACTERISTIC OF THE MANUFACTURING THE MASSIVE MOCK-UPS

The challenges in manufacturing massive mock ups can be discussed in general and with respect to two different cases with similar challenges. Also challenges can be described as expected and unexpected difficulties.

Expected challenges consist mostly from logistic and handling issues of the mock-up and manufacturing equipment. Difference between the cases consists from the situations where either the mock-up or equipment is moved. Other challenges consist from handling of the mock-ups. Smaller full size mock-ups can be moved and rotated to optimal position for manufacturing. Respectively transportable massive mock-ups e.g. bottom-head of the pressurizer can be moved to manufacturing system at workshop, but used manufacturing system shall be assembled to optimum position for manufacturing. Similar challenges consists in cases where manufacturing has done near mock-up e.g. full size reactor pressure vessel which is not transportable to the subcontractors due to the limitations of the workshops. Respectively field conditions set requirements for manufacturing systems. These are mainly consists from the limited yearly time window and also limited space around the reactor pressure vessel (RPV). RPV and other main components are stored to hall which used as a welding hall during the building time of the Loviisa power plant. Since then the hall has been modified to storage hall.

From the utility point of view, when deep surface or sub-surface cracks are needed to be fabricated into finished component surface, welding of solidification cracks is the easiest, cheapest and often representative enough as fatigue cracks, compared to other type of flaw options, to be used in ferrite and austenitic structures. Shallow solidification cracks are hard to produce as surface breaking. Logistic and handling issues, limited yearly time window among other challenges are presented in more detail via two similar cases. Challenges in flaw manufacturing are also presented.

MANUFACTURING OF THE PRESSURIZER BOTTOM HEAD MOCK-UP FOR INSPECTION QUALIFICATION

The simulation of the real inspection situation requires the same thickness as the bottom has. Also the frame structure around the bottom and the legs were designed at Loviisa NPP to simulate the inspection circumstances under the bottom. The solution was to order bottom from Germany with the same dimensions and shape as the pressurizer bottom. Welding of the cladding and manufacturing of the frame structure were done in Finland,
Figure **4**.

Figure 4. Half-finished bottom on the left and frame structure on the right.

Expected challenges were considered from the transportation and handling issues point of view in the workshops. Heavy lift transportation itself isn't a problem thus the pressurizer bottom head with the frames weight about 7 tons. Moving and handling the mock-up inside the workshop were assumed to be challenging, because a small fork lift would not be able to lift samples and bridge crane was not available.

Moving of test block inside the workshop was settled by using U-profiles beams as rails with roller set to roll along guides on the floor.

Expected challenges also observed to cause from undersized working facilities. Work shop facilities were updated to increase the work safety by improving ventilation and assembling curtains from floor to roof to limit grinding dust. Unexpected challenges caused from the repair and grinding of the cladding. The work took about four months of production time and caused extra costs. SAW welding of cladding layer on inner surface of bottom was a challenge for the welding company. Poor connection of parallel, adjacent strip welded passes and many welding defects in cladding caused long grinding job before the bonding of cladding could be inspected. Also due to the disturbing grinding work behind the curtains, other test blocks were not possible to be manufactured at the same time.

As mentioned, several types of artificial flaws have been manufactured. Used methods have been solidification cracks, aid-piece flaws, thermal flaws and EDM-notches. The deep cracks were produced by welding solidification cracks and shallow cracks with thermal fatigue by Trueflaw Ltd. Also narrow EDM notches with shape of crack front have been used.

Unexpected challenges did not occur during the flaw manufacturing by welding methods. Moisture was expected to occur during the flaw manufacturing and it removed with heating the mock-up. Remove of the hydrogen were daily time-consuming task. Anyhow work was necessary to do to avoid unexpected flaws.

Manufacturing of the EDM-notches did not cause either an unexpected challenges. Same typical challenges occurred which are also expected during the normal EDM machining. These were e.g. erosion of the electrode, re assembling of the electrode due to malfunction and impropriate parameters for current task. Usually parameters are needed to adjust during the manufacturing depending the material properties and size of the manufactured flaw size. To have acceptable process and tolerances to flaws in EDM machining, the head of the EDM machine shall be sturdy assembled. During the manufacturing process the head is not allowed to vibrate. Assembly system of the EDM machining is presented in the Figure 5.

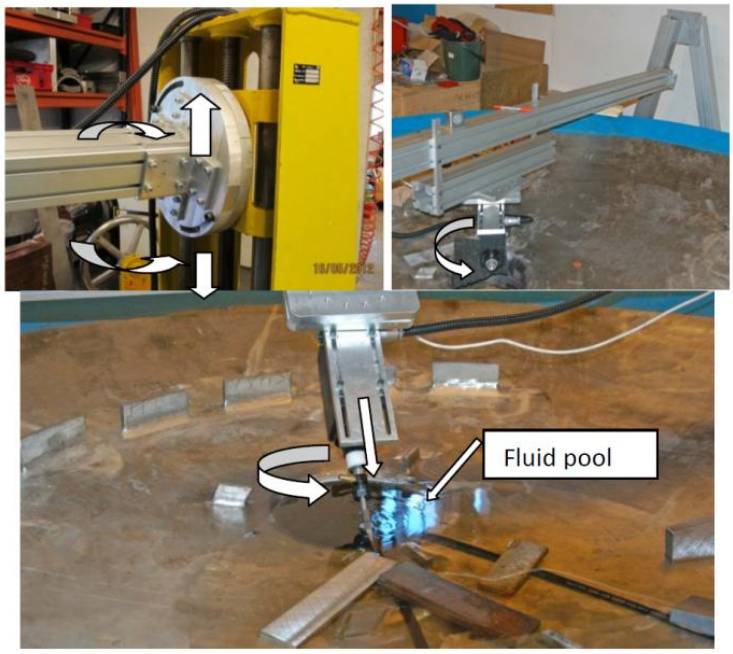

Figure 5. Assembly of the EDM machining system for YP-pressurizer bottom head flaw manufacturing. Adjustment movements are marked with arrows.

For Trueflaw, the pressurizer bottom was the largest mock-up to date. This caused some need for special arrangements. In particular, moving the heavy mock-up from transportation vehicle into suitable location at the shop floor and back to transportation vehicle required special attention (see Figure 6). The production location and transportation was well planned ahead and went accordingly. For flaw production, the mock-up size caused some additional challenges. The mock-up could not be rotated to optimal location for accessibility. Thus, the designated flaw locations were out of reach for normal flaw production tools. Special tooling with extended arm length was developed for this application. The extended arm also resulted

in increased tool flexibility, which necessitated some additional fixtures to allow reliable flaw production. Although the need for further tooling was foreseen, it was also recognized that the specific needs may change due to changes in flaw location or sample orientation. Thus, the tooling was completed when the sample was already in place and tools could be adapted to the exact requirements of the situation. Overall, combination of good preparation and adaptability made producing cracks to massive mock-up successful without major extra effort.

Figure 6. The Massive mock-up rolled into Trueflaw facilities.

Modification of the assembly system during the manufacturing is also expected. Manufacturing process is also a learning process and observed limitations in the design are addressed. As mentioned the mock-up cannot move to optimum position, the manufacturing system shall be moved. In some cases the assembly is not flexible enough due to the temporary assembly of the machining head.

MANUFACTURING OF THE DEFECTS TO TH-NOZZLE INNER RADIUS INSPECTION QUALIFICATION

Based to experiences form the flaw manufacturing to the pressurizer bottom head mock-up and other mock-ups during the resent year, flaw manufacturing to authentic RPV was ready to begin. In this time the flaw manufacturing systems were moved away from workshop to the field conditions. Manufacturing was done in the storage hall at the Loviisa power plant area. In field conditions more detail design for manufacturing arrangements and flaw placement. Thus the mock-up is lying down, all manufacturing systems have their optimal grades which to use. Also the work safety issues, manufacturing of the defect or documentation procedure were observed more detail than in workshop manufacturing.

First preparation work was done already on the 2008. Then the thermal shields from the nozzles were removed. During that work the firs unexpected challenge occurred. Machining work were notable larger and took longer than expected due that the thermal shields were fully welded to RPV. Assumption was that there is only sealing weld and screw fixing. Work with RPV continued on 2012 after manufacturing of the pressurizer. Trueflaw started the flaw manufacturing work at the end of the summer 2012.

Unexpected challenges were observed and also solved during the manufacturing processes due to the environment. The weather conditions were expected to cause challenges during the manufacturing of the defects to reactor pressure vessel. One of the biggest challenges was that the manufacturing time window had to be scheduled to the summer / autumn time. Used storage hall for manufacturing is equipped only with the power supply and is without heating system.

In generally manufacturing systems worked as expected. Mostly challenges were related to the auxiliary systems which are usually permanently installed to function in work shop. Thermal fatigue flaws and EDM-notches are manufactured with remote control and surveillance system via mobile phone net. To ensure reliable connection to net took more time than expected. During the EDM manufacturing similar requirements were not needed than during the fully remote controlled thermal fatigue flaw manufacturing.

For Trueflaw, the most significant challenge was moving the production to remote location and inside the reactor pressure vessel. Although the flaw manufacturing machines ("flawmakers") were designed to be modular and transportable, this had never been tried before. Also, all the flawmakers are connected to central control computer and central database. This provided several possible configurations for remote operation and it was decided to use single central database for all machines while using separate control computers for both locations. This allowed remote monitoring and control of the units while still supporting continued operation in case of intermittent network errors. The flawmakers are also designed to monitor possible error conditions and stop in case of error. The remote machines were connected to central database and control computers through 3G mobile data network. The arrangement was "dry-tested" in the shop floor to make sure it operated as planned.

The dry-tested arrangement was then moved to production location. The arrangements at the site were good and thus getting the machines into location and re-connecting the machines went well. Figure 7 shows the production machines in the location, inside the reactor pressure vessel. After production started, network connectivity provided additional challenges. While the mobile network had worked well during testing, in actual location the link was more error prone and network hardware experienced intermittent crashes that required rebooting the devices. The remote location also increased the occurrences of some (rather harmless) error conditions. This combined with network problems caused excessive machine down time and slowed flaw production in the beginning. It took numerous trials until robust network configuration could be established and the final system included both better hardware as well as local link-status monitoring and automatic recovery. Furthermore, as the final locations of the flaws were decided, it became evident that some of the planned production optimizations could not be used.

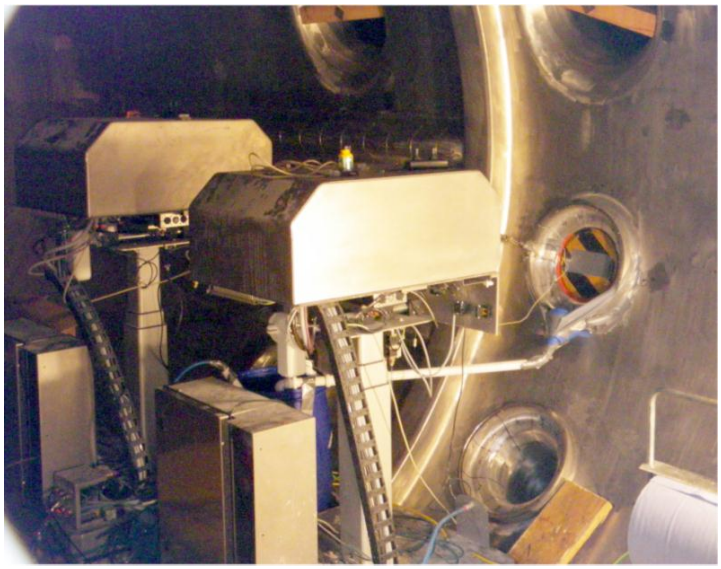

Figure 7. Flawmakers on location at Loviisa, inside reactor pressure vessel.

After the initial problems, the production advanced smoothly. However, the combined effect of the early delays provided its own problems. Over time, the approaching winter caused outside temperature to drop (sometimes to -20°C or below). This caused the working conditions to deteriorate. Furthermore, the flawmakers started to experience cooling water freezing problems. These were remedied by local heating and addition of anti-freezing agent to the cooling water. Despite these final problems due to outside temperature, the flaw production was completed successfully and the production quality for the flaws is as good as it would have been in the shop.

Manufacturing activities continued again on the summer 2013 with solidification cracks. After that all EDM notches have been manufactured. Changes in material properties caused unexpected challenges during the openings for welded flaws. Due to the hardness differences from expected the used manufacturing tools were needed to be changed. Local heating was also needed to avoid moisture based hydrogen problems.
Similar challenges in assembly of the EDM machining occurred as during the machining of the pressurizer bottom head. Also expected normal machining challenges at the beginning of the machining had to be solved. After optimal parameters were reached the position of the EDM head has been the most challenging

task to do. In this case the modification needs could not be excluded to predesigning. General view from the assembly of the EDM manufacturing system and assembly of the EDM machining head are presented in the Figure 8. A part of the system is located to outside of the reactor pressure vessel, the air filter of the local ventilation and fluid collector (see the Figure 9). There can be seen the plugged nozzle which is also used as the pool for fluid.

Figure 8. General view from the assembly of the manufacturing system on left and assembly of the EDM machining head on the right

Figure 9. General view from the assembly of the manufacturing system outside of the reactor pressure vessel. In the front right is fluid collector and on the left side behind is the air filter of the local ventilation

CONCLUSION

Massive mock ups are needed to verify inspection procedures with qualification process to ensure integrity of the components. As mention the geometry and used material should be as authentic as possible for all inspection mock-ups. Especially authenticity is probably most effective factor in the open-trials where selected inspection technique is demonstrated to fulfill determined requirements. Under the circumstances the massive-mock ups are used and manufactured for qualification purposes of the primary components inspection objects. In addition to verified inspection procedure, the quality of inspection system and most of all the nuclear safety are increased

At the moment Fortum has under construction with the subcontractors the biggest mock-up than before manufactured –full scale Reactor Pressure Vessel. RPV mock-up will be used for emergency cooling nozzle inner radius inspections. Later plans for the RPV-mock up for qualification purposes have been also considered.

Many kind of artificial flaw types have been manufactured to the mock ups, more detail designing were done compared to the previous manufacturing projects. In both presented cases, the mock-up could not be moved to the optimum position for manufacturing. Also sector locations were chosen in design according to the limitations of the used manufacturing system.

Experience gathered in resent year from manufacturing methods were notable advantage for designing and manufacturing of the mock-ups. During the manufacturing processes both expected and unexpected challenges were met. Unexpected problems were caused mainly from auxiliary systems. Movable flaw manufacturing systems were developed without any massive extra effort. Afterward can be even said that it were easier than expected. Logistics and handling issues related to the moving of the component or the manufacturing systems were solved in both cases. Other challenges in the field condition were mostly caused from the environment of the facilities due to the limited time window for all year defect manufacturing.

Although manufacturing were the first step in the process to have accepted mock-up for qualification. Finger print work will be also challenging, due the size of the mock-ups. There are only few companies which are able to give the feedback from the manufactured artificial flaws when scanning is performed externally. At the same time there are only few companies which can be qualified to do the actual inspection. This is one of the challenges which is still open. Qualification process continues and more detail results of the quality of the mock up will be received in near future after finger print and open trials. Now Fortum and subcontractors are more capably to carry out similar projects due to the gained experience from the presented cases.

POSITION CONTROL OF STRESS CORROSION CRACKING USING WELDING BEAD

B. Lee, Y. Woo, Korea Aerospace University, South Korea

Abstract

The Stress Corrosion Cracking (SCC) is one of the environmentally induced cracking.
SCC results from the combined action of a tensile residual stress, a structure with alloy and corrosive environment. Many researches about the cracks were done in a way of a slow strain rate test, U-bends and so on. But it has a little difference with actual crack generating conditions. These methods have a disadvantage which is long experiment time. So confirming the effect of experimental variables is some difficult. It is need to manufacture SCC in the simulated nuclear power plant environment with short experimental time and easy control possibilities. In this study, SCC was manufactured in the simulated corrosive environmental conditions with STS 304 tube that widely applied in the nuclear power plants. The residual stress which is one of the main factors to induce SCC occurrence was given by GTAW welding in the inner surface of specimen with pure argon shielding gas. The corrosive environment was simulated using the sodium hydroxide (NaOH) and sodium sulphide (Na2S). When the welding heat input was given to specimen enough, the longitudinal direction crack was generated near the welding bead which was affected by tensile residual stress. And the tangential direction stress which was generated by internal pressure was insufficient than yielding stress of STS 304. It is considered that the reason was due to the corrosive condition in the test specimen. The stress corrosion crack position can be controlled using welding heat input.

Keywords: Application areas of NDT (RPV-SG-Internals and primary circuit-Other component)

DIFFERENCES IN INDICATIONS OF DIFFERENT ARTIFICIALLY PRODUCED FLAWS IN NON-DESTRUCTIVE EXAMINATION

A. Koskinen, E. Leskelä VTT, Technical Research Centre of Finland

ABSTRACT

Qualification of non-destructive examination procedures for in-service inspections of nuclear power plant components is performed using different types of artificial flaws. The assessment of the reliability of a procedure requires sufficiently representative flaws compared to the real service-induced flaws.

Fatigue cracks can nowadays be produced artificially as thermal fatigue or mechanical fatigue cracks. Thermal fatigue crack production is very well controlled in matter of size and opening. That kind of cracks are very realistic option compared to the real service-induced cracks. Mechanical fatigue crack production is well known and widely used method and can produce very realistic cracks as well.

Ultrasonic indications are highly dependent on defect characteristics like roughness, crack opening, tilt and branching. This work studies the influence of different reflector properties on flaw indications. Two kinds of artificial cracks from different manufactures and one EDM reference notch were made in austenitic stainless steel test blocks. Flaws were examined using phased array ultrasonic testing (PAUT), scanning acoustic microscope (SAM) and time-of-flight diffraction (TOFD) techniques. Flaw images produced by two digital radiography techniques are used as reference. The aim of the study is to get a wider perspective to the differences in similar type of flaws from different manufacturers.

INTRODUCTION

This study was conducted to compare two different types of artificial defects to test and study the influence of different reflector properties on indications in non-destructive examination. Another objective was to produce new data on artificial reflectors for the needs of qualification as well as inspection.

There are many ways to produce artificial defects in different materials. Different defects produce different responses when they are inspected and it is crucial for the reliability to know how well artificial defects correspond to service-induced cracks. Fatigue cracks can nowadays be produced using thermal fatigue or mechanical fatigue. In this study thermal fatigue and mechanical fatigue cracks of similar size were produced in two test samples. These artificial defects were examined using manual and mechanized phased array ultrasonic testing (PAUT), scanning acoustic microscope (SAM) and time-of-flight diffraction (TOFD). Also digital radiography was used for crack imaging.

EXPERIMENTS

Fatigue crack samples

Two different fatigue samples were studied. Both samples were made of austenitic stainless steel 316L (ASTM) plate with a thickness of 25 mm. Samples were butt welded of two pieces and both weld face and root sides were ground. The cracks were produced on the root side along the fusion line (Figure 1 a). One of the samples contained one thermal fatigue crack and EDM reference notch and the other contained two mechanical fatigue cracks. Liquid penetrant indications of both thermal and mechanical fatigue cracks are shown in Figure 1 b and c. The branching shape of the thermal fatigue crack is well visible. The dimensions of the cracks in both samples were targeted to be 15 mm in length and 5 mm in depth. These dimensions will be confirmed after the final destructive investigation in 2013 as a part of the Finnish Research Programme on Nuclear Power Plant Safety 2011 - 2014 SAFIR2014 MAKOMON project [2].

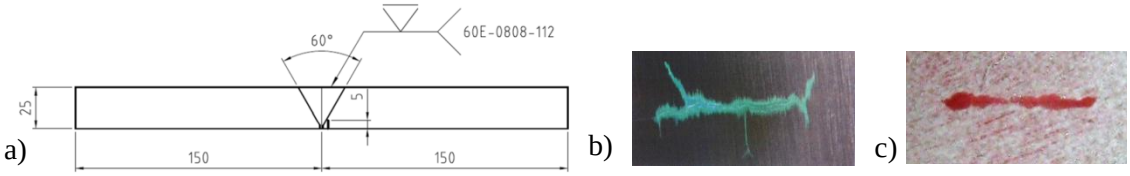

Figure 1. a) Schematic picture of the sample and liquid penetrant indications of b) thermal fatigue crack and c) mechanical fatigue crack.

Phased array ultrasonic examination

Phased array ultrasonic examination was performed using OmniScan 16/128PR with software control by UltraVision. Scanning in TRS and TRL techniques was carried out using Zetec's Manual Pipe Scanner and in the other techniques using motorized scanner (Phoenix ISL's SPIDER). More detailed information on the examination parameters can be seen in Table 1 and more detailed probe parameters in Table 2. The data was analysed using UltraVision software.

Table 1. Phased array examination details.

Technique	**Description**
TRS TRL	Scanning from weld face side using dual matrix PA probes with sectorial scan in pitch and catch mode. Line scanning from both sides of the weld using manual encoded scanner with several scan lines along the weld. Technique is qualified to be used in in-service inspections of piping welds in nuclear power plants in the USA. Procedure: Zetec OmniScanPA01 rev. C.
Sectorial 2 Sectorial 5	Scanning from weld face side using linear pulse-echo PA probes with sectorial scan. Raster scanning with a resolution of 1 mm from both sides of the weld using motorized scanner.
45° SW 55° SW 70° SW	Scanning from weld face side using linear pulse-echo PA probe with linear scan. Raster scanning with a resolution of 1 mm from both sides of the weld using motorized scanner.
MC	Scanning from weld face side using linear pulse-echo PA probe with sectorial scan generating inner surface creeping wave. Raster scanning with a resolution of 1 mm from both sides of the weld using motorized scanner.

Table 2. Phased array probe parameters.

Technique	**Probe**	**Wedge**	**Wavemode**	**Angles**	**Frequency (MHz)**	**Focus (mm)**	**Aperture (mm)**
TRS	1.5M5x3E17.5-9	ADUX576A	Shear	40° - 70°	1.5	25 TD	2x(9x17.5)
TRL	1.5M5x3E17.5-9	ADUX582A	Longitudinal	40° - 70°	1.5	25 TD	2x(9x17.5)
Sectorial 2	2L16A10	SA10-N55S	Shear	40° - 70°	2.25	25 TD	9.6x10
Sectorial 5	5L32A11	SA11-N55S	Shear	40° - 70°	5	25 TD	9.6x10
45° SW 55° SW 70° SW	5L32A11	SA11-N55S	Shear	45°, 55°, 70°	5	25 TD	9.6x10
MC	5L16A10	SA10-N60L	Longitudinal	60° - 89°	5	50 HP	9.6x10

Scanning acoustic microscope
The probe used in examination with scanning acoustic microscope (SAM) was a 5 MHz probe manufactured by Panametrics. The focal distance of the probe was 3 inches (76.2 mm) and the probe diameter 0.5 inches (12.7 mm). To evaluate the flaws in the test samples, a 45 degree transverse wave was chosen for examination. To produce a 45 degree transverse wave in steel, the probe was tilted 19 degrees in water according to Snell's law.

$$v_1/v_2 = \sin(\alpha_1)/\sin(\alpha_2) \quad (1)$$

where v_1 is the velocity of longitudinal wave in water, v_2 is the velocity of transverse wave in steel, α_1 is the transverse wave angle in steel and α_2 is the longitudinal wave probe angle in water (i.e. probe angle) [1]

Time-of-flight diffraction
The examination using time-of-flight diffraction (TOFD) was performed using basic 60° setup with 2.25 MHz and 5 MHz probes manufactured by Panametrics. The probe diameter was 0.25 inches (6.35 mm). OmniScan 16/128PR with manual scanner (Olympus HST-Lite) was used in data acquisition and the data was analysed using UltraVision software.

Digital radiography
Digital radiography was used to gather more information on the crack size, tilting, possible branching etc. Digital radiography examinations were done at Federal Institute of Material Research and Testing, Division 8.3, Radiological Methods in Berlin. The used methods included Vidisco RayzorX flat panel detector and TomoCAR which is equipment for X-ray tomography. The TomoCAR equipment has an ENIQ certification for detecting cracks in the tube with 25 mm wall thickness, the total penetration thickness 50 mm. The certified crack opening is min. 100 µm and the tolerance in crack height sizing is ±1 mm. In the equipment the X-ray tube moves along a straight bar over the examined specimen taking 400 images. The Cadmium telluride detector is made by AJAT Finland. The size of the detector is 100 mm x 25 mm with 0.1 mm pixel size. Tomographic data was processed and analysed using Analytical RT Inspection Simulation Tool (aRTist).

RESULTS

Signal-to-noise ratio (SNR) in phased array ultrasonic examination
In near side examination, all the flaws were detected with all techniques (Figure 2). Average SNR for crack MF A is a little bit lower than that for the other cracks. Variance in SNR with different techniques is clearly highest for TF crack and clearly lowest for EDM notch. The lowest SNR values are approximately 6 dB so also the techniques with higher frequency performed well.

As can be seen in Figure 2, the highest SNR values for mechanical fatigue cracks MF A and MF B were measured when scanning was performed from the crack side. The highest SNR value for crack MF A was measured when inspected with longitudinal wave and mode conversion technique whereas highest SNR value for MF B was measured when share wave was used. The highest SNR value for TF crack was measured with mode conversion technique. The lowest SNR for botch TF crack and EDM notch was measured with longitudinal wave.

In far side examination, thermal fatigue crack is detected with only one exception and EDM notch is detected with all of the techniques. Mechanical fatigue cracks are detected only with longitudinal wave, mode conversion and TRS techniques. There is only a minor difference in SNR between the flaws with longitudinal wave and mode conversion techniques. With mode conversion technique, the SNR for both mechanical fatigue cracks is similar when measured from crack side and vice versa. The highest SNR values in far side examination were measured for EDM notch. Variance between techniques is similar for both crack TF and EDM notch. The SNR for TRS technique is higher for both TF crack and EDM notch compared to the SNR of near side examination.

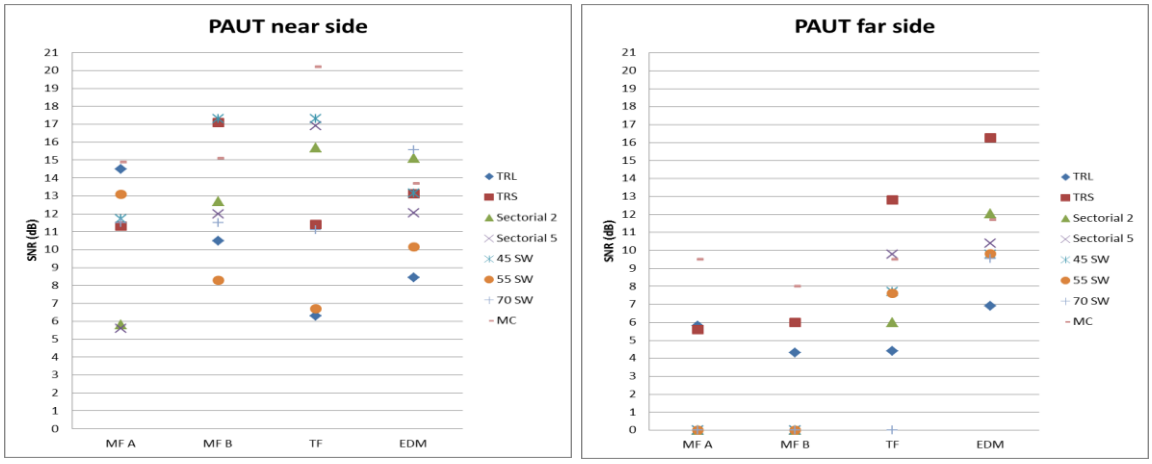

Figure 2. Signal-to-noise ratio in phased array examination.

Figure 3 (MF B) and Figure 4 (TF) show the examination results for TRS technique with similar gain settings. Difference in amplitude between inspection directions near/far side is remarkable with crack MF B. With thermal fatigue crack the amplitude is slightly higher when scanned through the weld and the indications are nearly similar regardless of the scanning direction.

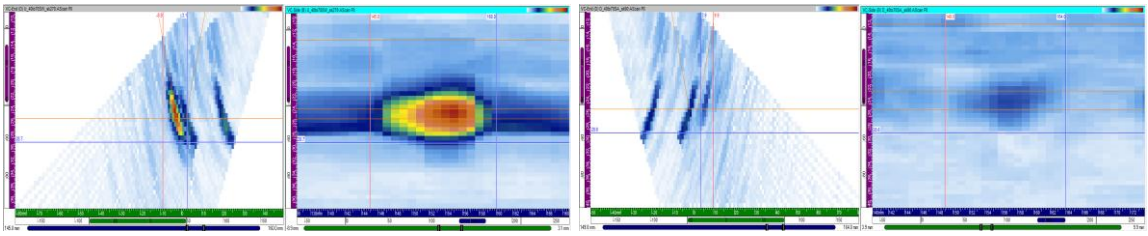

TRS near side TRS far side

Figure 3. D and B-scans of crack MF B inspected with TRS technique.

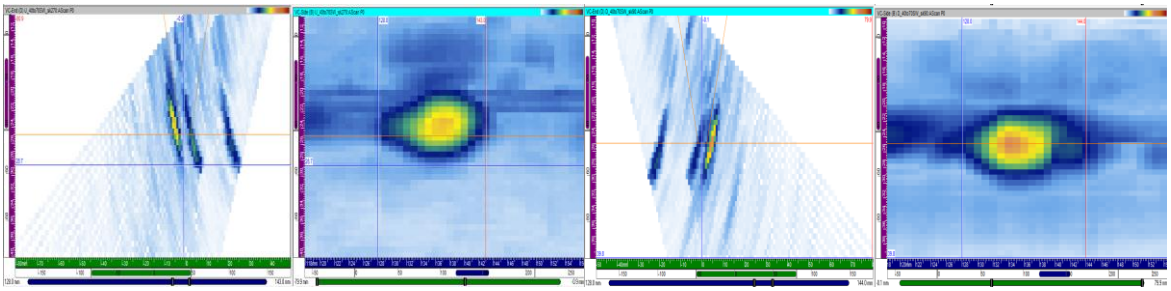

TRS near side TRS far side

Figure 4. D- and B-scans of crack TF inspected with TRS technique.

Frequency response

Frequency response was measured using FFT (Fast Fourier Transform). The results for each flaw with low frequency techniques are shown in Figure 5. There seems to be no remarkable difference between near/far side examinations.

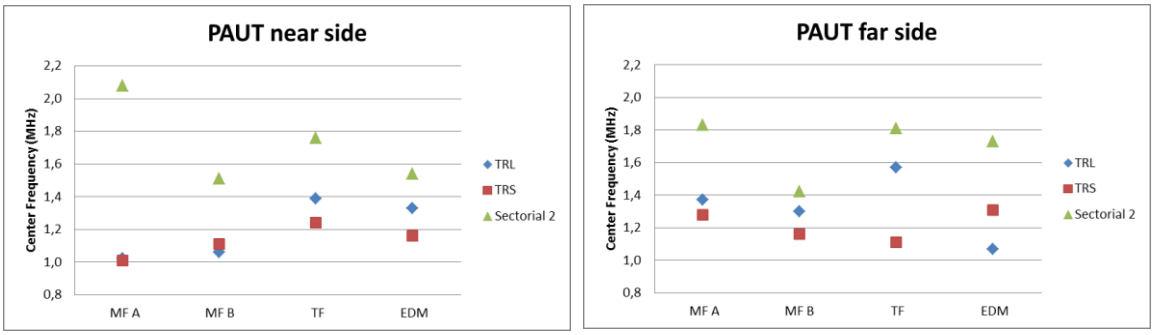

Figure 5. Center frequency for flaws with low frequency phased array techniques. On the left scanning from the flaw side. On the right scanning through the weld.

Amplitudes

Near side amplitude comparison for each flaw with phased array techniques is shown in Figure 6. The lowest amplitudes were measured with TRL technique. Variance between techniques is highest with thermal fatigue crack.

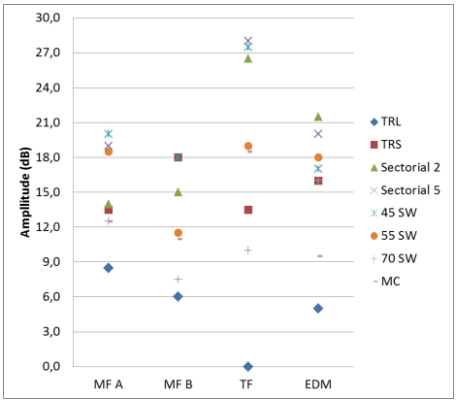

Figure 6. Near side amplitude comparison for each flaw with phased array techniques.

Scanning acoustic microscope (SAM) 45° transverse wave

B-scan images of examination with scanning acoustic microscope (SAM) are shown in Figure 7. Crack tip signal was detected for both of the mechanical fatigue cracks but not for the thermal fatigue crack. The amplitude of thermal fatigue crack indication is 9 dB higher than that of mechanical fatigue crack A. The difference in amplitude between the two mechanical fatigue cracks is 2 dB. There seems to be more interaction with crack morphology in the indications of mechanical fatigue cracks. The rather smooth indication of thermal fatigue crack does not show up the branching shape of the crack.

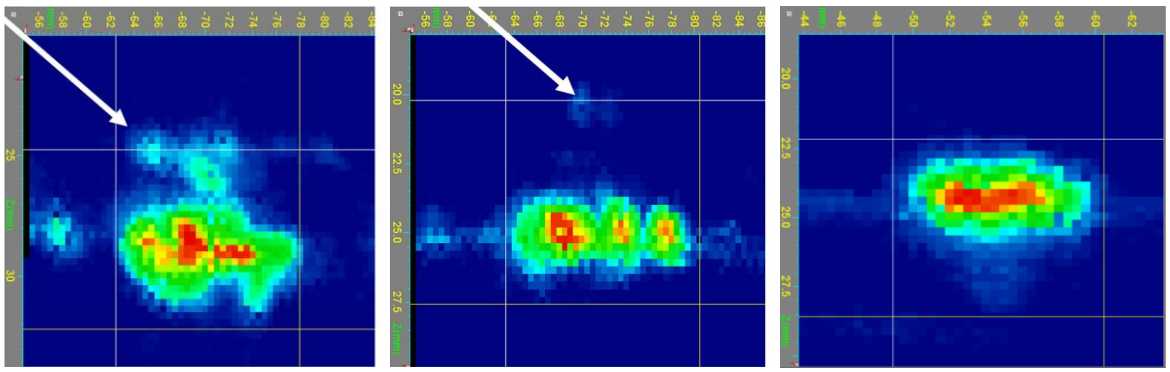

MF A MF B TF

Figure 7. B-scans of crack indications with SAM, 5 MHz 45° transverse wave. Crack tip signals are pointed with arrows.

Time-of-flight diffraction (TOFD)

The B-scan images of TOFD examination with 2.25 MHz probes are shown in Figure 8 and Figure 9. The challenge of TOFD inspection of rather shallow cracks in austenitic steel welds is realized in the images where no diffraction echo is detected. The result was rather similar with some more noise when 5 MHz setup was used. However, the amplitude drop in the back wall echo clearly proves the existence of surface-breaking flaws. The amplitude drop measured from the A-scans was significantly higher with EDM notch and thermal fatigue crack compared to the mechanical fatigue cracks: from 6 up to 12 dB.

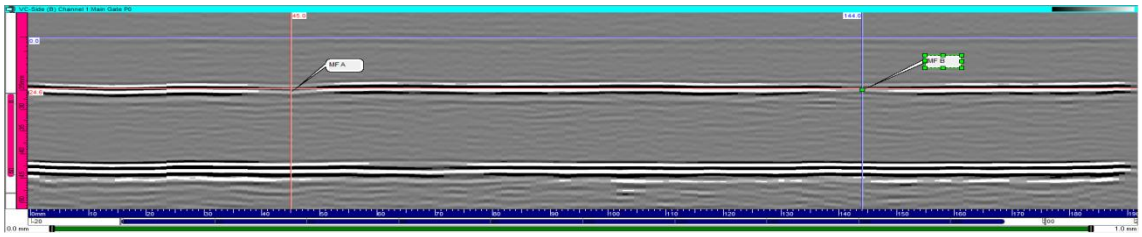

Figure 8. TOFD examination of mechanical fatigue cracks.

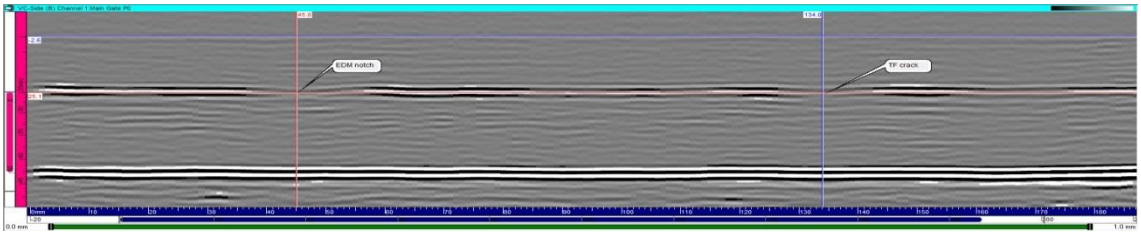

Figure 9. TOFD examination of EDM notch and thermal fatigue crack.

Digital radiography

Data collected with TomoCAR system was reanalysed and visualised at VTT. Crack surface was extracted and visualised from the original data using Matlab. Crack is very clearly visible in tomographic image as can be seen inFigure 10. Tomography shows the shape and the size of the crack relatively clearly. The confirmed results of the shape and the size will be evaluated and published after the destructive testing which will be done later this year.

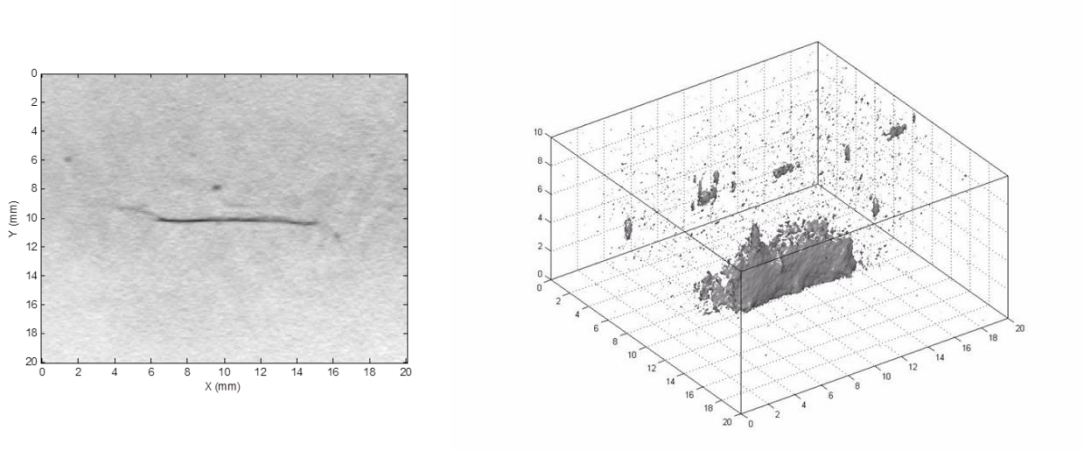

Figure 10. Thermal fatigue crack. On the left conventional digital radiographic image. On the right visualised tomographic image.

DISCUSSION

In this paper only some results of the on-going study concerning the differences in NDE reflectors are briefly presented. Flaw sizing results will be presented later together with the results of destructive examination. Even in these results it is clearly seen that the defect characteristics have a significant impact on indications – not only between different types of fatigue cracks but also between two similarly targeted mechanical fatigue cracks. Results presented in this paper encourage studying this subject more. Cracks examined in this study are rather shallow and short so the crack images do not show much variation caused by crack morphology.

Both the thermal fatigue crack and EDM notch were detected with almost all PAUT techniques also when scanned through the weld. In qualification process it is important to know how that kind of result corresponds to the real service-induced flaws to avoid overestimating the performance of a procedure.

Low frequency PAUT techniques which typically are preferred in the examination of austenitic welds did not show much interaction with crack morphology. Crack tip detection seems also be difficult which will make the height sizing more or less unreliable.

A very clear difference between cracks was seen in the examination by scanning acoustic microscope with 5 MHz 45° transverse wave. There is much more interaction with crack morphology in the B-scans of mechanical fatigue cracks while the image of thermal fatigue crack is rather smooth. Also the images of two mechanical fatigue cracks differ from each other.

The small changes in the coupling and in the shape of the scanning surface or in probe position together with flaw morphology can cause variation in the FFT measurements and diminish the repeatability of them. Signal response depends on the angle and measurement position.

Nowadays the interest for the use of digital radiography is rising also in the nuclear industry. Digital tomography seems to be performing well for crack characterization and sizing.

CONCLUSIONS

- More interaction with crack morphology was observed in mechanical fatigue cracks compared to thermal fatigue crack studied here.
- Higher frequency in ultrasonic testing can give more information of crack morphology and can also enable accurate height sizing of shallow cracks. Even then, e.g. branching of a crack may not be visible and noise can cause problems.
- Due to branching, a crack can be more easily detected when scanned through the weld.
- Both side access and weld cap removal makes a 5 MHz transverse ultrasonic technique applicable for crack detection in austenitic welds with thicknesses at least up to 25 mm.
- More measurements would be needed for reliable conclusions whether FFT measurements are applicable for crack characterizing.
- TOFD inspection of austenitic stainless steel weld is challenging and a basic setup does not seem to have a benefit compared to phased array or digital radiographic examination.
- A combination of PAUT technique (crack detection and sizing) and digital tomography (crack characterizing and sizing confirmation) can be effective in increasing the ISI reliability.

REFERENCES

1. Koskinen, A., Haapalainen, J., Virkkunen, I. & Kemppainen, M. Differences in Ultrasonic Indications – Thermal Fatigue Cracks and EDM Notches. 18th World Conference on Nondestructive Testing, 16-20 April 2012, Durban, South Africa.
2. Jäppinen T., Koskinen A., Leskelä E., Tuhti A., Haapalainen J., Sandlin S., Monitoring of the Structural Integrity of Materials and Components in Reactor Circuit (MAKOMON), SAFIR2014 The Finnish Research Programme on Nuclear Safety 2011-2014, Interim Report, Kaisa Simola (Ed.), Espoo 2013, Pp.292-301.

CURRENT STATUS OF JAPANESE PERFORMANCE DEMONSTRATION IN FY 2012

H. Shohji, K. Hide, K. Watanabe Central Research Institute of Electric Power Industry, Japan

ABSTRACT

The Japanese performance demonstration standard, NDIS0603, "Qualification and certification of personnel for performance demonstration of ultrasonic test system" was issued in 2005. The first Japanese Performance Demonstration (PD) qualification examination for IGSCC crack depth sizing in austenitic stainless steel piping welds for nuclear power plants began in March 2006 and has been operated by the PD center of the Central Research Institute of Electric Power Industry (CRIEPI).

At the end of FY 2012, 38 examination sessions have been completed and 44 candidates have passed the examination. The total number of tests administered including re-testing and re-certification was 89. The certified examiner can perform crack depth sizing of IGSCC flaws with a high level of accuracy. On the other hand, most of the failed candidates were extremely wary of the −4.4 mm critical miss call, but over 80% of the unsuccessful candidates failed to meet the requirement of an RMSE less than 3.2 mm.

Currently, in the spring of 2013, the NDIS0603 was revised to add the Weld Overlay performance demonstration (WOL-PD). The CRIEPI had started to prepare the WOL-PD examination. The Japanese WOL-PD system will be performed with EPRI examination facilities and test samples, and is based on Japanese code.

INTRODUCTION

In 2000, the Japan Society of Mechanical Engineers (JSME) published the first edition of a fitness-for-service (FFS) code [1]. In June 2005, the first Japanese performance demonstration (PD) standard, NDIS0603, "Qualification and certification of personnel for performance demonstration of ultrasonic testing system," was issued [2]. The NDIS0603 is fundamentally similar in its structure to Appendix VIII of Section XI of the ASME Boiler and Pressure vessel code with some modifications reflecting Japanese findings of the IGSCC with regard to 316L stainless steel welds. This code was focused on IGSCC crack depth sizing in austenitic stainless steel piping welds for nuclear power plants; however, it was decided to expand upon that target in the future.

In March 2006, the 1st Japanese PD qualification examination session was started [3]. At the end of FY 2012, 38 examination sessions have finished and 44 out of a total of 89 candidates have passed the examination.

THE PD SYSTEM IN JAPAN

Figure 1 shows the organizations that participated in the Japanese PD qualification examination system designed for crack depth sizing. The certification body of the Japanese Society of Non-Destructive Inspection receives direction from the PD Advisory Committee. The members of the PD Advisory Committee consist of academic experts, etc. The PD Advisory Committee reviews activities of PD-related organizations and provides them with recommendations.

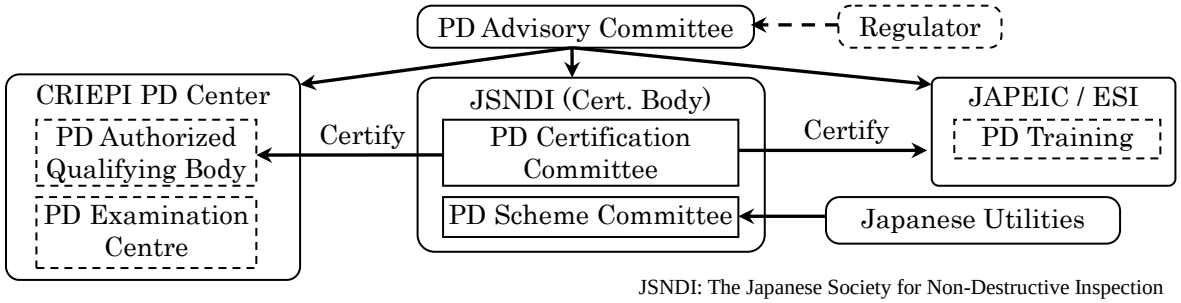

JSNDI: The Japanese Society for Non-Destructive Inspection
JAPEIC: Japan Power Engineering and Inspection Corporation
ESI: Electron Science Institute

Figure 1 Organization of Japanese PD qualification examination

EXAMINATION RESULTS

The first PD qualification examination began in March 2006. During the past 7 years, 48 (for a total of 89, including re-testing and re-certification) personnel took the examination with a total of 44 personnel passing the examination. **Figure 2** shows the history of the numbers of candidates and successful applicants from March 2006 to end of FY 2012. This figure shows that the number of candidates performing qualification activities in each period has gradually decreased over the past 6 years. It should be noted that the required number of qualified personnel to support the Japanese nuclear industry was almost satisfied within the first 18 months of starting the PD qualification examination process. After this period, the number of candidates performing the qualification examination during each period stabilized as candidates was primarily performing the examinations to support future activities within their organizations.

Although the pass rate of each period shows fluctuations, the data appears to present a gradual improvement in the pass rate with time. The information obtained by interviewing the candidates indicates that this improvement seems to be the result of educational efforts within their organizations.

Figure 3 shows the relationship between the RMSE and the average measurement errors of the successful and unsuccessful candidates. Approximately 70% of all successful candidates performed depth measurements on the IGSCC with average errors of 1 mm or less. This shows that depth sizing of IGSCC flaws can be performed with a high level of accuracy.

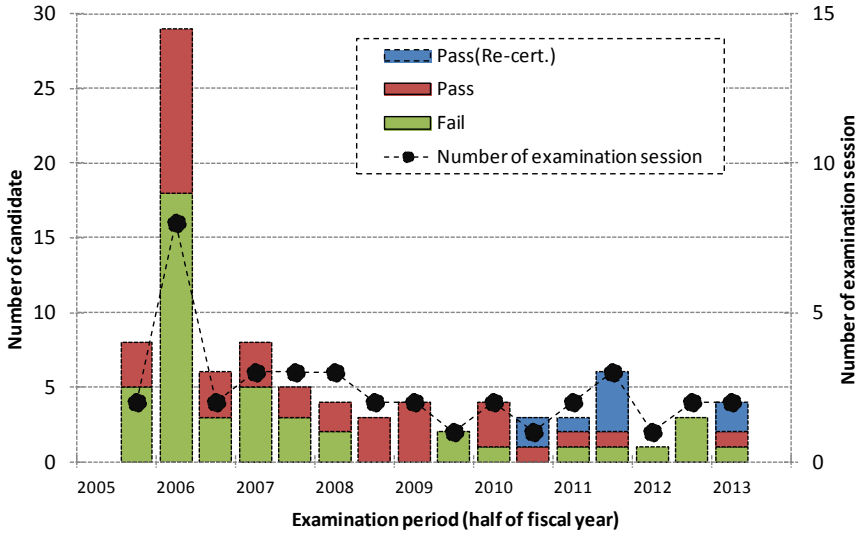

Figure 2 Number of candidates and successful applicants year by year

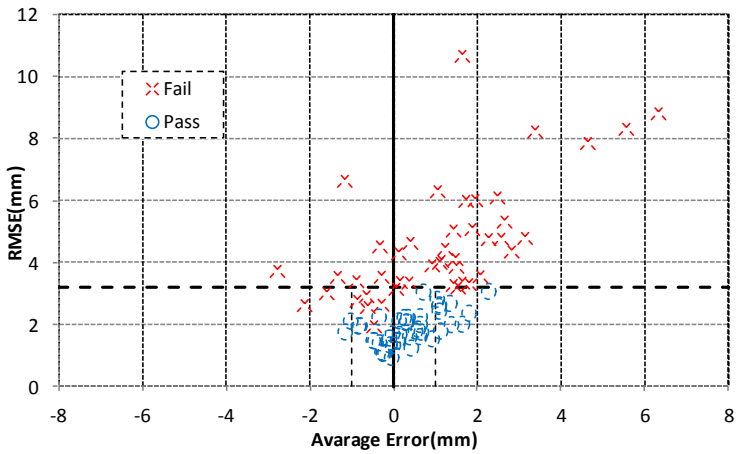

Figure 3 RMSE vs. average measurement errors

SIZING PROCEDURE

Figure 4 shows the number of applicants and all candidates for various types of crack depth sizing procedures used in the PD qualification examinations. In the figure, "PA" refers to phased array examination using either linear or matrix phased array transducers with encoded or automated scanning systems. "Others" refers to manual scanning techniques with a conventional A-scan-type UT instrument and conventional angle beam tip diffraction techniques. The majority of the candidates used the "PA + conventional" type procedure.

The test results shown in **Figure 4** indicate that the "PA + conventional UT" is the most successful procedure with the lowest RMSE. Using only the conventional procedure, a total of three candidates passed the examination in the first examination period. No candidate has recently performed the examination utilizing the conventional UT procedure. At present, the pass rate of the PA procedure is still low but its RMSE of passed candidates is better than that of the "PA + conventional UT" procedure.

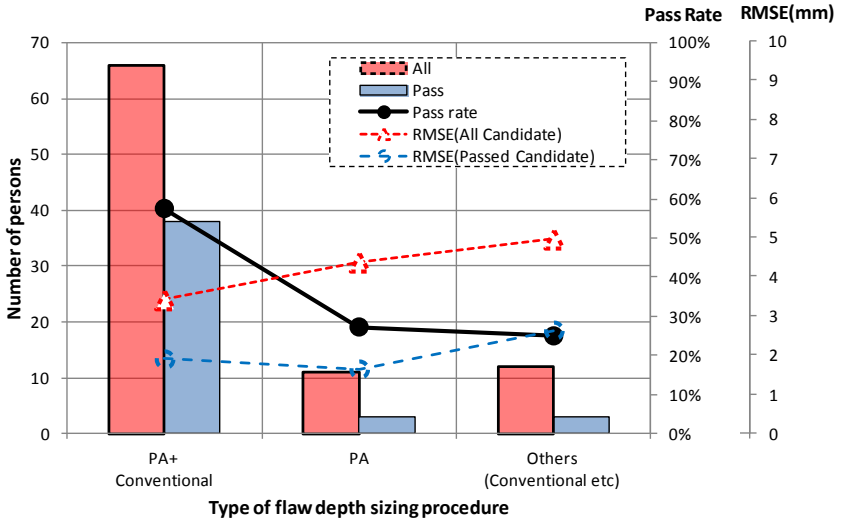

Figure 4 Number of candidates relative to the type of flaw depth sizing procedure

STATISTICAL ANALYSIS OF SIZING RELIABILITY

To clarify the depth sizing reliability, the PD center performed a statistical analysis using 890 depth sizing data points. **Table 1** shows the statistical analysis results of the IGSCC depth sizing error.

The mean error and the standard deviation of successful candidates were 0.33 and 1.92 mm, respectively, while the mean error and the standard deviation for failed candidates were 1.07 and 4.87 mm, respectively.

It is not necessary for the UT examiner to be very careful to avoid making a −4.4 mm critical miss call when the successful PD applicant subsequently measures the IGSCC depth in actual operations [4]. $P(x)$, which is the probability that the measurement of a successful PD applicant will make a −4.4 mm critical miss call, is derived from the mean errors and standard deviations of the pass group in Table 1 (0.33, 1.92^2) and the following equation [5].

$$P(x) = \int_{-\infty}^{-4.4} \frac{1}{\sqrt{2\pi\sigma}} e^{-\frac{1}{2}\left(\frac{x-\mu}{\sigma}\right)^2} \quad (1)$$

$P(x)$ is calculated to be 0.007 (0.7%) from Equation (1). Furukawa et al. have reported that the maximum probability that a −4.4 mm critical miss call will be made when a successful PD applicant measures the IGSCC depth sizing of 5% [6][7]. These results indicate that a successful Japanese PD applicant will measure the crack depth with sufficient precision and reliability.

Table 1 Statistical analysis of the IGSCC depth sizing error

Candidate group	Mean error μ (mm)	Standard deviation σ (mm)
All	0.70	3.73
Pass	0.33	1.92
Fail	1.07	4.87

Table 2 shows the statistical analysis of each final decided technique. As described above, most candidates use the "PA + conventional UT" procedure, but most candidates measured the crack depth by the PA technique as final decision. **Figure 5** contains the probability density curves for all candidates, both passed and failed, calculated from each standard deviation. From **Figure 5**, it can be presumed that the mode of frequency of the passed candidate is about 0 and the frequency distribution is almost symmetrical.

However, the frequency distribution of failed candidates has been obviously biased toward the positive side. This overestimation could be caused by a lack of skill of the examiner to differentiate the base metal to weld metal interface echo and the IGSCC tip echo. Moreover, the possibilities of human errors are also incontrovertible because the candidate is exposed to the stress of the potential for a −4.4 mm critical miss call, which could cause the examiners to bias their measurements toward the deeper value.

Table 2 Analysis result for each final decided technique

Candidates Group	final decided technique	No. of data	Mean error (mm)	Std. dev. (mm)
Pass	Phased Array	348	0.30	1.88
	Conventional	92	0.40	2.11
Fail	Phased Array	308	1.45	4.73
	Conventional	142	0.24	5.09

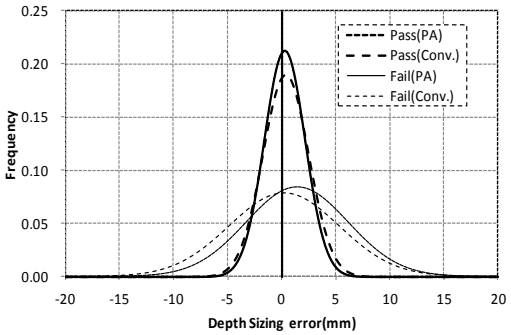

Figure 5 Distribution of depth sizing error

THE ACCEPTANCE CRITERIA THAT AFFECTED FAILED CANDIDATES

Figure 6 shows the various reasons due to which candidates failed the PD examination. As mentioned in Section 2.2, the Japanese PD examination regulation has two acceptance criteria. One is the critical miss call, which requires that all flaws cannot be under sized by an amount greater than 4.4 mm.

The other acceptance criterion is that the RMSE should be less than 3.2 mm, and the candidate should perform depth sizing of at least 10 IGSCC cracks. When the test set includes 10 IGSCC cracks, if the candidate sizes one IGSCC crack with a +10.1 mm error and sizes the other nine IGSCC cracks without error, the resultant RMSE will be greater than 3.2 mm. Therefore, another critical miss call is an overestimation of +10.1 mm when performing depth sizing.

The information obtained by interviewing the candidates indicates that most of the failed candidates were extremely wary of the −4.4 mm critical miss call. However, Fig. 6 shows that, for the failed candidates, the −4.4 mm critical miss call was the cause for only 19% of the failures. Over 80% of the unsuccessful candidates failed to meet the requirement of an RMSE less than 3.2 mm.

Almost half of the failures resulted from the +10.1 mm sizing overestimation. Finally, 30% of all failures were the result of the candidate's inability to meet the RMSE of less than 3.2 mm in conjunction with a −4.4 mm critical miss call.

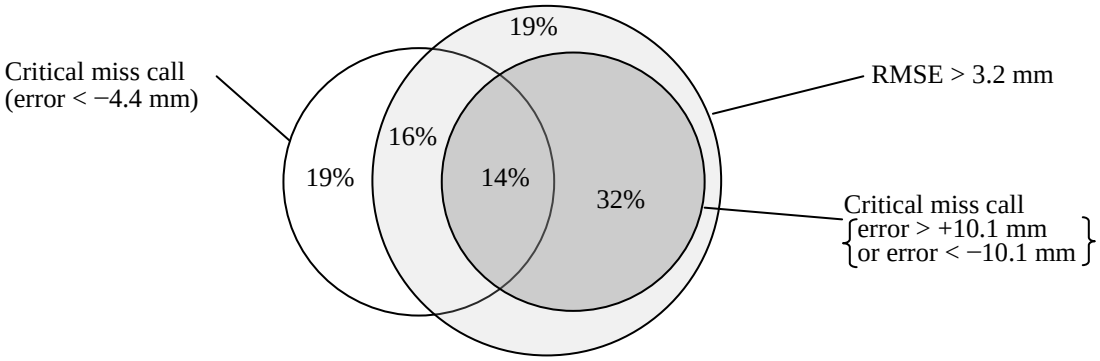

Figure 6 Reasons for candidate failure

THE FUTURE PROGRAM (WOL-PD SYSTEM)

Presently, in the spring of 2013, the NDIS0603 was revised to add the Weld Overlay performance demonstration (WOL-PD). CRIEPI had begun to prepare the WOL-PD examination. However, WOL is not a popular repair method in Japan; thus, it is expected that the number of candidates wishing to take the WOL-PD certification is limited. Therefore, the Japanese WOL-PD system is planned as a collaboration between the CRIEPI and the EPRI. The Japanese WOL-PD system will be performed with EPRI test samples, at EPRI examination facilities, and based on Japanese regulations (**Table 3**). In addition, the EPRI WOL samples are confirmed in their crack equivalency to SCC required by Japanese regulation [8].

CONCLUSION

The CRIEPI PD center has been operating Japanese PD examinations and has begun to prepare the WOL-PD examination. The outcome of the Japanese PD is as follows:

- ✓ The average depth sizing error for successful candidates is 0.33 mm with a standard deviation of 1.92 mm.
- ✓ The average depth sizing error was +1.07 mm for unsuccessful candidates. Reasons for candidate failure included candidate's inability to discriminate the crack tip echo along with the overestimation of the flaw due to the candidate being wary of the −4.4 mm critical miss call.
- ✓ The Japanese WOL-PD system is being prepared in collaboration with the EPRI and the EPRI PDI program.

Table 3 Outline of WOL-PD Administration (assumption).

Category	SUS-PD	WOL-PD	Note
Standards	NDIS0603：2005 Appendix (NDIS0603 : 2013 Appendix A)	NDIS0603 : 2013 Appendix B	
Category	Crack Depth Sizing	Detection Length and depth Sizing	
Qualifying Body	CRIEPI PD Center	CRIEPI PD Center (Probably)	
examination Administrator	CRIEPI PD Center Staff	CRIEPI PD Center Staff EPRI PD Administrator	
Examination Location	Japan	EPRI NDE Center (Charlotte NC USA)	
Test Specimen	Prepared in Japan	EPRI PDI Test Specimen (Include Japanese Specific Sample)	
Examination Session	Few times in Year	Any time (need to adjustment) (minimum two applicant)	
Acceptance Criteria	(Depth Sizing) *RMSE : < 3.2mm *No underestimation over -4.4mm	(Detection) (Length and Depth Sizing) Same as ASME	
Basic Certification	UT Level-2	NDIS0603:2013 Appendix A (SUS-PD)	

REFERENCES

[1] Kashima K, Nomura T and Koyama K, : "Current status of Japanese Code on Fitness-for-Service for Nuclear Power Plants" Proceedings of ASME/JSME 2004 Pressure Vessels and Piping Conference (PVP2004), San Diego, p.227-234 (2004)

[2] Sasahara T, Yamashita T and Nomura, : "UT Performance Demonstration in Japan" Proceeding of Fifth International conference on NDE in Relation to Structural Integrity for Nuclear and Pressurized Components, San Diego, p.163-167 (2006)

[3] Sasahara T, and Hide K, : "Japanese PD Examination of IGSCC Depth Sizing" Proceedings of eighth International conference on NDE in Relation to Structural Integrity for Nuclear and Pressurized Components, Berlin, p.124-130 (2010)

[4] Sasahara T, Jikimoto T, Hide K and Inoue H, : "Evaluation of SCC Depth Sizing Candidate and Performance" Maintenology, Vol.9 No.1, p.39-44 (2010)

[5] Watanabe K, Shohji H, and Hide K, : "Japanese PD examinations for depth sizing of SCC in austenitic stainless steel pipes from 2006 to 2012" Proceedings of Ninth International conference on NDE in Relation to Structural Integrity for Nuclear and Pressurized Components, Seattle, Number Tu.2.A.5 (2012)

[6] Furukawa T, Komura I, Yoneyama H, and Yamaguchi A, : "Guideline for the Direction of Instructional Training in SCC Depth Sizing by Ultrasonic Flaw Detection" Maintenology, Vol.4 No.3, p.50-55 (2005)

[7] Shohji H, Hide K, Watanabe K, : "Trends Identified Between Successful and Unsuccessful Candidates that have Participated in the Japanese Performance Demonstration (PD) Program of Stress Corrosion Cracking (SCC) Depth Sizing" E-Journal of Advanced Maintenance, Vol.4 No.4 p.125-132 (2013)

[8] Shohji H, Hide K, Watanabe K, : "Comparison of Ultrasonic Responses from Intergranular Stress Corrosion Cracking (IGSCC) and Man-made Flaws in Weld Overlay (WOL) Samples" Proceedings of Ninth International conference on NDE in Relation to Structural Integrity for Nuclear and Pressurized Components, Seattle, Number Tu.1.A.4 (2012)

USABILITY OF THE INSPECTION PROCEDURE – HUMAN FACTORS APPROACH

M. Bertovic, C. Mueller, BAM, Germany
U. Ronneteg, SKB Swedish Nuclear Fuel and Waste Management Co, Sweden
B. Fahlbruch, Tuv Nord Systems, Germany

Abstract

The inspection procedure is one of the most important tools in the application of NDT. A series of "Programme for the Assessment of NDT in Industry" (PANI) projects has shown that the inspection procedure has a significant effect on the inspection reliability (Mc Grath, Wheeler, & Bainbridge, 2009). In order for it to fulfil its purpose and guide the operator towards a successful completion of the inspection task, the procedure needs not only to contain all the relevant information, but also communicate the information in a way which allows the operator to conduct the task effectively and efficiently. The goal of this study was to evaluate the usability, generate improvements and reevaluate the usability of a selected procedure, i.e. the NDT instruction for the ultrasonic inspection of the cast iron insert (part of a canister used for permanent disposal of spent nuclear fuel in Sweden).

According to the international standard ISO 9241-11, usability is defined as an extent to which a product can be used by specified users to achieve specific goals with effectiveness, efficiency and satisfaction in a specified context of use. The effectiveness was measured through the successful and accurate completion of the data evaluation task following the procedure; efficiency through the effort invested into finding relevant information in the procedure; and user satisfaction through a questionnaire, specifically designed for this study. The majority of the study was conducted using the eye tracking methodology. An eye tracker records eye movements over a computer screen. By observing the eye movements of four operators doing the evaluation of UT data, it was possible to learn how the evaluation is conducted and in what way the procedure is being used. This observation enabled us to identify critical points in the procedure that were either not followed or where the information was missing, which finally led to defects being missed or wrongfully characterized. Taking this into consideration, together with the guidelines from the PANI 3 (regarding more structured information presentation and clearer writing), a new procedure format was proposed and tested in a follow-up study.

The preliminary results show improvement in the completion of the UT data evaluation task using the new procedure format, as well as higher used satisfaction. These results should lead to a unified approach to the procedure writing adopted by the Swedish Nuclear Fuel and Waste Management Co (SKB).

Keywords: Inspection procedure, NDT instruction, human factors, usability

NEW ISO NORM FOR TITANIUM WELDED TUBES

P. Gerard, Valtimet, France

Abstract

Today, the majority of tube specifications for titanium condenser tubes referred to ASTM B 338.
However, this standard covers many fields of applications, like the tube heat exchangers for the process industry, the tubes evaporator or condenser for the desalination industry, the tubes for condenser of power stations.
It covers also different types of tubes (seamless, welded, welded and cold worked).
Consequently, the requirements of this standard, and specially the non-destructive tests, are not exactly adapted for welded tubes for critical application like condenser tubes for nuclear power stations.
A new ISO norm is under preparation, precise and stringent requirements.
The paper reviews the NDT part of the new ISO norm in comparison with ASTM B 338 and gives justifications based on return of experience on the differences.

Keywords: Qualification inspection tubes control before installation heat exchangers.

ALTERNATIVES TO RT

USE OF COMBINED UT ADVANCED TECHNIQUES IN LIEU OF CONVENTIONAL UT ASSOCIATED TO RADIOGRAPHY FOR END OF MANUFACTURING OF PRIMARY COMPONENT CIRCUMFERENTIAL WELDS

F. Lasserre, J.Y. Gourdin, J.M Crauland, M. Jambon, AREVA, France
D. Verspeelt, D. Marois, ZETEC NDT Solutions, Canada

ABSTRACT

The steam generators (SG) and pressurizers (PZR) are assembled at AREVA-NP/SAINT-MARCEL (CHALON s/ SAÔNE) factory in France. After welding, surface (Magnetic Particle, Penetrant Testing) and volumetric (Ultrasonic Testing & Radiographic Testing) Non Destructive Testings are performed according to the French Design and Construction Rules for Mechanical Components of PWR Nuclear Islands (RCC-M) code. The UT examinations are performed manually with conventional probes before and after heat treatment and radiography is added before heat treatment.

Today, in several industries, NDT vendors look for replacing RT by other techniques for evident easy-going and productivity reasons. In nuclear domain, safety authorities encouraged more and more to propose less restrictive and optimized UT alternatives to RT as well. The present paper gives an overview of the file of equivalence being built-up by AREVA-NP to replace the current manual UT associated to RT examinations by automated phased arrays UT associated to UT TOFD examinations.

The parts of interest are pressurizer and steam generator circumferential welds between low alloy steel pieces, some being cladded at inner surface.

The file of equivalence gathers a set of elementary evidences that all the mandatory requirements of the reference code and standards of application are satisfactorily kept, and defines levels of equivalences between the replaced and the replacing NDT methods / techniques.

The main challenges of the process come from the change of NDT methods (RT to UT), namely concerning the management of the acceptance criteria and the associated changes in reference standards.

The new UT automated system is developed and tested by ZETEC Company. The manipulator equipment is based on a carriage supporting the UT probe arrangement tool for scanning, the part to be examined being rotated to be set in position. The actual frame of the development is open enough to include an extension of the equivalence to RPV shell welds examinations (thickness of 250 mm) or to ASME code requirements as well.

This file is intended at the end to support the implementation of this alternative in the RCC-M code.

The principles of the equivalence file and some results obtained on the "AFCEN" test block are discussed in this paper.

BACKGROUND

Current situation

According to the "RCC-M" code, the SG and PZR welds must be witnessed and their acceptance depends on several criteria including the Non Destructive Testing (NDT) assessment.

After welding, PT/MT, manual UT and RT are performed at AREVA Chalon factory. UT and RT are the methods/techniques to be replaced. The pulse-echo (PE) manual UT examinations are done with conventional probes before and after heat treatment, in complement to conventional radiography (mainly linear accelerator and radiograms) before heat treatment. Conventional 4 MHz 0° longitudinal waves (before SRHT), 2 MHz 45° (before and after SRHT) and 70° (before SRHT) shear waves probes are used.

The UT analysis required in RCC-M code for welds refers mainly to the process described in the NF EN ISO 23279 standard ("Non destructive testing of welds-Ultrasonic testing-Characterization of indications in welds"). Manual conventional pulse-echo UT + RT can be replaced neither by pulse-echo UT alone (even with enhanced phased array pulse-echo technique), nor by TOFD UT alone (due to possible limitations in zone coverage or capability of detection of volumetric defects). Combined pulse echo UT and TOFD UT seemed therefore the most reliable to reach an acceptable equivalence.

Besides, manual conventional pulse-echo UT technique is rather restrictive (regarding productivity, reliability and traceability aspects) for such large and thick (greater than 100 mm) welded components. It was obvious in our case to implement by the way automated combined system, as described in details in 1). Automated phased array pulse-echo UT combined with automated TOFD UT was thus retained.

Its further use will only be possible if a demonstration of sufficiently satisfying quality constant evolution is proposed and accepted.

Scope

The parts of interest are narrow gap submerged arc welds between low alloy steel parts, thicknesses between 100 mm and 180 mm, of pressurizer (Figure 1) and steam generators (Figure 2). The inner surface of the pressurizer welds and of the SG tube sheet to head are cladded.

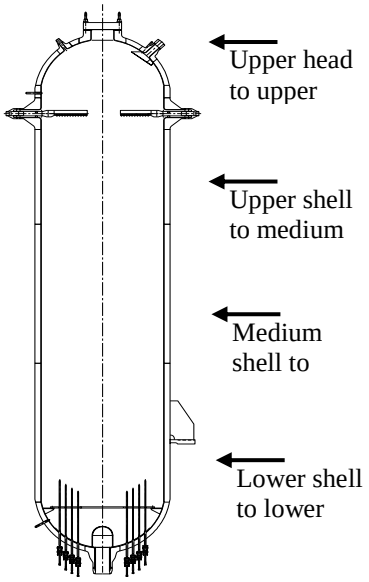

Figure 1: pressurizer welds of concern

The fusion faces are essentially perpendicular to the vessel surfaces and the width of the welds is approximately 22 mm (bevels are 0°15' tilted). The material is of 18 or 20 MND 5 grade (low alloy ferritic steel) and the wire is alloy steel with Mn-Mo-Ni. The classification of the welds according to RCCM is "Level 1".

The manual UT examinations are performed from outside and, when accessible, from inside of the component, depending on the stage of examination. In addition, these examinations deal in some cases with local obstacles which are known and identified for each type of joint, the overall examinations (UT + RT) complying with the requirements of the code.

Objectives

The main objective already introduced here above is to be able to replace the current examinations of the PZR and SG circumferential welds at the end of manufacturing by alternative UT techniques insuring a quality level of the welds against the reference standards and regarding the replaced technique that would be acceptable for the customer.

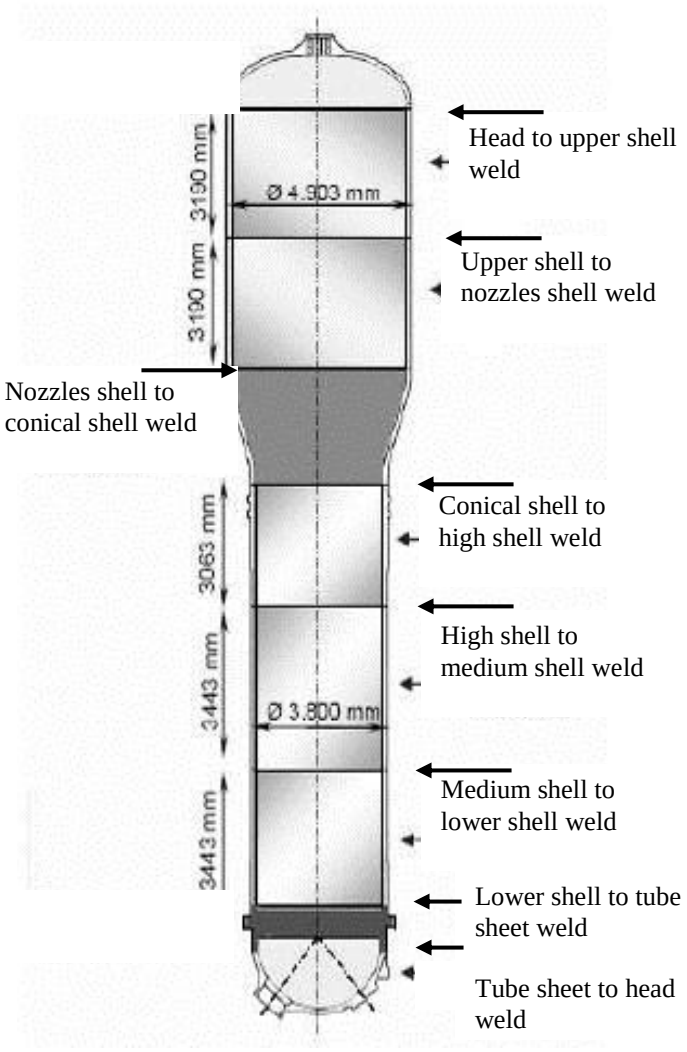

Figure 2: steam generator welds of concern

This will be achieved by including the alternative in the reference code with the support of adequate evidences taking into account experimental data on appropriate test blocks and engineer reasoning. This work is different of those to be performed for the automation of a technique (e.g. UT), that is possible and foreseen in the code (see an example in 2)).

The justification file will be dedicated to the scope of concern only and shall take into account the new developed automated combined system and the environment.

This new combined equipment includes the so-called “replacing techniques” UT phased array technology and UT TOFD (with either conventional or phased array probes for this latter depending on the set-ups). The development of this system and the equivalence tests on representative blocks are done by ZETEC Company.

ZETEC also develops the manipulator. The manipulator equipment is based on a carriage supporting the UT probe arrangement tool that supports all the probes and the TOFD set-ups (see more details in 1)). The scanning of an elementary sector of the part is provided by the carriage movements, and then the part is rotated to reach the following sector, until 360° coverage.

When shifting from conventional UT probes to phased array probes and TOFD techniques, the goal is to refer as far as possible to the dedicated standards. Some are already released and some are still under development. In the latter case, their contents are anticipated if possible.

Means for justification file

The main support for the demonstration file is experimental data acquisitions. Test blocks containing realistic and artificial flaws have been acquired with all the replaced and replacing methods/techniques.

The first test block referenced "AFCEN" contains cracks, lacks of fusion, lacks of penetration, aligned inclusions and clustered gas cavities. Its geometry and dimensions (thickness 120 mm) are representative of the scope of concern.

The second block referenced "BCCN" contains cracks, lacks of fusion, lacks of penetration and inclusions. Its thickness (255 mm) covers the present scope and could even be used later on for thicker components. Both blocks include a representative narrow gap weld.

All the flaws of different sizes are located through-wall at various depths.

A last block referenced "CIC" ("hot isostatic compacting") contains embedded planar artificial defects. It is used to determine and check TOFD set-ups capabilities (not presented in the paper).

STRATEGY AND CHALLENGE OF THE EQUIVALENCE FILE

The alternative to the current practices (conventional UT + RT) concerning the end of manufacturing examination of the PZR and SG circumferential welds could be proposed to the authorities for an implementation in the reference code if it is demonstrated that an acceptable quality level remains insured.

The guarantee of the quality is obtained by meeting all the requirements of the RCC-M standard. So the replacing methods/techniques need at least to fulfil the RCC-M demands.

The requirements of the code are numerous and some could be not hundred percent fulfilling; justifications are provided in these case.

One way to handle the process is to demonstrate: that the new replacing techniques fulfil satisfactorily the code requirements. Ignoring the links with the replaced methods/techniques would however make us missing additional important information regarding the experience feed back. One consequence would be for example to over specify the new NDT system thus leading, for example, to increase repairs.

The other way to proceed, followed in the present project, is to establish in parallel a level of equivalence between the replaced and the replacing methods/techniques.

All the RCC-M requirements are checked, studied and justified, and elementary equivalence levels are defined. At the end, a synthesis is done in order to state whether the obtained equivalences considered together are acceptable against the expected quality insurance demonstration.

The justification of the use of alternative NDT means in accordance with standards comes up against different problems.

When the examination method changes (e.g. RT to UT), the intrinsic domains of capabilities regarding defects likely to be found are not equals, and besides, the representation of the defects are of different types (indication for UT, image for RT).

When the examination technique changes (e.g. manual pulse-echo conventional UT to automated pulse-echo phased array UT), cumulative intrinsic uncertainties make difficult the determination of "equivalence".

In order to minimize as far as possible these issues, the following rules have been chosen.

Firstly, the equivalences are always made by considering the two replaced method/technique together and the two replacing techniques together (in order to avoid not obvious complete dissociations like "conventional UT is replaced by phased array" and "RT is replaced by TOFD").

An elementary equivalence is set for each requirement of the standards. The requirement concerning the fulfilment of the NF EN ISO 23279 standard process ("cascade" procedure), which is very complex, is divided in several sub parts. All the defects included in the "AFCEN" and "BCCN" tests blocks are taken into account. Examples on "AFCEN" block ("BCCN" data acquisitions analysis is under way) are detailed in the next sections.

In parallel, from the results obtained on the test blocks with the replaced and replacing techniques, elementary comparisons of capability are performed (e.g. amplitude of detection in a given direction of propagation) to strengthen the final conclusion.

Concerning RT, only the requirements concerning detection, classification and acceptability are considered.

Finally, the alternative will be considered as acceptable if the final diagnosis obtained with replaced and replacing method/techniques are equivalent.

If necessary and justified, the application of the TOFD standard NF EN 15617 is adapted to the present scope.

EQUIVALENCE DEMONSTRATION

All the requirements of the RCC-M code to be studied (mainly for UT techniques) in order to set the levels of equivalence between the replaced and replacing method/techniques are not of same level of complexity.

Some are rather easy to justify (e.g. the application of principles of general UT standards).

Other requirements (e.g. the number of directions of propagation) do not exhibit fundamental difficulties but reveal evident gaps between replaced and replacing techniques (automated UT examinations cannot be performed from inside) that shall be documented.

The task is getting more delicate when dealing with requirements of detection, classification or unacceptability, this due to the fundamental differences of approach between UT (dealing with "indications") and RT (dealing directly with "defects") and between pulse-echo (regarding RCC-M, dealing with amplitude and length) and TOFD (regarding the available standard, dealing with height and length); moreover, the equivalence is less easily quantified as for sizing or positioning.

The appropriate references to use are: the process of the NF EN ISO 23279 standard for UT pulse echo conventional or phased array, the application of criteria of S7714.4 article of RCC-M code for UT, the process (eventually with adjustment) of NF EN 15617 standard for TOFD UT and the application of criteria of S7714.3 article of RCC-M code for RT.

Theoretically, considering the philosophy introduced above, the replaced and replacing method/technique could be deemed equivalent as soon as the final level of equivalence in term of "unacceptability", and only this one, is 100% (all the defects being taken into account). However, the demonstration file will be stronger if there are also intermediate equivalences that are acceptable and justified on these defects, namely in detection, recording, and classification. A summary is presented in the flow chart of Figure 3.

Equivalence level for detection

The first sub requirement is the concept of detection. The background idea is to select the defects (or its indications for UT) which must be reported because potentially unacceptable. This selection has to be done in a correct way by both the replaced and by the replacing method/technique. In UT pulse-echo, an indication is recorded if its amplitude is $\geq$-6 dB, in RT, a defect is "seen" (and thus also recorded somewhere) if its image has been recognized by the operator and in TOFD, an indication is recorded (no threshold in the standards) as soon as it does not come from geometry or false calls ("indication of discontinuity is detected").

The answers to the relevant questions ("is the indication recorded?", is the defect seen?"…) for all the defects of the blocks by applying the replaced and replacing method/techniques together enable setting a level of equivalence for a "detection" requirement (see also figure 3).

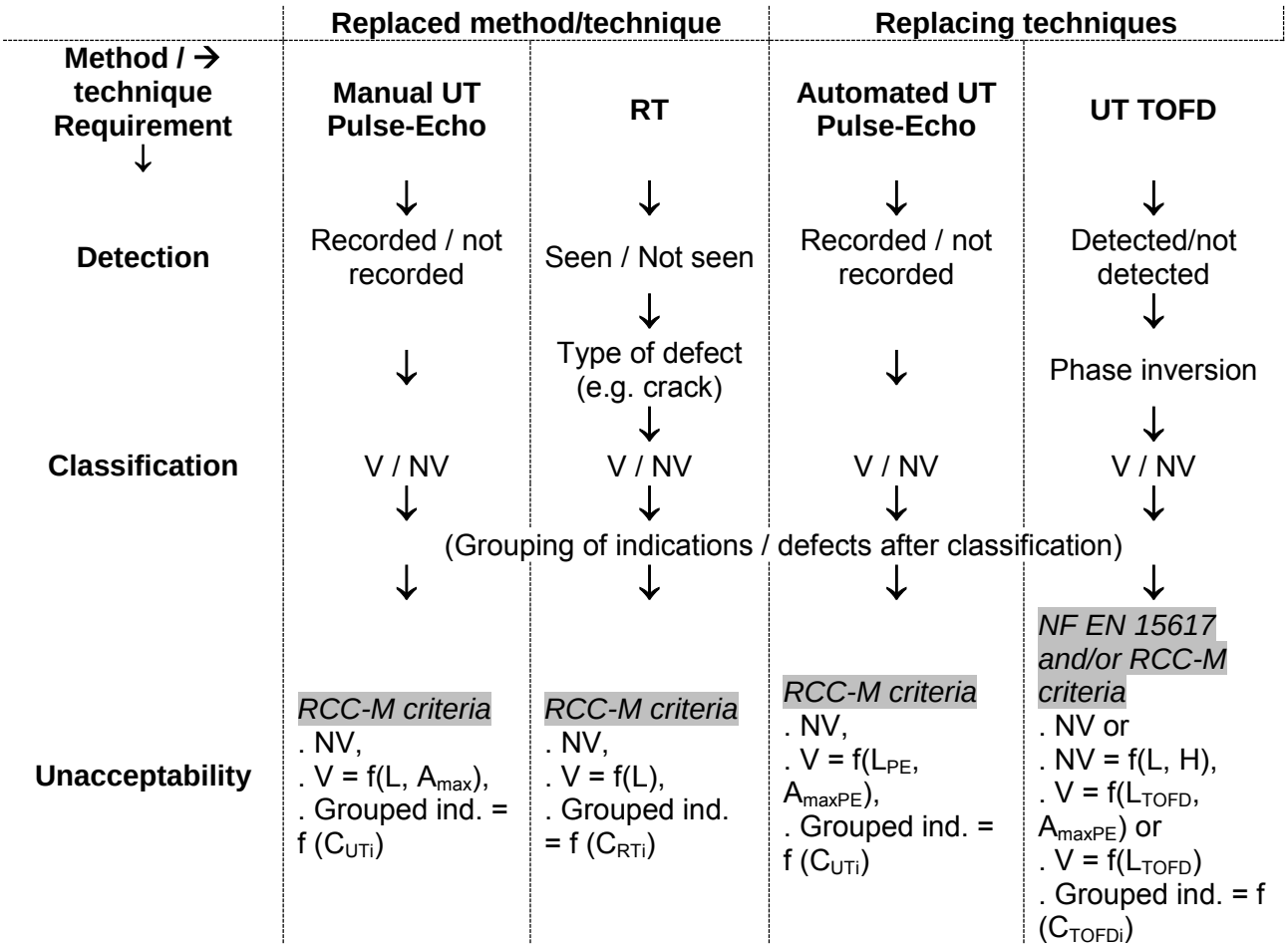

Figure 3: flow chart for characterization

Concerning pulse-echo UT techniques, the MC 2638a) article of RCC-M code requires a first gathering of indications prior applying the NF EN ISO 23279 standard process. It is thus possible in our case to set a level of equivalence of this sub requirement for conventional UT replaced technique and phased array UT replacing technique.

RCC-M requires indeed that indications detected at different directions of propagation are grouped (and thus considered coming from the same reflector) if they are closed enough together (basically in a range of 10% of the thickness of the component). When several indications are grouped, the maximum amplitude ("A_{max}"), the minimum depths ("P_{min}") and the maximum lengths ("L_{max}") are retained.

The level of equivalence between conventional UT (replaced technique) and phased array UT (replacing technique) of this requirement is not conclusive for the final equivalence level but is important as the values of A_{max}, P_{min} and L_{max} are used as input data for the equivalences on some other sub requirements.

For example, in the configurations for which outer surface access only is considered for both the replaced technique and the replacing technique, the A_{max} values for both techniques are within ±3,5 dB, the P_{min} values for both techniques are within ±4 mm and the L_{max} values for both techniques are within ±21 mm. We conclude then that, for this requirement, the automated phased array UT technique is equivalent to manual UT technique at ±3,5 dB, ±4 mm and ±21 mm for A_{max}, P_{min} and L_{max} , respectively.

The issue we have to handle here concerns one (1) lack of fusion ("LF") which features singular detection: depending on the technique and direction of propagation, several points of the defect are detected indeed and all the indications are not grouped on MC 2638 a) criteria (see Figure 4). This defect is handled in the requirement on grouping of indications after classification.

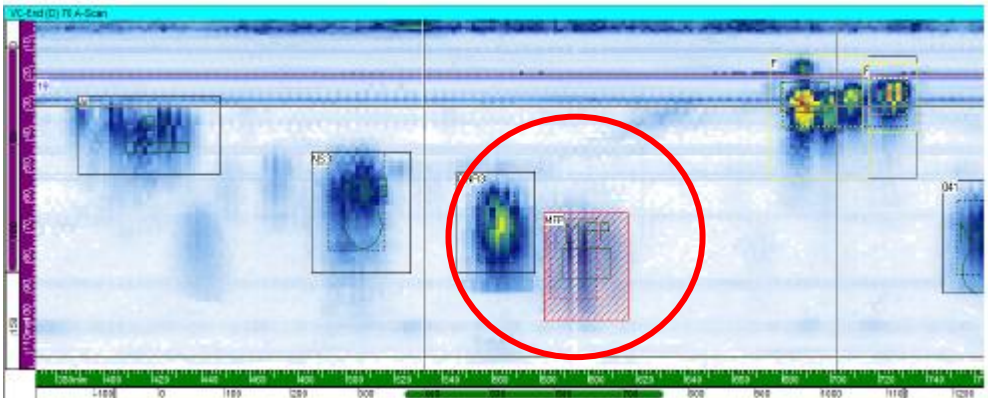

Figure 4: "AFCEN" test block. DSCAN view showing 2 main spots of detection of LF defect

Equivalence level for classification

According to the reference code, the unacceptability requirement for UT pulse-echo is based on the type of indication or defect: non volumetric indications/defects, volumetric indications/defects exceeding specific length and grouped indications/defects exceeding specific values, are not allowed. It is thus important to set a level of equivalence on this sub requirement "classification".

On this topic, RT can meet easily the denomination "Volumetric/Non Volumetric" as the criteria on the detected defects are defined on the kind of defects themselves (cracks are non volumetric, lacks of fusion are non volumetric…).

The issue comes up with TOFD (see figure 3). In the NF EN 15617 standard indeed, indications are "with" or "without" measurable height and, consequently, a height can theoretically be measured on a volumetric type indication (e.g. clustered gas cavities). The classification in volumetric or non volumetric indication is not used and, in addition, measured height and length are indeed not explicitly linked to a non volumetric discontinuity.

One way to deal with this is to impose a dedicated relation between the measurement of a height only with an association to diffraction echoes and then a classification "non volumetric". The direct consequence is that a volumetric indication will only be length characterised (see Figure 3). The assessment of this principle is under way because of the consequence on the new length criteria definition (see next requirement). In case of non acceptable justification at the end, we will have to come back with length criteria to apply also to volumetric indications.

However, the level of equivalence between the two replaced and replacing methods/techniques might become rather high.

Equivalence level for unacceptability

In order to get a level of equivalence (actually the final one) for this requirement between the replaced and replacing methods/techniques (under assessment), the unacceptability criteria of the dedicated line of Figure 3 are to be applied.

For (replaced) conventional manual UT technique, RCC-M criteria are used. Non volumetric indications are unacceptable. Volumetric indications are unacceptable depending on the measured length (-6 dB drop method) and the maximum amplitude. Grouped indications are unacceptable depending on specific criteria "C_{UTi}".

For (replaced) RT method, RCC-M criteria are used. Non volumetric defects are unacceptable. Volumetric defects are unacceptable depending on the measured length. Grouped indications are unacceptable depending on specific criteria "C_{RTi}" (applied on cumulated elementary lengths).

For (replacing) automated phased array UT technique, RCC-M criteria are used. Non volumetric indications are unacceptable. Volumetric indications are unacceptable depending on the measured length (-6 dB drop method) and the maximum amplitude. Grouped indications are unacceptable depending on specific criteria "C_{UTi}".

For (replacing) automated TOFD UT technique, some criteria from NF EN 15617 standard and RCC-M are used. The only way to get a conservative equivalence is to make non volumetric indications unacceptable whatever their size (however, a proposal of evolution is discussed in the next chapter). Volumetric indications detected by both techniques are unacceptable by applying the UT pulse-echo criteria with the greater value of the lengths measured in pulse-echo and TOFD. Volumetric indications only detected by TOFD technique are unacceptable depending on the measured length against already existing (in the standard) or specific TOFD criteria. These criteria are still to be defined regarding the whole results on the tests blocks and considering also the length criteria applicable for the other method/techniques. Grouped indications are unacceptable depending on specific density criteria "C_{TOFDi}".

Acceptance criteria for TOFD technique

As introduced here above, the use of UT TOFD technique as one of the replacing technique needs a particular demonstration in the file. Indeed, this technique being not introduced yet in the RCC-M code, no value of criteria exists (neither for NV nor V indication). Moreover, the fulfilment of these criteria shall take into account the other (phased array UT) combined technique.

The natural proposal to get an equivalence level on unacceptability at least conservative is to keep the unacceptability criteria of RCC-M for any non volumetric indication whatever its size. This could however involve more repairs, at least until the upgrade of the standard (introduction of recording levels is under study).

There is also the possibility to use the criteria of the TOFD standard for non volumetric indications that authorize to leave some in the parts, depending of their size. This was not allowed before but would be a way to take profit of the height sizing capability of the TOFD technique: the equivalence would be lower but the reliability in term of planar defect characterisation might be improved without increasing repairs rate.

So our aim is also to propose a level of equivalence that will state this gap, but providing in addition a justification that, mechanically, the remaining small defects can be left indeed in the components of interest over the total lifetime of the plant.

Acceptance level	**Acceptable Maximum Length l_{max} (in mm) if $h<h_2$ or h_3**	**Acceptable maximum height (mm) if $l \leq l_{max}$**		**Acceptable maximum height (mm) if $l > l_{max}$**
		Surface breaking indication h_3	**Embedded indication h_2**	
1	50	3	5	2

Table 1: set of acceptance criteria for acceptance level 1 of NF EN 15617 standard

This mechanical study (representative of our scope) aimed at justifying that, in one representative configuration (the most penalising weld of the pressurizer), at least one of the acceptance level of the standard refers to criteria in accordance with the allowed non volumetric defects. The calculations performed take into account the acceptable limits in initiation and propagation of defects over 60 years lifetime.

The results on the sizes of acceptable defects show with comfortable margins that one could refer to acceptance level 1 values of the NF EN 15617 standard (see Table 1).

REQUIREMENTS	QUANTIFICATION	OBSERVATIONS
Conformity to standards	Equivalence in the limits of application of new standards	Standards on phased array technology in progress
Qualification and certification of the operators	Partial equivalence	Provided adequate training and practices are managed
UT calibration blocks	Partial equivalence	In the limits of applicability to the replacing techniques and of availability of new standards
UT reference blocks	Partial equivalence	Non conformance on the reflector size in TOFD technique justified in the demonstration file
Reflectors sizes for UT calibration in UT pulse-echo (PE)	Equivalence	
Number of directions of examination in UT PE	Partial equivalence when manual UT are performed from one side No equivalence when manual UT can be performed from 2 sides.	The non equivalence can be compensated (TOFD, sectorial scan…)
Zone coverage	Partial equivalence	In progress
Amplitude and length measurement principles	Full equivalence	
Grouping of indications from several directions of propagation	Equivalence	Checked on one AFCEN block defect
Retained depth (Pmin) after grouping (UT PE only)	±4 mm when manual UT are performed from one or two sides	No interesting supply of T60° additional angle
Retained length (Lmax) after grouping (UT PE only)	±21 mm when manual UT are performed from one or two sides	To be confirmed
Retained amplitude (Amax) after grouping (UT PE only)	±3,5 dB when manual UT are performed from one side	When manual UT are performed from two sides: in progress
Depth positioning (UT PE); comparison defect by defect (intrinsic capability)	±7 mm when manual UT are performed from one or two sides	On BCCN block. To be confirmed
Recording level (UT PE)	Full equivalence	
X location	±35 mm when manual UT are performed from one or two sides	On BCCN block. To be confirmed
Depth positioning (UT PE + TOFD only) using Pmin for UT PE	±13 mm when manual UT are performed from one or two sides	On BCCN block. To be confirmed
Detection	Equivalence	
Classification	In progress	
Grouping of indications / defects	In progress	Checked on one AFCEN block defect
Unacceptability	In progress	Several proposals can be made

Table 2: summary of temporary results

FINAL EQUIVALENCE

The equivalence file that will be proposed at the end to the customer shall include the necessary demonstration of the suitability of the replacing techniques for all the RCC-M requirements (examples are summarised in Table 2). At the moment, the results are partially available and need to be completed.

Temporary levels of equivalence obtained so far however show a general tendency that might be further confirmed. The local specific remaining issues on a few defects will also be explained and documented.

Several final levels of equivalence can be proposed depending whether acceptance criteria of the TOFD standard for V and NV indications are used or not. Some levels would allow taking profit of TOFD capabilities but represent an important evolution.

In addition, the level of equivalence regarding the replaced and replacing equipments will be considered.

CONCLUSION

The replacement of current manual UT and RT examinations of welds of heavy components by advanced automated UT techniques at end of manufacturing would undoubtedly take a great step forward in term of environment issue, productivity and NDT reliability.

The goal is by the way very complex: several different NDT methods and techniques must be considered together, standards to be met are very demanding and component geometries involve enhanced developments. Alternative to RT is currently under way for several applications but, in the present case, the demonstration file to be provided is a first of a kind indeed.

The equivalence file is being constituted and data are still to be acquired and analysed. However, the first results obtained by the new UT equipment (ZETEC developments) are encouraging. Phased array probes have been developed in order to cover at least the same field as the replaced conventional one and the TOFD set-ups have been optimized to provide in addition all the capability of the technique.

One cannot obtain a pure comparison and equivalence between the replaced and replacing methods/techniques; our aim is to provide finally the customer and the safety authority with a package made of an appropriate combined system plus a related demonstration file presenting an overall documented level of equivalence between the means to be changed.

A more conservative equivalence reached by keeping the same criteria for non volumetric indication (unacceptable whatever the size) or a lower equivalence level (but associated to a more accurate diagnosis thanks to TOFD sizing capabilities, namely taking into account the planar defect size in the criteria, and without increasing repairs rate) could be proposed and discussed at the end by all parties. The determination of new possible TOFD length criteria for volumetric indication is also under study.

First results on “AFCEN” block have been introduced. They need to be confirmed indeed, adjusted and completed by those on “BCCN” test block to get an as large as possible panel of data on representative defect shapes. Besides, a few delicate comparisons on analysis of defects with complicated shapes are under way.

REFERENCES

1) Verspeelt D, Marois D, Cliché B, Crauland JM, Jambon M, Lasserre F, “Development and implementation of advanced UT techniques in lieu of manual and RT for inspection of narrow gap welds during manufacturing of primary component circumferential welds”, 10th Int Conf Non Destructive Evaluation in relation to structural integrity for nuclear and pressurized components, Cannes, 2013.
2) Lasserre F, Tchilian JM, Gien S, Paris JM, Meier R, Mouyade P, “Automated detection system for NDT of forged products”, 9th Int Conf on NDE in relation to structural integrity for nuclear and pressurized components, Seattle, European commission, 2012.

DEVELOPMENT AND IMPLEMENTATION OF ADVANCED UT TECHNIQUES IN LIEU OF MANUAL UT AND RT FOR THE INSPECTION OF NARROW GAP WELDS DURING MANUFACTURING OF PRIMARY COMPONENT CIRCUMFERENTIAL WELDS

P. Tremblay, D. Verspeelt, D. Marois, B. Cliche, ZETEC NDT Solutions, Canada
J. M. Crauland, M. Jambon, F. Lasserre AREVA, France

ABSTRACT

For productivity reasons the AREVA-NP/EFF/SAINT-MARCEL factory decided to replace manual UT and radiographic testing, as applied for SG and PZR circular welds, by advanced automated UT based on Phased Array and TOFD techniques.

The new method has to comply with the existing code requirements, i.e. French RCC-M, EN ISO 10863, etc, and has to satisfy severe exploitation criteria such as a limitation of the total examination time.

The presentation gives an overview of the implemented state of the art solutions for the examination of narrow gap submerged welds with thicknesses ranging between 100 and 180 mm. Pulse-echo phased array technique is implemented using 2D matrix probes. The probes can be applied for conventional raster as well as for sector scanning if needed, while their large beam skewing capability allows for optimized detection of misaligned defects. TOFD technique is implemented using conventional probes and linear Phased Array probes. The latter allows perfecting thickness coverage, optimizing signal-to-noise ratio and characterization.

The performance and the flexibility of this solution would make the extension of the work to RPV shell weld examinations (wall thickness of 250 mm) quite possible.

A dedicated scanner has been developed for shop use, and offers flexible installation and operation. A separate calibration bench allows fast verification of the UT parameters during the examinations.

The DYNARAY® system allows applying Pulse-echo and TOFD (conventional and phased array) in parallel, offering a single pass inspection of the welds in all orientations. On-line processing capabilities of the system drastically reduce the data volume.

The extended tools of UltraVision® software, such as the data merge functionality and the assisted analysis, offer a fast analysis solution as well as a comprehensive visualization of the data for final reporting. The developed equipment is intended to be implemented through a demonstration file of equivalence based on trials and justifications (see ref 1).

INTRODUCTION

Manufacturing of Steam Generators (SG) and Pressurizers (PZR) involves Non Destructive Testing of the circumferential welds according to the French Design and Construction Rules for Mechanical Components of PWR Nuclear Islands (RCC-M) code. This includes surface (Magnetic particle and Penetrant Testing) and volumetric NDT methods.

Radiographic Testing is currently applied before heat treatment while manual UT is used in complement for examination of the welds before and after heat treatment.

For productivity and environment reasons the AREVA-NP/EFF/SAINT-MARCEL factory decided to replace manual UT and Radiographic Testing with advanced automated Phased Array Pulse-Echo ("PE") and TOFD techniques.

The development of the new UT PE method is based as much as possible on the existing manual procedure to demonstrate equivalence since the qualification and acceptance of a completely new method may be very time consuming. This means that the main examination parameters, i.e. beam angles, orientations and probe frequency, are identical to those presently applied for the manual UT method. At this stage the PA beam steering capability is used for reducing the number of probes and for optimizing the beam with regard to the defect orientation.

The TOFD technique is implemented using conventional and phased array probes. This allows a very good depth coverage and flexible adaptation to different weld thicknesses as well as enhanced capabilities in characterisation.

SCOPE

The low alloy steel pieces of PZR and SG (Figure 1) are assembled by means of narrow gap submerged arc welds.

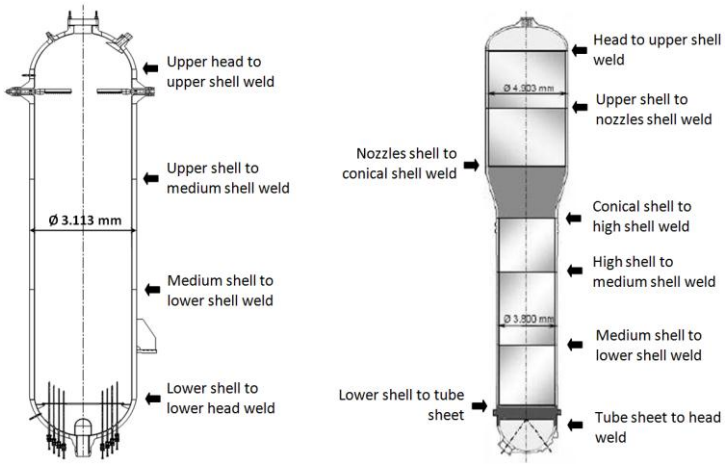

Figure 1: Pressurizer and Steam Generator weld outline

The weld thickness range varies between 100 mm and 180 mm. The bevels are slightly tilted resulting in almost perpendicular fusion faces. The width of the welds is approximately 22 mm. Shell diameters varying between 3.077 m and 5.165 m yield weld lengths up to more than 16 m.

INSPECTION REQUIREMENTS

PE technique requirements

The UT inspection method has to comply with the French RCC-M code regarding pulse echo techniques. The code requires 0°, 45° and 70° coverage of the heat affected zone of the welds. Following AREVA specifications, a 60° beam is added in the preliminary evaluation stage yielding directions of propagation as shown in the next figure:

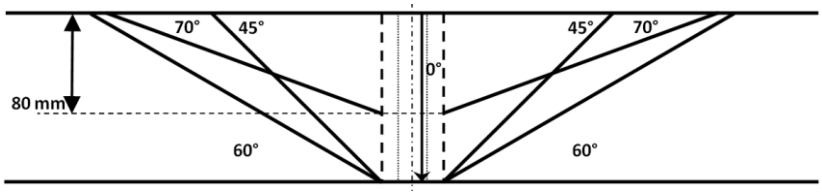

Figure 2: Weld coverage

Longitudinal as well as transverse defects are considered, therefore a total of up to 13 basic beam orientations are used considering a single face weld inspection.

The approach of validation of the new PE method is to demonstrate a level of equivalence with the presently applied manual inspection method (Ref 1) that could be acceptable. As the manual inspection allows for optimizing the indication amplitude by physically turning the probe (up to ±10°), the same capability is required for the automatic inspection. This is achieved by generating skewed beams for each of the considered basic orientations (except for the 0° beam):

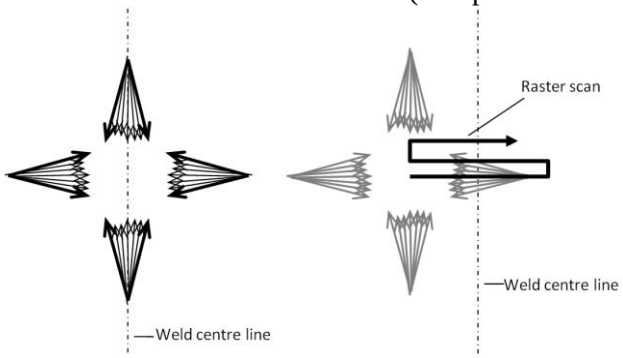

Figure 3: Beam skewing, probe orientations and scanning pattern

A single pass inspection is required for practical reasons and since discrete angles are used, a classical raster scan is performed to cover the weld volume.

TOFD requirements

The TOFD technique requirements do not come from RCC-M code and therefore could be those of the ISO 10863 standard with additional requirements concerning the coverage of the different inspection depth zones. Four or more depth zones are implemented based upon a -6dB diffraction coverage criteria while the standard requires a maximum of 3 zones for the considered weld thicknesses.

Exploitation requirements

The components to be inspected are horizontally positioned on turning rolls. As they are spread over the shop the inspection system must be mobile. The examination of a weld must be performed within a working day.

PE PROBE

Phased array technique has been chosen to generate a skewing beam to replace the manual optimisation process. This is achieved by a 2D matrix probe. The developed probe has similar beam characteristics as the conventional probes presently used for the manual UT inspection. The beam steering allows for generating refracted angles from 45° to 70° SW with a skewing range of ± 15°.

The following images show a 45° SW example of the obtained beams of the matrix probe compared to the beams of the probes used for manual inspection.

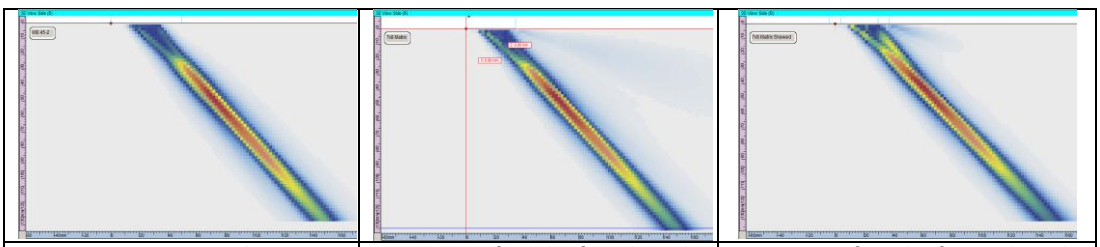

Beam WB45-2	Beam Matrix 7x8; skew 0 - 45°	Beam Matrix 7x8; skew 15° - 45°

Figure 4: Beam simulation comparison WB45-2 and 7x8 Matrix

As can be observed, the beam similarity with the manual probe is very good, even for the skewed beams. The lobe amplitude is for all cases (45-70°) more than 20dB below the main beam amplitude. Practical measurements on side drilled holes show a very good match of the DAC curves with those of the conventional probes (Figure 5).

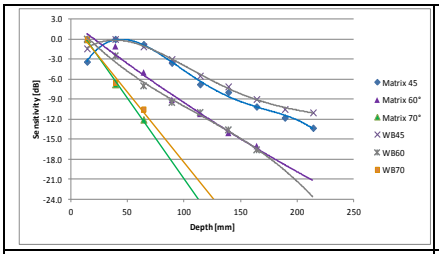

Comparison of DAC curve between Matrix probe and WB conventional probe (DAC on Ø2 mm)

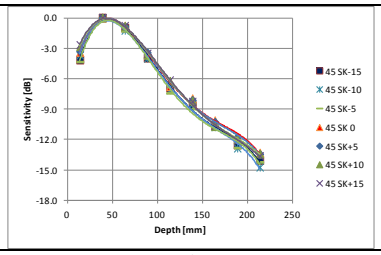

45°: DAC curves for all skew angles

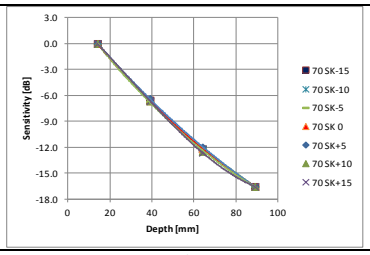

70°: DAC curves for all skew angles

Figure 5: Practical results on SDH

The DAC curves were recorded, for a given skew angle, by rotating the probe in order to orient the beam perpendicularly to the side drilled holes. As can be seen on the figure above the DAC curves for the skewed beams are almost identical.

Besides the generation of discrete angles the probe is capable generating sector scanning practically between 40° and 70°.

TOFD WITH PHASED ARRAY OR CONVENTIONAL PROBES

The TOFD technique covers weld thicknesses ranging from 100 to 180 mm by a combination of conventional and phased array transducers (
Figure **6**).

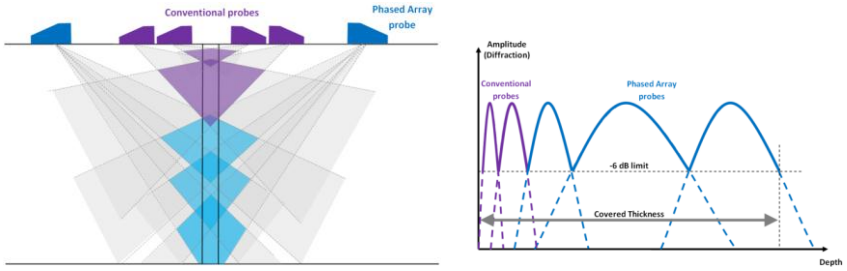

Figure 6: TOFD zone coverage

The thickness is divided in zones that overlap each other. The required number of zones is defined on the basis of a -6dB drop of the diffracted signal as shown in the figure above.

The upper depth range is covered by two conventional configurations. The phased array probe set covers the lower depth range. This offers, besides a reduction of the number of probes, a flexible adaptation of the zone division to fit the weld thicknesses and a good control of the beam spread for a given depth range resulting in a high S/N ratio and reduced back-wall dead zone.

The required TOFD configuration (probe frequency, aperture size, beam angle and probe centre separation) has been defined on the basis of beam simulations with UltraVision® and practical measurements on EDM notches.

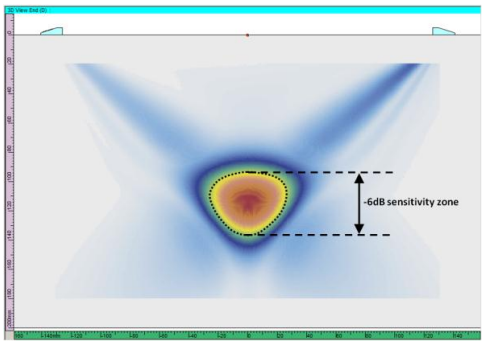

Figure 7: TOFD coverage beam simulation

ASSESSMENT TRIALS

UT PE techniques

The comparison of the UT methods capabilities was carried out from several test blocks containing artificial and realistic flaws such as cracks, lack of fusion, lack of penetration, aligned inclusions and clustered gas cavities.

The scope of the PA PE assessment was mainly based upon a comparison of the results obtained with the new method with those obtained with manual inspection. Additionally, the influences of some essential parameters, such as the scanning resolution, were determined based on acquisitions on different test blocks. Some measurement uncertainties have also been evaluated on the basis of multiple calibration scans spread over a long time period and taking into account all practical variables such as probe coupling and mounting-dismounting of probes, cables, acquisition and scanning system. This will be introduced in the demonstration file (see ref 1).

The PE inspection was carried out following the requirements of EN 583-1 and EN 583-2, as far as possible. The DAC technique is applied for measuring the amplitude of reflectivity of the imperfections. Length sizing is based upon a -6 dB amplitude drop technique.

A typical result obtained on a 120 mm thickness test block is shown for an inspection angle of 60° SW in an end-view below:

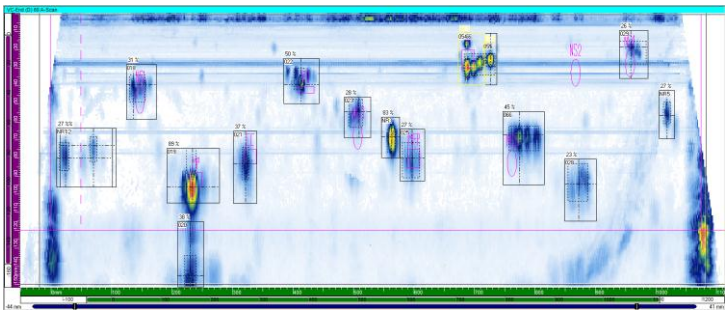

Figure 8: Test block AFCEN, End view, 60deg

The green axis of the end view represents the weld length, the purple axis the depth of the indications. The merged view shows the results of the maximum amplitudes obtained for all skew angles. It can be highlighted that the beam skewing also detects the side walls of the specimen (vertical indications at both sides of the view).

Basically, and independently of the demonstration of the equivalence file, PA PE technique performances have been found equivalent to the conventional manual PE technique. The beam skewing capability of the phased array probe allowed recording identical amplitudes as found manually. For some indications a skew of up to 15° was required for obtaining the maximum reflection amplitude. This will allow being equivalent to the replaced techniques in term of acceptability for these defects.

UT TOFD technique

TOFD examinations were carried out on the same test blocks as those used for PE UT and on specimens with EDM notches. Additionally a qualification of the technique was carried out on a 165 mm thick test block with artificial planar alumina inserts realised by means of hot isostatic compacting and on a clad specimen in order to evaluate the effect of the stainless steel cladding on the back wall echo.

An example showing the excellent signal-to-noise ratio obtained with the Phased Array TOFD configuration is shown for a test specimen containing alumina inserts. Although this kind of artificial defect is known to yield low diffraction amplitudes, the quality of the signal is very good and the obtained S/N is about 16 dB as can be observed from the left side picture below:

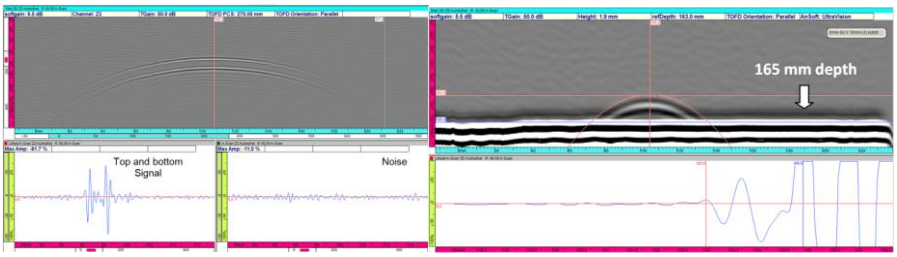

Figure 9: 5 MHz PA-TOFD; Result on a 4mm Alumina insert and on a 2 mm height ID EDM notch

The right side picture shows a 2mm ID surface breaking notch in a 165mm test block illustrating that the back wall dead zone is reduced to a minimum. These results will be used for the equivalence file as support of justifications. A typical TOFD perpendicular scan result is shown below for a test specimen containing real defects:

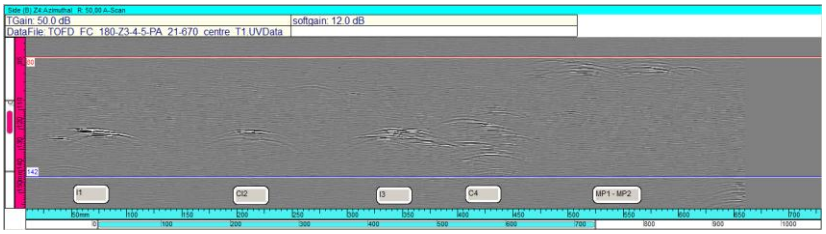

Figure 10: PA TOFD, perpendicular scan, specimen with real defects

It was found that the TOFD technique allows detecting all defects with a good S/N in all the considered blocks.

IMPLEMENTATION

Single scan data acquisition

The weld is inspected in sections (3 to 4 m) and each section is covered by a single scan performing PE and TOFD simultaneously. A complete inspection scan of a 1 m weld segment is done in less than 30 minutes. This is achieved thanks to the high data rate capability of the DYNARAY. Acoustic crosstalk is managed by positioning the probes adequately and by firing the laws in an appropriate order. The Firing Sequencer available in UltraVision® is used for this purpose.

On-line data processing

Since the component thickness is big, the weld length long and the number of beams large (4 orientations; 3 angles per orientation; 7 skewed beams per angle + 0° + TOFD) the amount of gathered data is impressive. The inspection of a SG weld with 135 mm thickness and a length of 16 m would generate about 750 GB of data considering all the applied techniques with “normal” data acquisition parameters. Besides the acquisition issue, this huge amount of data must also be analysed and all this within an acceptable time frame.

The DYNARAY system offers on-line compression and multi-peak detection processes to reduce the amount of data. Multi-Peak processing has been chosen since compression still generates too much data and would affect too much the time positioning. The multi-peak process allows storing the amplitude and position of the peaks found in an A-Scan. The picture below shows a comparison of Multi-Peak recording with normal A-Scan recording:

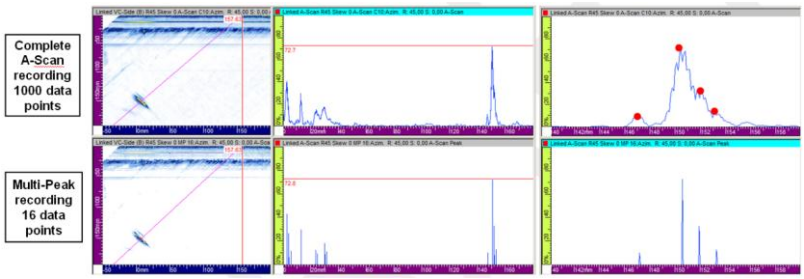

Figure 11: Multi-peak data reduction process

The advantage of this method is that no time shift is introduced: all peak position data is acquired with the resolution of the initial digitizing frequency of 100 MHz. The major advantage is of course the drastic data reduction: only a limited number of peaks (16 in the present case) for each A-Scan are recorded. Applying this data reduction process allows, for a typical weld, reducing the initial data size of 750 GB to 30 GB (Multi-Peak data reduction is not applied on the TOFD channels).

Dedicated scanner, calibration and acquisition system

A dedicated system has been designed and developed to allow for a fast and reliable inspection in the shop. The mobile system is subdivided in 3 main parts. The picture below shows the scanner system positioned on the component, the calibration-manipulation table and the data acquisition unit containing ZMC2 motor controller, DYNARAY acquisition unit, PC and screen:

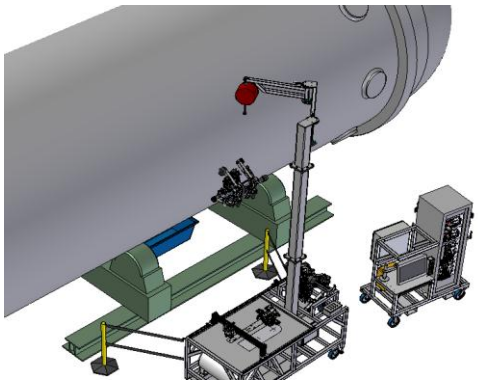

Figure 12: Inspection system

The scanner system (independent from the table) moves on the surface of the inspected component by means of magnetic wheels (Figure 13). Two motors are used for driving the movement in order to allow, in case of slight deviations with the weld centre line, corrections of the travel path. A detector on the scanner allows for steering the motors in such a way that the movement follows a trajectory which is projected by a laser trace on the component.

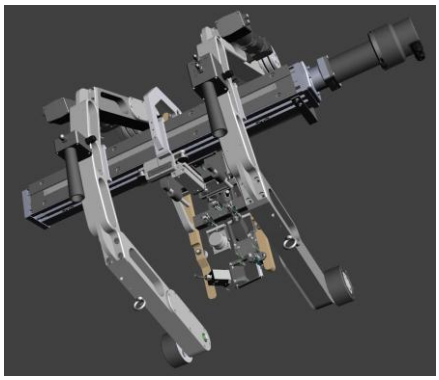

Figure 13: Scanner with magnetic wheels

The scanning movement is performed by a linear arm on which the probe holder is fixed.

The probe holder is applied on the surface. Contact ball bearings allow the probe holder to run smoothly on the component. Each probe has an independent suspension assuring a good wedge-to-surface contact.

The height of the linear movement is such that the scanner can travel over obstacles (nozzles etc) while the position of the legs can be adapted to allow moving between obstacles.

The calibration table holds the calibration blocks and an encoded X-Y axis manipulator (Figure 14). With an easy fixing system of the complete probe pane, the tool allows performing fast and reliable encoded calibration and verification scans. Local liquid coupling and recuperation is also provided.

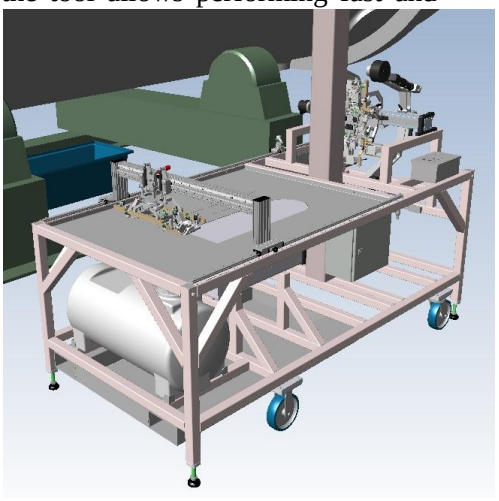

Figure 14: Calibration + manipulation table

The laser system can be positioned and oriented in such a way that it projects a line on the component which will guide the scanner system to follow a travel path parallel to the weld seam.

Data Analysis and reporting

The weld is inspected with different probe angles, orientations and skews yielding a total of more than 90 PE beams. Analysing the weld data beam by beam would require too much time. For this reason all the data of the PE angle beams is brought together into a new weld zone volume by using the UltraVision® Merge tool. The considered volume is subdivided in unitary cubes. The merge tool calculates, considering all the beams, the maximum amplitude found for each unitary cube by taking into account the time of flight, probe position, angle, orientation and skew of each beam. The principle of merging shall be taken into account in the equivalence file against the step by step study of the trials results (to check all the RCC-M requirements, see ref 1).
A typical result is shown in the next picture.

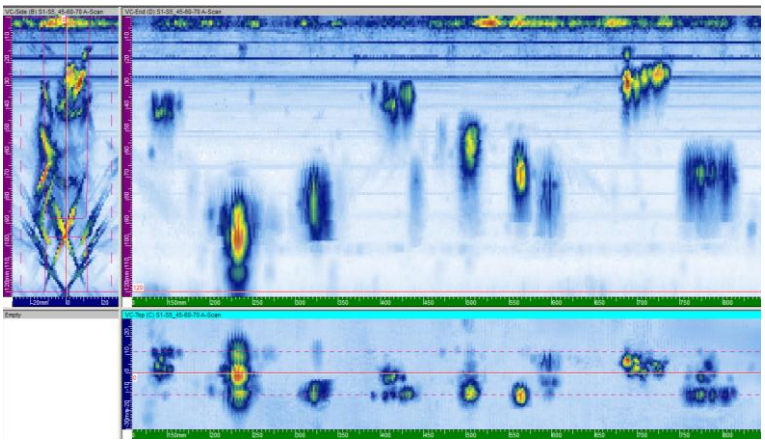

Figure 15: Typical view of Merged Data

The left view of Figure 15 shows a cross section of the weld with all indications found along the weld seam (gate cursors allow for isolating a particular indication). The end view shows a “front” view of the weld (green axis = along the weld length, purple axis = depth). The lower view shows the top view of the weld.

The combination of the Soft Gain tool and the high dynamic range offered by the DYNARAY allow visualizing indications having amplitudes far above the reference level without saturation. Increasing the Soft Gain allows analysing indications at noise level as well if needed.

The resulting volume is analysed with the tools offered by UltraVision®. Indications that cross the reporting level are automatically determined by means of the Assisted Analysis tool. The process automatically draws a contour on each detected indication which gives a visual feedback to the analyst. These functions will also be justified against the basic comparisons made in the equivalence file.

An automatically generated indication table lists all details, such as amplitude related to the reference, position, length size, etc of the found indications.

CONCLUSION

A dedicated system for the UT inspection during manufacturing of large narrow gap submerged welds has been developed and realized. Qualification on blocks with artificial and real defects shows excellent results with PA Pulse-Echo UT and PA TOFD. The acquisition unit and accompanying scanner system allow for a fast inspection of the weld seams.

The performance and the flexibility of the present solution make the extension to RPV shell weld examinations (wall thickness of 250 mm) quite possible. At this stage evaluations have been made regarding probe and system design. A 120-element probe would be required to generate a sufficiently small beam to allow dimensioning flaws located at 250mm depth.

Two DYNARAY acquisition units will operate in parallel in order to deal with a total of more than 500 channels (4 probes of 120 elements + additional PA TOFD and conventional probes). The two instruments will appear as a single unit in the UltraVision® software.

It is expected that this solution will allow full inspections of heavy wall components (single scan) at rates of more than 2m per hour.

All the characteristics and capabilities of the final system are currently being implemented and studied in the equivalence file that will make it possible to use as an alternative to conventional UT and RT in the RCC-M code.

Ref 1
Fredéric LASSERRE et al, Use of combined UT advanced techniques in lieu of conventional UT associated to radiography for end of manufacturing of primary component circumferential welds -- Justification dossier for equivalence demonstration, 10th International Conference on Non Destructive Evaluation, Cannes – France, 2013

THE CHALLENGE OF REPLACING RADIOGRAPHIC BY ULTRASONIC TESTING ON THIN AUSTENITIC PIPES

M. Bolander, A.M. Clairouin-Blais, E. Compagnon, R. Jansohn,
WesDyne International

ABSTRACT

Fabricated welds on austenitic pipes are widely inspected utilizing radiographic testing (RT). The requirement of limiting the personnel's risk to health induced by the expose of ionizing radiation and the demand for the avoidance of the security zone setup hindering other working activities close to the inspected component, gives reasons for establishing alternative volumetric inspection methods. It is well known that every non-destructive examination method possesses its strengths and its weaknesses. As a consequence replacing RT by an alternative method cannot be reduced to a comparison of the capabilities of RT with those of the considered substitute technique in general. The assessment of the applicability of an alternative inspection method should rather be adjusted to the actual task. This results in a justification including the reevaluation of input parameters and the comparison of the results expressiveness achieved by the application of RT and the alternative methods.

In this article we present an example of a practical approach for the non-destructive control of thin austenitic pipe welds beginning with the process definition, continuing with the possible defect identification and the evaluation of ultrasonic testing (UT) methods with respect to the recognized detection targets up to the substitutability decision of RT by UT.

INTRODUCTION

If a radiographic examination (RT) should be replaced by an ultrasonic examination (UT), at first the question arises, which procedure should be chosen. The attempt of proving, that the targets to be found utilizing RT can be detected with UT, falls short for two reasons. First, although RT and UT are both volumetric non-destructive inspection methods the used physical interactions are different. Second and much more important, non-destructive testing aims proving the integrity of the component with sufficient task-specific reliability, so the question whether the flaws, which are detectable with the aid of RT can also be found by the application of UT needs to be regarded as irrelevant.

From these basic considerations it can be concluded, that replacing RT by UT must include all steps of a qualification. Due to economic reasons the complex qualification process of an alternative test method should be preceded by a feasibility study verifying the performance of the UT methods to be implemented in terms of their flaw detection and sizing capability against the considered defects.

If it is planned to perform such a feasibility study, the question arises how to implement a structured and effective process, which delivers measures allowing objective decisions. Whereas many publications dealing with the use of UT in lieu of RT do not focus on the methodology, Chauveau et. al. presented an approach /1/ to develop a task related process resulting in a measure composed of the three contributions occurrence, performance and consequences (OPC), i.e.:

1. the frequency of certain flaws (occurrence),
2. the ability of the test method to detect these flaws (performance)
3. and the expected impacts if an existing fault is not found (consequences).

Hence the OPC-method comprises of component production, in-service usage, non-destructive inspection and component functioning aspects. To assign values to these items we need to investigate them:

1. The expected flaw types including their locations, orientations, sizes and probability of occurrence can be found during the development of the welding procedure qualification and by lessons learned gained in similar manufacturing processes.
2. An assessment of the performance of the examined non-destructive testing method for finding the expected flaws can be found by evaluating the probability of detection /2, 3/, by modeling or by a technical justification. In any case these examinations have to be carried out for all individual flaws types, sizes and orientations, in order to assign a quantity, which measures the reliability of the non-destructive examination method with respect to a certain defect type.
3. For the evaluation of the possible consequences caused by undetected flaws mechanical strength calculations are needed to gain information about the component state in the case of a defect induced fault condition. This examination should also include the consequences of such an event for man and environment.

The objective quantification of these three determinants, defining the acceptance of the considered method, represents a considerable expense. Within the feasibility study the concept of the OPC-method is applied as well, but instead of quantifying these determinants qualitative statements and derivations are taken into account.

If the feasibility study gives reasons for the assumption, that the chosen UT-method exhibits sufficient performance, the qualification process following the feasibility study will provide one of the following three results, where the probability of the third result can almost be treated as zero, due to the successful feasibility study.

1. The inspection can be executed with the chosen UT method completely without any restrictions.
2. The chosen UT method complements the established RT and improves, when used together with the established RT method, the detection and sizing capability of expected flaws that affect the integrity of the component.
3. The UT method cannot be used for the evaluated task.

This paper shows how a feasibility study, which estimates the likelihood of success of the envisaged qualification, can be implemented and carried out with moderate effort. We suggest making use of the available information to gain justified assumptions about the expected flaw types and about the acceptance criteria complying with the provisions taken from the applicable code.

As it is shown below, the feasibility study process is based on the evaluation of all characteristic conditions defined in referenced documentations, like fabrication procedure specifications, codes and lessons learned acquired when performing such or similar inspections. A reasonable project design ensures a methodology exploiting such available information and minimizes the economic risks of the project.

In this article hints are given for planning a feasibility study project in general. These are applied to the design of an implemented and ongoing project "feasibility study of replacing RT by UT on butt welds joining thin austenitic pipes". In that project we investigate whether RT after weld implementation, which is stipulated by the French RCC-M code /4/, can be replaced by UT. Figure 1 shows a mockup of the weld to be implemented and inspected after welding.

We experienced that the implementation of the project based on the conceptual ideas of the OPC-method /1/ provided an efficient process, so we present it here to provide a sample for similar tasks.

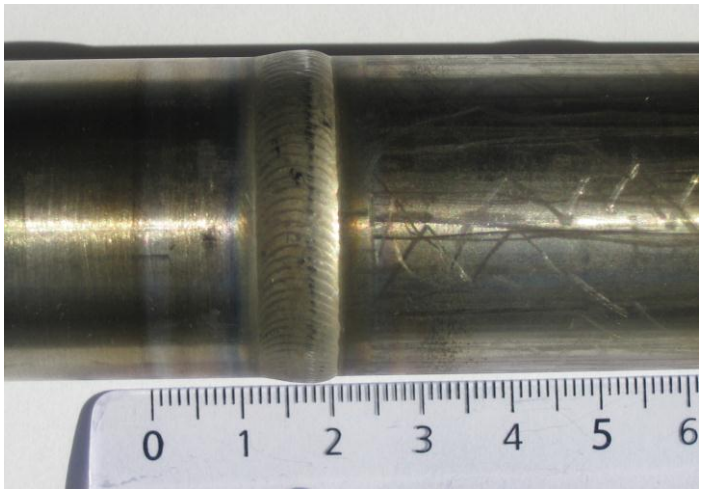

Figure 1: Mockup of the weld (ruler divided in cm)

PROJECT DESIGN

The effectiveness of a feasibility study aiming to prove whether it is possible to make use of UT in lieu of RT depends on proper project design. Such a process may be designed in the based on the OPC-method /1/ by identifying working packages, which can be assigned to the three major subjects of the method occurrence, performance and consequences. The creation of process accompanying documentation deliverables assures a close monitoring of the project.

Since the likelihood and the harmfulness of the expected defects determine the required performance of the non-destructive inspection we start the feasibility study with the evaluation of these items denoted as Defect Occurrence and Defect Consequence. As discussed below, this can be done utilizing the welding procedure specification development documents, lessons learned reports of similar projects, literature and codes.

The results of the evaluation of the Defect Occurrence and the Defect Consequence items are then used to examine the performance of the chosen UT method denoted as UT Performance working item. Based on the findings gained in the Defect Occurrence and the Defect Consequence items we build up the influential parameter list and to decide, which defects should be taken into account in the feasibility study. The next step is to build mockups and to perform practical trials. By means of preceding UT-modeling the experiments may be restricted to those exhibiting the highest potential. Based on the achieved results it is decided whether it is worth starting a qualification process.

Figure 2 shows the design of the project to prove the feasibility of replacing RT by UT on the thin austenitic butt weld.

As outlined above we designed the process to be started by investigating the component, i.e. we planned to identify possible defects that are the inspection targets to be detected by UT. We implemented a working item where the defects are classified according to EN ISO 6520-1 /5/ and their frequency of occurrence is estimated roughly.

The aim of the investigation of possible consequences, which may happen if a defect is not detected, is the definition of acceptance criteria for non-destructive examinations. These are given in the code. Although the RCC-M /4/ does not cover UT-inspections for the examined welds, such acceptance criteria can be derived from the acceptance criteria defined for RT. Hence we focused on code analysis for guidance of the acceptance criteria.

With the information collected the investigation of the achievable performance could be started with the creation of the list of input parameters gathering details of the component such as dimensions, material, geometry and expected defects /6/. Since we need to make sure that the feasibility study reflects the inspection task, this group of the influential parameters needs to be identified. However a comprehensive study of influential parameters and determination of the essential parameters as described in /6/ is regarded as part of the qualification process. Taking both, the input parameters and the derived acceptance criteria, into account it is decided which defects

should be treated in the feasibility study. By means of UT-modeling the most promising techniques and their parameters are identified, which will be examined in practical trials. The results of these experiments serve as a basis for making the decision whether a qualification process is initiated or not.

INPUT PARAMETERS

In our sample process we specified the evaluation of input parameters as the first work package. In the widest sense this work package corresponds to the occurrence item of the OPC-method /1/, since the scope of this work package includes the evaluation of the expected defects. In addition we consider the component to be inspected in terms of its geometry and material.

Component

The input parameters of the component are discriminated in geometry and material. These parameters have strong impact on the consideration of expected defects, because many defects are related to geometry. In addition the applicability of UT depends on geometry and material. Whereas the geometric input parameters and the associated tolerances can simply gathered from the drawings using the checklist given in /1/, the material analysis requires additional effort. For austenitic welds one recommended source of information is the "Handbook on the Ultrasonic Examination of Austenitic and Dissimilar Metal Welds" /7/.

In our project the creation of the welding procedure specification required a material analysis including microscopic investigations of the manufactured weld samples, which are perfectly suited as input parameter information. The forged components to be connected by welding and the weld filler consist of austenitic steel 316L. During welding the pipe axis are in vertical position, so the weld will be produced horizontally. This leads to a symmetrical grain structure with respect to the weld centre plane, if the weld preparations of both sides are symmetrical. In addition we can assume a constant grain structure in the weld cross section over the whole weld length. Figures 3 presents a cross sectional view of a weld sample. This figure shows the comparatively fine grained parent material. Close to the weld the structure of the parent material changes to the heat affected zone, where the grain size increases. Close to the bevel, in the welds volume the grains have an elongate shape perpendicular to the bevels of the weld preparation. In the weld center this orientation of grains cannot be observed, but the grain size is larger compared to the grain size of the parent material. The grain sizes according to EN ISO 643 /8/ were determined on the base of ASTM images. They are presented in table 1. In figure 4 a microscopic image of the transition between the base and filler material is shown. As mentioned above, the base material in that area, which is the heat affected zone, exhibits a larger grain size compared to the those grains lying in the unaffected material volume of the parts to be welded. The image especially presents the abrupt transition between the grain structure of the heat affected zone and the dendritic grains at the weld border. The direction of heat flow during the solidification of the weld bead is different at different positions of the weld. The heat flow mainly depends on the geometry of the weld preparation and is perpendicular to the bevel. At the edges and at the inner surface, where the weld preparation possesses a radius, the heat flow direction is more complicated. It can be seen that the orientation of the columnar grains reflects that process. Although the orientation of the dendritic grain structure differs in the cross section, we are able to detect areas with structural similarity as it is shown in figure 5.

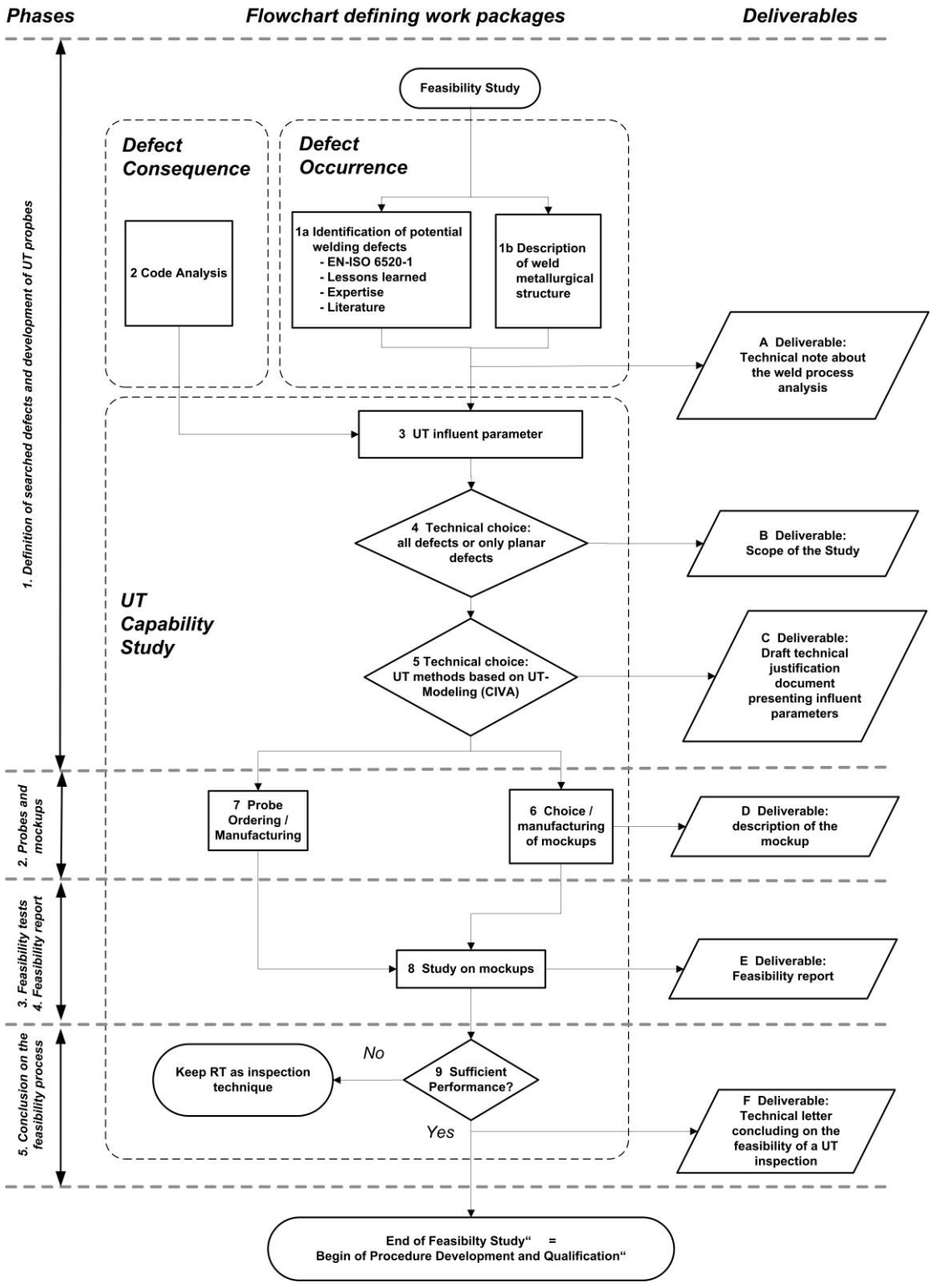

Figure 2: Feasibility study process

Table 1: Grain size of the component material

zone	**ASTM grain size number**	**grains / mm^2**
base material	G = 7	between 769 and 1536
heat affected zone	G = 3 – 4	between 49 and 192
melted zone	dentritic structure / impossible to measure	

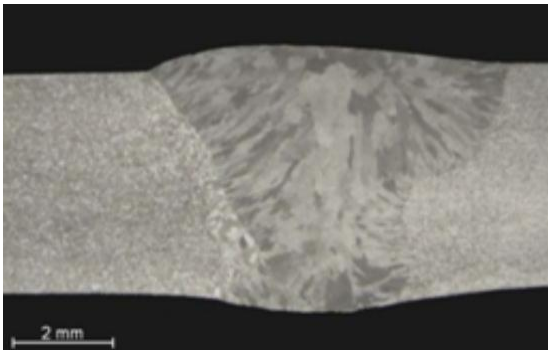

Figure 3: Cross sectional view of the weld

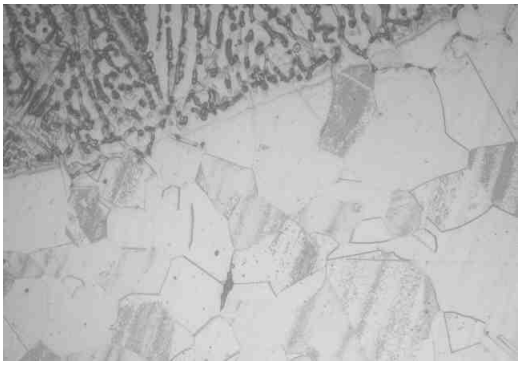

Figure 4: Heat affected zone

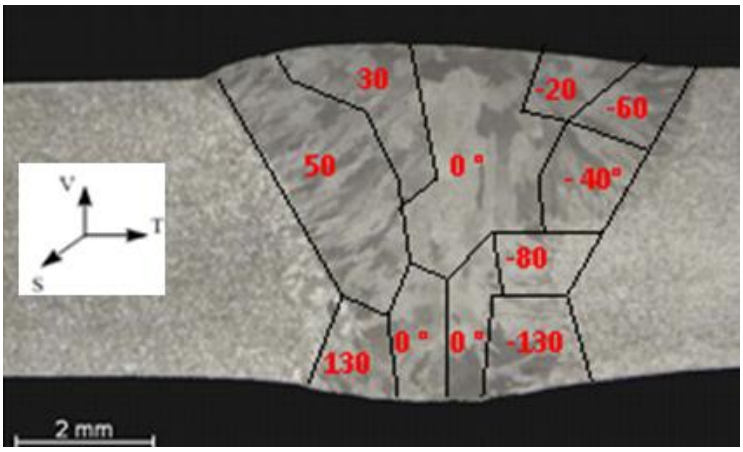

Figure 5: Identification of areas with similar grain size and orientations

Expected Defects

Which defect types, sizes, locations and orientations are to be expected needs to be communicated by the manufacturer of the component, who can use experience gained from similar productions or during the establishment of the component fabrication specification development.

During the welding procedure specification development for the welds examined in the example project 60 test samples were welded and inspected by visual, penetrant and radiographic testing. In addition macroscopic inspections were performed. The results of this work were used to determine and evaluate the defects we need to be aware of. We classified these defects with respect to their morphology as planar, volumetric or shape deviation and gathered for every defect the minimum size, the orientation of the defect normal vector and the risk level of occurrence according to the manufacturer in a table. In addition we provided icons similar to those given in /5/ to illustrate the inspection targets. Two samples are given in figures 5 and 7.

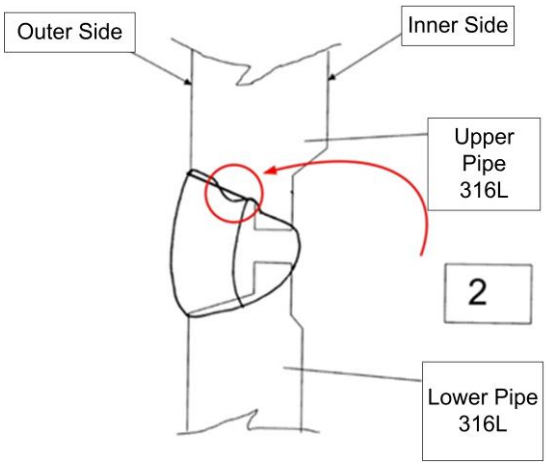

Figure 6:Lack of fusion at the bevel

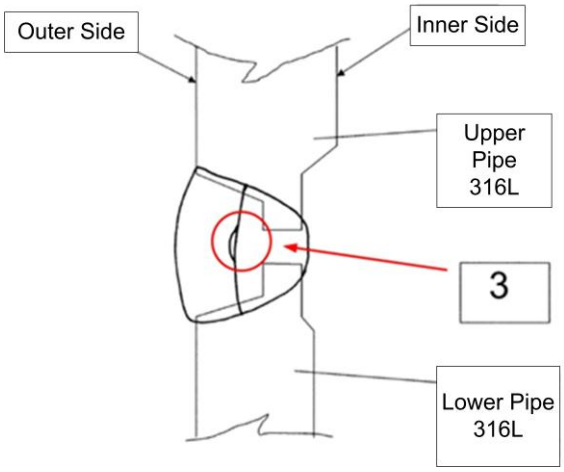

Figure 7: Lack of fusion between the passes

CODE ANALYSIS

The second work package in our sample process was code analysis. At a first glance this package differs from the consequences item identified in the OPC-method /1/. However if we keep in mind that the acceptance criteria for non-destructive examinations given in the underlying code were chosen to honor the risks and consequences of certain defects the relation becomes clear. Hence code analysis gives measures for the acceptance criteria and helps to classify possible defects according to their harmfulness for the component.

Depending on the applicable code, the acceptance criteria may be given in terms of geometric measures or as a method specific defect response, like amplitude, phase shift, etc.. For some applications only one method is treated by the code. If rules for RT are defined, but UT is not considered, we need to justify acceptance criteria on the base of those existing for RT. Since RT results are given as images, the acceptance criteria for RT are always given as geometric measures, which can be used to create test reflectors for the development of defect response related acceptance criteria for UT analysis.

According to the RCC-M /4/ the volumetric inspection after welding of austenitic butt welds needs to be performed by RT. UT is not accepted for that weld type. The acceptance criteria defined by the code depend on the weld classification. The examined weld is an austenitic class 1 weld. It is interesting to note that the RCC-M /4/ gives acceptance criteria based on the amplitude ratio of the defect echo and a reference echo, which do not distinguish between the inspection of ferritic and austenitic components. Hence we can also apply the acceptance criteria given as long we make use of UT-methods covered by the RCC-M /4/. Since the RCC-M /4/ only treats pulse echo methods in a central frequency range between 1 MHz and 6 MHz, the amplitude ratio dependent acceptance criteria defined in the RCC-M /4/ can only be applied for these UT methods. If we involve other UT methods like TOFD, we need to derive acceptance criteria from those found for RT, because these are given as geometric defect measures. Since the code does not allow any planar defects like lacks of fusion or cracks to be left in the examined volume, we conclude that the feasibility study needs to focus especially on these defect types.

EVALUATION OF THE PERFORMANCE

After the input parameters are gathered and the acceptance criteria are derived, the list of input parameters can be compiled, which is used to select the defects to be examined in the feasibility study. This selection should contain the defects, which are most harmful for the integrity of the component, most likely. By means of UT modeling the UT methods exhibiting the highest potential are identified. These techniques are then applied in the experimental program to show their inspection capability. Based on the results of the practical trials it is decided whether a qualification program should be initiated or not.

In our ongoing project, which serves as a sample here, we followed exactly the path which is described above. The modeling was performed with the aid of the CIVA simulation software. Based on the findings in literature especially in /7/ and experience we selected the following techniques to be modeled: 0° longitudinal wave, 70° longitudinal wave, 70° vertically polarized shear wave, vertically polarized 45° shear wave and TOFD. Figure 8 shows a sample setup and figure 9 the modeling result for a simulation of 70° TRL applied to a specimen containing a 1 mm x 1 mm lack of fusion defect in the root area of the weld as an illustrative sample. The following defects were modeled: planar defects parallel to the bevel (15°), planar defects parallel to the surface (90°), planar defects perpendicular to the surface (0°), porosities and tungsten inclusions. Table 2 serves as a sample of qualitative potential estimations of the different techniques for the detection of certain defects expressed in the three degrees low, medium and high.

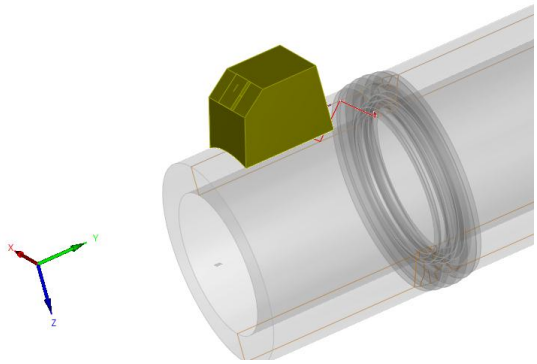

Figure 8: Probe and mockup in CIVA

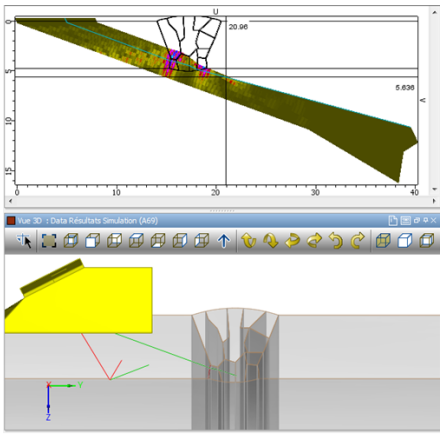

Figure 9: Sample simulation of a 70° TRL probe

Table 2: Qualitative potential estimations based on CIVA simulations

Defect	45ET	70ET	70EL	TRL70	TOFD	TRL0
Planar 0°	medium	high	low	low	low	low
Planar 15°	medium	high	low	low	low	low
Planar 90°	low	low	low	low	low	high
Porosities	low	low	low	low	low	high
Inclusion	low	low	low	low	low	medium

Based on the modeling results and the influent parameters mockups were planned containing test reflectors corresponding to the identified defects. These mockups are currently produced. To prepare the practical trials we also completed the inspection system by ordering probes and by writing the procedure for the experiments.

The next step of the ongoing project is the experimental verification of the result found by modeling. Based on the results we will decide whether sufficient performance can be achieved.

SUMMARY

It was found, that a feasibility project aiming to replace RT by UT for the testing of thin austenitic butt welds, can be implemented according to the OPC method published by Chauveau et. al. /1/. We showed how the recommendations given in /1/ can be applied to a feasibility study, in which the chances for success of a complex qualification project are evaluated to minimize the risk of such a project. We encourage using available information, which roughly corresponds to the three items occurrence, performance and consequences, to reduce the costs of such a study.

If the feasibility study confirms the principle suitability of the UT method, a qualification process needs to be initiated to justify UT as a replacement or supplemental non-destructive examination technique.

REFERENCES

/1/ Chauveau D., Blettner A., Abittan E., Hatsch J., "Présentation d'une démarche d'évaluation de la pertinence du remplacement d'une méthode ou technique CND par une autre: l'approche OPC (Occurrence / Performance / Conséquence)", Institut de Soudure, 2011

/2/ Gandossi L., Annis C., "Probability of Detection Curves: Statistical Best-Practices", ENIQ Report No 41, Publications Office of the European Union, Luxembourg, 2010

/3/ Annis C., "Nondestructive Evaluation System Reliability Assessment", MIL-HDBK-1823A., Department of Defense Handbook, Wright-Patterson AFB, USA, 2009

/4/ "RCC-M - Design and Construction Rules for Mechanical Components of PWR Nuclear Islands", acfen, French Association for Design, Construction and In-service Inspection Rules for Nuclear Island Components, Paris, 2007 edition and 2008 amendment

/5/ EN ISO 6520-1 "Welding and allied processes – Classification of geometric imperfections in metallic materials – Part 1: Fusion welding"

/6/ "ENIQ Recommended Practice 1 – Influential / Essential Parameters", Issue 2, ENIQ Report No 24, Publications Office of the European Union, Luxembourg, 2005

/7/ International Institute of Welding, "Handbook on the Ultrasonic Examination of Austenitic and Dissimilar Metal Welds", Document No. V-1321-5, 2005

ENCODED PHASED ARRAY ULTRASONIC TESTING OF SOCKET WELDED JOINTS

J. Hall, J. Fred Hall, J. Devers, T. Blechinger
ANATEC, USA

Abstract

This presentation will describe the development and application of encoded phased array ultrasonic testing (PAUT) of socket welded joints.

Background: Current US Regulation requires periodic testing of installed socket welded joints for plant life extension or licence renewal. Typically these joints are either radiographed or destructively tested for evidence of cracking from the root of the joint. In order to reduce the outage impact, radiological concerns and costs associated with radiography or destructive testing, LMT developed a technique to examine these joints with encoded phased array UT. This presentation will describe the development of the technique, including performance demonstration, and describe the PAUT application at US facilities.

Keywords: Development in volumetric

RADIOGRAPHIC SOURCE EJECTION REDUCTIONS BY ULTRASONIC TECHNIQUES FOR SOME IN-SERVICE INSPECTIONS

F. Vivier, C. Reece, EDF - CEIDRE, France
L. Blarel, EDF - UTO, France

ABSTRACT

In 2005, EDF launched a national project in order to reduce the risks associated with high energy gammagraphy carried out on its French fleet. One of the major parts of this project was the replacement of some in-service inspections historically performed using Radiographic techniques by new inspections using well-established Ultrasonic techniques.

A technical analysis was performed to determine the zones for which this replacement would be both technically possible and beneficial in terms of radiographic source ejection reductions. The secondary coolant loop pipe welds (Main Steam Line, Main Feedwater line, Auxillary Feedwater line), on which some UT was already being performed, were selected as the first area of interest.

In accordance with the French regulatory requirements, the new UT inspections were formally qualified according to the RSE-M methodology by an independent second party qualification commission before being implemented on-site.

This paper will detail the operational experience obtained and the main challenges faced while qualifying and implementing the new UT inspections, and will briefly discuss the impact, advantages and disadvantages of the technique change on the French fleet. This paper will also present the perspectives currently being investigated to reduce further the risks associated with gammagraphy.
Keywords: RT replacement – UT – Secondary loop – Qualification – Implementation

INTRODUCTION

EDF has a long history of using radiographic techniques for non destructive testing both during manufacturing and in-service inspections of Nuclear Power Plant components. Radiographic techniques allow sufficiently sensitive volumetric inspections of components or welds and create long term records of the inspection, the radiograph. However, Industrial Radiographic techniques use high energy radioactive sources which require special precautions, such as specific training for operators, shielding during transport and demarcation the area of the inspection during source ejection. These precautions can cause schedule constraints on an outage. Furthermore, despite these measures being taken, accidents involving radioactive sources have in the past caused human injuries and major delays during outages. To limit these risks, EDF have launched a national project to reduce the use of radiographic techniques for manufacturing and in-service inspections on their French fleet. This large project involves work with manufacturers on modifying the code inspection requirements (such as French RCC-M code) to allow the use of techniques alternative to radiography, as well as rethinking the way in-service inspection is carried out to limit the use of Radiography.

This paper will focus on the work carried out on reducing the use of radiographic techniques, specifically high energy gammagraphy, for in-service inspections, by replacing existing qualified radiographic inspections by alternative volumetric inspections using well established ultrasonic techniques.

This work was started with an study to identify the welds for which this replacement was both technically feasible and which would give the highest reduction of radiographic ejections. Then, inspections using well established pulse/echo Ultrasonic techniques were developed, qualified and implemented on selected sites. Finally, the inspection procedures were modified to take into account the operational experience obtained in order to be implemented on all the sites.

SELECTION OF THE SECONDARY LOOP PIPING WELDS

The first stage of the project was to select the Radiographic inspections to be replaced by UT inspections. The secondary Loop piping welds, shown in red in **Figure 1** were chosen as it was considered that:

- The replacement is technically feasible using pulse/echo UT techniques (ferritic material, favourable geometries)
- There was a high number of radiographic examinations being eliminated as a result of the replacement
- The Social, Organisational and Human impact of the replacement was manageable
- The potential dose impact of the replacement was small.

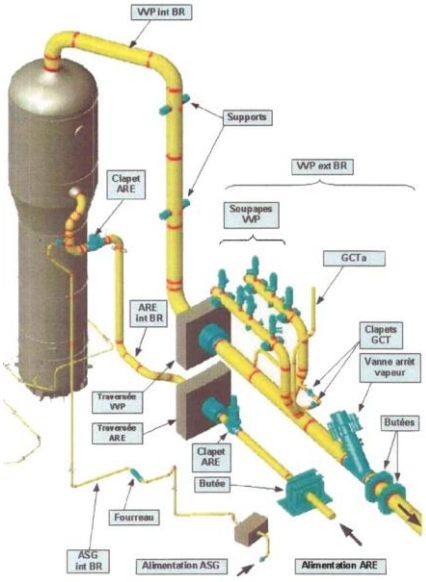

Figure 1: Schematic of the secondary circuit welds of a French NPP

The Main Steam Line, Main Feedwater line and Auxiliary Feedwater Line pipes were selected on the basis of their favourable geometries. An analysis of the existing radiographic inspection requirements showed that the target defects varied according to the positions of the weld along the secondary circuit. Therefore, three separate inspection specifications were drafted for:

- The Main Steam Line (MSL) and Main Feedwater line (MFL) welds up to the last valve before the steam generator for which the RSE-M qualification type is “conventional” (no defect specifically targeted)
- The Main FeedWater Line circular welds between the last valve and the Steam generator, for which the RSE-M qualification is “general” and internal surface breaking defects are targeted.
- The auxiliary Feedwater Line circular welds for which the RSE-M qualification is “general” and internal surface breaking defects are targeted

Due to the differences in requirements and geometries, it was decided to develop and qualify the three inspections separately. This paper will focus on the MSL and main feedwater line inspections, as those have already been implemented on site. The Auxiliary Feedwater inspection will be implemented for the first time by the end of the year 2013.

DEVELOPMENT AND QUALIFICATION OF THE MSL INSPECTION

Existing UT inspection and strategy

Some of the MSL and Main Feedwater line welds were already inspected using a qualified manual UT pulse echo techniques, using miniature shear wave transducers. A preliminary analysis showed that these UT techniques could also be used for the inspection of other circular and longitudinal welds, which were historically examined by RT techniques.

Therefore, it was decided to extend the qualification to welds which had dimensional characteristics in the range of the existing qualification. The qualification strategy was to demonstrate that this qualification extension to new welds did not have a negative impact on the existing qualified performance in terms of coverage, detection sensitivity and positioning uncertainties.

Preliminary analysis

The previous UT technique was qualified for several configurations seen in the French fleet, including nozzles, longitudinal and circular pipe or elbow welds.

The preliminary analysis showed that the replacement of RT technique by a UT technique would be feasible for all configurations for which the coverage of the inspection volume could be guaranteed. It was shown that this would only be achieved when the inspection could be carried out from both sides of the weld. Thus, the pipe/valve weld inspections, which feature limited access to the weld, were excluded from the qualification extension.

Development and qualification

The qualification extension was heavily dependent on the coverage of the inspection volume defined in the inspection specification. Therefore, it was decided to carry out a detailed analysis the geometries of some the welds impacted by the qualification. As it is very difficult to obtain detailed of all the welds on the French fleet (which comprises of 58 reactors), it was assumed that the worst case configurations in terms of inspection coverage were the smallest and biggest dimensions of the weld, and, the inspection coverage of those welds using different probes was evaluated on real weld profiles.

This study showed that sub-miniature probes (transducer size ∅6.35 mm) were needed additionally to the already qualified miniature probes in order to maximise the coverage of the volume, especially the internal area near the weld root. This meant that the detection capability and positioning uncertainties of the inspection had to be re-evaluated in order to extend the qualification.

As no defect is specifically targeted by these inspections, the recording threshold of the inspection procedure is based on the RSE-M code (using SDH as the reference reflector) and the corresponding sensitivity is determined in FBH diameters. This is done, for each probe, using DGS curves taking into account some of the influential parameters. The inspection sensitivity at a given depth can be read by comparing the recording threshold to the closest FBH curve at the corresponding sound path on the DGS diagram (**Figure 2**). In this case, it was shown that a defect which has the same ultrasonic response than a FBH equivalent ∅4 mm in the ultrasonic beam axis, can be detected in all cases.

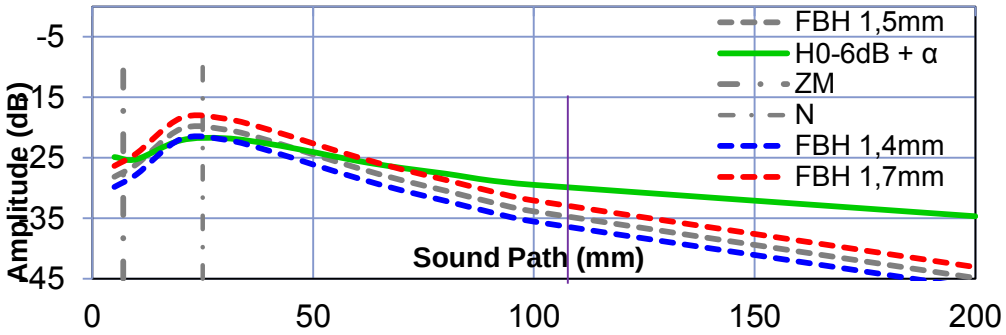

Figure 2: DGS diagram obtained for a 45° miniature probe

DEVELOPMENT AND QUALIFICATION OF THE MAIN FEEDWATER LINE INSPECTION

Choice of the inspection technique

An analysis of the geometries of the welds to be inspected showed that the major challenges to this inspection would be to be able to obtain full coverage of the target zone and to be able to differentiate the signals which could correspond to the defect sought from other echoes (point indications and geometric echoes). Due to the planar nature of the defect sought by the inspection, both pulse/echo based and diffraction based techniques would be able to fulfil the inspection requirements. Therefore, trials were performed on a representative mock up to test a classic manual pulse/echo based inspection and an encoded TOFD inspection. The results showed that all three techniques could detect all the defects in the mock-up, but that the TOFD inspection yielded the results faster than the manual pulse echo inspection.

However, the TOFD technique tested had several disadvantages which could not be seen during the trials. Firstly, it would be more difficult to implement on the site welds due to the presence of obstacles and elbows, which would not allow the use of a simple manipulator as was possible during the trials on the mock-up. Secondly, despite the fact that the encoded methods allowed for a quick pre-screening of the inspected area, a further inspection using a pulse/echo technique would still be required to confirm their presence. Finally, the training and certification requirements for operators are much higher for the TOFD inspection. Therefore, it was decided to first develop and qualify a manual pulse/echo technique using single element probes, and to re-evaluate the situation once some operational feedback would be obtained.

Preliminary inspection design and qualification strategy

The inspection was designed using existing practices of codes or standards (RCC-M code, Euronorms). The inspection was designed as a half-skip inspection using two standard "miniature" shear wave probes (transducer size 8×9 mm) with a 7 mm probe overlap during scanning. The reference reflector is a 2 mm diameter side drilled hole, as generally used in RSE-M code inspections. The objective is to detect the corner echoes generated by the defect.

The 60° and 70° beam angles were chosen to maximise the coverage in the presence of a weld bead, but their use made it impossible to fully inspect the inspection volume for the connection to the Steam generator nozzle. It was therefore decided to produce a separate inspection procedure for those welds, and to replace the 70° angle probe by a 45° miniature probe. To maximise the coverage of the inspection area, a sub-minature probe was also incorporated in the procedure.

To qualify this inspection according to RSE-M code, it was necessary to demonstrate that, taking into account all the possible errors linked to human errors, through the use of the equipment or the specificity of the technique used, the sought defect in the target will be detected by following the inspection procedure. This was achieved by:

1. Determining the characteristics of the ultrasonic response of the defect using modelling.
2. Analysing the influential parameters of the inspection in order to determine an appropriate "safety margin" to guarantee that the target defect defined in the inspection specification would exceed the recording threshold in all cases when the ultrasonic beam hits the defect,

Determination of the worst case defect and its ultrasonic response

The objective of this phase was to define a recording threshold with which the target defect would be recorded, but other, non targeted defects (such as volumetric defects) would not be recorded.

To achieve this, the characteristics of the ultrasonic response (amplitude and length) of the defect were modelled using the Civa modelling software. As corner echoes are highly dependent on the incident beam angle and the tilt of the defect (as shown in **Figure 3**) and length measurements are highly dependent on the beam width, the response of the defect was modelled for different combinations of thicknesses, defect tilts, probe angles and positions in the elbows in order to determine the amplitude response of the defect.

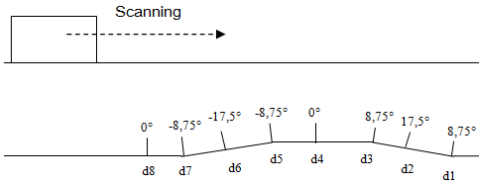

Reflecteur	Tilt	amplitude/reference (dB)
Reference	/	0
d1	8,75°	10,7
d2	17,5°	6,2
d3	8,75°	-2,1
d4	0°	2,5
d5	-8,75°	5,1
d6	-17,5°	15,3
d7	-8,75°	0,7
d8	0°	3,5

Figure 3: Impact of tilt of defect on the amplitude of corner echoes

The results show that the amplitude of the defect exceeds in all cases -12dB with respect to the reference reflector and differences of over 25dB can be obtained between the most and the least reflective configurations. It could also be noticed that the most tilted defects and the least reflective the amplitude of the defect is generally smaller in the intrados of the elbows, due to coupling issues.

The length of defect measured using the 6dB drop method was in some cases very small. Therefore, it was decided to use a length measurement using the 12 dB drop measurement method. Using this method, the defect's length was measured as always exceeding 18 mm, which would be more manageable to measure for the operators on site.

Analysis of the other influential parameters

In order to guarantee the recording of the defect defined in the inspection specification, safety margins were taken on the amplitude and length thresholds determined above, as well as for the positioning of the defect. These safety margins were determined by analysing the influential parameters using physical reasoning.

For the amplitude of the detect, the main influential parameters were the linearity of the flaw detector, the human errors during calibration and evaluation of echoes, as well as the overlap in the scanning pattern.

For the measurement of the length of the defect, the error made by operator was considered to be generally proportional to the width of the ultrasonic beam. This error was incorporated into the recording threshold.

For the positioning of the defect, it was determined that taking into account all the influential parameters (error or beam angle, velocity of the UT beam, errors during calibration, positioning errors due to the corner trap, error due to "profile" etc...) , the maximum positioning error approached 15 mm. The area to be inspected was therefore enlarged to take this into account.

The recording threshold of the inspection procedure was obtained by adding the "safety margin" to the nominal response of the defect obtained. This recording threshold was used successfully during the qualification trials on a representative mock up. These trials were performed to validate the modelling and reasoning carried out as well as to ensure that the inspection could be carried out successfully by two adequately trained operators.

During these trials, all the defects in the mock up were successfully found and positioned by the two operators, and the differences in results obtained with both operators were in line with the assumptions made in the technical justification documents.

IMPLEMENTATION TRIALS

The Main Steam Line and Main Feedwater line inspections were first implemented on several "voluntary" French NPPs. The objective of these implementation trials was to evaluate weld accessibility (**Figure 4**), to determine the time and dose impact of the replacement, as well as to identify difficulties and potential improvements to the inspection procedures. It was especially important to check whether different operators with different levels of experience could implement the procedure correctly.

Figure 4: Example of welds accessibility

The trials implementations were successful, but a few difficulties were encountered. The main technical issues discovered during implementation were:

- The surface condition of the welds did not always allow a full inspection of the inspection volume. The use of "sub-miniature" probes allowed for improved coverage in some cases. An example of a weld difficult to inspect is shown in **Figure 5**.
- The very high sensitivity of the UT inspections to geometric echoes (weld root and weld beads)

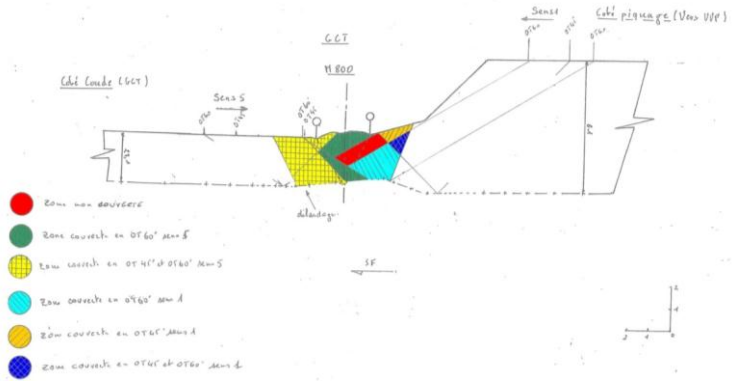

Figure 5: Example of an MSL for which a full volumetric inspection could not be achieved

Furthermore, the trial implementation showed that both the inspection time and the collective dose of operators were higher for the UT inspection than for the RT inspection. This can partially be explained by the technical problems described above, but also by the fact that the scheduling of the inspection during the outage was not optimised with respect to the other activities on the steam generators.

However, the trial implementation showed that the UT inspection was a viable alternative to the radiographic inspection and could offer significant advantages by allowing co-activity.

Therefore, further work will be carried out to:

- Modify the inspection procedure to take into account the operational feedback obtained,
- Optimise the outage schedule to minimise the collective dose of the inspection,
- Investigate more complex inspection methods such as phased array inspection and TOFD to carry out the inspection more effectively.

CONCLUSIONS

As a part of a national project to reduce the risks associated with gammagraphy, EDF has designed UT inspections using well established pulse-echo techniques to replace radiographic inspections on the main secondary loops of their nuclear reactors. These inspections were first qualified and then implemented on site. Despite the overall success of the trial implementations, which have demonstrated that these new UT inspections are viable replacements for the RT inspection, the operational feedback was not entirely positive, as unforeseen technical issues and organisational issues were discovered. Further work will be carried out to improve the qualified inspections as well as find alternatives to reduce the time and dose of the inspections or improve their performance (ability to detect small defects and to discriminate them from geometric echoes, positioning precision, etc.).

Further work will also be carried out to find new radiographic inspections to be replaced by UT inspections. This work will incorporate all the experience obtained while qualifying and implementing the secondary circuit inspections.

LINEAR ACCELERATOR FOR THE INSPECTION OF CAST IRON COMPONENTS

G. Mannessiez, L. Woisel, CEP Industrie-Bureau Veritas, France
M. Hernandes, XsCell, USA

Abstract

CEPI (a subsidiary of Bureau Veritas) carried out RT (Radiographic testing) on large steel thicknesses (70 mm to 300 mm) since 1987 with a mobile accelerator 4/6 Mev manufactured by Schonberg corp.
We will focus more specifically on the case study of casting elbows (both aspects: NDT tools and accelerator equipment)
The ageing of equipment and the evolution of standards and technology has naturally led to the revamping of the equipment and the qualification of NDT expertise.
The project conducted with EDF, CEPI and XCELL is both about setting the accelerator in conformity with regulations rules & European standard (CE, CEM, ..) and improving the operational reliability.
Radioprotection safety regulations have to be taken in account with the specific accelerator requirements such as the obligation for radiographer to hold certificate "CAMARI" option accelerator.
CEPI in collaboration with LCIE (1) and ASN (2) must validate/qualify the accelerator for a first intervention in February 2014 on a NPP (Nuclear Power Plant)
In partnership with EDF/DER (3), work is underway on the modelization of the beam RX as to master the expertise means.
Also will be presented some potential short term applications in the field of high energy X-ray such as carrying out NDT with RX generator from 0,4 to 2 MeV. It may be considered as a radioprotection safety improvement so as to replace radioactive sources such as cobalt 60.

(1) LCIE: French laboratories accredited for electric measurement
(2) ASN: French Nuclear Authorities
(3) DER: NDT Development department of EDF

MATERIAL PROPERTIES/ALTERNATIVE RT

QUALIFICATION OF A BUTT-WELD INSPECTION USING PHASED ARRAY IN LIEU OF RADIOGRAPHY

B. Dormoy, ALSTOM POWER, France
J. Delemontez, T. Le Guevel, EDF, France

1 Context

The low profile scanner named “Scan 13” and ultrasonic procedure allow for buttwelds to be inspected rapidly and without any shut down of production work as with radiographic process. This makes Alstom construction more competitive and safe. Since this scanner only requires 13mm of clearance, it opens up the door to do inspections that were previously not possible due to limited access. Since this scanner design adapts to various sized weld diameters, it can be used to inspect welds in virtually all business segments from turbine to HRSG, boiler, hydro, wind and transport
Butt welds made during repairs on boiler screens or pendular tubes are particularly difficult to inspect. These welds are usually inspected radiographically. The consequences and impacts of the choice of this method during a unit outage are known and are restrictive. In order to speed up examinations and reduce analysis time, Alstom has developed a method of examination by ultrasonic phased array to inspect an entire weld quickly and efficiently.

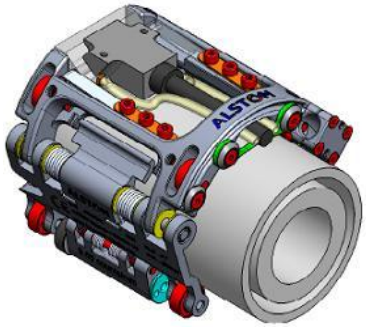

Figure 1 – Buttweldscanner Design

To facilitate monitoring and thereby promote effective management of the maintenance policy, the following are necessary:

- be able to characterize the indications located in the weld or HAZ (heat affected zone);
- perform the inspection, even if inspection conditions are not optimal (confined space, high temperature of the part being examined (up to 60° C);
- facilitate monitoring of machinery in the areas inspected by offering a reliable technique for recording the signals measured.

Alstom proposed EDF to apply this new ndt technique for the the control of boiler tubes butt welds in lieu of radiography according criterias of french decree of March 1978.

To meet the EDF requirements, a qualification dossier was constituted including:

- technical justifications and specifications,
- demonstrations of performance taking account of essential parameters,
- tests with representative mock-ups and representative CIVA simulation,
- specific ndt procedure,
- training program for the operators.

2 Specifications and objectives

The purpose of the technique developed by Alstom is to be able to detect indications that may appear when butt-welding steel tubes (stainless steels are excluded from this study).

Their position and orientation may vary, but possible indications are expected at the welded joint and oriented along the axis of welding. Figure 2 illustrates the position of expected defects in different parts of a weld (lack of fusion or incomplete fusion, excess or lack of penetration, porosity, inclusions, cracks, etc.)
From an operational perspective, it is necessary to develop a technique capable of taking into account the vagaries of site works (overlapping sites, confined space) so as not to penalize the rollout of the entire overhaul in progress during NDT. Moreover, it is also necessary to impact the inspection environment as little as possible so that NDT operators can be autonomous to carry out their work. Finally, the new inspection technique is semi-automated to ensure acquisition repeatability/ reproducibility and to record the acquisitions, which makes for proper monitoring. The semi-automated process will also save time because the analysis will be carried out almost simultaneously.

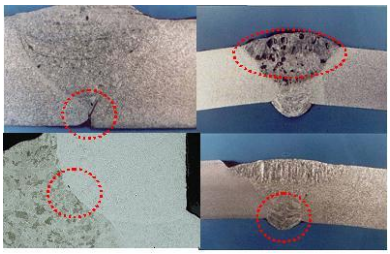

Figure 2 – Expected Defects

3 Justification for the choice of NDT technique

The choice of ultrasounds for weld inspection is a natural one, since the requested inspection turns out to be a volume examination. So even though some indications may be surface-breaking, they are scarcely, if at all, accessible to conventional surface techniques (PT, MT, ET). It is therefore necessary to use a so-called volumetric technique. Only ultrasounds and radiography can be used to examine the volume of a component. But here, radiography, used up until now, has drawbacks when being used, as it is not possible to locate faults detected in the depth direction. Positioning the film can be tricky, depending on the weld being examined. In addition, radiographic testing has a major drawback due to the presence of a dead zone (limit of elliptic RTs) that mean two different shots have to be realized to ensure complete coverage of the weld.

Moreover, the regulations on radiation protection imply major consequences in terms of site organization for the overhaul in progress. In addition, the use of radiography is becoming more and more subject to regulations due to changes in the Decree of 24 March 1978. The use of ultrasound will therefore be a definite advantage.

The methodology is based on ultrasounds because they can also be used to examine a component in its volume and locate defects using the sound path (PS). The multitude of variables to be taken into account when making settings for the examination (groove type, thickness, angle, tube diameter, grade of material, etc.) leads to a large number of ultrasonic configurations (position of sensors, refraction angles, etc.). The use of phased array transducers will allow delay laws to be applied; these are chosen so as to generate ultrasound in several directions sequentially and build ultrasound images in real time. Automated - and especially encoded - movement can accurately locate the indications on the ultrasound image.

To sum up, semi-automating acquisition allows for information repeatability (positioning relative to a physical reference), and reproducibility of the measurement (the various components of the UT channel can be interchanged without impacting performance). The impact of the human factor is strongly reduced.

4 Digital simulation of the inspection configuration

To ensure the feasibility of the inspection and accurately define the components used, ultrasonic simulation resources available on the market are used. We used the ESBeamTool3 software to define the phased array configuration to be used.

The simulations were carried out in several stages:

- **Ray tracing**. This stage is to get the work started and determine the delay laws to be used depending on the position of the probe on the tube. It also provides an initial estimate of defect detectability;
- **Definition and characterization of phased array transducers**. In this stage the deflection capacity of the sensors is checked based on the intrinsic parameters of the transducers. The beam is then characterized ensuring that there are no interfering network lobes that may hinder detection;

To perform simulations in a representative environment, the geometry of the weld + HAZ is drawn using ESBeamTool and this allows us to simulate a realistic configuration.

- Groove angle: 37°
- Tube thickness: 5mm
- diameter 63.5mm
- Gap between the two root faces: 2mm

4.1 Ray tracing

Ray tracing or ray path allows us to define the examination positions for each of the transducers used together with the optimum refraction angle to be used to detect an indication. Ray tracing can also be used to define the angular range of the sectors to be used.

These simulations allow us to choose the scan angles, the aperture and the depth of focus to be used for indications that may appear in this weld range. Several types of scanning can be chosen (linear or sector).

All the simulations have shown that the optimal configuration for inspecting a weld comprises an initial acquisition of one side of the weld (upstream) and then a second on the other side (downstream). These two acquisitions provide a 100% examination of the weld.

4.2 Beam/defect interaction

To digitally validate the inspection principles, new simulations have been conducted to define the nature of the interaction between the UT beam and the defect. Using these simulations in tandem with laboratory tests, it was possible to refine and validate the choice of scans, focusing and angles in order to obtain a configuration that is particularly sensitive to certain types of default. The linear scan turns out to be a perfect tool for detecting lack of fusion or incomplete fusion at the groove edge. This scanning is set so that the beam is incident perpendicularly on the groove. For example, for a groove at 37°, the beam will be set at an angle of 53°. Consequently, the ultrasonic response obtained is optimal. Conversely, sector scanning covering angles of 30° to 65° will allow indications such as porosity, inclusions, root crack, lack of penetration, etc. to be located.

The phenomena involved in the simulations and tests are:

- Corner echo (e.g. surface-breaking crack)
- Specular reflection (e.g. incomplete fusion, porosity)

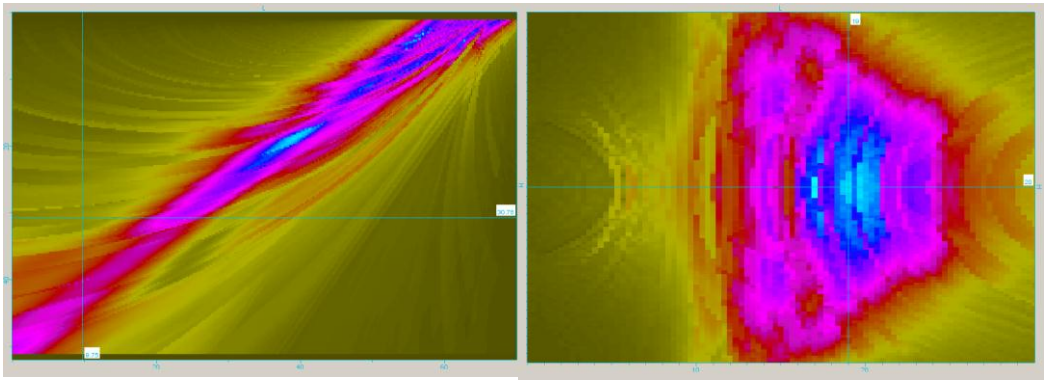

Figure 3: Focal spot size at -6dB of the elementary beam

Representative CIVA simulations have allowed us to determine the length of the smallest detectable plane defect (i.e. one whose response is ≥ 50% of baseline level) with the SCAN13 inspection procedure. A plane defect, oriented along the groove axis and located in the chamfer, of size 1x1mm² is detected with a greater than 50 % response compared to a calibration on a side drilled hole (SDH) ϕ1.5mm.

A plane defect, oriented along the weld axis and perpendicular to the surface, of size 2x2mm² is detected with a greater than 50 % response compared to a calibration on a side drilled hole ϕ1.5mm.
From our experience feedback, it is unlikely to get a defect of this kind in the welding configurations discussed in this article but these results allow to define the limits of the sensibility performance of the UT phased array.
A gas cavity greater than or equal to 3mm in diameter will be detected with a greater than 50 % response.
CIVA simulations have shown that a gas cavity of diameter ϕ = 3mm will be detected with a response of -1.1 dB.
An elongated gas cavity of diameter 1.5mm and length 6mm is detected with a greater than 50 % response.
CIVA simulations have shown that a gas cavity of diameter ϕ = 1.5mm and L=6mm will be detected with a response of +8dB.

A root crack size 1x1 mm2 positioned at the boundary with HAZ on the inner diameter side and detected on the ½ skip will have a response in the order of +19 dB (SDH at 16dB).
When a crack is positioned at the boundary with the HAZ, on the outside diameter side and detected on the full skip, the response is in the order of +6 dB (SDH at -3dB).

4.3 Identification of influential parameters and areas of change

4.3.1 Groove angle

According to the welding specifications, nominal groove angle is 37°30 +-2°30. For inspection, we define the groove angle as 37° +-2°50. The size of the incomplete fusion used for these simulations is 2x2mm². Simulations were performed on CIVA varying this parameter within the range of tolerance.
Additional simulations were performed to measure the reflectivity difference between a 35° and a 37° groove with an ultrasound beam at 53° (linear sweep with 16 elements opened).
The result obtained with these simulations indicates that there is a difference in reflectivity of 0.2dB.
As long as we keep within the range of tolerances established by the DMOS, the difference in reflectivity does not affect the detection capability of the process.

4.3.2 Weld bead

The width of the weld bead is an influencing parameter.
During any inspection, the inspector will therefore measure a number of beads to corroborate his simulations with reality. In cases where the actual size of beads differs from the theory, a new simulation is performed in order to confirm the feasibility and the "offset index" parameter will be amended accordingly. From laboratory tests, a weld bead wider by 2mm at the most will not affect detection provided that this difference has been taken into account. In the case of a bead overlapping onto an area of the tube, the latter will be ground so as to have as regular as possible a weld bead.

4.3.3 HAZ: Heat affected zone

Since no standard defines the size of the HAZ in tubes of thickness less than 8mm, we will define the size of the HAZ as being representative of a half thickness of the material considered on both sides of the weld bead. A specific test on mock-up is done to check the ultrasonic coverage of the volume to be examined.

***4.3.4** Surface coupling*

Surface roughness or loss of water may affect the good coupling of the probe and cause damage regarding the sensibility during the scan. Surface is prepared before the examination and a specific

focal law (0°) is generated during the scan in order to record the background echo. This allows the operator to check the good coupling and guarantee the sensibility of detection along the entire weld length.

5 Experimental measurements on artificial defects

Many simulations were performed to determine the positions and angles to be used for each transducer. These are checked on calibration blocks made to be used in existing inspections. The following sections describe the blocks and transducers used for validation measurements on artificial defects.

5.1 Models used for testing

The models used for the tests were made from a similar steel grade to that used in the majority of cases. The first model used represents a "forest" of pendular tubes containing butt welds. Some of these tubes have artificial representative defects such as incomplete fusion, porosity or inclusion.
This model is necessary for testing implementation by simulating real-world conditions.

Figure 4: Mock-up to test in real condition

5.1.1 Comparison between conventional ultrasound and phased array ultrasound

To make a comparison between conventional ultrasound and the phased array method, several specimens were manufactured. Each specimen includes a butt weld with real defects.
There are several tubes by diameter range (1,5", 2", 2,5"). Each of these tubes has 2 different real defects. These reference tubes were manufactured by Sonaspection.

The first tests were carried out by Sonaspection upon delivery of the manufacturing report. Their tests were performed using conventional ultrasound. An initial comparison could then be made, carrying out the inspection with the new process.

The vast majority of faults are detected by both methods with the exception of lack of fusion between passes (not detected with conventional UT). However, it should be noted that the tests at Sonaspection required the use of several probes (45°, 60° and 70°) whereas using the phased array method, it is possible to significantly reduce the inspection time (10 minutes on average per weld).
In addition, conventional ultrasound is feasible only when space permits. Using this method on the model, for example, is not feasible given the space between tubes.

5.1.2 Comparison between phased array ultrasound and radiography

This section will be devoted to the comparison made between the use of phased array ultrasound and radiography.
The 3 specimens cited above were X-rayed using an IR-192 source (36 curies).
The exposure time was 2min and 36sec.

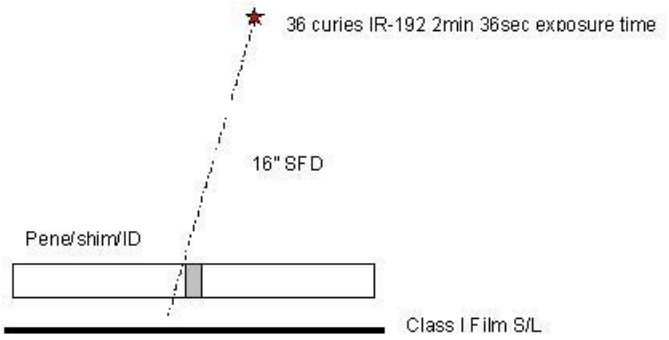

Figure 5 - Double-wall radiography of specimens

After analysing the results, it appears that lack of fusion was not detected during X-ray examination. It appears that leaving this type of fault as it is on small thicknesses can be critical when using a boiler.
Additional tests were performed on sleeves made of Z10CDNbV92 corresponding to a high-alloy steel. These comparative RT/UT tests have allowed us to identify all the defects in these sleeves.
These tests required a calibration block of identical grade made from Z10CDNbV92.

5.1.3 Sonaspection and EDF mock tests

Additional tests on Sonaspection reference tubes were made on identical tubes (same diameter, thickness and grade to those encountered during the RHT (final reheater header)
LE HAVRE 4 project in 2012.

These tests involved tubes made of 10CrMo9.10 and X10CrMoVNb9.1

- diam. 63.5mm th 4.5mm -> X10CrMoVNb9.1
- diam. 63.5mm th 4mm -> 10CrMo9.10
- diam. 44.6mm th: 6mm -> 10CrMo9.10

Tests were also carried out on EDF SC100 and SC101 mock-ups in order to demonstrate the good ultrasonic coverage of the SCAN 13 inspection process.
These tubes had electro-eroded notches located throughout the weld (melt zone, groove and HAZ).
The results mean that we can validate proper coverage of the process zone during the performance of a single scan per side.

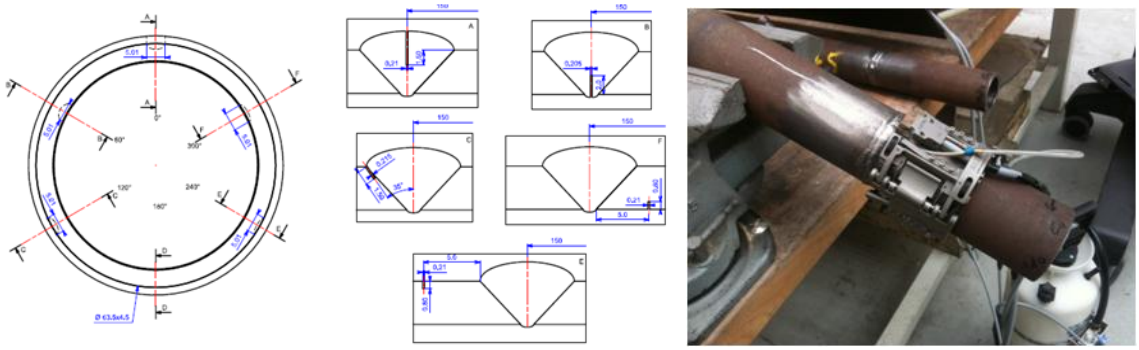

Figure 6: SC100 and SC101 EDF mock-ups – check of the ultrasonic coverage

Through these experimental tests, we were able to validate the fact of modifying the initial aperture of the linear scan by reducing. This allows us to cover a wider area of the groove zone without reducing detection sensitivity. Aditionnal CIVA simulations were added and confirmed the experimental results.

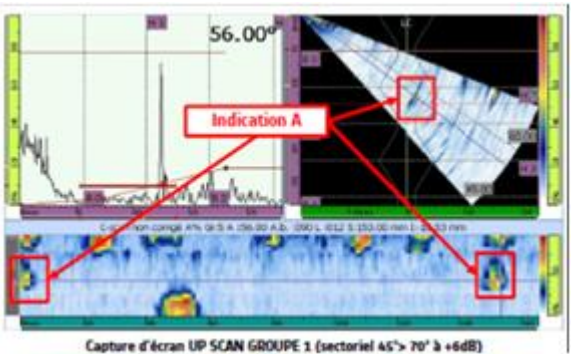

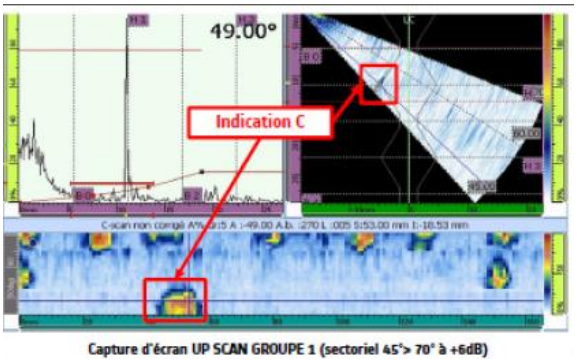

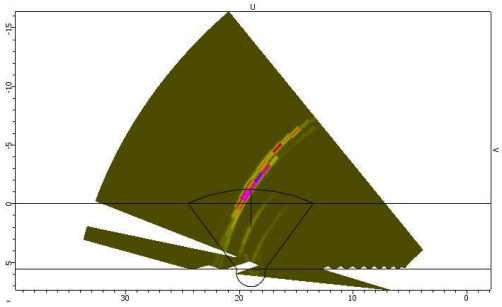

Figure 7: Planar defect perpendicular to the surface

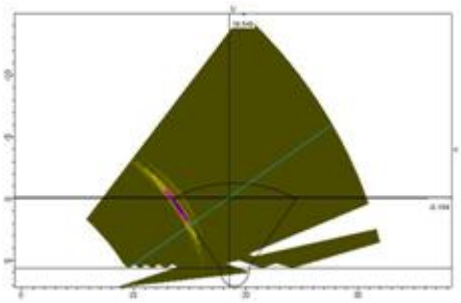

Figure 8: Planar defect in the chamfer

In addition, we developed:

- another group for monitoring coupling during the acquisition phase. This acquisition is performed with a sector scan, scanning from -6° to 6° with a criterion based on monitoring the background echo,
- specific criteria based on amplitude and location of indications in order to characterized them and apply acceptance criterias according frenc decree of march 1978.

5.1.4 Experience feedback

This method is already used regularly on projects abroad. The use of SCAN 13 has been validated by Lloyds (UK) and ASNT (USA). We can assert a relatively large amount of feedback concerning this inspection technique.

In the United States, 20 nuclear and conventional sites have already used this inspection method instead of radiography. Between 50 and 2200 tubes have been inspected per site.

In Portugal, this system is already widely used in production on the Alstom Portugal site. In total, more than 5000 tubes have been inspected by this method.

In France, we implemented this process during an outage that took place during the summer of 2012 on the site of Le Havre Tr4. During this overhaul the RHT was changed and we performed ultrasound inspections instead of radiography after EDF approbation of the qualification dossier.

608 welds were examined by the SCAN 13 method. EDF performed random X-ray shots on welds inspected using Scan 13 in order to confirm the results obtained by the ultrasonic method.

No differences were observed in this project. Some indications were reported with the scan 13 (classified as lack of fusion, ...) and repaired.

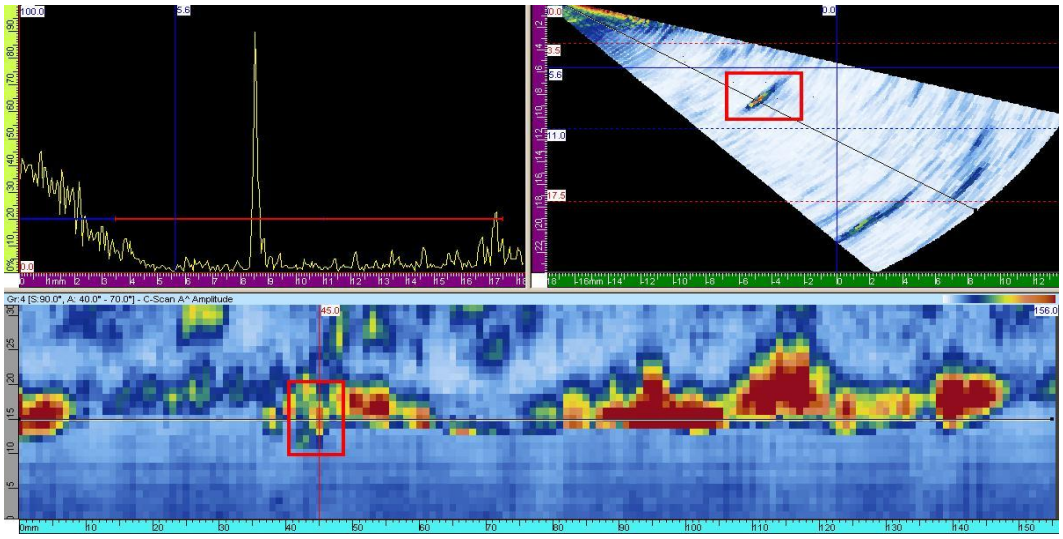

Figure 9: Lack of fusion

6 Conclusion

The technique developed by Alstom for the inspection of small diameter welds (**≤2.75"** and for a thickness of **≤8mm**) was developed and validated according to a study in several stages. Work on documentation, the study of plans, forecasting and evaluation of the most appropriate techniques helped define the outline and the principle of phased array ultrasonic technique. Then development also took place in several stages:

- ultrasound simulation to verify the original ideas using ESBeamTool 3 and CIVA;
- Experimental validation on scale models including artificial defects;
- validation on the Seabank Power Company project in Bristol (UK).

This last step was to verify that the new method performs much better than the usual technique because it allows us to characterize an indication by giving its length in a very short period of time.
In addition, the new technique is encoded which ensures repeatability of the measurement.
Finally, the inspection time can be reduced by using this device as compared to the use of radiographic examination. This technique allows complete inspection of a weld in less than 15 minutes (up to 60 welds inspected per day), whereas about several hours are required for a RT control.

In addition, it is important to emphasize that these examinations do not interfere with other projects.

In summary, semi-automation of the acquisition enables measurement repeatability and reproducibility, and so the impact of the human factor is strongly reduced.
Furthermore, the use of phased array technology assists in the analysis through the use of an imaging system instead of a simple A-scan type view. Finally, being able to overlay the plan of the part further enhances the comfort of the data analysis.

This technique is now implemented of the thermal power plant of EDF. To reach this, a complete qualification dossier with demonstration of performance, specific procedure and training program of the operators was approved from EDF.
Finally the benefits for the utility are:

- if necessary, checks can be made immediately without affecting the continuity of the site;
- operating time is reduced;
- signals are recorded and can be consulted later on request;
- indication sizing is now possible;
- monitoring equipment is easier;
- reduces operating and maintenance costs
- radioactive source management
- work in parallel

MULTI-POINT STRAIN MEASUREMENT USING FBG-OTDR OPTICAL FIBER SENSOR

K. Saruta Japan Atomic Energy Agency, Japan
T. Kobayashi, University of Fukui, Japan

Fiber Bragg grating optical fiber sensor based on optical time-domain reflectometry is proposed and experimentally demonstrated for multi-point strain measurement. All gratings have the identical reflection spectrum, thereby reducing the requirements for the bandwidth of the light source and overcoming the limitation on the number of gratings arrayed in a single optical fiber. Experimental results show that the presented method can measure strain with an rms error of 1.0 με for single grating measurement and 1.4 με for multi-point measurement using a 50 grating array.

1. Introduction

With increasing needs for safety and reliability, nuclear power plants are being driven to introduce structural health monitoring technologies [1]. Fiber Bragg gratings (FBG) are one of the promising sensor elements because they offer multi-point sensing capability with a high sensitivity and a superior spatial resolution [2]. A fiber Bragg gating is a periodic perturbation of the refractive index inscribed in the core of a single mode optical fiber. Such grating reflects a part of the incident light based on Bragg diffraction. The center wavelength of the reflected light is referred to as the Bragg wavelength and given by $\lambda_B = 2n_{eff}\,\Lambda$, where n_{eff} is the effective refractive index of the core and Λ is the grating period. Any change in strain and temperature results in a change in the grating period and effective refractive index. Consequently, strain and temperature applied to the grating can be measured by a shift in the Bragg wavelength.

A broadband light source and the wavelength division multiplex (WDM) technology are widely used to interrogate individual gratings in the sensor array [3]. In the FBG-WDM each grating is assigned a unique Bragg wavelength and spectrum range in which the Bragg wavelength shifts due to applied strain. Individual gratings are identified by the assigned Bragg wavelengths and their shifts are measured by means of spectrum analysis of the reflected light. To avoid overlapping the Bragg wavelengths, each grating exclusively occupies a specific spectrum range within the bandwidth of the light source. The number of gratings is in turn limited by the spectrum range assigned to the gratings and the bandwidth of the light source, typically limited up to several tens of gratings in a single optical fiber [3]. This number of gratings is insufficient to develop effective structural health monitoring systems by taking full advantage of multiplexing capability of grating sensors.

In this paper we report a design and experimental demonstration of FBG strain sensor based on optical-time domain reflectometry (OTDR) [4], which allows using gratings with the identical reflection spectrum, thereby reducing the requirements for the bandwidth of the light source and overcoming the limitation on the number of gratings arrayed in a single optical fiber. In the FBG-OTDR [5,6], short optical pulses alternately emitted from two single wavelength laser diodes are launched into the gratings. The reflectance of the gratings is sufficiently low so that the most of the incident power can pass through one grating and arrive at the others while suppressing cross talk caused by multiple reflections between gratings. Since each light source has a specific single wavelength, any change in the Bragg wavelength due to applied strain leads to a change in the power of the reflected pulse. The Bragg wavelength is then determined by a curve fit of the reflection spectrum of the gratings using the power of the reflected pulses. Individual gratings are identified by the time required for the reflected pulses to arrive at the detector. The FBG-OTDR can overcome the limitation on the number of gratings and enables strain measurement at more than several hundred sensing points with a high accuracy. In addition, the presented method does not need spectrum analysis to determine the Bragg wavelength. This shortens the measurement time and allows for real-time measurement.

2. Calculation of Bragg wavelength

In the FBG-OTDR the Bragg wavelength is calculated from the power of the reflected pulse. Assuming that the reflectance of a grating $r(\lambda)$ has a Gaussian profile, we can write the power of the reflected pulse as

$$P(\lambda) = P_0 r(\lambda) = P_0 R_{\max} \exp\left[-\frac{(\lambda - \lambda_B)^2}{2\sigma^2}\right] \quad (1)$$

where P_0 is the power of the incident pulse, $R_{\max}$ is the maximum reflectance of the grating, λ_B is the Bragg wavelength, and σ is the standard deviation of the Gaussian profile and is related to the linewidth $\Delta\lambda$ (FWHM) of the grating through $\sigma = \Delta\lambda/\left(2\sqrt{2\ln 2}\right)$. Taking a logarithm of the both sides, we can rewrite Eq. (1) as the following quadratic equation with respect to λ:

$$A\lambda^2 + B\lambda + C = \ln[P(\lambda)]. \quad (2)$$

The coefficients *A*, *B*, and *C* are decided by fitting Eq. (2) by means of the least square method to the reflected power $P(\lambda)$ measured at several different wavelengths. The parameters λ_B, $\Delta\lambda$, and $R_{\max}$ are then obtained by

$$\lambda_B = -B/2A, \quad (3A)$$

$$\Delta\lambda = 2\sqrt{\ln(1/2)/A}, \quad (3B)$$

$$R_{\max} = \frac{1}{P_0}\left(C - \frac{B^2}{4A}\right). \quad (3C)$$

If the linewidth and the maximum reflectance of the grating are given, the Bragg wavelength can be decided from the reflected power measured at two wavelengths.

3. System design

3.1 Configuration

The configuration of the FBG-OTDR system using two laser wavelengths is illustrated in Fig. 1. The gratings in the sensor array have the identical reflection spectrum; that is, all the gratings possess almost the same Bragg wavelength λ_B, the linewidth $\Delta\lambda$, and the maximum reflectance $R_{\max}$. The number of gratings is *N*, and the separation between adjacent gratings is ΔL. To interrogate the gratings two distributed feedback (DFB) laser diodes (LD) with the wavelength λ_1 and λ_2 are employed. These wavelengths are set away from the Bragg wavelength by a half linewidth of the grating in the shorter and the longer wavelength sides so that tensile and compressive strains are measured. Two LDs alternately emit short pulses at the repetition period T_{rep}, the pulse width of which is Δt. A small portion of the incident pulse is reflected at each grating and then detected by a photodiode. The output of the photodiode is amplified by an amplifier and then recorded by a data acquisition device.

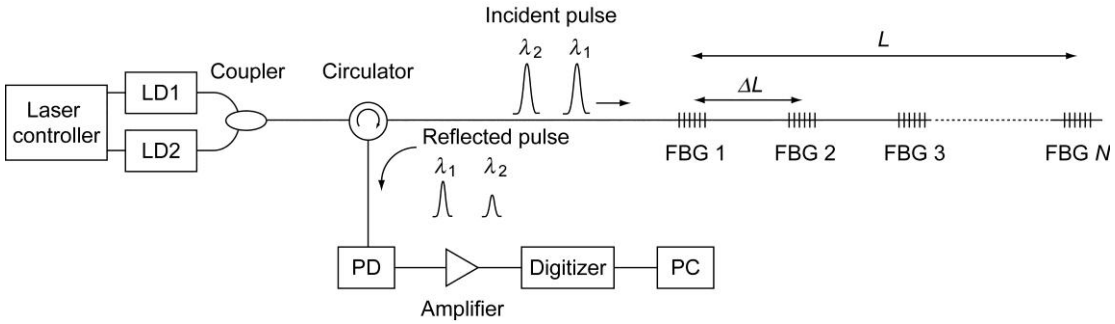

Fig. 1. Configuration of the FBG-OTDR optical fiber sensor.

As shown in Fig. 2, the reflected pulses for each LD arrive at the detector with a time difference $\Delta T = 2n_{eff}\Delta L/c$, where n_{eff} is the effective refractive index of the core of the optical fiber and c is the velocity of light in vacuum. Thus, individual gratings are identified by the arrival time of the corresponding reflected pulses. The Bragg wavelength of each grating is calculated using the corresponding pair of the reflected pulses obtained by LD1 and LD2 based on the algorithm described above in a personal computer.

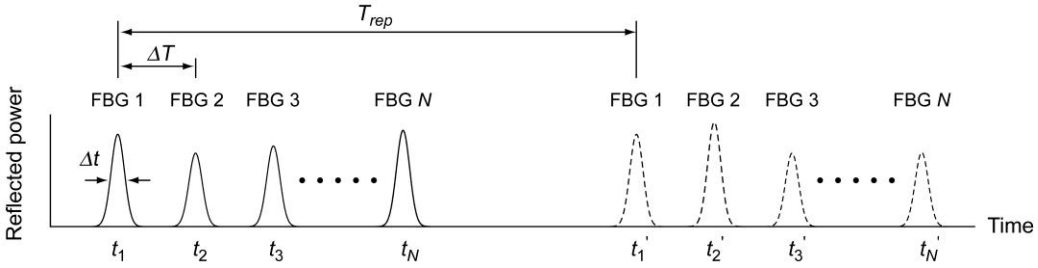

Fig. 2. Schematic of the reflected pulses.

3.2 System parameters

3.2.1 Separation of gratings

The minimum separation of the adjacent gratings is limited by the pulse width Δt of the LD pulse. To distinguish between the pulses reflected from the two adjacent gratings, the separation of gratings needs to satisfy $\Delta L \geq c\Delta t/2n_{eff}$. For instance, using the pulse width of our light source Δt = 4 ns and n_{eff} = 1.5, we have $\Delta L \geq$ 40 cm.

The spatial resolution of the FBG-OTDR system is determined by ΔL. A higher spatial resolution is achieved by narrowing the pulse width of the LD pulse. In a practical case, however, one can improve spatial resolution by simply arranging the gratings as close to each other as possible on a measurement object since the sensor array is flexible.

3.2.2 Repetition period

Repetition period T_{rep} is limited by the round trip time required for the reflected pulse from the farthest grating in the sensor array to reach the photodiode. In other words, T_{rep} is the delay required to avoid overlap of reflected pulses for LD1 and LD2 (see Fig. 2). When the distance between the first and the farthest gratings is L, the repetition period need to satisfy $T_{rep} \geq 2n_{eff}L/c$. Since our sensor array consists of 50 gratings separated by ΔL = 100 cm, then L = 49 m, leading to $T_{rep} \geq$ 0.49 μs.

The bandwidth of the FBG-OTDR system can be known from T_{rep}. It takes $2T_{rep}$ to interrogate all gratings in the sensor array. Thus, the basic bandwidth of the system is given by $1/4T_{rep}$ based on sampling theorem. If the reflection signals are averaged by m times, the bandwidth is accordingly reduced to $1/m$. In the experiment we set T_{rep} = 0.6 μs and average the reflection signals by 100 times. The actual bandwidth is approximately 4 kHz.

3.2.3 Measurement range of strain

The measurement range of strain is proportional to the linewidth of the grating and is calculated by dividing the linewidth by the strain sensitivity of the grating. The strain sensitivity is the proportional coefficient of the Bragg wavelength shift to applied strain and is experimentally found to be 1.44 pm/με for our system. We employ the linewidth of 0.77 nm in the experiment; the measurement range is calculated to be approximately $\pm$267 με.

3.3 Number of gratings and cross talk error

The incident pulse propagating in the sensor array is partially reflected at *N*-1 gratings before reaching the *N*th grating, and the reflected pulse also undergoes the same partial reflection in the return path to the detector. As a result, the reflected pulse of *N*th grating suffers the multiple reflections by the preceding *N*-1 gratings. Such multiple reflections potentially cause cross talk and consequently increase measurement error. Therefore, the cross talk should be taken into account in order to decide the maximum number of gratings in a single sensor array. The reflected power of *N*th grating is expressed as

$$P_N(\lambda) = P_0 r_N(\lambda) \prod_j^{N-1} [1 - r_j(\lambda)]^2. \quad (4)$$

As is evident by comparison with Eq. (1), the effect of the cross talk is determined by the third factor. Since it has the maximum of unity, the most significant cross talk will occur when it takes the minimum at $r_j(\lambda) = R_{\max}$. This means that all gratings except for the *N*th grating which is subject to the cross talk align at the same Bragg wavelength even after any strain is exerted on them. In this case Eq. (4) is expressed as

$$P_N(\lambda) = P_0 r_N(\lambda)(1 - R_{\max})^{2(N-1)}. \quad (5)$$

It is apparent from Eq. (5) that the cross talk depends on both the number of gratings *N* and the maximum reflectance $R_{\max}$ of the gratings.

Figure 3 shows the estimation of the cross talk error as a function of number of gratings and maximum reflectance. The cross talk error increases with increasing number of gratings, whereas it decreases with decreasing maximum reflectance. Therefore the use of low reflectance gratings is required in order to avoid significant cross talk. We employ 50 gratings with $R_{\max}$ = -36 dB. In the worst case the cross talk error can be $\pm$2.9 με. In the experiment we use cantilever configuration for multi-point measurement. In this case the Bragg wavelength distributes according to strain distribution generated on the cantilever. The expected cross talk error is $\pm$1.9 με. As is expected from this experimental case, actual cross talk will be further reduced in a typical case.

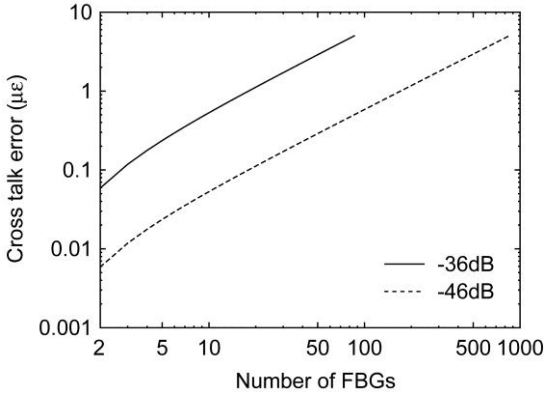

Fig. 3. Dependence of cross talk error on the number of gratings and the maximum

4. Experimental

The experimental setup to demonstrate the FBG-OTDR system is the same as shown in Fig. 2. The light sources are two DFB LDs with a power of 100 mW, which alternately emit short pulse light with a pulse width of 4 ns at a repetition period of 0.6 μs. The wavelengths of the LD1 and LD2 are set to 1549.62 and 1550.39 nm, respectively. The sensor array consists of 50 gratings with the maximum reflectance $R_{\max}$ = -36 dB, the linewidth $\Delta\lambda$ = 0.77 nm, and the Bragg

wavelength λ_B = 1550.00 nm. As shown in Fig. 4, the gratings are arranged in 5 rows on a cantilever (SUS304, 500 mm × 25 mm × 2 mm) in a way that the following gratings are placed on the next row. Resulting interval between adjacent gratings is 9 mm on the cantilever. One end of the cantilever is fixed and the other end is pushed down by a micrometer to generate strain distribution over the sensor array. The deflection of the cantilever is measured by a dial gauge placed under the cantilever. A strain gauge is also used to calibrate the strain sensitivity of the grating and as a reference for comparison. In the experiment the reflection signals are averaged by 100 times to obtain the signal to noise ratio greater than 20 dB.

Figure 5 shows an example of the signals reflected from 50 gratings. The first and the second groups of the reflection signals are obtained by LD1 and LD2, respectively. The reflection signals in each group are separated by 10 ns in accordance with the separation of gratings $\Delta L = 100$ cm. Since each reflection signal is detected at a fixed time corresponding to the position of the grating, individual gratings are clearly identified in time-domain. The signal voltage varies depending on the strain applied to the gratings.

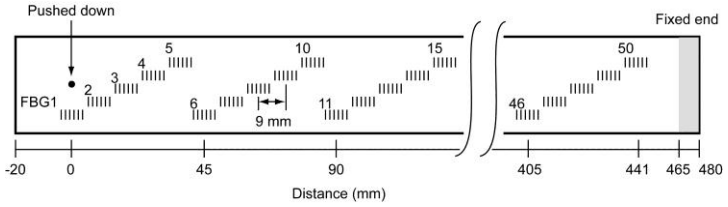

Fig. 4. Arrangement of FBGs on the cantilever.

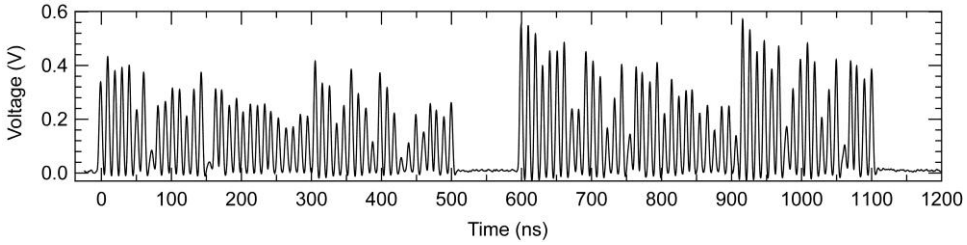

Fig. 5. Reflection signals of the 50 FBG array.

We have calibrated the strain sensitivity of the grating by measuring the Bragg wavelength shift as a function of applied strain. As a result the strain sensitivity was found to be 1.44 pm/με. This value was employed to convert the Bragg wavelength shift to the corresponding strain for all gratings in the sensor array.

To examine the measurement error free of the influence of the cross talk, strain measurement using a single grating was carried out. The measurement result compared with the strain gauge is shown in Fig. 6. The FBG measurement is in good agreement with the strain gauge measurement and shows a good linearity with respect to the deflection of the cantilever. The rms error and maximum error of the measurement are 1.0 and 2.2 με with reference to the strain gauge measurement, respectively. In the figure although tensile strain was measured up to around 275 με, compressive strain can also be measured up to the same value, resulting in the measurement range of approximately ±275 με, which is close to the theoretical measurement range of ±267 με, described in Section 3.

To demonstrate the capability for multi-point measurement, strain distribution generated on the cantilever was measured by 50 gratings at 9 mm interval. The result is shown in Fig. 7. The experimental data agrees well with the theoretical line, though one may notice that the deviation from the line tends to become relatively larger in the gratings deployed near the end of the sensor array. This can be understood as an effect of the cross talk illustrated in Fig. 3. A comparison of the grating measurement with the theoretical value shows the rms error of 1.4 με and the maximum error of -3.6 με. Compared with the single grating case, the measurement error becomes slightly larger mainly due to the cross talk, although the difference is not significant. This indicates that the contribution of the cross talk to the measurement error can be negligible.

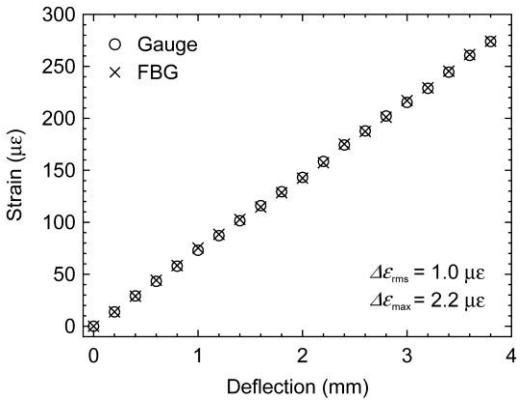

Fig. 6. Strain measurement result for a single FBG.

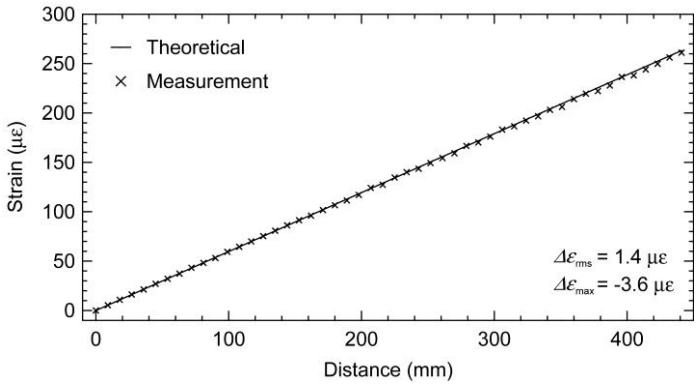

Fig. 7. Multi-point strain measurement result for the 50 FBG array.

5. Discussion

We consider the requirements for increasing the number of gratings multiplexed in a single optical fiber. The measurement error for the single grating measurement is considered as the minimum measurement error which our system can achieve when the cross talk does not take place. We obtained the maximum error of 2.2 με for the single grating case. The error induced by the cross talk must be smaller than at least this value to suppress its contribution to measurement error as small as possible. The experimental results show that the difference in the measurement error between the single grating measurement and the multi-point measurement is not significant despite the fact that the cross talk error is expected to be 1.9 με as mentioned in Section 3. Based on these findings, if the cross talk error is suppressed less than 1.9 με, the number of gratings can be increased without introducing additional errors from the cross talk effect. In the worst case illustrated in Fig. 3, the cross talk error can reach 1.9 με when the number of gratings is increased up to around 30 for the maximum reflectance of -36 dB. However, if the gratings with the maximum reflectance of -46 dB are employed, the number of gratings can be increased to more than 300 while the cross talk error is still below 1.9 με.

Using such low reflectance gratings, on the other hand, we also need to allow for the power of the light source because of a reduction of the power reflected from the gratings. Figure 8 shows the calculated power of the reflection signal as a function of number of gratings for the maximum reflectance of -46 dB. In the calculation a structural loss of 0.01 dB at each grating and a splice loss of 0.01 dB for every 100 gratings are assumed as practical conditions. The horizontal dotted lines indicate the minimum signal power required to yield a signal-to-noise ratio of 20 dB when the reflection signal is averaged by $m = 10^2$ and 10^4 times. This minimum signal power is calculated from the noise equivalent power of the detector used in the experiment. At the light source power of 100 mW, only several ten gratings are detectable if the signal is averaged by 10^2 times, though more than 300 gratings can be detected by increasing the number of averages up to 10^4. Alternatively if the power of the light source is increased to

1000 mW, by using an Er-doped fiber amplifier for example, the same number of the reflection signals can be measured even though the signal is averaged by 10^2 times. Use of a high power light source is more practical because of short measurement time. From these arguments it is expected that the number of gratings can be increased up to 300 without introducing significant cross talk error to the measurement when we employ gratings with the maximum reflectance of -46 dB and a 1000-mW light source.

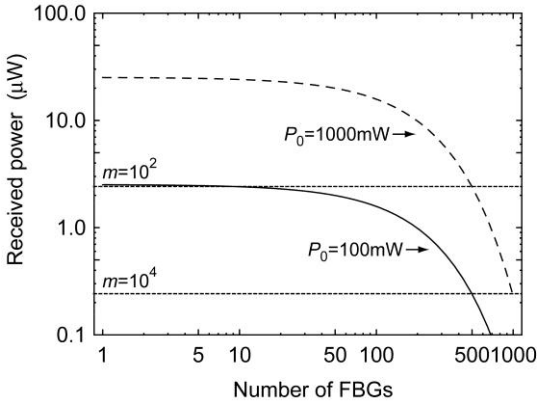

Fig. 8. Received power as a function of number of gratings for the maximum reflectance of -46 dB.

6. Summary

We have developed the FBG-OTDR optical fiber sensor, in which gratings with the identical reflection spectrum are used and the Bragg wavelength is calculated by a curve fit of the reflection spectrum of the gratings using the power of the reflected pulses measured with two laser wavelengths. We have demonstrated the strain measurement for the 50 grating array with the maximum reflectance of -36 dB. A comparison of the FBG-OTDR measurement with strain gauge measurement shows that the FBG-OTDR optical fiber sensor can measure strain with an rms error of 1.0 με over a measurement range of ± 275 με in a case of single-point measurement where the cross talk does not take place. The result of multi-point measurement indicates that an rms error of 1.4 με can be achieved when the cross talk is suppressed as small as possible with respect to the measurement error for the single-point measurement. Although the multi-point measurement was conducted only for 50 gratings, we shows that the number of sensing points can be increased up to 300 by increasing the power of the light source to 1000 mW and decreasing the maximum reflectivity of the gratings to -46 dB. It is our expectation that the FBG-OTDR optical fiber sensor will contribute to the structural health monitoring technology for nuclear power plants.

References

1) Matsuba K, Ito C, Kawahara H, and Aoyama T, “Development of fast reactor structural integrity monitoring technology using optical fiber sensors”, J Power Energy Syst 2008 **2** (2) 545–56.
2) Majumder M, Gangopadhyay T K, Chakraborty A K, Dasgupta K, and Bhattacharya D K, “Fibre Bragg gratings in structural health monitoring—Present status and applications”, Sensor Actuat A-Phys, 2008 **147** (1) 150–64.
3) Kersey A, Davis M A, Patrick H J, Leblanc M, Koo K P, Askins C G, Putnam M A, and Friebele E J, “Fiber grating sensors”, J Lightwave Technol 1997 **15** (8) 1442–63.
4) Barnoski M K, Rourke M D, Jensen S M, and Melville R T, “Optical time domain reflectometer”, Appl Opt 1977 **16** (9) 2375–9.
5) Kobayashi T, Enami Y, and Iwashima H, “Higly accurate fiber strain sensor based on low reflective fiber Bragg gratings and fiber Fabry-Perot cavities”, Optical fiber sensors, Cancún, Mexico, Optical Society of America, 2006.
6) Enami Y, Iwashima H, and Kobayashi T, “Fiber strain sensor using low reflective fiber Bragg gratings”, Conf Lasers and Electro-Optics/Quantum Electronics and Laser Science and Photonic Applications Systems Technologies, Baltimore, Optical Society of America, 2005.

FLAW GROWTH EVALUATION FOR DEEP SURFACE FLAW BASED ON FFS CODE PROCEDURE

F. Iwamatsu, K. Miyazaki, Hitachi Research Laboratory, Hitachi, Japan
M. Mochizuki, Osaka University, Japan

ABSTRACT

Rational and applicable flaw evaluation based on a fitness-for-service code is required due to ongoing developments in NDT techniques. In this study, SCC growth evaluation under several stress distributions was conducted using a conventional code procedure, a proposed code procedure, and a detailed finite element analysis method.

In-service inspection including evaluation for nuclear power plants was conducted on the basis of a fitness-for-service code, such as the ASME Boiler and Pressure Vessel Code Section XI. In flaw evaluation based on ASME Section XI, an aspect ratio of a detected surface flaw is defined by a/ℓ, where a is the flaw depth and ℓ is the flaw length, and the aspect ratio a/ℓ is limited up to 0.5. Therefore, a deep surface flaw, which has an aspect ratio a/ℓ greater than 0.5, is characterized as a semicircle with ℓ equal to $2a$. Meanwhile, deep surface flaws caused by stress corrosion cracking (SCC) were detected in Ni based alloy weld metal by the NDT technique. Since the limit of the flaw characterization rule seems to lead to conservative evaluation results for a deep surface flaw, more rational and applicable flaw evaluation is required to eliminate surplus conservatism. Therefore, in this study, flaw growth evaluation was conducted using a conventional code procedure, a proposed code procedure to deal with a deep surface flaw shape, and a detailed finite element analysis method. Since detection of deep surface flaws are assumed in Ni based alloy weld metal, a deep initial flaw caused by SCC and anisotropic SCC growth rates was considered in flaw growth evaluation. Membrane, bending, and residual stress distributions were assumed. Comparisons of these results show the applicability and effectiveness of flaw growth evaluation beyond current code limits.

INTRODUCTION

SCC has been detected in welded components of nuclear power plants[1)]. The detected surface flaw is characterized by a semi-ellipse for analytical evaluation in Fitness-for-Service (FFS) Code, such as ASME Section XI[2)], to calculate flaw growth until the next inspection or the end of service lifetime of the component. In the flaw evaluation based on ASME Section XI, an aspect ratio of a surface flaw is represented by a/ℓ, where a is the flaw depth and ℓ is the flaw length. To calculate stress intensity factors (SIFs), which are parameters affecting flaw growth evaluation, influence coefficients are prescribed for a/ℓ is from 0.0 to 0.5. Therefore, the aspect ratio of the characterized surface flaw shall not exceed 0.5. Some FFS Code prescribes a flaw evaluation procedure similar to that in ASME Section XI. API 579-1/ASME FFS-1—Fitness-for-Service[3)] (API/ASME) prescribes equations to calculate SIFs up to a/ℓ equal to 1.0 for a surface flaw in a plate under membrane or bending stresses.

Therefore, a deep surface flaw, which has aspect ratios a/ℓ greater than 0.5, is characterized in accordance with a limit of each flaw characterization rule. Meanwhile, deep surface flaws beyond these limits caused by SCC have been detected in the Ni based alloy weld metal by a NDT technique, such as an ultrasonic test. Therefore, more rational and applicable flaw evaluation is required for a deep surface flaw. The authors have proposed influence coefficients to calculate SIFs for surface flaws and summarized them as a tabular form on the basis of equations prescribed in ASME Section XI [4].

In this study, to verify applicability and effectiveness of proposed coefficients, flaw growth evaluation was conducted on the basis of ASME Section XI, API/ASME, proposed coefficients, and a detailed FEA method[5]. Since detection of deep surface flaws is assumed in Ni based alloy weld metal, a deep initial flaw caused by SCC and anisotropic SCC growth rates was considered in flaw growth evaluation. Membrane, bending and residual stress distributions were assumed. Comparisons of these results show the applicability and effectiveness of flaw growth evaluation beyond current code limits.

SIF SOLUTIONS BASED ON CODES

Generally, since flaw growth rates due to SCC or fatigue are represented as a function of SIF, flaw growth evaluation requires calculation of SIFs. In accordance with the ASME Section XI procedure, a detected surface flaw with an aspect ratio a/ℓ over 0.5 is characterized as a semicircle flaw with ℓ equal to $2a$ as shown in Fig. 1. Stress distribution σ on the surface flaw as driving force is represented by the third order polynomial.

$$\sigma = A_0 + A_1\left(\frac{x}{a}\right) + A_2\left(\frac{x}{a}\right)^2 + A_3\left(\frac{x}{a}\right)^3 \tag{1}$$

where x is distance in the flaw depth direction from flawed surface as shown in Fig. 2, and A_0 through A_3 are constants depending on stress distribution. SIFs at the deepest and surface points (points 1 and 2 in Fig. 2, respectively) are calculated in accordance with the following equation for a characterized surface flaw.

$$K = \left[\left(A_0 + A_p\right)G_0 + A_1G_1 + A_2G_2 + A_3G_3\right]\sqrt{\pi a/Q} \tag{2}$$

where A_p is internal pressure loading on the flaw surface and G_0 through G_3 are influence coefficients depending on a/t and a/ℓ (Coefficients G). Coefficients G are can be obtained from Tables A-3320-1 and A-3320-2 in the ASME code for a surface flaw with an aspect ratio a/ℓ between 0.0 and 0.5. The flaw shape parameter Q is calculated in accordance with the following equation.

$$Q = 1 + 4.593\left(\frac{a}{\ell}\right)^{1.65} \tag{3}$$

Eqs. (1) through (3) enable calculation of SIFs for an arbitrary semi-elliptical flaw shape with an aspect ratio a/ℓ between 0.0 and 0.5. To evaluate flaw growth behavior of a deep surface flaw, the application range of coefficients G should be extended to an aspect ratio over 0.5. Also, the flaw shape parameter Q should be converted into the following equations.

$$Q = 1 + 4.593\left(\frac{a}{\ell}\right)^{1.65} \quad for\ a/\ell \le 0.5$$
$$Q = 1 + 0.4663\left(\frac{\ell}{a}\right)^{1.65} \quad for\ a/\ell > 0.5 \tag{4}$$

To extend flaw growth evaluation for a deep flaw, coefficients G should be evaluated by a series of FEA depending on flaw sizes a/t and a/ℓ. Therefore, the authors have proposed coefficients G to calculate SIFs for surface flaws with an aspect ratio a/ℓ up to 4.0 and summarized them as a tabular form on the basis of equations prescribed in ASME Section XI. Several example problems are required to verify the applicability and effectiveness of proposed coefficients G.

API/ASME prescribes the equations to calculate SIFs for a surface flaw in a plate under membrane and bending stresses with an aspect ratio a/ℓ between 0.0 and 1.0. Stress distribution σ on the surface flaw as driving force is represented by the fourth order polynomial.

$$\sigma = A_0 + A_1\left(\frac{x}{t}\right) + A_2\left(\frac{x}{t}\right)^2 + A_3\left(\frac{x}{t}\right)^3 + A_4\left(\frac{x}{t}\right)^4 \tag{5}$$

where t is thickness of a plate. Equivalent membrane and bending stress distribution, σ_m and σ_b, respectively, are in accordance with the following equation.

$$\sigma_m = A_0 + \frac{A_1}{2} + \frac{A_2}{3} + \frac{A_3}{4} + \frac{A_4}{5} \tag{6}$$

$$\sigma_b = -\frac{A_1}{2} - \frac{A_2}{2} - \frac{9}{20}A_3 - \frac{6}{15}A_4 \tag{7}$$

SIFs on the flaw tip are calculated in accordance with the following equation.

$$K = \left[M_m\left(\sigma_m + p_c\right) + M_b\sigma_b\right]\sqrt{\pi a/Q} \tag{8}$$

where p_c is internal pressure loading on the flaw surface and the same as A_p in Eq. (2). M_m and M_b can be determined using equations. Q is the same as Eq. (4).

FLAW GROWTH EVALUATION USING FEA

Since it is difficult to conduct fatigue or SCC growth tests while maintaining a deep flaw shape up to the end of a test, flaw evaluation using FEA that enables flaw growth behavior to represent an arbitrary flaw shape was conducted for comparison with flaw growth evaluation based on code procedures. Flaw evaluation using FEA required repeated calculation considering flaw growth behavior, which means that an FE model considering a flaw shape has to be generated for each analytical step. Moreover, hundreds of analytical steps are needed to obtain accurate results. Therefore, the authors have proposed automatic flaw growth evaluation using the developed program and commercial software (FEA method). In evaluations using the FEA method, three-dimensional FE models considering the arbitrary planer flaw shape are automatically generated using the program in Visual Basic. SIFs are calculated using a commercial FEA program ABAQUS for generated FE models. The FEA method enables SIFs to be calculated on each flaw tip node and arbitrary planer flaw shapes to be estimated under

complicated stress distribution as shown in Fig. 3. Therefore, accurate SIFs calculated for a flaw with an aspect ratio a/ℓ over code limits.

ANALYTICAL CONDITIONS OF FALW GROWTH EVALUATION

To verify applicability and effectiveness of proposed coefficients G to flaw growth evaluation, SCC growth behaviors under membrane, bending, and residual stress distributions were evaluated on the basis of ASME Section XI, API/ASME, proposed coefficients G, and a detailed FEA method. Analytical conditions are as follows.

Initial flaw: A flaw model assumed a semi-elliptical flaw in a plate as shown in Fig. 2. Initial flaw depth a_0, was 1.0 mm, initial flaw length ℓ_0 was 0.2 mm, and thickness of a plate t was 10.0 mm. The initial aspect ratio a_0/ℓ_0 is 5.0 and flaw deep ratio a_0/t is 0.1. The initial aspect ratio a_0/ℓ_0 exceeds the limits of procedures, which are 0.5 in ASME Section XI, 1.0 in API/ASME, and 4.0 in proposed coefficients G. Therefore, the initial flaw length is expanded on the basis of each aspect ratio limit except the FEA method. In evaluation using the procedures except the FEA method, a semi-elliptical flaw shape is applied during flaw growth evaluation in accordance with the flaw characterization rule. In an evaluation using the FEA method, an arbitrary flaw shape is defined on the basis of flaw extension at each flaw tip node as shown in Fig. 3.

Stress distribution: Membrane, bending, and residual stress fields were assumed for flaw growth evaluation. Each stress distribution is represented as follows and shown in Fig. 4.

$\sigma = 300$ (Membrane)

$\sigma = 300 - 300(x/t)$ (Bending)

$\sigma = 470.0 - 3512.1(x/t) + 7182.7(x/t)^2 - 4018.3(x/t)^3$ (Residual stress)

Note that the bending stress field is not exactly pure bending but includes membrane stress. Residual stress field was considered with 100 MPa membrane stress as applied stresses from all forms of loading.

Calculation of SIFs: SIF, K, is calculated using coefficients G, equations, and the FEA method as described above.

Flaw growth rate: In consideration of deep surface flaws in the Ni based alloy weld metal caused by SCC, a SCC growth rate was applied for a Ni base alloy in a BWR environment with normal water chemistry[2)]. The applied SCC growth rate in a flaw depth direction is represented as follows and shown in Fig. 5.

$$\begin{aligned} \frac{da}{dt} &= 8.92\times10^{-14}K^{2.5} \quad \text{for} \quad K \le 27.5 \\ \frac{da}{dt} &= 3.53\times10^{-10} \quad \text{for} \quad K > 27.5 \end{aligned} \tag{9}$$

where t is time. A unit of da/dt is m/s. The 1/10 SCC growth rate in Eq. (5) was assumed in a flaw length direction. Anisotropic SCC growth rates are assumed to maintain a deep flaw shape for as long as possible during flaw growth evaluation. Time increments Δt were set to 0.01 years for evaluation using G values and within 0.1 years for evaluation using the FEA method to calculate flaw extension Δa for a step.

RESULTS OF FLAW GROWTH EVALUATION

Flaw growth evaluation was conducted on the basis of ASME Section XI, API/ASME, proposed coefficients *G*, and a detailed FEA method. Flaw growth behaviors until flaw depth *a* reached 8 mm, which means that flaw depth ratio *a*/*t* reaches 0.8, were obtained from each evaluation. Results of flaw growth evaluation for a deep surface flaw under membrane, bending, and residual stress distributions are shown in Tables 1 through 3 and Figs. 6 through 8. These figures compare of flaw depth versus time and SIF versus flaw depth ratio. As described above, the FEA method enables flaw growth evaluation to represent arbitrary planer flaw shapes. Therefore, flaw depth and length should be defined for an arbitrary planer flaw shape. In this study, flaw depth was defined as the distance from the flawed surface at the deepest node and flaw length as the length on the flawed surface.

Evaluation results for membrane stress distribution are shown in Table 1 and Fig. 6. Evaluated times differ depending on evaluation procedures, especially the time evaluated by the FEA method, which is over 10 times that evaluated by the ASME Section XI procedure. Since an aspect ratio a/ℓ is limited up to 0.5 in the ASME Section XI procedure, a flaw length with an aspect ratio a/ℓ exceeding 0.5 is expanded into $2a$. The initial SIF at the deepest point by the ASME Section XI procedure is over seven times that by the FEA procedure. In addition, flaw growth rate is represented as a function of the 2.5th power of SIF as shown in Eq. (9) in this evaluation. An aspect ratio limit has a significant effect on flaw growth evaluation in this case. SIFs at the end of evaluation calculated by the API/ASME procedure are approximately 20% different in regard to the FEA method, which caused over 10 years difference in evaluated times. Although SIFs by proposed coefficients *G* roughly correspond with those by the FEA method as shown in Fig. 6(b), evaluated times are about four years different.

Evaluation results for bending stress distribution are shown in Table 2 and Fig. 7. Evaluated times also differ depending on evaluation procedures, especially the time evaluated by the FEA method, which is over six times that evaluated by the ASME Section XI procedure. Although tendencies of SIFs calculated using API/ASME, proposed *G*, and FEA seem to correspond totally, differences in SIFs while the flaw is small remarkably affect the evaluated times. Because the evaluated time until the flaw depth reaches 2 mm was more than half the total time until the flaw depth reaches 8 mm in the cases of proposed *G* and FEA, the flaw characterization for the initial flaw is primarily of importance.

Evaluation results for bending stress distribution are shown in Table 3 and Fig. 8. The flaw depth evaluated by API/ASME did not propagate to 8 mm in 60 years. From Eqs. (6) and (7), equivalent membrane and bending stresses, σ_m and σ_b, are approximately 104 MPa and -27 MPa, respectively. These equivalent stresses seem to be underestimated for the assumed residual stress distribution. In this case, the polynomial approximation of the stress distribution would be appropriate and API/ASME also specifies the evaluation procedure using the polynomial approximation. Note that the aspect ratio limit for the polynomial approximation in API/ASME is the same as that in ASME Section XI: a/ℓ is limited up to 0.5. The evaluated results obtained by ASME Section XI, proposed *G*, and FEA were compared as described below. Evaluated time until the flaw depth reaches 8 mm relatively corresponds to results for membrane and bending stresses.

Since the residual stress is sharply decreased adjacent to the flawed surface as shown in Fig. 4, the flaw growth rate at the surface point while the small flaw is relatively higher. Therefore, the aspect ratio is sharply changed into the semicircle flaw, and the effect of deference of SIFs for the small flaw is not significant.

Although it is difficult to conduct fatigue or SCC flaw growth tests while maintaining a deep flaw shape up to the end of a test, the detailed FEA method obtained the most accurate results for the flaw growth evaluation. Therefore, it is verified that the code procedure including the application range is expanded into the deep flaw shape generally obtaining the conservative results for the flaw growth evaluation. From the comparison evaluation results between conventional code and proposed *G* to deal with a deep surface flaw shape, the expansion of the application range of the aspect ratio enables rational and applicable flaw evaluation.

SUMMARY AND CONCLUSIONS

Rational and applicable flaw evaluation based on a fitness-for-service code is required due to the ongoing developments in NDT techniques. SCC growth evaluation under several stress distributions was conducted using a conventional code procedure, a proposed code procedure, and a detailed finite element analysis method. The results are summarized as follows:

(a) It is verified that the code procedure including the application range is expanded into the deep flaw shape generally obtaining conservative results for the flaw growth evaluation.

(b) The expansion of the application range of the aspect ratio enables rational and applicable flaw evaluation.

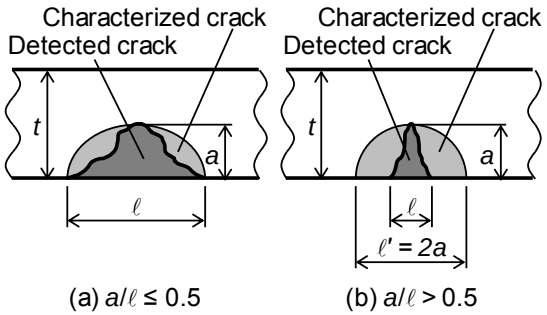

Figure 1 Flaw characterization in ASME Section XI

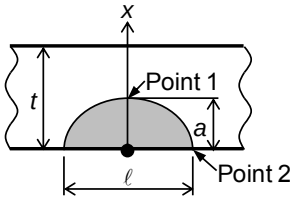

Figure 2 Schematic of characterized surface flaw

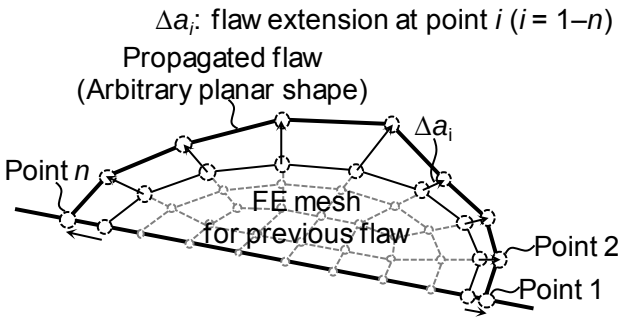

Figure 3 Renewal of flaw shape using FEA method

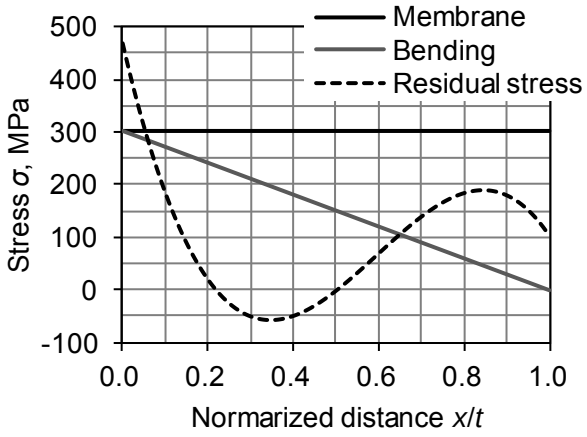

Figure 4 Assumed stress distributions for flaw growth evaluation

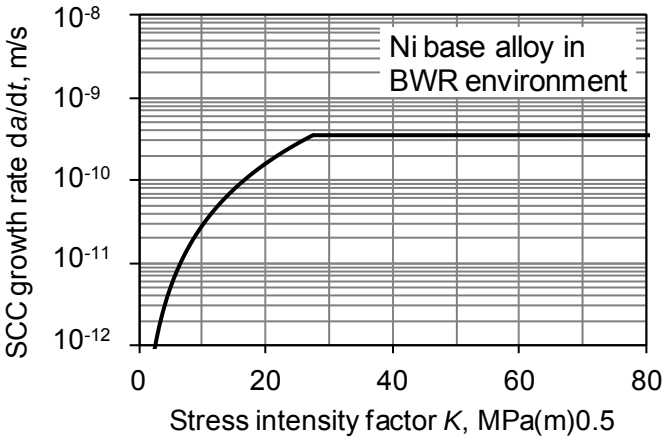

Figure 5 SCC growth rate for Ni base alloy in BWR environment[2)]

Table 1 Results of flaw growth evaluation for membrane stress distribution

	Initial conditions				Results of evaluation				
	a_0, mm	ℓ_0, mm	K, MPa(m)$^{0.5}$		t, year	a, mm	ℓ, mm	K, MPa(m)$^{0.5}$	
			Deepest point	Surface point				Deepest point	Surface point
ASME	1.00	2.00	11.1	12.3	1.4	8.09	16.17	33.6	45.1
API/ASME	1.00	1.00	7.1	11.0	4.3	8.04	8.04	20.2	34.7
Coef. G	1.00	0.25	2.0	6.4	10.6	8.03	6.27	17.3	31.5
FEA	1.00	0.20	1.5	4.9	14.5	8.03	6.54	16.6	30.1

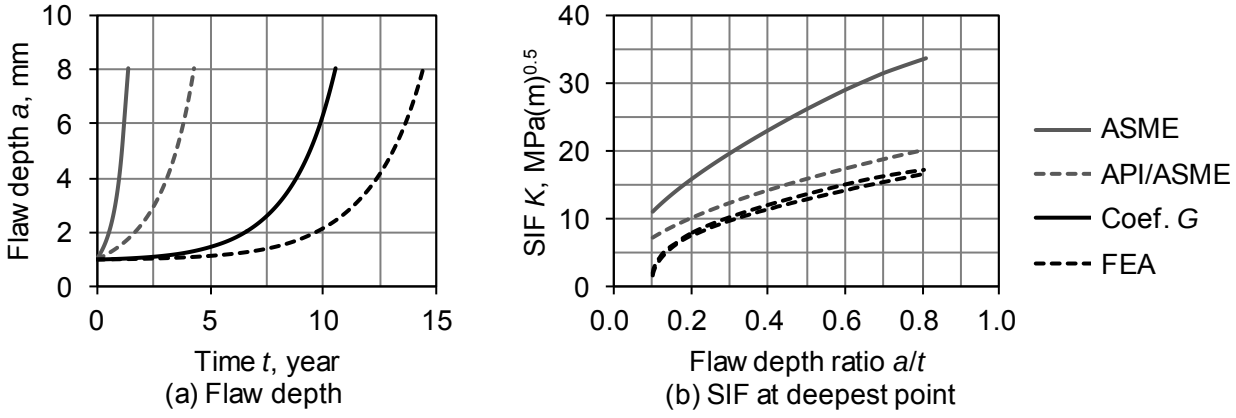

Figure 6 Transition of flaw growth under membrane stress distribution

Table 2 Results of flaw growth evaluation for bending stress distribution

	Initial conditions				Results of evaluation				
	a_0, mm	ℓ_0, mm	K, MPa(m)$^{0.5}$		t, year	a, mm	ℓ, mm	K, MPa(m)$^{0.5}$	
			Deepest point	Surface point				Deepest point	Surface point
ASME	1.00	2.00	10.3	12.1	2.8	8.02	16.04	14.5	37.6
API/ASME	1.00	1.00	6.5	10.9	8.8	8.00	11.52	10.6	32.7
Coef. G	1.00	0.25	1.8	6.3	14.2	8.00	11.32	10.7	33.7
FEA	1.00	0.20	1.4	4.9	18.5	8.02	11.49	10.9	33.8

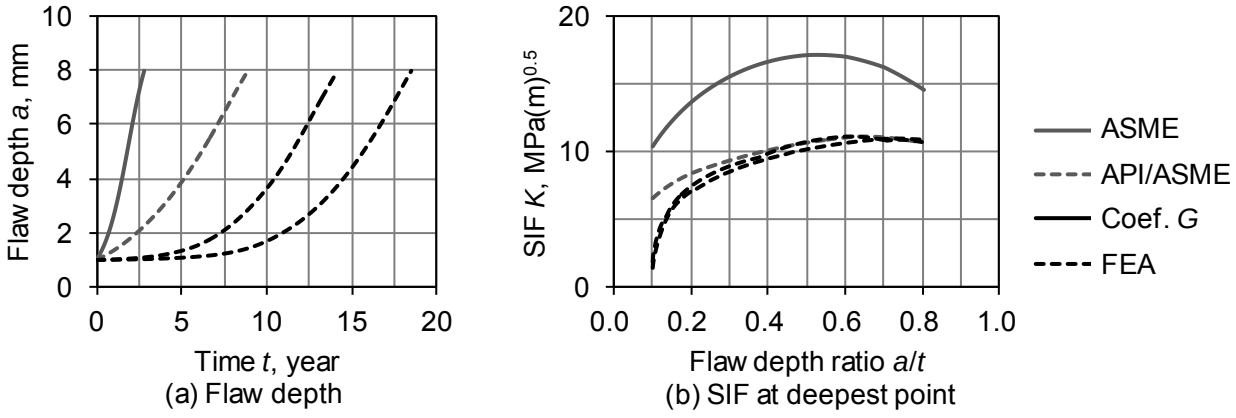

Figure 7 Transition of flaw growth under bending stress distribution

Table 3 Results of flaw growth evaluation for residual stress distribution

	Initial conditions				Results of evaluation				
	a_0, mm	ℓ_0, mm	K, MPa(m)$^{0.5}$		t, year	a, mm	ℓ, mm	K, MPa(m)$^{0.5}$	
			Deepest point	Surface point				Deepest point	Surface point
ASME	1.00	2.00	9.6	17.1	16.6	8.00	32.03	17.2	33.5
API/ASME*	1.00	1.00	1.9	2.8	> 60.0	(2.95)	(2.95)	(3.7)	(5.0)
Coef. G	1.00	0.25	1.3	9.5	20.4	8.00	32.03	17.2	33.5
FEA	1.00	0.20	1.0	7.5	22.1	8.12	31.41	15.5	32.0

* Flaw did not propagate to 8 mm in 60 years

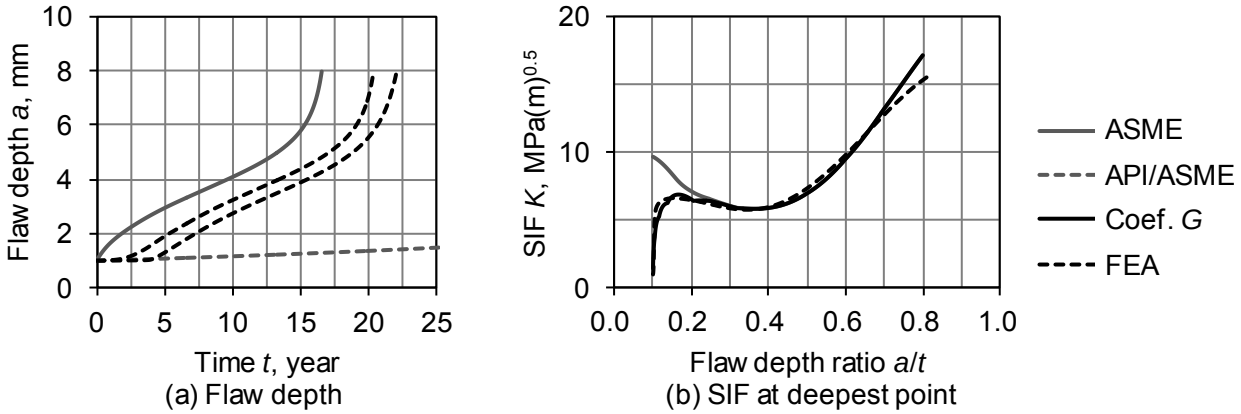

Figure 8 Transition of flaw growth under residual stress distribution

REFERENCES

1) T. Fujino, T. Terakado, K. Dozaki, N. Ito and K. Hasegawa “Crack Growth Behavior and Preventive Maintenance for Reactor Internals with Cracks in Tokai-2 Nuclear Power Plant”, ASME 2013 PVP Conference, Paris, France, 2013.

2) The American Society of Mechanical Engineers, 2010 BPVC Section XI, Rules for Inservice Inspection of Nuclear Power Plant Components, 2010.

3) American Petroleum Institute and the American Society of Mechanical Engineers, API 579-1/ASME FFS-1-Fitness-for Service, 2007.

4) F. Iwamatsu, K. Miyazaki, H. Miyata and H. Yuya, “Application of Stress Intensity Factors for Deep Surface Cracks to Crack Growth Evaluation”, ASME 2013 PVP Conference, Paris, France, 2013.

5) F. Iwamatsu, K. Miyazaki and M. Mochizuki, “Estimation of SCC Crack Growth Behavior under Weld Residual Stress in the Bottom of a Reactor Pressure Vessel by Finite Element Analysis”, ASME 2012 PVP Conference, Toronto, Canada, 2012.

ND-CHARACTERIZATION OF AGEING PHENOMENA - DEVELOPMENT OF SENSORS FOR ISI AND SHM

G. Dobmann, Fraunhofer-IZFP, Germany

Abstract

So far materials are ferromagnetic - as the most of the structural steels – micro magnetic and electromagnetic material properties are sensitive to monitor fatigue behavior. In the case of austenitic stainless steels we have to separate material which is prone to phase transformation under cyclic deformation or not. If a phase transformation to the body centered α'-martensite phase can be observed the ferromagnetic properties can be utilized for fatigue characterization. In all other cases, and when the material is fatigued at elevated service temperatures, e.g. when temperatures are greater equal 300°C, ultrasonic properties are of interest. A reasonable approach is based on the use of electromagnetic acoustic transducers (EMAT) which transmit a wave into the material without the need of a coupling media. The contribution summarizes results obtained in R&D programs in the last decade in the LCF- as well as in the HCF fatigue regime.

1. Introduction

Worldwide in countries with nuclear power generation there is the tendency to lifetime extent the components. Lifetime extension up to a total life of 80 years actually is discussed. As the primary circuit components are mainly exposed to thermo-mechanically induced cyclic deformation it is of interest to have non-destructive techniques available which sensitively can characterize the elapsed lifetime. From all components in the primary circuit of German nuclear power plants some – which are especially stressed thermo-mechanically – are manufactured in austenitic stainless steel, for instance in PWR the pressurizer surge line combining the pressurizer vessel with the hot-leg piping or the reactor pressurizer spray line system (Figure 1). It is well known for instance that during each heat-up of the plant in the surge line the hot water rides on a layer of cooler water, causing the upper part of the pipe to be heated to a higher temperature than the lower part. This causes stratification and in the cross-section of the pipe resulting in a stress gradient and low-cycle fatigue damage accumulation. The spray line system has the objective to reduce the actual pressure when higher than a limit by spraying cold water through a spray head into the steam atmosphere of the vessel in order to initiate condensation of water and therefore pressure reduction.

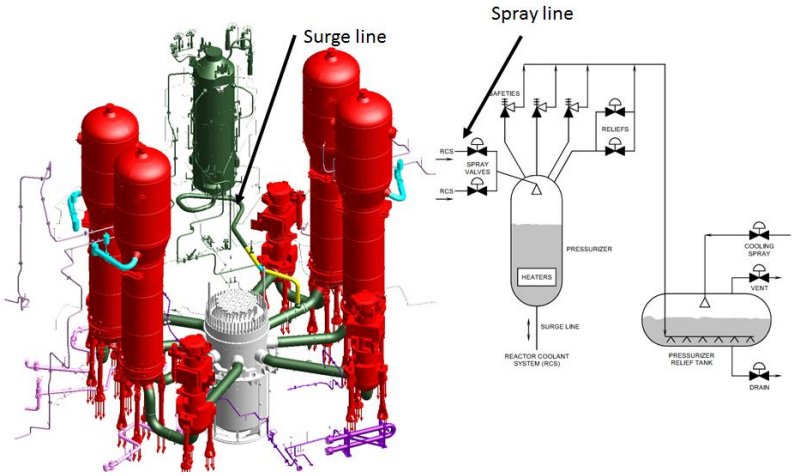

Figure 1: Pressurizer-surge-line and -spray line system

2. Materials

Austenitic steels of the grades AISI 321 (German grade 1.4541 - Ti-stabilized) and AISI 347 German grade 1.4550 - Nb-stabilized) are often used in power station and plant constructions so also in German NPP. The evaluation of early fatigue damage and thus the remaining lifetime of austenitic steels is a task of enormous practical relevance. Meta-stable austenitic steel forms ferromagnetic α' martensite due to quasi-static and cyclic loading. This presupposes the exceeding of a threshold value of accumulated plastic strain. The amount of martensite as well as its magnetic properties should provide information about the fatigue damage. Fatigue experiments were carried out at different stress and strain levels at room temperature (RT or AT, ambient temperature) and at T = 300°C [1, 2]. The characterization methods included microscopic techniques such as light microscopy, REM, TEM and scanning acoustic microscopy (SAM) as well as magnetic and electromagnetic methods, ultrasonic absorption, X-ray and neutron diffraction. Table 1 and table 2 show the chemical compositions.

Table 1: Material X6 CrNiTi 1810 (German material No. 1.4541), 2 heats (in mass %)

elements	C	N	Si	Mn	P	S	Cr	Mo	Ni	Ti
heat F producer specification	0,04	-	0,44	1,14	0,033	0,004	17,74	-	9,3	0,35
heat F WWK [1]	0,05	0,002	0,4	1,09	0,024	0,005	17,81	0,27	9,3	0,3
heat K producer specification	0,025		0,44	1,76	0,026	0,02	17,15		9,83	0,16
heat K WWK [1]	0,03	0,006	0,45	1,72	0,022	0,014	17,31	0,28	10,18	0,16

Table 2: X6 CrNiNb 1810 (German material No. 1.4550), (in mass %) [3]

C	Cr	Ni	Nb	N	Si	Mn	P	S	Al
0,040	17,600	10,640	0,620	0,007	0,410	1,830	0,020	0,007	0,016
Ti	Sn	Mo	W	Cu	Co	V	Pb	B	Fe
0,020	0,008	0,290	0,030	0,060	0,010	0,070	<0,008	<0,005	Rest

The Nb-stabilized material obviously has a higher Nb and Ni content compared with the Ti and Ni content of the 1.4541 material. That was primarily introduced into the specification in order to reduce the sensitivity for sensitization during heat treatments, i.e. to reduce the risk for inter-granular stress corrosion cracking. A secondary effect is that the material is only prone to show a phase transformation to α' martensite when fatigued at ambient temperature (AT).

Sufficient amounts of mechanical energy due to plastic deformation lead to this phase transformation from fcc austenite without diffusion to tetragonal or bcc ferromagnetic α'-martensite. As the martensitic volume fractions in the case of 1.4541 are especially low for service-temperatures of about 300°C [1, 2] highly sensitive measuring systems are necessary. Besides systems on the basis of a HTC-SQUID (High Temperature Super Conducting Quantum Interference Device) special emphasis was on the use of GMR-sensors (giant magnetoresistors) which have the strong advantage to be sensitive for dc-magnetic fields too without any need for cooling [4]. In combination with an eddy-current transmitting coil and a universal eddy-current equipment as a receiver hardware the GMR-sensors were used especially to on-line monitoring the fatigue experiments in the servo-hydraulic fatigue machine.

Figure 2 shows the sensor principle of a GMR [2, 4, 5]. An electrically conducting material, i.e. a Cu layer (A) of some nm thickness is embedded into a sandwich structure of two ferromagnetic layers (for instance a B-Fe- or Ni-alloy like Permalloy) of nm thickness (B). Because of the nm thickness of the layers the magnetic domains in the two ferromagnetic layers interact such that in the magnetic-field-free state (energetic low state) the magnetic moments in the domains are antiparallel oriented. If an electric current is sent through the Cu-layer the conducting electrons will be scattered at the closure domains of the interfaces. The scattering at the interface with anti-parallel magnetic moment direction to the moving direction of the electrons is much higher than at the other interface. Therefore the electric resistance is higher. When magnetizing the structure the moments are more and more aligned and the resistance is decreasing; the overall dynamic is about 14% resistance change.

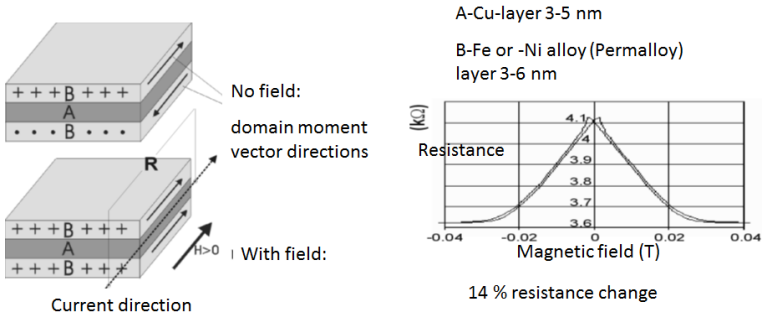

Figure 2: GMR principle

As GMR today are mass products, read heads in in magnetic hard discs are made by GMR; cheap sensors are available as integrated circuits.

3. Results obtained at 1.4541 austenitic stainless steel at room temperature (RT)

Figure 3 shows such a GMR-sensor embedded in a small ferromagnetic yoke together with a clip-gage for strain measurement at a fatigue specimen clamped in a servo-hydraulic machine for fatiguing. The yoke is used to locally magnetize the fatigue specimen in the measuring length by an alternating electrical current in the magnetizing coils. The yoke has 1 mm lift-off of the specimen and excites in the conductive material eddy currents. The GMR is affected by the primary magnetic field of the yoke and the secondary field of the eddy currents which lowers the primary field. The so-called transfer-impedance is measured. In Figure 4 cyclic deformation curves of one-step fatigue tests are presented in the case of stress controlled experiments (mean stress-free, R_σ=-1) at RT.

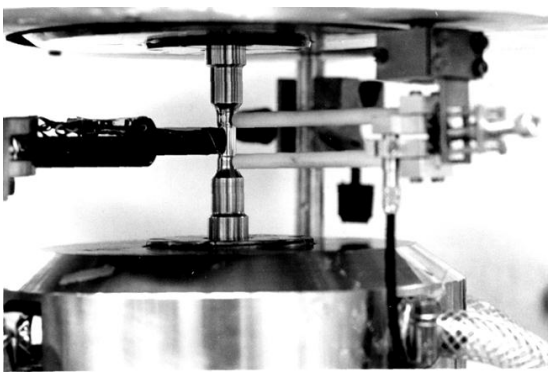

Figure 3: GMR-yoke sensor (left) together with a clip-gage (right) in the servo-hydraulic machine

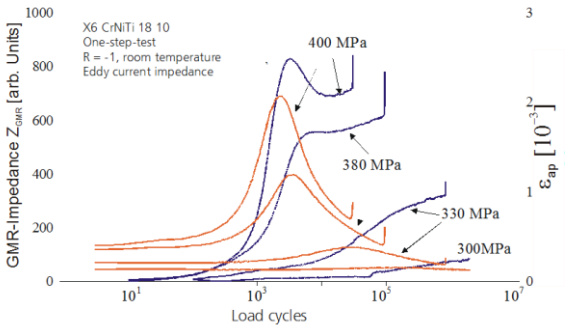

Figure 4: Cyclic deformation curves of on-step fatiguing (red color), stress controlled (σ = 300 MPa, 330 MPa, 380 MPa, and 400 MPa at RT and GMR-inpedance curves (blue color)

As the cyclic deformation curves (in red color, ε_{ap} – plastic strain amplitude) show a typical secondary hardening maximum due to the development of the martensite followed by a minimum before failure.This can be observed in the GMR-impedance (blue colored curves) only for higher stress amplitudes, i.e. the impedance needs some threshold in accumulated strain to show the effect due to the martensite. However, when performing a multiple-step loading experiment as shown in Figure 5, according to a loading time function as shown in red color the eddy current impedance (blue color) of the GMR sensor exactly follows this functional behavior. In other words, the impedance curve is a one-to-one image of the loading history but in addition a certain off-set is observed revealing the occurrence of α' martensite which is enhancing the magnetism of the specimen when fatigued in the geomagnetic field. In the case of a strain-controlled one-step fatigue test (mean strain free, R_ε=-1, ε = 0.2%) the GMR sensor was applied in a magnetometer circuit. Highly time-resolved the developing stress amplitude as well as the magnetic field in the specimen was measured. In each load cycle a hysteresis can be measured of which the area under the curve as well as the inclination is typically increasing with the cycling number.

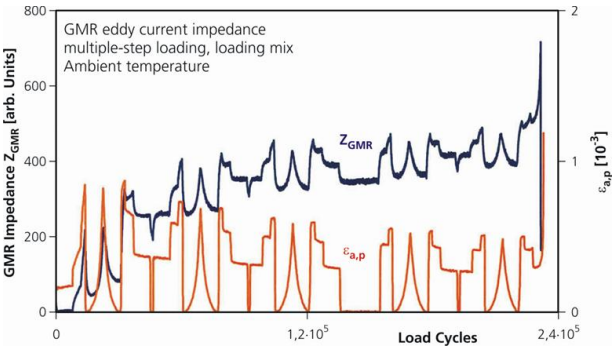

Figure 5: Multiple-step loading at RT

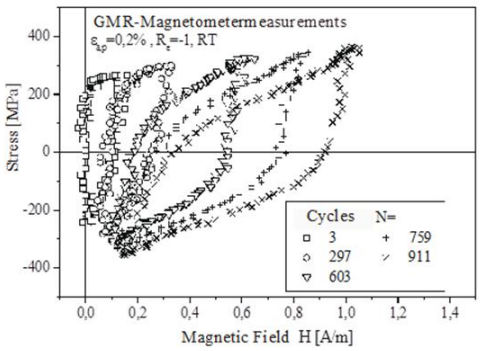

Figure 6:Stress/magnetic field hysteresis curves, strain controlled (mean strain free,R_ε = -1) one-step fatigue tests at RT, ε_{ap} = 0.2%

4. Results obtained at 1.4550 stainless steel at room temperature (RT) and 300°C [3]

The low cycle fatigue experiments were performed in the strain-controlled mode at room temperature and at 300°C what is the service temperature range of the components of interest. The electromagnetic properties discussed in the last chapter cannot be sensed at elevated temperatures and cooling of sensors cannot be accepted at real components in practice. Therefore the need for a new measurement technology was given. This is based on the use of electromagnetic acoustic transducers (EMAT). An EMAT is - in its simplest version no more than a spiral inductive coil (Figure 7) in which a high-frequency tone-burst (a couple of sine-periods) is excited by a pulse generator [6, 7]. The coil induces eddy currents in the conductive material of which the magnetic field of a permanent magnet (NdFeB) in normal direction is superimposed. The magnetic induction B_0 is perpendicular to the tangential direction of the eddy currents I_{Eddy} and the mechanical Lorentz forces F are the cross vector product of both, i.e. radially oriented, exciting radially polarized shear waves propagating in axial direction.

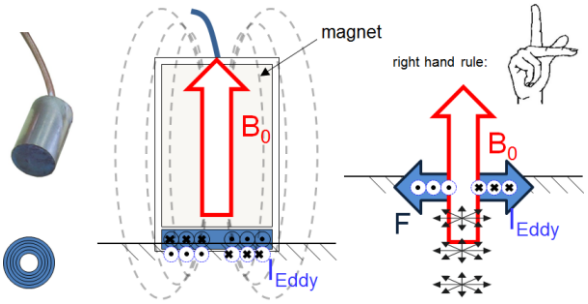

Figure 7: EMAT excitation of radially polarized shear waves by Lorentz-forces

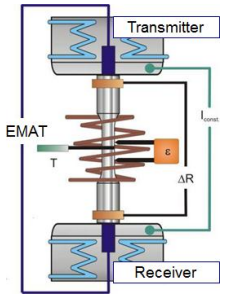

Figure 8: EMAT transmitter – receiver probes built in the clamping of the fatigue specimen

In Figure 8 one important fact concerning the experiments in the servo-hydraulic machine is shown. First of all, the clamping devices of the specimens are cooled permanently by water. That clearly results in heat sinks in the clamping and a continuous heat flow from the specimen into the clamping; the actual specimen temperature T can be measured by a thermal couple as function of the cycle number. Furthermore a constant electric current, $I_{constant}$, is fit-in the clamping and along the specimen length the electrical resistance change ΔR can be measured as function of the cycle number.

According to Figure 9 in the A-scan the time-of-flight (tof) of the through-transmitted ultrasonic shear wave and its amplitude is measured. As the tof during one load cycle varies between the smallest value (smallest elongation) and largest value (largest elongation) the tof_{mean}-value is calculated as a characteristic damage parameter as function of the load cycles. The tof_{mean}-value in the case of the total strain of ε = 1% as function of fatiguing at ambient (RT) temperature shows a characteristic behavior (Figure 9, right hand side). The enhanced increase of tof_{mean}, before the failure of the specimen, is due to the phase transformation to α'-martensite. The full information concerning the fatigue behavior at ambient temperature is documented in Figure 10 in the total strain range $0.8\% \leq \varepsilon_{at} \leq 1.6\%$. In addition to the the cyclic deformation curves (stress σ as function of the load cycles) the development of the martensite is shown by using a Feritescope® as a commercially available tool.

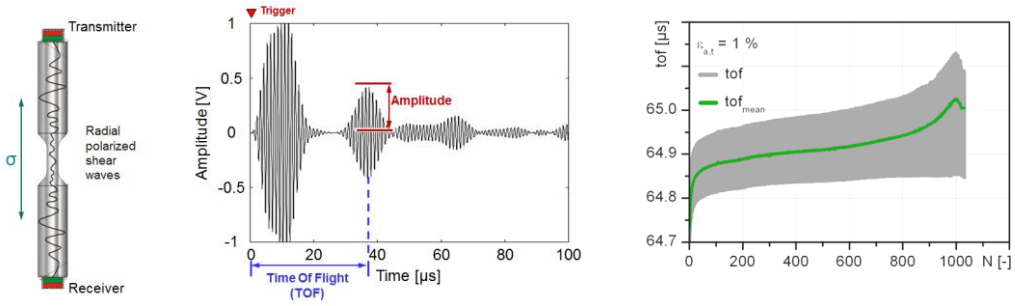

Figure 9: A-scan (HF) of the ultrasonic wave, time-of-flight (tof) and amplitude determination (left hand side); tof_{mean} determination (right hand side)

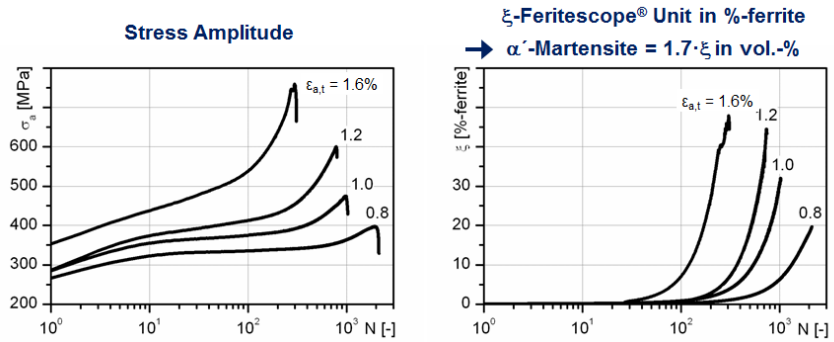

Figure 10: Cyclic deformation curves, developing stress amplitudes as function of load cycles and detection of the α' martensite by use of the Feritescope®

The cyclic deformation behavior is strongly influenced by the service temperature and totally changes its character when the temperature is enhanced from ambient temperature (AT) stepwise to 50°C, 240°C, and 300°C (Figure 11).

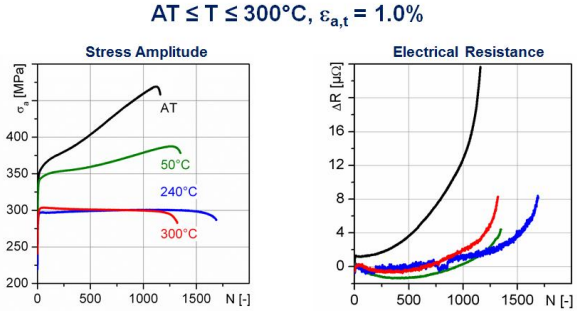

Figure 11:Temperature dependence of the cyclic deformation curves and the development of the electrical resistance in case of a total strain ε_{at} = 1%

Whereas the stress increases permanently at AT up to the break of the specimen at elevated temperatures after a rapid increase during the first cycles (strain hardening) a moderate increase (50°C) or a saturation behavior (240°C) or even a slight stress decrease (300°C) before the failure is observed. The development of the electrical resistance is also very informative. The resistance change is the largest at AT. This can be understood well as here the martensite is developing with a high increase of dislocations. At enhanced temperatures the behavior is not unique and not yet clear in interpretation. May be that dislocation cross slip, recrystallization processes and therefore dislocation annihilation plays a role?

Figure 12 compares in case of the full strain range $0.8 \leq \varepsilon_{at} \leq 1.6\%$ the curves of tof_{mean} obtained at 300°C with the cyclic deformation curves (σ as function of load cycles). Whereas, just discussed in Figure 11, the stress curves show no influence of a continuously increasing damage parameter because of this nearly constant behavior (saturation or slight cyclic softening) along the full life time, the tof_{mean} curves show a strong monotonic increasing during the last third of life and indicate therefore very early elapsing of life. That is mainly due to the fact that micro-cracking in the specimen surface is sensed.

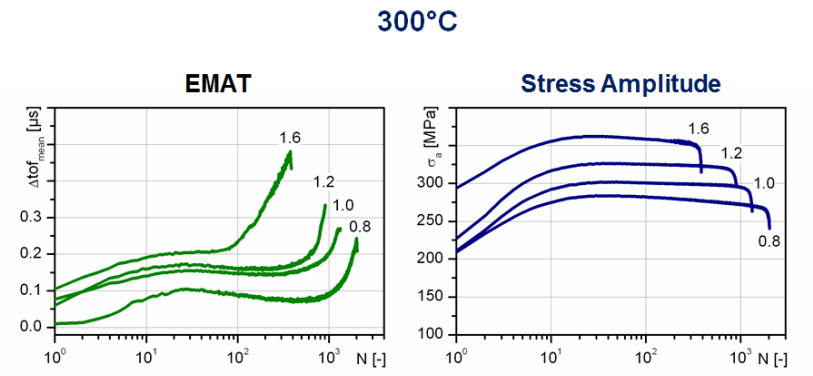

Figure 12: tof_{mean} curves and stress curves at 300°C

5. Sensors for ageing management

Fraunhofer IZFP will start with a new project in the German nuclear safety research program in 2014. In cooperation with AREVA the new developed tof_{mean} measurement by use of EMAT will be optimized for pipe condition monitoring. Two transmitter-receiver arrangements integrated as combination-EMAT in a joint housing are planned as shown in Figure 13.

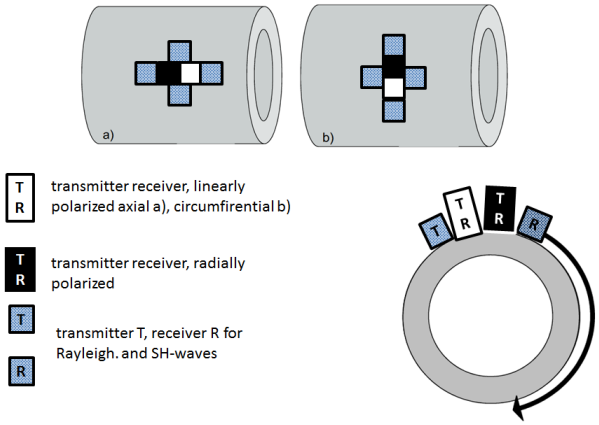

Figure 13: Transmitter-receiver arrangements for condition monitoring of pipes

In order to obtain a higher spatial resolution a higher number of combination-EMAT can be integrated in the hoop direction of the pipe. The sensor information will be read-out by time-multiplexing. As an EMAT coil is nothing else than a special shaped eddy current transducer, the eddy current impedance of the EMAT can be measured additionally and the information discussed in Figure 11 concerning electrical resistance effects can be collected. A theoretical model will be developed in which the temperature gradient in the pipe wall is modeled as piecewise linear in layers. As the phase velocities of the ultrasonic waves, respectively the tof for fixed T-R-distances,

as well as the eddy current impedance depend on temperature, besides the direct fatigue information discussed in the here presented paper these quantities should be used too to calibrate the model in the layered media. AREVA has developed in the last decade the fatigue monitoring system FAMOS [8] which is based on surface temperature measurements and FE-modeling of the temperature gradient. Based on this information by FE the stress gradient can be calculated. The plan is to combine FAMOS with the new EMAT/Eddy-Current system to have redundancy and diversity and to use FAMOS for calibration of the stress gradient in the pipes.

6. Conclusions

It was shown that electromagnetic properties like the GMR-transfer-impedance or the magnetic field of the α' martensite developing in the geomagnetic field when fatiguing Ti- or Nb-stabilized meta-stable austenitic stainless steels are sensitive to characterize the cyclic deformation when performed at RT. At service temperatures in the 300°C regime the time of flight of ultrasonic waves transmitted and received by an EMAT is a proper tool for fatigue characterization which especially in the last third of lifetime is more sensitive than the developing stress when strain-controlled experiments are performed. As with EMAT also electromagnetic properties can be sensed a combination system will be developed and calibrated with the FAMOS-calculation results.

7. Acknowledgements

The author very much acknowledges the high valued contribution of colleagues from Fraunhofer-IZFP which are Iris Altpeter, Klaus Szielasko, Ralph Tschuncky, and Gerhard Hübschen. The special thank is to the Institute of Material Science and Engineering, WKK, (Prof. Dietmar Eifler) at the Technical University Kaiserslautern with its team for the long-year fruitful co-operation. Last but not least, thank is to the ministry of economy and technology for the financial support in different projects beginning in 1979 up to now.

8. References

[1] Bassler, H.-J.: Cyclic deformation behavior and strain-induced development of martensite in case of the austenitic stainless steel X 6 CrNiTi 18 10 (in German), Ph.D.-thesis at the University Kaiserslautern, 1999

[2] Lang, M.: Non-destructive characterization of the cyclic deformation behavior and the development of strain-induced martensite in case of the austenitic stainless steel X6 CrNiTi 1810 by use of sensitive magnetic sensors (in German), Ph.D.-thesis at the University of the Saarland, Saarbrücken, 2000

[3] Altpeter, I. et al: Early detection of damage in thermo-cyclically loaded austenitic materials, ENDE 2011 proceedings, ISO press, ENDE 2011 conference, March 10-12, Chennai

[4] Yashan, A.: To eddy current (EC) and magnetic leakage flux (ET) testing with GMR sensors (in German), Ph.D.-thesis at the University of the Saarland, Saarbruecken, 2008

[5] German patent DE 3820475Magnetfeldsensor mit ferromagnetischer, duenner Schicht; filed on 16.06.1988

[6] Salzburger, H.-J.: EMATs and its Potential for Modern NDE - State of the Art and Latest Applications, Proceedings of the IEEE International Ultrasonics Symposium 1, 2009, 621-628

[7] Salzburger, H.-J., Niese, F., and Dobmann, G.: EMAT pipe inspection with guided waves, Welding in the world 56 (2012), 5-6

[8] Rudolph J., Bergholz S., Heinz B., and Jouan B.: AREVA Fatigue Concept - A Three Stage Approach to the Fatigue Assessment of Power Plant Components, in: Nuclear Power Plants, edited by Dr. Soon Heung Chang, KAIST Department of Nuclear & Quantum Engineering, South Korea, http://www.intechopen.com/books/nuclear-power-plants, ISBN 978-953-51-0408-7, Publisher: InTech, March 21, 2012

NON-DESTRUCTIVE DETECTION OF DEALLOYING IN CU-AL ALLOYS USING ULTRASOUND

R.Royer, Structural Integrity Associates, INC.,USA
C. Searfass, Jason Van Velsor, Jeff Milligan

Introduction

Dealloying is defined in a general sense as a corrosion process where a material becomes deficient of one or more of its constituent species. The dealloying process typically progresses by two primary mechanisms, which can occur in tandem. One mechanism is when one alloy constituent dissolves within a materials' bulk and then re-deposits on the surface. The second is a diffusion mechanism by which one of the constituent species migrates out of the bulk material, leaving behind a porous structure. Dealuminification is the specific process of the leaching of aluminum in aluminum-bronze alloys. The process of dealuminification is thought to be electrochemical in nature. In cases where dealuminification occurs in aluminum-bronze alloy components, the microstructure of the material contains both copper-rich α and aluminum rich γ-2 phases. When these alloys are exposed to solutions containing chlorine ions or an oxidizing acid, such as hydrofluoric acid, the aluminum rich γ -2 phase will preferentially corrode resulting in large losses of aluminum. The consequence of concern of dealuminification is its adverse affect on the ultimate tensile strength of components. Thus, dealuminification has been an issue plaguing nuclear power generation facilities utilizing aluminum-bronze alloy piping and piping components for the transport of brackish water.

Relatively severe forms of dealuminification can be detected visually and can be identified by the presence of a deep copper color. Fig. 1 contains an image of a sample where dealloying product has accumulated on the internal surface of an aluminum-bronze alloy component. With etching, dealuminification can be observed visually with greater ease, as is observed by the dark areas seen in the cross-section of the component. Other techniques for the detection of dealuminification include utilizing electrochemical impedance spectroscopy, chemical analysis, or the measurement of a samples linear polarization resistance or electrical resistance. However, these methods are either purely surface techniques or they require very specific environments, such as immersion in an ionic liquid, and are therefore confined to detecting dealloying in laboratory settings.

This paper discusses work on the development of an ultrasonic method for the characterization of dealuminification in aluminum-bronze alloy samples. Very little previous work has been performed on the detection of dealloying in this family of materials using ultrasonic methods; however, because dealuminification results in localized perturbations of the material's elastic modulii and density as the exodus of aluminum from the material progresses, it is intuitive that one could monitor dealuminification by analyzing ultrasonic wave velocity as this material characteristic is strictly dependent on the bulk/shear modulii and density.

Fig. 1 Specimen with indications of dealuminification

Furthermore, the industry wide acceptance of ultrasonic nondestructive evaluation methods for other types of material damage, such as cracking, pitting, and erosion, further motivated Structural Integrity's investigation into the detection of dealuminification using ultrasonic methods.

Determining Dealloying from Measurements of the Ratio of Longitudinal to Shear Wave Time-of-Flights

As dealuminification advances, localized changes in the materials' elastic modulii occur and inevitably lead to the lowering of the material ultimate tensile strength. This same phenomenon is what is to be exploited when attempting to detect dealloying with ultrasonic time-of-flight measurements. The ultrasonic longitudinal and shear wave velocities, v_L and v_s, respectively, are frequently expressed as

$$v_L = \sqrt{\frac{E(1-\vartheta)}{\rho(1+\vartheta)(1-2\vartheta)}} \tag{1a}$$

$$v_S = \sqrt{\frac{\mu}{\rho}} \tag{1b}$$

Where v, ρ. E and μ are the materials' Poisson's ratio, density Young's modulus, and shear modulus, respectively. As dealloying of the material increases, changes in the modulii, as well as the density, are to be expected and thus cause changes material wave velocity. Therefore, by monitoring the wave velocity in a material it should be possible to monitor the state of dealloying within a material. The wave velocity can be determined experimentally by noting that

$$v_{L,S} = \frac{2t}{TOF} \tag{2}$$

Where t is the thickness of the specimen being investigated and TOF is the time-of-flight of the ultrasonic wave. In a laboratory environment, careful measurements of a component's thickness can be made and it therefore follows that determining a specimens wave velocity is a fairly trivial procedure. On the contrary, for the inspection of in-service components, access to the internal surface of the component is not easily accomplished and a precise ultrasonic thickness measurement cannot be made due to the unknown localized variations in wave velocity potentially caused by dealuminification. It is therefore not possible to determine absolutely the material wave velocity or material thickness. To circumvent this conundrum, a technique was developed which focused on utilizing a ratio of the measured pulse-echo time-of-flights of shear and longitudinal waves. Mathematically, the ratio of the longitudinal to shear wave time-of-flight is given by,

$$\frac{V_S}{V_L} = \frac{{}^{2t}/_{TOF_S}}{{}^{2t}/_{TOF_L}} = \frac{TOF_L}{TOF_S} \tag{3}$$

Eqn. 3 show that by utilizing the time-of-flight ratio method, a metric for characterizing the time-of-flight of material is established and no specific knowledge of the material thickness or wave velocity.

A feasibility study was performed of a sample of an aluminum-bronze alloy which had experienced varying amounts of dealuminification was diced into segments. An image of the sample before dicing is shown below. The ratio of ultrasonic shear and longitudinal wave pulse-echo time-of-flights for each segment were recorded at each segment and compared to one another. The ratios of the shear and longitudinal wave time-of-flights for each segment are shown below in Fig. 3. After the time-of-flight measurements were made, the diced samples were etched with silver nitrate to determine the approximate amount of dealloying which had occurred within each coupon. A clear trend was observed between the etched samples and measured results that demonstrated that dealuminification results in a larger longitudinal-to-shear wave velocity ratios. Fig. 4 shows exemplary images of etched samples demonstrating, low, intermediate, and high levels of dealuminification (dark areas in indicate regions of dealuminification). Given this initial success, work is underway to characterize the dealloyed material samples such that a quantitative characterization of the dealloyed state will eventually be possible. These methods are also being explored for the characterization of dealloying in other common power plant materials, such as gray cast iron.

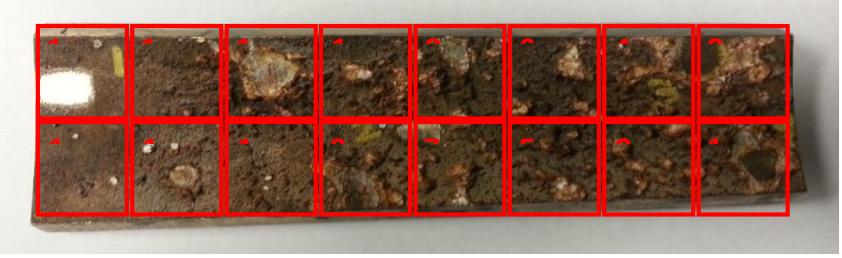

Fig. 2 Aluminum-braonze alloy specimen prior to dicing. Numbered boxes indicate coupon number corresponding to measured shear and longitudinal wave time of flights.

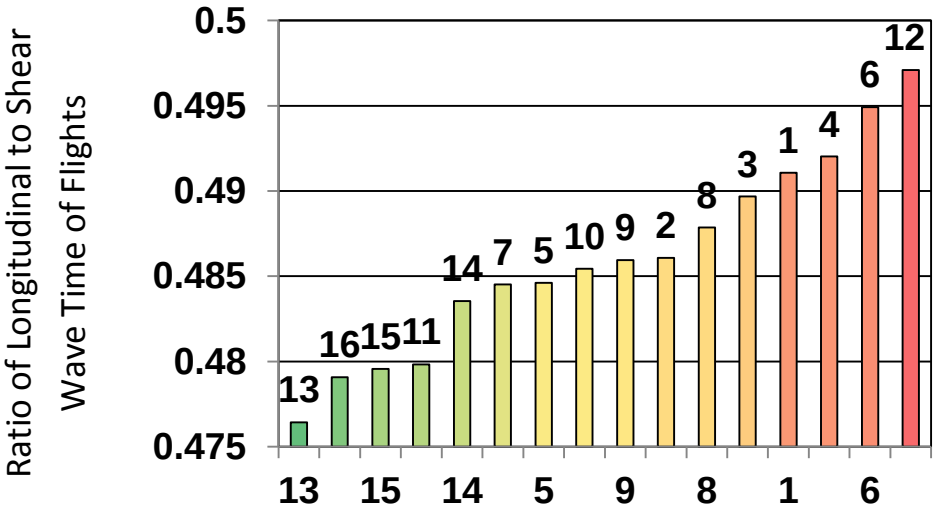

Fig. 3. Measured ratio of longitudinal to shear wave time-flight for test coupons shown in Fig. 2.

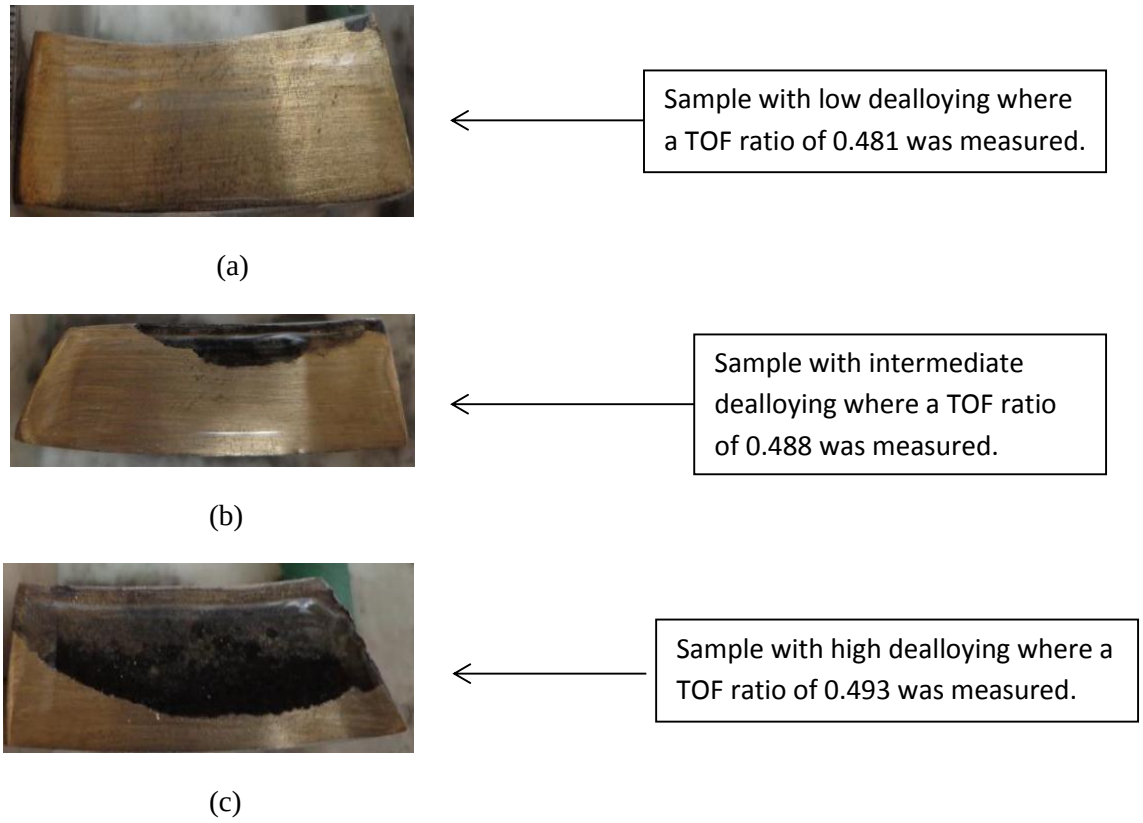

Fig. 4 Samples with **(a)** low dealloying, **(b)** intermediate dealloying, and **(c)** high dealloying and the corresponding measured ratios of longitudinal to shear wave time-of-flights.

Determining Dealloying with Time-of-Flight Diffraction (TOFD)

The time-of-flight diffraction (TOFD) technique is an ultrasonic through-transmission technique typically employed in crack detection. With TOFD, the actuating transducer sends an elastic bulk wave at angle into the material being investigated. A second transducer receives the ultrasonic wave which is reflected from internal defects, if present, and the specimen backwall. In the case of crack detection, if the material wave velocity is known, crack detection and sizing can be accurately performed. One of the primary advantages of TOFD is that commercially available systems exist. These systems are image based and require only a small amount of training for a technician to use for field applications. Fig. 5 shows an image of the operating principle of a TOFD set up, as well as an image generated during an inspection.

As the previous section demonstrated, dealuminification within a material alters the wave velocity within a material by decreasing its value. Thus, with a sample which has experienced some degree of dealuminification, one should anticipate that a TOFD system would measure an increase in backwall thickness in regions where wall thickness is constant. However, once again with testing in-service components, the thickness of sample under investigation is not known.

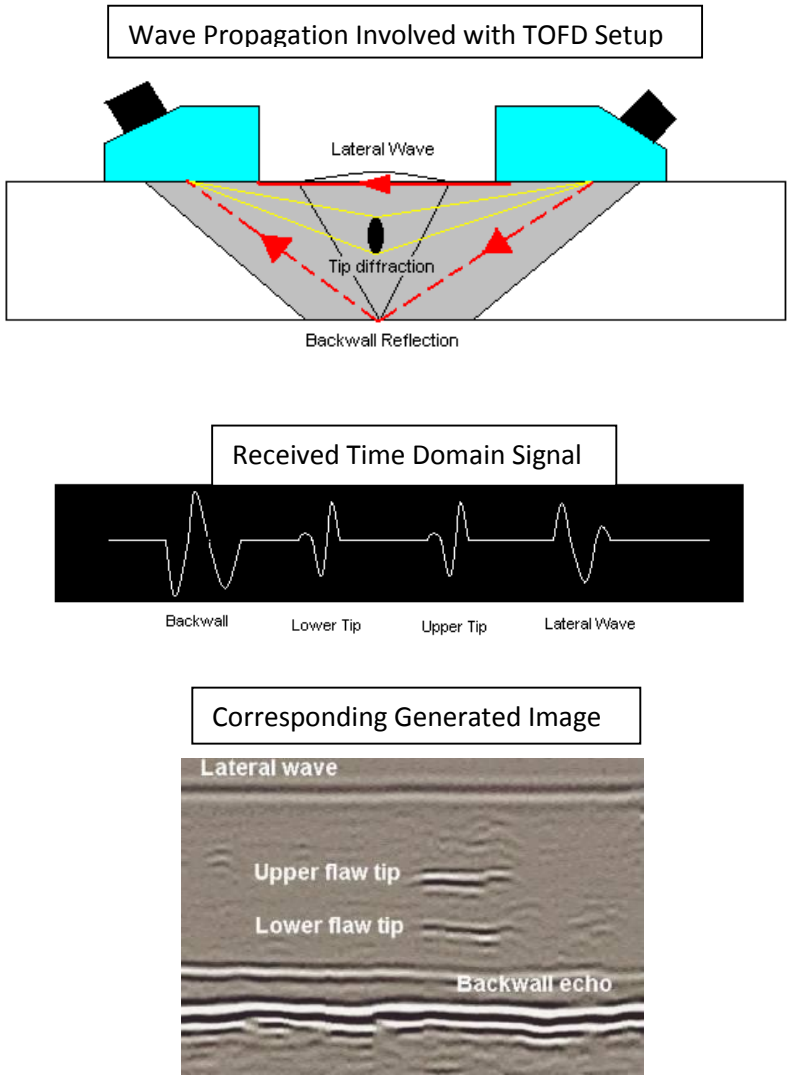

Fig. 5. Operating principle of the TOFD technique.

Therefore, in order to detect dealloying, an increase in the backwall must be measured in tandem with a reflection from the dealloyed-non-dealloying region. This premise for detection of dealuminification with TOFD has had initial success. Fig. 6 shows an image of aluminum-bronze alloy which contains a region where dealuminification was known to have occurred. Also shown in Fig. 6 is the corresponding image generated from a TOFD analysis on this region. In the image generated from the TOFD analysis, an increase in time-of-flight is recorded. Simultaneously, in the same region of the aluminum-bronze alloy sample where an increase in time-flight is logged, an echo from the dealloyed/non-dealloyed interface is recorded. Thus, here it has been demonstrated empirically that utilizing TOFD for detection of dealuminification is feasible.

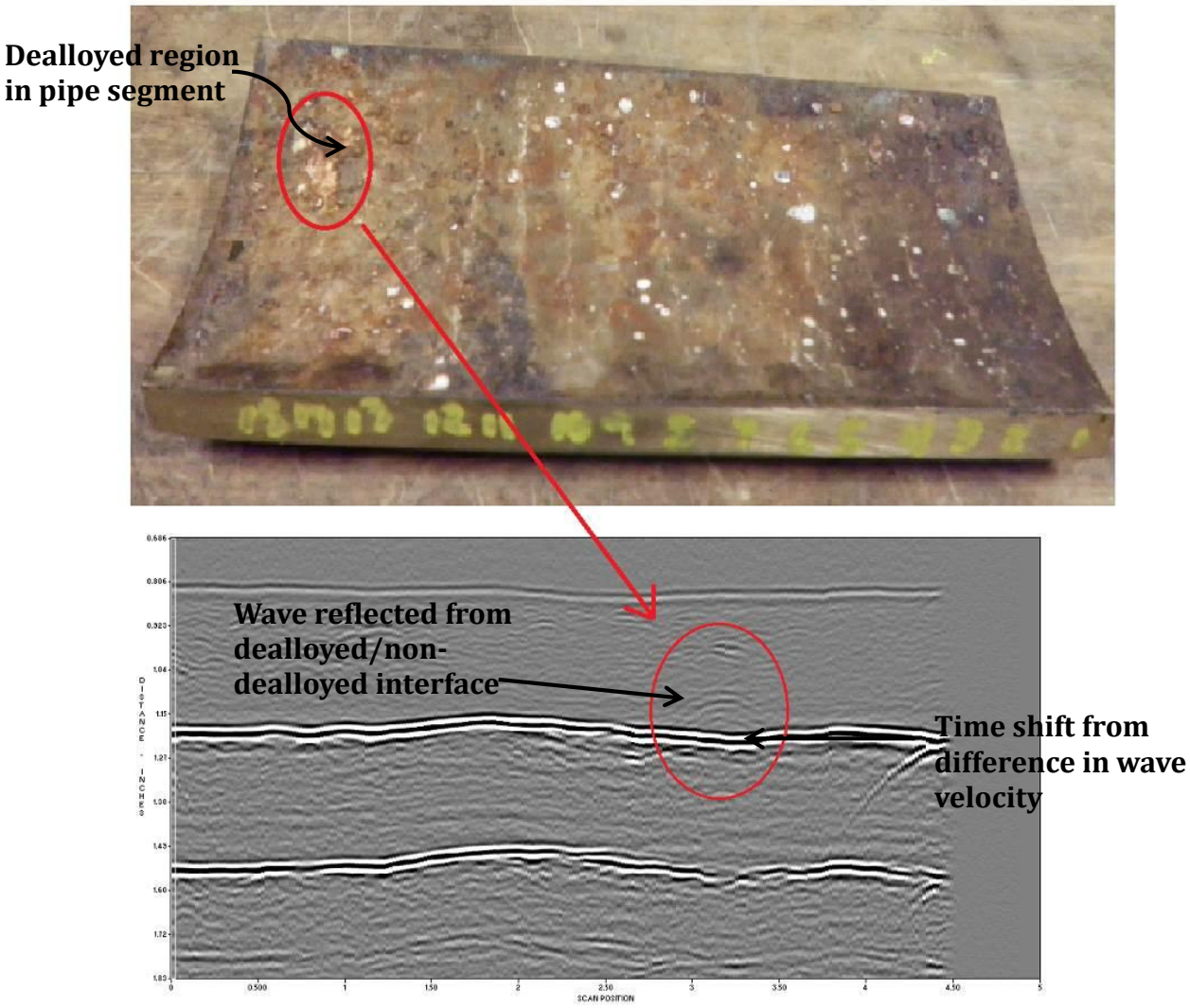

Fig. 6. Aluminum-bronze alloy specimen with region of known dealuminification and corresponding image generated from an investigation with TOFD.

Concluding Remarks

Two methods for successfully employing ultrasonic non-destructive evaluation for the detection of dealuminification have been presented and discussed here. One technique relies upon taking the ratio of measured time-of-flight of longitudinal and shear waves. This work has demonstrated that regions with higher degrees of dealuminification follow a trend of having larger longitudinal-to-shear wave time-of-flight ratios. It has been validated that this technique can detect regions where dealuminification has occurred, and it appears probable that this technique can be refined to give quantitative results as to the degree of dealuminification that has occurred. The second technique which has been employed is based upon standard TOFD techniques. This technique relies upon detecting both an increase in time-of-flight and detection of the reflection of wave a from the dealloyed/non-dealloyed region interface.

References

1) Heidersbach, R. “Dealloying” in *Uhlig’s Corrosion Handbook.* Revie, R. Winston, Ed., 145-151. Wiley, 2011.
2) Foster, M.L., Zanis, C.A., Crisci, J.R. “Dealuminization of Cast Aluminum Bronzes.” US Navy Technical Report. US Naval Applied Science Laboratory Naval Base, Brooklyn, NY, 1967.
3) Craig, B.D., Lane, R., Rose, D.H. “Corrosion Prevention and Control: A Program Management Guide for Selecting Materials.” Advanced Materials, Manufacturing, and Testing Information Analysis Center, Department of Defense. 2006.
4) Ferrara, R.J. “Dealloying of Aluminum Bronze and Nickel Aluminum Bronze Castings in Seawater.” Proceedings of the 1980 Tri-service
5) Shull, P.J., Tittmann, B.R. “*Ultrasound*”. In *Nondestructive Evaluation: Theory, Techniques, and Applications*, by P.J. Shull, 63-190. New York: Marcel Dekker, Inc., 2002.

NDE TOOLS SELECTION FOR COMPONENTS' STATE CHARACTERIZATION DURING NPP UNIT COMMISSIONING AND OPERATION

Arzhaev, A.I., Blokhin, V.N., Derij, V.P., Makhanev, V.O., Podlatov, M.A., Atomtechenergo, Russia
Dub, A.V., Razygraev, A.N., Razygraev, N.P., CNIITMASH, Russia
Pasmanik, L.A., Smirnov, INCOTEX, Russia

ABSTRACT

RF NPP Units operation experience indicates necessity of critical component state monitoring for possibility of long-term operation.

Components' initial state characterization during NPP Unit construction and commissioning is valid for improved life-time and structural integrity assessment.

"Road map" of Nuclear Energy development in Russia includes new NPP Units with light-water and fast breeder reactor types.

Quality assurance of new NPP Units should be provided by application of effective NDE technologies for components' initial state characterization which further could be used in operation also.

Applied inspection and diagnostic technologies have to provide initial records for reference zones (like a "finger print") for possibility of monitoring of trends in technical state of components during operation and decommissioning. It is also helpful for application of different inspection time schedule in operation for characteristic groups of NPP components.

NDE tools under consideration include some for stress-state measurement, for material characterization, for weld pre-service inspection. Requirements to these tools are discussed based on strength and integrity analysis.

Selection of components for structural integrity evaluation is based on results of safety analysis and economic estimates of repair and replacement in operation.

Approach based on structural integrity methodology and application of up-to-date technologies for technical state inspection and diagnostic provides possibility of cost-effective management of NPP Unit operation with optimization of ISI scope and schedule.

Program of Nuclear Power development in RF is being continued. Figure 1 from [1] presents "road map" of new NPP Units construction and commissioning with variety of reactor facility types: VVER-1000, VVER-TOI, BN-800, BN-1200 and BREST-300. JSC "Atomtechenergo" plays important role in commissioning of all new NPP Units designed in Russia.

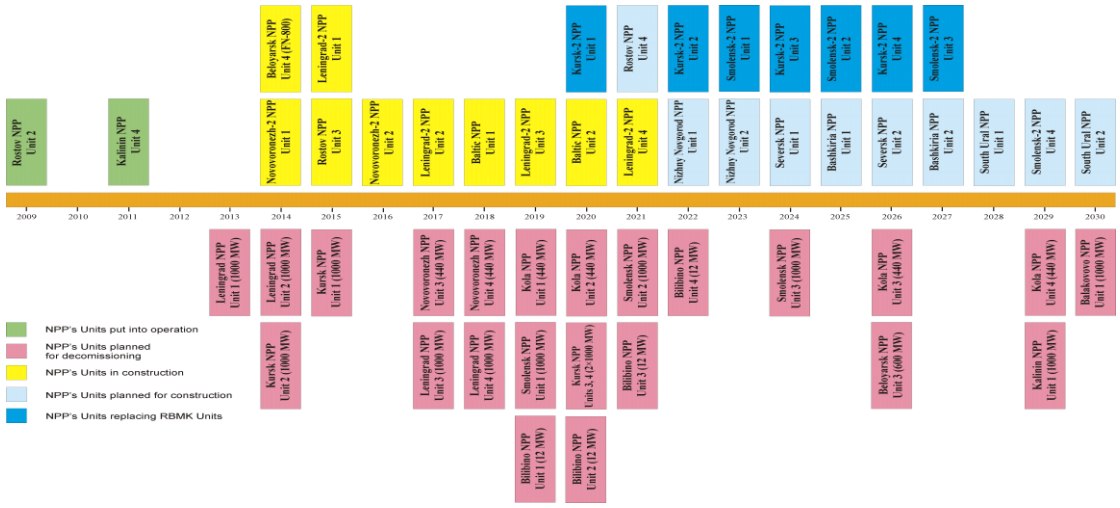

Figure 1. "Road map" of new RF NPP Units construction and commissioning [1]

Technologies of Life Cycle Management are being developed to support new NPP Unit design and construction [2]. Instrumental inspection of safety related piping and equipment actual technical state during construction and commissioning is intended to fix "as built" state. Results of such inspection should be kept in special electronic diagnostic passports (figure 2). Records with information on technical state of safety related components collected at the stages of operation and decommissioning will be added to these electronic information passports. Electronic information passports provide unified Life Cycle Management data platform for operative life-time assessments for the most important components [3].

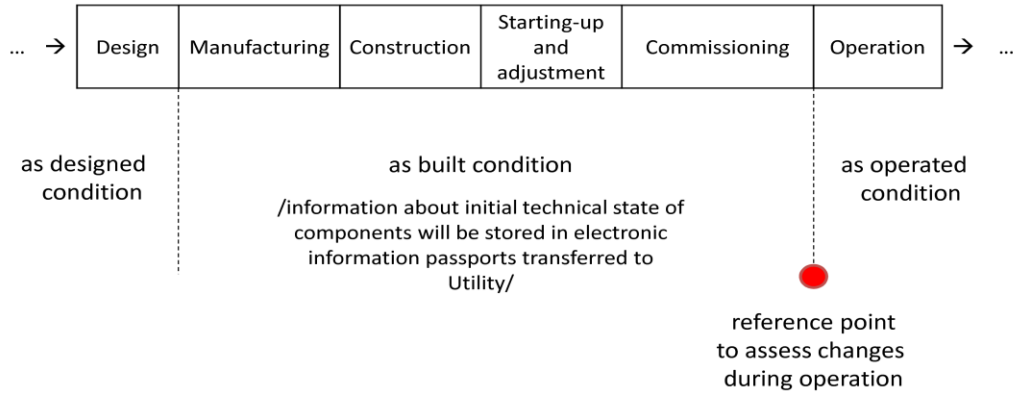

Figure 2. Life Cycle Management of Safety related components based in information from pre-operation stage

General requirements to safe operation of NPP passive components (piping and equipment) are based on terms of reliability and quality assurance at all stages of NPP Life Cycle: from selection of NPP site and up to decommissioning [4].

The purpose of present paper is to demonstrate capabilities of modern inspection and diagnostic technologies to ensure high quality of equipment manufacturing and assembling as well as commissioning of NPP Unit.

Statements on safety important component initial technical state recording based on modern technologies (table 1, [5]) are being introduced into set of regulatory documents and procedures valid for construction and commissioning [6].

Table 1. Tools for Component State Characterization

Technology	Stage of application	Benefits for operation stage
Measurements by acoustoelasicity method at piping and vessels	1) Measurements at manufacturing stage (zones between steam generator vessel branches and primary circuit headers of PGV-1000). 2) Measurements of SSS parameters during piping assembling (cold state) 3) Measurements of SSS parameters during hot testing at commissioning	Improved lifetime assessment. Ranging of components for differential ISI requirements.
Automated UT (UT holography*, TOFD, phased array) of safety important piping and vessel welds	Inspection of welds after assembling	"Finger print" to monitor changes during ISI. Ranging of components for differential ISI requirements.
On-line digital radiography of safety important piping and vessel welds	Inspection of welds during assembling (benefits of less labor costs, more high resolution and long-term data storage compared to film radiography)	Ranging of components for differential ISI requirements.

Measurement of component metal mechanical properties in referent zones (without cutting templates) *	Inspection of piping and vessel metal initial state during or after assembling	"Finger print" to monitor changes in mechanical properties during ISI. Improved lifetime assessment. Ranging of components for differential ISI requirements.
Inspection of components potentially susceptible to damages by FAC: – wall thickness measurements (including welds' zones) – bend dimension measurements* – chemical composition measurements*	Inspection of piping and vessel initial technical state parameters during or after assembling	"Finger print" to monitor changes in wall thickness during ISI. Improved lifetime assessment. Ranging of components for differential ISI requirements.

Note: * - experience comes from application for license extension of operating NPPs

Timeliness of such approach is supported by experience from RF NPP Units Life Time and License Extension and by analysis of world practice [7-9]. Application of modern inspection and diagnostic technologies for component actual technical state recording provided possibility of RF NPP Units Life Time extension for as minimum as minimum 10 years.

Structural Integrity Concepts like "Leak Before Break" [10] and "Break Preclusion" [11, 12] application in the framework of NPP Units License Extension supported substantiation of component acceptable safety level during prolonged operation. Requirements of these Concepts are more comprehensive than of regulatory document [13] and Utility document [14]

Provision of high quality design, equipment manufacturing and assembling, commissioning of NPP Unit forms the 1st basic principle of Structural Integrity Concepts [10-12] used for reliable guillotine piping rupture exclusion.

The following inspection and diagnostic technologies support high quality construction and commissioning of NPP Unit and eliminate level of uncertainties in initial technical state of NPP piping and equipment (table 1):

- automated high-resolution UT (first of all TOFD [7, 8, 15], phased array [16] and upgraded UT procedures [17-18]) providing record of so-called "finger print" for safety important weldments;
- experimental and calculation acoustoelasticity method for stress-strain state assessment of piping and equipment branches [6, 19-21];
- digital radiography [7, 8];
- modern technologies for wall thickness measurements in zones with non-equidistant out and inner surfaces [7, 8 ,15].

Application of systematic methodology [10-12] needs to take into account piping and equipment damage mechanisms potentially active in operation even if they are not covered by actual high-level regulatory documents (for example, [13]). Such unexpected damage mechanisms include FAC in low-carbon steel components in operating NPP Units with VVER reactor facilities (the secondary circuit) [22] and with Fast Breeder Reactor – FBR (the third circuit).

Initial wall thickness measurement for further comparison with ISI data is valid for components of new NPP Units which are potentially susceptible to FAC damages. This information should be kept in component electronic information passports. Technologies for wall thickness measurement in weldment zones currently used for purposes of Plant Life Extension based on requirements of regulatory document [23] need to be upgraded to up-to-date level due to lack of equidistant outer and inner surfaces in such zones.

Acoustoelasticity method is worth to be commented in more detail because it is reasonably new and very effective. The method is widely applied for gas and oil piping connected to equipment of transportation systems. Its application in nuclear industry has started in 2007. Now it is used in cold state (assembling, repair, etc.) and during hot testing for tightness and strength.

Procedure for measurement by acoustoelasticity method on NPP piping and equipment [24] in 2011 has been included into Utility list of actual technical documents [25].

Acoustoelasticity method is perhaps today the only one tool capable to measure through wall mean stress-state components in axial and circumferential directions of piping and thin walled vessels. The most widely used in nuclear field strain-gauge measurements provide only surface stress data.

Also strain-gauge measurements are extremely time consuming to find application in operative services during piping assembling and repair.

Acoustoelasticity method could be treated as effective up-to-date addition to Annex 5 of regulatory document [13]. Basic provisions of acoustoelasticity method are based on existing link between two axial stress state components in the range of elastic strains and velocities of volumetric elastic wave propagation in directions perpendicular to planes of acting stresses.

Practically the task is to form probing signals and to measure time delays of echo-signals for three ultrasound waves with mutually orthogonal polarization (two orthogonal shear waves and one longitudinal wave). There are high standard requirements to the precision of time delay measurements up to nanoseconds. Procedure of acoustoelastic measurement (PAM) of mechanical stresses in NPP components due to technological effects [24] have been successfully certified by Rostechregulirovanie in 2009. PAM rules parameters and algorithms of through wall mean stress value assessment in axial and circumferential directions due to inner pressure, applied forces and bending moments, etc. PAM could be applied to thin wall cylindrical components (piping and vessels) with outer diameter in the range from 300 to 1420 mm.

Accuracy of stress-state component measurements according to PAM is not worth than ±10%.

PAM [24] prescribes three measurement modes.

Mode 1 – "acoustic strain-gauge measurement". This mode provides measurement of actual stress-state components in reference point. One can measure values of the components if initial values before applying of loads are known.

Mode 2 – "differential acoustic strain-gauge measurement". This mode provides measurements in reference point and so-called "conventionally zero point". Some point with known stresses level (perhaps very small in comparison with stresses in reference point) could be used as "conventionally zero point". PAM provides criteria for substantiation of correct selection of "conventionally zero point" based on results of measurements.

Mode 3 – "non-nil acoustic strain-gauge measurement". Mode 3 corresponds to Mode 2 but "conventionally zero point" is positioned on a sample of component material free of stresses. This mode is used only in cases when there are no stress-free zone in object or if PAM criteria for "conventionally zero point" selection are not fulfilled.

Portable device IN 510A for stress component measurement by acoustoelasticity method is shown in Figure 3. Device provides generation of elastic waves and time delay measurement with given accuracy. IN 510A device has State certificate as a measuring tool [26].

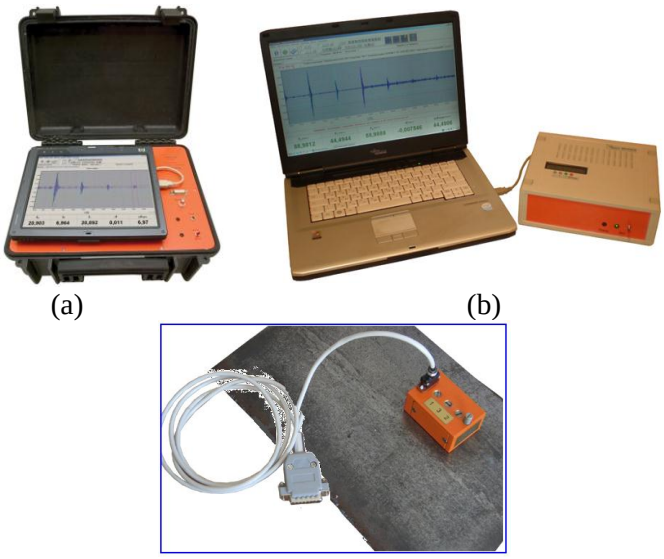

(a) (b)

(c)

Figure 3. IN 5101A device for on-site application:
(a) modification 00; (b) modification 01; (c) probe mounted on a pipe

Acoustoelasticity method has been used for measurements on components of operating NPP Units in "cold" state during outages and during equipment "hot" testing for tightness and strength. It has been applied to weld zones between steam generator vessel branch and primary circuit header at VVER-440 and VVER-1000 reactor facilities and also at Dia.300 mm RMBK-1000 piping far from weld zones.

Acoustoelasticity method for strain-stress state (SSS) assessment is positioned as combination of experiment and calculation. Experimentally measured data could be used for comparison with calculations and for improvement of boundary conditions accepted in finite-element model. Stress-state measurement in piping during assembling provides possibility of calculation improvement to fit experimental data and to reduce uncertainties in life time assessment for new NPP Units.

Application of acoustoelasticity method for Units under design and construction is worth for safety and reliability ensuring of safety important components (piping and equipment). Requirements for performance of such measurements at the stages of construction and commissioning should be included into design documentation (drawings and safety substantiation report) as well as in quality assurance programs developed according to requirements of [27] for all Life Cycle stages: design, manufacturing, assembling (construction), commissioning and operation. These requirements should be later implemented in working documentation used on-site.

Application of modern technologies for initial component state inspection and diagnostic (Table 1) to support structural integrity analysis [10-12, 21] allows to improve System of Commissioning Measurements (SCM) which is used at the stage of NPP Unit commissioning [28-29].

Improved SCM should be applied at new VVER NPP Units for important secondary circuit components as well as for reactor facility components. Also improved SCM could be recommended for 3rd circuit components of Units with FBR.

Application of systematic structural integrity methodology to NPP piping and vessels [10-12, 21] and on-site implementation of modern inspection and diagnostic technologies (Table 1) during NPP Unit commissioning and further operation provide favorable opportunities for elimination of operation expenses (compared to currently operating NPP Units) due to optimized requirements to ISI scope and inspection intervals (in accordance with utility procedure [30]) and condition-oriented maintenance.

REFERENCES

1) Ipatov P L, "Factors influencing formation of NPP "road map": replacement of RBMK Units and demand for medium-level power Units", 8th Int. public forum-dialogue «Atomic Energy, Society, Safety 2013», Moscow, Russia, 2013.
2) Limarenko V I, "Life Cycle Management at the Stage of Construction. Construction Control Information System", Results of the 2nd International Research and Practice Forum "Life Cycle Management of Complex Engineering Facilities. Development of Competitive Construction Technologies, Nizhniy Novgorod, Russia, 2012.
3) Arzhaev A, Evropin S, Petrov A, Savchenko V, "Effective technologies of PLIM elements application at Russian Federation NPPs", Nuclear power plant life management, Budapest, Hungary, 2002.
4) Rostechnadzor, General statements for NPP safety ensuring. OPB-88/97 (PNAE G-01-011-97).
5) Saakov E S, "Regulation of NPP Units Commissioning", Electric Stations, 2007 10 2-6.
6) Blokhin V, Derij V et al, "Up-to-Date Technologies of Component Technical Condition Inspection and Diagnostics During NPP Unit Construction and Commissioning", International Conference on Flow Accelerated Corrosion (FAC2013), Avignon, France, 2013.
7) Walaszek H, "New Benefits of Advanced Non-Destructive Techniques for Energy Industries", International Conference on Flow Accelerated Corrosion (FAC2013), Avignon, France, 2013.
8) Merck P, "NDT Methods Detecting/Monitoring FAC in Nordic Nuclear Power Plants", International Conference on Flow Accelerated Corrosion (FAC2013), Avignon, France, 2013.
9) Schiefner D, "The NPP Forsmark Program for the Prevention of Piping Degradation due to Flow-Accelerated Corrosion Phenomena", International Conference on Flow Accelerated Corrosion (FAC2013), Avignon, France, 2013.
10) RD 95 10547-99. Guideline for application of leak-before-break safety conception to NPP piping. R-LBB-01-99, 1999.

11) JSC “Concern Rosenergoatom”. Guideline for ensuring structural integrity of piping and equipment of coolant circulation circuit and safety important systems of reactor facilities, 2011.
12) Arzhaev A, Butorin S, “Improvement of Integrity Concepts for NPP Primary Circuit Piping”, 9th Biennial ASME Conference on Engineering Systems Design and Analysis ESDA08, Haifa, Israel, 2008.
13) Rostechnadzor. Norms of strength assessment of NPP piping and equipment. PNAE G-7-002-86.
14) JSC “Concern Rosenergoatom”. Guideline for Strength Assessment of Equipment and Piping of Reactor Facilities VVER, RBMK and EGP in Operation. 2012.
15) Delacoux D, “TOFD for Weld Rood Corrosion and Thickness Measurement”, International Conference on Flow Accelerated Corrosion (FAC2013), Avignon, France, 2013.
16) Vyazov D E, Dikov I A, Razygraev A N, Razygraev N P, “The study of ultrasonic testing technology”, 21st Conf. “Ultrasonic inspection of metal structures”, Saint Petersburg, Russia, 2013.
17) Razygraev A N, Vyazov D E, “Research and provision of testability, development of methods of ultrasonic testing of composite welded joints welding header to the steam generator”, 21st Conf. “Ultrasonic inspection of metal structures”, Saint Petersburg, Russia, 2013.
18) Razygraev N P, Kretov E F, “Ultrasonic testing technology development for anticorrosive (austenitic) coatings in Russia and new GOST (ISO/DIS) 17 405”, 21st Conf. “Ultrasonic inspection of metal structures”, Saint Petersburg, Russia, 2013.
19) Blokhin V N, Arzhaev A I, Makhanev V O et al, “About application of acoustoelesticity method for quality assurance of NPP piping assembling and repair”, 8th Int. Scientific and Technical Conf. “Safety, Efficiency and Economics of Nuclear Power”, Moscow, Russia, 2012.
20) Blokhin V N, Makhanev V O, Podlatov M A et al, “Quality assurance of NPP piping assembling and repair by application of acoustoelesticity method”, Int. Conf. “Structural Integrity and Lifetime of NPP Equipment, Kiev, Ukraine, 2012.
21) Makhanev V O, Pavlovich A A, Podlatov M A et al, “Application of acoustoelesticity method for ensuring of safe operation of NPP technological components”, Int. Conf. “Structural Integrity and Lifetime of NPP Equipment, Kiev, Ukraine, 2012.
22) Baranenko V I, Jantchenko J A et al, “About working norms of admissible thickness pipelines of the atomic power stations subjected to erosion-corrosion wear”, 12th Int. Conf. “Material Science Issues in Design, Manufacturing and Operation of NPP Equipment”, Pushkin-Saint Petersburg, Russia, 2012.
23) Rostechnadzor. Unified procedures of NPP equipment and piping base metal, welds and cladding inspection. Ultrasonic inspection. Part III. Thickness measurement of monometals, bimetals and anticorrosion cladding. PNAE G-7-031-91.
24) LLC «ENCOTES». NPP equipment components. Procedure of mechanical stresses due to technological effects measurement with acoustoelasticity method (Rostechregulirovanie certificate №633/17004; registration number FR.1.28.2009.06227 in the State List of procedures of measurement performance in the area of State metrological control and supervision).
25) JSC “Concern Rosenergoatom”. The list of technical documents for regulation of NPP Units safe operation ensuring (obligatory and recommended).
26) Rostechregulirovanie. Certificate № RU.C.28.011.A № 20395.
27) Rostechnadzor. Requirements to NPP quality assurance program. NP-011-99.
28) Saakov E S, Ryasny S I, Khaidretdinov V U, “Issues of NPP commissioning full-scale tests efficiency”, Electric Stations, 2007 9 10-14.
29) Saakov E S, “NPP commissioning regulation and optimization”, Author’s abstract of dissertation on competition of a scientific degree of the doctor of technical Sciences, 2008.
30) JSC “Concern Rosenergoatom”. Methodical recommendations for NPP equipment, piping and structures ISI scope and periodicity optimization.

PIPING INSPECTION II

A NEW METHOD FOR DRIVING 128CH MATRIX PHASED ARRAY PROBES WITH A VERY COMPACT AND HIGH PERFORMANCE SOLUTION

G. Dao, Advanced OEM Solutions, USA

ABSTRACT

As phased array UT continues to gain wide acceptance, matrix arrays are also becoming more common and easily attainable, creating a need for higher channel count instruments. The Nuclear and Power Generation industry has been a major influential force in driving NDT technology to its limits to further improve inspection speeds, while dealing with complex geometry. This paper will explore how pairing matrix arrays with new phased array (PA) technology opens doors to better inspections. A high performance PA instrument with faster data rates, a smaller form factor, and capability to adapt to specific applications will also be highlighted. Also, new system integration techniques for demanding applications are discussed.

INTRODUCTION

Matrix Phased Array definitely brings benefits to the table in various non-destructive testing applications, but it is important to have proper equipment to drive the transducer while still staying cost effective. Some benefits of a matrix probe are being able to steer and focus the beam in a 3D volume, point focusing, faster scanning speeds and the ability to correct focusing aberrations. Having at least a 128/128 PA instrument like OEMPA gives the ability to fire and receive 128 elements at the same time improving beam steering and spatial resolution.

Figure 1 represents a size comparison to see that high channel instruments like a 64/64 and 128/128 are so compact compared to a typical notebook computer.

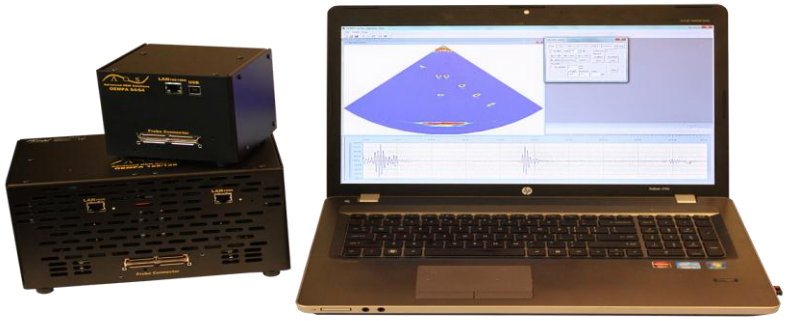

Figure 1: OEMPA 64/64 and OEMPA 128/128 with Laptop

UNIQUE BENEFITS OF OEMPA

OEMPA has many advanced features like excellent SNR, high parallel channel count instruments like 128/128, easy integration, fast data throughput, and more, however there are four benefits that make OEMPA even more unique.

- Size – Having a smaller size instrument opens the door to mounting the instrument anywhere and easier integration into automated systems.
- Openness – This provides research institutes, universities and integrators the opportunity to control the instrument in a flexible way.
- Cost Effective – Everyone loves new state of the art technology, but in a practical sense OEMPA's low price point allows easier adoption.
- OEM – Integrators can take advantage of an OEM model to save cost on research and development costs of a new instrument and concentrate on the final software application and final solution.

MATRIX ARRAY 3D FOCAL LAW CALCULATOR

Driving a matrix probe is not so trivial. The required delays that make up the focal laws is different and more complex than doing an electronic scan or sector scan with a linear phased array transducer. With the software development kit for OEMPA one can call software functions to input information like the probe parameters, wedge parameters and sweep parameters to setup the instrument. Often it is necessary to visualize what one input into the calculator to verify if that is where one would expect the beam to cover in the material.

Typically, with a linear array or a rectangle array element pitch can be defined by specifying the element spacing by a pitch in the primary axis and secondary axis. However, in the case of the Rho Theta probe you would require a custom element mapping where the X, Y coordinate for each element is input into the calculator. The software actually even supports an extra Z coordinate as well.

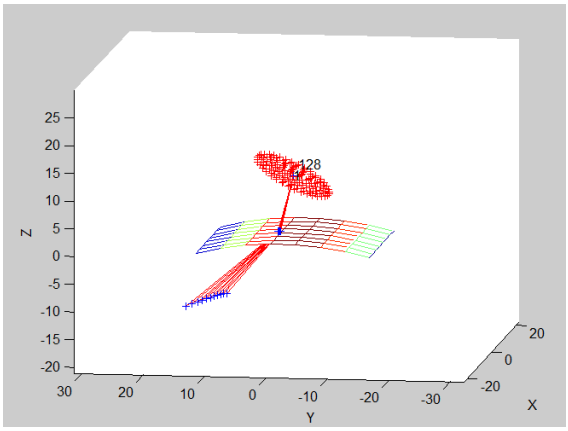

Figure 2: Rho-Theta Probe on a Curved Surface (e.g. Pipe)

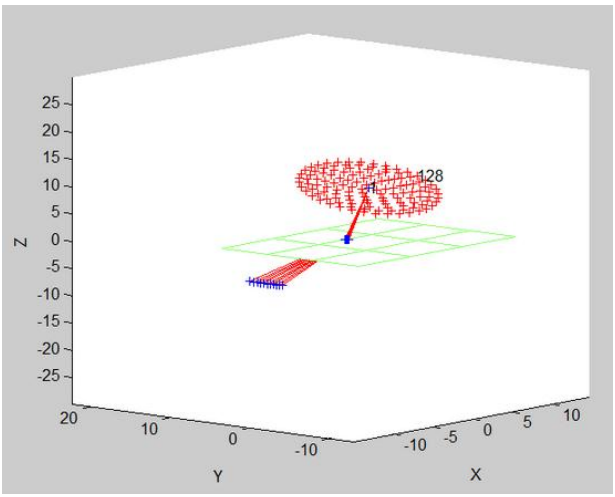

Figure 3: Rho-Theta on a Plane Surface

SMALL FORM FACTOR

Traditional systems for nuclear pressure vessel weld inspections require extremely long umbilical cables that can go upwards of 50 meters that mainly consist of separate coaxial cables for each phased array channel. It is well known that phased array has a large number of channels, in some cases as many as 128 or more. One can already imagine the thickness and diameter of such a cable. It is also important to consider the weight and the ease of handling. What happens when one of these cables fails or is damaged? Inspectors need to have spare cables readily available. When you add the cost of this complex cable with spares it can in some cases equal or exceed the cost of the phased array instrument itself.

Figure 4: OEMPA 64/64 Can Be Held in One's Hand

CONCLUSION

Matrix phased array will continue to grow in popularity as its benefits are understood, cost effectively implemented or adopted in procedures. Having the right instrument to drive the transducer is crucial in a successful inspection system. OEMPA demonstrates advanced capabilities like a focal law calculator powerful enough to generate delays for various types of matrix probes (custom mappings, rectangular

mappings and linear), compact size for easier integration and mounting closer to the transducer, low price point, OEM concept of freedom in branding, and openness in full control and access to the low level parameters.

REFERENCES

1) Dao G and Ginzel R, "New Customizable Phased Array UT Instrument Opens Door for Furthering Research and Better Industrial Implementation", The 40th Annual Review of Progress in Quantitative Nondestructive Evaluation, 2013.

ULTRASONIC PHASED ARRAY: APPLICATION TO A COARSE-GRAINED STAINLESS STEEL COMPONENT EXAMINATION

G.Garzino, J.M. Paris, AREVA, France

INTRODUCTION

The EPR™ primary piping circuit is made up of three different legs (the hot legs shown in **Figure 1**, the cold leg and the U leg) connecting the main components.

Figure 1 : View on hot leg

These pipes, made of forged austenitic stainless steel, are manufactured by AREVA NP Creusot Forge. An ultrasonic test of the entire pipe is required following manufacturing. This standard inspection is achieved with probes, whose active surface is adapted to the different external profiles of the legs. The principal test modes are 0° Longitudinal Waves (0°LW) and 45° Shear waves (45°SW).

In 2006, in support of the Flamanville EPR™, four hot legs and four cold legs had been produced. During the ultrasonic tests following manufacturing, the structural noise level in the running section and in the elbow was too high to detect the minimum target flaw to assure component integrety. Subsequently, other transducers, available on the market, were evaluated but they too did not give satisfactory results. Thus, the legs have been finally rejected and the material was returned to the forge to be remade at a significant cost to the manufacturer. The second attempt to manufacture these pipes included numerous process changes to improve the pipe inspect-ability.

Nevertheless, in parallel, AREVA NDE SOLUTIONS was asked to develop a technique to inspect hot & cold legs under an expertise mode contract. This is the subject of this work.

METALLURGIC AND ULTRASONIC LEGS ANALYSIS

In order to identify different influencing metallurgic and ultrasonic tests parameters, several tests were conducted on the affected legs.

Metallurgic Analysis

Samples were taken from one pipe section (referenced as Hot leg N°1) presenting the most important general structural noise. These samples were selected as shown in Figure 2 due to their different ultrasonic characteristics.

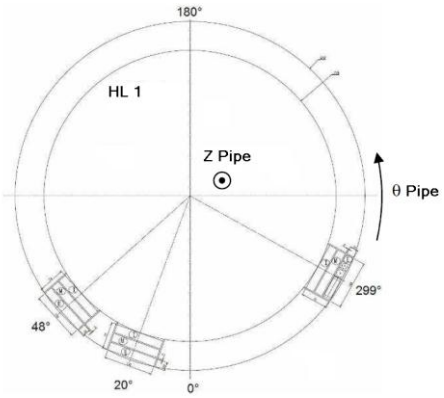

Figure 2 : Metallurgical sample locations on the Hot Leg N°1 pipe

Three areas of interest are identified.
The one at 299° presented a relatively low attenuation to the ultrasound; the area at 20° presents a medium level of attenuation to the ultrasound, and the one at 48° is highly attenuative to ultrasound.
Once the areas were selected, cuts were made separating the samples into three groups, depending on their positions within the pipe thickness.
The three groups were:

- Group I, located in the Inner diameter
- Group M, in the Middle section
- Group E, from the External part of the pipe wall thickness

Finally, for each group, samples are cut in the longitudinal direction (parallel to Z Pipe) and others in the transverse direction (parallel to θ Pipe). In total, 18 samples were available for the metallurgic tests.

The metallography tests were conducted by the laboratory of metallography Vulcain at AREVA NP Creusot Forge. The tests consisted of determining the average diameter of the grains (D) within each sample by using an automatic analysis package - Leica Qwin from Leica Microsystems. All 18 samples were analyzed following two directions:

- The axial direction (perpendicular to the main axis of the samples)
- The transverse direction (parallel to the main axis of the samples)

The data obtained are summarized in the Table 1.

Samples	Longitudinal (mm)						Transverse (mm)					
	Axial direction			Radial direction			Axial direction			Radial direction		
	I	M	E	I	M	E	I	M	E	I	M	E
48°	0,71	0,59	0,59	0,71	0,71	0,71	0,59	0,71	0,71	0,59	0,84	1,00
20°	0,30	0,35	1,00	0,30	0,41	1,00	0,30	0,35	1,00	0,35	0,18	1,00
299°	0,30	0,35	0,35	0,42	0,50	0,35	0,35	0,42	0,50	0,42	0,42	0,30

Table 1 : Synthesis of the average grain diameter (in mm) obtained on the 18 samples

Significant observations from the metallurgical study include:

- No significant difference between the average grain diameter for the samples taken at similar azimuth positions but tested in different directions (axial and radial).
- The evolution of the average grain diameter in function of the position of the sample in the thickness of the leg does not follow any specific trend.
- A difference in the average grain diameter was observed among the mean values obtained for each azimuth: 0,71mm for 48°, 0,58mm for 20°, 0,39mm for 299°.
- The evolution of the average grain diameter for each azimuth is in accordance with the first inspection conducted. Thus, the area determined as highly attenuative (48°) presents the grain with the largest dimensions.

Following these metallurgical assessments, additional ultrasonic tests were performed.

Ultrasonic Analysis

For the different samples, attenuation measurements using 0° longitudinal wave probes with varying frequency were evaluated. The data obtained are presented in Figure 3.

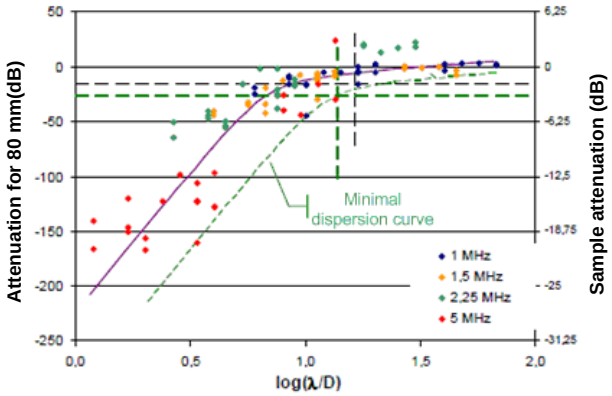

Figure 3 : Attenuation function of the ratio log(λ/D) for different frequency

For a clearer view of the expected attenuation on the component, the dB loss is also represented on the left side of Figure 3 for 80mm, which is the leg thickness. As expected, the least attenuation is observed for the lower values of the attenuation function ratio. Also, it is possible to extrapolate a curve representing the attenuation evolution as a function of log(λ/D). This facilitates selection of the working frequency depending on the average grain diameter and the maximum attenuation that the operator can accept. From these results, an inspection strategy was developed.

THE DEVELOPED INSPECTION STRATEGY

The aim of the development was to inspect pipe walls presenting an average grain diameter up to 1mm, corresponding to the maximum value identified in the samples.

General ideas

For developing the inspection, the sample pipe was cut into several samples presenting various noise characteristics. Eight separate mock-ups were prepared and each mock-up included side drilled and flat bottom holes that were then used for justifying the inspection performances.
A view of one of the mock-up is presented in Figure 4.

Figure 4 : Experimental leg mock-up

Based on experience, a phased array probe was designed and tested. The choice was made to work with annular concentric elements having equivalent emission surfaces. Following the results obtained during the first ultrasonic study, a 1MHz central frequency for the probe was chosen.
To maintain a complete contact between the planar probe and the pipe surface, contoured wedges were machined to the pipe's outer diameter and these were fit to the PA transducer face. Standard electronics were used for the data acquisition. The elements delay laws, necessary for focusing at different depths, were calculated via the acquisition & analysis ZETEC UT software Ultravision.

0° Longitudinal wave inspection development

After preliminary trials, it became obvious that optimized focal laws for the different depths would be required. Thus, for this inspection, six different focal laws have been defined.
Tests were conducted on the different mock-ups available for verifying the capability to detect and characterize the defects of interest. (Signal/Noise Ratio & depths into the mock-up).
The **Figure 5** & **Figure 6** present partial results obtained during the trials on a coarse grain mock-up.

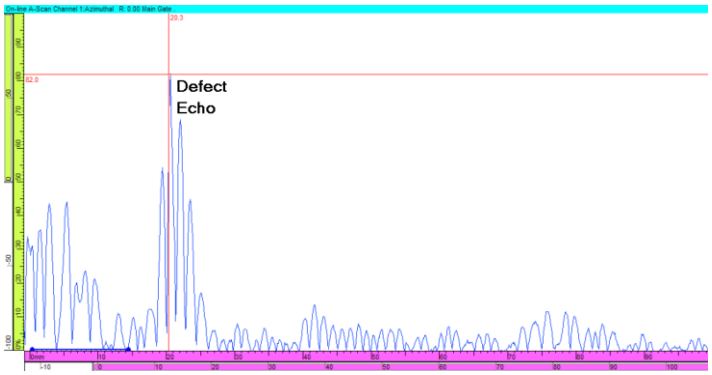

Figure 5 : A-Scan on a Φ3mm flat bottom hole having a 20mm ligament with the investigation surface into a coarse grain mock-up

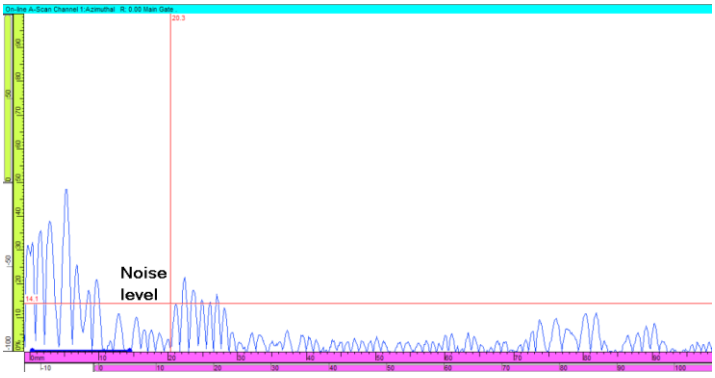

Figure 6 : A-Scan on an area without defects for measuring the noise level into a coarse grain mock-up

The **Figure 5** presents the echo obtained on a Φ3mm flat bottom hole having a 20mm ligament with the investigation surface into a coarse grain mock-up. A clear echo appears at a 20.3mm depth.
The **Figure 6** presents the noise level in the same coarse grain mock-up. For it, an acquisition is done in an area of the mock-up without defects. The noise level is then measured at the same depth than the one of the defect obtained previously by keeping the same settings.
For this defect, the signal / noise ratio (SNR) is equals to 15dB.
By this way, on an important number of mock-ups and defects, it has been possible to demonstrate the possibility to detect and characterize defects at various depths with sufficient SNR & a good positioning capability. Moreover, these acquisitions, achieved on mock-ups with different noise level, could be used as calibration values for future inspections on possible coarse grained legs.

Angled Longitudinal waves inspection development

Based on the previous ultrasonic results, the choice was made to work with angled longitudinal waves and not angled shear waves due to the high attenuation from the angled shear wave configuration.

Then, it has been necessary to identify the correct refraction angle into the mock-up for keeping sufficient longitudinal waves energy relatively to the shear waves energy. This identification has been conducted under the software CIVA 10.1 developed by the CEA.
Once this angle defined, tests have been conducted on the different mock-ups produced for the angled waves validation. The important parameters were the same ones as for the 0° longitudinal wave case.
The **Figure 7** & **Figure 8** present a part of the results obtained.

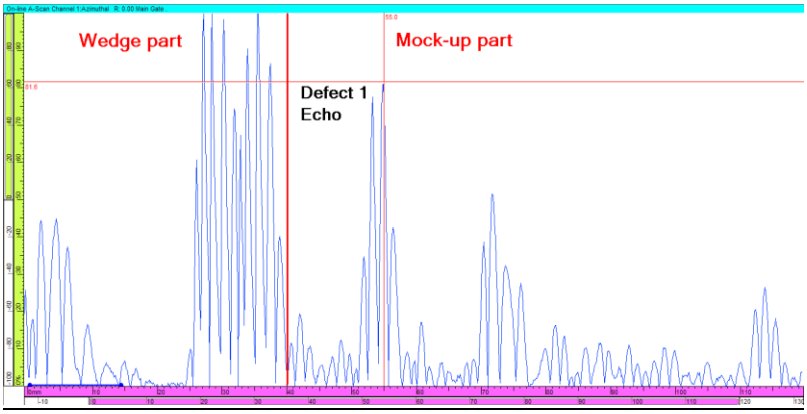

Figure 7 : A-Scan on a Φ3mm side drilled hole into a coarse grain mock-up

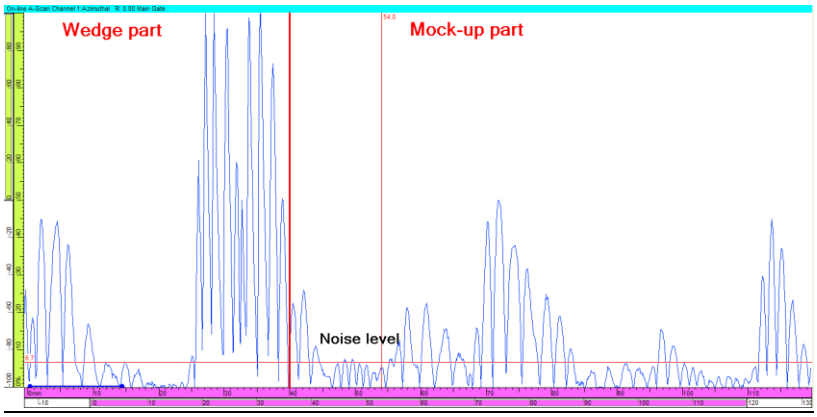

Figure 8 : A-Scan on an area without defects for measuring the noise level into a coarse grain mock-up

The **Figure 7** presents the echo obtained on a Φ3mm side drilled hole into a coarse grain mock-up. A clear echo appears at a 55mm depth. It has to be underlined that for this scan no delay was used under the acquisition software, which explains that the first 40mm corresponds to the wedges echoes. These permanent echoes have no effect on the measurements. Another permanent echo, due to the wedge configuration used, is visible at a 70mm depth. Nevertheless, trials showed that this echo was sufficiently low compared to a defect echo in this area, to assure that significant defects at this depth could be detected and distinguished from this permanent echo. The **Figure 8** presents the noise level in the coarse grain mock-up. For this case, data is acquired in an area of the mock-up without defects. Then, retaining all the same instrument gain settings, the noise level and the defect signal amplitude are measured on a similar sample with a representative reflector. For this defect, the signal / noise ratio (SNR) is equals to 21dB.
By this approach, as with the planar waves validation, the possibility to detect and characterize defects, at various depths, with sufficient SNR and a reasonable depth sizing capability has been demonstrated. Moreover, these acquisitions, achieved on mock-ups with different noise levels, could be used as calibration references for future inspections on possible coarse grained pipe legs.

CONCLUSION

These developments validated the possibility to detect and characterize defects within large-grain forged stainless steel pipe (up to 1mm grain-size and 80mm wall thickness) typical of the pipes manufactured for EPR hot and cold legs. From these results, a procedure has been elaborated to enable the implementation of this ultrasonic inspection procedure.

FLAW DETECTION IN HIGHLY SCATTERING POLYCRYSTALLINE MATERIAL: IMPROVEMENT OF THE PERFORMANCES BY THE USE OF PHASED ARRAY PROBES AND SMART FILTERING TECHNIQUE

F. Rupin, S. Shahjahan, B. Chassignole, EDF - R&D, France
A. Aubry, A. Derode, Institut Langevin, Université Paris Diderot, ESPCI, France

ABSTRACT

Flaw detection using ultrasonic non destructive testing on coarse grain steels commonly found in nuclear power plants is disturbed by a high backscattered noise. This leads to a decrease of the detection capabilities of common ultrasonic testing techniques, particularly at high frequencies and large depths for which multiple scattering dominates. Recent studies have shown that the contribution of single scattering could be extracted from multiple scattering in complex medium. These results were obtained on a model random medium made of parallel steel rods immersed in water. They showed that, when using a phased array probe, the ability to detect a target could be significantly increased using a smart filtering method, based on the application of the matrix theory on FMC (full matrix capture) acquisition, in supplement with the D.O.R.T. (French acronym for the decomposition of the time-reversal operator) method.

In this work, this new method is applied to an industrial material made of a nickel based alloy (Inconel600®) exhibiting a thermally-induced coarse grain structure. Experimental results on flaw detection of 2mm side drilled holes located at various depths in the mock-up are presented and compared to the classical detection techniques. Despite the existence of high structural noise when inspecting this material in the 2-5 MHz frequency range, a very significant improvement of the detection performances is observed. The advantages and limitations of the method are also discussed in this work.

Keywords: Ultrasound, Multiple Scattering, Noise, DORT Imaging, Array Processing, Flaw Detection

INTRODUCTION

Detection performances of ultrasonic techniques decrease for materials with a coarse grain structure. In particular, in the case where the characteristic grain size is comparable to the wavelength, scattering of ultrasonic waves at grain boundaries attenuates, distorts the wave and also generates a so-called “structural noise” which decreases detection capacities [1, 2].

Propagation of waves in a highly scattering medium has been the subject of many studies dealing with the development of theoretical backscattering models [3-6] or with the improvement of the signal-to-noise ratio [7-13]. From an experimental point of view, the development of phased array probes has also opened new perspectives for the UT characterization and inspection of heterogeneous materials. In particular, solutions to improve imaging in polycrystalline media using the advantages of phased array acquisitions emerge. Indeed, by means of the full matrix capture (FMC) [14, 15] and proper post-processing, it is possible to optimize target detection in homogeneous or weakly scattering media. For instance, the Total Focusing Method (TFM) allows creating an image as if the beam had been focused on every point of it. Consequently, it generally increases the signal-to-noise ratio compared to conventional imaging [16]. Time-reversal imaging is also possible by using a phased array to optimize target detection [11, 17, 18]. But both of these techniques are limited in presence of strong multiple scattering. Recent studies on the reduction of the multiple scattering contribution have been developed on synthetic model media (forests of steel rods immersed in water) in order to improve target detection in a scattering environment [19]. These studies, based on random matrix theory, discriminate single and multiple scattering contributions in the total backscattered signals. The technique relies on a particular property of single scattering: a deterministic coherence along the anti-diagonals of the response matrix.

The purpose of this paper is to apply this concept to an industrial metallic polycrystalline sample exhibiting strong ultrasonic scattering. Experiments were performed on a nickel-based alloy (Inconel600®) exhibiting a coarse grain microstructure in which four side-drilled holes (SDH) have been manufactured. First, the basic principles of the separation and detection method are described. Then the experimental results (particularly the detection rate and the signal-to-noise ratio) are presented and compared to the total focusing method (TFM). A significant improvement is demonstrated.

DENOISING OF THE ACOUSTIC SIGNAL

General principle

In highly diffusive material, the structural noise limits flaws detection and can create false alarms. A previous study has shown the possibility to separate the multiple scattering (noise) from the single scattering part of the signal. The details of the method have been published elsewhere [19, 20] but briefly, it is based on the acquisition of the transfer matrix of the material using a N-element linear array probe. A pulse is emitted from element i and the backscattered signal is recorded on the N elements of the array (**Figure** 1). The same operation is repeated with the N emitters. The response from transducer i to transducer j is then correlated with the emission signal to create $h_{ij}(t)$ impulse response of the couple (i,j). The N×N inter-element matrix **H** is finally composed of all impulse responses $h_{ij}(t)$.

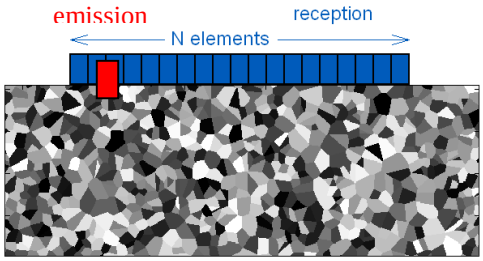

Figure 1: Principle of the full matrix capture sequences, here the signal $h_{ij}(t)$ with i=3 and j∈[1;19] is illustrated.

Once **H**(t) is acquired, a filtering method developed from the random matrix theory is used to reduce the multi-scattering part of the signal. The details of the method are explained in [19, 20]. Briefly, it is based on the fact that, in the Fourier domain, two typical behaviors of the inter-element matrix can be observed whether the Single Scattering (SS) or the Multiple Scattering (MS) dominates [21]. When MS dominates, the matrix was found to be similar to a classical random matrix, whereas when SS dominates it is similar to a Hankel matrix. As a consequence, it implies that whatever the medium, as long as there is only single scattering the elements of the matrix have a long-range deterministic coherence along their anti-diagonals. On the contrary, when multiple scattering dominates, there is no such coherence. This is the key to separate single and multiple scattering contributions. By and large, the idea consists in extracting from the total matrix the part that exhibits the particular form of coherence using a projection in an appropriate base.

Finally, the target detection is achieved by the DORT (French acronym for decomposition of the time reversal operator) method applied to the filtered matrix in order to detect more efficiently the manufactured defects [19, 20].

MATERIAL AND EXPERIMENTAL SET-UP

The inspected medium is a block of 90×90×280mm^3 made of Inconel600® which is a nickel-based alloy commonly used in the nuclear industry. It contains four side-drilled holes (SDH) of radius 1mm, located at depths 10, 30, 50 and 70mm from one face and 20 to 80mm from the other face (**Figure 2a**). This block was harvested from a forged bar and underwent a specific heat treatment to induce a growth of the mean grain size. Metallographic and EBSD analyses performed on a 17×13mm^2 sample yield the mean grain size (750 µm), and the standard deviation around the mean

value is 400 µm. In **Table 1**, the characteristics of the two 128-element linear arrays used in the experiments are summarized.
The block is immersed in a water tank and the probes are in contact configuration (**Figure 2a**). The acquisitions of **H**(t) in presence of a defect are realized at 11 different probe positions recorded along the axis of each flaw (y axis in **Figure 2b**). The probe is centered on the flaw position along the x-axis.

Table 1: Array probes characteristics; r is the average wavelength / mean grain size ratio.

	Central Frequency	-6dB Bandwidth	Element size (mm²)	Pitch (mm)	Sampling (MHz)	r
Array Probe 1	3 MHz	2.5 - 3.3 MHz	0.39×12	0.417	40	2.6
Array Probe 2	5 MHz	3.3 - 6.8 MHz	0.3×15	0.5	100	1.56

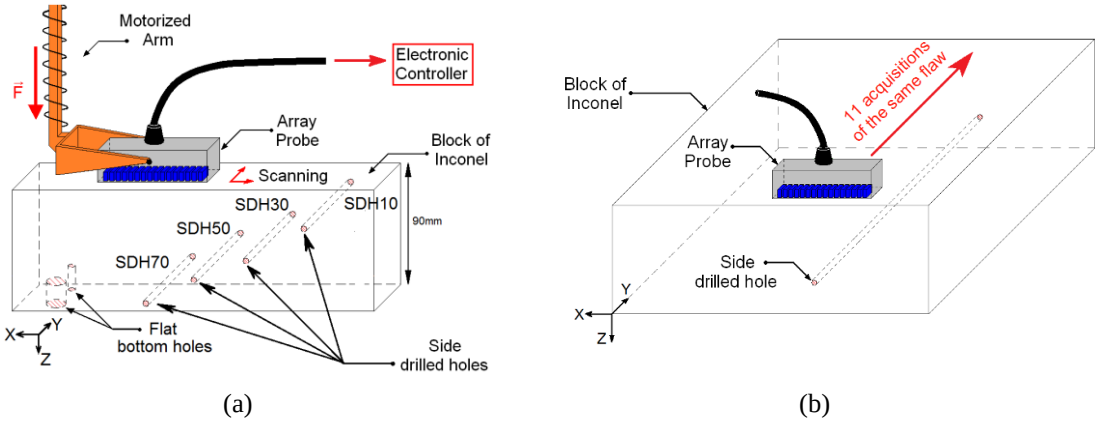

(a) (b)

Figure 2: Illustration of the experimental set-up (a) and the acquisitions along the flaws (b).

EXPERIMENTAL RESULTS ON VOLUMIC FLAW DETECTION

Total Focusing Method (TFM)

Once the matrix **H**(t) is acquired, classical post-treatment can be realized by summation and time shift operations on the $h_{ij}(t)$ signals in order to create a synthetic image of the medium [14, 22]. For example, adjacent elements responses can be added to create a plane wave or shifted and summed to steer the beam. Synthetic images can also be obtained using the total focusing method (TFM) [14, 22]. Signals from all the elements on the array are summed to synthesize a focus at every point (x,z) of the inspected zone as Eq. (1).

$$I(x, z = ct) = \sum_{i,j}^{N} h_{ij}\left(\frac{\sqrt{(x_i - x)^2 + z} + \sqrt{(x_j - x)^2 + z}}{c}\right). \quad (1)$$

c is the longitudinal wave velocity, x_i and x_j are respectively the emitter and receiver positions. This amounts to focus the ultrasonic beam, in emission as well as in reception. The resulting image can be interpreted as a reflectivity map. As typical examples, **Figure 3** shows TFM images obtained at different depths and frequencies. The structural noise level becomes so important that the flaws are hardly detectible beyond 70mm at 3 MHz (50mm at 5 MHz). For smaller depths, the flaws are correctly detected.

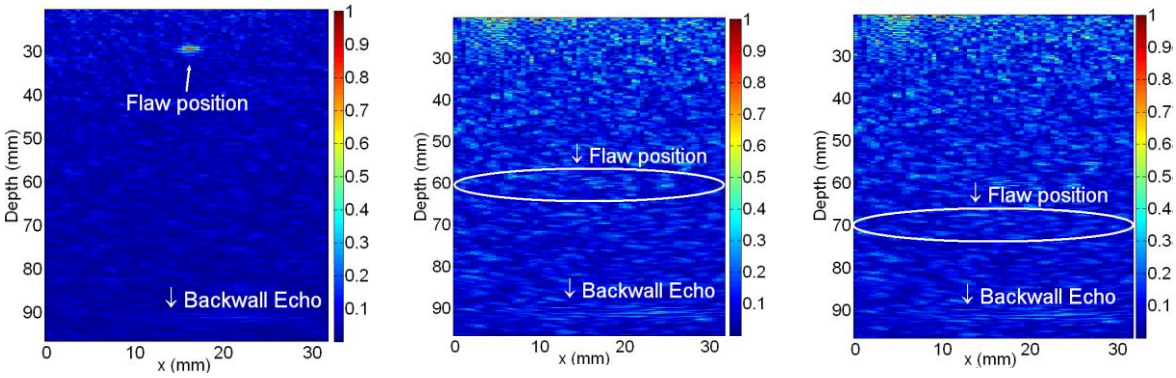

(a) (b) (c)

Figure 3: Example of TFM images with side drilled holes at z=30mm - 5 MHz (a); at z=60mm - 5 MHz (b); at z=70mm - 5 MHz (c).

DORT method combined with multiple scattering filtering

DORT imaging was then applied before and after filtering obtained in the flaw's area. An example of the images obtained for one of the deepest flaws (70mm) with the 5 MHz array is given in **Figure 4**. This corresponds to the worst configurations in terms of flaw detection. It undoubtedly shows the benefit of the MS Filtering (MSF) procedure, which is meant to eliminate multiple scattering. In **Figure 4a** and **b**, TFM and classical DORT images are too noisy and the defect is not detectable. On the contrary, the echo of the side drilled hole (SDH) is clearly visible once the "multiple scattering filter" is applied (**Figure 4c**). The MSF image also shows some spikes here and there (yet of much lower amplitude that the defect itself), which are false alarms.

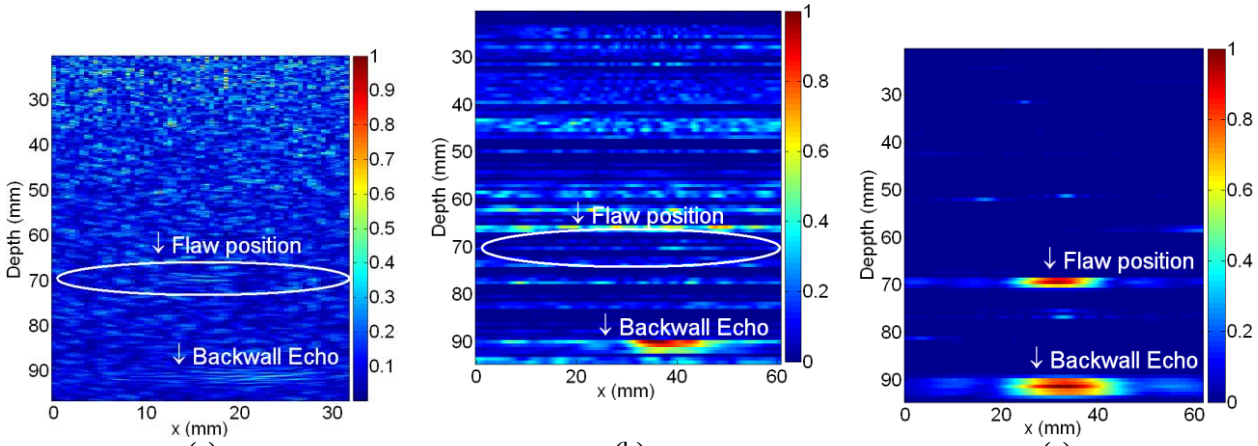

(a) (b) (c)

Figure 4: Comparison of three imaging techniques with the same data set, for the case of a SDH at 70mm with the 5 MHz array: TFM (a), DORT without MS filtering (b) and DORT with MS filtering (c).

Detection rate and SNR

Since we deal with a random structure, the spectacular result of **Figure 4** might be just a lucky strike. In order to compare the results of all three techniques, a systematic study was achieved for 11 realizations of each SDH (**Figure 2b**). Two indicators are used to furnish quantitative evaluation of the performances of the techniques. The first indicator is a signal-to-noise ratio (SNR) defined as:

$$SNR^X = 20log\frac{{A_{max}}^X}{{N_{max}}^X} \quad (2)$$

The superscript X represents the technique used (TFM, DORT, MSF DORT). It is computed, for each realization, as the ratio of A_{max} (the maximum amplitude in the flaw area) to N_{max} (the maximum noise amplitude for the same realization in a time window corresponding to depths between ±10mm around the flaw, see **Figure 5**).

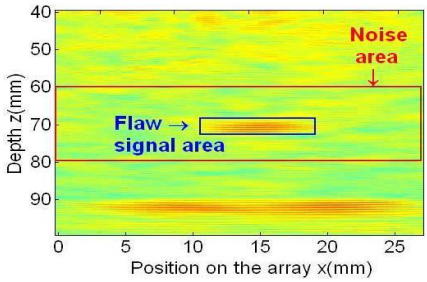

Figure 5: Example of the zone inspected in order to define the "signal-to-noise ratio" for a flaw at 70mm.

The second indicator is a detection rate: as often in NDT, the flaw is considered to be detectible if SNR≥3dB.

Table 2 summarizes the detection rates (evaluated on the ensemble of 11 positions along the same defect as illustrated in **Figure 2b**) and the mean SNR on the detected cases. First, these results show that for all three techniques, detection is more difficult at 5 MHz, which is not surprising since attenuation and structural noise increase with frequency in the stochastic domain. Second, a clear improvement of the detection rate is observed at large depths by using the combination of DORT method and MS filtering, particularly for the 5 MHz array. The mean SNR is also significantly increased which lets one expect that for less echogenic flaws than SDH, this technique might give interesting results.

Table 2: Experimental results: comparison of detection rates and means SNR for all three techniques.

Depth	Frequency of 3MHz			Frequency of 5MHz		
Imaging technique	TFM	DORT with K	DORT with KF	TFM	DORT with K	DORT with KF
SDH 30	100%	100%	100%	100%	100%	100%
SDH 40	100%	100%	100%	72.7%	100%	100%
SDH 50	100%	100%	100%	36.4%	90.9%	100%
SDH 60	100%	100%	100%	0%	0%	18.2%
SDH 70	54.5%	13.8%	82%	0%	0%	63.6%
SDH 80	0%	27.3%	9%	0%	0%	9.1%

Detection rate (%)

Depth	Frequency of 3MHz			Frequency of 5MHz		
Imaging technique	TFM	DORT with K	DORT with KF	TFM	DORT with K	DORT with KF
SDH 30	18 ± 1.0	17.7 ± 2.4	15.5 ± 3.6	8.9 ± 1.9	15.6 ± 2.1	24.8 ± 8.8
SDH 40	14 ± 1.5	17.9 ± 2.5	20.4 ± 7.0	5.5 ± 1.5	19.0 ± 3.6	21.7 ± 5.9
SDH 50	10 ± 1.5	18.8 ± 5.2	16.9 ± 4.5	3.8 ± 0.2	7.7 ± 4.3	17.9 ± 7.3
SDH 60	6.9 ± 1.3	16.0 ± 6.6	14.2 ± 5.8	X	X	18.4 ± 9.0
SDH 70	4.1 ± 0.6	13.8 ± 8.2	16.6 ± 9.2	X	X	11.1 ± 3.5
SDH 80	X	7.3 ± 2.7	9.93	X	X	7.7 ± 5.4

Mean signal to noise ratio (dB)

FIRST RESULT ON A PLANE DEFECT

An additional flaw was introduced inside block B4: an emerging notch of 20mm height perpendicular to the backwall face (**Figure 6**). The same experiment than for the SDHs was carried out with a 128-element linear array of 2 MHz. The results when applying the three post-processing techniques (TFM, DORT, MSF DORT) are given **Figure 7**. With the TFM, a discontinuity of the back-wall echo is observed due to the shadowing of the notch but the defect itself is not detected. Similarly, the classical DORT method fails though it shows strange artifact at higher depth. On the contrary, the MSF DORT reveals clearly an echogenic signature, roughly corresponding to the notch extension. However, it has to be noted that it is just a first attempt on one inspection configuration, so it is difficult to draw general conclusions but the potential of the MSF DORT is enhanced.

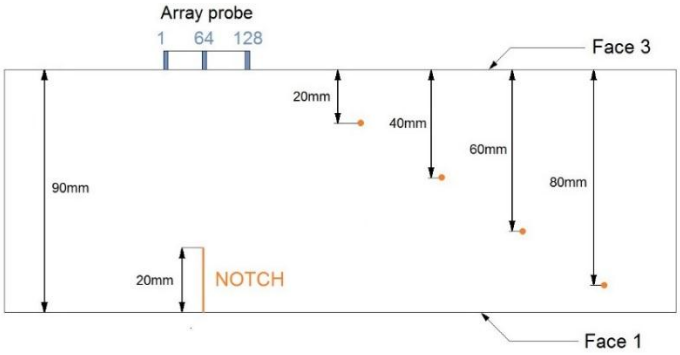

Figure 6: Characteristics of the mock-up after introduction of notch of 20mm height.

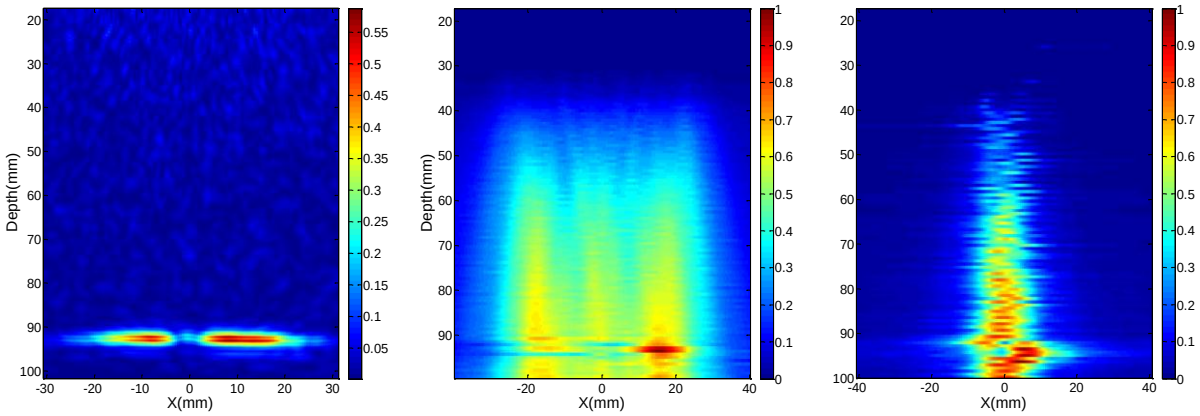

TFM Classical DORT Filtered DORT

Figure 7: Notch detection with the TFM, DORT and MSF DORT with a 2 MHz 128-element linear phased array.

CONCLUSIONS AND PROSPECTS

Experimental results regarding flaw detection on a nickel-based alloy block exhibiting a coarse-grain structure were presented. A novel imaging technique, the DORT method combined with the MS filtering, was compared to the Total Focusing Method. At large depths and higher frequencies, classical imaging techniques are clearly not adapted to detect flaws in such scattering microstructures. However the improvement of flaw detection by reducing the multiple scattering contribution is spectacular. Yet the method proposed here is naturally not perfect and, for instance, some false alarms were produced. The present experimental results must be completed e.g., by a study of the influence of the microstructure (grain size, etc.), on the SNR, the detection rates and the persistence of false alarms. New experimental results on more complex structures and defects are currently on hand, as well as numerical simulations on various microstructures, in order to challenge the robustness of this promising technique.

ACKNOWLEDGEMENTS

A. Derode is grateful for funding provided by the *Agence Nationale de la Recherche* (ANR-11-BS09-007-01, Research Project DiAMAN 2011-1015). EDF R&D (*Électricité de France – Recherche & Développement*) is grateful for funding provided by the *Association Nationale de la Recherche et de la Technologie* (ANRT).

REFERENCES

1. Yalda, I., F.J. Margetan, and R.B. Thompson, *Predicting ultrasonic grain noise in polycrystals: A Monte Carlo model.* The Journal of the Acoustical Society of America, 1996. **99**: p. 3445-3455.
2. Ghoshal, G. and J.A. Turner, *Numerical model of longitudinal wave scattering in polycrystals.* IEEE Transactions on Ultrasonics, Ferroelectrics and Frequency Control, 2009. **56**(7): p. 1419-1428.
3. Roth, W., *Scattering of ultrasonic radiation in polycrystalline metals.* Journal of Applied Physics, 1948. **19**(10): p. 901-910.
4. Turner, J.A. and R.L. Weaver, *Time dependence of multiply scattered diffuse ultrasound in polycrystalline media.* The Journal of the Acoustical Society of America, 1995. **97**(5): p. 2639-2644.
5. Turner, J.A., et al., *Radiative transfer and multiple scattering of diffuse ultrasound in polycrystalline media.* The Journal of the Acoustical Society of America, 1994. **96**(6): p. 3675-3683.
6. Reynolds, W.N. and R.L. Smith, *Ultrasonic wave attenuation spectra in steels.* Journal of Physics D: Applied Physics, 1984. **17**: p. 109-116.
7. Abbate, A., et al., *Signal detection and noise suppression using a wavelet transform signal processor: application to ultrasonic flaw detection.* IEEE Transactions on Ultrasonics, Ferroelectrics and Frequency Control, 1997. **44**(1): p. 14-26.
8. Chen, J., Y. Shi, and S. Shi, *Noise analysis of digital ultrasonic system and elimination of pulse noise.* International Journal of Pressure Vessels and Piping, 1998. **75**(12): p. 887-890.
9. Chen, Y., Y. Shi, and Y. Lei, *Use of a Wavelet Analysis Technique for the Enhancement of Signal-to-noise Ratio in Ultrasonic NDE.* Insight, 1996. **38**(11): p. 800-803.
10. Newhouse, V., et al., *Flaw-to-grain echo enhancement by split-spectrum processing.* Ultrasonics, 1982. **20**(2): p. 59-68.
11. Prada, C., et al., *Time reversal techniques in ultrasonic nondestructive testing of scattering media.* Inverse Problems, 2002. **18**: p. 1761-1773.
12. Russell, M. and S. Neal, *Grain noise power spectrum estimation for weak scattering polycrystalline materials using experimentally estimated backscatter coefficients: normal incidence.* Ultrasonics, 1994. **32**(3): p. 163-171.
13. Yue, L. and Y. Chong-Fu, *Two signal processing techniques for the enhancement of the flaw-to-grain echo ratio.* Ultrasonics, 1987. **25**(2): p. 90-94.
14. Holmes, C., B.W. Drinkwater, and P.D. Wilcox, *Post-processing of the full matrix of ultrasonic transmit-receive array data for non-destructive evaluation.* NDT & E International, 2005. **38**(8): p. 701-711.
15. Zhang, J., et al., *Defect detection using ultrasonic arrays: The multi-mode total focusing method.* NDT & E International, 2010. **43**(2): p. 123-133.
16. Wilcox, P.D., C. Holmes, and B.W. Drinkwater. *Enhanced Defect Detection and Characterisation by Signal Processing of Ultrasonic Array Data*. in *9th ECNDT*. 2006. Berlin, Germany.
17. Prada, C., M. Tanter, and M. Fink. *Flaw detection in solid with the DORT method*. 1997: IEEE.
18. Fink, M., et al., *Time-reversed acoustics.* Reports on Progress in Physics, 2000. **63**: p. 1933.
19. Aubry, A. and A. Derode, *Detection and imaging in a random medium: A matrix method to overcome multiple scattering and aberration.* Journal of Applied Physics, 2009. **106**(4): p. 044903.
20. Aubry, A. and A. Derode, *Random matrix theory applied to acoustic backscattering and imaging In complex media.* Physical Review Letters, 2009. **102**(8): p. 84301.
21. Aubry, A. and A. Derode, *Singular value distribution of the propagation matrix in random scattering media.* Waves in Random and Complex Media, 2010. **20**(3): p. 333-363.
22. Angelsen, B., *Ultrasound imaging. Waves, signals and signal processing*. Emantec. 2000, Trondheim, Norway.

STUDY OF THREE-DIMENSIONAL PHASED ARRAY ULTRASONIC INSPECTION TECHNIQUE FOR FLAW IMAGING

M. Tooma, H. Mori, A. Nishimizu, So Kitazawa
Hitachi Research Laboratory, Hitachi, Japan
K. Ehara, M. Koike, Hitachi-GE Nuclear Energy, Japan

Abstract

The pressurized components such as the main stop valve, casing and piping, etc, utilize cast steel and stainless material. The casting flaw pinhole and porous nest will be introduced in production process. Integrity confirmation by non-destructive inspection of the body and flange plays an important role in guaranteeing air-tightness of the components, therefore, ultrasonic testing, penetrant testing, and magnetic particle testing are currently applied. When in service inspection, stress corrosion cracking and wall thinning occurred by aging. In ultrasonic testing for cast steel material, grain, coarsening, anisotropic phenomena and wall structure reduce inspection accuracy. A new ultrasonic testing methodology was developed to overcome these difficulties; the methodology is derived from novel three-dimensional phased array ultrasonic imaging technique and characteristic of aperture size, i.e, transducer width, and frequency responses. So, I propose three-dimensional phased array ultrasonic inspection technique for flaw imaging, in order to improve the spatial resolution and signal-to-noise ratio (SNR) in flaw imaging. Verification testing using actual materials and mockups showed great improvement in defect visibility and flaw imaging. Therefore, this three-dimensional phased array ultrasonic inspection technique was confirmed powerful and useful technique for flaw imaging.

Keywords: Development in volumetric

DEFECT DETECTION AND SIZING TRIALS USING THE TOTAL FOCUSING METHOD AND SCATTERING COEFFICIENT MATRIX WITH A LINEAR PHASED ARRAY

S. Wedge, L. Carter, A. Rogerson
NDT, AMEC Clean Energy, UK
J. Zhang, B. Drinkwater, Bristol University, UK

ABSTRACT

Novel NDT techniques based on the use of ultrasonic phased arrays have been the subject of much academic research in recent years. In particular, the Total Focusing Method and Scattering Coefficient Matrix post-processing techniques have been developed at Bristol University for improved defect imaging and small defect characterisation as part of research funded by the UK University Research Centre for NDE (RCNDE). Potentially, these techniques offer many advantages over conventional pulse echo and phased array sector scanning techniques. In order to improve understanding of the limitations and capabilities of these techniques in a realistic industrial inspection, AMEC organised a "blind trial" test of these techniques on test specimens containing realistic defects on behalf of RCNDE.

Several 60 mm thick welded ferritic test specimens containing simulated planar and volumetric weld defects of different orientations and locations were examined by Bristol University in open and blind trials. The details of one specimen were revealed to Bristol for the purposes of the open trial, enabling an inspection procedure to be developed for the use of the Total Focusing Method and Scattering Coefficient Matrix on the remaining blind trial test specimens.

This paper reports the findings from this project and reveals evidence of the capability and limitations of these techniques and the overriding need for optimised inspection design to achieve the most effective inspection results in real industrial inspections.

INTRODUCTION

Many new techniques have been developed by academic research departments to take advantage of the flexibility of phased array ultrasonic probes. Often, these techniques have been described as "novel". In NDT, a novel approach can be useful to increase the capability of an inspection by providing a fresh technique independent of existing analysis tools. However, any new analysis technique will require experimental testing to provide evidence of its capability and to identify its region of applicability.

When a technique is in its infancy, it is often tested against a known defect population. This allows the technique to be shown to work against a range of defect species. Optimisation of the technique takes place until the defect is detected and determined to be of the correct size and character. The results are published and the technique labelled as being proficient in the detection and analysis of that particular defect type. Often, despite good intentions, these results feed in to the perception that the technique is capable of detecting a particular species of defect in all circumstances. However, the limiting factor of the capability of a technique is not just limited to the nature of the defect. It can rely upon a host of other parameters such as the geometry and material of the test subject, the crystal arrangement, frequency, size and placement of the ultrasonic probe etc. In order for a technique to be relied upon in an industrial application, it must have a defined inspection procedure to remove variation between inspections that could reduce this capability.

An inspection procedure is a set of instructions to be followed by an inspection operator. If designed and followed correctly, the variation due to operator choice is removed and the written inspection procedure will allow the inspection to be deployed with confidence in industrial applications.

The aim of this project was to test the novel ultrasonic techniques incorporated within Bristol University's Phased Array Full Matrix Capture (FMC) software package named Bristol Array Inspection (BRAIN). This software includes several post-processing algorithms including the Total Focussing Method (TFM) and the Scattering Coefficient Matrix (SCM). In order to achieve the goal of testing this system, the following tasks were required:

- A working inspection procedure was to be developed as part of this project in order to provide a repeatable inspection against which the performance can be assessed.
- An open trial was to be carried out to allow the development of the inspection procedure.
- A witnessed blind trial was to be conducted to test the performance of the operator following the procedure.
- To improve confidence in the capability of the techniques under test, destructive examination was to be conducted on defects in one of the ferritic steel welded test specimens.

For this project, Bristol University was responsible for the procedure development and for carrying out the open and blind trials. AMEC assessed the procedure and the open and blind trials, providing feedback and guidance where required. AMEC was also responsible for conducting the destructive examination.

INSPECTION PROCESSING ALGORITHMS

The BRAIN software includes many phased array post-processing algorithms based on data collected using the Full Matrix Capture technique. This paper is not intended to be a detailed narrative on the inner workings of these techniques. However, to aid in the understanding of the techniques featured in this paper, a brief description is provided below.

FULL MATRIX CAPTURE (FMC)

Full Matrix Capture is a technique whereby every element of a phased array probe is individually pulsed to generate sound that is received on every element including the transmitter. Thus, an a-scan is collected from every combination of transmitting and receiving elements across a specified range. These data can be stored for post-processing at a later time by summing together the a-scans with specific delays attached to each individual a-scan. It has been hailed as a technique that allows data to be processed multiple times from a single data set due to it recording every a-scan possible at a given probe position. This technique was used in this project to collect data from the phased array probe for later processing.

TOTAL FOCUSSING METHOD (TFM)

The Total Focussing Method is an imaging technique applied to FMC data. For a linear phased array probe, a two-dimensional grid is specified in the same plane as the probe. The FMC data are reconstructed to sum together the individual amplitude values that could have originated from each cell in the grid. Cells located at the true signal position will sum together in such a way as to dominate cells containing no true defect. In essence, the TFM image is focussed at every individual cell in the user-specified grid, with each cell incorporating data from multiple angles of incidence. This technique was used in this project to perform defect detection and location along with initial characterisation and sizing.

SCATTERING COEFFICIENT MATRIX (SCM)

This technique takes a single pixel in a TFM image and extracts each constituent of its amplitude. These constituent amplitude values are displayed as a function of incident and reflected beam angle. The resultant plot can be interrogated to provide information on the nature of a defect (planar or volumetric), the orientation of a defect (if planar) and the size of a defect. This technique was used in this project to perform defect sizing and characterisation, if deemed necessary by the initial interpretation of the TFM analysis.

INSPECTION SPECIFICATION

Three test specimens were available for this project, all of ferritic construction with geometry as described in Figure 1 a double-V ferritic butt weld, with the caps ground flat, runs across the width of the specimen. A series of volumetric and planar defects are located along its extent. These defects are typical of manufacturing and in-service defects:

- Lack of fusion at the weld interface
- Porosity
- Slag
- Rough crack
- Smooth crack

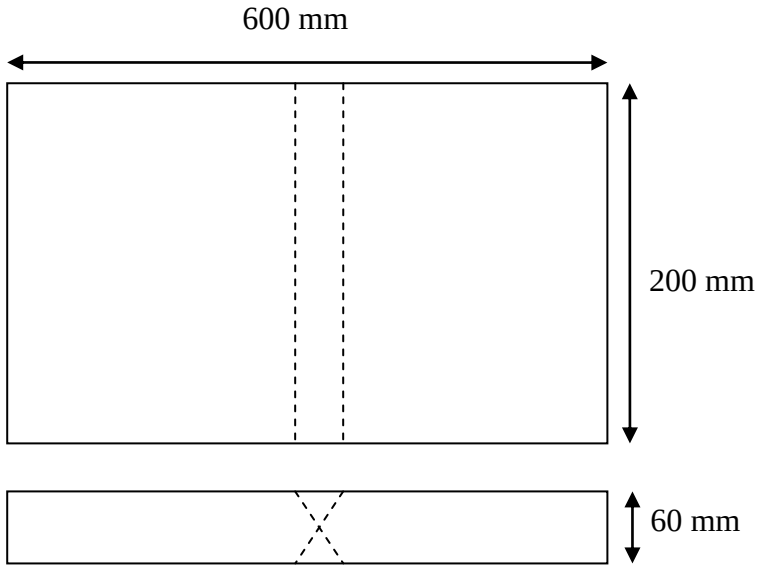

Figure 1: Test Specimen Geometry

An inspection specification was prepared by AMEC containing details of the planned trial process and reporting requirements. This was supplied to Bristol University at the project start and included details of the test sample dimensions, inspection volume and likely defect types to allow Bristol University to target the inspection procedure development.

DEVELOPMENT TRIAL PROCESS

Three specimens were used in this process: 4419-01, 4419-02 and 4419-03. 4419-02 was inspected independently from both major surfaces thus effectively increasing the total number of specimens to four. When inspected from the opposite surface, the specimen was labelled BT01. It was not revealed at the time of the inspection that the test specimen was the same and as such will be treated as a separate fourth sample from this point onwards.

Figure 2 depicts the flow of the development trials on each of the four test samples. Feedback was provided following the inspection of each sample, which was used to develop the procedure prior to the next stage.

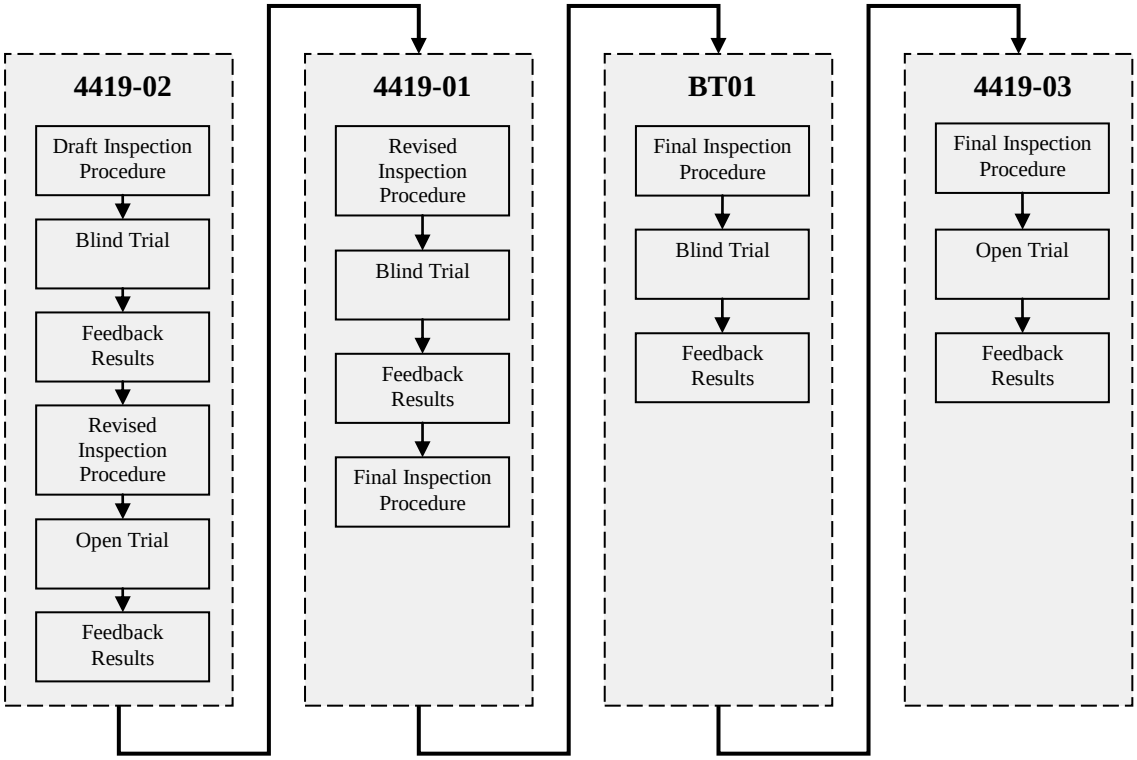

Figure 2: Flowchart of the Inspection Procedure Design and Testing Process

INSPECTION OF 4419-02

The first inspection to take place was carried out on the welded test specimen 4419-02. The purpose of this inspection was to develop the draft procedure to comply with the inspection specification and to define the parameter settings for use within BRAIN.

1. A blind inspection of 4419-02 was performed using the draft inspection procedure.
2. Results were submitted to AMEC in the form of TFM images (B and D scan) along with accompanying tabulated results listing the suspect defect volume dimensions and judgements on defect character based on a draft defect characterisation procedure.
3. Feedback was provided on the submitted results with the intended defect population details.
4. Revisions made by Bristol to the draft inspection procedure.
5. 4419-02 was re-inspected in an open trial using the revised inspection procedure.
6. Results submitted to AMEC for assessment.

INSPECTION OF 4419-01

The second inspection to take place was carried out on the welded test specimen 4419-01. The purpose of this inspection was to test out the revised procedure against an addition set of defects and allow further development of the procedure to comply with the inspection specification.

1. Blind inspection of 4419-01 took place using the revised inspection procedure.
2. Results submitted to AMEC for assessment.
3. Feedback given by AMEC on the comparison of the submitted results with the intended defect population details.
4. Following a further revision to the defect characterisation procedure, a final inspection procedure was produced

INSPECTION OF BT01

Following a review of the defects in the remaining test samples, it was decided to perform this final blind trial on test sample 4419-02 from the opposite inspection surface to that inspected previously (with the test sample identified as BT01). The inspection of test sample BT01 was performed as follows:

1. Blind inspection of BT01 using the final inspection procedure
2. Results submitted to AMEC for assessment.
3. AMEC compared the results with information on intended defect types and locations in test sample BT01.

INSPECTION OF 4419-03

It was thought to add benefit to this project to use the final specimen as a test of sizing and characterisation only. The defect locations were provided to Bristol.

1. Open inspection of four identified defect regions in 4419-03 using the final inspection procedure (for characterisation only)
2. Results reported to AMEC for assessment.

RESULTS

Table 1 - **Table 7** present the sizing results of all intended defects within the test samples. The intended size for each defect (as specified in the manufacturing drawings) is presented alongside the measured size.

RESULTS FOR 4419-02

ID	**Length (mm)**			**Height (mm)**		
	Intended	**Measured**	**Difference**	**Intended**	**Measured**	**Difference**
E	23	21	-2	4.9	5.5	0.6
F	10	27	17	2.3	7.5	5.2
G	10.1	10	0.1	2.5	2.2	-0.3
H	21.5	21	-0.5	5.4	5.5	0.1

Table 1: Sizing results from 4419-02

As observed in Table 1, defects E, G and H were all sized within a reasonable tolerance. However, Defect F was significantly over-sized in both length and through-wall extent. Figure 3 shows the TFM image of this defect. The rough nature of this defect can be observed in the spread of small reflected facets of sound rather than a single large reflected signal. In fact, this defect is a buried vertical rough crack, which makes it particularly difficult to defect. This particular defect was chosen for destructive analysis (see Figure 5) and was measured to have a through-wall extent of 1.49 mm at its mid-point. This confirms that this defect was over-sized in the through-wall dimension and not the result of a mistake made during the defect manufacturing process. The true length of the defect was not recorded during the destructive examination.

4419-02 was used to develop the characterisation techniques and so no defects were characterised on this sample.

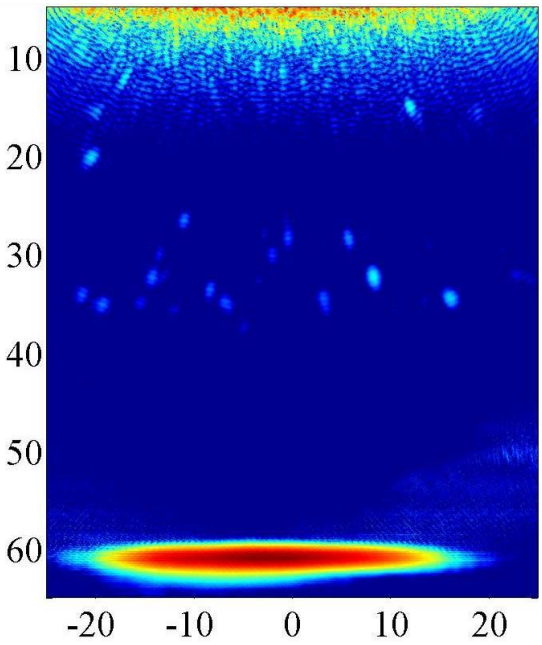

Figure 3: Defect F in Specimen 4419-02 with probe parallel to defect

RESULTS FOR 4419-01

Table 2 presents the sizing results from the sample 4419-01. Defect D was not identified as reportable and so was not sized or characterised. It was noted on the final list of defects but was not carried forward on the grounds of low amplitude. As a result of this, the threshold criteria were modified in the inspection procedure. Defect D is small (2 mm through-wall) and is distant relative to the probe, being located near the far surface. All other defects are within a reasonable tolerance.

ID	Length (mm)			Height (mm)		
	Intended	**Measured**	**Difference**	**Intended**	**Measured**	**Difference**
A	9	11	2	2.1	7	4.9
B	18	21	3	5	8	3
C	6.8	7	0.2	1.9	4.5	2.6
D	8	-	-	2	-	-

Table 2: Sizing results from 4419-01

Of the detected planar defects, both were characterised as rough instead of smooth. The images of these defects showed some amplitude variation across the length of the defects and hence this classification. Traditional fixed-beam angle inspections have been carries out on these samples and a variation was also noted. However, this variation was small (a few dB) and so the defects were interpreted as smooth. More work will need to be conducted into TFM as it fuses together data from multiple incident angles and so the interpretation of traditional "pattern" indications is not as straightforward.

It was interesting to note that Defect A was misclassified as a lack of fusion. This defect was intentionally used to test a common misclassification. Two parallel horizontal lines of slag, one directly above the other, could give the appearance of two diffracted signals from the tips of a planar defect. This defect emphasised a benefit of traditional multiple fixed-beam ultrasonic inspections where an analyst could study each beam angle independently to assess the reflected energy for each angle and attempt to achieve specular reflection to distinguish the two defect types. Additional amplitude criteria were inserted into the procedure as a result of this defect.

ID	Defect Type	
	Intended	Measured
A	Two Parallel Slag	Lack of Fusion
B	Lack of Fusion	Rough Crack
C	Smooth Crack	Rough Crack
D	Lack of Fusion	-

Table 3: Characterisation results from 4419-01

RESULTS FOR BT01

All defects in the sample BT01 were sized within a reasonable tolerance.

ID	Length (mm)			Height (mm)		
	Intended	Measured	Difference	Intended	Measured	Difference
E	23	22	-1	4.9	6	1.1
F	10	11	1	2.3	3	0.7
G	10.1	10	-0.1	2.5	2	-0.5
H	21.5	21	-0.5	5.4	5	-0.4

Table 4: Sizing results from BT01

The characterisation results for defects E, F and G were correct. To al intents and purposes, the result for Defect H was correct given that the intended and measured defect types are both rough and planar – Rough Lack of Fusion was only specified given the location of the crack on the weld fusion face.

ID	Defect Type	
	Intended	Measured
E	Lack of Fusion	Lack of Fusion
F	Rough Crack	Rough Crack
G	Slag	Slag
H	Rough Crack	Rough Lack of Fusion

Table 5: Characterisation results from BT01

RESULTS FOR 4419-03

All defects in this sample were sized within a reasonable tolerance.

ID	Length (mm)			Height (mm)		
	Intended	Measured	Difference	Intended	Measured	Difference
I	25	30	5	5	2	-3
J	8	10	2	8	10	2
K	15.1	18	2.9	5	5	0
L	6.3	5	-1.3	1.9	2	0.1

Table 6: Sizing results from 4419-03

The characterisation results for Defects I and K were both correct. The result for Defect L was reasonable given that the intended and measured defect types are both rough and planar. As in BT01, a Rough Lack of Fusion was only specified given the location of the crack on the weld fusion face. Defect J, however, was incorrect. Upon feedback of the defect type, it was noted that this was the first porosity observed in this process and so it was not directly linked in to the procedure. The defect type was given as a rough crack because of the multiple individual signals observed on both defect types. Differences were noted between the signals of the two defect types by way of the voluminous features of porosity – this would differentiate these in the future.

ID	Defect Type	
	Intended	**Measured**
I	Lack of Fusion	Lack of Fusion
J	Porosity	Rough Crack
K	Rough Crack	Rough Crack
L	Rough Crack	Rough Lack of Fusion

Table 7: Characterisation results from 4419-03

DESTRUCTIVE EXAMINATION

A destructive examination, followed by metallographic examination was carried out to confirm the true nature of the defects in the test sample 4419-02 / BT01. This allowed a comparison to be drawn between the TFM images and the optical microscope image of the defect cross section. Defect E is intended to be lack-of-fusion 23 mm in length and 4.9 mm through-wall tilted at 11°. The destructive examination of this defect can be seen in Figure 4. The through-wall extent of this defect was observed to be 5.8 mm and tilted at 7.8°.

Figure 4: Destructive examination of Defect E in Specimen 4419-02 / BT01

Defect F is intended to be a vertical rough crack 10 mm in length and 2.3 mm through-wall. The destructive examination of this defect can be seen in Figure 5. The through-wall extent of this defect was observed to be 1.49 mm. The gape of this defect is observed to be very tight, which would act to reduce the ultrasonic reflection at certain areas of the defect. The roughness is not clearly observed in this plane.

Figure 5: Destructive examination of Defect F in Specimen 4419-02 / BT01

Defect G is intended to be a horizontal line of slag 10.1 mm in length and 2.5 mm in diameter. The destructive examination of this defect can be seen in Figure 6 which depicts a cross section along the length of the defect. The true length is 9.52 mm and the through-wall extent was observed to be 2.45 mm.

Figure 6: Destructive examination of Defect G in Specimen 4419-02 / BT01

Defect H is intended to be a rough crack 21.5 mm in length and 5.4 mm through-wall tilted at 30°. The destructive examination of this defect can be seen in Figure 7. The through-wall extent of this defect was observed to be 4.28 mm and tilted at 36.3°. Its rough nature can be clearly observed.

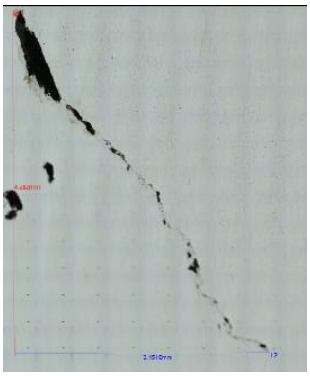

Figure 7: Destructive examination of Defect H in Specimen 4419-02 / BT01

DISCUSSION

The open and blind trials and associated procedure development provides important information on the strengths and weaknesses of FMC imaging techniques for the inspection of ferritic butt welds and their potential use as part of a diverse and redundant inspection procedure for such welds.

The importance of good inspection design in ensuring full weld coverage and optimised defect discrimination and characterisation for the full range of potential defect types has been reinforced. The inspection process was independently witnessed throughout. As a result, there were no performance weaknesses that could be attributed to human reliability factors.

The sizing of defects provided, in general, good results. Defect F in 4419-02 was grossly oversized during the initial trial. However, a revision was made to the procedure following this. When inspected as part of BT01, a good result was achieved on this defect. On average, defects were oversized more often than they were undersized and by a larger amount. This is likely to be partly due to the small size of most defects in the inspected test samples.

Some false calls relating to spurious echoes were noted in the analysis of FMC data. In most cases, these indications were sentenced as insignificant point indications following the application of the characterisation process. Some of these echoes were also noticed and sentenced as such during conventional pulse-echo inspections. Inevitably, with improved FMC imaging techniques, the cost of higher sensitivity is the increase in false call rate from small insignificant reflectors. This is reminiscent of the TOFD technique. Care is needed therefore in selecting a reliable calibration technique regarding inspection sensitivity and selecting a robust characterisation process. Also, further optimisation of the FMC, TFM and SCM inspection procedure for the full range, types and orientations of likely defects would increase the amplitude difference between very small (innocuous) and larger defects, so simplifying defect identification and discrimination.

CONCLUSIONS

The testing of the FMC/TFM post-processing algorithms available within the BRAIN software in this development trial has

1. prompted the development of effective FMC/TFM inspection procedures for ferritic welds which can be further optimised for improved defect detection, sizing and characterisation/discrimination
2. demonstrated the capabilities of the FMC/TFM algorithms and procedures in a simulated industrial application
3. provided valuable insights into the strengths and weaknesses of the FMC/TFM algorithms and identified areas for further research and development
4. provided the first known testing of the use of the BRAIN software and TFM- based inspection procedures in a realistic industrial inspection application
5. Rules have been created for differentiating between defects and noise and to characterise defects
6. Routes have been identified for facilitating rapid FMC/TFM imaging technology transfer into industry as part of a diverse and redundant inspection procedure

REFERENCES

1. AMEC Report, 2013, RCNDE Technology Transfer Project – Results from Development Trial on Bristol Phased Array FMC/TFM Imaging Techniques
2. Zhang, J, Drinkwater, BW & Wilcox, PD 2012, 'Effect of Roughness on Imaging and Sizing Rough Crack-Like Defects Using Ultrasonic Arrays'. *IEEE Transactions on Ultrasonics, Ferroelectrics, and Frequency Control*, vol 59., pp. 939-948
3. Zhang, J, Drinkwater, BW & Wilcox, PD 2010, 'The Use of Ultrasonic Arrays to Characterize Crack-like Defects'. *Journal of Nondestructive Evaluation*, vol 29., pp. 222-232

PHASED ARRAY TRANSDUCER OPTIMIZATION FOR COMPLEX NUCLEAR COMPONENT INSPECTION

A. Vanhoye, O. Casula, CEA - LIST, France
D. Moussebois, Laborelec, Belgium

The inspection of 3D components such as a nozzle weld requires overcoming the difficulties due to the complex geometry and metallurgical characteristics, and assumes the development of a fitted transducer. Considering the case of a weld inspection on a cast steel nozzle, this study presents the different steps which conducted to the computation of an optimized transducer configuration.

The nozzle cast steel metallurgical characteristics and geometry were first studied in order to determine the best fitted transducer technology. A low frequency flexible array transducer was retained due to the coarse grain material and highly curved saddle surface.

Considering a 3D scanning trajectory obtained using a zone coverage tool, the detection and characterization performances of the inspection were assessed thanks to the computation of a sensitivity map, which directly depends on the transducer used for the inspection. On this basis, the transducer configuration was optimized using a genetic algorithm in order to ensure an efficient coverage of the region of interest. The transducer optimization was refined considering sidelobe minimization and generated field shape on specific key areas.

Keywords : Inspection, Trajectory, Nozzle, Flexible Phased Array, Optimization

INTRODUCTION

In this study, we will consider the inspection of a weld around a 14'' nozzle. Made of cast stainless steel, its metallurgical structure includes coarse grains resulting in highly anisotropic and heterogeneous material. This structure induces severe attenuation, changes in velocity and scattering of the ultrasonic energy. Therefore, the ultrasonic inspection becomes difficult to perform with a conventional transducer.

TRL solid wedge transducers give good result on cast steel on a plane surface. But since we are considering a nozzle, with curved surface, that kind of transducer will not fit perfectly to the surface. Indeed, due to mismatching, the probe must be removed from the weld, resulting in higher acoustical path and high beam steering angle.

The solution is to use a flexible array transducer that can fit the saddle shape whatever strong distortions and thus reduce the acoustical path and beam steering angle. However, the transducer array configuration should be designed wisely in order to overcome the attenuation issue of the material and support the required acoustical beam deviation on the inspection trajectory.

A first transducer, a 60-element, 600 kHz, flexible transducer composed of 6x5 units, was designed for this application. Its working frequency was selected in consideration of material properties, in order to provide the best compromise between wavelength and resulting attenuation. Nevertheless, its array configuration was chosen without previous advanced optimization. The good results obtained with this transducer suggest that better can be achieved with an additional optimization step.

The purpose of this study is thus to optimize the 600 kHz transducer sparse array configuration for best detection performance in a fixed region of interest of the nozzle. The first part of the study presents the inspection trajectory computation and the transducer assessment method while the second part describes the optimization process.

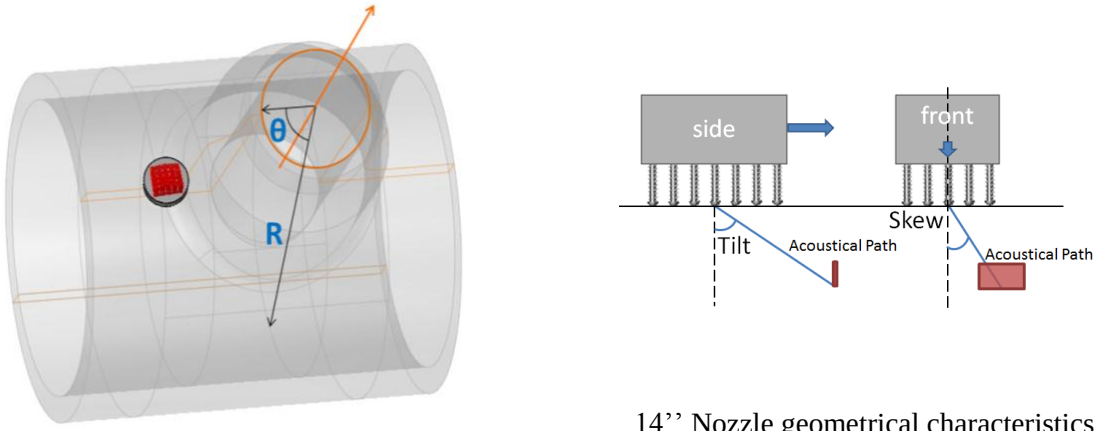

FIGURE 1. Cylindrical coordinate system on the nozzle, acoustical focusing parameters definition and nozzle geometrical characteristics.

14'' Nozzle geometrical characteristics

Primary cylinder ext. diameter	862.5 mm
Primary cylinder thickness	60 mm
Secondary cylinder ext. diameter	490 mm
Saddle curvature radius	50 mm

TRAJECTORY COMPUTING AND TRANSDUCER ASSESSING METHODOLOGY

Nozzle geometrical definition

In order to determine a 3D trajectory for the transducer, a geometrical description of the nozzle and its saddle was defined. We have based our calculation on a parametrical definition of the nozzle which characteristics is presented on figure 1. The cylindrical coordinate system centered on the secondary cylinder axis was retained in order to describe transducer or flaw position. All following results will be presented within this coordinate system.

Region of interest and transducer location area

Before computing a trajectory, one should define a region to cover during inspection, were alleged flaws are located. This region, named region of interest (ROI), was here determined according to the ASME code, which defines the required area to consider for a given weld geometry.

Figure 2.a is an illustration of ASME code application on our considered nozzle weld geometry. On a given angular position, the ROI starts 1" from the weld vertical side and ends 1" from the weld extremity once projected on the backwall.

Considering this ROI, the associated transducer positioning area which provides the best detection performance was computed using a developed zone coverage tool. This tool computes the transducer area assuming that the best detection performance is obtained when the acoustic beam hits the bottom of the flaw with a 45° angle. Thus, the ideal transducer position for a given notch is obtained by the reverse operation, when firing a 45° oriented ray from the notch bottom to the nozzle surface. In this study, we will only consider h10x30mm² ortho-radially oriented flaw, and the transducer location area was computed on this basis. The result of this computation is presented on figure 2.b.

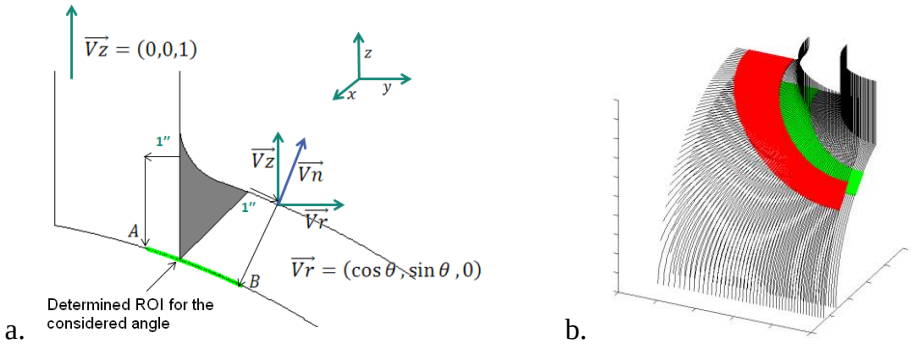

FIGURE 2. Region of interest determination using the ASME code (a) and its result on the nozzle (b).

Trajectory computation

The most suitable trajectories for robot inspection are meander like trajectories. The retained trajectory was thus a regular meander, for which the only parameter to determine is the angular step. Indeed, the length of each scan is automatically set by the width of the transducer location area.

The angular step of the regular meander should be as large as possible to limit the number of scans, but should not overcome a limit value which ensures area coverage. It was computed using the zone coverage tool, which considers the maximum gap that occurs between two consecutive scans for a given angular step. This gap must necessarily be inferior to the transducer minimum focal spot size, which was set at 10mm considering conducted simulation with the 600 kHz transducer used so far for this application. After computation, the trajectory was decided to be a 53 scans regular meander trajectory with an angular step of 1.73°.

Acoustical parameters

For the inspection trajectory to be entirely set, we must associate to the 3D scanning definition the required acoustical focusing parameters. Three parameters were considered: the tilt, the skew and the acoustical path (figure 1.b). For each position on the trajectory, their exact values can be compute thanks to the geometrical definition of the nozzle. However, in order to limit the number of delay law to consider, these values should be rounded. Previous conducted studies established that the following rounding does not significantly affect the acoustical field transmitted to the flaw [1]:

- +/- 1° for the skew angle
- +/- 0.5° for the tilt angle
- +/- 2mm for the acoustical path

Figure 3 presents an illustration of the rounding methodology applied on the skew values. Since the skew varies from 0 to 18°, the rounded skew will take a value within the 10 following one: 0, 2, 4, 6, 8, 10, 12, 14, 16, and 18, decreasing significantly the number of acoustical focusing setting to consider. Once rounded, the trajectory is divided in 242 areas, each of them associated to a specific acoustical focusing setting (i.e. delay laws).

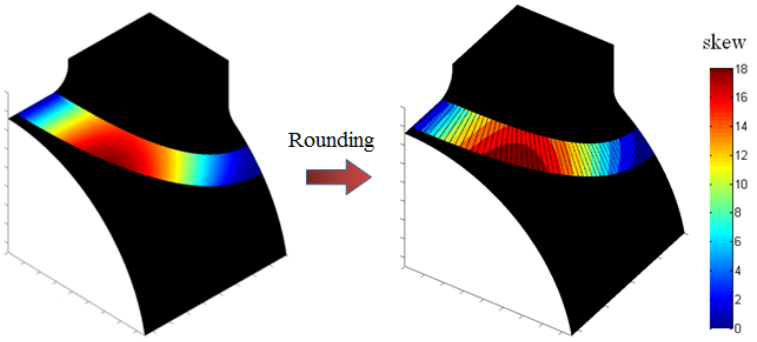

FIGURE 3. Rounding methodology applied for the skew values.

Transducer assessing methodology: sensitivity map

Since the inspection trajectory is completely set, the purpose was to assess the detection performance of a given transducer along it. To do so, the trajectory was sampled in a high number of points on which acoustical modelling was performed thanks to CIVA modelling tool. On each test points, a flaw response was computed considering the following configuration:

- The transducer to be assessed is located such that its flexible array is centered on the trajectory test point
- The used delay laws are computed considering the focusing setting presented above
- A flaw, with geometrical characteristics identical to the researched flaws, is positioned where the transducer delay laws focalize

The simulation took into account all geometrical aspect of the nozzle, but also the material properties including structural noise and wave attenuation. From each single flaw response, the maximum response amplitude is extracted and plotted on a map, so called sensitivity map, representing the detection sensitivity of our transducer along the trajectory and for the considered flaw geometry.

Since the flaw response mainly depends on the used transducer, sensitivity map is a proper way to evaluate a transducer performance, and can be used to find the best fitted one on a given control configuration. Figure 4 presents an example of a sensitivity map obtained with the 600 KHz used so far for this application.

The computation of the sensitivity map did enlighten specific areas on the nozzle:

- On the saddle, where the transducer has to be bent in order to fit the surface, leading in lower tilt value. This configuration is the most acoustically favorable, giving the highest detection performance.
- At high angular position (close to 90°), where the acoustical path is the shortest. This configuration is also acoustically favorable, fiving good detection performance.
- At angular positions close to 40°, where the non-parallelism between the surface and the backwall require using the highest skew values. This configuration is the less acoustically favorable configuration.

The signal loss with current array configuration goes up to -6dB, which is sufficient for efficient flaw detection on the nozzle. However, the study aimed at improving this result using a more fitted transducer.

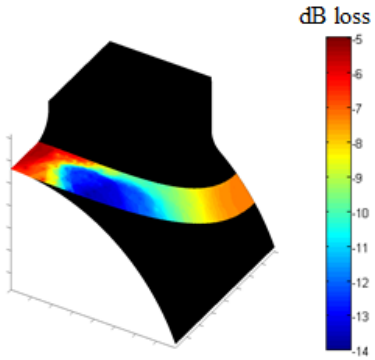

FIGURE 4. 3D representation of the sensitivity map for the 600 KHz transducer along the trajectory.

TRANSDUCER OPTIMIZATION

This paragraph presents the results of the optimization study conducted in order to determine a more efficient array configuration for h10x30mm² notch characterization in 45°LW on a 14” nozzle weld. In first place, we used CIVA optimization tools, which will be briefly described, to sort out the ten best optimized configurations. Then, the optimized configurations were assessed on the basis of their signal-to-noise ratio (SNR), sidelobe and sensitivity map on our considered inspection trajectory.

CIVA optimization tool

CIVA optimization tool is based on a genetic algorithm, classified as an evolutionary algorithm (EA). Genetic algorithm aims to evolve a population of candidate solution through mutation, crossing and selection operation, in order to determine the optimal solution. A candidate solution, also called individuals, is a n-dimension vector containing the values of the parameters to optimize. By assessing individuals though an objective function, defined by the user, the EA algorithm seek for the one that minimize it. Thus, the objective function should be defined in consideration of which aspect we want to minimize.

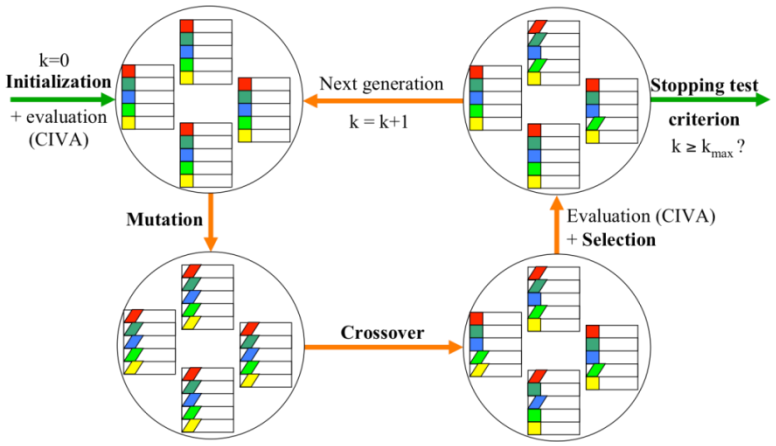

FIGURE 5. Differential Evolution diagram involving main evolutionary operators: initialization, mutation, crossover, and selection.

The algorithm is divided in four steps, presented on figure 5:

- The first step is an initialization step. A population of candidate solution is randomly selected within the working domain to form an initial population.
- Then, through mutation operation applied on the existing population, the algorithm breed a generation of muted individuals. A mutation is a perturbation applied on the value of each parameter, according to a normal distribution.
- By crossing this muted generation with the previous one, the algorithm generate a crossed-muted generation which characteristics will be assessed by the objective function.
- The last step is a selection step. The algorithm selects the best candidates within the former and crossed-muted generation. That is to say, the individuals that returned the lowest values through the objective function. Those individuals form the new generation.

Step 2 to 4 are then repeated for the new generations until an individual that returned a value lower than a fixed threshold through the objective function is found.

Since this threshold is arbitrary and not necessarily reachable, an alternative is to breed a fixed number of generations, large enough to ensure sufficient exploration of the working area, and then select the best produced individuals.

CIVA optimization tool configuration

In our case, the purpose is to determine the best fitted array configuration for the 14'' nozzle inspection. We retained six parameters to optimize:

- Number of element (along row and column)
- Size of the elements (along row and column)
- Pitch between elements (along row and column)

A range was defined for each of these parameters in order to limit the domain within which the genetic algorithm can evolve. In consideration of mechanical feasibility, the parameters ranges were set as following:

- Number of element : $8 < N < 14$ in row, $7 < N < 14$ in column
- Size of the elements : $3mm < S < 8mm$ in row and in column
- Pitch between elements : $3.5mm < P < 7mm$ in row and in column

The genetic algorithm needs an objective function in order to assess the potential candidate solutions. To do so, CIVA optimization tool interacts with CIVA modelling tool in order to assess the candidate transducers on a given configuration. This configuration, defined by the user, should be as representative as possible to the final expected application.

Along the inspection trajectory detailed on the previous paragraph, the transducer presents configurations that can highly differ each from another. Since we didn't want to give preferential treatment to a configuration, we decided to consider a generic configuration, however close to the application.

Indeed, we decided to consider the inspection of a h10x30mm² notch located in a 65mm thick plane piece made of cast stainless steel, same thickness than the actual nozzle (Figure 5). The ability of the transducer to meet the desired application is assessed by computing the SNR of the corner and diffraction echoes when firing using 45° longitudinal waves. The higher the SNR is, the better it is.

Thus, for each potential transducer, CIVA modelling tool generates a specific configuration on this basis, computes an inspection simulation to determine the associated SNR, and returns this value to CIVA optimization tool. Since we want to maximise the SNR value, the objective function was simply defined as the opposite of the RSB value returned by CIVA modelling tool.

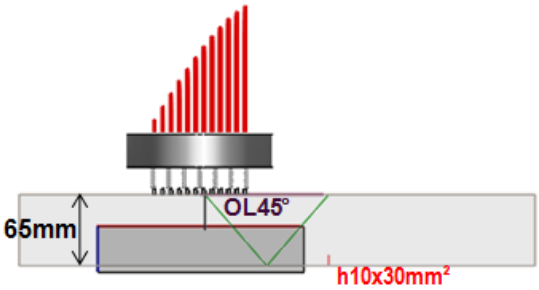

FIGURE 6. Assessment configuration for corner and diffraction echoes SNR evaluation.

Optimization results

The first optimization aimed to determine the array configurations that maximise SNR of the corner echo. The computation was performed using the configuration and the parameters range exposed above. It was performed several times in order to ensure that the algorithm did converge to the expected solutions. The second optimization computation was made considering the diffraction echo. In each case, the five best candidate solutions were retained, forming a group of ten candidate solutions to decide between.

The diffraction echo SNR was computed for the solution obtained considering the corner echo SNR optimization, and the corner echo SNR was computed for the solution obtained considering the diffraction echo SNR optimization. Then, was only retained the three best candidate solution on the consideration of both diffraction and corner echo SNR. Those solutions are presented on figure 7.

	Solution 1	**Solution 2**	**Solution 3**	**Reference**
Number of element	10x6 (60)	10x9 (90)	8x8 (64)	10x6 (60)
Element size	3 x 7 mm²	3.5 x 4 mm²	4.5 x 3.5 mm²	5 x 8.5 mm²
Element pitch	5mm and 6.5mm	5mm and 5.5mm	5mm and 6mm	1&5mm and 5mm
Total aperture	75 x 74.5 mm²	80 x 80 mm²	71 x 70 mm²	75 x 76 mm²
Corner echo SNR	**5.6 dB**	**6.1 dB**	**5.7 dB**	**2.5 dB**
Diffraction echo SNR	**4.5 dB**	**5.3 dB**	**4.6 dB**	**1.2 dB**

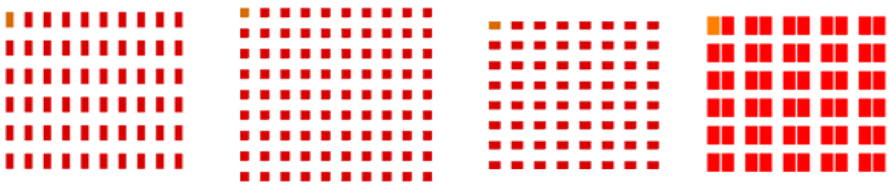

FIGURE 7. Best candidate solution characteristics, considering the corner and diffraction echoes SNR.

An average improvement of +3dB is to notice between the candidate solutions and the current transducer, taken as reference. Nevertheless, on the consideration of SNR, the three candidate solutions remain close to each other. In order to select the best solution for our application, we've studied the amplitude of their grating lobes and assessed their performance along the inspection trajectory, thanks to the sensitivity map presented above.

Grating lobe computation

Grating lobe can induce unwanted echoes on our signal that can affect the notch detectability. The aim of this study was thus to determine the ratio of the parasitic backwall echo due to grating lobe compared to the echo coming from the notch. The computation was performed using the same configuration as the one used for the optimization (cf. Figure 6), excepted that structural noise and attenuation were not taken into account.
The result of the computation performed on solution n°1 is presented on figure 8. On the modelled Bscan, the maximum amplitude coming from the notch is extracted. Then, the maximum of the grating lobe is extracted considering the contribution found beside.

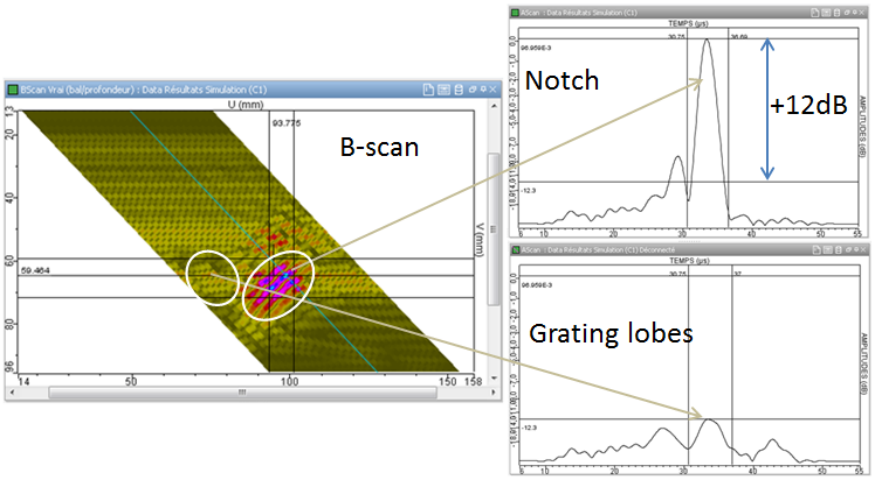

FIGURE 8. Illustration of grating lobe ratio determination for the solution n°1

The ration between the two extracted amplitude is computed, reflecting the potential consequence that may have grating lobes on our signal. The results for all considered transducer are presented below:

	Solution 1	Solution 2	Solution 3	Reference
$A_{notch}/A_{side\ lobe}$	12 dB	11 dB	7 dB	6 dB

TABLE 1. Result of grating lobe ratio computation for the candidate solutions and reference.

The solutions n°1 and n°2 stand out from the solution n°3, even if it still gives better ratio than the reference. However, before selecting a transducer among the three, we wanted to assess their detection performance along the trajectory using sensitivity map.

Sensitivity map assessment

Using the developed sensitivity map tool, the sensitivity maps associated to the three candidate solutions were computed. The result is presented on figure 9

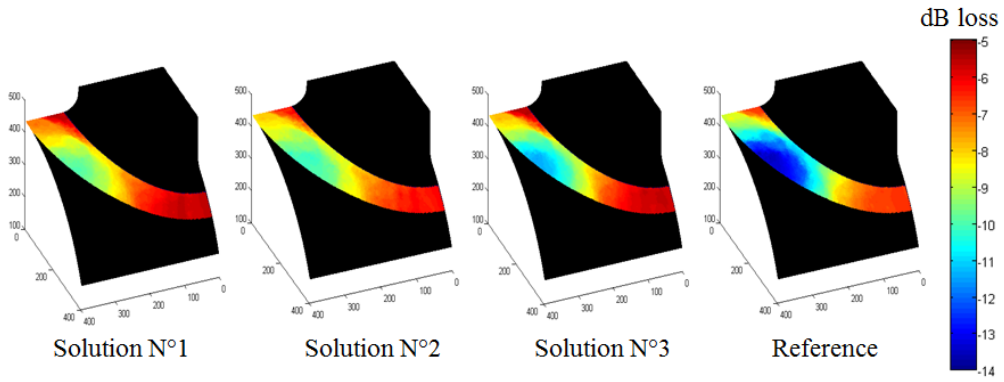

FIGURE 9. Result of sensitivity map computation for the candidate solutions and reference.

The sensibility map of the three candidate solutions enlighten a clear improvement compared to the reference transducer used so far. Indeed, optimized transducers present more efficient and more homogeneous detection sensitivity along the trajectory, thus seem to be more fitted for the expected application. Among the three candidate solutions, the solution n°1 presents the more favourable sensitivity map and is moreover, the array configuration that requires the least element. Therefore, for having the best grating lobe ratio and the most favourable detection sensitivity along the trajectory, solution n°1 was retained to be the new transducer array configuration for the 14" nozzle application.

CONCLUSION

On this paper, we presented the consecutive steps which conducted, from a nozzle geometrical definition and its material characteristics, to the generation of an inspection trajectory for weld notch detection associated to the computation of an optimized transducer to ensure sufficient performance along it. The development of sensitivity map generation tool allows us to dispose of a proper way to assess the detection performance of a given transducer along an inspection trajectory. Combined with CIVA optimization tool, an optimization tool based on a genetic algorithm, the sensibility map helps in determining the best fitted transducer for the expected application. The presented methodology can easily be extended to other geometry and material restraint, in order to determine the adequate inspection trajectory and the best fitted transducer to achieve notch detection along it.

REFERENCE

1) A. Vanhoye, O. Casula, D. Moussebois, "Design by simulation of the UT array inspection of a nozzle with a flexible probe: Definition of 3D trajectories and focusing parameters", QNDE, Denver, 2012.

2) L. Ganjehi, C. Poidevin, G. Cattiaux, T. Sollier, "Experimental and numerical Study of Ultrasonic Propagation in Cast Stainless Steel, 8th Int. Conf. on NDE in relation to Structural Integrity for Nuclear and Pressurized Components, Berlin, 2010.

3) O. Casula, G. Toullelan, L. Doudet, A Le Brun, N. Etchegaray, « Flexible multi-elements transducers, new applications in NDT », SFEN-COFREND, Paris, 2009.

4) O. Paris, O. Casula, B. Chassignole, L. de Roumilly, "Ultrasonic inspection through CVCS nozzle weld with flexible array", Cofrend Conference, Dunkerque, 2011.

5) G. Maes, S. Turgeon, D. Reilly, "Advanced phased array UT inspection through complex surfaces", 7th Int. Conf. on NDE in relation to Structural Integrity for Nuclear and Pressurized Components, Yokohama, 2009.

6) D. Richard, G. Maes, D. Reilly, J. Berlanger, "Advanced software tools for design and implementation of phased array UT inspection techniques on complex components, 8th Int. Conf. on NDE in relation to Structural Integrity for Nuclear and Pressurized Components, Berlin, 2010.

7) M.T. Anderson, A.D. Cinson, S.L. Crawford, A.A. Diaz, T.L. Moran, "Improvements in low-frequency, ultrasonic phased-array evaluation for thick-section cast austenitic stainless steel piping components", 8th Int. Conf. on NDE in relation to Structural Integrity for Nuclear and Pressurized Components, Berlin, 2010.

PIPING INSPECTION (NOZZLES/COMPLEX)

ADVANCED INSPECTION TECHNIQUE FROM INSIDE SURFACE FOR DISSIMILAR METAL WELD OF STEAM GENERATOR NOZZLE

T. Yamaguchi, T. Shichida, T. Matsuura, Y. Tsuruta, S. Kawanami
Mitsubishi Heavy Industries, Japan

1. Abstract

In 2012, several axial flaws were not detected by Ultrasonic Testing (UT) from outside surface of nozzle. The flaws were located in Dissimilar Metal Weld (DMW) of an inlet (hot leg) Steam Generator (SG) nozzle at North Anna Power Station Unit 1. One of the causes of missing flaw seems to be particular geometry of nozzle outside surface with large taper angle [(1)].

100% coverage by UT from outside surface was very difficult, because there are some areas where ultrasonic beam cannot reach. On the other hand, the inspection from inside surface of nozzle has a merit uninfluenced by the nozzle outside surface geometry. Therefore, we have developed an advanced inspection technique from nozzle inside.

This technique mainly consists of a new robot to access from inside surface and a new inspection technique with accurate depth sizing. The robot has high performance movement characteristic and easy installation structure which make it easy to apply not only UT but also Eddy Current Testing (ECT) and Visual Testing (VT) to DMW of SG nozzle remotely. This robot with state-of-art robotic technology has already been applied in the field service in Japan successfully. Up to date, accuracy in UT depth sizing from defect opening surface had been insufficient, so we developed both small Transmit-Receive type with L-wave Phased Array (TRL-PA) UT probe and matrices type with L-wave PA-UT probe. As results, it is verified that our advanced UT improves defect sizing capability remarkably even for a swallow defect [(2) (3)].

In this report, we will introduce our new solution from nozzle inside surface and show experimental results and some field experiences.

2. Background

To prevent the occurrence of PWSCC, Ultrasonic Shot Peening (USP) was applied to SG nozzle in Japan. Before application of peening, ECT for soundness check was applied. In these inspections, some axial PWSCCs were detected on the nickel alloy surface (Alloy 600) of SG nozzle in some plants (shown in Figure 1). After detection of PWSCC, Nuclear and Industrial Safety Agency (NISA) requested the application of ECT from inside surface for DMW of SG nozzle once in decade as In-Service Inspection (ISI).

On the other hand, in 2012, 5 Primary Water Stress Corrosion Crackings (PWSCC) were detected in the DMW in an inlet (hot leg) SG nozzle at North Anna Power Station Unit 1.

These PWSCCs were not detected by primary UT inspection from outside surface. However after outside surface machining in preparation for a full structural weld overlay, PWSCCs were founded by visually. One of the potential causes for the miss of the detection of these PWSCCs seems to be large taper angle of safe-end configuration (see Figure 2).

100% coverage by UT from outside surface was very difficult, because there are some areas where ultrasonic beam cannot reach. On the other hand, the inspection from inside surface of nozzle has a merit uninfluenced by the nozzle outside surface geometry. Therefore, Advanced inspection technique from inside surface for DMW of SG Nozzle have been developed to fulfill the ISI request in Japan. This technique is also effective for the case like North Anna Power Station Unit 1. This technique mainly consists of a new robot to access from inside surface and a new inspection technique with accurate depth sizing. (see Figure 3).

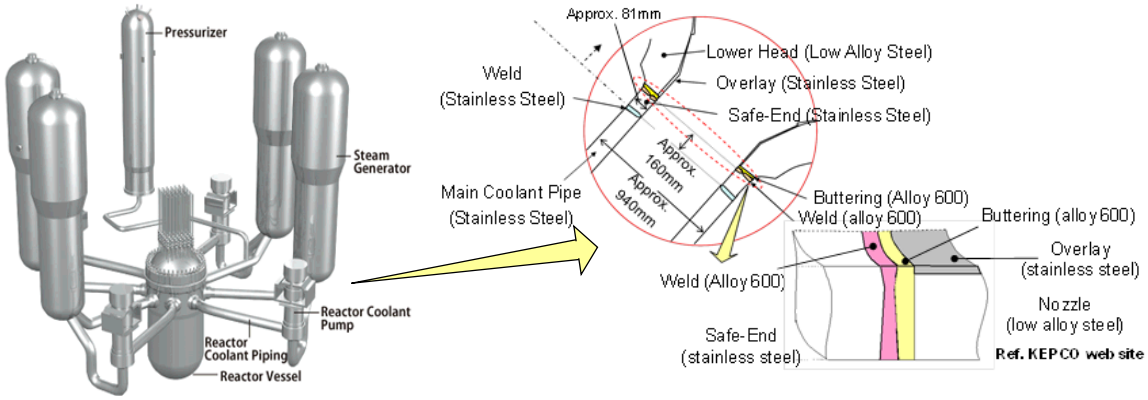

Figure 1 Location of defect at DMWs of SG

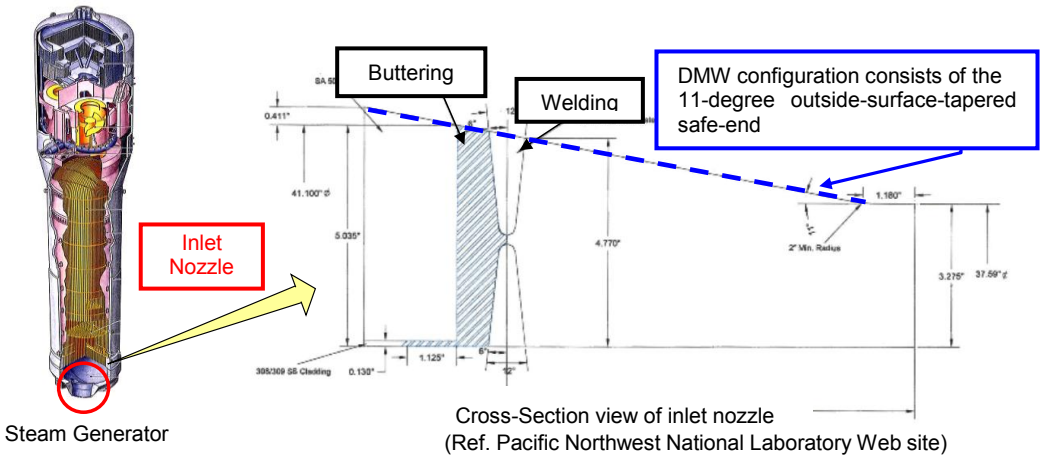

Figure 2 Safe-end configuration of North Anna Power Station Unit 1 SG

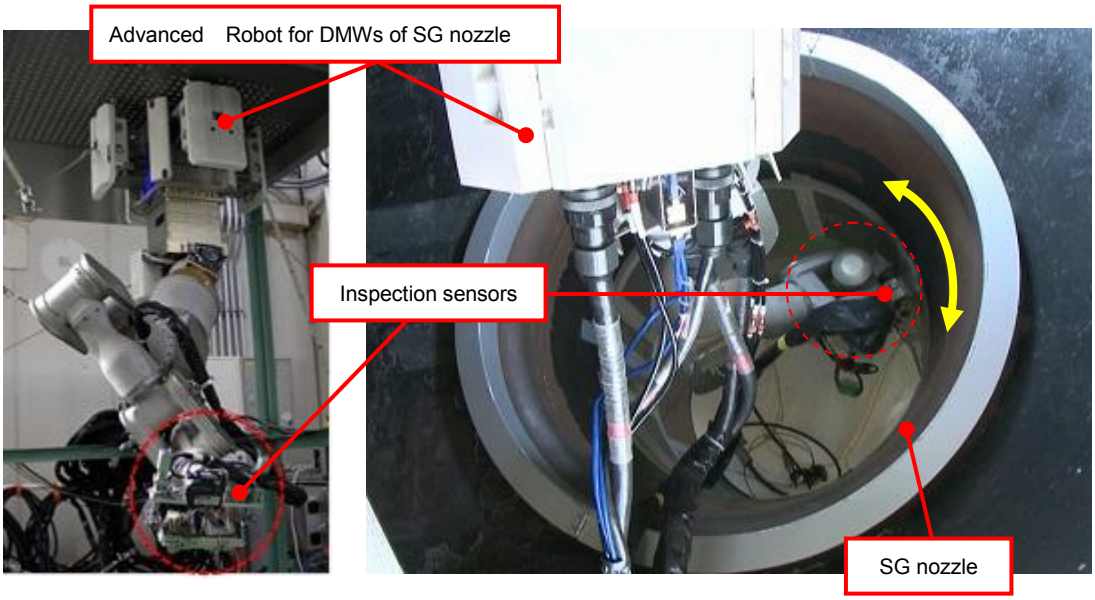

Figure 3 Advanced Robot for DMW of SG nozzle

3. Robot Technique

3.1 Target and feature of Advanced Robot for DMWs of SG nozzle design

The Advanced Robot was designed to achieve 3 functions for domestic inspection requirement such as quick installation, accurate coverage of inspection area and multiple inspection techniques. Details of these functions are shown in Table 1.

Table 1 Target and feature of Advanced Robot design

Target		Feature
Quick Installation	• Installation through primary manhole	• Module structure • Special tools for installation from outside of manhole • Self moving function on tubesheet
Accurate Coverage of Inspection Area	• All circumference inspection • High accuracy inspection	• 100% coverage of inspection area • Accurate tracking with auto rectification of sensor position by laser measurement
Multiple Inspection Technique	• Application of ECT, UT, and VT	• Retouchable sensor head

3.2 Quick Installation

To achieve the quick installation, the Advanced Robot consists of four modules. Each module is lightweight, so easy assembly is possible. Moreover, by using of the special tools for installation from outside of manhole, working in channel head is unnecessary. Outline of assembly procedure is shown in Figure 4. After the Advanced Robot is attached on the installation position, the Robot has to move to the inspection position by itself. Therefore it has moving capability on tube-sheet remotely by using MHI's SG tube robot technology. The outline of Advanced Robot movement is shown in Figure 5.

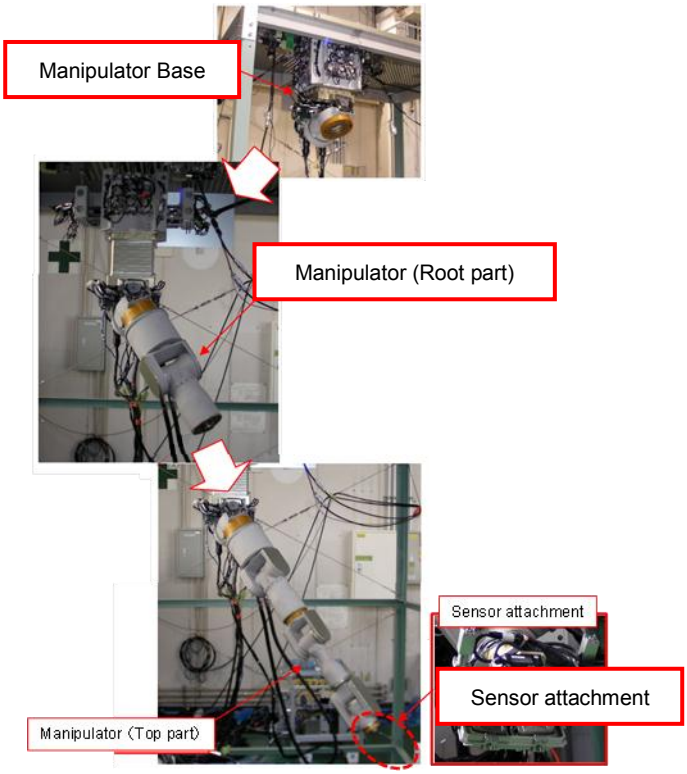

Figure 4. Outline of assembly procedure of Advanced Robot [4]

Figure 5 Outline of Advanced Robot movements

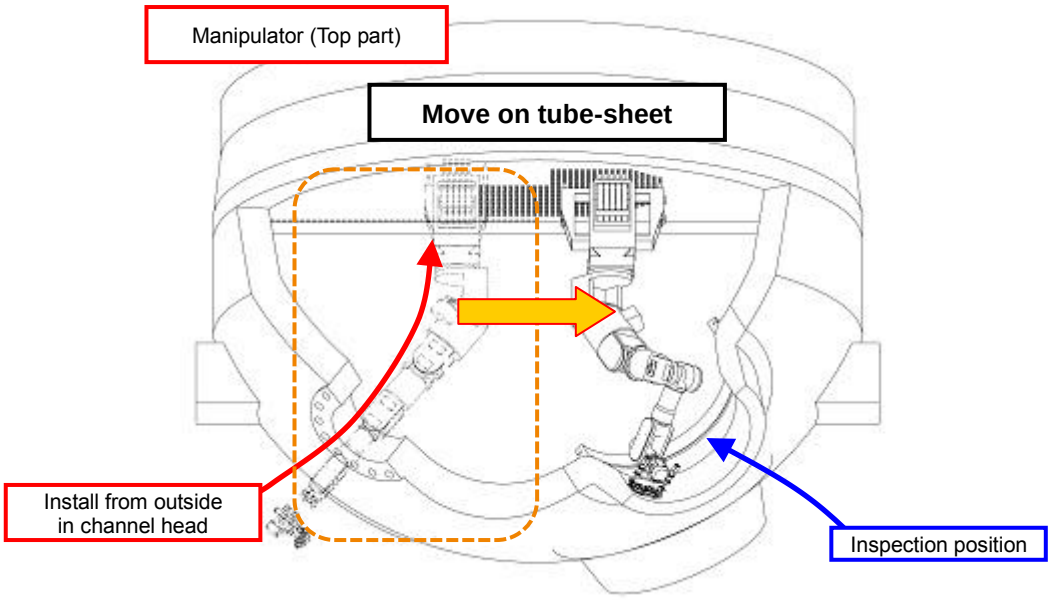

3.3 Accurate Coverage of Inspection Area

To achieve 100% coverage of inspection area and accurate tracking, seven axes manipulator was adopted. This manipulator has the wide movable range and high flexibility so that it is possible to control the sensors smoothly like a human's arm. Moreover, by laser measurement instrument, the distance between nozzle inside surface and the sensor attachment is kept constant and the forcing load to sensors is also controlled even for slight distortion on nozzle with auto rectification. The apparatus of the seven axes manipulator is shown in Figure 6.

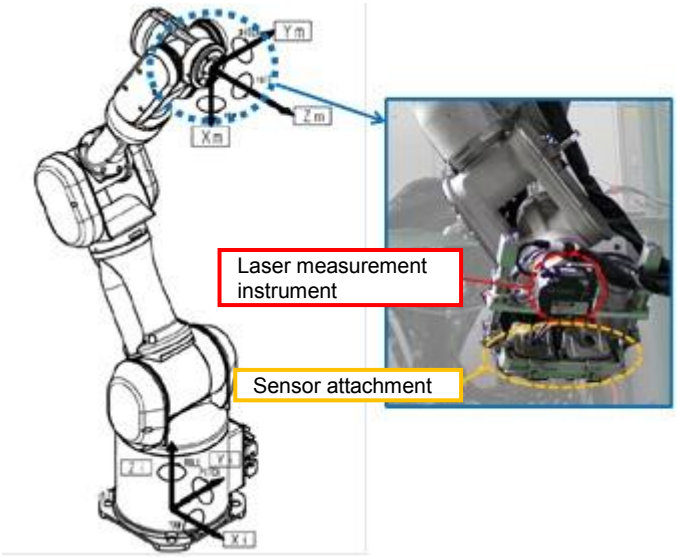

Figure 6 Apparatus of seven axes manipulator

3.4 Multiple Inspection Technique

In inspection, ECT is first applied to detect flaws. When flaws are detected by ECT, VT will be applied to check the characteristics of them and finally UT will be applied for depth sizing. Thus, the Advanced Robot can carry the ECT, UT and VT sensor head respectively. Attachments of each inspection technique are shown in Figure 7. Sensor exchange can be performed without removing a robot from channel head. The time for sensor exchange is approximately 3 minutes.

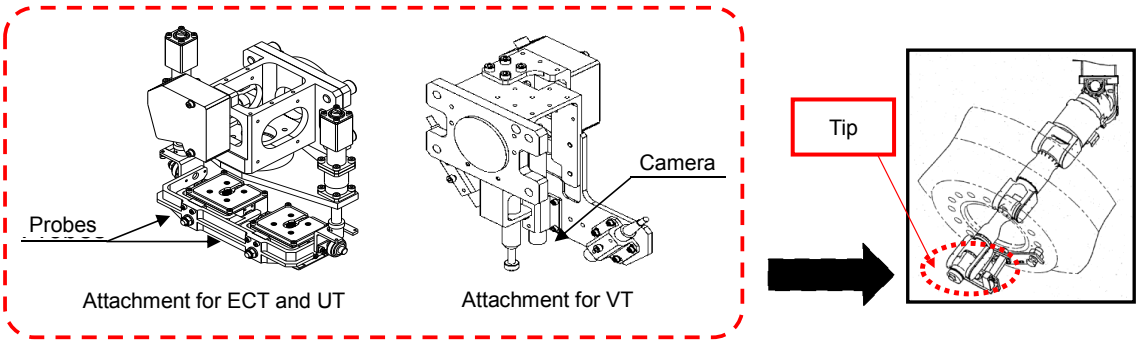

Figure 7 Attachment for each inspection technique

4. ECT Detection Technique

ECT is applied to check the soundness of nozzle weld. Both normal and magnetic biased ECT probes with cross-coil are used (see Figure 8). The magnetic biased ECT probe can decrease noises due to permeability change between safe-end weld and stainless overlay.

The results of EDM notch mock-up test are shown in Figure 9 and 10. All EDM notches including EDM notches with 0.5 mm depth are detected. Moreover, SCC mock-up test was performed. The result showed 0.5mm depth SCC is detectable (see Figure 11) [(5)].

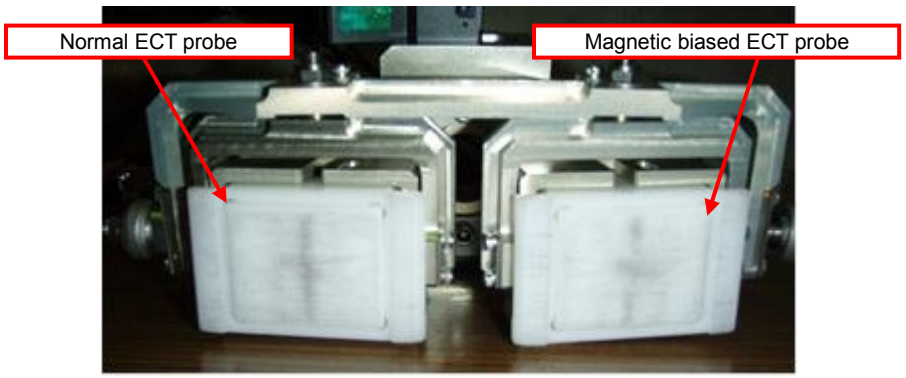

Figure 8 Normal and magnetic biased ECT probes with cross-coil

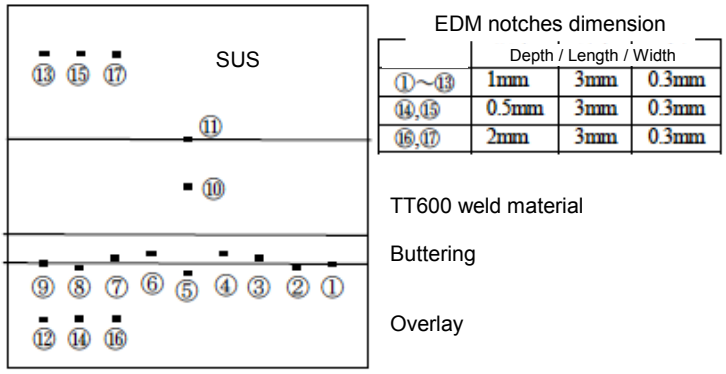

Figure 9 Layout of EDM notch on mock-up

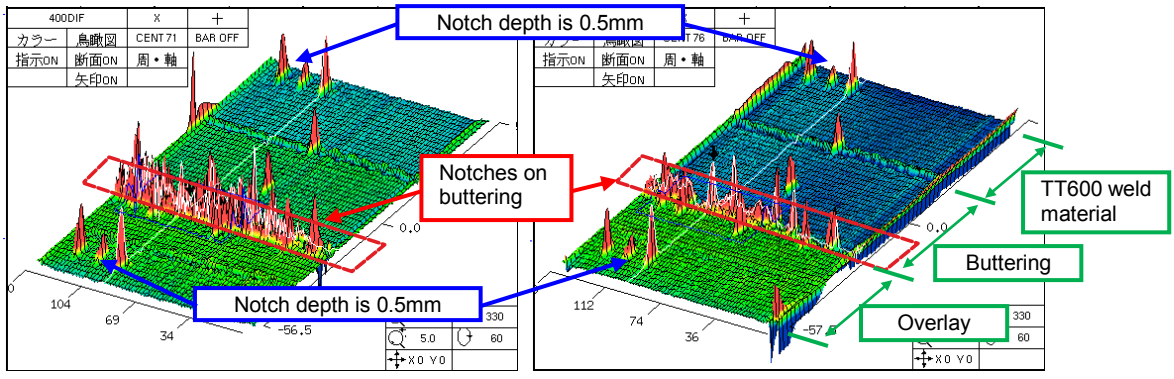

Figure 10 ECT Results of mock-up test

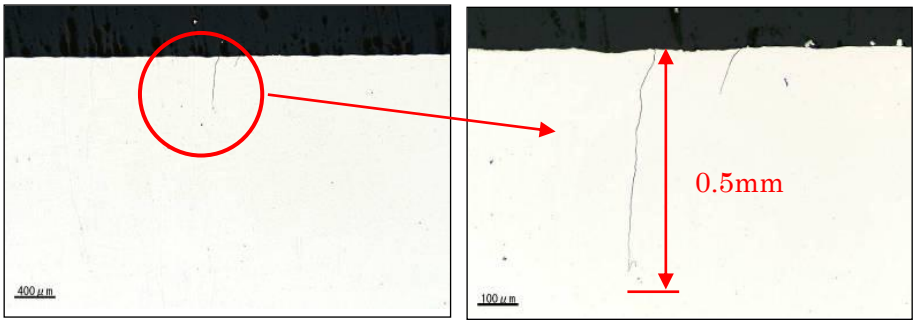

Figure 11 Cross-section of SC on mock-up

5. Field Application of Robot Technique with ECT

Since 2010, MHI has applied the Advanced Robot successfully in ISI of Alloy 600 DMWs on SG nozzles of 2 PWR plants as shown in Table 2. ECT was performed in ISI and no indication was verified. In future, the Advanced Robot will be applied for about 4 plants per year.

Table 3 shows the typical schedule of ECT application in ISI. Installation of Advanced robot can be carried out in only one day. Then, critical schedule can be finished in about 3 and half days. The work in the inside of channel head is not required by introduction of the Advanced Robot. Therefore, as compared with the case using old type equipment for USP, numbers of total workers have been reduced by about 50%. In addition, amount of radiation exposure reduced by about 30% compared with the case using old type equipment for USP.

Table 2 Experiences of ISI of SG nozzles

Unit	Type	Data
Plant A	PWR 2 - Loops	09/2010
Plant B	PWR 2 - Loops	10/2011

Table 3 Typical schedule of ECT by Advanced Robot [(a) (b)]

(days)

Work	1	2	3	4
Installation of NDT Robot to channel head				
Inspection (Data acquisition / Analysis) [(c) (d)]				
Tear down				

Estimated Condition
(a) Schedule is daytime shift (b) Equipment conveyance is excepted
(c) Inlet nozzle only (d) When there is a problem in data, re-inspection will be carried out

6. UT Depth Sizing Technique

In order to improve depth sizing of shallow and deep defects, the PA-UT technique was developed. A large size matrix PA-UT probe was developed for depth sizing of deep defects. This probe can utilize 3-Dimensional beam scan. Small size TRL PA-UT probe was developed for depth sizing of shallow defects. This probe can utilize a large refraction angle. Figure 12 shows these two PA-UT probes and two conventional probes with different refraction angles used in ISI for the comparison of depth sizing test. The depth sizing test was performed using artificial SCCs. In this test, a total of 17 test pieces were made. After ultrasonic inspection, all test pieces were cut and the depth size and shape of cracks was measured. Figure 13 shows a representative artificial SCC. Results of PA UT and conventional UT probes are shown in figures 14 (a) and 14(b) respectively. The conventional UT showed a good sizing performance in depth region less than 15mm, but it became extremely degraded in around 20mm depth region. On the other hand, the PA-UT technique showed a better accurate sizing result up to around 40mm depth region. The Root Mean Squire Error (RMSE) of the conventional UT was 9.35mm, the RMSE of the PA-UT with small TRL PA and Matrix PA is 2.54 mm. From these results, it is verified that the newly developed PA-UT achieved conquest of the weak point of the conventional UT and has adequate sizing capability up to approximately 40mm depth. The example of Advanced PA UT sizing result is shown in Figure 15. Just for information, volumetric inspection by normal UT probe and angle UT probe is also applicable.

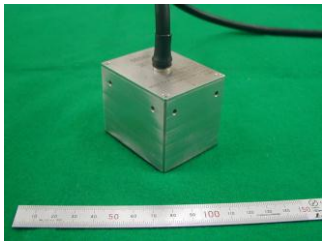

Matrix PA probe
Specs: 2MHz-96ch
Apply to: Middle to deep defects

Small type TRL PA probe
Specs: 5MHz-40ch
Apply to: Shallow defects

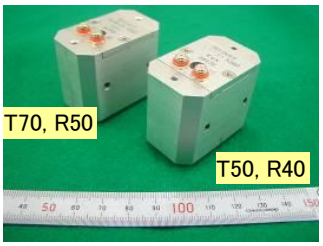

Conventional TRL probe
Specs: 3MHz-TR
Apply to: All defects

Figure 12 UT probes

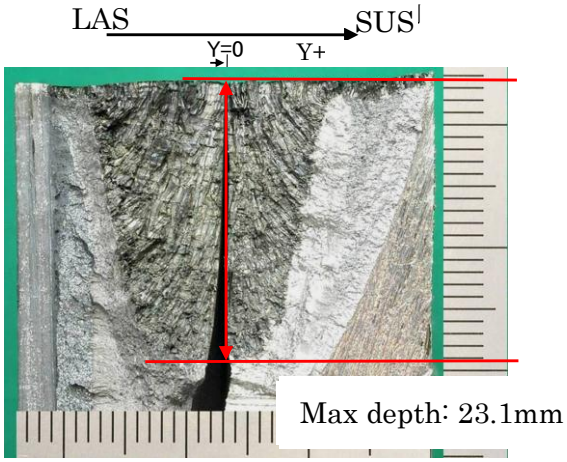

Figure 13. Representative artificial SCC

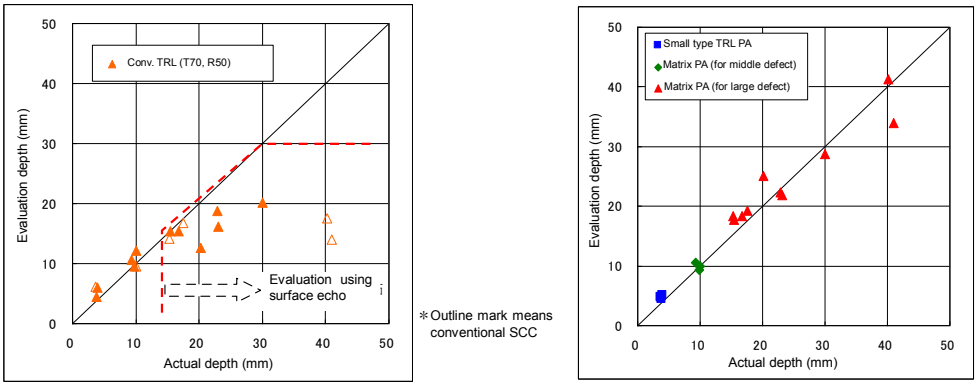

	Conv. TRL（T70, R50）
RMSE	9.35 (1.36 at <20mm)

(a) Conventional method

	Advanced method combined Small TRL PA with Matrix PA
RMSE	2.54

(b) Advanced method

Figure 14 Sizing accuracy of SCC

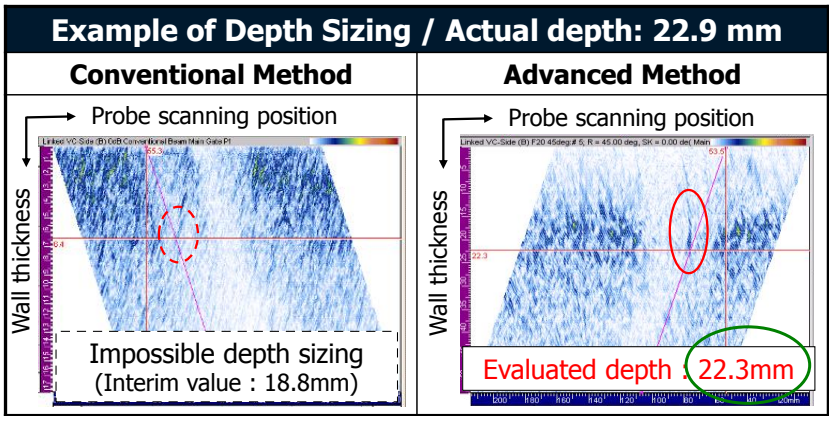

Figure 15 Example of Advanced PA-UT sizing result

7. Field Application of UT

The PA-UT method is designed to be used with the Advanced Robot. However, we had field experience of this method for Reactor Vessel (RV) outlet nozzle inspection in 2011 introduced below.

Two defects were detected and the PA-UT method which is described in section 6 was carried out for depth sizing. Figure 16 shows the location of the detected defects. Estimated depths of defects are less than 3mm and 4.7mm respectively. UT results (B-scope) for each defect is shown in Figure 17. The actual depths of defects estimated in 2.7mm and 4.8mm respectively as the grinding process of the nozzle for repair. This shows that deviation between estimated and actual depth of defects is very small. Thus, effectiveness of the PA-UT method in power plant inspection was proven.

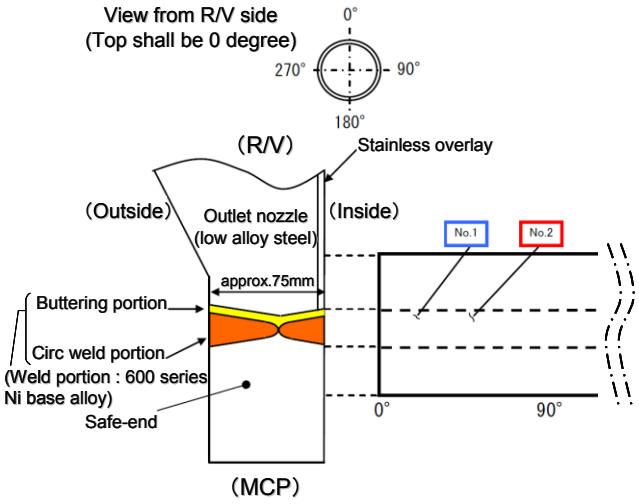

Figure 16 Location of SCC indications in Outlet nozzle of RV

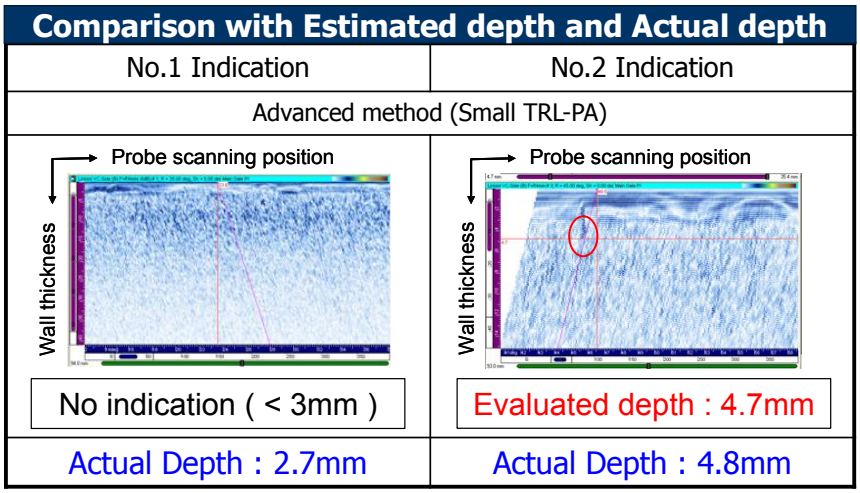

Figure 17 UT Sizing Result of Outlet DMWs

8. Conclusion

Advanced Robot for DMWs of SG nozzle and PA-UT (inspection technique from inside surface) have been developed. Advanced Robot with state-of-art robotic technology has been applied in the field service in Japan successfully. The PA-UT has been also applied to the RV outlet nozzle and effectiveness was proven by field experiences. These techniques will be effective ISI method for particular geometry of nozzle outside surface with large taper angle. MHI will intend to introduce these advanced techniques to contribute to the maintenance of power plants hereafter.

Reference

1) MT Anderson, AA Diaz, SR Doctor, "Evaluation of Manual Ultrasonic Examinations Applied to Detect Flaws in Primary System Dissimilar Metal Welds at North Anna Power Station", *PNNL-21546, Pacific Northwest National Laboratory*, 2012
2) T. Yamaguchi, T. Kawashima, M. Takatsugu, K. Unate, "Advanced NDT Robot for Dissimilar Metal Weld of Steam Generator Nozzles", *Proceeding of the 9th International Conference on NDE in Relation to Structural Integrity for Nuclear and Pressurized Components*, pp.763-769, May 2012.
3) S. Kawanami, T. Kimura, M. Kurokawa, J. Nishida, T. Yamaguchi, T. Matsuura, T. Tsuruta, "Advanced Phased Array UT Sizing Technique on Stress Corrosion Cracking in Dissimilar Metal Welds of Nozzle" , *Proceeding of the 9th International Conference on NDE in Relation to Structural Integrity for Nuclear and Pressurized Components*, pp.676-683, May 2012.
4) Y. Kohata, J. Fujita, K, Onishi, H. Tsuhari, F. Hosoe, "The Application of Manipulator Robot for Nuclear Plant Maintenance", *Preprints of 7th Annual Conference of the Japan Society of Maintenology*, Omaezaki, pp.400-405, July 2010. (in Japanese)
5) Y. Asada, K. Tokuhisa, M. Takatsugu, K. Kurokawa, K. Kawata, N. Hirano, T. Sera "Development of Eddy Current Testing Method for PWR Vessel's Dissimilar Metal Weld", *Japan Society of Maintenology, Maintenology,* Vol.6-No.4, pp.38-43, 2008. (in Japanese)

CRDM NOZZLES CRACKING OF REACTOR HEAD IN KOREA

E. Doh, Y. Kim, J. Kim, G. Lee, KEPCO KPS, South Korea

Abstract

Since the first CRDM nozzles of reactor head at Kori unit 1 in Korea have been inspected in 2003, CRDM nozzles were not revealed any crack before the inspection at Yonggwang unit 3 on October 2012, even though many foreign plants have been reporting PWSCC detection. We found 7 axial cracks from 6 CRDM nozzles at Yonggwang unit 3 which is a KSNP (Korean Standard Nuclear Plant) type, and confirmed them as PWSCC by Dye Penetrant Testing and Replica on the surface of J-groove weld of CRDM nozzles. All flaws started from the surface of J-groove weld, but did not grow to the top of J-groove weld, and did not make any Leak path of the welds, fortunately. PDI system of CRDM nozzle inspection has been applying in Korea since July 2011, and contributed for the detection and evaluation of these PWSCC of CRDM nozzles at Yonggwang unit 3. The experimentally based procedure of flaw detection and enhanced detection technique of examiners made possible to detect and to decide the indications as PWSCC. The repair process is still under study and will be approved by government authority shortly, and the repair of 6 CRDM nozzles will be completed by late spring of this year. CRDM nozzles of others plants in Korea, for example, Yonggwang unit 4 and a Framatome plant are questioned to have some potential PWSCC with reviewing previous inspection data, recently. And the secret of the conclusion will be un-covered in this year by performing field inspection of those plants in short future in accordance with their outage schedule.

Many experts attribute the detection of PWSCC to the application of PDI system, but also worry about the safety of nuclear plants in Korea.

Keywords: Qualification-Inspection, PWSCC, RPV

DEVELOPMENT OF AN ULTRASONIC INSPECTION METHOD FOR THE INTERNAL CORNER REGION OF A PIPE TO DOME NOZZLE ON A NUCLEAR COMPONENT

P. Sévrain, P. Bergalonne, Comex-Nucleaire, France
N. Hankinson, K. Quirk Phoenix ISL, UK

1 CONTEXT

COMEX-NUCLEAIRE was awarded to develop and to implement on site an automated NDE-UT process to inspect the internal corner region of a "pipe to dome" nozzle of a nuclear component.

For now, this project is engaged on exploratory basis (expertise mode) and is not submitted for qualification but NDE development has been instructed close to conventional qualification's method. Inspection will be performed as part of the "defense-in-depth". It does not search for particular defects but disorders are possible to first seek out in the radial plane of the nozzle (the most restrictive to the mechanical strength of the nozzle in the presence of discontinuities).

NDE Process will be implemented on 5 selected NPP within the upcoming years (4 x 900MW NPP and 1 x 1450MW NPP). Intervention is classified as significant radiological challenge level 2.

2 COMPONENT

Overall height of this IPS nuclear component (part of primary circuit) is roughly 15m and its overall diameter is about 2.5m, for around 100 tons (dry weight). This element is manufactured in low alloy steel (16MND5 type) with stainless steel internal cladding (AISI 308L/309L type).

Top of it consists in a dome (radius around 1200mm). At the periphery are 4 nozzles (lines to relief valves) and a manway. In the center is the pipe to dome nozzle that must be inspected. This nozzle is produced by forging of low alloy steel huge blocks (16MND5 or 18MND5 type) huge blocks. Pipe's OD is either 4" (900MW NPP) or 6" (1450MW NPP).

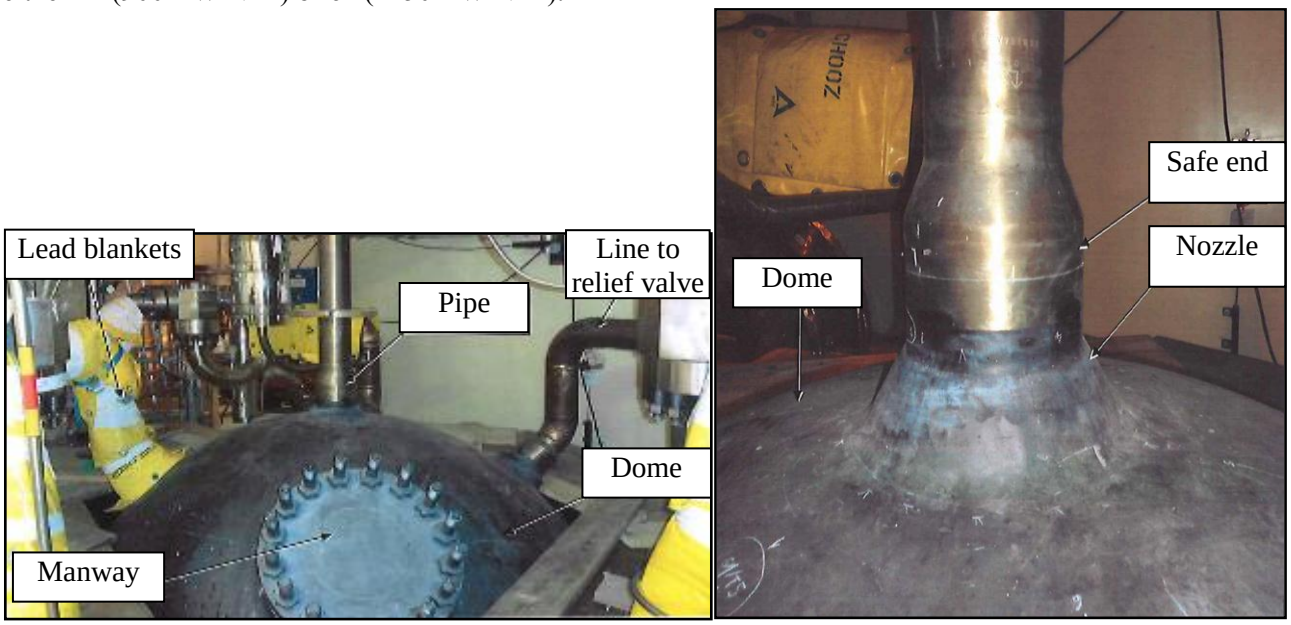

Figure 1: Top of the nuclear component

3 AREA TO INSPECT

At the dome's level, pipe's connection consists on a vertical nozzle (carbon steel) connected to the component, a safe end, the pipe (stainless steel), the bimetallic weld between the nozzle and the safe end, the weld between the safe end and the pipe (stainless steel/stainless steel one) and finally the coupling on internal side of the dome.

NDE process needs insonification of an annular volume of at least 35mm in radius at the corner region of the nozzle, for 360°.

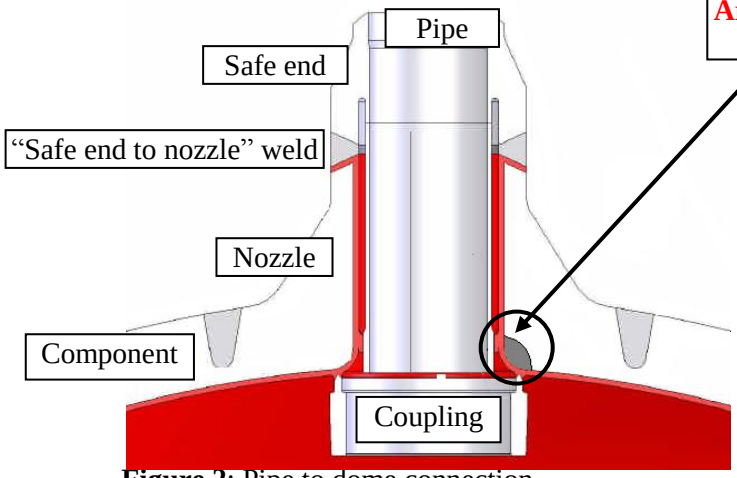

Figure 2: Pipe to dome connection

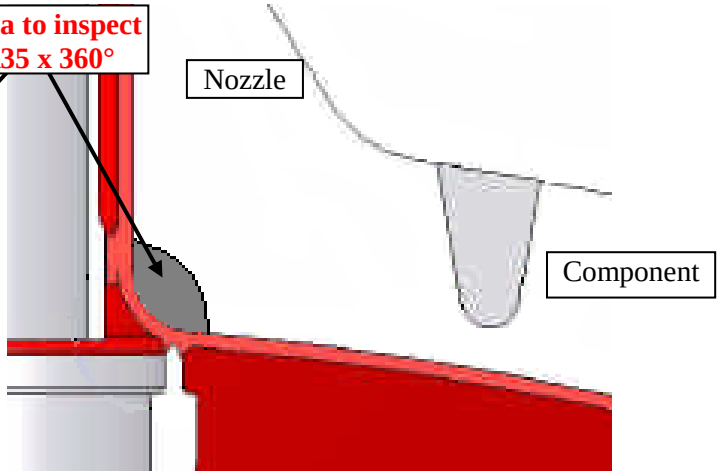

Figure 3: Area to inspect

4 DEVELOPMENT

4.1UT PROCESS

UT process was designed and developed using **CIVA 10** digital modeling software:

- Definition of validation's mockup
- Characteristics of defects (EDM notches and surface defects) to manufacture in the mockup
- Definition of UT probe
- Optimization of:
  - ✓ crystal's size
  - ✓ angle of refraction
  - ✓ skew angle
  - ✓ frequency
- Study of scanning movements
- Analysis of UT indication responses

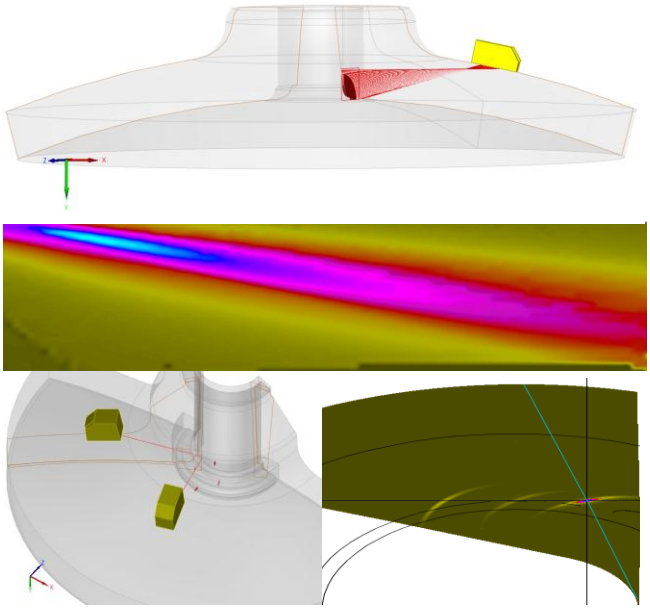

Figure 4: Digital modeling using CIVA 10 software

4.2 Mockup for development and validation tests

A mockup was designed, representative of a 900MW NPP configuration of the upper part of the dome and nozzle, including cladding and pins. A 4'' pipe was added to the mockup to support the scanner.

This mockup was used for development and validation tests.

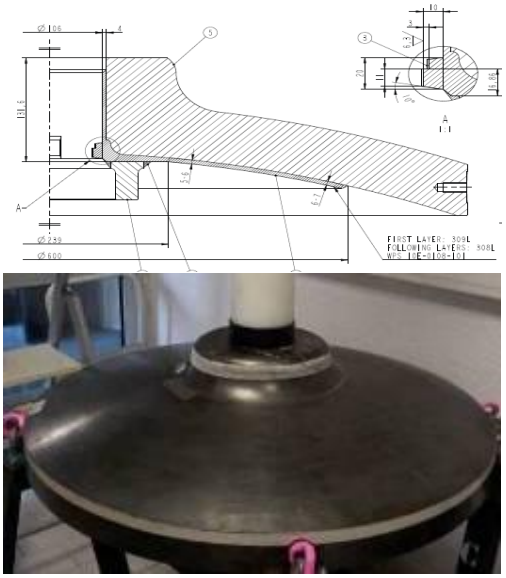

Figure 5: Mockup for development and validation tests

Some EDM notches were manufactured in dedicated area of the mockup, top, middle and bottom of the **R35** area to inspect, with variable tilts and skews. Some surface defects were also machined. For examples:

Critical blind planar defect, in radial direction from axis of pipe, located in the middle of area to inspect.

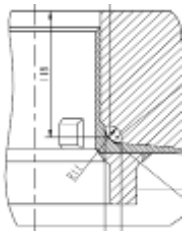

Radius= 11mm / width= 200µm
Surface: 190mm^2

Blind planar defect, in radial direction from axis of pipe, located in the upper part of area to inspect

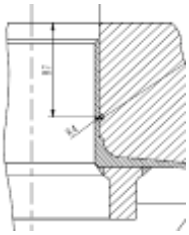

Radius= 4mm / width= 200µm
Surface: 25,1 mm^2

Blind planar defect, in radial direction from axis of pipe, located in the lower part of area to inspect

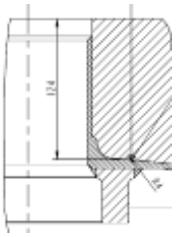

Radius= 4mm / width= 200µm
Surface: 25,1 mm^2

Figure 6: Example of EDM notches manufactured in the mockup

4.3 Scanner

For the inspection of this nuclear component, a scanner named **SIRUS** (**S**pray-nozzle **I**nner **R**adius **U**ltrasonic **S**canner) and developed by **PHOENIX ISL** needs to be used.

SIRUS scanner could be installed and sets within 5mn by 2 operators.

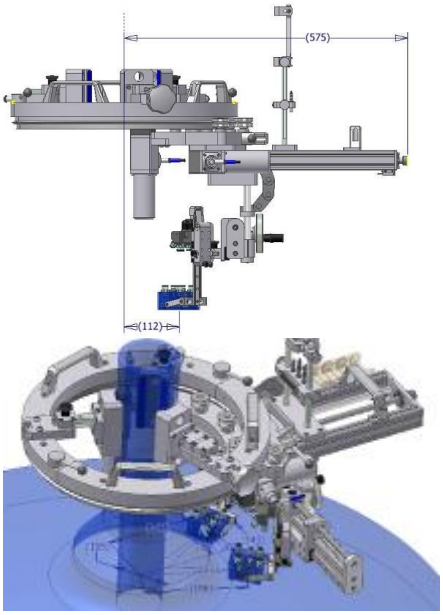

Figure 7: SIRUS scanner

SIRUS scanner has to be installed around the pipe. For that purpose, the support ring is split into two halves. Locking the two halves together is performed by hand via two quick release levers. Attached to the ring are three support feet, two of the feet have fixed bracket and interchangeable aluminum feet (for 4'' or 6'' pipes) and the third one has an adjustable clamping screw with compliant polyurethane pads (PMUC) to grip the pipe. Wholesomeness of the fastening on the pipe was verified during acceptance tests.

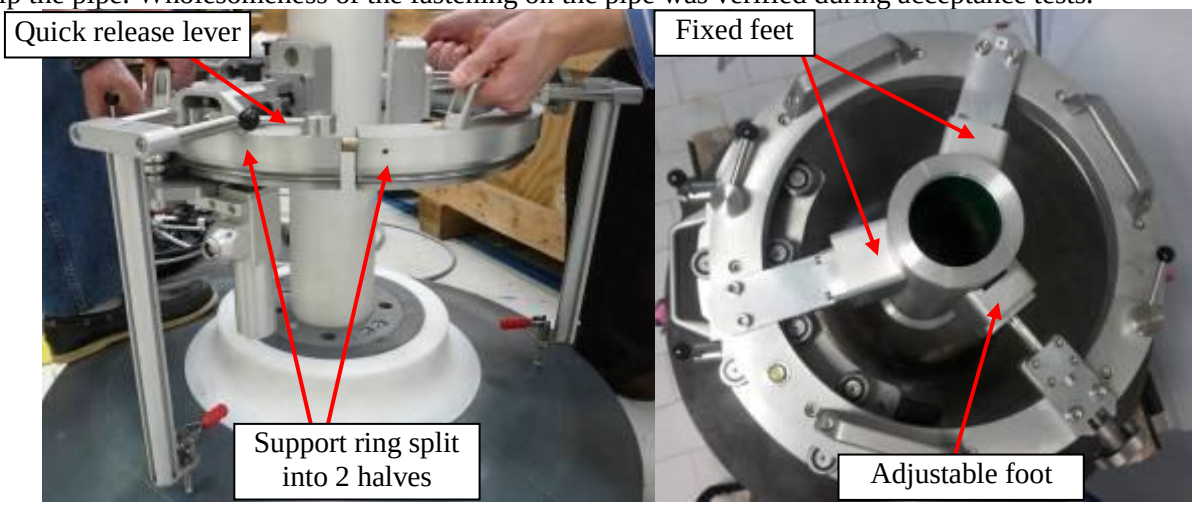

Figure 8: Installation of support ring around the pipe

For accurately positioning the scanner at the right altitude on the pipe and with the appropriated flatness of the support ring, 3 tripods forced by 3 braces are installed on the foot fixtures. Suitable horizontality of the support ring can be verified by checking the spirit level embedded on the scanner. Tightening of the adjustable foot can then be adjusted.

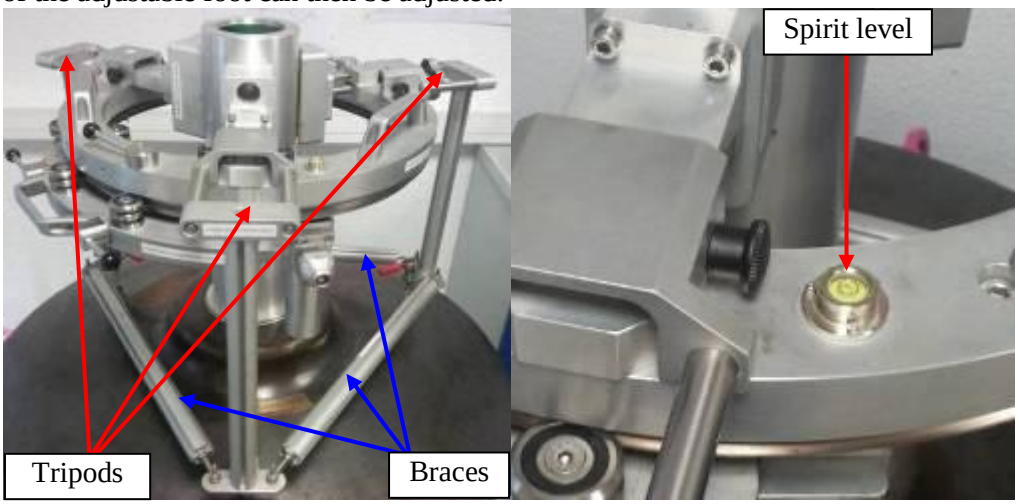

Figure 9: Accurate positioning of the scanner and check for horizontality

After removing braces and tripods, the radial module pack with probe separation module, toolposts, transducers and umbilical could be installed on the circumferential module (locked by hand via two quick release levers)

Figure 10: Installation of radial module pack

The radial module supports the probe separation module. This module holds 2 probe toolposts with a centralized slide which is manually adjusted with a handle. The module is self-locking, fixing the transducers' position (PCS) once the separation has been set. The module also includes a laser marker which, when active, shines a cross onto the surface of the dome This enables the scanner to be referenced to a datum position on the component for repeatability of inspections and positioning of the defects**.**

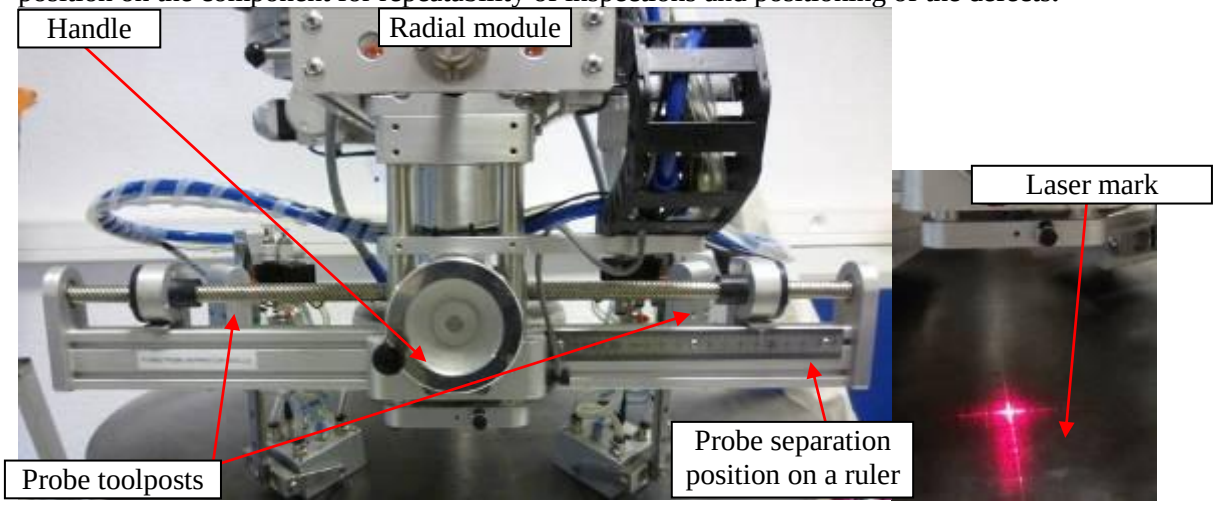

Figure 11: Probe separation module

At the top of the toolpost is a couplant feed and retrieval manifold. The transducers themselves include integrated couplant feed and retrieval channels to prevent the excessive loss of couplant during inspection

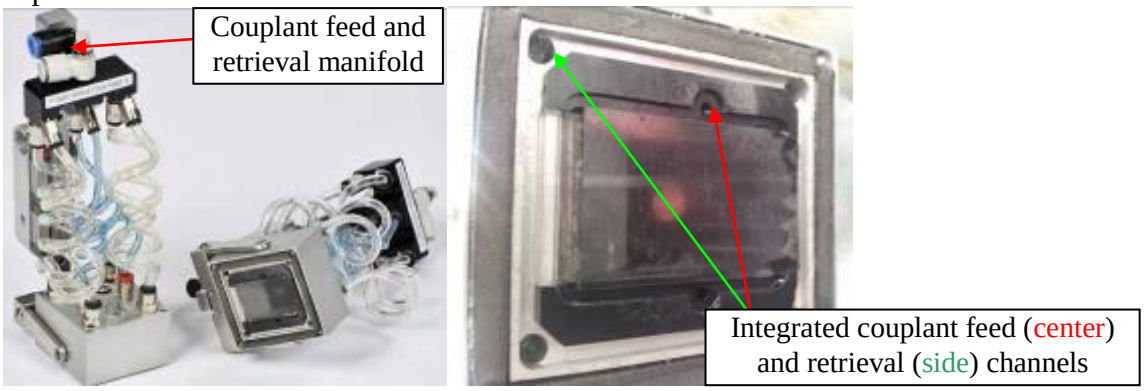

Figure 12: Couplant feed and retrieval system

5 UT CONFIGURATION FOR INSPECTION

5.1 Acquisition for detection

Probes are using **30°** skew angle from axis preferentially searched defect propagation (radial from the axis of the nozzle). This configuration will:

- Ensure maximum cover of the area to inspect
- Optimize the "corner echo" effect
- Confirm the presence of an indication according to 2 different directions of inspection
- Optimize the reflectivity of an indication with orientation other than radial

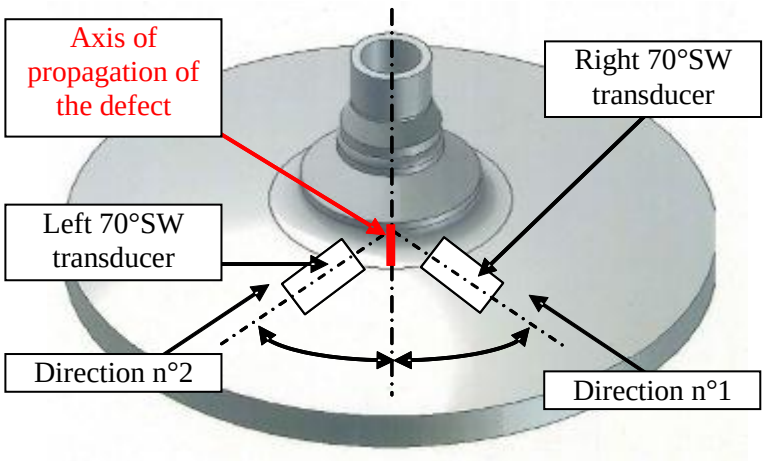

Figure 13: Inspection with 30° skew angle

5.2 Complementary inspections

Complementary inspections are performed with 45° skew angle and different separation values. Aims of these configurations are:

- To accurately cover top and bottom portions of area to inspect
- To confirm the indication by varying skew angle ±15°
- To obtain complementary information for the characterization of the indication (confirmation of diffraction echo, sizing, artifact/defect discrimination, etc).

5.3 Coupling monitoring

To monitor the ultrasonic coupling, a 0° Longitudinal Wave probe (5MHz, ∅6mm) is embedded with the 70° Shear Wave probe, in the same case. Both probes have the same index point and are driven the same UT generator.

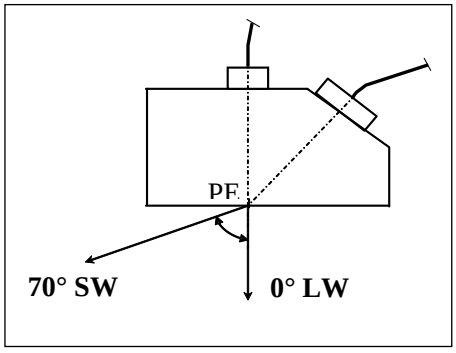

Figure 14: Coupling monitoring

6 UT DATA ACQUISITION

Data ACQUISITION is performed using ZIRCON , ZMC2 and Ultravision III software FROM **ZETEC**. Data from all inspections (skew 30° and skew 45°) are used for the analysis, with A-scan, B-scan or C-scan views.


UT acquisition equipments

Inspection sequence

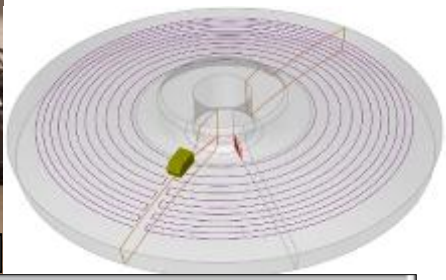

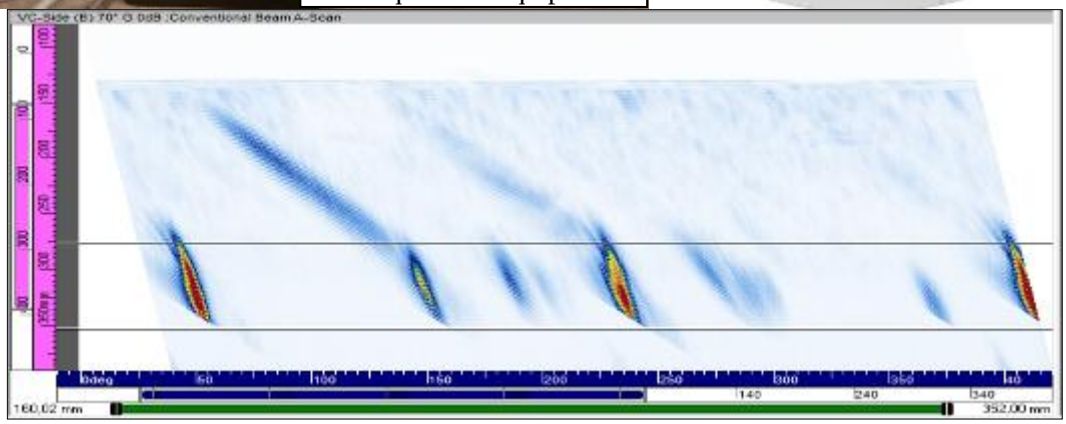

Figure 15: UT Data acquisition

7 UT DATA ANALYSIS

Data analysis is performed using **Ultravision III- 3D** to determine:

- the localization of the indication in the area to inspect.
- the time of flight (beam path)
- the reflectivity of the indication
- the sizing of the indication
- to discriminate defect from artifact

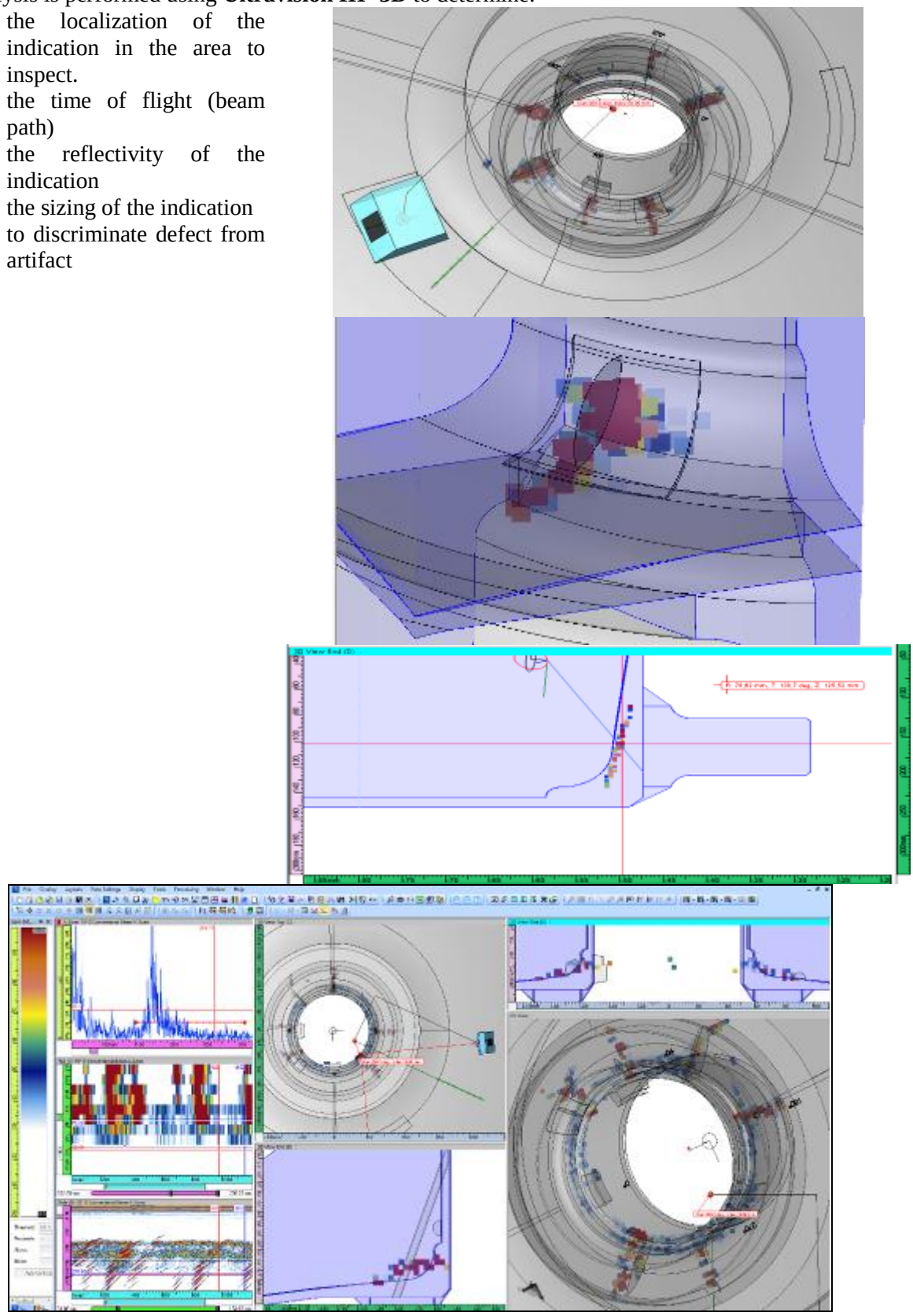

Figure 16: UT data analysis with Ultravision III-3D software

9 TECHNICAL JUSTIFICATIONS

As for a conventional qualification method, technical justifications were performed for the UT process. In addition of the reminder of the customer's requirements and related expected NDE performances, the description of the component, of the NDE equipment, of the calibration blocks, of the NDE process and the summary of expertise procedure were added to the technical justification file.

List of **I**nfluential **P**arameters (**IP**) was established. IP were sorted by group (Component, Technique, Scanner and Environment), with identification of systematic or random nature, nominal value and min/max limits of variation, impacted functions (coverage of the area to inspect, sensibility, localization, sizing or artifact/defect discrimination) and applicable methods to quantify impacts of each IP, in its variation range, on each functions (theoretical methods: computer simulations using CIVA software or analytical thinking, practical methods: design, tests, procedure or lessons-learned).

We first established the NDE performances of the process has the nominal state using IP with nominal values. At the end of the development phase, 34 IP were still under investigation (10 regarding the component, 12 for the technique, 3 for the environment and 9 for the scanner). 7 IP were also classified as "essential" (real value measured on site). After defining the equations to summarize global impact of all IP on each function, we calculated the NDE performances of the process has the nominal degraded state.

$$S_{final} = \sum_{Pi=1}^{Pi=11} S_i + k\sqrt{\sum_{Pi=15}^{Pi=30} \left| Z(S_i) \right|^2}$$

Figure 17: Example of equation to summarize global impact of all IP on "Sensibility"

For each impacted functions, we evaluated and justified:

- For sensibility : sensibility of the process at required detection and characterization limits (in the reference of the flat bottomed holes),
- For coverage of the area to inspect : percentage of the "area to inspect" that is effectively covered by UT, at the required level of sensibility,
- For localization : analytical expression leading to localize an indication from parameters of inspection and NDE measurements
- For sizing : reflectivity of the defect and equivalent to flat bottom hole dimensions
- Instruction or analysis method to discriminate physical defect from artifact (cladding, "nozzle to component" weld).

Most critical IP are:

- For sensibility : pipe OD, component thickness,
- For coverage of the area to inspect : angle of refraction and accuracy of this angle's measurement,
- For localization : angle of refraction, component's thickness,
- For sizing : scan and index steps
- For artifact/defect discrimination : cladding, "nozzle to component" weld

10 CONCLUSIONS

The development of this NDE process insures the following points:

- ♦ All defects manufactured in the mockup were detected according to the appropriated level of sensibility
- ♦ All defects were located within the right level of accuracy
- ♦ NDE process perfectly covers the required area to inspect : defects detected at upper, middle and lower limits of the R35x360°
- ♦ Discrimination of defect from artifact

DEVELOPMENT OF A FLEXIBLE CROSS WOUND EDDY CURRENT ARRAY PROBE FOR WELD INSPECTION

A. Lamarre, B. Lepage, Olympus NDT Canada

Abstract

Conventional cross wound eddy current sensor have been used for years in the non-destructive testing industry for surface detection of cracks on welds. Olympus recently developed a way to reproduce the sensor response of this three-dimensional transmit-receive structure on a flexible circuit board leading the path to the manufacture of a flexible cross wound eddy current array probe. This array permits a fast and reliable inspection of weld surfaces. This paper describes the method used and results of weld inspection will be presented.

Keywords: Development in surface examination, eddy current, array, weld

EDDY CURRENT PROBES BASED ON MAGNETIC SENSORS FOR COMPLEX NUCLEAR PARTS INSPECTION

B. Marchand, JM. Decitre, CEA - LIST, France
G. Cattiaux, T. Sollier, IRSN - DSR, France

ABSTRACT

Eddy Current Technique (ECT) is a powerful mean of inspection to check the integrity of metal parts. In nuclear industry, ferritic steel as for instance 18MND5, are often used. Because of skin depth effect, the magnetic permeability of this material leads to a limited efficiency of EC into the parts. Low frequency is therefore required and the control becomes less effective when conventional technologies are used. Furthermore, remanent magnetic field may occur into the parts and then disturbs EC measurements. That the reason why new methods and technologies have to be investigated to improve the inspection of such material and bring more efficient solutions.
Preliminary studies achieved in the framework of a joined R&D program between CEA LIST and IRSN, led to the development of a prototype probe, based on one Giant Magneto-Resistance Sensor (GMR). Such sensor has the asset to be effective at low frequency. First experimental results have demonstrated its efficiency in the detection of flaws into magnetic parts. Thanks to modelling tools included into CIVA software, a new 8-GMR probe has been designed and optimized. Magnetic sensors are arranged into a staggered rows matrix (2x4) so that the spatial resolution is enhanced. Sensors are wired on a flexible Kapton film set on a conformable mount. An electronic loop has been embedded into the probe, in order to monitor the polarization point of every GMR, and then balance offsets that may happen when remanent magnetic field occurs.
Design of the probe will be given in this article and experimental results of complex 18MND5 part inspection will be shown. They reveal how the flexible technology reduces the lift-off noise, optimizes the coupling between the sensors and the part and consequently enhances the detection of defects.

INTRODUCTION

A lot of critical components in a Pressurized Water Reactor are made of ferritic steel material as 16 or 18 MND5. For safety reasons, their integrity has to checked, in the production line as well as in service. Traditionally, Ultrasonic, X-Ray and Dye Penetrant methods are used. They have already proven to be efficient but have also revealed some limits, mainly in terms of accessibility and implementation difficulties. Eddy Current Technique has assets which makes it a promising alternative technique to control such parts. Nonetheless, the nature of the material itself leads to difficulties. Because it is a ferromagnetic material, it has a rather high magnetic permeability (μ_r) which prevents the induced current from penetrating deeply into the part. The relationship between penetration depth, magnetic permeability and frequency shows that the higher the permeability, the lower the frequency. When conventional EC probes based on classical winding coils are used, the size of the sensor can become pretty large to match the low frequency. In consequences, probes become rather bulky and flexibility is hardly achievable, which makes the inspection of complex parts non effective and accessibility to some areas impossible. On the contrary, the use of magnetic chip as sensors appears to be a promising solution. Such sensors are very small (one hundred of micrometers) and have a large bandwidth. Therefore, they offer the possibility of developing arrays working at low frequency embedded into a flexible mount.
In the framework of a joined R&D program between CEA LIST and IRSN, magnetic sensors and their performances for NDT application on magnetic parts has been investigated. Preliminary studies have led to the development of a first prototype probe, based on one Giant Magneto-Resistance Sensor (GMR) [1]. The first part of this paper details the probe, the way it works and the reason why embedded electronic is required. Experimental results are given and demonstrate its efficiency in the detection of flaws into magnetic parts.

Thanks to modelling tools included into CIVA software [2], an array composed of 8 GMR sensors has been designed and optimized. A new prototype probe has then been developed. The second part of the paper describes this probe and experimental results on magnetic mocks-up are provided and discussed.

DEVELOPMENT OF AN EC PROBE BASED ON A GMR SENSOR

Context

Magnetic sensors have the assets to be very small, large bandwidth and low cost, that makes them attractive to be used as receivers into EC probes. Making an array of Eddy Current sensors on a conformable substrate is feasible and developments at CEA LIST have already proven their efficiency. For these reasons, this technology appears to be promising for the inspection of components made out of magnetic material as 16 or 18 MND5. Nonetheless, one inconvenient of GMR is their need to be correctly polarized. Indeed, the external magnetic field has to be such that the response of the GMR is linear. So, the use of a polarization coil, close to the sensor, is required. As GMR are sensitive to continuous magnetic field, like the Earth's magnetic field or like remanent magnetic field that may occur into magnetic materials, this polarization is required to make the GMR works in normal condition [3, 4].

To explain the principle of magnetic material inspection with a magnetic sensor, three cases can be considered. For the three following cases, V_{GMR}, V, H, H_{POL}, H_{CF}, S and S' stand for:

- V_{GMR} (H): characteristic of the magnetic sensor (GMR)
- V_{GMR} (t): voltage given by the GMR sensor [V]
- V (t): voltage corresponding to the amplitude of the signal V_{GMR}(t), After demodulation, [V]
- H_{POL}: magnetic field required to polarize the GMR [A/m]
- H_{CF} (t): variation of the magnetic field at the Eddy Current frequency (due to the emitter) [A/m]
- S: polarization point without remanent magnetic field
- S': polarization point with remanent magnetic field

When there is no defect and no remanent magnetic field into the inspected material the response of the correctly polarized GMR sensor is a sinusoidal curve which frequency is the same as the Eddy Currents one (Figure 1). After demodulation, the signal will be the continuous voltage corresponding to the amplitude of the signal V_{GMR}(t).

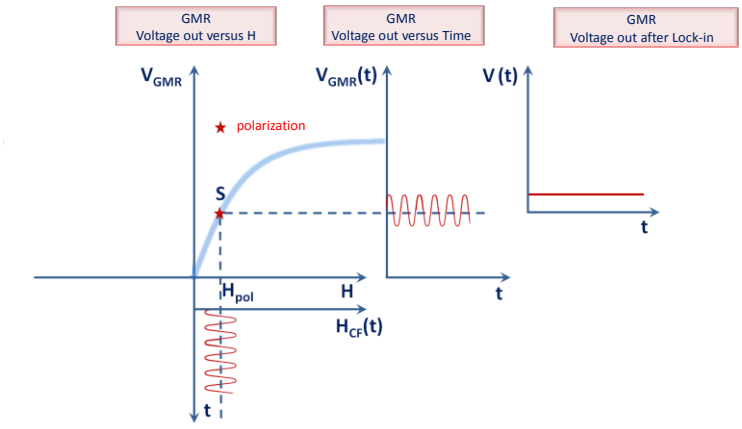

Figure 1 : Inspection of a part without defect, without remanent magnetic field, with a GMR.

When there is a defect but no remanent magnetic field into the inspected material, the response of the correctly polarized GMR sensor is a sinusoidal curve which frequency is the same as the Eddy Currents one. The defect produces an amplitude modulation of the response of the sensor (Figure 2). After demodulation, a variation of the voltage out from the sensor appears: the defect can be detected.

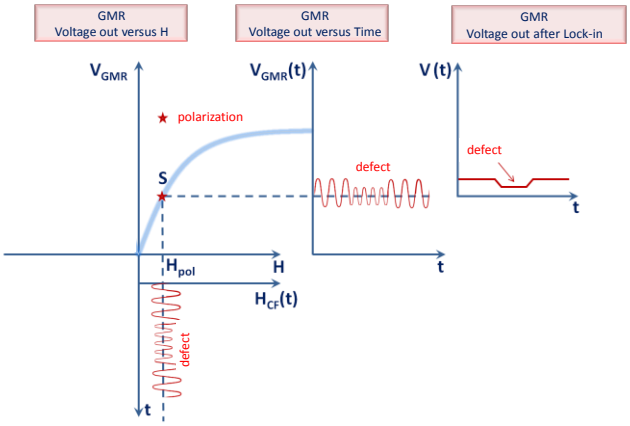

Figure 2 : Inspection of a part with a defect, without remanent magnetic field, with a GMR

Finally, when there are both a defect and a remanent magnetic field into the inspected material (Figure 3) the defect produces an amplitude modulation of the response of the sensor. But, the remanent magnetic area adds a continuous magnetic field which is measured by the sensor. In consequences, the polarization point of the GMR is modified and moves from state S to state S'. In this state, the sensitivity of the GMR and then, the amplitude of $V_{GMR}(t)$, have decreased, as shown on Figure 3.
After demodulation, two variations of the output voltage are detected: one comes from the defect while the other one is due to the remanent magnetic field. This signal may be interpreted as a defect one and leads to a false alarm. Or else, this signal may be superimposed to the one of the defect and conceals it.

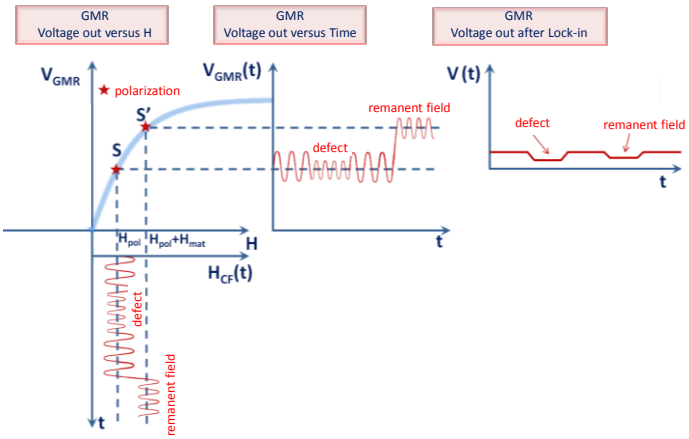

Figure 3 : Inspection of a part with a defect, with a remanent magnetic field, with a GMR

Development of the probe and its embedded electronic

One objective of the embedded electronic is to avoid a change of the polarization in case of remanent field happens when magnetic material is inspected [5]. The principle is to balance the effect of the continuous magnetic field by setting the suitable current into the polarization coil. The block diagram of the electronic loop is given on Figure *4*. The polarization voltage is compared to the output voltage of the GMR. The difference between these two voltages is injected to the corrector. The corrected voltage is then injected to the polarization circuit, and the GMR has a new output voltage. This feedback loop is run until the difference between the two voltages is equal to zero. Thus, when remanent field occurs, the polarization voltage will be automatically corrected.

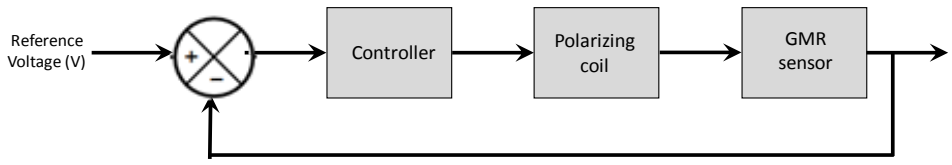

Figure 4 : Block diagram of the feedback loop

A drawing and photos of the prototype Eddy Current probe are given on Figure 5. The emitter is a classical winding coil, without ferrite. The receiver is a GMR sensor which measures the vertical component of the magnetic field. The distance between the emitter and the receiver can be set from 10mm to 25mm and therefore optimized with regards to the frequency of the Eddy Current. Emitter and receiver are as close as possible to the inspected surface. Housing allows a mounting on a mechanical bench. A LED signal shows if the GMR is well polarized. It is possible to activate or not the feedback loop thanks to a switch.

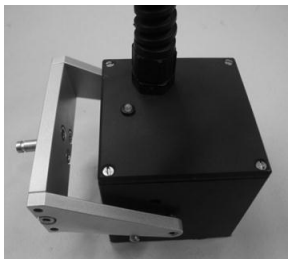

Top view of the EC probe

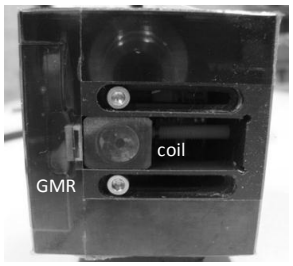

Bottom view of the EC probe

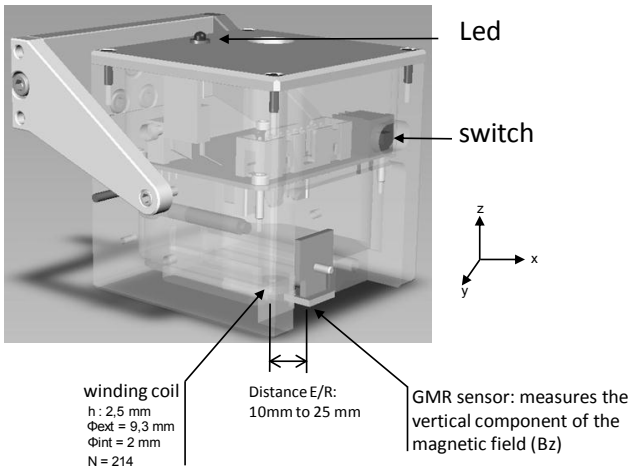

Figure 5 : Photos and drawing of the new EC probe based on GMR sensor

First evaluation

The new Eddy Current probe has been evaluated using a 16MND5 mock-up. It contains two surface holes which characteristics are given in Tab 1. A little circular magnet has been horizontally put on the surface of the part and then removed.

	Diameter (mm)	Depth (mm)
Hole #1	5	2.5
Hole #2	4	2

Table 1 : Characteristics of the defects into the 16MND5 plate

The experimental CSCANs obtained at 70 kHz are given on Figure 6. As expected, when the feedback loop is not used, both holes but also the remanent fields are detected (Figure 6b). For an unknown part, such signature could be interpreted as a third defect or could hide the response of an adjacent defect. On the contrary, when the feedback loop is activated, the signature of the remanent field has almost disappeared (Figure 6c). Besides, both holes are better detected and SNRs have increased. The electronic circuit has proven its efficiency and the inspection of magnetic parts using magnetic sensor EC probe is now possible.

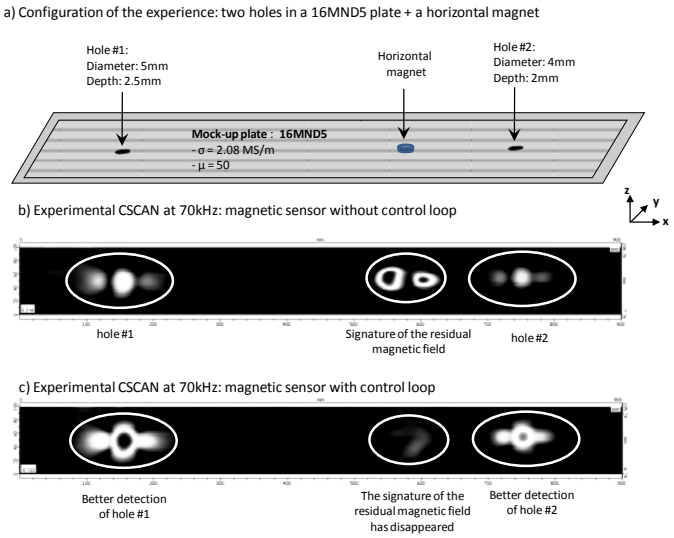

Figure 6 : a) Configuration: two holes and a horizontal magnet into a 16MND5 plate - b) Scan without using the feedback loop – c) Scan with the feedback loop

A second testing has been performed using an 18MND5 cylinder in which artificial notches have been realized in the inner wall. A photo of the mock-up and characteristics of the notches are given on Figure 7.

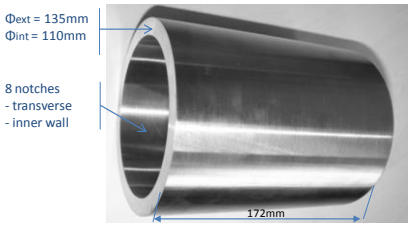

N°	Length (+/- 0.1mm)	Width (0/+0.05mm)	Ligament (+/-0.05mm)
1	20 mm	0.2 mm	2 mm
2	20 mm	0.2 mm	4 mm
3	20 mm	0.2 mm	6 mm
4	20 mm	0.2 mm	8 mm
5	10 mm	0.2 mm	1 mm
6	10 mm	0.2 mm	2 mm
7	10 mm	0.2 mm	4 mm
8	20 mm	0.3 mm	4 mm

Figure 7 : Photo of the 18MND5 cylinder and characteristics of the notches

The notch #01 has been inspected from the outer wall of the cylinder. Experimental CSCANs given on Figure 8 show that without electronic, the notch is hardly detected. Noise coming from the material itself is too important. However, when electronic is switch on, this noise has been greatly reduced and the signature of the notch appears clearly. Comparison of both lines of the CSCAN leads to the same conclusion.

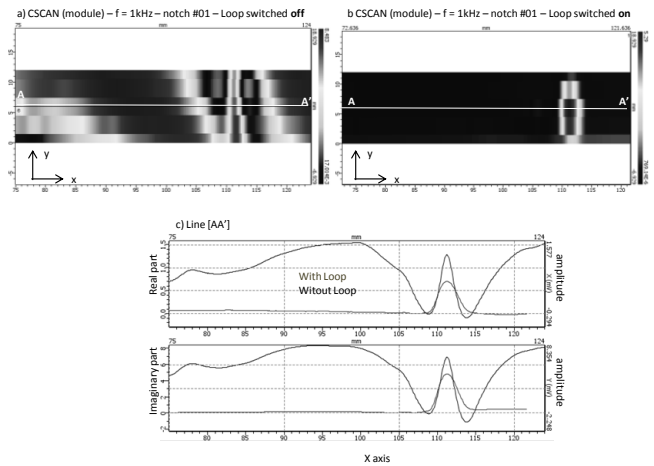

Figure 8 : CSCANS of notch #01 at 1 kHz, with and without feedback loop

DEVELOPMENT OF AN EC FLEXIBLE PROBE BASED ON A GMR SENSORS ARRAY

Design

Design and simulation of the performances of the probe has been performed using CIVA software. A lot of different geometries have been studied, and parameters have been optimized taking into account feasibility and limits of technology. The scheme of the final design is presented on Figure 9. The probe is composed with rectangular coils as emitters and a matrix of eight GMR, ordered in a matrix 4x2, as sensors. GMR are oriented along the [0x] axis so that they measure the tangential X component of the magnetic field. Thus, the expected response of one notch will be a mono-polar signal, which eases its detection and analysis. The pitch between sensors gives the spatial resolution of the probe. It has been defined from the required specifications in terms of size of defect to be detected while regarding the space requirement of each chip. Thanks to a staggered row arrangement, the pitch has been reduced to 1.25mm.

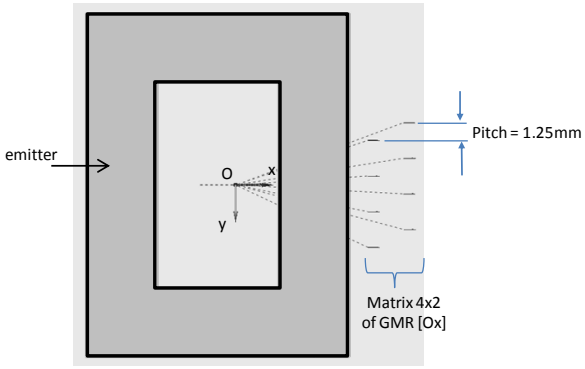

Figure 9 : Final scheme of the 8-GMR probe

When designing a multi-element probe, disparity between signals given by every sensor has to be estimated. Simulations have been done and CSCAN obtained from two separated chip are presented on Figure 10. It turns out that in the worst case (the most separated sensor) the difference between both amplitudes is less than 6% which confirms the homogeneity of the matrix.

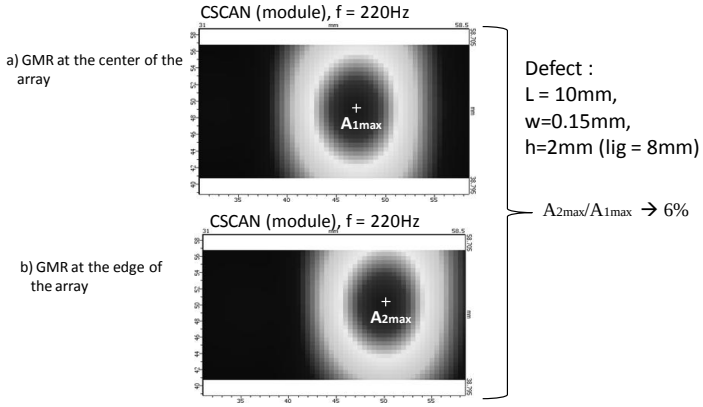

Figure 10 : Evaluation of the disparity between elements of the array

The probe has then been developed and a photo of it is given on Figure 11. Emitters and polarization coils are etched on a Kapton film when GMRs are connected thanks to “Flip-Chip” technique on this very film. This film has a flexible mount which makes the inspection of complex geometry parts achievable. Besides, the flexibility ensures a good and constant contact of the probe with the inspected surface that reduces lift-off noise and then enhances the SNR. Embedded electronic amplifies both emitted and received signals and monitors the polarization of each sensor. An embedded multiplexer 8→1 is required to drive each GMR. The probe can be manually or mechanically used.

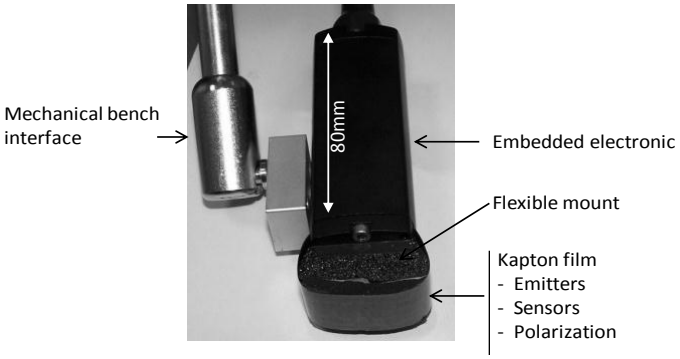

Figure 11 : Photo of the flexible EC probe based on an 8-GMR array

First evaluation

The experimental CSCAN of a 5mm surface notch located into a stainless steel plate is presented on Figure 12. This CSCAN corresponds to a one line inspection: the 8 GMR are activated thanks to the multiplexer and each line of the CSCAN corresponds to the response of one sensor when excited at 500kHz. The notch is detected by three GMR with a good SNR.

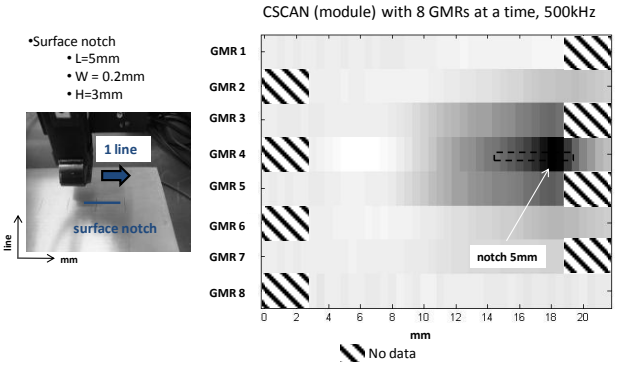

Figure 12 : Experimental CSCAN – 8GMR probe - notch 5mm – 500kHz

A second experimental CSCAN of a 10 mm sub-surface notch, located in a stainless steel cylinder with a 2 mm ligament is presented on Figure 13. The inspection is performed from the outer wall. Only one GMR is activated.

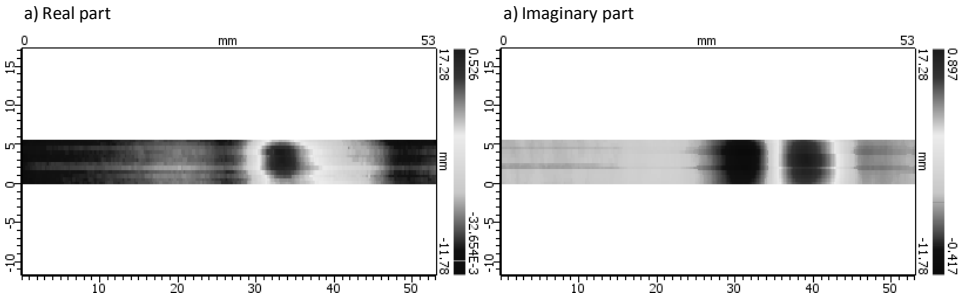

Figure 13 : CSCAN of a 10mm sub-surface notch in a SST cylinder at 2mm ligament with one GMR from the array - f = 10kHz

The defect is detected with a good SNR of 20dB. This first result is promising and shows that it is possible to detect a sub-surface crack into a complex part thanks to the multi-element flexible EC probe.

CONCLUSION

Eddy Current Technique is an efficient method for the inspection of metal parts. Nonetheless, specific constraints occur when the material is ferromagnetic. Because of skin depth effect, low frequency is required which implies the use of sensors sensitive at such frequencies. Because of their large bandwidth, GMR sensors seem to be well adapted for such applications, but they are sensitive to the remanent magnetic field that may occur into the part.
To bring a solution to this issue, a new Eddy Current Probe based on a GMR sensor has been developed, with optimized electronic embedded. It consists in a control loop which monitors the polarization of the GMR so that it remains in its linear range. Experimental testing performed on magnetic materials has demonstrated the efficiency of the electronic and the ability of the EC probe to detect defects even when remanent field happens.
To go further in this study, more experimentation considering defects with different sizes and depths should be done.

REFERENCES

[1] Dogaru T. and Smith S. T., "Giant Magnetoresistance-Based Eddy-Current Sensor", IEEE Transactions on Magnetics, Vol. 37, No. 4, pp.2790-2793, July 2001.
[2] http://www-civa.cea.fr
[3] Chikazumi, Sōshin (1997). Physics of Ferromagnetism. Clarendon Press. ISBN 0-19-851776-9
[4] Mayergoyz, Isaak D.; Bertotti, Giorgio, eds. (2005). The Science of Hysteresis (3-volume set). Academic Press. ISBN 978-0-12-480874-4
[5] Marchand B., Decitre JM., Casula O., "Innovative Flexible Eddy Current Probes for the Inspection of Complex Parts", World Conference on NDT, Durban, April 2012.

DEVELOPMENT OF ULTRASONIC AND EDDY CURRENT TESTING TECHNIQUES FOR CURVED STRUCTURES

T. Miura, S. Yamamoto, N. Kobayashi, J. Senboshi, S. Ueno,
M. Ochiai, I. Chida, H. Adachi, S. Yamamoto
Toshiba, Japan

INTRODUCTION

In nuclear power plants, some parts have complex surface structures, therefore it is difficult to inspect such structures by conventional testing technique. Especially, welded area near nozzle of pressure vessel and J-groove welded area have a curvature, therefore new inspection technique is needed. In this paper, we present a developed new ultrasonic testing and eddy current testing technique for curved structures and confirmed its performance.

ULTRASONIC TESTING

Conventional Phased Array Ultrasonic Testing (PAUT), which can vary its refraction angle and so forth by pulsing multiple elements of a probe separately, has been applied to many components as a superior alternative technique for a conventional single element probe testing. Toshiba has developed a ultrasonic beam control PAUT technology itself and that with easily formable gel (soft shoe) as propagation medium [1-2]. The schematic diagram of the application to R60 (Radius of curvature 60 mm) nozzle is shown in Fig.1. In a case that the conventional PAUT applies to R60 nozzle, the incident ultrasonic beam is reflected diffusely or refracted with an incorrect angle because of the surface profile (Fig.1 (a)). In the case of newly developed PAUT, incident ultrasonic beam refracts in the correct angle (Fig.1 (b))

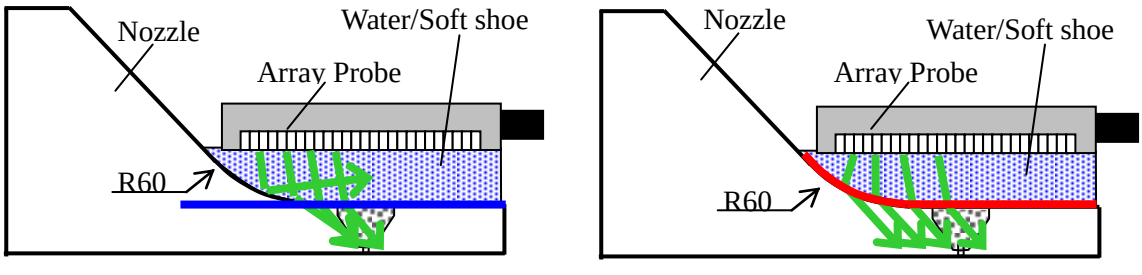

(a) Conventional PAUT (b) PAUT with Surface Correction

Figure 1 The schematic diagram of the application to R60 nozzle

The inspection procedure by using this technique is shown in Fig.2. Before inspection, there are two steps: surface profile measurement and calculation of delay time depending on the surface profile. In the surface profile measurement, ultrasonic wave is transmitted by each element that composes an array probe. Reflected ultrasonic wave on the measurement surface is received by all elements (from "element 1" thru "element n"). Therefore n×n patterns for raw wave pattern will be acquired. Intensity of reflecting waves from material surface is visualized by the Synthesis Aperture Focusing Technique (SAFT) using this wave patterns. This method enables higher precision surface profile measurement.

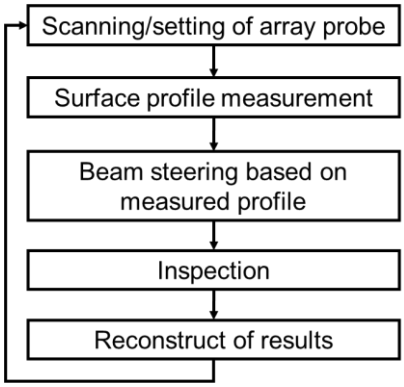

Figure 2 Inspection procedure

The schematic diagram of controlling ultrasonic beam to inspect partly dented surface is shown in Fig.3 for illustration. In the case of the conventional PAUT, the delay time is controlled by the assumption that the surface is flat. Therefore the refracting angle deviates from the right direction shown as the red line in Fig. 3 (a) because the ultrasonic beam is diffused with the same delay time. In this case, inspection refracting angles are changed by surface profile as Fig.3 (a). In this figure, green line shows successfully and accurately aimed ultrasonic beam, red line shows failed and uneven incident angle of ultrasonic beam because of the curved surface.

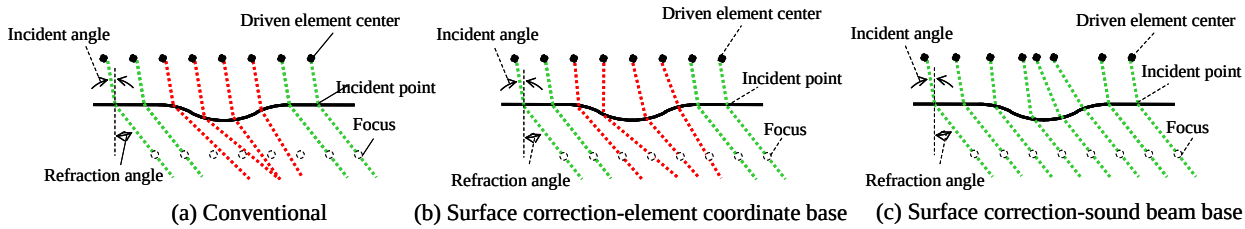

Figure 3 Schematic diagram of controlling ultrasonic beam

In the case that the delay time is calculated after fixing positions of a drive element and its paired focus (like the conventional linear scan) even if only the surface profile is compensated, although the ultrasonic beam can be incident in focus, the refracting beam deviates irregularly from the right direction with parallel angle shown as the red line in Fig.3 (b). Toshiba has succeeded in controlling ultrasonic beam to enter the material in the right direction corresponding to the surface profile. In this technology, firstly the focus point and inspection refracting angle are determined, then the incident point and optimum incident angle are uniquely determined. Lastly the elements are determined as driven elements on the incident angled extension line. This method makes it possible that ultrasonic beams in material are controlled to refract parallel to each other as shown in Fig.3 (c).

In addition, a soft shoe made by hydro-gel has been developed for inspection in air. The soft shoe has similar acoustic properties to water, the sound speed in which is 1450 m/s and the specific gravity is 0.82. Inspection sensitivity using this soft shoe is about 6dB less than the immersion method. With only gain control, inspection accuracy of this method achieves the same level as immersion method. Though the inspection for R60 nozzle is only taken up as an example to illustrate this technique here, it is also applicable to the distorted surface by welding or the curved surface by grinding.

Result of 2-Dimentional structures

The result of the surface profile measurement on R60 nozzle is shown in Fig.4 along with the results of laser displacement measurement defined as the true (reference) value. Comparing the results using by Time of Flight (TOF) and Synthesis Aperture Focusing Technique (SAFT) with the true value, while the mean error of TOF is 0.98mm and that of SAFT is 0.05mm or smaller.

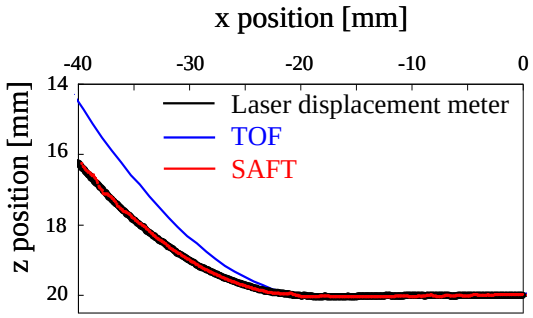

Figure 4 Comparison of surface measurement accuracy

The inspection results of nozzle shaped specimen are shown in Fig.5. Fig 5 (a) shows a result of the conventional PAUT where the delay time is calculated for the flat surface. The spurious echo is observed and the slit corner echo is unclear. Fig.5 (b) shows the inspection result in which the PAUT delay time is compensated for actual surface geometry. The spurious echo is suppressed and the slit corner echo is observed clearly.

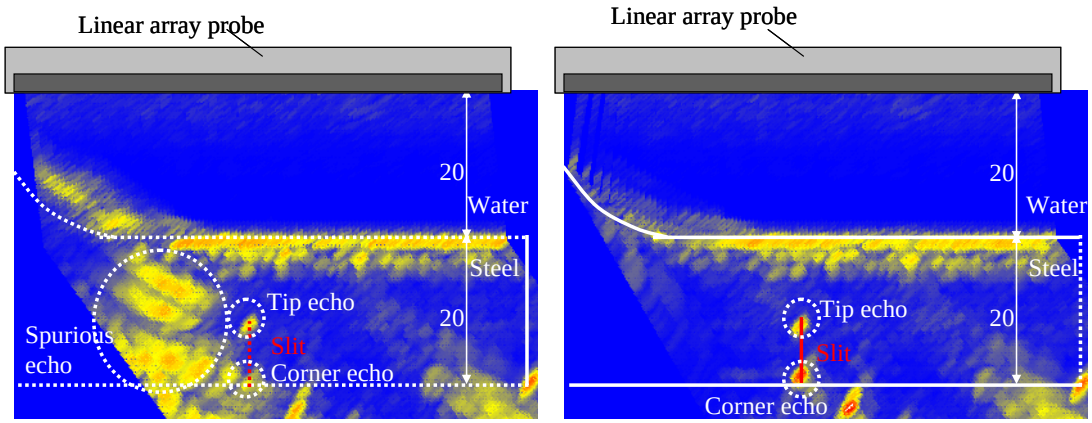

(a) Delay time without surface correction (b) Delay time with surface correction

Figure 5 Inspection result of nozzle shaped specimen

Result of 3-Dimentional structures

This technology has been expanded into 3-dimensions by using a matrix array probe. The inspection result is shown in Fig.6. Test specimen is R60 spherical material with 50mm in thickness shown in Fig. 6 (a). Fig 6 (b) is a result of the conventional PAUT, where the delay time was calculated for the flat surface. To evaluate the capability of the PAUT, the test specimen with drilled holes was prepared. The conventional method cannot observe the drilled holes echo at all. The bottom echo is not observed. Fig.6 (c) is the PAUT result in which the delay time was calculated for the actual surface geometry. The bottom echo is observed clearly.

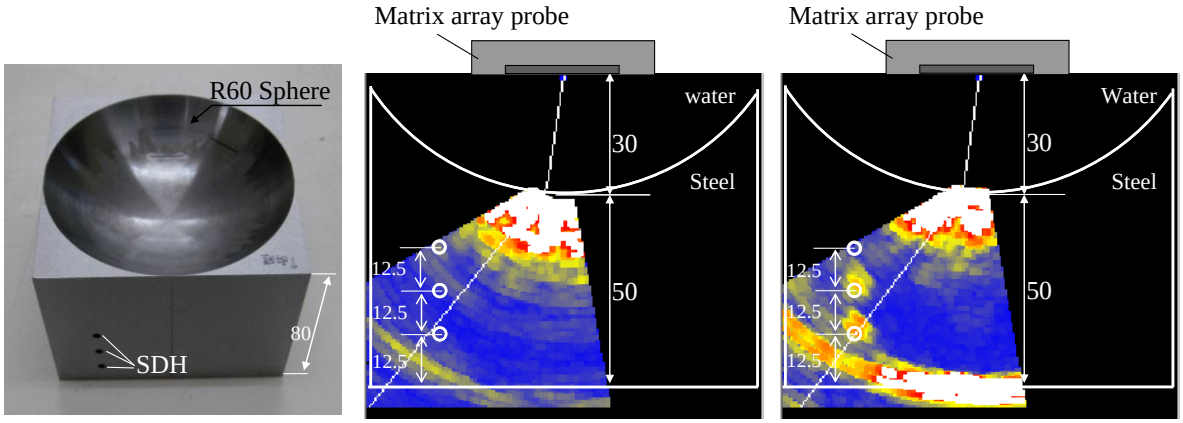

(a) Photo of a specimen (b) Conventional PAUT (c) PAUT with Surface Correction

Figure 6 Inspection results of spherical surface (R60) specimen

Result of practical use

We verified the detectability of developed technique in practical nozzle. Fig.7 shows the appearance of measured nozzle and experimental setup. There are many curved parts within weld to be measured. A matrix probe has a soft shoe, therefore ultrasonic beam can propagate into the nozzle.

We measured surface profiles at each measurement position by SAFT, and calculated beam steering delay time with consideration for surface profile information. The result is shown in Fig.8. The backwall echo signal of conventional technique shown in Fig.8(a) appeared in the middle part of thickness. On the other hand, developed technique shown in Fig.8(b) acquired

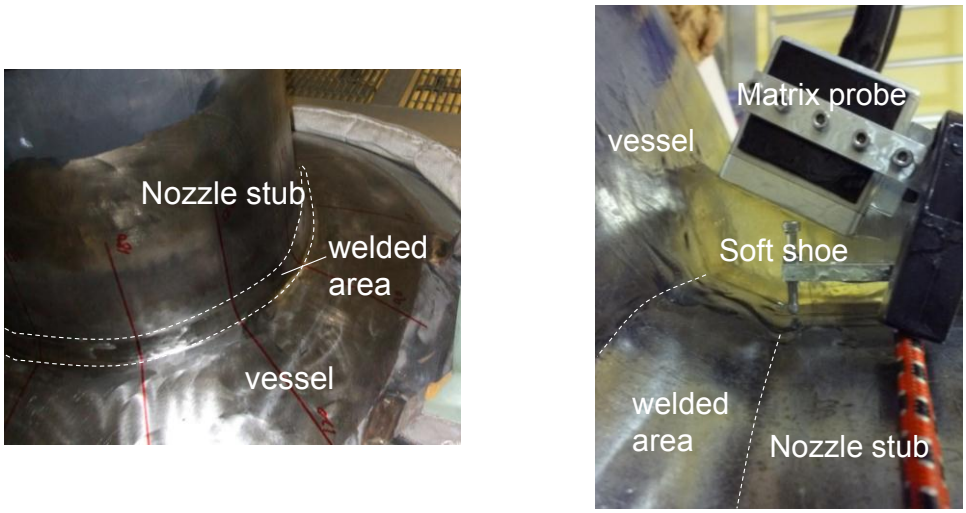

(a) Nozzle stub and welded area (b) Experimental setup

Figure 7 appearance of measured nozzle

accurate echo position and more clear echo signal.

As a result, the performance of developed technique was verified for inspection of complex surface.

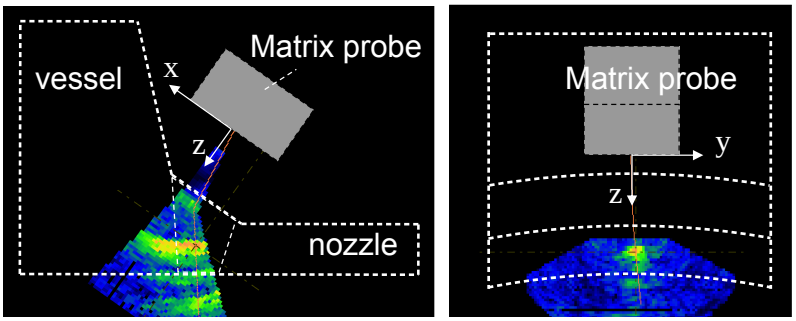

(a) conventional

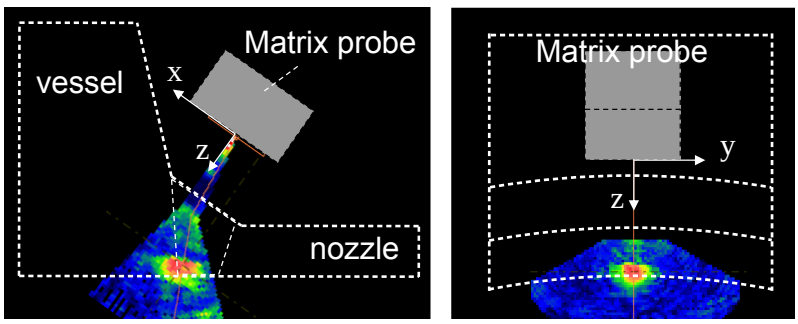

(b) developed

Figure 8 result of measured area

EDDY CURRENT TESTING

Eddy current testing (ECT) as a surface inspection technique has been developed for internals of nuclear power plants [3-4]. In this paper, we described confirmation of the defect detection performance of the eddy current testing (ECT) system in order to inspect the bottom-Mounted instrumentation (BMI) nozzle in reactor pressure vessel. Difficulties of BMI inspection are scanning equipment for complex surface, and ECT sensor for narrow space and small radius surface. We have developed equipment for scanning BMI surface for portable laser peening system [5], which can scan the surface of J-groove weld surface on BMI. However this equipment has a positioning error of ±3°, therefore reducing sensitivity has to suppress though ECT probe is tilting. In addition, ECT probe has to be installed for narrow and small radius surface of J-groove weld.

ECT probe for narrow and small curvature

Need for small but high sensitivity ECT probe for BMI inspection, ECT coil configuration changed. Conventional ECT coil has a distance between coil and magnetic material (Fig.9(a)), therefore coil size is difficult to be small, and magnetic flux diffuses in the case of inspection surface with 5 mm radius (Fig.9(b)). In the developed probe, magnetic materials are located in the interspace of the cross coil. As a result, probe becomes smaller and magnetic flux concentrates on the surface of R5 mm (Fig.9(c)).

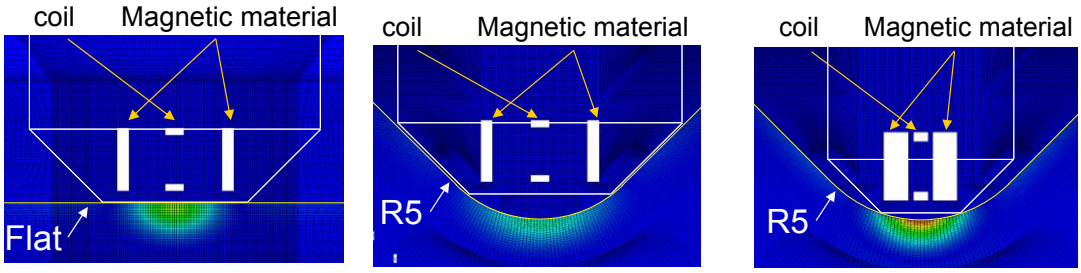

(a) Conventional (flat surface)　(b) Conventional (R5)　(c) developed (R5)

Figure 9 result of magnetic field analysis

Effect of probe tilting

The developed ECT probe has to be effective sensitivity by tilting due to mounting for the scanning equipment. Experimental result of tilting effect is shown in Fig.10. Cylindrical specimen with a diameter 38 mm has a slit with 0.5 mm depth and 0.4 mm width. Sensitivity is calibrated and set to 0 dB by reference specimen with 1 mm depth slit on flat Alloy600 surface. By tilting ECT probe, sensitivity is decreasing (Fig.10). Comparing the conventional and developed probe, the developed probe suppresses decreasing sensitivity. As a result, we achieved small and high sensitivity ECT probe having enough performance for J-groove weld surface inspection.

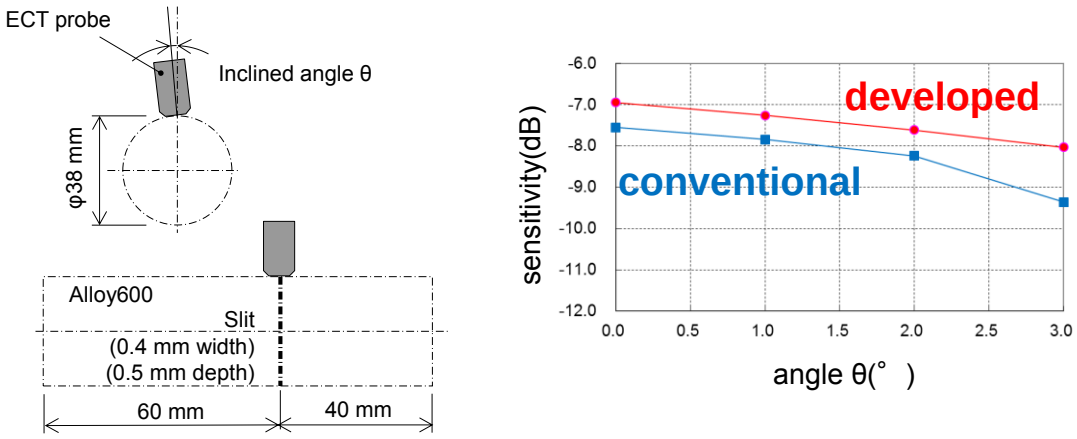

(a) Experimental setup (b) Sensitivity effect

Figure 10 experiment of probe tilt dependence

Detectability of artificial SCC by mock-up

Finally, we verified the performance by using artificial SCC on surface of J-groove weld. Experimental setup and scanning area are shown in Fig.11(a). Developed ECT probe scanned 10x6 mm area that has artificial SCC by scanning equipment. The result is shown in Fig.11(b). Indication appeared and its shape is similar to the result of penetration testing. Therefore, developed ECT probe has a performance of detectability of SCC on the surface of J-groove weld.

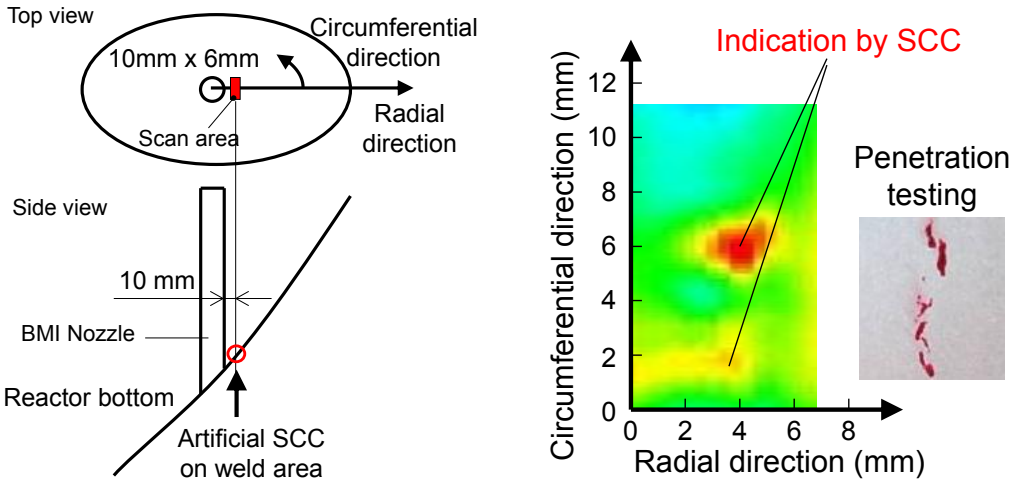

(a) Experimental setup (b) Result of detecting SCC

Figure 11 experiment of detectability of SCC

CONCLUSION

For inspection in nuclear power plants having complex surface structures, we developed new PAUT and ECT system. Volumetric inspection for nozzle of pressure vessel is effective by using developed shape adaptive beam steering technique. Surface inspection for the surface of J-groove welded area is effective by developed small ECT probe. Both development techniques were tested in practical structure or mock-up testing and their performance were verified.

REFERENCES

1) S. Yamamoto, J. Senboshi, M. Ochiai, T. Mitsuhashi, H. Adachi and S. Yamamoto: Shape Adaptive Beam Steering Technique for Phased Array Ultrasonic Testing, 38th Annual Review of Progress in Quantitative Nondestructive Evaluation, Burlington, VT, July 17-22 (2011)

S. Yamamoto, J. Semboshi, T. Miura, T. Mitsuhashi and M. Ochiai: Beam Steering Phased Array Ultrasonic Testing System for Complex Surface Shape Strucutures, Journal of The Japanese Society for Non-Destructive Inspection, Vol.62(2), pp.95-101 (2013)

3) N. Kobayashi, T. Kasuya, S. Ueno, M. Ochiai, Y. Yuguchi, C. S. Wyffels, Z. Kuljis, D. Kurek and T. Nenno, “Utility Evaluation of Eddy Current Testing for Underwater Laser Beam Temperbead Welding”, Proceedings of the 8th International Conference on NDE in Relation to Structural Integrity for Nuclear and Pressurised Components, Berlin, 2010, We.2.B.2.

4) S. Ueno, N. Kobayashi, T. Kasuya, M. Ochiai and Y. Yuguchi, “Defect Detectability of Eddy Current Testing for Underwater Laser Beam Welding”, Proceedings of the 19th International Conference on Nuclear Engineering (ICONE19), Osaka, 2011, ICONE19-43658.

5) I. Chida, T. Uehara, M. Yoda, H. Miyasaka and H. Kato, “Development of Portable Laser Peening Systems for Nuclear Power Reactors”, Proceedings of the 2009 International Congress on Advances in Nuclear Power Plants (ICAPP’09), Tokyo, 2009, ICAPP09-9029.

MODELLING (T6/T6.1) I

NUMERICAL SIMULATIONS OF ULTRASOUND NDE: A HYBRID MODEL WITH IMPROVED EFFICIENCY BY A NEW BOUNDARY FORCING METHOD

E. A. Skelton, R. V. Craster W. Choi, M. J. S. Lowe,
Imperial College, UK

ABSTRACT

For ultrasonic NDE, modelling tools able to represent the entire domain are desirable. However, different tools are attractive for different tasks. The finite element (FE) method, for example, is good for scattering by complex shapes, but for large volumes the calculation becomes unwieldy. The ability to utilise suitable small models for different features (sources, scatterers, receivers etc), and link them together to perform accurate modelling with manageable sized models would be advantageous. The generic hybrid method takes output from one region and processes it to use as input to another separated region. Previous work at Imperial College on this prototype method tested the concept using the values of displacements and stresses on the boundary of region 1 to calculate the values of displacements/velocities and stresses elsewhere: in particular on the boundary of region 2. (This takes place in the frequency domain, but is applied in the time domain by using Fourier transforms and inverse transforms). This allows region 2 to be excited in the FE model by **specifying** time-series for **either** stress or displacement/velocity along a line in front of region 2. Here, we introduce an extension to the method by modifying the forcing presented to the second region. This allows suitable point forces to be **applied** to the boundary of the second region to reproduce the incident field within that region, without introducing numerical scattering at its boundary and hence allowing both the size of the modelled region to be reduced substantially and the extraction of the scattered field on the boundary to be simplified. Some animations demonstrating the successful test of this concept will be included. In a separate presentation some examples of industrial interest, calculated using this method, will be presented and discussed.

INTRODUCTION

The concept behind the hybrid model is that different numerical methods are most appropriate in different situations. The FE model is good for very detailed modelling near a complex feature. Analytical methods are good for open spaces. For examples containing some complex features (e.g. sources and defect) which are widely spaced the hybrid approach seeks to use appropriate small models near to the complex features and link them together using a hybrid interface, as illustrated schematically in figure 1, and discussed in [1,2], for example

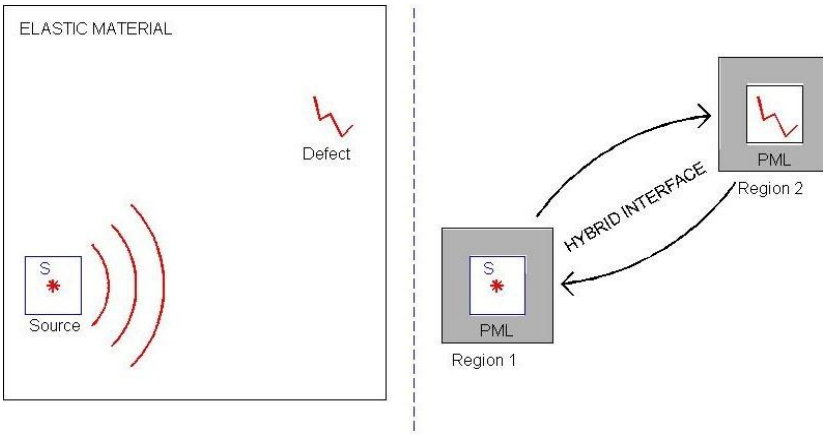

Figure 1 Simplified schematic geometry for source & defect: Whole region or Hybrid Interface

A GENERIC HYBRID MODEL

For simplicity of exposition only the 2-dimensional case is discussed in detail here. As it is convenient to work in the frequency domain, any output from the local modelling in the time domain is first subject to a FFT.

The generic hybrid model in the frequency domain for in-plane elastic motion is based here on a Green's function approach, using the displacement potentials. In dimensionless variables the equations of motion may be written as

$$-\omega^2 u_x = \frac{\partial \tau_{xx}}{\partial x} + \frac{\partial \tau_{xy}}{\partial y}$$

$$-\omega^2 u_y = \frac{\partial \tau_{xy}}{\partial x} + \frac{\partial \tau_{yy}}{\partial y}$$

$$\tau_{xx} = \gamma^{-2}\frac{\partial u_x}{\partial x} + (\gamma^{-2} - 2)\frac{\partial u_y}{\partial y}$$

$$\tau_{xy} = \frac{\partial u_y}{\partial x} + \frac{\partial u_x}{\partial y}$$

$$\tau_{yy} = (\gamma^{-2} - 2)\frac{\partial u_x}{\partial x} + \gamma^{-2}\frac{\partial u_y}{\partial y}$$

in which τ_{xx}, τ_{xy}, and τ_{yy} are the stress components, u_x and u_y are displacement components, $\gamma = {c_T}/{c_L}$ is the ratio of the shear (c_T) and compressional (c_L) wave speeds in the elastic material, and ω is the angular frequency of the time-harmonic motion. The displacement potentials are introduced via

$$u_x = \frac{\partial \Phi}{\partial x} + \frac{\partial \psi}{\partial y}$$

$$u_y = \frac{\partial \Phi}{\partial y} - \frac{\partial \psi}{\partial x}$$

and they satisfy the Helmholtz equations

$$(\nabla^2 + \omega^2)\psi = 0$$

$$(\nabla^2 + \omega^2\gamma^2)\Phi = 0.$$

Green's theorem allows us to use the values of the potential and its normal derivative on a closed curve to calculate the potential elsewhere. For example, for the shear potential

$$\psi(\boldsymbol{x}_0) = -\oint_S \left(\psi \nabla G_\psi - G_\psi \nabla \psi\right).\mathbf{n}\,\mathrm{dS}$$

in which **n** is the outward normal to the contour S and $G_\psi(\boldsymbol{x}, \boldsymbol{x}_0)$ is the Green's function of the Helmholtz equation for ψ,

$$G_\psi(\boldsymbol{x}, \boldsymbol{x}_0) = -\tfrac{i}{4} H_0(\omega|\boldsymbol{x} - \boldsymbol{x}_0|)$$

and for the longitudinal potential

$$\Phi(\boldsymbol{x}_0) = -\oint_S (\Phi \nabla G_\Phi - G_\Phi \nabla \Phi).\mathbf{n}\,\mathrm{dS}$$

$$G_\Phi(\boldsymbol{x}, \boldsymbol{x}_0) = -\tfrac{i}{4} H_0(\omega\gamma|\boldsymbol{x} - \boldsymbol{x}_0|).$$

Here, we make use of these properties to construct a hybrid model for scattering in a large region by defining two smaller areas, one containing the source (region 1) and the other containing the scatterer (region 2), and surrounding them with PML or absorbing material, [3], as shown in figure 1. Any numerical model appropriate to the source region can then be used to obtain suitable outputs on the boundary from which the potentials and their normal derivatives there, in the frequency domain, can be extracted and used, as above, to calculate values on the second boundary. For convenience we choose the boundary to be rectangular.

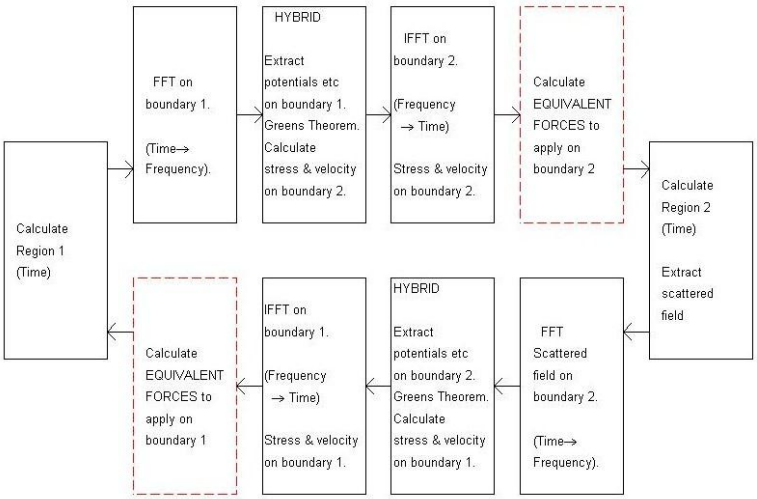

Figure 2 Flow Chart for Hybrid Model with Additional Applied Forces Element

Having found the values for displacement and stress components on the second boundary in the frequency domain, inverse Fourier transforms may be applied to obtain the displacements, stresses and velocities there in the time domain. The problem then arises as to how to make use of this information to force a small numerical model of this second scattering region. One option is to specify either the velocity or the stress have the given values there. Both of these options however lead to problems: (i) Reflections will occur at the artificial boundary, so the calculation area must be large enough that these don't have time to interfere with the extraction of the quantities required. (ii) This generates waves which travel away from the artificial boundary, which is acceptable on those faces which are between the source and the scatterer, but clearly unacceptable on those faces where the source and the scatterer are on the same side and in such cases an ad-hoc decision is made not to force on those sides.

A NEW BOUNDARY FORCING METHOD

The approach which we adopt here is different. We no longer require the values of the stress or velocity to have given values on the boundary. Instead we construct the times series for the forces around the artificial boundary which, when added to the system reproduce both the velocities and stresses of the incident wave field on the artificial boundary, and hence also the incident field within the calculation area. This procedure is summarised in the flow chart shown in figure 2. In order to achieve this, the time domain form of the elastic equations using velocity and stress are considered:

$$\frac{\partial v_x}{\partial t} = \frac{\partial \tau_{xx}}{\partial x} + \frac{\partial \tau_{xy}}{\partial y}$$

$$\frac{\partial v_y}{\partial t} = \frac{\partial \tau_{xy}}{\partial x} + \frac{\partial \tau_{yy}}{\partial y}$$

$$\frac{\partial \tau_{xx}}{\partial t} = \gamma^{-2}\frac{\partial v_x}{\partial x} + (\gamma^{-2} - 2)\frac{\partial v_y}{\partial y}$$

$$\frac{\partial \tau_{xy}}{\partial t} = \frac{\partial v_y}{\partial x} + \frac{\partial v_x}{\partial y}$$

$$\frac{\partial \tau_{yy}}{\partial t} = (\gamma^{-2} - 2)\frac{\partial v_x}{\partial x} + \gamma^{-2}\frac{\partial v_y}{\partial y}$$

We use a small finite difference scheme for the computation area, with no scatterer present and surrounded by a small PML, as shown in figure 3. As no scatterer is present there is no need for a detailed mesh for this part of the calculation.

The velocities on the boundary are known at times nδt and the stresses at intermediate times (n+1/2)δt. The equations are integrated for one time step throughout the computation area. Thus, when time-stepping for the velocities

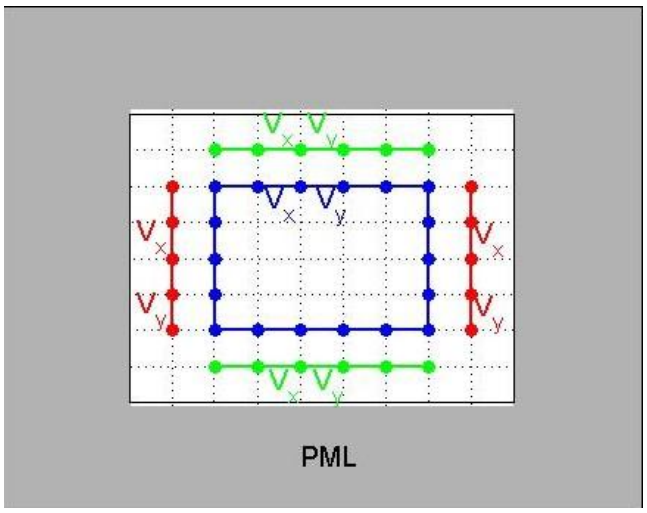

Figure 3 Finite Difference Grid for Applied Forces Calculation

$$v_x\big((n+1)\delta t\big) = v_x(n\delta t) + \delta t\left(\frac{\partial \tau_{xx}}{\partial x}((n+\tfrac{1}{2})\delta t) + \frac{\partial \tau_{xy}}{\partial y}((n+\tfrac{1}{2})\delta t)\right)$$
$$v_y\big((n+1)\delta t\big) = v_y(n\delta t) + \delta t\left(\frac{\partial \tau_{xy}}{\partial x}((n+\tfrac{1}{2})\delta t) + \frac{\partial \tau_{yy}}{\partial y}((n+\tfrac{1}{2})\delta t)\right)$$

in which the spatial derivatives are obtained using centred finite differences. We require that both velocity components on the artificial boundary 2 should have the values $v^H(\boldsymbol{x},(n+1)\delta t)$. Thus, an additional velocity $v^A(\boldsymbol{x},(n+1)\delta t)$ must be added there:

$$v^A(\boldsymbol{x},(n+1)\delta t) = v^H(\boldsymbol{x},(n+1)\delta t) - v(\boldsymbol{x},(n+1)\delta t)$$

for **x** on the boundary, and for both velocity components.

Next, we note that if we had instead added forces $\boldsymbol{F}^A$ to the right hand side of those equations of motion it would have resulted in an additional velocity of $\boldsymbol{F}^A\delta t$. Hence, our added velocities may be equated to an additional applied force:

$$\boldsymbol{F}^A(\boldsymbol{x}) = \frac{\boldsymbol{v}^A(\boldsymbol{x})}{\delta t}.$$

These values for the forces which need to be applied to the boundary are recorded for later use and the values of the velocity components on the boundary are updated to $v^H(\boldsymbol{x},(n+1)\delta t)$ there, ready for the next step. In order to mimic the incident field inside the region both the velocities and the stresses on its boundary must have the values predicted by the hybrid theory. The analysis above demonstrates how to fix the velocity there. It now remains to fix the stress there too. This requires the normal gradients of the velocities to have the correct values there, and this can be achieved by adding suitable values to the velocities at points which are one grid point outside the boundary, and recording the equivalent additional forces to be added there.

For example, on faces with x=constant, updating $\tau_{xx}(\boldsymbol{x},\big(n+\tfrac{1}{2}\big)\delta t)$ and $\tau_{yy}(\boldsymbol{x},\big(n+\tfrac{1}{2}\big)\delta t)$ to achieve $\tau^H_{xx}(\boldsymbol{x},\big(n+\tfrac{3}{2}\big)\delta t)$ and $\tau^H_{yy}(\boldsymbol{x},\big(n+\tfrac{3}{2}\big)\delta t)$ requires an additional velocity $v^A_x(\boldsymbol{x}\pm\boldsymbol{\delta x},(n+1)\delta t)$ to have been applied previously, where the ± is chosen to ensure this location is outside the boundary.

Similarly, updating $\tau_{xy}(\boldsymbol{x},(n+\frac{1}{2})\delta t)$ on this face requires an additional $v_y^A(\boldsymbol{x}\pm\boldsymbol{\delta x},(n+1)\delta t)$ to have been applied. These are found by time-stepping the equations

$$\frac{\partial v_x}{\partial x}=\frac{1}{4(\gamma^{-2}-1)}\left(\gamma^{-2}\frac{\partial \tau_{xx}}{\partial t}-(\gamma^{-2}-2)\ \frac{\partial \tau_{yy}}{\partial t}\right)$$

$$\frac{\partial v_y}{\partial x}=\frac{\partial \tau_{xy}}{\partial t}-\frac{\partial v_x}{\partial y}.$$

Hence,

$$v_x^A(\boldsymbol{x}\mp\boldsymbol{\delta x},(n+1)\delta t)=v_x\ (\boldsymbol{x}\pm\boldsymbol{\delta x},(n+1)\delta t)-v_x\ (\boldsymbol{x}\mp\boldsymbol{\delta x},(n+1)\delta t)$$

$$\mp\frac{\delta x}{2(\gamma^{-2}-1)}\left(\gamma^{-2}\left[\frac{\tau_{xx}^H\left(\boldsymbol{x},(n+\frac{3}{2})\delta t\right)-\tau_{xx}^H\left(\boldsymbol{x},(n+\frac{1}{2})\delta t\right)}{\delta t}\right]\right.$$
$$\left.-(\gamma^{-2}-2)\left[\frac{\tau_{yy}^H\left(\boldsymbol{x},(n+\frac{3}{2})\delta t\right)-\ \tau_{yy}^H(\boldsymbol{x},(n+\frac{1}{2})\delta t)}{\delta t}\right]\right)$$

and

$$v_y^A(\boldsymbol{x}\mp\boldsymbol{\delta x},(n+1)\delta t)=v_y\ (\boldsymbol{x}\pm\boldsymbol{\delta x},(n+1)\delta t)-v_y\ (\boldsymbol{x}\mp\boldsymbol{\delta x},(n+1)\delta t)$$

$$\mp 2\delta x\left(\left[\frac{\tau_{xy}^H\left(\boldsymbol{x},(n+\frac{3}{2})\delta t\right)-\tau_{xy}^H\left(\boldsymbol{x},(n+\frac{1}{2})\delta t\right)}{\delta t}\right]\right.$$
$$\left.-\left[\frac{v_x(\boldsymbol{x}+\boldsymbol{\delta y},(n+1)\delta t)-\ v_x(\boldsymbol{x}-\boldsymbol{\delta y},(n+1)\delta t)}{2\delta y}\right]\right).$$

These added velocities are then equated to additional applied forces, as before, recorded for later use and the values of the velocity components exterior to the x=constant parts of the boundary are updated by adding $v^A(\boldsymbol{x}\mp\boldsymbol{\delta x},(n+1)\delta t)$ there. The grid points exterior to the y=constant parts of the boundary are then considered in a similar way, but making use of the ∂/∂y derivatives. Hence time series are obtained for the force components to be applied to the boundary points and points one grid point outside the boundary to reproduce the velocities and stresses on the boundary and the field inside the boundary of the incident excitation. These forces are then also available to be input into any other numerical model for the scattering region, where they will also reproduce the incident field in the presence of a scatterer and will not result in reflections at the artificial boundary. Thus measuring the values on the boundary from this model and subtracting the known values for incident stresses and velocities there directly gives the scattered field there which is needed for a further application of the method to calculate the scattered field at a distance.

NUMERICAL EXAMPLES

The original hybrid model has previously been shown, [1,2], to be able to predict the time series for the values of stress and velocity of the incident wave on the boundary of region 2. Here we show a numerical example demonstrating the modified forcing part of the method.

Finite Difference Example

To test out the concept a finite difference model for elastic material excited by a point source which generates a pulse consisting of both longitudinal and shear waves is run in the time domain. The time series for values of stress and velocity on the boundary of region 2 are extracted and recorded. These are then used as input to the new part of the method to generate the forces which would need to be applied on and just outside of the region 2 boundary, in order to excite the same incidence wave inside Region 2, if only that small area, surrounded by PML, is used for the calculation.

An animation showing the pulse propagating across Region 2, both from the whole area calculation and the small area calculation using the applied forces calculated as described above will be presented. A still, taken from that animation while the pulse is crossing Region 2 is included here as figure 4. The plot shows the velocity in the x-direction. At the time shown there have already been 332 time steps. There is excellent agreement between the methods at each of the time steps as the pulse crosses the region. Plots of other variables are as expected and also exhibit good agreement.

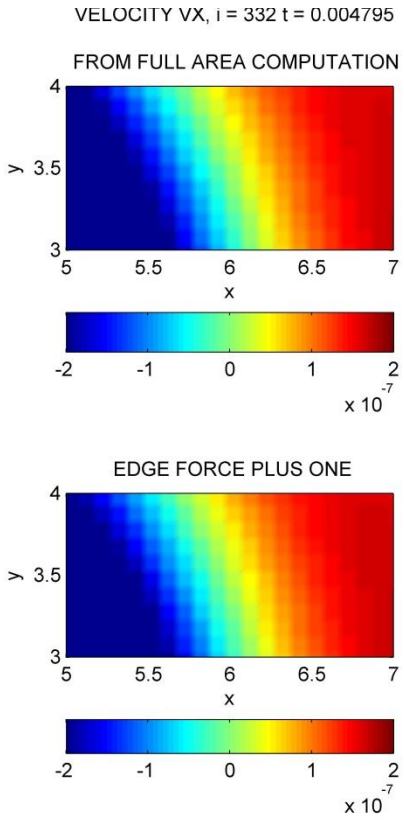

Figure 4 Finite Difference Comparison of Whole Region Calculation and Forcing Region 2 with Applied Forces from Hybrid Calculation

Finite Element Example

As the analysis and coding to generate the values of the applied forces has been implemented using finite difference methods, a more demanding test of the concept is to use a different calculation method in both the whole area calculation and the two small area calculations and to link them, as intended, using a 'black-box' hybrid method to generate the forces to be applied. Thus, we again set up a source box (Region 1) and a defect box (Region 2). The system is excited by a plane wave pulse from the source box. With no defect present in the Region 2 box, comparing the values for the incident wave on the boundaries of the defect box shows good agreement between the whole area calculation and the hybrid calculation with applied forcing on the region 2 boundary, as shown in Figure 5. In addition, the method has been applied when the defect box *does* contain a defect – in this case a side-drilled hole. Figure 6 shows a comparison of the values on the bottom edge and the left hand edge of Region 2 for this case, as a function of node-number along the edge (y-axis) and time (x-axis) for both the full FE calculation and using the hybrid method with applied forcing at the edges of the defect box. Again there is good agreement between the full, whole area, FE calculation and the hybrid result.

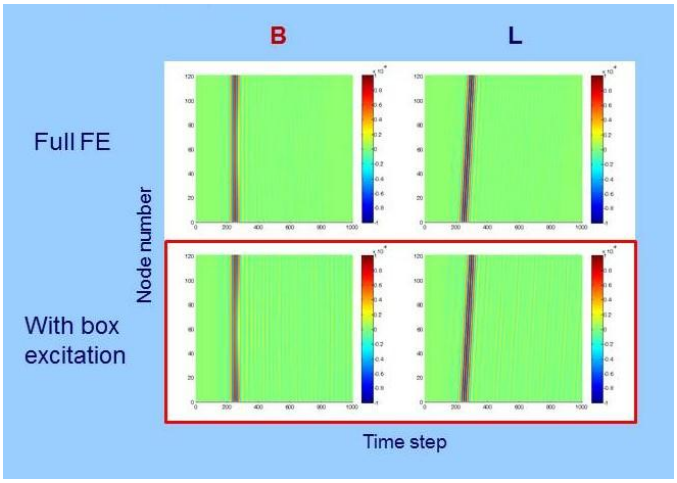

Figure 5 Finite Element Comparison of Incident wave from full FE calculation and Hybrid Method with Applied Forces

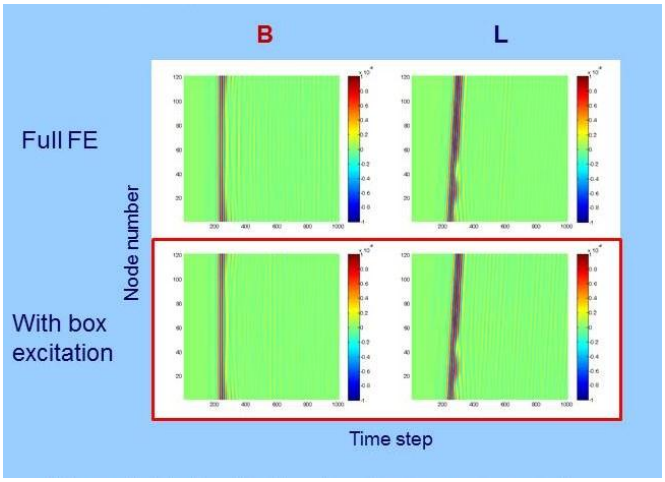

Figure 6 With Defect: Finite Element Comparison of Incident wave from full FE calculation and Hybrid Method with Applied Forces

The hybrid method has correctly reproduced the incident field, and this applied force modification also allows the field scattered by the defect to pass through the numerical boundary without introducing unwanted numerical scattering there.

CONCLUDING REMARKS

It has been demonstrated that the concept of linking two smaller calculation domains by this hybrid model to calculate the forces which need to be applied to the second domain in order to reproduce the incident wave there is feasible. This method of forcing the second region allows the field scattered by the defect to pass through the computational boundary without introducing numerical scattering there. Hence, this forcing technique permits the size of the second domain to be reduced compared to the version of the hybrid model with line forcing in front of region 2. As the values of the incident field on the domain boundary are available from the hybrid method it is straightforward to extract the scattered field there from the total field obtained from the numerical calculation in Region 2. This is then directly available for a further application of the hybrid method to obtain the scattered field elsewhere, at a distant receiver, for example, or for scattering at a different defect.

The model has also been extended to three-dimensions, in which case there are more variables to include, and more corners and edges which need special treatment. Further development of both the 2D and 3D versions of the codes is on-going.

ACKNOWLEDGEMENT

This work was carried out at Imperial College, London, with support from Simposium Project, a project co-funded by the European Commission under the 7th Framework Programme for Research and Technology Development.

REFERENCES

1) Rajagopal P, Skelton E A, Choi W, Lowe M J S, Craster R V, "A Generic Hybrid Model for Bulk Elastodynamics, With Application to Ultrasonic Nondestructive Evaluation", IEEE Transactions on Ultrasonics, Ferroelectrics and Frequency Control, 2012 59 1239-1252.
2) Rajagopal P, Skelton E, Lowe M, Craster R, Russell J, "Generic Time-Domain Hybrid Models for Ultrasonic NDE", Review of Progress in Quantitative Non-Destructive Evaluation, 18–23 July 2010: Volume 30A; Volume 30B , AIP Conf. Proc. 1335, pages 67-74;
3) Rajagopal P, Drozdz M, Skelton E, Lowe M J S, Craster R V, "On the Use of Absorbing Layers to Simulate the Propagation of Elastic Waves in Unbounded Media Using Commercially Available Finite Element Packages", NDT&E International, 2012 51 30-40.

THE RECONSTRUCTION OF THREE-DIMENSIONAL ROUGH SURFACES FOR ULTRASONIC NDE MODELLING

W. Choi, E. Skelton, M.J.S. Lowe1, R. Craster
Imperial College, UK

ABSTRACT

For ultrasonic NDE modeling, it is useful to be able to generate realistic rough surfaces in order to model the scattering from them. Previously, rough surfaces have been simulated, usually in two dimensions, by a line profile on a cross-section of the surfaces whose heights follow an ideal probability distribution. Three-dimensional rough surfaces can be reconstructed by random fields, but they are generally more difficult to generate because of the multiple directionality on the surface and expensive computational cost due to the additional dimension. However, rough surface generation, rather than line profile generation, is becoming more accessible due to recent investigations in random field theory and rapid increase in computation speed over the last decade. In this paper, rough surfaces are generated, simulating real surfaces. Firstly, the basic theory of surface generation is introduced. Then, rough surfaces are reconstructed based on the statistics of real surface samples. Rough cracks can also be generated and introduced in a finite element domain, and an example of scattering from a crack is simulated using a generic hybrid method for an ultrasonic inspection.

1. INTRODUCTION

In the power plant industries, ultrasonic inspection is one of the most widely used methods for Non Destructive Evaluation (NDE). Transducers emit waves into structures inspected and receive the waves reflected from cracks. When the reflected amplitude is larger than a certain threshold, it is regarded as signifying the existence of a reflector. Therefore, the amplitude of the reflected signal is an important factor to find cracks in power plant components. Since the amplitude depends on crack geometry, its roughness plays a significant role in crack detectability in the inspection.

The reflecting energy is mainly concentrated on the reflections at the specular angle, when the crack is smooth relative to the wavelength of the incident wave. Estimation of the amplitude based on the crack dimension has been investigated for many years and the level of confidence for the prediction has been increased based on real experimental results with known defects as well as on results from modeling methods such as Kirchhoff theory [1] or Geometrical Theory of Diffraction (GTD) [2]. However, crack morphology is not always smooth in real inspection. Then the reflection energy concentrated at the specular angle with a smooth crack can deviate to different angles with rough cracks, which decreases the amplitude at the specular angle and consequently increases it at the other angles. Because of these effects, it is common to add an additional attenuation factor to the threshold for rough cracks. The factor is normally set to be conservative and thus detectability decreases for rough cracks relative to smooth ones. Therefore, it is important to quantify the relation between crack roughness and the reflection from the crack for more accurate crack detection.

Roughness of cracks can be characterized in statistical manners using the random process theory in two-dimensional (2D) space and the random field theory in 3D, in which surface heights are treated as a random function on one and two dimensional axes, respectively. Using those theories, estimating real rough surfaces has been investigated in many engineering fields, for example, for simulating reflections from rough surfaces in underwater acoustics [3] and NDE as well as wear mechanisms between rough surfaces in contact mechanic [4].

The estimation process can be explained by linear filter theory, in which a rough surface is an output of filtered data with a random input noise. Then, the filter design becomes an important factor in the estimation. Moving-Average (MA) and Auto-Regression (AR) are the fundamental methods [5] which will be briefly covered in this paper. In NDE, the MA method has been widely used mainly because of its direct applicability using the Fast-Fourier Trasform (FFT).

If a surface is known to be one realization of a group (or an ensemble) of surfaces sharing similar characteristics, then the ensemble statistics represent the ensemble which includes the specific surface itself. In order to estimate the ensemble characteristics, real surfaces are required to be collected for statistically meaningful results. However, in many cases, ergodicity [6] is assumed in analyzing random data, which means that characteristics of a surface represent those of the ensemble if data collected from the surface is sufficient, and sometimes this is the only way to obtain the ensemble properties because of practical limits in time, labour and technology to collect a lot of surface data, even though the capability of collecting surface date has been enormously developed in the past decades. We will also assume the ergodicity in this paper and thus refer one real surface to estimate the ensemble characteristics.

Reflection from rough surfaces can then be investigated using the surface estimates. The perturbation theory and the Kirchhoff theory are the most widely used models [1] for simulating the reflection. However, their usability is limited to cases with moderately rough cracks. Alternatively, the Finite Element (FE) method is known to be suitable to generate very rough cracks. However, the roughness of a crack introduces practical difficulties in modeling the geometry in the FE method. As the roughness of the crack increases, a smaller size of elements is required to model the geometry properly. This difficulty becomes more serious in three dimensional models, since the number of elements is inversely proportional to the cube of the mesh size compared with the square in 2D. We will use a hybrid method [10] in order to overcome the difficulties in the FE simulation.

In this paper, a brief background of the underlying methods, the MA and AR methods, is introduced first. Surfaces are reconstructed using the methods, based on a real rough surface sample, and then the results are investigated. A generic hybrid model is used for efficient FE modeling with a rough crack, for which introducing a rough crack into an FE domain is described. The FE simulation results will be discussed and then conclusion will be presented.

2. BACKGROUND

Rough surfaces have been described using the random process theory in 2D, in which surface height is a random function on a spatial axis. The extension of the theory in 3D space is called the random field theory for a random function on a plane surface. In this section, brief background of basic surface generation methods will be introduced in a 2D discrete domain based on the random process theory for simplicity, although the surface reconstruction will be conducted in 3D in the later sections.

Rough surfaces for NDE modelling have often been generated using two parameters, Root Mean Square (RMS) value of surface heights *h*, often called roughness, and correlation length λ_0 where correlation function *C* falls into 1/*e*,

$$\sigma_h = \sqrt{\langle h^2 \rangle} \tag{1}$$

$$C(\tau) = \langle h(x)h(x-\tau) \rangle / \sigma_h^2 \tag{2}$$

where $\langle\rangle$ means 'spatial average of' and τ is a spatial distance. The length is known to represent a distance within which heights are statistically related. Two widely-used correlation function, Gaussian and exponential, are shown in Fig. 1.

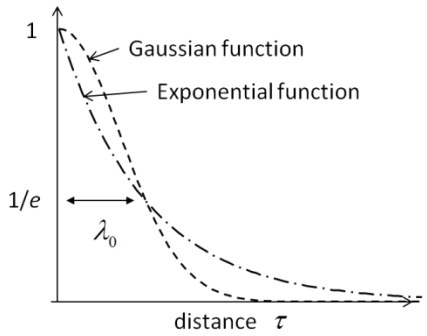

FIGURE 1. Gaussian and exponential correlation coefficient functions with the correlation length λ_0 .

Moving-Average (MA) and Auto-Regressive (AR) methods are the two fundamental estimation methods, which can be explained from the following linear system equation for height *h*,

$$\sum_{\tau} \alpha(\tau) e(x-\tau) = \sum_{\tau} \beta(\tau) h(x-\tau) \tag{3}$$

where *e* is random noise, and α and β are the weighting factors. The MA method has been widely used for generating random surfaces in the NDE community since a random surface can be readily generated via convolution and on the other hand the AR method can apply a linear relation between neighbouring heights to a rough surface.

The MA equation can be obtained by Eq. (3) with $\beta = 1$ at $\tau = 0$ and $\beta = 0$ otherwise,

$$h(x) = \sum_{\tau} \alpha(\tau) e(x-\tau) . \tag{4}$$

Substituting the equation into Eq (2), the correlation coefficient function becomes

$$C(\tau) = \sum_{m} \alpha(\tau)\alpha(\tau - m) . \tag{5}$$

Thus the weighting factors can be found by Eq. (5) if the correlation coefficient *C* is known. Gaussian and exponential surfaces can be readily generated based on the MA method via convolution as in [7] since we know the correlation functions as shown in Fig. 1.

The AR method can be expressed by Eq. (3) when $\alpha = 1$ at $\tau = 0$ and $\alpha = 0$ otherwise,

$$h(x) = \sum_{\tau} \beta(\tau) h(x-\tau) + e(x) . \tag{6}$$

In this equation, it is shown that the neighbouring heights *h* are linearly related. The relation between the weighting factors and the correlation coefficient can be obtained by multiplying $h(x-p)$ and then spatial averaging both sides of Eq. (6),

$$C(p) = \sum_{\tau} \beta(\tau) C(p-\tau) \qquad \text{when } p > 0. \tag{7}$$

It is relatively difficult to estimate the weighting factors from the correlation coefficient, particularly in 3D. However, it contains a linear relation of heights as can be seen in Eq. (6), which can be explained by height gradient, and may be an important factor in UT inspection as is stated for the Kirchhoff approximation [1].

In this paper, selected regions of a rough surface which has been measured by our industrial partner AMEC will be used as a reference for the reconstruction and compared with realizations with one AR surface and three MA surfaces with spectral, Gaussian and exponential methods. For generating random fields in 3D, the MA and the AR methods have been investigated extensively for image processing and there are many ways to generate the fields. We will follow methods in [8] for the AR method, [9] for spectral method and [7] for Gaussian and exponential methods.

3. SURFACE RECONSTRUCTION

3.1 Reference surface

For rough surface reconstruction, a real surface was provided by our industrial partner AMEC. A compact tension specimen of A533B ferritic steel was selected for the surface generation, which is a common material in power plant components. Fig. 2a shows the specimen. The 45 mm × 75mm surface consists of three regions: fatigue, ductile tearing and brittle fracture regions. The rough surface heights were measured using an optical microscope; a map of these heights is plotted in Fig. 2b. The three regions have different statistical properties, and for example RMS heights are 68, 344 and 204 μm for the three regions respectively. The roughest section, the ductile region, is selected to be a reference surface for surface reconstruction in the next section.

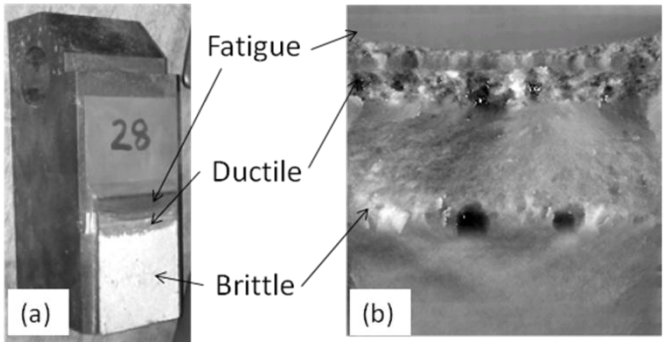

FIGURE 2.Real surface sample provided by AMEC. (a) the specimen and (b) heights on the rough surface

3.2 Surface reconstruction

Rough surfaces are generated using the four estimation methods: AR method, spectral method, Gaussian and exponential correlation. A 10 mm × 10 mm section of the real surface was selected as a reference in the ductile region, shown in Fig. 3a, on which there are approximately 40,000 height points with 50 μm interval in the *x* and *y* directions. The four reconstructed surfaces are shown in Fig. 3b-e. Note that all the five surfaces shown in Fig. 3 have an identical RMS height, 229 μm, and their correlation lengths are similar within maximum 15% of that of the reference surface as shown in Table 1.

Compared to the reference in Fig. 3a, the Gaussian surface in Fig. 3d shows visually smoother texture whereas the exponential surface in Fig. 3e shows a sharper image. The difference can be explained by the correlation coefficient function in Fig. 1. In the MA method, the sharpness of the surface texture depends directly on the shape of the tip of the function at zero. In the two surfaces, correlation lengths only in the *x* and the *y* directions are defined and the lengths of the other directions are calculated in ellipsoidal manner so they are in between the two correlation lengths. Thus the Gaussian and exponential surfaces are limited to describe characteristics in the other direction in 3D if they exist. Surfaces with the AR and the spectral methods shown in Fig. 3b and 3c look much closer to the reference than the other two.

The Probability Density Functions (PDF) of heights and gradients are shown in Fig. 4 for the reference and the reconstructed surfaces. For the PDF heights, all the height points on a surface are taken for the density function, and for the PDF gradients height the difference between the closest neighbouring heights are calculated and divided by the spatial step, 50 μm, in the *x* and *y* directions. The PDF heights of the realizations are very similar to the reference as shown in Fig. 4a, since their RMS value are identical, but the PDF gradients are all different. The Gaussian surface is the only one that shows larger probability at zero, while the others are all smaller. Intuitively, more near-zero gradients mean a smoother surface, which can be confirmed by the visual texture of the Gaussian surface in Fig. 3d comparing with the reference surface in Fig. 3a. The PDF gradients in Fig. 4b and 4c show that the AR surfaces are the closest to the real surface at zero, among the ones smaller than the real one.

For statistics with a lot of realizations, 100 surfaces in each method are generated and the PDFs are calculated as shown in Fig. 5. The PDFs are smoothed to have Gaussian distribution following the central limit theorem due to the increase in data size. Another significant difference compared to Fig. 5 is that the PDF gradients of the AR surfaces are much closer to the PDF of the reference. Except for this, in general, the trends of the PDFs are similar to the ones shown in

Table1. Correlation length in the x and the y directions (*mm*)

Correlation lengths	Real	AR	Spec.	Gauss.	Exp.
x direction	0.80	0.90	0.75	0.70	0.80
y direction	1.00	0.95	0.90	0.95	0.95

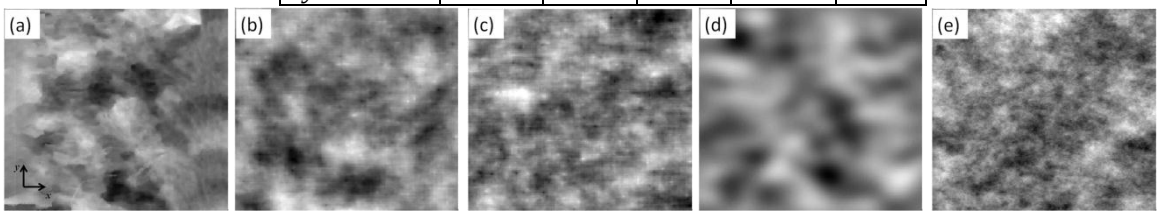

FIGURE 3. Surfaces for comparison. (a) the reference, and the reconstructed surfaces with (b) AR method, (c) Spectral method, (d) Gaussian and (e) exponential coefficients.

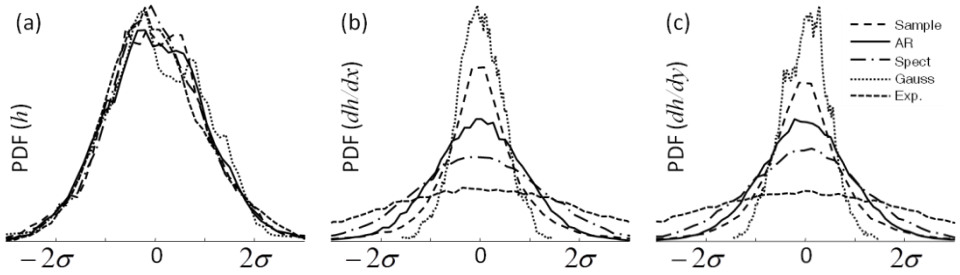

FIGURE 4. Local statistics of the surfaces. PDF of (a) the height and the gradients (b) in the *x* direction and (c) in the *y* direction, from a reference surface and one realization using the four methods.

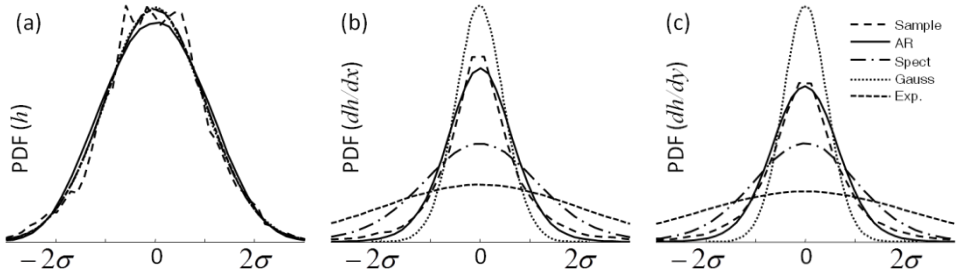

FIGURE 5. Local statistics of the surfaces. PDF of (a) the height and the gradients (b) in the *x* direction and (c) in the *y* direction, from a reference surface and 100 realization using the four methods.

Fig. 4. Thus different reconstruction methods result in different surface characteristics in the local statistics, which can have effect on the UT reflection from the surfaces. The relation between the characteristics and the reflection can be investigated by FE simulation as in the following section.

4. A FE SIMULATION USING A HYBRID METHOD

4.1 Background

Statistics of waves reflected from random surface cracks can be investigated by collecting a set of reflections from many different crack samples that have common statistical characteristics. In order to simulate reflection from a crack, the FE method has been frequently used when the crack geometry is irregular. However, introducing roughness into the FE model requires fine meshes, which increases computational time and memory requirements particularly with long wave propagation distance. Thus it can be difficult to simulate 3D FE model in such cases, and thus most of the statistical works have been conducted in 2D space. For efficient modeling, a hybrid method has been introduced for ultrasonic NDE by Imperial College [10] and expended to 3D application [11]. We introduce the hybrid method as a means for executing a lot of simulations to gather the statistics.

In the hybrid method, the UT inspection process is divided into several steps with smaller domains and a hybrid interface connects the domains as shown in Fig. 6. In the interface, Green's functions link the physically separated domains in the frequency domain. For a practical simulation in the time domain, the Fast Fourier Transform (FFT) and inverse FFT (IFFT) are used in order to transform the time-signal format.

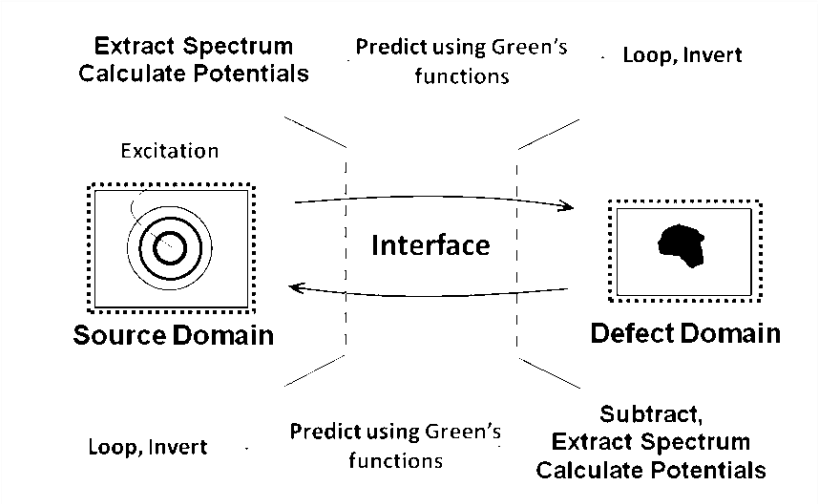

FIGURE 6. A schematic diagram for the hybrid method

4.2 FE Simulation

An example case for the reflection from a rough crack is shown in Fig. 7. A 3 mm × 3 mm rectangular crack is located 20 mm from a transducer in a steel medium (Young's modulus:200 Gpa, Poisson ratio: 0.3 and density 8000 kg/m3). We are simulating this pulse-echo model using the hybrid method. A rough crack is reconstructed using the AR method as in Section 3 and introduced to a FE model within the hybrid method. In this model, a plane P wave is insonified on the crack assuming far-field incidence, which is generated by exciting nodes on a surface with constant force as shown in Fig. 7. Thus, only the defect FE domain (no source FE domain) is created for modelling wave reflection against a defect. The wave reflected is monitored on a Defect Monitoring Box (DMB) surrounding the crack, which is fed into the hybrid interface, and the displacement at a source location is estimated by the interface.

In order to complete the hybrid process, it is needed to create the defect domain with finite elements. In this example, our aim is to use ABAQUS explicit [12] to run a simulation for the hybrid method. Heights of a rough crack are first generated on a 0.05 mm grid, using the AR method based on a real surface. The height points are connected to be a set of triangular facets. An identical surface was generated but located one element size below the original and the two surfaces are connected to be a solid feature as in Fig. 8a, which was done in MATLAB [13]. In ABAQUS, it is imported into a hexagonal domain of 4 × 4 × 2 mm^3 size as shown in Fig. 8b, and subtracted from the domain so that the crack has zero stress boundary condition. The steel domain with a crack is meshed nominally in 0.05 mm size, approximately 1/30 input wavelength, and tetrahedral linear elements (C3D4) were used for the free mesh. In order to simulate an infinite exterior boundary condition, an additional FE region is required outside the main domain. To ensure the additional domain has not too dense or too course mesh density, we generate regular tetrahedral elements and attach them to the main domain as in Fig. 8c.

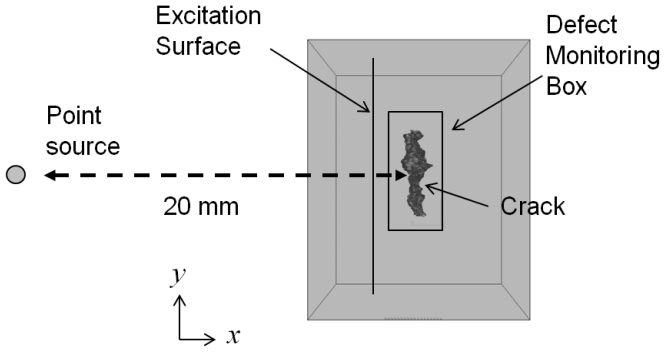

FIGURE 7. An example of hybrid method.

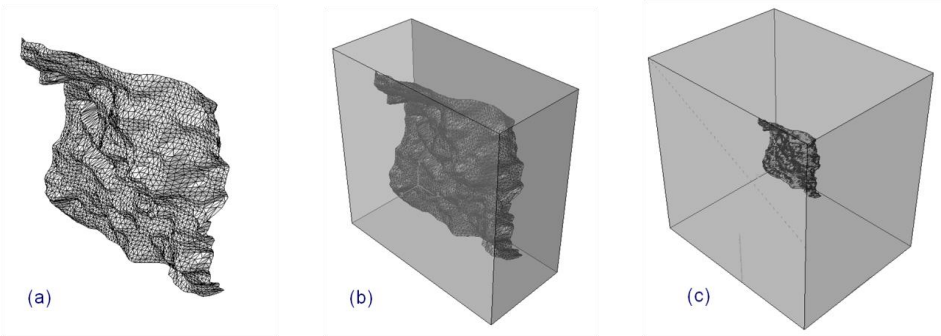

FIGURE 8. Defect FE domain in a generating sequence: (a) A crack shape, (b) a main domain, and (c) a defect FE domain including the main domain and the absorbing region.

A Stiffness Reduction Method (SRM), newly-developed by Imperial College [14], is used for the absorbing region, in which stiffness decreases and damping increases with distance from the boundary, resulting in an efficient absorbing capability.

The time signal detected on the DMB in Fig. 7 includes reflected as well as incident waves. Since the DMB is close to the crack, it is difficult to separate the two wave fields in time. Thus a FE model without a crack was run to monitor the incident wave only, and it is subtracted from the signal to obtain the reflected wave only. Fig. 9 shows the reflected wave extracted along a line on the DMB. Due to the roughness of the crack surface, it shows an irregular pattern across the line. Then the reflected wave on the point source location is estimated by the hybrid interface, and Fig. 10 shows the displacements in the *x*, *y* and *z* directions. Since the incidence is P wave, the *x* direction displacement has maximum amplitude as shown in Fig. 10a, but the amplitudes in the other directions are also noticeable since the rough crack scatters the incident wave in all directions while a smooth crack reflects it in a specular direction. How the scattering pattern depends on the crack roughness is an interesting question and the statistical analysis is planned with a lot of simulation using the hybrid method.

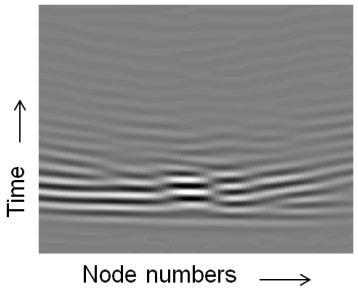

FIGURE 9. Bscan-type signal for wave reflection extracted along a middle line on the DMB.

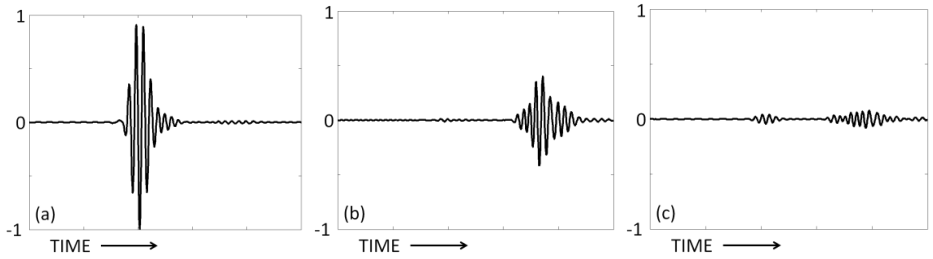

FIGURE 10. Displacements estimated from the hybrid interface, at a transducer location shown in Fig. 7, in the (a) *x*, (b) *y* and (c) *z* directions, normalised by the maximum amplitude of the *x* direction displacement.

5. CONCLUSIONS

Reconstruction methods for realistic rough cracks were investigated based on the random field theory. MA and AR methods were briefly reviewed and, based on a real rough surface, surface realizations were reconstructed with one AR method and three MA methods: spectral, Gaussian and exponential surfaces. Comparing the surfaces with identical RMS height and similar correlation lengths, the limitations of Gaussian and exponential surfaces were discussed. Statistics of the surfaces were investigated in terms of the PDFs of the heights and the gradients, and the AR method was shown to best simulate the real surface according to the local property statistics. A generic hybrid method is beneficial in simulating reflections from rough cracks, which can alleviate the computational burden. A 3D rough crack was reconstructed based on a real surface and it was explained how to introduce the crack in an FE domain. The wave reflection was monitored near the crack and estimated on the transducer location, showing a random pattern due to the roughness of the crack. A statistical study using the hybrid method with reconstructed cracks is under investigation.

ACKNOWLEDGEMENT
This project is supported by the SIMPOSIUM project, a project co-funded by the European Commission under the 7th Framework Programme for Research and Technology Development.

REFERENCES

1. J. A. Ogilvy, The Theory of Wave Scattering from Random Rough Surface, Adam Hilger, 1991.
2. J. B. Keller, "Geometrical theory of diffraction", J. Opt. Soc. Am, 52(2), 116-130, (1962).
3. J. L. Uretsky, "Relfection of a plane sound wave from a sinusoidal surface", J. Acoust. Soc. Am. 35(8), 1293-1294 (1963).
4. W. P. Dong, P. J. Sullivan and K. J. Stout, "Comprehensive study of parameters for characterizing three-dimensional surface topography I: Some Inherent Properties of Parameter Variation", Wear, 159, 161-171, (1992).
5. S. M. Kay, Modern Spectral Estimation: Theory & Application, Prentice-Hall, 1988.
6. J. S. Bendat and A. G. Piersol, Random Data: Analysis and Measurement Procedures, 3rd ed., Wiley, 2000.
7. J. A. Ogilvy and J. R. Foster, "Rough Surfaces: Gaussian or Experimental statistics?", J. Phys. D:Appl. Phys., 22, 1243-1251, (1989).
8. J. A. Velázquez-Muriel, C. O. S. Sorzano, J. J. Fernández, J. M. Carazo, " A Method for estimating the CTF in electron microscopy based on ARMA models and parameter adjustment", Ultramicroscopy, 96 (1), 17-35 (2003).
9. E. I. Thorsos, "The validity of Kirchhoff approximation for rough surfaces scattering using a Gaussian roughness spectrum", J. Acoust. Soc. Am, 83(1) 78-92 (1998).
10. P. Rajagopal, E. A. Skelton, W. Choi, M. J. S. Lowe and R. V. Craster, "A generic hybrid model for bulk elastodynamics, with application to ultrasonic nondestructive evaluation", IEEE Trans. Ultrason. Ferroelectr. Freq. Contrl. 59(6), 1239-1252, (2012).
11. W. Choi, E. Skelton, M. J. S. Lowe, R. Craster and P. Rajagopal, "Generic hybrid models for three-dimensional ultrasonic NDE", in Review of Progress in Quantitative Nondestructive Evaluation 31, edited by D.O. Thompson and D.E.Chimenti, AIP Conference Proceedings vol. 1430, American Institute of Physics, Melville, NY, pp. 126-133, (2013).
12. SIMULIA, ABAQUS v 6.12, http://www.simulia.com,
13. MATLAB R2010b, The MathWorks Inc., united Kingdom, 2012.
14. J. R. Pettit, A. Walker, P. Cawley, M. J. S. Lowe, "A stiffness reduction method for efficient absorption of waves at boundaries for use in commercial Finite Element codes", Ultrasonics, submitted.

OVERVIEW OF THE RECENT DEVELOPMENTS ON GRAIN-SCALE MODELING TO SIMULATE ULTRASONIC SCATTERING WITH A 2D FINITE ELEMENT CODE

P. E. Lhuillier, C. Trottier, S. Shahjahan, F. Rupin, B. Chassignole, T. Fouquet, EDF - R&D, France
I. Zeriouh EDF - CEIDRE, France

Abstract

Numerous studies were undertaken by EDF R&D for a few years to improve the NDT process on these applications and to help to their qualification. In many cases, the inspected components may exhibit a coarse grain microstructure which induces severe beam disturbances and reduces the reliability of the control. Moreover, modeling is more and more used to evaluate the beam to structure or to defect interaction and to perform parametric studies. However, the modeling of the scattering phenomena - attenuation and structural noise – must be based on accurate input data for the material description.

The methodology proposed by EDF R&D to simulate the inspection of coarse grain structures is to combine the finite element code ATHENA 2D with a grain scale description of the materials. The method reproduces the beam perturbations, the attenuation and the appearance of structural noise due to scattering of the wave at grain boundaries. It enables to compute macroscopic attenuation coefficient. In the case of anisotropic structure like austenitic welds, the anisotropic evolution of the attenuation in the inspection plane can be simulated.

The performances and the limits of the grain-scale modeling approach are illustrated on several configurations. Firstly the influence of the microstructure model on the accuracy of simulation results have been investigated on isotropic coarse grain INCONEL 600 components. Two specific illustrations are presented and compared to experimental results, which are the modeling of a multi-layer isotropic structure (centrifugally cast stainless steel) and a complex anisotropic structure (austenitic weld).

Introduction

For several years, EDF has extensively used numerical models to improve the design, qualification and implementation of NDT processes. Several studies and experimental validations have already been carried out with the ATHENA code to simulate ultrasonic inspections in simple and complex cases. In particular, the ability of the code to accurately reproduce complex phenomena occurring during the propagation in heterogeneous media like welds (beam deviation, division or attenuation…) has already been the subject of several publications [1-4]. In these studies, the heterogeneous medium is described as a set of homogeneous anisotropic domains characterized by their elastic and attenuation properties.

In addition to the development of the finite elements (FE) code ATHENA, EDF has recently carried out studies on the grain-scale modeling of the ultrasonic scattering in coarse grain structure. The method relies on the coupling of the FE simulation and a modeling of the microstructure at the description level of the grain.

The objective of this paper is to give an overview of the recent developments achieved by EDF R&D in the field of the grain-scale simulation of ultrasonic inspections with the 2D version of the ATHENA code.

Firstly, a brief description of the features implemented in ATHENA 2D is given. Then the models used to describe the microstructure of polycrystalline materials are detailes. Eventually, the results of grain scale modeling are presented. It gives an evaluation of the main parameters of the microstructure models impacting the reliability and the performances of the simulations.

1. Numerical modeling

The main features of the 2D version of the ATHENA code are presented here, more details can be found in [5].
ATHENA2D is a finite element code for elastodynamic developed by EDF R&D. The code solves the equation of elastodynamic expressed in a mixed formulation combining stress and velocity terms. The code is dedicated to the simulation of wave propagation in all kinds of elastic media and in particular, heterogeneous and anisotropic materials. One important feature of the code is the use of the fictitious domain method [6]. It relies on the combined use of a regular discretization of the calculation zone with a non-regular meshing of the defects. It allows taking advantage of the rapidity of regular mesh calculation with the possibility to model arbitrary shaped defects. Furthermore, ATHENA 2D gives the possibility to use Perfectly Matched Layers (PML) to define the boundaries of the calculation domain [7]. The use of PML removes spurious reflections on artificial edges of the calculation zone and thus enables to model virtually infinite components. Finally, ATHENA 2D integrates the possibility to simulate various inspection configurations (pulse-echo, tandem, TOFD) with a wide range of transducers (single element and phased array), inspection mode (contact or immersion), materials and defects. The code has been widely used by EDF to simulate the inspection of complex structures such as austenitic welds [3, 8, 9].

2. Polycrystalline material modeling

The aim of the grain-scale modeling is to combine the accuracy of the FE simulation of the ultrasonic propagation in heterogeneous and anisotropic media with a fine description of the microstructure of polycrystalline materials. The approach enables to simultaneously simulate the structural noise and attenuation due to ultrasonic scattering in coarse grain structures.

2.1. Microstructure modeling

In 2D grain scale modeling, the inspected component is modeled by a 2D tessellation of the plane which mimics the morphology of polycrystalline microstructure. In this paper the polycrystalline microstructure was modeled by several variety of plane tessellation based on Voronoi diagrams.

Voronoi tessellations are a mathematical tool which enables to subdivide the plane with convex cells. Each variety of Voronoi diagram relies on a basic construction procedure. A set of points, called seeds, is withdrawn on the portion of plane to be subdivided. The plane is subdivided in cells which contains the points closer from a given seed than any other. The way to withdrawn the seed in the first step and the metric used to compute the distances in the second step define the variety of Voronoi tessellations. Three kinds of Voronoi tessellations have been used to model the polycrystalline microstructure: the Poisson-Voronoi, Laguerre-Voronoi and heterogeneous Voronoi diagram.

a) The Poisson-Voronoi diagrams use an uniform distribution of seed and the Euclidian metric [10] (Figure 1.a).
b) The Laguerre-Voronoi diagrams also use a uniform distribution of seeds but the distance to the seeds is computed via the Laguerre distance [11] (Figure 1.b).
c) The variety of tessellation called heterogeneous diagrams in this study is generated by a recursive procedure based on Poisson-Voronoi diagram. A macroscopic Poisson-Voronoi tessellation with an average cell size greater than the final expected grain is constructed. A set of seeds is withdrawn on each cell of the macro-diagram with a local uniform distribution and a given density which varies from one macro-cell to another. The set of all the seeds belonging to the macro-cells is used to compute the final tessellation (Figure 1.c).

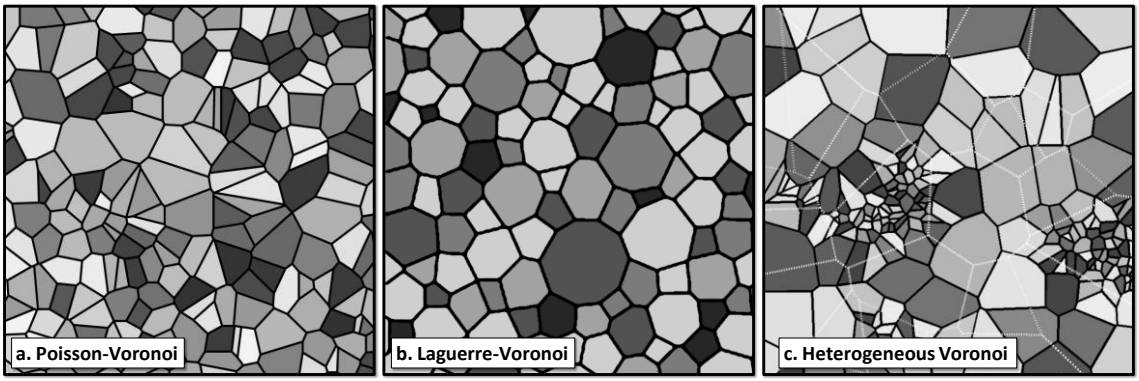

Figure 1 : Models of 2D microstructure: a) Poisson-Voronoi, b) Laguerre-Voronoi, c) Heterogeneous Voronoi diagrams.

The Poisson-Voronoi model has been used because of its ease of implementation whereas the Laguerre-Voronoi and heterogeneous Voronoi models have been chosen in order to control the shape of the grain size distribution. In terms of basic morphology, Poisson-Voronoi diagrams model grains exhibiting a sharp grain size distribution. On the contrary, the heterogeneous Voronoi diagrams provide highly inhomogeneous grain size repartition with local concentration of small and large grains.

2.2. Material properties

Once the inspection plane is partitioned into cells representing the grains, each domain is assigned with a random orientation – defined by three Euler angles - accounting for its crystallographic orientation. The elastic properties of each grain are derived from the single crystal's stiffness tensor and the three Euler angles. To accurately reproduce equiaxed materials, the 3 Euler angles are drawn following a random statistical law chosen to ensure the creation of a macroscopically isotropic medium. One set of random grain orientations plus one tessellation of the computation area give in one ‘‘realization’’ of the random microstructure.

3. Results and discussion

Thereafter, the recent results obtained by EDF R&D in the field of the grain-scale modeling are presented.

3.1. Influential parameters in grain-scale modeling

The aim of this section was to investigate the impact of the main parameters characterizing the description of the microstructure on the simulation performances. In particular, the objective was to evaluate the influence of the grain size distribution on the simulations.

We focused on the inspection of a homogeneous and isotropic block. The configuration implemented in both experimental set-up and simulations is shown in Figure 2. The mock-up is made of INCONEL 600 alloy which was thermally treated and exhibits a mean grain size of ~750 µm. The mock-up was inspected with a single element probe at 2.25 MHz generating longitudinal waves at 45°. The elastic coefficients of the INCONEL 600 single crystal are given in Table 1. In this study, we analyze the beam-to-defect interaction for a side-drilled hole (SDH) located at a 30 mm depth.

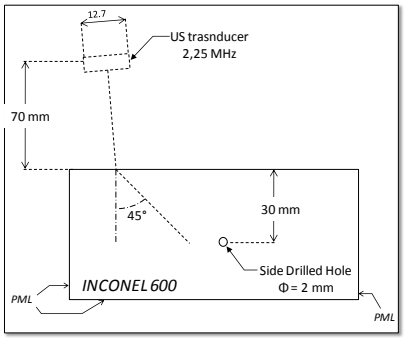

Figure 2: Inspection configuration of the study of the impact of microstructure description on the simulation performances.

INCONEL 600			
Mean grain size (µm)	Elastic coefficients (GPa)		
	C_{11}	C_{12}	C_{44}
750	235	145	126

Table 1: Elastic coefficients of INCONEL 600 single crystal.

The three different Voronoi models detailed in section 2.1 were chosen to study the impact of the grain size distribution on the simulation results. Figure 3 shows the grain size distributions obtained with the three models. The distributions have been computed so that they exhibit the same average grain size, ~750 µm. They are compared to the experimental grain size distribution obtained after micrographic observations on the mock-up.
One can see that the Poisson-Voronoi model exhibits a sharp grain size distribution. The "heterogeneous Voronoi" and Laguerre-Voronoi enable to compute simulated microstructure with grain size distributions which are much more similar to the measured grain size distribution. In particular, the models allow reproducing the high amount of small grains and also allow to account for the tail of the experimental distribution corresponding to the large grain sizes. Nevertheless the implementation of the Laguerre-Voronoi and heterogeneous Voronoi algorithms is much more complex and time consuming. As a consequence, the question of the level of refinement of the microstructure model required as regard to the expected simulation accuracy is an important issue.

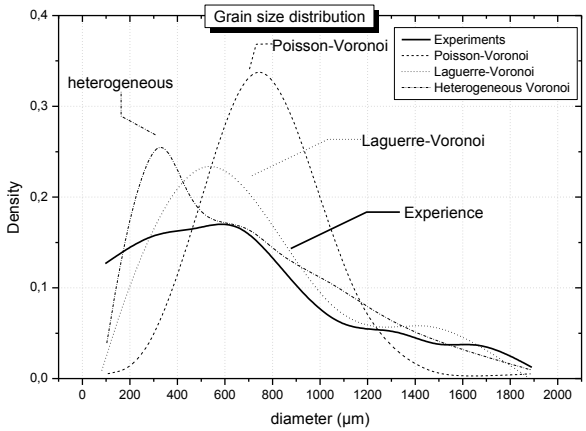

Figure 3: Grain size distribution obtained from metallographic experimental observations and from simulated microstructures.

As a preliminary study the Poisson-Voronoi model has been used to investigate the stability and convergence of the simulated results. It has thus been shown that about 10 simulations are required to constraints the average SDH echo amplitude within a confidence interval of 5%. Moreover 30 simulations are hardly enough to constraint the average value in a 1% confidence interval. Nevertheless the estimation of the required number of simulations is only valid for the considered configuration and need to be evaluated for each study.

As a consequence in the following study, the amplitude of the SDH located at 30 mm was simulated with 30 realizations of each microstructure model. In order to compare the simulated and experimental data, the echo of a SDH located at 10 mm in depth in a homogeneous block was used as reference for amplitude and time scales. bThe results are shown in Figure 4.b. One can see that the mean value of the three models are very close from each other. It thus shows that the differences in the grain size distribution due to the microstructure description seem to induce a very shallow impact of the simulated results. In addition, the differences between the mean simulated amplitudes of the 3 models and the experimental data are lower than 3 dB. The grain scale model is thus in this configuration rather efficient to reproduce the amplitude of SDH echoes in a highly scattering material. One can also note that the simulated results exhibit a slight time divergence (~1 µs) as regard to the experimental echo. The difference is more likely to be due to the uncertainties of the homogenized elastic coefficients used to simulate the time reference.

The trend of the noise profiles averaged over 30 simulations for the three simulation models and over 25 transducer positions for the experimental data are displayed in Figure 4. The three microstructure models show very similar trends for the noise. Indeed, each of the averaged profile is contained in the standard deviation of the two others. This observation confirms the previous conclusion on the slight influence of the grain size distribution on the results. Moreover, Figure 4 shows that the simulation does not well reproduce the experimental noise profile.

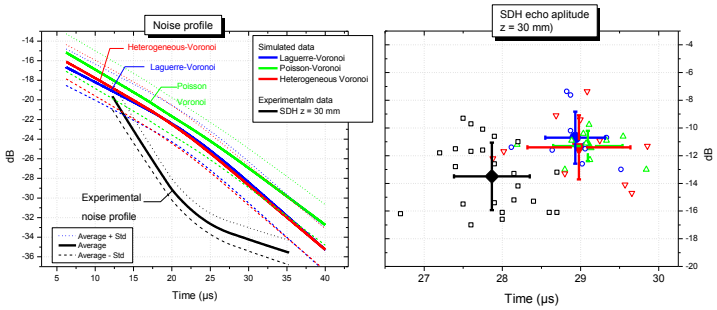

Figure 4 : a) Noise profile (trend computed over 30 simulations) and b) amplitude of the SDH located at z = 30 mm obtained experimentally and simulated with 3 different microstructure models.

This preliminary study has shown that the grain-scale modeling exhibits great efficiency to reproduce the decay of the SDH echo and thus the attenuation due to the scattering of the wave at the grain boundaries. In addition, the grain-scale modeling generates a high level of structural noise. Nevertheless, the average trend of the noise profile is highly overestimated by the grain-scale modeling. Finally, the 3 microstructure models implemented show highly similar results both in terms of attenuation and noise level.

3.2. Multi-layer isotropic structure : Centrifugally Cast Stainless Steel

This section deals with the inspection of Centrifugally Cast Stainless Steel. The microstructure of CCSS components may be highly complex and depends on the solidification conditions.

In the present case, the studied component is made of biphasic austeno-ferritic stainless steel. The metallographic observations (Figure 5.a) revealed that the microstructure varies along the depth in the block. The component was thus modeled as a multi-layer microstructure (4 layers) with a mean grain size varying along the depth (Figure 5.b). A second level of microstructure description was also introduced in order to take into account the subdivision of the initial ferritic grains into austenite colonies during the solidification process (usually called A type solidification). The corresponding simulated microstructure is obtained by subdivising each grain with a second poisson-Voronoi based procedure (Figure 5.c).

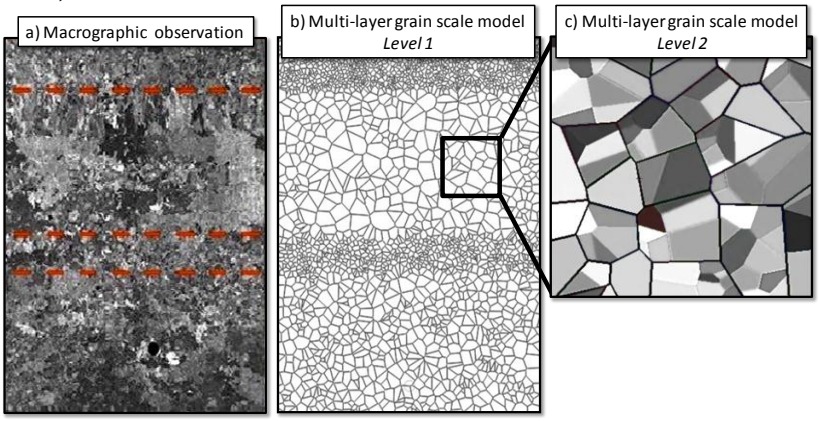

Figure 5: a) Metallographic observation of Centrifugally Cast Stainless Steel, b) Multi-layer microstructure model of CCSS, c) Multi-layer microstructure model of CCSS including a second refinement level of the microstructure.

In addition, the studied CCSS is a biphasic material containing 88% of austenite and 12% of residual ferrite. As a consequence 2 different set of elastic coefficients were used and assigned to the grains. The first set of elastic constant corresponds the austenite single crystal. Those input properties neglect the residual ferrite. They have been used in models #1 & #3 (see Table 2). The second set includes the residual ferrite by using a homogenized elastic tensor computed with the frame of the Voigt model (see model #2, Table 2). Eventually, 3 different models have been used and are described in Table 2. One aim of this study was thus to investigate the influence of the material modeling on the UT simulation results.

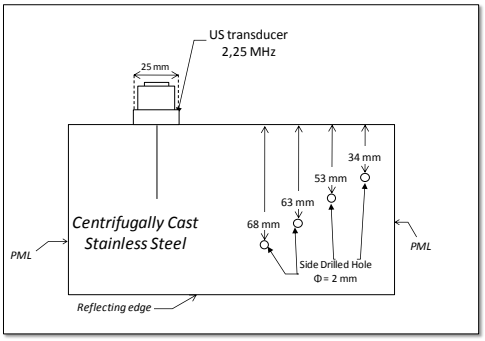

Figure 6: Inspection configuration of Centrifugally Cast Stainless Steel (CCSS).

CENTRIFUGALLY CAST STAINLESS STEEL					
	Description	Elastic coefficients (GPa)			
Model	level	Designation	C_{11}	C_{12}	C_{44}
#1	Primary (Level 1)	Austenitic	206	133	119
#2	Primary (Level 1)	Homogenised (Ferritic + Austenitic)	274	105	141
#3	Secondary (Level 2)	Austenitic	206	133	119

Table 2: Elastic coefficients of CCSS used for the simulation.

The 3 models have been used to compute the amplitude of the 4 SDH presented in Figure 6 and the amplitude of the backwall echo. The results are displayed in Figure 7. The echo amplitudes obtained with the three microstructure models are compared to the measurements performed for three probe position along the direction of the SDH axis. The SDH at 34 mm has been chosen as reference for the amplitude comparison. The general trend of the experimental data is well reproduced by the three simulation models. Especially the high amplitude difference between the SDH echoes and the backwall echo is well estimated. Nevertheless all three models globally overestimate the amplitude of the SDH echoes. It means that the attenuation due to the ultrasonic scattering generated by the microstructure is underestimated by the numerical model. In addition, as in the previous section, the 3 different models exhibit very similar results. It is thus highly difficult to discriminate the models.

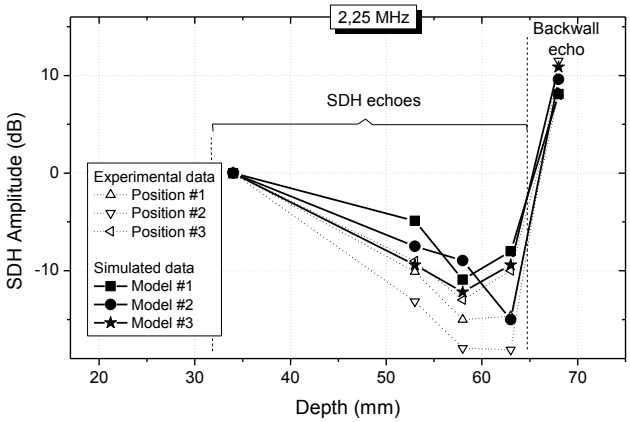

Figure 7: SDH echo amplitudes simulated with the 3 microstructure models and experimentally acquired on 3 different positions on the mock-up.

3.3. Complex anisotropic structure: Austenitic weld

In this application, the grain-scale modeling approach has been implemented in order to compute the anisotropic attenuation coefficient in an austenitic weld. The structure of austenitic weld is characterized by columnar grains generated by epitaxic growth during the solidification. The microstructure exhibits a crystallographic fiber axis and is thus highly anisotropic. In those conditions, the ultrasonic propagation through the structure highly depends on the angle α between the ultrasonic beam propagation direction and the fiber axis. Nevertheless, the determination of the variations of the attenuation coefficient as a function of the α angle is very hard to achieve experimentally[12].

In order to obtain this data for longitudinal waves, a simulation approach based on grain-scale modeling has been proposed. The simulated configuration is displayed on Figure 8 and consists on a single element immersion transducer at normal incidence on the inspected block. The mock-up is made of anisotropic austenitic INCONEL weld modeled at the grain scale.

The morphologic columnar structure was modeled by a Poisson-Voronoi tessellation which was elongated in the direction of the crystallographic fiber axis. The grain size is characterized by the mean length in the fiber direction and the width in the transverse direction. The grain size has been characterized by metallographic observations and was set to 5×0.25 mm.

The assumption of a transverse isotropic symmetry is made for the elastic properties assigned to the grains. The grains exhibit a common <100> crystallographic axis corresponding to the fiber axis. The elastic coefficients used are displayed in Table 3 and correspond to the values for INCONEL 600.

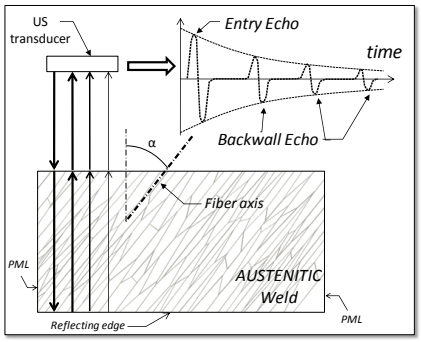

Figure 8: Simulation configuration for the determination of the anisotropic attenuation coefficient of P-waves vs the α angle between the beam propagation and the fiber axis.

INCONEL 600				
Mean grain size (µm)		Elastic coefficients (GPa)		
length	width	C11	C12	C44
5000	250	234	145	126

Table 3: Elastic coefficients of INCONEL 600 single crystal used for the simulation.

The objective of the study was to determine the contribution of the attenuation due to the wave scattering at the grain boundaries. In order to avoid the contribution of the beam divergence, a second computation was done with a homogeneous medium and was subtracted to the initial computation. The α value was incremented from 0 (vertical fiber axis) to 90° (perpendicular fiber axis) in order to investigate the attenuation variations versus the fiber axis orientation. For each set of input parameters the attenuation coefficient was averaged over 30 realizations of the microstructure. The computation of the attenuation coefficient uses the amplitudes of two successive backwall echoes.

The variations of the attenuation coefficient have been computed for 2 different frequencies – 2 MHz and 8 MHz- and are displayed in Figure 9. The simulated values at 2 MHz are compared to the experimental data available. They were estimated from attenuation measurements with a specific set-up on 316L weld samples, slightly adjusted from experimental data on SDH [13].

Unlike an isotropic medium, the results show strong variations of the attenuation depending on the direction of propagation. The maximum attenuation is obtained for propagation perpendicular to the fiber axis (α = 90°). This evolution of the attenuation as a function of the angle is in good agreement with the results of previous experimental and theoretical studies [3, 14, 15].

Moreover, the simulation results show a very good agreement with the experimental data at 2 MHz. The modeling approach seems to be highly reliable to estimate the scattering attenuation in an anisotropic weld.

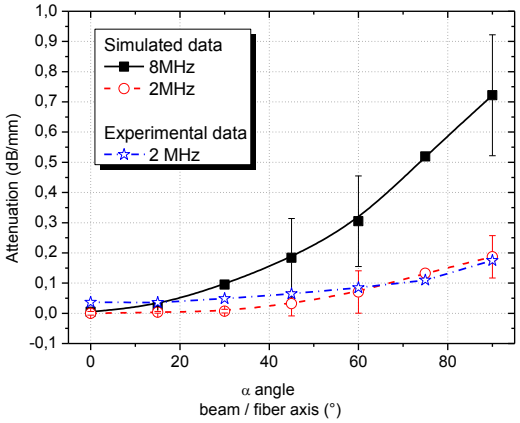

Figure 9 : Evolution of the attenuation coefficient as a function of the α angle between the propagation direction of the ultrasonic beam and the crystallographic fiber axis of the austenitic weld.

Conclusion

The objective of this paper was to give an overview of the recent developments achieved by EDF R&D in the field of the grain-scale simulation of ultrasonic inspections with the 2D version of the ATHENA code developed by EDF R&D. The method relies on the coupling of the FE simulation and a modeling of the microstructure at the description level of the grain. The main functionalities of the finite element code ATHENA 2D has been given. Three different mathematical models based on Voronoi diagram have been used to describe the microstructure of polycrystalline materials and to control the grain size distribution.

The grain-scale approach has been implemented on three different cases.

The first case deals with the simulation of the inspection isotropic coarse grain structure made of INCONEL 600 and was dedicated to the investigation of impact of the description of the microstructure on the reliability of the simulations. Three different models of microstructure based on Voronoi diagrams have been implemented in order to control the grain size distribution. Then the grain-scale approach has been applied on two others applications which are the inspection of multi-layer isotropic structure made of centrifugally cast stainless steel and the determination of the attenuation in an anisotropic structure of an austenitic weld.

Globally, the grain-scale modeling has proven a great efficiency to reproduce the decay of the SDH echo and thus the attenuation due to the scattering. The modeling enables to generate a high level of structural noise. Nevertheless, the average trend of the noise profile is highly overestimated by the grain-scale modeling. In the first application, the different microstructure models implemented show highly similar results both in terms of attenuation and noise level. It suggests that the grains size distribution is not a major influential parameter of the computation. In addition, the grain-scale modeling appears to be en efficient way to estimate the attenuation properties of complex structures when the data is experimentally hard to achieve.

Eventually, the discrepancy between experiment and modeling as regard to the noise level can be due to the 2D approximation of the finite elements code or the mathematical tool used to describe the microstructure of coarse grain material. The consequence of the 2D hypothesis would be to virtually concentrate the ultrasonic backscattered energy in the inspection plane and may raise the backscattering phenomena. The future perspective of the grain-scale modeling at EDF R&D will implement the 3D version of the ATHENA finite element code. Nevertheless the creation of 3D microstructure usually requires more than 100.000 grains and become a challenging issue of the grain-scale approach.

References

1) Moysan, J., et al., Modelling the grain orientation of austenitic stainless steel multipass welds to improve ultrasonic assessment of structural integrity. International Journal of Pressure Vessels and Piping, 2003. 80(2): p. 77-85.
2) Apfel, A., et al., Coupling an ultrasonic propagation code with a model of the heterogeneity of multipass welds to simulate ultrasonic testing. Ultrasonics, 2005. 43(6): p. 447-456.
3) Chassignole, B., et al., Modelling the attenuation in the ATHENA finite elements code for the ultrasonic testing of austenitic stainless steel welds. Ultrasonics, 2009. 49(8): p. 653-658.
4) Chassignole, B., et al. Ultrasonic propagation in austenitic stainless steel welds approximate model and numerical methods results and comparison with experiments. in AIP Conference Proceedings. 2000.
5) Becache, E., P. Joly, and C. Tsogka, Fictitious domains, mixed finite elements and perfectly matched layers for 2D elastic wave propagation. 2000.
6) Bécache, E., P. Joly, and C. Tsogka, An analysis of new mixed finite elements for the approximation of wave propagation problems. SIAM Journal on Numerical Analysis, 2000. 37(4): p. 1053-1084.
7) Berenger, J.-P., A perfectly matched layer for the absorption of electromagnetic waves. Journal of Computational Physics, 1994. 114(2): p. 185-200.
8) Chassignole, B., et al. Ultrasonic examination of a weld repair in Ni-based alloy. in 9th International Conference on NDE Relation to Structural Intergity for Nuclear and Pressirized Components. 2012. Seattle, Washington, USA: European Commission.

9) Chassignole, B., et al., Ultrasonic and structural characterization of anisotropic austenitic stainless steel welds: Towards a higher reliability in ultrasonic non-destructive testing. NDT & E International, 2010. 43(4): p. 273-282.
10) Marthinsen, K., Comparative analysis of the size distributions of linear, planar, and spatial Poisson Voronoi cells. Materials Characterization, 1996. 36(2): p. 53-63.
11) Borouchaki, H., N. Flandrin, and C. Bennis, Diagramme de Laguerre. Comptes Rendus Mécanique, 2005. 333(10): p. 762-767.
12) Bodian, P.-A., Propagation des ultrasons en milieu hétérogène et anisotropie : Application à l'évaluation des propriétés d'élasticité et d'atténuation d'aciers moulés par centrifugation et de soudures en inconel. PhD Thesis INSA Lyon. 2011, Ecole Doctorale Matériaux de Lyon: Lyon. p. 165.
13) Chassignol, B., O. Dupond, and L. Doudet. Ultrasonic and metallurgical examination of an Alloy 182 welding mold. in 7th International Conference on NDE Relation to Structural Intergity for Nuclear and Pressirized Components. 2009. Yokohama, Japan: European Commission.
14) Ahmed, S. and R. Thompson. Effect of preferred grain orientation and grain elongation on ultrasonic wave propagation in stainless steel. in Review of Progress in Quantitative Nondestructive Evaluation. Vol. 11B. 1992.
15) Seldis, T. and C. Pecorari, Scattering-induced attenuation of an ultrasonic beam in austenitic steel. The Journal of the Acoustical Society of America, 2000. 108: p. 580.

MODELING INSPECTION OF STEAM GENERATOR TUBES IN CIVA PLATFORM: PREDICTION OF INDUSTRIAL EC PROBE RESPONSE (X-PROBE® AND +POINT® EDDY CURRENT PROBES)

S. Paillard, A. Skarlatos, E. Demaldent, CEA - LIST, France
T. Sollier, G. Cattiaux, IRSN, France

ABSTRACT

Eddy current inspection modeling of Steam Generator (SG) tubes with industrial probes is beneficial for the evaluation of performances and limitations of industrial Non Destructive Testing (NDT) techniques. The detection of narrow cracks due to fatigue or corrosion in Steam Generator tubes is important for the safety of the nuclear plants.

The aim of this collaborative work between CEA and IRSN is to extend the capabilities of the CIVA software by developing a simulation tool for the evaluation of industrial non-destructive testing method used for the tube inspection with industrial probe such as X-Probe® and +Point® probe.

For the numerical modeling of this problem, a combination of different models such as Boundary Element Method (BEM), Finite Integral Technique (FIT) and Volume Integral Method (VIM), is used in order to combine the advantages of different techniques (speed, effectiveness…). According to this approach, the primary field is calculated using one of these models whereas the flaw response is calculated via another method.

First, we will introduce the principle of the hybrid method, we will describe the models used in the hybrid models. Then, we will present X-Probe® and +Point® probe simulated responses to narrow cracks in SG tubes. Finally, we will compare the simulated responses with results from non-hybrid model.

Keywords. Eddy Current modeling, X-Probe®, +Point®, ferrite core.

Introduction

The inspection of Steam Generator (SG) tubes in Pressurized Water Reactor (PWR) is a great challenge.The SG tubes are part of the second barrier for the confinement of radioactive material in PWR. Performing efficient inspections requires the development of reliable probes and data analysis. Eddy current array probes are used in the industry thanks to their flexibility, their imaging capabilities and the gains in productivity. The bobbin coil is used worldwide for baseline inspection.

IRSN, as technical support organization to the French Safety Authority (ASN), surveys the technical evolution of Non-Destructive Testing techniques (NDT) and support research activities. IRSN uses simulation codes to support its technical assessments in NDT [1].

Taking into account these requirements, CEA-LIST has focused its researches on the development of numerical models added to the CIVA software.

A long term research collaborative program between CEA and IRSN is ongoing for the development within CIVA of functionalities related to NDT used in the nuclear industry.

Numerical modeling of probes helps to assess their performances for detection and characterization of flaws. It also gives insight to their sensitivity to influential parameters and therefore their limitations. Numerical modeling is now often part of the technical justification of the qualification files of an inspection procedure. Probe modeling of techniques used widely by utilities, such as the +Point and the X-probe, gives IRSN and CEA a better understanding of the international operating experience

The first part of this paper is devoted to the X-Probe®. The probe and the acquisition modes are described, and a comparison between simulation using CIVA and experimental data are presented. The second part presents results of simulations of the +Point® probe. This study focuses on demonstrating the performance of the finite element model (FLUX) and the new developments in CIVA. The objective is to develop and validate models for accurate simulations results for these two probes.

1. Modeling the X-Probe®

The X-Probe® is an ET array probe. This probe is used for the evaluation and characterization of SG tube's degradation. The main advantage of this probe versus motorized rotating probes is its capacity to detect circumferential cracks with a high translation speed. The inspection of tubes along all their length is not economically achievable with motorized rotating probes due to a low translation speed of typically 5 mm/s. However, corrosion cracks might be located in the free span of the tube bundle such as an ODSCC crack detected at Seabrook Station, Unit 1 on an alloy 600 TT tube at a dent/ding location 2). It is therefore useful for utilities to have the option to inspect tubes over their full length with an array probe at a speed exceeding 100 mm/s.

A view of the X-Probe® is given in Figure 1. The specific array probe used for this research program has 2 bracelets of 19 coils operating in transmit/receive mode 3). For each bracelet, the coils are regularly distributed, and electronically switched, over the tube circumference 4). For the detection of circumferentially oriented flaws (transversal mode), both transmit and receive coils belong to the same bracelet. For the detection of longitudinally oriented flaws and volumetric flaws (longitudinal mode), the driving and receiving coils are located on bracelets spaced along the tube axis. A view of CIVA for the X-Probe® modeling is given in Figure 2.

The X-Probe® parameters are not detailed by the vendor. Based on available published information and visible design, the parameters chosen for simulation are given in Table 1. Although actual probe parameters might differ from those values, it is expected that calibration will compensate most of the deviations.

Data acquisition on reference tubes was done by TECNATOM using Teddy+® generator and software. Simulations were done using CIVA version 10.1 and FLUX version 11.1. Simulation results with the X-Probe® using a model (CIVA) based on the Volume Integral Method (VIM) 5) and a finite element model (FLUX, **Figure 3**) are compared to experimental data in **Figure 4**, **Figure 5** and **Figure** 6.

The calibration is done according to the ASME standard: 5 Volts in amplitude for a long external groove with a depth of 30% and 0° in phase for a lift-off signal. A good agreement is observed between CIVA and FLUX for the Electromotive Force induced in the reception coils for a reference flawless configuration with a frequency of 200 kHz.

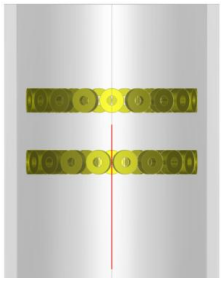

Figure 1: View of the CIVA configuration for the 2 bracelets of the X-Probe® model and for an axial notch.

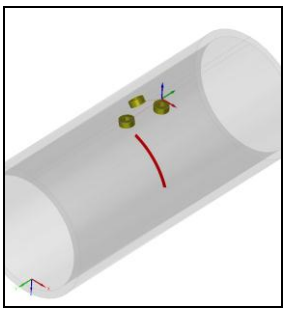

Figure 2: View of the CIVA configuration for 3 active coils of the X-Probe® model and for a transversal notch.

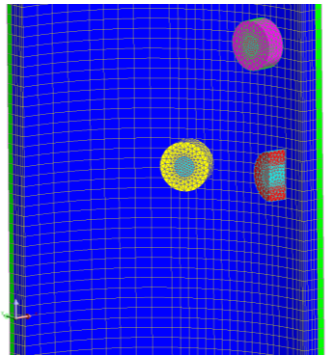

Figure 3: X-Probe® model based on Flux ; only one half of a driver coil, one receiver coil for the transversal mode and one receiver coil for the longitudinal mode are modeled.

Parameter	Value
Tube Outer Diameter	22.22 mm
Tube Wall Thickness	1.27 mm
Tube Conductivity	1 MS/m
Tube Relative Permeability	1
Coils Outer Diameter	2.5 mm
Coils Inner Diameter	1 mm
Coils Height	1 mm
Coils Lift-off	1 mm
Coils Number of Turns	50
Number of Coils per Bracelet	19
Number of Bracelets	2
Distance between Bracelets	6.4 mm
Frequency	200 kHz

Table 1. Parameters chosen for simulation of the X-Probe® response with a 7/8" OD tube.

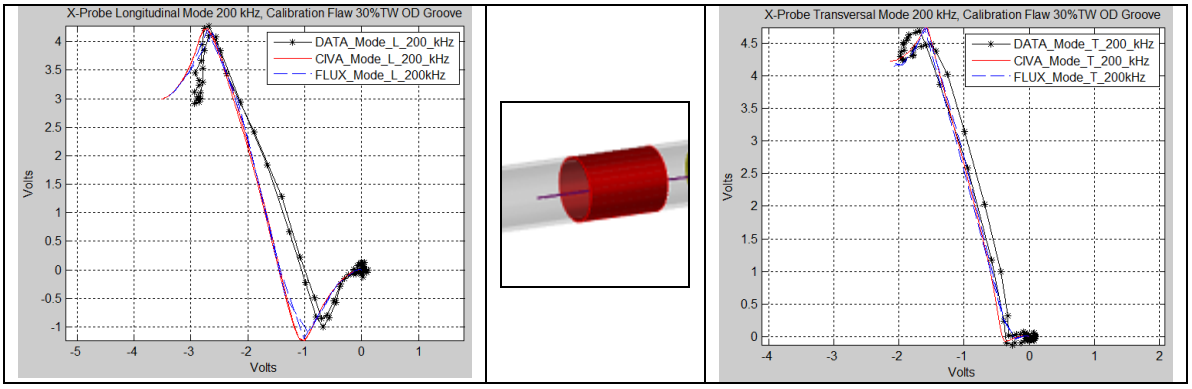

Figure 4. Comparison for the reference 30%TW OD groove between simulations with CIVA (solid line), FLUX (dashed line) and data (stars); left: X-Probe® longitudinal mode; center: External Groove 30%TW; right: X-Probe® transversal mode.

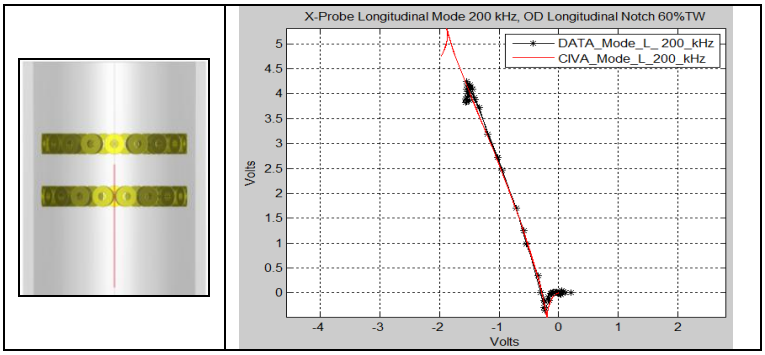

Figure 5. Comparison between CIVA simulations (solid line) and data (stars); 60%TW OD longitudinal notch X-Probe® longitudinal mode.

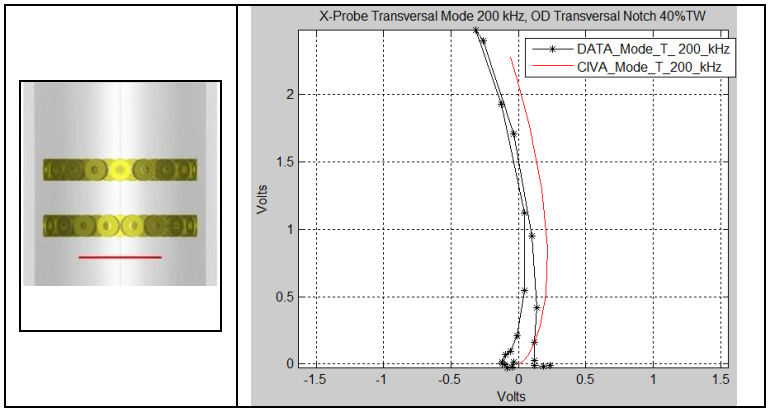

Figure 6. Comparison between CIVA simulations (solid line) and data (stars); 40%TW OD transversal notch X-Probe® transversal mode.

2. Modeling the +Point® Probe

The +Point® is a rotating probe widely used for the inspection of steam generator tubes. This probe is based on two orthogonal coils operated in differential mode 6) with a complex 3D ferrite core.

While CIVA allows the definition and use of most "standard" EC probes (axial, punctual, array) there is no possibility today to define probes with various element shapes as the +Point® Probe. Modeling is under development to take into account this kind of probe. The first results are shown here: calculations of the magnetic field on a work piece. The real and imaginary parts are presented in **Figure 8** and

Figure 9. The figures represent the C-Scan of the Z component of magnetic incident field on the surface of the plate created by the +Point® Probe at 200 kHz with a 150 µm lift-off. The input parameters of the simulated +Point® Probe are postulated.

A lift-off variation is presented in **Figure 10** (real part) and **Figure 11** (imaginary part). The lift-off has an impact on both parts, real and imaginary parts.

New development has been done 7) to take into account a tilted ferrite core. This allowed us to do a study on the tilt of the probe (or rotation). A rotation variation has been done from 0° to 10° between the plate and the probe. The results are illustrated in **Figure 12** and

Figure 13 (real part) of the Z component of magnetic incident field and **Figure 14** and **Figure 15** present the imaginary part.

In the framework an international collaboration with IRSN, Argonne National Laboratory has provided the authors with a set of data on a reference tube including 18 EDM notches of various length and depth. The outer diameter of the tube is 22.22 mm (7/8") and the average thickness is 1.23 mm. The calibration is done on a longitudinal EDM notch 100%TW with a length of 9.52 mm (0.375") and a width of 0.127 mm (0.005") accordingly to EPRI guidelines 8). The signal is normalized on this 100%TW notch to 20 Volts peak-to-peak. The phase is set at 0° for the lift-off variation. Four frequencies were used (100 kHz, 200 kHz, 300 kHz and 400 kHz).

Parameter	Value
Plate Thickness	1.27 mm
Plate Conductivity	1 MS/m
Plate Relative Permeability	1
Coils Outer Diameter	2.2 mm
Coils Inner Diameter	1.8 mm
Coils Height	1 mm
Coils Lift-off	1.5 mm
Coils Number of Turns	120
Frequencies	100 kHz; 200 kHz; 300 kHz; 400 kHz

Table 2. Parameters chosen for the simulation of the +Point® Probe response (estimated parameters for the probe)

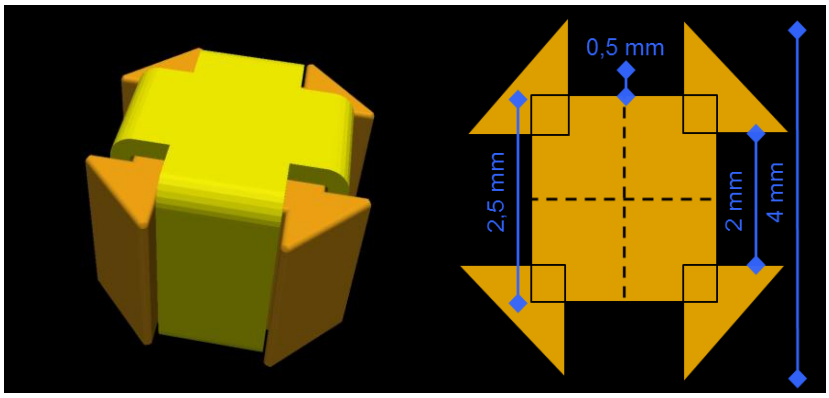

Figure 7: +Point® model using CIVA: 2 circular cross wounded coils with the ferrite core in differential mode: left: 3D View; right: input parameters.

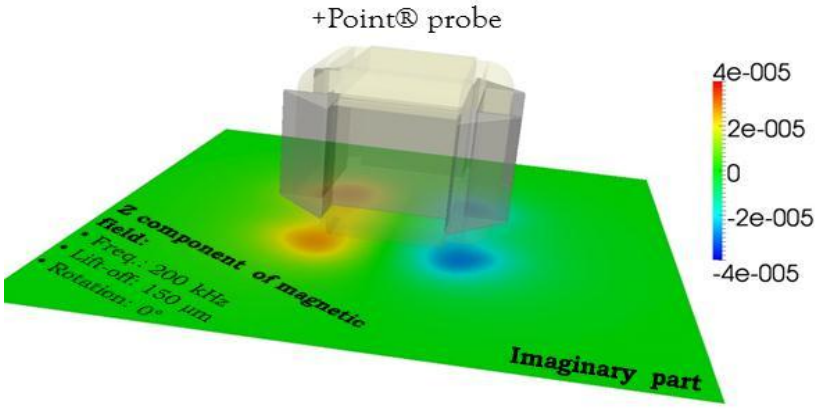

Figure 8. . Imaginary part of the Z componentof magnetic incident field on the work piece for the +Point® at 200 kHz for a lift-off 150 µm, a rotation of 0° and a conductivity of the plate of 1 MS/m.

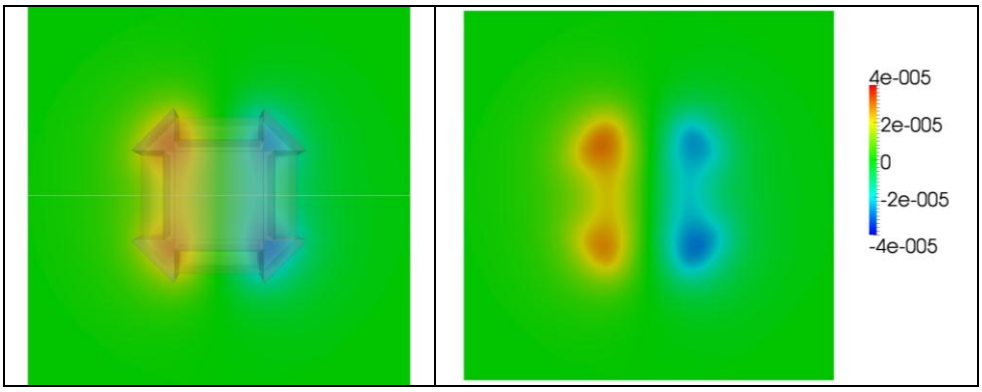

Figure 9. Imaginary part of the Z component of magnetic incident field on the work piece for the +Point® at 200 kHz for a lift-off 150 µm, a rotation of 0° and a conductivity of the plate of 1 MS/m; left: C-Scan is seen in transparency through the +Point® probe; right: C-Scan only.

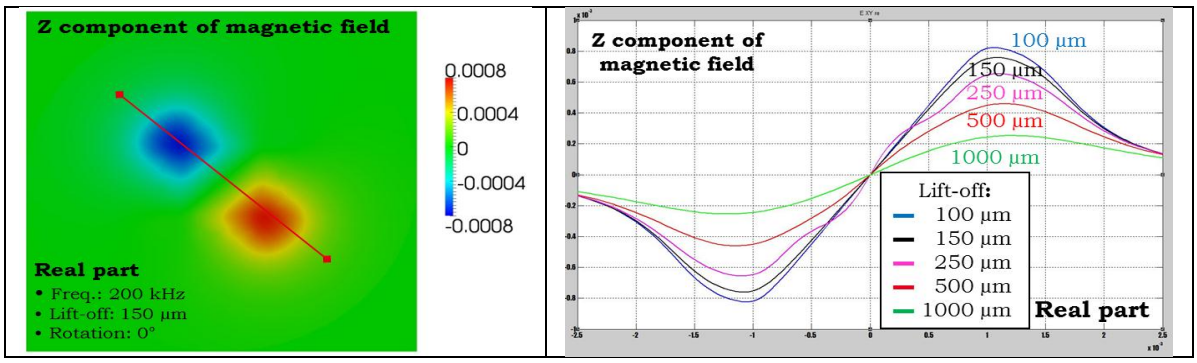

Figure 10. Real part of the Z component of magnetic incident field on the work piece for the +Point® at 200 kHz, a rotation of 0° and a conductivity of the plate of 1 MS/m; left: C-Scan with a lift-off of 150 µm; right: 1D signal on the red line marked on the C-Scan with a lift-off from 100 to 1000 µm.

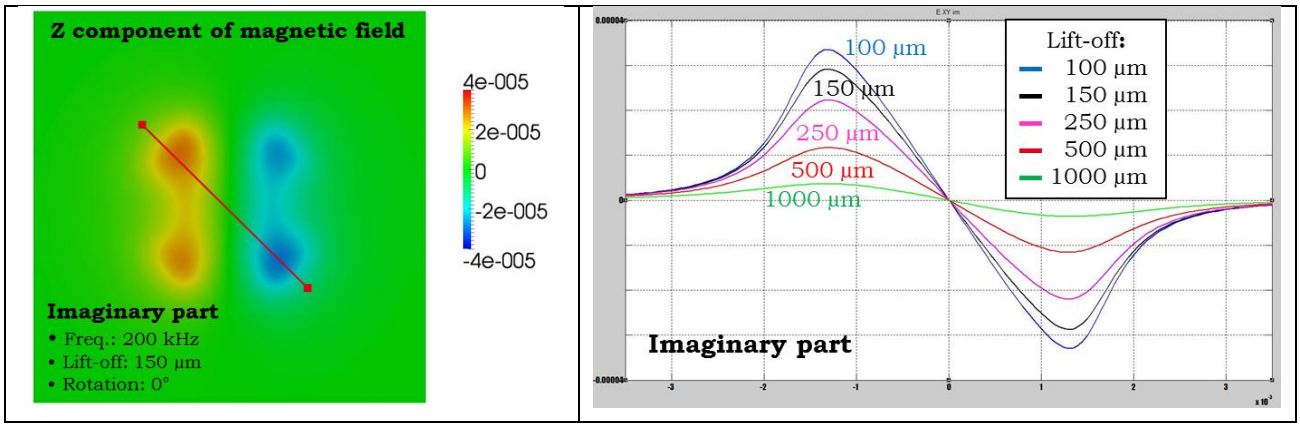

Figure 11. Imaginary part of the Z component of magnetic incident field on the work piece for the +Point® at 200 kHz, a rotation of 0° and a conductivity of the plate of 1 MS/m; left: C-Scan with a lift-off of 150 µm, right: 1D signal on the red line marked on the C-Scan with a lift-off from 100 to 1000 µm.

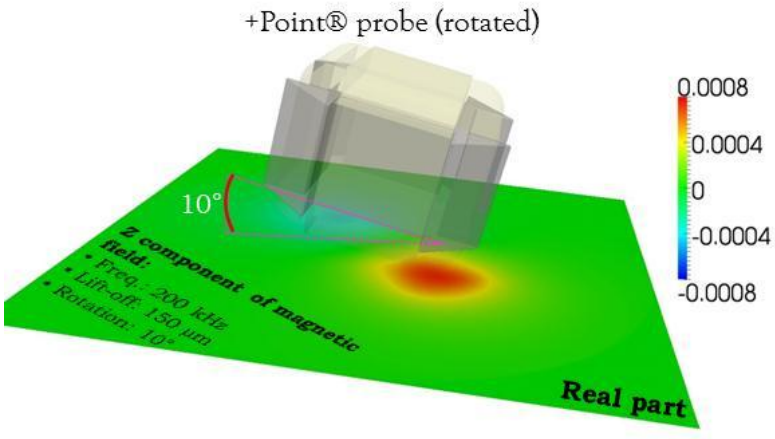

Figure 12. Real part of the Z component of magnetic incident field on the work piece for the +Point® at 200 kHz for a lift-off 150 µm, a rotation of 10° and a conductivity of the plate of 1 MS/m.

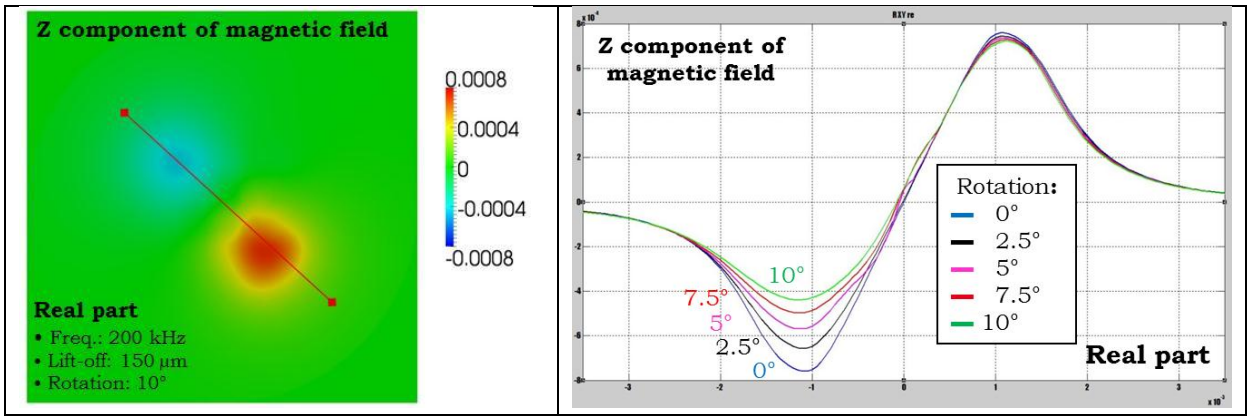

Figure 13. Real part of the Z component of magnetic incident field on the work piece for the +Point® at 200 kHz for a lift-off of 150 µm, and a conductivity of the plate of 1 MS/m; left: C-Scan at 10°, right: 1D signal on the red line marked on the C-Scan with a rotation from 0 to 10°.

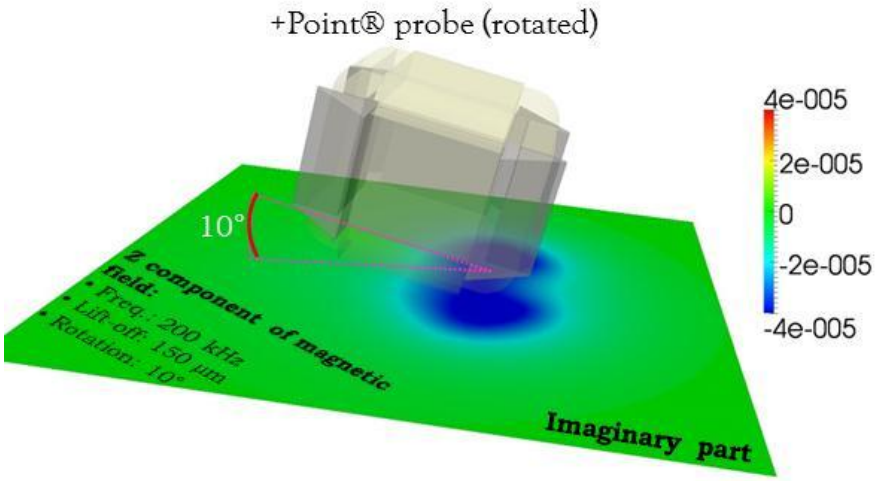

Figure 14. Imaginary part of the Z component of magnetic incident field on the work piece for the +Point® at 200 kHz for a lift-off 150 µm, a rotation of 10° and a conductivity of the plate of 1 MS/m.

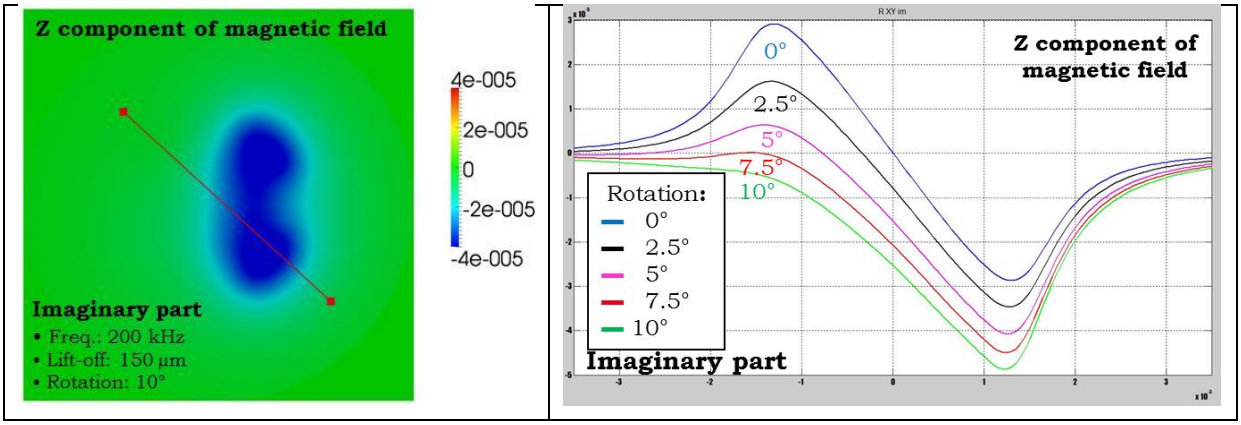

Figure 15. Imaginary part of the Z component of magnetic incident field on the work piece for the +Point® at 200 kHz for a lift-off of 150 µm, and a conductivity of the plate of 1 MS/m; left: C-Scan at 10°, right: 1D signal on the red line marked on the C-Scan with a rotation from 0 to 10°.

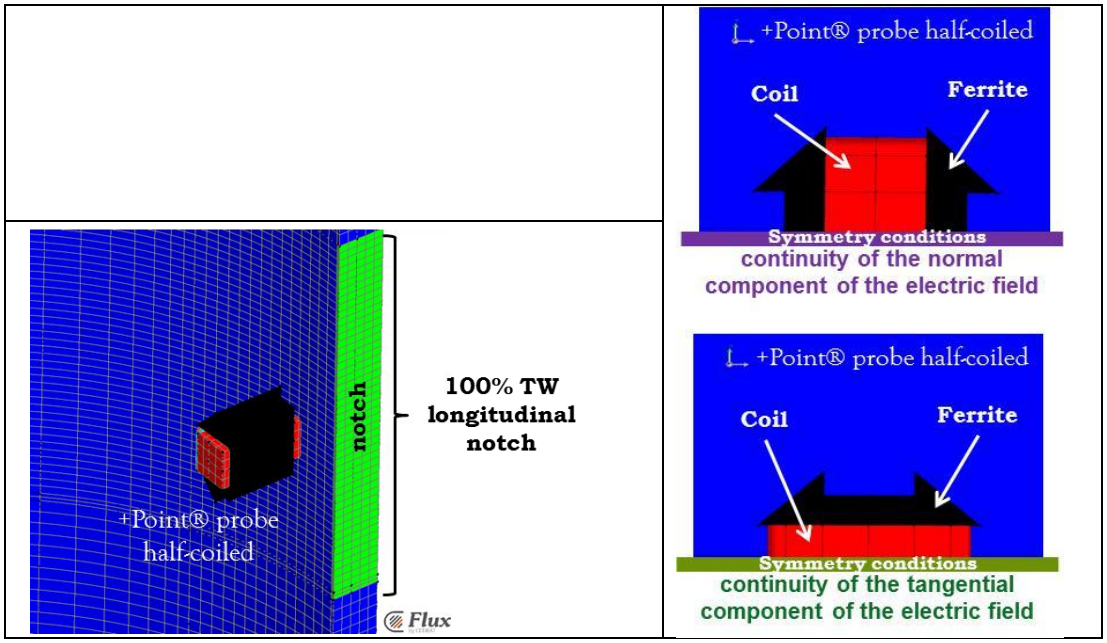

Figure 16. Input parameters; left: view of FLUX with the probe and the 100% TW notch; right: modeling the probe response for the horizontal coil and the vertical coil.

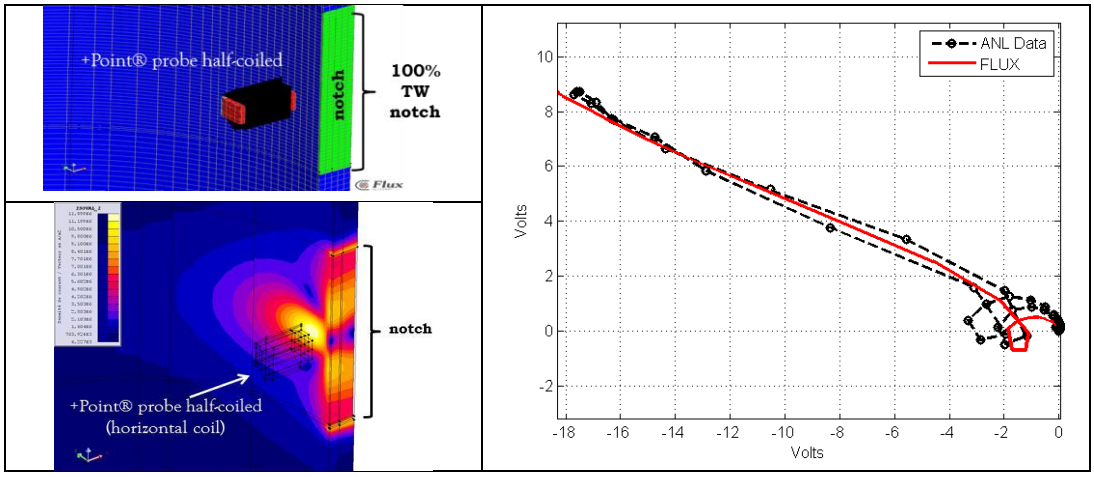

Figure 17. Comparison between FLUX simulations (solid red line) and data (black dash line); left, up: view of FLUX; left, down: Plot of the current density, horizontal coil, 100% TW longitudinal notch; right: reference flaw for calibration: 100% Through Wall Axial Notch (Magnitude = 20 Vpp).

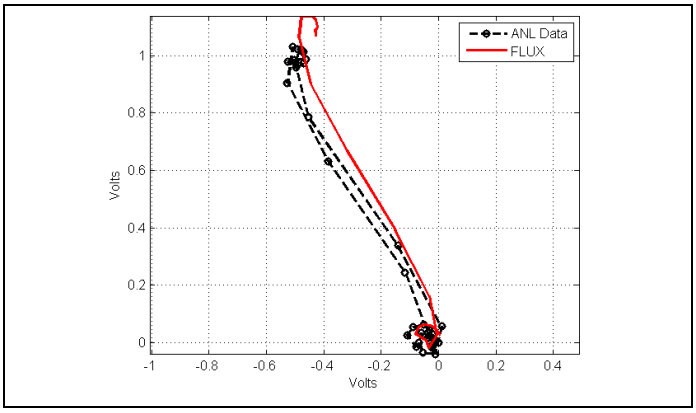

Figure 18. Comparison between FLUX simulation (solid red line) and data (black dash line); 60% TW Outer Axial Notch.

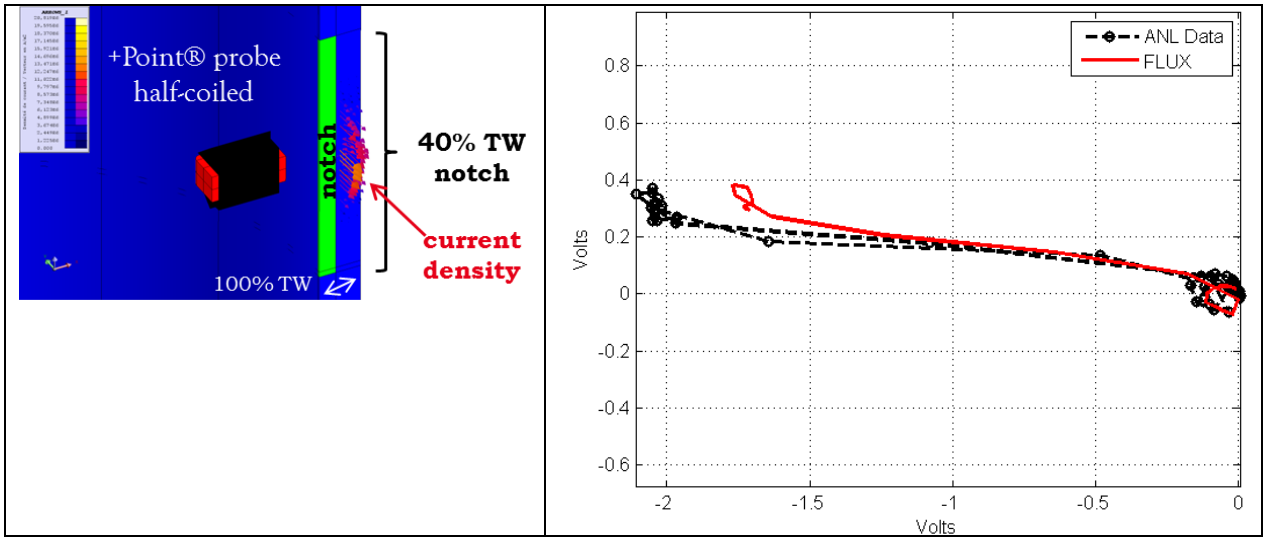

Figure 19. Comparison between FLUX simulations (solid red line) and data (black dash line); left: current density for a 40% TW Inner Axial Notch; right: 40% TW Inner Axial Notch.

3. Conclusions

The use of modeling tools for the evaluation of NDT techniques is part of IRSN policy in order to sustain his technical assessments and to sustain its technical expertise.

Benchmarks are effective to evaluate numerical models. Several benchmarks and model developments have been done and have been presented in this paper with industrial probes including X-Probe® and +Point®. In this work, we have postulated parameters for simplified models for the X-Probe® and the +Point® Probe

Several Benchmarks with X-Probe® has been done with experimental data and gives confidence in the results. Benchmarks with +Point® probe has been done with FEM code (FLUX3D) on notches (100%, 60% and 40% TW) with good agreement with experimental data. +Point® probe coupled model is under development and the first results show the influence of parameters like lift-off and rotation on magnetic field.

The authors believe that modeling is an efficient tool for that purpose and provides support to physical reasoning for the industry and for experts.

The very next step of the simplified models developed with CIVA is to model EC probes with a ferrite core of complex shape (like +Point® probe) in order to simulate a flaw response.

Acknowledgements

The authors are very grateful to Dr. Sasan Bakhtiari from Argonne National Laboratory for providing experimental data on references flaws for the +Point®.

References

1) "Modeling the X-Probe® and the +Point® Eddy Current Probes", ENDE conference, Bratislava, T. Sollier et al, June 24-29, 2013.
2) NRC Information Notice 2013-11, Crack-like indication at dents/dings and in the freespan region of thermally treated alloy 600 steam generator tubes, July 3, 2013
3) B. Marchand, JM. Decitre, O. Casula, G. Cattiaux, T. Sollier, Flexible Eddy Current Probes for Nuclear Parts Inspection, *Proceedings of the Eighth International Conference on NDE in Relation to Structural Integrity for Nuclear and Pressurized Components*, 28 September – 1 October, 2010, Berlin
4) G. Lafontaine, F. Hardy, J. Renaud, X-Probe ECT array: A high-Speed Replacement for Rotating Probes, *Proceedings of the Third International Conference on NDE in relation to Structural Integrity for Nuclear and Pressurised Components*, 14-16 November, 2001, Seville

5) Skarlatos, A.; Pichenot, G.; Lesselier, D.; Lambert, M.; Duchene, B.; , "Electromagnetic Modeling of a Damaged Ferromagnetic Metal Tube by a Volume Integral Equation Formulation," Magnetics, IEEE Transactions on , vol.44, no.5, pp.623–632, May 2008
6) N. Lei, J. Xin, L. Udpa, S. Udpa, Modeling of New/Commercial Eddy Current Probe for Steam Generator Inspection, *Review of Progress in Quantitative Nondestructive Evaluation*, Vol. 31A, 2012, 351-357
7) Modelling of Specimen Interaction with Ferrite Cored Coils by Coupling Semi-Analytical and Numerical Techniques", ENDE conference, Bratislava, A, Skarlatos *et al*, June 24-29, 2013
8) Steam Generator Management Program: Pressurized Water Reactor Steam Generator, Examination Guidelines: Revision 7. EPRI, Palo Alto, CA: 2007. 1013706.

AXIAL PROBE EDDY CURRENT INSPECTION OF STEAM GENERATOR TUBES NEAR ANTI-VIBRATION BARS: PERFORMANCE EVALUATION USING FINITE ELEMENT MODELING

L. Maurice, EDF - CEIDRE, France
V. Costan, P. Thomas, EDF - R&D, France

ABSTRACT

In order to carry out performance demonstrations of the Eddy-Current NDE processes applied on French Nuclear Power Plants, EDF studies the possibility of using simulation tools as an alternative to measurements on steam generator tube mock-ups. This paper investigates the effect of influential parameters on wear detection, defects which may appear in the U-shape region of steam generator tubes due to the rubbing of anti-vibration bars.

Keywords: NDE Qualification, Modeling, Validation, Eddy currents, Benchmarks
PACS: 06.60.Mr, 07.05.Tp,

INDUSTRIAL CONTEXT

EC NDE Performance Demonstration

Electricité de France (EDF) carries out Eddy Current (EC) Non Destructive Examinations (NDE) in order to ensure the integrity of steam generators (SG) tubes. According to the French ministerial order of 1999, the performances of these techniques have to be demonstrated. Namely, the ability to fulfill detection and sizing requirements has to be evaluated, taking into account the influential parameters (e.g. defect geometry, material characteristics, temperature, etc). These parameters can significantly affect the EC signal [1].

For this purpose, parametric studies are carried out. They are commonly performed through acquisitions on a large number of artificial flaws set on SG tube mock-ups. Nevertheless, this approach is costly and time consuming, remains quite empirical and does not give a deeper understanding of the implied phenomena.

EC NDE Performance Demonstration using numerical models

Numerical finite element models (FEM) have been considered as a potential alternative since 2000 and it has become more efficient thanks to the growth of available computer resources. On the one hand, this technique has several advantages including:

- Limiting the number of mock-ups and experimental trials, therefore decreasing the time and the cost of the inspection.
- Ability to model different defect shapes which would not be possible to machine on mock-ups, and which would be more representative to on-site observed flaws.
- Consider a larger variability of influential parameters, or, in a more general way, it makes it possible to study parameters not easily reachable on mock-ups.
- Improve the knowledge of involved physical phenomena.

On the other hand, it should not be forgotten that:

- This strategy implies the use of accurate input data such as probe geometries, or material characteristics, which are sometimes known with some uncertainty.

- Another drawback is that Finite Element modeling requires specific skills in mesh computation and in a more general way in use of numerical tools.

- Last but not least, as numerical techniques are quite different than on site EC techniques, their reliability must first be proved, as required in the RSEM [2].

EC NDE Simulation Tools Reliability Assessment

At EDF, reliability and performance demonstration of the EC NDE simulation tools has been a key issue since 2000, and it is still the case today, as illustrated by recent publications [1] . It was also investigated by the European Network for Inspection Qualification (ENIQ) who published the Recommended Practices in 2011[3]. The strategy commonly used is to cross-validate codes on specific benchmarks, representative of actual NDE situations. It is a necessary strategy that allows to have an overall view of the ability of each model. This has led to the creation of the "EC simulation" working group [4] in the frame of the COFREND, the French association for NDE. The aim of this group is to gather experts from different areas, such as users of electromagnetic codes, code developers, and proposes to test codes on specific realistic benchmarks.

Nevertheless, it appears, as a conclusion of the COFREND benchmarks studies that the ability of a given code for a specific configuration cannot predict the performances of the same code for another different configuration. That is the reason why reliability and performance demonstrations have to rely directly on the NDE application or on similar applications.

NDE APPLICATION OF INTEREST

In order to support the tubes of a SG tube bundle and to protect the U-bend from vibration caused by reactor coolant flow, Anti Vibration bars (AVBs) are placed in the U-bend region. However, this can lead to wear-fretting at the AVB-to-tube contact. Since 2010, EDF Nuclear Engineering Division and EDF R&D have performed studies dedicated to the detection of such wears with an axial probe, the SAX probe, as can be seen on FIGURE 1. Wear may appear in the U-shaped region of SG tubes, due to rubbing of anti-vibration bars (AVB's), and is therefore only external.

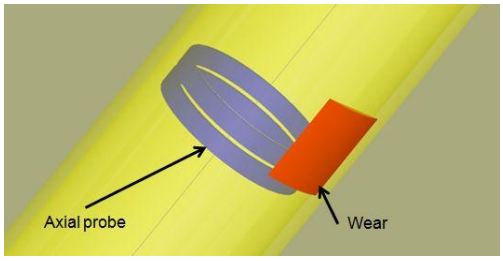

FIGURE 1 : 3D representation of a tube, wear and an axial probe.

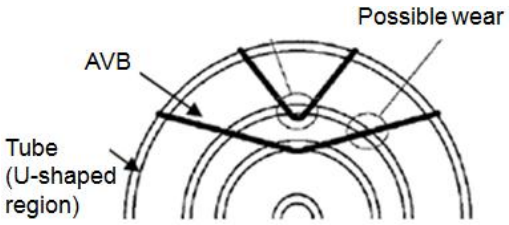

FIGURE 2 : Schematic representation of a tube bundle and AVB's

For this application, the axial probe is used in the differential mode, at an operating frequency of 240 kHz or 280 kHz respectively for 22,22mm and 19,05mm diameter tubes. The notation criterion is related to the Y projection, that is to say the imaginary part of the probe signal.

Calibration of the signals is performed on four through-wall holes located on a dedicated calibration mock-up, with the same characteristics (material, dimensions) than the real tubes. Calibration mock-up and tube to be inspected are placed in line. All EC signals presented in this work have been calibrated on this defect to 1.3V, -30° and 1.7V, -35° for the 22,22mm and 19,05mm diameter tubes respectively, according to the on-site procedure.

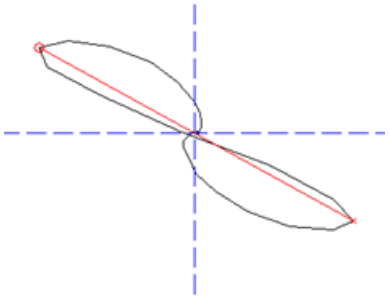

FIGURE 3 : Experimental signal on the 4phi1 flaw after calibration

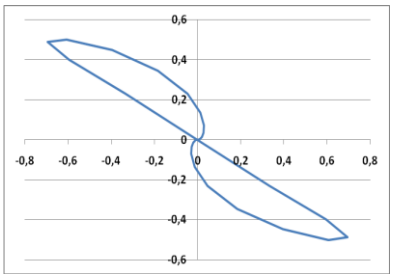

FIGURE 4 : C3D simulated signal on the 4phi1 flaw after calibration

The calibration of the numerical model is performed exactly in the same way, in taking a great care for the meshing of the 4phi1 flaw, so that the numerical error obtained is under 3%.

SIMULATIONS TOOLS

Considering EC NDE Performance Demonstration using numerical models, EDF mainly works with two codes: code_CARMEL3D (C3D for short) and CIVA.

Code_CARMEL3D

The code_Carmel3D (C3D) is a 3D FEM software for eddy current investigations. This software is based on Whitney's elements and is developed by the LAMEL ("Laboratoire de Modélisation du Matériel Electrique", a common laboratory between EDF R&D and L2EP). Two 3D FEM dual potentials formulae are implemented, and are applicable to a large scope of problems in the domain of electrotechnics. The pre and post processing is achieved using the SALOME software [5]. In this study, the v_2_2_2 version of C3D has been used, and the 5.1 version of SALOME.

CIVA

CIVA is a semi-analytical model, implementing a volume integral method (VIM). It is developed by CEA and distributed by EXTENDE [6] . Using the 10.0a version of CIVA software is not capable of modeling the wear, as represented in FIGURE 5, but only cylindrical shaped defects, as represented in FIGURE 6.

Therefore, CIVA has not been used to study the effect of influential parameters, only for the cross-validation of C3D in the cylindrical configurations.

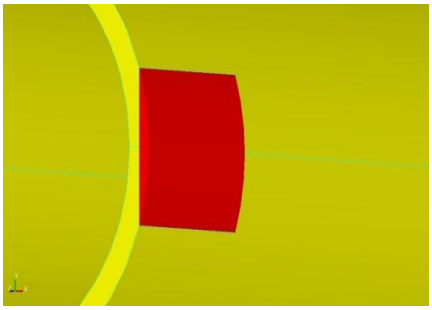

FIGURE 5. Target defect shape : flat wear – SALOME picture

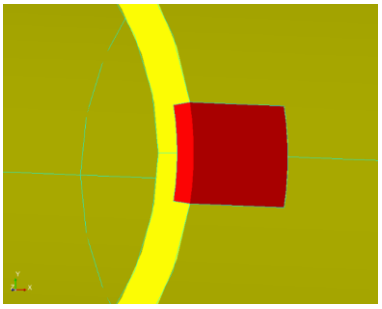

FIGURE 6. Cylindrical shaped defect – SALOME picture

VALIDATION OF THE CODES

The purpose of this section is to illustrate the reliability and performance demonstration of C3D to model the detection of wear using the SAX. C3D has been tested on different configurations and the results have been compared to experimental measurements and / or CIVA results.

1st Step: Simple Shaped Defects

Comparisons between simulation and experimental data have been carried out ([7]) on a set of "simple" shape defects, as represented in FIGURE 7. The defects are considered as "simple" from an experimental point of view: they are easy to machine. They consist of 360° circular notches or grooves with varying depths or axial lengths. Therefore, they are convenient for acquisitions on SG tube mock-ups, and often chosen for that purpose. The experimental data were defined on the base of a statistical exploitation (RMS and standard deviation) of approximately 90 EC measurements for each defect. Comparisons between simulation and experimental data reveal good agreement for both codes, CIVA and C3D. An example of comparisons of the EC signals magnitudes on internal circular notches with different widths from 20% to 80% of the wall thickness, on a 22,22mm tube mock-up, at 240 kHz in differential mode, is given in **FIGURE 8**. Therefore it can be considered that numerical approach is valid for such simple defects.

FIGURE 7 : 360° circular notch - using CIVA ET

However, the shape of those defects is very different from the shape of AVB-to-tube contact wear (FIGURE 5). It is for this reason that the ability of the models to take into account the actual defect shape has to be studied.

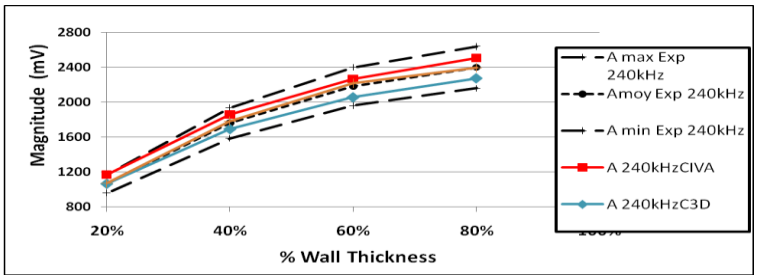

FIGURE 8: Example of comparisons of EC signals magnitudes, obtained with C3D and CIVA, and compared with the statistical exploitation of experimental data

2nd Step: Cross comparisons on more realistic defects

As the 10.0a version of CIVA only allows the user to model cylindrical shaped defects, two types of cylindrical defects approaching the flat wear type defect have been defined in [9]. Computations are performed using C3D and CIVA on 6 defects of varying volumes, corresponding to those of the flat wear. Comparisons reveal good agreement between CIVA and C3D.

These results enable cross-validation of the models on configurations close to the actual NDE configuration.

3rd Step: Comparing with Experimental Data on representative defects

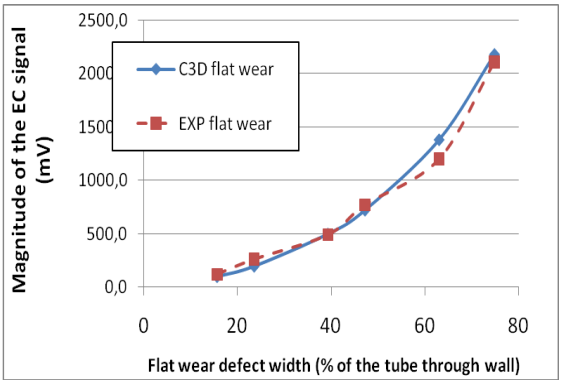

FIGURE 9 : Magnitudes of flat wear defects, obtained with C3D and by experiment

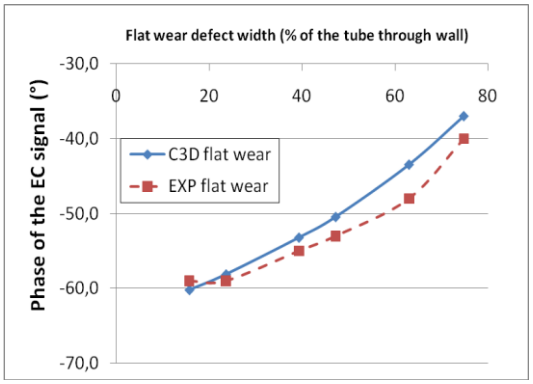

FIGURE 10 : Phases of flat wear defects, obtained with C3D and by experiment

FIGURE 9 and FIGURE 10 show the EC signal amplitudes and phases of flat wear, with depths varying from 15 to 75%, obtained with C3D and from experimental data. Quantitatively, the disparity between C3D results and experimental data is about 11,7% in magnitude (average value of the 6 considered defects) and around 2,3° in phase.

These results validate the numerical approach for both codes. FEM software was chosen for the remainder study because it is more suited to 3D configurations.

STUDY OF INFLUENTIAL PARAMETERS

The study of two influential parameters will be presented here: the AVB's constitutive material and the angle between AVB and tube. In both cases, the AVB has a square section of 7,9 x 7,9 mm. The tube features a 40% depth flat wear just below the AVB and the AVB relative position to the tube is chosen so that it would be in contact with the tube if there were no wear, that is to say that the distance between the AVB and the back of the wear is equal to the depth of the wear, as represented on FIGURE 10. The effect of the distance between AVB and tube on the EC signal was presented in [8]. The nominal chosen angle between the tube and the AVB is 90° and is represented in FIGURE 12.

AVB material

Depending on the SG model, AVB are made of inox, or of alloy 600 with a 15µm- or 30µm-thick chrome layer. The C3D simulation provides visualization of the effect of the AVB material on the EC signal. FIGURE 14 compares the impedance plane diagrams of a 40% depth external wear in the presence of a rectangular cross-section AVB. Three types of the AVB material are considered: alloy600 – based AVB, alloy 600-based AVB with a 30µm-thick chrome layer, and inox AVB. Alloy 600-based AVB is never used in steam generators, but this configuration gives a reference result and enables a better understanding of the effect of the thin chrome layer. The finite element mesh used to analyze the AVB material effect is illustrated in FIGURE 12.

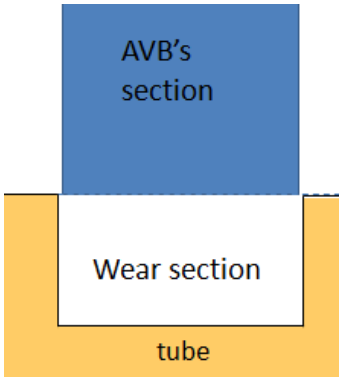

FIGURE 11: AVB's position relative to the tube, 2D section

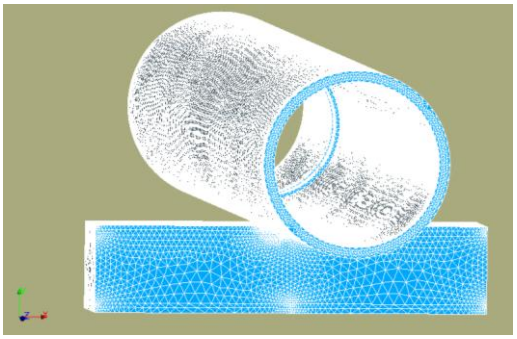

FIGURE 12 : AVB's position relative to the tube, 3D view (obtained with Salomé)

Regarding the 30µm-thick chrome layer, the model of the thin conducting sheet is based on so-called "Impedance Transmission Conditions". The implementation in C3D and the validation of this approach is described in [9].

The 15µm-thick chrome layer was not considered, because the 30µm-thick layer has a stronger effect than the 15µm-thick, but the Impedance Transmission Conditions is adapted to this configuration.

The TABLE 1 provides the EC signal values for three AVB materials. It can be concluded that there is a difference of approximately 4% between the chrome layer on the alloy600 – based AVB and inox AVB on the Y projection and the magnitude, and less than 1 degree on the phase.

TABLE 1 : Quantitative comparisons on EC signals depending on the AVB material

	YF2 (V)	Magnitude (V)	Phase (°)
Alloy 600	0,68	0,68	-89,12
Alloy 600 + chrome layer	0,65	0,65	-89,20
Inox	0,67	0,67	-90,28

Orientation of the AVB relative to tube axis

As can be seen from the schematic representation of a tube bundle and AVB's on FIGURE 2, the angle between the AVB and the tube axis is not always the same; it depends on the row of the tube and of the AVB. As a first approximation, and for simplicity reasons, the results above were obtained for an angle of 90°. But it is necessary to evaluate the effect on the EC signal considering another angle value.

The angle between the AVB and tube axis was set to 75°, as represented in FIGURE 13, to test the modification of the electromagnetic interactions with a change in the angle.

The impedance plane curves results for 90° and 75° inox AVB are compared in FIGURE 15. The quantitative values of the Y projection, magnitude and phase are reported in TABLE 2, and it is concluded a difference of less than 3% between the two angles, and less than 1 degree on the phase, that is to say it has a very low influence.

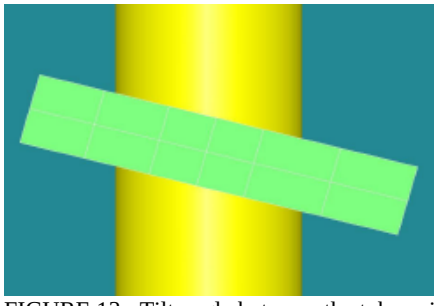

FIGURE 13 : Tilt angle between the tube axis and the AVB main axis

TABLE 2: Quantitative comparisons on EC signals depending on the AVB - tube angle

	YF2 (V)	Magnitude (V)	Phase (°)
Inox AVB - 90°	0,67	0,67	-90,3
Inox AVB - 75°	0,66	0,66	-88,9

CONCLUSION

Simulation tools use represents an interesting alternative for EC ND technique inspection performance demonstration, but the reliability and performance demonstration of these tools have first to be assessed. The present work focuses on the detection of wears, which can be caused by AVB's fretting in the U-shape region of SG tubes, with an axial EC probe.

Simulation of this application with the presence of the AVB requires the use of 3D FEM software. Code_Carmel3D was assessed by cross comparisons with CIVA, and compared with experimental data, obtained on configurations very close to the target configuration. This reveals a good agreement between both models and experimental data.

Finally, the effect of two influential parameters was studied: the different AVB's materials used on French nuclear plants are taken into account, and a variation of the angle between the tube and AVB is considered. The effect of these both parameters on the EC signal is very low.

A lot of influential parameters have been studied in 2012 and Code_Carmel3D proves its efficiency to take them into account. Results will be used with a view to demonstrate performance of the detection of wear under AVB. This strategy will be extended to other EC NDE applications.

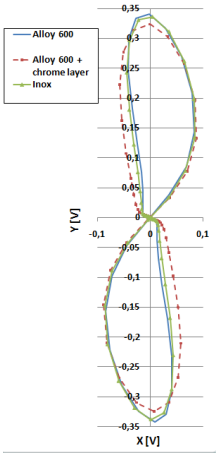

FIGURE 14 : Plane impedance diagrams of EC responses of a 40% depth external flat wear in presence of the AVB.

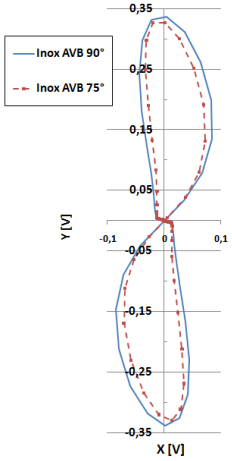

FIGURE 15 : Impedance plane curves of EC signals, obtained with an inox AVB, for two AVB-tube angles

REFERENCES

[1] Mayos M., Moreau O., Dupond O., Schumm A., "The use of modeling in support to NDE qualifications", Zagreb, IAEA Symposium on RI Inspection for Integrity of System Structure and Components through Advanced ISI/NDE Technologies, 2011, pp. 11-14.

[2] AFCEN, Règles de Surveillance en Exploitation des Matériels Mécaniques des Ilots Nucléaires REP, AFCEN, 2010, Annexe 2, 4.3.

[3] ENIQ, ENIQ Recommended Practice 6: the Use of Modeling in Inspection Qualification, ENIQ report No. 45, vol. 6, 2nd issue, 2011.

[4] Mayos M., Lambert M., Gilles-Pascaud C., Dessendre C., Dominguez N., Foucher F., Abakar A., "COFREND Working Group on eddy current NDE simulation - Review of activities", Journées COFREND 2008, Toulouse, May 2008.

[5] http://www.salome-platform.org/

[6] http://www.extende.com/

[7] Maurice L., Costan V., Guillot E., Thomas P., "Comparaison de modèles numériques pour le calcul d'interactions électromagnétiques : application aux examens non destructifs par courants de Foucault pour l'industrie nucléaire", Numelec 2012, 2012, pp. 178-179.

[8] Maurice L., Costan V., Guillot E., Thomas P., « EDDY CURRENT NDE PERFORMANCE DEMONSTRATIONS USING SIMULATION TOOLS", AIP, 1511, Review of Progress in Quantitative Non Destructive Evaluation, Volume32, Denver, Colorado, USA, 15-20 July 2012, Vol. 32A, pp 464-471

[9] T. Abboud, F. Béreux, N. Béreux, V. Costan, "Thin Conducting Sheet (TCS) in non-destructive testing simulations: implementation in Code_Carmel3D and validation", Compumag 2013.

THE USE AND VALIDATION OF THE OPERA SIMULATOR FOR EDDY CURRENT SIMULATION MODELLING

J. Taggart, A. Kyrieleis AMEC, UK

Abstract

OPERA-3D is a finite-element simulator for representing electrical and magnetic fields, and associated circuits, and in the UK is vended by Cobham Ltd. As it has a general geometric capability, and a wide range of coil types can be represented, it can readily be used to model eddy current applications.

A number of different eddy current applications have been modelled by AMEC in support of inspection design and qualification in a varied set of industrial applications, comprising inspections and tests on steel, graphite, and aluminium components, and examples are detailed. For steel inspections, most models have been of austenitic (non-ferromagnetic) steel, but some modelling of ferritic steel applications has also been carried out. Both conventional eddy current and ACFM applications have been modelled.

It is important to confirm the validity of eddy current loci resulting from OPERA simulations. Accordingly, comparisons between experimental test and simulated loci have been made for several applications, and examples are given here. The comparisons indicate reasonable to good agreement between test and simulation. Contributing factors to the differences include material property variations, and the representation of test loci processing.

1. Introduction

In the nuclear industry, eddy current inspections are carried out on a number of plant components. It is desirable in designing and analysing these inspections to simulate the responses of eddy current probes to defects and other features. This can be done readily using a numerical simulator of electromagnetic fields and electrical circuits. The finite element simulator OPERA-3D [1] has been used in this respect for a number of years by NDE staff at AMEC (previously Serco).

In this paper, the use and validation of OPERA-3D in simulating eddy current probe responses are described. In Section 2, the method for representing eddy current probe response using OPERA is outlined. Some examples of its use by AMEC for different inspected materials are given in Section 3. A discussion of its development in this respect is given in Section 4, and conclusions are stated in Section 5.

2. The representation of eddy current probe response using OPERA

2.1. General

In this section, the general method for simulating eddy current probe response, representing what is obtained in an inspection scenario is described. In most cases the OPERA simulator has been used to represent inspections of non ferromagnetic materials, in which the relationship of magnetic flux density (B) to magnetic field strength (H) is linear, i.e.:

$$B = \mu_r \mu_0 H \,, \qquad (1)$$

where

μ_r is the relative magnetic permeability of the component, and is effectively constant, and

μ_0 is the magnetic permeability of free space.

This linearity has the consequence that the magnetic (B) and electric fields (E) in the component have a time dependence that is the same as that of the current in the eddy current coils:

$$B(t), E(t) \propto \cos(2\pi f t), \qquad (2)$$

where

f is the frequency of the coil excitation current.

This means that explicit time dependence of the field variables does not need to be modelled, in turn meaning that a quasi-steady-state solution (space-dependent only) is possible, significantly reducing simulation time relative to a full time-dependent solution.

2.2. Geometry

Geometrically, an OPERA eddy current simulation model always comprises a component, one or more eddy current coils, and a surrounding air box. A typical model geometry is illustrated in Figure 1.

The component geometry is created by combining simple geometrical shapes (boxes, cylinders, etc). More complex geometrical features can be obtained by specifying a surface and a path along which it is to be swept in order to define a volume.

Probes are represented by modelling their constituent coil(s). Most commonly, solenoidal coils are modelled, as in Figure 1. However, other coil shapes, such as saddle coils, can readily be represented.

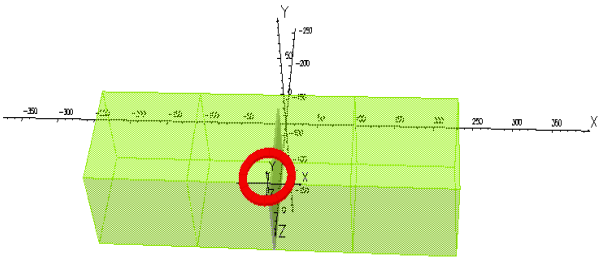

Figure 1. Typical OPERA eddy current model

2.3. Material properties

Each component material is specified by its electrical conductivity and relative magnetic permeability. Values can be specified along each of the Cartesian axes, enabling representation of anisotropic materials.

2.4. Element specifications

OPERA offers a powerful meshing engine producing tetrahedral and prism-shaped elements. Typically, the maximum element size is specified in sub-volumes of the model (though also to ensure the element dimensions are fine enough to capture the geometrical details of the model and large variations in field variables. The elements created by OPERA smoothly vary between the sizes set by the user in the sub-volumes. In this way the elements are fine enough to describe detail where needed, but the number of cells and hence the computation effort is kept to a minimum. Nevertheless, a typical number of elements in a simulation ranges from about one to five million. Typically, the run time for such simulations is in the region of 10 minutes on a current desktop PC

2.5. Boundary conditions

Boundary conditions on either the electric field or the magnetic flux density have to be set on outside surfaces in order to fully define the simulation. The most common boundary conditions set either the electric or magnetic field vectors to be normal or parallel to an outside surface, usually of the surrounding air box – Section 2.2. In the case of effectively symmetric models, the simulation effort can be significantly reduced by modelling only a (symmetric) fraction of the model and imposing normal electric boundary conditions at the cut surface.

2.6. Calculation of impedance plane components

Evaluation of normalised coil impedance components, inductive and resistive, at a given frequency, is carried out by calculating (in OPERA) the total energy (E) and power losses (P) in the model at the frequency f, and comparing with the energy at 0Hz (E_0). The reactance X and resistance R are given by:

$$X = 2\frac{E}{E_0}$$
$$R = \frac{1}{2\pi f}\frac{P}{E_0} \qquad (3)$$

2.7. Validation of simulation models

The validation of OPERA is based on loci from scans of known slots or defects. The loci are either directly compared (see Section 3.1.1) or the phases of the loci with respect to e.g. the lift-off locus are compared. Loci are produced by running OPERA simulations for a set of probe positions. The possibility to write scripts in OPERA has been of great use in automating the calculation of loci. A script has been written that moves the probe by a certain amount and re-runs the case. Another script extracts the power and energy values from all cases. In this way a locus can be obtained simply by executing two scripts, in contrast to the manual set up and execution for each point on the locus.

3. Application examples

Simulation models have been constructed and comparisons made with test results, for several different component materials. Here, examples are given for graphite, stainless steel and aluminium components, spanning a range of electrical conductivities from about one tenth to about ten times that of stainless steel.

3.1. AGR graphite inspections

3.1.1. AGR graphite bricks

Eddy current measurements have been carried out on virgin AGR bricks (resistivity 10μΩm) with machined slots using a 70mm absolute probe in a bridge configuration. Zetec TC 5700 and MS5800 instruments have been used for the measurements. In OPERA, a 180° brick sector of axial extent was modelled to limit the number of elements. This extent was found to be sufficient to represent the magnetic and electric fields of the coil, while using a number of elements that is small enough to be practical. Typical model geometry is illustrated in Figure 2.

For the comparison of simulation and experiment, scans over slots extending 50% and 74% of the distance from the keyway base to the bore have been used (see Figure).

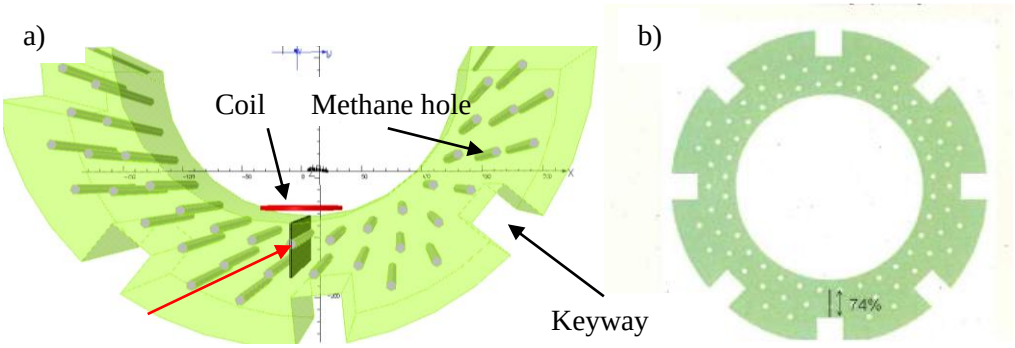

Figure 2. a) AGR Brick as modelled in OPERA, b) defect considered in comparison of experiment and simulation. The slot extends to 74% (shown) and 50% of the brick wall.

The loci obtained from the TC5700 or MS5800 system are dependent on the instrument drive voltage and gain settings as well as on certain delays which cause rotation of the display. A method of orienting and normalising a measured defect locus was therefore used to enable

comparison with the modelled loci in the normalised impedance plane. This is illustrated schematically in Figure 3.

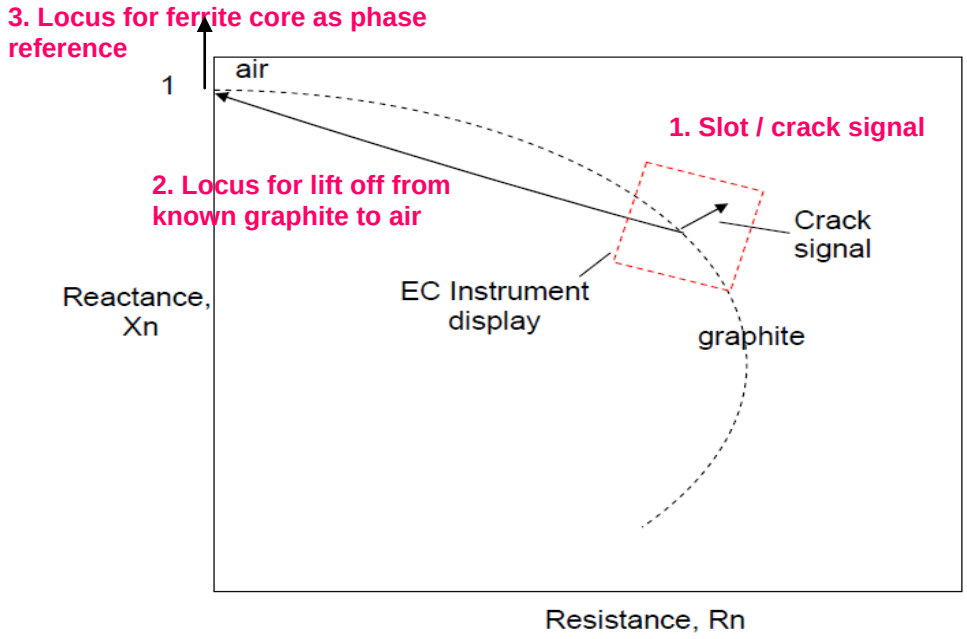

Figure 3. Schematic of method for mapping a measured locus onto a normalised impedance plane

The measured slot / crack signal is shown (Step 1). In order to normalise the measured locus, two approaches have been used. In the first approach, the measured loci (at one frequency) have been scaled so that the sizes of the measured and the modelled lift-off loci are the same (Step 2). To orient the measured lift off locus, a measurement with a ferrite core was made (Step 3). Ferrite can be considered to have essentially infinite resistivity but a large magnetic permeability. The signal locus caused by approach from the air point to the ferrite is therefore presumed to increase the reactive (inductive) component of the coil impedance and not affect the resistive part of the impedance. The direction of this locus is set to be vertically up in the normalised impedance plane. In this way the direction of a measured locus is translated to the direction in the normalised impedance plane.
Using this way of normalisation, good agreement (i.e. to within about 10% on amplitude and phase) between model and experiment has been achieved for slot extensions of 50% and 74% at 4kHz (Figure 4), corresponding to a skin depth of about 20mm. It was noted that it was important to represent the resistivity of the brick reasonably accurately in the simulations.

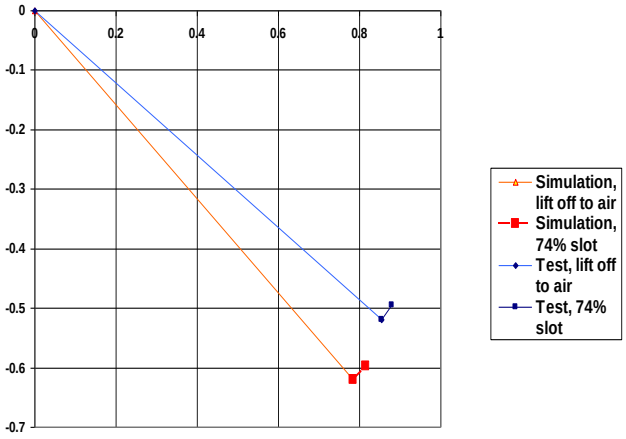

Figure 4. Measured and simulated loci for graphite (Ring X, 74% slot).

An alternative way to scale the measured loci has been developed. Accurate impedance measurements have been taken at single points on the two blocks for different frequencies. The modelled normalised impedance is compared to the experimental signal at each frequency and the ratio between the two calculated for both components (horizontal and vertical).The mean ratio is used as a scaling factor to apply to the experimental defect loci, so that they can be plotted on the impedance plane with the modelled data.

Using the same brick model as before, a range of other defects has been modelled (Figure 5). These results can be used to discern defects based on measured loci. The advantage of the OPERA software lies in the possibility to extrapolate and to make predictions for various defects based on the validation of the model using limited experimental data.

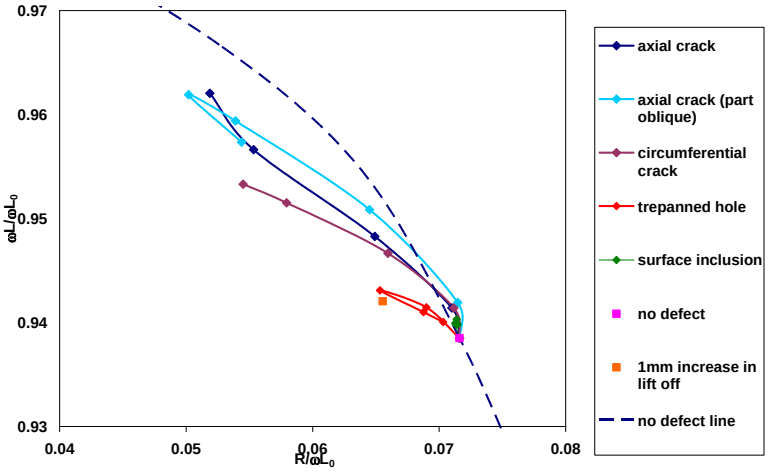

Figure 5. Simulated loci for various defects in graphite at 4kHz and a resistivity of 10μΩm.

3.2.1 Graphite block scans

Measurements of sub-surface slot loci on two graphite blocks of resistivities 10μΩm and 35 μΩm were carried out using a similar probe to that used for the graphite brick measurements (Section 3.1.1). An OPERA model of the block was constructed, and comparisons of the phase of the locus of each slot, relative to the lift off locus were made (an absolute comparison of loci, as in Section 3.1.1, was not made, as ferrite data were not available). These showed reasonable to good agreement.

3.2. Steel inspection examples

It is important to validate the use of OPERA for eddy current inspections of stainless steel components. Several inspections on stainless steel have been modelled by AMEC.

A relevant example of a comparison between measured and simulated data is that of the response of a pencil probe to a shallow slot in a stainless steel block. The probe contained a pancake coil 2mm in diameter and was operated at a frequency of 1MHz; the slot was 1mm in through wall extent, which compares with the skin depth of about 0.5mm at this frequency. This comparison was made to support measurements using such a probe on shallow cracks in a plant component.

In Figure 6 are shown the measured and simulated loci for the slot, together with the lift off locus. The measured loci have been normalised to the phase of the simulated lift off locus (an absolute comparison of loci, as in Section 3.1.1, was not made).

It can be seen that the relative phases of the measured loci (32°) and simulated loci (26°) are in reasonable agreement. Other similar comparisons using this block and probe also showed reasonable agreement.

OPERA validation data for stainless steel components are relatively sparse, so that further comparisons are sought. It is noted that design simulations (without direct comparisons) have been undertaken for surface defects in one stainless steel component; these effectively indicated a suitable probe size and frequency to be used for an inspection of this component.

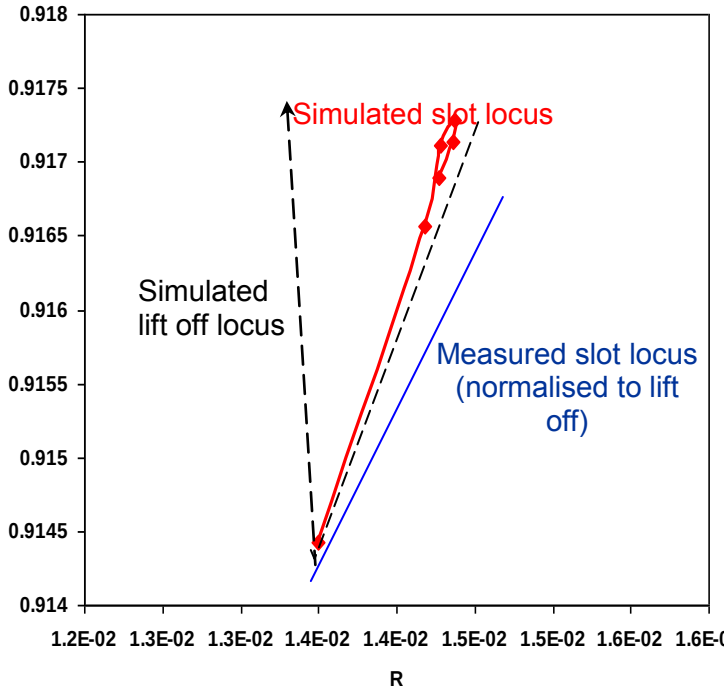

Figure 6. Measured and simulated loci of a shallow slot in a stainless steel block, using a small pencil probe

3.3. Aluminium test block example

A comparison with a literature example of measured eddy current data for aluminium was made. The response of a 25mm pancake absolute eddy current probe over a 5mm surface slot in an aluminium plate of thickness 12mm, at a frequency of 900Hz (giving a skin depth of about 5mm) was detailed in [3]. An OPERA model was constructed of this situation. Comparisons were made of the inductive and resistive components of the probe impedance, and example results are shown in Figure 7. The plot shows changes in impedance relative to that for the probe situated distant from the slot. For all of the points, agreement to within about 10% of total impedance change was observed.

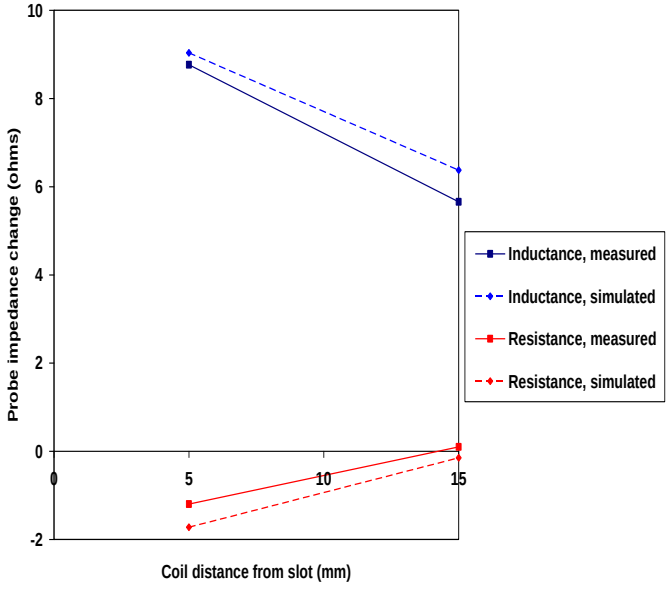

Figure 7. Measured and simulated impedance changes for a pancake probe near an aluminium slot

3.4. Other applications

The OPERA simulator has also been used for other electromagnetic inspection types. These include ACFM (alternating current field measurement), and MPI (magnetic particle inspection), with reasonable success. For the MPI application, difficulty with long run times was experienced, arising from the need to represent a non-linear magnetic flux density against magnetic field strength relation, for a ferromagnetic material.

4. Discussion

The OPERA simulator has been used for a range of eddy current inspection situations, and it is clearly a practical tool in representing such situations, particularly for non ferromagnetic materials.

Validation evidence has been obtained for different component materials, covering conductivities from about $1*10^5$S/m to $1*10^7$S/m. Comparisons between measurement and simulation have been made in different ways. A method for comparing absolute loci has been worked out (Section 3.1.1), and used in one set of examples on graphite components. More commonly, comparisons between relative phases and / or amplitudes have been made (Sections 3.1.2 and 3.2), and these do not require additional measurements with a ferrite core.

The agreement between measurement and simulation has generally been reasonable to good, at about 10-20% difference between measurement and simulation. Differences can be attributed to the specification of component resistivity, imprecisions in lift off, and coil geometry and position. Considering a combination of likely errors (perhaps 5-10%) from each of these sources, the typical error in locus amplitude and / or phase is likely to be at least 10%. The results therefore give an indication that the probe response is modelled with reasonable accurately in the cases given.

Notwithstanding these examples, the validation base for OPERA-3D for eddy current inspection is limited. In particular, for nuclear applications, data on stainless steel for a range of probe sizes and frequencies would be useful.

5. Conclusions

The following conclusions can be made on the use and validation of OPERA-3D in modelling eddy current inspections:

- The simulator is a practical tool for inspections in non-ferromagnetic materials, and inspection scenarios can be readily set up and run.
- Validation evidence, with reasonable to good agreement between measurement and simulation, has been obtained for inspections of graphite, stainless steel, and aluminium components. However, more evidence, particularly for stainless steel, is desirable. The quality of agreement indicates that reasonably accurate models of the inspection have been constructed.
- Simulation models for non-ferromagnetic materials have much longer run times than those for non ferromagnetic materials.

References

1. OPERA-3D, Cobham Limited, www.cobham.com.
2. J. Taggart, T. Bloodworth, M. Brown, Simulation modelling of eddy current measurements on AGR graphite bricks, Paper No. NDT-0084-2010-JT, BINDT Conference, Cardiff UK, 2010.
3. S.K. Burke, Eddy current inversion in the thin skin limit: determination of depth and crack opening for a long crack, Journal of Applied Physics, 76 (5), pp. 3072-3080, 1994.

MODELLING (T6/T6.1) II

A MODELING APPROACH TO OPTIMISE IP RESPONSE FOR LARGE WALL THICKNESSES

A. Schumm, EDF - R&D, France
D. Tisseur, CEA - LIST, France
F. Mathy, CEA - LETI, France

ABSTRACT

Computed radiography (CR) using imaging plates (IP) have widely replaced film radiography in the medical domain, and is gaining momentum in NDE applications. For nuclear NDE, however, the application of imaging plates is still limited to small and intermediate wall thicknesses, mainly due to the strongly marked sensitivity to scattered radiation.

Computer modeling should allow to better understand the current limitations of industrial radiography using imaging plates, and to optimize operating procedure for inspection situations. We present a modeling approach using a cascade model for the IP response and the digital read-out of the imaging plate, which helped to understand why the transition from silver film to imaging plates is difficult, and which can potentially help to design an adapted stack of filters and intensifying screens.

1. INTRODUCTION

Photographic film is still the most widely used detection technique in industrial radiography, and as such is considered to be the reference detector other techniques have to be compared with. Digital detectors, on the other hand, promise a number of advantages in terms of handling, exposure and total turnaround-time, cost, radiation hazards etc, and have shown to be very successful in medical applications, where they replaced photographic film almost entirely.

Of all available options, imaging plates (IP) appear as the most direct replacement for photographic films, because of their similar handling, replacing the photographic film by an IP made of a photostimulable layer, but keeping the rest of the equipment. The flexibility of the imaging plate makes it particularly attractive for piping applications, since it can be wrapped around a weld like traditional film. After exposure the IP is read by a scanner using photostimulated luminescence, providing a digital image to the user.

However, the quality and productivity gains reported from the medical field after the introduction of imaging plates have for some reason not yet been transferred to industrial radiography applications. We understand that the reason for this difficulty lies in the different energy ranges used in medical and industrial radiography, highlighting the need for a careful choice of operating conditions: We can not apply the same source/filter/intensifying screens combinations as in conventional radiography.

Should not computer modeling play a key role in implementing imaging plates as a replacement detector for traditional photographic films? It seems a given that the NDT community would benefit from a simulation tool for computed radiography, for applications such as inspection procedure definition and validation, performance demonstration, POD etc.

2. STUDYING THE DETECTOR RESPONSE

Based on the observation that imaging plates show reasonably good results on lower energy sources and correspondingly small wall thicknesses, and decrease in performance with increasing wall thicknesses and increasing source energy, CEA-LETI and EDF collaborated on a prospective study to better understand the difficulties encountered in the application of imaging plates in industrial radiography. To that end, CEA-LETI developed a model based on the Monte-Carlo code Penelope [1], modeling the response of an imaging plate in terms of deposited energy for a given incident radiation beam.

In this model, a certain number of assumptions are necessary to model the imaging plate stack with the substrate material, the active phosphor layer and the protective layer, both in terms of thickness and in terms of material composition, as shown schematically in figure 1. In this study, a high resolution and a high sensitivity IP were modeled, using different densities of BaFBr:Eu2+ for the active layer with 70-100mg/cm2 for HS screens and 40-50mg/cm2 for HR screens, knowing that the thickness of the phosphor layer determines sensitivity and spatial resolution (see figure 1). Furthermore, an optional metal screen could be modeled on top of the protective layer.

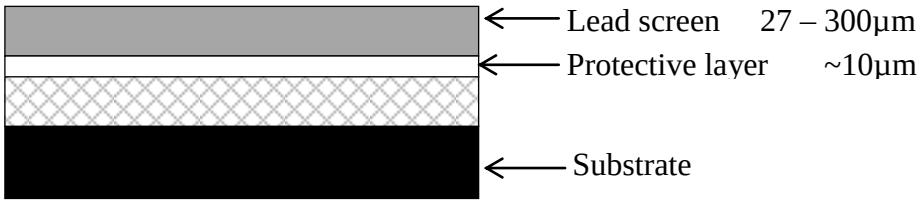

Figure 1 : Image plate modeling

The Penelope Monte-Carlo code used for this study simulates photon interaction with matter, as well as the propagation of electrons produced by photoelectric absorption or Compton scattering, and also models the related effects of Bremsstrahlung and fluorescence. In order to determine the detector response, a monochromatic pencil beam with normal incidence to the IP is modeled and propagated across the material stack, taking due account of scattering and electron production and propagation (see figure 2).

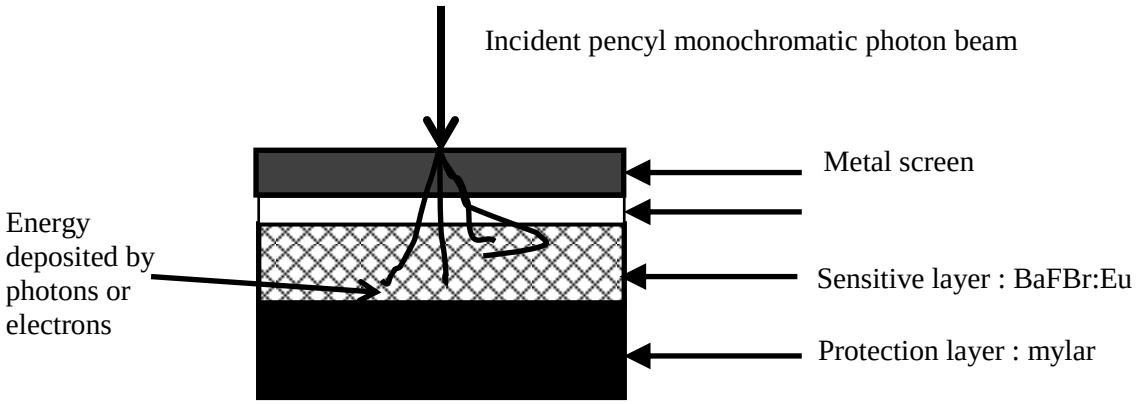

Figure 2 : Penelope setup modeling

The actual detector response is accounted for in terms of energy deposit in the phosphor layer, and a linear relationship between deposited energy and gray level after read-out is supposed, which in itself is an approximation. By scanning the entire energy range, it is possible to obtain the spectral response (or quantum efficiency) of the imaging plate.

Figure 3 shows the raw IP response for different IP compositions. As expected, the iodine content modifies the spectral response for low energy, but all IPs show similar behavior at higher energies. The spectral response explains many of the difficulties encountered in industrial radiography with imaging plates: At energies used in Co and Ir-sources, the response is rather attenuated, while the peak of spectral sensitivity is located below 100keV.

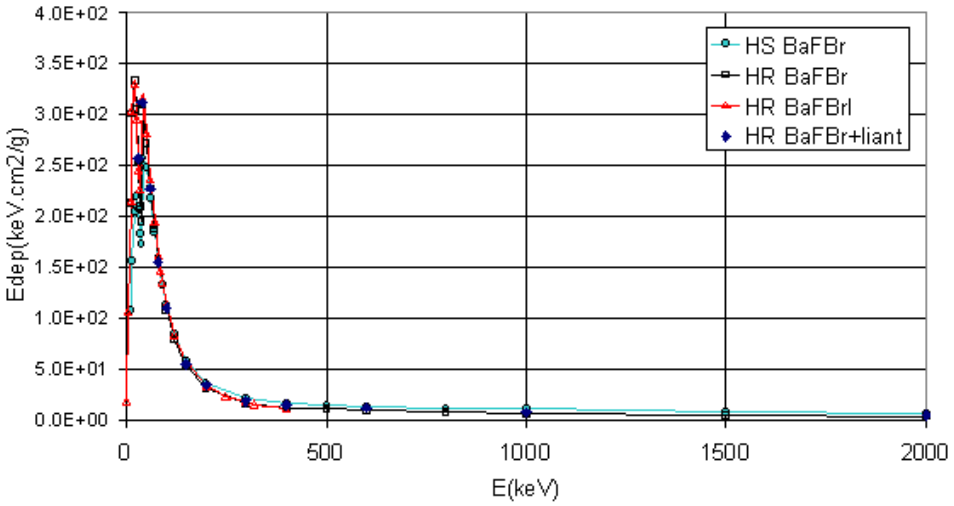

Figure 3: IP spectral response

2.1 A modeling approach: using equivalent cross section data for the spectral response

While it is not computationally feasible to use a code like Penelope to calculate an entire radiographic inspection, it is possible to use the spectral response to determine equivalent absorption coefficients, which can then be used in an engineering model to take the spectral detector response into account. Figure 4 shows the response for a number of different IP and filter combinations.

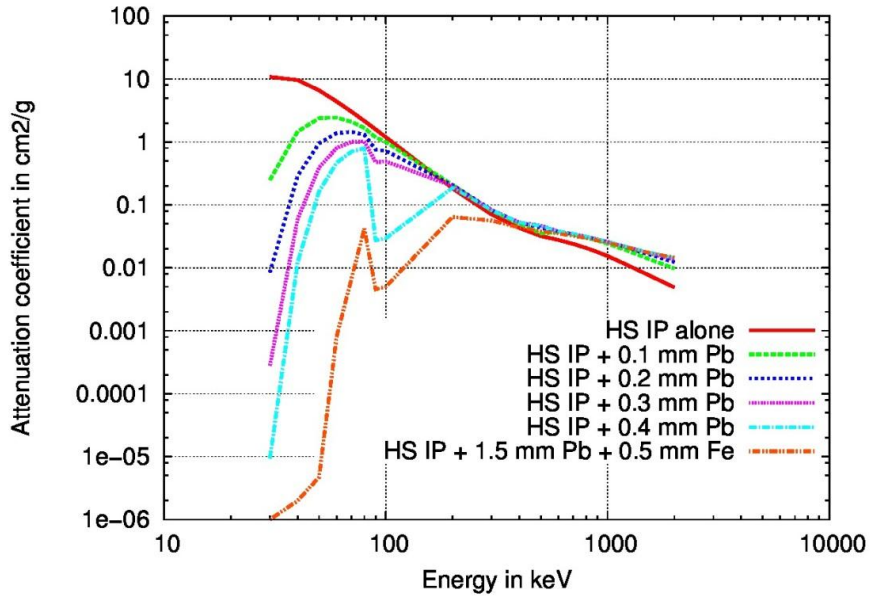

Figure 4: Attenuation coefficient for different IP/filter combinations

This figure shows that by choosing the appropriate filter, the response curve can be “tweaked” to be less sensitive at lower energies, where scattered radiation is likely to mask image details.
An interesting observation can be made for the sandwich filter of 1.5mm lead and 0.5mm steel, where a significant part of the fluorescence produced by the lead screen is filtered by the steel layer. It is important to keep in mind that an engineering model using tabulated cross section data obtained using a Monte Carlo model requires an IP stack characterization for each IP/filter combination.

2.2 Modeling spatial resolution

The spatial resolution of imaging plates is limited by two effects, namely the propagation of scattered photons/electrons within the IP and the optical scattering during the readout process. The MC model provides the information on intrinsic unsharpness due to particle scattering, which is in fact the same effect that also is responsible for inherent unsharpness in photographic film. The model does not, however, handle the unsharpness introduced by optical scattering during the readout process in the scanner. A comparison of our results with MTF data (Modulation Transfer Funtions) provided by manufacturers showed that the optical scattering dominates the MTF in most cases. A different approach was therefore necessary to model spatial resolution in the CIVA implementation of our model. Figure 5 shows experimentally obtained MTF data.

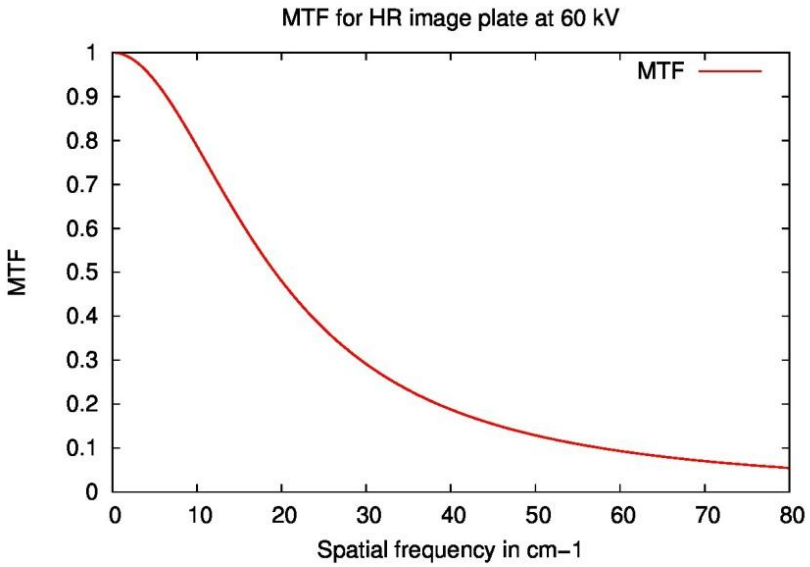

Figure 5: Experimental MTF data

2.2 Modeling noise

In this model we use a global noise of the detection system [2]. We compute the standard deviation of the global noise versus the gain (G), the variance image (σ_{Eabs}) and the Detection Quantum Efficiency (DQE):

$$\sigma^2_{signal} = G^2.(\frac{\sigma^2_{E_{abs}}}{DQE})$$

The DQE takes into account all phenomena:

- photonic noise
- noise of the detection of the radiographic inspection parameters

3. The IP model in CIVA and its validation

For the imaging plate detector model in CIVA [3], two types of imaging plates (Kodak HS high sensitivity and HR high resolution) were characterized using the Monte Carlo approach just described. For each plate, the IP alone without any filter and a range of lead filters between 0.1mm and 0.4mm were characterized and the tabulated absorption coefficients implemented into CIVA. A further characterization concerns the filter stack of 1.5mm lead and 0.5mm of steel. The model was validated using Durr and GE scanners, using the following parameters in the experiments and the simulation:
- Ir192 source 3x3mm
- Source-detector distance 500mm
- Ferritic steel step wedge with 7 different thicknesses (4 to 18mm)
- 0.2mm Pb + HR Kodak IP
- Dürr NDT CR35 scanner with 50 µm pixel size

Figure 6 summarizes the validation setup.

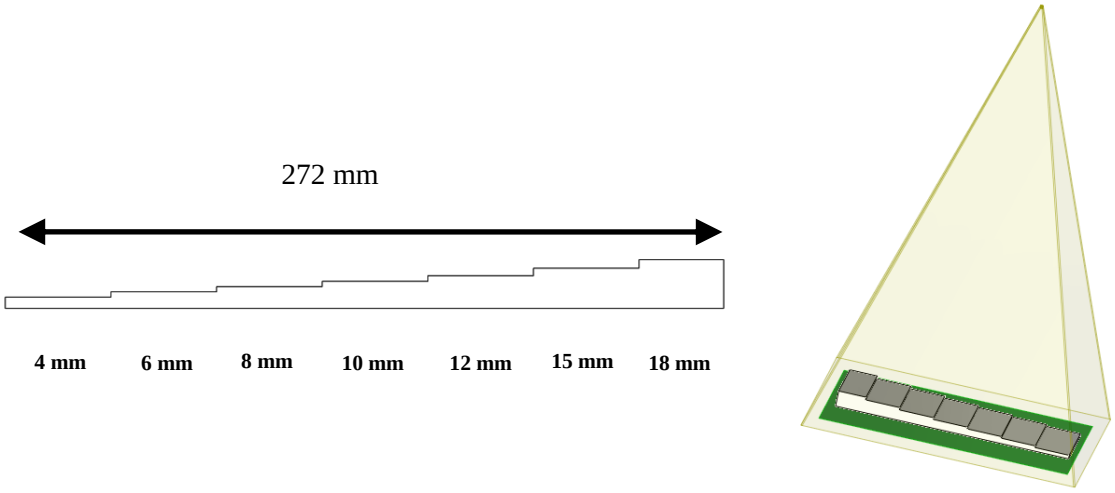

Figure 6: Validation setup with ferritic steel step wedge.

Figure 7 shows the gray value profile obtained in the experiment and the simulation, and table 1 resumes the obtained results for gray values and signal to noise ratio and indicates the relative differences. The error is less than 5% in terms of gray level.

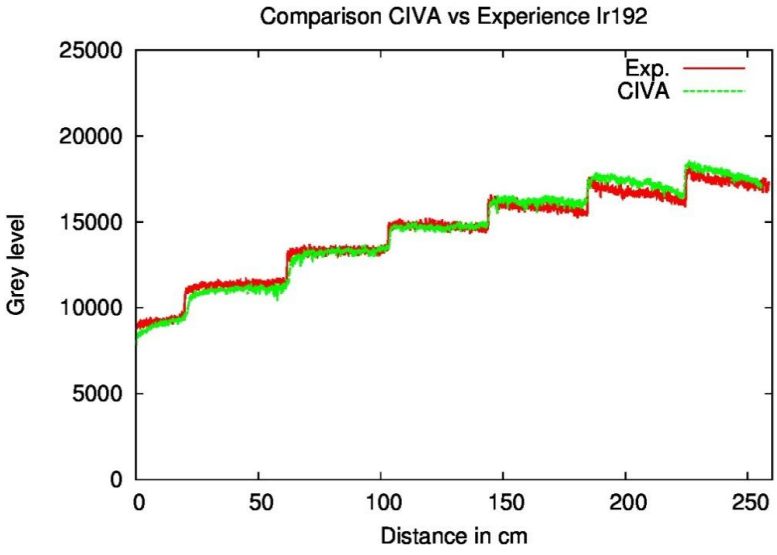

Figure 7: Gray value profiles obtained over step wedge with CIVA and experimentally

	Experimental			CIVA		
Step thickness in mm	Mean gray level	Standard deviation	SNR	Mean gray level	Standard deviation	SNR
4	17851	152	117	17365	148	117
6	17245	145	119	16470	145	114
8	16482	135	122	15891	139	114
10	14703	120	123	14760	133	111
12	13256	115	115	13304	126	106
15	11228	117	96	11322	119	95
18	9069	96	94	9089	111	82

Table 1: Gray level and SNR obtained experimentally and in the model

In order to validate the spatial resolution, duplex wires were used [4], and an excellent agreement between experiment and the model was observed (see figure 8). Since experimental MTF data was used to implement the MTF model, this was expected, however.

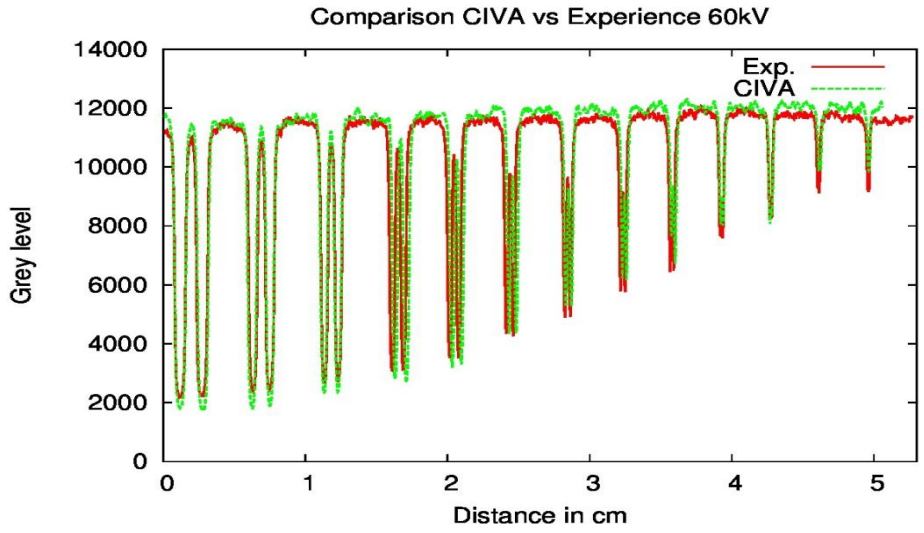

Figure 8: Validation of spatial resolution using duplex wires

3. DISCUSSION

We presented a modeling study using the Monte Carlo code PENELOPE to obtain quantum efficiency data for various IP/screen combinations. From these, equivalent materials were derived in terms of absorption coefficients and used in an engineering model implemented in CIVA. Since the Monte Carlo model only gave incomplete information on spatial resolution, not taking into account the unsharpness produced throughout the optical read-out process, we used experimentally obtained MTF data to correctly model the spatial resolution.

The study brought inside to the difficulties we have to use CR for higher wall thicknesses with high energy sources, and highlighted the necessity to carefully choose the right screen/filter combination. The first preliminary results show a good agreement between simulation and experimental data. Further characterizations for other IP/screen combinations will be added and further validations using other sources and wall thicknesses are planned.

4. REFERENCES

[1] F. Salvat, J. M. Fernandez-Varea, J. Baro, J. Sempau, "PENELOPE, an algorithm and computer code for Monte Carlo simulation of electron-photon showers," Informes Tecnicos Ciemat, 799, CIEMAT,Madrid, Spain (1996)

[2] J. Tabary, "Detector modelling report" Europen project VERDICT report 2005-154

[3] http://www-civa.cea.fr

[4] EN 462-5:1996, "Image quality of radiographs- Image quality indicators, duplex wire type", European standard for non-destructive evaluation

EXPERIMENTAL STUDY FOR THE VALIDATION OF CIVA PREDICTIONS IN TOFD INSPECTIONS

R. Raillon, G. Toullelan, M. Darmon, CEA - LIST, France
S. Lonne, EXTENDE, France

Abstract

Numerical modelling is nowadays currently used in inspection qualification process. The simulation enables to investigate a much wider range of complex cases than that obtained using only measurements. In this context the validation of the models and codes is of great importance.

A long-term validation work is being done at CEA-LIST in collaboration with EXTENDE in order to quantify the level of reliability of the predictions provided by the code and determine its range of capabilities and limitations. The validation process is based on comparisons with accurate experiments.

After first studies performed on pulse-echo techniques and previously reported for instance at ICNDE 2012 [8], we present here a validation study dedicated to TOFD techniques. Experiments have been achieved using blocks containing artificial notches. Results concerning diffraction echoes from the top edges of the notches are reported. The experimental validations are completed by considerations about hypotheses and approximations of the models, allowing to draw conclusions on their validity.

Keywords: Ultrasounds; simulation; experimental validation; CIVA, TOFD.

1. INTRODUCTION

The CIVA modules allow calculating the echoes from defects during a postulated NDT inspection [1]. The calculations are based on several semi-analytical models depending on the physical phenomena involved in the inspection [2, 3]. It is important to evaluate the level of reliability of their predictions and this can be done by considering the models (physical basis, domain of applicability and approximations made for their implementation), the list of code inputs and their values (it helps to check if the influence of the essential parameters of the inspection are taken into account by the code) and also data used to the validation of the code in similar inspection configurations (data from literature, data from other codes, experimental validation data…)

To collect experimental validation data, a long term validation work is being done at CEA-LIST for 3 years. It consists in performing comparisons between experiments and predictions of the CIVA-UT models in series of chosen inspection cases dealing with various items (responses of calibration reflectors, corner echoes of notches, echoes of the specimen geometry, obtained in pulse echo mode with mono-element or phased array probes…).

This paper comes within this validation work and presents quantitative comparisons, performed following the recommendations of ref [4], which aim at investigating the CIVA's capabilities to predict notch edge responses in TOFD mode. For brevity, only a part of the study results are presented in this paper, the whole results being available on the EXTENDE web site [5].

2. EXPERIMENTAL AND SIMULATION PROCEDURES

Specimen

The reference block, of 30mm thickness, is composed of steel and incorporates 11 artificial notches of extension 15mm and heights varying from 0.5mm to 15mm (Figure 1)

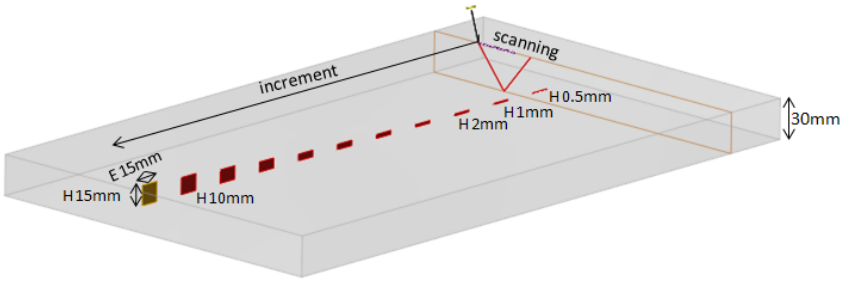

Figure 1: Steel specimen, 30 mm thickness, with back-wall breaking artificial notches of height 0.5mm, 1mm, 1.5mm, 2mm, 3mm, 4mm, 5mm, 7.5mm, 10mm, 12.5mm and 15mm (15 mm extension).

The material homogeneity was experimentally checked and the specimen material (steel) was modelled as isotropic, homogeneous and the attenuation was ignored. The longitudinal (L) and transversal (T) velocities were estimated using successive backwall echoes (V_L = 5900m.s^{-1} and V_T = 3230m.s^{-1}), the density was 7.8g.cm^{-3}.

Probes displacement

The two probes arranged in TOFD mode were moved in two directions over the notches with a scanning step of 0.2 mm and an increment step of 1mm.

Probes

Shape and wedge: the probes used were single element conventional round probes with a centre frequency of 5MHz and a diameter of 6.35mm.

Probe arrangement: two couples "transmitter-receiver" were used: one with probes mounted on wedges designed to generate longitudinal waves at 45° and another one with probes generating L waves at 60° in the specimen. Concerning the material properties of the wedges the longitudinal and transversal velocities are respectively V_L = 2730m.s^{-1} and V_T = 1340m.s^{-1} and the density is 1.18g.cm^{-3}. For each couple, the TOFD inspection of the back-wall breaking notches was performed for probe centre space "PCS" varying from 35mm to 100mm, allowing various incidence angles of the L waves on the top edge and various positions of the "L axis crossing point" (point where the L axis of the transmitter and receiver intersect) relative to that of the top edge (Figure 2).

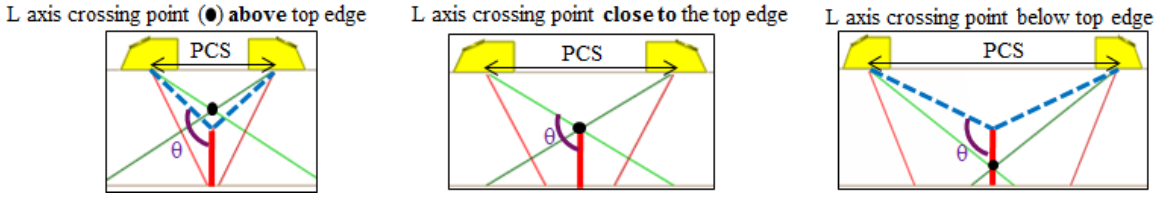

Figure 2: CIVA schematics of TOFD configurations with different PCSs, showing the variation of the L waves incident angle on the top edge of the notch (θ) and of the L axis crossing point position relative to that of the top edge with the PCS.

Calibration in pulse echo mode: the transmitter and receiver of each TOFD arrangement were used separately in a pulse echo mode to perform a calibration inspection over SDHs Ø2mm at different depths. The two experimental scanning echodynamic curves thus obtained were superimposed to check the probe resemblance in terms of sensitivity and L refraction angle. A good agreement was obtained. The refraction angle of the longitudinal waves in the specimen was estimated from this calibration: we obtained 44.5° with the wedge designed to generate L waves at 45° in the specimen and 59° with the L60° wedge. Another calibration block was used to measure the index point and the wedge height.
CIVA input signal: finally, the probe input signal was a synthetic signal generated by CIVA whose parameters (centre frequency, bandwidth and phase) were precisely adjusted so as to ensure a good matching of the experimental and simulated wave forms of a SDH Ø2mm L direct echo obtained in pulse echo mode (figure 3, case of a L60° probe).

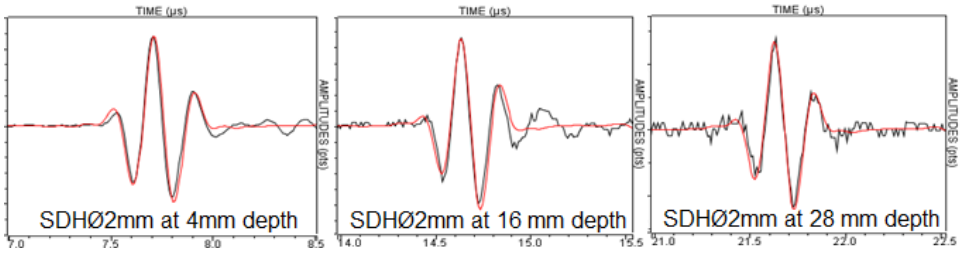

Figure 3: Superposition of measured and simulated L direct echoes of a SDH Ø2mm obtained in pulse echo mode with the L60° probe.

Artificial notches
Shape: the profile of an artificial notch provided by the manufacturer is represented in the left of Figure4.

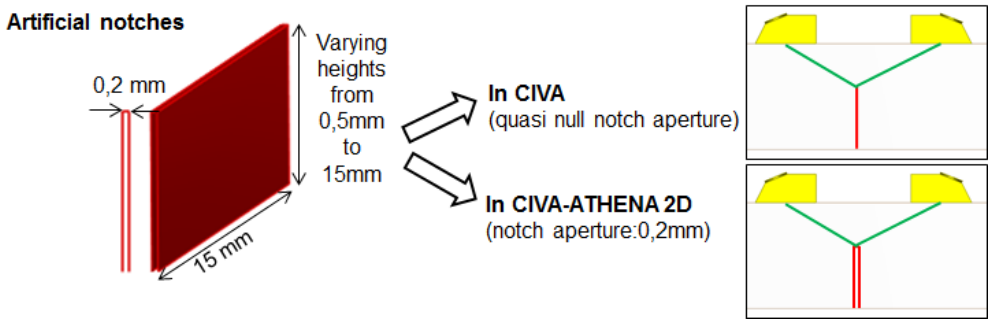

Figure 4: Shape of the artificial notches and description of the notch in CIVA and CIVA-ATHENA-2D.

Echoes studied: during the TOFD inspection the amplitude of the longitudinal top edge echo of the back-wall breaking notches were measured.
Model used to compute the L top edge echoes (TOFD mode): the appropriate model in CIVA to compute the top edge diffraction echoes is based on the GTD (Geometrical Theory of Diffraction) [6]. In this model, a quasi null aperture of the defect is assumed. This null aperture assumption is particularly well-suited for the description of a real fatigue crack but is not consistent to deal with the aperture shape of artificial notches.
Account of the notch aperture: previous studies carried out at the CEA-LIST had shown that, in the case of artificial notches, the notch aperture is an important parameter that may affect the amplitude of

the top edge echo. As such, to take this parameter into account, we have also computed the top edge echo with the module CIVA-ATHENA-2D, a hybrid module using both conventional semi-analytical methods of CIVA and the FEM (Finite Element method) code ATHENA from EDF. The connection with Finite Elements allows taking into account more complex flaw scattering phenomena that can occur during the echo formation (and not only the diffraction phenomena as the GTD does).

To illustrate the influence of the notch aperture on the longitudinal top edge echo amplitude, we have simulated in CIVA a symmetrical TOFD configuration studied by Ravenscroft [7] and using circular contact probes of 10mm diameter and 5MHz centre frequency. The amplitude of the top edge echo were compared for three configurations:

- with CIVA-2D: GTD model and notch modeled by a rectangular defect of quasi null notch aperture
- with CIVA-ATHENA 2D and notch modeled by a rectangular defect of quasi null notch aperture
- with CIVA-ATHENA 2D and notch modeled by a multi-faceted defect composed by 3 facets, two vertical and one horizontal of 0.2mm length simulating the notch aperture.

NB: In all cases, the field and the flaw interaction are computed in 2D.

The Ravenscroft configuration and the results of the 3 cases are presented Figure 4. They show that, at incident angles θ greater than 130°, the amplitude of the top edge echo is much more important in the case of the notch with the aperture of 0.2mm than in the case of that with a quasi null aperture. This difference is attributed to an additional specular echo coming from the horizontal part of the notch top. The GTD model does not compute this specular echo.

These results show the necessity to take into account the aperture of the artificial notches whose influence on the longitudinal top edge echo amplitude depends on the L waves incident angle.

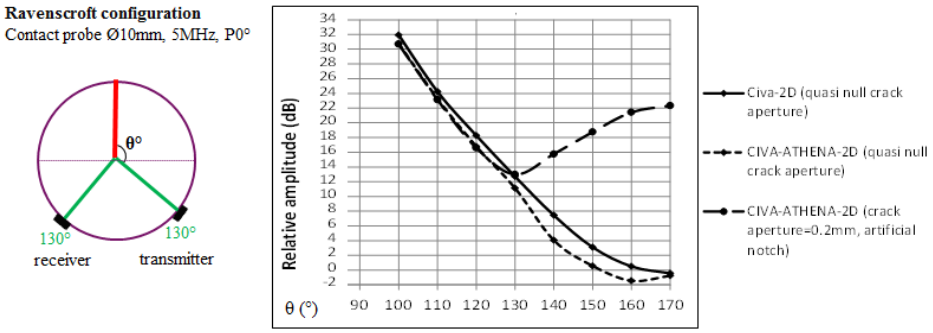

Figure 5: Left) Ravenscroft configuration modeled with CIVA. Right) simulated results.

Reference for the amplitude

The physical quantity considered for the comparisons presented in this paper is the echo amplitude. Previous experimental validation study concerning Side Drilled Holes reflectors of 2mm diameter (SDH Ø2mm) inspected in TOFD mode had showed the reliability of CIVA predictions for L direct echoes of SDHs [8]. So, the amplitude reference for all the results of the current study is the longitudinal echo of a SDH Ø2mm (precise information concerning this reference will be given for each graph).

Experimental results

A rigorous experimental protocol has been followed in order to minimize the sources of inaccuracies. The reproducibility of the results has been checked and the confidence interval of the experimental data presented in this paper has been evaluated to +/-3dB.

3. EXPERIMENTAL VALIDATION, RESULTS AND DISCUSSION

As announced above, the experimental amplitudes of the top edge echo are compared to their corresponding simulated ones obtained with the CIVA GTD model and also with the CIVA-ATHENA-2D coupling code. This last code is a "2D" code (the field and the flaw interaction are computed in 2D) and the comparison between its predictions, experiments or "3D" code predictions (GTD of CIVA) is allowed only if the "3D" aspect of the echo formation can be ignored. To check that point, all the simulated amplitudes obtained with CIVA (GTD) were compared with that obtained with CIVA-2D ("2D" code using the GTD available in CIVA). The results of these comparisons are not shown in this paper, but they demonstrate that it is fair not to consider the "3D" aspect of the echo formation in the case of the studied configurations.

On the graph presented below, we have plotted the L top edge echo amplitudes against the PCS obtained:

- 1) experimentally
- 2) with CIVA: GTD, "3D" model and notch modeled by a rectangular defect of quasi null notch aperture
- 3) with CIVA-ATHENA 2D: "2D" coupling code and notch modeled by a rectangular defect of quasi null notch aperture
- 4) with CIVA-ATHENA 2D: "2D" coupling code and notch modeled by a multi-faceted defect with an horizontal facet mimicking the 0.2mm notch aperture (see above).

On each graph, the vertical line on the left will indicate the PCS for which the "L axis crossing point" is 4mm above the top edge, the dotted line will correspond to the PCS for which the crossing point is very close to the top edge and the vertical line on the right to the PCS for which the "L axis crossing point" is 4mm below the top edge.

3.1 L60° TOFD inspection of the artificial notches

Figure 6 shows the experimental and the three simulated amplitudes of the top edge echo obtained for the TOFD inspection of the 15mm height notch performed with the probes generating longitudinal waves at 60° in the specimen and for various PCS. The reference for the amplitude is the L direct echo of the SDH Ø2mm at 20mm depth obtained in TOFD mode with a PCS of 70mm.

When the PCS increases, the "L axis crossing point", situated above the top edge for the PCS of 35mm, moves deeper, reaches the top edge for PCS = 50 mm and then drops below it. The amplitude of the top edge echo reaches its maximum when the crossing point is close to the top edge.

We have a good agreement between experiment and CIVA or CIVA-ATHENA-2D predictions whatever the notch aperture. In this case, we observe almost no effect of the notch aperture as expected according to the results obtained in the Ravenscroft configuration. Indeed we can see on the right of Figure 6 that, whatever the PCS, the incident angle θ is less than 130°, and the influence of the notch aperture on the top edge echo amplitude occurs only for θ greater than 130° (Figure 5).

The same agreement between experiments and the three simulations (with CIVA and CIVA-ATHENA-2D with quasi null or 0.2mm aperture) was obtained for the notches of 10mm and 5mm (Figure 7).

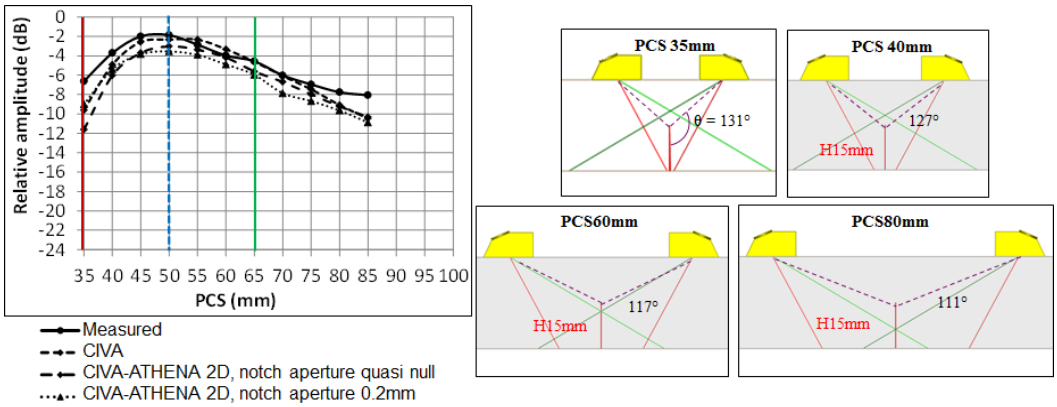

Figure 6: L60° TOFD inspection, notch of 15mm height. Left) Compared experimental and simulated amplitudes of the L top edge echo versus the PCS. Right) CIVA schematics showing the relative positions of the notch and the probes for different PCS.

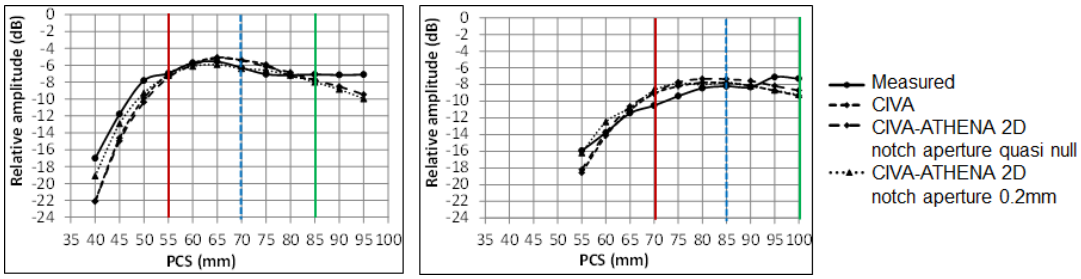

Figure 7: L60° TOFD inspection, notch of 10mm height (left) and of 5mm height (right). Compared experimental and simulated amplitudes of the L top edge echo versus the PCS.

3.2 L45° TOFD inspection of the artificial notches

Figure 8 shows the experimental and simulated longitudinal amplitudes of the top edge echo obtained for the TOFD inspection of the 15mm height notch performed with the probes generating longitudinal waves at 45° in the specimen and for various PCS. The reference for the amplitude is the L direct echo of the SDH Ø2mm at 20mm depth obtained in TOFD mode with a PCS of 40mm.

The "L axis crossing point", situated above the top edge for the PCS of 25mm, reaches the top edge for PCS = 30mm and then moves below it. The amplitude of the top edge echo reaches its maximum when the crossing point is close to the top edge.

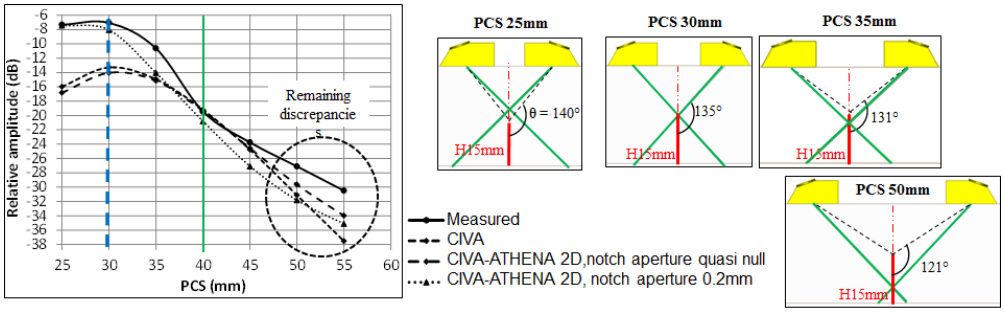

Figure 8: L45° TOFD inspection, notch of 15mm height. Left) Compared experimental and simulated amplitudes of the L top edge echo versus the PCS. Right) CIVA schematics showing the relative positions of the notch and the probes for different PCS.

We can see Figure 8:
- a good agreement between experiment and CIVA or CIVA-ATHENA-2D predictions, whatever the notch aperture, is obtained only for PCS values of about 40mm.
- an effect of the notch aperture: for the small PCSs, only the CIVA-ATHENA-2D amplitudes obtained for the 0.2mm notch aperture match the experimental ones: the real notch aperture has to be taken into account for the top edge echo computation at these PCSs. This need for taking account of the notch aperture can be evaluated by considering the results obtained in the Ravenscroft configuration (see Figure 5). Indeed we can see on the right of Figure 8 that, for the PCS smaller than 35mm, the values of the incident angle θ are greater than 130°, values for which the influence of the notch aperture on the top edge echo amplitudes is significant (see Figure 5).
- discrepancies between experiment and simulations: for the great PCSs, taking into account or not the notch aperture for the echo computation does not modify the L top edge echo amplitude. This is consistent with the predictions from the Ravenscroft configuration because, for the PCS up to 45mm, the incident angle θ is less than 130° (see right of Figure 8 and Figure 5). So, some discrepancies between experiment and simulations remain, and their origin may come from an approximation made in CIVA: hypotheses are assumed in the echo computation to simplify the description of the field. For instance the wave fronts are supposed to be locally plane at the vicinity of a notch edge mesh point and emitted wave-form is supposed to be modified during the propagation in the specimen by nothing but an amplitude factor, a phase shift and a time-delay, which means that distortions of the transient signal will not be taken into account. These hypotheses are less verified when the notch is located far from the probe L axis. It is the case of the top edge of the notch when inspected in TOFD mode with a PCS greater than 50mm.

For the notches of 10mm and 5mm we observed also an influence of the notch aperture for the smallest PCSs corresponding to an incident angle θ greater than 130° (Figure 9).

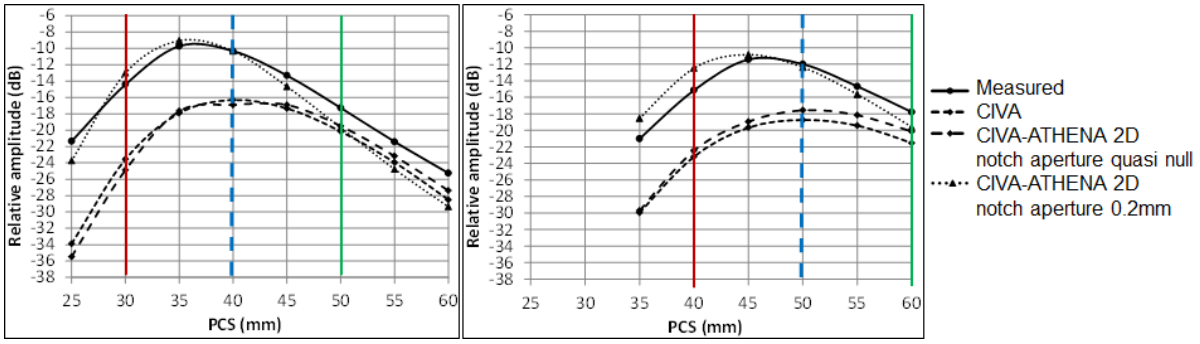

Figure 9: L45° TOFD inspection, notch of 10mm height (left) and of 5mm height (right). Compared experimental and simulated amplitudes of the L top edge echo versus the PCS.

4. CONCLUSION

We have reported results of an experimental validation study aiming at quantifying the reliability of CIVA UT predictions for the amplitude of the longitudinal top edge echo of artificial notches inspected in TOFD mode with conventional probes. The simulations using the GTD code have been performed using the CIVA 11 release and that using the coupling code have been performed using the CIVA 10 release and revalidated with CIVA 11 through automatic non regression testing of the successive releases of CIVA.

The experimental and simulation procedures were described.

In the case of artificial notches (aperture of 0.2mm) and for some values of the L beam incident angle on the top of the notch, the notch aperture is an important parameter that has to be taken into

account in the simulation. In CIVA, the GTD model is the appropriate one for diffraction echo computation in the case of realistic cracks of quasi null aperture. Since the GTD model doesn't take into account the real aperture of the artificial notches we compute the top edge echo with the coupling code of CIVA-ATHENA-2D which allows taking into account the real aperture.

The comparisons between experimental and simulated amplitudes showed a good agreement for the studied cases in the zone of interest. Where the notch aperture influence was not expected according to a previous study based on the Ravenscroft configuration [7], the predictions of the GTD model and of the coupling code were in good agreement with experiments. Then, where the notch aperture influence was expected, the coupling code predictions were in good agreement with the experiment unlike the GTD model.

Some discrepancies, not due to the non account of the notch aperture remain, when the top edge is located far from the zone of interest. Hypotheses assumed in the echo computation to simplify the description of the field (plane wave approximation) may explain these discrepancies. To avoid the consequences of this simplification, work is in progress at CEA to take into account a real description of the incident beam for echo response.

REFERENCES

1) CIVA website http://www-civa.cea.fr
2) Darmon M, Chatillon S, "Main Features of a Complete Ultrasonic Measurement Model: Formal Aspects of Modeling of Both Transducers Radiation and Ultrasonic Flaws Responses." Open Journal of Acoustics, 3A (2013)
3) Darmon M, Leymarie N, Chatillon S, Mahaut S, "Modelling of scattering of ultrasounds by flaws for NDT", Ultrasonic wave propagation in non homogeneous media ed A Léger and M Deschamps (Springer Proc. Phys. 128) 61 2009 and also Darmon M, Chatillon S. Mahaut S, Calmon P, Fradkin L J and Zernov V, "Recent advances in semi-analytical scattering models for NDT simulation", J. Phys.: Conf. Ser. 269 012013, 2011..
4) Calmon P, Recommendations for the use and validation of NDT simulation, V, IIW Best practice document, IIW 2363-13(2013).
5) EXTENDE website http://www.extende.com
6) Darmon M, Chatillon S, Mahaut S, Fradkin L J and Gautesen A "Simulation of disoriented flaws in a TOFD technique configuration using GTD approach", Review of Progress in QNDE 27, ed D O Thompson and D E Chimenti (Melville: AIP Conf. Proc. 820) 155 2008
7) Ravenscroft F A, Newton K and Scruby C B, "Diffraction of Ultrasound by Cracks: comparison of Experiment with Theory", *Ultrasonics,* Vol 29, pp 29-37, January 1991.
8) Raillon R, Toullelan G, Darmon M, Chatillon S and Lonne S, "Validation of CIVA ultrasonic simulation in canonical configurations", 9th International Conference on NDE in Relation to Structural Integrity for Nuclear and Pressurized Components, (2012)

RECENT COMPUTER MODELING ACTIVITIES AND ACHIEVEMENTS IN PAUT APPLICATIONS

L. Horacek, UJV Rez, Czech Republic
P. Mares, Centrum vyzkumu Rez, Czech Republic
V. Kopal, CEZ Czech Republic

INTRODUCTION

This paper is devoted to review predominantly phased array ultrasonic testing (PAUT) results and their comparison with computer modeling PAUT simulation by CIVA s/w for selected WWER type piping systems. The results of these studies were used in practice for comparison with other at present applied or developed UT techniques especially with pulse echo and TOFD.

The importance of mathematical models to assist in predicting in-service inspection results for WWER type components and piping systems has increased with the need to properly and effectively demonstrate nondestructive evaluation (NDE) procedures separately or within NDE qualification process prior to field use. UJV Rez applies one of the most commonly used programs to aid in this task, the CIVA software, developed by CEA (France).

CIVA licenses allow us and are mainly used to perform simulations for ultrasonic and eddy current inspection methods. The most frequent CIVA applications are devoted to phased array ultrasonic testing (PAUT) and TOFD techniques in Czech Republic at present.

This paper tries to provide assessment regarding the capabilities and accuracy of this software using a series of practical examples focused on WWER type piping system configurations. The CIVA simulation results are taken from 1:1 scale test assemblies fully representing from the point of applied original base and weld materials, welding technology the field WWER type piping system weld configurations equipped with a variety of prepared artificial defects.

The CIVA PAUT simulation results are compared directly against PAUT experimental data. It is at least partially demonstrated here that CIVA simulation can reproduce reflections from prepared defects. It has to be highlighted that the comparison is strongly dependent on choice of user input data of modeling parameters. In conclusion, some strengths and weaknesses of the comparison are highlighted and discussed.

TOFD UT examinations presented in the second part of the paper are expected to be used either as single qualified examinations or as additional/alternative examinations focused on either height and ligament sizing of defects in the Czech Republic for Temelin NPP, Dukovany NPP, Metsamor NPP (Armenia) and Ukrainian NPPs with a focus on support in Long Term Operation NDE issues for WWER type NPPs.

The latest most important objectives of CIVA simulations for piping and nozzle to piping areas are simulations of defect response for phased array, pulse-echo and TOFD technique application to determine an estimate of defect height (through wall extent). The progress in phased array applications on circumferential welds and longitudinal elbow welds of different piping systems is also accompanied by extensive computer modeling simulation by CIVA s/w. Several WWER 440 and WWER 1000 type examples of compliance of PAUT examination and PAUT simulation results are provided for defects in the 1:1 piping weld test assemblies.

The other part of the paper contains a summary of the progress in PAUT and TOFD applications on circumferential welds of different piping systems that are also accompanied by extended computer modeling simulation by CIVA s/w.

Examples of compliance of PAUT and TOFD examinations with PAUT and TOFD simulation results are provided for defects in the 1:1 piping test assemblies with intended defects in welds. Experience and lessons learnt from computer modeling of PAUT and TOFD UT examinations compared with PAUT and TOFD UT inspections performed on the same test assemblies with intended defects are summarized as well.

PAUT EXPERIMENTS ON TEST ASSEMBLIES

PAUT experiments on PMPN test assembly

Phased array UT experiments were performed on the test assembly with the pressure measurement piping nozzle (PMPN) to WWER 1000 primary circuit Dn 850 piping weld. There were observed on this type of weld and in the vicinity suspicious indications of corrosion degradation mechanisms. The test assembly with the PMPN respectively the 3D drawing suitable for CIVA simulations is on the Figure 1 respectively Figure 2.

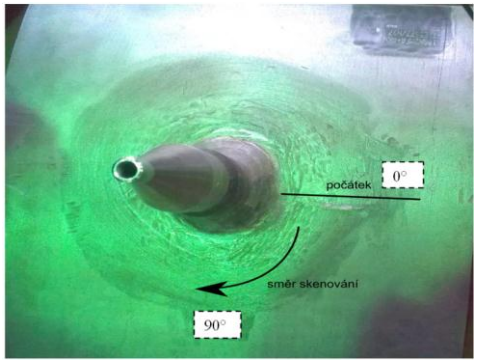

Fig. 1: Pressure measurement piping nozzle on WWER 1000 primary circuit Dn 850 piping

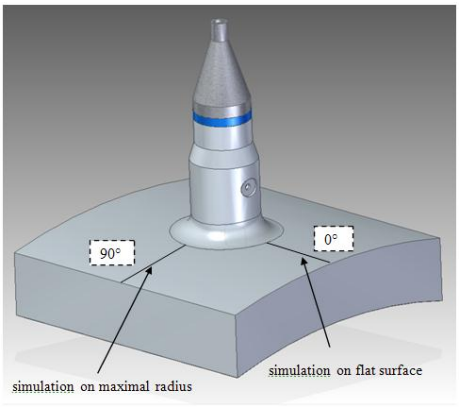

Figure 2: 3D drawing of the pressure measurement piping nozzle to WWER 1000 primary circuit Dn 850 piping weld test assembly

The appropriate layers of cladded material with the defects proposed on the interfaces can be seen on the Figure 3.

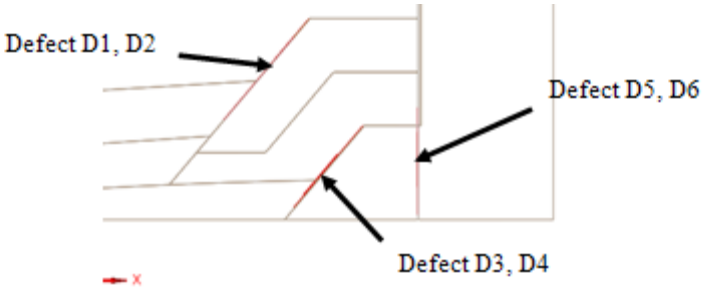

Figure 3: Defect locations and dimensions on PMPN test assembly

The defect distribution with proposed locations and dimensions are on the Table 1.

Defect number	Dimensions [mm]	Location on interface
D1	6x10	BM to cladding (40° slope)
D2	8x8	BM to cladding (40° slope)
D3	4x8	BM to cladding (40° slope)
D4	8x8	cladding to weld (40° slope)
D5	8x8	weld to nozzle
D6	4x8	weld to nozzle

Table 1: Defect locations and dimensions on PMPN test assembly

The phased array UT examination was performed using linear 16 elements 3.5L16-A3 (25.6x16 mm, Rexolite) search unit with flat contact surface wedge SA3-N45S (30°-60°).

The increased noise from the inner surface shape of the pressure measurement piping nozzle on WWER 1000 primary circuit Dn 850 piping and cladding layer to layer or base metal to cladding interfaces can be clearly seen on Figure 4.

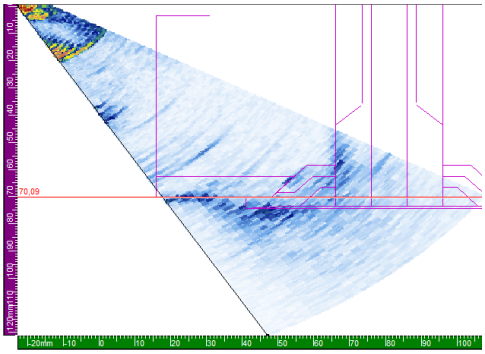

Figure 4: PAUT measurement by search unit 3,5L16-A3 on the defect free part of the PMPN test assembly

Practical examples of defect indications on S-scans measured by search unit 3,5L16-A3 for index offset 55 mm (IO 55mm) can be seen on Figure 5a and Figure 6a. Appropriate CIVA version 10 simulation results for the same LOF type defect number D3 and D4 can be seen on Figure 5b and Figure 6b.

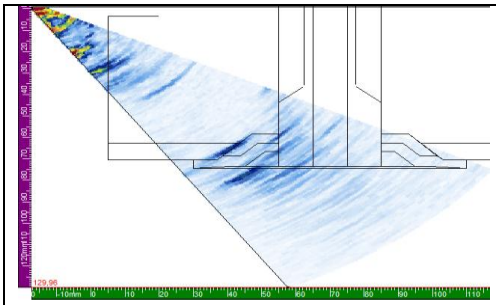

a) D3 defect indication measured by 3,5L16-A3 for IO 55 mm (length 41°-44°, height 4,5 mm)

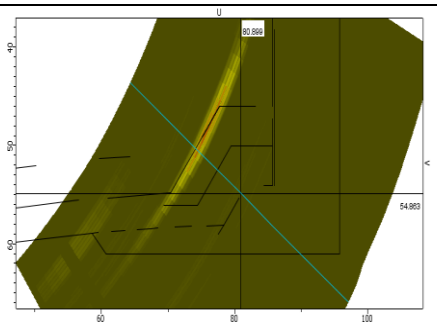

b) CIVA simulation of D3 defect indication

Figure 5: D3 defect indication S-scan measured and simulated for search unit 3,5L16-A3 with SA3-N45S wedge (IO 55 mm)

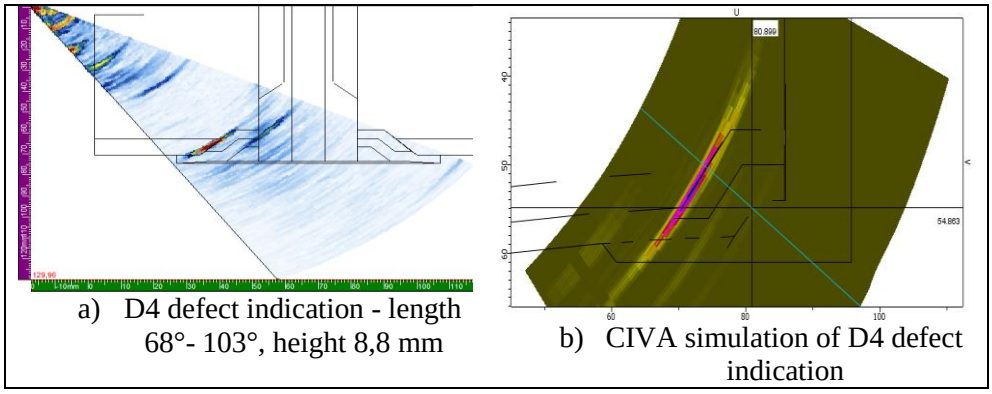

a) D4 defect indication - length 68°- 103°, height 8,8 mm

b) CIVA simulation of D4 defect indication

Figure 6: D4 defect indication S-scan measured and simulated for search unit 3,5L16-A3 with SA3-N45S wedge (IO 55 mm)

PAUT and pulse echo experiments on SG collector DMW welding procedure test assembly

High level attention at WWER type NPPs in relation to lifetime extension is devoted to ISI, NDE qualification, ISI site feedback and in time readiness of repair technology of dissimilar metal welds. Here there is a specific example of WWER 440 type steam generator collector DMW.

Simplified macrograph drawing of welding procedure qualification test block (WPQTB) section with manufacturing LOF of 1.16 mm height in the weld root area was used for CIVA simulation of conventional UT and PAUT inspections (see Figure 7). The real macrograph of WPQTB section with a detail of real and simulated manufacturing LOF of 1.16 mm height in the weld root area can seen on Figure 8. Pulse echo and PAUT inspection and simulation results with indication of the manufacturing LOF of 1.16 mm height in the weld root area can be seen on Figure 9 and Figure 10. Both PAUT and pulse echo inspection results were effectively simulated and confirmed inspection results.

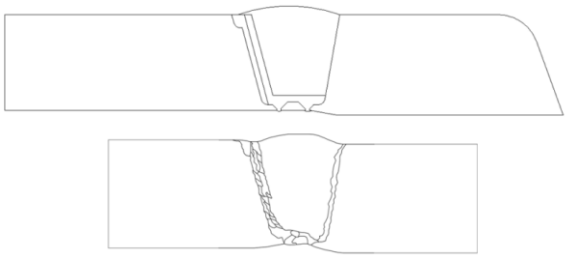

Figure 7: Simplified macrograph drawing of WPQTB section for CIVA simulation of UT examinations

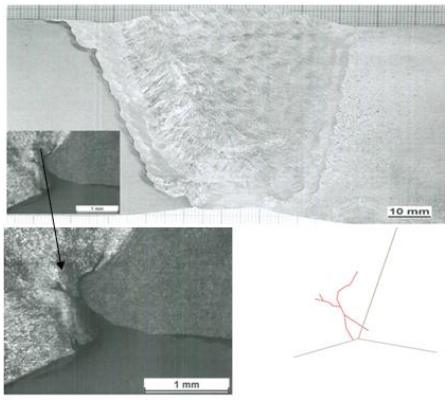

Figure 8: Macrograph of WPQTB section with a detail of real and simulated manufacturing LOF of 1.16 mm height in the weld root area

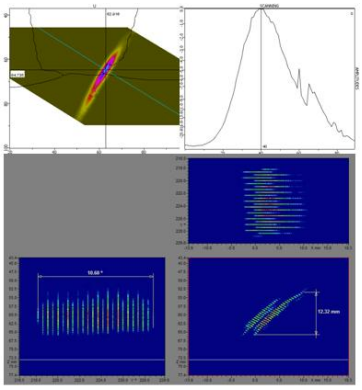

Figure 9: Pulse echo UT inspection and simulation B, C, D-scan results with indication of the manufacturing LOF of 1.16 mm height in the weld root area

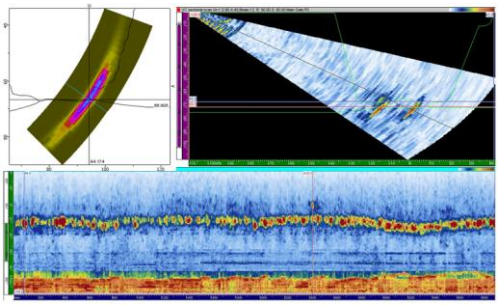

Figure 10: PAUT inspection and simulation results with indication of the manufacturing LOF of 1.16 mm height in the weld root area

TOFD EXPERIMENTS ON THE 273x16 MM TEST ASSEMBLY

Material specification
Base metal: ST20
Weld metal: OK 48.00
Piping diameter and wall thickness:
Nominal outer diameter: 273 mm
Nominal wall thickness: 16 mm

Defect distribution in the test assembly

The defect distribution details in the 273x16 mm piping test assembly are provided in the Table 2. As can be seen there are also smaller defects of the range 3 mm height in the 273x16 mm piping test assembly.

Label	Type	Length /mm/	Height /mm/	Position
BA1	FCC	10	2.5	WCL
BA2	LOF	12	5	-WFL
BA3	FCC	15	5	+WFL
BA4	PISC-A	21.5	6	+WFL
BA5	FCC	30	10	+WFL
BA6	PISC-A	24.1	6	WCL
BA7	FCC	24	8	-WCL
BA8	LOF	12	5	-WFL
BA9	PISC-A	18.5	4	WCL
BA10	PISC-A	16	3	+WFL

Table 2: Defect distribution in the test assembly 273x16 mm

As can be seen the 273x16 mm test assembly contain not only artificial defect types like PISC type A (PISC-A) defects and lack of fusion defect types, but also four fatigue crack simulations (3 point bending cycling defects) more realistic than simple artificial type defects.

TOFD examination has been performed using CDTOF 10MHz 3mm search unit and WTOF 12/70 wedge with longitudinal waves for 3 PCS from 36 to 58 mm showing different UT fields suitable for different defect height distributions (see Fig.11).

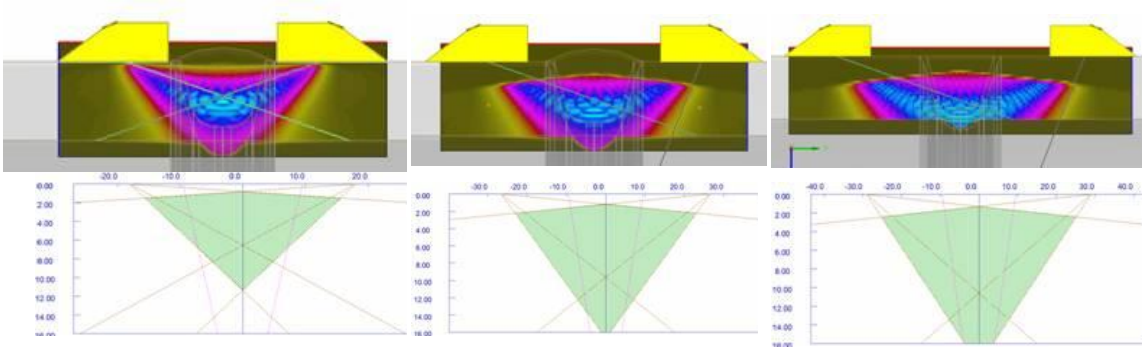

PCS=36 mm PCS=42 mm PCS=58 mm

Figure 11: TOFD UT fields presented for different PCS, CDTOF 10MHz 3mm search unit and WTOF 12/70 wedge

PAUT examination has been conducted with 2L16-A1 search unit and compared with CIVA simulation results (see Table 3).

	Inspection			Simulation			
Defect	**Hm (mm)**	**dH (mm)**	**Sizing method**	**Hm (mm)**	**dH (mm)**	**Sizing method**	**Side**
BA1	3.5	1.0	Tip diffraction	2.5	0.0	Tip diffraction	Minus
BA2	4.9	-0.1	Tip diffraction	4.0	-1.0	6 dB drop	Plus
BA3	5.6	0.6	Tip diffraction	5.0	0.0	Tip diffraction	Plus
BA4	6.0	0.0	Tip diffraction	6.0	0.0	Tip diffraction	Plus
BA5	10.1	0.1	Tip diffraction	9.5	-0.5	Tip diffraction	Plus
BA6	7.0	-1.0	6 dB drop	8.5	0.5	Tip diffraction	Minus
BA7	7.4	-0.6	Tip diffraction	7.5	-0.5	Tip diffraction	Plus
BA8	5.7	0.7	Tip diffraction	5.5	0.5	Tip diffraction	Minus
BA9	3.8	-0.3	Tip diffraction	4.5	0.4	Tip diffraction	Minus
BA10	3.4	0.3	Tip diffraction	2.5	-0.6	Tip diffraction	Plus

Legend:

Hm – Examined/simulated defect indication height

dH – (delta H) Difference between examined/simulated and As built defect height

Table 3: Comparison of PAUT simulation and examination results for 2L16-A1 PAUT search unit on the 273x16 mm Piping Weld Test Assembly

As can be seen from the Table 3 the PAUT examination and CIVA simulation results have the maximum height oversizing or under-sizing below or equal to 1 mm and height sizing methods have been based in majority of cases on tip diffraction signal measurements.

As a final step the TOFD and PAUT examination results for 2L16-A1 PAUT search unit on the 273x16 mm piping weld test assembly have been compared in the Table 4.

Based on this comparison can be told that both TOFD and PAUT examinations provide useful applicable results within expected tolerance limits for height sizing.

273x16	TOFD Inspection			PAUT Inspection		
Defect	**Hm (mm)**	**dH (mm)**	**Sizing method**	**Hm (mm)**	**dH (mm)**	**Sizing method**
BA1	2.0	-0.5	Tip diffraction	3.5	1.0	Tip diffraction
BA2	5.1	0.1	Tip diffraction	4.9	-0.1	Tip diffraction
BA3	5.4	0.4	Tip diffraction	5.6	0.6	Tip diffraction
BA4	5.9	-0.1	Tip diffraction	6.0	0.0	Tip diffraction
BA5	8.7	-1.3	Tip diffraction	10.1	0.1	Tip diffraction
BA6	5.8	-0.2	Tip diffraction	7.0	1.0	6 dB drop
BA7	6.8	-1.2	Tip diffraction	7.4	-0.6	Tip diffraction
BA8	4.6	-0.4	Tip diffraction	5.7	0.7	Tip diffraction
BA9	4.1	0.1	Tip diffraction	3.8	-0.2	Tip diffraction
BA10	3.3	0.3	Tip diffraction	3.4	0.4	Tip diffraction

Table 4 – Comparison of TOFD/PAUT simulation and examination results on the 273x16 mm Piping Weld Test Assembly

CONCLUSIONS

Phased array UT experiments and CIVA simulations comparison results are presented at first for two NDE issues at inspection areas covered by the test assembly with the pressure measurement piping nozzle (PMPN) to WWER 1000 primary circuit Dn 850 piping weld and WWER 440 SG collector DMW welding procedure qualification test assembly.

Pulse echo and PAUT inspection results with indication of the manufacturing LOF of 1.16 mm height in the weld root area were effectively simulated and confirmed inspection results.

Further comparison results of UT experiments and CIVA simulations are presented for TOFD and PAUT experiments on WWER 1000 type piping welds.

TOFD examination and CIVA simulation compared with PAUT examination and simulation results are presented on 273x16 mm piping weld test assembly with altogether10 intended artificial and realistic fatigue type defects. TOFD and PAUT examinations provide similar comparable results within very acceptable height sizing.

Suitable assessment of inspected areas and NDE qualifications are necessary condition for covering of safety service of NPPs. Implementing of NDE methods like TOFD and other supporting activities like computer modeling ensures increasing of examination quality of selected areas, that is why computer modeling is becoming an integral part of NDE qualifications. Qualifications are extended by further additional information and by means of computer modeling, which can help in examination of components on NPP.

Other benefit is the possibility to predict responses from defects, which are not manufactured in test block or even a simulation of a whole test block, which is not manufactured for given weld joint; or verification of usage of certain probe or method belongs to possibilities of utilization of simulations.

GENERIC GTD-KIRCHHOFF SCATTERING MODEL FOR THE ULTRASONIC RESPONSE OF PLANAR DEFECTS

M. Darmon, R. Raillon, V. Dorval, S. Chatillon, CEA - LIST, France
L. Fradkin, Sound Mathematics, U.K

Keywords: Ultrasonics, Flaw Scattering, Planar Flaw, Kirchhoff & GTD.

ABSTRACT

Simulation is helpful for evaluating the performances of inspection techniques and requires the modeling of waves scattering from defects.

Two classical flaw scattering models have been previously evaluated and implemented in the CIVA platform developed by CEA/LIST to deal with planar defects: the geometrical theory of diffraction (GTD) and the Kirchhoff approximation (KA). These two approaches appear to be complementary. Combining them so as to retain only their advantages, we have developed a combined model (the so-called Kirchhoff & GTD) using a procedure similar to the physical theory of diffraction (PTD).

Both theoretical and experimental validations of the Kirchhoff & GTD model have been carried out in various practical NDE (pulse echo and TOFD) configurations studying both direct and corner echo modes. Theoretical validations have consisted in comparisons between this new model and other scattering models (GTD, KA and a finite-element method).

Whereas the previously existing models were notably useful to respectively simulate specular reflection echoes for Kirchhoff and edges diffractions for GTD, the performed validations have shown that the Kirchhoff & GTD model provides a generic modeling of both the two main scattering phenomena arising from a planar flaw: specular reflection and edges diffraction.

INTRODUCTION: AVAILABLE SCATTERING MODELS IN CIVA

The CIVA software platform is developed at CEA-LIST and partners in the aim of simulating non-destructive evaluation [1]. Most of the developed models are based on semi-analytical methods.

The ultrasonic simulation tools in CIVA allow one to fully predict the results of an ultrasonic inspection in a range of applications which requires the computation of the beam propagated, as well as its interaction with flaws [2]. The transducer field is calculated using a pencil method derived from the Rayleigh integral for acoustic radiation [3]. Indeed, inside the coupling material, the Rayleigh integral is computed directly by summing the contributions to the field of each source point of the discretized transducer surface [2]. In the specimen the pencil method which is an extension of ray theory [4] is applied.

The beam to flaw interaction is dealt with different modelling approaches depending on the defect and the inspection characteristics. Three kinds of models for the scattering of ultrasound by flaws have been integrated: approximate analytical solutions, exact analytical solutions and numerical modelling methods. In the last release CIVA 11, numerous improvements of these methods have been added as described hereafter.

The developed approximate analytical solutions are respectively:

- the Kirchhoff approximation [5] to deal with specular reflections from volumetric voids (spherical or hemispherical holes, SDHs) and cracks (rectangular, CAD or elliptical planar, FBHs, multifaceted, branched). This approximation is mostly valid if the observation direction is close to reflection and is particularly suitable to simulate specular reflection, corner effects, etc. The corresponding integrated model requires the meshing of the defect surface. The Kirchhoff model has been extended in Civa11 to deal with anisotropy and impedant (non-rigid) interfaces [6].

- the geometrical theory of diffraction (GTD) to treat scattering from crack edges [7,8]. This approximation is valid away from specular angles and forward paths. The corresponding integrated model requires the meshing of the flaw contour. In Civa 11, the GTD model has been extended to deal with indirect echoes (diffraction echoes after reflection on the specimen surfaces) and has become a 3D GTD model which uses 3D GTD diffractions coefficients.

- the modified Born approximation to deal with solid inclusions. It provides an analytical solution for some flaw geometries (spherical, cylindrical and ellipsoidal) without any meshing of the flaw [9]. The modified Born model has been extended in Civa11 to deal with any incidence on inclusions.

An exact analytical solution for the scattering from a cylindrical cavity, based on the Separation Of Variables (SOV) method, has been used since Civa 10 to simulate the response of a side drilled hole [5]. This model is in addition available in CIVA 11 for solid spherical inclusions.

The main general assumptions applied to deal with the application of the semi-analytical models are described in [2,5].

These previous methods have been experimentally validated in the most commonly used configurations [10].

Since CIVA10.1 release, it is also possible to use a 2D numerical method to model the beam/flaw interaction especially in some complex configurations. Indeed, the hybrid model CIVA/ATHENA [11] is available for simulating the 2D response of SDHs and cracks (rectangular, CAD, multifaceted, branched) and uses the following principle. The pencil method used for CIVA beam calculations is applied to deal with most of the propagation, while intricate interaction phenomena located in a small region surrounding the defects are computed numerically by the finite elements (FEM) code ATHENA developed by EDF.

In Civa 11, another approximate analytical solution has led to the development of a new model called Kirchhoff & GTD (as shown in Figure 1) which is the subject of this paper.

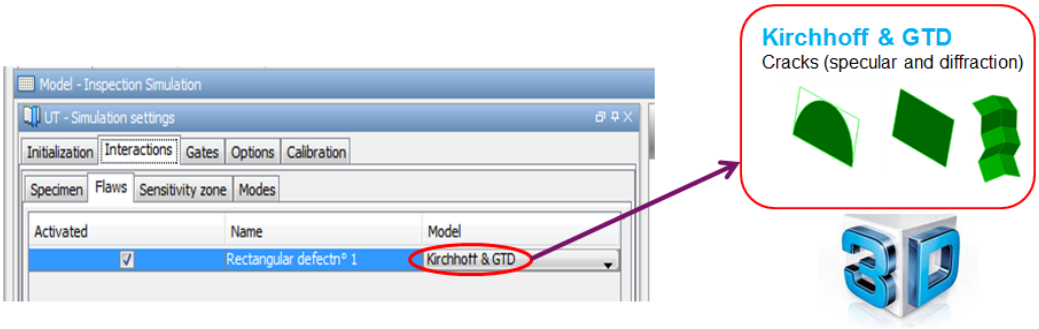

Figure 1: choice of the Kirchhoff & GTD in CIVA 11.

PRINCIPLE OF THE KIRCHHOFF & GTD MODEL

The Kirchhoff & GTD model [12] is devoted to the simulation of both reflection and diffraction echoes from crack-like flaws.

The two previous approaches (Kirchhoff and GTD) appear to be complementary. Combining them so as to retain only their advantages, we have developed a hybrid model (the so-called Kirchhoff & GTD) using a procedure [12] similar to the physical theory of diffraction (PTD)[13].

Indeed, the Kirchhoff model is useful for the modelling of echoes due to specular reflections but is less accurate for observation directions far from the specular one since it doesn't model correctly and quantitatively edges diffraction. On the other hand, contrary to Kirchhoff, the GTD model is not valid for specular observation direction since the GTD coefficient diverges but GTD is very effective to predict edge diffractions echoes in most configurations.

In the PTD formalism, an approximation for the Kirchhoff scattered field in far field from the flaw is done. It assumes that the Kirchhoff scattered field can be decomposed in an approximate manner in two parts: a geometrical field which includes the specularly reflected field and a contribution arising from the flaw edges corresponding to the edges diffraction field. This diffraction field contribution at the observation point x has the same form as the GTD field but a different edge diffraction coefficient (depending on the α incidence and β observation directions and polarizations):

$$\mathrm{U}^{\mathrm{KA(Diff)}}(\mathrm{x}) = D_{\alpha\beta}^{KA}(\mathrm{x})\frac{\mathrm{e}^{ikr}}{\sqrt{kr}} \tag{1}$$

Note that this coefficient characterizes the directivity of the Kirchhoff edge diffraction contribution.

The physical theory of diffraction (PTD) consists in correcting the Kirchhoff edge diffraction field by that modelled by GTD.

This correction leads to add a corrective term to the KA scattered field (without far-field approximation). This corrective term is the difference of wave amplitudes diffracted by the edge given by GTD and KA.

$$\mathrm{U}^{PTD}(\mathrm{x}) = \mathrm{U}^{\mathrm{KA}}(\mathrm{x}) + \left[D_{\alpha\beta}^{GTD}(\mathrm{x}) - D_{\alpha\beta}^{KA}(\mathrm{x}) \right] \frac{\mathrm{e}^{ikr}}{\sqrt{kr}} \tag{2}$$

The PTD field is the sum of the Kirchhoff field and a GTD modified field in which the GTD coefficient has been replaced by the difference between GTD and Kirchhoff edge diffraction coefficients.

At the specular observation direction, the Kirchhoff field (without far-field approximation) is finite leading to an effective prediction of specular reflection. But the KA diffraction coefficient $D_{\alpha\beta}^{KA}(\mathrm{x})$ for edge diffraction contribution (previously obtained from a far field approximation of the Kirchhoff field) diverges and has the same singularity as the GTD edge diffraction coefficient $D_{\alpha\beta}^{GTD}(\mathrm{x})$ .When making the difference of the two coefficients, their singularities cancel each other and the diffraction coefficients difference $D_{\alpha\beta}^{GTD}(\mathrm{x}) - D_{\alpha\beta}^{KA}(\mathrm{x})$ is finite. Consequently the PTD scattered field is spatially uniform and presents no singularity at the specular observation direction unlike GTD.

When the observation direction is close to the specular direction, the Kirchhoff field is predominant compared to the edge diffraction contribution and the Kirchhoff & GTD model leads to similar results than the Kirchhoff model:

$$\mathrm{U}^{PTD}(\mathrm{x}) \approx \mathrm{U}^{\mathrm{KA}}(\mathrm{x}) \tag{3}$$

When the observation direction is far from to the specular direction, edge diffraction effects are predominant compared to reflection phenomena, the Kirchhoff field is equal to the Kirchhoff edge diffraction contribution and so cancels it so that the Kirchhoff & GTD model leads to similar results than the GTD model.

$$\mathrm{U}^{\mathrm{KA}}(\mathrm{x}) \approx D_{\alpha\beta}^{KA}(\mathrm{x})\frac{\mathrm{e}^{ikr}}{\sqrt{kr}} \quad \text{and} \quad \mathrm{U}^{PTD}(\mathrm{x}) \approx D_{\alpha\beta}^{GTD}(\mathrm{x})\frac{\mathrm{e}^{ikr}}{\sqrt{kr}} = \mathrm{U}^{GTD}(\mathrm{x}) \tag{4}$$

Flaws which can be modelled thanks to Kirchhoff & GTD are the same than with the GTD model: planar flaws (rectangular, semi-elliptical or CAD contour planar flaws), multi-facetted flaw and branched flaw.

VALIDATIONS OF THE KIRCHHOFF & GTD MODEL

Both theoretical and experimental validations of the new developed Kirchhoff & GTD model have been performed on steel specimens.

a. Theoretical validations: direct modes in pulse echo configurations

Theoretical validations have consisted in comparing different models including the new developed one for the simulation of direct echoes in pulse echo configurations. In most configurations, the hybrid CIVA/ATHENA model using finite elements (FEM) for flaw scattering modeling is employed as reference model.

The first studied configuration is presented in **Figure 2**.a and deals with the pulse echo inspection with SV45° waves at 5MHz of a rectangular 5mm high defect of various tilt angle α. In **Figure 2**.d is compared the amplitude (in dB) of the flaw simulated echoes versus the tilt angle α for different Civa11 models: GTD, Kirchhoff (KA) and Kirchhoff & GTD (PTD). This comparison illustrates the unified modeling provided by the GTD-KIRCHHOFF (PTD) model. Indeed, when the flaw is observed by the probe near specular reflection (for α=-45°, **Figure 2**.b and yellow area of **Figure 2**.d), GTD is invalid (the theoretical divergence is avoided by a treatment in the CIVA integrated GTD model without removing the invalidity) but KA is very effective and consequently, the PTD model leads to results equivalent to Kirchhoff ones. When diffraction effects are observed (in blue areas of **Figure 2**.d), KA leads to prediction errors: for instance for the classical case of a vertical flaw inspected with S45° waves (for α=0°, **Figure 2**.c), the KA error compared to FEM (see **Figure 3**) is of 6dB order. For diffraction modeling, GTD is much more effective than KA and PTD leads to equivalent simulation than GTD in the blue areas.

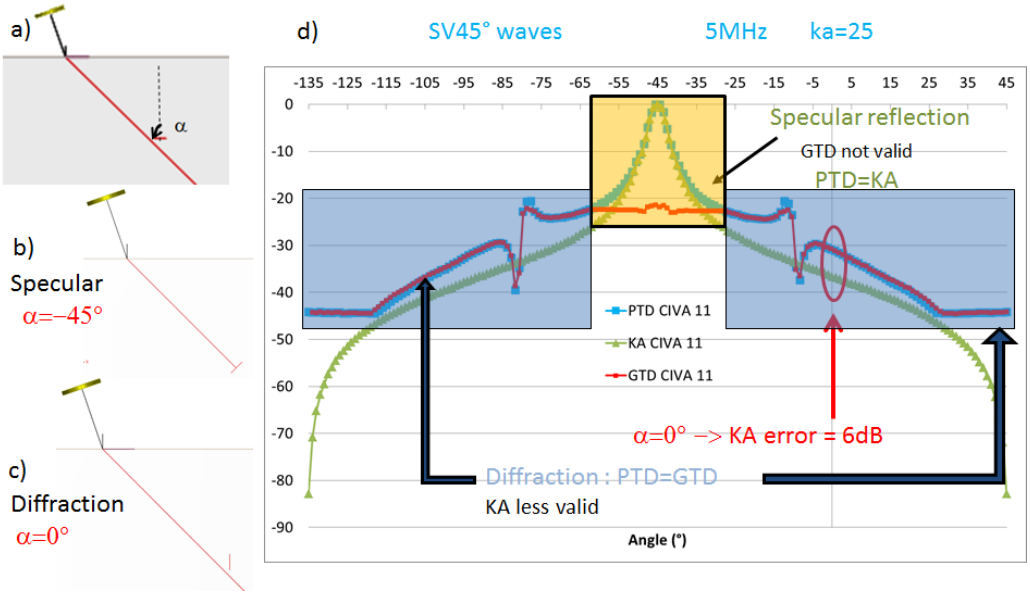

Figure 2: a) pulse echo inspection with SV45° waves at 5MHz of a rectangular 5mm high defect of various tilt b) specular reflection configuration for α=-45° c) for α=0°: classical case of a vertical flaw inspected with S45° waves and observed diffraction effects d) comparison of the simulated echoes amplitude (in dB) versus the tilt angle α for different Civa11 models: GTD, Kirchhoff (KA) and Kirchhoff & GTD (PTD).

In **Figure 3**, the same configuration as in **Figure 2** is still studied but the results from 2D FEM CIVA/ATHENA are also provided. The simulated amplitudes shown in **Figure 3**.b are this time absolute and still represented versus the tilt angle; **Figure 3**.c is a zoom devoted to small amplitudes. A perfect agreement between PTD and FEM is obtained near specular direction (reflected echoes) in **Figure 3**.b for α=-45°. On the other hand, the PTD model can lead to some prediction errors in diffraction compared to the FEM reference model but only for S incident waves. Indeed, the FEM curve presents beyond L critical angle oscillations due to interferences between head waves (detailed in Figure 4) and the S->S diffracted wave which are not accounted by the PTD model. This

phenomenon appears for angles between observation and specular directions more than 33° (in steel). The PTD error is generally still acceptable except exactly at the critical angle (α=-78° or -12°). When increasing flaw height, the oscillations phenomenon fades and an improvement in the prediction for diffraction is observed.

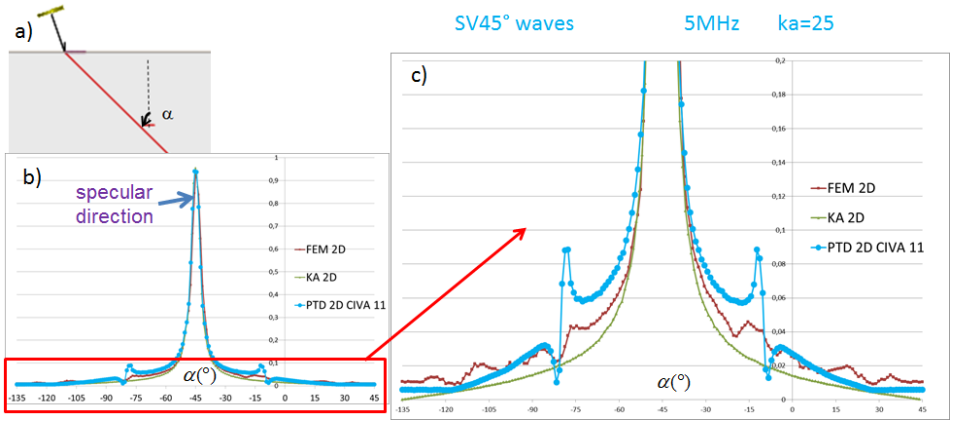

Figure 3: a) pulse echo inspection with SV45° waves at 5MHz of a rectangular 5mm high defect of various tilt b) and c) zoom: comparison of the simulated absolute echoes amplitude versus the tilt angle α for different 2D Civa11 models: FEM, Kirchhoff (KA) and Kirchhoff & GTD (PTD).

Figure 4 details the paths of the waves that interfere together at critical incidence. These waves arise only from the bottom edge and consists in: a) classical diffraction of the incident SV bulk wave into a SV bulk wave; b) due to critical incidence of the S wave, creation of a P creeping wave propagating along the flaw which is diffracted by the bottom edge into a S wave notably in the backscattering direction; c) diffraction at the bottom edge of a P creeping wave propagating along the flaw which radiates a S head wave along the critical direction (equal to the backscattering one). The interferences between these three contributions lead to the PTD peaks at critical angles (**Figure 3**.c) and to the less effective prediction for SV waves near L critical angles (notably for small flaws).

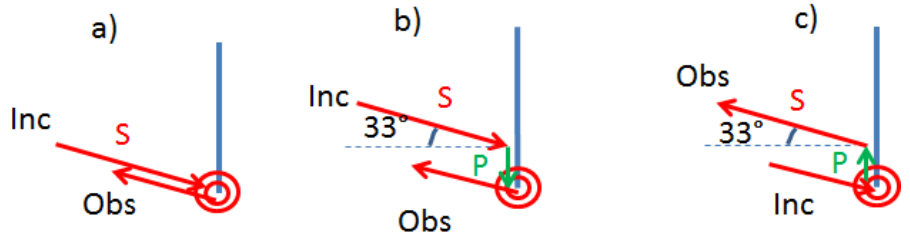

Figure 4: a) Classical diffraction of the incident SV bulk wave into a SV bulk wave b) diffraction of a P creeping wave by the bottom edge c) radiation of a S head wave along the critical direction.

P waves are now considered. The last presented theoretical validation involves the pulse echo inspection of a rectangular 5mm high defect at 5MHz with P waves of various incidences. To impact the flaw with various α incidences, a cylindrical specimen is used and the probe is rotated along the specimen surface and positioned so as to be at normal incidence to this entry surface (**Figure 5**.a). Using such a procedure, the beam impacts the flaw with different P wave incidences during the probe scanning. In **Figure 5**.b is compared the amplitude (in dB) of the flaw simulated echoes versus the tilt

angle α for different Civa 11 2D models: CIVA/ATHENA (FEM), Kirchhoff (KA) and Kirchhoff & GTD (PTD). **Figure 5**.c is a zoom devoted to small amplitudes. The Kirchhoff & GTD model leads to a very good agreement with FEM for all tilt angles. A logical equivalence with KA is observed near the specular reflection configuration (α=90°, see **Figure 5**.b) and with GTD (not represented here for simplification) for a diffraction configuration. In the latter case, the Kirchhoff model leads to prediction errors for tilt angles corresponding to observation directions far from the specular one.

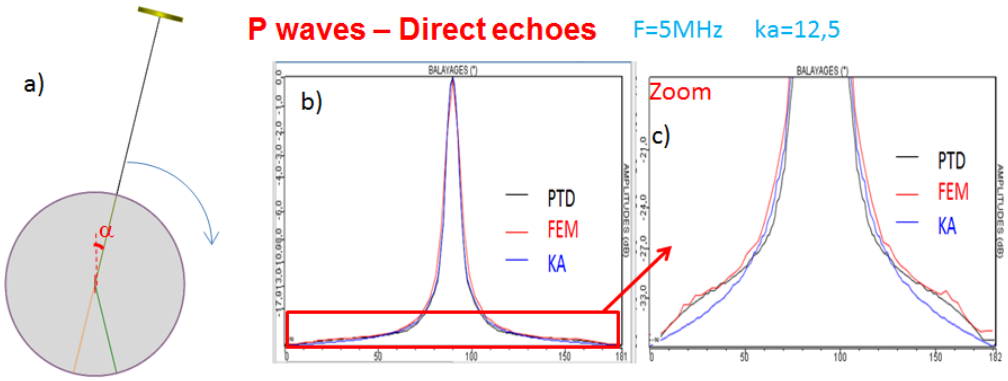

Figure 5: a) inspection at 5MHz with P waves of various incidences of a rectangular 5mm high defect b)and c) zoom: comparison of the simulated echoes amplitude in dB versus the tilt angle α for different 2D Civa11 models: FEM, Kirchhoff (KA) and Kirchhoff & GTD (PTD).

Note that for both P and SV waves, a deterioration of the PTD prediction can be observed for small flaws (rarely encountered in NDT) in diffraction configurations since the diffraction at edges of the Rayleigh waves propagating along the defect are not currently predicted in the Kirchhoff & GTD model.

b. Experimental validations

Intensive experimental validations of the developed PTD model have been carried out both in pulse echo and TOFD configurations by studying both diffraction echoes and corners echoes resulting from specular reflections.

In order to validate simulation of corners echoes in pulse echo configuration, measurements were performed on a mock-up with vertical backwall breaking notches of various heights (**Figure 6**a). A 64 elements contact matrix phased-array probe with a wedge dedicated to generate 45° longitudinal waves was used (**Figure 6**.c and d). A 2D scanning of the probe was performed over each reflector. At each probe position, different focusing laws were applied: several depths focusing (from 10 to 40mm depth) with L45° deviation. The reference amplitude corresponds to the maximum amplitude of the specular L45° direct echo obtained on a 2mm diameter SDH at 72mm depth. To check the experimental reproducibility, the experimental measurements were carried out several times (minimum 2 times for all the flaws); a maximum difference of less than 1dB was obtained. **Figure 6**.c and d present experimental and CIVA 11 simulated reconstructed B-scans obtained over the 15mm height backwall breaking notch obtained for a L45° deviation with focusing at 30mm depth. A very good agreement between experimental and simulated Bscan is obtained. Note that in this case, the corner echo is due to a specular reflection on both the backwall and the flaw and consequently the CIVA 11 Kirchhoff & GTD simulation is equivalent to the Kirchhoff one with Civa 10.

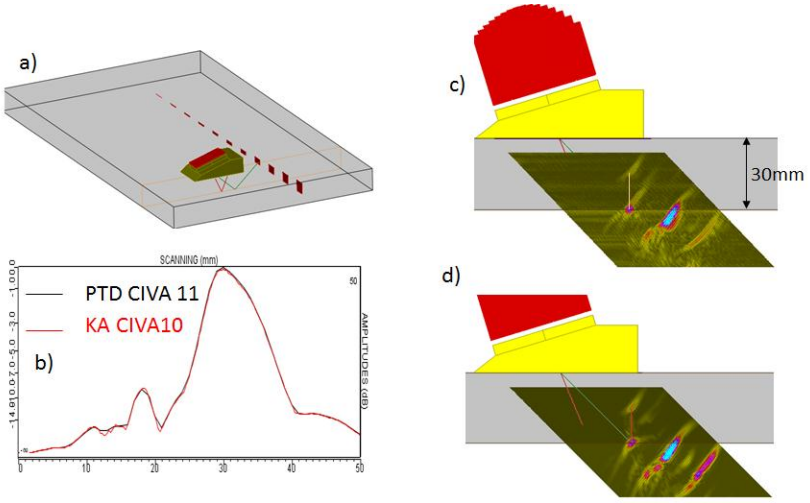

Figure 6: a) Mock-up and defects implemented inside b) Comparison of CIVA11 Kirchhoff & GTD simulated echodynamics and Civa10 Kirchhoff one. Comparison of measured c) and CIVA11 simulated d) reconstructed B-scans over the 15mm height backwall breaking notch. Delay law: L45° deviation with focusing at 30mm.

Applications to TOFD inspection are then considered. First a detailed comparison with Ravenscroft's results [14] is discussed hereafter. Ravenscroft notably employed a symmetrical TOFD arrangement (**Figure 7**.a) of both transmitting and receiving probes over a cylindrical mock-up containing a fatigue crack (mimicking a real one) and investigated the theoretical and experimental behaviour of the amplitude of the flaw edge diffraction echo versus the transmitting (and receiving) orientation of the beam (**Figure 7**.b).

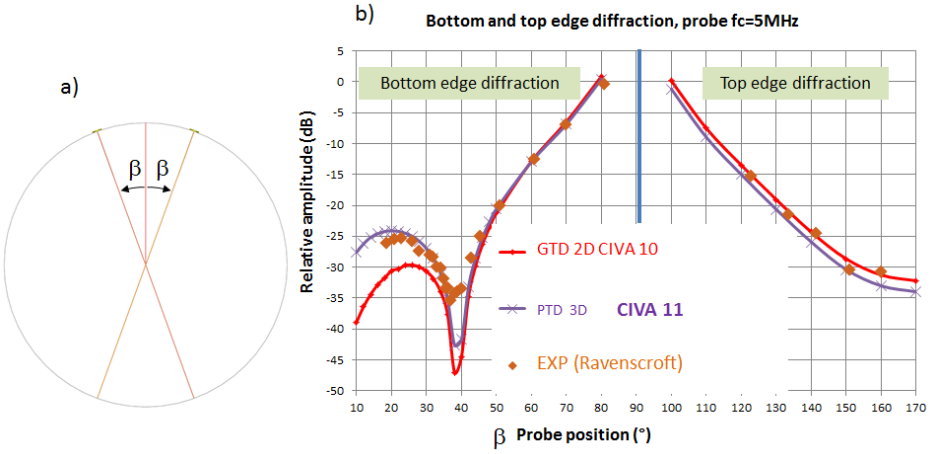

Figure 7: a) Influence of the emission and observation angle for a symmetrical TOFD inspection over a cylindrical mock-up. b) Comparison of 2D GTD Civa 10 and 3D PTD Civa11 simulations with experimental results published by F. Ravenscroft et al [8].

On the simulated curve one clearly observes a minimum amplitude of the flaw response about 38°, which accurately corresponds to the minimum of the longitudinal-longitudinal GTD coefficient [14]. CIVA 11 simulation results show a pretty good agreement with Ravenscroft's results. The Civa 11 PTD model leads to an improvement for small incident angles on bottom edges compared to 2D GTD Civa 10.

Another experimental validation was performed to evaluate the effect of skew flaw angle on edge diffraction amplitude. Tests were carried out on a planar rectangular backwall breaking flaw using a pair of transducers (2.25 MHz, 45° longitudinal wave, 6,35 mm diameter). The probes were

positioned in a TOFD configuration with a 60mm Probe Space Center and with flaw skew angle varying from 0° to 70° (Figure 8.a).

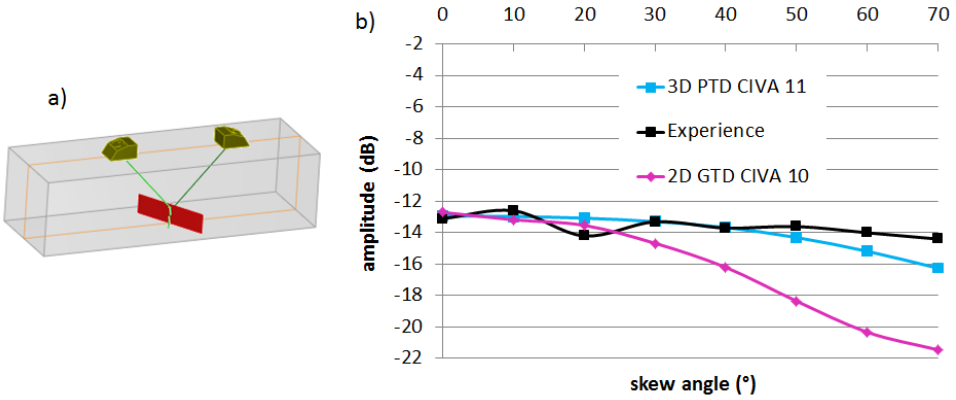

Figure 8: a) TOFD configuration for measuring skew angle effect on edge diffraction b) top edge diffraction echoes amplitudes versus skew angle for measure, 2D GTD Civa 10 and 3D PTD Civa11 simulations.

The experimental and simulated results are presented in Figure 8.b. Experimental results show that there is negligible effect of the skew angle on the diffraction echoes amplitudes. Moreover there is a good agreement between experimental and simulated results with a maximum difference of about 2 dB for 3D PTD CIVA 11 model whereas the 2D GTD CIVA 10 model breaks down for important skew (>40°).

CONCLUSIONS

An elastodynamic GTD-Kirchhoff model based on physical theory of diffraction (PTD) has been developed in Civa 11. This model provides a unified modeling of both specular reflection and diffraction phenomena. Whereas corner echoes were previously (CIVA 10) simulated by the Kirchhoff model and direct diffraction ones by the GTD (geometrical theory of diffraction) model, all phenomena are accounted by the CIVA 11 GTD-Kirchhoff model. Theoretical comparisons carried out on direct echoes with a FEM model has shown a very good overall prediction for P waves and also for S waves except in the latter case for incidences near the longitudinal critical angle (existence of head waves). A deterioration of the GTD-Kirchhoff prediction can be observed for small flaws (less significant case in NDT) in diffraction configurations. Successful experimental validations have been obtained in numerous NDT configurations: 2D and 3D, pulse echo and TOFD, on diffraction or corner echoes.

REFERENCES

1) CIVA software website, http://www-civa.cea.fr
2) Darmon, M, Chatillon, S, “Main Features of a Complete Ultrasonic Measurement Model: Formal Aspects of Modeling of Both Transducers Radiation and Ultrasonic Flaws Responses.” Open Journal of Acoustics, 3A (2013)
3) Gengembre N and Lhémery A “Pencil method in elastodynamics. Application to ultrasonic field computation Ultrasonics 2000 38 495
4) Červený V Seismic Ray Theory (Cambridge U. Press) 2001
5) Darmon M, Leymarie N, Chatillon S, Mahaut S, “Modelling of scattering of ultrasounds by flaws for NDT”, Ultrasonic wave propagation in non homogeneous media ed A Léger and M Deschamps (Springer Proc. Phys. 128) 61 2009
6) Dorval V, Chatillon S., Darmon M. and Mahaut S., “A general Kirchhoff approximation for echo simulation in ultrasonic NDT”, Review of Progress in QNDE, ed. by D. O. Thompson and D. E. Chimenti (AIP Conference Proceedings).
7) Achenbach J D and Gautesen A K “Edge Diffraction in Acoustics and Elastodynamics”, Low and High Frequency Asymptotics - Vol 2 ed Varadan V K and V V (Elsevier) 335-401 1986

8) Darmon M, Chatillon S, Mahaut S, Fradkin L J and Gautesen A “Simulation of disoriented flaws in a TOFD technique configuration using GTD approach”, Review of Progress in QNDE 27, ed D O Thompson and D E Chimenti (Melville: AIP Conf. Proc. 820) 155 2008
9) Darmon M, Calmon P and Bele B “An integrated model to simulate the scattering of ultrasounds by inclusions in steels” Ultrasonics 42 237 2004
10) Raillon R., Toullelan G., Calmon P., Darmon M. “Validation of CIVA Ultrasonic Simulation in Canonical Configurations, ” 18th WCNDT, 2012
11) Leymarie N., Calmon P., Fouquet Th., Schumm A., “A Semi-analytical-FEM Hybrid Model for Ultrasonic Simulation of Complicated Wave Defect Interaction, ” International Conference on NDE in relation to structural Integrity for Nuclear and Pressurised Components (2006)
12) Zernov V, Fradkin L, Darmon M, "A refinement of the Kirchhoff approximation to the scattered elastic fields ", Ultrasonics 2012, 52, Issue 7, pp 830–835.
13) Ufimtsev P Y Fundamentals of the Physical Theory of Diffraction; John Wiley & Sons.: Hoboken USA, 2007.
14) Ravenscroft F A, Newton K and Scruby C B, “Diffraction of Ultrasound by Cracks: comparison of Experiment with Theory”, Ultrasonics 1991, 29, pp 29-37.

INVESTIGATIONS ON THE CRITICALLY REFRACTED LONGITUDINAL WAVE FOR OPTIMIZED USE IN THE NDT/E FIELD

W. K. Yaacoubi, S. Yaacoubi, Institut de Soudure, France

Abstract

Despite the abundance of studies linked to the critically refracted longitudinal wave (L_{CR}), and the fact that this technique has been used in practice for long time, the behavior of L_{CR} and the critical refracted beam components has not been studied in great detail. In this work, investigations based on finite element modeling are performed. Its aim is to determine the main parameter which should be optimized. Some optimizations are achieved. Numerical results validated experimentally are presented.

Keywords: L_{CR}, Finite element modeling, optimization, ultrasonic beam, experiment validations

1. Introduction

The LCR has been employed for various applications in the field of nondestructive evaluation and testing. They can be mainly used to:

- detect surface and sub-surface defects, and
- measure residual stress.

In both cases, accuracy in the measurement is required to reduce the false alarm. Overvaluation or underestimation of the defect size for example can give rise to serious accident or to economic loss due to too early replacement of equipment's and eventual stop in manufacturing. A good knowledge of the field distribution radiated by transducers and propagated in the structure to be evaluated is required. Due to lack of deep knowledge from previous works and systematic experimental procedures, various questions with different difficulty degrees and deepness remain, such as:

i. how is it the behavior of the L_{CR} field, when propagating in the medium to be evaluated or tested?
ii. how L_{CR} behaves with regard to the incidence angle?
iii. is the transducer shape has any effect?
iv. is there any influence of the driven frequency on this behavior?
v. Is the Snell-Descartes law sufficient to understand the behavior of the L_{CR} propagation?
vi. is the numerical simulation analysis able to answer on these questions?

Next sections are developed to answer on these questions.

2. Components of the critically refracted acoustical field

The well-known Snell-Descartes law is given mathematically by this equation:

$$\frac{c_1}{\sin\theta_1} = \frac{c_2}{\sin\theta_2} \tag{1}$$

which can be written as:

$$k_1 \sin\theta_1 = k_2 \sin\theta_2 \tag{2}$$

From this equation, we can deduce that the Snell-Descartes Law is independent of the frequency. That's mean L_{CR} should be also independent of the frequency derived by the emitter. To confirm this result, the last section of this paper will be devoted to study numerically the effect of this parameter.
Figure 1 shows schematics of the Snell-Descartes Law when the incident angle is different from (left) and equal to the critical incident wave (right). As shown in this figure L_{CR} is expected to be in surface or underneath the surface. One among the next sections is devoted to determine the critical incident wave which allows obtaining the maximal longitudinal wave amplitude at 90°.

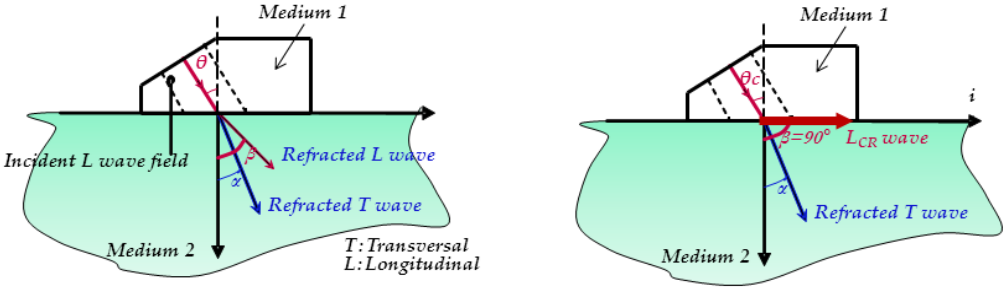

Figure 1 : Snell-Descartes law: incident angle different from (left), and equal to (right) critical angle.

The schematic given in Figure 1 (right) was simulated numerically in time domain, in 2-dimensions to reduce the computation time. The chosen driven frequency is 2.25 MHz which is equal to the central frequency of the transducer to be used in experiments. The gained result, which is 2D total displacements time propagation field at different time steps, is shown in Figure 2. In this figure, the gray panel is related to the amplitudes of the total displacement. We can remark:

- the 1st arrived are LCR with displacement parallel to the propagation direction,
- a longitudinal wave with displacement perpendicular to its wave-front, followed by
- a head wave remarked with a plane wave-front,
- Rayleigh wave, and finally
- a transversal wave which is overlapped with surface wave in the subsurface region which can be distinguished through the wave-length.

As an answer to a question asked previously, Snell-Descartes Law is not appropriate to determine the components of the critically refracted beam and analyze the behavior of LCR wave.

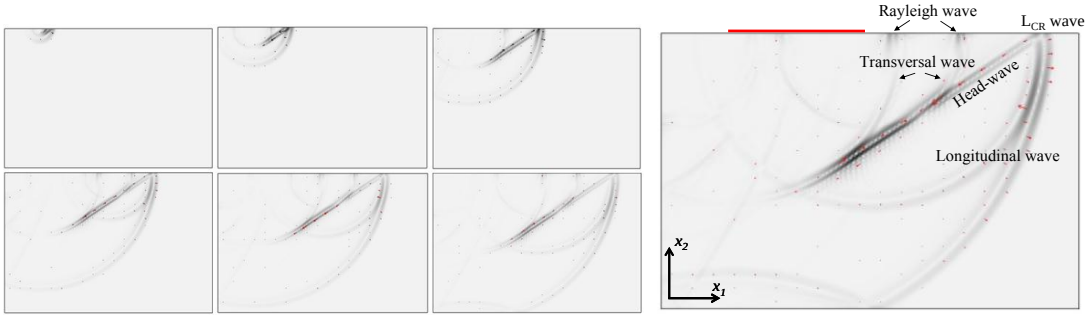

Figure 2 : Snapshots of 2D-total displacement time propagation field at different time steps (in increased order from left to right).

As it can be remarked in **Figure 2**, it is not practical to characterize directivity by monitoring wave-front on the simulation results in time domain. To overcome this problem, simulations will be carried out in frequency domain in the next section.

3. Effect of the transducer edge

To determine the effect of the transducer edge, numerical simulations was driven in frequency domain. The chosen shapes of the excitation signal in the space domain are two: square windowed and Gaussian windowed harmonic function. These excitations are given respectively from left to right in Figure 3 - top. Figure 3 – bottom represents the corresponding total displacement amplitudes simulated, in frequency domain, at f = 2.25 MHz.

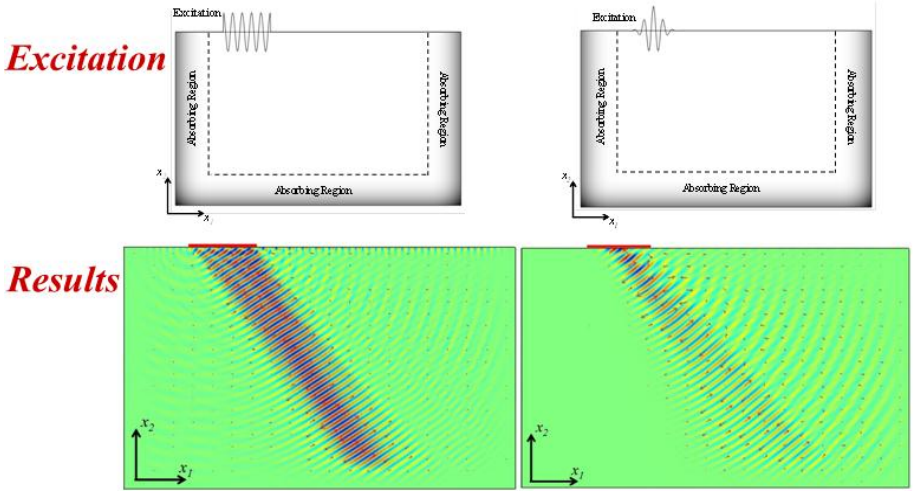

Figure 3 : Schematics of the space excitations signal (top) and corresponding snapshots of the obtained total displacement (bottom): square window (left) and Gaussian window (right).

As it can be remarked, all wave-fronts are overlapped, and so, wave modes cannot be separated straightforwardly. To overcome this problem, spatial Fourier transform is needed to be applied for wave's separation. After accomplishing this step, several steps have to be followed to carry out the polar displacement distribution. Some other steps are needed. Figure 4 shows a flowchart of the procedure which is developed for determining the directivity diagram.

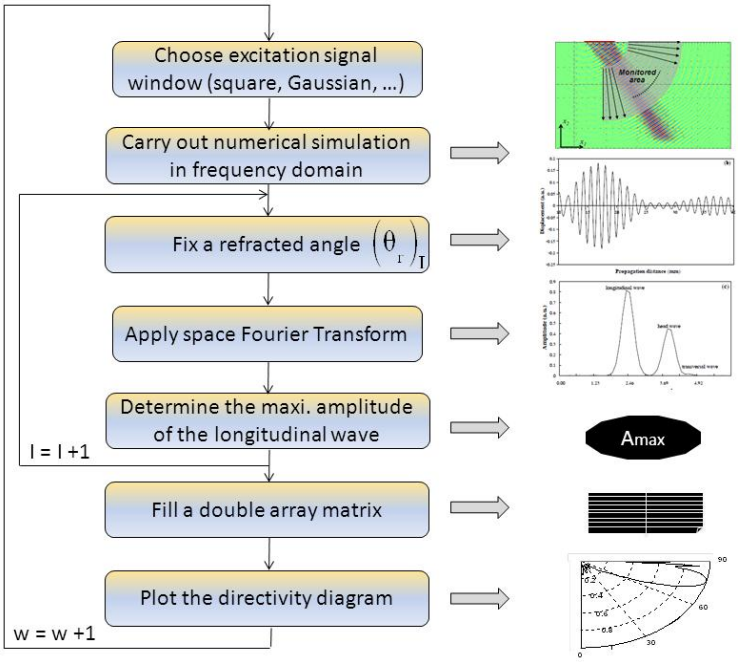

Figure 4 : Procedure flowchart for determining the directivity diagram, where the increments w and I correspond the excitation signal window order and the refracted angle (between 0° and 90°), respectively.

By applying the post-processing algorithm which is based on this procedure flowchart, directivities displacements in both cases are plotted. The results are given in Figure 5. As it can be seen, corresponding directives are clearly different. In the near surface region, the distortion which can be distinguished is due to the superposition of longitudinal wave and head-wave. This distortion is more highlighted in the case where the square window is used. The amplitude is bigger in this case. Consequently, in real life and following this modeling study, it is advisable to use a piston transducer.

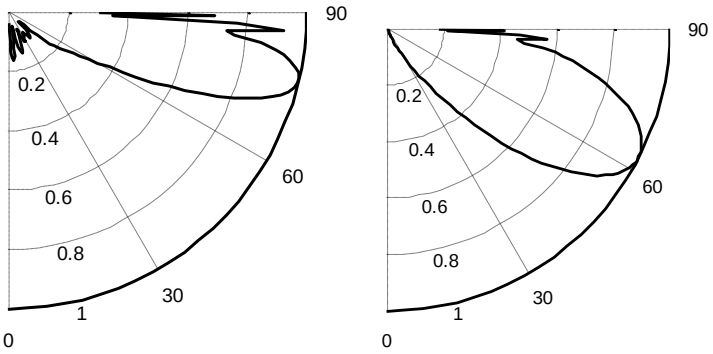

Figure 5 : Directivity of the total displacement field, at 2.25 MHz: square window (left) and Gaussian window (right).

4. Effect of the incidence angle

To study the effect of the incidence angle, numerical simulations are carried out in time domain as well as in frequency domain. In both cases, and as in the previous section, the central frequency is equal to 2.25 MHz. However, the wedge is chosen to be water as it is available in experimental set-up. This choice allows generating only longitudinal waves since shear ones don't propagate in light liquid, like water. Figure 6 (left) shows a schematic of the experimental set-up designed and manufactured to characterize the refracted beam. The structure is circular to allow:

- moving easily the sensor to perform a circular scan, and
- keeping the same distance between the emitter and the receiver for all the points of acquisition, for easy comparison of the collected data.

Comparatively to the structure used in the previous section, a part between 90° and 135° was added. The principal roles of this extended part are:

- avoiding the edge effect (interactions between waves and the top edge of the structure). This permits as far as possible to collect cleaner signals, particularly near 90° since the hot-spot is underneath the top surface of the structure (normal configuration, as shown **Figure 3**).
- enabling the receiver to measure the waves which propagate along the refracted direction (90°).

Figure 6 (right) shows a time signal acquired at a refracted angle equal to 0°. Note that this signal is one among several signals acquired for different refracted angle going from 0° to 112° by 2°, but to alleviate the paper, only one signal is shown. The first four echoes correspond, respectively from left to right, to longitudinal wave, head wave, shear wave, and a shear wave generated by the longitudinal one at the intersection between the horizontal and inclined surfaces. The other trailing waves are due to the interaction with the sample boundaries. This signal confirms what it found via numerical simulations.

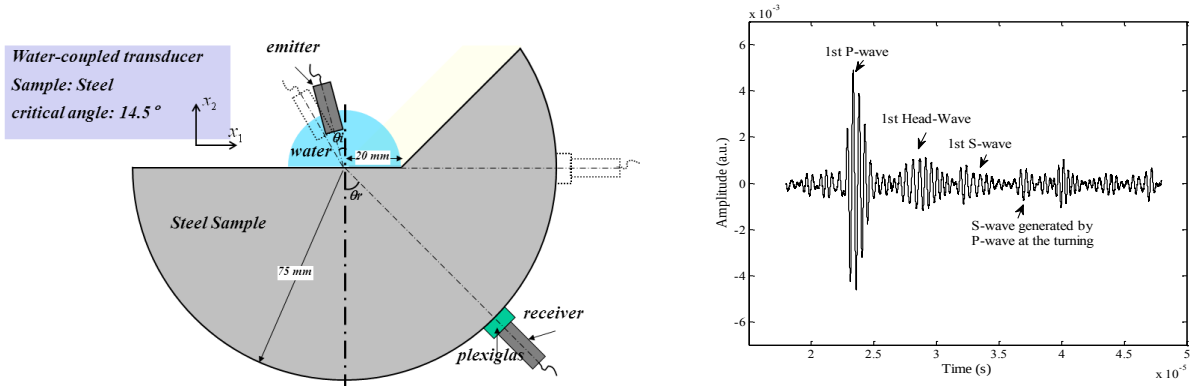

Figure 6 : Experimental set-up designed and manufactured to perform a circumferential scan for different incidence angle (left), and a time signal obtained experimentally at a refraction angle = 0° (right).

The Numerical simulation in time domain permits to have a global view and quick idea about the components of the refracted displacement field. Figure 7 shows snapshots of 2D-total displacement time propagation field at different time steps (in increased order from top-left to bottom-right). The three main component waves can be identified clearly.

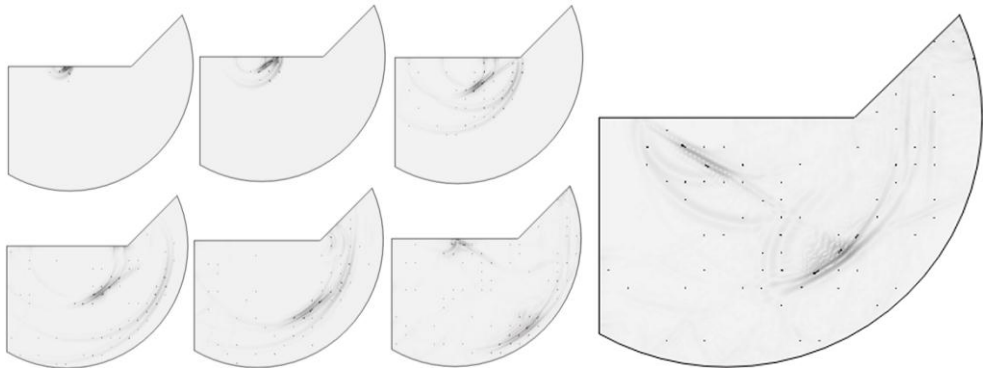

Figure 7 : Snapshots of 2D-total displacement time propagation field at different time steps (in increased order from left to right).

As explained previously, numerical simulation in time domain is not suitable for collecting the angular distributions of displacement amplitude, and so, numerical simulation in frequency domain is needed. As it can be remarked in Figure 8 (left) which presents the model setting, an absorbing region was used. The role of this kind of area is:

- reducing the time of computing (by reducing the size of the simulated structure);
- vanishing the spurious reflection to help make the analysis easier.

Eight incident angles are tested (from 12° to 19° by step of 1°). A typical result is shown in Figure 8 (right). This one corresponds to the incident angle which is equal to 14°. For better understanding, the same procedure developed and used in section 3 was applied, in this case, to plot planar refracted beam directivities.

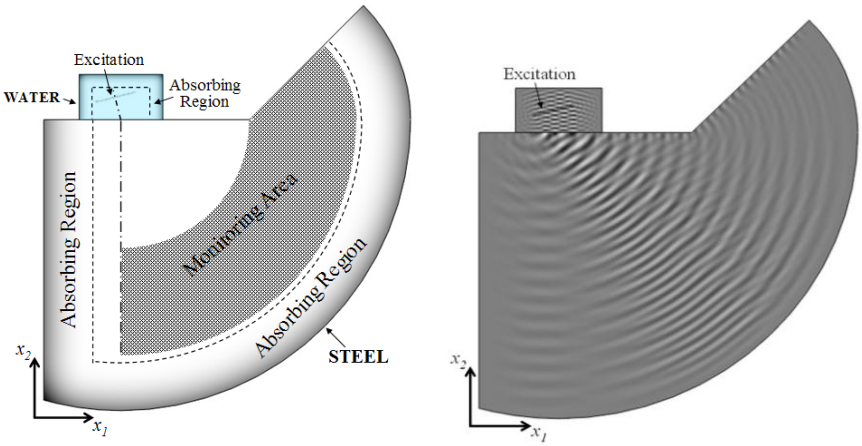

Figure 8 : Numerical simulation in frequency domain: model statement (left), and total displacement at f=2.25 MHz (right).

The obtained result is given in Figure 9 which plots numerical (black) and experimental (red) directivity (longitudinal displacement amplitude distributions), generated at a frequency = 2.25 MHz, and at different incidence angle. A well concordance between numerical and experimental results can be seen. The refracted beam consists of one main lobe and several side lobes. When the incidence angle increases, the main lobe turns (its principal refracted angle grow up), and secondary lobe number and sizes increase. At 18°, secondary lobes size is quasi-equal that of the main lobe. After that, the main lobe degenerates (at 19°). In the last cases, following these results, it is not advisable to work with these parameters because ultrasonic energy is not focused in one place.

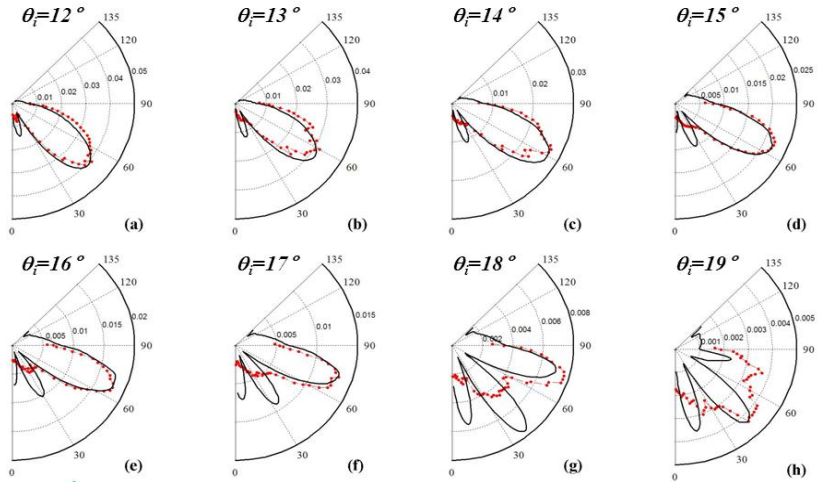

Figure 9 : Numerical (black) and experimental (red) directivity (longitudinal displacement amplitude distributions), generated at a frequency = 2.25 MHz, and different incidence angle. A well concordance can be seen.

At 90°, the maximum displacement amplitude is measured for all the incidence angles (from 12° to 19° by a step of 1°). The highest displacement amplitude is found at 15°, which is roughly 1° more than the critical incidence wave. The critically longitudinal refracted wave (generated at 15° in the case of water/steel) is different from the Creeping wave, which can be generated at critical angle (~14° in the case of water/steel) and decays quickly, after starting from the emitter.

5. Effect of the driven frequency

Numerical simulations were conducted to collect and plot refracted beam directivities at different angle of incidence. As in the previous section, the incidence angles chosen are around the critical one which is 14° (or approximately). The driven frequency chosen in this case is equal to 5 MHz which is more than two times that used in the previous section (Figure 9). In Figure 10, the collected longitudinal displacement amplitude distributions are plotted. As it can be remarked in this figure, and with Figure 9 kept in mind, subsidiary lobes are absent. From this side, operating with higher frequencies seems to be better than lower ones since secondary lobes can interact:

- with the top surface (surface where the transducer emitter is placed) of the structure to be tested/evaluated, as well as
- with the eventual defects and/or pre-stressed areas near that where the main lobe is,

In both cases, these phenomena may false the result.

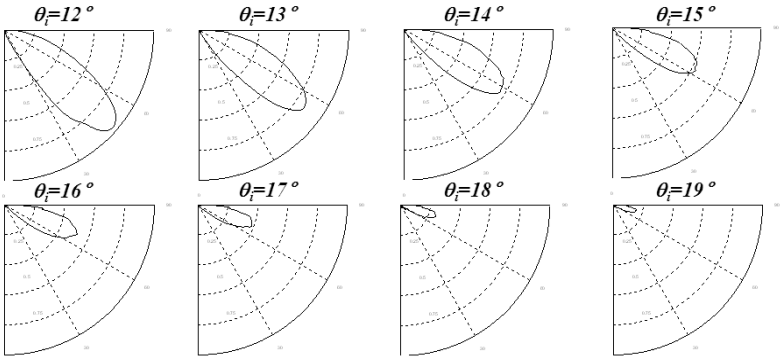

Figure 10 : Numerical directivity (longitudinal displacement amplitude distributions), generated at a driven frequency = 5 MHz, and different incidence angles.

The second point which should be underlined, and what is the aim of this section, is the displacement amplitude at the L_{CR} (refracted angle = 90°) versus the angle of incidence. For the sake of clarity, we dedicate the Figure 11 to this important information. This figure presents a barogram showing the measured amplitude at L_{CR} for such an incident angle (11°, 12°, 13°, 14°, 15°, 16°, 17°, and 18°), divided by the maximal directivity amplitude (refraction angle go from 0° to 90°), and multiplied by 100. As it can be seen, the maximal amplitude is obtained at 15°, as when the driven frequency is 2.25 MHz (see the previous section). In conclusion, with regard to numerical simulation results performed for two frequencies, and with respect to Snell-Descartes Law given by equation 2, we can affirm that L_{CR} is independent of the driven frequency.

We note that the amplitude of the displacement was not compared numerically with that obtained at a lower frequency (2.25 MHz). But, what it can be expected is that the displacement should decreases when the driven frequency increases. This implies that the higher the frequency, the shorter the distance between the transducer and the area of interest (either to detect subsurface defect or to measure residual stresses) is. In conclusion, a compromise between different and nested parameters such as:

- the driven frequency,
- the characteristics of the expected defect with its criticality level or
- the size of the prestressed area,
- accessibility (work *in-situ*),
- performance of the equipment,
- etc.

should be find to obtain an accuracy result.

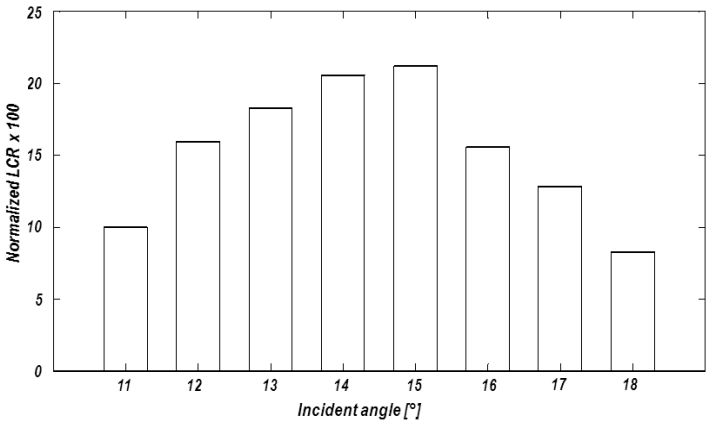

Figure 11 : Barogram showing the measured amplitude at L_{CR} (refracted angle = 90°) for such an incident angle (among 11°, 12°, 13°, 14°, 15°, 16°, 17°, and 18°), divided by the maximal directivity amplitude, and multiplied by 100.

6. Conclusion and perspectives

Conclusions from this parametric study are as following:

- Snell-Descartes law is not sufficient to understand the L_{CR} field behavior.
- The L_{CR} acoustical field is composed of several waves: longitudinal wave, transversal wave, head wave and surface wave.
- The edge effect of transducer (non-continuity of source) on the excited acoustical field was shown, and quantified with radial distribution.
- Driven frequency has no effect on the incident angle (which permits to get the maximal energy at 90°).
- The bigger the driven frequency, the lower the side lobes are.

Perspectives are:

- If the structure under test is relatively hot, what is the effect of T° on the behavior of LCR field?
- How and which parameters should be optimized to obtain the bigger depth penetration to detect subsurface, for example?
- To evaluate residual stress near weld, what is the optimal distance between it and the transducer?
- How to optimize overcoming the effect of roughness?
- ...

OPTIMIZATION OF THE FULL MATRIX CAPTURE PARAMETERS OF ULTRASONIC TRANSMIT–RECEIVE ARRAY DATA FOR NON-DESTRUCTIVE CHARACTERIZATION OF DEFECTS

F. Koubaydatt, S. Chaki, S. Hariri, M. Douai, TPCIM, France
B. Dupont, F. Berthelot, F. Koubaydatt, CETIM, France

ABSTRACT:

One of the interesting functions offered by the phased array technology for defects characterization is the Full Matrix Capture (FMC) associated with the reconstruction algorithm Total Focusing Method (TFM).
The defects Characterization using this function depends on the ultrasound beam shape, which depends itself on the choice of some control parameters such as: central frequency, transducer opening (pitch and number of elements), angle of refraction, transducer position and attenuation.
The aim of this paper is, firstly to study the influence of these parameters on the ultrasonic beam and especially on the FMC-TFM resolution. Secondly, these parameters are optimized in order to allow a quantitative characterization of defects.
A series of simulations with CIVA software were performed to carry out this study according to an experimental design approach, which was established taking into account all the previous parameters.
The obtained results show the importance of certain parameters such as number of elements, frequency and attenuation on the ultrasonic beam width and consequently on a quantitative defect characterization.

Key words:
Phased-array, Non-destructive testing, Full matrix capture, Total focusing method, Excitation parameters, Experimental design method.

1. Introduction

For obvious safety reasons, the presence of an indication in a weld of an item of Pressure Equipment requires knowledge of its harmfulness. This is why the indication needs to be best characterized through various destructive or non-destructive testing methods. Currently, the non-destructive methods used to inspect welds are surface methods (such as dye penetrant inspection and magnetic particle inspection) as well as volume methods such as conventional ultrasounds, X-ray examinations and Time Of Flights Diffraction (TOFD). All these methods are standardized.
Due to the possibilities that it offers, ultrasonic phased array technology represents an interesting alternative to X-ray examination (reference but costly and harmfulness method for people and the environment) for detecting and characterizing defects [1]. Phased array ultrasonic inspection does not yet propose acceptance criteria nonetheless; there are promising possibilities of defect characterization.
A number of interesting functionalities for characterization such as Full Matrix Capture (FMC) associated with the TFM (total focusing method) reconstruction algorithm can be obtained with this technology [2].
The aim of this study is to use the FMC functionality coupled with the TFM reconstruction algorithm to examine how certain phased array ultrasonic inspection parameters influence the characterization of defects.

These parameters include in particular the frequency, transducer opening (pitch and number of elements), the angle of refraction, the position of the defects regarding the axis of the transducer and the defect placement depth. Series of simulations were carried out with the CIVA software for this study according to an experimental design approach taking into account all the previous parameters.
The first part of the paper is an overview of the principles of the FMC functionality and the TFM algorithm as well as a few points of theory regarding the ultrasonic beam. The second part analyses the results of the experimental design implemented to optimize the testing parameters and thereby improve defect characterization.

2. Reminders: FMC-TFM and focusing of the ultrasonic beam

Figure 1 below explains the principle of the FMC functionality.

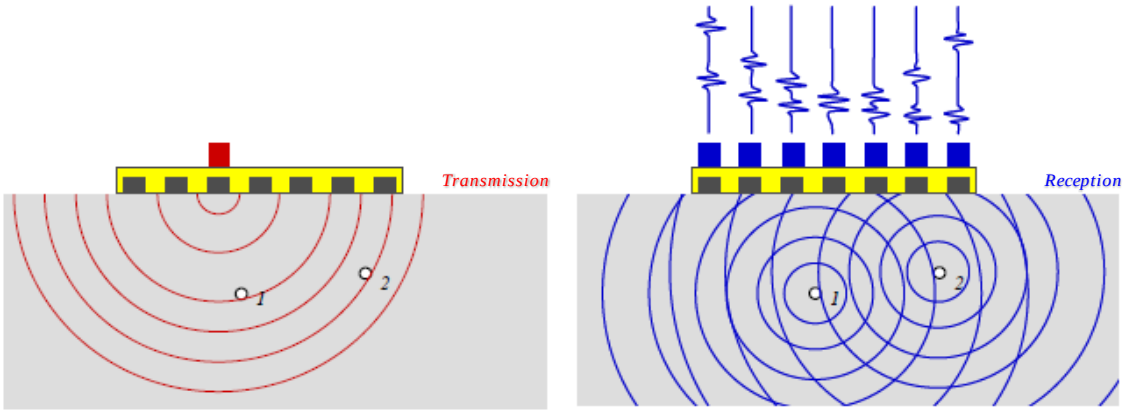

Figure 1: Block diagram of the FMC operation [3]

The FMC functionality involves successively transmitting with each element j of the transducer and receiving for each shot all the elementary signals i received by the elements of the network. A set of NxN elementary signals $k_{ij}(t)$ is therefore recorded in a matrix referred to as an Inter-element Matrix, where N is the number of activated elements transmitted and received. Once the inter-element matrix is acquired, the entire data is post-processed with the TFM reconstruction algorithm.
This post-processing implemented in the CIVA software involves defining a reconstruction zone *ROI* (position, dimensions and meshing), then calculating the theoretical time of flight $T_{ij}(P)$ for each point P of the zone corresponding to the time of flight between the transmitter j and the receiver i through point P (see Figure 2).
The synthetic focusing is carried out by adding in each point P the amplitudes $A_{ij}(P)$ extracted from the signals $k_{ij}(t)$ at the time of flight $t = T_{ij}(P)$ [4].
This algorithm is also used to reconstruct the image I in each point P:

$$I(P) = \left|\sum_{i=1}^{N}\sum_{j=1}^{N} A_{ij}(P)\right| \quad (1)$$

Where: $A_{ij}(P) = k_{ij}[t = T_{ij}(P)]$ at point P.

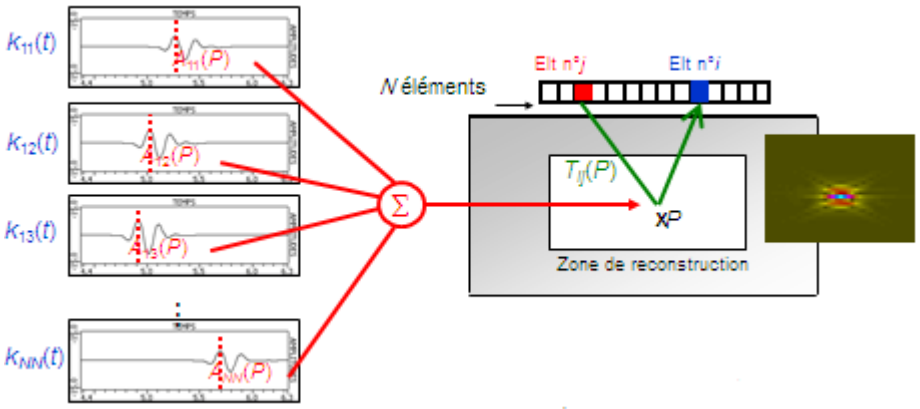

Figure 2: Principle of the TFM reconstruction. (CEA)

A fine characterization of the defects requires control of a few parameters directly influencing the characteristics of the ultrasonic beam. The main characteristic is the beam opening which depends on the geometric dimensions of the active element, the frequency and velocity of propagation of the inspected medium.

Two zones are considered in the propagation axis of the ultrasonic beam from a non-focused transducer: the Fresnel zone and the Fraunhofer zone.

The Fresnel zone (near field) is characterized by a severely disturbed acoustic field which makes it difficult to inspect this zone. The pressure field suffers a succession of amplitude maxima and minima [5]. The last acoustic pressure maximum corresponds to the limit of the near field zone, which, for a circular tip, depends on the square of the diameter of the transducer *D* and the wavelength *λ*.

$$l_0 = \frac{D^2}{4\lambda} \tag{2}$$

In the case of a phased array transducer (linear arrangement), the length of the near field depends on the active transducer opening *D* (mm) which depends on the number of active elements *N*, pitch *p* and the inter-elements space *ei*, the frequency *f (Hz)*, the velocity in the medium *v (m/s)* and a correction factor *K* to switch from a circular transducer to a rectangular transducer. This factor *K* depends on the ratio between the width and the length of the active transducer opening [6].

$$l_0 = K * \frac{D^2}{4\lambda} \tag{3}$$

Where, $D = N * p - ei$, and $\lambda = \frac{v}{f}$ is the wavelength.

Beyond the Fresnel zone is the ***Fraunhofer zone*** (or far field), where the ultrasonic energy is optimum and features a regular attenuation profile. This latter zone is also characterized by a divergence of the beam, which has negative effects on the assessment of the defects [5].

The TFM algorithm is used to focus the ultrasonic beam in all points. This TFM reconstruction applied to the inter-element matrix in a point *P* amounts to determining the ultrasonic energy in this point when *N* elements are used with a focusing type delay law in this point. The focusing region is called the *focal zone*. The width of this focal zone at -6dB depends on the focal distance *F* of the transducer opening *D* and the wavelength *λ*.

$$l_{-6dB} = \lambda \frac{F}{D} = \frac{v*F}{f*D} = \frac{K*D*F}{4l_0} \tag{4}$$

Note that according to equation 3 and equation 4 if the opening and the frequency of the transducer increases then the length of the near field increases and the width of the beam decreases.
This study of the influential parameters on the characterization of the defects is presented below.

3. Definition of the influential parameters

In NDT domain, it is becoming increasingly common to firstly study the phenomena with numerical simulations for economic reasons and also to help interpret experimental results. Moreover, it is often difficult to study several parameters involved in a phenomenon all the more so as there are many and that there may be interactions between them. It is therefore advantageous to organize the simulations to be carried out within the framework of an experimental design.

Table 1 presents the various parameters studied with their low level (-) and high level (+). The definition of the values of the parameters stems from the usual NDT configurations.

No.	1	2	3	4	5	6
Parameters / Level	Depth of the defect (mm)	Position of the defect with regard to the axis of the beam (mm)	Angle of refraction (°)	Number of elements	Pitch (mm)	Frequency (MHz)
-	10	0	0	16	0.5	5
+	30	2	45	64	0.8	10

Table 1: Parameters taken into account

The studied defects are side drilled holes (SDH) of 0.2 and 3 mm diameters located to 10 and 30 mm in depth.
The strategy of the experimental design adopted to carry out the simulations involves taking into account all the parameters and all possible interactions between them. This amounts to implementing a type 2^k factorial design (k is the number of parameters to be studied and the Figure 2 refers to the number of levels given to each parameter) [7]. For this study, k = 6 and therefore 64 simulations must be carried out for each SDH diameter where the level of a single parameter is changed by switching from one testing configuration to the other. The width of the dynamic echo at -6 dB of the wave/defect interaction signal was designated as the result of a simulation. The best testing configuration will be that which will give a width of the same order of magnitude as the diameter of the studied SDH.
This experimental design approach will make possible to prioritize the 6 parameters studied with respect to their effect on the result.

4. Results and discussion

The results of the parameters influence on the width of the dynamic echo obtained on the SDH will be presented in this section. This study will allow us to define the best configurations for characterizing a defect independently to its size.

4.1 Widths measurements

Figure 3 shows the width of the dynamic echo at -6 dB as a function of the applied configuration for the two SDHs of 0.2 mm and 3 mm diameters.

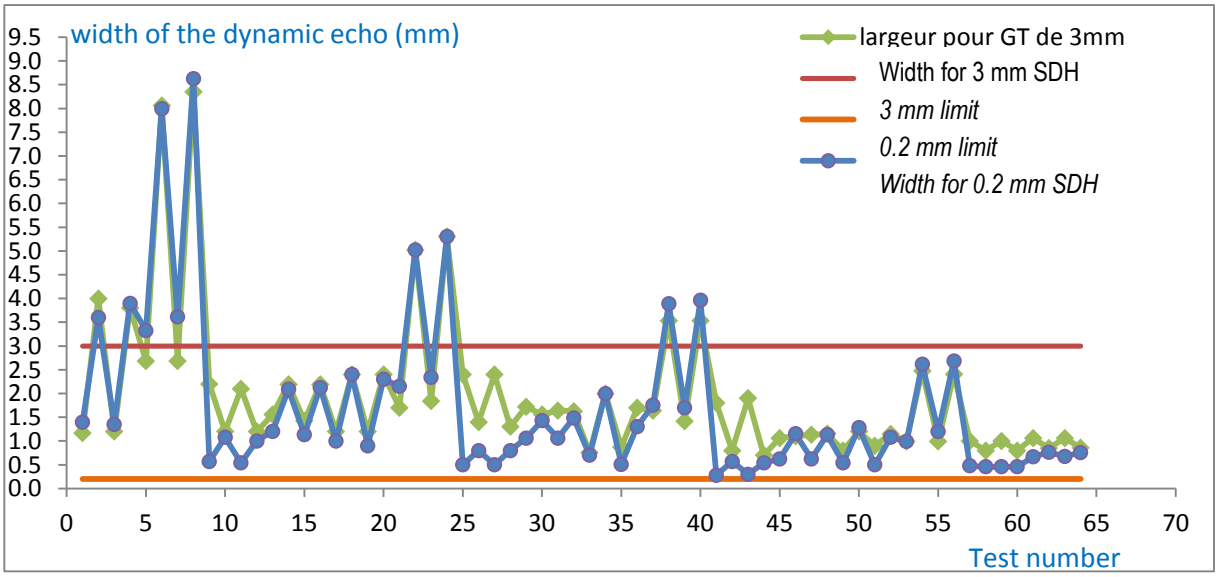

Figure 3: Width of the dynamic echo obtained for the 0.2 and 3 mm SDH

Two groups of configurations can be identified from figure 3:

1. Those configurations which give the same results irrespective to the SDH size. They are not suitable for the defect characterization.
2. Those configurations whose results differ as a function of the SDH size. Amongst these, the configurations with wide variations (see Table 2) will be analysed to select the optimum configuration for the defects characterization.

Test numbers	Depth of the SDH (mm)	Position of the defect with respect to the axis of the beam (mm)	Angle of refraction (°)	Number of elements	Pitch (mm)	Frequency (MHz)	Width obtained on SDH (3 mm)	Width obtained on SDH (0.2 mm)
9	10	0	0	64	0.5	5	2.2	0.57
11	10	2	0	64	0.5	5	2.1	0.54
25	10	0	0	64	0.8	5	2.4	0.5
27	10	2	0	64	0.8	5	2.4	0.5
41	10	0	0	64	0.5	10	1.8	0.28
43	10	2	0	64	0.5	10	1.9	0.3

Table 2: Configurations for Group 2: The result varies as a function of the SDH diameter

Note that configurations 9 and 11 yield the most varied results compared with the other configurations in the table as regards the actual width of the studied defects. These configurations are therefore not suited to characterization of the indications.
Configurations 41 and 43 are suited to the testing of 0.2 mm SDH whereas configurations 25 and 27 are better suited for the 3 mm SDH. The only difference between configurations 41 and 43 (respectively 25 and 27) concern the position of the centre of the SDH with respect to the beam axis.

This parameter therefore does not have a lot of influence on the result (width of the dynamic echo) as both SDHs are always positioned in the transducer field.
However, the difference between configurations 25 and 41 (respectively 27 and 43), which justify selecting one over the other for a given SDH, concerns parameters involved in the construction of the ultrasonic beam that is to say the frequency (5 MHz /10 MHz) and the pitch (0.8 mm / 0.5 mm).
Nonetheless, and in the reality of an industrial testing, the size of the defects is unknown in principle hence the need to find a testing configuration which helps to characterize the defect irrespective of its size. To this end, the focus will now be placed on assessing the deviations obtained for all configurations between the measured width and the actual diameter of the SDHs.

4.2 Dimensioning deviation

The deviations obtained between the measured width and the actual diameters of the SDH are displayed on figure 4.
Many configurations give markedly different measured values than the actual value (deviation exceeding 400 %). For the purpose of clarity, only the configurations for which the deviation is less than 400 % are displayed.

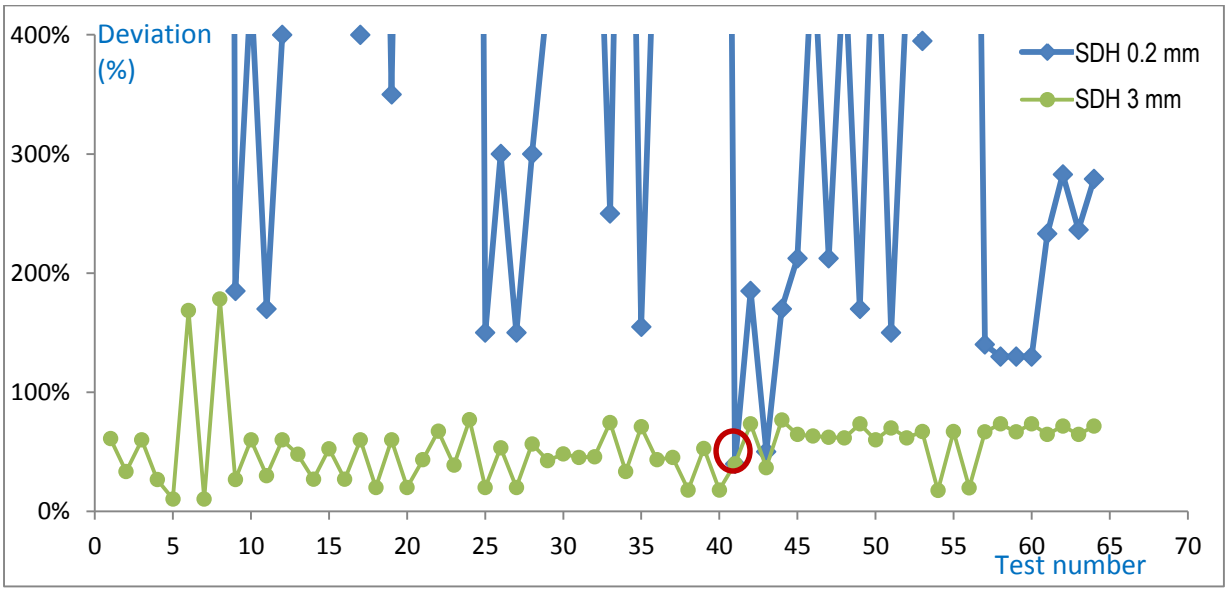

Figure 4: Measurement deviation for each configuration

Figure 4 makes it possible to identify:

1. The ***best configurations as a function of the defect***. As was previously mentioned, configuration 41 is best suited to characterizing the 0.2 mm diameter defect as here it generates the lowest deviation (~40 %). However, by analysing the measurement deviations, configurations 5 and 7 are best suited to characterizing the 3 mm diameter defect (10 %). Between configurations 5 and 7, only the position of the defect with regard to the beam axis changes.
2. Configuration 41 gives both ***the lowest and the same measurement deviation*** (40 %) irrespective of the SDH size. Therefore, this last configuration is selected for characterizing the defects ranging between 0.2 and 3 mm.

4.3 Analysis of the results

The 40 % deviation obtained with configuration 41 for the dimensioning of the 0.2 and 3 mm diameter SDHs is very significant. This deviation is partly explained by the cylindrical shape of the reflecting surface of the SDH. The ultrasonic energy is therefore reflected in all directions and not only towards the transducer.

In order to validate this assumption, configuration 41 was applied on two flat defects of 0.2 mm and 3 mm in width.

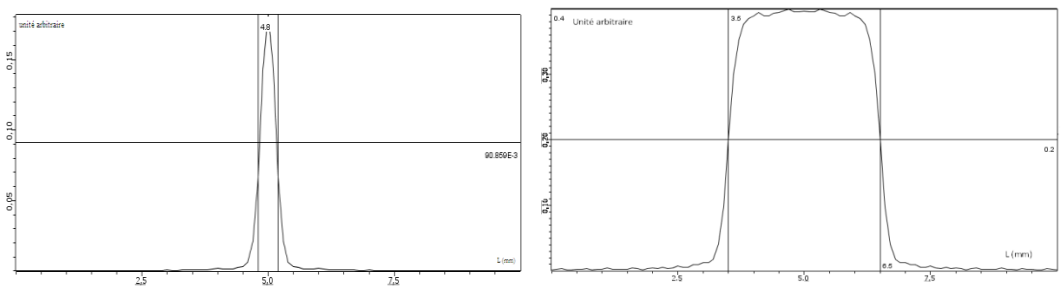

Figure 5: Echo dynamic curves obtained with configuration 41 on a flat defect of 0.2 mm width (left) and 3 mm with (right).

The width obtained for the 0.2 mm defect is equal to 0.33 mm i.e. 65 % deviation and that obtained for the 3 mm defect is equal to 3 mm, that is 0% deviation.

It is clear that this configuration has improved the characterization for the 3 mm defect. In this case, the previous assumption is validated according to which the ultrasonic energy reflected by a flat defect is fully returned to the transducer. However, the width measured (0.33 mm) for the flat 0.2 mm defect remains comparable to that obtained for the SDH (0.28 mm) and the deviation is still significant. By calculating the field for configuration 41, the following beam is obtained:

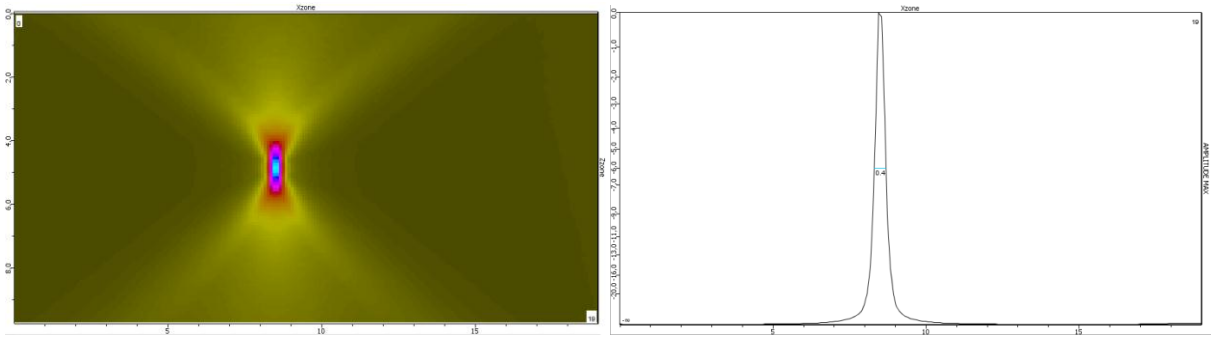

Figure 6: Beam generated by configuration 41 with focus at 10 mm depth (left) and width of the focal zone at this depth (right).

Note that the width of the beam at 10 mm depth (0.4 mm) is greater than the size of the defect studied (0.2 mm). Consequently, a defect that is smaller than the width of the beam irrespective of its shape cannot be finely characterized.

In a theoretical point of view, the length of the near field of the transducer with this configuration is equal to 425 mm (equation 3), i.e. forty times more than the depth of the SDH at 10 mm. Moreover, if the focal distance is small with respect to the limit of the near field (in our case the focal distance is equal to 10 mm), the width of the focused beam decreases (see equation 4). This configuration is therefore logically more optimal for characterizing a defect irrespective of its size.

The same configuration is thus applied for the defects located at 30 mm in depth (configuration 42). The results are given in the table below.

Size of the defect	0.2 mm	3 mm
Deviation for the SDHs	180 %	70 %
Deviation for the flat defects	200 %	0 %

Table 3: Deviations obtained with configuration 42 for the studied defects.

Compared with configuration 41 (defect at 10 mm depth), a degradation of the results for the 0.2 mm defects (almost constant with an absolute value) is noted. In fact, the focal distance (30 mm) increases with respect to the limit of the near field and accordingly the width of the focused beam also increases. The width of the beam is once again markedly higher than the size of the defect (see image below).

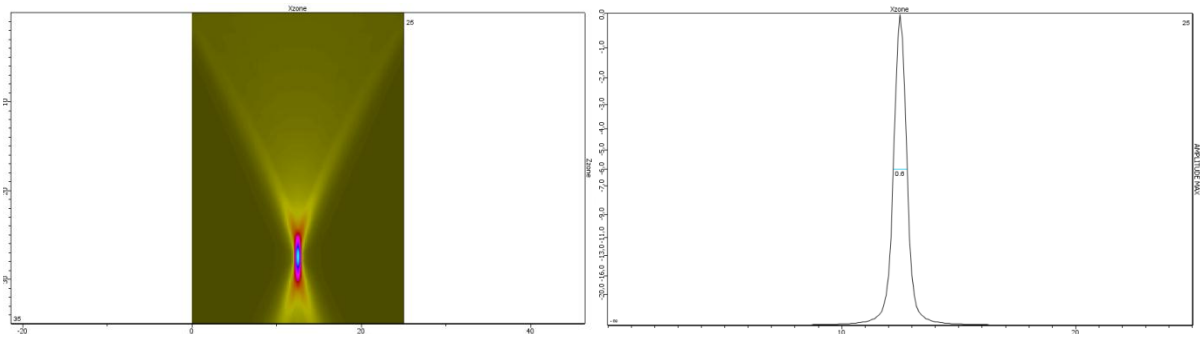

Figure7: Beam generated by configuration 42 with focusing at 30 mm depth
and width of the focal zone at this depth

With regard to the 3 mm defect, a degradation of the result in the case of the SDH defect (70 % deviation instead of 40 % previously) can be noted whereas the flat defect is properly characterized (0 % deviation). This degradation stems, on the one hand, from the width of the beam which increases with the focal distance (30 mm) and, on the other hand, the cylindrical shape of the SDH.
Applying the TFM algorithm to the matrix obtained by FMC therefore amounts to generating a beam focused at the indication depth.

5. Conclusions and perspectives

In this paper, an experimental design was carried out to study as accurately as possible, how the testing parameters such as frequency, transducer opening (pitch and number of elements), the angle of refraction, the position of the transducer with respect to the defect and the depth of the defects, influence the characterization of the defects by using the FMC functionality and the TFM reconstruction algorithm. The configurations which are not suited to the defect characterization were identified given that the results obtained were identical irrespective of the size of the defect.
Furthermore, the configuration which gives the same deviation for the dimensioning of two defects of different size was identified. This configuration proves to be optimal for the characterization of defects. As a matter of fact, the deviation obtained even though it was significant due to the type of defect modelled (SDH), was greatly reduced on a flat defect. However, a defect that is smaller than the beam cannot be accurately characterized. The field calculations confirmed this truth that has been long known in NDT. The electronic focusing applied by the phased array ultrasonic technology or synthetically applied using the FMC coupled with the TFM algorithm, improves the characterization up to a certain limit with regard to the smallest-sized defect that can be detected (function of wavelength and beam size).

For the future work, this experimental design should help to firstly calculate effects of the various parameters studied on the width of the wave/defect interaction beam. Secondly, it should help to establish a mathematical model that compares the results of the simulations and consequently saves a significant amount of time. The interest of this model will be calculating all the responses of the studied domain without being obliged to perform the tests (simulation or experiments). Finally, these results will be applied to the inspection of welds.

References

[1] L. D. ROUMILLY, "Introduction à la technique ultrasonore multiéléments," *Techniques de l'ingénieur*, 2012.

[2] P. C. M. L. S. P. S. C. A. Fidahoussen, "Imaging of Defects in Several Complex Configurations by Simulation-helped Processing of Ultrasonic Array Data," *Review of progress in QNDE,* vol. 29, 2010.

[3] B.DUPONT, *"Etudes numérique et expérimentale des technologies ultrasonores multiéléments en vue d'une application en Contrôle Non Destructif des matériaux",* thése de doctorat: Université de Technologie de Compiègne, CETIM, 2010.

[4] O. C. M. N. O. R. S. Robert, "Méthodes ultrasonores de détection et d'imagerie temps-réel implémentées dans les systémes d'acquisitions," *NDT, Cofrend,* 2011.

[5] A. LAMBERT, "Les faisceaux acoustiques des traducteurs utilisés en contrôle par ultrasons," CETIM, 1987.

[6] N. Dubé, Phased Array Technical Guidelines, USA: R/D Tech, 2005.

[7] J. Demonsant, Comprendre et mener des plans d'expériences, AFNOR, 1996.

[8] J.Goupy, Les plans d'expérience, Revue Modulad, 2006.

REACTOR PRESSURE VESSEL I

A REVIEW OF INSPECTIONS CONDUCTED ON BELGIAN REACTOR PRESSURE VESSELS AFFECTED BY HYDROGEN FLAKING

Ph. Dombret, A.S. Bogaert, F. Somville, Tractebel Engineering, Belgium

ABSTRACT

During the 2012 outage at Doel 3 Nuclear Power Plant, specific ultrasonic in-service inspections were performed to check for underclad cracking in the Reactor Pressure Vessel (RPV). No such flaws were found but a large number of nearly-laminar indications were detected, mainly in the lower and upper core shells. A second inspection was performed with ultrasonic probes able to inspect the whole thickness of the vessel and identified the same type of indications deeper in the material. A similar inspection performed in September at Tihange 2 Nuclear Power Plant showed similar indications but to a lesser extent. The observed indications could subsequently be attributed to hydrogen flaking induced during the component manufacturing process.

As a consequence, both units stayed in cold shutdown pending the elaboration of an extensive safety case demonstrating that they can be operated safely. Among other measures, they were subjected to a pressure test monitored by acoustic emission, and to additional UT examinations aiming at verifying that no material condition modification was caused by the pressure test.

The paper reviews the methods and results of the various examinations conducted on the Doel 3 and Tihange 2 Reactor Pressure Vessels, from their manufacturing up to the latest outcomes.

THE ACCIDENTAL DISCOVERY

In July 2012, Unit 3 of Doel Nuclear Power Plant started its third 10 year outage. Doel 3 is a three-loop 1000 MWe PWR of Framatome design, operated by Electrabel. It was constructed and is operated according to the ASME Code (1), transposed to the Belgian national context.

The outage program included a regulatory inspection of the Reactor Pressure Vessel (RPV) and an additional examination of the RPV beltline region that was planned following the international experience return to verify the absence of manufacturing-induced underclad cracking. Ultrasonic Testing (UT) revealed no such underclad cracking but many unexpected echoes were observed by straight beam transducers (Fig. 1).

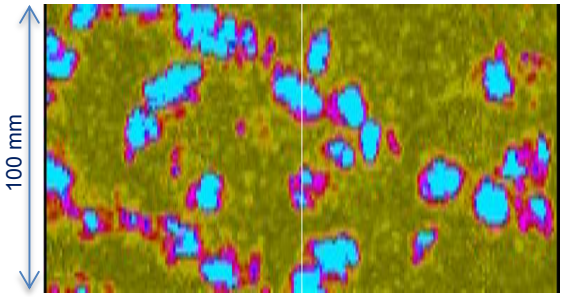

Fig. 1 – Flaw indications observed by straight beam search unit in the RPV beltline region of Doel 3

The UT indications morphology led to suspect some manufacturing-induced flaw type. As the underclad cracking inspection was restricted to the RPV beltline region over a maximum depth of 25 mm from the ID surface, a decision was made to extend the inspection to the full thickness of all RPV forged components in order to fully document the extent of the flaws.

As Unit 2 of Tihange NPP was constructed at the same period, by the same contractors and under the same orders as Doel 3, a similar examination of its RPV was also readily planned during its next refueling outage, i.e. in September 2012.

DOCUMENTING RPV CONDITION IN DOEL 3 AND TIHANGE 2

UT equipment and method

The equipment commonly used in Doel and Tihange for RPV inspection is the MIS-B developed by Intercontrôle (Fig. 2). It operates a number of independent tools that bear UT, ET and VT sensors dedicated to the various RPV zones subjected to in-service examination. The MIS-B equipment and the associated NDE methods have been qualified years ago, according to domestic rules. In order to characterize the laminar flaw population in all forgings, three tools were mobilized, addressing the cylindrical shells, the transition ring and the vessel flange. In parallel, the head flange was subjected to manual UT.

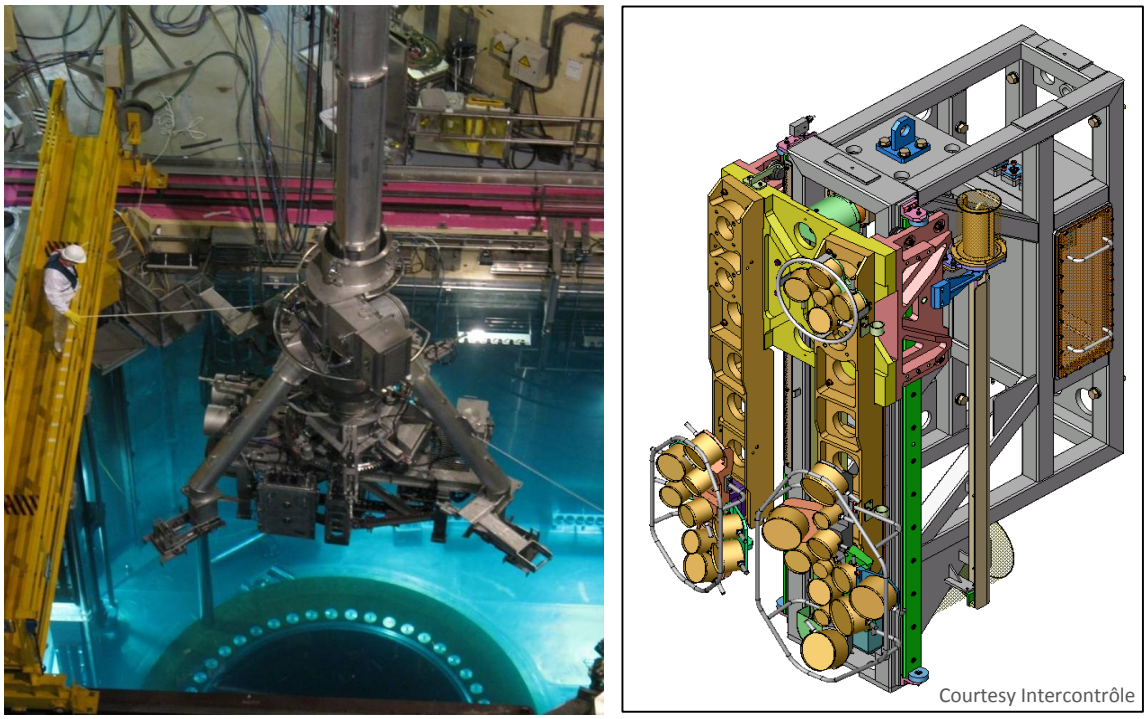

Fig. 2 – The MIS-B equipment (left)
and the tool implemented for RPV circular weld examination (right)

The examination method relies on beam focusing. For each sound propagation orientation, the full wall thickness (200 mm) is covered by three transducers with overlapping depth ranges ; this allows minimizing the acoustic beam width variation through depth. Fig. 2 illustrates the cylindrical shell and flange examination tools.

Experimental trials were carried out on site to determine the reporting threshold needed to document all significant indications. Based on the signal reflected by a 2 mm dia. hole side-drilled in an unclad calibration sample, a threshold of -12 dB was selected, except in the first 25 mm, where the threshold was lowered to -18 dB.

Inspection results

Figure 3 displays the number of flaw indications observed in both core shells of Doel 3 and in the upper core shell of Tihange 2 ; all other RPV forgings appear to be free from significant degradation.

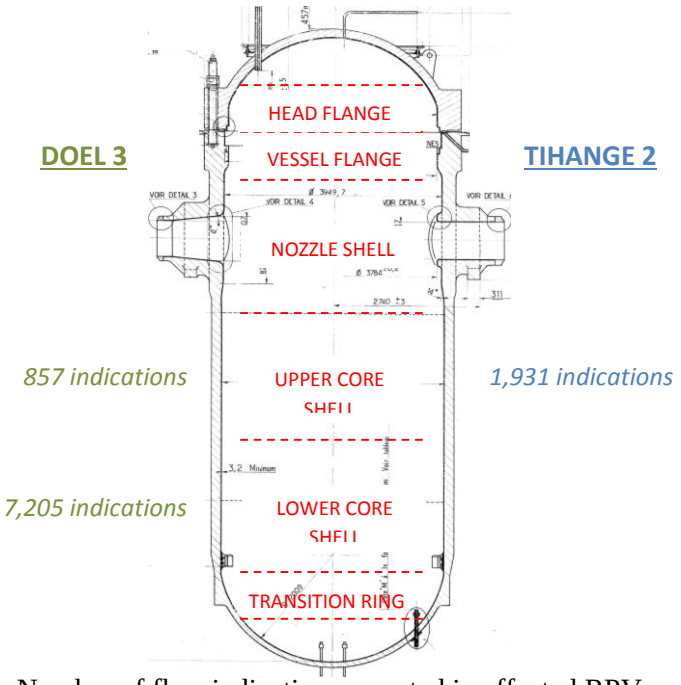

Fig. 3 – Number of flaw indications reported in affected RPV components

The laminar character of flaws was confirmed, with an off-axis orientation of up to 10° ; indeed, the detailed analysis of angle beam examination data associated to about 30% of the indications observed in Doel 3 and Tihange 2 revealed that angled insonification does not contribute effectively in the flaw detection and characterization capability.

The flaws form a large cluster sinking with decreasing altitude. In all cases, the upper and lower edges of the shells are sound, which explains why weld in-service inspections never reported such indications.

Most indications are located in the first half of the shell thickness, between 20 to 80 mm from the inner surface (Fig. 4). In Doel 3 however, some of them were found close to the 7 mm thick clad interface. The largest dimension of flaws is typically 5 to 15 mm ; larger sizes appear to result from unresolved flaw clusters.

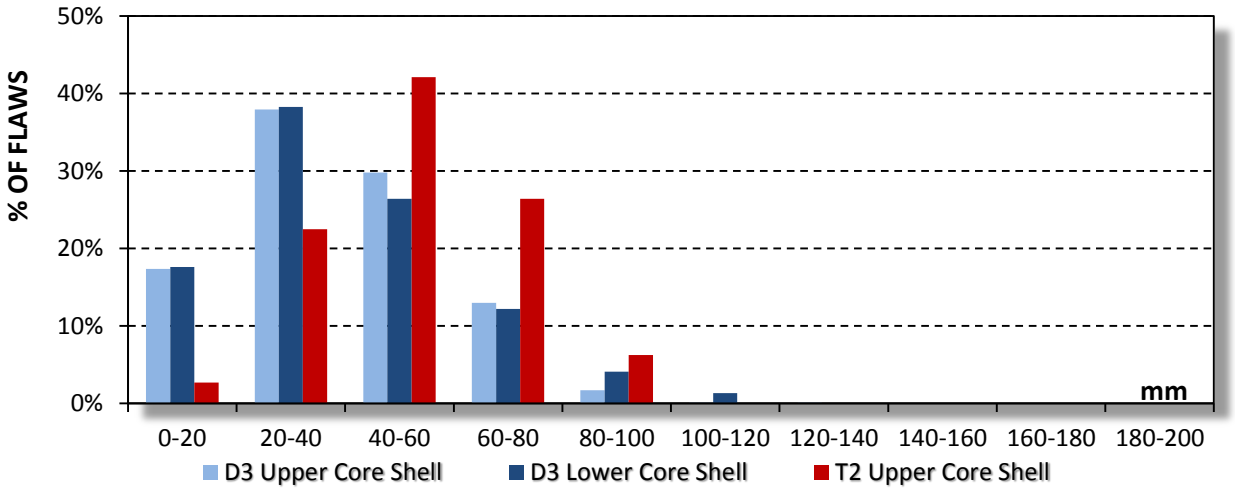

Fig. 4 – Distribution in depth of flaw indications

ELABORATION OF A SAFETY CASE

The Licensee decided to keep both Doel 3 and Tihange 2 units in cold shutdown with the core unloaded, and initiated various analyses and a testing program supporting a Safety Case to be submitted to the Belgian Safety Authorities in support for a request to restart of operation. Extensive investigations addressed reviewing the construction files, material testing on sound and flawed steel specimens, validating the UT inspection capability and elaborating original tools to assess structural component integrity.

Also, a thorough root cause analysis was conducted, which eventually confirmed hydrogen flaking as the most likely origin of the indications. Hydrogen flakes are crack-like laminar flaws (Fig. 5) that may occur during the manufacturing process, particularly in ghost lines, which feature the highest positive segregation coefficient.

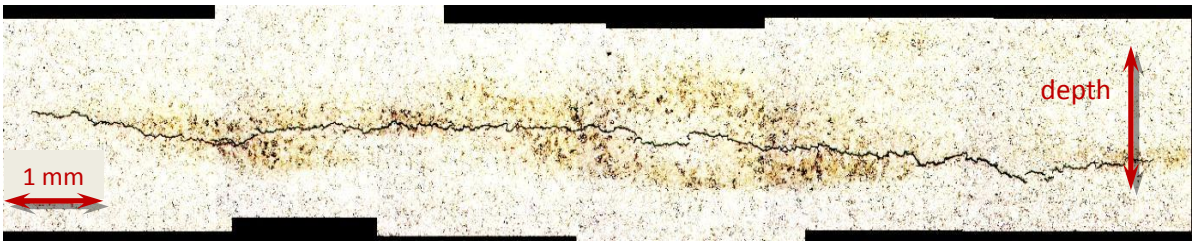

Fig. 5 – Macrograph of hydrogen flake

Comparison of shop examination and in-service inspection results

The review of the Doel 3 and Tihange 2 construction files could retrieve all manufacturing inspection reports requested by contractual provisions and by the applicable regulations, i.e. ASME Section III. None of those documents mentioned indications comparable to the 2012 in-service data, except an internal UT examination form, issued by the manufacturer, that was shortly after superseded by a blank official report countersigned by the customer.

Knowing that the flaws were already present at that time, such observations questioned the absence of reporting during the fabrication process and, more essentially, the rightful acceptance of the RPV shells. Although it remains difficult to reach absolute certainty about what happened nearly 40 years ago, significant insights could be gathered in spite of the impossibility to reproduce nowadays the shop examination of the actual shells.

It should be first realized that the examination conditions differ greatly between 1975 and 2012 : shop inspection was conducted manually from the outer surface, with contact search units (B4S), and rejection criteria essentially based on back wall echo extinction, whereas in-service inspection is fully automated and insonifies the component from the inner surface, through the stainless steel clad layers ; in addition, the narrow beams generated by focusing probes enhance testing sensitivity, and the reporting level is fairly low.

The experimental implementation, on a specimen affected by hydrogen flaking, of 3 manufacturing UT procedures, including the one applied in 1975 on the Doel 3 and Tihange 2 shells, showed that the latter is quite sensitive in terms of flaw reporting, yet very tolerant regarding component rejection (2).

Parallel UT modelling works lead to believe that the flaws were indeed detectable and reportable by the original shop inspections, but that the rejection threshold was most probably not reached (3) ; that conclusion was subsequently reinforced by another study (4). The reason why flaws were not reported at that time remains unclear.

Evaluation by Safety Authorities

At the end of 2012, the Licensee submitted for each unit a Safety Case documenting the safe serviceability of the RPV (5, 6). After evaluation of the files, Safety Authorities concluded that some issues remained open, which however did not represent conditions requiring a definitive shutdown of the units, but that the Licensee still had to resolve ; some new requirements were prerequisites to the restart of both units, while others could be addressed during the next operating cycle (7).

Several short-term actions were conducted to supplement the Safety Cases in the field of mechanical testing and UT validation (3). The program also included performing in each unit a load test, at a pressure slightly higher than the design pressure, and to be complemented by acoustic emission (AE) testing and UT to demonstrate that the RPV condition was not modified by the overpressure.

RPV LOAD TEST INSPECTIONS

In each unit, the load test was carried out for about 9 hours in total, at a maximum pressure of 175 bars and a minimum temperature of 117°C. No unexpected event occurred.

Acoustic emission testing

The test was performed during the whole load test, according to the AFIAP guidelines (8). Six sensors were positioned onto the RPV head, 6 on the inlet and outlet nozzles and 3 in the in-core instrumentation room (Fig. 6). The methodology classifies AE events into 3 categories, from I (insignificant signals) to III, which imposes further local inspection; events classified under II lead to recommend additional inspection.

Care must be taken however in interpreting AE results, as test conditions departed from the ideal environment assumed by the AFIAP guidelines: the RPV was not isolated from the primary circuit, and operating conditions generated intensive acoustic activity, which precluded discriminating between categories I and II events. As no source was attributed to category III, the test eventually concluded in recommending a UT examination of one 60° sector of the RPV in Doel 3 and 2 sectors in Tihange 2.

Noteworthy, the Doel 3 sector corresponds to the lower core shell part featuring the highest flaw density, whereas the Tihange 2 sectors appear randomly positioned with reference to UT indications.

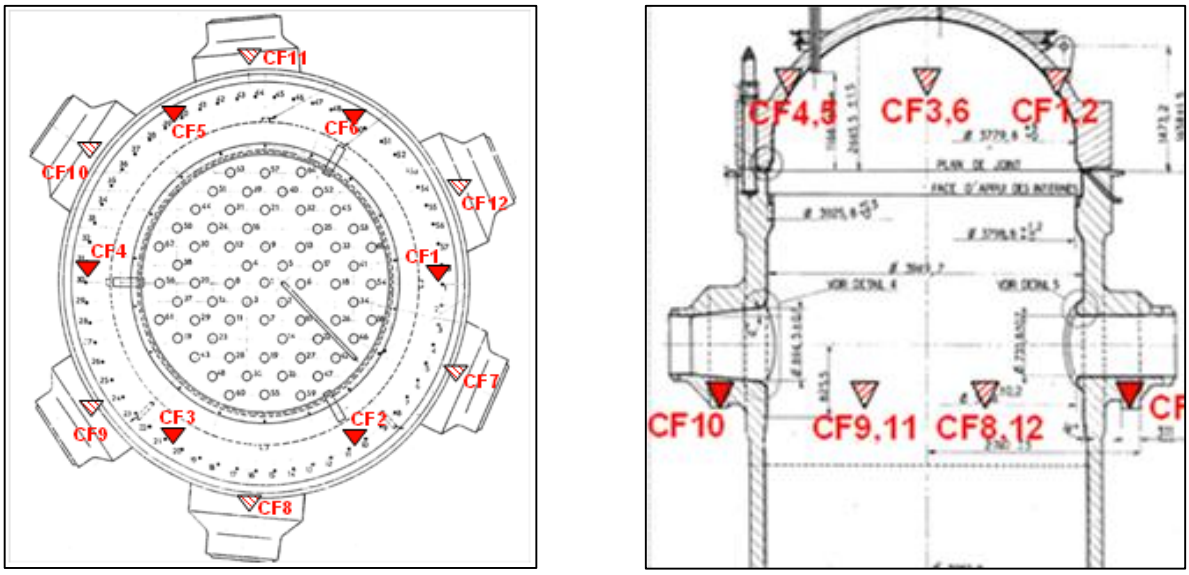

Fig. 6 – Disposition of AE sensors on the RPV

Ultrasonic examination

UT was requested to compare flaw indications observed before and after the load test in both core shells of Doel 3 and in the upper core shell of Tihange 2, in order to demonstrate that pressure had no effect on material condition.

Flaw evolution criteria

The ASME Code applied in Belgium does not require comparing ultrasonic signatures recorded by successive examinations. Consequently, a decision was made to rely on comparison rules prescribed by French regulations : a no-growth diagnosis is reached if the following conditions are simultaneously met by any indication in successive examinations :

1. the amplitude variation does not exceed 6 dB ;
2. the variation of each dimension does not exceed 150% of the sound beam width (at the flaw indication depth).

A linear model fitting accurately the beam profiles of the 3 0° transducers was devised to make easier and faster the comparison process (Fig. 7).

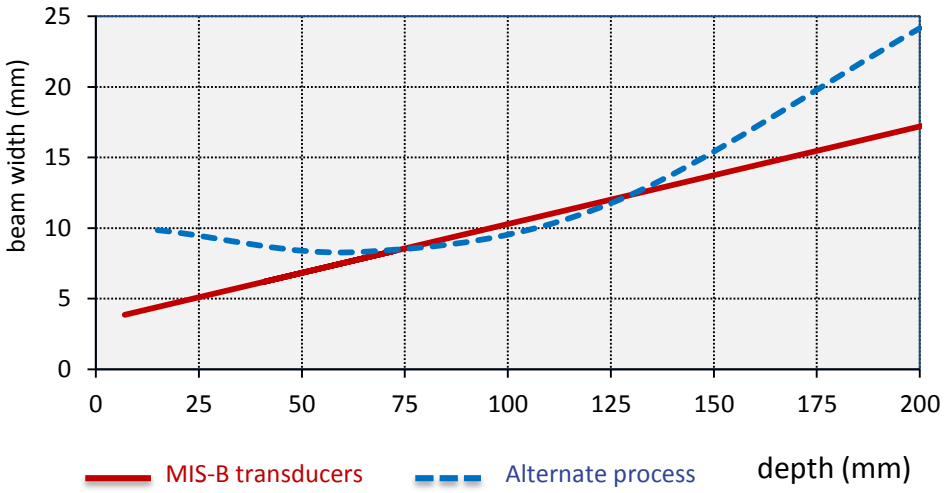

Fig. 7 – Ultrasonic beam width models

Doel 3 alternate pre-load test examination

As the MIS-B equipment could not carry out both interventions without significant delay, the Licensee decided to entrust the Doel 3 examination to another experienced and recognized company, and requested firstly a pre-load test inspection to define a comparison baseline. Using standard immersed 0° search units, about 30% of the flaw indications observed in 2012 could be detected, but repeated scans of a small area demonstrated that the evolution criteria could not be complied with, because resolution was penalized by too large values of acoustic beam width (Fig. 2) and scanning step.

It was consequently decided to start with the load test and to wait then for the return of the MIS-B. As already planned in Tihange 2, 2012 records were used as pre-load test data.

Comparison to 2012 data

Noteworthy raw data reproducibility was achieved in both spring 2013 interventions, which were carried out with the same method, equipment and settings as in 2012 (Fig. 8).

All flaw indications of the Doel 3 core shells and of the Tihange 2 upper core shell could be compared between 2012 and 2013 according to the pre-set evolution criteria, leading to the amplitude and size distributions displayed in Fig. 9 and 10.

Attempts to identify any correlation between the 3 sectors pinpointed by AE testing an UT data remained unsuccessful.

Globally, the various NDE measurements conducted in the framework of the short-term action program showed conclusively that no modification had been induced by the load tests in the condition of both Reactor Pressure Vessels.

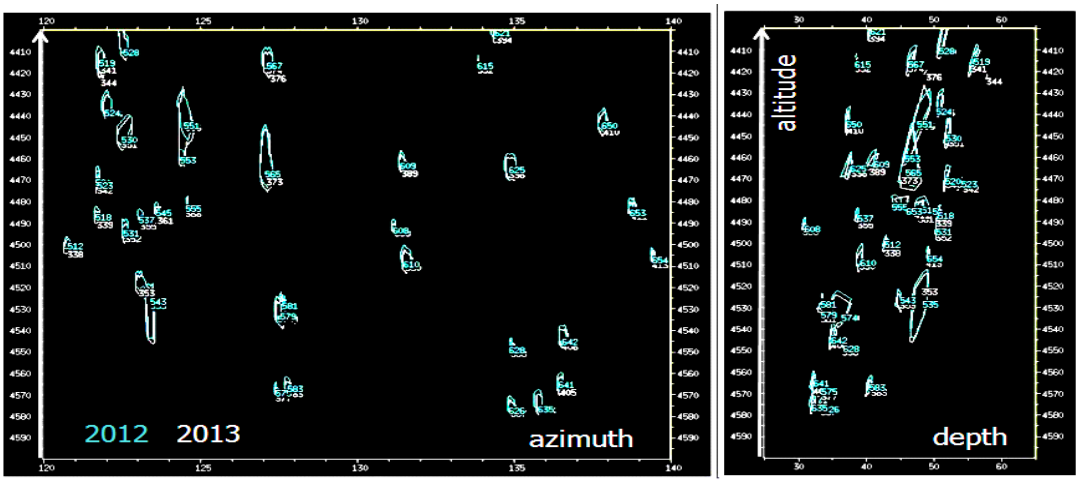

Fig. 8 – Superimposed data of 2012 and 2013 examinations in Tihange 2

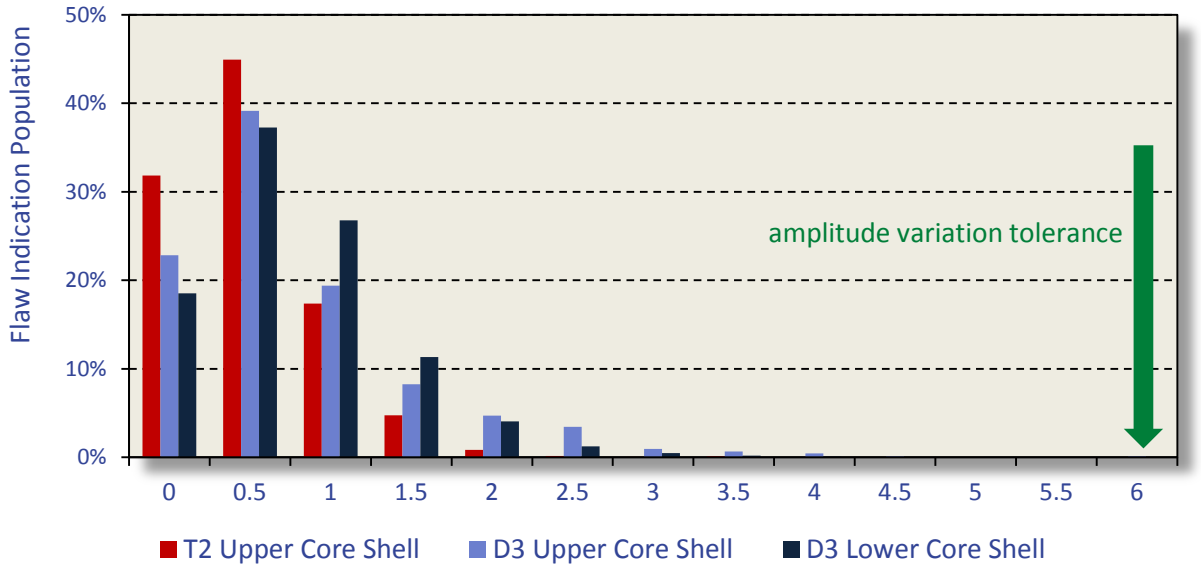

Fig. 9 – Distribution of amplitude variation

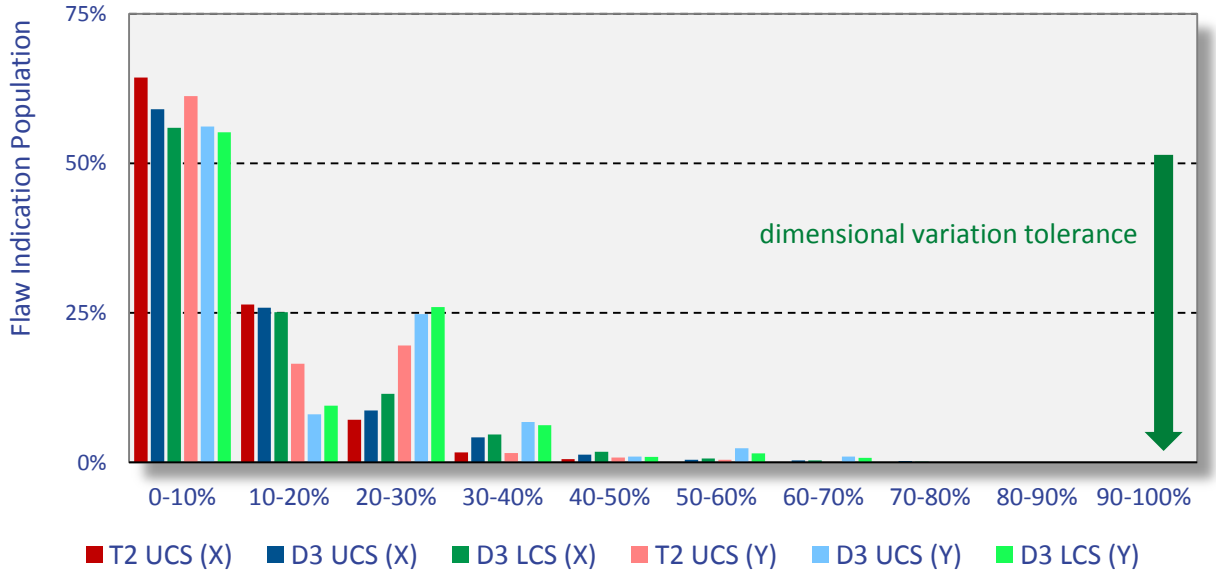

Fig. 10 – Distribution of dimensional variation

FINAL SAFETY ASSESSMENT AND FURTHER ACTIONS

The outcomes of all additional actions requested are documented in Addenda to the original Safety Cases (9, 10), which led Safety Authorities to consider that the short-term safety concerns raised in their first evaluation had been solved in a satisfactory manner, and that Doel 3 and Tihange 2 could consequently be restarted (11). Both units resumed operation early in June 2013.

UT inspections contributed significantly in the outcome, by providing detailed, reliable and reproducible information on the flaw population.

Mid-term actions still need to be fulfilled in the future: in the field of NDE, a specific qualification of the inspection system is in progress, and the core shells of Doel 3 and Tihange 2 will be subjected to the same examination after one cycle. In addition, identical inspections have been carried out on the RPV of Tihange Units 1 and 3 in April and September 2013 respectively, and have shown the absence of hydrogen flaking ; Doel Unit 4 RPV will be similarly examined in 2015.

REFERENCES

References 5, 6, 7, 9, 10 and 11 are publicly available on the Federal Agency for Nuclear Control website (www.fanc.fgov.be).

1. ASME Boiler and Pressure Vessel Code, The American Society of Mechanical Engineers
2. AREVA, private communication
3. Moussebois D and Pasquier T, "Ultrasonic examination of hydrogen flaking in large forgings: from validation to site inspections", 10th Int. Conf. on NDE, Cannes, Eur. Comm. JRC, 2013
4. Lareau J P and Bamford W, "A review of the shop inspections performed on US reactor vessels, and the potential for indications such as those found in the recent Doel 3/Tihange 2 inspections", WCAP-17786-NP Rev. 0, Westinghouse, 2013
5. Safety case report: Doel 3 – Reactor Pressure Vessel Assessment ; Electrabel, 5/12/2012
6. Safety case report: Tihange 2 – Reactor Pressure Vessel Assessment ; Electrabel, 5/12/2012
7. Doel 3 and Tihange 2 reactor pressure vessels: provisional evaluation report ; FANC, 30/01/2013
8. AFIAP, "*Guide des bonnes pratiques pour le contrôle par émission acoustique des équipements sous pression, 2ème édition*", Sadave, 2009
9. Safety case report – Addendum: Tihange 2 – Reactor Pressure Vessel assessment ; Electrabel, 15/04/2013
10. Safety case report – Addendum: Doel 3 – Reactor Pressure Vessel assessment ; Electrabel, 26/04/2013
11. Doel 3 and Tihange 2 Reactor Pressure Vessels: Final evaluation report ; FANC, 17/05/2013

ULTRASONIC EXAMINATION OF HYDROGEN FLAKING IN LARGE FORGINGS: FROM VALIDATION TO SITE INSPECTION

D. Moussebois, Laborelec, Belgium
T. Pasquier, AREVA, France

ABSTRACT

During 2012 RPVs inspections, nearly-laminar indications were detected in the lower and upper shells of Doel 3 and Tihange 2 RPVs.

As a consequence, the Doel 3 and Tihange 2 NPPs have to stay in cold shutdown until it has been proved that they can be safely operated.

The performance and capability of the applied UT technique to detect and characterize DDH flaws have to be confirmed.

To achieve this objective, an investigation has been launched on a block of limited size extracted from a steam generator shell known for containing hydrogen flaking.

The paper describes the UT measurements performed on the block and the results of the destructive tests which enable to demonstrate the capability of a straight ultrasonic beam to detect and size laminar and nearly laminar indications and to correctly identify ligaments between two adjacent indications. It also address the in-service inspection techniques and procedures used for the site inspections and the lessons learned from the experiments.

RPV INSPECTIONS IN BELGIUM

The ASME Code Section XI, Edition 1992, is fully applicable to the regular in-service inspection of all Belgian units.

The current in-service inspection program starts from this ASME framework, but in addition, national and international operating experience is constantly being integrated in order to continuously improve the inspections programs. This implies that the inspection planning and methods are re-evaluated at regular intervals.

The in-service inspection program of a ten-year interval covers the volumetric examination of all welds, studs and bolts as well as the visual inspection of the inner surface of the vessel. It must be completed by the end of the interval.

The inspection procedures are qualified by the licensee's qualification body (EQB). The work is supervised by the safety authorities.

Equipment and techniques for RPV shell inspection

Since the 1982 Pre-service Inspection of the Doel 3 RPV, regulatory ultrasonic examinations have been carried out by Intercontrôle (France) using the automated MIS-B (Machine d'Inspection en Service Belge).

The MIS-B equipment uses the acoustic beam focusing technique, concentrating sound energy in a restricted volume. The RPV wall thickness is divided into three depth ranges, to be insonified by different ultrasonic transducers. For the shell welds inspection, one 0°L probe and four 45°T shear wave transducers, orthogonally oriented, are dedicated to each depth range.

All transducers are immersed within the RPV and are actuated in pulse-echo mode without contact with the examination surface.

The acoustic beam focusing technique generates narrow acoustic beams, which require, in order to assure full material coverage, small scanning steps and increments between emission of acoustic pulses.

Scanning steps of 2 mm and increments of 2 or 5 mm, depending on flaw density, have been used in the hydrogen flaking inspection. Indications dimensions were measured by the standard 6 dB amplitude drop technique.

Figure 1 - MISB 3G In Service Inspection Machine

DOEL 3 2012 RPV core zone inspection

During the 2012 outage at Doel 3 NPP, specific ultrasonic in-service inspections were performed to check for underclad cracking in the reactor pressure vessel. No underclad defects were found but a large number of nearly-laminar indications were detected mainly in the lower and upper shells.

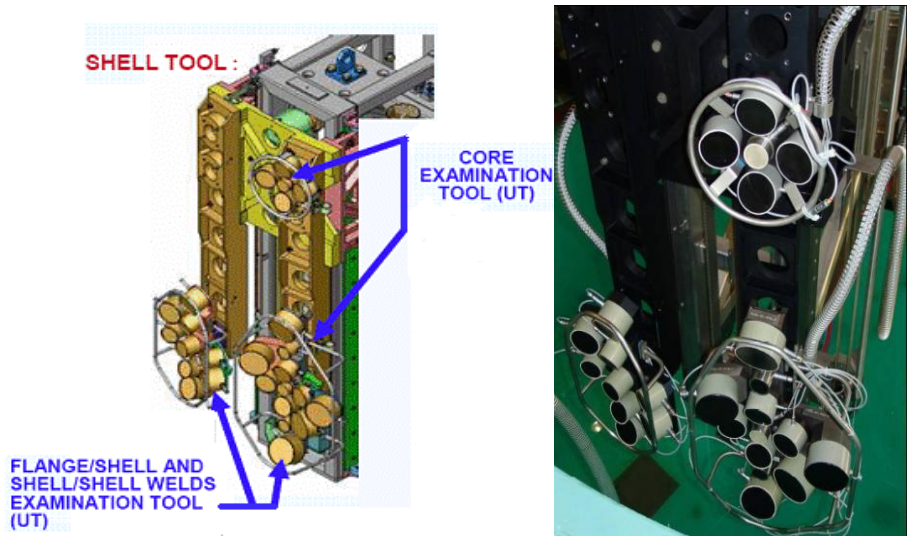

Figure 2 - MIS shell and core zone inspection Tool

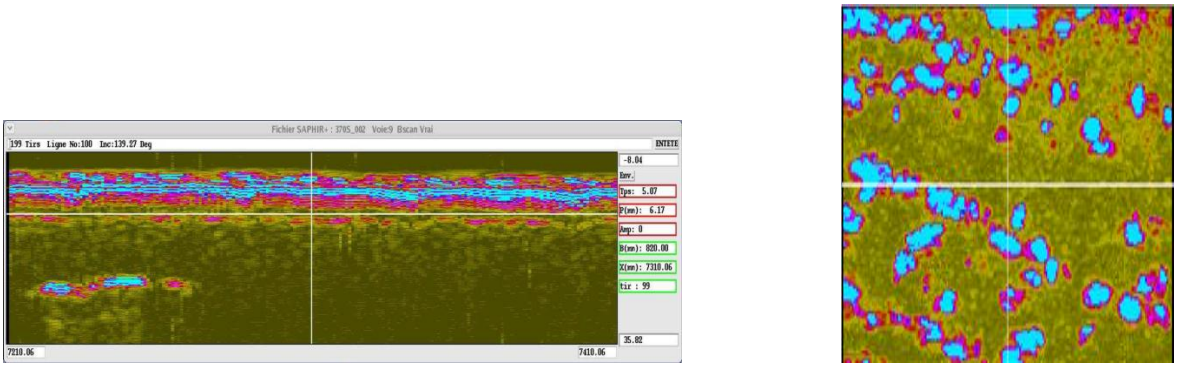

Figure 3 - Example of atypical quasi-laminar detected indications

Doel 3 and Tihange 2 2012 RPV complementary inspections

A second inspection was performed with UT probes able to inspect the whole thickness of the vessel and identified the same type of indications deeper in the material. A similar inspection performed in September at Tihange 2 NPP showed similar indications but to a lesser extent.

As a consequence, the Doel 3 and Tihange 2 NPPs have to stay in cold shutdown until it has been proved that they can be safely operated. A Safety Case (a case per unit) for requesting their restart has been launched by the operator, Electrabel.

UT VALIDATION

Background of the investigation

The predominantly laminar orientation of the indications detected during the inspections of the reactor vessel at Doel 3 and Tihange 2 NPPs was clearly established from the ultrasonic responses.

The MIS in-service inspection machine is equipped with straight and angle beam transducers. The application of all these transducers showed the superiority of the straight ones to detect and size the laminar indications.

The root cause analysis identified hydrogen flaking as the most likely degradation mechanism.

The information received from the metallurgists and collected in the literature emphasizes the nearly laminar aspect of the hydrogen flaking flaws, their faceted appearance and their possible slight inclination.

Ultrasonic strategy

The performance of the inspection technique specifically applied to detection and sizing of nearly laminar flaws has to be verified.

Therefore, it was decided to conduct at Laborelec an UT investigation on a selected block of an AREVA shell (identified as VB395/1), known to contain numerous hydrogen flakes by exploiting the capability of a phased array transducer to generate an ultrasonic beam of defined dimensions with very good accuracy.

Different transducers and beam sizes were considered for this exercise.

More specifically, the beam sizes of the straight transducers present on the MIS in-service inspection machine and used to cover the full thickness of the shells were taken into account.

In addition to the straight beam, different refraction and skew angles were applied, going from -20° to +20°. Doing this allowed to evaluate the impact of a limited ultrasonic beam angle on the ultrasonic response of the flakes that are slightly tilted and facetted. The choice of a limit of 20° takes into account a conservatism on the information obtained from the metallurgists about this type of flaws.

However, the exercise also enabled to assess the ability of the current control techniques applied on the MIS inspection machine to correctly detect and size the laminar or quasi-laminar flaws similar to those detected in the reactor vessels of Doel 3 and Tihange 2 NPPs.

In addition to this straight beam and associated small angle beams, a 45° shear wave transducer was applied on the block in order to confirm the behavior observed in Doel 3 and Tihange 2 and leading to the finding that the information from this angle beam inspection on that type of indications did not modify the conclusions obtained by the inspection with the straight beams transducers.

The 45° angle beam transducers are also part of the set of transducers present on the MIS inspection machine and formally qualified for a large range of applications mainly related to welds inspection and detection of indications perpendicular to the wall thickness. As such, they are part of the full inspection system.

Figure 4 - AREVA shell VB 395

UT PA examination of the block VB 395/1

Basically, it is considered that, if ultrasonic sets of parameters are chosen in an appropriate way, it is possible to recreate in the material a beam similar to that produced by the focused single element straight transducers of the MIS. Experience shows that, to achieve such a goal with a good accuracy, the number of UT elements is an important parameter, the larger, the better.

Due to the fact that different transducers are used on the MIS to cover the whole thickness (200 mm) of the reactor vessel with a similar sensitivity, different set of ultrasonic focal laws were needed to recreate the ultrasonic beams of the different straight transducers of the MIS used to detect and size the flaws.

This was achieved by using a CEA 2D matrix phased array conformable probe and different set of focal laws allowing for a beam shaping, by electronic means.

The CEA CIVA software has been used in order to select the appropriate settings of the 12*7 elements 2 MHz transducer. In fact, this modelling tool is used in defining needs and later in verifying that the selected settings enable to reach the desired beam characteristics.

In addition to the straight beam, different ultrasonic beams are generated with variable refraction angles (in the incidence plane) and skew angles (in the plane perpendicular to the incidence plane) within the inspected volume.

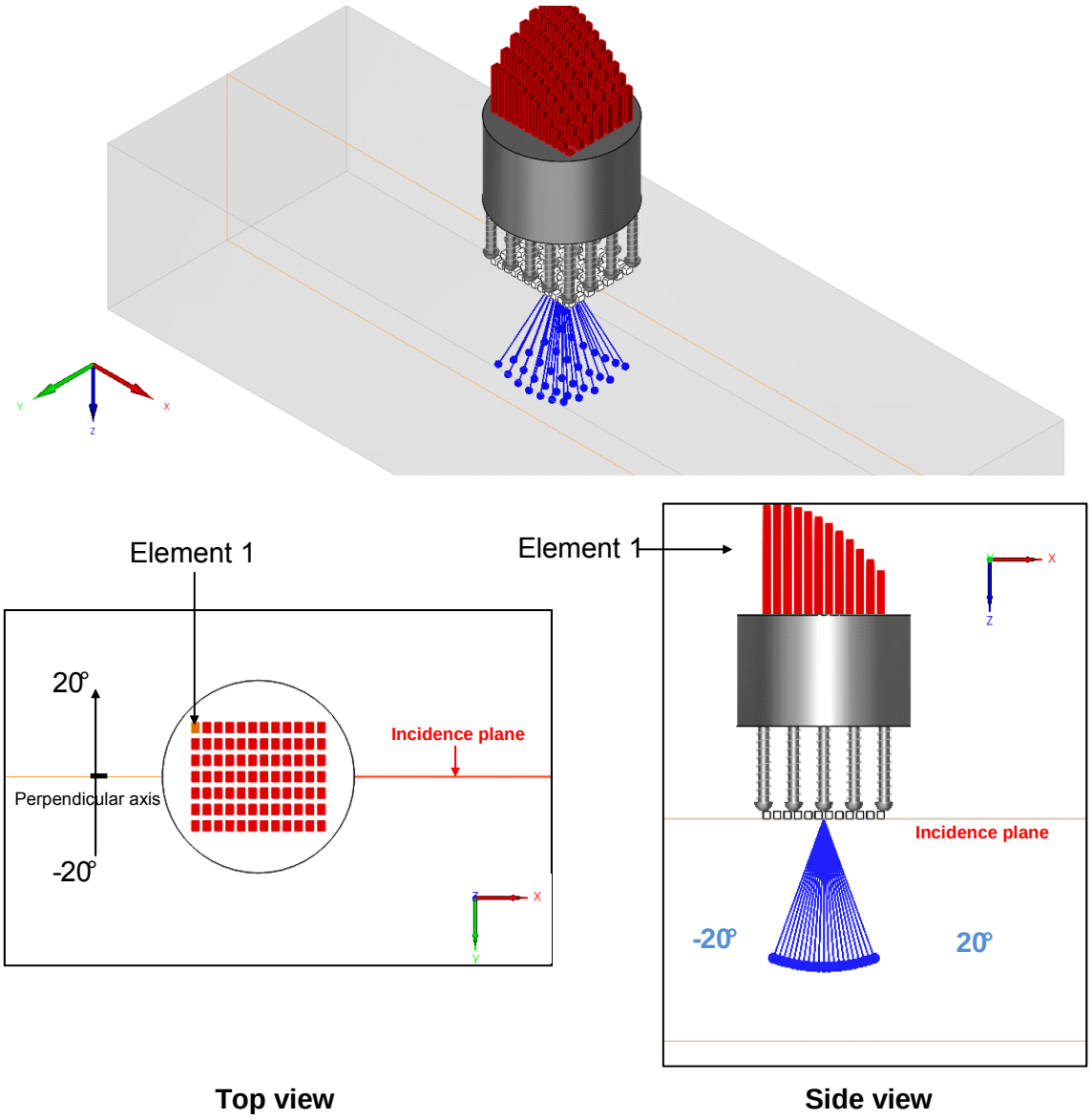

Figure 5 - CEA UT PA conformable transducer used for the UT validation

UT results

About 380 flaw indications were detected and sized within the block with the 0°L beams. Figures 6 and 7 show different view of the UT results.

The ultrasonic acquisitions made at angles between -20° and +20° in refraction and skew directions, as described above, showed that 20% of the flaw indications identified in the block have ultrasonic amplitude responses larger on one of these angles than on the 0°L.

However, if the amplitude of detection can be larger for these indications, it has to be noted that :

- The sizing of the indications made on the small angles showed often an under-sizing of the final ultrasonic dimensions of the indications.
- All indications detected with the small angles beams were detected with the straight beam.
- No indications were missed with the 0° straight beam.

In the light of the numerical results obtained on the concerned indications and more particularly those of them that have been cut later and whose real dimensions have been verified, no need to pursue this process in the future actions was identified.

Cumulated C-scan, top view of a half block D-scan, side view along Y axis

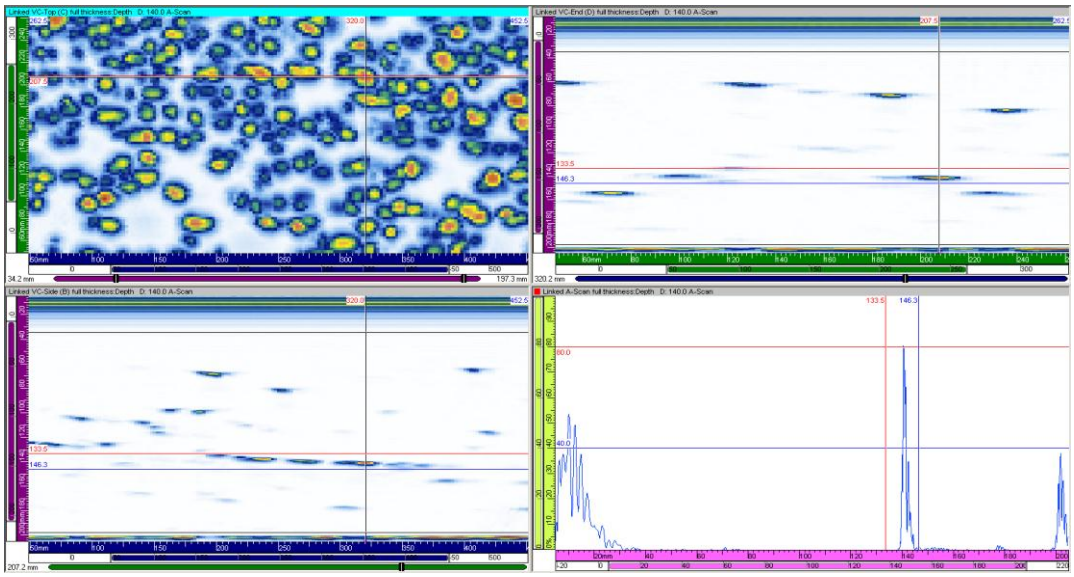

B-scan, side view along X axis A-scan, UT Energy from a given reflector

Figure 6 - UT results on the block VB 395/1

Cumulated C-scan, top view of a half block D-scan, side view along Y axis

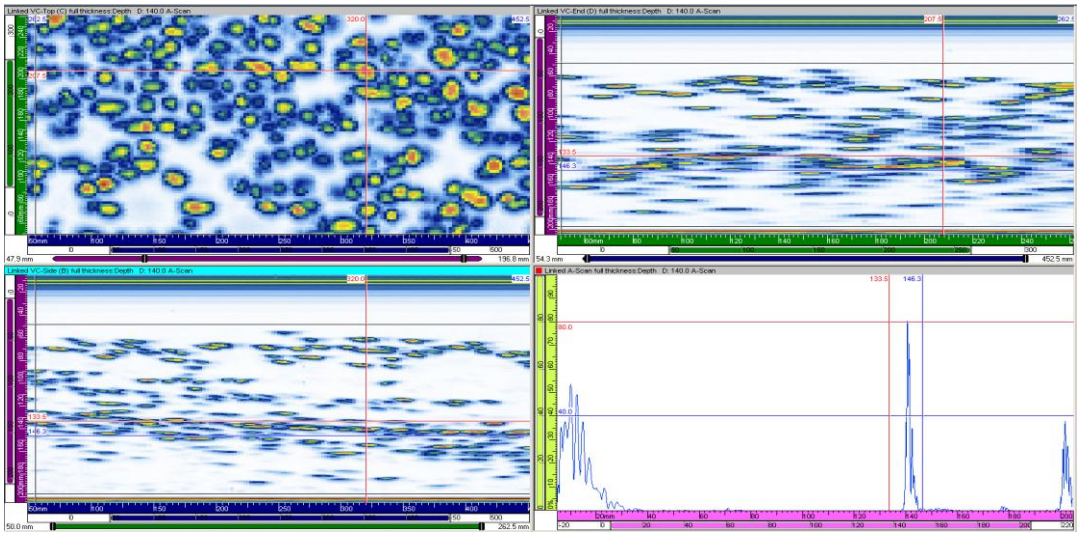

B-scan, side view along X axis A-scan, UT Energy from a given reflector

Figure 7 - Cumulated UT results on the block VB 395/1

45°T UT examination

A 45° angle beam transducer was applied on the block. The number and reflectivity of the indications detected by the 45° angle beam transducer are significantly lower than the ones of the indications detected by the straight beam inspection.

These results lead to the conclusion that the information from this angle beam inspection on that type of indications did not modify the conclusions obtained by the inspection with the straight beams transducers.

Destructive examination

Material examinations were conducted on a selection of indications selected as the most representative for the distribution and morphologies of flaws in the material.

Cuttings of samples and their slicing by EDM (Electro Discharge Machining) were performed in order to identify the 2D profile of the indication on each slice and to give indications about the global morphology and profile of the real indication.

Sloping flaws were deliberately sought in order to define the inspection techniques capability on inclined flaws.

Also, the real nature of the 45°T UT very low amplitude responses was investigated since no such response is expected from nearly laminar hydrogen flakes.

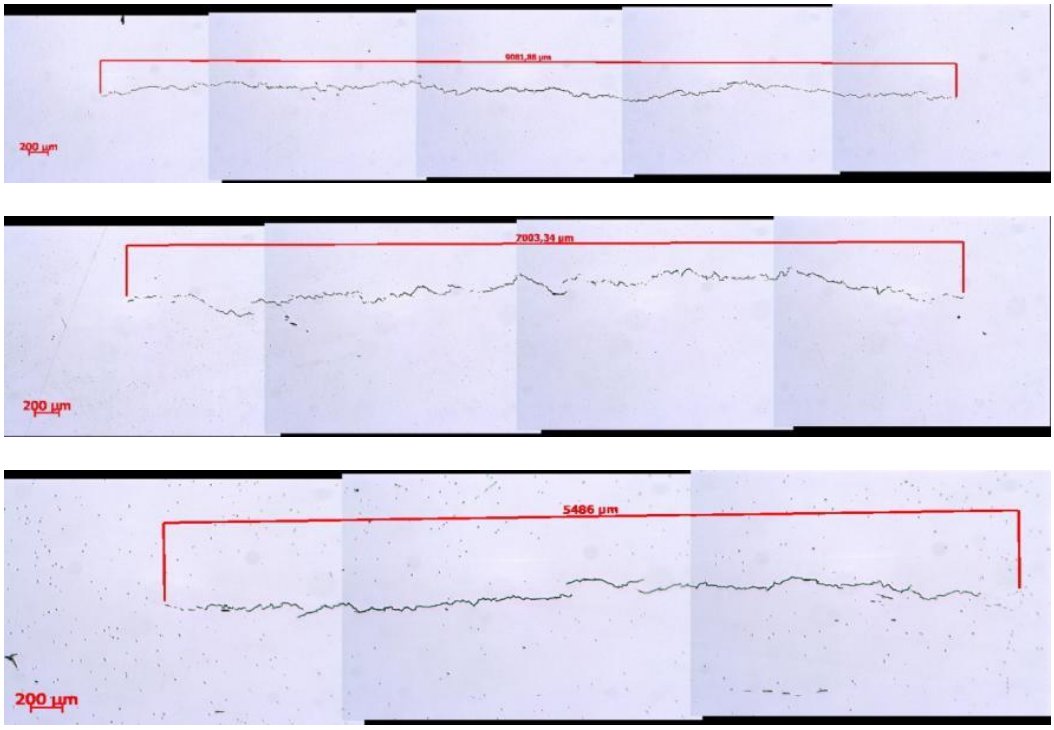

Figure 8 - Examples of hydrogen flakes profiles

The destructive results show that the hydrogen flakes are mostly almost purely laminar and confirm 14° maximum slopes.

To date, a total of 27 flaw indications were cut, i.e. 8% of the flaw indications contained in the block VB 395/1.

Destructive examination did not show any material discontinuity that was not reported by the ultrasonic examination.

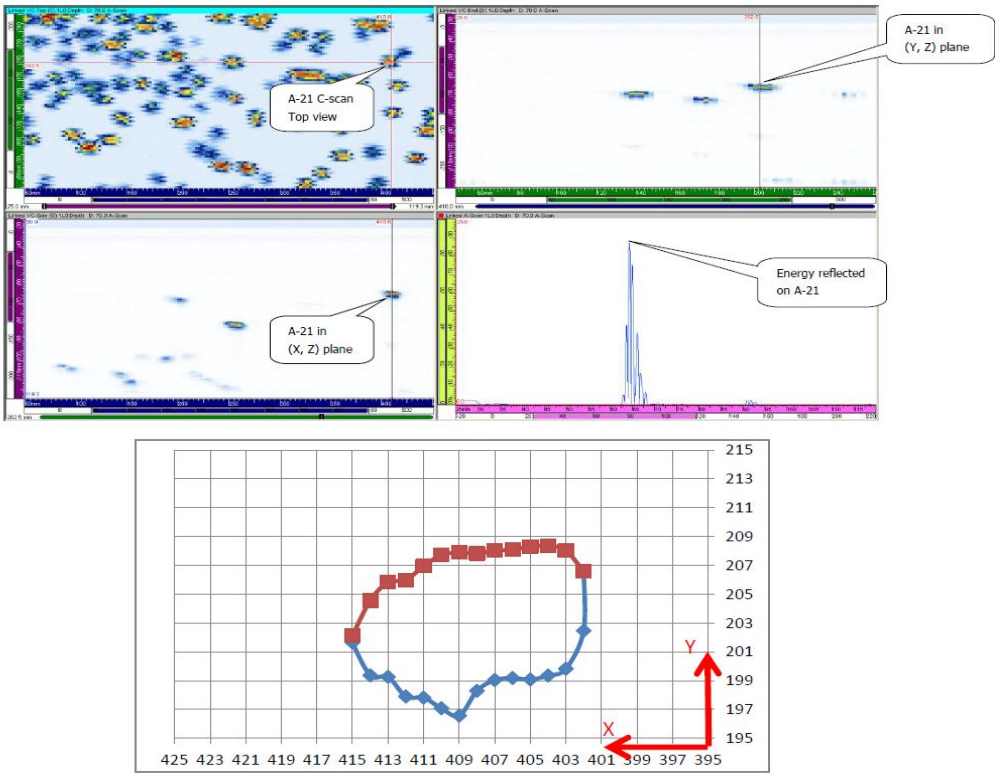

Figure 9 - Example of UT response and destructive examination of a flake

Conclusions of the validation

The UT sizing based on the 6 dB drop method on the straight beam UT response is most generally conservative and when it is not, the error is in the range usually considered acceptable and inherent in any dimensioning process by non destructive methods.

An under-sizing of the ligaments was observed on the UT responses, which is conservative. It was noted that, between two adjacent indications, the material was perfectly sound.

It was verified on inclined flaws that the sizing of the indications was not improved by using the UT laws based on angle different from 0°.

2% of the flaws (8) in the block VB 395/1 are highly tilted, between 10° and a maximum of 15°. In total, 5 from these highest tilted flaws were destructively examined, confirming that they were correctly detected and sized by the UT straight beam.

Finally, the destructive examination shows no correlation between 45°T UT responses and a radial or volumetric component of a flake.

Comparison with the Doel 3 and Tihange 2 situation

It was observed that the flaws present in the block were of slightly larger dimensions that those in the reactor vessel shells of Doel 3 and Tihange 2.

After applying a sensitivity transfer, a difference can be noted between the amplitudes observed for this investigation and these noted for the MIS inspection with the 1L0 transducer.
This finding is totally in line with the observation already made that the flaws present in the block are of larger dimensions than those in the reactor vessel shells of Doel 3 and Tihange 2.

It also supports the hypothesis that the flaws in the reactor vessel shells of Doel 3 and Tihange 2 are close to the beam dimensions or even smaller, implying UT responses of limited amplitude.

CONCLUSION

Extensive ultrasonic and material investigations took place on an AREVA steam generator shell known for containing hydrogen flaking. All these operations lead to conclude that the AREVA shell is representative for the RPVs. This was acknowledged by the safety authorities.

The UT validation confirms that inspection techniques using a straight UT beam allow a correct detection and sizing of DDH flaws.

For a given beam size of the UT PA transducer used for the investigation, it has been shown that the range of accuracy of the sizing depended mainly on the scanning increments and was usual for this type of inspection techniques.

This implies that no other inspection technique than those present on the MIS inspection machine have to be deployed to cover the needs of the Safety Case for Doel 3 and Tihange 2 reactor pressure vessels.

The formal extension of qualification of the MIS procedures is currently ongoing in order to confirm the capabilities of the current applied UT MIS inspection procedures to correctly detect and size hydrogen flaking present in Doel 3 and Tihange 2 RPVs.

REFERENCES

1) Safety Case Report Doel 3 – Reactor Pressure Vessel Assessment – Electrabel, 05-12-2012.
2) Safety Case Report Tihange 2 – Reactor Pressure Vessel Assessment – Electrabel, 05-12-2012.
3) Safety Case Report Doel 3 – Reactor Pressure Vessel Assessment – Addendum - Electrabel, 26-04-2013.
4) Safety Case Report Tihange 2 –Reactor Pressure Vessel Assessment – Addendum – Electrabel, 26-04-2013.
5) Doel 3 and Tihange 2 Reactor Pressure Vessels – Provisional Evaluation Report, Federal Agency for Nuclear Control, FANC-AFCN, 30-01-2013.
6) Doel 3 and Tihange 2 Reactor Pressure Vessels – Final Evaluation Report, Federal Agency for Nuclear Control, FANC-AFCN, 17-05-2013.

INSPECTION OF THE REACTOR PRESSURE VESSEL WALL LOOKING FOR HYDROGEN FLAKES AT RINGHALS USING QUALIFIED UT – IMMERSION TECHNIQUE

J. Benitez, T. Sjö, DEKRA Industrial AB, Sweden

ABSTRACT

DEKRA Industrial AB successfully performed a mechanised Ultrasonic Inspection looking for Hydrogen Flakes at the Reactor Pressure Vessel at Ringhals NPP unit 2 in October 2012.

DEKRA Industrial AB developed the NDE technique and qualified a procedure according to the ENIQ and Swedish rules (by SQC-Swedish Qualification Center) in a very short time frame.

The procedure was qualified for inspection of the RPV wall looking for lamination type defects at depths from 10mm to 195mm. The target was to detect planar defects ≥ Ø10mm parallel to the RPV surface (with ±10° tilt) and length size found defects.

Due to the long delivery time of Phased Array probes, it was chosen to use standard UT immersion probes in an array setup to quickly respond to the Ringhals needs.

A mechanized inspection of the full volume of the Reactor Pressure wall was performed using UT immersion technique with a water path of 50mm allowing the inspection of the full volume between the entry signal and the first multiple of the entry signal.

Two types of unfocused normal beam (with nominal frequency 5MHz) transducers were used in order to cover the whole depth: one type of transducer with crystal diameter Ø 12.5mm to cover from 10mm to 120mm and one transducer with Ø 20mm to cover from 100mm to the rest of inspection volume.

An array arrangement for each type of probe was designed in order to increase the step increment and reduce the inspection time.

The probes were mounted in the lightweight manipulator, Skidbladner, which was successfully used at all three 10-year RPV inspections in Ringhals.

The experience from Ringhals shows that the inspection is very trustworthy. With the results it was possible to make an assessment of the status on hydrogen flakes in the Ringhals RPV.

INTRODUCTION

As results of the presence of a large amount of quasi-laminar indications (Hydrogen Flakes) found in the Reactor Pressure Vessels of Doel 3 and Tihange 2 in June –July 2012, the Swedish Radiation Safety Authorities (SSM) required Ringhals AB to perform an inspection looking for Hydrogen Flakes at Ringhals NPP unit 2 during the September -October outage 2012.

DEKRA Industrial AB developed the NDE technique and qualified an inspection procedure according to the ENIQ and Swedish rules (by SQC-Swedish Qualification Center) in a very short time frame using UT immersion technique.

INSPECTION REQUIREMENTS

The inspection shall be performed according to the EN-10228-3 quality class 3 which described the techniques to be used for the ultrasonic testing of forgings manufactured from ferritic and martensitic steel.

Inspection Volume

Inspection of a 90°-sector (4th Quadrant, 270°-360°) of the RPV wall looking for lamination defects located at depth from 10mm to 195mm.

Material: Carbon steel with cladding, thickness 195mm, including cladding (cladding thickness ~ 5-7mm).

Figure 1- Reactor pressure vessel

Defect Specification
The Inspection System is required to detect planar defects ≥Ø10mm parallel to RPV (with ±10° tilt).

Tolerances
Detected defects will be sized with the following tolerances:

Length

Table 1 - Length sizing Tolerances

Direction	Depth from 10 to 120mm	Depth from 120 to 195mm
Scan Direction - Circumferential	±5mm	±16mm
Step Direction - Axial	±16mm	±22mm

Positioning

The global and local positioning error, taking into account all error sources is:

Table 2 - Positioning accuracy

Axis	Global Positioning Error When scan is performed with Rotation axis (X-axis)	Local Positioning Error
Scan axis (Rot.)	• X position: ± 28mm	• X position: ± 9mm
Step axis (Vertical)	• Y position: ± 21mm	• Y position: ± 8mm

Surface Conditions
The examination surface shall be free of irregularities, loose material or any other matter that may interfere with the probes.

Apart from the known geometry changes, the scanning surface should be uniform and without any abrupt changes. However, it is necessary to consider the roughness of the clad surface of the RPV.

INSPECTION METHOLOGY

In order to ensure a good contact it was decided to use UT immersion technique. Due to the long time for delivery of Phased Array probes it was chosen to use standard UT immersion probes in an array setup.
The target was to detect planar defects ≥ Ø10mm parallel to the RPV surface (with ±10° tilt).

The developed NDE technique and qualified procedure can be summarized by the following methodology description:

- A mechanized inspection of the full volume of the Reactor Pressure wall was performed using UT immersion technique.
- A water path of 50mm permits inspection of the whole volume between the entry signal and the first multiple of the entry signal.
- The inspection was performed with two types of immersion probes with the following characteristics:
- Unfocused 5MHz (nominal frequency) normal beam transducer with crystal diameter Ø 12.5mm to cover from 10mm to 120mm
- Unfocused 5MHz (nominal frequency) normal beam transducer with crystal diameter Ø 20mm to cover from 100mm to the rest of inspection volume

EQUIPMENT

Manipulator

The inspection was performed using the manipulator Skidbladner.
Skidbladner manipulator is controlled by DEKRA system Muspelhem and software Embla.

Ultrasonic Equipment

Ultrasonic System: Zetec Z-scan
Acquisition Program: Zetec UltraVision 1.1Q5
Analysis Program: Zetec UltraVision 1.1Q5

Inspection Probes

Table 3 - Nominal Probe Specification

Type	*Angle (º)*	*Freq. (MHz)*	*Probe Shoe Profile*	*Focal Depth (mm)*	*Crystal Size (mm)*	*Working Range (mm)*	*Comments*
Normal beam	0	5	flat	N/A	∅12.5	10 to 120	Immersion Probe
Normal Beam	0	5	Flat	N/A	∅20	80 to 195	Immersion Probe

QUALIFICATION

DEKRA Industrial AB developed the NDE technique and qualified procedure according to the ENIQ and Swedish rules (by SQC-Swedish Qualification Center).

According the EN-10228-3 quality class 3, the sensitivity of the transducers needs to be set on the Flat Bottom Hole (FBH) Ø3mm.

The calibration was performed on the calibration block (see figure 2) with FBH Ø3mm at different depth. A TGC (Time Gain Compensation) was applied for each transducer.

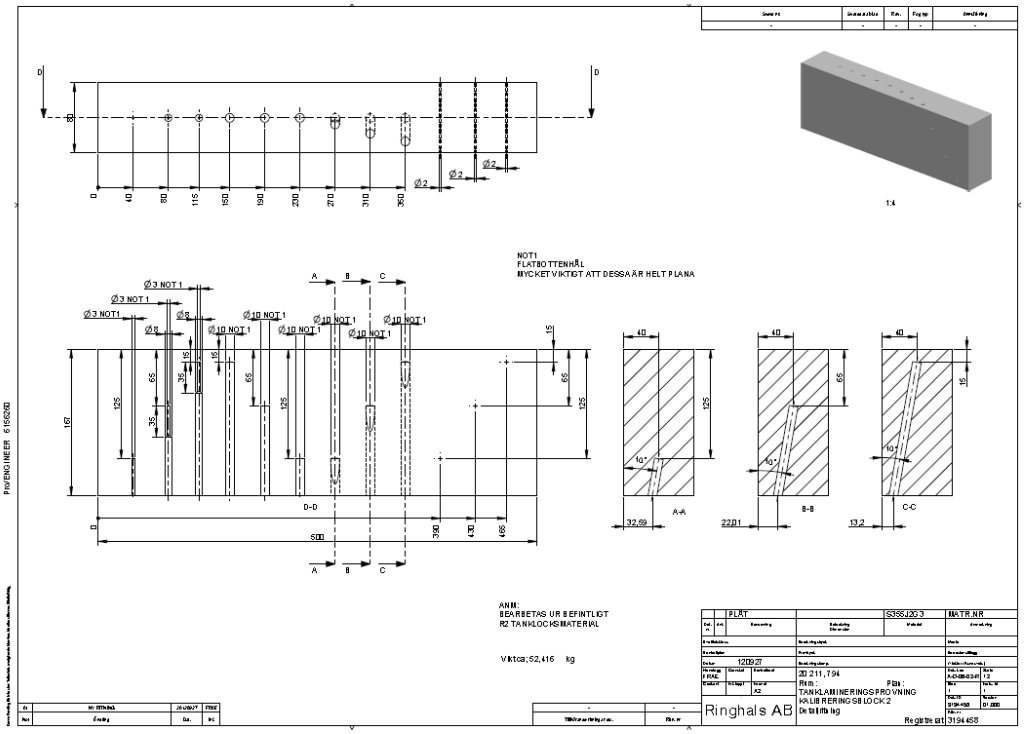

Figure 2 - Calibration Block

The qualification was successfully demonstrated on the Test sample with representative Flat Bottom Holes (FBH), see

Figure 3 and Figure 4.

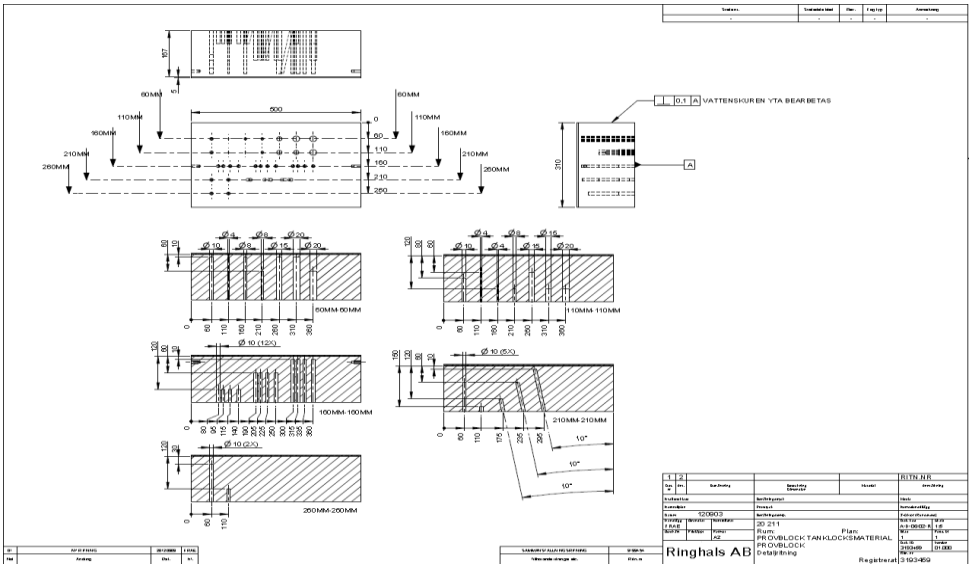

Figure 3 - Test sample used during the qualification

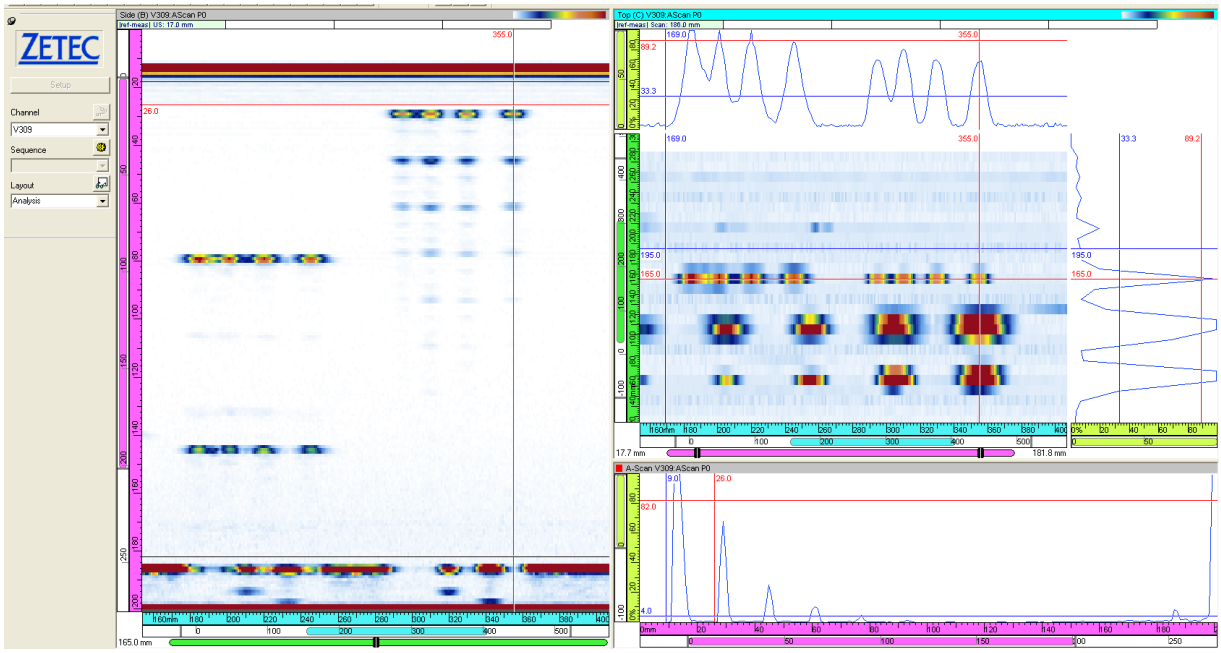

Figure 4 - Example of evaluation layout

PERFORMANCE AT RINGHALS UNIT 2

The task was to perform the inspection of a 90° sector at Ringhals unit 2 with the qualified inspection procedure.

A probe array arrangement for each type of probe was designed in order to increase the step increment and reduce the inspection time.

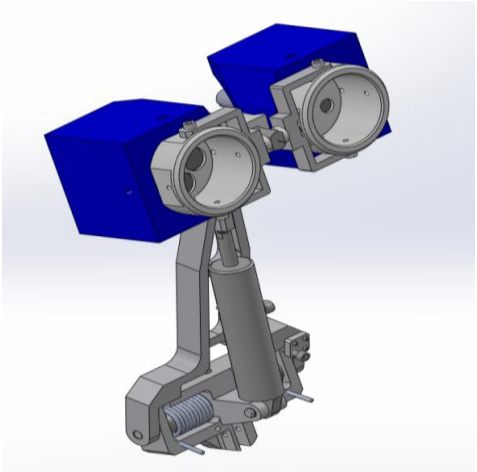

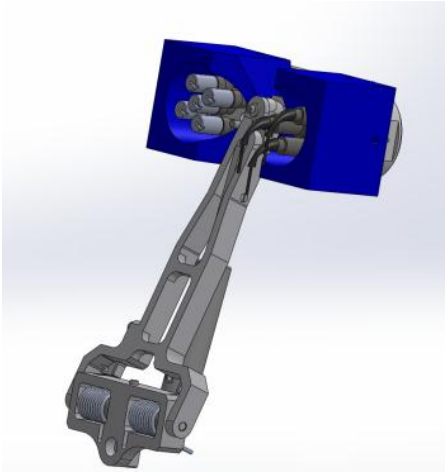

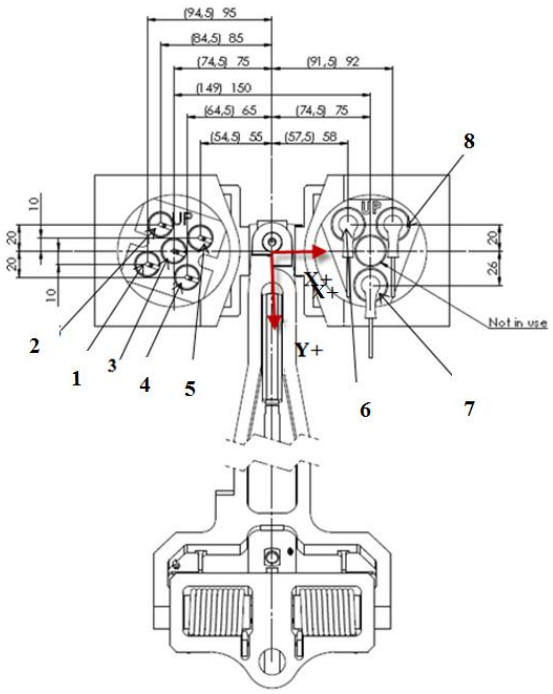

Figure 5 - Probes Holders with UT-immersion Probe Array arrangement

The probes were mounted in the light weight manipulator Skidbladner that was successfully used at all three 10-year RPV inspections in Ringhals, see Figure 6 and Figure 7.

Figure 6- Manipulator for inspection of PRV lower position

Figure 7 - Manipulator for inspection of PRV Upper position

Results

The inspection of the 90°-sector (4th Quadrant from 270° to 360°) was performed from 800 mm to 8400 mm from the flange according Figure 8.

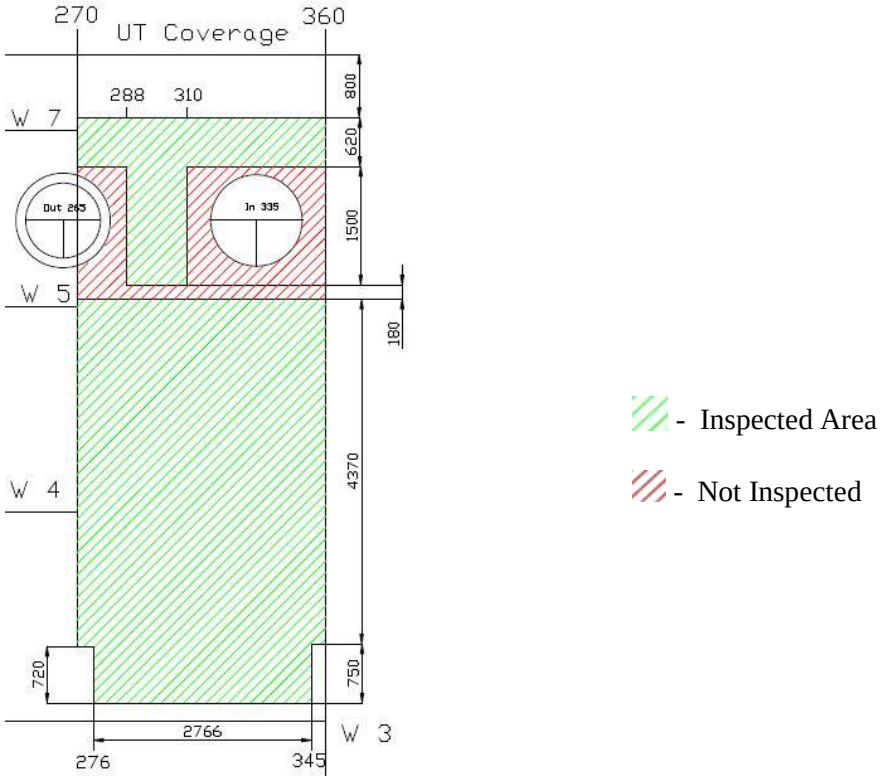

Figure 8 - Inspection Coverage in the 4th Quadrant (270°-360°)

The inspection was performed in the planned timeframe. The real time for the performance for the UT inspection of the 4th Quadrant of the RPV Shell was 36 hours from when we got access to the RPV until the manipulator was on the stand on the refuel floor after performance of the inspection.

No Hydrogen Flakes were found in the inspected area.

CONCLUSIONS

- The development of the NDE technique, qualification of the procedure and the inspection of the RPV wall looking for Hydrogen Flakes at Ringhals unit 2 was performed in a very short period of time (less than 8 weeks). This process could be performed in less time; however, the delivery time of the probes was the limiting factor.

- The solution of using standard immersion probes to perform the inspection was a good solution to quickly respond to the Ringhals needs.

- The inspection was successfully performed in the planned timeframe. The real time for the performance a 90°-sector of the RPV Shell was 36 hours from when we got access to the RPV until the manipulator was back on the refuel floor after performance of the inspection.

- The experience from Ringhals that the inspection is very trustworthy. With the results it was possible to make an assessment of the status on hydrogen flakes in the Ringhals RPV.

FUTURE PERSPECTIVE

DEKRA Industrial AB is developing a new procedure for inspection of the Hydrogen Flakes based on Phased Array immersion technique. This will give the possibility to focus the Ultrasonic beam through the whole depth. This will give a more accurate length sizing and increases the ability to separate defects in close proximity.

The technique and procedure will be qualified by QSt (Swiss Qualification Body) next spring and will be used during the inspection of the two RPVs at Beznau, Units 1 & 2 next autumn.

COMPARISON OF PRE- AND IN-SERVICE INSPECTION TECHNIQUES IN BELGIUM AND GERMANY AGAINST THE BACKDROP OF ULTRASONIC INDICATIONS FOUND AT THE REACTOR PRESSURE VESSEL OF DOEL-3

A. Erhard, BAM, Germany
S. Dugan, X. Schuler, Materialprüfungsanstalt Universität Stuttgart, Germany

Abstract

The Belgian Federal Agency for Nuclear Control (FANC) informed the public in August 2012 about the finding of thousands of flaws in the core area of the reactor pressure vessel of the nuclear power plant Doel-3. This information also prompted activities in Germany. The relation to Germany was very close, since the ingots of the forged rings came from Germany. That is why questions have arisen concerning quality management during fabrication: heat treatment, pre-service inspection in general, and NDT methods in particular. The focus will be on the rules and standards at the time of fabrication in relation to the required NDT methods and their failure sensibility levels. In addition, NDT registration levels and documentation and acceptance criteria at that time are also of interest.
In the German Nuclear Safety Standard KTA, it is required that the employed NDT method is based on the state-of-the-art of science and technology. After having obtained the knowledge of the flaw situation in Doel-3, the discussion regarding the inspection areas for in-service inspection of the reactor pressure vessel rose up in Germany: Is it still enough to examine only the welds, including the head affected zones, or is it necessary to examine the whole rings, i.e. including the base metal? This paper will try to give answers to these questions in the light of the standards used in Germany. In addition, the information and experiences gained from pre-service inspection as well as many in-service inspections - which are required to be carried out every 4 to 5 years – will be described.

Introduction

The Belgian nuclear power plant (NPP) operator Electrabel shut down the 1006 MWe pressurized water reactor on 2nd June 2012 for a scheduled mandatory ten-year in-service inspection of the reactor pressure vessels (RPV) according to ASME XI. Since 1982, when Doel 3 started its operation, several in-service inspections have been performed on the RPV. During these inspections, the whole reactor pressure vessel was examined in addition to the regular requirements in the code. Following the rules of the ASME Code Section XI, volumetric in-service-inspections of the beltline area are limited to the circumferential welds and the heat affected zone. The reason for this change in the inspection procedure was a concern about under clad defects, which are normally generated during the welding process of the cladding (1-4), and were found in the beltline area of the nuclear power plant Tricastin in France (5). As explained in (6), no under clad defects were detected at Doel 3. Further, it is reported in (7) that 158 defect indications of an apparently different type were recorded on the basis of the criteria used for this UT-inspection optimized for under clad defect detection. These indications appear to be a quasi-laminar type of flaw, which means the flaws are more or less parallel to the inner/outer surface of the pressure vessel and not like under clad cracks perpendicular to the surface. The result of the first interpretation of the origin was that hydrogen flakes could have such measured specular reflectivity. With an optimized and qualified UT inspection system approximately 7800 indications were detected in the core lower shell ring and approximately 900 indications in the upper core shell ring (7). Based on the pattern of the indications in relation to those known from other heavy forgings (8), and their number and position in relation to the original ingot, it can be assumed that the indications found are caused by hydrogen flaking (6).

The news about the high number of indications in the base metal of the core rings of Doel 3 RPV raised questions in Germany regarding the inspection during manufacturing as well as during in-service inspection. These questions are summarized as follows:

Against the background of the defects found in Doel 3 and Thiange 2, do the inspections methods for the RPV employed in Germany reflect the state-of-the-art of science and technology? Are there additional inspection techniques necessary for the examination of the base metal of the RPV shell?

Were the examinations, the quality control and the data documentation during fabrication of the RPV, especially after heat treatment steps, carried out in such a manner that defects of the type found in Doel 3 and Thiange 2 could have been detected?

To answer those questions, the non-destructive testing techniques at the time of fabrication, in particular the ultrasonic techniques and the procedures (codes and specifications) should be known. Those must be compared to the ultrasonic techniques and codes now applicable. In the present paper, the NDT examinations as they have been carried out at the beginning of the 1970s in Germany will be compared to the examinations required in the ASME code. In a next step the methods used for the in-service inspection 2012 in Doel 3 will be compared to the techniques used in Germany as required in the regulations of the Nuclear Safety Standards Commission (KTA).

Finally, some information about mechanical tests during fabrication and the documentation of these results are described for a German nuclear power plant of generation II (9). In addition, some information on the pre-service inspection will complete the answering of the questions under bullet two.

NDT Examination during Fabrication

Since the time of fabrication of the reactor pressure vessel of Doel 3, there were many changes in the application of NDT methods due to the permanent development of NDT methods. But even then, depending on the codes used, differences occurred e.g. in the heat treatment, in the time of the inspection during the production process, and in the methods used for the inspection. In (8) the differences between the ASME code and the regulations employed in Germany at that time, especially the AVS 13 (10), are explained. In Fig. 1 these differences are printed. Obvious is that the inspection methods, i.e. the probe positions and the point in time of the inspection are not comparable.

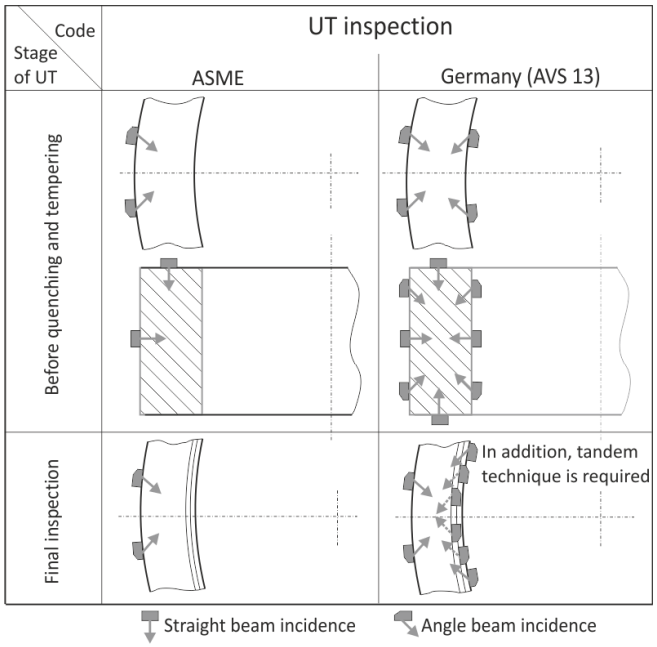

Fig. 1: Comparison of Incidence of UT Required by ASME and German Regulations (8)

The differences are clearly visible in the higher number of probe positions and beam incidence from each of the surfaces. Another significant difference is the application of the tandem technique for the detection of planar defects more or less perpendicularly oriented to the spherical surfaces of the forged components. The different steps in the machining of the inner diameter (ID) are controlled for each step by UT inspection (schematically printed by dotted lines).

Not only the numbers of probe positions and the beam incidence are different, but also the recordable indications as well as the acceptance criteria of those indications. The task to compare the Siemens AVS 13 requirements with the ASME Code Section XI is a challenge due to the different history and inspection philosophy in the two countries. In detail the following differences were found between the inspection based on ASME and the requirements of AVS 13 (Table 1).

<table>
<tr><td colspan="2">Product</td><td colspan="6">Flanges and tube sheets</td></tr>
<tr><td colspan="2">Detectable sensitivity (defect size or equivalent diameter using 2 MHz ultrasound)</td><td colspan="6">0.5 mm at 200 mm
0.8 mm at 400 mm
1 mm at 800 mm</td></tr>
<tr><td rowspan="3">Recordable indication</td><td>ASME</td><td colspan="6">• Defect echo with ≥10% of adjacent back reflection
• Continuous indication ≥ 2 twice the diameter of the transducer crystal
• Planar indication ≥ 25 mm long
• Travelling indication ≥ 5% of back reflection, 25 mm long
• Cluster indications ≥5 in 50 mm cube</td></tr>
<tr><td rowspan="2">AVS</td><td>Thickness [mm]</td><td>15 ~ 30</td><td>30 ~60</td><td>60 ~ 120</td><td>120 ~ 250</td><td>> 250</td></tr>
<tr><td>DGS [mm]</td><td>1.5</td><td>2</td><td>3</td><td>4</td><td>6</td></tr>
<tr><td rowspan="2">Acceptance criteria</td><td>ASME</td><td colspan="6">Indication which cause to complete loss of back reflection (Smaller than 5% of screen height)</td></tr>
<tr><td>AVS</td><td colspan="6">• Defect with recordable size + 18 dB
• Defect with length
½ wall thickness for "recordable size + 12 dB"
wall thickness “recordable size + 6 dB”
• No recordable indication in near surface (< 10mm ~ 30 mm)</td></tr>
</table>

Table 1: Detectability of defects and acceptance criteria by ultrasonic inspection of heavy forgings for NPP (8)

This comparison is trying to concentrate on points where significant differences are noticed for flanges and tube sheets as shown in table 1. These components are of course not equal to the RPV shell but the values are representing the difference in the inspection procedures. The sensitivity of the ultrasonic technique for defect detection is independent of the code. Differences are in the recordable level, where the ASME code has recordable levels which include the material properties and the reflection behavior of the used calibration reflector. An example for a material property which influences the detectability is the noise, mostly produced due to the grain boundaries. Indications are documented as soon as the echo exceeds the noise by 10% (noise at the adjacent back reflection).

In contrast to that, and typical for codes and standards in Germany, the AVS 13 applies the so called DGS method (Distance-Gain-Size). The DGS method is based on artificial reference “defect” which is a circular disc with a diameter depending on the wall thickness. For the wall thickness of the Doel 3 RPV shell of 205 mm, a 4 mm diameter disc is recordable. But there is a difference between angle beam and straight beam incidence in such a way that for angle beam the recordable size is smaller than for straight beam: 3 mm for angle beam and 6 mm for straight beam. Acceptance levels are based on the reflected amplitude or the length extension and depend on the wall thickness. In the near surface area (<10 mm ~ 30 mm) no indication is acceptable. In general, acceptance levels are always a combination of the defect size and length or size and accumulation. In relation to the defect characteristics found in Doel 3 and in Thiange 2 with an orientation more or less parallel to the cylindrical surface of the RPV shell ultrasound straight beam techniques are preferred.

For this sound beam incidence and wall thicknesses between 150 mm – 300 mm the following levels are accepted according to AVS 13:

Additional conditions	Acceptance level	
	Size	Length
	1000 mm^2 or 15 mm disc diameter	No extension
	6.5 mm disc diameter	150 mm
Welding area (100 mm above the end face)	11 mm disc diameter (max. 6 per m^2)	No extension
Near surface area (cylindrical surface)	minimum distance of 30 mm from surface for indications	

Table 2: Acceptance levels for wall thicknesses between 150 to 300 mm

A further difference between the German specifications and the ASME requirements are the hardness measurements after quenching and tempering, which were not part of the ASME code requirements at that time. The numbers of samples for the mechanical tests are also not comparable. As noted in (12), only 2 samples from the top of the forging in 180° positions are tested in accordance to the ASME code valid at that time. In contrast to that, 6 samples i.e. 3 from the top and 3 from the bottom in 120° circumferential positions must be tested in accordance with the AVS 13.

In the following, we will come back to the sensitivity of the ultrasonic system employed during Doel 3 RPV shell fabrication. In (11) the estimated defect sizes during the inspection in 2012 are described. In Doel 3 average diameters of 10 - 14 mm were found by the inspection in 2012, while some indications have diameters of more than 20-25 mm. Tables 1 and 2 show the basis for the detectability required in 1978 (12). When comparing the detectable defect sizes of table 1 to the sizes found in Doel 3, no lack in the detectability is recognizable. From the ultrasonic system sensitivity, available from the start of the fabrication, the detection capability for the described defect was given. Moreover the potential presence of hydrogen flakes in steel ingots was known at that time. In (8, 13) such a kind of imperfections during solidification of large mass of steel is described. Furthermore, this phenomenon was well known in Germany and was analyzed in the so called *Research Program Ccomponent Safety* (FKS) in 1981 (14). During the ultrasonic inspection on RPV rings, after tempering (Fig. 2), indications were detected in the middle of the wall, to find out why the rings were rejected.

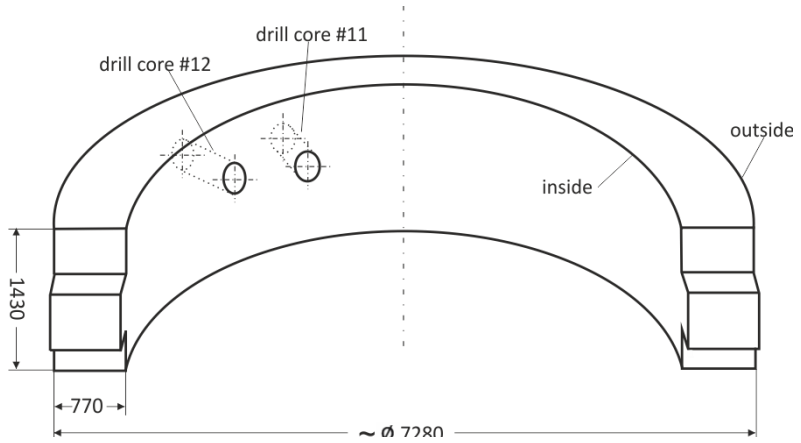

Fig. 2: RDB flange ring (FKS KS02) for a 1300 MW PWR embedded in the MPA pressure vessel

The result of the metallographic examination of the drill core #11 is pictured in Fig. 3. The macro crack is visible at the top of the Figure were as a detail of this crack is presented as section A. In addition to this section, another detail is shown in section B.

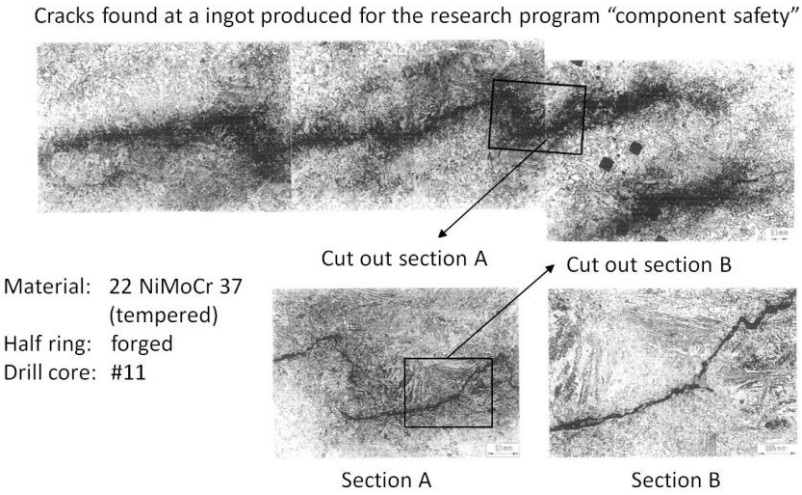

Fig. 3*:* RPV ring (FKS KS02) drill core #11, macro and micro cracks

In addition to these micrographs made from the drill cores of the flange ring (FKS KS02), the mechanical properties were a main focus, especially when a RPV has such cracks. Is the toughness of such a RPV high enough to withstand the pressure under normal operational conditions of a nuclear power plant? To answer this question, two tensile test specimens were prepared from an ingot with cracks. The chemical composition and fabrication conditions for this ingot (melt KS07C) were modified to achieve low toughness and maximize the risk of hydrogen cracking. This way, the melt KS07C represents a “lower-bound” condition.

Visual inspection and magnetic particle testing of the ingot showed macro and micro cracks. These cracks are also clearly recognizable at the tensile test specimens. The tensile test specimens had a diameter of 100 mm and were tested at temperatures of 90 °C and 280 °C. The tensile test specimens are shown in Fig. 4. The fractured surface of one of these specimens is pictured on the right side. The fissured fracture surface is a typical outcome when hydrogen flakes and oxides are present.

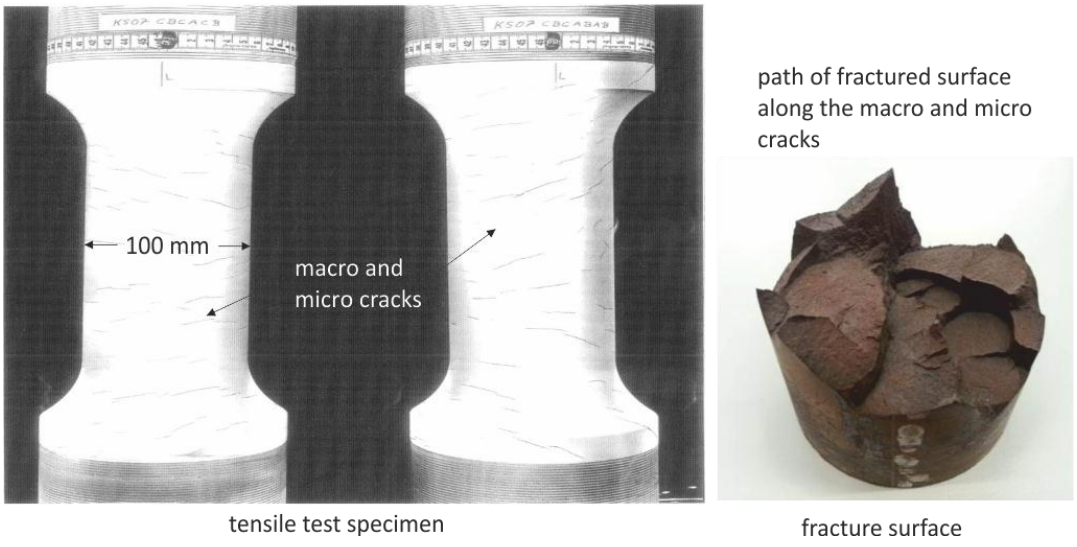

Fig 4: Tensile test specimen in the frame of the FKS research program

The chemical composition of the melt KS02 (rejected RPV ring) is comparable to Doel 3 as shown in table 3. Only in the chromium content, there is a distinct difference.

		C	Si	Mn	P	S	Cr	Mo	Ni	Al	Cu	V	Sn	Co	As
KS02	PA	0.21	0.20	0.95	0.007	0.007	**0.51**	0.57	1.30	0.02	0.09	<0.01	0.007	0.014	0.025
Doel	PA	0.22	0.26	1.25	0.009	0.009	**0.08**	0.48	0.72	0.011	0.04	0.01	-	0.013	

Table 3: Comparison of the chemical composites of the FKS specimen and RPV of Doel 3

In summary, the results of the FKS program on those special specimens show that from the fracture mechanics point of view the components withstand the pressure under normal operating conditions even with the described defects. The result of standard tensile and notch impact test specimens taken from uncracked but segregated regions shows no significant difference compared with specimens taken from non-segregated material

The experiences collected by the fabrication of the FKS specimens showed that the quality of the melt for RPV is guaranteed if the specifications are fulfilled. These results were used as input for some codes in Germany.

Pre-service and In-service Inspection

Following the rules of the ASME Code Section XI, as well as German KTA 3201.4, volumetric in-service-inspections of the beltline area are normally limited to the circumferential welds (there are no axial welds in the Belgian RPVs and in German RPVs which are still in operation) and the surrounding heat affected zone and base material, within the limits set by the code. To compare both codes in relation to the pre- and in-service inspection is not easy. Therefore, the focus will be merely on the parts with significant differences.

One of the important differences during the pre-service inspection by using NDT-techniques, also required for the in-service inspection, is the inspected area on the RPV. In Germany the scope of pre-service inspection covers the whole RPV. Exceptions are only permitted in the zones inaccessible for the sound beam due to the stud boreholes in the head and nozzle flange (15). For RPV of a pressurized water reactor (PWR) the exception areas are marked in Fig. 5. That is the first time where the sound propagation into the base metal is influenced by the stainless steel cladding if the inspection is carried out from the inside. During the inspection from the outside, the sound reflection at the inner surface is affected by the cladding.

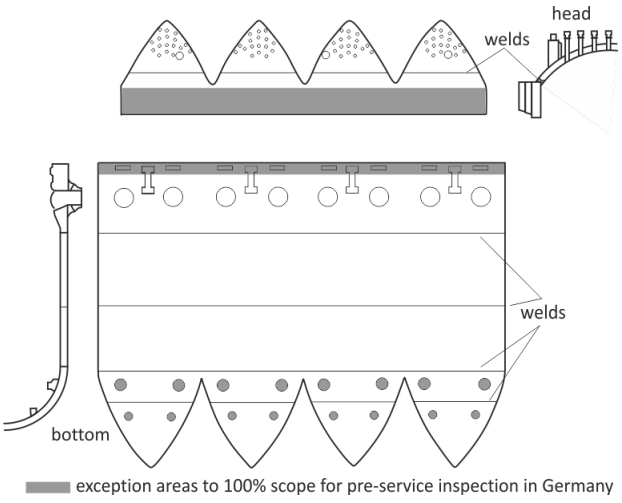

Fig. 5: Pre-service inspection of the RPV of a PWR type nuclear power plant

The inspection in general can be carried out from the outer surface as well as from the inner surface. If the inspection is carried out from only one surface, it must be guaranteed that the inspection from the complimentary side is exactly comparable. The sensitivity of the ultrasonic system is in accordance with the sensitivity employed for the in-service inspection. In accordance with the Nuclear Safety Standard for in-service-inspection, KTA rule 3201.4, the pre-service inspection must be carried out on all the areas required for the in-service inspection. In addition to those areas, it must be guaranteed that all base metal areas are inspected too. The results of the UT-examination of the welds and surrounding heat affected zones are the basis for the following periodic in-service inspections. If some defects or imperfections generated during the production are in the base metal and are not detected during the quality control in the frame of the fabrication, they will most likely be detected during the pre-service inspection, because of the smaller recordable defect size, and additional techniques applied (tandem technique). Indeed, the sensitivity setting of the ultrasonic system required by the Nuclear Safety Standard is sufficient to find defects with extensions found in Doel 3 and Thiange 2. Therefore, it can be assumed that the nuclear power plants in Germany which are still in operation do not contain such imperfections.

The periodic in-service inspections in Germany, which are conducted every 4 years for older plants and every 5 years for the newer plants, the so called convoy plants, are carried out according to the KTA 3201.4. For PWR type reactors the RPV inspections are carried out from the inside, for BWR types they are done from the outside, while a mechanized ultrasonic system is employed for both. The in-service inspection has to cover all welds, the nozzle inner radii, the control rod ligaments at the head (PWR) or the bottom (BWR). Further tested areas are the studs, nuts and threaded stud boreholes (Fig. 6).

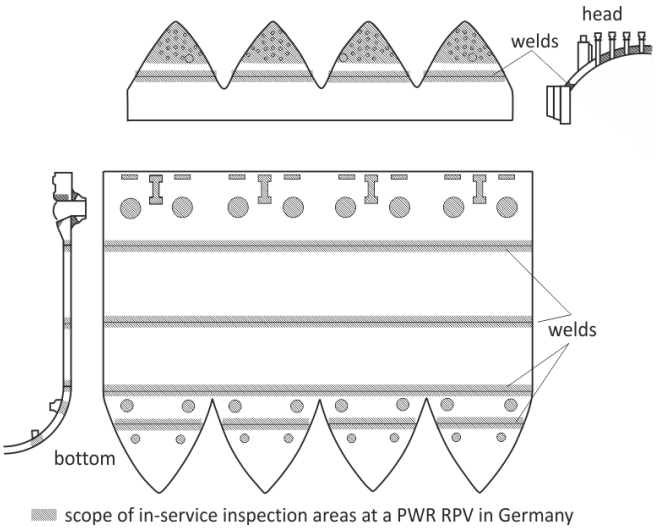

Fig. 6: In-service inspection of a RPV (PWR type) according the KTA rule

The scope of German in-service inspection requirements is comparable to that of ASME Sect. XI, except for the inspection of the control rod ligaments. The in-service inspection techniques must comply with the KTA rule 3201.4. The reference for the sensitivity of the ultrasonic volumetric examination with pulse-echo techniques using a single ultrasonic probe is a 3 mm flat bottom hole. Surface inspection on the RPV is carried out using a 3 mm deep and 20 mm long notch for the sensitivity setting. These techniques are comparable to those used in accordance with the ASME Sect. XI, except for the calibration reflectors which are used for the sensitivity setting of the ultrasonic system. For the volume inspection the ASME code requires side drilled holes. The difference in the reflectivity between side drilled holes and flat bottom holes can be calculated using a well-known, simple formula:

$$d_{flat-bottom} = \sqrt{\frac{\sqrt{2}}{\pi}\lambda\sqrt{d_{side-drilled} \cdot s_{path}}}$$

where: $d_{flat\text{-}bottom}$, diameter of the flat bottom hole

$D_{side\text{-}drilled}$, diameter of the side drilled hole

λ, wavelength

S_{path}, sound path

The biggest difference in the German inspection philosophy compared to the ASME code is the application of the tandem technique or mode conversion techniques. These methods, required for wall thicknesses up to 100 mm, are sensitive for planar defects oriented approximately perpendicular to the inner or outer surface.

For a validation and confirmation of the pre-service inspections in the German plants, a mechanized ultrasonic examination of the base metal in a circumferential segment of 30° using a sensitivity setting according to AVS 13 was carried out in one plant. The result of this additional inspection can be summarized as follows: There was no indication detected in the selected area of the base metal of the RPV. This result was a confirmation of the production quality at the time of the fabrication of the RPV.

Conclusions

The results of the *Research Program Component Safety* (FKS) confirm that the specifications for the melting of RPV were suitable to ensure good quality. Furthermore the rupture stress related to the nominal cross section of the big tensile test specimen including macro and micro cracks are in the range of the rupture stress measured on flawless tensile specimens. Moreover, the experiences made in the FKS program served as a basis for the preparation of the German KTA rules.

Based on the information about the defect situation of Doel 2 and Thiange 2, the assessment of the detectability of the defects in these two plants in comparison to German nuclear plants (only the plants which are still in operation for the time being) was carried out. According to the specification AVS 13 valid for ultrasonic testing during the fabrication of the RPV rings, and the results of the pre-service inspection, it can be assumed that agglomerations of defects with orientations and sizes given for the Doel 3 defects were detectable using straight beam probes with radial incidence of the ultrasound. The examination of a selected area of the base metal at a RPV in a German nuclear power plant (PWR) in addition to the normal in-service inspection shows that the quality control during the fabrication was successful. No defect was detected in the inspected area.

References

1) Handbook on the ultrasonic examination of austenitic steel components; IIW 1994, European Commission EUR 15786 EN
2) *A. G. Vincker, A. W Pense*: A Review of Underclad Cracking in Pressure Vessel Components WRC-Bull. (1974) H. 197, S1/35
3) *H. Cerjak, W. Debray*: Erfahrungen mit austenitischen Schweißplattierungen an Kernreaktor-komponenten, VGB-Werkstofftagung 1971, Tagungsband Seite 23 - 31
4) *G. Bartholome, H. Dorner*: Diskussion zum Vortrag Erfahrungen mit austenitischen Schweiß-plattierungen an Kernreaktorkomponenten, VGB-Werkstofftagung 1971, Tagungsband Seite 42144
5) *L. Hernandez, J. C. Barbant, Ph. Bastin, T. Pasquier*: Characterization of Crack-Like Sub-Surface Defect Located in Nuclear Reactor Core Region, Proceedings 15th WCNDT Rome 2000
6) *Electrabel*: Safety Case Report Doel 2, Reactor Pressure Vessel Assessment, 5 December 2012
7) *FANC*: Flaw indications in the reactor pressure vessel of Doel 3, This note provides a summary of the information available on the 27th of August 2012.
8) *S. Onodera, Y. Ohkubo, M. Takeya and M. Wataya*: Defects and their inspectability by UT in current heavy section steels for nuclear power plant, Proceedings of the Fifth International Conference on Nondestructive Evaluation in the Nuclear Industry, San Diego, California, 10-13 May 1982, pp. 231 – 236

9) *E. Gelfort*: Kernkraftwerke der I., II., III. und IV. Generation; Was heißt das für die Fortführung der Entwicklung?, atw 57. Jg. (2012), Heft 7 Juli, Seiten 486 – 494
10) *Siemens RT 4, Arbeitsvorschrift AVS 13 b*: Zerstörungsfreie Prüfung von Schmiedeteilen vom 21. 2. 1973
11) Flaw indications in the reactor pressure vessel of Doel 3, This note provides a summary of the information available on the 3rd of September 2012, www.fanc.gov
12) *JSW Technical Report TR-012-GN*: Difference in Material Manufacture between ASME Code and German Requirements, June 1978
13) *B. I. Voronenko*: Hydrogen and Flakes in Steel, Metal Science and Heat Treatment, Vol. 39, Nov. 11 - 12, 1997, pp. 462 – 470
14) FKS RS 304A, Einzelvorhaben EV 01 Werkstoffe und Schweißen: Technisch-wissenschaftlicher Bericht TWB 1/1, 1981
15) *G. O. Engl, H. J. Elsner*: Comparison of Requirements for In-service Inspection in Germany with Section XI, ASME, BAPV Code, Nondestructive Evaluation in the Nuclear Industry 1980, Proceedings of the Third International Conference, 11-13 February 1980, Salt Lake City, Utah, pp. 291 – 302

ULTRASOUND & SUBMARINE ADVANCEMENTS FOR RPV INTERNALS BAFFLE BOLT INSPECTION

S.W. Glass, B. Thigpen, AREVA, USA
A. Bleuze, E. Brau, AREVA, France

ABSTRACT

As many nuclear plants approach the end of their initial 40 years license period, inspection or replacement of their reactor internals bolts must be considered. This is consistent with the Materials Reliability Program (MRP 227/228) guideline for plant life extension. Assurance of the internals structural integrity is essential for continued safe operation of these plants. If there is no suspicion or indication of bolt failure, simple inspection is normally more cost-effective than replacement. Inspection specialists have inspected thousands of internals bolts with conventional or Phased Array UT. In some cases, complex bolt and head geometries coupled with counter-bore and locking bar interferences render classical UT inspections difficult. Additionally, different bolt head configurations and bolt capture mechanisms mandate specific qualifications for each bolt type.

AREVA has used advanced modeling approaches to optimize transducer designs to efficiently inspect these complex bolt shapes and has improved the SUSI submarine delivery platform for bolt inspection. This paper firstly discusses advances in the UT inspection methods for particularly challenging bolt designs including: the ID Hexagonal socket bolts characteristic of the WESTINGHOUSE 2 loops plants, the locking bar configuration characteristic of WESTINGHOUSE and FRAMATOME 3 and 4 loop plants and the B&W button head bolts. Secondly the results of the corrosion crack growth study engaged for UT inspection qualification is presented. At the end, advancements in position control of the SUSI submarine to assure correct identification of the internals bolts during the inspection are discussed.

INTRODUCTION

The reactor internals baffle plate assembly channels cooling water through the fuel assemblies. The assembly is comprised of rectangular plates nominally parallel to the vessel wall bolted into edge plates nominally aligned with the vessel radius and former rings located at multiple elevations within the vessel (Figure 1). Bolt shank diameters are typically 2 to 3 cm. The internals baffle assembly operates at elevated temperature (280-365 ºC) and is highly irradiated due to its close proximity to the nuclear fuel. These conditions are known to increase stainless steel material susceptibility to inter-granular stress corrosion cracking.

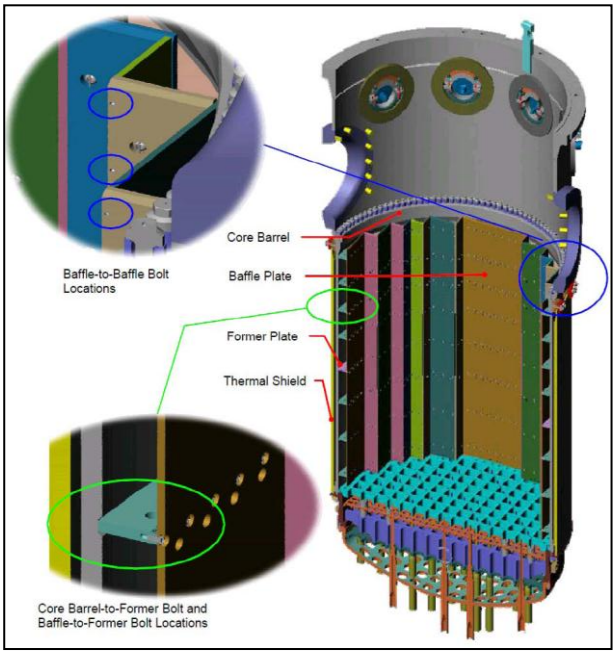

Figure 1: Internals Assembly highlighting baffle bolt locations

Normally this component is not readily observable. The lower internals are rarely removed from the vessel except to allow access for vessel wall ultrasonic examination. In the 1980's Visual Test (VT) inspections of several reactor internals discovered indications of baffle bolt cracking [1]. Most of these bolts were made of 316 cold worked stainless steels.

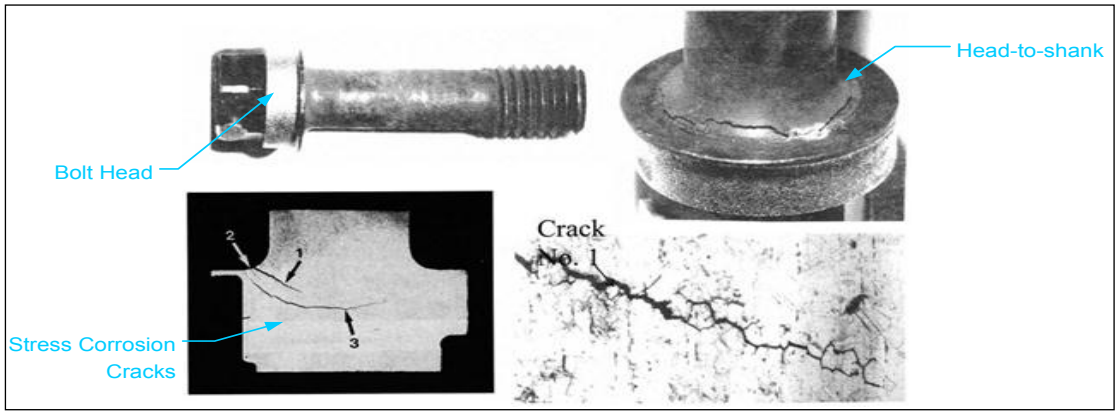

Figure 2: SCC can present various orientations with a tilt angle of up to 30 degrees from the head face.

Temperature and the water environment alone coupled with the relatively low stress levels on these bolts should not have been sufficient to cause cracks. Most of the cracked bolts though were located in the second and third rows from the bottom, corresponding to the highest neutron irradiation region. This indicated that the neutron irradiation coupled with stress and elevated temperatures increased the bolts crack susceptibility and in some cases led to cracking. The failure mode was identified as irradiation assisted stress-corrosion cracking (IASCC). Typically cracks are located in the head-to-shank region and along the shank even to the first thread in the body of the bolt (Figure 2). The cracks propagate along grain boundaries and therefore present a complex surface for UT signals to reflect from. This can be significantly different from EDM notch flaw representations.

Although the specifics are quite varied, most regional codes and regulatory bodies now require a bolt management program that includes VT, a prudent volumetric inspection (ultrasound) sample (typically every 5 to 10 years), or limited replacement of accessible bolts. Inspection vendors have invested heavily to automate and reduce the cost and schedule for bolt inspection thereby encouraging utilities to select the lower-cost inspection option. This gamble usually pays off. Moreover, the baffle structure is tolerant of a large number of failed bolts without compromising the structural integrity but there is still concern for loose parts. The global statistics are difficult to verify but on the AREVA built French CPO plants, between 1 and 11% of inspected bolts are confirmed cracked.

Bolt inspection frequency has increased in the US with plant-life extension programs performed in accordance with MRP 228 guidelines [2]. This document provides numerous internals inspection recommendations but the major automated inspection focuses are the guide-card channel wear measurements and baffle-bolt inspection.

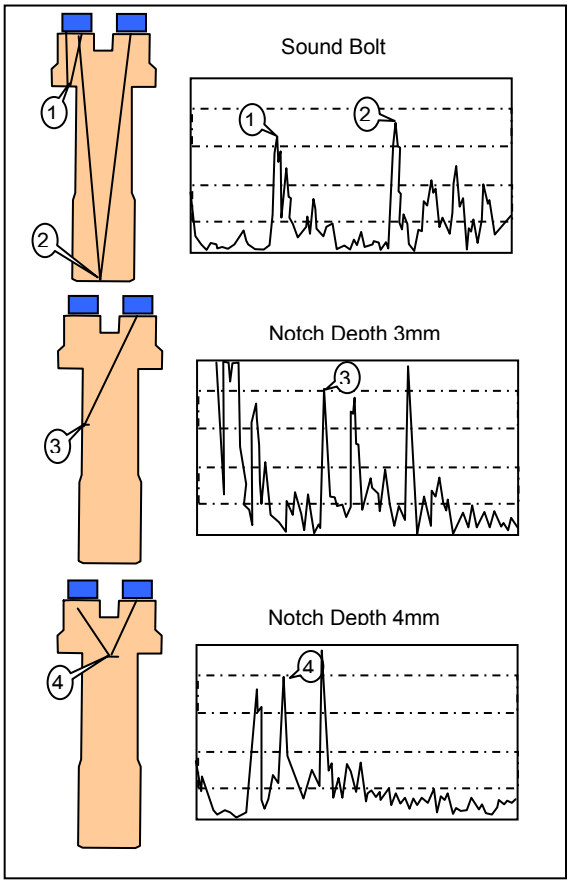

Figure 3: Conventional UT bolt integrity

ULTRASOUND TECHNIQUES

Conventional ultrasound (UT) techniques have long been known to be able to detect cracks and flaws in bolts. Transducers are coupled to the bolt head allowing sound to be transmitted through the shank of the bolt. If a strong reflection is observed from the bottom of the shank with minimal additional reflections, the bolt integrity is confirmed. If however, reflections are observed before the bottom-of-shank reflection is detected and/or the bottom-of-shank reflection is reduced, a compromised bolt is indicated or suspected (Figure 3). A typical transducer suitable for inspection of a flat-head bolt may have transmit and receive elements distributed in four quadrants. Transmit and receive interrogations can be from circumferentially adjacent or circumferentially opposite elements (Figure 4).

Figure 4: Four quadrant UT probe

In some cases, the bolt shank is made of highly attenuative materials so use of a back-wall echo is not possible. The most likely location however for cracks to occur are in the head-to-shank area, through the shank and into the bolt down to the first thread. The sound does not have to travel as far to interrogate this bolt region as it does to reach and return from the end of the bolt.

QUALIFICATIONS

Although the general inspection approach is straight-forward, each particular bolt geometry requires a specific qualification and technique adaptation. Technique development and qualification typically begin with a 3-D bolt model coupled to a planned UT transducer or transducer set (Figure 5). The UT and coupling configuration parameters are then optimized to produce a prototype probe. A series of bolts are then prepared with verification flaws to confirm the model predicted inspection capability. Flaws are determined in accordance with the client and sometimes the regulatory body but generally they include elliptical cuts or straight cuts in the locations of greatest concern and with a distribution of depths and orientations including the minimum target detectible flaw depth. Elliptical cuts are most representative of real flaw growth but straight cuts are easier to manufacture and typically yield similar results. Controlled fatigue cracks or weld-embedded cracks are also becoming more wide-spread as the costs for these more realistic cracks are becoming more manageable.

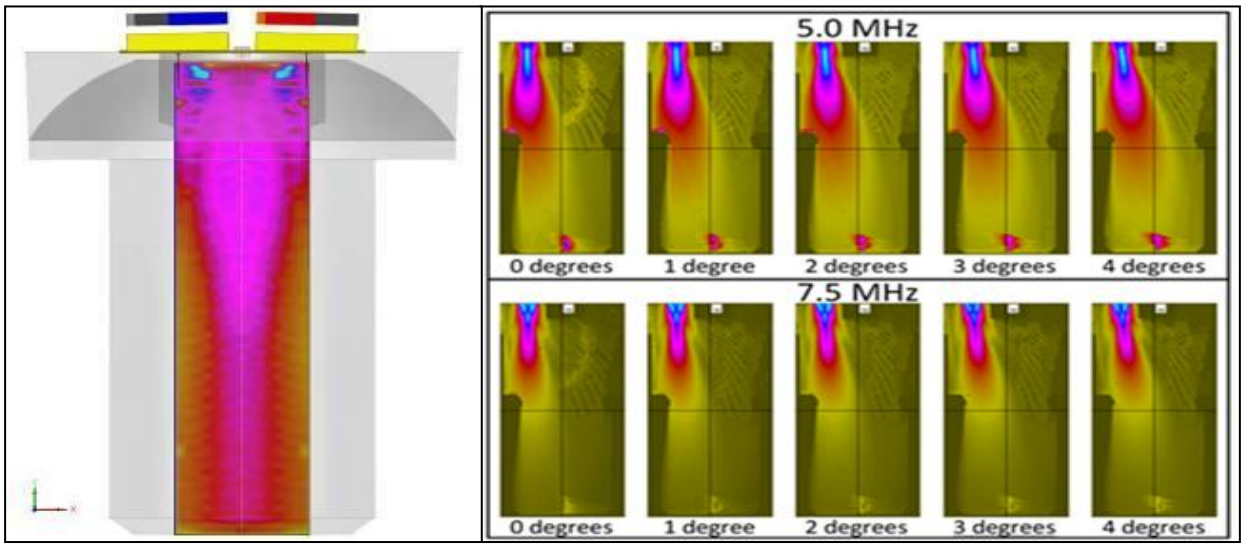

Figure: 5. CIVA modeling used to optimize frequency, element size, and angle prior to fabricating transducer

Through the years, several vendors have acquired a substantial portfolio of bolt inspection qualifications. In 2007, a comprehensive catalog of bolt designs associated with AREVA's key clients was assembled. The information included design geometry, material, access considerations, and an indication of the inspection technique and qualification status. This encompasses a high percentage of the possible bolt configurations but certain bolts still represent a challenge and/or availability of newer techniques coupled with an interest to improve the inspection quality have prompted continued advancement of techniques. Recent AREVA advancements have been focused on the B&W button head bolts, the Westinghouse 2-loop ID Hex bolts and the external hex head bolts with a locking bar typical of AREVA French plants (Figure 6).

Figure 6: Recent advancements have focused on 3 separate bolt types

B&W BUTTON HEAD

For the B&W button head bolts, the challenge was to couple ultrasound into the curved head with a sufficiently controlled beam angle to interrogate the shank area of interest. Following the CIVA model optimization, transducers were manufactured and verified to detect all target flaws. This system was successfully deployed in 2013 using the SUSI submarine delivery tool.

WESTINGHOUSE ID HEX SOCKET BOLT

This configuration poses a particularly interesting challenge. The ID socket is made by drilling the basic socket hole then placing the hexagonal socket faces within the head using an EDM machine. The intuitively obvious face for introducing ultrasound into the bolt shank is the bottom of the socket. This however was not a controlled feature of the bolt design. Efforts to use a nominal profile of this surface have resulted in a poor percentage of successful inspections. Underwater dental molds of the hex socket bottom surface confirmed the variability of this surface. AREVA has developed an alternate technique using the well-controlled faces of the ID hexagonal socket. The ultrasound is reflected off the OD cylindrical side of the head sending the ultrasound into the bolt shank. The transmit and receive elements are located on a single face, adjacent faces, and opposing faces of the hexagonal socket. All combinations of transmit and receive elements are

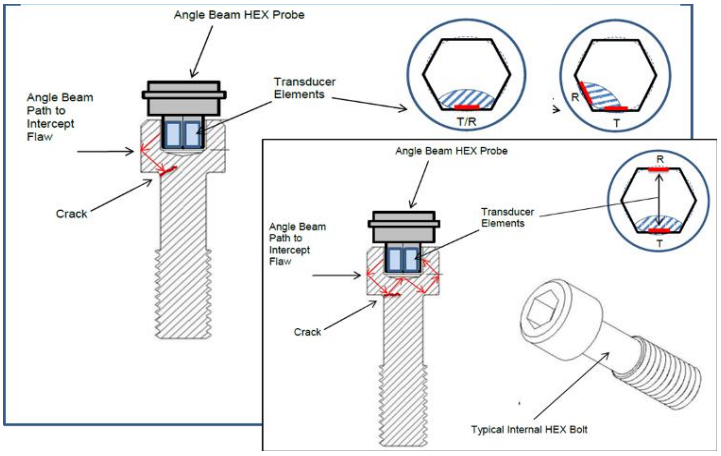

Figure 7: ID hex socket inspection from a single face, adjacent, and opposing socket faces detect all target flaws near head.

automatically interrogated to complete an inspection (Figure 7).
This inspection system was deployed to one plant on a rush basis following schedule difficulties for a large-scale replacement plan resulting in significant savings in critical path time [3].

AREVA OD HEX WITH LOCKING BAR

These bolts represent a significant portion of the overall bolt population and also represent a particular challenge due to the limited clean surface area available to insonify the bolt. Moreover, this kind of limited surface caused concerns about the relative amplitude for edm notch reflections vs. stress corrosion cracks. A series of bolts was developed with induced SCC cracks. These cracks were then examined with focused immersion UT (Figure 8) and with X-ray tomography (Figure 9) to confirm actual flaw locations in support of a new qualification effort. This qualification is on-going at the time of this paper's publication but the techniques used to demonstrate the true shape of induced flaws that can serve as inspection references represents a significant advance in the level of technology that can and has been applied to this overall inspection challenge.

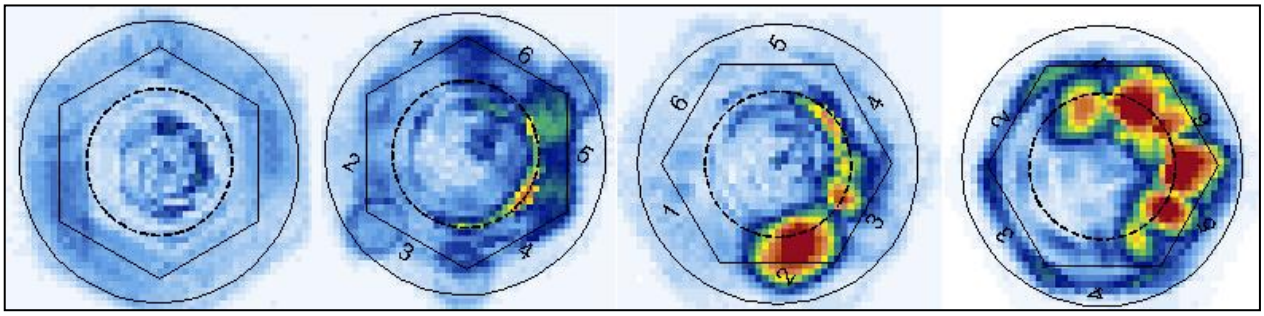

Figure 8: Reference un-cracked (left) and induced SCC samples (center and right) immersion UT showing full extend of induced SCC flaws.

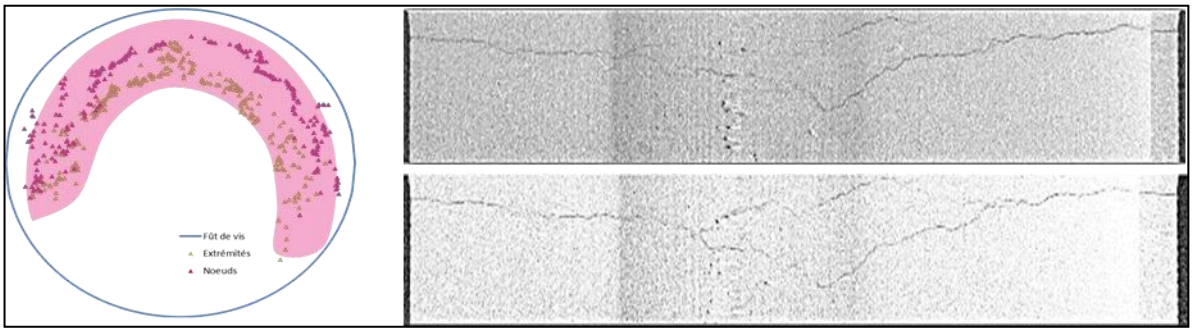

Figure 9: X-ray tomography by ERSF Synchrotron gives indication of crack morphology.

ADAPTING TO SUBMARINE

Internals bolt inspection requires precise delivery of the transducers to the bolts and a well-organized program to manage the data from the hundreds of inspections performed during each intervention. AREVA's Submarine System for Inspection (SUSI) has been adopted as a preferred delivery approach (Figure 10). A small neutrally buoyant cable is connected to a joy-stick controller manned by the trained SUSI operator. Video feedback of the view in front of SUSI aids the submarine driver to position the system. A lateral and rotational fine-position mechanism was added to the submarine base to facilitate transducer positioning. All of the added components are weight compensated so that the submarine is essentially neutrally buoyant requiring little energy to maintain depth and trim.

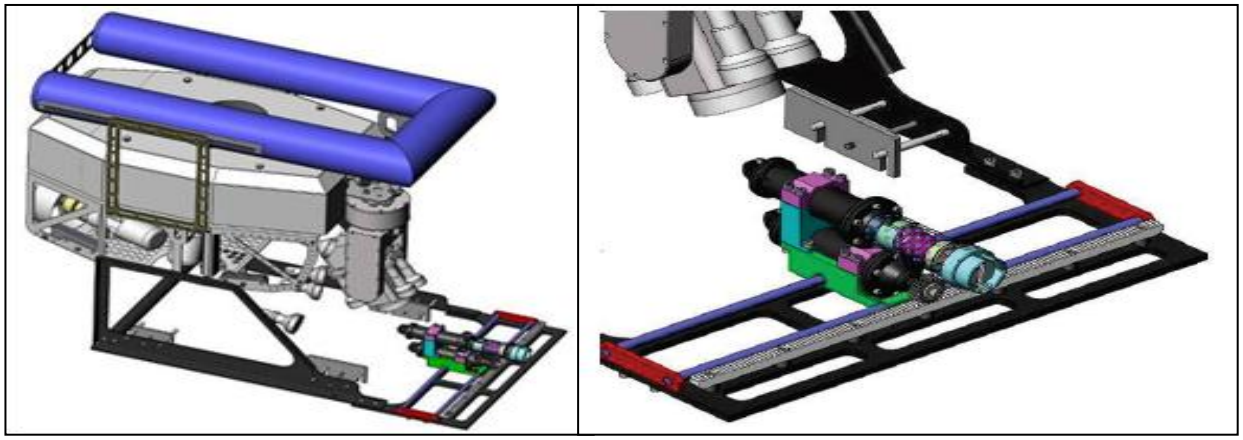

Figure 10: SUSI submarine with cameras plus linear traverse for higher productivity

The submarine is launched and piloted from the side of the reactor and internals stand pool. The operator has an overview perspective either by eye, and/or from an overview camera. After driving near the first bolt to be inspected, the fine-positioning mechanism with aid from the video camera focused on the transducer is used to position the transducer until a UT signal is recognized indicating proper coupling to the bolt. The UT data is captured and verified then the operator is released to go to the next location.

The examination strategy is to position over the first baffle plate and inspects the top row (typically 3 bolts) then change elevation and repeat the process. This allows the operator to register which bolt is being inspected. The data is captured and managed with custom software that allows the bolt identification to be associated with the data. Vertical position is managed with vertical thrusters and monitored with a pressure sensor to better than +/- 3 cm. This is adequate to assure correct identification of the bolt being inspected. Speed of inspection is partially a function of the operator skill and the particular bolt configuration but typical inspection rates exceed 20 bolts/hour. This allows a typical full internals inspection intervention in less than 3 days. This system has been used for more than 300,000 bolts over more than 10 years.

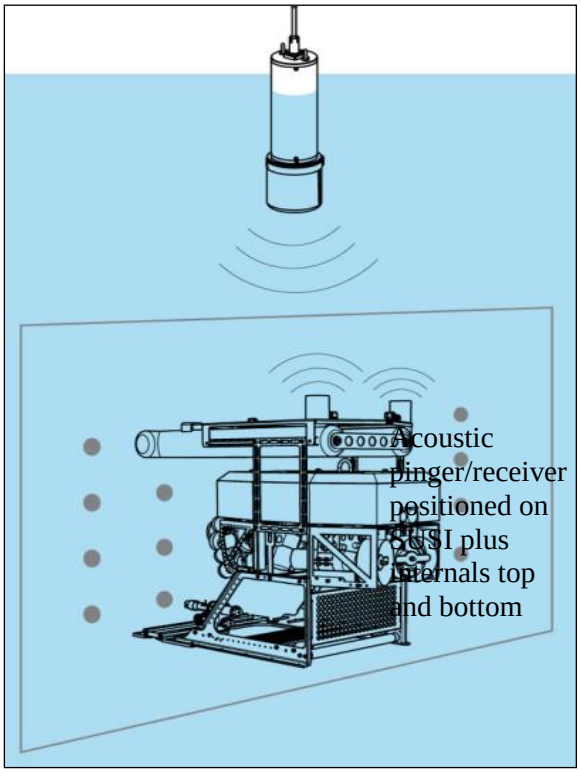

Figure 11: Acoustic location tool provides position feedback better than +/- 20 mm

Recent developments of the SUSI delivery platform include addition of a centrally located acoustic position sensing system. Acoustic chirpers are located on SUSI and are detected by the listening hydrophone. By triangulation on these signals, the absolute position of the submarine can be determined within the internals or vessel to within +/- 20mm (Figure 11). This is more than adequate to assure correct bolt identification and adds to the certainty and inspection verification completeness.

SUMMARY and CONCLUSION

A range of bolt inspection techniques for reactor internals bolt examination has been developed and most RPV internals baffle bolts can be inspected to some degree. New techniques however are being applied in response to rising customer expectations and in some cases re-qualification efforts are being performed in order to introduce new and better methods. These techniques are deployed on the SUSI submarine inspection platform to maximize the inspection speed and minimize intervention schedules. This paper has addressed the particular case of the B&W style button-head bolt, the Westinghouse ID hexagonal head bolt, and the French style OD hex-head locking bar design where techniques have been or are being developed and qualified. In addition, an acoustic position verification system has been developed to allow the low-cost submarine mounted inspection approach to have confirmed and verified position feedback to assure the correct bolt identification.

ACKNOWLEDGEMENTS

Developments were performed by French, German, and US operational units of AREVA NDE-Solutions plus the AREVA NDE Technical Center (NETEC).

REFERENCES

[1] IAEA Tec Doc 1557 Assessment and Management of Ageing of Major Nuclear Power Plant Components Important to Safety: PWR Vessel Internals June 2007 Update
[2] Materials Reliability Program: Inspection Standard for PWR Internals (MRP-228), EPRI, Palo Alto CA: 2009. 1016609
[3] L. Friant and T. Richards; Innovative Solution to Baffle Bolt Inspection and Structural Integrity, 9th International conference on Non Destructive Evaluation in relation to Structural Integrity for nuclear and pressurized components, May 2012.

ULTRASONIC INSPECTION OF BAFFLE TO FORMER BOLTS IN PRESSURIZED WATER REACTORS

M. Bolander, L. Alerts, C. Bies, F. Bonitz Westinghouse Electric, Germany
R. S. Devlin, P. Minogue, WesDyne International,USA

ABSTRACT

Industry-wide Aging Management Programs, as well as specific operating experience has resulted in increased interest in the inspection of the baffle to former bolts found in the internals of many Pressurized Water Reactors (PWR's). Age related degradation mechanisms, such as Irradiation Assisted Stress Corrosion Cracking (IASCC) may lead to the failure of these bolts over time. Sufficient baffle bolt failures may lead to the loss of structural integrity of the baffle-former assembly, or damage to the fuel.

Ultrasonic testing is used for the inspection of these bolts. The heads of the bolts are accessible from the core side when all the fuel is offloaded. The core barrel may remain in the reactor vessel, or be moved to the storage stand, but it is generally submerged due to the high radiation emanating from the baffle region.

Because of the large variation of the configuration of baffle to former bolts in different nuclear power plants, different types of ultrasonic inspection techniques have been developed and qualified. Conventional, phased array, contact, and immersion techniques have been developed to inspect the various bolt types. Qualifications have been undertaken for reactors in Europe, the United States, and Asia.

Besides the ultrasonic inspection technique, specific manipulators have been developed to deliver the ultrasonic probe to the bolts to be inspected. In this context the manipulator MIDAS VI used by Westinghouse is introduced. The MIDAS VI is a remotely operated underwater vehicle which positions the ultrasonic probe via camera observation. With MIDAS VI, the time for an on-site inspection, especially the installation time for the manipulator system is substantially reduced. Even the ultrasonic inspection itself can be realized in a shorter time.

Longtime experience with the manipulator SUPREEM™ for European power plants will be also a topic of this contribution.

INTRODUCTION

In a pressurized water reactor the fuel elements, which possess a quadratic cross section, are assembled in the core during power operation. The core barrel forms an adaptation between these fuel elements and the cylindrical reactor pressure vessel. It consists mainly of the horizontally aligned former plates providing the transition between the reactor pressure vessel to the fuel assembly and the vertically oriented baffle plates constituting the inner shape of the core barrel. The baffle plates are bolted to the former plates by the baffle to former bolts (short: baffle bolt) and the former plates are bolted by the barrel to former bolts (short: barrel bolts) to the core barrel, which is the outer shell of the core assemblies. Figure 1 shows the core barrel and its internals, figure 2 a collection of baffle and barrel bolts used in German nuclear power plants.

Depending on several boundary conditions, like material properties, bolt geometry, manufacturing technique of the bolt, chemical water composition, mechanical stress, radiation, etc., the baffle bolts are subject to material damages leading to the fracture of the bolt. The failure of individual baffle bolts distributed on the baffle plate does not affect the proper fixation of the baffle plates at the former plates. If adjacent baffle bolts are broken, the baffle plate may undergo slight displacements yielding to gaps between the baffle plates.

These gaps can cause irregular flow conditions causing abrasion at the fuel elements. Since demolishing of the bolt head is avoided by means of weld spots, lock washers (locking rings) or lock bars (locking pins), a broken bolt cannot be recognized by visual inspection.

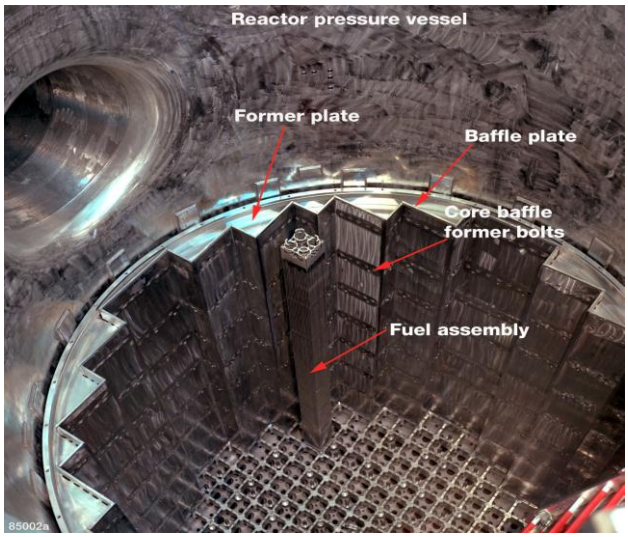

Figure 1: Core barrel and its internals inside of the reactor pressure vessel

Figure 2: Collection of baffle and barrel bolts used in German nuclear power plants

Ultrasonic examinations are carried out to detect cracked baffle bolts. To get access to the bolts the fuel assembly needs to be removed from the core barrel. The high dose rates enforce a mechanized underwater inspection. Different tools, like mast manipulators or complex multiple axis robot systems, were developed, qualified and used to perform these investigations. All these tools required considerable logistic efforts, especially crane support, for their installation.

An extended flexibility can be achieved utilizing remotely operated underwater vehicles (ROVs). Due to economic reasons the application of such ROVs is restricted to inspections, where a new qualification of the inspection technique is required or where the expenses of a new qualification are low.

Westinghouse Electric Germany developed MIDAS VI, a ROV for the inspection of baffle bolts. This ROV was presented in [1] and [2]. This article reviews the design of MIDAS VI and describes the recent qualifications and inspections, where MIDAS VI was used to apply the ultrasonic probe to the baffle bolt.

THE REMOTELY OPERATED UNDERWATER VEHICLE MIDAS VI

The remotely operated underwater vehicle MIDAS VI, shown in figures 3 and 4, was designed by Westinghouse for visual inspections in the primary system of nuclear power plants and to replace stationary manipulators used for baffle bolt inspections. It consists of the following components:

- the remotely operated vehicle (ROV),
- the end-effector allowing the positioning of the ultrasonic probe so sufficient coupling on the bolt head can be achieved,
- the radiation tolerant camera system including illumination and video recording unit,
- the operator console,
- the power and control unit (see figures 7 and 8) and
- the control and supply lines from the power and control unit to the ROV.

An overview underwater camera located on the top of the core barrel allows the surveillance of the MIDAS VI activities during the inspection.

The ROV consists mainly of a basic frame carrying a buoyancy vessel, which is driven and maneuvered by four propellers (see figures 3 and 6). By means of these driving and steering elements the ROV can be moved forward, backward, sideward, upward, downward and turned around the vertical axis. A pressure sensor based depth control supports the operator to keep the ROV at constant depth.

The radiation tolerant camera possesses a wide angle lens with fixed focal length of 9 mm allowing the visual surveillance of the probe applied on the inspected bolt. Eight 50 W spotlights ensure homogenous illumination of the end-effector with limited shadow casting.

The end-effector is mounted under the camera. It can be arranged in a left or in a right position, to reflect the location of the inspected baffle bolts on the baffle plate. That means depending on the accessibility of the baffle bolt the camera and the end-effector are installed on the left or right side of the ROV. A pneumatic cylinder presses the ultrasonic probe onto the bolt head. To turn the probe around its main axis a motor-resolver unit is build into a waterproof housing. The end-effector of MIDAS VI carrying a probe for the inspection of hexagonal bolts with a lock bar is presented in figure 5.

During the inspection of the bolt the end-effector is kept in position by suction cups applied to the baffle plate. These suction cups are connected to a vacuum pump connected at the ROV. Figure 6 shows the ROV attached to a mockup.

The ROV is brought into the water with the aid of a gripper, which can be connected and disconnected to a bracket located at the top of the ROV. A rack, which is positioned close to the pool, serves as a storage for the ROV between two dives. All ROV operations do not require crane support.

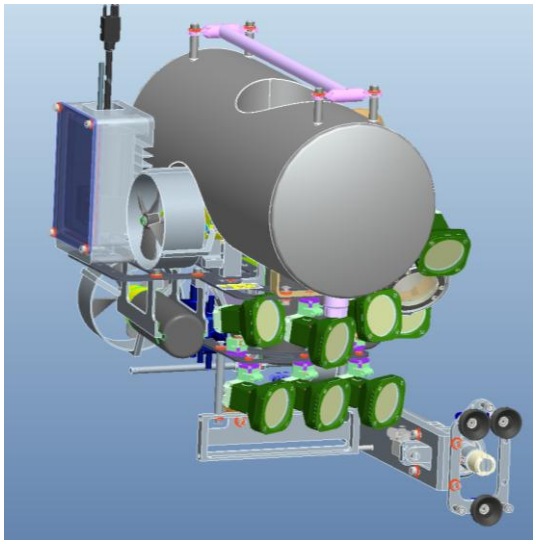

Figure 3: Schematic illustration of MIDAS VI

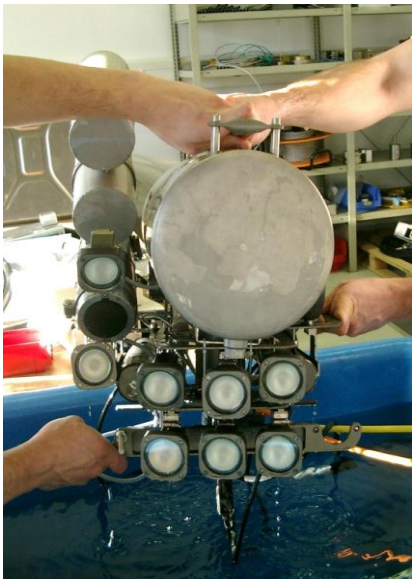

Figure 4: Front photgraphy of MIDAS VI

All ROV movements are operated utilizing the MIDAS VI control and surveillance equipment shown in figures 7 and 8. The movement of the whole ROV and the end-effector is performed from the operator console (see figure 8). A screen showing the camera image of the overview camera helps the operator to position the ROV close to the bolt. This screen is located on the top of the control and surveillance equipment (see figure 7). The camera located over the end-effector delivers an image of the bolt so the operator can move the probe directly in front of the bolt head. This screen is also shown in the top figure 7 under the overview screen and as a detailed image in figure 9. The operator moves the ROV close to the bolt utilizing the surveillance camera image, adjusts it with the aid of the end-effector camera, activates the suction cup mechanism to hold the ROV in position, presses the probe onto the baffle bolt head with the pneumatic cylinder and starts the probe rotation required for the inspection.

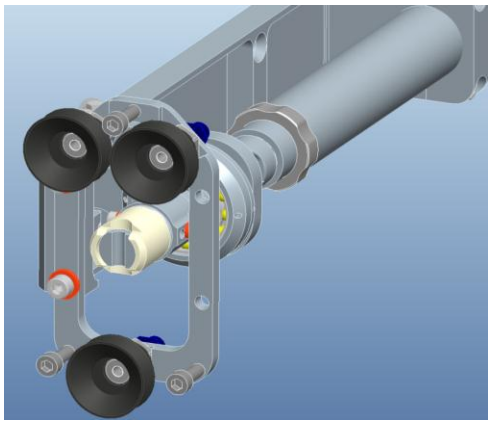

Figure 5: MIDAS VI end-effector

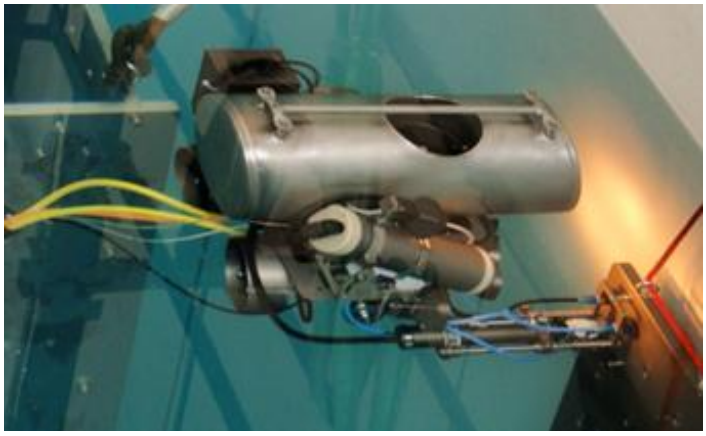

Figure 6: MIDAS VI attached to a mockup

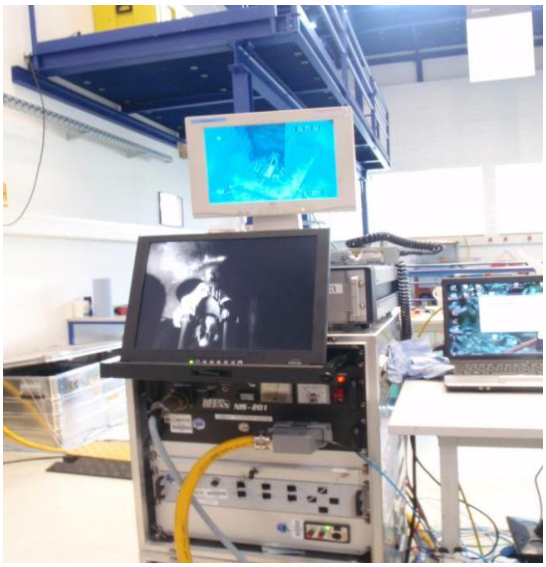

Figure 7: MIDAS VI control and surveillance equipment

Figure 8: MIDAS VI operator console

Figure 9: End-effector camera image

ACTUAL QUALIFICATIONS

General Steps

During the preparation of an ultrasonic technique for the inspection of baffle bolts it must be verified if an existing ultrasonic probe can be applied. The applicability of an ultrasonic depends mainly on the shape of the baffle bolt head, the material properties and the inspection targets to be found.

After the ultrasonic probe characteristics are known the question of the accessibility must be answered. That means the geometric boundary conditions need to be examined. These conditions include the evaluation of obstacles like fuel alignment pins at the bottom of the core barrel or niches formed by the baffle plate. If the environment of the baffle bolts to be inspected is known, the next task is to determine whether the baffle bolts can be reached utilizing the end-effector mounted on MIDAS VI or not. This task can be solved by performing experiments or by CAD modeling.

If the probes are available and the accessibility of the bolts is proven, the qualification process can be initiated. This process is finalized by an integral performance demonstration.

Actual Qualifications in Europe

Since major components of the inspection equipment used for an existing qualified inspection of baffle bolts in Belgium power plants were substituted, the inspection technique for these examination was qualified utilizing the new inspection system. The existing technique was widely kept due to the reliable results achieved in the past. In 2005 baffle bolts exhibiting indications had been removed after ultrasonic inspection. The indications found were confirmed by penetrant testing.

The equipment was modified as follows.

1. The ultrasonic device PARAGON was replaced by the DYNARAY / Ultravision inspection system.
2. The SUPREEM manipulator was replaced by the MIDAS VI remotely operated underwater vehicle.

In addition the technique was qualified for baffle bolts possessing lock bars (see figure 10) and replacement bolts with a safety flange.

Figure 10: Baffle bolts possessing lock bars

The ultrasonic probes used for that qualification were not modified, since these have shown excellent detection capabilities in the past. Figure 11 shows schematics of the probe used in pulse-echo and pitch-and-catch mode.

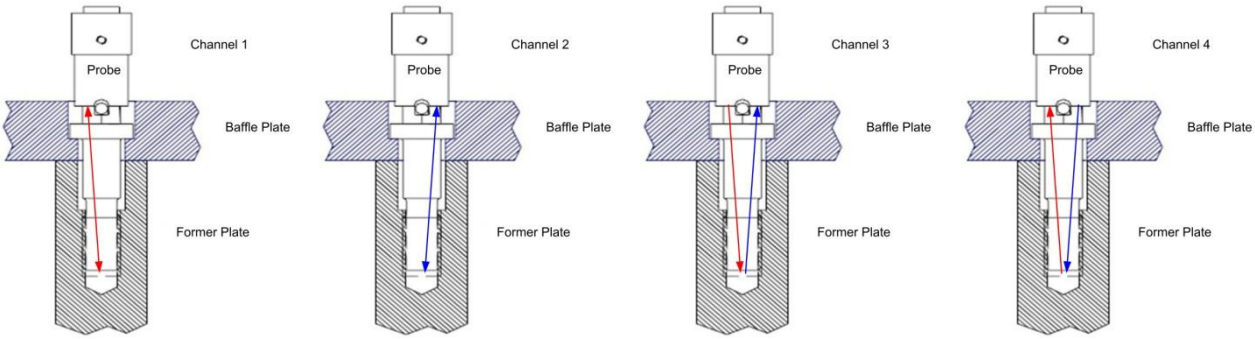

Figure 11: Schematic of the probe and configured channels

In figure 12 a sample of an indication is given. The test reflector located under the bold head is clearly detected in pulse-echo mode.

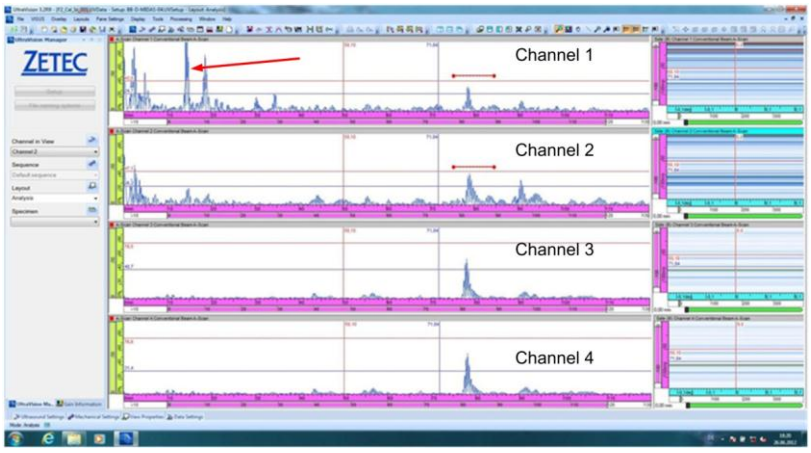

Figure 12: Reflector underneath the bold head detected with channel 1 (see arrow)

Actual Qualifications in the US

In order to inspect baffle bolts, which could not be examined with ultrasound in the past, two ultrasonic techniques were developed and qualified. For both qualifications MIDAS VI was used to attach the probe at the baffle bold.

1. The inspection of inner socked bolts (allen screws) secured by a lock bar with a technique utilizing the few areas at the edge of the bolt head for the coupling of the a multi-element ultrasonic probe. This bolt type is shown in figures 13 and 14.
2. The inspection of inner socked bolts (allen screws) secured by a lock washer with a technique utilizing the conical bottom of the hexagonal socked for the coupling of a phased array probe. This baffle bolt type is displayed in figures 15 and 16.

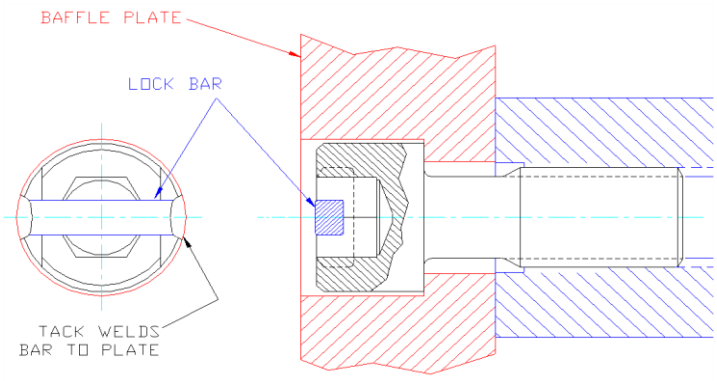

Figure 13: Installed inner socket bold with lock bar

Figure 14: Bold with lock bar

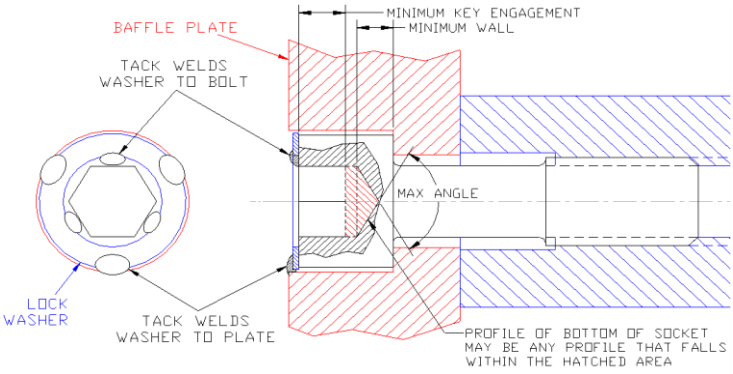

Figure 15: Drawing of an installed inner socket bold with lock washer and weld pins

Figure 16: Bold with lock washer and weld pins

During the examination the shape of the cone is determined utilizing a sector scan. As an example for the results, two sector scans are given in figure 17. The left image displays an indication underneath the bold head, the right image the back-wall echo from the bolt bottom.

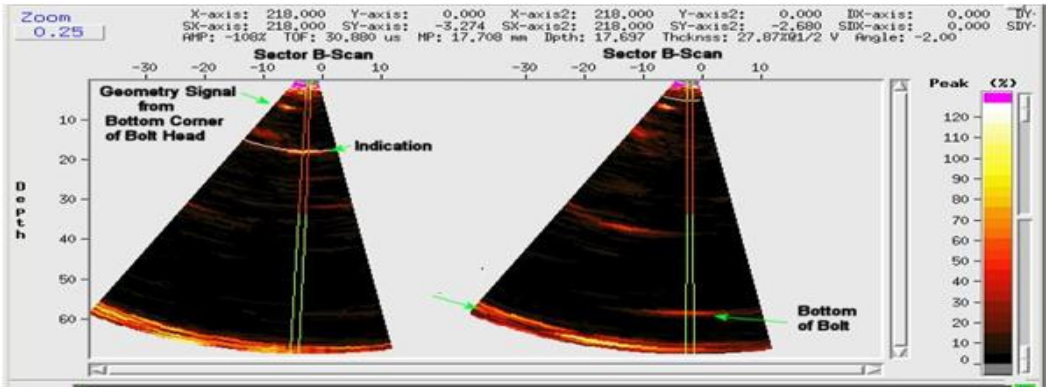

Figure 17: Sector Scan of a phased array baffle bolt inspection

The phased array technique for inner socked baffle bolts was qualified in December 2011 and successfully used in spring 2013 at the Point Beach 1 nuclear power plant. By means of the qualification of these ultrasonic examination techniques, the power plant owners avoided the replacement of baffle bolts, which were regarded as not inspectable by the authorities.

Experiences gained during inspections in French nuclear power plants

In 2009 inspection techniques for the original and the replacement baffle bolt built into French power plants (900 MW / 1300 MW) were qualified. In contrast to the examinations described above, the SUPREEM inspection robot, which originally was developed by WesDyne for the inspection of the reactor pressure vessel, was used (see figure 18). The examination of the original hexagonal baffle bolts was performed utilizing a four element ultrasonic probe; for the inspection of the replacement bolts a two element ultrasonic probe was applied. The inspection techniques have proven their practical applicability during the following interventions:

- Bugey 4 September 2009 3-loop plant
- Bugey 5 December 2009 3-loop plant
- Belleville 1 May 2010 4-loop plant
- Bugey 2 August 2010 3-loop plant
- Bugey 4 February 2011 3-loop plant
- Fessenheim 2 May 2011 3-loop plant
- Bugey 5 June 2011 3-loop plant
- Dampierre 2 March 2012 3-loop plant

Figure 18: SUPREEM inspection robot

General comments on the analysis

The analysis of the collected signals is generally based on pattern comparison, evaluation of the indications signal to noise ratio and the surveillance of the back-wall echo generated at the bolt bottom.

Further actual activities

The present development efforts concentrate on the inspection of barrel bolts, which can only be accessed through the 25 mm wide gap between the thermo shield and the core barrel. Such configurations are found in pressurized water reactors exhibiting a Westinghouse design. Figure 19 illustrates how the probe is attached to the barrel bolt. The recent qualification in that area focuses on the development of an inspection specification of barrel bolts with a lock bar [3]. The probe used for that purpose was developed with the aid of a simulation of the sound field described in [4].

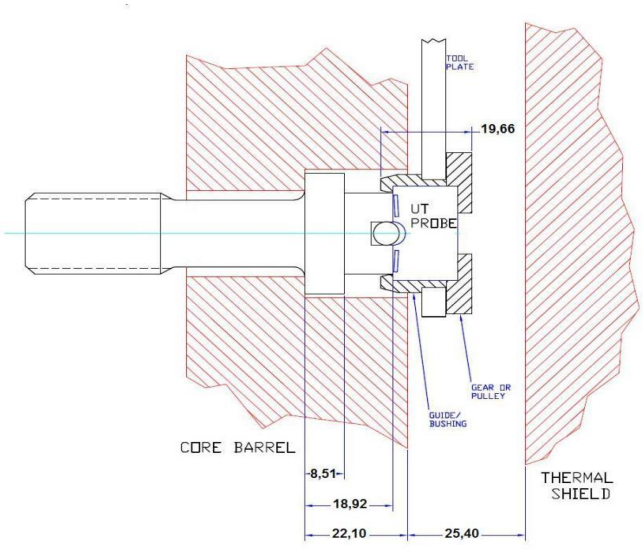

Figure 19: Ultrasonic probe attached to a barrel bolt

Summary
This article was meant to provide insight in some existing inspection technique of baffle and barrel bolts. These challenging inspections underwent permanent improvements during the last 15 years. The improvements comprise both, the manipulator technique and the inspection technique. The manipulator used became more and more flexible and complicated by means of adding axis providing a higher degree of freedom and finally by changing the basic design towards the application of remotely operated underwater vehicles. The inspection techniques evolved from simple transducers, over multi-element probes to phased array probes used in the recent designs. Due to the presence of a qualification, techniques established over that development period are still in use and serve as a base of future improvements.

References

1) Debnar A., Spies M., Bonitz F., "Prüfung der Kernumfassungsschrauben in Druckwasserreaktoren", DGZfP Jahrestagung 2010
2) Debnar A., Alaerts L., Spies M., Minogue P., Epineau C., "Recent Experiences with Ultrasonic Inspection of Baffle Former Bolts", Proceedings of the 8th International Conference on NDE in Relation to Structural Integrity for Nuclear and Pressurised Components, Berlin, 2010
3) Bonitz F., D'Annucci F., Knierriem L., Franke H., Kappes W., "Auslegung, Herstellung und Qualifikation einer Prüfeinrichtung für Kernbehälter von Druckwasserreaktoren", DGZfP Jahrestagung 1997
4) Spies M., "Semi-analytical elastic wave-field modeling applied to arbitrarily oriented orthotropic media", Journal of the Acoustical Society of America 110 (1), July 2001

SG&BOP

NON INVASIVE HEAT EXCHANGER TUBE INSPECTION USING TWO MODALITIES OF PULSE REFLECTOMETRY

N. Amir, Y. Harel, Acousticeye, USA

Abstract

Pulse Reflectometry (PR) is a non-traversing method for inspection of various tubes and pipes. In Acoustic Pulse Reflectometry (APR), for example, acoustic pulses are injected into the air inside the tube. Internal Diameter (ID) defects create reflections which propagate back up the tube, where they are recorded and can later be analysed. However, APR cannot detect cracks and Outer Diameter (OD) defects. In this paper we first present a novel implementation of PR based on the well-known technique of "guided waves", in which ultrasonic pulses are propagated in the tube wall itself. This method, which we term Ultrasonic Pulse Reflectometry (UPR), is complementary to APR: it can detect both cracks and OD defects. It cannot defect blockages or very small through holes, which however can be detected by APR. We therefore present a combined APR and UPR system, which can detect a very wide range of ID and OD defects, and demonstrate its capabilities through various case studies.

Keywords: Qualification-Inspection

MANUFACTURE AND NON-DISTRUCTIVE TESTS OF HIGH PRESSURE STAINLESS STEEL FEEDWATER HEATER TUBES

P. Gerard, Valtimet, France

Abstract

Today, the stainless steel feedwater heater tubes are more and more manufactured from welded tubes.
Two main categories of grade are available on the market: The austenitic stainless steels (304, 304N…) and the ferritic grades, (439) specially for nuclear power plants.
The specification for the tubes are generally based on A 688 for the austenitic grades and A 803 for the ferritic ones.
No one of these standards recommend the utilization of the ultrasonic test.
The paper reviews the different types of tube manufacture and focuses on the NDT parts.
The efficiency of the utilization of the ultrasonic test is clearly demonstrated for both products through many concrete examples.

Keywords: heat exchanger inspection tubes before installation.

HELIUM LEAK TESTING: A COMPLEMENTARY SG INSPECTION TECHNIQUE. TECHNOLOGY AND LESSONS LEARNED

F. Lesage, B. Bittard, L. Riquelme, Westinghouse Electrique, France
H. Henaff, EDF - CEIDRE, France

Abstract

The method presented in this paper allows detecting tubes with micro gas leaks, estimating the size of each leak and, if applicable, locating it in the tube detected as leaking. This method is based on the use of helium as a tracer gas and mass spectrometers as detectors.

The goal is to detect any global leak on a tube ? 3 cm3/h of gas with a Sf/Sn signal ratio (examined tube indication/gastight tube indication) ? 1.1 and if applicable, to locate the leak in the concerned tube. The helium leak testing process is applicable to all unplugged tubes of every SG type, independently of the plugging of neighboring tubes.

The helium leak testing process, as applied to steam generator tube bundles, includes two phases:

- Basic inspection: Systematic Inspection of all unplugged tubes of the tube bundle, in order to detect leaking tubes,
- Complementary Inspection: Inspection used to determine the approximate location of the leak, should a tube be detected as leaking during the basic inspection phase.

The principle for preparation and inspection is the following:

- Steam Generator (SG) drained and as hot as possible,
- Secondary part of the SG dried, leak tested and isolated,
- Primary part of the SG dried,
- Secondary side of SG pressurized to 6 bar absolute (6.105 Pa) with a homogenous mixture of air and helium.

The Concetration of helium obtained in the secondary side of the SG is 25%

- Application of a sweeping flow rate of 1200N/h established in the tubes to examine,
- The concentration of helium in the outlet air of the tubes is measured using a mass spectrometer set according to the helium peak. The measurement is performed after a certain amount of time, that includes the tube discharge time plus a sufficient delay and the response time of the sniffer.
- Location of the leak in the tube, if applicable, using the double flow speed variation method.

The Helium Leak Testing process implemented by Westinghouse is qualified in France for EDF Steam Generators.

The paper will describe:

- The technology and equipment,
- The Capability and performance of the inspection,
- The lessons learned from site jobs.

HELIUM LEAK TEST IN LINE: ENHANCED RELIABILITY FOR HEAT EXCHANGER TUBES

M. Lheureux, P. Gérard, Vallourec, France

ABSTRACT

Pneumatic test using air under water or air pressure differential method is a Non Destructive Test specified by current ASTM standards (A1016/A1016M) for welded tubes.
This paper reviews these two leakage testing methods and introduces a new in line helium leak test method developed by Vallourec. The first results obtained by this method demonstrate its advantage to substitute and improve the current pneumatic tests with lower detection level and higher reliability. Besides, this system is closer to the final testing methods used on assembled heat exchangers.

PNEUMATIC TESTING METHODS

The Air Under Water method (AUW)

Fig 1: AUW bench

Pressurized air is introduced into the tube and the tube is placed in a well-lit tank. After a stabilization time, an operator walks along the tube looking for bubbles. If the operator is detecting bubble coming out the tube, there is a leak and the tube is rejected and if no bubble is detected during the inspection, the tube is considered as conform. The limit of detection mentioned with the method C1 of the EN1779 is 10^{-3} mbar.l/s but in an industrial environment it is commonly considered that the sensitivity of the air under water method is ranging from 10^{-3} mbar.l/s to 10^{-2} mbar.l/s depending on factors like lighting, water, air bubble trapped outside and when the first bubble will appear. The high dependence on operator judgment and possible plugging of the defect by water contamination are significant disadvantages that can cause to lower significantly the sensitivity even more and the repeatability of the AUW test.

The Pressure Differential method (PD)

Fig 2: PD bench

The PD method is based on the measurement of the pressure drop over a constant period of time. A tube is pressurized with air and after a stabilization time, the pressure drop is measured by differential method, comparing the tested tube pressure to a reference volume pressure over a certain amount of time. If the pressure of the tube drops above a threshold specified, the tube is automatically rejected and if the pressure keeps below the threshold specified, the tube is conform.
On top its good sensitivity, the automatism makes this method independent of human mistake or misjudgment.
The sensitivity of the test is linked with the testing time and the pressure values. Besides, several factors can disturb the sensitivity and repeatability of the test as mentioned in the EN1779:

- Internal temperature gradient influencing the results
- Variation of the elasticity of the tube due to the variation of mechanical properties
- Mechanical deformation of the equipment itself
- Precision of the transducer
- Thermal fluctuations

Finally the PD method doesn't allow the leak localization which can be a significant disadvantage for process/quality continuous improvement.

The limit of detection of the current pneumatic tests

Strip defect or weld defect can be very narrow with a complex geometry as illustrated below. Such "defects" could pass successfully standard Non Destructive Tests on tubes during production but generate some leaks during more stringent tests performed on assembled equipment.

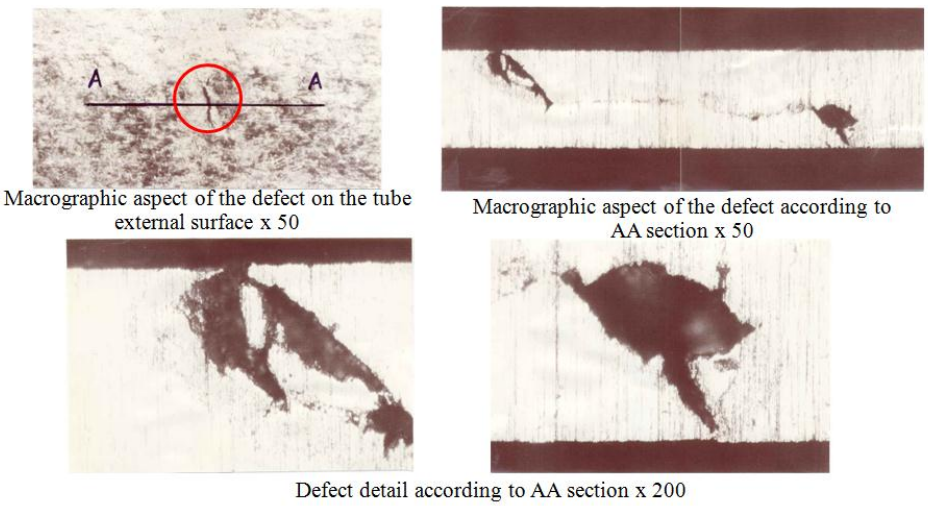

Fig 3: Strip defect N°1

THE DEVELOPMENT OF A NEW TECHNOLOGY FOR TUBE LEAK DETECTION: THE HELIUM LEAK TEST ON TUBE

Fig 4: Helium bench

Vallourec developed the helium leak test on tube using the sniffing method by accumulation. A tube is set on a bench and the inside is pressurized with a gas tracer.

Why helium is used?

- *Thanks to its low mass and low viscosity, it can rapidly pass through very small and very complex leaks*
- *It is a noble gas so it does not react or combine with metallic surface*
- *The very small amount of helium gas is naturally present in the atmosphere (5ppm) so the background noise is very low and any increment of helium concentration can be detected easily*

The sniffers will be displaced on top of the whole length of the tube and they will detect eventual leak by sniffing concentration of helium in the chamber above the threshold specified.

The detection of the increment of helium concentration is performed thanks to a mass spectrometer. It will detect the presence of helium molecule thanks to their mass and will convert them into an electrical signal.

Assuming that the sniffing probes don't detect any leak of helium, the tube is exhausted and automatically released. In the event of a leak failure, the tube is not released and a visual and noisy alarm is alerting the operator.

Experimentation

To study the reliability of the test, two sets of tests have been carried out:

- The capability and repeatability test
- The comparison test with others pneumatic methods

The minimum threshold is fixed at 1.10^{-5} mbar.l/s which is corresponding to double the helium rate in the air (usual concentration of 5ppm). The setting of the threshold is validated by measurement of helium stability in the surrounding air at the helium test bench place.

Capability and repeatability tests

Objective

- Evaluation of the capability and the repeatability of an automatic helium test on tubes. Detection on 1m long tubes of 1, 3 and 5 microns diameter laser drilled holes.

Tests of sample tubes in dynamic

- Tests were carried out with two pressures 1 bar and 7 bars on three hole diameters (1 micron, 3 microns, 5 microns)
- For each condition (corresponding to one pressure and one hole diameter), the tube was tested in four position: with the leak above, with the leak below, with the leak on the right side and with the leak on the left side

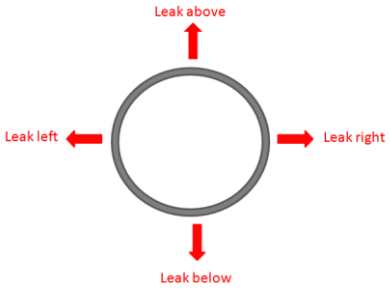

Fig 5

Presentation of results

The results are presented like a graph with the leak rate in ordinate and the passes in abscissa. For example, we can see in the graph below that for a hole of 3 microns and an internal pressure of 1 bar, the leak is detected for all positions with a threshold at 1.10^{-5} mbar.l/s with the maximum signal when the hole is above:

	Above (blue)	Right (red)	Below (purple)	Left (green)
Signal	7.10^{-5}	$1{,}2.10^{-5}$	$1{,}7.10^{-5}$	2.10^{-5}

Table 1

We can also conclude that the test is repeatable as the leak is detected five times over five passes.

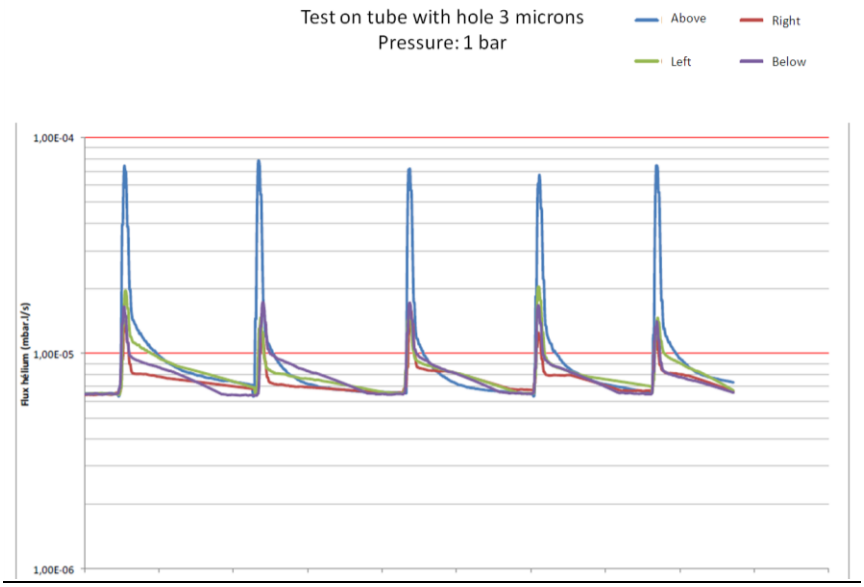

Fig 6: Graph of helium signal

Results

	1 bar				7 bar			
	Top	Right	Below	Left	Top	Right	Below	Left
1µm	$2{,}5x10^{-5}$	$1{,}2x10^{-5}$	$0{,}95x10^{-5}$	$0{,}9x10^{-5}$	$8x10^{-4}$	$1x10^{-4}$	$4x10^{-5}$	$1x10^{-4}$
3µm	$7x10^{-5}$	$1{,}2x10^{-5}$	$1{,}7x10^{-5}$	$2x10^{-5}$	$1{,}5x10^{-3}$	$1x10^{-4}$	$2x10^{-4}$	$3x10^{-4}$
5µm	$6x10^{-4}$	$3x10^{-5}$	$2x10^{-4}$	$1x10^{-4}$	$3x10^{-3}$	$3x10^{-4}$	$4x10^{-4}$	$7x10^{-4}$

Table 2

→ In all conditions, 100% of leaks have been detected

Comparison between pneumatic tests

Objective

- Comparison between the, air under water method, the air pressure differential method and the helium sniffing method. The thresholds have been fixed according to common industrial practices and standards like ASTM A1016/A1016M and ASTM A1047/A1047M.
- Two sets of titanium tubes grade 2 were tested in order to compare and evaluate the efficiency of the methods with tubes having artificial and industrial defects
    - Set 1: tubes with an outside diameter of 25mm with artificial defects of diameter 1 µm and 3 µm.
    - Set 2: tubes with an outside diameter of 19mm with "industrial" defects (tube 1 and tube 2)

Methods	Time of control	Pressure	Thresholds by current standard
Air Under Water	1 min	7 bars	Detection of bubble with a detection speed of 1m/s, equivalent to 1 bubble per second
Air Pressure Differential	5s	7 bars	Difference of pressure more than 150Pa
Helium Test	Vallourec specific conditions compatible with in-line control	7 bars	Leak rate more than 10^{-5} mbar.l/s

Table 3

Results

	1 µm	3 µm	Tube 1	Tube 2
AUW	**Below threshold**	**Below threshold**	**Below threshold**	**Below threshold**
PD	**Below threshold**	**Below threshold**	**Below threshold**	**Below threshold**
He	**Detected**	**Detected**	**Detected**	**Detected**

Table 4

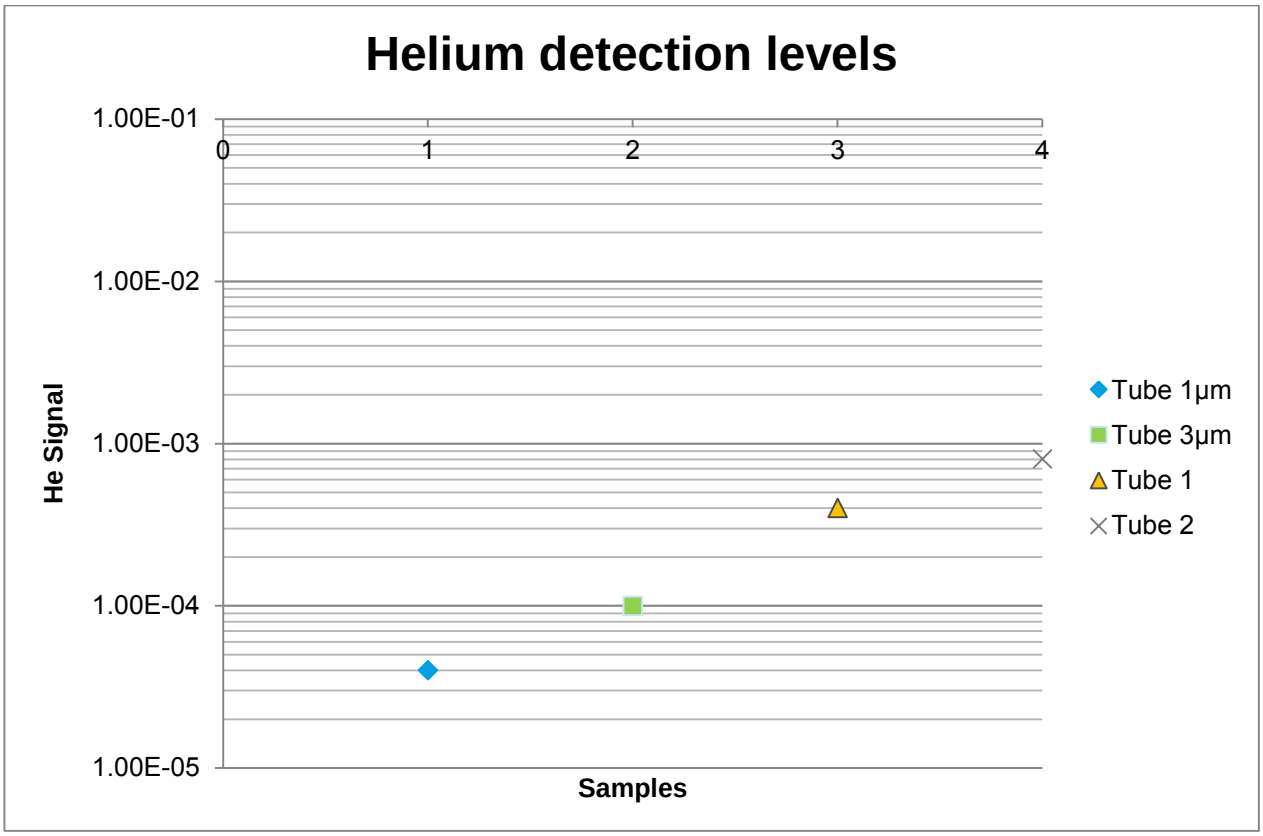

Fig 7

CONCLUSION

With a sensitivity up to 10^{-5} mbar.l/s the helium test proved a very high sensitivity, a hole diameter as small as 1 micron can be detected with a good repeatability. The comparison with the other standard pneumatic testing methods PD and AUW turned clearly to the advantage of the helium test.
Thanks to its higher sensitivity, its repeatability and its automatism, the helium test inline is a perfect candidate to achieve the zero defects during complementary tests requested by our customers for stringent operations.

PIPES FOR LIFE - AN NDE INSPECTION OF AGR BOILER TUBES

C. R Bird, D. Maclennan, Doosan Babcock, UK

Abstract

As part of the Lifetime Extension Programme for gas cooled reactor power stations EDF Energy has embarked on a detailed study of the condition of their boiler tubes. As part of this study Doosan Babcock were requested to develop an inspection system for the measurement of the wall thickness and bore diameter of the superheater boiler tubes.

An ultrasonic head has been designed to negotiate pipes with a 13mm internal bore after first negotiating 5 off 45 degree bends. The requested probe deployment distance was approximately 30m. To add a further challenge there is a restriction which forces the maximum diameter of any probe to approximately 11mm.

The tubes are finned on the external surface adding to the complication of generating a wall thickness measurement.

This paper describes the technical challenges, the inspection solution and the application of the developed techniques in the field.

Keywords: Boiler Tube Inspection, Signal Processing, Restricted Access.

1. INTRODUCTION

The aim of the NDT development and application has been to provide boiler tube wall thickness measurements to enable a quantitative assessment of the boiler tube condition forming part of the boiler lifetime monitoring programme.

The boilers were manufactured in 1976, they were not designed with in service inspection as a consideration, resulting in consequential access and inspection challenges. The boilers layout is shown in Figure 1a.

This paper highlights the extreme challenges associated with the inspection problem and provides an outline of the solutions developed to solve these challenges.

The challenges can be divided into mechanical and NDT. Both the mechanical and NDT challenges were at the boundaries of current best practise forming an intriguing development project. This paper first discusses the mechanical challenges followed by the NDT challenges. The paper then goes on to describe our solutions to the technical challenges.

2. INSPECTION CHALLENGES

2.1 Mechanical challenges.

As introduced these boilers were not designed with inspection in mind, resulting in difficult NDT access. The boiler design utilises a compact and complex helical tube pattern, to achieve high thermal efficiency. Figure 1a presents an overall drawing of the boiler.

The only feasible NDT access point for tube inspection of the superheater outlet headers is the top of the boiler. To provide access to the tubes the header dome is cut off and then reinstated after the inspection. The probe is lowered 10m (vertical) through a tail pipe, containing a number of 45° bends to a bifurcation (BIF) where two superheater tubes feed into the tailpipe. (Figure 1b).

Figure 2 provides a section through the BIF. The vertical pipe has an internal diameter of approximately 20mm.

The two smaller pipes that feed the tailpipe have an initial bore diameter of 13.8mm. The forging has no blend radius and a bend angle of 80°, additionally any probe has to identify and navigate around either the top or bottom superheater tube.

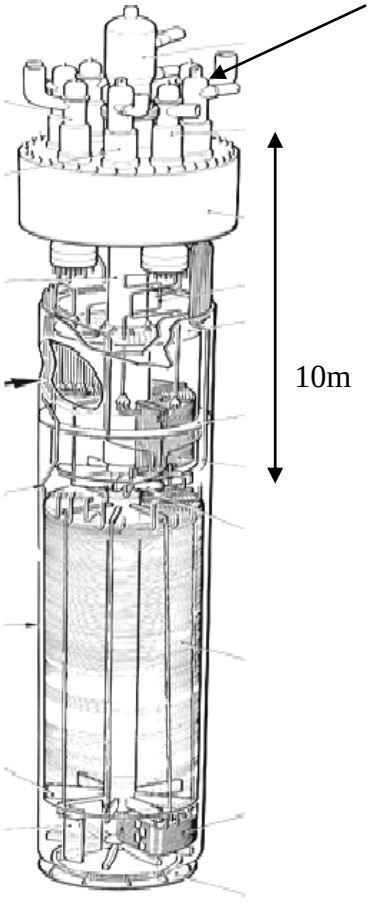

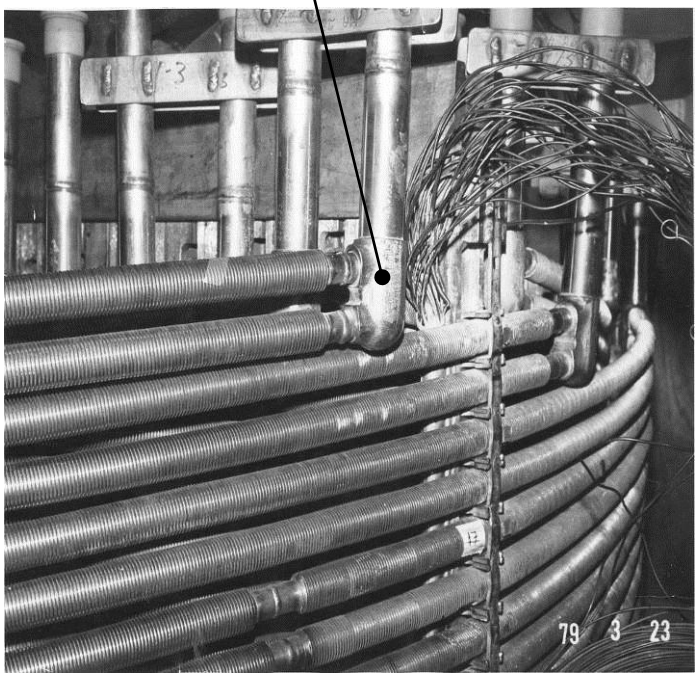

Figure 1a Drawing of boiler layout

Figure 1b Photograph of the boiler tube bifurcation (BIF).

The superheater tube forms a helical spiral is ~100m and undergoes material and dimensional changes throughout the height of the boiler. The first of theses obstacles is a transition joint approximately 11m upstream of the BIF where the material changes from 316 stainless steel with a 13.8mm bore, to 9%Cr, 1%Mo carbon steel with a bore of 12.7mm.

Eddy-current probes are frequently used for PWR steam generator inspection but they are only subject to 1 or 2 small radius bends. After 360° of bends the capstan effect takes hold and prevents deployment via pushing or pulling any cable.

An access solution was required. Self propulsion systems are regularly used e.g. “PIGS”, but these normally have pipe diameters of many centimetres (50mm minimum) and are not subject to bends where the diameter of the pipe equals the bend radius to be navigated.

Ultrasonics inspection was chosen as the NDT method to provide wall thickness measurement. Given the dimensional limitations imposed by the requirement to pass around the BIF, it was decided that an immersion technique was the only feasible solution given the mechanical complexity of providing a contact probe. A further advantage of an immersion solution was the possibility of providing bore diameter measurement.

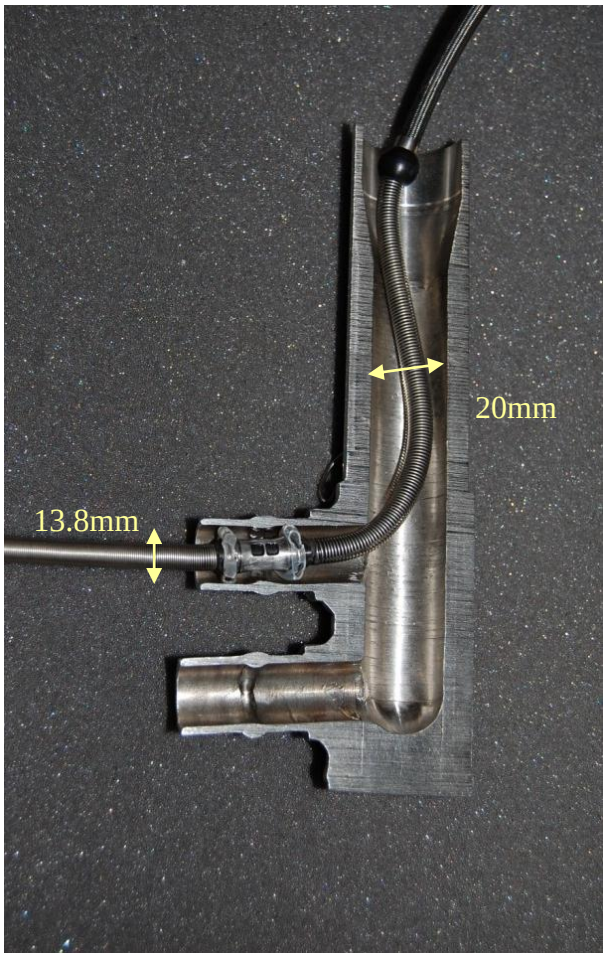

Figure 2. Section through BIF

The consequence of using water immersion was that the probe would be small relative to the bore of the tube. It was important that the probe could be held central within the tube to ensure the beam was near perpendicular to the surface. A flexible centralisation system was required to ensure high accuracy measurements.

In common with all boiler circuits there are strict Foreign Material Exclusions. In short what goes into the tube must come out. Being a nuclear installation these rules are strictly adhered to and the probe design was required to demonstrate that it would not break and even more importantly would come out after deployment. Furthermore all materials used in the construction of the probe are required to be nuclear compatible.

2.2 NDT Challenges

The NDT challenges can be divided into four areas:

i) Tube dimensions and length
ii) Probe alignment
iii) Finned tube
iv) Probe size

2.2.1 Tube Dimensions and Length.

The inspection technique was required to measure wall thickness reliably with accuracy better than 0.2mm. Whilst this is not difficult on flat plate with a good surface finish where the probe can be manoeuvred to be at normal incidence to the surface the task is far more challenging when the probe is 35m away from the instrument down a 13.8mm tube after navigating an 80° bend with no radius.

The as built tube wall thickness ranged from 1.8mm to 2.4mm depending upon the location within the boiler. This thickness of tube would normally require a high frequency probe (greater than 10MHz and if possible 20MHz) to provide accurate thickness measurements.

The cable length and diameter causes high frequency attenuation lowering the possible probe frequency. To date the maximum centre frequency transmitted by this length of cable has been 8MHz. It should be noted that to achieve the required flexibility in the cable and to negotiate the BIF 40AWG, coaxial wire has been used for the cable construction.

In order to negotiate the very small radius bends, see Figure 2 the space envelope for the probe must have a smaller diameter than ideal (6mm at the transducer) and must also be relatively short (20mm in axial direction). Further, the cable was limited to be less than 4mm diameter including the outer tri-axial sheath. When taking measurements this small probe then requires to be centralisation and aligned axially.

2.2.2 Probe Alignment

To obtain accurate bore diameter and wall thickness measurements the ultrasonic beams need to be near normal to the internal surface of the tube. The small tube radius creates a condition where a very small probe eccentricity causes a high degree of radial beam misalignment for example 1mm eccentricity causes a 17° radial beam misalignment. Poor probe alignment causes pulse shape distortion and reduction in measurement accuracy.

As introduced the probe is required to navigate around a 80° bend and then down a spiral tube of two different diameters. To navigate around the 80° bend a dog bone, (Figures 2 and 5), shaped probe was designed and manufactured incorporating centralisation features. It was recognised at the technique design stage that alignment to the surface within 2.5° would not be achieved in all occasions, and that it would be necessary to use the ultrasonic data to discriminate between aligned and non aligned ultrasonic beams.

The dominant ultrasonic energy is received from the beam path which is at normal incidence to the bore of the tube, represented in Figure 3 as a solid line. The dashed line represents the normal beam direction from the transducer face. In this case the 6dB half angle beam spread is approximately 2.5°. Hence the algorithm used to measure the bore diameter determines a best fit circle taking into account the three beam paths normal to the inner surface of the tube.

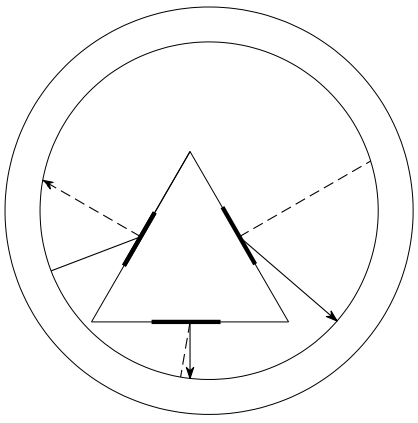

Figure 3. Exaggerated illustration of measurement accuracy challenge due to radial alignment

In addition to probe concentricity, axial misalignment must also be taken into account. The energy normal to the tube bore will dominate but when the beam is non normal to the tube bore the ultrasonic signal becomes extended, this leads to difficulty discriminating the correct signal peak.

2.2.3 Finned Tube Wall Thickness Measurement

The majority of the tubes to be inspected were manufactured with fins as shown in Figure 1b. The fins are manufactured with rounded "roots" causing the signals from the outer surface (at the base of the fin) to be severely reduced and scattered by the radius. Furthermore the beam will detect the fin root even if it is not perpendicular in the radial plane. Figure 4 provides a picture of a sectioned tube and illustrates the thickness measurement challenge. Incorrect alignment will cause a distortion in the pulse shape and a potential inaccurate beam path.

The finned tube was manufactured by a rolling process similar to bolt manufacture, ensuring that the fins have a consistent and accurate pitch, (2.5mm), and shape. It is possible to take advantage of this regular pattern in the signal processing as discussed in Section 4.

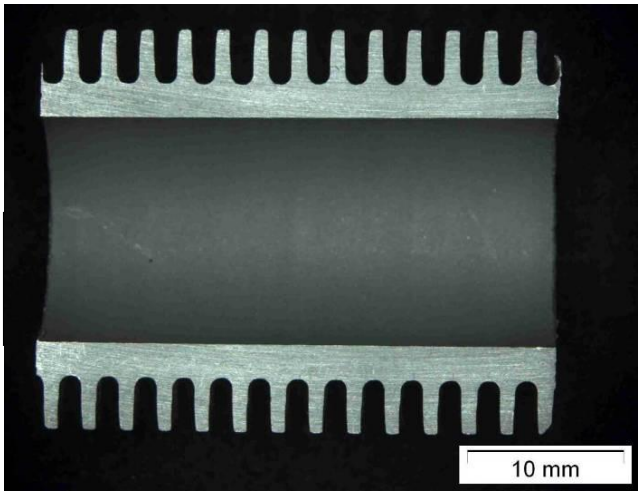

Figure 4. Section through fined tube.

2.2.4 Probe Size

To achieve larger beam spread and greater tolerance to beam alignment, small crystals are required (typically <2mm diameter) but for transmission of power and matching crystal impedance to that of the cable a larger crystal is required. The probe case is currently too small to fit a matching amplifier circuit.

3. INSPECTION SOLUTIONS

The probe consists of 6 off pulse echo elements forming three pair spaced at 120° intervals. The probes are not twin probes but two rows of pulse echo elements. The two rows are used to measure probe tilt in addition to tube diameter and thickness. Measurement of probe tilt and the concentricity of the probe is an essential parameter in assessing the accuracy of the measurements achieved and selection of the appropriate signals.

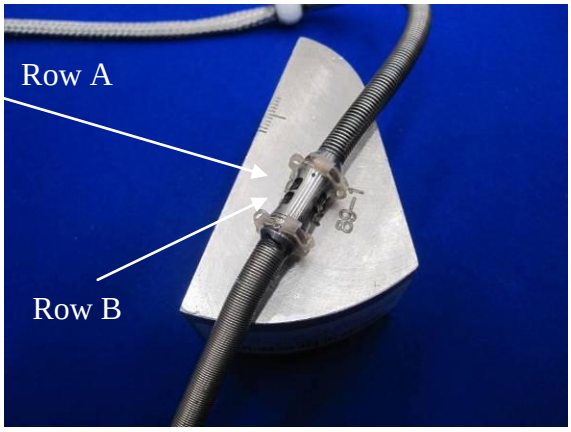

Figure 5. Photograph of deployed probe showing centralisation features.

Probe deployment is via a mixed air/water deployment system and the data is collected during probe withdrawal via a patent water propulsion system. Beads are fitted along the length of the probe to provide propulsion during deployment and retrieval. The probe is mounted into a spring section to enable a high level of mechanical flexibility to aid the deployment around the 80° Bifurcation port. Figure 5 illustrates the physical size of the probe and the centralisation features used to align the probe once deployed.

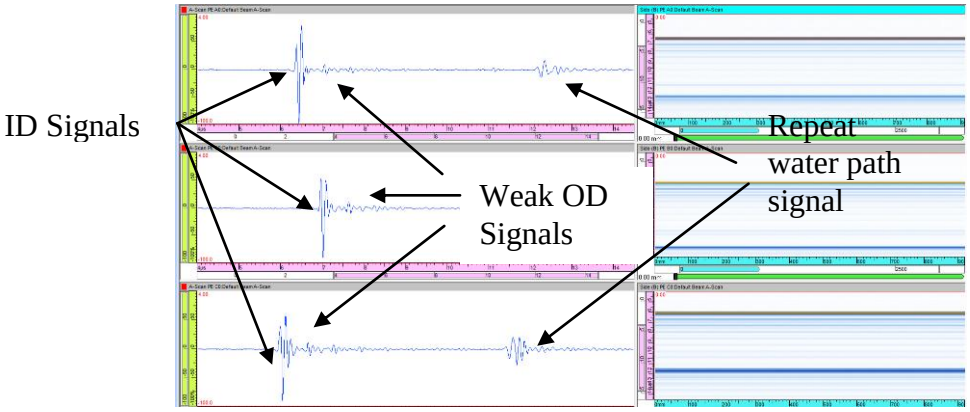

Figure 6 provides data from a probe in a finned test piece.

The water to steel interface generates a large signal but the OD generates as small signal due to the loss of energy at the interface. In this case we have to detect the signal from the finned root which generates an even weaker scattered signal. Due to the signal scattering conventional repeat OD signals cannot be use for the thickness measurement normal thickness measurement. To accommodate this dynamic range a 12 bit 100MHz digitisation instrument was selected. Signal processing algorithms were developed to facilitate data interpretation.

4. SIGNAL PROCESSING AND DATA PRESENTATION

The signal processing is performed in three stages.

i) Water to steel interface echo detection and straightening.
ii) Water path determination and bore diameter computation
iii) Wall thickness determination.

4.1 Water to steel interface detection and straightening

Figure 6 shows A-scan and B-scan plots for one row of beams, (the three zero degree beams at the 120° positions), from a plain calibration pipe. The plot shows the water to pipe internal diameter (ID) signal and then the small amplitude pipe outside diameter (OD). Further it shows that the water path is not equal in each direction.

Correct peak detection in the data is essential but eccentric probes will cause a distortion in pulse shape and incorrect thickness determination. To aid the processing the data processing straightens the ID interface signal with respect to axial position. This effectively lines up the OD signal and eases the correct identification of the fin root signal. The software includes a number tools to simulate manual data interpretation. The process identifies the ID and OD signal over a length of tube, to generate an accurate mean position of the two interfaces. It is pointed out at this point that the data analysis is designed to identify general trends in the wall thickness (as opposed to corrosion pits or other defect types). An example of some date after this processing is provided in Figure 7.

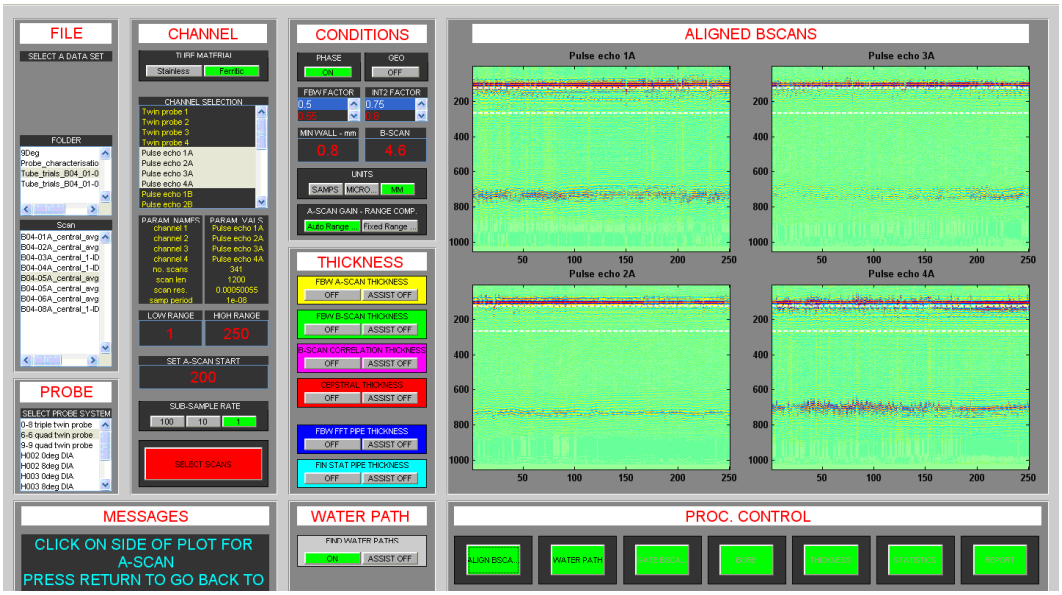

Figure 7 Image of Heterodyned data and interface echo straightened data.

4.2 Water Path and bore diameter determination

After the data is straightened the water path is measured and a best fit circle approach is used to determine the tube bore diameter. This calculation takes into consideration the skewing of the beams due to non–normal propagation as discussed section 2.2.2.

4.3 Wall Thickness Determination

The signal processing for wall thickness employs four methods for plain tube and two methods for finned tube. Plain tube processing can take into account repeat back wall reflections to provide very accurate wall thicknesses. Finned tube as already stated, only uses the water to steel interface to finned root path. To this end a calibration scan is performed in a test tube with a known bore diameter to determine the system delay for each element.

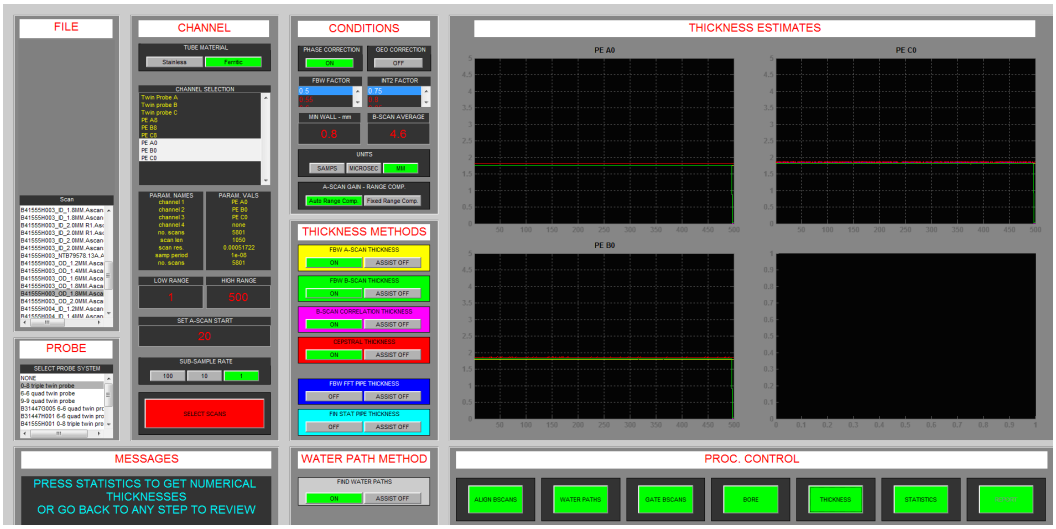

Figure 8 Screen shot of data analysis after plotting the wall thickness for the three probes

Figure 9 shows data from a finned test piece with a photograph of the sectioned tube above. This finned test tube has five wall thicknesses with a constant bore diameter. The data is presented as a B-scan view, the horizontal axis is encoded distance along pipe. The data shows a series of fin root signals with a selected A-scan at the central position of a fin. To ensure that data is captured from the centre of the fin roots data is captured every 0.5mm along the tube bore both in test pieces and on the plant. Automated data analysis poses two challenges: firstly identification of the central root fin signal and secondly, identification of the correct point on the wave form to provide acceptable wall thickness and diameter measurement.

As introduced the tube is finned but has a regular pitch. This feature is used by the pattern recognition system to identity the centre of the fin root. The signal processing method used is called heterodyning. Once the fin root signal is identified from each root the remaining data is discarded and the data is re-plotted as if the OD signal is continuous. The data is then processed using peak detection software to provide wall thickness measurements.

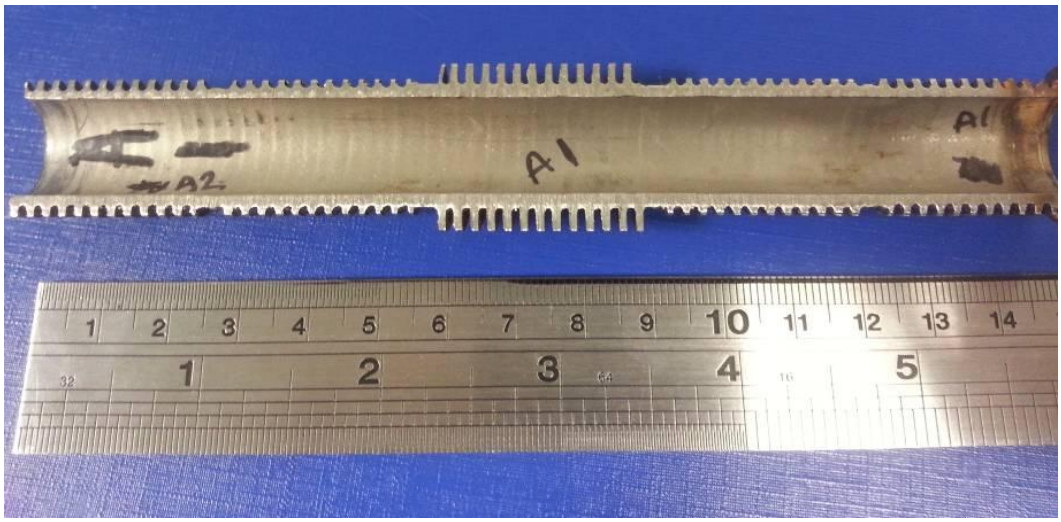

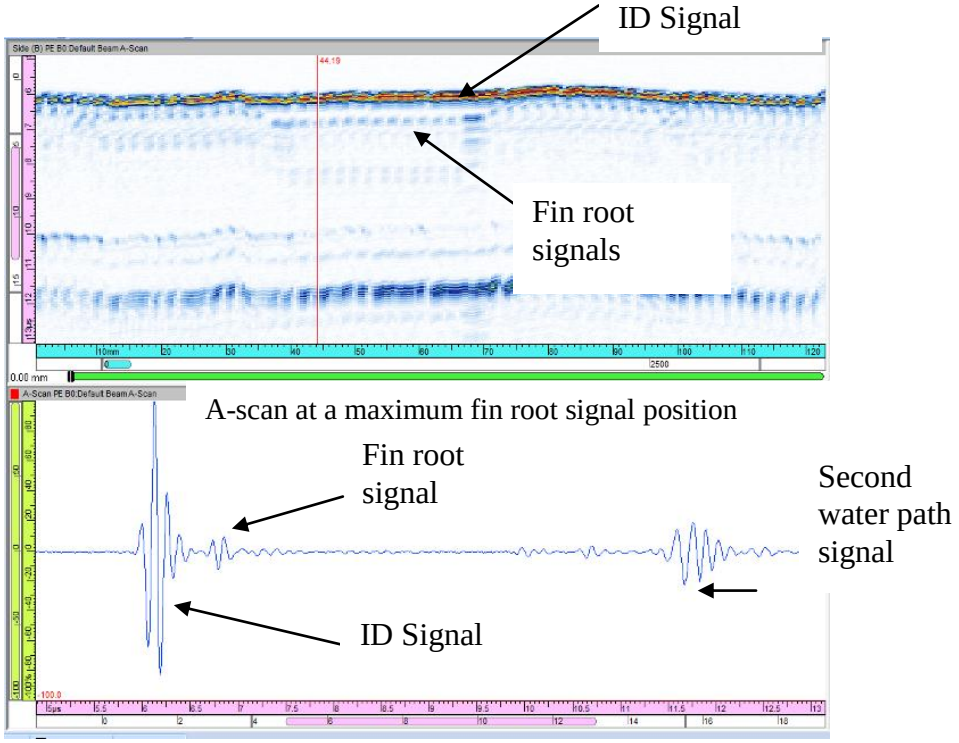

Figure 9 Screen shot of the ultrasonic responses a finned test tube with different wall thicknesses.

4.4 Data Presentation

The software outputs the mode, mean and standard deviation for the bore diameter and tube thickness for the section of pipe being analysed. This output is shown in Figure 10.

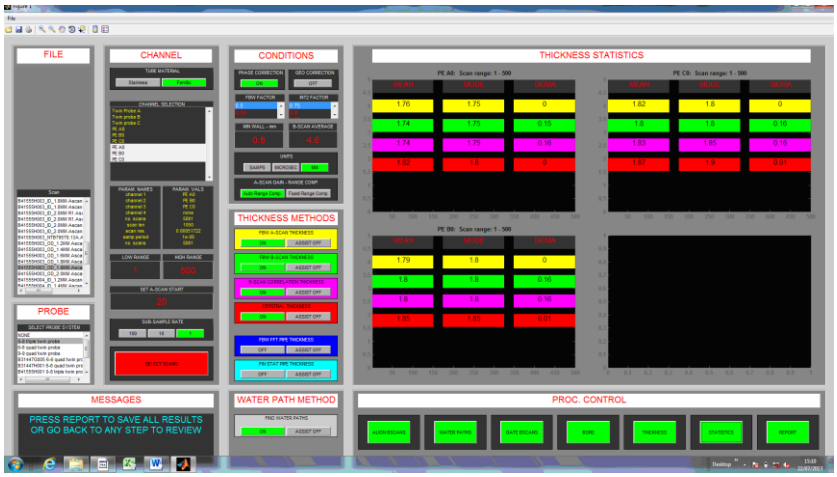

Figure 10 Statistical output of analysis software.

5. SYSTEM DEPLOYMENT

The inspection system has been deployed under strict trial conditions at two power stations. This has allowed identification of operating constraints and verification of mechanical reliability. The next stage is to assess the reliability and accuracy of the bore diameter and thickness measurements.

6. Conclusions

1 A tube wall thickness and bore diameter system has been developed and deployed down 30m of spiral tube and negotiated 80° bends.
2 A data analysis system and software has been developed and successfully deployed to account for probe misalignment whilst maintaining accurate measurements.
3 The system has proved to be mechanically reliable and is now undergoing the early stages of qualification.

Acknowledgements

1 The authors wishes to acknowledge EDF Energy for their support in this development and application project.
2 The authors acknowledges the advanced signal processing support provided by SNAPE signal processing.
3 The authors of this paper wish to acknowledge the assistance of AMEC towards the mechanical deployment solution.

DISCUSSION OF THE USE OF REMOTELY OPERATED MANIPULATORS AND VPN TECHNOLOGY FOR EDDY CURRENT TESTING FIELD PROJECTS

C. J. Speas, ANATEC, USA

Two applications of technology in support of eddy current inspections will be discussed.

Remotely Operated Manipulator Development and Deployment

Summary
The advantages of manipulator use in Balance of Plant Heat Exchanger (BOP HX) inspections have been recognized for several years. Inspection of components in radiologically controlled areas and increased production through automation were primary drivers leading to manipulator development and wider use. When a US utility required a replacement manipulator system due to obsolescence, system requirements were detailed, and a purchase specification was generated. During the manipulator design process, several design and flexibility options were incorporated into the system design. The manipulator system was delivered, and was utilized in a limited field trial for the client in the spring of 2012. Additionally, the system was deployed at several other US utility sites in the fall of 2012 and the spring of 2013. This presentation will detail design considerations, features and capabilities, general field experience from several deployments, and possible future capabilities and design revisions.

Discussion
The use of remotely operated manipulators is driven by numerous considerations and provides several benefits. The most obvious benefit is the ability to inspect heat exchangers that are not typically inspected due to environmental factors (high dose rates, high contamination areas, etc.). The use of a manipulator to perform these inspections reduces the time personnel must spend in an area from hours to minutes, thus reducing the impact of the hazard.

Manipulator use also increases productivity and accuracy when performing inspections. Retests due to mis-encoded tubes are reduced, saving valuable schedule time. The ability to operate acquisition stations nearly continuously, while using the same, or fewer, numbers of inspectors provides tangible benefits in work schedules and overall inspection cost.

Increased production provides additional benefits because more tubes can be inspected in the same amount of schedule time; increased sample sizes provide a clearer picture of component condition.

The combination of these factors makes manipulator use an easy choice for inspection projects in environmentally challenging areas, and for projects involving notable numbers of tubes where increased production rates can help to minimize inspection schedule.

When a US utility required a replacement manipulator system due to obsolescence, system requirements were detailed, and a purchase specification was generated. The major requirements for this system included:

1. A minimum 24” working envelope

2. Ability to deliver the inspection probe.

3. Control system compatible with Windows

4. Encoded positioning (Row and Tube information) that interfaces with the eddy current data acquisition software.

With general needs identified, additional design parameters were considered. Other design features incorporated were:

1. Quick and easy to install

2. Reliable and robust hardware

3. Current actuator technology

4. Adjustable length of manipulator

5. Various mounting options

6. Hardware and Software designed with future applications considered (tube plugging, tube cleaning, dual probing, automated acquisition.

With input from Anatec-LMT, the engineering team at Corestar International developed the IM-2 manipulator system to meet all of the design parameters specified. The system was delivered to the utility, and has been utilized on clean as well as radiologically contaminated components.

The IM-2 manipulator has been deployed for inspection work at the following sites:

1. Oconee – Turbine Lube Oil Cooler and LPI Heat Exchanger Inspection

2. Prairie Island – Residual Heat Removal Heat Exchanger Inspections

3. Susquehanna – Spent Fuel Pool Cooler eddy current and tube cleaning

4. Perry - Residual Heat Removal Heat Exchanger Inspection

Conclusion

The design and deployment of a remotely operated manipulator system allows inspection of many heat exchangers that must be inspected for license renewal and are often vital to safe plant operation and shutdown. Improved accuracy and productivity gains over current processes have been demonstrated, and further improvements to the manipulator systems are on-going.

Use of VPN Technology for Eddy Current Inspection Data Transmission

Summary
Currently in the United States, point-to-point T1 data connections are used widely for transmission of steam generator eddy current inspection data offsite for remote analysis. Remote analysis of the data is performed to minimize the number of personnel on-site. This results in cost savings for the utility clients by minimizing the costs for travel, office space, and site badging. Due to the rising costs and decreased reliability of point-to-point T1 technology a replacement technology was needed. Virtual Private Networking (VPN) technology, which is a mature technology and provides for excellent data security, increased bandwidth, and reduced cost has been successfully utilized for inspections in the US and abroad.

Discussion
Remote data analysis for PWR Steam Generator inspections is common practice in the US and abroad. The main technology used for data transfer for the past twenty to twenty-five years has been point-to-point T1 connections. At one time, this technology provided an excellent value for bandwidth. Over the last several years, however, the cost of point-to-point T1 connections has risen dramatically. This is primarily due to the fact that point-to-point T1 technology has reached the useful life in the eyes of the providers.

Point-to-point T1 is a private data connection securely connecting two or more locations with T1 data speeds (1.554Mbps). A T1 point to point circuit is a closed network data transport service and is considered to be inherently secure with no data encryption needed. Point to Point T1 services are available in higher bandwidth speeds by combining multiple T1's and multiplexing them, by using point-to-point Ethernet, or by using point-to-point DS3.

A replacement for point-to-point T1 connections was needed. Virtual Private Network (VPN) technology is a suitable replacement that provides for reliable security, increased bandwidth, and decreased cost. The primary requirement for utilizing VPN technology is a high speed (3-5 megabit minimum) internet connection at both work locations. While this type of connection was unheard of twenty years ago, it is commonplace today. This can also allow for these connections to remain active if remote access is required between outages.

A Virtual Private Network (VPN) is a private, secured tunnel through the public internet backbone joining one location with another. The size of the VPN tunnel, and therefore how much data can be sent at once, is dependent upon the bandwidth available from either point. For example if one side of the VPN tunnel has a 1.4 megabit (upload and download) connection and the other side has a 10 megabit (upload and download) connection then the data transfer would be limited by the lesser of the two bandwidths at 1.4 megabits.

Conclusion
Functionally, the point-to-point T-1 network and the VPN network are identical. VPN has the advantages of lower cost and scalable bandwith.
VPN technology provides a lower cost, secure solution for transmission of eddy current inspection data for the purpose of remote data analysis.

REACTOR PRESSURE VESSEL II

DEVELOPMENT OF NEW MANIPULATORS FOR PWR AND BWR NOZZLE INSPECTION

M. Wendel, T. Sjö, DEKRA Industrial, Sweden

ABSTRACT

Flexibility has been the key word for the development of nozzle manipulators for PWR and BWR vessels.
By using standardized concepts for propulsion and controllers we succeeded to fulfill the customer demand with an effective solution.
The new manipulator concept has been developed for reactors of several PWR designs as well as for BWR's.
Our goal was also to minimize the time in the reactor containment with the possibility to prepare the equipment in only one day for a full nozzle exam. Furthermore, the manipulators are neutrally buoyant in water and work in parallel with ROV functions totally independent of each other and with minimum support from the crane and service bridge. No pre-installation in the vessel is needed.
All control systems are identical and will thus increase the redundancy.
The NDE techniques are being qualified according to the ENIQ and respective Swedish and Swiss rules. The qualifications are valid for detection, characterization and sizing.
The following objects can be inspected using ET, UT and VT:

- Inlet and Outlet Nozzles, nozzle to shell welds, inner radius and connection welds
- Feedwater Nozzles, shell welds and safe-end welds
- Steam outlet Nozzles, nozzle to shell welds and connection welds
- Bottom nozzles

The nozzle exam can be done in a very short time frame; typically the time for one nozzle is a matter of some hours. All manipulators can be used in parallel with other vessel equipment and thus reducing time on critical path.

Development of tooling

DEKRA Industrial AB – Mechanized Inspection has designed manipulators for several types of nuclear power plants as well as for conventional plants. This includes development of scanners and manipulators for the inspection of the RPV Shell Welds, Nozzle Welds and BMI Welds (Bottom Mounted Instrumentation nozzles) as well as visual testing of internals in PWRs.
The new set of manipulators will now address the inspection task of nozzles in BWR's.

All manipulators have been designed to minimize the time in the reactor vessel and also in the reactor containment. The equipment can be prepared in only one shift for a full vessel exam. Furthermore, the equipment will work in parallel totally independent of each other and with minimum support from the crane and service bridge. No pre-installation in the vessel is needed.
The main principle with all equipment is to make them neutral buoyant in water and also to use thrusters for independent movement.

The NDE technique has been qualified according to the ENIQ and the Swedish regulations. The data gathered will be sufficient for detection, characterization and sizing.
The personnel resources cover all needs for development of manipulators and NDT, as well as probe design. All equipment has been tested in a pool with mockups before the first outage performance.

Fig. 1 The nozzle tool during set up at Ringhals

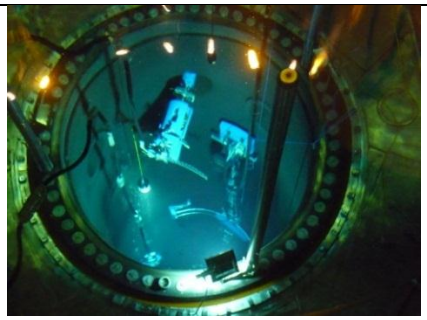

Fig. 2 Nozzle manipulator used in parallel with vessel weld exam

THE EQUIPMENT

Three new equipment and one replica tool have been designed with the focus to allow for parallel inspection in the vessel without obstructing or delaying the other ongoing inspections.

- **SÄRIMNER**, Manipulator for large Nozzles
- **GUNGNER**, Manipulator for BMI Nozzles and J-groove welds
- **GRAM**, Manipulator for small Nozzles
- **DRAUPNER,** Replica tool for BMI J-groove weld

The concept is based on the idea of lightweight and remotely operated vehicles, ROV- equipment, independent of cranes and platforms. The manipulators for nozzle inspection and the manipulator for bottom nozzles can freely "swim" between the different objects, while the vessel inspection manipulator keeps on scanning in segments. Inspection of the vessel wall is performed in 90 degrees sectors with repositioning of the manipulator.

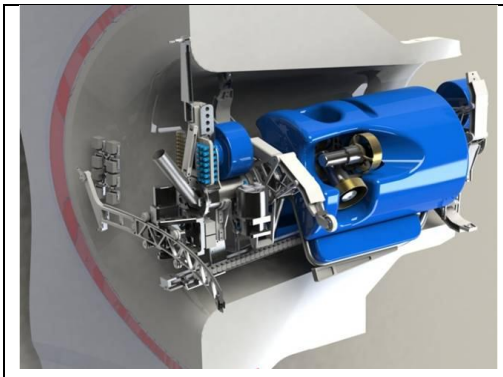

Fig. 3 The Nozzle inspection manipulator Särimner

Fig. 4 The BMI nozzle manipulator Gungner

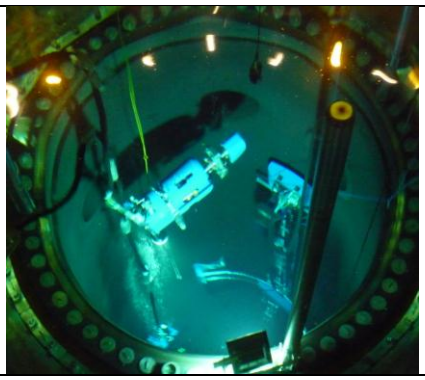

Fig. 5 The Nozzle inspection manipulator Särimner swimming

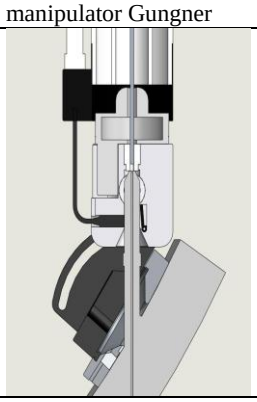

Fig. 6 The BMI manipulator Gungner

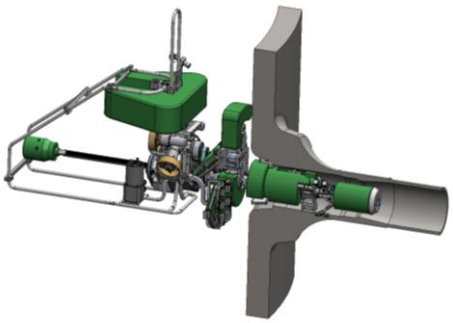

Fig. 7 Manipulator GRAM, Configuration for Feed Water Nozzle BWR

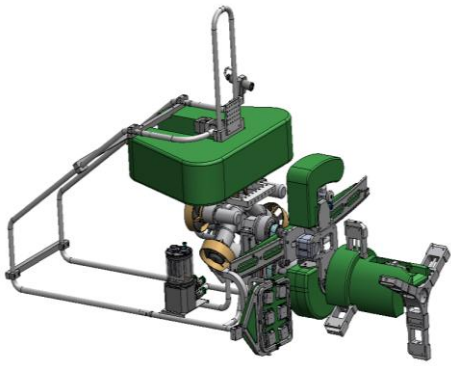

Fig. 8 Manipulator GRAM, Configuration for Steam Outlet Nozzle BWR

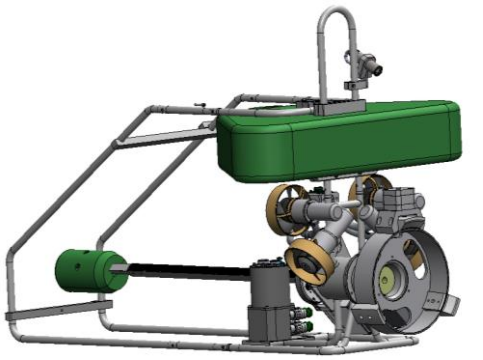

Fig. 9 Manipulator GRAM, Configuration for Safety Injection Nozzle PWR

Fig. 10 Remote control

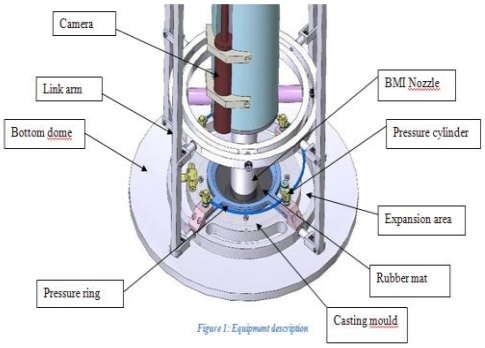

Fig. 11 The moulding VT tool Draupner

Fig. 12 The moulding VT tool Draupner

NDE

PWR Nozzle area qualification

The following describes the qualification performed for Ringhals. The nozzles were inspected with pulse echo, TOFD and ET probes manufactured by DEKRA.

Object	*Height*	*Tolerance*	*Length*	*Tolerance*	*Ligament*
RPV to nozzle weld UT	5*	±3.3	40	±15	≤3mm
Inner radius UT	5*	±3.3	40	±15	≤3mm
Inner radius ET	2		10	±15	N/A

Table 1 Qualification defects for nozzles

Plant	Weld type	Defect location	Defect mechanism	Detection target h x l ±(sizing tolerance) (mm)	Skew / Tilt	Orientation
R2	Nozzle to pipe	Weld + HAZ*	Fatigue crack	6 x 18 ± (4.4 x 10)	±10°/ ±10°	Long
R3/R4	Nozzle to safe end	Weld + HAZ*	IDSCC	6 x 12 ± (3.0 x 10)	±10°/ ±10°	Long / trans
R3/R4	Safe end to pipe	Weld + HAZ*	Fatigue crack	6 x 18 ± (4.4 x 10)	±10°/ ±10°	Long

Table 2 Detection targets for nozzles

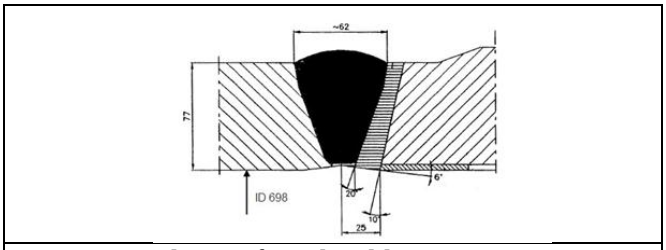

Fig. 13 Nozzle to safe end welds

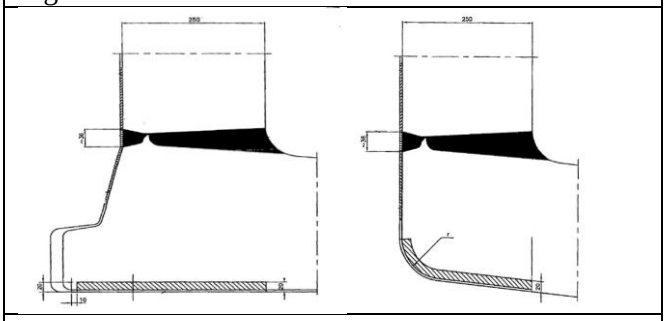

Fig. 14 RPV to Nozzle welds

The following describes the qualification for Beznau.

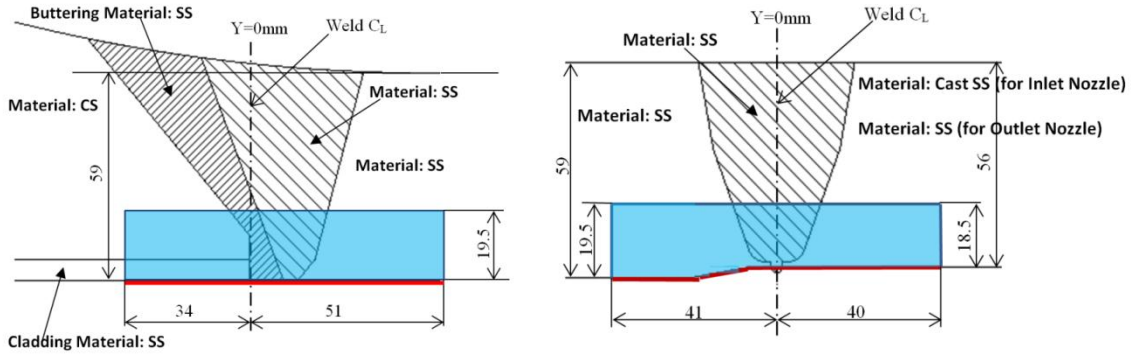

- Inspection with ET; - Inspection with UT;

Fig. 15 1:st and 2:nd Connection Weld: Inlet and Outlet Nozzles

Inspection Object	*Object Nomenclature/ Weld No*	*Defect Location*	*Defect Mechanism*	*Detection Target h x l ±(sizing tolerance) (mm)*		*Skew / Tilt*	*Orientation*
Nozzle Bore Inlet & Outlet Nozzles	• **Clad 60°** • **Clad 240°** • **Clad 120°** • **Clad 300°**	ID surface	UCC	6 x 18 mm	±(3.0x10)	±0°/ ±0°	Circ. / Axial
1:st Connection Weld Inlet & Outlet Nozzles	• **DM 60°** • **DM 240°** • **DM 120°** • **DM 300°**	Weld + ½T	Fatigue cracks and IGSCC	6 x 18 mm	±(3.0x10)	±0°/ ±0°	Circ. / Axial
2:nd Connection Weld Inlet & Outlet Nozzles	• **53** • **26** • **29** • **2**	Weld + ½T	Fatigue crack	6 x 18 mm	±(3.0x10)	±0°/ ±0°	Circ. / Axial

Table 3 Defect specification

BWR Nozzle area qualification

The qualification for Oskarshamn covers the areas presented below.

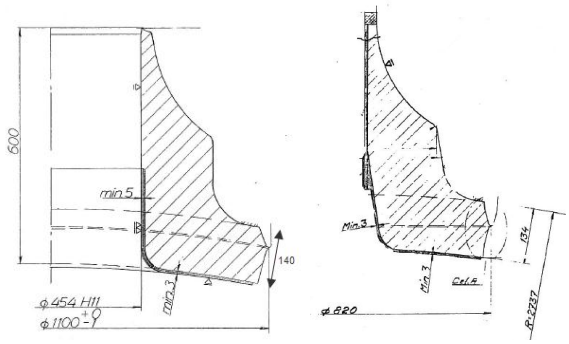

Fig. 16 Nozzle to Shell overviews Left: Steam Outlet Nozzle, Right: Feed Water Nozzle

Nozzle Type		*Feed Water*	*Steam Outlet*
Position in Vessel (°)		*0 / 90 / 180 / 270*	*60 / 120 / 240 / 300*
Materials	*Nozzle*	ASTM A508 Cl2 (ferritic steel)	
	Vessel	ASTM A533 Cl1 (ferritic steel)	
	Weld	AWS E8018G and EF1 (ferritic steel)	
	Cladding	AWS ER308L, E309 and E308L (stainless steel)	
Weld Type		Double U	Double U
Weld id.		W29.1-4	W32.1-4
*Weld Angle**		15° against Vessel 4° against Nozzle	0° against Vessel 15° against Nozzle
Weld Width		52 mm	34 mm
Weld Center Line		Ø 820 mm	Ø 1100 mm
Wall thickness		140 mm	140 mm
Cladding		Nom. 5mm (min 3 mm)	
HAZ		10 mm on each side of the weld fusion face	
Surface		Flat / vessel curvature	
Surface finish		< 25µm Ra	

Table 4 Nozzle to Shell Object Specification

* Within the inspection volume of 50 mm from cladding surface

Location	*Defect*				*Detection target (h x l)*	*Accuracy (h x l)*
	Type	Orient.	*Max Tilt*	*Skew*		
Weld and HAZ	Mechanical fatigue	Long.	±15°	± 10°	15 x 30 mm	± (4.2 x 20)mm
Fusion zone	Lack of Fusion, embedded	Long.	±15° [1)]	± 0°	15 x 30 mm	± (4.2 x 20)mm

Table 5 O2 Nozzle to Shell Weld Defect Specification

[1)] The lack of fusion will be equal to the fusion face angle and therefore can be either ±15° or ±4°. Volumetric defects are not required to be detected or characterized. However, they must not be misinterpreted as planar. The procedure includes characterization even though it is not a requirement.

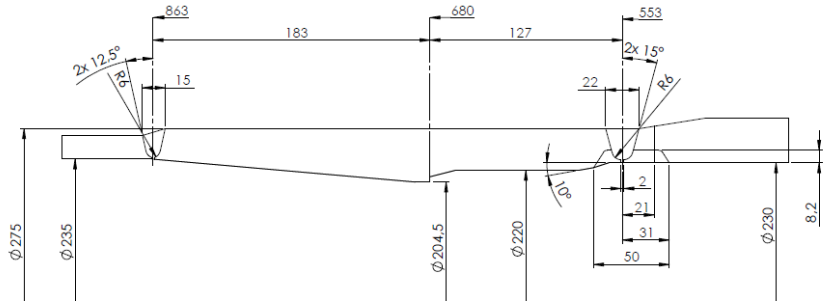

Fig. 17 Feed water nozzle schematic; 1:st and 2:nd connection welds and safe-end in between.

Parameters	*1:st connection*	*Safe End*	*2:nd connection*
Identity	W30.1-4	W30SE.1-4	W31.1-4
Weld type	U-joint	N/A	U-joint
Base Material	CS/Inconel 600	Inconel 600	Inconel 600/SS
Buttering	Alloy 182	N/A	N/A
Cladding	SS	N/A	N/A
Weld overlay	Alloy 82, min 6mm	N/A	Alloy 82, min 6mm
Old weld	Alloy 182	N/A	Alloy 182
Wall thickness (mm)	22.5	21-35	21-16.5
ID (mm)	230	204.5-233	233
Surface finish	≤Ra 6.3	≤Ra 6.3	≤Ra 6.3

Table 6 Object Specification

ID Surface breaking defects			
Parameters	*1:st connection*	*Safe End*	*2:nd connection*
Defect type	IDSCC* / IGSCC / Mech. fatigue	Thermal fatigue	IDSCC* / IGSCC / Mech. Fatigue
Location	Weld + HAZ	Parent material	Weld + HAZ
Orientation	Ax. / Circ.	Ax. / Circ.	Ax. / Circ.
Tilt/Skew IDSCC, fatigue	±10º / ±10º	±10º / ±45º	±10º / ±10º
Tilt IGSCC	-33º	N/A	±33º
Detection target (mm)	3 x 6	3 x 6	3 x 6
OD Surface breaking and embedded defects			
Parameters	*1:st connection*	*Safe End*	*2:nd connection*
Defect type	Mech. Fatigue / LOF	N/A	Mech. Fatigue / LOF
Location	Weld + HAZ		Weld + HAZ
Orientation	Circ.		Circ.
Tilt/Skew fatigue	±5º / ±5º		±5º / ±5º
Tilt LOF	±33º		±33º
Detection target (mm)	5 x 10		5 x 10

Table 7 Connection Weld Defect specification

* Only when fatigue cracks has propagated into the old Inc 182 weld, therefore no surface breaking IDSCC

BMI demonstration

Location	Defect				Detection target h x l ± (sizing tolerance)
	Type	Orientation	Tilt	Skew	
Fusion zone	Lack of fusion	N/A	N/A	N/A	4 x 5 ± (3.5 x 10)* mm
Nozzle ID including connection weld	Surface breaking IGSCC	Circumferential / Axial	± 10 °	± 10 °	1 x 5 ± (2.5 x 10) mm
Nozzle OD					2 x 10 ± (2.5 x 20) mm
J-Groove weld	Surface breaking IGSCC	Circumferential / Axial	± 10°/ 45°**	± 10 °	2 x 5 ± (3.5 x 10) mm

Table 8 Detection targets for bottom nozzles

The technique was demonstrated for Ringhals. The BMIs were inspected with a combination of pulse echo, TOFD and ET probes, manufactured by DEKRA. Test blocks were supplied by EPRI, Ringhals AB and SQC.

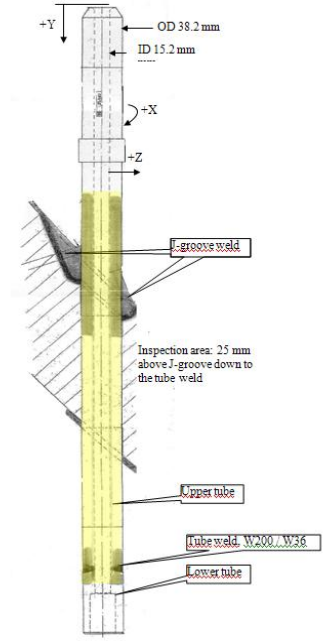

Fig. 18 BMI with inspection areas

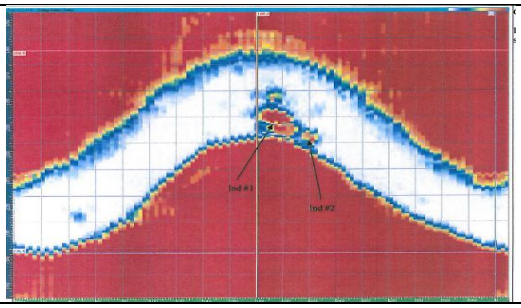

Fig. 19 Fusion face inspection, with reportable defects

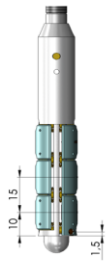

Fig. 20 DEKRA BMI probe with, 0° TRL, 2x TOFDT and ET

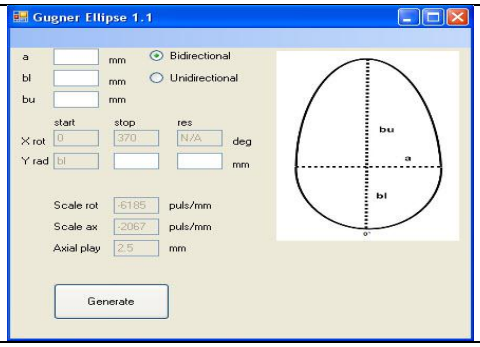

Fig. 21 Ellipse program to ensure coverage of the weld and HAZ.

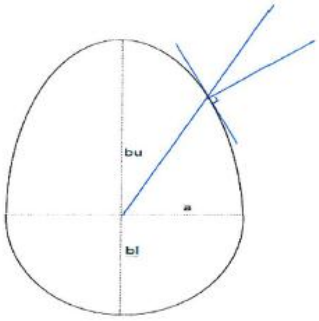

Fig. 22 Probe skew relative to the weld, depending on nozzle geometry.

VVER

A new set of tooling is now under development for the VVER market where demands exist to perform part of the inspection with the water level under the nozzles during part of the outage.
There is also a demand to perform extensive visual inspection as well as ultrasonic and eddy current testing.
The concept is similar to our PWR solution and works with two different nozzle manipulators.
The concept is based on the idea of lightweight and remotely operated vehicles, ROV- equipment, independent of cranes and platforms. The manipulators for nozzle inspection can freely "swim" between the different objects.
The VVER equipment can perform a vessel exam in only 8 days considering the demand to start the inspection with the water level below the nozzles.

Performance

The task was to perform a qualified inspection of all vessel welds including nozzles, bottom nozzles and VT of the radial supports for all 3 PWRs in Ringhals Sweden. The full inspection was done in just 5 days!
The ability to perform parallel activities results in less impact on critical path.
The next inspection projects with the vessel manipulators will be the feed water nozzles in a BWR in Oskarshamn, Sweden and the vessel and nozzles in the PWRs in Beznau, Switzerland. The existing qualification will be adapted to fit the requirements in Switzerland. This includes scanning on test blocks at EPRI.

APPLICATION OF OVERLAPPED SKEW SCAN TECHNIQUE FOR NOZZLE INNER RADIUS USING PHASED ARRAY

T. Hamano, S. Matsuda, E. Shiina, R. Horikoshi, N. Shiokawa, IHI, Japan

ABSTRACT

In ISI of Japanese BWR nuclear power plant, a nozzle inside corner region of RPV has been inspecting by the conventional UT technique from a nozzle outside radius, according to the JEAC4207 code [1]. In 1995-2005, Japan Nuclear Energy safety organization (JNES) conducted the "Ultrasonic Test and Evaluation for Maintenance Standards" (UTS) project [2]. The UTS project included flaw detection and sizing test at the nozzle inside corner region by the conventional UT technique. All flaws at the nozzle inside corner region of mock-up are detected. However, many length sizing results of conventional UT technique at the nozzle inside corner regions were underestimated in the UTS project.

The sizing technique for the nozzle inside corner region has not been approved by the Japanese regulatory commission. Until now, a flaw has not been detected at the actual Japanese RPVs. However, when it will be detected, flaw length cannot be measured by the approved UT technique. The present work is intended to improve the accuracy of length sizing at a nozzle inside corner region.

We investigated the cause of sizing error. The cause is the complicated geometric shape of the nozzle outside radius and the nozzle inside corner radius. Detectability of the notch has been found to reduce at the both ends of the nozzle inside corner radius. Therefore, the "overlapped skew scan technique" for improvement of length sizing accuracy, using the phased array is proposed. In this study, the maximum error of length sizing by the conventional technique is -13 mm. However, the maximum error of length sizing by "overlapped skew scan technique" is +14 mm. Considering beam spread, error of length sizing by this technique is appropriate. It was confirmed that the "overlapped skew scan technique" conservatively evaluate length by our nozzle mock-up.

BACKGROUND

In 1995-2005, JNES conducted the "Ultrasonic Test and Evaluation for Maintenance Standards" (UTS) project in Japan. The UTS project was confirmed flaw detectability and sizing accuracy in the various components such as the pipes and the vessel, according to the JEAC 4207 Code. The UTS project included inspection program of detectability and sizing at the nozzle inside corner regions. The inspection method of the nozzle inside corner region by the conventional UT technique and model of nozzle mock-up of N4 are shown in Fig 1. At the nozzle inside corner region, the conventional UT technique is angle beam, and the example of refracted angle is 21 degrees. The search unit is moved along a circle at the nozzle outside radius. Contacted angles of search unit at nozzle outside radius are defined as the inspection angle. The inspection angle is changed repeatedly and inspected repeatedly, after inspection of one scan is completed. Each of the several inspection angles for the covering inspection region are calculated before inspection. The inspection angles pitches are from about 1.5 to 2 degrees and inspection angles are about 25 angles at the N4 nozzle. In UTS project, all flaws were detected at mock-ups of primary loop recirculation nozzle of inside corner regions. However, results of length sizing by the conventional technique were underestimated.

Therefore, sizing technique for a nozzle inside corner region has not been approved by the Japanese regulatory commission.
Until now, a flaw has not been detected at actual Japanese RPVs. However, when it will be detected, flaw length cannot be measured by the approved UT technique.

We first inspected the nozzle inside corner region of our N4 nozzle mock-up from the nozzle outside radius by means of angle beam technique, simulating ISI. The conventional technique is simulated by the phased array fixed angle control. Three reflectors were processed to the nozzle inside corner region of our N4 nozzle mock-up. The nozzle boss outside diameter of our N4 nozzle mock-up is 356 mm, the nozzle inside diameter is 290 mm, and the nozzle inside corner radius is 60 mm. The sizing results are shown in Table 1. The length of all notch are underestimated. Our results are same as results of the UTS project. Therefore, cause of undetectable corner reflection from notch is investigated, and the "overlapped skew scan technique" using phased array is proposed.

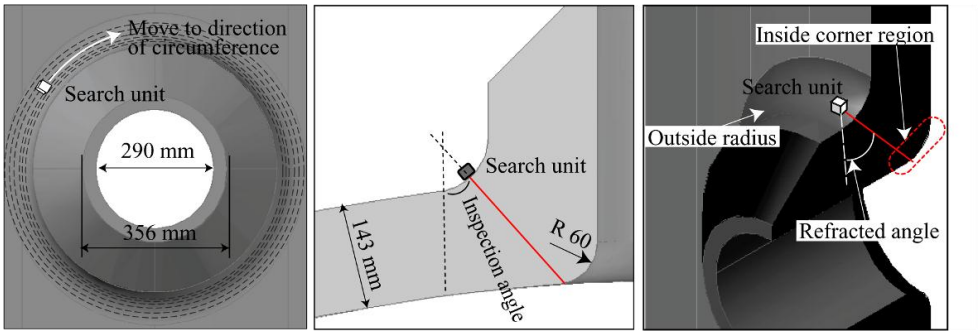

Fig. 1 Inspection method of nozzle inside corner region by the conventional UT technique

Table. 1 Sizing results of our N4 nozzle mock-up by Conventional UT

Notch	Length (mm)		
	Actual	Conventional UT	Measuring error
1	42	29	-13
2	41	31	-10
3	40	28	-12

CAUSE OF LENGTH SIZING ERROR

We have investigated cause of short length evaluation in the nozzle inside corner region with clad. The investigative experiment that moved the search unit of angle beam along the direction of the nozzle outside radius (normal direction) is conducted. In this case, the search unit is moved in parallel to the direction of the notch. The search unit fixed the position of circumference direction, varying the inspection angle from 30 degrees to 85 degrees, and refracted angle is set at 19 degrees. The inspection method of this experiment is different from ISI. The experimental results are shown in Fig. 2. Indication of corner reflection is confirmed in the range of inspection angle from 47 to 52 degrees. However, calculated lengths from the detected inspection angle are shorter than actual length. Corner reflection is not detected, although corner reflection should be detected more than 52 degrees. Considered the following cause of undetectable corner reflection from notch. The scanning surface (nozzle outside radius) and the inner surface (nozzle inside corner radius) are not parallel, and it is different from a pipe or a plate. If the scanning surface is not parallel to inner surface, corner reflection of the angle beam technique is generally decreased.
Therefore, it was confirmed inclination to the scanning surface and inner surface by the experiment using N4 nozzle mock-up.

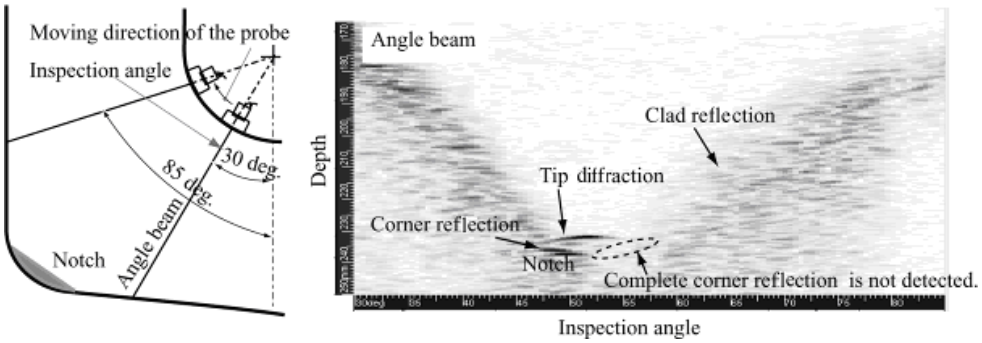

Fig. 2 Results of a parallel scan to the direction of the notch.

The method of confirming inclination at the scanning surfaces is a straight beam method. If the scanning surfaces and the inner surface are parallel, back wall reflection will be received, and if the scanning surface inclined with the inner surface, back wall reflection will not be received. Inner surface shape can be confirmed, although the straight beam cannot detect a notch. The results of the straight beam method are shown in Fig. 3. The inspection angles which can receive back wall reflection are 46 degrees to 54 degrees, but other inspection angle cannot receive back wall reflection.

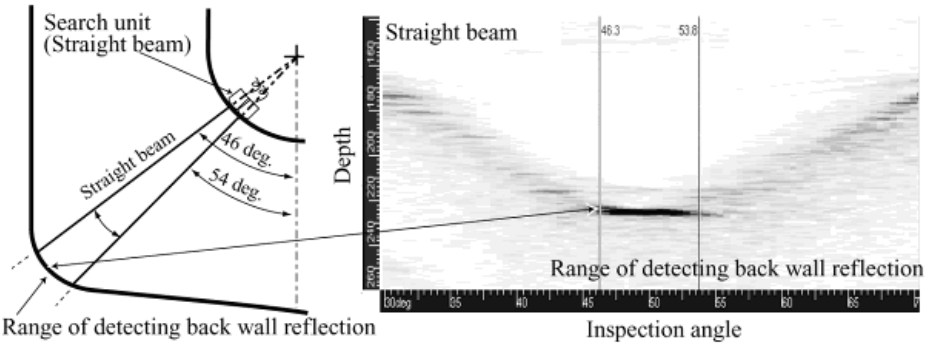

Fig. 3 Result of range of inspection angle detecting back wall reflection by straight beam

Probably, the scanning surface is inclined with the inner surface at the inspection angle in which back wall reflection is not received. Then, the receiving range of experimental results from corner reflection of the notches by the angle beam and from back wall reflection by the straight beam is compared. At receivable range of back wall reflection by the straight beam, the corner reflection is generally received by the angle beam. However, at unreceivable range of back wall reflection by a straight beam, the corner reflection is not received by the angle beam. Furthermore, in order to confirm position in large inclination of the scanning surface and the inner surface, the inclination angle in each inspection angle is calculated using CAD. The inclination between the scanning surface and the inner surface is defined as inclination angle. When the scanning surface and the inner surface are parallel, the inclination angle is 0 degrees. The calculated results of the inclination angle using CAD are shown in Fig 4. The horizontal axis shows the inspection angle, and the vertical axis shows the inclination angle.

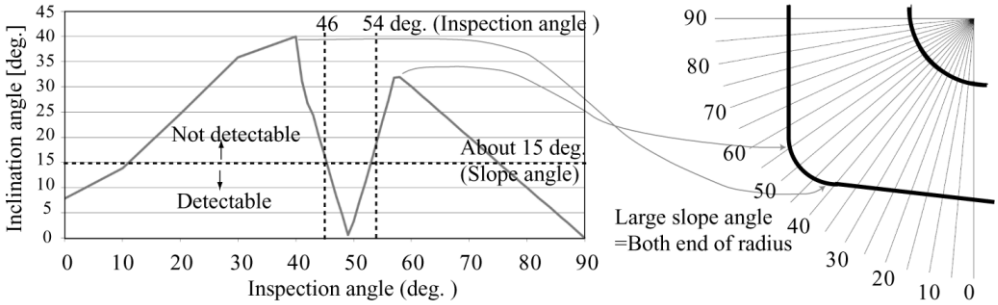

Fig.4 Calculated results of the inclination angle θs.

The inclination angle changes with inspection angle at the nozzle corner. Near the inspection angle of 48 degrees, scanning surface and inner surface are completely parallel, and the inclination angle is 0 degrees. Near the inspection angle of 40 degrees and 58 degrees, the inclination angle is the largest. The positions of large inclination angle are both ends of nozzle inside corner radius. Inspection angle from 46 degrees to 54 degrees that detected back wall reflection by straight beam experiment are inclination angle under about 15 degrees, referencing Fig4. Consequently, it was confirmed that detectability of the notch corner reflection at the both ends of the nozzle inside corner radius of inclination angle more than 15 degrees is decreased.

IMPROVEMENT OF LENGTH SIZING ACCURACY

In order to solve this problem, we merged acquiring several data which changed the inspection angle, by means of skew scanning beam of the phased array method. The skew scanning beam can be approached to inclination angle of 0 degrees at the both ends of nozzle inside corner radius. The inclination angle in case of the skew beam angle -15, +15 and 0 degrees using the phased array is shown in Fig 5. The horizontal axis is the inspection angle and the vertical axis is the inclination angle.

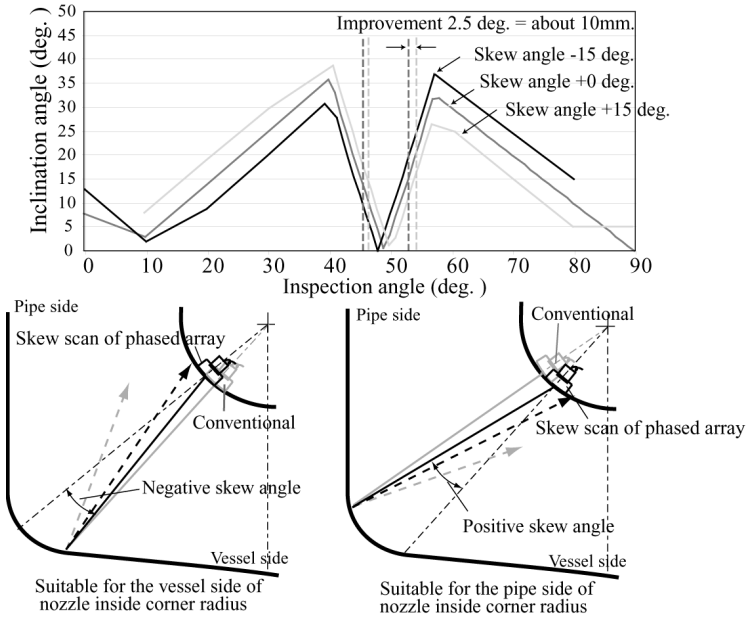

Fig. 5 Inclination angle in case of skew angle -15 degrees and +15 degrees using phased array

If inclination is large, detectability is decreased. In case of the skew beam angle -15 degrees, the inclination angle is decreased at vessel side of nozzle inside corner radius, and the inclination angle is increased at the pipe side of nozzle inside corner radius. In case of the skew beam +15 degrees, the inclination angle is increased at vessel side of nozzle inside corner radius, and the inclination angle is decreased at the pipe side of nozzle inside corner radius. The positive skew beam angle will be suitable for the pipe side of nozzle inside corner radius, and the negative skew angle will be suitable for the vessel side of nozzle inside corner radius. Consequently, if the inspection results which performed skew electronic scanning in the angle range of positive from negative by the phased array method in addition to the angle beam method, and performed the direction circumference at several inspection angles by means of skew scanning method is merged, detectability at both the side of the vessel and the pipe of the nozzle inside corner region will improve, and length sizing accuracy will improve. This technique is defined as the “overlapped skew scan technique”.

INSPECTION TECHNIQUE OF OVERLAPPED SKEW SCAN

The overlapped skew scan technique is shown in Fig. 6. The search unit of phased Array is moved into a circle at the nozzle outside radius. After inspection of one scan is completed, the inspection angle is changed repeatedly and inspected repeatedly. On the other hand, the beams are scanned in the right-angled direction to the moving direction of the search unit by the skew scan method of the phased array. Consequently, beams are overlap and nozzle inside corner region is inspected by several skew beam angles.

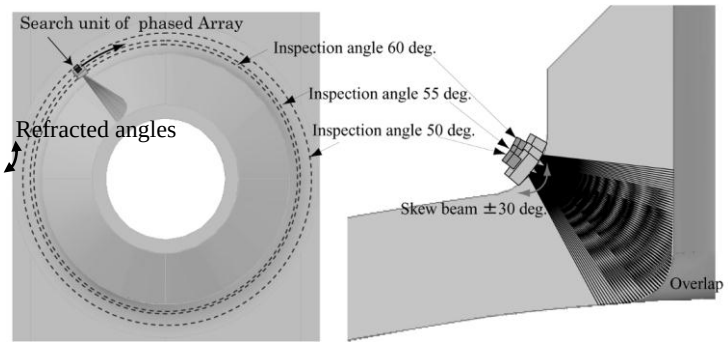

Fig. 6 Inspection method of overlapped skew scan technique

Then, several results acquired by the plural inspection angle is merged on three dimensional coordinates. The incident points *Pi*(*x*, *y*, *z*) are first calculated. The incident points *Pi* (*x*, *y*, *z*) are calculated from the position of circumference of search unit θz and inspection angle θx. *Rb* is the vessel outside radius, *Ra* is the nozzle boss outside radius, *Rs* is the nozzle outside radius. The original point of Z-coordinates is the center of RPV, and the original point of X, Y-coordinates is the center of nozzle. Three dimensional coordinates may be described by the following equation.

$$Pi(x) = \{Ra + (Rs - Rs \cdot \sin\theta x)\} \cdot -\sin\theta z \quad (1)$$

$$Pi(y) = \{Ra + (Rs - Rs \cdot \sin\theta x)\} \cdot \cos\theta z \quad (2)$$

$$Pi(z) = Rb \cdot \cos\left(\sin^{-1}\left(\frac{(Ra + Rs) \cdot -\sin\theta z}{Rb}\right)\right) + Rs - Rs \cdot \cos\theta x \quad (3)$$

The temporary beam coordinates *Ps'*(*x*, *y*, *z*) is calculated from sound path *w*, skew angle θs and refracted angle θy.

$$Ps(x)' = -w \cdot \sin\theta y \quad (4)$$

$$Ps(y)' = -w \cdot \cos\theta y \cdot \sin\theta s \quad (5)$$

$$Ps(z)' = -w \cdot \cos\theta y \cdot \cos\theta s \quad (6)$$

The coordinates *Ps''*(x, y, z) after inspection angle θx rotation is

$$Ps''(x) = Ps'(x) \quad (7)$$

$$Ps''(y) = Ps'(y) \cdot \cos\theta x + Ps'(z) \cdot \sin\theta x \quad (8)$$

$$Ps''(z) = Ps'(y) \cdot -\sin\theta x + Ps'(z) \cdot \cos\theta x \quad (9)$$

The coordinates *Ps'''*(x, y, z) after search unit position θz rotation is

$$Ps'''(x) = Ps''(x) \cdot \cos\theta z - Ps''(y) \cdot \sin\theta z \quad (10)$$

$$Ps'''(y) = Ps''(x) \cdot \sin\theta z + Ps''(y) \cdot \cos\theta z \quad (11)$$

$$Ps'''(z) = Ps''(z) \quad (12)$$

The beam coordinates *Ps*(*x*, *y*, *z*) is added *Ps'''* (*x*, *y*, *z*) and the incident points *Pi*(*x*, *y*, *z*).

$$Ps(x,y,z) = Pi(x,y,z) + Ps'''(x,y,z) \quad (13)$$

The echo amplitude is inputted into coordinates *Ps*(*x*, *y*, *z*), and three-dimensional volumetric data is created.

EXPERIMENTAL RESULTS

We conducted the experiment using the N4 nozzle mock-up added to three notches. The inspection equipment for the nozzle inside corner region is shown in Fig. 7. The inspection equipment attached the nozzle inspection mechanism to the ring truck for pipe. The functions of the ring truck are to move the nozzle inspection mechanism in the direction of a circumference, and to measure the position of circumference of search unit θz. The functions of the nozzle corner inspection equipment are to trace the shape of the vessel radius, to measure the inspection angles θx and to push the phased array search unit to the nozzle outside radius. After setting inspection angle, the ring truck is moved in the direction of circumference. After the ring truck rotates one time, the inspection angle is changed and the ring truck is again moved in the direction of circumference. The pitch of the inspection angle is set at 5 degrees, and the range of skew beams angle is set at ±30 degrees. The pitch of the inspection angle of the overlapped skew scan technique can be set larger than the conventional method, and it increased inspection efficiency. Then, the data of several inspection angles acquired by experiment are merged. The three-dimensional volumetric data are acquired using formulas from (1) to (13). The three dimensional volumetric data are displayed by means of volume rendering software. The results of three-dimensional volumetric merged data that are acquired at inspection angle of 55 degrees, 50 degrees and 45 degrees are shown in Fig 8. In the nozzle inside corner region, the three notches can be confirmed and the length can be measured. Moreover, the zoomed volumetric data of notches and the impression of the notches have been confirmed to similar.

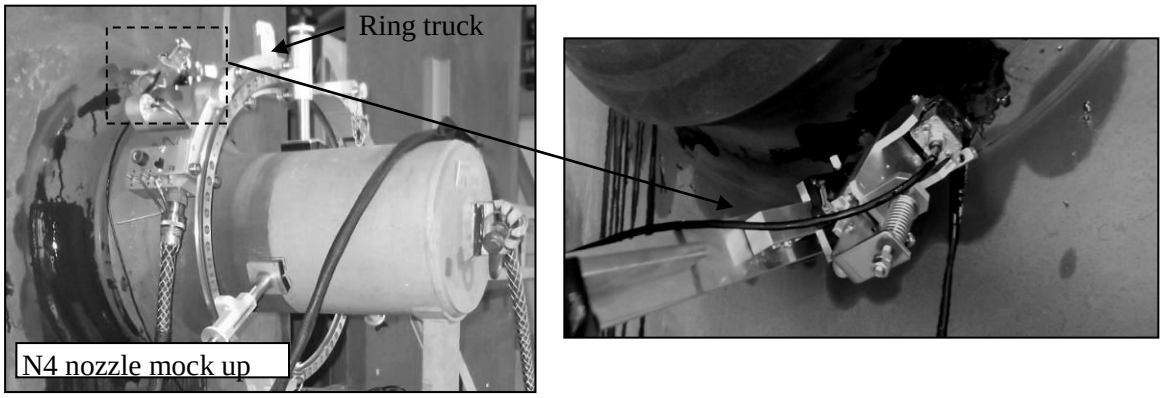

Fig.7 Inspection equipment

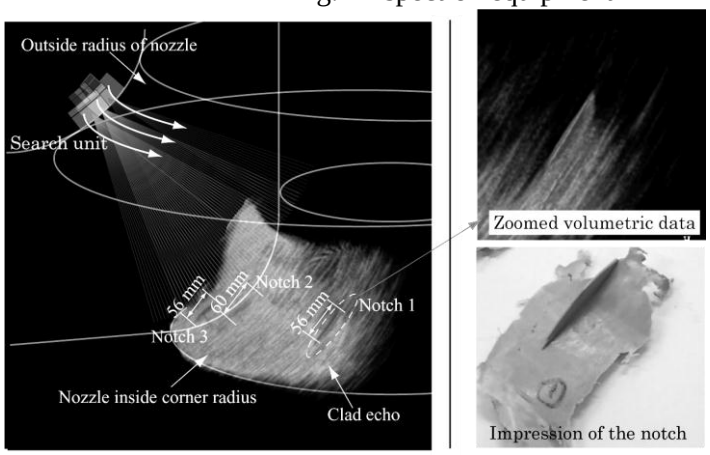

Fig. 8 Results of three-dimensional volumetric merged data that acquired by the inspection angle 55 degrees, 50 degrees, and 45 degrees.

LENGTH SIZING RESULTS

The length sizing results in this experiment are shown in table 2. The results in the UTS project, results of our conventional method, and the results of overlapped skew scan technique are superimposed and are shown in Fig 9. The lengths sizing results of UTS and our results by the conventional method are evaluated shorter than actual length. Evaluation of conventional method is non conservative. However, the overlap skew scanning method is evaluated longer than actual length. Evaluation of overlapped skew scan is conservative. The overlap skew scanning method estimated that the detectability of the both ends of nozzle inside corner region has been improved. Considering beam spread, error of length sizing by the "overlap skew scanning technique" is appropriate.

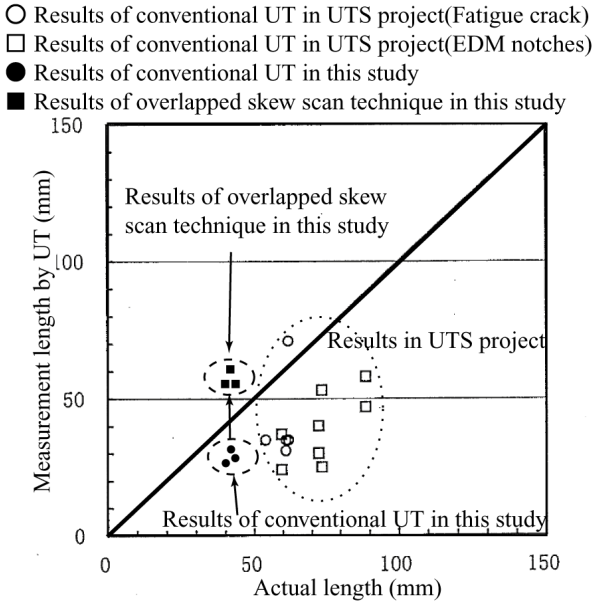

Fig. 9 Results of length sizing by UTS project and results of length sizing by our experiment

Table 2. Results of length sizing in this study

No.	Length (mm)		
	Actual	Conventional UT	Overlapped skew scan
1	42	29	56
2	41	31	60
3	40	28	56

Reference: JNES, "Report of ultrasonic test and evaluation for maintenance standards", 2008, pp.948.

CONCLUSIONS

The present work is intended to improve the accuracy of length sizing at the nozzle inside corner region and to increase efficiency in inspection. The cause of length sizing error has been investigated by experiment. The cause is the complicated geometric shape of the nozzle outside radius and the nozzle inside corner radius. It was confirmed that the detectability of the notch was lowered in the both ends of a nozzle inside corner region radius our mock-up. Consequently the overlapped skew scan technique for improvement of length sizing accuracy, using the phased array was proposed. The pitch of the inspection angle of the overlapped skew scan technique can be set larger than the conventional method, and it increased efficiency in inspection. In this study, the maximum error of length sizing by the conventional technique is -13 mm. However, the maximum error of length sizing by "overlapped skew scan technique" is +14 mm. Considering beam spread, error of length sizing by this technique is appropriate. It is confirmed that the "overlapped skew scan technique" conservatively evaluated length by our nozzle mock-up. In the next step, it will be necessary to confirm an effect with more specimen and natural flaw.

REFERENCES

1) Japan Electric Association, “JEAC 4207 Ultrasonic examination for in-service inspection of light water cooled nuclear power plant components”, 2008. (in Japanese)
2) Japan Nuclear Energy safety organization, “Report of ultrasonic test and evaluation for maintenance standards”, 2005. (in Japanese)

RPV NOZZLE INNER RADIUS (NIR) INSPECTION WITH A 5 AXIS ROBOT: DEVELOPMENT, QUALIFICATION AND IMPLEMENTATION ON FRENCH REACTORS

P. Ancrenaz, E. Brau, AREVA
S. Deydier, L. Truchetti, B. Ruos, EDF

ABSTRACT

As part of the 3rd 10year outage, the nozzle inner radius (NIR) of -six 900MWe generation reactor vessels of the French nuclear power plant fleet had to be inspected. Both the type H (output) and G (input) nozzles are impacted. The objective of the examination was the detection and characterization of under-cladding cracks.

Due to the NIR complex geometry and the different geometries of H and G nozzles, AREVA NDE Solutions decided to develop a robotic solution. The 2 different types of nozzles were to be inspected using Ultrasonic Testing (UT) with a 5 degrees axis arm able to work underwater
In order to reduce the vessel occupation time, this tool was integrated on the MIS (machine for the reactor vessel in service inspection). The inspections must be conducted during the full vessel inspection.

Taking into account the performance to be achieved regarding the detection demands and the sizing accuracy, the non destructive technique chosen is the immergion focused probe.

Finally, the first in service inspection was carried out in September 2012 with success. The operational performance complied with the requirements. The main problem concerned the shape of the component which was slightly different from the theoretical one. This issue was solved by using the technical justification document in order to adapt the analysis methodology.

CONTEXT

As part of the 3rd 10yr outage, the NIR of -six 900MWe generation reactor's vessels of the French nuclear power plant (NPP) fleet were to be inspected. Both the type H (outlet) and G (inlet) nozzles are impacted. The objective of the examination is the detection and characterization of under cladding cracks.

COMPONENT GEOMETRY AND MATERIAL

Two different nozzles are considered for the examination:

1. Outlet nozzle: the area to be inspected is the area of the nozzle located inside the vessel. The shape of this area is cylindrical. The nozzle material is ferritic steel with stainless cladding (Figure 1).

2. Inlet nozzle: The area to be inspected is the conical shape and the toroidial shape of the nozzle. The nozzle material is ferritic steel with stainless cladding (Figure 2).

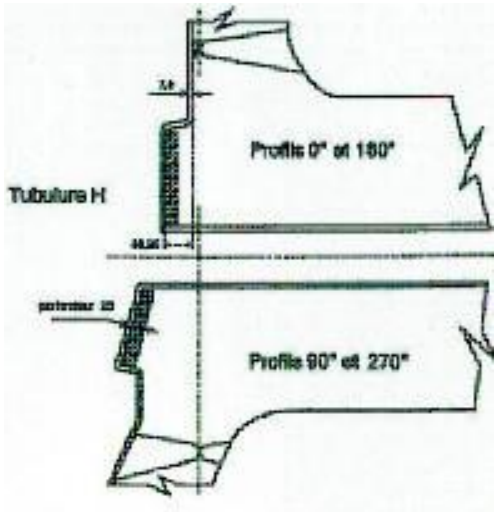

Figure 1 : view of the outlet nozzle according to the 0° and 90° plane

INSPECTION OBJECTIVE

Defects to be detected are under-cadding cracks initiated during the fabrication process of the nozzle. The defects are located at the base metal/cladding interface, and the concern is for propagation into the base metal. Relative to the nozzle axis, defect orientation of concern is longitudinal and circumferential for both nozzles.

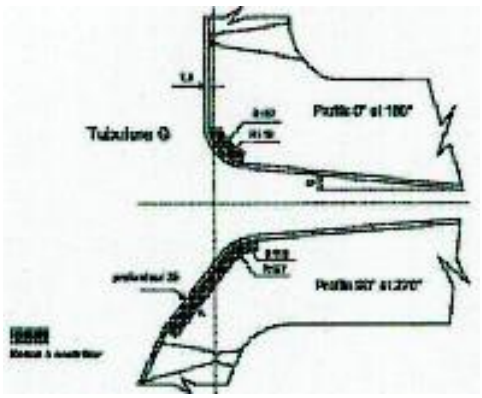

Figure N°2 : view of the inlet nozzle according to the 0° and 90° plane

NDE TECHNIQUE

The UT technique uses the diffraction echoes from the top and bottom defect ends for detection, sizing and positioning [2]. The technique chosen is based on a focused immersion UT probes used without contact with the nozzle surface. Considering the different inlet and outlet nozzle geometries, two different sets of probe were developed and tested. For both nozzles, the principle of detection, characterization and sizing are identical.

Outlet nozzle probe configuration:

- 4 x LW 63° probe (detection and sizing)
- LW 0° : cladding thickness measurement

Inlet nozzle probe configuration (Figure 3):

- 4 x LW 63° probe (detection and sizing) for the conical shape
- 2 x LW 63° probe + 2x LW 45° probe (detection and sizing) for the toroidial shape
- LW 0° : cladding thickness measurement
- All these transducers are integrated on the same mounting plate

Figure 3: view of the mounting plate used for the inlet nozzle

CHALLENGES OF THIS NEW EXAMINATION TECHNIQUE

This examination is performed with the MIS 3G manipulator which has been used for all the In Service Inspection (ISI) in France [1]. A new tool had to be developed in order to inspect this new area (Figure 4). This new tool had to be sufficiently flexible to scan the two substantially different geometries associated with either the inlet or outlet nozzles.

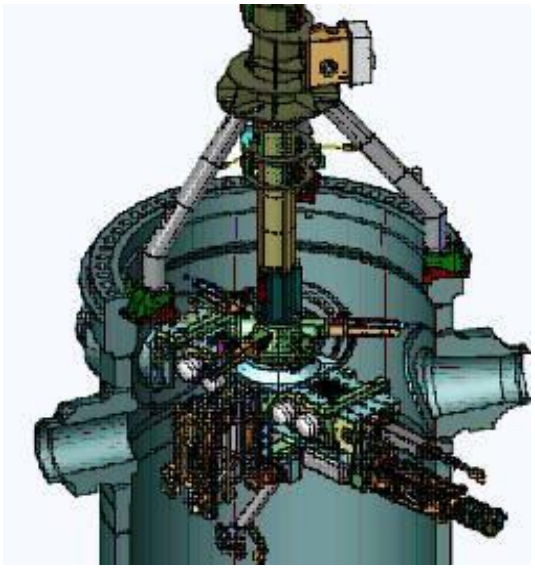

Figure 4: view of the MIS with the NIR tool attached to the lower portion.

An important issue concerns the knowledge of the component geometry. Because the surface was finished by hand during the original fabrication, the precise geometry is not known. The NDE technique and the tool must be flexible enough to manage this issue.

The MIS concept is predicated on the philosophy that the complete tooling for all inspections is in place when the MIS is mounted to the vessel to minimize the chance to remove the MIS robot following the initial installation and setting on the vessel. This assures minimum vessel occupation time and correspondingly minimum overall outage time as well as minimizing overall personnel radiation exposure associated with installing and removing the tool. .

IMPLEMENTATION ON THE MIS 3G

Due to the inner radius complex geometry to be inspected and the different geometries of the H and G nozzles, INTERCONTROLE decided to develop a robotic solution. The 2 different types of nozzles to be inspected using Ultrasonic Testing (UT) required a 5 degree-of-freedom (DOF) robotic arm able to work underwater. The 5 axis arm was developed and manufactured by AREVA to support a payload of 7 Kg at full extension. The 5 axis arm and the robotic control system were integrated into the overall MIS control system to support the multi-DOF control challenge (Figure 5).

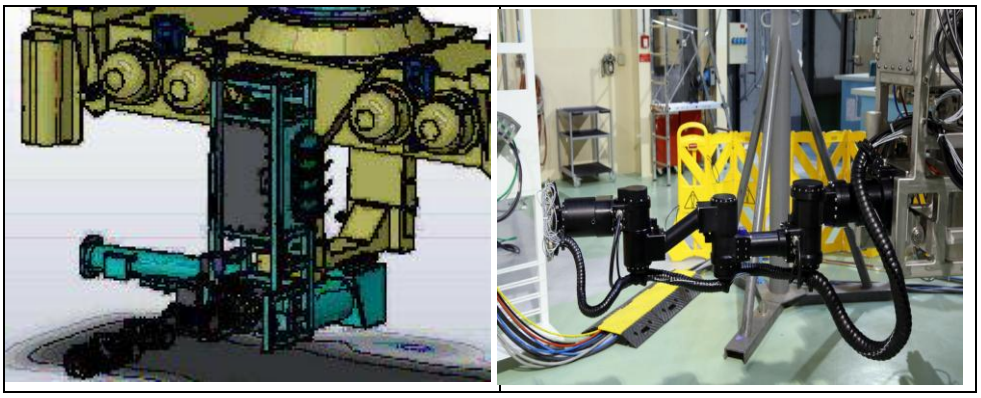

Figure 5: Picture of the 5 axis arm and the apparatus for his installation on the MIS

The robotic control system is an industrial solution which manages the trajectory, the manual and automatic mode, the safety function, plus the configuration of all 5 DOFs of the arm. This robotic system is integrated into the existing control command software of the MIS 3G (MIS Control

Command). The operator pilots the MIS and the 5 axis arm through a single software with both manual and automated scanning control modes. In addition, the MIS Control Command interface manages the NDE data base and the UT acquisition (Figure 6).

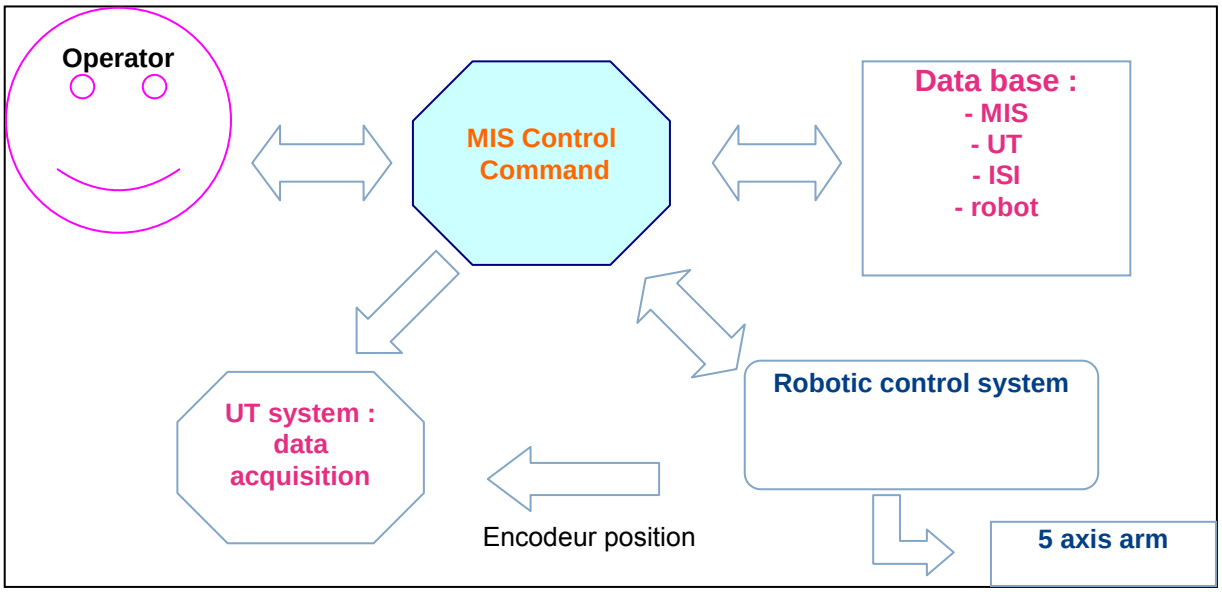

Figure 6: Overview of MIS plus 5 axis arm control and command

The UT-data are stored according to the position of the 5 DOF robot and the MIS 3G. The data coming from the encoders are sent to the UT equipment to activate the UT shot. Safety functions of the system include the following:

- Dual loop motion control (1 absolute encoder plus 1 resolver),
- Only fully developed, tested and qualified pre-programmed trajectories are used during the inspection ,
- Secure management of all trajectories are used for inspection,
- The environment is taken into account during the trajectories via real time collision avoidance calculations

As a consequence of these functions, the inspection is safe with a high quality level.

INLET AND OUTLET EXAMINATION

The examination is performed according to the following phases:

- PHASE 1: centring the arm to the nozzle face using an automatic sequence. After the centering measurement, the scan trajectory used for the inspection is automatically modified.
- PHASE 2 : scanning and data acquisition :
  - Inlet nozzle: 2 scans are done; one for the conical shape and a second for the Toroïdal part. Data acquisition is made during the rotation around the nozzle axis. Iindexing is done along the nozzle axis (3 axis of the arm are used).
  - Outlet nozzle: Scanning is performed by the MIS (rotation of the whole MIS) and indexing uses 3 axis of the arm. While scanning, data acquisition is performed and the probes are oriented toward the center of the nozzle (figure 7).
- PHASE 3: data analysis.

The data acquired includes all data required for the detection, characterization, and also the sizing process. No supplementary acquisition is needed.

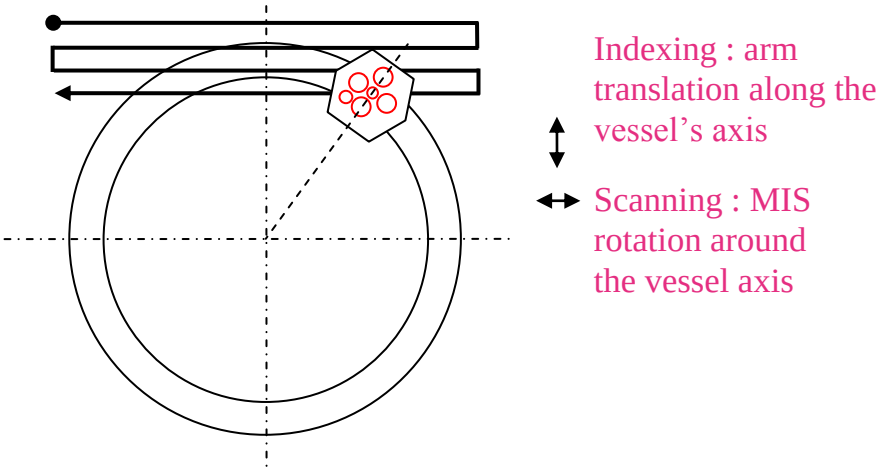

Figure 7: Principle for the outlet nozzle scan

QUALIFICATION PROCESS

Three full scale mock-ups were used for the development and the qualification: 1 outlet nozzle and 2 inlet nozzles. These mock-ups contain side drilled hole to analyse the effect of the cladding and geometry, and around 25 notches per mock-up to analyse the detection capability and the sizing accuracy.

The qualification methodology included two main steps:

1. The first consisted of a technical justification document based on computer models, analytical calculations and also some laboratory's measurements. At this stage, the detection capability, the sizing and the localization accuracy were justified. The examination procedure was then written using this input.
2. The second step was the qualification test series using 2 full scale G type and H type nozzle mock-ups containing artificial flaws. These tests confirm the demonstrated performance as calculated in the technical justification document (Figure 8).

Figure 8: View of the environment during the qualification tests

IN SERVICE INSPECTION

The first Inlet nozzle in service inspection was carried out in September 2012 at GRAVELINES NPP with success. The operational performance complied with the requirements. The main problem concerned the surface finish presenting an unrefined roughness and the shape of the component which was slightly different from the theoretical shape. These issues were solved by using the technical justification document in order to adapt the analysis methodology.

The first Outlet nozzle in service inspection was carried out in May 2013 at the SAINT-LAURENT NPP.

The quality of the UT data was identical to the quality obtained during the qualification test, and was better than the historical NDE technique. In particular, the resolution and the capability to discriminate planar defect from other defect or artefact were observed.

CONCLUSIONS

The choice of a robotic solution for the inspection has been validated through the qualification tests and the inspections performed on site. Several advantages can be highlighted as shown below:

- Reduction of the number of tools to be developed: the robotic tool is a versatile tool easily adaptable to both target inspections
- High quality of the inspection: possibility to adapt the trajectory before the acquisition to take into account the component specificity,
- High level of safety: trajectory qualified before the inspection,
- Operator training: the choice has been made to integrate the robotic control system into the MIS Supervisor. No need to train the operator to the robotic control system.

A new development is in progress to perform other examinations in the reactor pressure vessel using this robotic tool.

REFERENCES:

1. *ENC 2005*, M. ALGAROTTI, Ph. DUBOIS, L. HERNANDEZ, JP. LANDEZ, **PWR reactor vessel inspection according to RSEM**,
2. *5th International Conference on NDE in Relation to Structural Integrity for nuclear and Pressurized components, French* **reactor pressure vessels – non destructive examination of the core area – Detection performance demonstration of the « ZDC » process,** K.ZAMOUM, T.PASQUIER.

NEW DEVELOPMENTS FOR AUTOMATED NOZZLE INNER RADIUS AND PIPING INSPECTIONS

D. Eargle, WesDyne International, USA

ABSTRACT

WesDyne has recently engaged in developing and deploying methods for automated Inner Radius Inspections for Boiling Water Reactor (BWR) vessel nozzles from the outside surface. The system is also capable of performing automated dissimilar metal weld and piping examinations using the same base platform as the automated inner radius scanner. This system was developed to replace the existing automated piping scanner which used a flexible spring steel track with magnetic drive wheels. The newly developed scanner utilizes a modular scanner mounting platform and a rigid round track and integral gear rack for an adaptable scanning platform and robust drive train.

Many BWR plants require periodic inspections of the reactor vessel nozzle inner radius regions and dissimilar metal welds. The varying clearances and nozzle and piping geometries provide difficulties for automated inspections. WesDyne has developed a modular design that is adaptable to multiple configurations, geometries and a variety of nozzle sizes. This allows for one base design to be used for multiple applications and configurations.

These inspections have been demonstrated in accordance with the requirements of the American Society of Mechanical Engineers (ASME) Code, Section XI, Appendix VIII and through the Performance Demonstration Initiative (PDI) program.

The first automated inner radius inspection was completed on four feed-water nozzles at a BWR Type 4 reactor with a Mark I type containment. The simplified and modular design allows for improved performance, reduced site support, lower personnel dose and reduced inspection durations. Other projected uses for this system are steam generator dissimilar metal weld and nozzle inner radius examinations and feed water heater nozzle dissimilar metal weld examinations for Pressurized Water Reactors.

EXAMINATION OF NOZZLE INNER RADIUS AND PIPING FROM THE OUTER SURFACE

Inspection Background

Many existing BWR plants require periodic UT inspections of the reactor vessel nozzle inner radius (IR) regions from the outside diameter (OD) of the vessel shell, the OD blend radius area and nozzle barrel surface searching for nozzle inner radius (IR) flaws oriented in the radial-axial plane. This UT process must be qualified to ASME Section XI, Appendix VIII [1] as modified by the EPRI/PDI performance demonstration program. The inspection areas are shown in Figure 1.

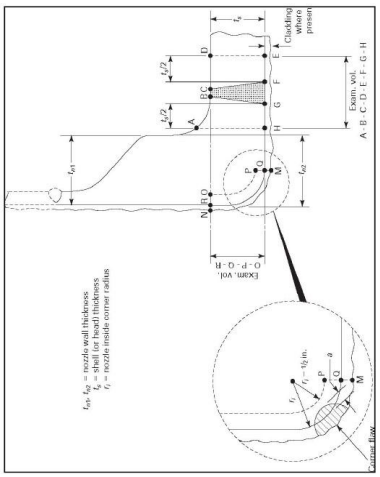

Figure 1: ASME Section XI, Figure IWB-2500-7,
Nozzle Inner Radius and Nozzle to Shell Weld Examination Areas

Previously, WesDyne performed manual conventional UT inspections of the nozzle IR regions from the OD. These inspections required personnel to remain at the nozzle in high dose areas for extended periods of time, and the data cannot be stored for later review. With the benefits of lower dose exposure and data storage, many customers in the BWR industry were interested in an automated OD inspection of the IR regions. WesDyne already provided automated OD inspections of the reactor vessel nozzle safe- end welds; however, the existing system was not capable of performing the additional inspection of the IR region.

Approach

Given the variety of nozzle sizes, plant dry well configurations and inspection environment obstructions, a modular and adaptable design approach was developed for automated inspection of the nozzle IR regions. Improvements over the existing safe-end weld inspection system were incorporated in the design and a common platform for IR and safe-end examinations was pursued to improve inspection performance, reduce site support requirements, lower personnel dose, reduce inspection durations and maximize inspection coverage.

The scanner is installed locally, but all equipment is designed for quick installation, reconfiguration and disassembly to require inspection personnel to remain in the inspection area as little as possible to reduce dose. The automated piping portion of the scanner was designed to carry conventional or phased array probes, as required for the given inspection. The automated inner radius scanner was designed to carry conventional probes with a quick disconnect end-effector for rapid changes between probe and wedge configurations.

The 2- or 4-axis scanner design, piping and inner radius respectively, includes two elevated track sections that can be customized for each individual pipe and mounting location geometry. The track is assembled in two halves with an integral dovetail and key providing track alignment at assembly and positive interlocking of the track sections. The lower track section is pre-set prior to installation and the top track assembly holds the encoded circumferential motor assembly and scanner mount trolley. Once the track sections are locked together, the upper track section is adjusted to secure the track to the pipe. The scanner arm is then installed using the integral dovetail and fastened to the scanner trolley. Any scanner arm can be mounted in multiple configurations to the scanner trolley as required and configured for the given inspection(s) through the integral dovetail connection.

The piping scanner consists of a single axis scanner arm with encoder feedback for axial probe positioning. The inner radius scanner consists of three independent encoded axes allowing for single and coordinated axis motion to accommodated scanning of both simple and complex geometries. Each scanner incorporates constant force springs for probe delivery and constant and reliable probe contact over the entire scanning surface. The inner radius scanner end-effector incorporates a self locking, manually operated skew axis that is preset prior to mounting the end-effector. Figure 2 shows the inner radius scanner installed on a full size BWR N4 feed-water nozzle mock- up.

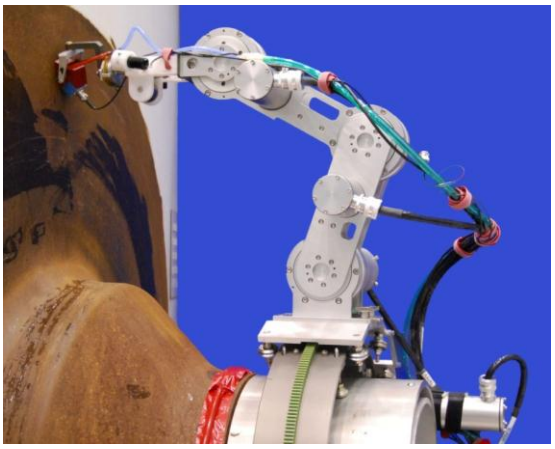

Figure 2: Inner Radius Scanner Installed on Feed-water Nozzle Mock-up

Remote operation and multiple on-board and overview cameras are used to allow the operators to calibrate the scanner position, set-up and execute scans and verify probe contact from a remote location; this process eliminates the need for a track handler in the high dose areas around the pipe at all times. In addition, dose reduction is achieved by the operator manipulating the scanner arm out of the nozzle window to allow inspection personnel to change end-effectors out of the high dose areas.

The UT process consists of a conventional shear wave transducer mounted to a flat wedge for vessel and barrel scans and a contoured wedge for blend radius scans. Using the EPRI 3D Modeling Toolkit V1.0R1, the probe skew, beam angles, scan surfaces, required radial position and metal paths are determined. Data acquisition and analysis is performed using the WesDyne IntraSpect^{TM} system. Figure 3 shows a WesDyne IntraSpect™ UT image of notch located along the nozzle bore ID surface; the scans were conducted from the OD surface of the nozzle barrel.

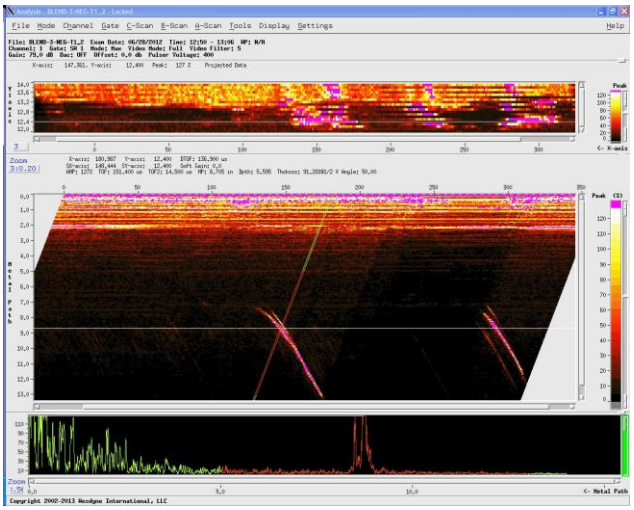

Figure 3: Inner Radius Data Collected Using WesDyne IntraSpect^{TM} System

System Qualification

Internal scanner qualifications and UT process development were conducted on a full size feed-water nozzle mock-up representing a BWR N4 nozzle. Scanner positional and environmental calibration processes were developed, along with completion of scanner kinematic and positional accuracy testing. From the testing, the system global positional accuracy and repeatability was determined to be less than 4.6mm. UT scan parameters were also tested and optimized for data quality and achievement of maximum scan speeds. Additional procedure and personnel qualifications were completed at EPRI on various size test samples in accordance with the EPRI/PDI performance demonstration process and using nozzle modeling [2]. The samples consisted of BWR N1, N2, N3, N8 and N9 nozzles ranging in pipe mounting location sizes from 5.12 (130mm) to 30" (760mm). The data was collected on all samples at a maximum scan speed of 3"/sec (75mm/sec). The WesDyne procedure WDI-STD-1117 [3] was qualified for detection of flaws along with several WesDyne inspection personnel.

Field Application

The inspection system was applied in the field in September 2012. It was specifically applied in four BWR N4 feed-water nozzle inner radius region inspections. Figure 4 shows the scanner installed on one of the feed-water nozzles.

Figure 4: Inner Radius Scanner Installed on Feed-water Nozzle at Site

Bioshield wall obstructions prevented >90% automated coverage on three of the four feed-water nozzles. The additional >90% coverage was obtained using a qualified manual UT process. However, after identification of the scanning limitations, additional end-effectors were developed to improve the scanner performance. These additional end-effectors are shown in Figures 5 and 6. These new end-effectors allow for an inverted scanner arm orientation around the bioshield wall obstructions and provide improved transducer contact over the inspection surfaces.

Figure 5: 90° Oriented EE for Improved Nozzle Barrel Scanning

Figure 6: 45° Oriented EE for Improved Nozzle Blend Radius Scanning

In addition to BWR reactor vessel nozzles, other proposed inspections for the WesDyne Track mounted ROSA based EXamination (T-REX) system include PWR reactor vessel nozzles, new plant steam generator to reactor coolant pump welds, new plant reactor coolant pump to main coolant pump welds, cast SS piping, UT in lieu of RT applications, and feed-water heater nozzle and piping inspections.

REFERENCES

[1] American Society of Mechanical Engineers, Section XI: Rules for Inservice Inspection of Nuclear Power Plant Components, Appendix VIII: Performance Demonstration for Ultrasonic Examination Systems, 2004 Edition.

[2] WesDyne Nozzle Examination Qualification, EPRI, Palo Alto, CA, IR-2012-514. [3] Automated Ultrasonic Procedure for Examination of Nozzle Inner Radius Corner Radius Areas in Accordance with ASME Section XI, Including Appendix VIII, WesDyne International, WDI-STD-1117.

MULTIELEMENT ULTRASOUND AND EDDY CURRENT INTEGRATED PROBE FOR NON-DESTRUCTIVE EVALUATION OF NUCLEAR REACTOR PRESSURE VESSEL HEAD PENETRATIONS

M. Budimir, N. Pavlović, R. Gracin, M. Kekelj, INETEC, Croatia

ABSTRACT

An integrated combined UT (ultrasound testing) and ECT (eddy current testing) multielement probe prototype for inspection of gaps in nuclear reactor pressure vessel head penetrations (RVHPs) was numerically modelled, designed, assembled and tested in this work. The probe prototype consists of an acoustically active head and an acoustically passive body. The active part consists of an axial and a circumferential UT TOFD (time of flight diffraction) configuration pairs of central frequency of 6.2 MHz, of a normal beam 0° single element disc shape UT probe of central frequency of 2.25 MHz and a cross wound ECT probe. All these elements have been integrated in the polymer probe head of dimensions 29mm x 24.4 mm x 2.8 mm, with the OD (outer diameter) of 69.85 mm. The head is mounted on a flexible stainless steel probe body, able to follow the complicated structure of narrow gaps between penetration pipes and thermal sleeves. The prototype was assembled according to numerical optimizations results, and its electromechanical properties were tested on a stainless steel calibration block. The modelled and experimental results of electromechanical probe signals showed excellent agreement and all the artificially made indications on the calibration block were successfully detected and sized.

INTRODUCTION

Among compulsory activities for nuclear power plants inspections during regular and periodic outages prescribed by the standards, codes and regulations [1-3], it is of great importance to inspect the RVHPs. The penetration stainless steel pipes are mechanically expanded into the head and welded at the bottom (J-weld), see Figure 1.

A crack may appear in the heat affected zone of the weld and the space between the penetration pipe and the vessel head can, in such cases, be filled with water. Within the expanded penetration pipe, there is a thermal sleeve that protects the safety rods that control the nuclear reaction. Such a geometrical configuration creates a complex inspection environment, with a very narrow gap (3 mm – 9 mm) between the thermal sleeve and the penetration pipe, and the thin gap (filled with air, or with water in a case of a failure) between the penetration pipe, with the wall thickness of 15.9mm, and the reactor pressure vessel head. It is thus important to have a tool capable of inspecting the welds, the heat affected zones for cracks and the thin air gap for water leakage.

Figure 1. INETEC Lab RVHPs mock-up (welds, pipes and thermal sleeves configuration).

An inspection solution for such a configuration is proposed in this work – an integrated multielement probe consisting of a polymer probe head, a flexible probe body made of stainless steel and the probe connector with coaxial cables. The probe head contains two TOFD pairs of central frequency of 6.2 MHz, a normal beam probe of central frequency of 2.25 MHz, and a cross wound EC element. The flexible probe body houses the thin coaxial cables and the couplant, in this case water, supply. The design and construction procedure of this probe consisted of several steps: finite element modelling and theoretical optimization of the probe design, engineering of the acoustically active and passive materials, assembly, electronics engineering and the probe testing on a standard calibration block.

FINITE ELEMENT MODELLING OF THE PROBE PERFORMANCE

The theoretical modelling and optimization was performed within the PZFlex software package [4]. The software uses a finite element and wave – propagation analysis algorithms that are designed specifically for piezoelectric and ultrasound applications. In this work, the software was used for modelling of 6.2 MHz TOFD and 0° normal beam 2.25 MHz ultrasound probes with different designs and material properties in order to find the optimal configuration. The analysis model in this software package could be imported from a CAD format (Figure 2) or written in the PZFlex code. The second approach was finally applied in this work as it provided more options for user to configure different scenarios.

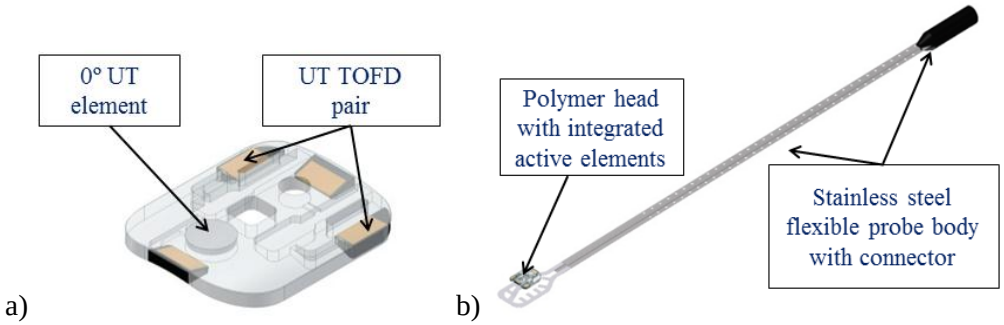

Figure 2. CAD model of the integrated multielement NDE probe for testing of the penetration gaps: a) the polymer probe head containing active testing parts (piezoelectric elements in TOFD and normal beam configurations and an ECT element); b) the probe head mounted on a probe body made of a flexible stainless steel strip, able to bend and to follow the complex thermal sleeve-penetration pipe gap geometrical configurations.

To perform the complete analysis of both axial and circumferential configurations of TOFD and of an additional zero degree probe, three separate models were created. Figure 3 shows the initial models of axial and circumferential ultrasound TOFD configurations, while Figure 4 presents the zero degree UT single element in the normal beam pulse-echo configuration. All three models are individual 2D projections in the same material body.

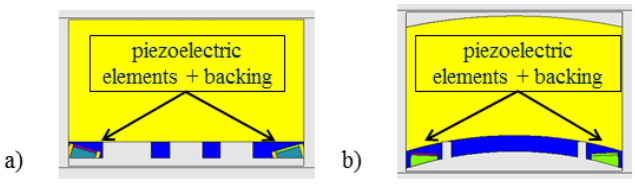

Figure 3. 2D model of piezoelectric pairs in axial (a) and circumferential (b) TOFD UT configuration together with the pipe material (coloured in yellow) to inspect. The models were made by taking two perpendicular planar cross sections of the prototype probe head (Figure 2a). The blue areas are the polymer head housing cross sections.

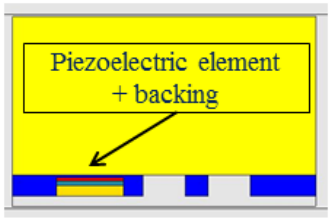

Figure 4. 2D model of piezoelectric disc shape normal beam UT 0° pulse-echo configuration, together with the pipe material.

The model was set to run with different number of finite elements, excitation functions, boundary conditions etc. Setting all the input parameters correctly was generally the key to have comparable results with ones in real applications. Also, adding different electronic components in serial or parallel connections made the obtained simulation results significantly differ among themselves. Figure 6 shows a caption of a video in the user interface during a simulation. The video clips can greatly facilitate understanding of wave propagation in material and determine if the simulation procedure is converging in a desired direction.

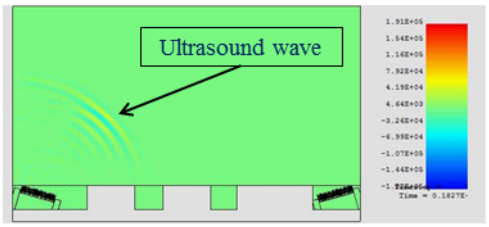

Figure 5. Caption of a video in user interface during simulation of the axial TOFD 6.2 MHz UT configuration.

In the PZFlex software package, the output results of the simulations can be specified by the user. In this work, the wanted output was the voltage amplitude as a function of time on the receive port of the TOFD pairs. In that way, the simulation results could be compared with the assembled probe measured signals in the experimental phase of the work. Another advantage of this theoretical approach is the modelling of different flaw indications in the inspected material and comparison of the results. In that way, the optimization of the probe for certain specific flaw indications is possible. Figure 6 shows the voltage resulting from an inspection of a healthy material, and Figure 7 shows the response of the probe positioned in front of an OD indication – in the latter case an additional reflection is visible if compared with the result in the Figure 6.

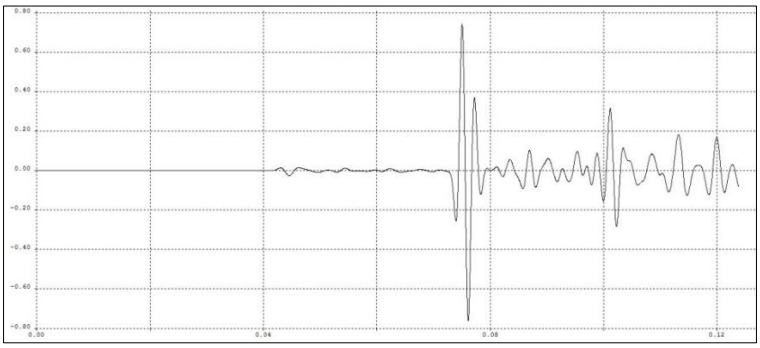

Figure 6. Receive port voltage signal of axial TOFD 6.2 MHz resulting from an inspection simulation by using a healthy testing material (no defects).

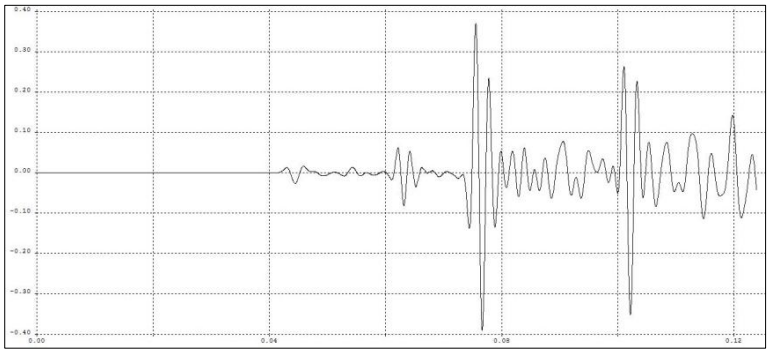

Figure 7. Receive port voltage signal of axial TOFD 6.2 MHz resulting from an inspection simulation by using a testing material with a small OD defect.

The goal of numerous simulations performed in this work was to determine the optimal materials for ultrasound wave's excitation and for the backing material. Also, the angles and positions of the piezoelectric material were set to have better voltage responses regarding to different indication positions in the inspected material. The later experimental results showed very little difference from the simulated results. This modelling procedure has pointed to the main benefit of such an approach – reducing the invested time and resources during the development phase and speeding up to the final stage of probes construction and assembly.

PROBE ASSEMBLY

Several prototypes have been assembled in this work, as shown in Figure 8. Prior to the final assembly, the electrical and acoustical properties of the building parts, comprising piezoelectric elements, eddy current coils, backing materials, and polymer housing, were characterized. Figure 9 shows, as an example, the frequency dependence of the electrical impedance of the coils in the cross wound ECT element. It can be seen that the properties of both the element coils tested were identical, which is a confirmation of the precision of the construction of the ECT element in the probe. The spring system holding the polymer head to the stainless steel housing was specially designed to cover the testing in the gaps of 2 mm to 9 mm width. In this interval the spring holds the polymer head tightly adjusted to the wall of the penetration pipe – there is no lift-off. The water supply was made by a polymer tube to be used as an ultrasonic couplant. The stainless steel body of the probe was made to be flexible enough to bend and to follow the configuration of the thermal sleeve and the penetration pipe system, see Figure 1.

Figure 8. Assembled prototypes of the integrated multielement UT/ECT probe.

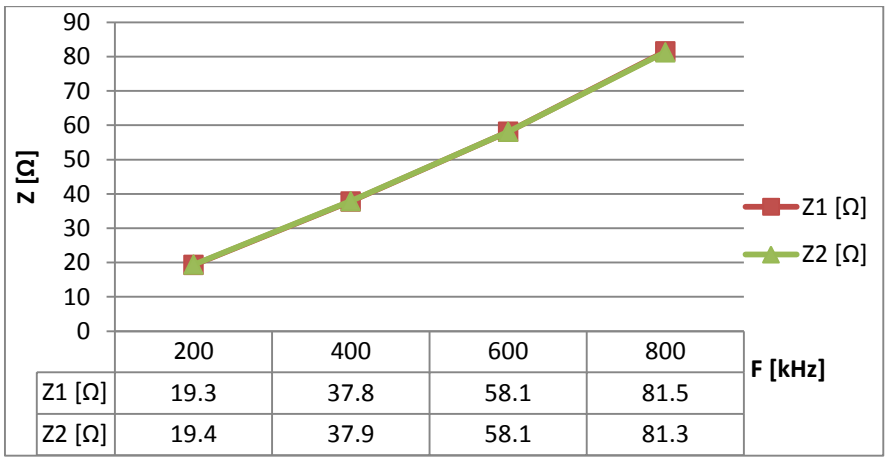

	200	400	600	800
Z1 [Ω]	19.3	37.8	58.1	81.5
Z2 [Ω]	19.4	37.9	58.1	81.3

Figure 9. Measured frequency dependence of the electrical impedance for the two coils used in the cross-wound eddy current element.

PROBE PERFORMANCE TESTING

A common procedure for testing ultrasound and eddy current NDE transducers is performed by using standard calibration blocks. A CAD design of such a calibration block is shown in Figure 10. One can see the axial and circumferential artificially made cracks that are suitable for testing of the UT TOFD and ECT techniques, as well as the abrupt block thickness change, that is convenient for the testing of the normal beam 0° UT transducer.

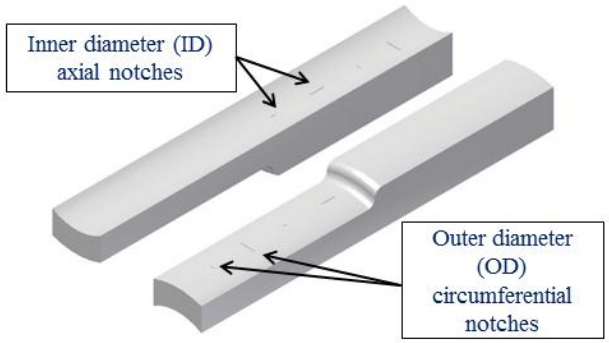

Figure 10. CAD design of a calibration block for the UT/ECT transducers characterization.

The experiments were performed on the block by using a ZETEC Tomoscan III commercial NDE pulser-receiver, accompanied by TomoView 2.29 software package for the pulser-receiver control and signal acquisition and analysis. Figure 11 shows representative A and B scans for axial TOFD, circular TOFD and 0° normal beam scanning of the calibration block, that were chosen from the set of the experimentally obtained results. The comparison of the measured results with those obtained by modelling in the PZFlex showed excellent agreement (see Table 1).

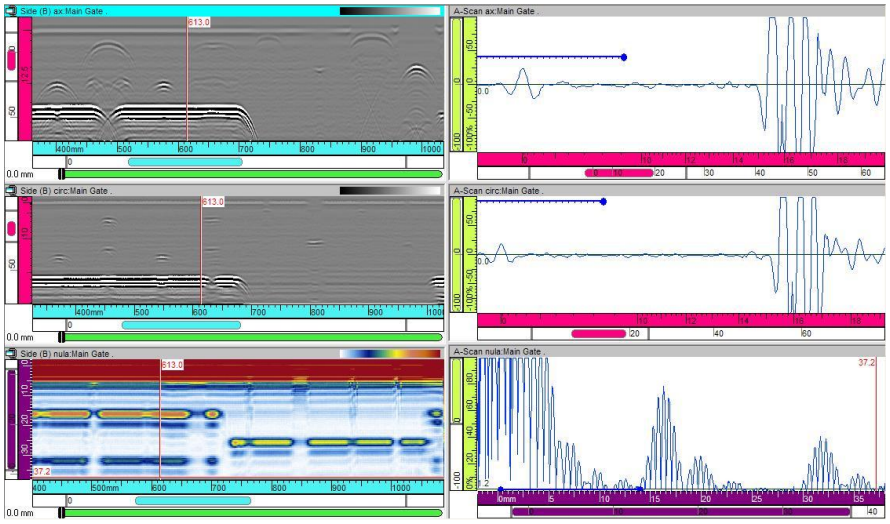

Figure 11. Typical A and B scans for (from top to bottom) axial 6.2 MHz TOFD, circumferential 6.2 MHz TOFD and 0° 2.25 MHz normal beam ultrasound scanning of the calibration block.

Label	Actual size	Modelled size	Measured size	Shooting direction
ID circ. Notch	3.5mm depth	3.1mm	3.3mm	axial
ID circ. Notch	10mm depth	-	10.3mm	axial
ID axial notch	3.5mm depth	3.0mm	3.6mm	circumferential
ID axial notch	10mm depth	-	10.5mm	circumferential
OD circ. Notch	3.5mm depth	-	4mm	axial
OD circ. Notch	10mm depth	9.2mm	9.9mm	axial
OD axial notch	3.5mm depth	-	4mm	circumferential
OD axial notch	10mm depth	-	10.5mm	circumferential
Block thickness	15.8mm	-	15.8mm	normal beam

Table 1. Comparison of the notches and thickness sizing results, obtained by modelling in the PZFlex software package ("modelled size" column) and measurements by a fully assembled probe prototype ("measured size" column), with the real sizes on the calibration block ("actual size" column). The "shooting direction" column displays the direction of the testing ultrasound beam for each measurement.

CONCLUSIONS

NDE inspections in nuclear power plants can get really challenging when it comes to testing of complex geometrical configurations such as the gap between the thermal sleeve and the penetration pipe in the nuclear reactor pressure vessel head, as discussed here. Such places call for somewhat non-orthodox NDE tools. Such a tool has been presented in this work – an integrated combined UT and ECT multielement probe prototype was modelled, designed, assembled and tested. The probe prototype acoustically and electrically active part consists of several important and independent elements: an axial and a circumferential UT TOFD configuration pairs, a normal beam disc shape UT probe and a cross wound EC probe.

Those elements have been integrated in the acoustically and electromagnetically transparent polymer probe head and mounted on a flexible stainless steel probe body that is able to follow the complicated geometrical structure in question. The UT TOFD elements were designed by using specifically made composite piezoelectric elements utilized as ultrasound signal generators and receivers, additionally backed with special acoustic polymer-metal powder mixtures in order to produce the ultrasound testing signals of high quality. The pulse duration of the signal for the TOFD pairs was measured to be 0.5 μs, the bandwidth 71% and signal-to-noise ratio 40:1. For the normal beam single element, a classic commercial PZT piezoelectric disc was used, together with the specially made backing to reduce the ringing, and the pulse duration of the signal was measured to be 1.6 μs, the bandwidth 48% and signal-to-noise ratio 8:1, which was more than enough to have high quality testing signals. The modelled and the experimental results of electromechanical probe signals, when finally compared, showed an excellent agreement and all the artificially made indications on the testing calibration stainless steel block were successfully detected and sized. This probe has a very high commercial potential.

REFERENCES

1) ASME B&PV Code, Section XI, 2007 Edition, Appendix VIII, Supplement I
2) ASTM Guidelines for Evaluating Characteristics of Ultrasonic Search Units, Designation: E 1065-08
3) EN 12668-2, Non-destructive testing – Characterization and verification of ultrasonic examination equipment – Part 2: Probes
4) PZFlex Version 4.0, Weidlinger Associates Inc., http://www.pzflex.com/default.aspx

GUIDE TUBE INSPECTION

M.Montero, M.Grataloup, P.Blachon, CEGELEC, France

CONTEXT

The SIRIUS equipment has been developed for EDF / UTO to inspect the card control guides component in nuclear reactors. The goal of the equipment is to evaluate by a NDT technique the wear of the guide before performing maintenance (possible replacement of tube guide).
To point out the benefit of SIRIUS equipment the context is recalled below.
The control of the activity of the nuclear reactor is critical for obvious safety reasons, but also to control the power supplied. The regulation of power is carried out by means of control rods which are inserted directly into fuel assembly (see fig1). The card guides are the components which allow this insertion. The functionality of card guide must guaranty the perfect position of control rod cluster in front of the fuel assembly.

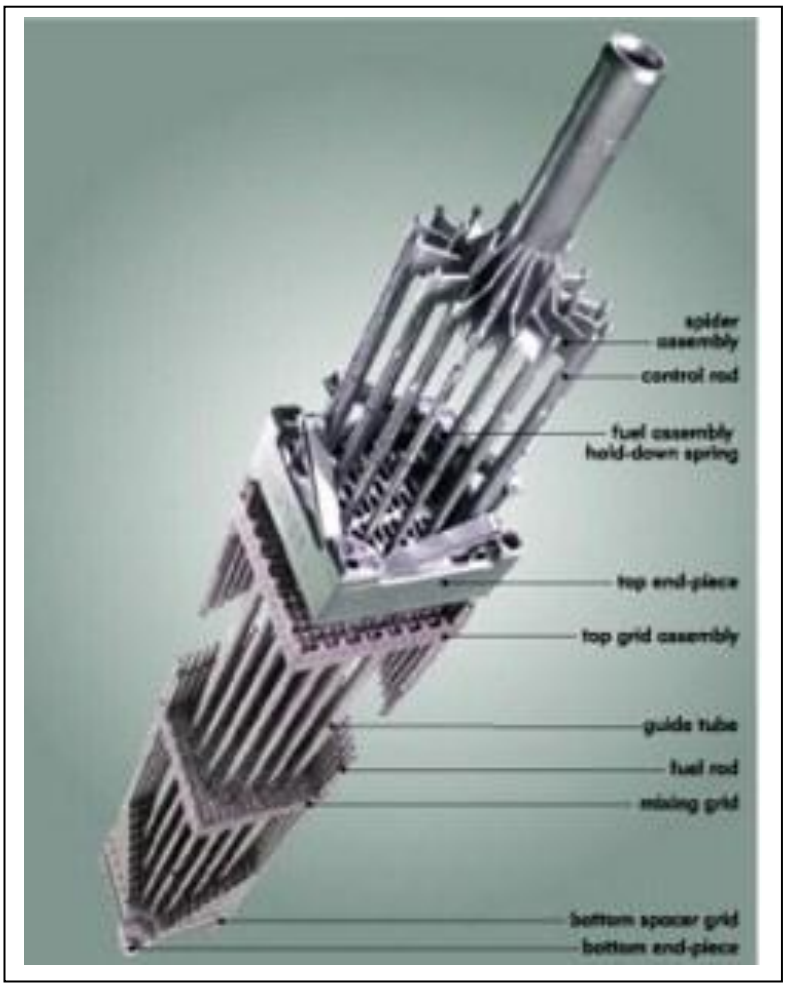

fig 1

The control rod cluster (RCCA) is an assembly of 24 thin tubes (see fig 2) of zirconium of 9,7mm diameter and about 5m long. They are filled with neutron absorber hanged to a spider control part. These clad are inserted in fuel assembly at different depth to regulate the activity or shutdown the reactor.

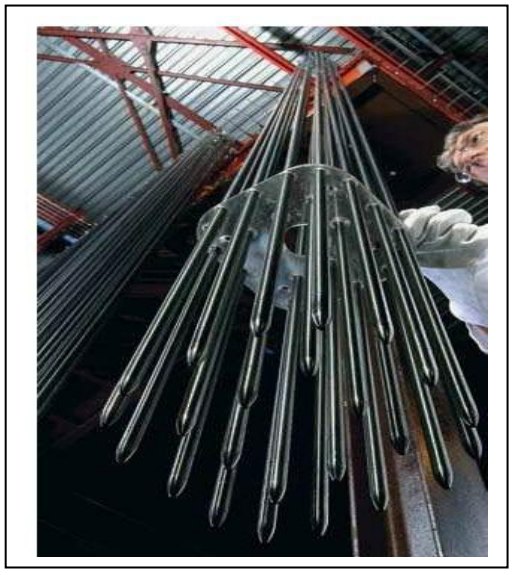

fig 2

This set of clad is very flexible and requires a guidance system which allows aligning each ones facing the orifices of the fuel assembly to obtain a perfect insertion.

During the phase of the full production control clusters are positioned over the fuel assemblies and maintained perfectly in position in the guide tubes in front of the fuel assembly (see Figure 3). The supports are called RCCA guide tube cluster (see Figure 4)

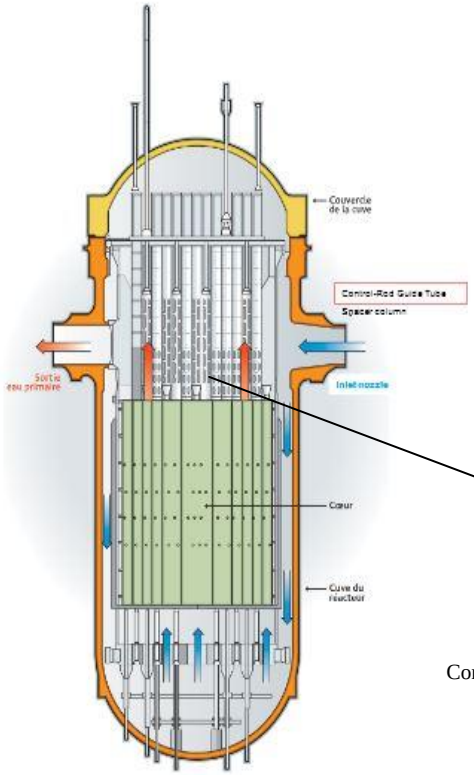

fig 3

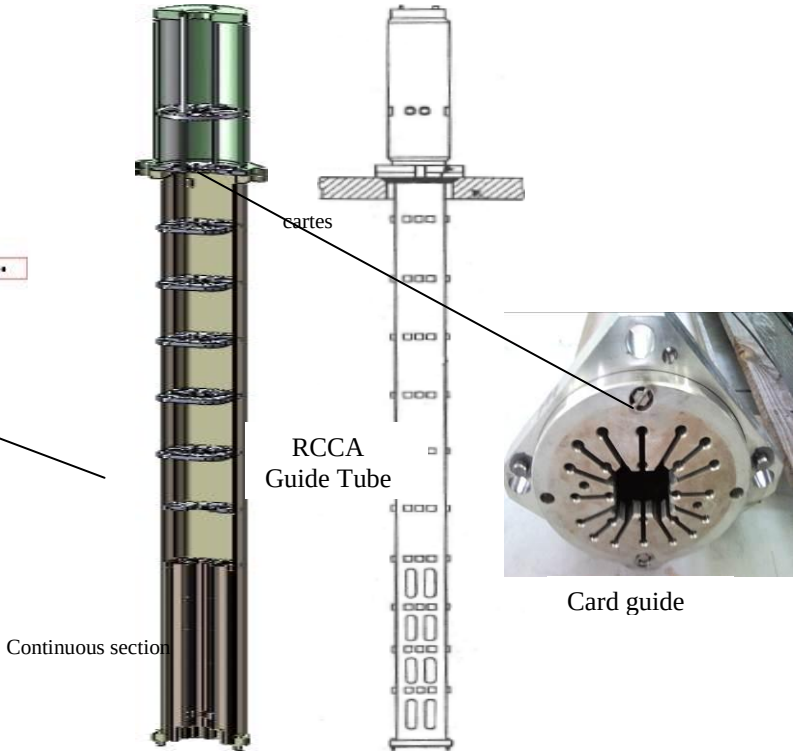

fig 4

INSPECTED COMPONENT

Tube Guide consist of a welded assembly card guide (24mm in thickness) on the top side and at lower side continuous guide section of length about 800mm.

These guide elements (cards and continuous section) are formed by bores vertically aligned fixing in position clads of the cluster control rod. This system aims at power regulation phases but also in case of emergency shutdown of the reactor (automatic control rod drop).

The way of reactor activity regulation by inserting the control rods with small movements in the assembly fuel, the vibration of clad, the water flow circulation of reactor naturally lead to the wearing of the holes by friction.

The clearance due to wear could lead to a misalignment between the clad and openings of fuel assemblies, with a risk of blockage during the insertion phase.

As part of maintenance programs and extend life of nuclear power stations EDF / UTO has set up an inspection program of tube guides to determine the status of these components related to the safety.

INSPECTION ENVIRONMENT

Constraints associated with these tests are mainly related to the environment. The inspection must be carried out, tube guides installed in the Upper Internal Assembly (see Figure 5), and immersed in the pool of the reactor building by 20m deep. Tube guides clusters are highly activated and the high dosimetry rate

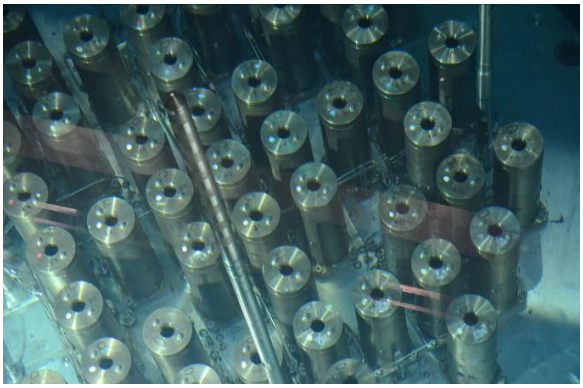

fig 5

WEAR DEGRADATION DEFINITION

Here after the solicited area of card guide and zone to measure (in red see fig 6).
EDF/UTO requirements for measurement are the followings, diameter, residual ligament and slot width. All measurements should be done at the middle of thickness, and 3 slice profiles must be done in continuous section.
To take into account the dimensions to measure, it was essential to propose a technique to fulfill all requirements.

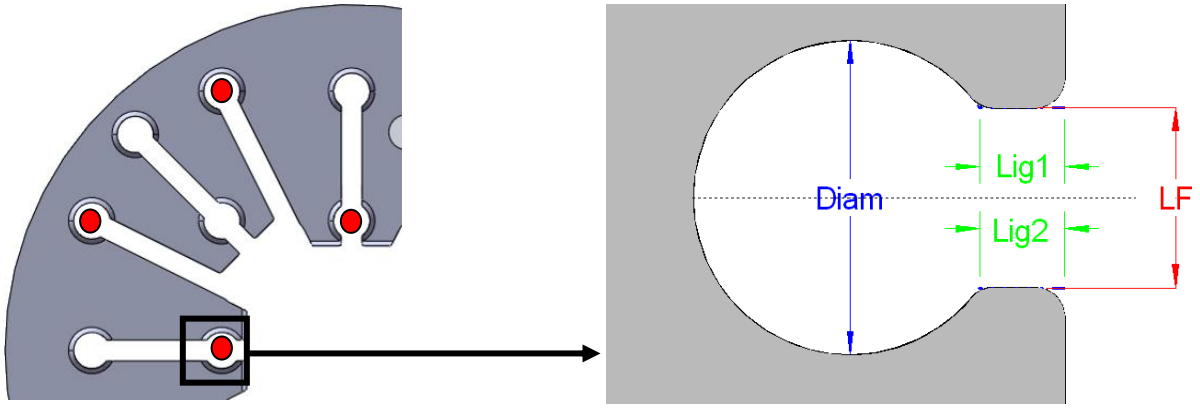

fig 6

As techniques based on vision (cameras) cannot carry out measurements inside the cards or in continuous section we have decided to work with an ultrasound technique.
The principle is show on fig 7. An UT beam is generated from the center of bore to the edge, to measure de distance r. If the bore hasn't degraded by a wearing this distance is Constant in other case the variation is related to the wearing.

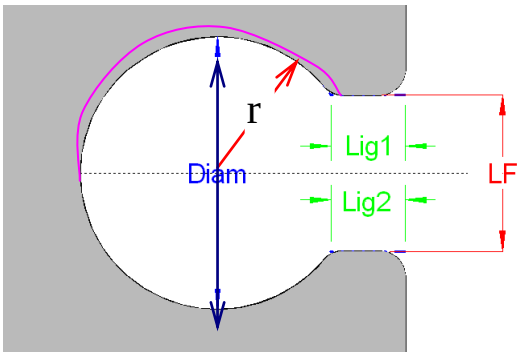

fig 7

NDT TECHNIQUE

With a beam rotation it's possible to build a complete profile. As the nominal diameter of bore is 10,67mm the design of UT measurement device introduces a mirror beam deviation (See fig 8).

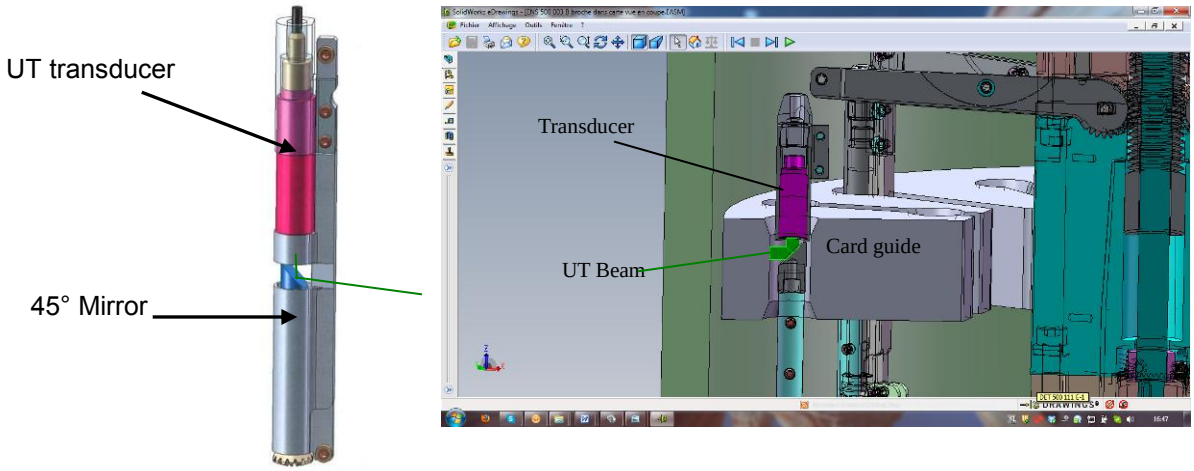

fig 8

As twelve bores must be inspected at same time we design the equipment with retractable capabilities.

MEASURING PERFORMANCES AND INFLUENT PARAMETERS

The accuracy of measurements is theoretically affected by the influent parameters. The following type of influent parameter has been evaluated:

- Component and defect
- UT measuring technique and calibration
- Measuring unit position in the card and geometry
- UT equipment
- Environment

To determine the theoretical accuracy we have studied 33 parameters.

The uncertainties related to these influent parameters lead to the following performances which have confirmed during qualification process.

Measure	Uncertainty
Diameter	***U* globale (Ø) =+/- 0,141mm**
Ligament	***U* globale (Lig) =+/- 0,204mm**
Slot Width	***U* globale (LF) =+/- 0,492mm**

SIRIUS EQUIPMENT

The 12 measuring unit are retracted at the introduction of equipment in the tube guide and deployed before to reach the measuring position.

To achieve this mechanical function it was designed a device like "sugar tongs" based on parallelograms (see fig 9).

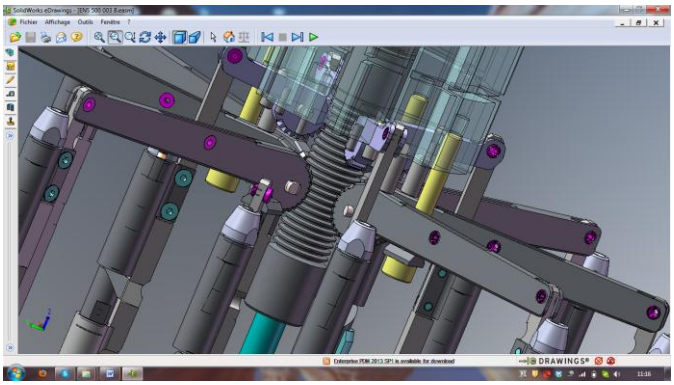

fig 9

The mirror rotation is achieved by conical gear set with calibrated stiffness axes (see fig 10) to ensure permanent contact on 12 transmission lines.

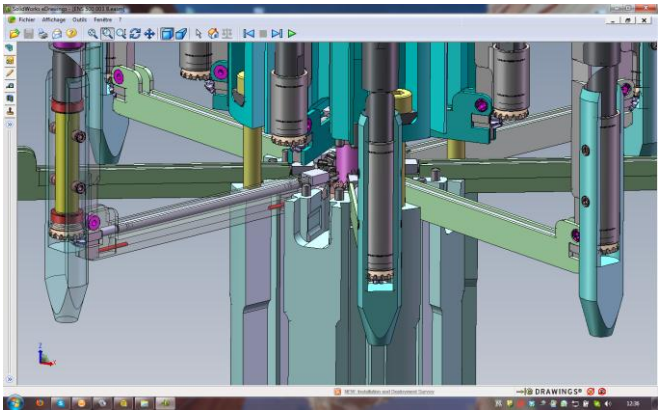

fig 10

The equipment introduction is done by the cover top plate of tube guide through a hole of 58,6mm (see fig 11) the total size of equipment is 56mm.

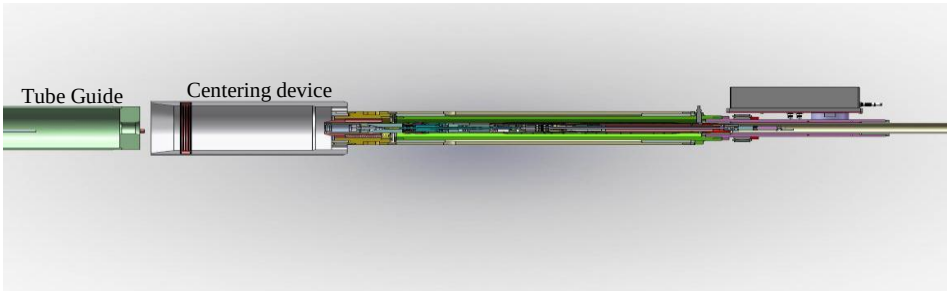

fig 11

Alignment between equipment and tube guide is done by means of centering device with locking ring (see fig 11) and fine adjustment with conical part (see fig 12).

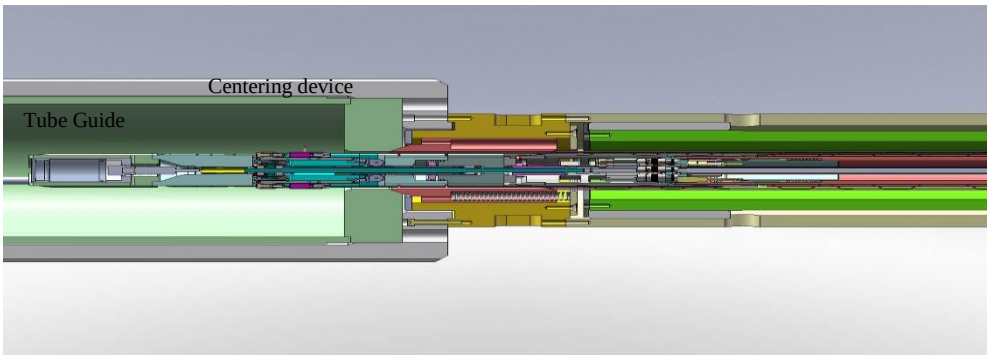

fig 12

The alignment of slot in card and arms of measuring system (see fig 13) is obtained by a frontal camera at the bottom of measuring system. (see fig 14).

Clearance between arms and slot in card is about 1mm at 5m of distance from the top of tube guide.

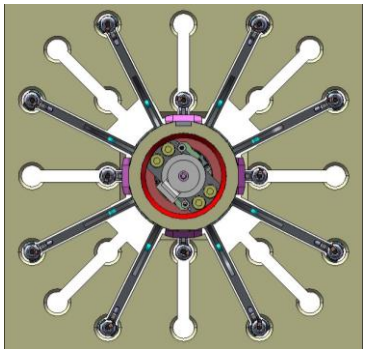

fig 13

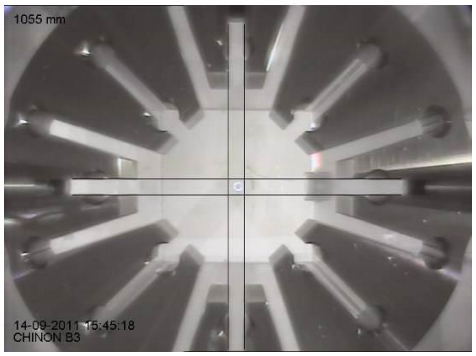

fig 14

The measuring system is connected to a matt of 6m long which is used for translation along the tube guide. This is done by the means of control loop motor installed on centering device (see fig 15).

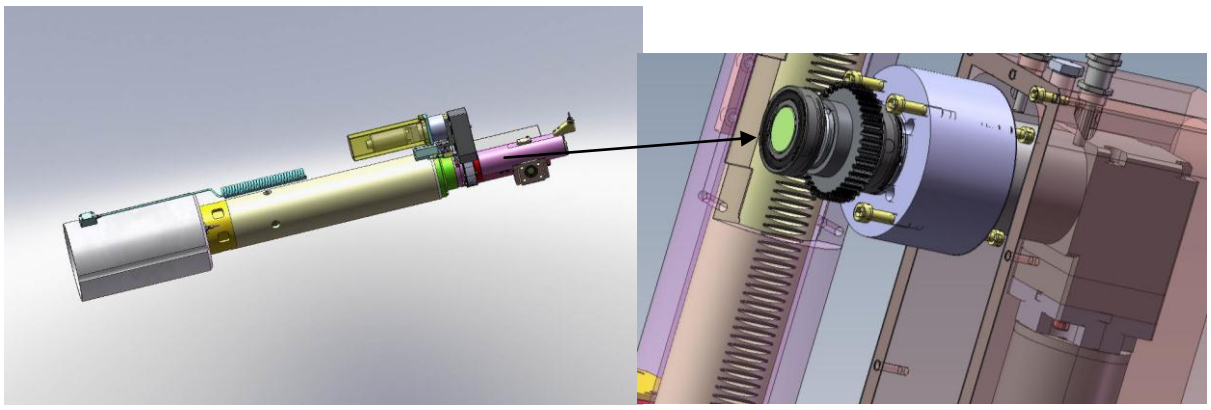

fig 15

INSPECTION CONTROL SOFTWARE

Automated movement cycles that optimize the inspection time. The software is also used for secure operation of the tool. Software continuously records images and the dynamic torque required to move. In case of over-torque especially in the approach area zones (introduction of measuring unit in cards) an automatic shutdown of the descent is enabled, then retract movements and new insertion are started to ensure the integrity of the devices and in all circumstances allow the extraction of tool from tube guide. The software allow a reel time visualization of measuring system inside de tube guide and inspection plan status (see fig 16)

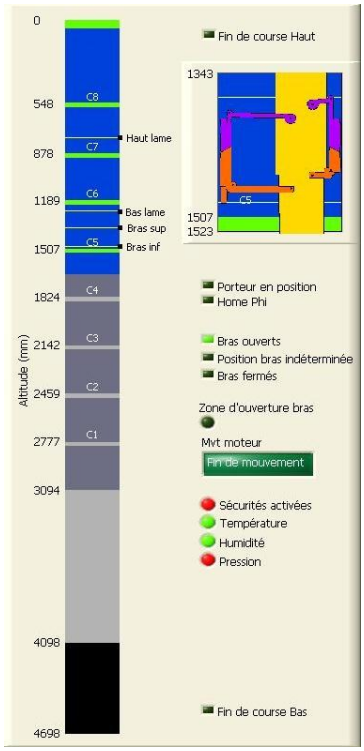

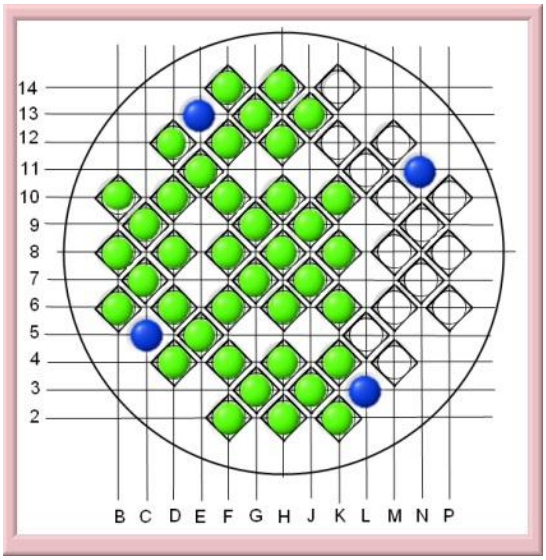

Plan des EIS avec les guides de grappes contrôlés

fig 16

ANALYSIS SOFTWARE

Analysis software has been developed to calibrate and measure the different values of guide.
This software performs automated dimensions measurements required through complex processing algorithms signal (see fig 17 et 18).

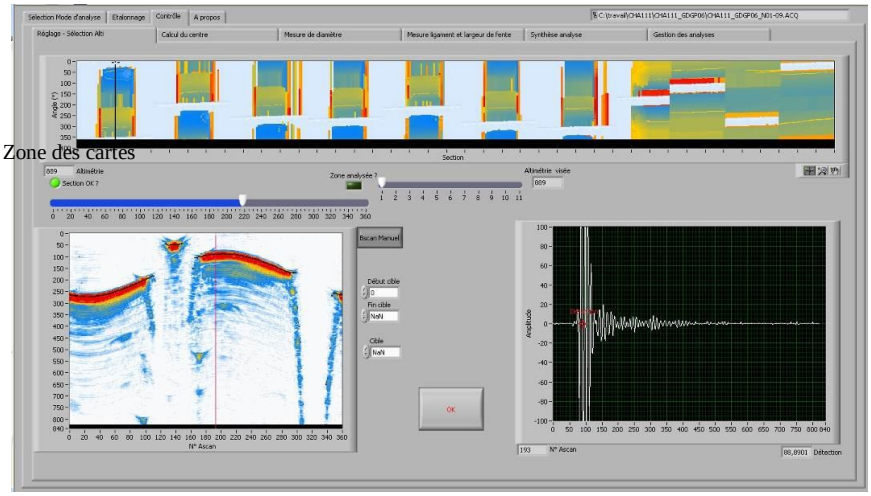

General view of measurements in cards and continuous section
fig 17

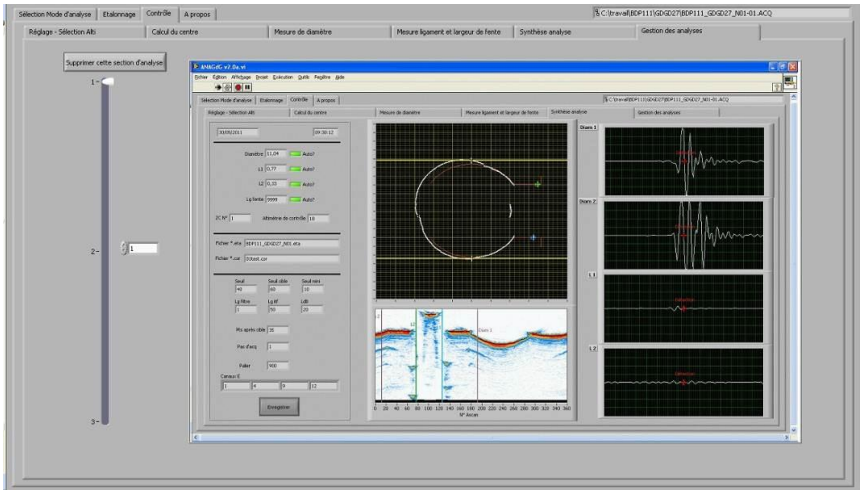

Profile characterization at center of card
fig 18

RESULTS AND PERSPECTIVES

SIRIUS equipment has been implemented on 8 sites. We have inspected about 500 guide tubes 1300Mw or 900Mw. Relevant results offered by the device convinced our customer to extend the inspection to more sites.
SIRIUS is the first equipment to give simultaneously 12 measurements of degradations wear in guide tube allowing relevant information to utilities to proceed with maintenance action in association with other criteria.
The perspective for the future is to extend the inspection to other sites and countries and to implement the equipment few cycles after guide tube replacement to evaluate the kinetic of degradation.

REACTOR PRESSURE VESSEL III

DEVELOPMENT OF A FUEL ROD GUIDED WAVE INSPECTION SYSTEM

J.L. Fisher, S. Vinogradov, E. Laiche Southwest Research Institute, USA
K. Krzywosz, EPRI, USA

ABSTRACT

Fuel failures are an expensive and undesirable event for nuclear utilities. The presence of leaking fuel is identified during plant operation; however, identifying the individual leaking fuel rod presents a challenge. Individual leaking fuel assemblies are identified during plant outages using nondestructive examination (NDE) techniques to prevent the re-insertion of failed fuel rods back into the reactor and to aid in root cause failure analyses. Due to false and missed calls experienced by traditional inspection techniques, alternative inspection methods are needed that can reliably identify individual leaking fuel rods in a leaking fuel assembly. A magnetostrictive transducer (MsT) probe was developed to perform guided wave inspections of sample fuel rods containing simulated fretting flaws and simulated circumferential, axial, and 45° cracks. In addition, a mechanical delivery unit was built to facilitate remote operation of the probe in conditions similar to field conditions. The complete system was tested in a dry laboratory environment as well as in a simulated spent fuel pool environment. The effect of nonlinear dependence of signal amplitude on the depth of the anomalies was investigated for data processing. The results showed that 100% through-wall defects can be identified and reliably distinguished from other non-through-wall defects. This paper presents the results of the examinations conducted to date in air and under water on simulated machined flaws located both in free spans and under supporting grids.

INTRODUCTION

Fuel rods in nuclear reactors consist of uranium fuel pellets that are encased in hollow metal tubes made from zirconium alloys. They are grouped together into fuel assemblies of up to 250 or more fuel rods. A reactor core typically contains several hundred fuel assemblies. Due to the elevated temperature, pressure, and radiation inside of a reactor, fuel rods can fail during operation. The most common failure mechanism in Pressurized Water Reactors (PWRs) is grid-to-rod fretting wear while for Boiling Water Reactors (BWRs), debris fretting is most common [1]. Other mechanisms include crud and corrosion failures, and pellet cladding interaction (PCI) cracks. The failure of a fuel rod can potentially lead to leaking of radioactive material into the primary coolant system. Because this release of radioactive materials is a safety concern, fuel rod failures can cause unscheduled plant shut downs, which may cost as much as $40 to $80 million dollars [2].

Failed fuel assemblies may be identified through “sipping” techniques, in which the water surrounding the fuel assembly is sampled to determine the presence of radioactive materials. However, testing methods for identifying individual failed fuel rods are more costly and time-consuming. Visual, eddy current, and ultrasonic techniques have been in use for this purpose, but all are time-consuming and require scanning of the fuel rod. Long-range guided wave inspection is a method for rapidly surveying a long length of pipe or tube for flaws from a single test location without scanning [3]. Now widely used for examining pipelines in processing plants, this method could be used for identifying individual fuel rods with through-wall flaws.

Inspecting fuel rods with guided wave technology requires addressing the following issues:

- Development of a small diameter (less than 5 mm) guided wave probe
- Development of a reliable probe coupling mechanism
- Development of a testing procedure allowing discrimination of rods having through-wall flaws from all the other rods
- Development of a probe positioning system

- Development of a data acquisition system capable of conducting rapid screening of an entire fuel assembly at a rate of 15 min/assembly
- Development of a method for deploying guided wave inspection without the need to disassemble the fuel assembly, or ideally, in place in the reactor

Prior to the investigation presented in this paper, preliminary work on fuel rod samples showed good potential for using a torsional mode guided wave inspection for screening the entire length of the rod [4]. In this paper, the results of the second phase of the project will be described. A new probe was developed, together with a novel method for probe coupling. Also, a multi-frequency inspection approach was applied, along with the advanced signal processing.

PROBE DESIGN

MsT technology was chosen as the basis for the inspection probe [5]. In an MsT probe, an excitation coil is wound around an iron cobalt (FeCo) strip; this produces time-varying magnetic fields in the circumferential direction of the strip, as illustrated in Figure 1. The FeCo strip generates torsional waves that are mechanically coupled through a protective outer coating to the waveguide connected to the fuel rod.

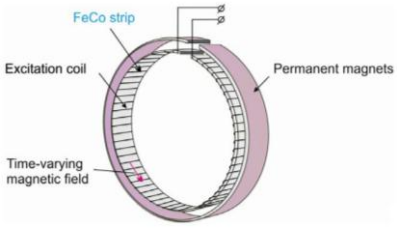

Figure 1. Configuration of MsT

There were a few reasons for the selection of the MsT-type probe. One was the ability of the MsT-type coil to introduce relatively high magnetization in the sensor strip, providing magnetostrictive strains up to 5 times that of conventional MsS sensors [6]. Another reason was the ability of the probe to generate high amplitude nonlinear harmonics utilized in signal processing [7]. The predominant effect allowing effective generation of the higher order harmonics is based on a relatively high strength magnetic field forcing the magnetic domains to rotate (in lower magnetic fields only the domain oscillation or movement of domain walls occurs). The domain rotation typically produces two cycles of magnetostrictive strains per cycle of input frequency. Compared to the testing when only one center frequency is utilized at a time (frequency sweep), simultaneous generation of several frequencies allows normalizing amplitude information more accurately since data over a range of frequencies are acquired simultaneously and no variations in coupling or rod temperature occur.

PROBE COUPLING

In order to minimize the size of the probe to meet the geometric constraints of the fuel rod assembly, a self-coupling waveguide was developed, as shown in Figure 2. A small axial force from a mechanical manipulator caused the waveguide to compress on the top surface of the fuel rod cap. This coupling provided for good signal strength and detection capabilities at a wide range of frequencies.

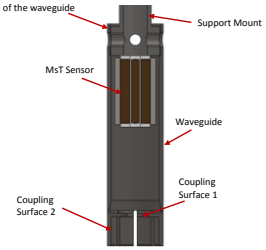

Figure 2. Schematic of the probe design and coupling concept

The MsT probe was positioned in the waveguide at a distance from the cut off end allowing constructive interference of waves traveling in the forward and the backward directions at discrete frequencies.

FUEL ROD SAMPLES & LAB SETUP

The MsT probe was tested on four empty fuel rods with simulated defects. Each rod contained a different type of defect – axial notch, circumferential notch, 45° notch, and volumetric flaw – in three different depths – 50% though-wall, 75% through-wall, and 100% through-wall. The defect layout is shown in Figures 3 and 4.

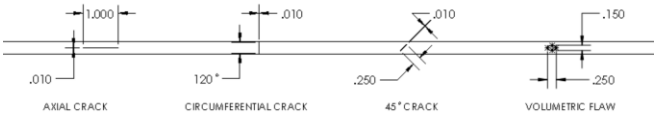

Figure 3. Sample defect sizes by type

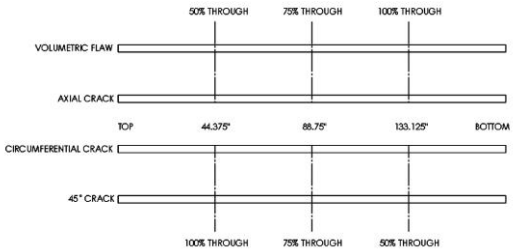

Figure 4. Defect layout in the four sample fuel rods

The system was first validated on a dry laboratory mockup. The sample fuel rods were mounted horizontally in spacer grids, and inspections were performed using a mechanical manipulator and remote camera system. The dry laboratory mockup is shown in Figure 5. The sample rods were moved to various positions in order to assess the effects of the spacer grids on defect detection signals.

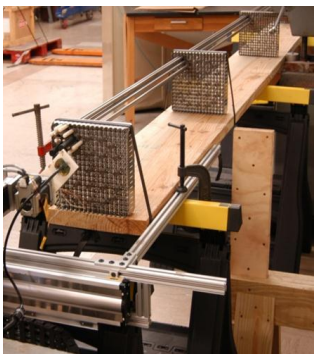

Figure 5. Dry laboratory test setup the fuel rod assembly in a horizontal orientation

After successfully completing the dry lab tests, the inspection system was taken to a water tank facility to be evaluated on the four sample fuel rods in conditions similar to field conditions. The rods with artificial defects were mounted vertically underwater in an assembly structure with defect-free empty fuel rods, grids, and control rods, as shown in Figure 6. As in the dry lab tests, the probe's defect detection capabilities were evaluated with the sample fuel rods in various positions.

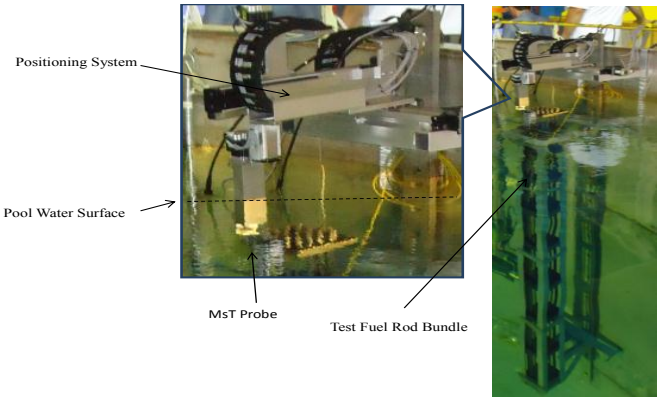

Figure 6. Overall water tank test setup

DATA COLLECTION & ANALYSIS

In the dry laboratory tests at 20 kHz, it was determined that an MsT probe allowed detection of all through-wall defects regardless of the type or placement of the defect. Grids and near through-wall (75% deep) flaws did not produce any significant indications. Dry laboratory data also showed that 200 kHz was the most effective frequency at which to locate the grids and other (75% and 50% through-wall) defects. Sample data obtained from the rod with axial flaws at 200 kHz (a) and 20 kHz (b) is shown in Figure 7.

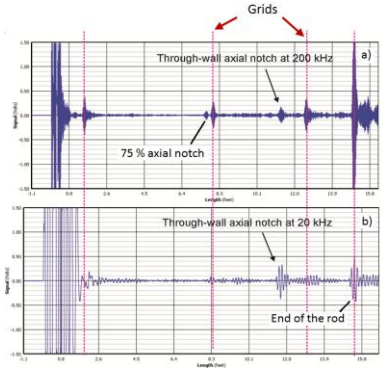

Figure 7. A-scan traces obtained from a sample rod with an axial notch at 200 kHz (a) and 20 kHz (b). The 100% through-wall defect is positively discriminated from grids and other defects.

For the simulated spent fuel pool tests, MsT inspections at 20 kHz and 200 kHz were initially targeted, but the results of the tests were inconclusive. It was found that a 20 kHz inspection was not sufficient to positively identify 100% through-wall defects. This was possibly due to tighter mechanical contact between the fuel rods and the grids, causing the guided wave energy to leak into the grids. In actual fuel bundles after a few years of operation, it is expected that the grids will be not be as tight due to vibration caused by water flow. The option of using 20 kHz frequency as a discriminator for through-wall anomalies may still be viable.

To continue testing of the supplied fuel assemblies, a wider range of frequencies was examined to positively identify 100% through-wall defects. A multi-frequency scan on each rod was performed in the range of 20 – 200 kHz, with an increment of 1 kHz. New target frequencies were identified that allowed the discrimination of through-wall anomalies based on amplitude criteria. These new target frequencies varied depending on the type of defect, as shown in Table 1.

Table 1. The frequency at which different types of through-wall defects are positively discriminated from spacer grids and other defect signals, using a multi-frequency approach.

Through-wall Flaw	Optimal Frequency
Volumetric	160 kHz
Axial	60 kHz
Circumferential	200 kHz
45° Flaw	200 kHz

This summary was made taking the multiple responses from the grids as a baseline noise floor level. The response from a through-wall anomaly was considered to be discriminated if its amplitude was at least 6 dB higher than the grid response or the response produced by near through-wall flaws. As shown in Table 1, each type of flaw was discriminated at a specific frequency. Also, a unique behavior was noticed with respect to the signal amplitudes as well as the signal's frequency content as a function of the flaw geometry during the frequency sweep. The behavior is believed to be related to a specific transfer function introduced by each type of flaws to a signal response. The understanding of the parameters of the transfer function should allow qualitative, and in some cases, quantitative explanations of the phenomena and how it can be utilized for enhanced flaw characterization.

NONLINEAR DEPENDENCE OF THE SIGNAL AMPLITUDE ON THE AXIAL EXTENT OF THE FLAW

As shown in Figure 3, four types of simulated flaws were examined in this research – a volumetric flaw, axial notch, circumferential notch, and 45° notch. The volumetric flaws and axial notches were of most interest due to their similarities to some of the most common defect mechanisms in fuel rods – grid-to-rod fretting and PCI cracks. Each different flaw type produced a specific backscattering signature.

Volumetric flaws in fuel rods typically have a specific shape resembling the shape of the supporting springs, with pronounced edges. The front and the rear edges of the flaw both produce guided wave responses that become superimposed. Figure 8 shows that the flaw response amplitude is strongly dependent on the ratio of the signal wavelength to the flaw length. This effect has been shown on tubing mockups in the past [7]. As long as the axial extent and the depth of the flaw allow the front and rear edge signals to interfere, either destructive or constructive interference may be observed in the response amplitude at discrete frequencies. Significant gain in the amplitude is expected when a near through-wall flaw becomes a 100% through-wall flaw. This effect occurs due to the interruption in propagating the reflection from the rear side of the opening. Total gain in the signal amplitude can be expected on the order of 12 dB (transition from point D to point E in Figure 8). This effect could be diminished if the guided wave reaches the rear edge of the flaw from the sides. This might be the case if the circumferential extent of the flaw is a small fraction of the wavelength. However, the volumetric flaw simulated in the sample rod for this research had a circumferential extent of approximately 25% of the wavelength.

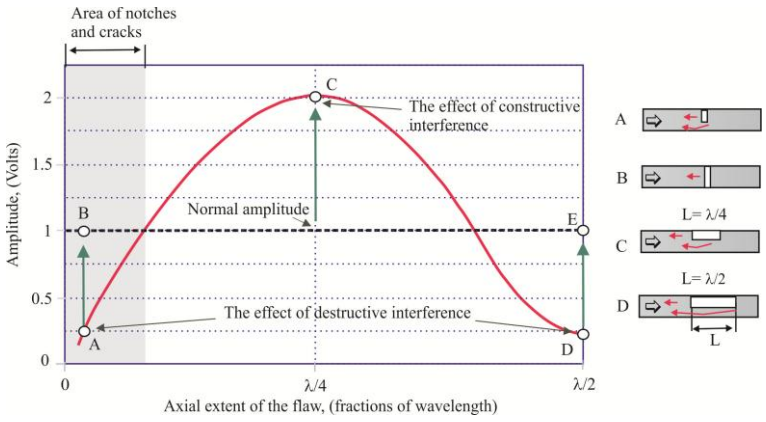

Figure 8. Simulated dependence of the signal amplitude on the axial extent of the flaw.

Axial notches represent a flaw with a near zero cross-section to the incident guided wave. Torsional mode guided waves produce a response from this type of flaw, which includes conversion of the fundamental T (0,1) mode to the SH (0,1) mode traveling around the rod circumference, followed by conversion of the SH (0,1) mode back to the T (0,1) mode [9]. Since the response is formed by a chain of mode conversion events, some discrete frequencies may affect the efficiency of this process. For the given rod dimensions, the highest signal amplitude for the axial through-wall notch was obtained in the range of 55 – 65 kHz, while responses for a near through-wall notch (75% deep) and a grid were more than 16 dB and 9 dB lower, respectively.

Circumferential notches have a very short axial extent, representing a small fraction of the wavelength, and causing the front and the rear side flaw responses to interfere destructively (point A in Figure 8). This is believed to be the reason why even a rather deep notch might produce a rather small response. On the other hand, when the notch is 100% through-wall, approximately 12 dB amplitude gain can be expected (transition from point A to B in Figure 8).

Backscattering from 45° notches was similar to the backscattering from the circumferential notch. In addition, this type of flaw produced pronounced, flexural vibrations that can be used for flaw characterization.

UNDERWATER TEST RESULTS

The goal of this testing was to create a more realistic situation with the probe operation and the probe coupling under water. Since fundamental torsional mode guided waves T (0,1) do not couple with water, no changes in performance were expected as compared to the dry test. As stated above, however, the grid springs used for this testing were much tighter than those used in the dry lab test. Figure 9 shows an A-scan trace obtained from the rod without defects at 200 kHz after distance amplitude correction at a rate of 1.2 dB/m was applied. The amplitude of the grid responses, marked with the red dotted line, was taken as the baseline noise floor level for further tests.

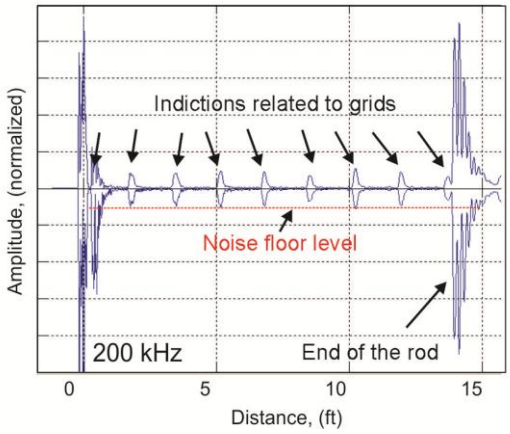

Figure 9. A-scan trace obtained from the rod without defects at 200 kHz after distance attenuation correction at a rate 1.2 dB/m was applied

Figure 10 shows four A-scan traces obtained from the rods with a volumetric flaw: (a) axial notch, (b) circumferential notch, (c) and 45° notch, using 160, 60, 200, and 200 kHz, accordingly. Each rod was inspected twice: first with grids placed near the through-wall defect (Test 1) and then with grids placed on top of the through-wall defects (Test 2). The data acquired during Test 1 are rectified positive and the data acquired during Test 2 are rectified negative on all four pictures. This was done to evaluate the effect of interference between the indications produced by grids and the indications produced by flaws.

Indications produced by through-wall flaws as well as indications produced by near through-wall flaws are shown with arrows. As shown in the data, all four through-wall anomalies produced indications 6 – 9 dB higher in amplitude compared to the noise floor level determined by the amplitude of the gird indications. It should also be noticed that near through-wall (75% deep) flaws produced responses either lower or only slightly higher (75% circumferential notch on C) in amplitude compared to the noise floor level.

Considering the applied amplitude-frequency criteria, the multi-frequency inspection approach correctly distinguished the 100% through-wall flaws in both locations – in the free span and underneath the grids.

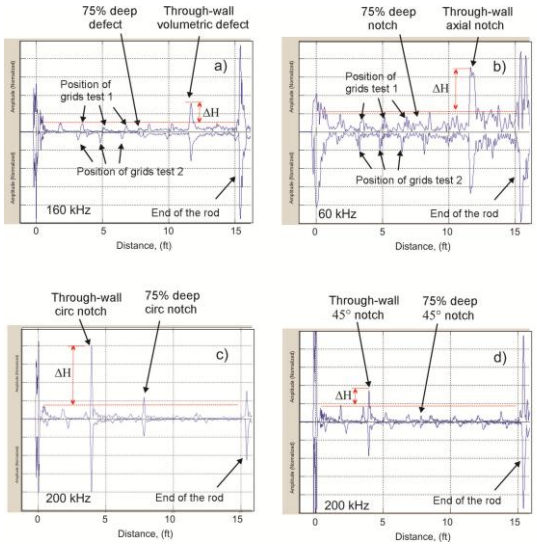

Figure 10. A-scan traces obtained from the rods with (a) volumetric flaw, (b) axial notch, (c) circumferential notch, and (d) 45° notch, using 160, 60, 200, and 200 kHz, accordingly

SUMMARY

A prototype MsT guided wave fuel rod inspection system was developed to inspect individual fuel rods in an assembly for 100% through-wall defects. In a dry laboratory environment, a two-frequency inspection was adequate to positively discriminate all 100% through-wall defects, regardless of their type and location. However, conditions in the simulated spent fuel pool tests were different, prompting a multi-frequency approach to identifying the same defects.

This project is ongoing, and further evaluation of the system on more realistic full assembly mockups is planned. Also, further research and development is recommended to understand the detailed interaction mechanisms of guided waves with flaws of different types and sizes in order to improve flaw characterization.

REFERENCES

1. B. Tompkins, “Advancing the cause of fuel reliability,” Nuclear News, June 2008, pp. 34-37.
2. Frequently asked questions; Fuel Reliability Guidelines, Electric Power Research Institute, 2008.
3. H. Kwun, S. Y. Kim, and G. M. Light, “The Magnetostrictive Sensor Technology for Long-Range Guided-Wave Testing and Monitoring of Structures,” Material Evaluation 61, pp. 80–84 (2003).
4. H. Kwun, E.V. Mader, K.J. Krzywosz, Guided wave inspection of nuclear fuel rods. NDT.net, 2010
5. S. Vinogradov, "Magnetostrictive Transducer for Torsional Mode Guided Wave in Pipes and Plates," Materials Evaluation, Vol. 67, N 3, 2009, pp. 333–341.
6. Vinogradov, S., Kwun, H., Light, G., Wagar, D., “Applications of MsT Probes for Guided Wave Testing of Components,” Spring ASNT Conference 2012.
7. S. Vinogradov, “Development of Enhanced Guided Wave Screening Using Broadband Magnetostrictive Transducer and Nonlinear Signal Processing ,” Fourth Japan-US Symposium on Emerging NDE Capabilities for a Safer World, Maui Island, Hawaii, USA, June 7-11, 2010.
8. H. Kwun, S. Y. Kim, H. Matsumoto, and S. Vinogradov, “Detection of Axial Cracks in Tube and Pipe Using Torsional Guided Waves,” Review of Progress in Quantitative Nondestructive Evaluation, Vol.27A, pp. 193-199 (2008, American Institute of Physics).

EXPERIMENTAL AND ANALYTICAL EVIDENCE OF USING NONLINEAR ULTRASONIC TESTING TO MONITOR RADIATION DAMAGE

K. H. Matlack, J. Kin, L. J. Jacobs, Georgia Institute of Technology, USA
J. J. Wall, EPRI, USA
J. Qu, Northwestern University, USA

Abstract

Radiation damage occurs in reactor pressure vessel steels, causing microstructural changes that lead to embrittlement and/or stress corrosion cracking. Many nuclear reactors throughout the US have entered a period of licence renewal, meaning reactor components will be exposed to higher levels of neutron fluence than was originally anticipated. An NDE technique to monitor radiation damage in the reactor pressure vessel could provide quantitative for the technical basis for long term operation of nuclear reactors. Nonlinear ultrasonic testing is known to be sensitive to microstructural changes in metallic materials, and has recently been shown to be sensitive to microstructural changes that occur throughout radiation damage in ferritic steels, such as precipitate and cluster formation, and changes in dislocation density. Recent experimental results are presented that show the trend of the acoustic nonlinearity parameter over various irradiation conditions on reactor pressure vessel steel material. An analytical model is presented to interpret these results in terms of irradiation-induced microstructural features. This model and its verification can be used to predict the sensitivity of nonlinear ultrasonic techniques to radiation damage in other RPV steels under different irradiation conditions.

Keywords: Material characterization

DEVELOPMENT AND DEPLOYMENT OF BOTTOM MOUNTED INSTRUMENTATION (BMI) NOZZLE INSPECTION

O. Burat, M. Taglione, F. Jacquinot, AREVA, France
C. Gibert, EDF - CEIDRE, France

ABSTRACT

This paper deals with the recent developments, the qualification and the first deployments of the new BMI (Bottom Mounted Instrumentation) Nozzles Inspection Solutions for the French 900, 1300 MWe and N4 NPP (Nuclear Power Plants). AREVA had performed the first Inspection of the BMI Nozzles in 1993, but this was improved with a first RSEM qualification (2005) and after a new call to tender by EDF, in 2009: EDF decided to increase their inspection program through 2016.
Most BMI nozzles are made of 600 alloy material which is susceptible to SCC (Stress Corrosion Cracking). Qualified UT (Ultrasonic Testing) by TOFD (Time Of Flight Diffraction) methods allow detecting these cracks, including the nozzle to weld interface examination. This RSEM qualified Inspection includes additional control by ID 0° LW (Longitudinal Waves) UT coupled with VT (Visual Inspection), for both the nozzle ID and OD surface.

1. INTRODUCTION

In the context of ageing and life extension of the NPP, Inconel 600 components and alloy 182 weld material require particular attention, due to its susceptibility to SCC (Stress Corrosion Cracking). This has been known since the 1980s. As early as 1993, AREVA has performed In Service Inspection (ISI) of the Inconel 600 Bottom Mounted Instrumentation (BMI) Nozzles for EDF French 900, 1300 MWe and N4 Nuclear Power Plants (NPP). In this paper, we present firstly the component to be inspected, followed by the history of this inspection, a description of the latest requirements from EDF, the NDT methods developed and the equipment deployed to achieve the new target inspection, then lastly, we show the performance of the qualified process and tooling associated with Inspection Implementation.

2. BMI NOZZLE

A Bottom Mounted Instrumentation nozzle is a tube welded into the reactor vessel bottom. Its role is to allow the introduction of nuclear instrumentation into the core of the reactor. A leak in the BMI tube or J-weld constitutes a break of the primary coolant system. Fifty BMI nozzles are typically welded at the bottom of the vessel for a 900MWe unit and there are 58 for a 1300MWe unit. Inspection of the BMI nozzle is performed from inside the vessel and it requires removing the Reactor Pressure Vessel (RPV) Internals (Figure 1).

Figure 1 : BMI Forest, with internals removed

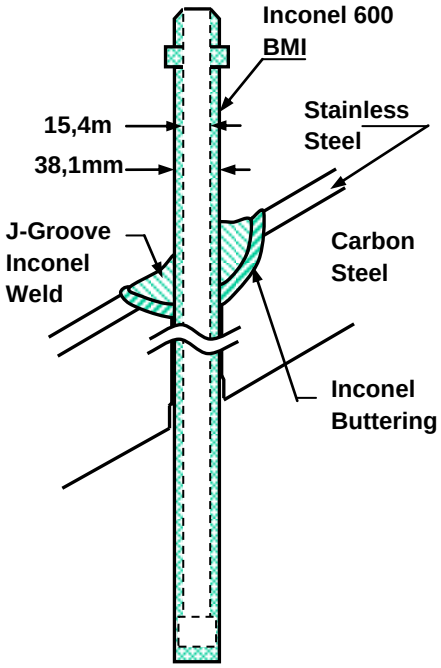

Figure 2 : BMI Nozzle configuration

The union between the bottom of the vessel (16MND5 carbon steel, with a 308 or 309 stainless steel cladding added) and the BMI Nozzle (Inconel 600) is formed by a buttering and a J-groove weld (alloy 182) (Figure 2).

3. HISTORY

Starting in 1993, EDF began to require ISI of these components and AREVA has inspected about 2 plants per year until 2011. In United States, a first inspection (including nozzles and J-welds) and repair was performed in 2003, due to a leak of 2 BMIs in the South Texas Nuclear Station [1, 2]. After an RSEM qualification in 2005, EDF decided (in 2009) to increase inspection program of BMI Nozzles for 900, 1300 MWe and N4 NPPs through 2016, with a second RSEM qualification. In 2011, an indication was discovered in Gravelines [3]. This prompted the qualification completed in January 2013. This improved inspection has been deployed on six RPV and is planned to be implemented on three additional RPVs before the end of 2013.

4. INSPECTION REQUIREMENTS

The areas to be examined are:

- The entire wall thickness of the nozzle base metal.
- The interface base metal / weld.

The examination doesn't include the volume of the weld.

The axial extend of the examination volume, defined in Figure 3 is as follows:

- On the nozzle tube inner wall, the area extending from 15mm above the high point of the weld to 50mm below the low point of the weld.

- On the nozzle tube outer wall, the area following the profile of the weld, including a band between 15mm above the high profile (transition radius) and 15mm below the low profile of the weld.

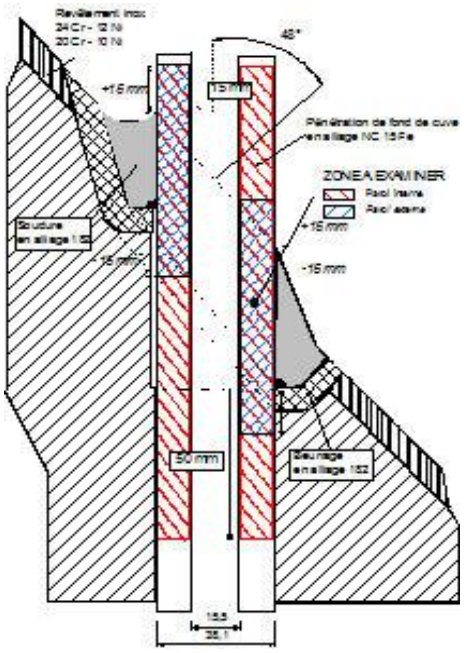

Figure 3 : Zones of the nozzle to be examined

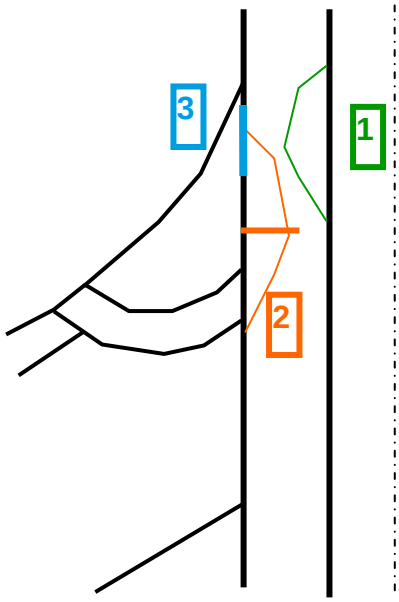

Figure 4 : Researched defects

The defects to be detected (Figure 4) in the base metal are :

- Internal Longitudinal (IL) Stress Corrosion Cracks (SCC), deeper than (or equal to) 3 mm with a length more than (or equal to) 10 mm (1).
- External Longitudinal (EL) and Circumferential (EC) SCC, deeper than (or equal to) 4 mm with a length more than (or equal) 10 mm (2).
- A complementary inspection is made at the level of the interface base metal to the weld (3), if one of the following defects is found :
- Longitudinal SCC started on the ID, deeper than (or equal to) 7 mm with a length more than (or equal to) 10 mm.
- Longitudinal or circumferential SCC started at the OD, deeper than (or equal to) 4 mm with a length more than (or equal to) 10 mm.

5. NDT METHODS

Two steps of inspection are deployed:

- A basic and systematic inspection of each nozzle, considered RSEM. This step is led by UT Time Of Flight Diffraction (TOFD) – Longitudinal (L), whose objective is to detect SCC in the base metal of the nozzle.
- A complementary inspection, depending on the basic inspection results. This step is led with :
  - UT TOFD - Longitudinal and Circumferential (C) probe, (this complementary inspection is also considered RSEM),
  - Plus a 0° UT Longitudinal wave probe,
  - Plus a Visual Testing (VT) probe, after brushing to remove surface deposits inside the nozzle,
  - Plus an external VT probe.

The UT TOFD technique overview is described in Figure 5 : Without a defect (or with an external defect), this technique shows a continuous echo (lateral wave – 1). Faced with a crack, the UT beam is diffracted by the tip of the crack and some of this diffracted energy returns to UT receiving transducers (2). The UT wave Time Of Flight (TOF) is linked with the depth of this defect.

A second continuous echo (backwall echo - 3) is present, only interrupted by an external defect or the base metal – weld interface.

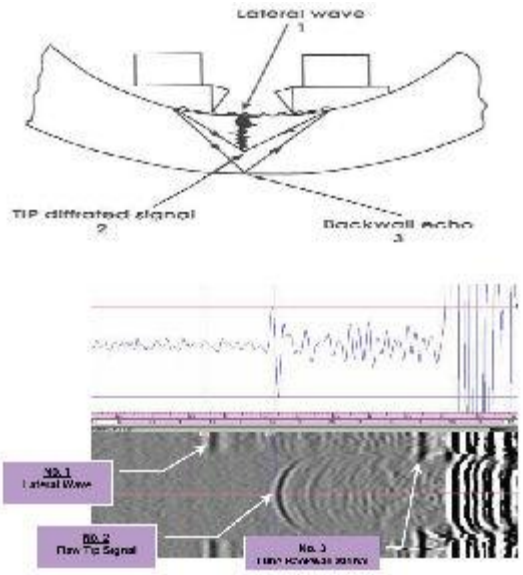

Figure 5 : UT TOFD Technique Overview

Figure 6–a: UT TOFD L and C Probes

Figure 6-b: 0°LW UT probe

- The two types of UT TOFD probes developed for the BMI nozzles inspection are shown in Figure 6-a. For the UT TOFD – L probe, orientation of the two sensitive crystals is fit to characterize axial flaws while the orientation for the UT TOFD C probe is fit to characterize circumferential flaws.
- 0° Longitudinal Waves (0°LW) presented in Figure 6–b is designed for weld profiling and characterization of Lack Of weld Fusion (LOF) at the base metal to weld interface (such functionalities are also provided by the two UT TOFD probes).
- VT inspection is used to improve the diagnosis, when a surface indication is detected, and/or to complement the exam where disturbances like surface damage surface or acoustic noise preclude clear interpretation of the UT signals.

6. EQUIPMENT DEVELOPED AND DEPLOYED

Besides the UT and the VT probes described above, the deployed equipment includes:

- The manipulator ‘’OBTEUS’’ (see Figure 7), for the Inner Diameter (ID) inspection includes both UT and VT sensors. The manipulator ensures coordinated rotation and translation movement of the UT transducer and optimized positioning of the VT equipment inside the nozzle.
- The manipulator ‘’OTEVEX’’ (see Figure 8) has been developed for OD visual inspection. It allows VT equipment positioning outside of the BMI Nozzle.

  It can be noted that these manipulators are qualified for Foreign Material Exclusion (FME).
- Other supporting equipment is linked to the tool via a cable bundle and is positioned on the floor reactor cavity. These equipment include :
  - the carrier OBTEUS remote control,
  - the UT acquisition hardware (Z-scan from ZETEC), associated with a PC containing the qualified UT software – Ultravision,
  - forty meter cable bundle linking equipment operating in the vessel and these OBTEUS remote controllers and UT acquisition hardware / software.

Figure 7 : Manipulator ''OBTEUS"

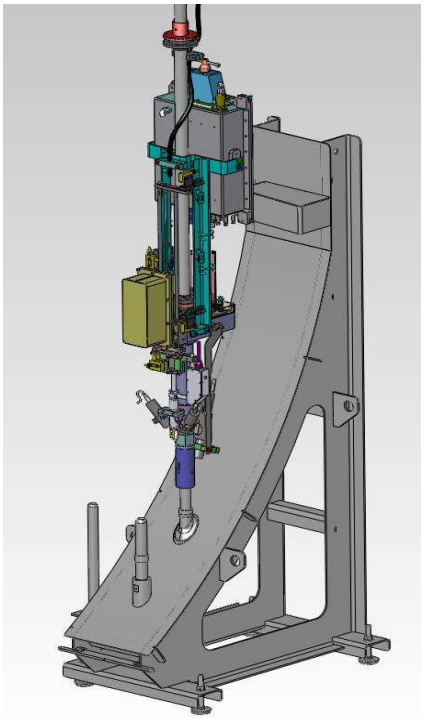

Figure 8 : Manipulator ''OTEVEX"

7. QUALIFICATION PROCESS

The RSEM qualification objectives are to :

- Check accessibility of every BMI Nozzle, whatever its position in the bottom of the RPV.
- Confirm UT data quality to allow a clear diagnosis, considering the health of the inspected BMI nozzle.
- Check NDT performances in term of detection / characterization.
- Confirm repeatability and reproducibility of NDT results.
- Validate the inspection duration (inspection rate for basic UT inspection).

7.1. Qualification Principle

This qualification principle is to show and justify the performances of :

- The base metal inspection, on the one hand.
- The complementary interface base metal / weld inspection on the other hand.

Base metal inspection includes area coverage, SCC detection (see §4), location, depth and length measurement, while complementary interface inspection concerns area coverage, detection, location, surface measurement and weld profile definition.
These performances have been evaluated in two conditions:

- Best case performances considering a "perfect and ideal" environment.
- Reliability and reproducibility performances taking into account the presence of complicating parameters (CP) considering the component (including nozzle distortion and rough surface conditions), the equipment deployed (ex. : UT probes and manipulator characteristics), extending to the specific type of Stress Corrosion Cracks (ex. : morphology, ID/OD wall initiation, etc).

To supply these two conditions, a series of mock-ups (without and with CP) was defined and manufactured. Reflectors representative of targeted flaws were implanted in these samples. Performance evaluations of the techniques described above have been achieved based on experimental testing (see Figure 9, examples of experimental test results that are exploited for detection and characterization of external notches detected with the UT TOFD – L probe).

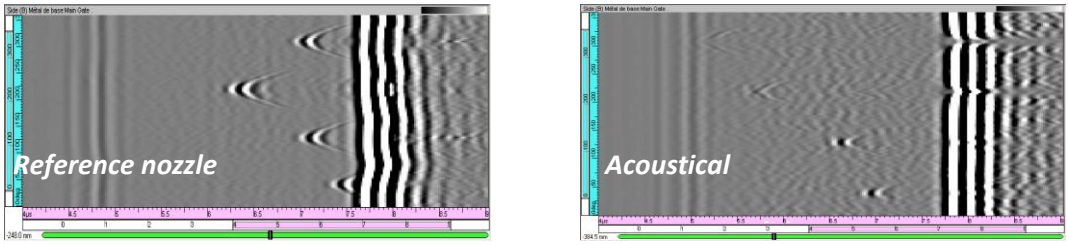

Figure 9 : B scan cartography of external notches

To improve the experimental validation, inspection models using CIVA software were developed to predict the UT performance allowing detectability to be inferred based on a limited number of implanted sample flaws. An example of the UT TOFD signal taking the expected morphology of a reflector into account is shown in Figure 10.

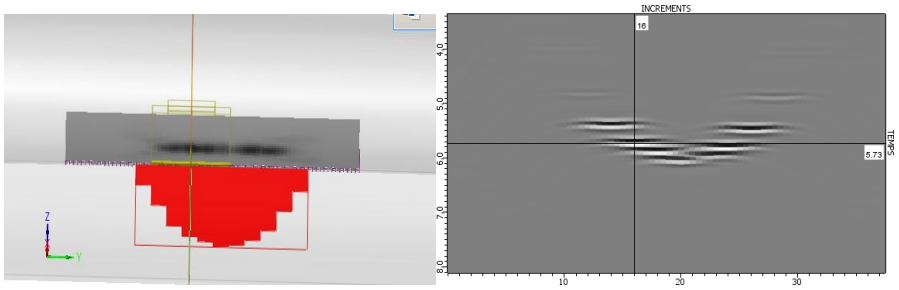

Figure 10 : CIVA modeling configuration and D scan result

7.2. Qualified UT Performances

Considering the inspection requirements (described in §4), the qualified UT performances (including the contribution of every complicating parameters) are the following :

- Area coverage is in accordance with the requirement, excepted for some nozzles of the N4 PWR, for which the area extension is limited to 10mm below the low point of the weld,
- Base Metal Stress Corrosion Cracks (SCC) to be detected, that's to say :
  - Internal Longitudinal (IL) SCC (ID SCC) deeper than (or equal to) 3 mm with a length more than (or equal to) 10 mm,
  - External Longitudinal (IL) and Circumferential (IC) SCC (OD SCC) deeper than (or equal to) 4 mm with a length more than (or equal to) 10 mm,

  can be detected,

- Base Metal SCC detected can be sized, if their depth are between :
  - 3 and 9 mm, for ID SCC
  - 4 and 8 mm for OD SCC.

  Deeper SCC are said to be potentially crossed SCC

Depth and Length and locating SCC accuracies are given in the table below. These are systematically better than accuracies that are required.

Type of defect	Height Accuracy	Length Accuracy (mm)	Longitudinal Location	Azimut Location
Inspection Requirements	±1,5 mm	±5 mm	±5 mm	+/-30°
ID Long SCC	±0,50 mm	-2.5 mm / +3 mm	±2 mm	+/-15°
OD Long SCC	±0,50 mm	-0.5 mm / +5 mm	±2 mm	+/-15°
OD Circ SCC	±0,50 mm	-1.5 / +3 mm	±2 mm	+/-15°

Table 1 : Height, Length and Location accuracies of SCC detected (requirements and performances)

- Interface flaws to be detected and sized (diameter more than (or equal to) 3 mm) can be detected and sized,
- Interface flaws surface sizing accuracy is -0/+1,5 mm; Required surface sizing was -0,5/+1,0 mm.

8. INSPECTION IMPLEMENTATION

The equipment implementation conditions during an inspection includes the following :

- The pool is full during the inspection. The water is necessary to shield bridge workers from high levels of radiation inside the vessel.
- The refueling machine is used during the operation of installation (see Figure 11).
- Once the appropriate probe is attached to the tool and placed in-line with the calibration nozzle, the manipulator is lowered into the reactor vessel cavity and positioned on the nozzle to be inspected. With the help of a funnel, it is centered (to ensure the proper alignment for the probe to be inserted without damaging the nozzle) and fixed to this nozzle.
- For each UT probe, the initial tool setup requires calibration of the tool motors and encoders.
- The UT probe is then driven down to the designated start position. Once in position, the examination begins by a continuous helical rotation movement of the UT probe.

The UT calibration standard is ultrasonically scanned as the probe exits the top of each BMI nozzle.

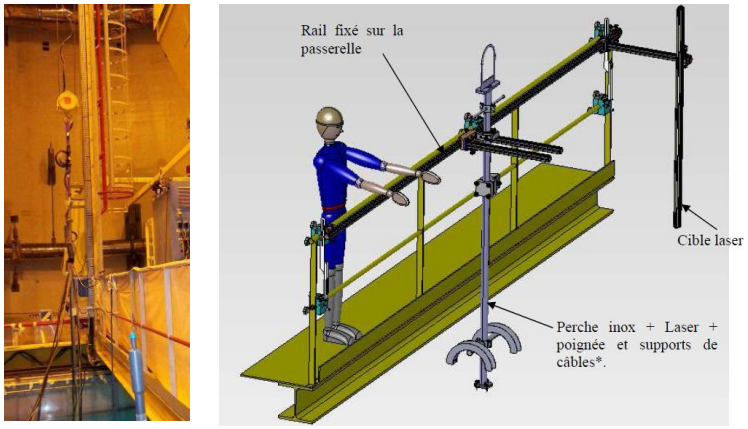

Figure 11 : Use of the refueling machine during the inspection operation

The duration of a vessel bottom inspection is approximately 112 hours as broken down below:

- Installation of the equipment in the reactor building (24h).
- Inspection duration (56h), including :
  - initialization in reactor vessel,

- UT examination,
- withdrawal of the equipment from the reactor vessel (including a vessel bottom VT inspection).

- Removal (32h), including decontamination and packing.

9. INSPECTION EVOLUTION

AREVA NDE Solutions has already performed six inspections following the RSEM Qualification, which was obtained in January 2013. The main milestone events for these inspections are :

- The implementation with the first set of equipment by INTERCONTROLE - AREVA NDE - Solutions at Tricastin 2 in March 2013.
- The use of second equipment at BUGEY 3, deployed in June 2013.
- After six inspections already achieved, three more are planned before the end of this year.
- Third equipment is expected to be qualified by EDF for 2014. It will allow AREVA to make three simultaneous operations.

REFERENCES

[1] NRC Bulletin 2003-02 - NUREG 1863, Leakage from Reactor Pressure Vessel Lower Head - Penetrations and Reactor Coolant Pressure Boundary Integrity, August 23, 2003, OMB control No: 3150-0012

[2] Inspection Technology for BMI Penetrations (M.S. Lashley, South Texas Project, S. W. Glass and R.F. Cole, Framatome ANP Inc.) – Conference on Vessel Penetration Inspection, Crack Growth and Repair - Washington Center Gaithersburg, MD (September 29 – October 2, 2003)

[3] Note d'information de l'ASN (20/12/2011), concernant la Réparation de défauts détectés dans une PFC du réacteur de Gravelines 1

A COMPUTERIZED SYSTEM FOR THE ADVANCED INSPECTION OF REACTOR VESSEL STUDS AND NUTS BY COMBINED MULTI-FREQUENCY EDDY CURRENT AND ULTRASONIC TECHNIQUE

W. Kelb, KontrollTechnik, Germany
J. M. Sarteel, CapTech, France
R. Leriche, CEGELEC NDT, France

Introduction

Studs and nuts of reactor vessels have to be examined periodically by non-destructive techniques. The requirements according to ENIQ or RSEM lead to improved demands regarding examination and consideration of influent parameters, accuracy in determination of the defect lengths, the axial and circumferential positions of indications as well as the reproducibility of the inspection result. With the newly developed computerized scanning system both eddy current as well as ultrasonic technique can be applied to the inspection of both studs and nuts. All scanning procedures are pre-programmed ensuring a maximum possible accuracy for determination of the indication position and a maximum in reproducibility of the inspection result especially for testing of complex geometric areas like the transition zones from the threads to the shaft. Due to their long lifetime, bolts and nuts show in many cases a high quantity of mechanical imperfections like dents, scratches, missing material, corrosion, etc. leading to extensive signal analysis and documentation work. Particularly for the eddy current testing the probe guiding was heavily improved in order to achieve a high signal to noise ratio and preventing multiple indications from imperfections allowing automatic signal evaluation techniques. Additionally the automatic data analysis software allows the fast, safe and uncomplicated evaluation of indications and direct result storage including all relevant signal and position data to the indication list. The overall concept and operation of the system and examples of results from qualification and practical inspections are presented.

Requirements to stud and nut inspection systems

The requirements of e.g. ENIQ, RSEM, KTA certifications regarding detection capacity, defect length determination, accuracy, etc. led to improvements of the entire testing systems for studs and nuts. Figure 1 shows the main requirements and the influenced part of the testing system.

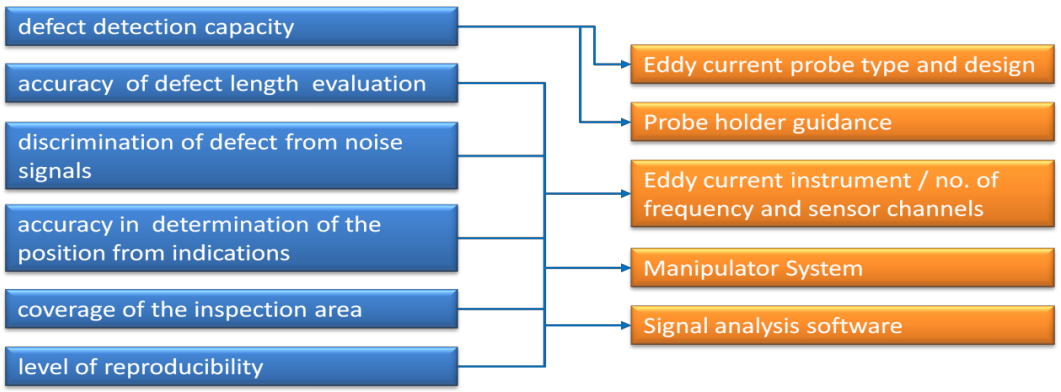

Fig. 1:Main requirements to the testing system by ENIQ, RSEM, KTA certifications

Evolution of stud and nut testing systems

Kontrolltechnik GmbH is working in the development of mechanized inspection systems for reactor stud and nut inspections as well as in the execution of inspection services for several years. Within this period the functionality and size of the manipulator systems, the sensor technique as well as the signal analysis software were subject to permanent improvements. Figure 2 shows the evolution of the testing system representative for the manipulators.

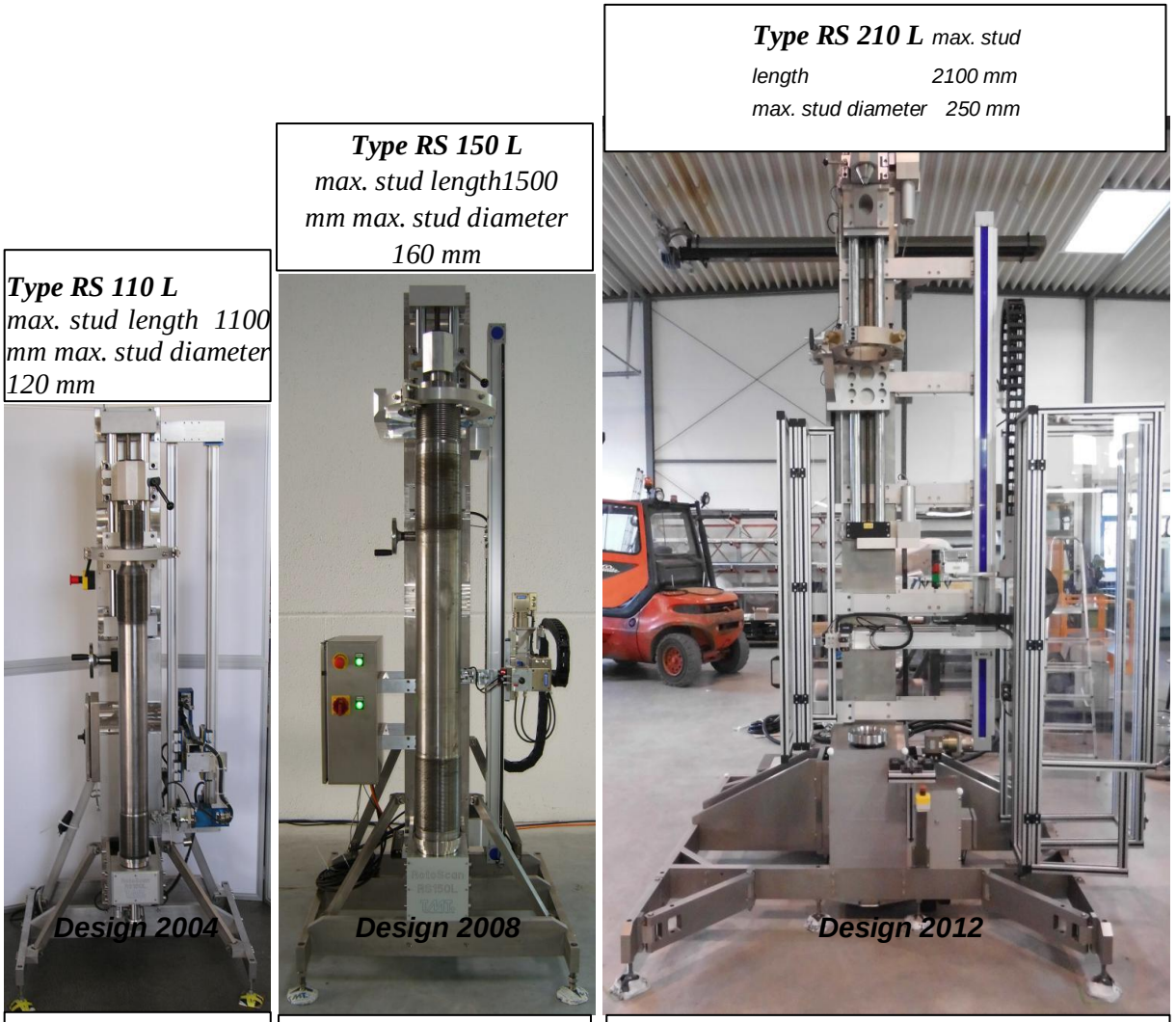

Fig. 2: Evolution of manipulator systems for the inspection of reactor studs and nuts

Function and Features of the Manipulator Type RS 210 L

The stud and nut testing manipulator Type RS 210 L is the latest design. From its dimensions the manipulator is constructed to test studs of the EPR reactor, which are currently the longest in place. Figure 3 shows the main functions and features of the manipulator type RS 210 L. The concept of the manipulator took into consideration that besides the requirements in accuracy and reproducibility, the studs can be installed in an easy, time effective and safe manner. By the safety cabinet and several emergency stop switches all requirements concerning human safety are ensured. Additionally the functionality of the RS 210 L type manipulator took into consideration the minimization of human errors in operation of the unit.

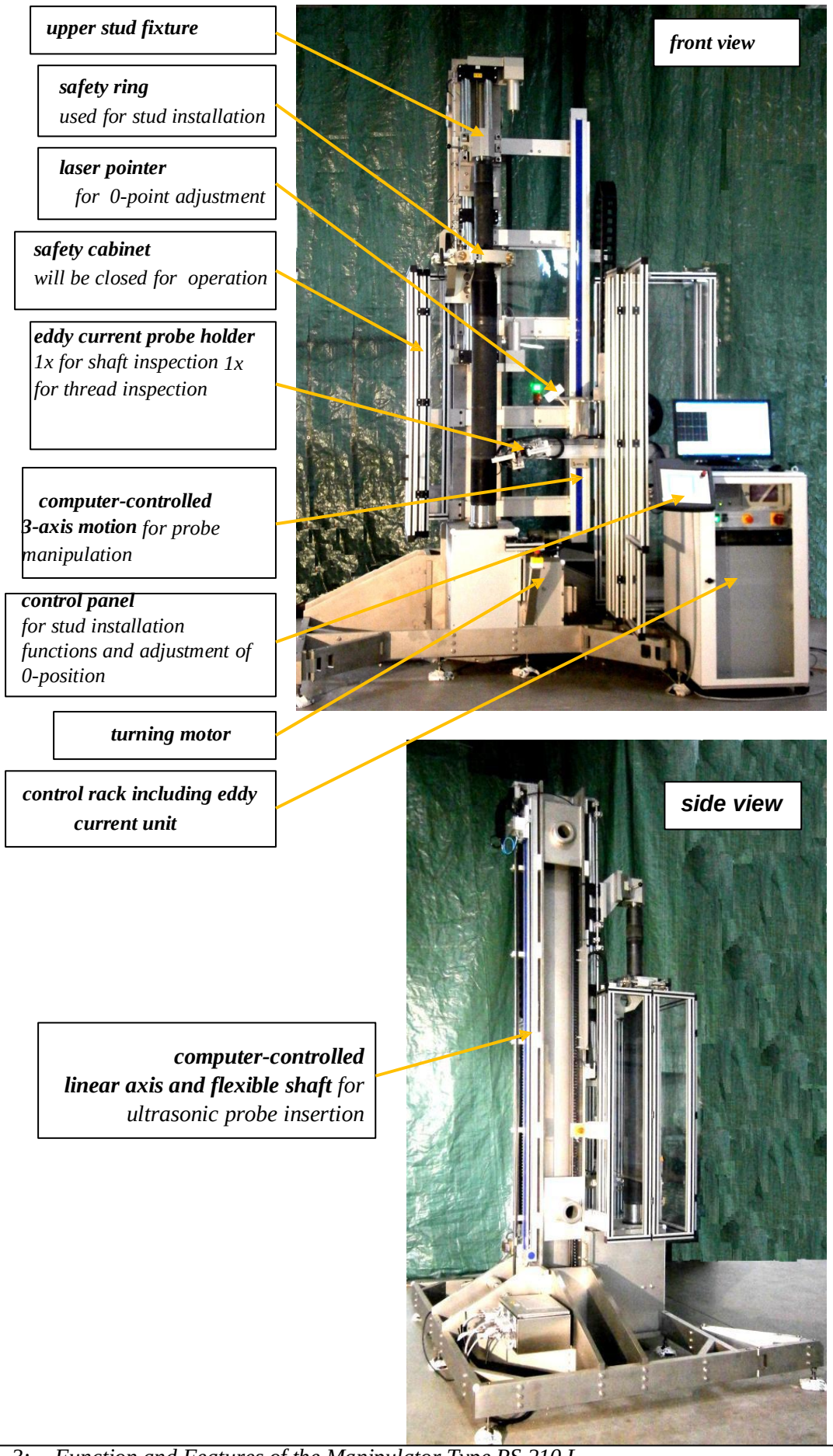

Fig. 3: Function and Features of the Manipulator Type RS 210 L

While the previous manipulator types are designed for eddy current testing only, the type RS 210 L includes an additional ultrasonic testing facility through the bore of the stud. The ultrasonic probe is connected to a flexible shaft positioned at the rear side of the manipulator. The flexible shaft will be pushed into the bore of the stud via a roller guiding as shown in figure 4.

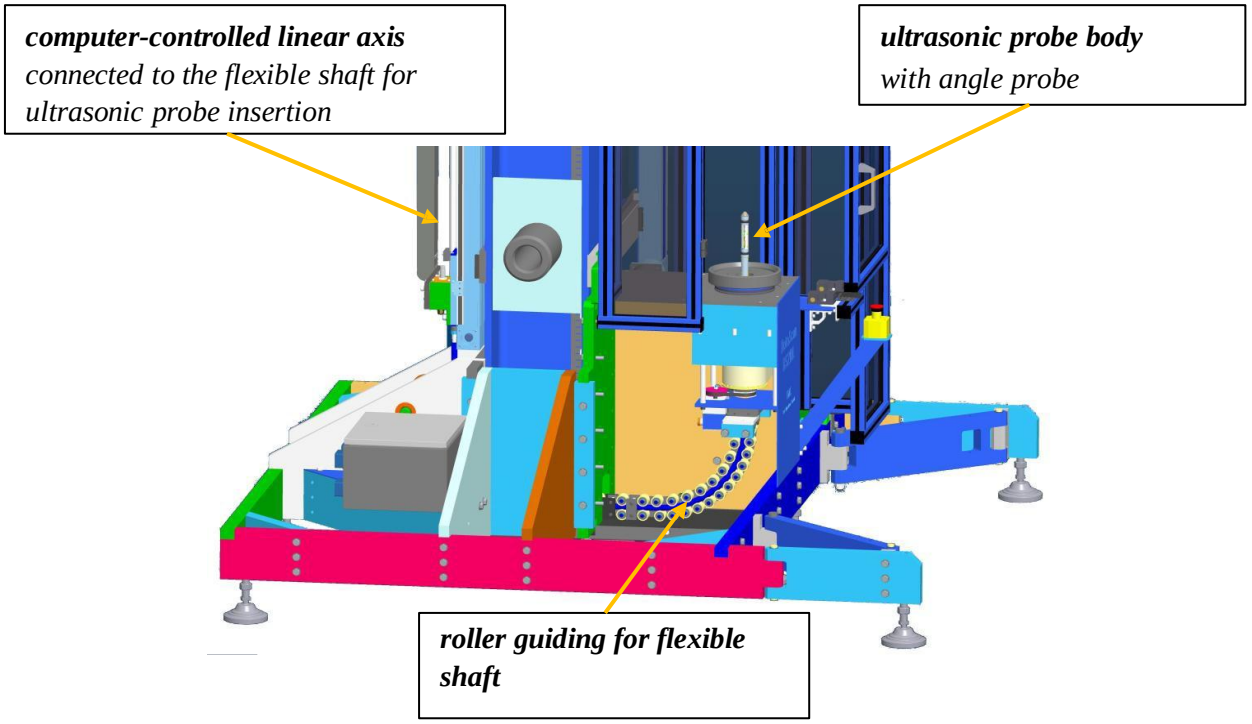

Fig. 4: Connection of the ultrasonic probe in the manipulator type RS 210 L

Installation and adjustment of studs

In general the studs are provided in upright position placed in a transport cradle. For installations into the manipulator the studs are lifted out of the cradle and can be directly placed into the adapter piece (figure 5 and figure 6).

Fig. 5:stud lifted out of the transport cradle

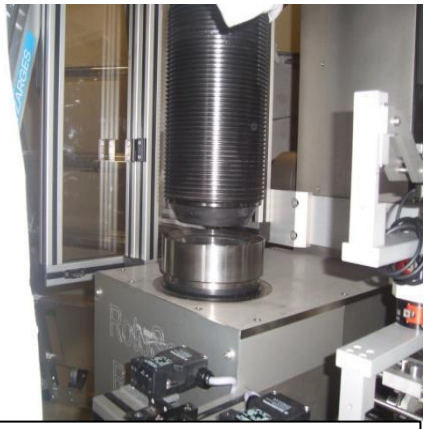

Fig. 6:stud placed into the adapter piece

Once the stud is placed in the adapter piece it has to be secured against falling over. Therefore the safety ring will be closed, and the eye bolt at the top of the stud can be unscrewed. Afterwards the upper bolt fixture will be driven down to fix the stud (figure 7).

Fig. 7:stud placed in the anipulator secured by the safety ring

The stud is now ready to be turned into the 0-position. Depending on definition, the 0-position can be either a special marking on the stud or the start of the thread. For 0-position alignment, a laser pointer is used, which can be fixed either to the sensor arm or to the upper bolt fixture (figure 8). The bolt will be turned using the control panel until the laser is aligned with the defined 0-position and the encoder is set to zero.

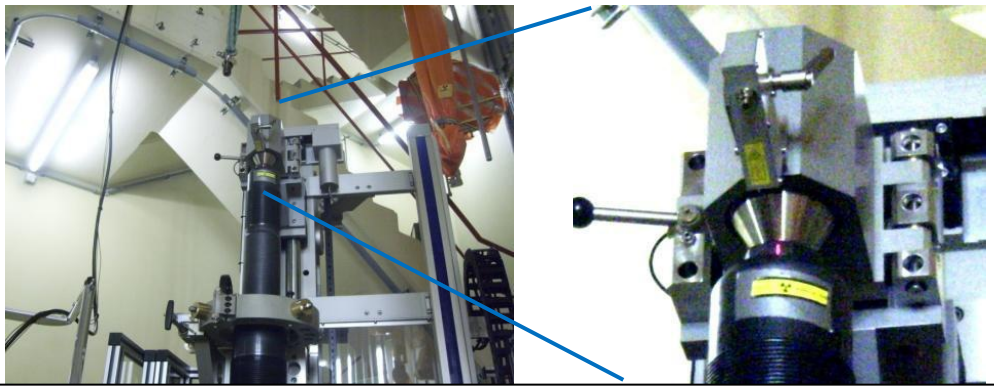

Fig. 8: Application of the laser pointer for 0-position alignment

The eddyMax – RotoMax data acquisition software

The eddyMax – RotoMax data acquisition software combines the signal data acquisition, signal display in different modes and control of the manipulator. Figure 9 shows the screen display and functions.

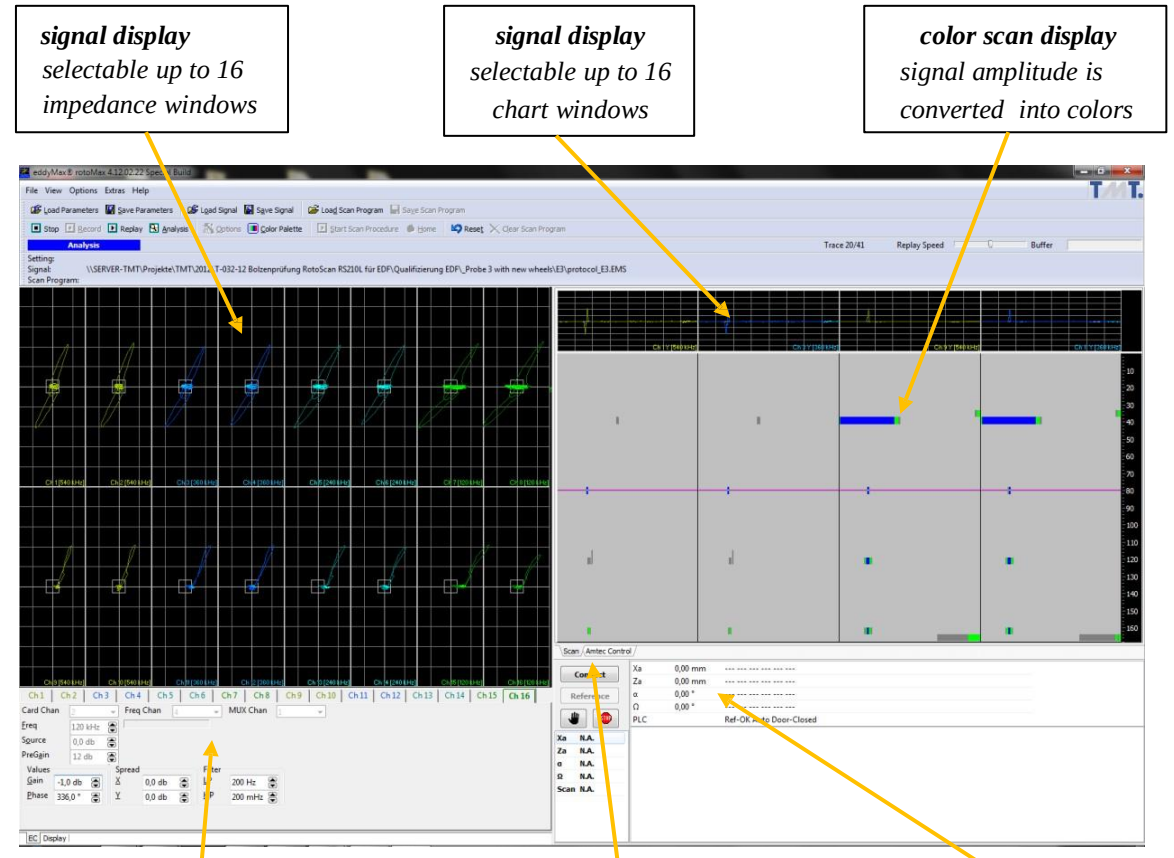

Fig. 9: Screenshot of the eddyMax RotoMax data acquisition software, with display in scan mode

The testing multi-frequency mode is necessary for signal phase discrimination of defect signals from noise signal caused e.g. by mechanical damage or corrosion. All signal data are stored inclusive the entire parameter setting. By the toggle the operator can switch between the signal chart display and the manipulator control window. The manipulator control window shows the active scanning procedure and allows manual manipulator control as well as generation of scanning procedures by teach-in or keyboard input. Figure 10 shows the screenshot of the RotoMax software toggled to the manipulator control window.

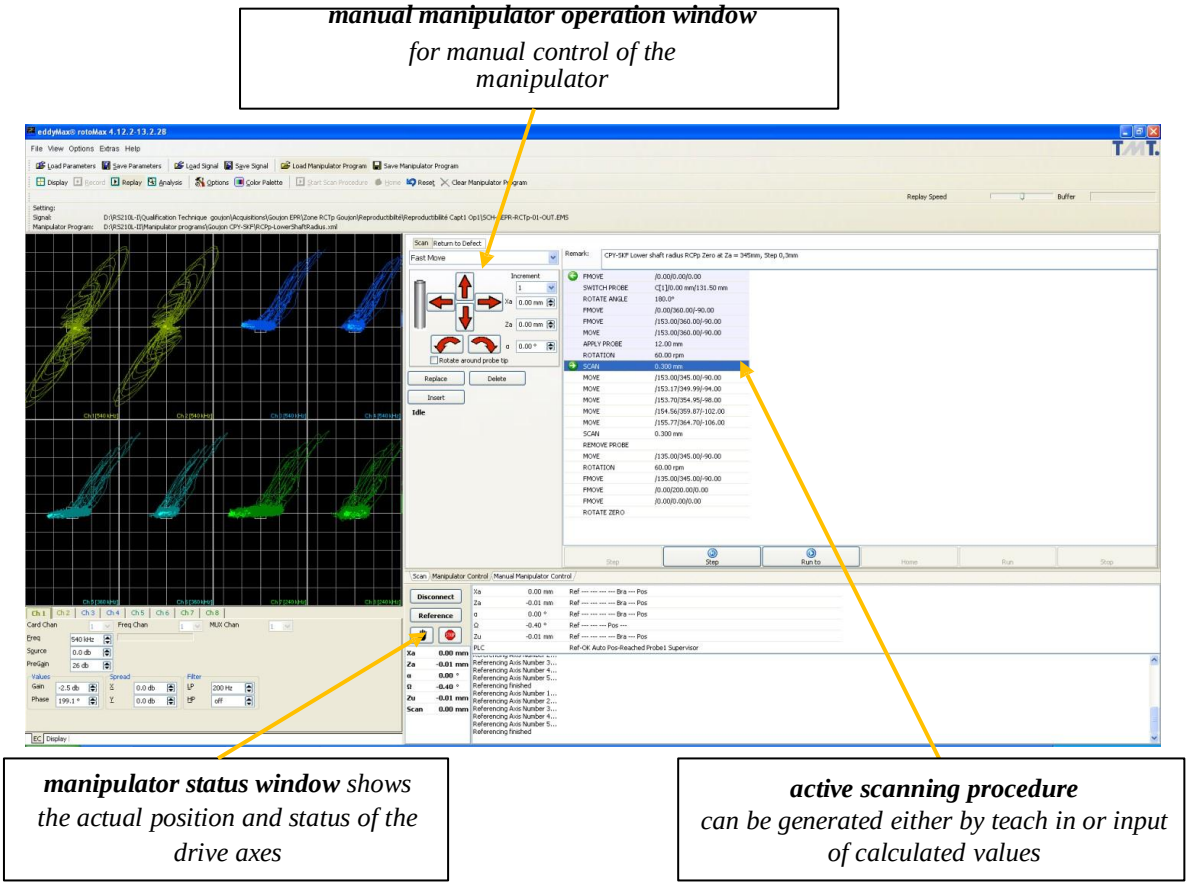

Fig. 10:Screenshot of the eddyMax RotoMax data acquisition software, with display in manipulator control mode

Computer-controlled scanning procedure

Figure 11 shows an example for a scanning procedure of the transition zone from the shaft to the thread. The scanning procedure determines the axial and radial position of the probe, the inclination of the probe to the vertical axis as well as the rotating speed of the stud and the trace feed of the probe. For each section to be tested a scanning procedure will be established, ensuring a reliable, reproducible and fast coverage of the area to be tested.

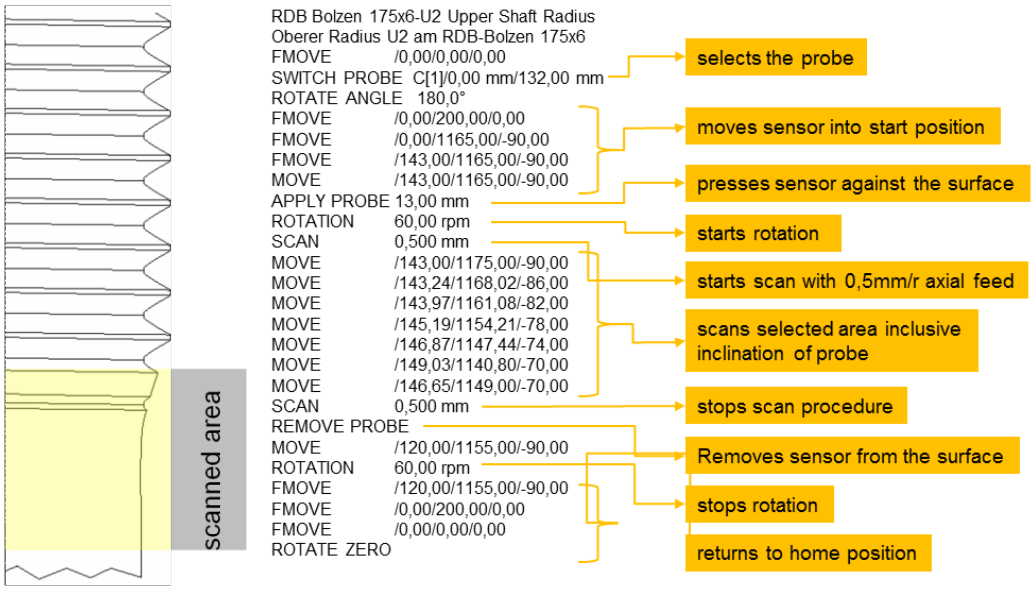

Fig. 11: Example for a computer-controlled scanning procedure

Eddy current probe and probe guiding

Due to their long lifetime bolts and nuts show in many cases a high quantity of mechanical imperfections like, dents, scratches, missing material, corrosion, etc. leading to extensive signal analysis and documentation work. Particularly for the eddy current testing an important point was made to the improvement of the probe guiding in order to achieve a high signal to noise ratio and preventing multiple indications from imperfections allowing automatic signal evaluation techniques. Therefore the following requirements are valid for the performance of eddy current sensors and probe guiding.

Requirements to the performance of the eddy current sensors

- the eddy current sensor has to work in absolute mode to allow the evaluation of the defect length and defect profile display.
- the eddy current sensor should be focused. Especially for the testing of threads the use of compensation coils in the neighbor turns should be prevented - avoiding double indications from one source.
- the eddy current sensor for threat testing shall have the highest sensitivity in the root of the thread.

Requirements to the performance of the probe guidances

- the probe guidance shall follow the contour caused by unroundness and bending of the bolts in order to minimize signals caused by sensor lift-off.
- the probe guidance shall have a minimal contact area not to transmit mechanical imperfections from the neighbor area and turns to the probe.
- the probe guidance shall cause minimal lift-off change in transition zones with changing diameter.

Extensive tests on different probe configurations led to the result, that sensors with two separated ferrite cores in differential and absolute mode show the best results according to the above requirements. Special attention was turned to the fact to have a sensitive absolute mode, because all signal evaluations are using the absolute signal, whereas the differential signals are used for confirmation or extended signal analysis purposes only. Figure 12 show the eddy current probes and the wiring of the sensors.

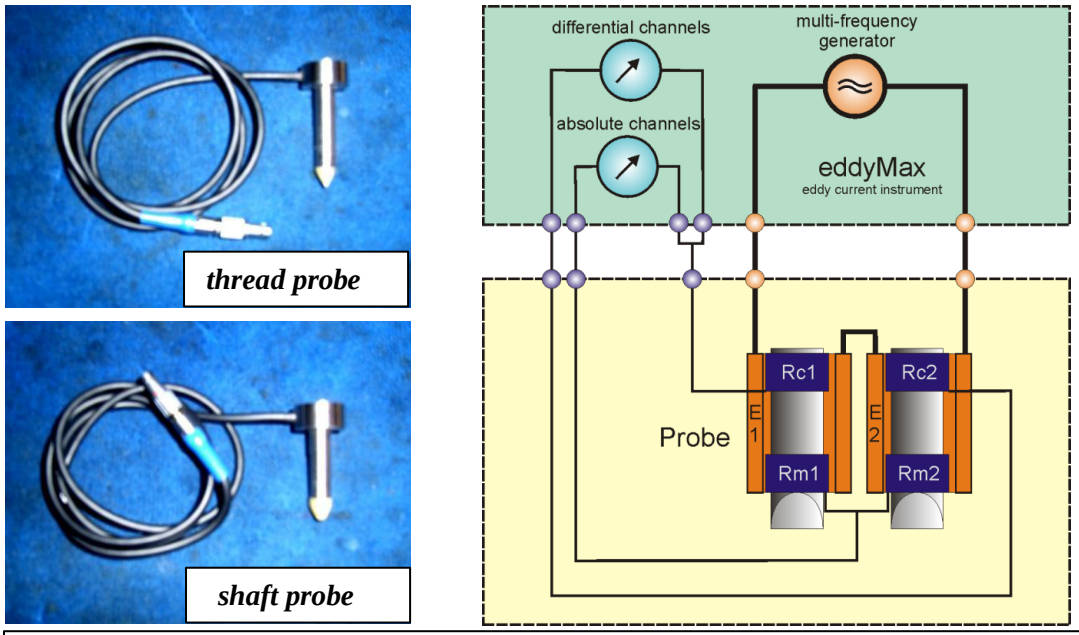

Fig. 12 : eddy current sensors for shaft and thread testing

Both the thread and the shaft probe have the same configuration and wiring, using internal compensation coils (Rc1 and Rc2) to get a better matching of the absolute coils. The tip and the ferrite cores of the thread sensors are tapered to fit into the thread contour, whereas for the shaft sensor the ferrite cores in the tip remain round. Figure 13 shows by the example of a long notch the necessity for sensitive working of the absolute channel. Figure 13 shows the signal response from a 174 mm long notch in the threaded section of the bolt for the differential channel, absolute channel without high-pass filtering and absolute channel with 0.2 Hz high-pass filtering. It can clearly be seen, that only the absolute channel without high- pass filter shows the real contour of the notch and thus allow the evaluation of the notch length.

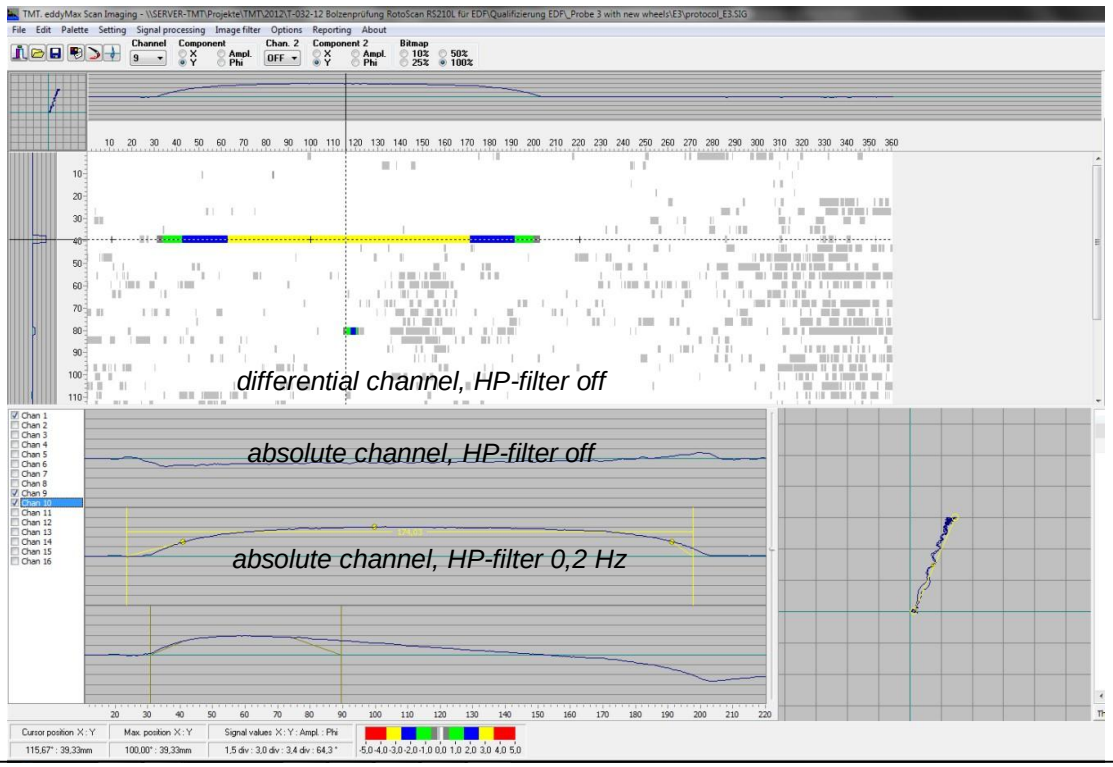

Fig. 13: signal response from a 174 mm long notch in the threaded section of the bolt for the differential channel, absolute channel without high-pass filtering and absolute channel with 0.2 Hz high-pass filtering

The probe guidance for the shaft and transition has 2 grades of freedom and the guidance for threads has 3 grades of freedom in order to compensate out-of-roundness and bending of the studs. Both guidances are using rollers to ensure a minimal contact area and therefore minimize noise and phantom signals due to superimposed lift-off at mechanical imperfections. The optimized probe guidance is an essential factor for the application of computerized signal evaluation, defect length determination and reproducibility of the testing result. Figure 14 shows the design of the probe guidance for the shaft and thread testing and figure 15 shows the guidances in operation placed to the stud.

Probe guidance for shaft and transition zone	Probe guidance for threaded area

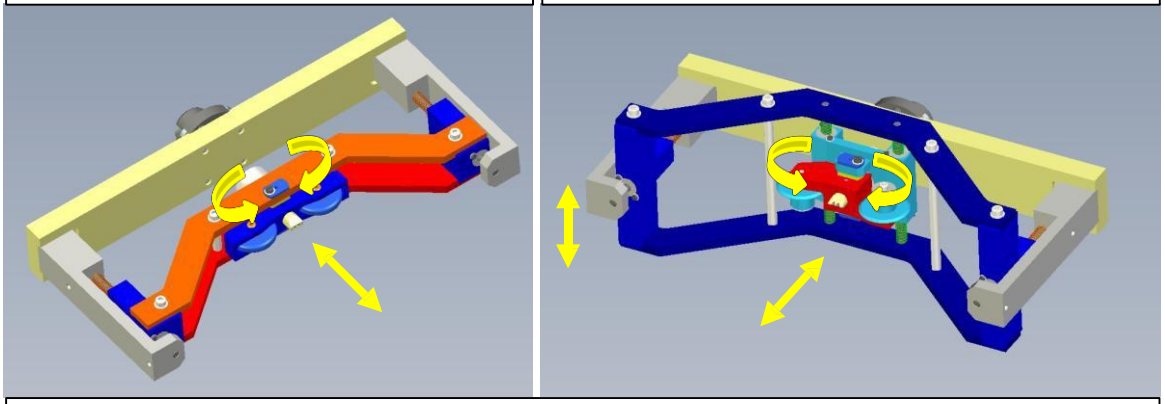

Fig. 14: probe guidances for shaft and thread testing

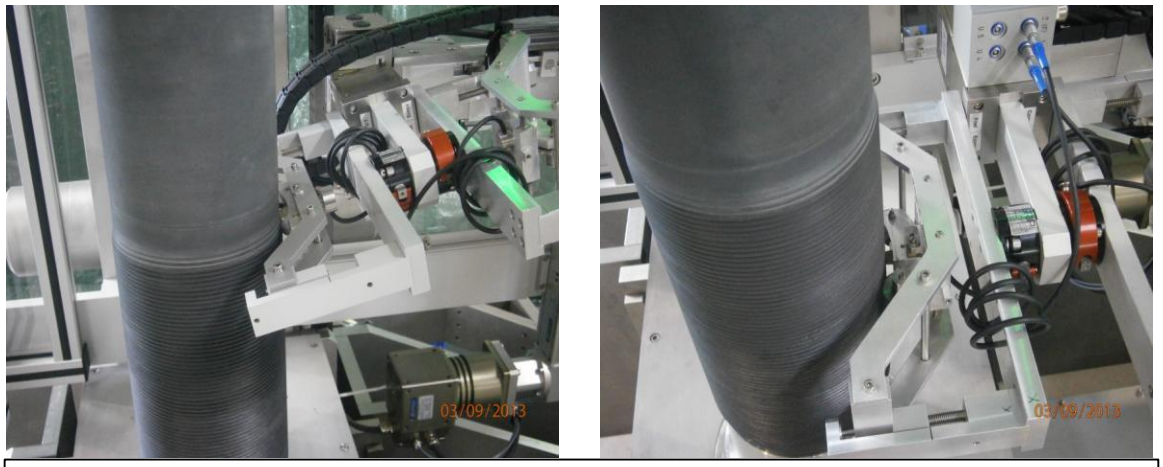

Fig. 15: probe guidances for shaft and thread testing in operation placed to the stud

To give an example of the signal quality reached by the optimized probe guidance, Figure 16 shows the signal response of a 1.0 mm deep notch recorded with a former model of probe guidance compared to signal response of the same notch recorded with a improved probe guidance. The former guidance shows a relative high lift-off signal in horizontal direction superimposed to the signal from the notch. In such a case the determination of the signal phase is unreliable. With the new probe guidance lift-off changes are completely suppressed resulting in a clear and defined notch signal.

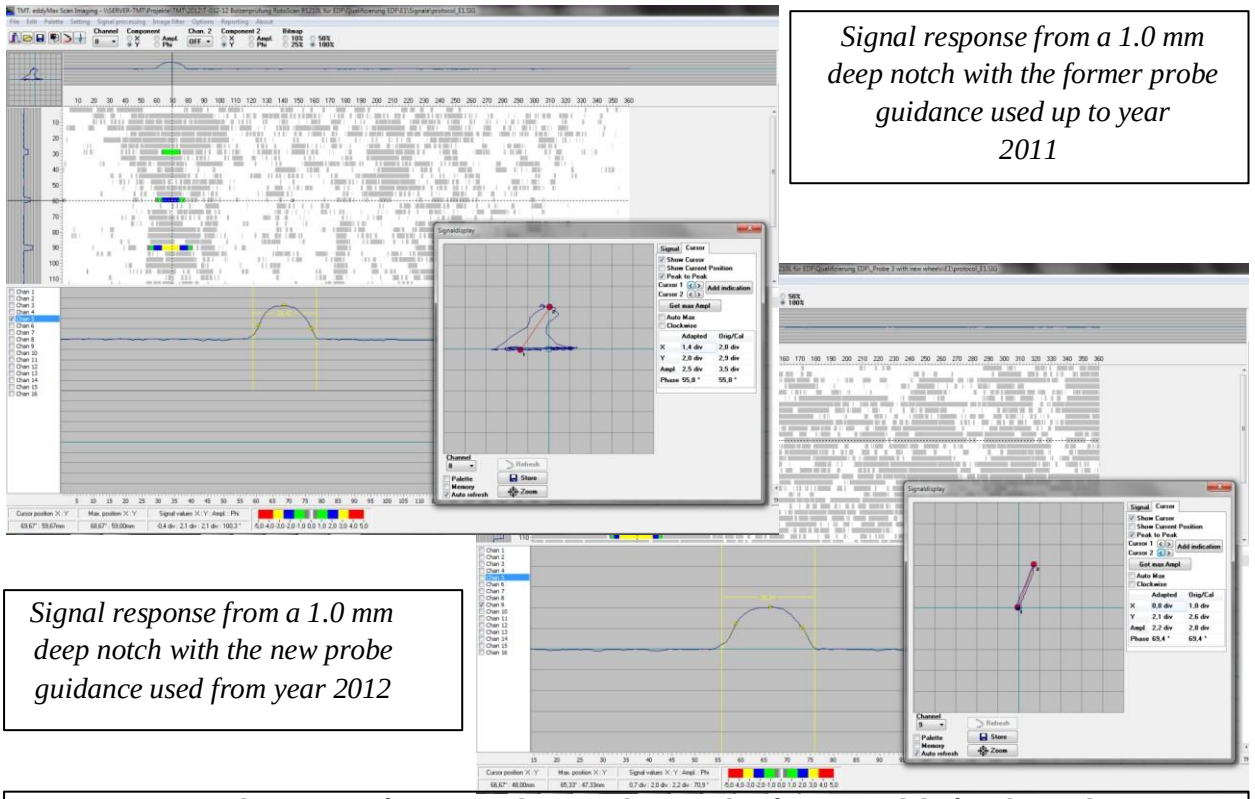

Signal response from a 1.0 mm deep notch with the former probe guidance used up to year 2011

Signal response from a 1.0 mm deep notch with the new probe guidance used from year 2012

Fig. 16: signal response of a 1.0 mm deep notch got with a former model of probe guidance compared to signal response of the same notch got with a improved probe guidance

The eddyMax data analysis software

Due to their long lifetime studs and nuts show in many cases a high quantity of mechanical imperfections like, dents, scratches, missing material, corrosion, etc. leading to extensive signal analysis and documentation work. Additionally reproducibility is an important factor for follow-up inspections which shall indicate differences to previous inspections. The eddyMax data analysis software is developed under consideration of these factors. Figure 17 shows a screenshot and a description of the main features.

The testing result for each tested area is shown in a colored scan display. With the cursor a sector can be selected and the impedance signal from this sector is shown. The analysis function automatically evaluates the signal phase, signal amplitude and defect length as well as defect position of the signal in the sector. All data can be exported for reporting e.g. to Excel. This feature ensures an operator independent, reliable, fast and comprehensive signal evaluation and reporting.

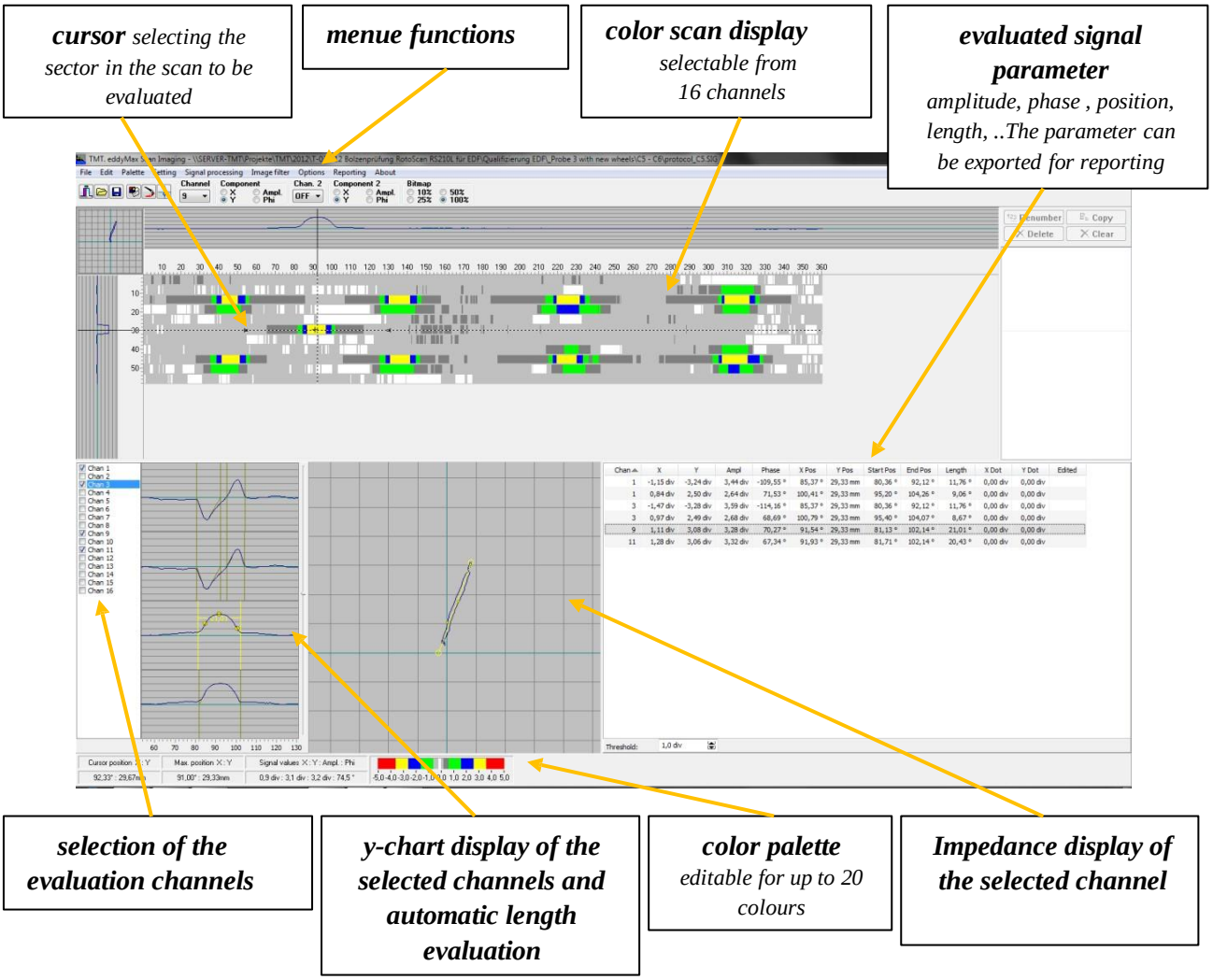

Fig. 17: screenshot and a description of the main features of the eddyMax data analysis software

Another feature of the analysis software was made for the evaluation of signal data from the shaft and transition zone. Whereas for testing of threaded areas a notch will only be passed one time by the eddy current sensor and therefore will only generate a single signal, for testing of unthreaded areas the signal display is different. For testing the shaft or transition zone, the feeding path is approximately 0.5 mm per turn, meaning that a notch will pass the influence zone of the sensor on several turns and generate a signal on each turn. For length evaluation only the turn with the maximal signal amplitude has to be evaluated. In the eddyMax data analysis software the signal of all relevant turns can be selected and will be automatically evaluated. The turn with the highest signal amplitude can easily be selected and the result exported for reporting (see figure 18).

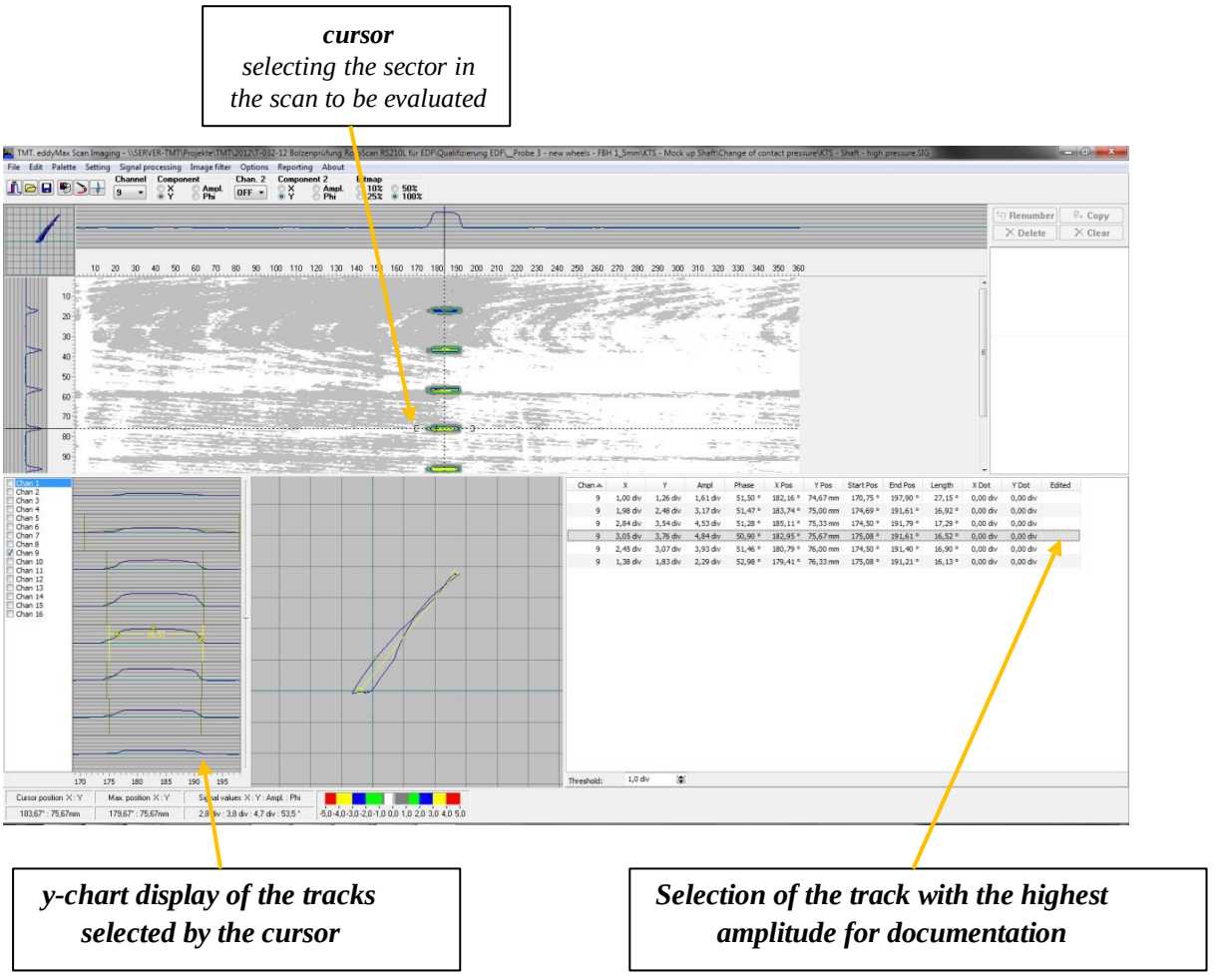

Fig. 18: evaluation of indications in the shaft and transition zone by the eddyMax data analysis software

Summarization

The main features and advantages of the inspection system can be summarized as follows:

- The manipulator is designed for safe, easy and fast installation and zero alignment of bolts and nuts
- The manipulator fulfills all necessary safety regulations
- Easy teach-in or input of precise and reproducible scanning procedures
- Advanced design of probes and guidances to reach a high signal-to-noise ratio
- Powerful multi-frequency / multi-channel data acquisition and data analysis software
- ENIQ qualification of the system for swiss nuclear plants
- RSEM qualification in process

MECHANIZED NDE ON REACTOR PRESSURE VESSEL (BWR) NOZZLES AT NUCLEAR POWER PLANT LEIBSTADT 2012

I.Vinzelberg, Westinghouse Electric, Germany
R.Schwammberger, H.Lipke, Nuclear Power Plant, Switzerland

Abstract

One of the most challenging tasks for NDE is the inspection of austenitic welds and dissimilar metal welds. If the examinations are hampered by poor accessibility of the inspection areas in combination with high dose rates, high temperature and scaffolding work the inspection equipment has to fulfill special requirements.

In support of the outage 2012 at Nuclear Power Plant Leibstadt, Switzerland (KKL), Westinghouse/WesDyne International performed automated ultrasonic (UT) and eddy current (ET) Examinations from the outside surface of Reactor Pressure Vessel nozzle safe-ends and associated piping. The inspection scope included 42 welds on 20 nozzles of various thicknesses and diameters. All welds were located between the biological shield and the reactor pressure vessel.

Especially for these inspections a manipulator system (SM5-KKL) was developed by Westinghouse Electric Germany, which allowed performing the inspection in a very short time frame with a minimized collective dose. The volumetric ultrasonic examinations were carried out with a qualified examination system according to the HSK-policy B07 utilizing PDI qualified equipment, personnel and procedures.

With the UT-inspection according to the KKL-procedure VOP/0264 a reportable indication was detected in one of the feedwater nozzles (Ø 374 mm, thickness 28 mm). The indication was planar and axial oriented, contained wholly inside the buttering and the weld material and was connected to the inner surface. In addition to the UT-techniques of the VOP/0264 several other techniques (UT, TOFD, and ET) were used to confirm the measured data of the indication and to achieve further information about the weld contour.

The subsequently performed repair of the affected weld was carried out with a so-called overlay welding. The nuclear regulatory authority ENSI (Federal Nuclear Safety Inspectorate) has released the repaired feedwater pipe at a nuclear power plant Leibstadt in Aargau for operation. It accepts the repair of the crack but only with conditions - until 2015, the repair should be reassessed.

Scope Procedures

In order to support safe and reliable operation of the KKL plant, in-service inspections of pipe welds associated with the following nozzles are required at an interval of 10 years.

- N2 Recirculation Outlet Nozzles (2)
- N3 Recirculation Inlet Nozzles (10)
- N4 Main Steam Nozzles (4)
- N5 Feedwater Nozzles (6)
- N6 Core Spray Nozzles (2)
- N7 RHR/LPCI Nozzles (3)
- N10 Jet Pump Instrumentation Nozzles (2)
- N11 CRO Nozzle (1)

In the period 2004 – 2014 this inspections are performed by Westinghouse. These inspections, involving a mechanized ultrasonic test (UT) process (iD) and an eddy current (ET) process (oD) are primarily required to detect service related degradation in the dissimilar metal welds (DM) and the similar metal welds (SM). Both, UT- and ET-inspection must be in compliance with the Swiss Regulatory HSK requirements which dictate that the process must be qualified in terms of the procedure, equipment and personnel.

KKL has adopted a Qualification Concept where the UT examination system to be used on the listed nozzle welds is based on the Performance Demonstration Initiative Program (PDI).

The Qualification Concept also adopts the principals of an ENIQ-based qualification process which varies from the PDI-based process.

Using physical reasoning and experimental evidence, these differences are resolved such that the requirements of the Swiss Qualification Body NDE are satisfied.

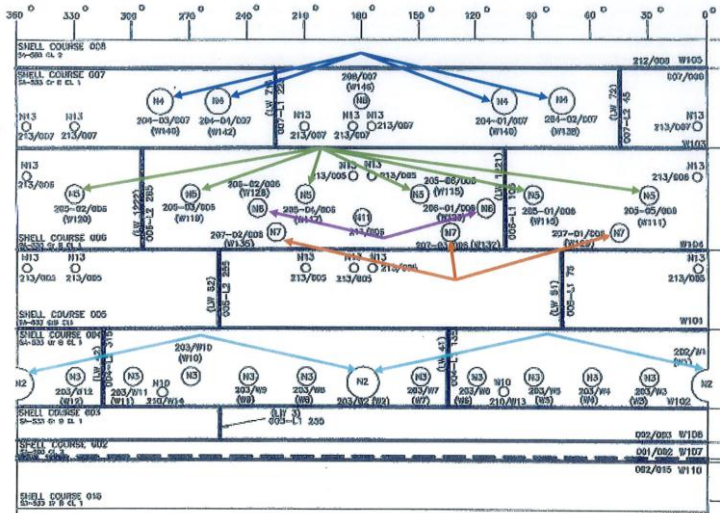

Figure 1: Automated UT & ET Examination on 17 RPV-Nozzles DN > 150

Environment

All austenitic and dissimilar metal welds are located in the area of the biological shield and difficult to access. For the inspection crew this results in increased workloads due to high radiation level, limited space, high temperature and work on scaffolds.

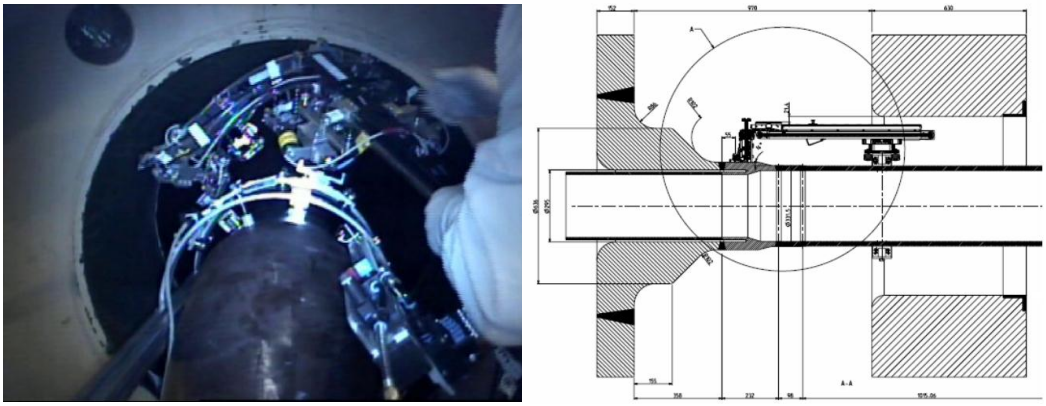

Figure 2: Manipulator Setup

Manipulator SM5-KKL

Based on the Manipulator Concept used for the Inspection in JHR 2004 Westinghouse Electric has developed the SM5- KKL – Manipulator. In 2009 the System was qualified for the inspection of N3-nozzle-welds according to ENIQ requirements and to the ENSI-Guideline B07. In 2012 it was adopted and qualified for the inspection of N2-, N4-, N5-, N6- and N7-Nozzle welds using technical justifications and demonstrations on nozzle mockups.

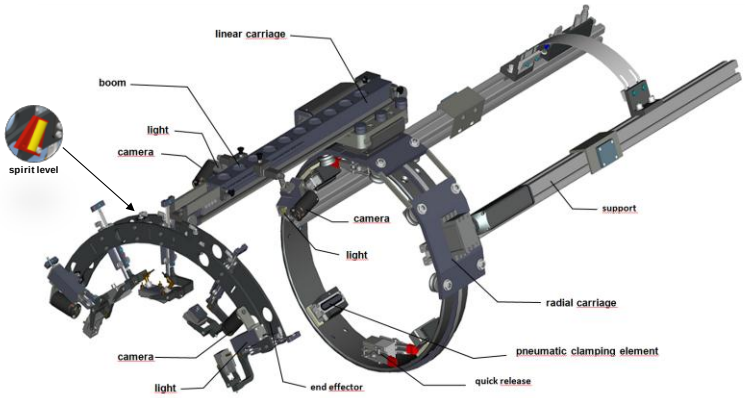

Figure 3: SM5 KKL

As a result from “lessons learned 2009 and 2010” modifications were also implemented to make the system easier to handle, which led to a shorter setup-time and thus to a lower radiation exposure of the personnel. Quick release connections and a dovetail and key design for the guiding ring and all changeable parts like scanner arms and probe systems allow for a precise and rapid assembly of the manipulator outside of the biological shield in an area with a low radiation level.

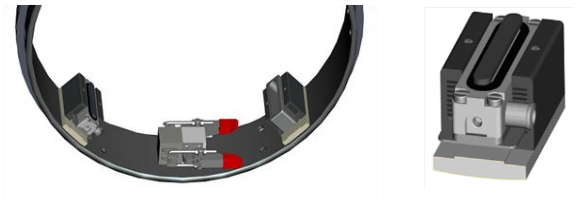

Figure 4: Quick Release Connection and Pre- Adjustable Pneumatic Element

Through the use of pneumatic elements, pre-adjustable to different diameters, rapid adaption to the pipe is ensured. Changes to probe-holders (spring-loaded instead of pneumatic) and probes resulted in reproducible data of excellent quality.

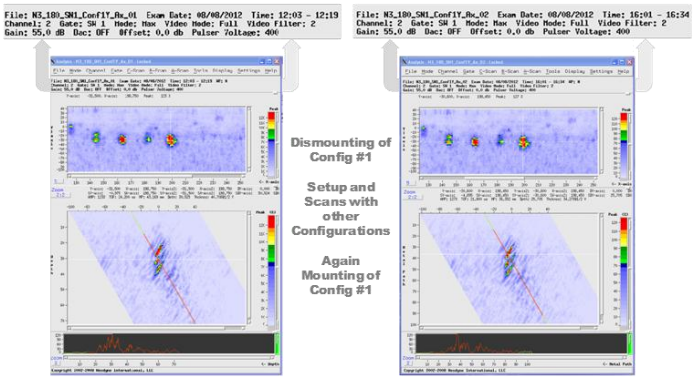

Figure 5: Integration Test - Reproducibility

All changes to the system have been extensively tested and demonstrated to the customer (KKL) and supervisory authority (SVTI) at the Westinghouse service center in Mannheim and on site prior to inspection.

Probes and Connectors

For the UT inspection (detection and sizing) of the RPV nozzle-welds > DN 150 at the nuclear power plant Leibstadt the following codes and WesDyne procedures are used.

- ASME Section XI, Article VIII-4000,
- WDI-STD-119-A
- WDI-STD-119-B
- WDI-STD-119-C

These procedures specify that probes of the type GEIT MSWQC (North American Standard) shall be used for detection and sizing. Frequency and crystal-diameter are defined as a function of the wall thickness and the diameter of the test object.

The previously conducted inspections on the RPV nozzle-welds and lessons learned have led to reconsider the use of the GEIT MSWQC probes (North American Standard) and to replace probes of this type with probes of the type “European Standard”, which have the same acoustic characteristics, but are better suited for mechanized ultrasonic UT-inspections because of their design.

Probe Characteristics

North American Standard

Probes of the type "North American Standard" consist of a 0° transducer in a cylindrical housing with thread that is screwed onto an interchangeable Plexiglas wedge. By choosing the Plexiglas wedge the required angle of incidence is determined. Advantage of these probes is that each transducer can be fixed to various wedges with different angles to obtain the required angle of incidence. They provide a maximum versatility, but are mainly designed for manual UT inspections.

Figure 6: North American Standard

One of the disadvantages is that a coupling layer of oil or a similar medium must be present between transducer and wedge, which dries up over time and has influence on the test sensitivity.

Furthermore, these probes are less suitable for mechanized UT inspections because they don’t have metal housings with holes for the fittings of the probe holders used in mechanized inspections.

Most of the “North American Standard” probes have an uneven weight distribution due to the lack of metal housings, which makes it difficult to guide the probes on the surface with contour changes in scan direction (nozzle radius, tapered areas).

Due to this problem special metal probe housing were developed for the inspection in 2010 to accommodate the GEIT MSWQC-probes (transducers and wedge). This enlarges the dimensions of the sensors. To perform reference checks the probes had to be removed from the housings and the proper re-installing was difficult.

The Microdot connectors of the GEIT MSWQC -probes are not optimal for the use in mechanized systems because they are very small and must be bolted, which is difficult wearing gloves in the controlled area of a NPP.

European Standard

Figure 7: European Standard

Probes of the "European Standard" are specifically designed for mechanized ultrasonic inspection. The transducer is directly bonded to the wedge and together with the damping mass integrated in a metal housing.

The housing provides seats for the fittings of the probe holders and connectors for the coupling supply. The design of the housing provides optimum couplant distribution on the component surface.

Disadvantage of the probes of the type "European model" is that for each beam angle a separate probe is required.

Advantages of the probes of the type "European Model" are the constant sensitivity, since no liquid medium between the transducer and wedge is needed, the even weight distribution and a better suitability of this type for mechanized systems, because the housings are specially adapted to the requirements of mechanized inspections.

Usually European Standard probes use LEMO 00 connectors. Compared to Microdot connectors the handling during the setup of the manipulator system is easier, faster and less error-prone.

Replacement probes

To replace the GEIT MSWQC-probes matching probes were manufactured by the company HQSonics from the Netherlands. These probes have identical acoustic characteristics (essential parameters). To prove that both types of probes have the same characteristics, the parameter of the GEIT MSWQC and the HQS probes were measured by HQS. The GEIT MSWQC probes were measured with the bolted wedge in order to have an identical basis for comparison with the HQS probes.

Sensitivity and Signal to Noise Ratio

To verify that the Sensitivity and the S/N-Ratio of the HQSonics probes is comparable to the Sensitivity and S/N-Ratio of the GEIT MSWQC probes, tests were performed with the complete specified equipment for the inspection in KKL on the KKL N3 test piece. Basis for evaluation were the notches in the weld N1.

The comparison of the essential parameters and the results of the examinations on the KKL N3 test piece show that within their tolerances the acoustic characteristics of the HQSonics probes are comparable or better than the characteristics of the previously used GEIT MSWQC probes.

All requirements for replacement search units according to ASME Section XI, Article VIII-4000 and to the WesDyne procedures were met by the HQSonic UT-Probes.

Since the mechanical properties of the HQSonics probes are better suited for mechanized ultrasonic inspections these probes instead of the GEIT MSWQC probes were used at the following inspections of the RPV-nozzle welds > DN 150 at NPP KKL.

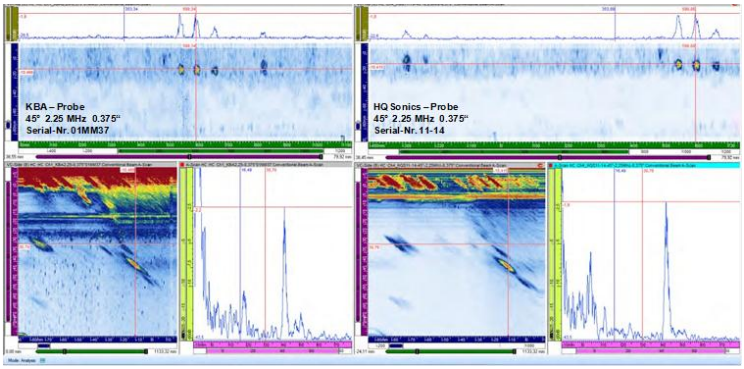

Figure 8: Improvement of Data Quality

Identification of Weld Center Lines

Because of the poor accessibility of the nozzles and the high radiation exposure since 2010 the positions of the weld center lines and their relative position to one another are measured with sufficient accuracy by performing an axial scan of all welds with a 0° UT probe.

The measurement is performed with a 4 MHz T/R-Probe (e.g. Krautkrämer MSEB 4), which is included in all probe configurations. The measurements are carried out in accordance with WDI-STD-119-C.

The SM-5 scanner is installed in such a way that all welds can be covered during a scan and the acquisition gate is set so as to display the first two back wall echoes over the whole scan area and the first back wall at 80% BSH.

The probe system is positioned over the SN1 weld buttering/ferrite transition in such a way that the index point of the 0° probe (beam exit point) is located directly over the buttering/ferrite fusion line.

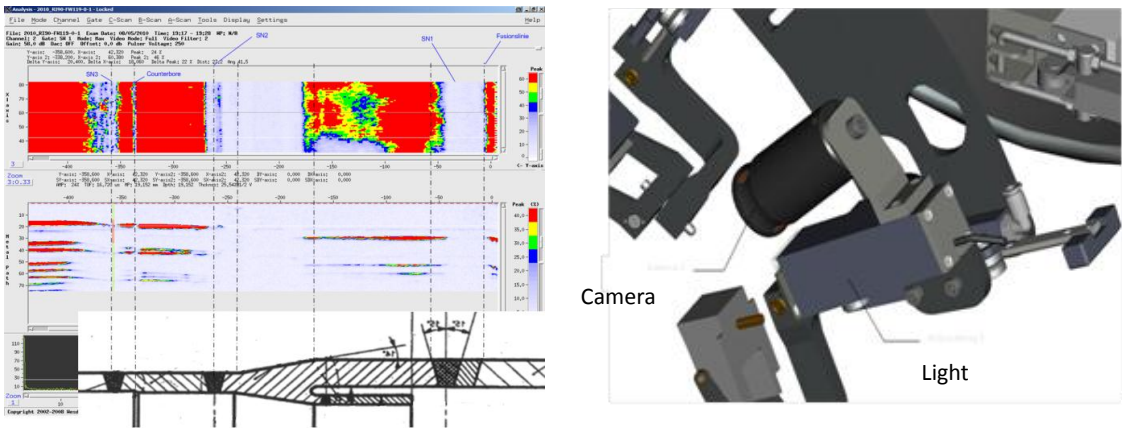

Figure 9: Identification of weld centerlines / Positioning Camera

The position of the probe is verified via the positioning camera, which is fixed at the same level as the probe tipping point. For later inspections this position is set as the 0-point for axial positioning. Approximately 50 tracks (index) were recorded in circumferential direction. The accuracy tolerance of the measured weld positions is ± 3mm.

Indication in Nozzle N5@150° SN1, (W116)

With the UT-inspection according to VOP/0264 a reportable indication of interdendritic stress corrosion cracking (IDSCC) was detected in nozzle N5 at 150° on 24.08.2012. The Indication was located in Weld SN1, Number W116. The indication #1 was planar and axial oriented, contained wholly inside the buttering and the weld material and is connected to the ID.

Weld Information		
Diameter OD	374 mm	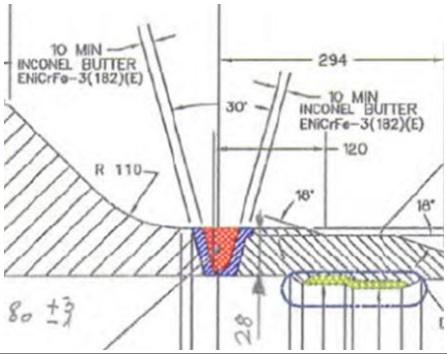
Thickness	28 mm	
Weld Crown Width	62 mm	
Configuration	Ferritic Nozzle - Inconel Butter (both sides) – Inconel Weld – Ferritic Safe-End	

Table 1: Weld Information Nozzle N5@150° SN1, (W116)

UT-Inspection

The dissimilar weld W116 was examined with automated UT and the techniques listed in the table below, according to VOP/0264 (based on WesDyne procedure WDI-STD-119A).

Probe Type	45 TRL 1	45 TRL 2	60 TRL 2	45 S 1.5	45 S 1.5(20°skew)
Axial Scans	x	x	x	x	
Circumferential Scans	x	x			x

Table 2: UT-Techniques used on weld W115

The indication was detected with a 45° TRL 2 MHz probe in scan direction (-) with a tip signal showing a remaining ligament of about 2 mm.

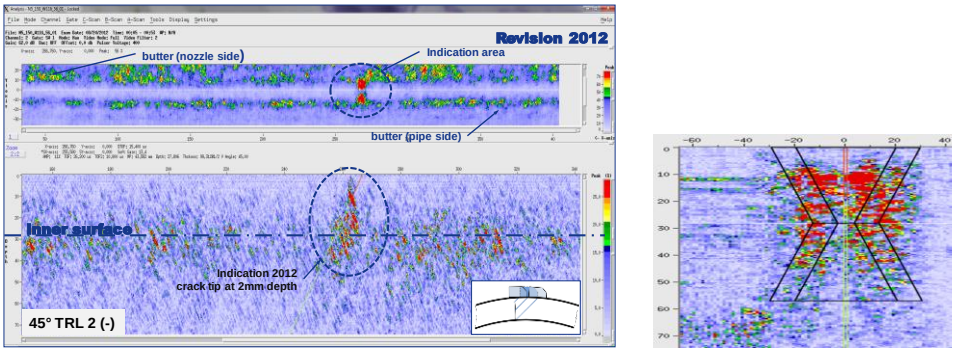

Figure 10: Indication detected in SN1 at Nozzle N5 @ 150° (W 116)

Additional Techniques

In addition to the UT-techniques of the KKL-procedure VOP/0264 the following techniques were used to confirm the measured data of indication #1 and to achieve further information about the weld contour:

- 70° TRL 2 MHz
- 80° TRL OD-Creeper
- 0° TRL
- ET-probes
- TOFD – Technique

The Signals of the 70°TRL 2MHz (+) and the OD-Creeper 80° TRL 2 MHz (+) show typical patterns of a planar flaw, not connected to OD with a ligament of ~ 2 mm.

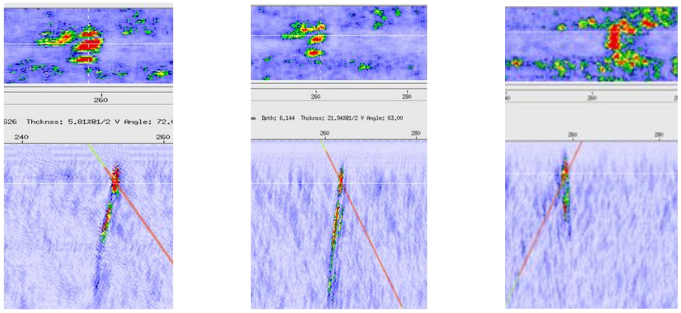

Figure 11: Flaw Signals of 80°TRL OD-Creeper, 70 TRL 2 (+) and 70 TRL 2 (-)

Time of flight diffraction (TOFD) technique

To verify the indication #1 detected with the qualified UT-inspection scans with different TOFD-setups were performed. In dependence on the TOFD setup ligaments between 2.2 mm and 4.2 mm were measured.

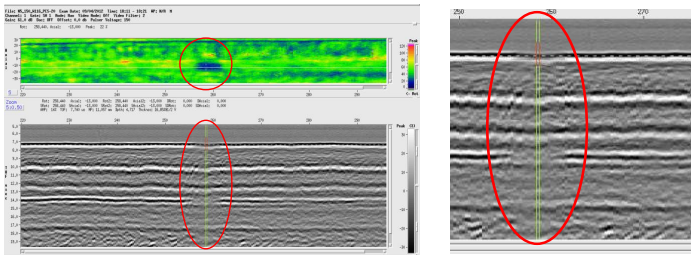

Figure 12: TOFD Inspection Results

Eddy Current (ET) technique

To verify the indication detected with the qualified UT-inspection an ET-probe (Type: TRC-X) with a frequency of 50 kHz was used. The measured indication length was 11.7mm.

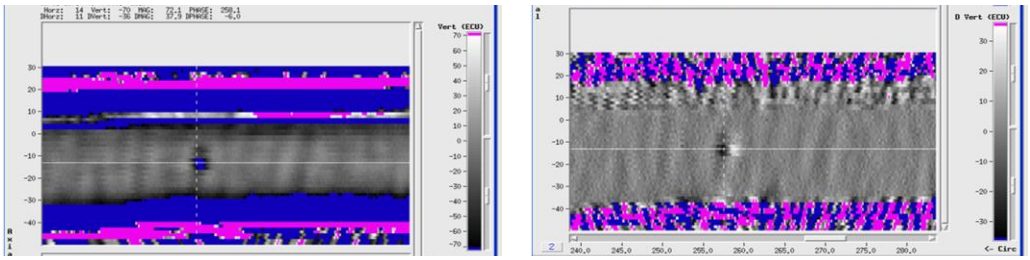

Figure 13: ET Inspection Results

0°- Technique

At the probe position on Weld center line without flaw the 0°- backwall signal shows typical patterns of a dissimilar weld with buttering while in the flaw area the backwall signal of the 0° TR probe is not present.

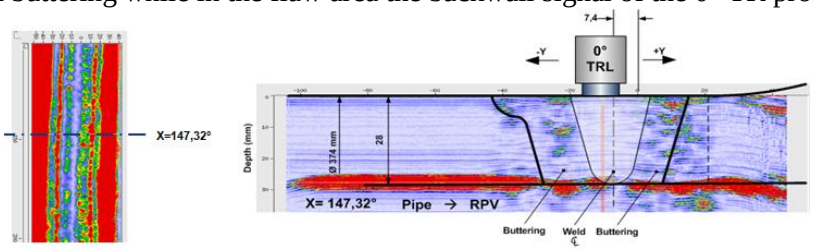

Figure 14: 0° - Signal at weld position without flaw

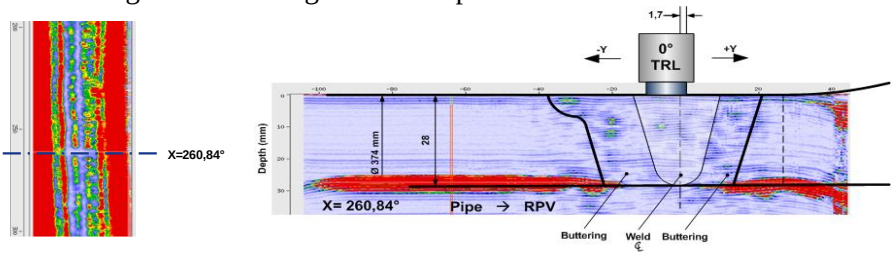

Figure 15: 0° - Signal at weld position with indication #1

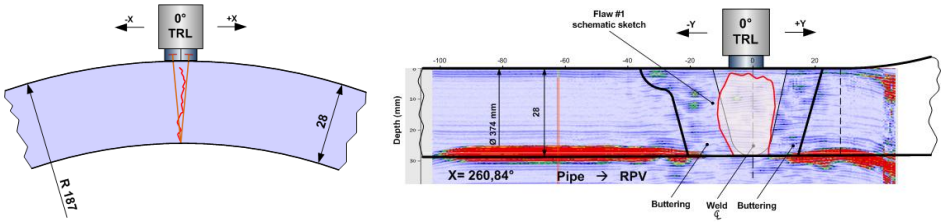

Figure 16: Schematic presentation of the indication in nozzle N5 @ 150° / SN1 (W 116)

History

The indication was already detected in 2004. At that time it was determined to be a non planar, non surface connected indication in the weld and/or butter material. Therefore it was considered non relevant.

In light of the results of the inspection in 2012, a review of the previous data found the indication to have been 5 mm in length (contained wholly in the nozzle side butter) and a maximum height of 15 mm; however connection to the ID surface was difficult to determine or confirm.

As a result of the mischaracterization in 2004, no fracture analysis, increased inspection frequency or repairs were conducted or implemented. The subsequently performed repair of the affected weld was carried out with a so-called overlay welding and resulted in a lengthy extension of the outage.

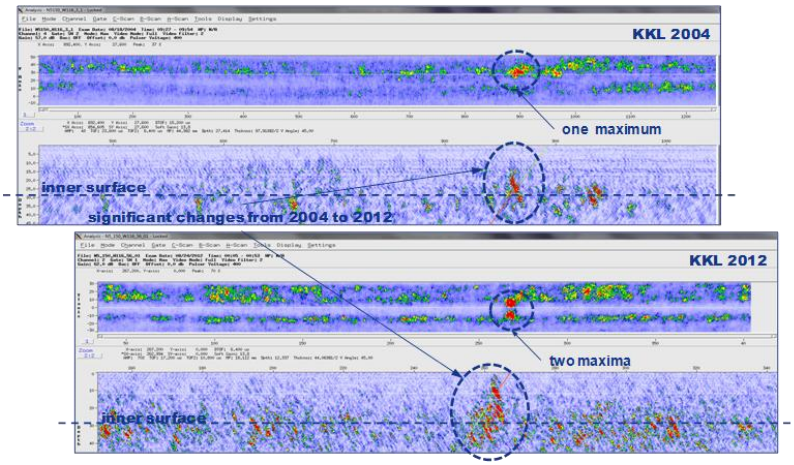

Figure 17: Examination Results 2004 <> 2012

Contributing Facts for the Mischaracterization

Westinghouse, KKL/EPRI evaluated independently why this flaw was characterized as subsurface flaw during the 2004 examination. The following reasons were identified:

- Echo dynamic responses and amplitudes were lower and less pronounced
- Length of flaw was shorter, thus making it more difficult to see
- Difficult to see connection to inner surface (Colortable)
- Flaw confirmation from both directions (CW, CCW) was difficult
- Inexperience with the use of the procedure (by all parties),
- Lack of relevant operating experience did not trigger to identify the flaw as in-service related.
- Numerous implementation issues shifted focus from the actual analysis and oversight processes needed to assure detection and characterization of the flaw using the recorded data.
- Time and schedule pressure due to equipment malfunctions and lack of communication with the rest of the team
- Implementation issues and schedule pressure forced the entire crew to work extended hours for several weeks with no time off. This included KKL oversight personnel.

Corrective Actions

All corrective actions recommended by EPRI/KKL to prevent mischaracterizations were implemented out of lessons learned 2004 before the inspection 2012 to perform a high quality inspection in a short time and led to a clear inspection result.

- Redesign of the manipulator and probe system as described.
- Strictly defined operating procedures and guidelines for data collection, analysis, data-flow and creating and handling of data packages and documents
- Intense and documented tests on all changes made to the inspection equipment. Readiness reviews are performed to determine if the proper preparations are being performed.
- Documented KKL-related hands-on training for the inspection personnel (track handler, data acquisition -, and data analysis personnel
- Track handling personnel is familiar with automated UT-inspections (UT Level II)
- Interpreter on each shift to bridge the communication barriers if the inspection is performed with a multinational crew.

Scope Expansion

Due to the detected in Nozzle N5@150° SN1, (W116) the DM welds of two more nozzles were identified by KKL to be subject to qualified inspection.

Therefore new manipulator systems based on the KKL SM5 had to be developed. Between the inspection inquiry (19.09.2012) and the nozzle inspection (06.10.2012) Westinghouse had about 3 weeks to modify and build the special manipulator systems. Before using them in the drywell, integration tests including track handler training was performed.

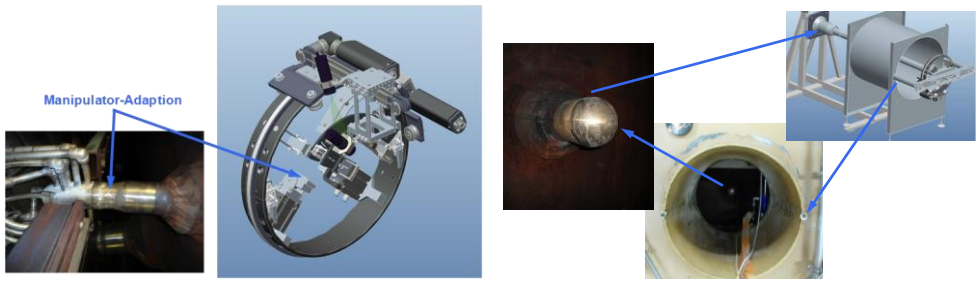

Figure 18: Modified SM5-Systems for Nozzle N10 and N11 Inspection

The DM-welds of two N10 and one N11-nozzle were inspected. No crack-like indications were seen in any of the inspected welds of these nozzles. All proposed examination coverage was achieved.

Conclusion

With the use of the corrective actions the JHR 2012 in NPP Leibstadt was carried out successfully.

- All Project Steps within scheduled Timeframe
- Data Acquisition (UT) Finished 6 Days before scheduled Date
- Data Acquisition (ET) Finished 5 Days before scheduled Date
- Actual Collective Dose ~ ½ Planned Collective Dose
- Good Data Quality in all Examined Areas with no rescans
- All the proposed examination coverage was achieved
- No crack-like indications were seen in any of the inspected welds except Nozzle N5 @ 150° SN1 (W116)
- Improvement measures from 2010 (implemented and demonstrated before outage 2012) demonstrated their effectiveness on actual components under field conditions
- No problems with setup and functionality of the new Manipulator-systems for N10- and N11-Nozzles

As a result of the detected indication KKL implemented an increased inspection frequency.

In JHR 2013 DM welds (12) and SM welds (6) were inspected on six N3-Recirculation Nozzles. No crack-like indications were seen in any of the inspected welds.

MECHANIZED INSPECTION OF CORE SHROUD SUPPORT LEGS AT FORSMARK 1 – FROM IDEA TO INSPECTION WITH MANIPULATOR NEMO

J. Danielsson, Westinghouse, Sweden

Abstract

During routine visual examination of the Core Shroud Support Legs in Forsmark Unit 1 in May 2011, two new crack-like indications were discovered on two separate legs. As a response the Nemo inspection system and associated inspection techniques were developed and qualified in record-breaking time. The Nemo system is capable of inspecting the Core Shroud Support Legs using both qualified Visual and Ultrasonic technique. The manipulator design allows for a minimum of Control Rod Guide Tubes to be rotated/removed while able to inspect all legs; thus reducing the risks typically associated with Guide Tube handling. The Nemo system employs state-of-the-art design features to optimize both inspection coverage and time.

Qualified camera systems (according to the general qualified Swedish visual inspection procedure VT-01) and qualified UT techniques (as developed for this application) is applied to detect, size and characterize any identified defects on the Support legs or in the adjacent weld/buttering areas. Development work started in August of 2011 and a site Acceptance Test (SAT) was performed in Forsmark Unit 2 in May 2012, with the full-scope inspection carried out in Unit 1 in August 2012. The inspection was performed in a safe and error-free way in significantly shorter time than initially estimated. An issue encountered on site was mitigated and solved according to a pre-set handling plan, as developed from Risk Analysis sessions as well as Lessons Learned from personnel training.

Keywords: Application areas of NDT (RPV-SG-Internals and primary circuit-Other component)

ADVANCED TECHNOLOGIES

ADVANCED 3D VISUALIZATION AND ANALYSIS OF PHASED ARRAY UT INSPECTION DATA

G. Maes, J. Berlanger, D. Reilly, D. Richard, ZETEC, Canada

ABSTRACT

Phased array is now a mature and widely adopted technology, and allows for highly efficient UT inspections on critical components in aerospace, oil & gas, heavy industry and power generation plants.

Still, the industry is continuously looking for innovative and efficient inspection solutions to more challenging inspection configurations, and this requires advanced software features.

This paper will present recently developed and enhanced software tools to support inspections on components with complex geometries:

- accurate CAD models can be imported from files, or can be generated using either a manual profiling tool, position C-scan UT data, or a laser scanning device
- advanced phased array probe types can be designed, simulated and controlled, to improve inspection capability for challenging inspections
- a versatile scanner simulation tool now supports various scanner types; linking of the phased array probe assembly with the scanner allows to generate accurate coverage maps
- rapid and efficient plotting of inspection data on complex surfaces in the 3D model, including rebounds and correction for couplant gap
- use of both Cartesian and polar coordinate systems, with appropriate tools for visualization, positioning and sizing of indications (cutting planes, 3D cursors, drawing tools)

Various practical examples will be presented, to illustrate the potential of the new software tools for design of advanced phased array probes and inspection sequences, and for display and analysis of inspection results in a 3D environment.

INTRODUCTION

Advanced 3D visualization tools can be used for the design and validation of various UT inspections, and are also very useful during the analysis of the examination data, and for the detailed investigation of reported indications. This is true for both conventional UT and phased array UT inspections. However, advanced software tools are probably more essential for inspections involving phased arrays, as these are often applied on complex geometries (1), and can involve multiple beams generated from a single probe: for example, the increasing application of 2D arrays that can generate beams with a range of refraction and skew angles.

3D ray tracing can be utilized, for a given component and defect combination, to determine where a probe should be placed and what refraction and skew angles are required to insonify the defect. If a representative CAD model of the component is available, accurate information can be extracted regarding the incidence angle on the defect, thus enabling an initial assessment of detectability. Ray tracing also provides information regarding travel times for echoes scattered from the defect and for geometric echoes in the component. 3D rays can be used to provide a graphical representation of focal laws and their formation. Multiple rays can provide an indication of coverage achieved either for a single crystal or a phased array probe.

Beam simulation can be utilized to design probes and wedges, and to assess whether or not an available probe will be suitable for a particular application. Beam simulation can also provide useful information about specific probe characteristics: can a specific beam be adequately generated; presence of side lobes and grating lobes; relative strength of shear and compression wave components when using a wedge; the effect of 'dead' elements on the acoustic beam.

Accurate representation of the probe trajectory on the considered component (inspection sequence), in combination with the above-mentioned ray-tracing, will allow the UT technique developer to assess inspection coverage and to optimize the inspection technique.

Finally, accurate and realistic 3D visualization of UT examination data in the CAD model of the inspected component will drastically facilitate and expedite the analysis process for phased array inspections on complex components. This 3D representation, in combination with adequate software tools will allow for accurate positioning and sizing of flaw indications. In addition, flaw characterization may be improved by corroborating indications with 3D ray-tracing on the same CAD model.

Zetec introduced the new UltraVision® 3 software platform in 2008, and completed the migration of its earlier 3D package in 2010 (2). Since then, requests from multiple users and custom application development projects have led to many incremental improvements and several fundamental enhancements in the newest UV 3.5 release version.

COMPONENT SPECIFICATION

The input information for any UT inspection technique development consists of the detailed inspection objectives, and a complete and accurate description of the inspection configuration.

The inspection objectives include a complete description of the flaw(s) to be considered: type, size, location, orientation and other characteristics; as well as the detailed requirements for detection and sizing of these flaws.

The description of the inspection configuration should include an accurate graphical representation of the component or weld to be examined, detailed information about base materials and weld materials, and any access restrictions that could be relevant to the implementation of the inspection techniques and equipment.

Obviously, the ability to use a CAD model of the component to be inspected in the UT and phased array inspection software package will greatly facilitate and expedite the inspection preparation. UltraVision® 3 offers various alternatives to achieve this goal.

For some inspection configurations, typically with complex but regular inspection surfaces, the software offers a set of pre-defined components with welded configurations that can be modified by the operator to represent the actual configuration.

In other cases, a realistic CAD file of the existing component is readily available, in which case it can be simply imported, using the *.SAT file format

However, for a large number of cases in the field, no accurate as-built CAD models are available. To deal with this, UltraVision 3 offers a "Specimen Generator" tool that enables the creation of a 3D specimen from a complex surface shape replicated with a manual profile tool.

Furthermore, CAD files generated by 3D laser scanning of the component surface using a flexible portable scanning device can be easily imported in the UltraVision environment.

A recently developed alternative is the creation of the surface profile from position C-Scan UT data acquired from a 0° channel (either phased array or conventional). In order to accurately create the rough and wavy surface, the raw position data needs some cleaning up. This processing of the position UT data is shown in Figure 1: on the left the raw position data with missing interface reflections, the middle image shows the result of the "Aberrant Point Removal" algorithm, whereas the right picture shows the smoothed final data.

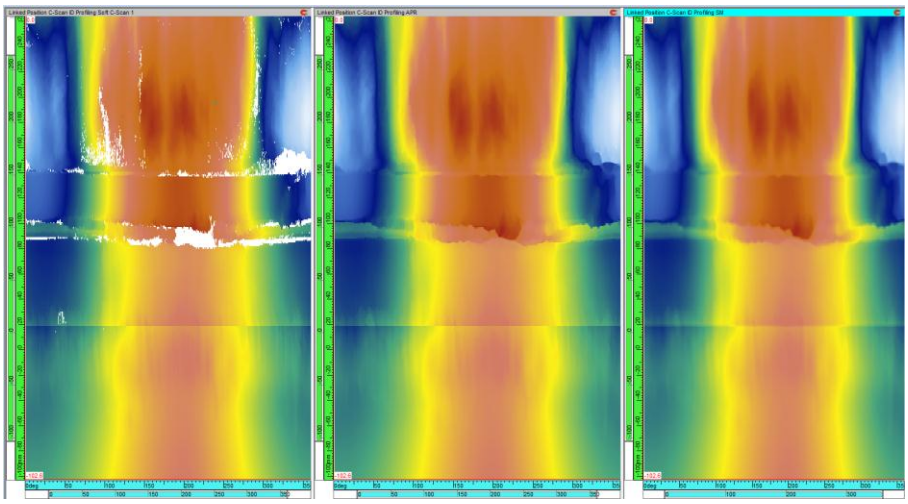

Raw position data Aberrant Point Removal Smoothing

Figure 1: Position C-Scan Data on DMW ID specimen (Courtesy of AREVA)

This smoothed position C-scan UT data can now be used to generate the ID profile of the component to be inspected.

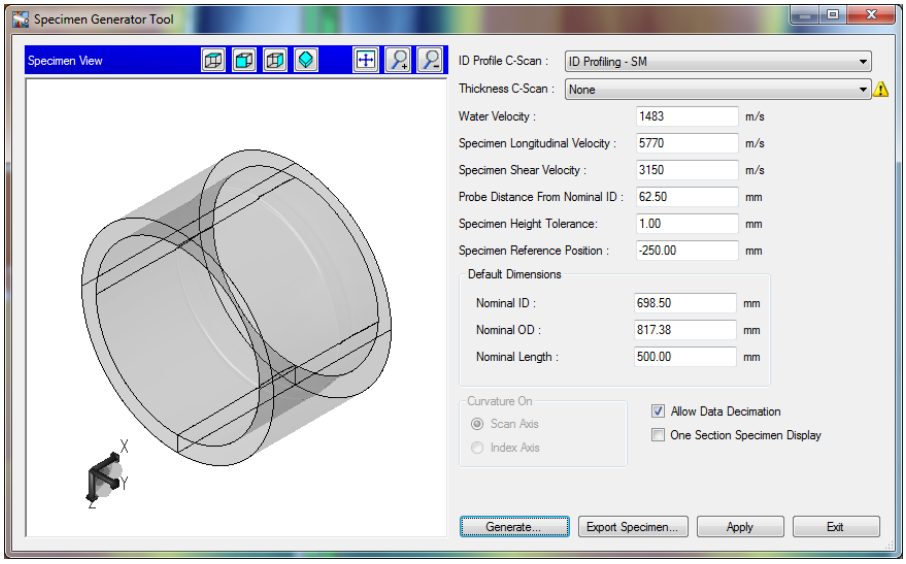

Figure 2: Creation of ID profile for DMW specimen (Courtesy of AREVA)

Independent of the method used to generate the CAD model, the component material can be specified and postulated defects that should be covered by the inspection method can be inserted. Currently, elliptical, circular and rectangular reflectors can be used, embedded or surface-breaking, in addition to custom shapes that can be imported from *.SAT files.

ADVANCED PHASED ARRAY PROBE TYPES

Inspection technique development starts with the identification of ray paths that will be efficiently redirected towards the emission point, and that will adequately cover the examination volume. Obviously, computerized 3D ray-tracing can greatly improve the efficiency of this operation.

Once ray paths and wave modes for adequate insonification of the considered flaws have been determined, the next task is designing the phased array probe assemblies required to generate these beams. Acoustic beam simulation is an ideal tool to efficiently optimize the design parameters of phased array probes and wedges. UltraVision 3 allows the user to compute, visualize and quantitatively characterize the energy distribution in the acoustic beam generated by various probe types, from single element conventional UT probes to advanced 2D matrix arrays and flexible arrays.

As phased array has become a mature and widely adopted technology, more and more dedicated probes can be found on the market. In order to correctly implement these special probes within the UltraVision platform, a "custom" array type probe has been added to the Advanced PA Calculator. This gives the operator the complete freedom to define his own dedicated probe through means of an xml file.

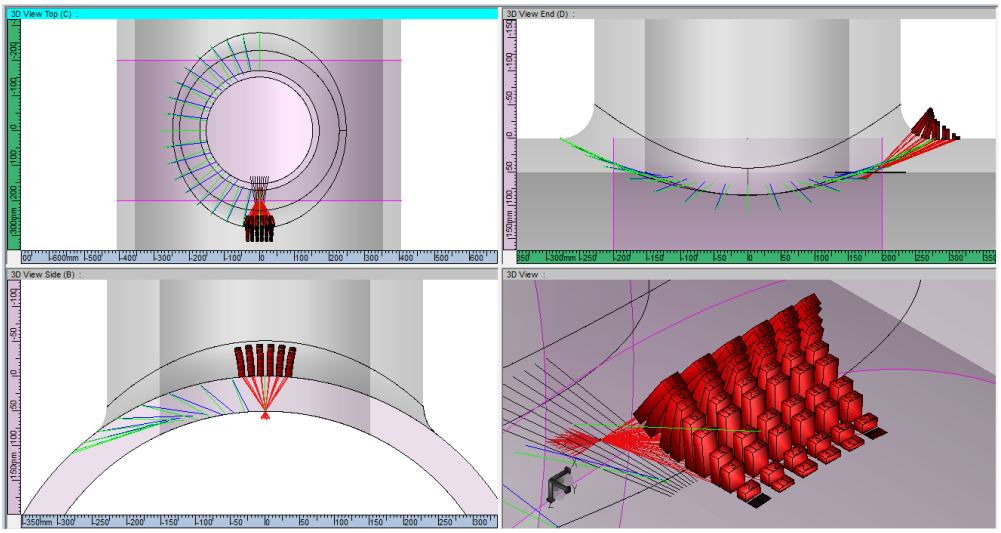

Figure 3: Custom 2D Matrix Flexible Array (Courtesy of Laborelec)

Figure 3 shows an example of a "custom" flexible 2D matrix array used for the inspection of saddle welds (3). Within this probe, each 2 elements are grouped together and spring-loaded so that the probe always fits to the saddle surface. As a result of this grouping, the primary pitch varies hence the reason for defining this type of matrix as a custom array.

Another example of a custom array is shown in Figure 4 where a dedicated annular array is built through an xml file. Each annular ring consists of multiple elements with different element sizes for each ring. The xml file allows, for each individual element, to define the element size, the element position, the normal direction and rotation of each element as well as the element numbering. Once the xml file is imported in UltraVision, it behaves as any "normal" probe and can thus be easily mounted on a wedge.

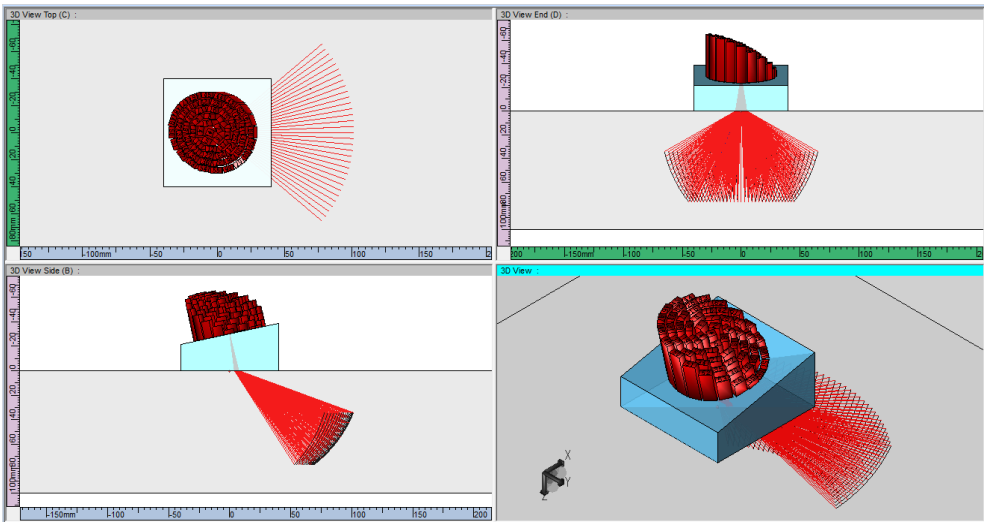

Figure 4: Custom Annular Array (xml file) Mounted on Wedge

Figure 5 shows Zetec's solution for the inspection of heavy forging turbine components (4). The QUAD probe consists of four 2D matrix arrays (8x8 elements) that are mounted together and fit to the surface. As the distance between the individual arrays depends on the component diameter, the secondary pitch varies so the only correct way of setting this up is through a custom array.

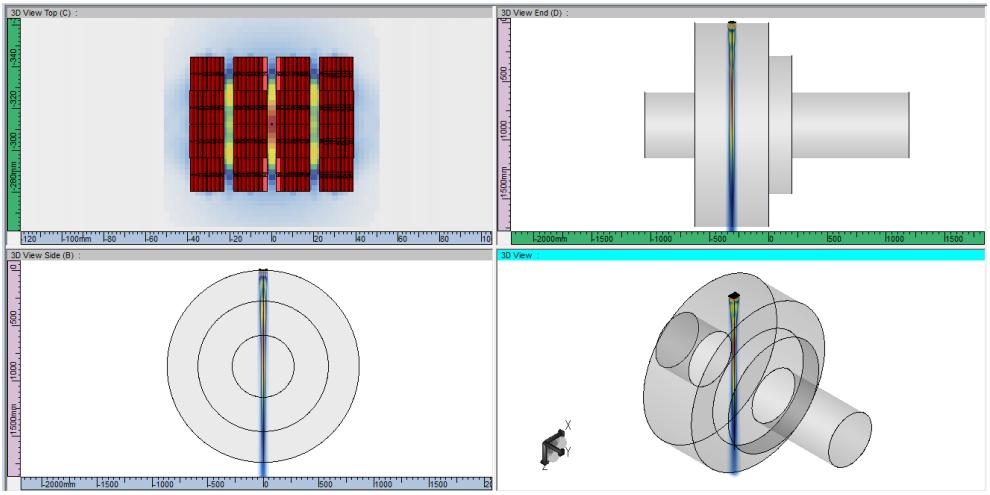

Figure 5: Custom Flexible 2D Matrix Array (QUAD Probe)

Acoustic beam simulations can be performed for custom array types as well, so, the development engineer can assess both the detection capability and lateral resolution of his inspection technique in various regions of the volume to be examined. Important technical decisions can be taken early in the inspection preparation, to avoid extra costs for alternative probes or extended inspection time for technique optimization.

SCANNER SIMULATION TOOL

Another important aspect of inspection technique development is to provide an accurate assessment of the coverage of the volume to be examined, taking into account as-welded conditions, complex geometry and access limitations.

UltraVision 3 includes a Scanner Simulation Tool that performs a simulation of the inspection scanner movement of the probe on the specimen. At each probe position, a complete set of rays can be created, thus allowing a complete coverage map for each refracted/skew angle used during the inspection to be generated.

Furthermore, the actual probe/wedge assembly can be linked to the scanner so that at each location, optimized focal laws can be calculated and the acoustic beam can be simulated.

Various common scanner types are supported: a simple one-line scanner, a XY table scanner, pipe scanner for ID and OD inspections, a polar scanner and a projected line scanner for complex geometries.

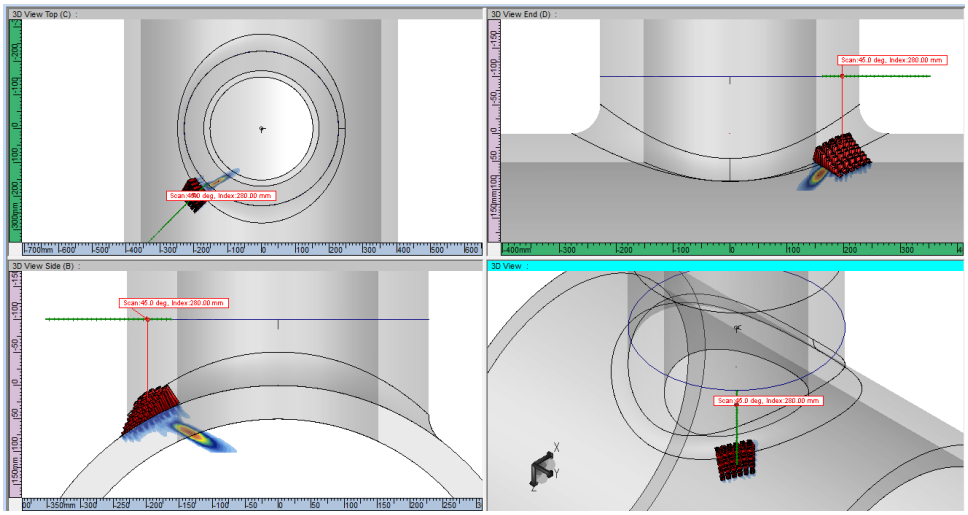

Figure 6: Flexible 2D Matrix Array Linked to Polar Scanner (Courtesy of Laborelec)

The example above shows a polar scanner mounted on the shell. The flexible 2D matrix array is linked to the scanner and spring-loaded so that it rides on the surface of the nozzle and is oriented according to the normal to the surface. The image shows the simulated acoustic beam at the current position.

Figure 7 shows multiple probes linked to a pipe ID scanner for the inspection of dissimilar metal welds from the inside diameter. All probes are individually spring-loaded and the actual size of the wedge footprint can be taken into consideration to calculate the position and orientation of the probe on the specimen surface. Rays can be attached to the probe/wedge assembly and can even be corrected for the couplant gap between the wedge and the component's surface. The ray in blue is the nominal ray whereas the red ray is couplant-corrected. The influence of the couplant gap on the refracted angle and flight time are automatically calculated.

These couplant-corrected rays are used afterwards for the actual data plotting in the 3D environment.

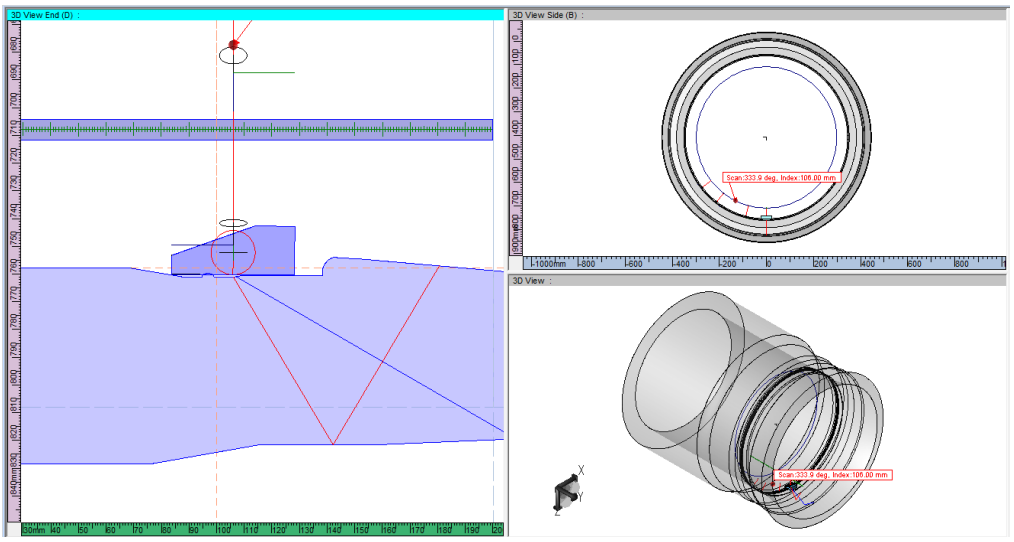

Figure 7: Multiple Probes Linked to Pipe ID Scanner with Length Contact Option (Courtesy of AREVA) Rays Attached to Probe Assembly: Nominal Ray (Blue) – Couplant Corrected Ray (Red)

For more complex specimens where the scanning pattern is not a simple geometry, the projected line scanner can be used. A line is defined in 3D space which is then projected down until it reaches the component's surface. When the probe/wedge assembly is attached to the scanner, it will follow the complex surface. Figure 8 shows the attached assembly and the calculation of the focal laws taking into account the orientation with regards to the normal on the surface.

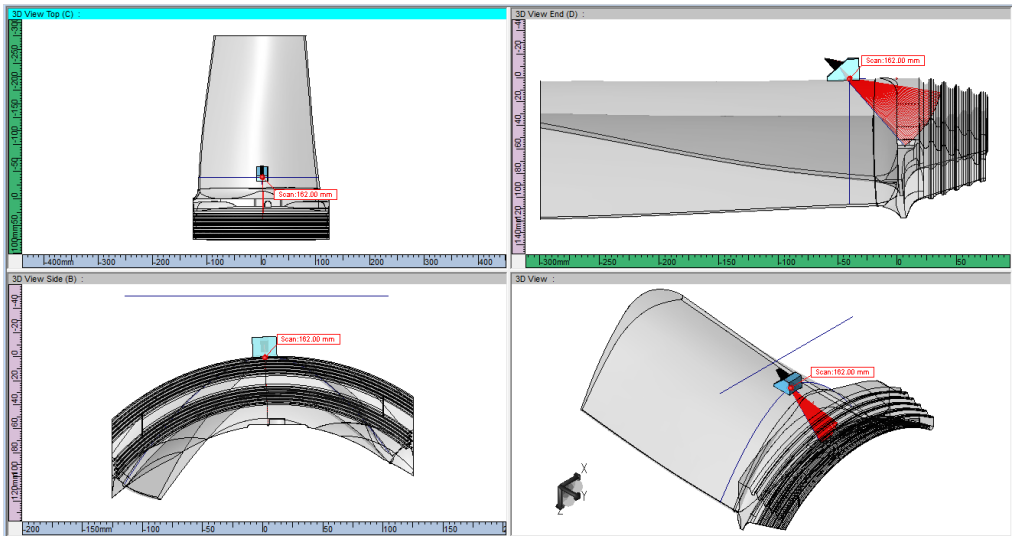

Figure 8: Projected Line Scanner on Turbine Blade

3D VISUALIZATION AND ANALYSIS OF INSPECTION DATA

The capability of a software package to visualize the recorded data in a 3D CAD model of the actual component under inspection can drastically improve the quality and the efficiency of the data analysis process. This feature enables the evaluation of each relevant indication in a 3D environment, where its size and position with regards to the geometry can be measured.

In order to create an accurate 3D image of the ultrasonic data, several steps need to be accomplished, involving various tools in UltraVision 3. The Scanner Simulation Tool is used to calculate the probe location and orientation on the actual component, from the Scan/Index coordinates of the inspection sequence and the surface profile of the component. Then, the beam path is calculated using the 3D ray-tracing feature. Finally, the raw A-scan signals are converted into 3D coordinates.

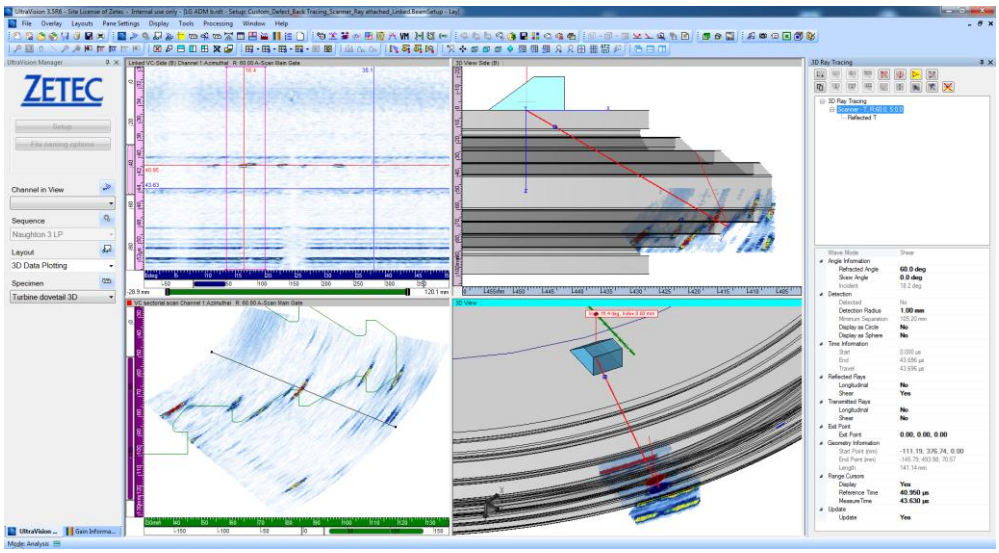

Figure 9: Ray Tracing and 3D Data Plotting on Turbine Dovetail
(Courtesy of Structural Integrity Associates)

Figure 9 shows the various steps of this process: the scanner is linked to the reference cursor in the 2D views and moves automatically to this position, the probe/wedge assembly is attached to the scanner and thus moves along, a ray is attached that represents the current focal law, and the A-scan data is superposed along the ray path to create a realistic representation of the data in the 3D environment.

Figure 10 shows the projected 2D images and the 3D representation of phased array UT data recorded from the inside diameter on a dissimilar metal weld specimen with an as-welded surface condition. Taking into account the actual "wavy" surface profile of the component and the complete footprint of the wedge enables accurate orientation of the probe with regards to the surface. Subsequently, by applying the correction for the couplant gap, the software can accurately plot and show the through-wall size of ID surface breaking flaws.

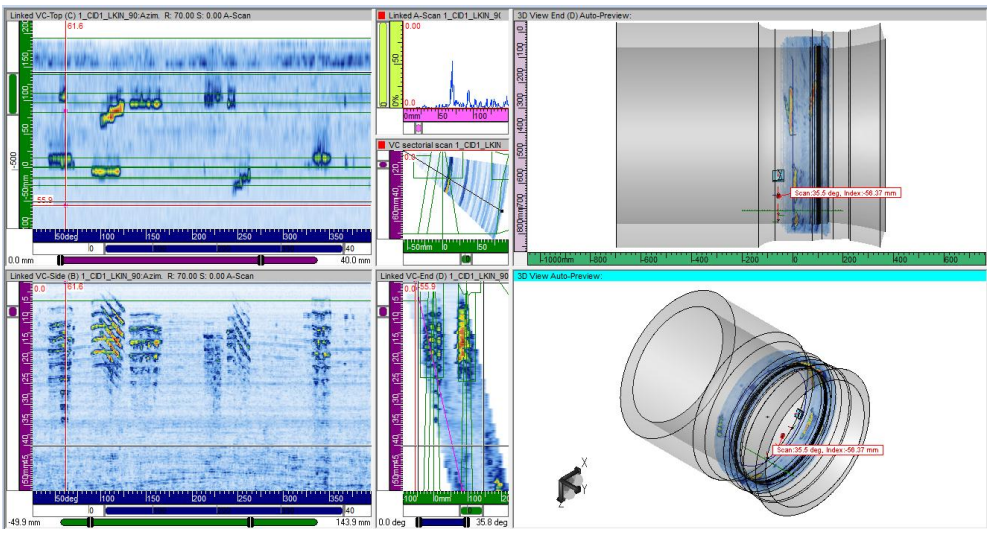

Figure 10: 3D Data Plotting on DMW ID Specimen (Courtesy of AREVA)

In order to efficiently analyze the data from cylindrical or disk-like specimens, the UltraVision software allows for easy switching from a Cartesian to a polar coordinate system. This includes polar measurement cursors as well as polar cutting planes for slicing through the 3D data.

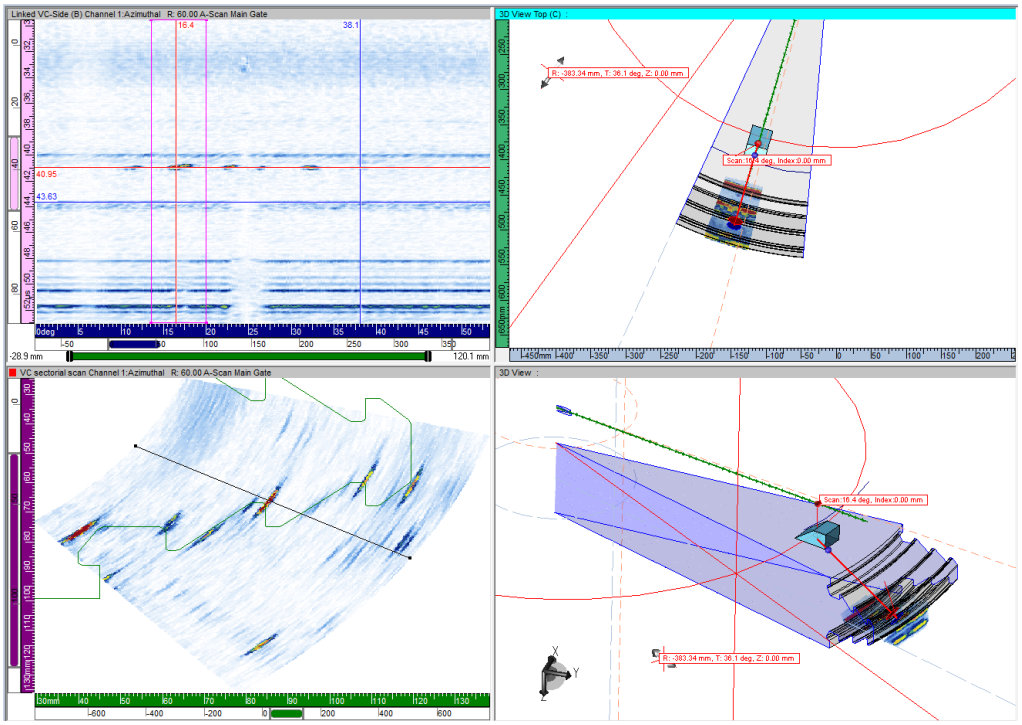

Figure 11: Polar Coordinate System and Cutting Planes on Turbine Dovetail
(Courtesy of Structural Integrity Associates)

CONCLUSIONS

1. The availability of accurate CAD models of the components to be examined is a necessary condition for successful PA UT technique development and inspection on complex geometries.
2. Advanced phased array probe types may be required to improve the inspection capability in challenging configurations; it is important for the software to support adequate focal law generation and acoustic beam simulation for such probe types.
3. Simulating the actual scanning mechanism and probe interface allows to generate accurate coverage maps during inspection technique development, to simulate the actual scanning conditions, and to define the environment for the 3D data plotting.
4. Accurate 3D UT imaging, taking into account actual component geometry, scanning mechanism, and probe contact, can drastically improve the interpretation of the examination data, specifically the characterization and sizing of potential flaws.
5. State-of-the-art software, including a complete 3D environment and powerful analysis tools is commercially available, and is being used to support various advanced inspection solutions.

REFERENCES

1) G. Maes, S. Turgeon, D. Reilly, "Advanced Phased Array UT Inspection through Complex Surfaces", 7th Int. Conf. on NDE in Relation to Structural Integrity for Nuclear and Pressurized Components, Yokohama, May 2009
2) D. Richard, G. Maes, D. Reilly, J. Berlanger, "Advanced Software Tools for Design and Implementation of Phased Array UT Inspection Techniques on Complex Components", 8th Int. Conf. on NDE in Relation to Structural Integrity for Nuclear and Pressurized Components, Berlin, October 2010
3) D. Moussebois, "Inspection of Complex 3-D Surfaces with Conformable UT PA Transducer", 9th Int. Conf. on NDE in Relation to Structural Integrity for Nuclear and Pressurized Components, Seattle, May 2012
4) P. Tremblay, D. Verspeelt, "Design and Validation of a Semi-Flexible Phased Array UT Probe for the Inspection of Large Forged Rotors", 9th Int. Conf. on NDE in Relation to Structural Integrity for Nuclear and Pressurized Components, Seattle, May 2012

INNOVATIVE PRACTICAL PHASED-ARRAY ADAPTIVE FOCUSING APPLIED TO THE COMPENSATION OF A WELD CAP PROFILE

A. Lamarre, J. Habermehl, Olympus NDT, Canada

Abstract

Ultrasonic inspection of welds through the cap is a major issue as it creates all kinds of beam propagation distortion. While different complex focusing technics address that issue, Olympus has investigated the use of practical phased-array adaptive focusing applied to the compensation of weld cap profiles. By means of reversal ray-tracing, it is now possible to determine an inspection scenario referencing the weld, instead of the array. Linear scans at specific angles and pitches defined relative to the weld as well as sector scans with refracted angles relative to the weld improve flaw detection and volumetric representation. The advantages of this method and practical results will be discussed in this paper.

Keywords: Development in volumetric, weld, adaptive focusing, phased-array

AUTOCOVERAGE – AN AUTOMATED ASSESSMENT OF THE COVERAGE ACHIEVED IN INSPECTION OF A NOZZLE INNER RADIUS BY UT BEAMS

T Cherraben, D Cornez, B J Dikstra, Doosan Babcock, UK

A key requirement of the RSE-M code is that un-inspected areas must be described in the inspection report. In many applications this is a relatively simple process, but in the inspection of components of complex geometry it can be difficult to assess, and report the location and extent of un-inspected areas.
In order to assess coverage of the inspection volume situated in the inner radius of branch nozzles in PWR primary circuits, a Mathcad routine, "Autocoverage", has been developed to calculate the actual coverage achieved by the wide variety of ultrasonic beams used to provide detection in these complex geometries.

Given the inspection geometry, the best detection mechanism for surface-breaking defects of radial/axial orientation is normally the corner effect. For a defect to be detected by corner effect, an ultrasonic ray within the beam must intersect the corner in a direction normal to the surface breaking edge. Of course the ray must also be launched from a position on the component surface at which ultrasonic coupling is suitable.

This paper describes the Mathcad routine, how it is used to simulate coverage that could be achieved on the basis of the component geometry, the techniques applied and the scan plan that is followed. The paper further explains how the actual coverage is determined based on these parameters but also by taking account of the actual coupling conditions obtained during automated inspection.

Objective

The RSE-M code, which governs PSI/ISI of nuclear power plant in France, requires for any inspection that, in addition to demonstrating that defects can be detected and localised or characterised, the actual coverage of the examination volume be assessed and reported.

For inspections of components with constant cross section, such as pipe-to-pipe butt welds, coverage can be established without difficulty but where the component has more complex geometry coverage assessment requires calculation. This is an onerous task where phased-array techniques involving multiple beams are applied. Branch nozzle geometries typically require many beams and present significant challenges to inspection design and also to the assessment of inspection coverage. This is especially true for inspections of the nozzle inner radius.

Experience shows that the geometry of branch nozzles in primary-circuit piping may deviate from the theoretical configuration given in plant drawings. While these deviations are normally small in relation to the overall dimensions of the nozzle, they can have a significant effect on the coverage achievable in practice, given that this is almost always limited by the constraints of the component geometry (for example, the axial extent of the nozzle reinforcement). Experience also shows that the surface form of a branch nozzle may not allow for good coupling of the ultrasonic probe, particularly around the boundary of the nozzle-to-shell weld where manual grinding is applied. A proper assessment of the coverage achievable in inspection of a branch-nozzle inner radius must therefore take account of the as-built geometry of the nozzle. A proper assessment of the actual coverage of such an inspection must also take account of the quality of coupling achieved.

To facilitate assessments of this kind, a routine called "Autocoverage" has been developed using Mathcad software to simulate the geometric characteristics of an inspection and to quantify the coverage which it achieves both in theory and in practice, taking account of the ultrasonic techniques applied, the scan plan which is optimised to maximise coverage of the particular nozzle under investigation and the quality of coupling achieved.

The "Autocoverage" routine is designed to assess the coverage of phased-array inspections for inside-surface breaking defects in typical branch-nozzle geometries. Current versions provide for inspections carried out from the outside surface of the nozzle reinforcement (including its conical part) or

from the outside surface of the main pipe. They provide for assessment of coverage of the inside surface comprising the nozzle bore, the inner radius and the inside surface of the main pipe.

The examples presented in the present paper are for detection of surface-breaking, radial/axial planar cracks in the inner radius of a branch nozzle where the ultrasonic beams are deployed on the cylindrical surface of the nozzle reinforcement. This inspection makes use of the "corner-effect", in which the ultrasonic beam is reflected from the corner formed by the plane of the defect and the local surface of the component. For effective detection of defects by this technique, the beam should be incident on the defect in a direction close to normal to the line of the corner. Where a defect has a significant extension the line of the corner may vary along the defect length; at any position along the defect, the corner is characterised by the orientation of the tangent line to the curve of intersection of the defect and the surface.

In the examples presented, a phased-array probe is used to generate a number of beams at a variety of refraction angles and skews so as to obtain suitable incidence conditions over the range of geometries encountered around the nozzle. The use of a phased-array probe also allows a straight (0°) beam to be included so that the effectiveness of coupling can be continuously monitored by observing the signal reflected from the internal surface of the nozzle. This feature allows the production of detailed maps of the coverage actually achieved in application of the inspection.

A schematic representation of the inspection configuration for a single ultrasonic beam is shown in Figure 1.

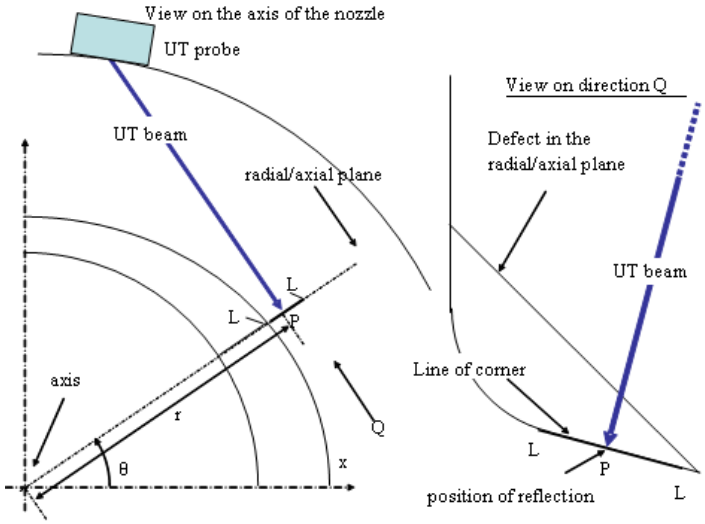

Figure 1 Schematic showing ultrasonic beam in radial/axial plane in the bore configuration (on the left) and in the inner radius (on the right)

The Autocoverage routine

The purpose of the Autocoverage routine is to provide a computerised means of assessing and quantifying ultrasonic coverage actually obtained for each nozzle inspected. This assessment is based on the geometry of the component, the techniques and scan pattern applied and the amplitude of the backwall echo at each point on the scan plan.

The adequacy of coverage at any given point of the inside surface of the component is defined in terms of the angle of incidence on the target area.

The routine can be broken down in 3 main functions: (a) the *input data* module groups all parameters required to set up the simulation; (b) the *calculations* module evaluates coverage by applying criteria defined in (a); and (c) the *output data* module synthesises the results obtained from various computations and defines the display format for cell maps and coverage statistics.

The flowchart in
Figure 2 shows how the routine operates.

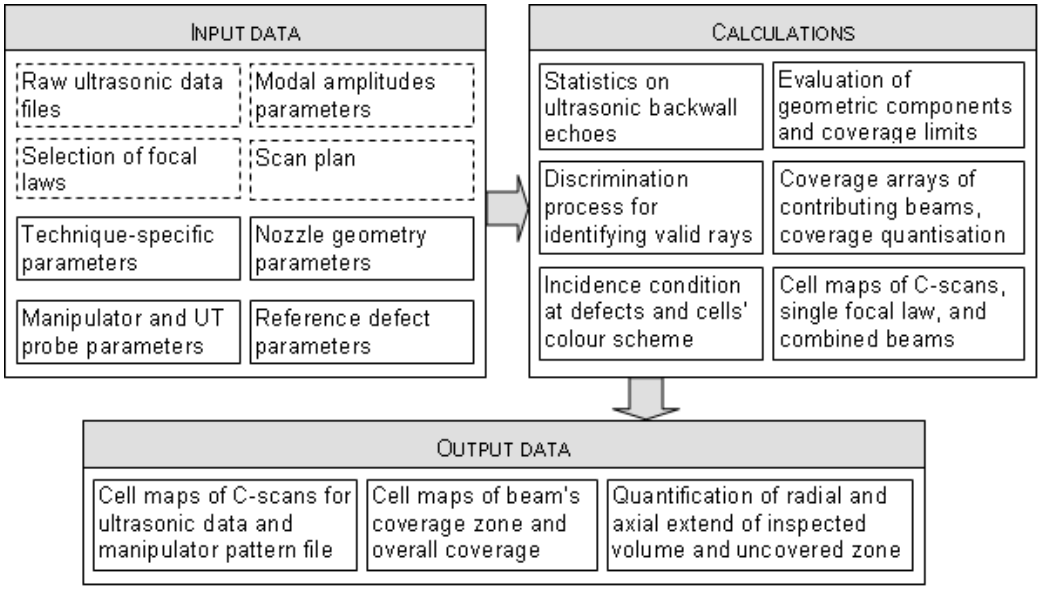

Figure 2 Flowchart of main Autocoverage's functions.

The input module verifies that the geometrical dimensions of the component are within the acceptable range of variation allowed by the Technical Justification of the inspection. It also uses the data from acquisitions to determine those probe positions where adequate coupling has been achieved. The criterion for this is that the amplitude of the back-wall signal at the position considered differs from the modal value over the whole inspection by less than a tolerance defined in the examination procedure. Positions where the insonification is not effective either because of a failure of coupling or due to local surface degradation are excluded from the subsequent calculations.
The calculation module first defines a grid of potential reflection positions over the examination area (on the inner surface of the nozzle/pipe).
Figure 3 illustrates the establishment of this grid and a map of valid probe positions.
For each of the ultrasonic beams applied, the calculation then proceeds as follows. For each combination of reflection position and valid probe position, the ray joining the points is examined. The reflection point is said to be insonified if the following criteria are met:

- the ray lies within the cone of divergence of the beam (where the divergence is defined by a given dB drop relative to the beam axis);
- the distance between the reflection point and probe position is such that the reflection point lies within the range gate applied.

If the beam reaches the reflection point according to these criteria, then the angle between the ray and the surface tangent line at the reflection point (i.e. the line of the corner formed were a surface-breaking defect of the relevant orientation to be present) is calculated. The incidence angle is defined as the difference between this angle and 90°. At each reflection point, the minimum incidence angle over all combinations of grid points is retained.

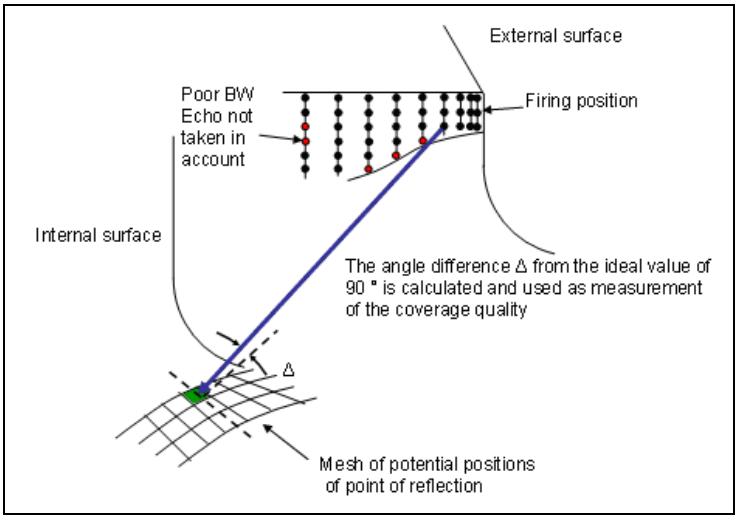

Figure 3 Schematic illustrating the coverage mapping process.

The output module presents maps of the incidence angles calculated for each beam individually and of the minimum incidence angle for the combination of all beams. An example of such a map for a small group of beams is shown in Figure 4. In this example of the map for a group of beams applied to inspection of the inner radius of a 14 inch nozzle, the cell size in the radial (R) direction is 4mm, and the lower edge of the map corresponds to the junction between the inner radius and the inside surface of the main pipe. The map shows immediately the sectors of the inside surface of the main pipe adjacent to the inner radius over which coverage is effective and the sectors where it is not effective.

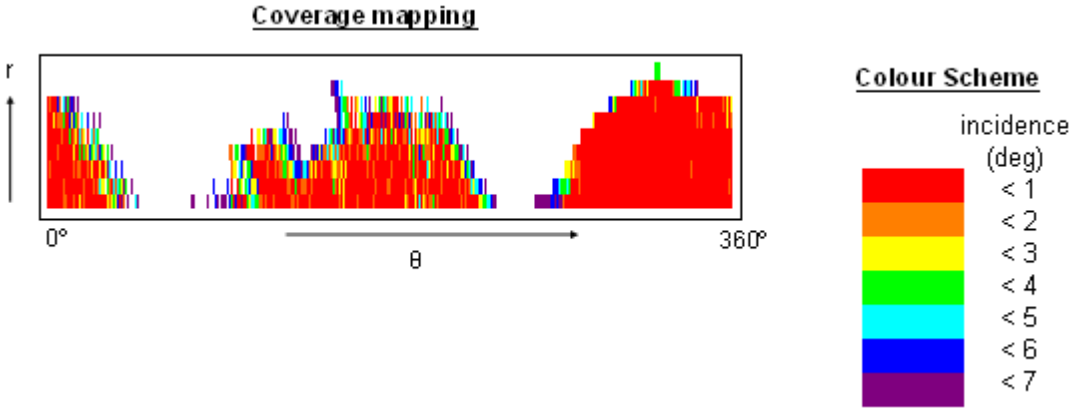

Figure 4 Example of coverage mapping of a group of 52° beams on a 14 inch nozzle. Axes are radial, r and azimuthal, θ. Colours represent the deviation of incident beam from the direction normal to the defect edge.

Examples of coverage maps

The coverage result for a typical case of a phased-array inspection of the inside surface of the main pipe adjacent to the inner-radius of a 14-inch branch nozzle is shown in Figure 5. A study of the detection conditions conducted as part of the Technical Justification for the inspection concluded that radial/axial defects of the size of interest would be detected by the corner effect provided that coverage was achieved at the inside surface of the main pipe over a strip adjacent to the inner-radius/inside surface junction of minimum width 12mm. The Autocoverage result shows coverage of 100% of this strip. It can be seen that there is a slight difference in the mapping between the intended coverage, based only on the extent of the surface scanned, and the actual coverage taking account of the coupling achieved (as deduced from the amplitude of the backwall echo with the 0° beam). The coverage result is the same because the critical area (first 3 cells or 12mm, measuring from the bottom of the map) is filled in red, indicating that the angle of at

least one of the beams intersecting the cells concerned does not deviate by more than 1° from the local direction of the defect edge passing through the cell; the 1° criterion having been established as adequate for detection in the Technical Justification for the application.

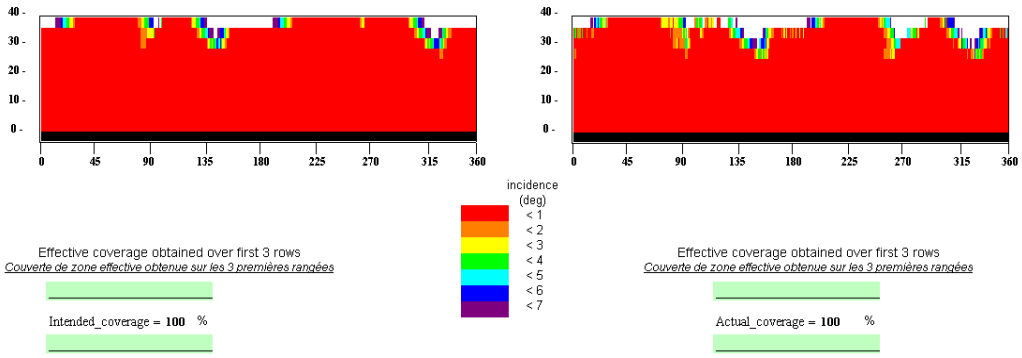

Figure 5 Example of overall coverage: coverage corresponding to the area scanned is shown on the left and actual coverage taking account of coupling on the right (vertical scale mm, horizontal scale degrees).

An example of an Autocoverage result where coverage did not reach 100% is shown in in Figure 6. Here the strip adjacent to the inner radius has some "missing cells" where the colour indicates that the angle of deviation of the beam from perpendicularity exceeds 1°. While the coverage map indicates that these areas are insonified, the incidence conditions are not ideal so that defect detection is less certain than for areas where the 1° criterion is met.

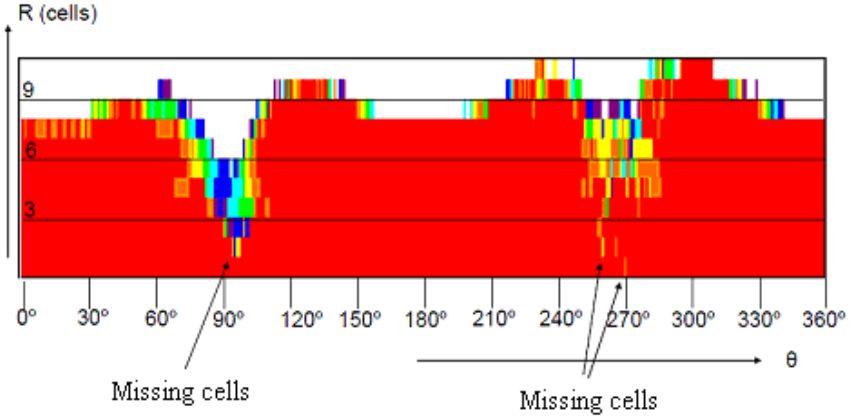

Figure 6 Example of mapping showing missing cells in the critical area (row n°1, 2, 3) around 90° and 270° (i.e. cells where the criterion: deviation from perpendicularity ≤ 1° was not met)

Analysis of this result showed that the missing cells were due in part to the axial extent of the surface available for scanning on the nozzle boss being less than expected and in part due to areas where the surface conditions prevented effective coupling.

Site application

The use of Autocoverage for coverage mapping has now been integrated into the ultrasonic inspection procedures deployed by Doosan Babcock for the inspection of certain 6 inch and 14 inch branch nozzles in EDF 900MWe plants in France. Several interventions have been carried out and Autocoverage has allowed the extent of coverage on each nozzle inspected to be established and documented in detail.

Conclusion

A software tool “Autocoverage” which allows assessment of the coverage which is potentially and actually achievable in the inspection of the inside surfaces of branch nozzles in primary circuit piping has been established and demonstrated.
The tool has been deployed successfully on site.

Acknowledgement

“Autocoverage” has been developed and applied in the context of the EDF application “Inspection of Boron Injection and Surge Line Brach Nozzles on 900MWe PWRs”.
We acknowledge the helpful comments of EDF CEIDRE in developing and finalising Autocoverage and in integrating it within the site procedures for implementation of the inspection application.

ZONE SENSITIVITY OPTIMIZATION FOR THE ULTRASONIC INSPECTION OF COMPLEX 3D GEOMETRIES USING CIVA SOFTWARE

B. Chapuis, F. Jenson, CEA - LIST, France
F. Vivier, L. De Roumilly, EDF - CEIDRE, France
B. Chassignole, P.E. Lhuillier, EDF - R&D, France

ABSTRACT

The development of an ultrasonic inspection method to guarantee the detection of a critical defect whatever its position in the examination zone is often a long process when phased array probes are involved on complex 3D geometries. The use of CAD may be useful to perform geometrical calculations. In order to take into account the physical effects specific to UT examination, simulation tools and a dedicated methodology are being developed in CIVA software. The aim is to define an optimized trajectory, to determine a set of associated focal laws suitable for the inspection of a given examination zone of a complex specimen and to evaluate the sensitivity.

The first step of this methodology consists in geometrically determining a number of optimal probe positions to inspect the whole examination zone. Based on these optimal points, a probe trajectory can be computed. Then, the focal laws associated to that trajectory are calculated. These focal parameters are used to steer the ultrasonic beam in order to avoid any zone that is not properly insonified when the probe travels along the previously determined trajectory. Finally, sensitivity maps are calculated to evaluate the effectiveness of the proposed solution (the trajectory and associated focal laws) in order to verify that the sensitivity requirements are met.

This methodology will be illustrated considering the case of the examination of a notch in the internal surface of a nozzle using a flexible matrix probe.

INTRODUCTION

The development of an ultrasonic inspection method to guarantee the detection of a critical defect whatever its position in a given examination zone is often a long process when phased array probes are involved on complex 3D geometries. In addition to the practical difficulty of the implementation of such an inspection technique (use of a robot, synchronization between the robot and the electronic system, precision on the positioning of the probe at the surface of the specimen,…), it must be demonstrated that the targeted sensitivity is guaranteed for detection of a critical defect whatever its position in the examination zone. The use of the simulation is very useful to construct the solution and anticipate its performances before the practical implementation.

This methodology is developed using the CIVA software and it will be illustrated considering the case of an examination zone where a notch has to be detected in the internal surface of a nozzle (Figure 1) using a flexible matrix probe of 12x7 elements at 2 MHz (Figure 2).

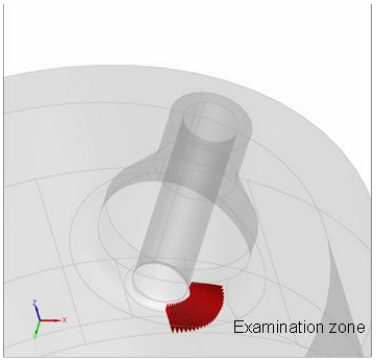

(a) (b)

Figure 1: (a) Example of a nozzle, (b) Illustration of the examination zone in the internal surface of the nozzle.

Figure 2: Flexible matrix array probe.

METHODOLOGY AND RESULTS

The principle of the methodology is the following. After the definition of the examination zone by the user (a), the first step consists in geometrically determining a set of optimal probe positions to inspect the whole examination zone (b). Based on these optimal points, the user defines a probe trajectory (c). Then, the focal laws associated to this trajectory are calculated by CIVA. These focal parameters are used to steer the ultrasonic beam in order to avoid any zone that is not properly insonified when the probe travels along the previously determined trajectory. Finally, sensitivity maps are calculated to evaluate the effectiveness of the proposed solution (the trajectory and associated focal laws) in order to verify that the sensitivity requirements are met (d).

Notations: The position and orientation of the probe at the surface of the specimen is described Figure 3. R is the distance to the center of the secondary pipe, θ the angle to the axis of the primary pipe and β the orientation of the probe. Y, the distance from the top of the nozzle, is specified by the geometry of the structure.

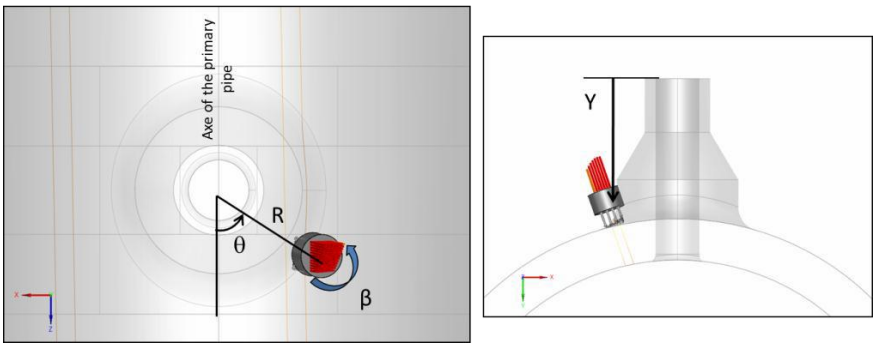

Figure 3: Positioning of the probe at the surface of the specimen.

a. Definition of the examination zone

The examination zone is the zone on which the performances of the inspection method must be guaranteed. In CIVA this zone is defined by describing the position of a set of defects.

The aim is to guarantee to detect all these defects, which will be considered to be equivalent to cover the whole examination zone. This is true only if the density of the defects is sufficient (compared to the size of the focal spot) to be representative of all the possible positions inside the examination zone. In this paper the defects are located in the internal surface of the nozzle, from θ = 0° to θ = 90° (Figure 4). We have considered N = 22 x 5 = 110 defects to define the examination zone.

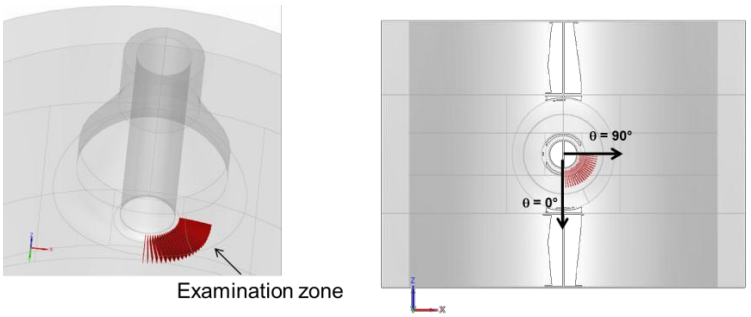

Figure 4: In this paper the examination zone is the internal fillet of the nozzle.

b. Optimal probe positions and accessibility zones

The next step of the methodology consists in determining a set of optimal probe positions from which all the defects of the examination zone are detected.

For each defect an acoustic ray is traced from a focal point on the defect to the surface of the specimen. The angle of the ray and the position of the focal spot on the defect are defined by the user and are the same for all the defects of the examination zone (Figure 5). The points at the surface are considered to be the optimal positions of the probe to inspect the whole examination zone (Figure 6).

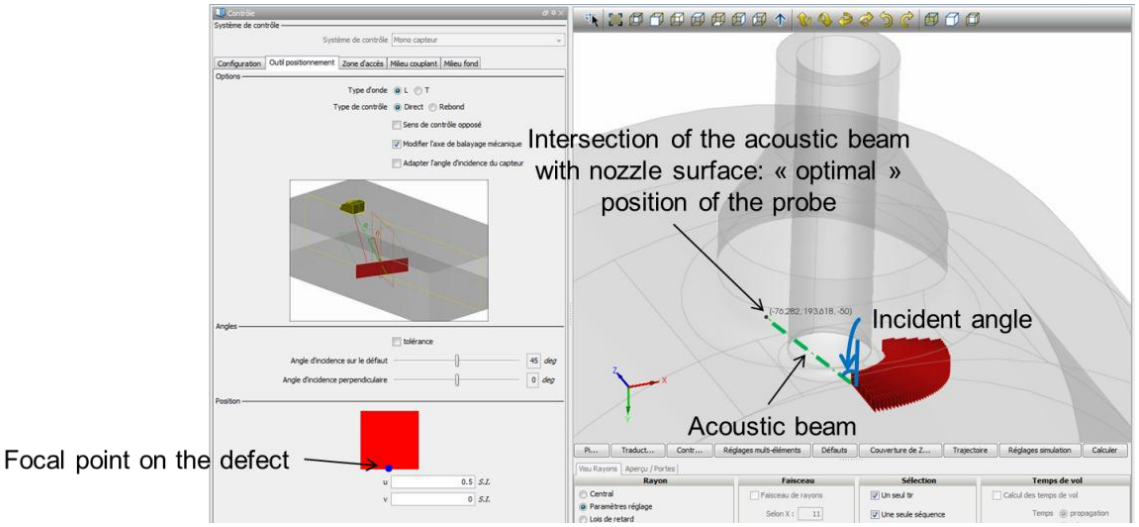

Figure 5: CIVA GUI for the definition of the angle of the acoustic beam and the position of the focal spot on each defect of the examination zone.

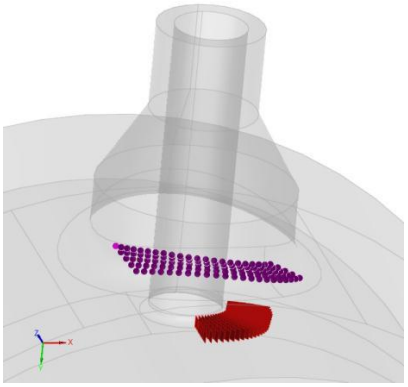

Figure 6: Set of optimal probe positions at the surface of the specimen for an incident angle of 45° on the defects.

However, in some cases it is not possible to place the probe on some or all of these positions. To deal with these cases the user can define a tolerance on the incident angle (Figure 7). He can also limit the parts of the specimens that are accessible, i.e. on which the "optimal" positions can be found: this is the accessibility zone. These parts are selected among those defined on Figure 8. A margin can also be defined to avoid positions being too close to the boundaries of the selected parts. This margin is a rough method to take into account the volume of the probe that can restrict its accessibility.

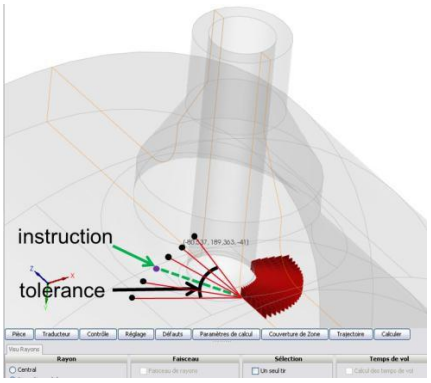

Figure 7: Tolerance on the incident angle on the defect.

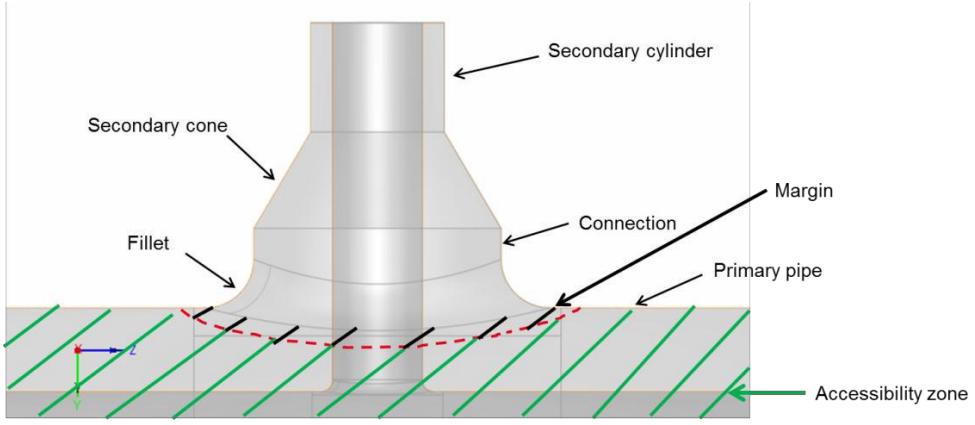

Figure 8: Accessibility zone.

The "optimal" positions (without any accessibility constraint) of Figure 6 were on the internal surface of the nozzle. Anyway, if the only accessible zone is the primary pipe with a margin of half of the probe diameter and a tolerance of [-30°; +10°] on the incident angle on the defect, we obtain a new set of "optimal" probe positions presented Figure 9. The "optimal" positions are now at the boundary of the accessibility zone.

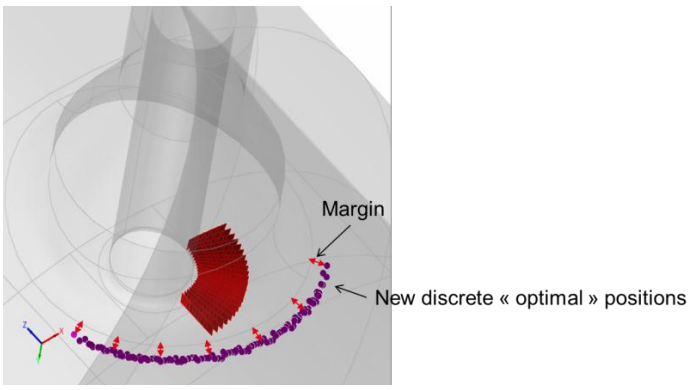

Figure 9: Set of optimal probe positions taking into account the accessibility constraints.

c. Trajectory and focal laws

These positions are used to guide the user for its definition of the probe trajectory. Indeed, the trajectory is not calculated automatically by CIVA but chosen and parameterized by the user, and must be as close as possible to the optimal points determined previously.

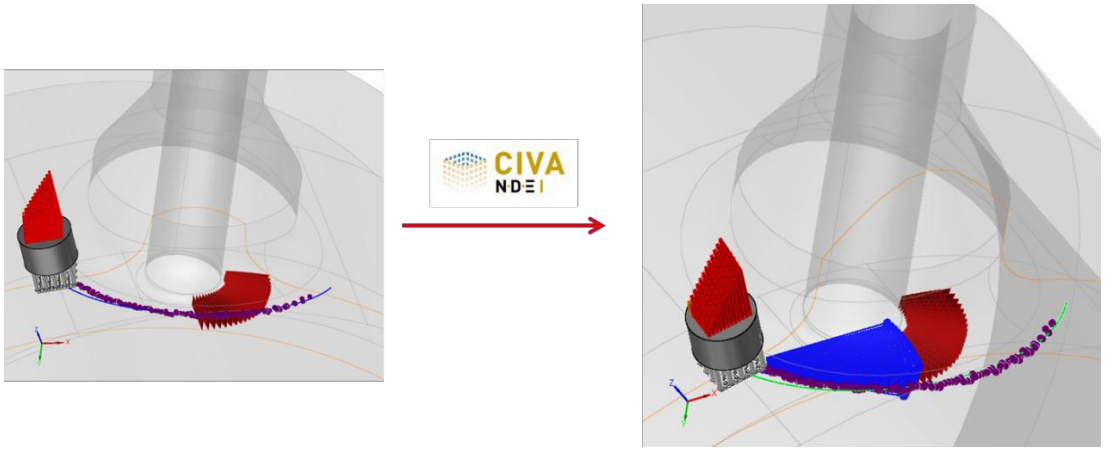

Figure 10: Computation of a matrix of focal parameters adapted to the inspection of the examination zone from the trajectory defined by the user.

From this trajectory (represented on the left of Figure 10 for the present configuration), CIVA computes a matrix of focal parameters adapted to the inspection of the examination zone, the electronic delay laws can therefore compensate the fact that the probe position and orientation is not optimal on the trajectory. On each point of the trajectory the full set (matrix) of focal laws is applied. These focal parameters are computed to guarantee that for each defect of the examination zone at least one law focuses on it when the probe travels along the trajectory. This matrix consists in focusing at different refraction and skew angles defined from the center of the probe (Figure 11).

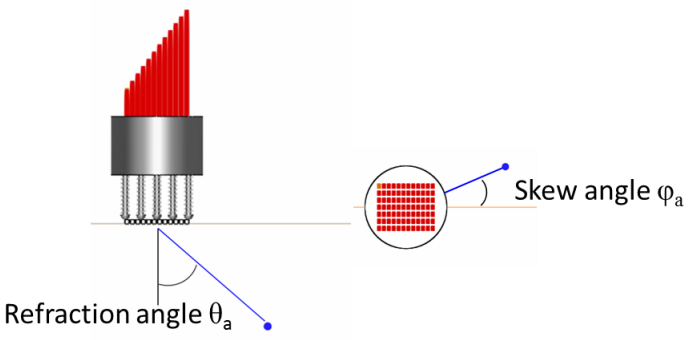

Figure 11: Acoustical angle defined from the center of the probe.

The algorithm is the following:

- *Initialization of $\theta_{a\,min}$, $\theta_{a\,max}$, $\varphi_{a\,min}$, $\varphi_{a\,max}$ = 0*
- *For each defect of the examination zone:*
  - *The closest point of the trajectory to the "optimal" probe position determined previously is considered as the new position from which the defect will be detected (*Figure 12*)*
  - *From this point the refraction angle θ_a and the skew angle φ_a necessary to focus on the defect are determined*
  - *If θ_a (respectively φ_a) is outside the actual values of [$\theta_{a\,min}$, $\theta_{a\,max}$] (resp. [$\varphi_{a\,min}$, $\varphi_{a\,max}$]), then update the new boundary $\theta_{a\,min}$ or $\theta_{a\,max}$ (resp. $\varphi_{a\,min}$ or $\varphi_{a\,max}$)*

At the end of the algorithm the minimal deviation in every direction ($\theta_{a\,min}$, $\theta_{a\,max}$, $\varphi_{a\,min}$, $\varphi_{a\,m}$) necessary to focus at least once on each defect from the trajectory is obtained. The user then defines the number of laws (= density of the matrix of focal spots) in accordance with the focal spot size to have a sufficient overlaying between two adjacent shots.

For the trajectory presented previously the matrix has *M* (refraction) x *L* (skew) = 13x13 = 169 focal parameters (Figure 13).

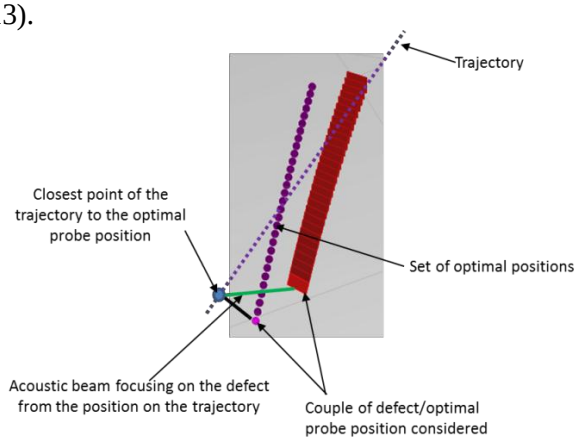

Figure 12: Determination of the position to detect the defect from the trajectory.

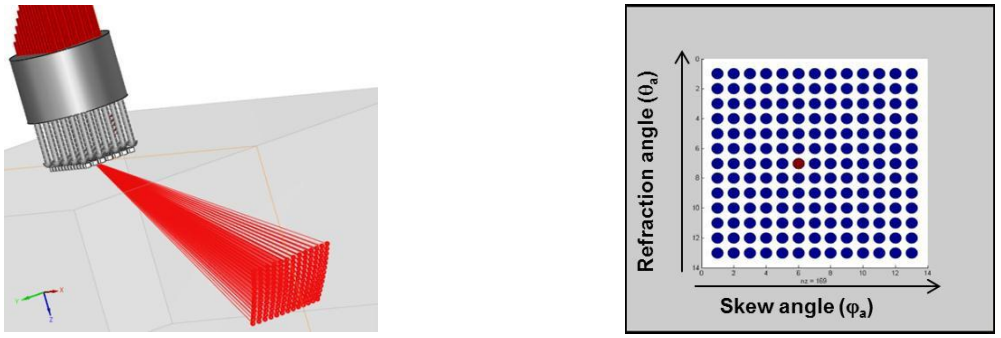

(a) (b)

Figure 13: Matrix of focal parameters.

d. Sensitivity maps

In order to verify the quality of the solution (trajectory + associated focal parameters) determined in the previous steps, sensitivity maps are computed. The procedure used to compute these cartographies is the following:

- *For each defect the probe is placed at the position on the trajectory determined in the previous paragraph (projection of the optimal position on the trajectory).*
  The echo from the defect is computed using CIVA defect response module for each of the focal laws of the matrix.

At the end of these *N* x *M* x *L* (defects x refraction angles x skew angles) computations, the results are calibrated determining the response of side drilled holes (SDH) of 3 mm situated at the focal points for each of the *M* shots without skew (Figure 14). The value of calibration is kept for the *L* shots with the same refraction angle but different skew.

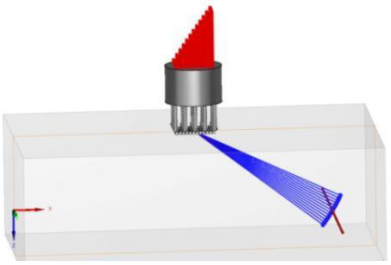

Figure 14: Calibration on SDH ∅ 3 mm situated at the focal point for each shot without skew, on a plane specimen.

Examples of sensitivity maps for different law of the matrix are presented Figure 15. As expected on a complex 3D geometry that requires the use of a phased array probe, it can be noticed that each law has a limited coverage of the examination zone. However, considering the full set of focal laws we obtain the global sensitivity map of Figure 16, which shows that the full examination zone is inspected with a sufficient sensitivity. The closest region to the secondary cylinder is the most difficult to inspect (lowest amplitude) since it requires the most important angle of acoustic skew from the probe (in that case 20°). Due to the rectangular shape of the array of the probe's piezoelectric elements, steering the beam with an important skew with this probe is not favorable which can explain the reduced sensitivity in this region.

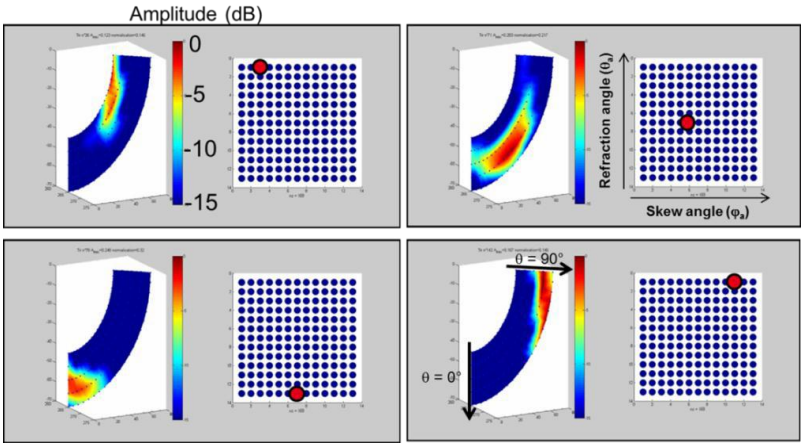

Figure 15: Sensitivity maps for 4 different focal laws.

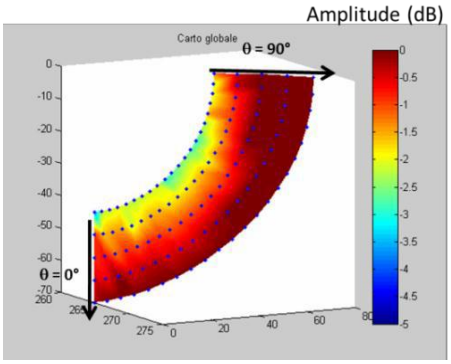

Figure 16: Global sensitivity map.

CONCLUSIONS

We have presented in this paper a methodology to determine a trajectory and the associated focal parameters to inspect a given examination zone in a specimen of complex geometry taking into account accessibility constraints. The methodology provides the required beam steering (skew in particular) that the probe must be able to ensure given the constraints.

The relevance of the solution is evaluated through the computation of sensitivity maps which can highlight zones for which inspection is difficult.

In the context of UT development for the inspection of a 3D complex component, these simulation tools seem to be very helpful to design the NDE process; of course the solution derived from this methodology would have to be compared to experiments to validate the performances while developing the process.

The simulation tools were developed in order to be applicable to various configurations (other geometries, mono-element probes …) and the methodology has been successfully simulated on a specific application (inspection of the internal surface of the nozzle using a flexible matrix array probe). This tool is not yet available in a CIVA commercial version and is being progressively implemented into the software.

DYNAMIC TRACKING OF ULTRASONIC PROBE AND REAL-TIME VOLUMETRIC RAY-TRACING AS A SUPPORT TO MANUAL PHASED-ARRAY INSPECTION OF COMPLEX COMPONENTS

A. Lamarre, J. Habermehl, Olympus NDT, Canada

Abstract

Ultrasonic inspection of complex components usually requires the use of complex 3D scanners to assure full volumetric inspection of the part and volumetric reconstruction of the data. In order to ease the use of manual phased-array, Olympus is currently developing a package integrating a real-time 3D phased-array probe tracking camera with real-time volumetric ray-tracing taking into account the rebounds from the complex geometry. Economic and easy to deploy, it is designed to meet the requirements of ASME standards. This paper will present how this package could prove to be a great benefit for the inspector allowing precise and reliable manual inspection of complex components such as nozzles.

Keywords: Development in volumetric, 3D tracking, ray-tracing, phased array, manual, complex components

ADVANCES IN ULTRASONIC FLAW CHARACTERISATION

L. Carter, Allan Rogerson, AMEC, UK

Introduction

This paper will discuss the progress of techniques for the ultrasonic characterisation of flaws over the last 40 years and describe in more detail one of the most recent studies performed by AMEC in an attempt to validate characterisation for small (~3 mm in through-wall extent) flaws using a combination of an updated objective flaw characterisation software and post-processing algorithms for linear phased array Full Matrix Capture data.

Background

The principles of good ultrasonic inspection design are based on an understanding of the interaction of ultrasound with defects are now well established within the nuclear industry. As long ago as the 1970's (Reference 1) it was recognised that accurate sizing and characterisation of manufacturing and service induced defects in major nuclear reactor pressure vessels and piping posed particular problems for conventional code defined ultrasonic inspection methods. Improved techniques were required to provide meaningful and reliable location, through-wall and length sizing and characterisation (planar or volumetric) information on manufacturing and service induced defects to support plant structural integrity assessments. Research and development programmes were underway in Europe and the USA investigating improved ultrasonic inspection technologies, some of which are now in common use worldwide, others which have been largely discarded.

Reference 1 summarised 1970's research being performed in the areas of

- Improved probe designs (large focused and transmit-receive longitudinal probes) and optimised inspection parameters for specific components and materials based on physical understanding of ultrasound propagation and defect interaction characteristics
- Signal processing techniques for enhancing defect signal to noise ratios and defect discrimination (including adaptive learning networks)
- Defect imaging and sizing using ultrasonic holographic techniques
- Defect length and through-wall sizing using ultrasonic time of flight diffraction (TOFD) and synthetic aperture processing (SAFT) techniques
- Defect characterisation using ultrasonic spectroscopic and multi-parameter regression techniques
- Defect sizing based using Ultrasonic phased and sequential arrays.

It was concluded that more quantitative information was required from defect sizing and characterisation programmes on the relative merits of both conventional and advanced characterisation techniques for specific defect types.

Quantitative information regarding the capabilities of research and best practice industrial ultrasonic inspection techniques for nuclear reactor pressure vessel and piping components emerged (Reference 2) in the 1980-90's from international round robin inspection programmes (DDTs, PISC II and III) in and supporting national experimental and theoretical modelling research programmes. In the UK, the good performance of the multi-probe pulse echo and TOFD/SAFT methods (Reference 3) in the DDT and PISCII round robin tests led to their specification for use in the manufacturing and pre/in-service inspection programmes for the Sizewell B PWR.

In parallel, the benefits of a formal demonstration of the capabilities of the ultrasonic inspection techniques, systems and personnel in circumventing the thorny issue of quantifying overall inspection reliability were recognised and led to the establishment of the UK Inspection Validation Centre (Reference 2). This was mirrored sometime later by the establishment of the European Network for Inspection Qualification and the Performance Demonstration Initiative (PDI) programme in the USA.

The widespread adoption of formal Inspection Qualification as the preferred means of demonstrating the capabilities of nuclear NDE systems, procedures and personnel is evidenced by the large number of technical papers on specific qualification exercises and reviews of national Inspection Qualification programmes presented in recent Conferences (References 4 and 5). Additionally, some of the recognised best practice ultrasonic methods for the detection, sizing and characterisation of defects are now captured in national codes and standards (References 6, 7 and 8).

The status of current best practice defect sizing and characterisation techniques

Almost without exception, Inspection Qualification target defect sizes are based on either structural integrity defect tolerance and crack growth assessments, with an allowance of a reserve factor, or established knowledge of best practice inspection capability in the component in question. This usually ensures that the target qualification defect sizes are large with respect to known inspection capability and hence can be achieved with high reliability. Where this is the case, the current approach to Inspection Qualification is considered fit for purpose. Concerns regarding the existing limitations of existing ultrasonic techniques for sizing and characterising defects, and the lack of a complete theoretical understanding of the processes involved, are of only limited concern.

Emerging requirements for improved small defect sizing and characterisation techniques

Current best practice inspection qualification approaches are challenged when the required qualification target defect sizes for defect detection approach the defect detection limit. This may be the case when refinements to component design, unexpected degradation of component material properties or up-rating of plant service demands lead to smaller start of life tolerable defect sizes. Pressures to minimise intrusive in-service inspection or the impracticality of routine ISI over long operational periods (Reference 9) would also demand further improvements in ultrasonic defect detection, sizing and characterisation capabilities for small start of life defects. For such applications, a reliable capability to discriminate between small crack-like and volumetric manufacturing flaws in new and replacement nuclear plant components is needed. This in turn places extra demands for the use of realistic flaw types in test specimens used for inspection capability, reliability and qualification programmes (References 10 and 11).

Progress in phased array based small defect sizing and characterisation

The major technological advances (in computer processing power, mathematical modelling, sensor technology (composite transducers, and phased arrays) over the last 20 years have not in themselves led to comparative improvements in defect sizing and characterisation performance. They have enabled inspection optimisation for complex geometry components and fast collection, storage and processing of large full RF waveform A-scan data files with the potential for further refinement of defect detection, sizing and characterisation capabilities. However, they have mainly re-confirmed the capabilities achieved with less technologically advanced best practice inspection techniques and systems in the 1980-90's. In particular, the known limitations regarding the detection, sizing and characterisation of small defects evident with earlier best practice inspection design have remained.

Significant advances have been made recently (References 12-15) through academic research into the use of ultrasonic phased arrays for improved small defect sizing and characterisation. Full matrix capture (FMC), Total Focusing Method (TFM), scattering coefficient matrices (SCM) (References 12-14) methods, supported by hybrid modelling of the interaction of ultrasound with rough cracks (Reference 15), have been studied in depth. The potential and limitations of amplitude based, scattering coefficient matrices based and image based techniques for sizing small misoriented crack-like defects of height h have been assessed support by limited experimental trials. In summary, amplitude based techniques appeared most applicable for $h<\sim 0.2\lambda$ (λ = ultrasonic wavelength), scattering coefficient matrices techniques for $\sim 0.2\lambda < h < \sim 1.4\ \lambda$, and imaged based techniques for $h > \sim 1.4\ \lambda$. These finding regarding very small and large defects are largely consistent with current ultrasonic best practice but the applicability of scattering coefficient matrix technique to realistic defects in engineering components has not been tested.

Objective flaw characterisation (OFC) methods

In the early 1980-90's, objective ultrasonic physically-based pattern recognition techniques (References 16 and 17) were developed to aid reliable discrimination between crack-like and volumetric flaws/defects. Ultrasonic full RF waveform data files were collected from raster scans over a suspect defect volume using immersion pulse echo with a variety of inspection angles. Three physically based numerical features derived from the ultrasonic signal amplitude variation with incidence angle (amplitude ratio), the ultrasonic waveform peakedness (kurtosis) and ultrasonic signal volume distribution (sphericity) in three dimensional space are calculated for each suspect flaw volume. These features were stored in a large diverse flaw feature database and plotted in a three dimensional feature space. A clear separation of purely crack-like and purely volumetric defects was evident in the feature space. Calculated features from an unknown flaw could then be plotted in this feature space to determine the flaws relative crack-like or volumetric characteristics within defined confidence limits. The size range of flaws studied in References 16 and 17 were generally larger than those of current interest.

Current study

In the study reported here, we have sought to extend the objective flaw characterisation (OFC) method to smaller flaws by including additional evidence derived from phased TFM images and SCMs.

A series of rectangular (600mm x 600mm x 57mm) ferritic test specimens containing implanted small (≥3mm through wall extent) geometric and realistic weld defects were examined using multi-probe pulse echo techniques and a new small flaw feature database constructed. FMC phased array inspections were then performed over identified flaws from which TFM images and SCMs of each defect were produced.

The multi-probe pulse echo data were collected using 10 mm single crystal diameter 4 MHz (0°, 45, 60°, 70° and 45° tandem) probes and the Micropulse 5PA automated flaw detector running MIPS and GUIDE data collection and processing software. The RF waveforms were collected with a sample rate of 50 MHz on a raster grid of 0.5 mm by 0.25 mm. FMC phased array inspections were performed with 5MHz 64 element probes.

A procedure for assessing the evidence on flaw character from the OFC features (amplitude ratio, kurtosis and sphericity), TFM images and SCMs was then developed and described in a written technical justification of the approach.

The resulting capability was tested in a blind trial performed on an additional ferritic test specimen containing implanted defects. The results from this blind trial are summarised here.

One test specimen was destructively examined to determine the true nature of the implanted defects. A comparison of the ultrasonic and metallographic evidence from four of these defects are presented in images below.

Results

Figure **1** presents a typical plot of two of the flaw features from the flaw feature database.

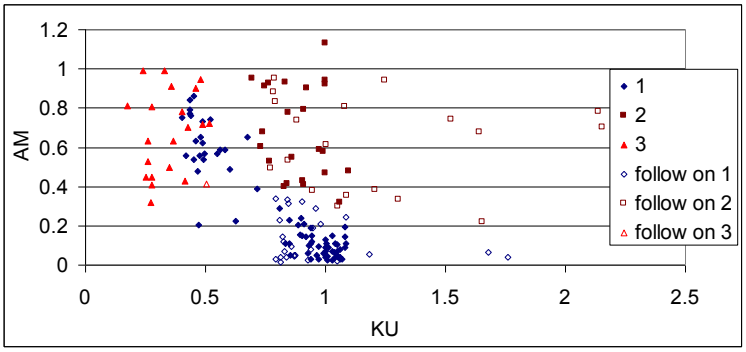

Figure 1 The Amplitude ratio (AM) against the Kurtosis (KU) for the original flaw database and the newly collected results

Figure **1** shows several results with high Kurtosis values which places these particular results away from the other results in 3D space. On closer examination, these results were usually vertical planar defects and the parameters were calculated using the data collected by the tandem technique, which was only introduced during this current project and not in the original OFC program.
The next set of figures show the comparison of a small smooth planar defect with a small planar defect with a complex nature; a mix between volumetric and planar. The figures show the automated multi-probe pulse echo, TFM, SCM and the metallographic images. These defects are from the specimen that was destructively examined.
Figure 2 B, C and D scan for a small (3.7 mm TWE) smooth planar defect

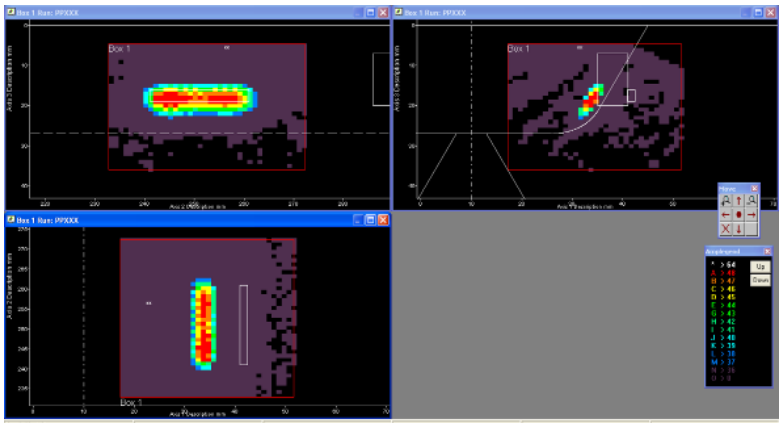

Figure 2 shows the ultrasonic response in three projections for the specified lack of fusion defect indicating a smooth planar defect.

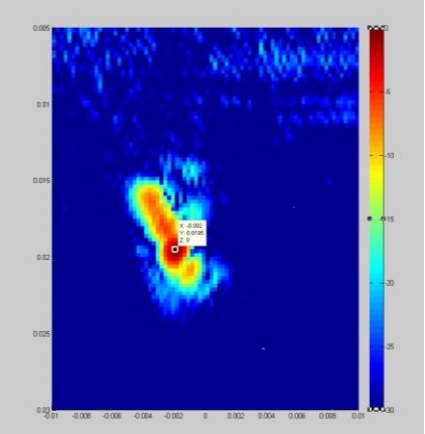

Figure 3 TFM image showing one high amplitude spot but generally an even amplitude distribution along the defect

The nature of the defect can also be clearly seen with the TFM image in Figure **3**. From observation of the image, a smooth planar shape with an even distribution of amplitude would indicate a smooth planar defect.

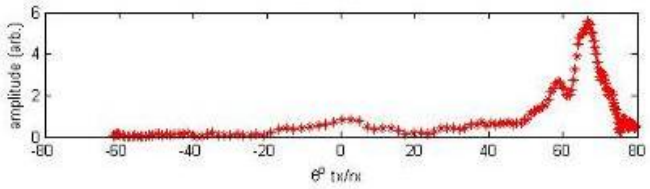

Figure 4 SCM plot showing highest amplitude at approximately 60°

The SCM plot (Figure 4) for the lack of fusion flaw shows a maximum amplitude at approximately 60°, indicating that the defect is orientated at 60° from the horizontal. The shape and amplitude of this distribution also can be used to determine whether the defect is planar or volumetric. In this case a narrow peak and a large amplitude with respect to a side drilled hole indicates a planar defect. A broad peak with a similar amplitude to a side drilled hole would indicate a volumetric defect.

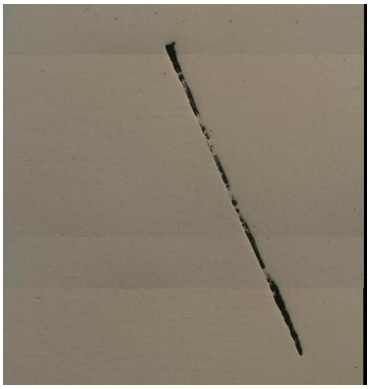

Figure 5 Cross-sectional view of the lack of fusion defect under an optical microscope

Figure **5** shows a smooth lack of fusion defect as expected from the specification of this defect. The OFC software characterised this defect as a planar defect with 100% confidence and the evidence from TFM and SCM compliment this result.

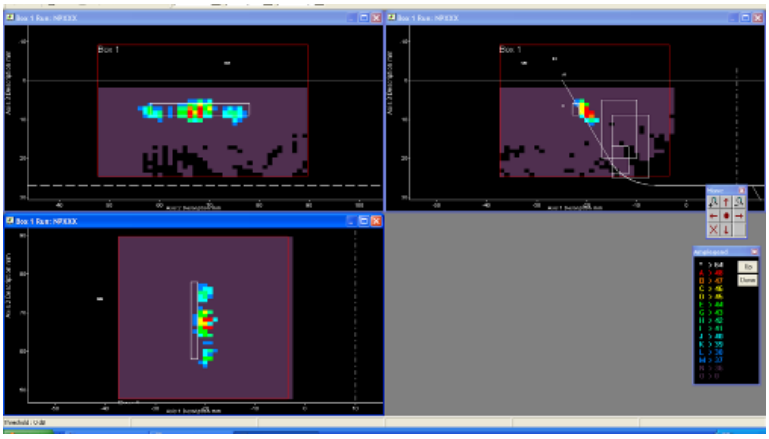

Figure 6 B, C and D scans for a small (3.1 mm TWE) rough heat affected zone defect

The ultrasonic response in
Figure **6** is indicative of a rough defect and at this size it is difficult to make an interpretation as to the type (volumetric or planar) of the defect.

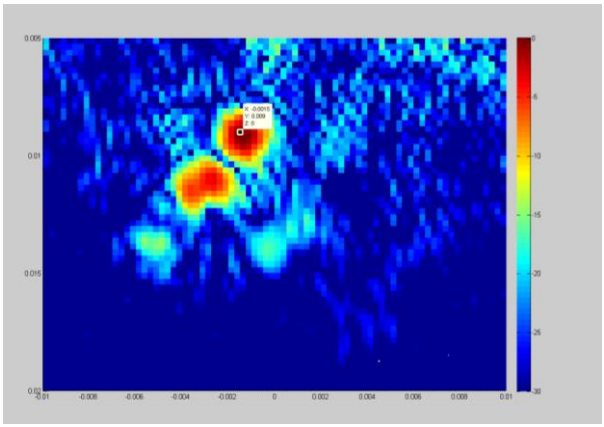

Figure 7 TFM image of the rough heat affected zone defect

The TFM image in Figure 7 shows two large amplitude indications (red) with some surrounding artefact signals. As with the automated pulse echo data it is difficult to determine the true nature of this defect from this image.

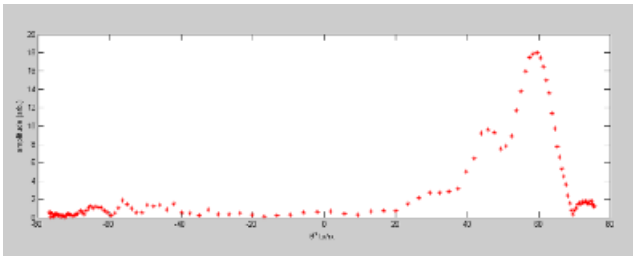

Figure 8 SCM image for the rough heat affected zone defect

The SCM image (Figure 8) again shows a high amplitude peak around 60° indicating a planar defect.

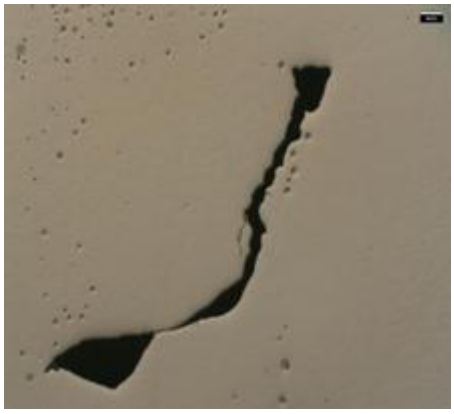

Figure 9 Small mixed characteristic defect

The true nature of the defect is shown in Figure 9 which appears to be a mix between a volumetric and a planar defect. The OFC programme characterised the small smooth planar defect as planar with high confidence but mis-classified the small mixed characteristic defect as volumetric (with lower confidence). However, using a combination of the alternative methods (TFM, SCM) an overall decision with higher confidence can be made.

- After complete destructive examination of this test specimen, it was found that:
- Two defects correctly classified with 100% confidence were smooth planar.
- Two of the defects correctly classified but at lower confidence were planar defects with non-uniform orientation.
- The remaining two defects were misclassified as volumetric with less than 100% confidence and were more complex, with volumetric features.
- The OFC code alone was unable to discriminate between volumetric defects and mixed planar/volumetric defects. However, it was found that the routine was able to provide the data interpreter with a level of confidence, by backing up the original assessment from GUIDE data (or indicating when something has gone wrong).

The TFM and SCM algorithms were able to provide complimentary information, to aid in the characterisation of defects. SCM provided a measure of the scattered amplitude due to the defect as a function of beam angle (thereby allowing an estimate of defect tilt to be calculated), while TFM provided an image focussed at every point, providing a visual guide as to the shape of the defect.

For smaller defects (<4 mm), the SCM technique was particularly useful, as it allowed a determination to be made of both the defect character (planar/volumetric) and the defect tilt (if applicable).

The overall conclusions of the study were -

- OFC classified 88% (150 out of 170) of the current defects in the database correctly.
- OFC classified seven out of the eight blind trial defects correctly.
- SCM performed well on the defects that were misclassified by OFC and on small defects (less than 4 mm extent).

- On the defects that were destructively examined, TFM images showed characteristics that were evident in the defect macrograph e.g. non-uniformly orientated defects had areas of high amplitude along the defect in the TFM image.
- Some defects do not fall into one of the three distinct categories used within OFC. However, the analysis procedure defined in the inspection procedure combining OFC and TFM and SCM information reduces the likelihood of misclassification.

Proposed way forward

Where further improvements in defect sizing and characterisation capability for small defects are needed over and above that achievable by best practice ultrasonic inspection design and inspection qualification methods, an approach based on combined analysis of OFC, TFM and SCM methods offers the potential for significant progress. In this project a start has been made in subjecting some of the more recent phased array based methods to the rigorous capability assessments performed on existing best practice ultrasonic techniques in the 1980-90's.

References

1. A Rogerson and R A Murgatroyd. Defect characterisation using ultrasonic techniques. Research Techniques in Non Destructive Testing Vol. IV, Ch. 12.Edited by R S Sharpe. Academic Press 1980.
2. A Rogerson. A personal perspective on the early developments in inspection qualification and reliability assessment in the nuclear industry and comparison with similar developments in other industries. Procs. of the 9th Int. Conf. on NDE in Relation to Structural Integrity for Nuclear and Pressurized Components. Seattle. 22-24 May 2012, pp.97-106.
3. JP Charlesworth and JAG Temple. Engineering Applications of Ultrasonic Time of Flight Diffraction. Second Edition. Research Studies Press Ltd. 2001.
4. Procs. of 8th Int. Conf. on NDE in Relation to Structural Integrity for Nuclear and Pressurised Components. Berlin. 29 Sept- 1 Oct 2010.
5. Procs. of 9th Int. Conf. on NDE in Relation to Structural Integrity for Nuclear and Pressurised Components. Seattle. 22-24th May 2012.
6. BS EN ISO 23279:2010. Nondestructive testing of welds- ultrasonic testing-characterisation of indications in welds.
7. BS EN 10863:2011. Nondestructive testing of weld-ultrasonic testing-use of time of flight diffraction technique (TOFD)
8. ASME Boiler and Pressure Vessel Code 2013 Edition. Section V. Nondestuctive Examination.
9. J Pitkanen, T Salonen, A Lipponen, M Sarkimo, and R Paussu. Ultrasonic testing of copper welds. Procs of 8th Int. Conf. on NDE in Relation to Structural Integrity for Nuclear and Pressurised Components. Berlin. 29 Sept- 1 Oct 2010. pp 974-983.
10. I.Virkkunen, M Kemppainen, R. Paussu, J Pirinen and P Luostarinen. Proposed improvements for use of different qualification defect types – three generations of defects. Procs of 8th Int. Conf. on NDE in Relation to Structural Integrity for Nuclear and Pressurised Components. Berlin. 29 Sept- 1 Oct 2010. pp 137-146.
11. W. Daniels and D Ludlow. NDE of stress corrosion cracks. Procs of 8th Int. Conf. on NDE in Relation to Structural Integrity for Nuclear and Pressurised Components. Berlin. 29 Sept- 1 Oct 2010. pp 839-844.
12. J Zhang, BW Drinkwater and PD Wilcox. Defect characterisation using an ultrasonic array to measure the scattering coefficient matrix. IEEE Trans.on Ultrasonics, Ferroelectrics and Frequency Control. Vol. 55, No. 16, October 2008, pp2254-2265.
13. J Zhang, BW Drinkwater and PD Wilcox. The use of ultrasonic arrays to characterise crack-like defects. Journal of Non Destructive Evaluation. 2010, Vol. 29, No. 4, pp. 222- 232.
14. PD Wilcox. Ultrasonic arrays in NDE: Beyond the B-scan. AIP Conf. Proc. 1511, 33(2013).

15. J Zhang, BW Drinkwater and PD Wilcox. Longitudinal wave scattering from rough crack-like defects. IEEE Trans. In Ultrasonics, Ferroelectrics and Frequency Control, Vol. 58, No. 10, Oct. 2011.
16. SF Burch. Objective ultrasonic characterisation of welding defects using physically based pattern recognition techniques. Review of Progress in Quantitative NDE. 1987. Vol 7A, pp.1495-1502. Plenum Press, New York.
17. SF Burch, AR Lomas and AT Ramsey. Practical automated ultrasonic characterisation of welding defects. Brit. J. NDT 1990, 32, pp347-350.
18. S Wedge, L Carter, A Rogerson, J Zhang and BD Drinkwater. Defect detection and sizing trials using the Total Focusing Method and Scattering Coefficient Matrix with a linear phased array. To be presented at 10th Int. Conf. on NDE in Relation to Structural Integrity for Nuclear and Pressurised Components, Cannes, Oct 2013.

EMERGING TECHNOLOGIES

IMPROVEMENT OF AN ACOUSTIC SENSOR DEDICATED TO THE INTERNAL GAS CHARACTERIZATION OF A LWR NUCLEAR FUEL ROD IN A HOT LABORATORY FACILITY

JY. Ferrandis, G. Lévèque, E. Rosenkrantz,
Southern Electronic Institute, CNRS, France
J.C. Segura, R. Blachier, EDF - SEPTEN, France
G. Thouvenin, M. Martino, EDF - DCN, France

ABSTRACT

We presented in 2010 [1] an acoustic method to assess the pressure and the composition of the internal gas mixture of a standard LWR fuel rod. It was possible to determine the composition with an uncertainty of about 1% and the pressure with an uncertainty of about 10 bars (for around 50 bars and a gas mixture containing 20% Xe/Kr). The limit of detection was established around 35 bars. A full-scale hot cell test of this acoustic method was also carried out successfully on irradiated fuel rods in the LECA-STAR facility at CADARACHE Centre [2].

We have developed an improvement of this sensor allowing us to divide by two the uncertainty on the pressure measurement. In the case of hot-cell measurements, viscous liquid can be used to couple the sensor with the rod. For gas content with a pressure exceeding 15 bars and a 10% Xe/Kr ratio, such coupling may reduce relative acoustic method accuracy by ±7% for pressure measurement result and ±0.25 % for the assessment of gas composition.

INTRODUCTION

We developed a non-destructive acoustic method allowing measurement of the pressure and the composition of the internal gas mixture in the upper plenum of a standard LWR fuel rod. The sensor is directly in contact with the fuel rod (Fig. 1).

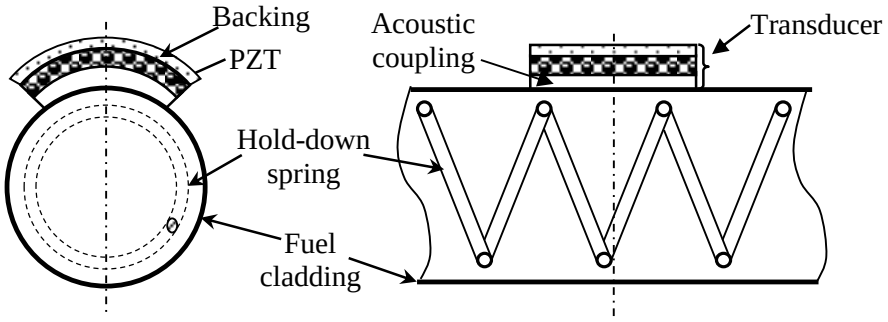

Figure 1. Schematic representation of measurement process, tube inner diameter D=8.36 mm and tube thickness e=57 mm (from [1]).

Several non-destructive methods coexist to assess the internal gas pressure, e.g. measurement by gamma scanning of ^{85}Kr, which requires heavy devices [3, 4]. Other methods had been investigated in the past, but no satisfactory solution has been proposed since; then there is no easy and accurate non-destructive method for determining the fission gas internal pressure and gas composition without puncturing the fuel rod in a hot cell.

Rod internal pressure is a safety criterion, such as e.g. cladding corrosion, giving the range for using the fuel. These parameters constitute a fuel behaviour indicator and reflect the overall fuel performance. Their knowledge is also required to validate engineering code simulations. These data are currently assessed in hot cells.

Our method for pressure measurement has been developed since 1993. It consists in injecting an acoustic pulse in the fuel rod through the cladding and in analysing the signal received by the transducer after a back and forth path of the sound wave through the gas [5].

A full-scale hot cell test of the internal gas pressure and composition measurement by an acoustic sensor was carried out successfully between 2008 and 2010 on irradiated fuel rods in the LECA-STAR facility at CADARACHE Centre. The acoustic sensor has been specially designed in order to provide a non-destructive technique to easily carry out the measurement of the internal gas pressure and gas composition (mainly Helium-Xenon mixture, with a small amount of Krypton) of a LWR nuclear fuel rod. [6].
The representation of the device is described in Fig.1. The central frequency f_0 of the transducer is chosen to be equal to the first transparency frequency of the tube wall:

$$f_0 = \frac{c_D}{2e} = 4.14\,MHz \qquad (1)$$

where c_D is the speed of the longitudinal wave in the metallic wall and e its thickness. The thicknesses of the PZT transducer and of the clad are equal to half wavelength at the frequency f_0. Our sensor is efficient in the 3.5-4.5 MHz range. Several designs optimizing the sensor sensibility were found [7], depending on whether the gain, the bandwidth or both were considered. If the acoustic coupling is low impedance material as water or honey, the best solution is a $\lambda_0/2$ layer instead of the standard solution in $\lambda_0/4$ (Fig. 2).

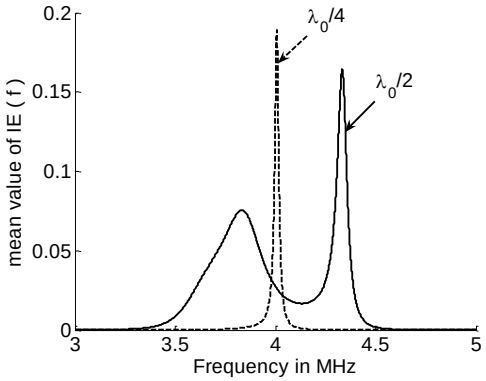

Figure 2. Comparison of the sensor sensibility obtained either with a $\lambda_0/2$ or $\lambda_0/4$ layer of water (theoretical results). For clarity the $\lambda_0/4$ curve has been divided by 4 to be in the same range to the $\lambda_0/2$ one. IE is the power injection efficiency and is representative of the sensor sensibility. (from [1]).

A specific sensor has been designed for an easy use in the hot cell. The specificities do not concern the acoustic part of the sensor but the use of LEMO connector and an auto-positioning system.

Fig. 3. A specific acoustic sensor for hot cell measurements including auto-positioning system and LEMO connector from [6].

An auto positioning system has been proposed to ensure the repeatability of the coupling between the tube and the sensor. It consists in two metallic masses tied to the sensor. With these two masses, the centre of gravity of this heavy system is under the rod: It gives a good stability and a constant coupling

force between the sensor and the rod. Besides, the large size of this system allows handling the device using the tele-manipulators fitted to the hot cell.

The method and the principles of measurement are widely discussed in [4, 5]. The speed of sound can be computed from the gas resonances period measured in frequency spectrum and the molar mass of the mixture, and its composition (volume ratio) can then be deduced. The amplitude of gas resonances in frequency spectrum and of echoes in echogram increases with the pressure. This phenomenon makes it possible to determine the pressure via a calibration process.

We presented in 2010 [1] an application of the acoustic method to assess the pressure and the composition of the internal gas mixture of a standard LWR fuel rod. With a transducer called LMF6, it was possible to determine the composition with an uncertainty of about 1% and the pressure with an uncertainty of about 10 bars (for around 50 bars and a gas mixture containing 20% Xe/Kr). The limit of detection was established around 35 bars. A full-scale hot cell test of this acoustic method was also carried out successfully on irradiated fuel rods in the LECA-STAR facility at CADARACHE Centre [2].

IMPROVEMENT OF THE SENSOR

When a voltage burst excites the system, three kinds of vibrations appear: the transducer vibration (piezoelectric element, coupling layers, 1D-rod), flexural vibrations of the rod and the gas vibration, which has to be measured.

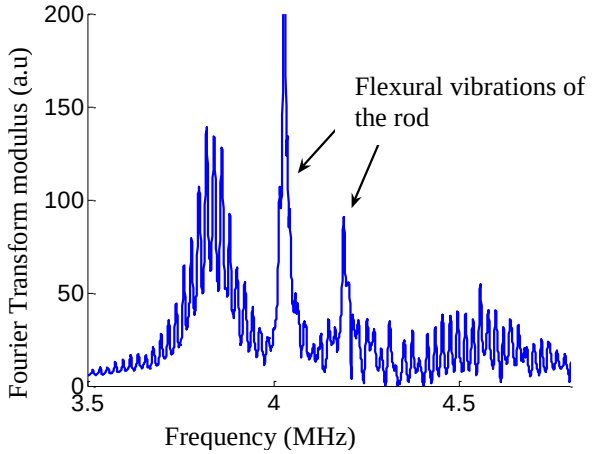

Fig. 4. Spectral response of the system between 3.5 and 5 MHz. The sharp peaks correspond to the gas resonance. The two flexural vibrations of the rod are the main parasites.

The three kinds of resonances are not at the same frequencies in the spectral domain and they do not have the same amplitude. For instance in the case of a rod without a spring and for 150 bars pressurised gas, the resonances of the gas have a high amplitude which constitutes the major part the signal (Fig. 5a). Echoes are separated in time domain without any treatment. The gas signal is higher than the parasite. When the gas signal is low, a Fourier transform can separate parasites, filtering the domain of the flexural vibration of the tube. For instance, in figure 4, the zone between 4 and 4.2 MHz can be excluded. In figure 5b, the parasite (blue curve) is higher than the signal of the gaz. After a signal treatment, gas echoes appear (green curve). But the main problem with such a signal treatment is that it also excludes gas signal in the spectral zone which in not taken into account. The effect can be important in the case of low gas signal and it reduces the low limit pressure of measurement

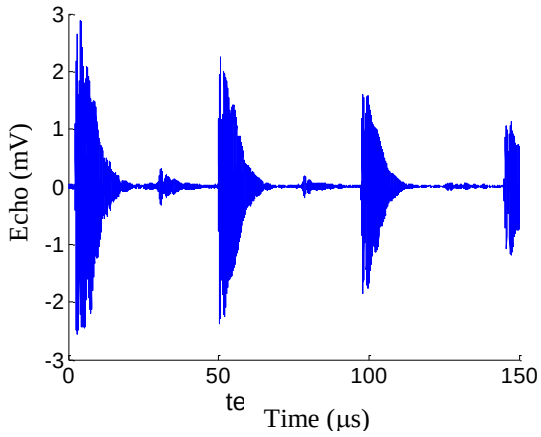

Fig. 5a. Time domain response for a rod without a spring and for 150 bars pressurised gas. The resonances of the gas have a high amplitude which constitutes the major part the signal. The echoes are separated from noise.

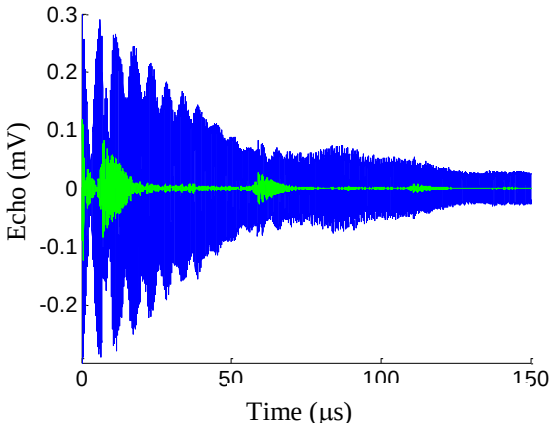

Fig. 5b. Time domain response in the case of the signal is low (blue curve). The echoes are in the noise. After a signal treatment, parasites are separated and gas echoes appear (green curve).

Then it appears important to physically reduce the amplitude of the parasite resonance and to optimize the signal to noise ratio, independently of the signal treatment. The improvement of the device consists in decreasing the influence of the parasite resonance on the measure. If we are able to separate the parasite resonance, we increase the useful signal. The main problem consists in rejecting a frequency domain in which the sensor in not very sensitive to the gas resonance. Il will allow to increase the signal to noise ratio and then to get a lower limit for pressure measurement and a higher accuracy. Two ways have been investigated:

- A new sensor design to shift of the resonance of the transducer in order to minimize the sensitivity in the parasite resonance zone.
- The choice of an acoustic coupling which quickly attenuates the parasite in time domain.

OPTIMISATION OF THE SENSOR DESIGN

A new sensor has been designed. It consists in modifying the width of the matching layers. The minimum of the sensitivity to the gas has been put at the frequency of the parasite resonance. In the figure 6, we present the theoretical curve of the sensitivity to the gas of the sensor versus frequency. The blue curve is the response of the LMF6 sensor used in the past. The response is not so bad but it can be optimized by shifting the minimum of this curve to 4.14 MHz. It is the response of the red curve.

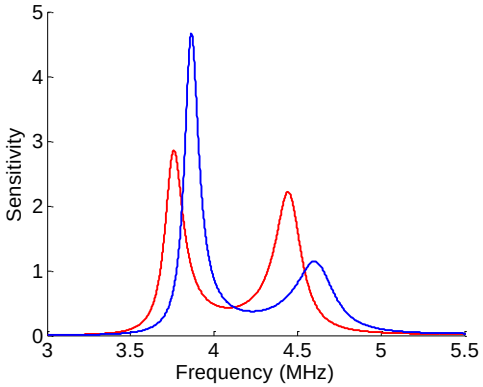

Fig. 6. Sensitivity to the gaz of a new sensor (red curve) compared to the first one (blue curve). The peak of sensitivity has been shifted to minimize the influence of the parasites (around 4.14 MHz)

The experimental responses are presented in the figure 7. We present the measured voltage (dB) versus frequency. Thin curves represent the raw response with the parasite resonance. The thick curves are interpolated responses. We can observe that the LMF10 response (new sensor) has a minimum of the sensitivity in the parasite resonance frequency domain but also present a higher sensitivity in the 4.5 MHz domain witch slightly increase the global sensitivity of the system. This modification of the sensor response allows increasing performances by rejecting the parasite in a low sensitivity zone.

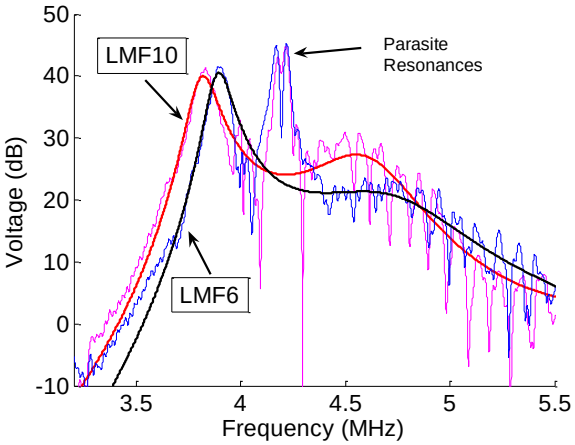

Fig. 7. Experimental response of LMF6 sensor (black curve) and LMF10 sensor (red curve).

OPTIMISATION OF THE ACOUSTIC COUPLING

A second way to reduce the influence of the parasite is to use an acoustic coupling that physically attenuates the parasite. A viscous fluid has been chosen. As we can see on the figure 8, the time decay of the parasite when a viscous fluid is used as acoustic coupling is about 25 microsecond. Above this time, the noise keeps the same value and comes from electronic devices. In the case of water coupling, even above 80 microseconds, the parasite has not disappeared and so interfered with the gas signal. Indeed, the first echo of the gas appears after 40 microsecond (it obviously depends of the mixture) and its amplitude is lower than the noise amplitude.

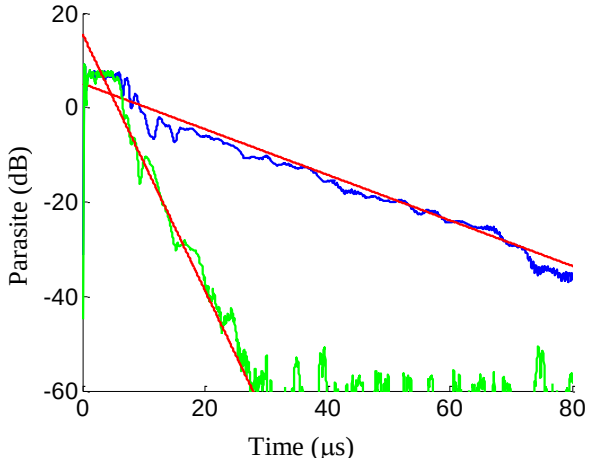

Fig. 8. Time decay of the parasite in the case of water coupling (blue curve) and of viscous fluid coupling (blue curve).

This phenomenon is lightly observed in the figure 9. The blue curves represent the raw signal in the time domain. In the case of water coupling, the parasite is high and last in time. For instance

when the first echo should appear (red curve is obtained after separation of the parasite by Fourier transform treatment as presented before), the parasite widely interferes with the signal. In the case of viscous liquid coupling, at 45 microseconds, the parasite noise is pretty equal to zero and the raw signal is the gas signal.

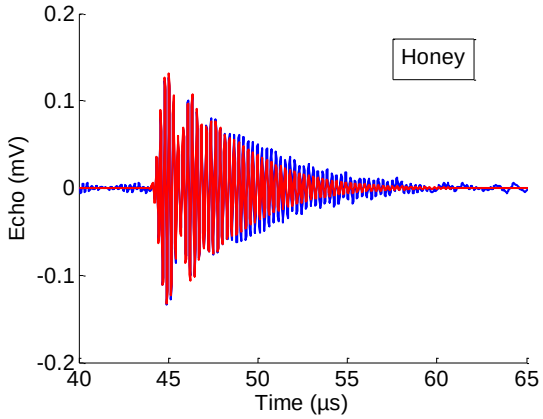

Fig. 9a. LMF10 sensor time domain reponse in the case of honey coupling. Red curve is obtained after separation of the parasite

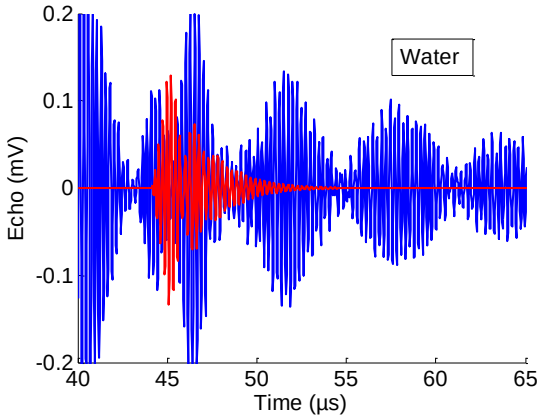

Fig. 9b. LMF10 sensor time domain reponse in the case of water coupling. Red curve is obtained after separation of the parasite

FINAL RESULTS

We have developed an improvement of the sensor allowing us to divide by two the uncertainty on the pressure measurement. In the case of hot-cell measurements, viscous liquid can be used to couple the sensor with the rod. For gas content with a pressure exceeding 15 bars and a 10% Xe/Kr ratio, such coupling may reduce relative acoustic method accuracy by ±7% for pressure measurement result and ±0.25 % for the assessment of gas composition. These results are obtained above more than 500 measurements on gas mixture (pressure varying from 10 bars to 100 bars and composition from 5% of Xenon to 20%)

	Composition uncertainty	**Pressure uncertainty (At 50 bars)**	**Low pressure limit**
Classical Sensor	± 1%	± 10%	35 bars (for mixture above 20% Xe)
New generation of sensor	± 0,25%	±7%	15 bars (for mixture above 10% Xe)

Table I. comparison of performances between classical and new generation of acoustic sensors.

CONCLUSION

With the last generation of acoustic sensors devoted to characterization of fission gas, it was possible to determine the composition with an uncertainty of about 1% and the pressure with an uncertainty of about 10 bars (for around 50 bars and a gas mixture containing 20% Xe/Kr). The limit of detection was established around 35 bars. Now, for gas content with a pressure exceeding 15 bars and a 10% Xe/Kr ratio, such coupling may reduce relative acoustic method accuracy by ±7% for pressure measurement result and ±0.25 % for the assessment of gas composition. The improvement of

this sensor allows us to divide by two the uncertainty on the pressure measurement. Viscous liquid can be used to couple the sensor with the rod.
Such improvement, associated to specific instrumentation and signal treatment, allows proposing our device as a new reliable instrumentation for gas characterization in hot-cell environment.

REFERENCES

1) E. Rosenkrantz, JY. Ferrandis, G. Lévêque, D. Baron, Ultrasonic Measurement of Nuclear Released Gas Pressure and Composition by Ultrasonic Method, 8th International Conference on NDE in Relation to Structural Integrity for Nuclear and Pressurised Components, September 29 – October 1, 2010, Berlin (Germany).
2) JY. Ferrandis, E. Rosenkrantz, G. Lévèque, D. Baron, J.C. Segura, G. Cécilia, O.Provitina, Full-scale hot cell test of an acoustic sensor dedicated to measurement of the internal gas pressure and composition of a LWR nuclear fuel rod, ANIMMA 2011, the 2d International Conférence on Advancements in Nuclear Instrumentation, Measurement Methods and their Applications, June 6-9, 2011, Ghent (Belgium).
3) D.R. Olander, Fundamental Aspects of Nuclear Fuel Elements, chapter 15, TID-26711-P1, Us Dept of Energy 1976.
4) J. Siefken, SCRAP/RELAP5/MOD3.3Code Mannual, NUREG/CR-6150, Vol.2, Rev.2, INEL-96/0422 2001.
5) E. Rosenkrantz, J.Y. Ferrandis, G. Lévèque and D. Baron, "Ultrasonic measurement of gas pressure and composition for nuclear fuel rods," Nuclear Instruments and Methods in Physics Research Section A: Accelerators, Spectrometers, Detectors and Associated Equipment, vol. 603, no. 3, pp. 504-509, 2009.
6) J.Y. Ferrandis, E. Rosenkrantz, G. Lévèque, D. Baron, J.C. Segura, G. Cécilia, O.Provitina, Full-scale hot cell test of an acoustic sensor dedicated to measurement of the internal gas pressure and composition of a LWR nuclear fuel rod, Nuclear Science, IEEE Transactions on, 60 (4), pp.2894-2897 2013.
7) G. Lévêque, E. Rosenkrantz, and D. Baron, "Acoustic Injection Into a Pressurized Gas Through a Metallic Wall," Acta Acustica united with Acustica, vol. 93, pp. 722-729, 2007.

PROPERTY STUDY ON EMATS WITH VISUALIZATION OF ULTRASONIC PROPAGATION

T. Yamamoto, T. Furukawa, I. Komura
Japan Power Engineering and Inspection Corporation, Japan
R. Urayama, T. Uchimoto, T. Takagi, Tohoku University, Japan

INTRODUCTION

In ultrasonic testing, a transducer placed on a test object generates ultrasonic waves in the test object according to applied voltage and converts returning echoes into electrical signals. A discontinuity in the test object can be found by examining echo signals that represent returning ultrasonic waves reflected or diffracted by the surface of the discontinuity. However, the surface condition of a discontinuity or the material property of a test object sometimes makes ultrasonic waves propagate along unexpected paths, which leads to inappropriate evaluation of the discontinuity. Visualization of ultrasonic propagation is a powerful tool to verify actual behavior of ultrasonic waves inside a test object. For ultrasonic testing with a piezoelectric transducer, many studies for visualization of ultrasonic propagation have so far been conducted to confirm how ultrasonic waves propagate inside a test object. In these studies, visualization of ultrasonic propagation is realized by a numerical simulation or experimental measurement.

Ultrasonic testing is usually performed with a piezoelectric transducer. While a piezoelectric transducer requires a coupling medium to transmit an ultrasonic wave into a test object efficiently, an electromagnetic acoustic transducer (EMAT) directly generates an ultrasonic wave at the surface of a metallic test object by the electromagnetic interaction [1)]. Some studies have shown the results of numerical calculations to visualize ultrasonic propagation generated by an EMAT for improvement of inspection using an EMAT [2, 3)]. Such calculations need to be performed as a coupled analysis of electromagnetic forces and elastic waves. Establishing an experimental approach to visualize ultrasonic propagation for EMATs makes it possible to verify the results of these complicated calculations. The reference 4) introduces a method to visualize ultrasonic waves that propagate in a metallic block by scanning the side surface of the block with a piezoelectric transducer. In our experiment, this method is applied to visualization of ultrasonic propagation for an EMAT. This paper shows the results of experimental and computational visualization methods and compares these results to confirm that the computational results well reproduce the experimental results.

An EMAT usually consists of a coil and magnets. The coil to which driving pulses are applied induces eddy currents in the surface of a test object. There is a static magnetic field due to the magnets near this surface. Lorentz forces caused by the eddy currents and the static magnetic field generate ultrasonic waves in the test object. In ferromagnetic materials, ultrasonic waves are also generated by magnetostriction forces arising from a combination of the static magnetic field of the magnets and the dynamic magnetic field created by the coil. In this study, we concentrate on nonmagnetic materials and do not consider magnetostriction forces.

EXPERIMENTAL VISUALIZATION

Figure 1 describes the configuration of the experimental visualization method we exploit. An EMAT is placed on the top of the specimen as the transmitting probe. A scanning mechanism which can hold a piezoelectric transducer is mounted on the side surface of the specimen to scan a two-dimensional area parallel to the travelling direction of the ultrasound generated by an EMAT. The scanning result provides images that represent transient changes in the intensity distribution of ultrasound on the side surface. Then it is desirable to place the transmitting probe as close to the side surface as possible so as to make the central axis of the ultrasound beam closer to the side surface.

The specimen used in the experimental measurement for the visualization is 50 mm in the *x*-direction, 200 mm in the *y*-direction and 30 mm in the *z*-direction. The material of the specimen is 316 austenitic stainless steel (JIS G 4305 SUS316). Figure 2 shows the structure of the EMAT used in this measurement [5]. The EMAT consists of a coil and permanent magnets. The coil is a race-track type and wound with a single layer of 40 turns of copper wire of 0.12 mm in diameter. The alternating current flowing through the coil induces eddy currents in the surface of the specimen. Only the straight line part of the coil (20 mm×11 mm) is utilized for generation of ultrasound. Two samarium-cobalt magnets of vertically opposite polarities are combined and placed on the top of the coil to create a static magnetic field. The eddy current induced in the surface of the specimen and the static magnetic field created by the magnets work together to give rise to Lorentz forces, which generate ultrasonic waves in the specimen.

Because the coil and magnets are not axisymmetric, the view of ultrasonic propagation observed on the scanned surface becomes different according to whether the scanned surface is parallel to Side A or Side B of the EMAT (Figure 2). Then we conducted the measurements in both cases. The eddy currents in the surface of the specimen are basically parallel to the current flowing through the coil, and the dominant direction of the static magnetic field created by the magnets is perpendicular to the surface of the specimen. The direction of the Lorentz forces is perpendicular to both the eddy currents and the magnetic field. Therefore the dominant direction of vibration of the shear waves generated by the Lorentz forces is supposed to be also perpendicular to both the eddy current and the magnetic field (Figure 3). As the receiving probe, a shear wave transducer is used when the scanned surface is parallel to Side A, and a longitudinal wave transducer is used when the scanned surface is parallel to Side B.

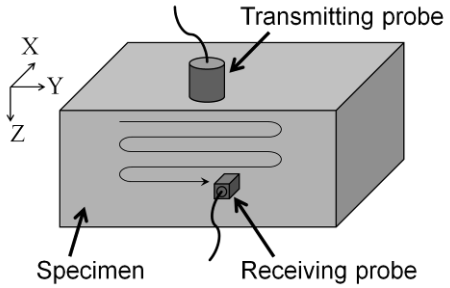

Figure 1. Measurement configuration for visualization of ultrasound.

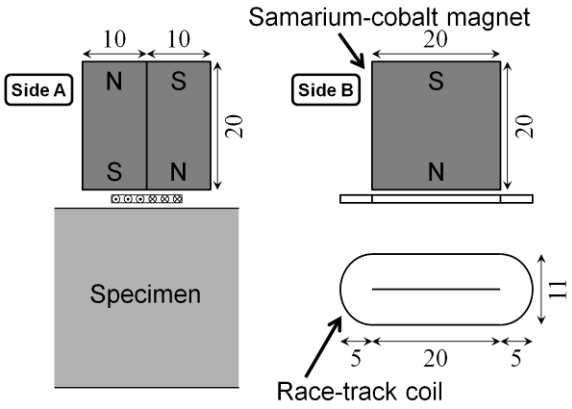

Figure 2. Structure of EMAT.

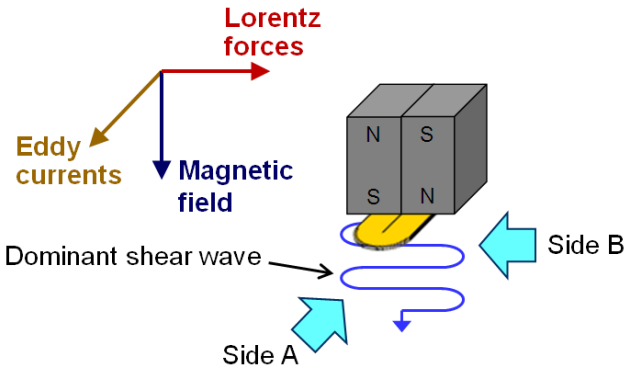

Figure 3. Observing directions for behavior of ultrasonic waves.

Driving pulses applied to the coil of the EMAT are produced by the pulser-receiver (RITEC RPR-4000). Each pulse is a three-cycle sinusoidal pulse of a center frequency of 2 MHz, and its peak-to-peak voltage is approximately 700 V. The automated multi-channel UT inspection system (Just R&D UT station) is used to manage a transmitting probe and a receiving probe separately and record the signals obtained by the receiving probe while the UT inspection system controls a scanning mechanism to move the receiving probe. A driving pulse transmitted by the UT inspection system is converted to a rectangular pulse as a trigger signal for the pulser-receiver to synchronize the EMAT as the transmitting probe and the piezoelectric transducer as the receiving probe. The center frequency of the piezoelectric transducer used as the receiving probe is 2 MHz, and the size of its oscillator is 2 mm square.

Because the amplitude of ultrasonic waves generated by an EMAT is generally smaller than that by a piezoelectric transducer, the SN ratio with an EMAT tends to be worse than that with a piezoelectric transducer. This hinders experimental visualization of ultrasonic propagation generated by an EMAT. To compensate this problem, the signals obtained with the receiving probe are amplified by the pre-amplifier and the internal amplifier of RPR-4000 and noises on the signals are reduced by the bandpass filter (NF FV-628B).

Figure 4 shows actual devices that realize a scanning mechanism. In the picture, the scanned surface faces upward. The specimen is mounted in a thin stainless plate which has a hole of the same size as the cross section of the specimen to prevent the receiving probe from inclining at the edge of the specimen. The probe holder in the center of the picture moves the receiving probe on the scanned surface. The scanning pitch is 1 mm.

The results of the experimental visualization are shown in a later section to be compared with the results of the computational visualization.

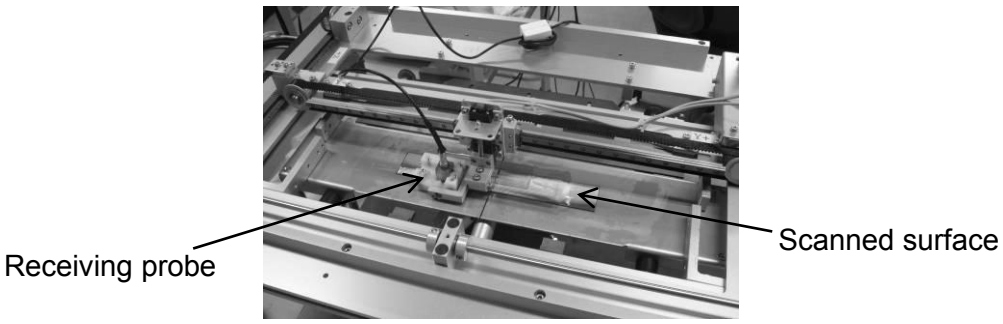

Figure 4. Actual devices for scanning mechanism.

COMPUTATIONAL VISUALIZATION

A computational approach to visualize ultrasonic propagation generated by an EMAT has two steps: calculation of Lorentz forces that generate ultrasonic waves and simulation of propagation of the generated ultrasonic waves. Two bunches of commercial software are used for these steps respectively. EMSolution, developed by Science Solutions International Laboratory (Japan), is software for numerical electromagnetic analysis based on the edge element finite element method (FEM) and used to calculate Lorentz forces generated by an EMAT. ComWAVE, developed by ITOCHU Techno-Solutions Corporation (Japan), is software for simulation of ultrasonic propagation based on the voxel-based FEM and used to calculate propagation of ultrasonic waves generated by the Lorentz forces obtained above.

Figure 5 shows the calculation model for EMSolution. Only half part of the considered objects is modeled using geometric symmetry. The size of the specimen region is 50 mm×100 m×20 mm. The air region extends 30 mm in the direction of each horizontal axis, 50 mm toward the top and 10 mm toward the bottom from the specimen region. The conductivity and the relative permeability of the specimen region are set to 1.35×10^6 S/m and 1.0 respectively. The dimensions of the EMAT are made the same as shown in Figure 2. The thickness of the coil and the gaps above and under the coil are set to 0.5 mm. To suppose the number of turns of the coil is 40, the cross-sectional current of the coil is given by multiplying the input current by 40. The input pulse is given by

$$w(t) = \sin(2\pi ft)\left\{1 - \cos\left(\frac{2\pi f}{n}t\right)\right\},$$

where t is the time variable (the unit is second), f is the center frequency and set to 2×10^6 Hz and n is the number of waves and set to 3 (Figure 6). The magnetization vectors of the two magnets are respectively set to 1 and −1 T in the vertical direction. The material of the magnets is treated as nonconductive and nonmagnetic objects.

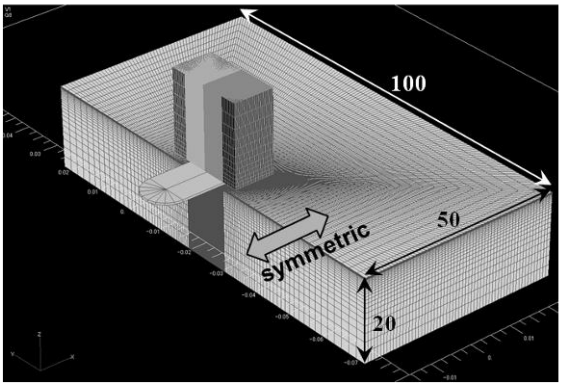

Figure 5. Calculation model for EMSolution.

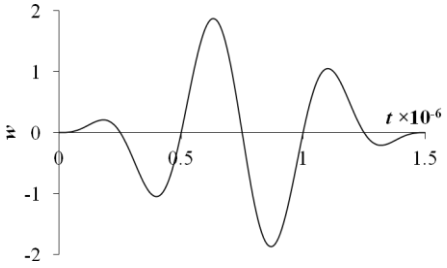

Figure 6. Waveform of input pulse.

In the numerical electromagnetic analysis, the mesh of the calculation model can be made sparse with the increasing distance from the EMAT because calculation errors in regions distant from the EMAT do not have considerable influence on the calculated Lorentz forces we need. However, simulation of ultrasonic propagation requires its calculation model to be uniformly meshed because ultrasonic waves emanate all over the model and may reflect back to a significant region. Therefore the calculation model for ComWAVE is built up with only 0.1-mm voxels, and the distribution of Lorentz forces should be given at the vertices of these voxels to ComWAVE. To transport the distribution of Lorentz forces to ComWAVE easily, in the model for EMSolution, the region where Lorentz forces are calculated as the input data for ComWAVE is meshed with 0.1-mm cubes. This uniformly meshed region is a 6 mm×12 mm×0.5 mm block around the point where the EMAT is placed on the surface of the specimen region.

In the experimental visualization, the scanned surface is parallel to Side A or Side B of the EMAT. Then, the computation by ComWAVE was performed for these two cases. This can be realized by exchanging the horizontal axes of the distribution of Lorentz forces. Figure 7 shows one moment of the ultrasonic propagation computed by ComWAVE. The two-dimensional view on the surface corresponding to the scanning surface is used to compare the results of the experimental and computational visualization methods in the next section.

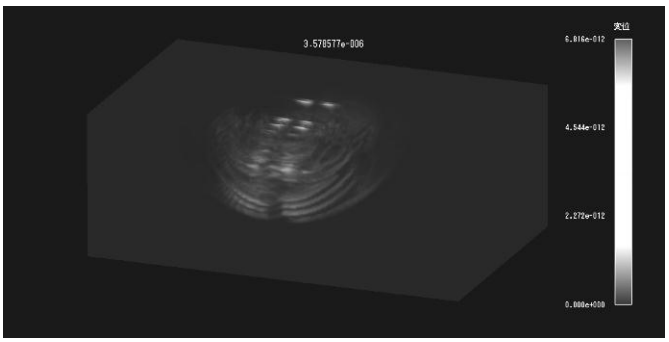

Figure 7. Visualization image of ComWAVE.

COMPARISON OF EXPERIMENTAL AND COMPUTATIONAL RESULTS

Figures 8 and 9 provide comparisons of the results of the experimental and computational visualization methods. The experimental results are shown as the distribution of the received signal amplitude obtained with a piezoelectric transducer at each point, and the computational results are shown as the distribution of the absolute value of the displacement at each point. The origin of the coordinates is the point where the EMAT is placed.

Figure 8 shows the results when the scanned surface is parallel to Side A, and Figure 9 shows the results when the scanned surface is parallel to Side B. In these figures, distributions after the same time elapsed from the emission of the input pulse are aligned in a row. In austenitic stainless steel, the sound velocities of longitudinal waves and shear waves are about 5790 m/s and 3100 m/s respectively. It is confirmed that the longitudinal waves precede the shear waves in these images. Although the images obtained with the experimental approach include superfluous waves, the results of both visualization methods depict very similar transitions of ultrasonic propagation. After the longitudinal waves are reflected by the bottom surface, another group of shear waves occur due to mode conversion. Propagation of these shear waves are also observed by both visualization methods.

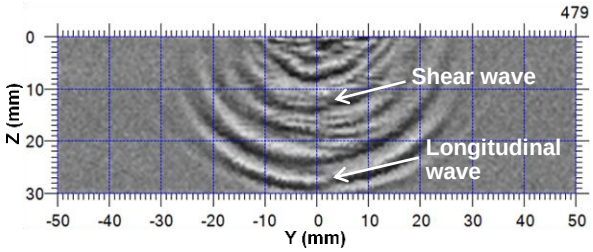

(a) Experimental result (5.3 μs)

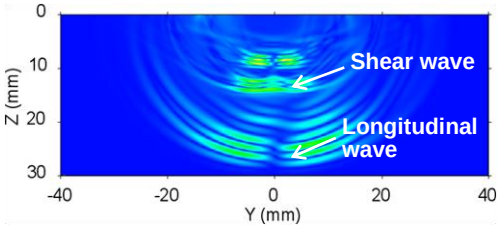

(b) Computational result (5.3 μs)

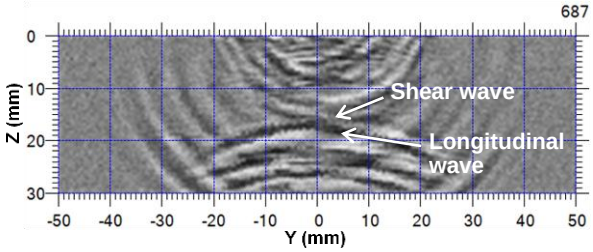

(c) Experimental result (7.4 μs)

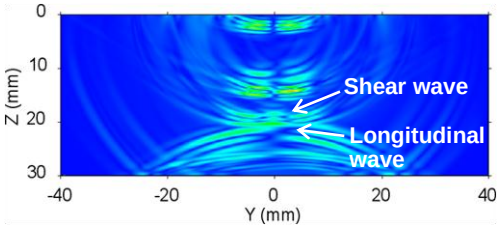

(d) Computational result (7.4 μs)

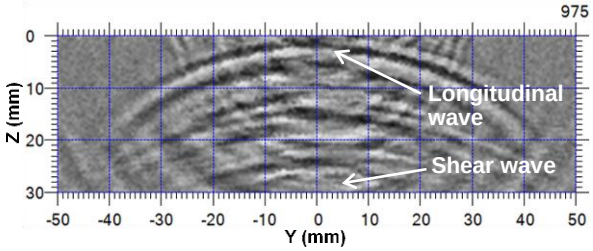

(e) Experimental result (10.3 μs)

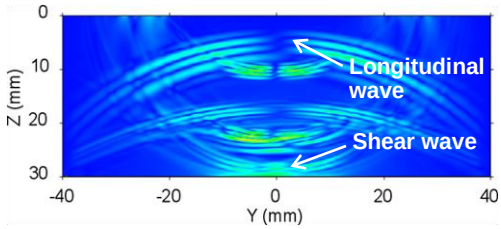

(f) Computational result (10.3 μs)

Figure 8. Comparison of experimental and computational results (Side A)

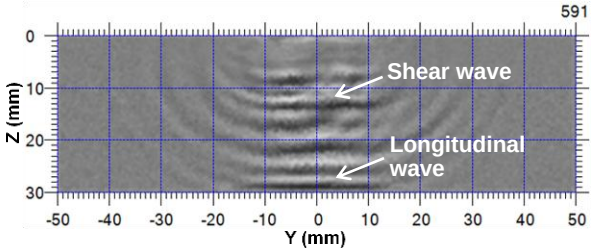

(a) Experimental result (5.9 μs)

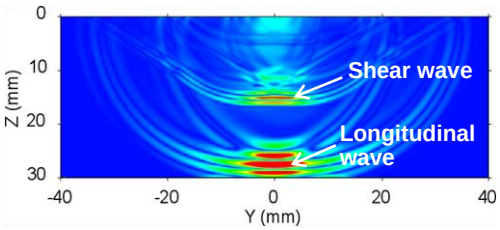

(b) Computational result (5.9 μs)

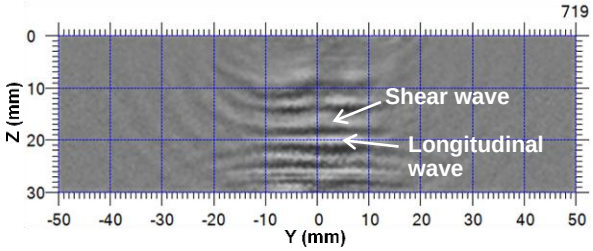

(c) Experimental result (7.2 μs)

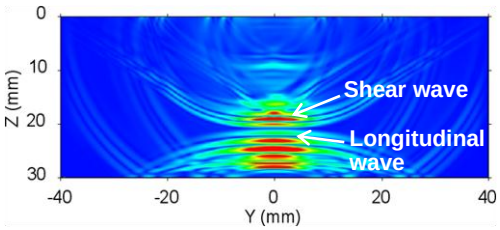

(d) Computational result (7.2 μs)

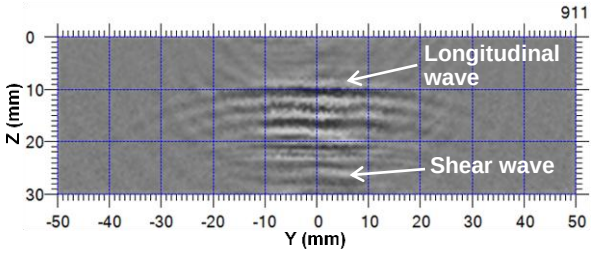

(e) Experimental result (9.1 μs)

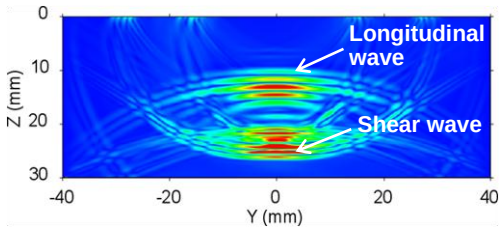

(f) Computational result (9.1 μs)

Figure 9. Comparison of experimental and computational results (Side B)

SUMMARY

Ultrasonic propagation generated by an EMAT was visualized by scanning the side surface of the specimen with a piezoelectric transducer as an experimental approach and by a combination of numerical electromagnetic analysis and simulation of ultrasonic propagation as a computational approach. The computational results well reproduced the experimental results.

The results of the experimental visualization provide evaluation criteria to assess the validity of computational results. The comparison results shown above validate that this computational approach is an appropriate method to find how the structure of an EMAT affects the generation of ultrasonic waves and to improve inspection using an EMAT.

From another aspect, it is desirable to calculate the signal received by an EMAT to be compared with the corresponding signals in an experiment for validation of the computation. To avoid considering magnetostriction, this study focuses on nonmagnetic materials. Taking account of magnetostriction in numerical electromagnetic analysis enables us to calculate ultrasonic propagation generated by an EMAT in ferromagnetic materials as well.

REFERENCES

1) Hirao M and Ogi H, *EMATs for science and industry: Noncontacting ultrasonic measurements*, Boston/Dordrecht/London, Kluwer Academic Publishers, 2003.
2) Sugiura T and Maruyama S, "Numerical analysis of ultrasonic detection by an EMAT," *Review of Progress in Quantitative Nondestructive Evaluation*, 2001, **20**, 898–905.
3) Itoh H, Sugiura T, Maruyama S, Yokota S and Enoeda M, "Numerical analysis of joint inspection using electromagnetic acoustic transducers," *International Journal of Applied Electromagnetics and Mechanics*, 2002, **15**(1–4), 3–8.
4) Furukawa K, Yoneyama H, Horii Y and Uesugi N, "Measurement of ultrasonic wave propagation in austenitic stainless steel welds—(I)," *Proceedings of the Second International Conference on NDE in Relation to Structural Integrity for Nuclear and Pressurized Components*, 2000, B195–201.
5) Urayama R, Uchimoto T and Takagi T, "Application of EMAT/EC dual probe to monitoring of wall thinning in high temperature environment," *International Journal of Applied Electromagnetics and Mechanics*, 2010, **33**(3–4), 1317–1327.

DETECTION OF INCIPIENT SCC DAMAGE IN PRIMARY LOOP PIPING USING FIBER OPTIC STRAIN GAGES

B. K. Jackson, D. Bosko, M. T. Cronin, J, W. Warwick, Intertek AIM, USA
J. J. Wall EPRI, USA

Abstract

Current nondestructive examination (NDE) technology detection capabilities limit our ability to detect stress corrosion cracking (SCC) damage until it has progressed significantly. This work describes the continued development of an *in-situ* monitoring technique to detect and characterize mechanical damage caused by SCC, allowing the detection of the incipient stages of damage to components/piping. The application of this study is to prevent failures in the primary cooling loop piping in nuclear plants. The main benefit to the industry will be improved safety and component lifetime assessment with fewer inspections.

The technique utilizes high resolution fiber optic strain gages mounted on the pipe outside diameter (OD). This technique has successfully detected changes in the residual stress profile caused by a crack propagating from the pipe inside diameter (ID). The gages have a resolution of < 1 με. It has been shown experimentally for different crack geometries that the gages can readily detect the changes of ~10 – 60 με caused on the OD of the pipe due to crack initiation on the ID.

This paper focuses on the latest in the development of the technology. Details of the previous work in this effort may be found in in [1-3]. A short summary is provided in this paper. The main recent development was the full scale accelerated SCC cracking in boiling magnesium chloride ($MgCl_2$) experiment. In conjunction with experimentation, both 2D and 3D finite element (FEA) models with thermal and mechanical analyses have been developed to simulate the changes in residual stresses in a welded pipe section as a SCC crack progresses.

Background & Motivation

One of the biggest challenges for the nuclear power industry is SCC in aging materials as plants continue to run beyond their original design lifetimes. This occurs in structural materials of Pressurized Water Reactors (PWRs) and Boiling Water Reactors (BWRs) primarily in the sensitized heat affected zones (HAZ) of welds. Current NDE technology is limited in its ability to detect SCC cracks in their incipient stages. Previous laboratory-based studies undertaken by EPRI suggest that component lifetime in the field is more often governed by the initiation and growth of short stress corrosion cracks than by the growth of long (deep) cracks [4]. SCC is especially dangerous as it can propagate rapidly once initiated with little or no change in external environment. The inspection interval for each individual weld may be as long as 10-15 years of operation. This is likely sufficient time for a through wall crack to form from an initiation point that currently is too small to detect.

The purpose of this work has been to develop a real time in situ technique to allow the earliest possible detection of incipient stage damage to components/piping. This is achieved by monitoring the change in residual stress on the pipe OD as an ID SCC crack initiates, using highly sensitive fiber optic strain gages.

The technique has gone through proof of concept (work presented in [1-3]), and this work now presents the results from the most realistic damage simulations (both experimental and modeling based) to date. The main benefit to EPRI members will be improved component lifetime assessment with fewer inspections.

Overview of Monitoring Technology Development to Date

A more complete description of the various stages and experimental methods may be found in [2-4].

Firstly, a proof of concept study was conducted on a flat welded plate. A "crack" front was simulated by electrical discharge machining (EDM) that introduced a linear advancing crack front from the weld root towards the crown. A second experiment set used an EDM electrode to simulate a more realistic semielliptical crack front progressing through a circumferential weld in a pipe section. These experiments both showed that there was a measureable and distinct strain response to crack initiation and propagation, independent of temperature change, on the weld crown side (OD for the pipe) of a crack initiated on the opposite side.

In an effort to correlate strain response with crack depth, the initial portion of the data for each semielliptical crack front experiment was taken and normalized to remove the time component. Figure 1 shows the strain response data for the central strain gage for the first 5 mm of cut for each of the normalized data sets. It can be seen that the relationship between cut depth and strain response is approximately linear for the first 3 mm. Experimental limitations prevent constant cut rate beyond this depth. With further data sets it may be possible to develop a semi-quantitative relationship between crack depth and strain response for a single crack. The presence of multiple, interacting, or branched cracks will likely make this significantly more challenging.

The experiments were limited in their ability to accurately simulate an SCC crack, as the cracks produced were not branched, and they did not follow the path of the sensitized region in the HAZ. There were also some equipment limitations that prevented a constant crack growth rate. However, it was considered sufficient to prove the concept that changes in residual stress could be used to monitor for crack initiation.

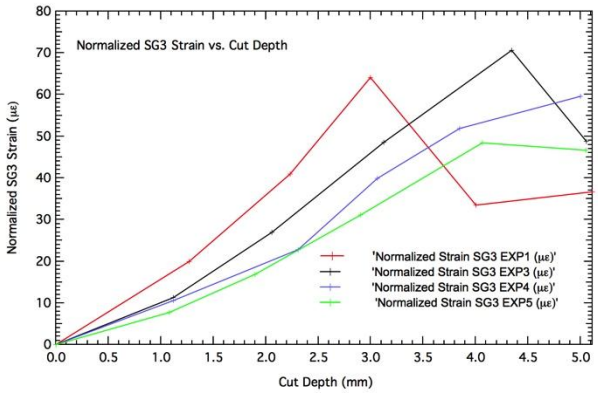

Figure 1 – Normalized Strain vs. Depth Correlation Elliptical EDM Crack Experiment

Full Scale Boiling $MgCl_2$ Accelerated SCC Experimental Method

This experiment represents the most realistic simulation of SCC cracking to date. The specimen used was, as in the semielliptical EDM experiments, a 12" OD 304L pipe section with a 1" wall thickness, and a height of 22". There was a single V-groove circumferential weld half way along its length.

The experimental method is based on ASTM G36 - 94(2013): *"Standard Practice for Evaluating Stress-Corrosion-Cracking Resistance of Metals and Alloys in a Boiling Magnesium Chloride Solution"* [5]. This standard uses small test coupons (~0.5-1.0 in^2) immersed in boiling $MgCl_2 \bullet 6H_2O$ in a 1 L Erlenmeyer flask. The boiling magnesium chloride test is applicable to wrought, cast, and welded stainless steels and related alloys. It is a method for detecting the effects of composition, heat treatment, surface finish, microstructure, and stress on the susceptibility of these materials to chloride stress corrosion cracking [5]. The boiling $MgCl_2$ solution reacts with the stainless steel to achieve chloride stress corrosion cracking in an accelerated time frame. The experimental method employed here uses a scaled up specimen in the form of the entire pipe section, and an accordingly scaled up volume of corrosive media.

Figure 2 shows a diagram of the experimental set up with an image of the as-built apparatus. 18 fiber optic strain gages (SG) and 6 temperature compensation (TC) gages were evenly spaced around the OD of the pipe spanning the weld. .

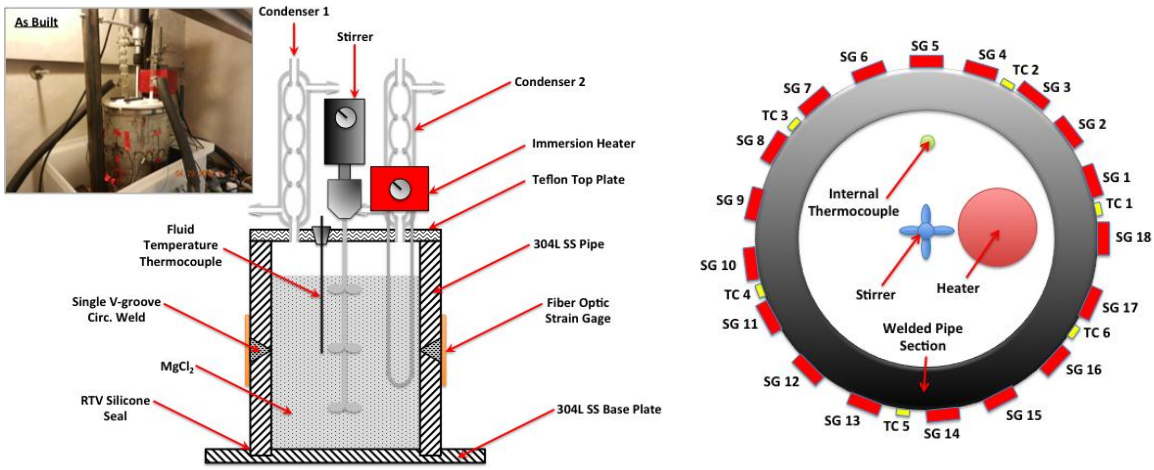

Figure 2 – Boiling $MgCl_2$ SCC Experiment Set Up

An immersion heater with titanium (Ti) coated heating elements is used to initially melt the solid powdered $MgCl_2 \bullet 6H_2O$ and to maintain it in a boiling molten state. An independent thermocouple is used to monitor the fluid temperature and maintain it at 155 °C. The fiber optic strain gages and their associated temperature compensation gages record data at a rate of 10 Hz throughout the experiment. The external thermocouple records fluid temperature at a rate of 1 Hz.

The boiling solution is maintained until through wall cracking is observed or significant cracking is observed in the strain responses. Additional $MgCl_2 \bullet 6H_2O$ powder is added as necessary to counteract any evaporative fluid losses.

Full Scale Boiling $MgCl_2$ Accelerated SCC Results & Discussion

The experiment ran for a total of 12 days before the heater failed, causing the $MgCl_2$ solution to solidify. Importantly, the solution in contact with the weld and HAZ area on the ID remained molten throughout the experiment. The apparatus was disassembled and the ID surface of the weld inspected using dye penetrant (DP) to check for indications of cracking around the weld. Figure 3 shows the results of the DP inspection. Indications of cracking were evident in the HAZ regions both above and below the root of the weld pass around almost the entire circumference of the pipe ID.

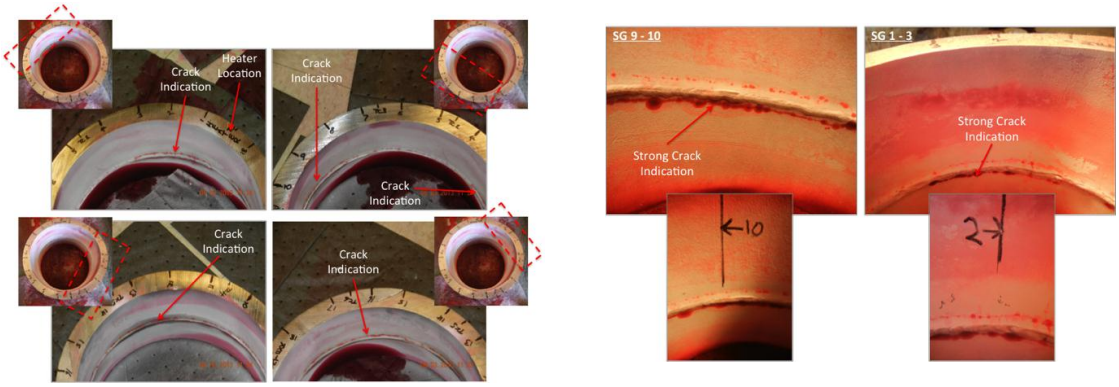

Figure 3 – Dye Penetrant Testing Results on Weld ID.

Two regions showing the strongest indications were chosen for detailed metallographic analysis, and the pipe was sectioned to expose the cross section of the welds in these locations. Close up images of these regions are shown in Figure 3. The sections were taken underneath SG2 and SG10. SG2 was located close to the heater and SG10 was approximately opposite SG2, furthest away from the heater. The cross sections were mounted, ground, polished, and etched (Marbles) according to standard metallographic procedures. Figures 4 and 5 show the as polished, etched, and a magnified collage of the cracked regions for SG2 and SG10 respectively. It is clear from Figures 4 and 5 that the experiment has successfully generated SCC cracks. Classic branched cracks typical of SCC are clearly visible. In the SG2 region, the cracking extends ~ 50% of the wall. Cracks initiate at the root of the weld in the HAZ, grow along the HAZ, and terminate in the weld metal. This is a typical example of SCC. In this case cracking is both intergranular and transgranular in nature. This result is significant, as it is highly challenging to induce SCC in a large specimen in an accelerated laboratory test.

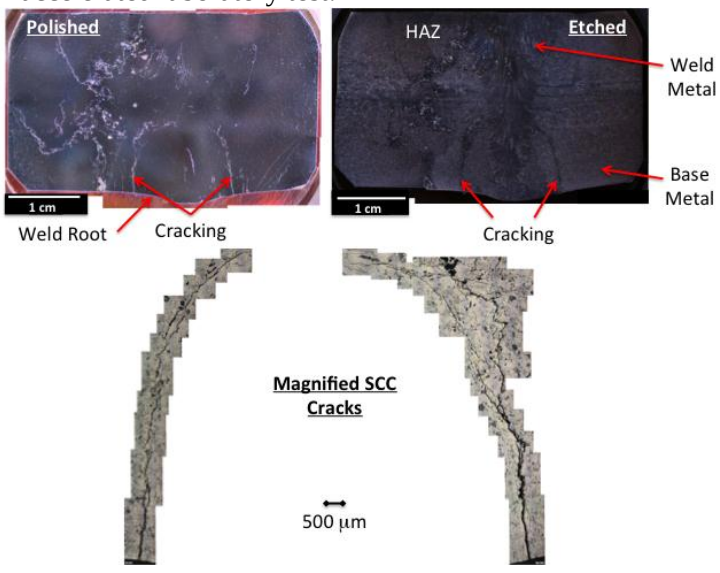

Figure 4 – Metallurgical Evaluation of Weld Cross Section at SG2

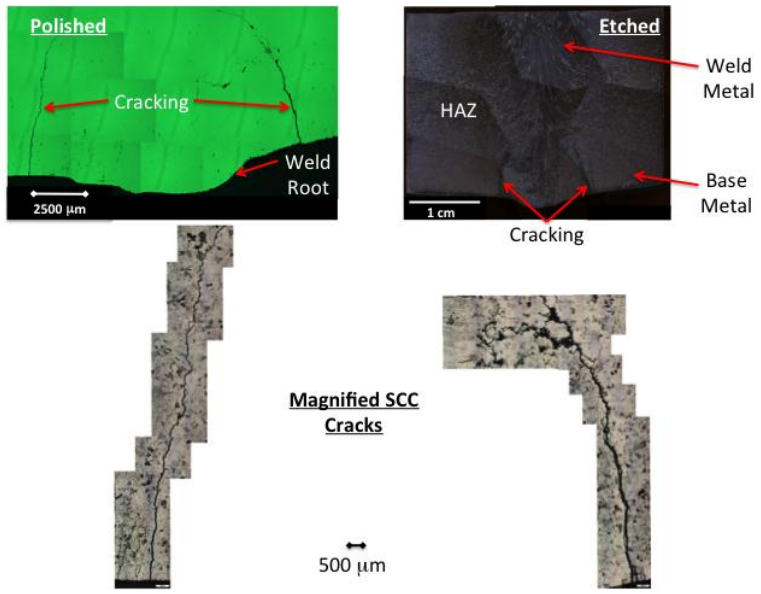

Figure 5 – Metallurgical Evaluation of Weld Cross Section at SG10

The SG and TC data were processed and analyzed upon completion of the experiment. Strain events that were independent of temperature events were identified, and are summarized below:

- Figure 6 shows strain and temperature data for a select time period near the beginning of the run. There is a strain event indicated on all of the SGs simultaneously at time stamp $105.5x10^3$ s. There are no corresponding temperature responses. This is the first large strain change. The response is characterized by a sharp change in slope for a response of approximate magnitude of ~50 με. This is similar to the EDM experiments. The strain change measured on all gages simultaneously and to similar magnitude. This is the likely initiation point of one or multiple SCC's.

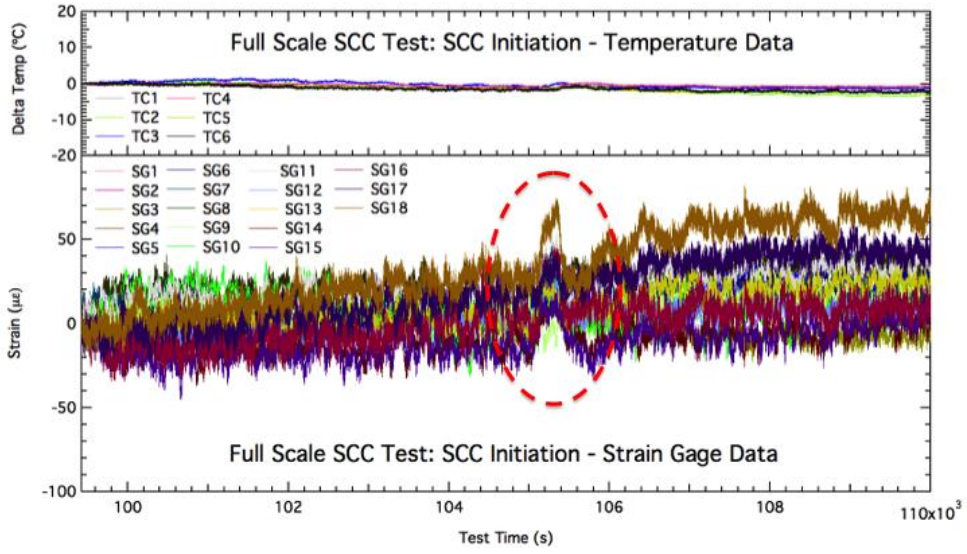

Figure 6 – SCC Initiation

- Figure 7 shows strain and temperature data for a subsequent time period. The plot shows a divergence of SG10 (green) and SG18 (brown) from the baseline strain. This is a more gradual slope change, followed by a steady strain response. SG10 and SG18 are approximately opposite each other around the pipe OD, suggesting that a single cracking event puts one side of the pipe into compression and the other into tension. Given that this is a gradual slope change compared to that observed in Figure 6, this is likely the strain response to steady state crack growth. There are some thermal events also shown on the plot. The drop in temperature likely closed up the SCC crack as indicated by the sharp strain increase in SG10. There is a gradual decrease in temperature throughout the time period, which corresponds to the gradual increase in baseline strain. The data shows interaction of multiple initiating and growing cracks. Unlike the previous EDM tests, it will likely be very challenging to relate strain responses for multiple cracks to location and length. However, sharp changes in slope in the strain response may still be distinguished and flagged as a crack initiation/growth event for further inspection. Multiple other examples of steady state growth were found in the data.
- Figure 8 shows strain and temperature data for a subsequent time period. The event at time stamp ~320-325x10^3 s shows a sudden strain increase, followed by steady state, then a similar sharp decrease (a "hat shaped" profile). The magnitude was largest at SG10, but was registered on all the other gages. The event could have been a "pop" when the crack progressed through a localized region of lower toughness, and then arrested once it progressed through this region, perhaps passing from HAZ to weld metal or weld bead to weld bead. The hat shaped profile strain event was observed several times after this as the experiment progresses. There is a continued increase in strain over the baseline at SG1 and SG2 as crack progresses. A possible explanation for the resetting of the stress is local deformation at the crack tip.

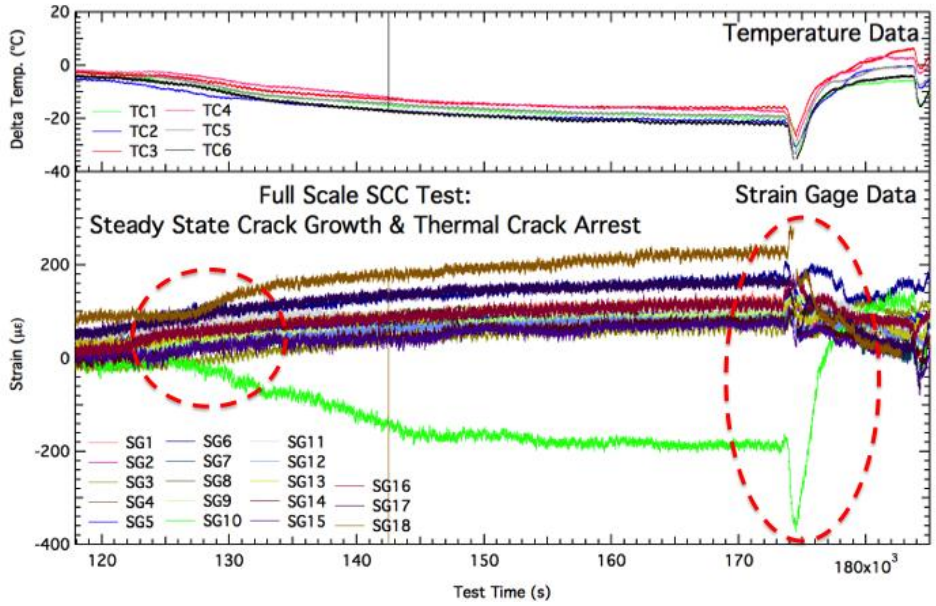

Figure 7 – Steady State SCC Growth & Arrest

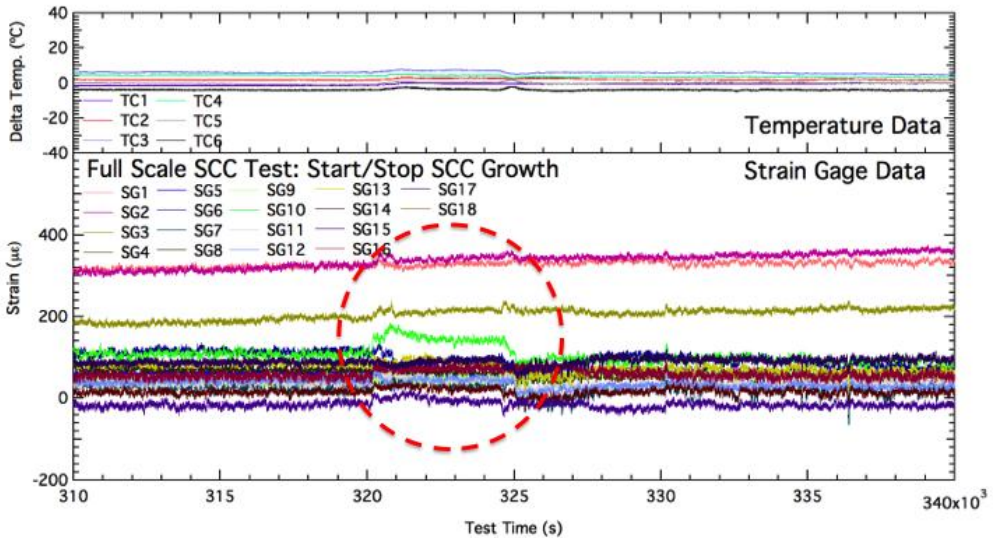

Figure 8 – Start/Stop SCC Growth

FEA Modeling of Weld Induced Residual Stresses

In order to accurately simulate the real life multi-pass weld process in a full 3D thermo-mechanical model, a 2D thermo-mechanical model was first developed to refine the process of setting up a welding mechanics FEA model. Once the process for analysis was determined and reasonable results were acquired with the 2D analysis, a full 3D model was then created and analyzed. Both models take all non-linearity associated with the welding process into account. These non-linearities include temperature-dependent material properties, moving heat source, material deposition, latent heat, and large deformations.

Two-Dimensional Thermo Mechanical Analysis

The 2D model was created using 2D axisymmetric elements with a greater mesh density in the area of interest.

The initial analysis was set up to include a seven "Lumped Pass" weld model. A lumped pass model is used to reduce computation time. Multiple weld beads are considered as one lumped pass. Heat fluxes for each pass in a layer are added and distributed over the weld elements. A separate heat flux array table was defined for each weld pass.

Various thermal analyses were conducted with each time-step result from the thermal analysis used as input conditions for the mechanical analysis. The maximum equivalent stresses were found to be on the order of 45 ksi. This initial 2D analysis helped to define the process of the weld analysis with further refinements to the model to be done using the 3D model and analysis.

Three-Dimensional Thermo Mechanical Analysis

The 3D analysis includes all the material property data of the 2D study with the added properties of temperature-dependent Poisson's ratio as well as enthalpy.

The 3D model was created with thermal brick and pyramid elements. There are a total of 1,216 individual weld volumes. The V-shaped weld groove cross-section is comprised of 32 individual beads. Each of the 32 circumferential weld beads is composed of 38 individual 1-inch

length nuggets which, during the analysis, are activated one at a time every 6 seconds to simulate a traveling weld arc.

Heat input arrays were created for each of the individual weld nuggets, which are then called on as heat loads as needed. Each array can be customized for a particular ramp rate and total heat input.

The solution macro increments through each of the 1,216 weld nuggets, saving each of the solved time step results. These thermal time step results are fed into the mechanical analysis as loading inputs much the same way that the thermal analysis uses the heat arrays as loading.

Results of the Three-Dimensional Thermo Mechanical Analysis

The initial 2D analysis revealed maximum equivalent stresses of 45.8ksi. As can bee seen in the Figure 9, the 3D analysis also produced comparable results of approximately 43.6ksi.

The axial and hoop stresses shown in Figure 10 did not produce smooth patterns or believable results. This is believed due to the coarseness of the mesh in the HAZ as well as the stiffness of the tetrahedral elements.

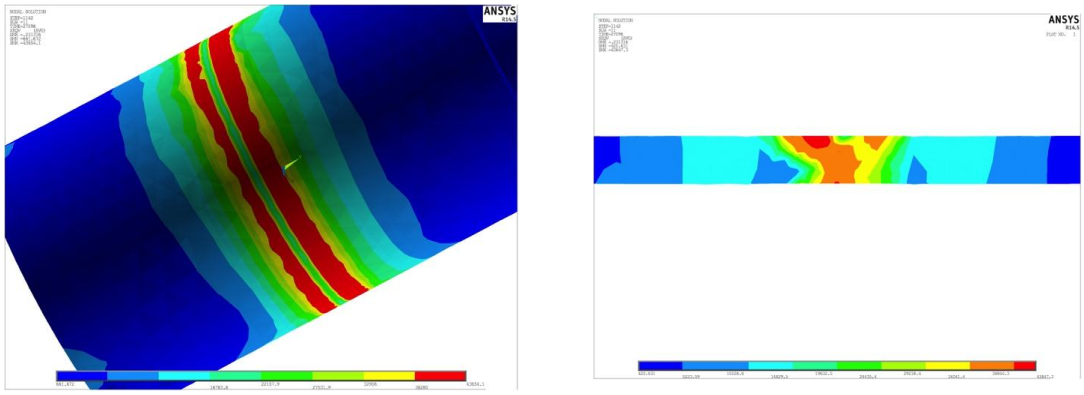

Figure 9 – Von Mises Stress & Cross-Section Von Mises Stress

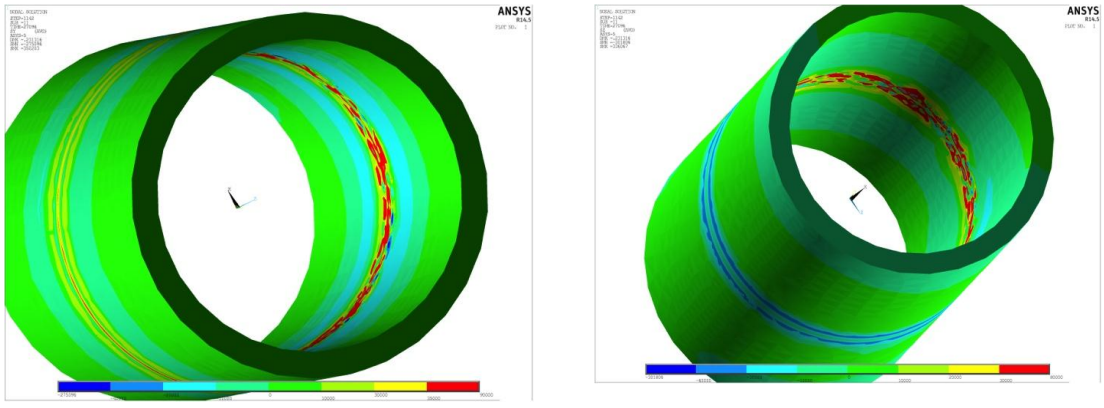

Figure 10 – Axial Stress & Hoop Stress

With the initial three dimensional analysis complete, a sensitivity study needs to be done to discover how much detail can be removed or needs to be added to retain sufficient accuracy to be used to analyze the effects of SCC.

These initial results show that more fidelity is needed in the HAZ. This will be accomplished by extending the fine detailed mesh in the weld zone out further through the HAZ. Tetrahedral elements will be kept away from the areas of interest.

The model will be further reduced by taking advantage of the axial symmetry and processed as a half model. Stress distribution changes due to cracking can then be introduced by freeing boundary constraints along the symmetry line thus simulating crack propagation.

Other possible areas to explore to reduce computing time would include combining multiple passes into a single lumped pass, taking advantage of lateral symmetry, or applying single weld passes at once instead of simulating a moving welding arc.

Conclusions & Further Work

In summary there are 3 distinct types of strain/cracking event that have been detected in this experiment:

- Initiation of SCC cracking in the form of a ~60 με spike in strain in all gages, similar to that observed in previous EDM experiments.
- Steady state crack growth indicated by a gradual and sustained divergence from the baseline strain.
- Start/stop or "pop" crack growth characterized by "hat shaped" strain profiles as a crack progresses through a localized region of lower toughness, and then arrested once it progressed through this region.

It is also evident from the complexities of crack interaction observed in this more realistic simulation of SCC that it would be highly challenging to correlate crack depth and location around the circumference with strain response. However, sharp changes in slope in the strain response may still be distinguished and flagged as a crack initiation/growth event for further inspection.

The main conclusions from the initial results of the weld simulation model were:

- We have successful developed and documented a procedure for analyzing weld residual stresses using the ANSYS finite element software package. A complete set of input macros have been written to allow for easily changing the parameters such as weld and piping dimensions, number of weld beads, heat input, meshing of the model, and solving. Comparative studies can now be efficiently solved and analyzed.
- The axial and hoop stresses did not produce smooth patterns or believable results due to mesh coarseness in the HAZ and the stiffness of the tetrahedral elements.
- A sensitivity study should be performed to ascertain the level of detail that can be removed or needs to be added to retain sufficient accuracy to be used to analyze the effects of SCC.
- A greater degree of fidelity is required in the HAZ. This will be accomplished by extending the fine detailed mesh in the weld zone out further through the HAZ. Tetrahedral elements will be kept away from the areas of interest.
- The model will be further reduced by taking advantage of the axial symmetry and processed as a half model.
- Once fidelity has been improved, stress distribution changes due to cracking may then be introduced by freeing boundary constraints along the symmetry line thus simulating crack propagation.

This experiment has confirmed that it is possible to generate real SCC cracks on a large scale. They can be detected using fiber optic strain gages monitoring the change is residual stress on the OD of a pipe section as a result of ID initiated SCC cracks. The strain events are all characterized by an abrupt change in strain with respect to time. Such an abrupt change is unlikely to be due to external events in a plant. In order to automate cracking event detection,

data could be analyzed by taking a running average of the data to reduce noise, then taking its first derivative. The sharp changes of slope associated with strain events will then be flagged in a first derivative of strain response vs. time plot. The results of this and future large scale SCC experiments will then be used to calibrate the weld simulation model. This model may then be used and adapted to simulate a variety of damage mechanisms and geometries.

References

1. B. Jackson (2010), "Interim Status Update: EDM Crack Simulations", *EPRI Project Status Report AES 10067465-2-1*.
2. B. Jackson et al. (2011), "Detection of Incipient SCC Damage in Primary Loop Piping using Fiber Optic Strain Gages", *EPRI Conference: Welding & Fabrication Technology for New Power Plants & Components,*Orlando, Fl, USA,
3. B. Jackson et al. (2011), "Detection of Incipient SCC Damage in Primary Loop Piping using Fiber Optic Strain Gages", *MS&T 2011, Columbus, OH, USA.*
4. J. Hickling et al., "Status Review of Initiation of Environmentally Assisted Cracking and Short Crack Growth," Electric Power Research Institute Report 1011788, December 2005.
5. ASTM G36 - 94(2013): *"Standard Practice for Evaluating Stress-Corrosion-Cracking Resistance of Metals and Alloys in a Boiling Magnesium Chloride Solution"* [5].
6. Materials Safety Data Sheet (MSDS) for Magnesium Chloride Hexahydrate ($MgCl_2 \cdot 6H_2O$), CAS# 7791-18-6, ACC# 13365, Revised 8/02/2000.

ULTRASONIC TRANSDUCERS FOR SODIUM COOLED REACTORS

.F.Saillant, O.Martin, S.Charrier, J.Sibilo, AREVA, France
F.Baqué, CEA - DEN, France

1. INTRODUCTION

The framework of the French Act, dated June 28th 2006, which requested an assessment of the industrial perspectives of transmutation by 2012, concluded that Generation IV systems, and especially the sodium-cooled fast reactors, seemed to be the most suitable technologies to be developed. Thus, since 2007, French partners CEA, EDF and AREVA launched a coordinated research program on Sodium cooled Fast Reactors (SFR) which is now being used for the next ASTRID (Advanced Sodium Technological Reactor for Industrial Demonstration) prototype.

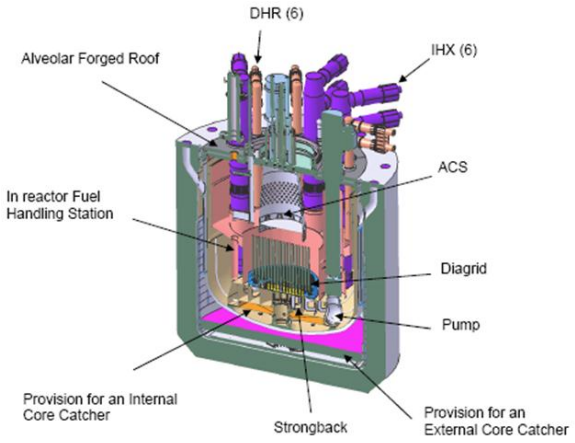

Fig. 1. Pre-conceptual Design for ASTRID reactor block

Several axes of improvement are targeted in this program [1] [3]. Amongst them, the improvement of the reactor's In-Service Inspection and Repair (ISI&R) is a major transverse issue. This includes:

- Safety analysis
  - checking the state of structures during the reactor's life span
  - detection of premature failures
  - in-operation detection of significant failures
- Economic reliability (implementation of delays),
- Investment protection (repair).

Deployment of ISI&R in sodium cooled reactors is not an easy task. Sodium has several characteristics which tend to make ISI&R complex, especially by comparing with that of Light Water Reactors:

- Sodium is very reactive with air and water. This leads to monitor carefully the confinement and steam generators leakage (if any), and to control the tightness during the interventions.
- Due to the risk of under stress caustic corrosion formation, sodium draining of the reactor is only planned for exceptional interventions. Routine inspections and operations have to be realized in immersion under liquid sodium.
- ISI&R devices have to work at high temperature levels. Because of sodium's melting point (97.8°C), the temperature corresponding to plant cold shutdown condition is maintained to a minimum of 180°C. Operation temperatures are comprised between 400°C and 550°C.

Liquid sodium being opaque, each intervention (inspection / repair) beneath the free surface of sodium cannot be performed using optical devices. Ultrasonic techniques are largely studied to provide means of under sodium investigations [2].

This paper reports on the development and tests of ultrasonic transducers specifically designed for performing Non Destructive Testing (NDT) on structures immersed under liquid sodium. First, the technical objectives will be specified. Then, the experimental setup and the design of transducers will be presented. Finally, experimental results will be shown and discussed.

2. NDT ULTRASONIC TRANSDUCERS FOR IMMERSION UNDER LIQUID SODIUM

The harsh environment of Sodium Fast Reactors makes the design of ultrasonic transducers difficult. Next paragraphs will detail the specifications for the different transducer design parameters.

2.1 Temperature

NDT of the reactor's structures will be performed during cold shutdown phases. Sodium temperature is then kept at 180°C. This temperature is not conventional for ultrasonic transducers. Especially, the transducer will have to be immersed continuously for periods of time of several days. Cooling down the transducer will also be difficult as it can be immersed under 20m of hot sodium, meaning that the coolant can difficultly be cold when reaching the transducer. Moreover, sodium in the reactor has to be very pure and the risk of having coolant leaking in the sodium primary circuit is not acceptable. Therefore we aim at making a transducer that can work continuously at 200°C (180°C + 20°C margin) without external cooling.

Several technologies can be envisaged for generating ultrasound. The choice here was made to use piezoelectric transduction for converting electrical energy into ultrasonic pressure waves, and vice-versa. If the choice is made to use a ferroelectric ceramic, then one has to pay attention that its Curie temperature is not be exceeded so that it remains piezoelectric.

High temperatures means that passive materials conventionally used in NDT transducers fabrication cannot be used, their physical integrity could be damaged. Moreover, thermal expansion coefficients of the materials of the different components (backing, matching layers, piezoelectric material …) leads to different strains at the interfaces, generating stresses which may cause adhesion failure and therefore malfunction of the transducer.

Electrical connections are also affected by the temperature level. Cabling and soldering have to be chosen carefully.

2.2 Chemical compatibility

It was mentioned in Section 1 that sodium was reactive to air and water. Sodium can also be aggressive towards different materials and much care has to be taken for the conditioning of the probe. For instance, epoxies are not all compatible to sodium. All materials used for the external packaging of the probe must be compatible to sodium. Chemical compatibility tests are mandatory to determine the potential use of particular nuances of materials. Materials inside the probe do not necessarily need to be compatible; however, particular attention has to be paid to the sealing of the packaging.

2.3 Acoustic parameters

Pure sodium is a metal and one would expect acoustic properties similar to that of steel or alloys. However, the acoustic properties of sodium at 200°C are surprisingly relatively similar to that of water:

- Density = 903.5 kg/m^3
- Velocity = 2472.5 m/s
- Acoustic impedance = 2.23 MRayl

Consequently, the same design rules as those for underwater immersion transducer can be applied. The problem mainly consists in finding suitable backing and matching layer materials for operating at a continuous temperature of 200°C. The objective in terms of acoustics is to produce a reasonably short pulse shape: a maximum of 4 cycles at -20dB, or a relative bandwith > 40%. Short pulses are necessary to have sufficient resolution during the inspection.

Controlling the pulse shape is necessary; however, the most critical acoustic issue to be addressed is the acoustic transmission at the interface between sodium and the transducer's emissive face. Indeed, liquid sodium does not wet all material surfaces. By comparison, it has similar behaviour to a drop of mercury on a table which would always remain more or less spherical, rather than spreading flat like water.

When a liquid does not wet a surface, it means that there is a thin film of gas in between. Transmission of acoustic energy between solid/gas or between liquid/gas is very inefficient; the acoustic transmission coefficient is in the order of 0.001% compared to optimal state. This means the transducers emissive face should be made from a material that can be wetted at 200°C. Temperature again is an influent parameter in the wetting of materials. For example, sodium does not wet stainless steel at 200°C; however, it wets well at a temperature above 400°C (note that when wetting is achieved, it remains wetted even if temperature decreases). Surface state is also an important parameter. A non oxidized polished surface helps wetting at lower temperature.

2.4 Irradiation

Transducers will be exposed to high levels of gamma irradiation. Indeed, unlike PWRs, fuel rods won't be removed when performing NDT inspections. Preliminary calculations stated that when the transducer is located near the assembly rods, it could be exposed to approximately 2.10^5 Gy/hr which is considerable.

3. TUCSS TRANSDUCER DESIGN

Transducers developed in this project are called TUCSS, french acronym for "Ultrasonic transducer for NDT under sodium" (Transducteur à Ultrasons pour CND Sous Sodium). We previously reported in [2] on the TUCSS G1, the first generation of TUCSS which showed that we were able to make a transducer emitting ultrasound at a temperature < 180°C and to last for more than 2 weeks in sodium (expected duration of NDE campaign) without degradation. However, its performances were quite low in terms of sensitivity and pulse length.

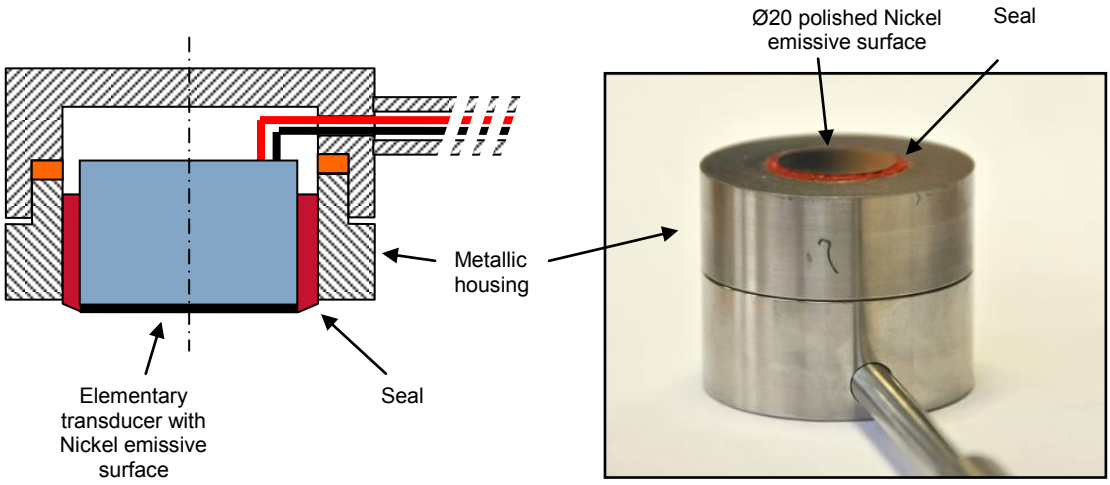

Fig 2. Sketch and photograph of a TUCSS G2 transducer.

The transducers presented in this paper, TUCSS G2, are designed to have improved performance, especially in terms of sensitivity. A photograph of a TUCSS is shown in Fig.2. The piezoelectric element is based on PZT material.

Its resonant frequency is 2 MHz and the emissive surface is a Ø20 mm diameter disc. Acoustic transmission was obtained by using a polished Nickel front face. An elementary transducer was fabricated and then encapsulated in a metallic housing by means of a silicone seal.

Two transducers were fabricated and tested.

4. EXPERIMENTAL SETUP

Under sodium tests were performed at CEA facilities in Cadarache, France. They took place in the glove box named PENELOPE, which had a Nitrogen atmosphere.

The objective of the study was to show that it is possible to detect a flaw inside a stainless steel structure immersed under liquid sodium. Fig. 3 illustrates the setup that was used to carry out this demonstration.

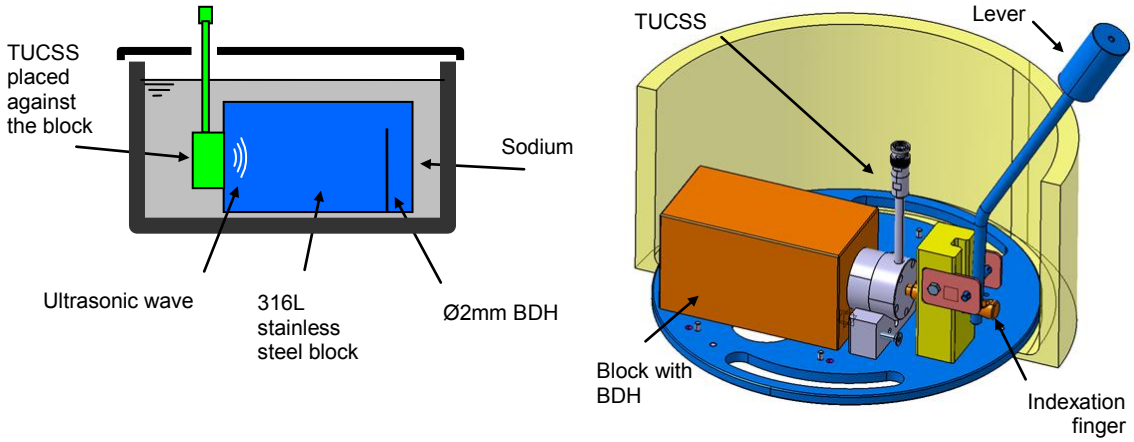

Fig 3. Sketch and CAD view of the under sodium NDT demonstration device

This device is made of:

- A 316L stainless steel block including a Ø2 mm Bottom Drilled Hole (BDH),
- A system for locating the transducer so that the BDR would be on the trajectory of the ultrasonic beam,
- A system for pressing on the transducer against the block with a controlled force.

The block was 140 mm long and the BDR was located 30 mm away from the backwall. The hole was made from the bottom and not drilled through so that there would be no sodium inside (therefore filled with Nitrogen gas). The positioning of the transducer is done by a V-block. Once it is placed on the V-block, an indexation finger pushes it against the block to enable a firm contact. The momentum generated by the mass at the end of the lever allows producing a controlled 10N contacting force.

All the parts are mounted on a support plate which is put on the bottom of a 300mm diameter pot filled with sodium. For reasons of clarity, several parts have not been represented on the CAD view of Fig.3. For instance: legs to pull the device in and out of the sodium, a lid to prevent sodium aerosols to diffuse in the glove box, or the slide way to guide the transducer to the V-block.

Note that although the temperature of the test is 200°C, the stainless steel block needs to be wetted before trying to sending ultrasound in it. As mentioned earlier, stainless steel wets at 400°C and our TUCSS G2 transducer can only withstand a maximum temperature of approximately 220°C. Wetting of the structure and wetting of the transducer have to be separate and testing has to be carried out according to the following sequence:

- Immersion of the test device without the transducer in low temperature sodium (approximately 110°C),
- Sodium temperature risen to 400°C to achieve wetting,
- Sodium cooled down back to approximately 110°C
- Immersion of the transducer at 110°C to minimize thermal shock,
- Sodium temperature risen to 200°C.

The transducer was excited using a SEPEMA pulser/receive circuit was made of an amplifier (Data precision, Analogic D1000) and a bandpass filter (KH3940). Acquisitions were done using a Lecroy Wave surfer 24MXs oscilloscope.

5. RESULTS

This TUCSS G2 transducer was immersed in the pot containing liquid sodium at 105°C and the test device. Fig. 4 shows the oscillogram obtained from the pulse/echo measurement when the transducer

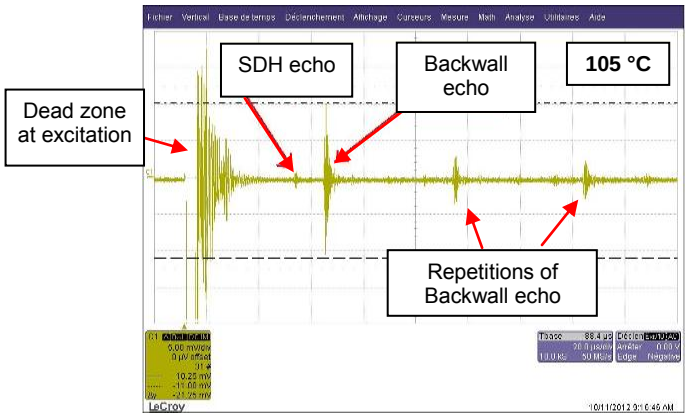

Fig 4. Oscilloscope snapshot showing echoes from the Ø2mm Side Drilled Hole and multiple reflections from the backwall at 110°C

was placed in contact against the block's front face. The BDH could clearly be seen as well as multiple backwall echoes. The amplitude of the backwall echo was 20 mV and the echo from the BDH was 2.5mV (square excitation of 50V, gain = 0).

The temperature was then increased. The level of noise became much more important, making the identification of the echoes impossible. Fig. 5 shows an oscillogram taken at 130°C. The length of the dead zone is considerably increased.

This increase in noise was due to the thermal expansion of the seal around the Ni emissive face. It expended more than foreseen, preventing a close contact between the transducer and the block to be made. This gap consequently generated multiple reflections between the transducer and the block, hence an important amount of noise. Integrity tests of the TUCSS were carried out in liquid sodium up to 200°C. These tests showed that this type of transducer can survive in conditions representative of the In Service Inspection conditions for ASTRID. However, some additional design work is required to make an effective contact between the transducer's front face and the test block.

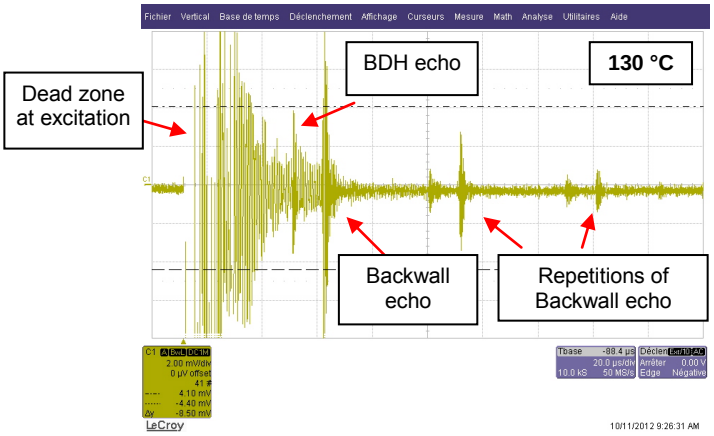

Fig 5. Oscilloscope snapshot showing echoes from the Ø2mm Side Drilled Hole and multiple reflections from the backwall at 130°C

6. CONCLUSIONS AND PERSPECTIVES

The present work is an important step towards the improvement of In Service Inspection of sodium fast reactors. This significant milestone indicates that NDT can be performed in a structure immersed under liquid sodium.

The results shown in this paper are work in progress. Optimization of the design of the probe has to be done for operation at 200°C. Once this optimization done, future work will consist in performing NDT in a mock-up that includes representative welds and flaws. This will require special designs for L0°, angled or phased array probes. Irradiation has yet not been taken into account: tests are planned for end 2013.

7. REFERENCES

[1] F. Jadot, F. Baqué, J.Ph. Jeannot, J.M. Augem, G. De Dinechin, J. Sibilo, "Astrid sodium cooled fast reactor program for improving in service inspection and repair," Animma Int. Conf., Ghent, 6-9 June 2011.

[2] C. Lhuillier, O. Descombin, F. Baqué, B. Marchand, J.F. Saillant, J.M. Augem, "In Sodium Tests of Ultrasonic Transducers," Animma Int. Conf., Ghent, 6-9 June 2011.

[3] F. Baqué, F. Jadot, F. le Bourdais, J. Sibilo, JM. Augem, O. Gastaldi, "ASTRID In Service Inspection and Repair : review of R&D program and associated results" FR13, Paris mars 2013

VALIDATION OF A HIGH RESOLUTION X-RAY TECHNIQUE WITHIN THE PARENT PROGRAM

L. Hammar, H. Wirdelius, Chalmers University of Technology, Sweden

ABSTRACT

The PARENT Round Robin Test (RRT) comprises a study of the efficiency of different non-destructive examination (NDE) techniques to detect and size stress corrosion (SCC) crack in Ni-base material. This report describes an x-ray technique that has been used for detection and characterization of these defects.

The x-ray source is a 450 kV x-ray machine and the detector is CCD-based with fiber optic lens and glass fiber optic scintillation screen. The imaging area of the detector is only 27 x 27 mm but the spatial resolution is very high. The un-sharpness in the image plane is measured to be less than 0.08 mm.

X-ray radiography is a volumetric method and to be able to detect cracks or parts of cracks the orientation has to be reasonably parallel with the x-ray beams. Therefor each defect is radiographed in series of projections. The projection angle is from -10° to +10°, with increments of 2°. To determine the size or the depth of the cracks a method are developed which describes the depth as function of the movement of the observed crack tip between the end positions in the series of exposures.

INTRODUCTION

The Nuclear Regulatory Commission (NRC) in United States has proposed the formation of an international cooperative project, PARENT, to address primary water stress corrosion cracking (PWSCC), materials aging management, and materials degradation. The intended focus of the new work is on reliability of non-destructive evaluation (NDE) to detect and characterize PWSCC in nickel alloy nuclear power plant components.

A Round Robin Test (RRT) RRT has been carried out as an international study of the efficiency of different non-destructive examination (NDE) techniques for detecting, characterizing and sizing SCC type of defects in nickel based materials with program members from North America, Asia and Europe.

The Round Robin tests will include demonstrations of emerging techniques in open tests and commercial techniques in blind tests. The purpose of the RRT is to assess commonly applied NDE techniques, preferably qualified, and also evaluate new and experimental NDE techniques that show promise for the future. All NDE performance categories (i.e. detection, characterization and sizing) are to be evaluated (quantified) during the RRT. Definition of characterisation means distinguishing between flaws and non-flaws.

This report describes an x-ray technique [1] that has been developed for detection and characterization of service induced defects, e.g. intergranular stress corrosion cracking (IGSCC). The x-ray source is a 450 kV x-ray machine and the detector is CCD-based with fiber optic lens and glass fiber optic scintillation screen.

EXPERIMENTS

Test block

Two different test blocks were used. One rectangular type with thickness of 30.3 mm with nickel based material (22 NiMoCr 3 7) and weld of Alloy 182 (addressed as P28-P30 below). The other test block, refered to as P41, was a simulated circular attachment weld of stainless and carbon steel, welded with Inconel material. Wall thickness was 32 mm and double wall exposures was performed. i.e. a total penetrated thickness of 64 mm.

Equipment

X-ray machine

The X-ray machine is a GE Titan 450 kV constant potential with ISOVOLT 450 M2/0.4-1.0HP tube. This is a high power tube with a small focus, f, of only 0.4 mm (25 % modulation). The geometrical unsharpness is less than 0.04 mm.

$$U_g = \frac{f \cdot ODD}{SOD} \qquad [mm] \qquad (1)$$

Figure 1. X-ray machine.

The source to object distance (SOD) has been 650mm and object to detector distance (ODD) was 50mm. In this case the crack opening is defined as the object. The objects are positioned and rotated by a rotation unit which is stepper motor driven.

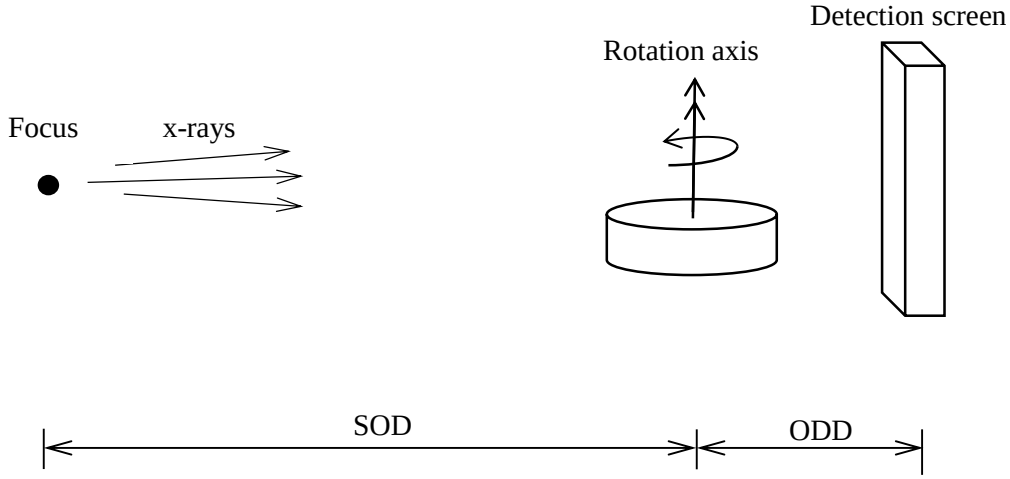

Figure 2. Set up.

Digital detector

The x-ray camera is an imaging detector with a scintillating screen of glass fiber optics [2]. It is a new design of a proven concept where the design issue was to minimize the amount radiation induced noise. This was done by bending the fiber optic lens (image conduit) which moved CCD-chip out of the primary beam. The spatial resolution is increased by using a new type of scintillating face plate. The new scintillating faceplate [3] has unique properties which have eliminated the internal light spread [4] and increased the spatial resolution.

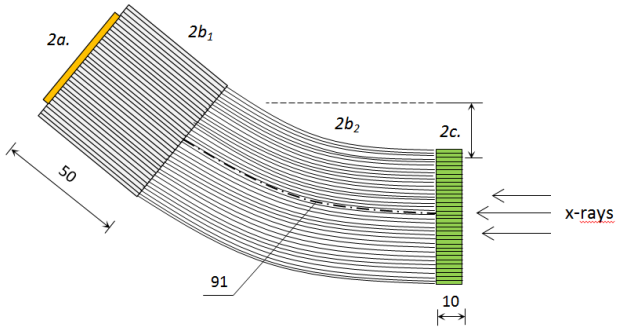

Figure 3. Fiber optic lenses and scintillating faceplate.

The new detector is based on a front illuminated full frame CCD camera (EEV CCD42-40) (2K x 2K) with pixel size of 13.5x13.5 µm. It is Peltier cold down to -30°C and is equipped with fiber optic input window. The input window is a fiber optic lens with fiber diameter of 4.5 µm with a length of 50 mm (see Figure 3). In the front of the camera, the bended fiber optic lens with the scintillating screen is mounted. The imaging area is only 27 x 27 mm (see Figure 4) but the spatial resolution is very high. The detector unsharpness is measured to be less than 0.08 mm. Better than 50% modulation of the 13:th wire pair with the EN462-5 double wire IQI.

Figure 4. The x-ray detector with a Cu-filter in front.

Image processing

Each x-ray image is divided in eight exposures. They are then integrated to improve the signal-to-noise (SNR) ratio. As each image also can contain radiation induced noise they are compared statistically and the noise (white dots) are removed. Conventional background and flat field correction to remove the structural noise is done in the next step. Finally a "lifting"-operation is done by multiplying the corrected raw image with an interpolated surface based on curve fitting in the perpendicular direction of the cracks. The Fourier-series of third grade is used as function for curve fitting as it can adapt nearly any shape in a "smooth" way.

The images are presented in an animation. By using animations the crack can be seen clearly and it thus easy to characterize them as either been produced by the manufacturing process or service induced. Models of human visual sensing [5] show that the human brain is designed to see motion with direction and speed. By interpreting the x-ray images as moving images (animations) we increase the contrast sensitivity with about two wire pair with single wire IQI. This is a simple way to dramatically increase the sensitivity of industrial radiography.

Procedure

Coordinates

The object coordinate system is placed so the crack opening is coincident to the axis of rotation in the object manipulator. The defects in test block P41 are orientated in two directions, axial and circumferential and P41 test block is thus in two different positions.

- The test block P28-P30 (square bars) is placed in such a way that its X-axis is parallel to the axis of rotation of the object manipulator in the coordinates Y=0 and Z=30.3 [mm] (see Figure 5).
- In the position for testing axial defects in test block P41, the Y-axis of the test object coincident to the axis of rotation of the object manipulator in coordinate Z=0 [mm] and the polar coordinate X [degrees]of the defect.
- In the position for testing circumferential defects the tangent of the defects polar X-coordinate coincident with the axis of rotation of the object manipulator.
  The Y-coordinate is the value for the actual defect and Z=0 [mm] (see Figure 6). X-ray radiography is a volumetric method and to be able to detect cracks or parts of cracks the orientation has to be reasonably parallel with the x-ray beams. Therefor each defect is radiographed in series of projections. The projection angle is from -10° to +10°, with increments of 2°.

Exposure data

For the test blocks P28-P30 the following data was applied:

- U= 300 kV; I= 2.25 mA; 30 mm Iconel
- Exposure time: 8 x 60 s (18 mAmin)

For the test block P41 is following data used:

- U= 450 kV; I= 1.5 mA, 64 mm Inconel
- Exposure time: 8 x 120 s (24 mAmin)

The reason to use such a long exposure time is that it corresponds to an optical density between 3.0-3.5 with Agfa D5 industrial x-ray film. We are using the cooled CCD to be able to integrate for long exposure times. In other word we have similar exposure time as film but much better image quality.

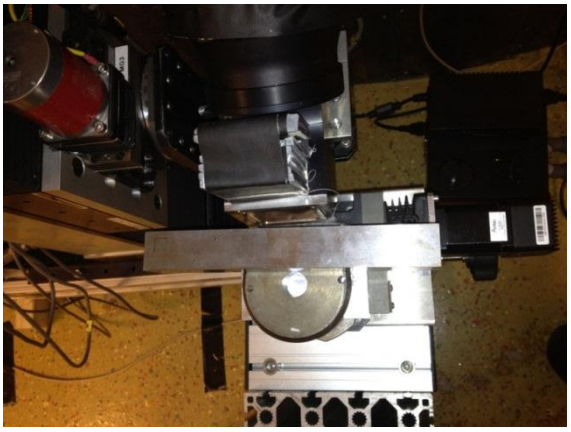

Figure 5. Test block P28-P30 (seen from above).

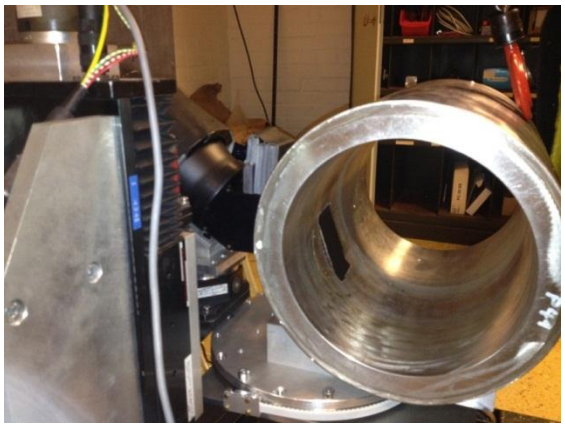

Figure 6. Test block P41 axial position (seen from the side).

RESULTS

To determine the size or the depth (z-coordinate) an expression (see Figure 7) is developed which describes the depth, d, as function of the movement of the observed crack tip between the end positions in the series of exposures.

$$d = \frac{nopx \cdot pxsize}{2 \cdot M \cdot \cos\theta \cdot \tan\alpha} \quad [mm] \qquad (2)$$

Where, Θ, is the projection angle of the crack tip in the center position of the projection series. The angle, α, is half the angle between the end positions. The distance, nopx, is measured between the end positions of the crack tip. The pixel size is pxsize=0.0135 [mm]. The geometrical enlargements is M=1.045. And finally, d, is the depth of the defect (Z_{max}-coordinate). The measured width (nopx) can be seen in Figure 8.

The crack opening is clearly visible at the left marks (green lines) in Figure 8.

Figure **8**The crack tip is difficult to identify in a single image but is visible in the animation because the human vision is more sensitive to motion than individual still images.

This is thus not possible to visualize in this contribution but the original inspection report also included a number of animations as parts of the result. The measurement presented below has not yet been verified since the project is ongoing but based on previous experiences the system has high capacity when it comes to characterize, size and positioning a defect in 44 mm Inconel weld.

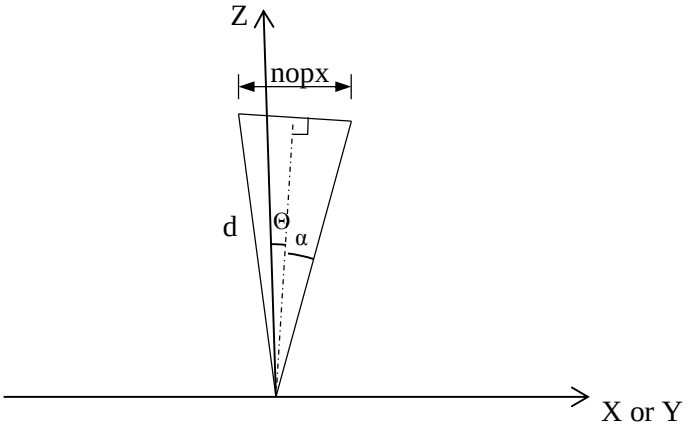

Figure 7. Crack depth calculations.

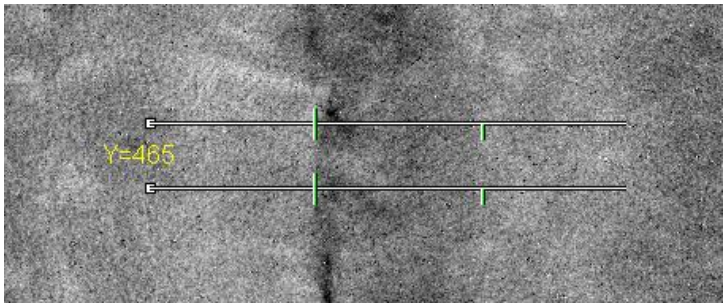

Figure 8. Measurement of the distance, nopx.

Sizing of each defect is presented in a table with:

X	X-coordinate of the defect [mm or degrees].
X_1 , X_2	Coordinates of the line profile.
nopx	No. of pixels (projected width).
Z_{max}	Maximum Z-coordinate (=d, maximum depth of the defect).
Length	Real length in the image plane.

All images are of same size, 26.45 x 26.45 mm^2, which is the real size in the image plane. The size in the detector plane is compensated by the geometrical enlargement, M.

The Z_{max} is systematically underestimated in the case of "real" defects such as SCC and fatigue in P28-P30. This since the volume close to crack tip diminish to less than detectable by the system.. Experience from earlier work with SCC gave an under estimation of about 1 - 2mm. In the test block P41 where the defects are artificially produced the Z_{max} estimation is more correct.

P28 (SCC)

α=10°and Θ=8°; From -10° to +10°; 2°/pos; 11 positions

X [mm]	**X_1**	**X_2**	**nopx**	**Z_{max} [mm]**
27.8	85	341	256	9.5
22.7	71	323	252	9.3
17.5	93	329	236	8.7
12.3	93	381	288	10.6
7.2	97	358	261	9.7

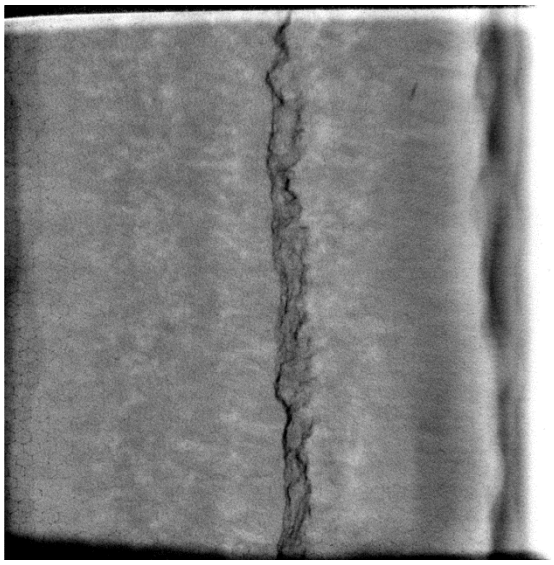

Figure 9. U6, 6:th position (Image size 26.45 x26.45 mm^2).

P28 MN 220 AD U6 spline 8 bit 512 inv.avi

P29 (SCC)

α=10°and Θ=6°; From -10° to +10°; 2°/pos; 11 positions

X [mm]	X_1	X_2	nopx	Z_{max} [mm]
27.8	90	260	170	6.2
22.7	81	309	228	8.4
17.5	186	462	276	10.1
12.3	136	386	250	9.2
7.2	149	411	262	9.6

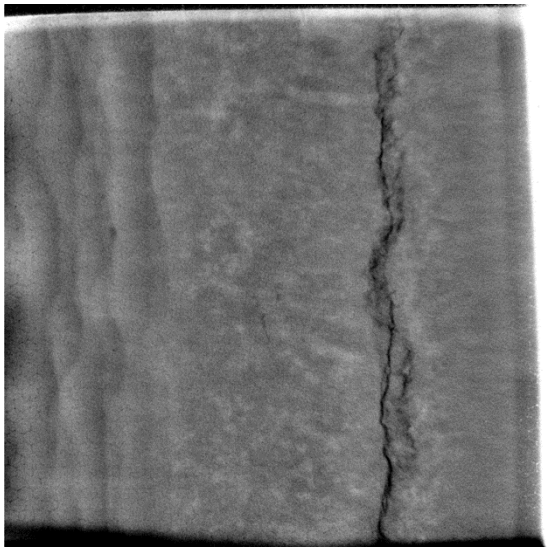

Figure 10. U10, 6:th position (Image size 26.45 x26.45 mm2).

P29 MN 220 AD U10 spline 8bit 512 inv.avi

REFERENCES

[1] Hammar L., Wirdelius H., 16th World Conference on Nondestructive Testing, Montreal 2004.
[2] H. Shao, D.W. Miller, C.R Pearsall, Nucl. Instr. and Meth. A299 (1990) p.528.
[3] Hammar L., 18th World Conference on Nondestructive Testing, Durban 2012.
[4] Hammar L., Wirdelius H., Int. Symposium on Digital Industrial Radiology and Computed Tomography, Lyon, 2007.
[5] Watson A., Ahumada A., J. Opt. Soc. Am. A/Vol. 2, No. 2, February 1985.

PROPOSAL FOR NDT STRATEGIES TO ASSESS THE STRUCTURAL INTEGRITY OF NUCLEAR PIPINGS

S. Yaacoubi1, W. K. Yaacoubi, P. Dainelli, Institut de Soudure, France
D. Chauveau, and M. Riethmuller, Institut de Soudure Industrie, France

ABSTRACT

To ensure reliable testing with optimum efficiency, a technique package consisting of Ultrasonic Guided Waves (UGW), Time of Flight Diffraction (TOFD), phased-array (PA) and Multi-skip (MS) is proposed. Different tests based on theoretical understanding and numerical simulations of different scenarios were performed to make sure that this package is complete, and can answer all the non-destructive need for testing pipework, especially in nuclear power plant (NPP). Some numerical results are shown without bring details. For all techniques, a brief description is delivered to allow a non-specialist reader to have a quick background, and how such a technique is suitable for pipes testing in NPPs. Furthermore, results from experienced feedback of Institut de Soudure (IS), obtained *in-situ* are presented. Prospective to use smart welds as guided waves sensors is discussed.

INTRODUCTION

Hollow cylinders (pipings, pipelines, tubes...) are widely used nowadays' in many industrial fields where NPP is one among them. They are used in various applications such as convoying water and industrial fluids (liquid or gas) which are carried on the facilities. These fluids can be under high-pressure, with various temperature, flammable, corrosive... They are although identified in France under the generic term TRICE (Toxic and / or Radiological, Flammable, Corrosive and Explosive[1]). Consequently, these pipes are exposed to two main natural phenomena: corrosion and mechanical and thermal fatigues. All parts of pipings can subject to these phenomena. Tubes are connected each to other via joint-welds, and defects can appear there. In addition, to avoid direct contact between these structures and ground, supports are needed. These supports have various shapes and sizes, and they can be in free contact with the structure, glued or welded to it. The neighborhood of this contact promotes the onset of defects. Far from welds, supports, flanges, Tees ..., these structures are not exempt of defects, which can be inner or outer.

Regular inspections should be conducted on these components to avoid any human or environmental catastrophe. Various non-destructive testing and monitoring (NDT&M) techniques can be used to detect these defects even in early stage. Each technique has its advantages and limitations with regard to the sought defect characteristics (shape, localization, size, orientation...), and some other parameters such as

- pipes accessibility, likewise area under supports, sleeves, insulation, coating, and pipes underground, crossing walls and slabs, …
- its geometries (tubes having variable cross-section, presence of several elbows, supports, branches, drains,…)
- materials (stainless steel for tubes, polymer layers for coating, concrete at pipe crossing wall or foundation,…)

Therefore, a single technique may not be able to detect defects appearing in such a structure. A smart association of appropriate NDT&M techniques is needed. As main requirements, this techniques association should be:

- able to detect defects in pipes by screening. This allows saving operating time, and consequently testing costs.
- deployable *in-situ*, that is to say, operating equipment should be efficient, portable, offers the possibility to test inaccessible areas.
- able to quantify the detected defects with high accuracy level, and without any false-call.

Consequently, this techniques association may allow to:

- better manage the key repairs to perform during shut-down,
- increase the service life of critical pipings keeping a high safety level,
- increase the examination volume of a piping.

To ensure a high level of safety throughout the plant's operating lifetime, a technique package consisting of Ultrasonic Guided Waves (UGW), Time of Flight Diffraction (TOFD), phased-array (PA) and Multi-skip (MS) is proposed. Different tests based on theoretical understanding and numerical simulations of different scenarios were performed to make sure that this package is complete, and can answer all the non-destructive need for testing pipework, especially in NPPs. Some numerical results are shown without bring details in every section allowed to each technique. For all techniques, a brief description is delivered to allow a non-specialist reader to have a quick background, and how such a technique is suitable for nuclear pipings. Furthermore, results from our experienced feedback, obtained *in-situ* and on laboratory structures of scale 1/1, is presented.
NDT of some parts of pipes in NPPs[2] can be helped or replaced by Structural Health Monitoring (SHM) technique. In this technique, the actuators / sensors accompany permanently the structure in-service[3]. This offers the possibility to monitor these structures in real-time where remote system can be used. Some problems linked to in-service environmental conditions can make the SHM difficult to achieve. Prospective to use smart welds as guided waves sensors, to overcome these problems, will be discussed.

PRINCIPAL DEFECTS

Most efforts concerning the safety of nuclear power plants are focused on reactors, boilers and turbines. Piping that acts as a hose-pipe to convey flow from one component to another is in most cases assumed to be less critical since it has no obvious moving parts. Over the years some utilities realized that the piping may be a critical component. In many cases, piping failure would result not only in massive loss of revenue, but the consequences of a violent failure would be devastating and could result in potential loss of life. Despite the common opinions, piping is far from being passive, it is subjected to a severe temperature changes and it usually operates well into the creep range. Cyclic operation of the plant subjects the piping to mechanical and thermal fatigue mechanisms and poor or defective support assemblies can impose massive loads onto the structure. With regard to the nature of the fluid fed through the tube and thermal and mechanical stresses exerted by the tube during its life-cycle, different defects can appear.

Figure **1** schematizes the main defects. They are, from left to right, general corrosion, stress corrosion cracking, erosion-corrosion, fatigue cracking, crevice (under deposit) corrosion, pitting corrosion, mesa corrosion, weld HAZ sensitization corrosion, hydrogen blisters, and hydrogen induced cracking.

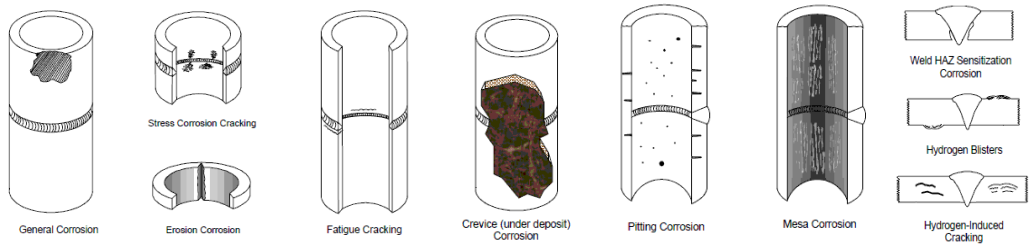

Figure 1 : Schematic of major defects which can appear in pipework[4].

Other defects, especially those which may occur in a weld such as porosity, gas inclusions, and cracks exist. More about weld defect is given in old paper written by one among the authors[5] of the current paper.

GUIDED WAVES (UGW)

Brief description

This technique has been developed over about 20 years. It relies on guided waves which are mechanical waves propagating through the wall of a structure (tube in this paper). They are generated at frequencies well above the range of human hearing (around 20 kHz), that's why they are called ultrasonic. Note that in some cases of tubes embedded in high attenuating medium such as bitumen or cement, to overcome the problem of wave's leakage, lower frequencies (< 20 kHz) are sometimes chosen. To test such a tube, two experimental arrangements may be used, as shown in Figure 2.

Figure 2 In pulse-echo measurement, the transducer plays in general case a dual role: emission and reception. However, in pitch-catch case, two transducers are needed, and should be placed on either side of the area to be tested. This arrangement is not preferred in inspection field because it needs a baseline data, which is not easy to get in most cases (see paragraph 3). Standard equipment exists nowadays, and allows performing both measurements. More details can be found in websites of companies which manufacture and market systems such as MsS, ULTRAWAVE, TELETEST, WAVEMAKER,…). Some standards linked to the concept of guided waves and the use of these equipment are currently available[6,7,8,9].

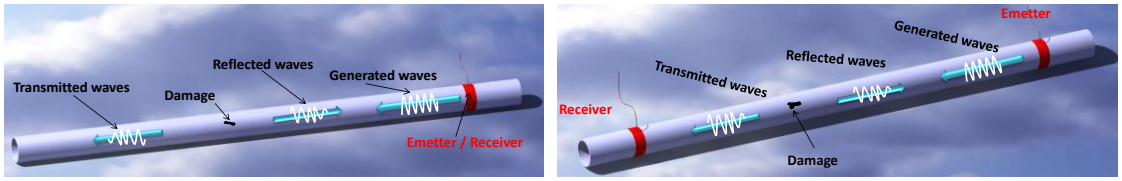

Figure 2 : Experimental arrangement: pulse-echo (on the left hand-side), and pitch-catch (on the right hand-side).

The principal advantages of guided wave measurement in nuclear area are:

- non-invasive: simple installation, probes can be protected from contamination;
- intrinsically safe: can be used in hazardous process environments without further protection;
- capable of providing information that is difficult or impossible to obtain by conventional measurements;

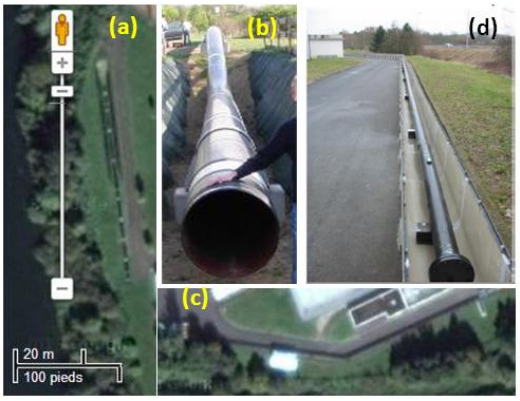

Figure 3 : Loops installed at IS Yutz: satellite view of loop 1 (a), and a correspondent photography (b), and satellite view of loop 2 (c) and a correspondent photography (d).

- real-time response: suitable for control;
- not expensive in comparison to other techniques, like for example C-scan point-to-point.

With regard to its wavelength, ultrasonic guided waves testing involve Short range UGW and Long range UGW[10,11]. The latter which is a screening tool is used to detect the presence of significant reflectors which are then examined locally in detail using conventional methods of NDT.

This technique, which is well adapted to cylindrical tubular structures for detecting especially corrosion, is used by IS since 1999 in industrial assessment sites, and through a joint industrial projects (JIP)[12,13]. Tow long loops were installed at IS facility to master guided waves testing and make it more reliable. The length and diameter of these two loops are around 100 m and 70 m where the diameters are 6'' - 8'', and 24'' respectively. They contain elbows, clamps, supports, branch and flanges. Different defects, with different sizes and shapes, are intentionally created on it. Some parts are coated by high attenuating polymer. The longest loop can be installed in a gutter, as can be seen in Figure 3 (d). The gutter can be filled by water, humid clay, …The loop can be also filled by water, gas, oil, …

Some results

Ultrasonic guided waves have two behaviors which can make the interpretation of testing results problematical: dispersive and multimodal. To alleviate this paper, we will not enter in details and the reader can refer to some academicals books like[14,15]. Theoretically speaking, infinity of propagative and evanescent modes with different degrees of dispersion exists. Among them T(0,1), which is frequently used thanks to its ease of excitation and reception, not-or-weak dispersive behavior, axisymmetry (probability of detection independent of the revolution angle), etc. This will help to make the interpretation easier and the analysis more reliable.

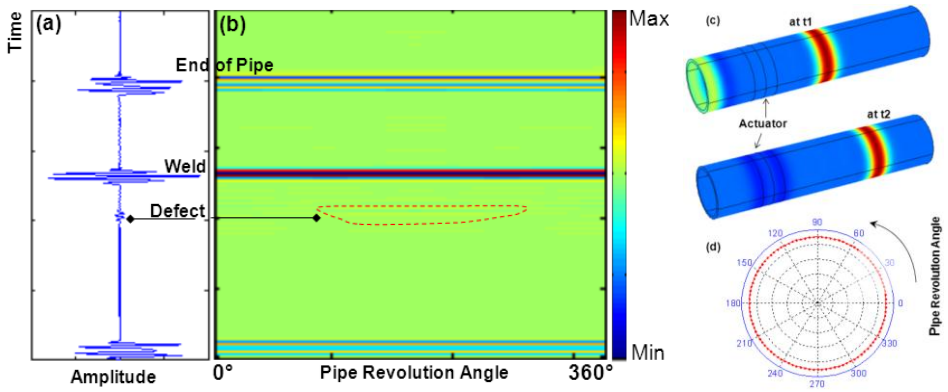

Figure 4 : T(0,1) numerical simulation: A-scan (a), B-scan (b), time-domain propagation at two instants t1 and t2 where t2 > t1 (c), and directivity (torsional displacement versus pipe angle revolution) (d).

Figure **4** presents an example of pulse-echo arrangement numerical simulations carried out in the case of two tubes matched by a circumferential joint weld. These tubes have the same diameter and cross-section, and one among them contains a relatively small defect. The calculation is performed in time-domain which allows displaying the propagating displacement field, as shown in

Figure **4**(c), which presents the torsional particle displacement at two moments t1 and t2 where t2 > t1. This displacement is independent of the angle of revolution, as can be seen in

Figure **4**(d). Waveforms, as that given by

Figure **4**(a), are acquired in every finite element node to simulate phased array transducer (see section 4). This permits to plot a B-scan (signal amplitude versus pipe revolution angle and testing distance which easily deduced from time of propagation through the T(0,1) velocity). From this B-scan, we can distinguish effortlessly the presence of axisymmetric reflectors (weld, end of pipe, flange in real world,…) and asymmetric reflectors (defect in the present case). Furthermore, the amplitude of the weld echo is, in general, much larger than that of the defect, as it can be seen in the next example, which describes results obtained in the field.

Under ideal conditions, roughly 100m can be inspected in a single test. The length of pipe that can be inspected is heavily dependent on several factors, and inspection distance can be much lower than ideal case. Following our field experience, guided waves testing and monitoring techniques are mainly dependent of:

i. size of the tube to be tested;
ii. dimensions and material of the coating (mainly: viscoelastic properties, thickness, and length);
iii. nature and quality of the coating/tube interface;
iv. characteristics of the defect to be detected (mainly: size, shape, and orientation);
v. distance between the sensor (and/or actuator) and the defect;
vi. presence of geometrical reflectors such as welds, supports, clamps, tees, elbows,…
vii. presence or not of inner deposit

All these parameters are evidently linked to the carrier frequency and the frequency-band. Figure 5 presents a result acquired *in-situ* where the goal was to test a pipe at bonded support locations.

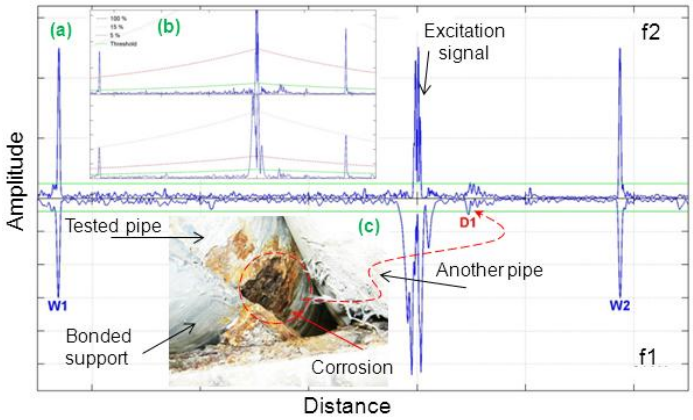

Figure 5 : Result gained in field presenting detection of corrosion under support: waveform acquired for two frequency f2 > f1 with Time Correction Gain (a), with Distance Amplitude Curve (b), and photography showing the detected corrosion (c).

Corrosion under support was detected successfully. We can remark, as it was mentioned in the previous paragraph, the amplitude of the welds echo are much bigger than that of the defect. This argues the need to several carrier frequencies, especially where the pipe is in doubtful status. This example is one among others which justify the ability of guided waves to be a suited tool for detecting corrosion in pipes at supports. However, detection of corrosion at supports is not always too evident, especially when propagating waves interact several times with features (as weld, drain, bend, …) before impinging the support to be tested. It depends also of the experience feedback of the data analyst, and the result is qualitative. To gain on accuracy, a complementary technique is needed. Multi-skip is an appropriate technique for these configurations (see section 3).

Besides, the detection of a localized defect in close proximity of a weld may not be feasible in several cases. This depends of various parameters such as:

- its characteristics (shape, orientation, and size),
- characteristics of the weld (mainly, bead width, and bead height),
- the distance separating it from the weld,
- its location with regard to the weld and the sensor (upstream and/or downstream the weld),
- axial and circumferential uniformity shape of the weld,
- i, ii, iii, v, and vi (see details given previously),

An optimization of the excitation parameters and the extracted features from the collected data is essential.

Figure **6** gives an example of a defect created voluntary in the neighborhood of a weld (defect 2).

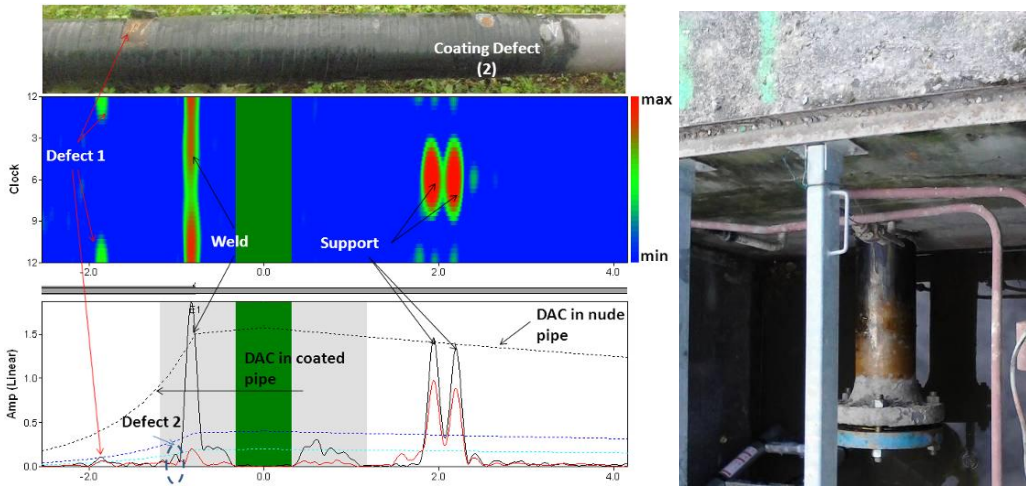

Figure 6 : Results showing the detected defects: B-scan (Top left), and A-scans on axisymmetric and non-axisymmetric propagating modes (bottom left), and an example photography of a case of study.

The second case concerns a defect performed in a highly attenuating coating. This was to mimic pipes crossing walls, concrete foundation, streets, rails, … where they are wrapped in polymer layers to be protected from humidity and water infiltration, to avoid corrosion attack.

Figure **6** (right) shows an example of this configuration where the pipe passes through a wall. Its accessible part (between the flange and the first boundary of the wall, as it can be seen in the figure) was cleaned to allow installing the guided wave transducer. This example shows that guided waves technique is able of testing crossing wall, slab, floor, ….

As last example of guided waves testing, we present in Figure 7 concerning detecting and sizing of corrosion defect under support. Figure (a) and (b) show the area on interest, which was identified by Visual Testing. Due to its size relatively big (axial and circumferential), NDT techniques as TODF and Phased Array cannot be applied. Testing via High frequency Short Range UGW was achieved. A specific procedure was developed for this complex configuration of testing. One among the collected results is plotted in Figure 7 (c) and (d) which represent respectively waveforms saved at two different central frequencies (f1 and f2), and a time-frequency diagram. As it can be seen, the echo corresponding to the defect is clearly apparent. To size the defect, the special procedure, developed for implementing this technique allowed determining the axial and circumferential extents. Basing on a mathematical model and exploiting all the collected data (data not shown here to alleviate the paper), the 3rd dimension which is the depth, is calculated. The wall-loss value was 26% of the total thickness. The decision was consequently to move the support.

The support was moved and the corrosion product was cleaned, as it can be seen in the Figure 8 (a). Upper the pipe, we put a hold to show the wall-loss (the defect zone is surrounded by a dashed yellow line, showing clearly, under the hold, the expected wall-loss). For validating short rang UGW testing result, a thickness gauge was used to measure accurately this wall-loss. Figure 8 (b) shows photography of the used equipment, indicating the measured value. The maximal wall-loss value is 23% of the total thickness.

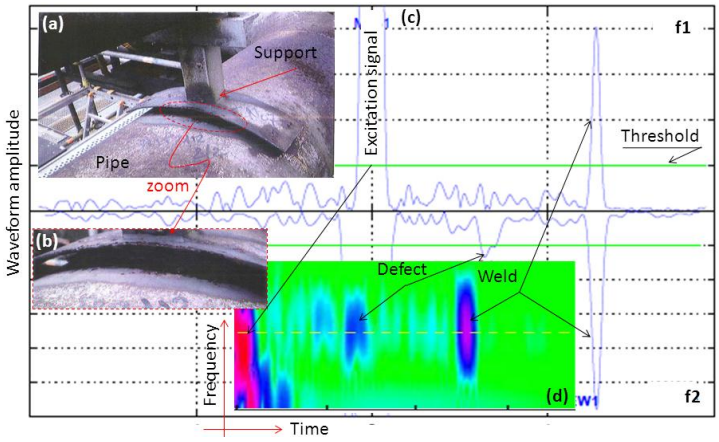

Figure 7 : Detection and sizing of corrosion under support: photography (a, and b), waveforms collected at two carrier frequencies f1 and f2, and time-frequency diagram (d).

The error is then 3%, which is a small value. This result confirms that Short Rang UGW has the ability to detect and size defects. Some other results may be needed to consolidate more the developed procedure and mathematical model.

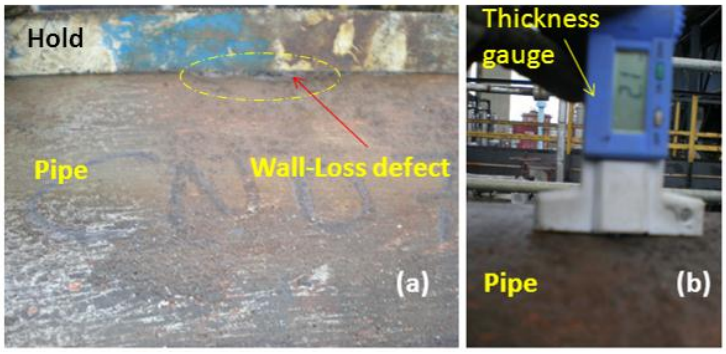

Figure 8 : Validation of the wall-loss carried out by means of short RUGW: photography of the tested area after moving out the support (shown in Figure 7 a, b) and cleaning it (a), and a thickness gauge showing the measured loss-wall value (b).

Guided wave testing is not limited to corrosion defect, and it can be applied to detect cracks in complex geometries like bent. Cheong et al. applied it to detect axial cracks in bend[16], and in feeder[17] pipes, and demonstrate its ability to assess the structural integrity of such a complex geometry.

SWIS: Smart Weld Institut De Soudure

To overcome the logistical difficulty due to periodical testing preparation, reduce the cost, increase operators safety, and improve the detectability, SHM of pipes and some other structures in NPPs is needed[18,19]. In this technique which is slightly different from a periodical testing, the sensor leaves permanently with the structure to be monitored. Sensors based on various physical effects such as magnetostriction and piezoelectricity can be used. In both technologies, sensors should be glued to the tube. However, this glue is sensitive to external factors (loads, humidity, temperature, Ultraviolet radiation, water condensation, atmospheric oxygen, concentrations of gases, solvents, salts ....) which may accelerate its natural ageing. The ageing of an adhesive or an adhesive bonding is defined as the change in its quality as a function of time and external effects that provoke the change[20]. This change in the behavior of the glue is random since, in most cases, external factors are not predictable. Consequently, it will impact the data (signals) by for example, polluting noise, outlier, etc which can give rise to corruption of the amplitude and aberration of the phase. As in SHM technique the anterior data is compared with the current one to determine the state of the structure, noise and outliers which have a stochastic behavior complicate the analysis, and can then cause a false call. Consequently, this makes the monitoring less reliable than what is hoped.
To help solving these kinds of problems which are linked to ageing of glue, IS has developed and patented various solutions to confer a weld or a structure adequate magnetostrictive properties such as: incorporating adequate elements during welding, applying appropriate spraying on the surface, applying heat treatment. These solutions don't need any adhesive substance, and the magnetostrictive elements which are a part of the whole sensor are matched to the tube. Figure 9 gives an example of results.

Figure 9 : Example of signals obtained with SWIS (top) compared to original method (bottom).

In conclusion, this original concept should permits to overcome the effects of environmental and operational variability on structural health monitoring. Furthermore, it can be used in NPPs to overcome problems linked to irradiation, and offers consequently better safety for operators.

MULTI-SKIP: The bulk-guided waves

Brief description

To certain extent, Multi-Skip technique is similar to Guided Waves technique, concerning the cases of wave propagation in waveguides. It can be considered as a simple derivative of it for the reason that there is no mode-conversion when the waveguide is healthy. This behavior is similar to that of bulk-waves (longitudinal and shear) when propagating in unbounded homogeneous medium. To avoid mode conversion, shear angle beam transducer is used. The incidence angle is thus chosen to be bigger than the first critical angle (longitudinal critical angle). In this technique, both experimental arrangements (pulse-echo and pitch-catch) can be used. Operating procedures, data process, and analysis are evidently not the same.

When the waveguide contains defect(s), some other modes can appear due to interaction between defect and propagating waves. This interaction phenomenon may give rise to signal dispersion (this means basically, "frequency components" will propagate at velocities different from shear bulk velocity). However, in healthy waveguide, signals are actually not dispersive. In practical case, this depends of several parameters such as spreading angle of the incident beam, wavelength (frequency), frequency-band (narrow or wide), transducer size, thickness of the tube to be tested, distance between emitter and receiver, etc. To ensure a reliable testing via this technique, an optimal combination of these main parameters must be found.

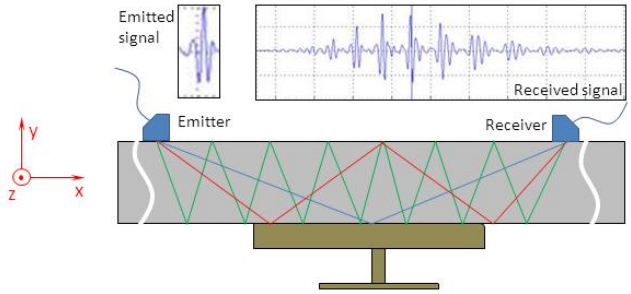

Figure 10: Schematic representation of wave propagation with multi-skips (bottom), and an example of emitted signal (top- left), and received one (top- right).

Note that Multi-skip should not be confused neither with T(0,1) guided mode (described in section 2) nor with SH_0 (propagating in plate or in tube which must be large and thin enough, with regard to the wavelength and transducer size, to behaves as an unrolled plate). Even if, the emitted initial beam waves is shear, particles displacements are not similar in both cases: in-plane for T(0,1) and SH0 (through z-direction in Figure 10, where the direction of propagation is x), and out-of-plane in Multi-skip (through x- and y-directions simultaneously). Consequently, in healthy waveguide (tube or an infinite plate) with uniform section,

- there is no interaction between T(0,1) (or SH_0) propagating waves and boundaries, and thus, only one echo is expected at the receiver, however,
- multi-interaction between propagating waves and boundaries can occurs in the case of multi-skip technique, and thus, several echoes are expected at the receiver, as can be seen in Figure 10. It schematizes the multi-skip wave propagation in a part of a wall of tube upper a support (bottom), and an example of emitted signal and received one (top).

This difference in these characteristics offers some complementarities towards inspection distance, metal defect characteristics, accessibility, etc. While T(0,1) mode is suitable for screening long distances, accordingly to the tube wall thickness (since it imposes the selection of the wavelength), Multi-skip is only appropriate to short distances. It may be applied on pipe support for corrosion mapping, pipe passing through short wall, and short casing. Wall-loss corrosion can be measured without the need to move these obstructions which can prove costly and time consuming.

In the next paragraph, we give some numerical and experimental results showing the ability of this technique to assess the integrity of some special case of structures. IS has started to use this technique in pulse echo mode around 15 years ago. Some examples (numerical and experimental are outlined in the next paragraph.

Some results

Numerical simulations are helpful to understand the wave's behavior even in complex waveguides, to simulate the interaction between waves and realistic defects (with arbitrary fashions and sizes), simulate the generation of a pure mode and supply accurate data,... Figure 11 presents an example of simulation carried out in two-dimensional time domain showing wave's propagation in circumferential tube wall (a), in axial tube wall (b), waves/wall-loss defect interaction at different instants (from c to h), and post-interaction (i). Some conversion mode can be remarked during the interaction between propagating waves and the current case of defect. This will affect the shape of the expected echoes, the time-of-flight, and amplitude. Basing of these main parameters, IS has developed and advanced analysis software for the interpretation of data obtained, to detect and size possible defects by means of this technique.

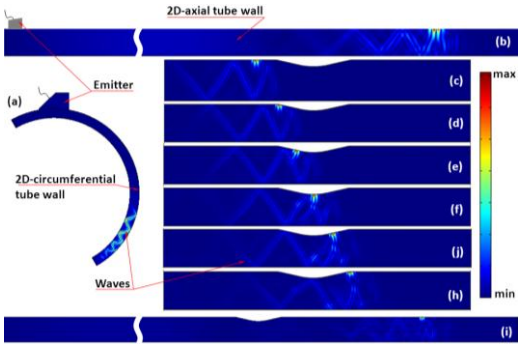

Figure 11 : An example of time domain numerical simulation of Multi-skip technique: Wave's propagation in 2D-circumferential tube wall (a), in 2D-axial tube wall (b), waves/wall-loss defect interaction at different instants (from c to h), and post-interaction (i).

Figure 12 (right) shows an example of experimental result received on a tube containing 4 defects with different depths (D1 = 10%, D2 = 20%, D3 = 30%, and D4 = 40%). From this B-scan (signals amplitude versus scan distance and time), we can deduce that all defects are detected successfully and get an idea about their sizes (D1 < D2 < D3 < D4). This experimental result has been obtained by means of IS's facility shown in Figure 12 (left).

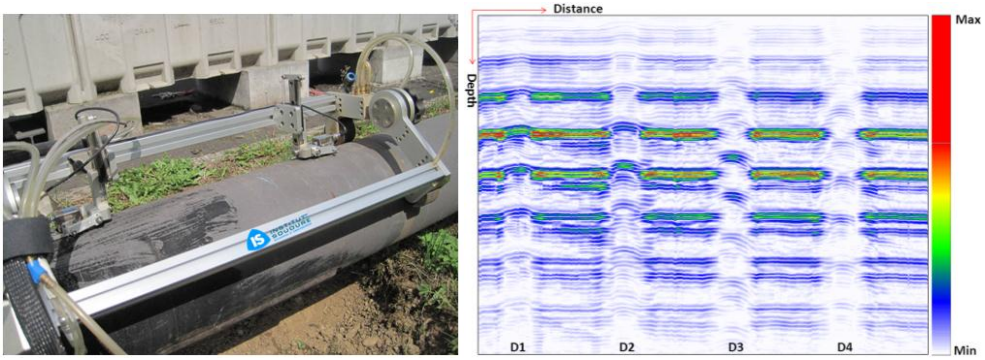

Figure 12 : An example of IS's facility (left) and experimental result obtained on scale 1/1 specimen (right) for an area containing 4 defects with different depth (D1 < D2 < D3 < D4).

TIME OF FLIGHT DIFFRACTION (TOFD)

Brief description

Time Of Flight Diffraction, known by its acronym TOFD, is a non-destructive technique which birth in early 1970s[21]. It was standardized in Europe in 2009[22,23]. This technique is useful mainly to detect defects in welds whether manufacture-originating or in-service[24].

It is based on the detection and analysis of ultrasonic waves diffracted from the extremities of discontinuities. It is a well-established technique and has been applied successfully for accurate sizing of defects in thick material sections[25,26]. The main advantage of this technique is its higher probability of detection and reduced inspection time. Faster scanning also makes TOFD a preferred technique for high temperature applications[27]. This makes TOFD a necessary tool in in-service inspection of nuclear reactors, pressure vessels etc.

A typical TOFD set-up and the corresponding A-scan signal and D-scan image are shown in Figure 13. Two longitudinal beam transducers of similar nature are arranged in a pitch-catch configuration, where one send and the other receive waves. The transducers are symmetrically positioned over the axes of the weld, and separated by a distance which depends mainly of the weld size, tube thickness, incidence angle, and beam spreading. The longitudinal wave which travels just below the surface from the transmitter (T) to the receiver (R) is called the lateral wave (LW). The wave which is reflected from the opposite surface of the wall of the tube is called the back wall echo (BW). The LW and the BW echoes are used to define the thickness of the material. Additional signals that appear in between LW and BW are the diffracted waves from the top and bottom extremities of the discontinuity. By knowing the transit time between different signals, the location and height of the discontinuity can be obtained.

The difference in arrival times of the diffracted waves are directly related to the size of the discontinuity and hence the name time of flight diffraction (TOFD) technique.

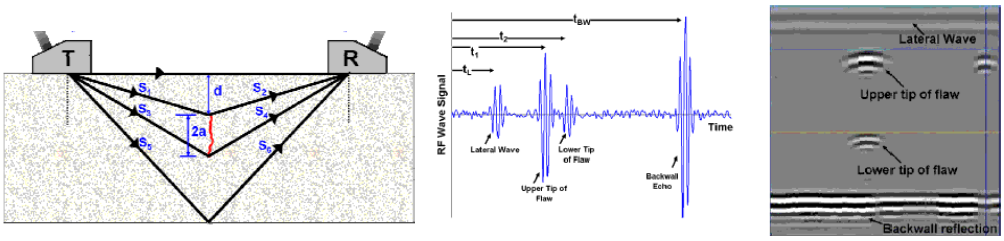

Figure 13 : TOFD principle: schematic (Left), Resulting A-scan (Middle), and D-scan (Right). TOFD t_L, t_1, t_2, and t_{BW} correspond to lateral wave, (S_1+S_2) tarjet, (S_3+S_4) tarjet, and (S_5+S_6) tarjet, respectively.

Deep details concerning theoretical basis, equipment design, processing, display and analysis, application of codes and standards,… can be found in the book written by Charlesworth and Temple[28]. Papers of Wedgwood[29], and A. Hecht[30] may also be helpful.

Some results

IS had started to work on the TOFD technique since the 1980s, through the project entitled "Non Destructive testing characterization of weld defects and their mechanical significance".. IS launched some research and development in an ongoing European Commission funded industrial project such as RAPINSPECT[31], RAYSQUIN[32], TOFDPROOF[33,34]... We present here two results from these projects.

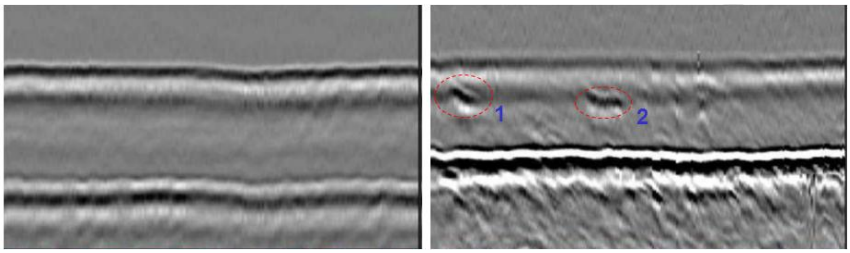

Figure 14 : An example of TOFD D-scan cartography: healthy weld (left), and a weld containing defects (right).

In Figure 14, we show D-scan cartographies obtained in the case of healthy weld and weld containing two defects, namely 1 and 2. In the healthy weld, only lateral wave and back-wall wave can be seen. However, in a weld containing defect, some echoes can appear between the lateral and back-wall waves.

Through the projects mentioned above, the TOFD technique had proved the most effective for the height dimension of the defects (y-direction). This technique allows also estimating essential information, which is the depth of the detected defect, as it can be deduced from Figure 13 (Right). The image TOFD can as well measure the length of different indications (z-direction). In the European project TOFDPROOF, various tests had showed that it was possible to obtain these values with an average error of 0.3 mm for the height (standard deviation 1.9 mm), and of 4.5 mm in length (standard deviation 6.5 mm). Besides, IS performed a signal processing algorithm which allows enhancing defect detection. Figure 15 presents a result example in which continuous wavelet transform was applied. By comparison to figure 14 (a) which represents the original image, defect can be easily detected in figure 14 (b) which is the result of this kind of post-processing.
Among the tools of signal or image processing used in TOFD inspection, the linearization of the lateral wave is prominently. The purpose of this tool is to correct subsequent changes in arrival time of the ultrasonic signal due to pipe surface irregularities and/or coupling thickness. Figure 15 (c) and (d) gives an example of result obtained via an algorithm developed in IS. The improved result obtained allows a better measurement of the height and depth of a possible indication whether opening-out or inner.

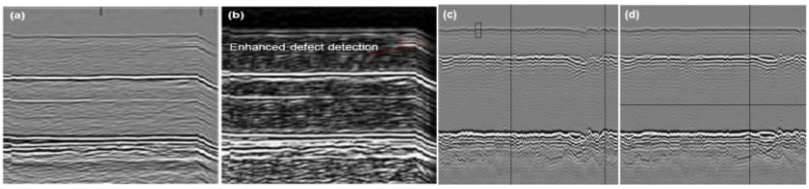

Figure 15 : Some post-processing algorithms: basing on continuous wavelet transform (a) and (b), and linearization, original image (c) and resulting image (d).

As we can see, the TOFD has many technical advantages, but as any other NDT technique, limitations exist. Indeed, it is not possible to conclude with certainty, on the basis of D-scan images, if the detected indication is volumetric (inclusion or porosity) or not (lack of fusion or crack). Phased-Array can be a suitable technique to overcome this problem. Further details can be found in reference[35].

PHASED ARRAY

Brief description

Phased array technique (PA) is based on the use of multi-transducers where each can be independently driven. These probes are connected to specially-adapted drive units enabling independent, simultaneous emission and reception along each channel. These units should also be able to effect, during emission and reception, the different electronic time delays for each channel. By using these multi-transducers (all or some among them) and adapted phased delays, different beamformings can be achieved such as scanning (Figure 16 a), deflection (Figure 16 b and c), and focusing (Figure 16 d). Further details concerning concepts, probes and applications of Phased Array technology can be found in reference[37].
The PA technique allows at least to[36]:

- map corrosion areas
- simplify testing and reduce operating time, so the testing cost
- improve the diagnosis of equipment (provide size and morphology defects)

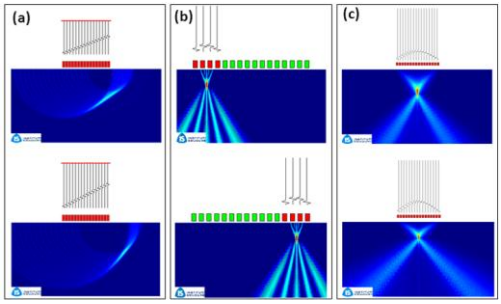

Figure 16 : Some schematics representing the principle of Phased array technique: electronic deflection (a), Electronic scanning (b), and an example of electronic focusing (d)[37].

- test areas of difficult access, complex shapes or large thicknesses
- improve the traceability of their results by digital processing.

Some results

For this technique, we present two examples. The first one concerns crack detection in Heat Affected Zone (HAZ) of inner side of a weld, as schematized in Figure 17 (left). The second example depicts a high temperature hydrogen attack (HTHA) defects, and will be presented hereafter.

Concerning the first one, as it can be remarked in the same figure, the weld to be tested is near a flange. The distance between the weld and the flange is too short, and don't allows using TOFD technique (previous section). The challenge is so to test it from only one side. PA technique by using the electronic deflection (schematized in Figure 16 b and c) permits achieves this goal.

The result obtained is plotted in Figure 17 (right). From the S-scan, we can deduce easily that this weld is not healthy (the red-yellow area in this image corresponds to the presence of defect). In addition, the location of the detected defect and its high can be deduced from the same image. This example shows the ability of PA technique of detecting and characterizing defects. This example reflects also how the technique can be a complementary to other techniques (TODF for example), especially in accessible area, but not limited to. A case of *in-situ* study showing the complementary between TOFD and PA in a straightforwardly accessible area can be found in reference[35].

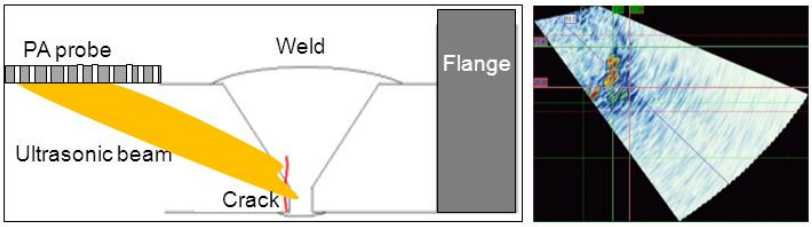

Figure 17 : Schematic of crack in inner side of a flange weld (left), and example of the obtained S-scans showing detection and localization of this defect.

Another example of the application of PA technique concerns the high temperature hydrogen attack (HTHA) defects. HTHA is a metal degradation phenomenon that is well known to occur in carbon and low steels exposed to high partial pressure of hydrogen at elevated temperature. It can occur in the base metal as well as the weld HAZ. HTHA increases the ultrasonic backscatter and reduces the ultrasonic velocity in the metal[38].

PA is suitable technique for testing this kind of damage. Indeed, visualization of the image makes interpretation easier than analyzing the A-scans. As an example, Figure 18 represents a three case of sectorial scan (S-scan) obtained in a reactor in refinery. They are obtained, from left to right, in healthy area, in area containing some inclusions, and then a HTHA damaged area. Further details can be found in reference[39].

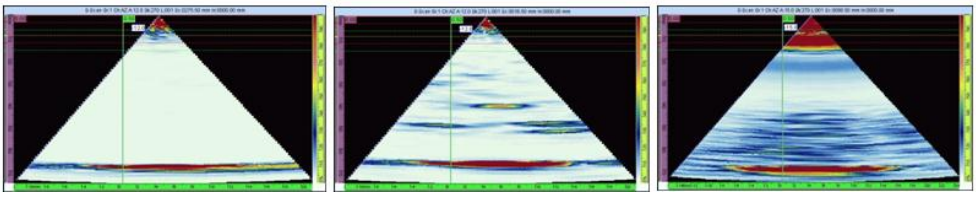

Figure 18 : S-scans from -15° to 15° with focal low calculated every 0.2° obtained in three area of a tested reactor: soundness area (left), detected inclusions (middle), and high temperature hydrogen attack damaged area (right).

CONCLUSIONS AND DISCUSSIONS

The majority of damage kinds which can appear during life-service of pipework in NPPs have been highlighted. Since such a pipe is a set of parts having various materials and geometries such as tube, welds, supports, clamps, elbows, flanges, etc, resulting defects have different characteristics. Hence, one NDT technique may not be sufficient to ensure a reliable testing. Knowing the variety of these defects, a NDT package of 4 techniques to assess the structural integrity of pipes in NPPs has been proposed. These techniques are complementary, and allow having a good probability of defect detection. This NDT package consists of UGW, M-Skip, TOFD, and Phased-Array. Some numerical and experimental results from either laboratory or *in-situ* have been shown. These results are collected in refineries. Their validation proves the maturity of these techniques. They can be transposed to NPPs pipings. Some other techniques such as Eddy current, EMAT UT, … are available in IS, and can be applied in various configurations.
In the next table, we summarize the most common pipe configurations related to the main possible defects, and we propose to apply the correspondent techniques by order of priority. This proposition shall be optimized for a given application in order to take into account: defect size, problem of accessibility, wave's attenuation, etc.

Configuration	D1	D2	D3	D4	D5	D6/D7/D8	D9	D10
Straight pipe, Sleeve	1	/	1,2	3,4	1,2	1	4,3,1	/
Bend	1,4	4,3	1,2	3,4	1,4	4	4,3,1	3,4
Tee, vent, drain	1,4	4	/	4	1,4	4	4,3	4
Support (welded or not), clamp	2,1,4	2,3,4	2,1	2,4	1,2,4	2,4	2,4	3*
Wall, slab crossing/ entrance	1,2,4	1,2,4	1,2,4	1,2,4	1,2,4	2,4	2,4,1	4
Insulation, coating	1,4	1,4	1, 4	/	1,4	1,4	1,4	/
Near and/or at Weld	3,4,1	4,3,1	3,4,1	3,4	3,4,1	3,4	3,4	3*

Table 1 : Summary of the most pipe configurations and the main possible defects, and a proposition of the correspondent techniques by order of priority. Key: D1 = General corrosion, D2 = Stress corrosion cracking, D3 = Erosion corrosion, D4 = Fatigue Crack, D5 = Crevice under deposit, D6 = Pitting corrosion, D7 = Mesa corrosion, D8 = hydrogen induced cracking, D9 = Hydrogen blisters, D10 = Weld HAZ sensitization, 1 = UGW, 2 = M-skip, 3 = TOFD, 4 = PA (it includes also guided waves phased array). / = not possible (defect cannot exist there or any technique not adapted or another problem, like accessibility, * = access is needed

REFERENCES

[1] EDF Division production nucléaire, Note d'information : La maitrise des risques lies a l'utilisation de fluides industriels sur les centrales nucléaires, Mars 2010. Available in : http://energie.edf.com/fichiers/fckeditor/Commun/En_Direct_Centrales/Nucleaire/General/Notes_Info/note%20information_maitrise_des_risques_lies_aux_fluides_industriels_avril2011.pdf

[2] "Periodic safety review of nuclear power plants", IAEA Safety Standards Series, Safety Guide No. NS-G-2.10, International Atomic Energy Agency, 2003.

[3] Daniel Balageas, Claus-Peter Fritzen, Alfredo Güemes, Structural Health Monitoring, ISBN 10: 1-905209-01-0.

[4] EWI Project No. 45891GTH, "Evaluation of methods for detecting and monitoring of corrosion and fatigue damage in risers", November 2003

[5] D. Chauveau, "Bilan de 5 années de travaux sur la caractérisation de défauts de soudure", 1er congrès COFREND sur les essais non destructifs - Nice 1990 - pp 141 – 150.

[6] BS 9690-1-2011, Non-destructive testing – Guided wave testing part 1: General guidance and principles.

[7] BS 9690-2-2011, Non-destructive testing – Guided wave testing part 2: Basic requirements for guided wave testing of pipes, pipelines and structural tubulars.

[8] ASTM E2775 – 11, Standard Practice for Guided Wave Testing of Above Ground Steel Pipework Using Piezoelectric Effect Transduction.

[9] ASTM E2929 – 13, Standard Practice for Guided Wave Testing of Above Ground Steel Piping with Magnetostrictive Transduction.

[10] S. Yaacoubi, W. K. Yaacoubi et S. Ramadan, "A propos des ondes guidées: partie 1", Soudage et Techniques Connexes, vol. 66, N° 8/9, 2011.

[11] S. Yaacoubi, W. K. Yaacoubi et S. Ramadan, "A propos des ondes guidées: partie 2", Soudage et Techniques Connexes, vol. 66, N° 9/10, 2011.

[12] Projet associatif N° ME824, "CND Non Intrusif".

[13] Système de MOnitoring de Structures Offshores vis-à-vis de leur endommagement par la corrosion,. Citeph project http://gep-france.com/citeph/files/49-INSTITUT%20DE%20SOUDURE%20Projet%20MOSCO%20reunion%20Mars%202012%20diffusable.pdf

[14] J. L. Rose, "Ultrasonic Waves in Solid Media", 476 pages, 1999, ISBN-10: 0521548896

[15] Cheeke, "Fundamentals and Applications of Ultrasonic Waves", 2002, ISBN-10: 0849301300

[16] Yong-Moo Cheong1, Sang-Soo Kim, Dong-Hoon Lee, Hyun-Kyu Jung, and Young H. Kim, "Detection of axial cracks in a bent pipe using EMAT torsional guided waves",

[17] Y. M Cheong, D, H Lee, S. S. Kim, and H. K. Jung, "Analysis of circumferential guided wave for axial crack detection in a feeder pipe", 11th APCNDT, Nov. 3-7, 2003, Jeju island, Korea.

[18] Fumio Kojima, "Structural Health Monitoring of Nuclear Power Plants using Inverse Analysis in Measurements", proceeding in Workshop Kobe".

[19] Tadeusz Stepinski, "Structural Health Monitoring of Piping in Nuclear Power Plants– A Review of Efficiency of Existing Methods", Report number: 2011:17 ISSN: 2000-0456

[20] http://www.adhesiveandglue.com/adhesive-ageing.html

[21] M.G. Silk, B.H. Lidington, "The potential of scattered or diffracted ultrasound in the determination of crack depth", Non-Destructive Testing, Volume 8, Issue 3, June 1975, pp. 146–51.

[22] EN 583-6, Non-destructive testing – Ultrasonic examination – Part 6: Time-of-flight diffraction technique as a method for detection and sizing of discontinuities

[23] EN 15617, Non-destructive testing of welds – Time-of-flight diffraction technique (TOFD) – Acceptance levels.

[24] http://www.isgroupe.com/fr/metiers/controle/controles-non-destructifs/Controle-par-TOFD.aspx

[25] J.A. Ogilvy, J.A.G. Temple, "Diffraction of elastic waves by cracks: application of time of flight inspection", Ultrasonics 21 (1983) 259–268.

[26] J. Verkooijen, "TOFD used to replace radiography", Insight 37 (6) (1995) 433–435.

[27] R. Subbaratnam, Saju T. Abraham, M. Menaka, B. Venkatraman, Baldev Raj, "Application of time of flight diffraction technique for evaluation of austenitic stainless steel weldments at elevated temperatures", Materials Evaluation 66 (3) (March 2008) 332–337.

[28] J. P. Charlesworth, J. A. G. Temple, "Engineering Applications of Ultrasonic Time-of-Flight Diffraction", Second Edition, Research Studies Press LTD, 2001, ISBN: 0 86380 239 7, 254 pages.
[29] F. A. Wedgwood, "TOFD Comes of Age"; Inspection, January 1995, S. 35 – 37.
[30] A. Hecht, english version by Rolf Diederichs, "Time of Flight Diffraction Technique (TOFD) -An Ultrasonic Testing Method for all Applications?, Ultrasonic testing online Journal, 1997, Vol.2, No.09
[31] Rapid Quality Weld Inspection without Surface Preparation, European project number BRPR950007, http://cordis.europa.eu/projects/rcn/30925_en.html
[32] EU-BRITE-EURAM III project, "Development of a Portable Remote Controlled Real-time Radioscopy System for Quantitative Industrial Inspection of Large Thickness Steel Pipes and Welds (RAYSQUINS)", BE95-1164, CT95-0096.
[33] Projet TOFDPROOF: Effective application and acceptance criteria of TOFD method at the manufacturing stage for weld inspection of pressure equipment, contrat n° G6RD-01-00626, 2002 - 2005).
[34] D. Chauveau, D. Flotté, C. Boucher, "Main Issues of the European TOFDPROOF Project", ECNDT 2006.
[35] D. Flotté, S. Demonte, "Association of phased-array and TOFD for a detailed analysis of defects", Journées COFREND, 2008.
[36] http://www.isgroupe.com/fr/metiers/controle/controles-non-destructifs/Controle-par-Phased-Array.aspx
[37] D. Chauveau, W. KE, "Basic principle of phased array", 66th annual IIW assembly – Essen September 2013.
[38] A. S. Birring, M. L. Bartlett, and K. Kawano, "Ultrasonic Detection of Hydrogen Attack in Steels". Corrosion: March 1989, Vol. 45, No. 3, pp. 259-263.
[39] Birring, A.S., Riethmuller, M., and Kawano, K. "Ultrasonic techniques for detection of high temperature hydrogen attack", Material Evaluation, pp. 110-115, Feb. 2005.

CONCRETE

FDR FOR NON DESTRUCTIVE EVALUATION: INSPECTION OF EXTERNAL POST-TENSIONED DUCTS AND MEASUREMENT OF WATER CONTENT IN CONCRETE

F. Visco-Comandini, G. Six, F. Sagnard, Université Paris Est, France
T. Bore, D. Placko, SATIE, ENS Cachan, CNRS, France
S. Delepine-Lesoille, Andra, France
G. Moreau, F. Taillade, J.Salin, EDF - R&D, France

Introduction

The water content in concrete (nuclear structures and nuclear waste repositories) is a major topic to understand and predict the behaviour at the end of the operating period. That is the reason why ANDRA and EDF are involved in research programs dedicated to concrete Thermo-Hydro-Mechanical (THM) modeling and to in situ water content assessment technologies [1].
Another example concerns the bridges which include "external" post-tensioned cables to reinforce these structures. These cables are not into the concrete material, hence potentially accessible for measurement. They are generally placed in High Density Poly-Ethylene (HDPE) ducts, where the residual space is filled under high pressure with a cement grout intended to prevent corrosion. Nevertheless, in some cases, the cables breaking occur in non-protected zones [2, 3] due to the presence of a "white paste" or grout voids.
To remote diagnosis anywhere and in real time of post tensioned ducts or to measure the water content in concrete, we propose a structural health monitoring method based on Frequency Domain Reflectometry (FDR). Today's, advanced reflectometry methods provide an efficient solution for the fault-detection and for their diagnosis in electric transmission lines [4, 5].
This paper presents a direct model of the FDR method based on Telegrapher's equations. An analysis of these signals, based on scattering theory, enables one to retrieve the impedance distribution of the electric line. The impedance distribution depends on damage into the duct or the water content in concrete. An inversion algorithm is realized with software ISTL provided by INRIA. FDR method has been applied to two real cases: measurement of the water content in concrete and the diagnostic of the external post tensioned duct.

Theorical Background

The idea presented in this paper is based on examining the concrete walls and bridge cables thanks to the FDR method as they were a transmission line. The transmission parameters along an electric line (as velocity and attenuation) depend on the complex permittivity of the material that is placed between the wires of the electric line. It is well known that permittivity depends on the nature of the dielectric material which is function of water content, void, etc. The electric line is connected to a calibrated vector network analyser (VNA) which measures the reflection coefficient $S_{11}(\omega)$. The FDR method is detailed through the diagnostic of the external post-tensioned cable. This first study allows us to give the way for measuring the water content in concrete.

For the post-stressed cable, we consider which is filled with cement, white paste and air. We characterize each material by the relative complex permittivity $\varepsilon_n = \varepsilon'_n - j\,\varepsilon''_n$ ($j=\sqrt{-1}$) where n can be air, HDPE, cement, white paste or concrete which the relative permittivity is respectively 1, 2.5, 5, $63+j2.6/(2\pi\varepsilon_0\omega)$ and of the order of 10.
The height of each material h_n in the transversal section depends on the position variable $z\epsilon$ [0,*l*] along the electric line and *d* represents the diameter of the cable (see Figure 1).

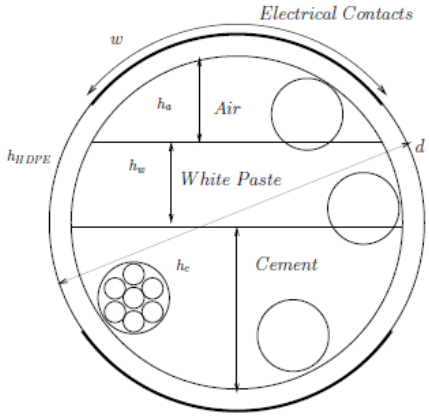

(a) Section of a duct

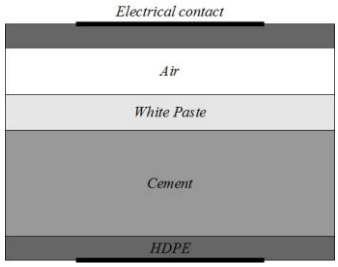

(b) Equivalent electrical model of duct

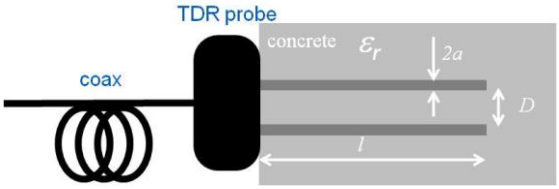

(c) Water content measurement with TDR probe

Figure 1: Electric line model: a) and b) for post-tensioned duct and c) for water content measurement probe

In the post-tensioned duct diagnosis case, the principle of our method consists in adding two electrically conductive tapes of width *w* on the upper and lower parts of the duct. Initially, we assume that cable model (Figure 1a) is equivalent to a coplanar geometry (Figure1b). Practical micro-strip lines have width-to-height ratios $w<d$. The electric conductors and the ducts form an electrical line between tapes. Given a post-stressed cable, we can calculate an apparent permittivity ε_{app} using the basic formula of a multi-layers planar medium material's permittivity [6]:

$$\frac{1}{\varepsilon_{app}(z)} = \frac{1}{d}\sum_{n}\frac{h_n(z)}{\varepsilon_n(z)}$$

In the water content measurement case (Figure 1c), the electric line is constituted by a two parallel wires placed into a material (relative permittivity ε_r). The table 1 gives the different electric line parameters for the two electric lines used.

Table 1: Electric line parameters

Parameter	**For the strip-line**	**For the two parallel wires**
Permittivity $\varepsilon_{rel}(z)$	$\frac{\varepsilon_{app}(z)+1}{2} + \frac{\varepsilon_{app}(z)-1}{2}\frac{1}{\sqrt{1+12d/w}}$	ε_{rel} of the material
$L(z) = \mu.\eta$ $C(z) = \varepsilon'(z).\eta$ $G(z) = \omega C(z)\frac{\varepsilon''}{\varepsilon'}$	with $\eta = \frac{1}{2\pi} ln\left(\frac{8d}{w} + \frac{w}{4d}\right)$	$\eta = \frac{1}{\pi} acos\left(\frac{D}{2a}\right)$
$R(z)$ with $\delta_r = \frac{1}{\sqrt{\mu\sigma\pi f}}$	$\frac{2}{\sigma w \delta_r}$	$\frac{2}{\sigma\pi 2a\delta_r}$

The high-frequency impedance $Z_\infty(z)$, the loss terms $\frac{R(z)}{L(z)}$ and $\frac{G(z)}{C(z)}$ are related to the material permittivity ε. Finally, the high frequency impedance is given by [6]

$$Z_\infty(z) = \sqrt{\frac{R(z)+jL(z)\omega}{G(z)+jC(z)\omega}}$$

Electric model of the transmission line

The electric signal transmission is generally modeled using the "telegrapher's equation" and characterized by the line parameters *R*,*L*,*C* and *G*, representing, respectively, the resistance, the inductance, the capacitance and the shunt conductance.
In the harmonic regime, telegrapher's equations are written as follow:

$$\partial_z V(\omega,z) - j\omega L(z) I(\omega,z) + R(z) I(\omega,z) = 0$$
$$\partial_z I(\omega,z) - j\omega C(z) V(\omega,z) + G(z) V(\omega,z) = 0$$

where the intensity $I(\omega,z)$and the voltage $V(\omega,z)$depend on the space position *z* and the pulsation $\omega = 2\pi f$ where f is the frequency in a range of frequencies from 1 MHz to 1GHz with the step $\Delta f = 1$ MHz.
The following boundary conditions are verified at both ends at *z*=0 and z=*l*

$$V(\omega,0) - Z_S(\omega) I(\omega,0) = V_S(\omega)$$
$$V(\omega,l) - Z_T(\omega) I(\omega,l) = 0$$

$Z_S(\omega)$ is the internal source impedance of the VNA connected at *z=0* and $Z_T(\omega)$ is the terminal impedance connected at *z=l*. $V_S(\omega)$ represents the harmonic source generator.

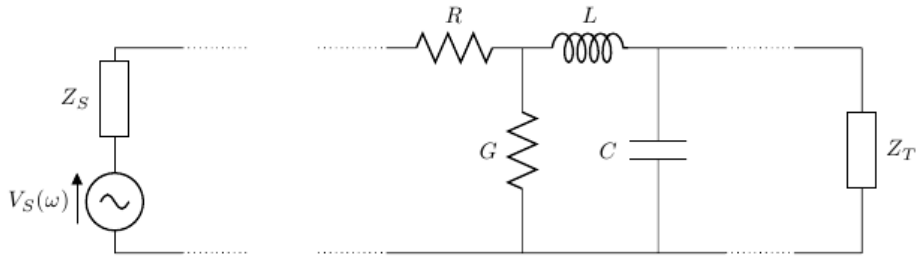

Figure 2: Transmission line model with one source generator

Direct problem: Riccati Equation

Reflectometry technique consists in exciting a cable with a given signal and analyzing the returning signals, composed by all signals reflected by the heterogeneities of the line. Reflectometry experiments lead to observing voltages and currents as a function of the time at some position: only the traveling times and amplitudes of waves are accessible by such experiments. A fault can only be localized in terms of the traveling time of the reflected test wave starting from the test point. It becomes natural to work with the traveling time instead of the spatial coordinates. The traveling time is also called the *electrical distance*.
The *Liouville transformation* allows to transform the spatial coordinate *z* into the electrical distance *x*, which writes as follow:

$$x(z) = \int_0^z \frac{ds}{v(s)}$$

$x(z)$ corresponds to the wave traveling time from position *0* to *z*.
The electrical distance $\tau = x(l)$ corresponds to the physical length *l* and we will be able to write any function $g(x) \equiv g(z(x))$.
The wave velocity associated with the complex permittivity is defined as:

$$v(z) = \frac{c}{\sqrt{\varepsilon'(z)\frac{1+\sqrt{1+tan\delta(z)^2}}{2}}}$$

where $tan\delta(z)^2 = \varepsilon''(z)/\varepsilon'(z)$.
Reflection coefficient is modeled by a set of Riccati equations [7].
For a fixed frequency $f \in [1MHz, 1GHz]$, the corresponding Riccati equation, denoted by *R(f)* shows the behavior of the reflection coefficient along the line $[0,\tau]$. We define the high-frequency impedance such as:

$$Z_\infty(x) = \sqrt{L(x)/C(x)} \quad (1)$$

then the set of Riccati equations *R*(f)

$$\frac{d}{dx}Z_{app}(x,\omega) = \left(j\omega + \frac{G(x)}{C(x)}\right)Z_\infty^{-1}(x)Z_{app}^2(x,\omega) - (j\omega + \frac{R(x)}{L(x)})Z_\infty(x) \quad (2)$$

$$Z_{app}(\tau,\omega) = Z_T(\omega)$$

where $\omega = 2\pi f$.

The reflection coefficient $S_{11}(\omega)$ is defined by

$$S_{11}(\omega) = \frac{Z_{app}(0,\omega) - Z_s}{Z_{app}(0,\omega) + Z_s} \quad (3)$$

where Z_S is the internal impedance of source.

Inverse problem: ISTL software

The inversion method is processed by a software ISTL (Inverse Scattering Transform Lossless) developed at INRIA[1] by the team SISYPHE. ISTL is based on an inverse scattering method applied to transmission lines [7].

The inverse scattering transform consists of the following steps for computing the profile of L(x)/C(x)= $Z_\infty^2(x)$, from the reflection coefficient $S_{11}(\omega)$ (see [2] for details).

1. Let the Fourier transform of the reflection coefficient $S_{11}(\omega)$ be

$$\rho(x) = \frac{1}{2\pi}\int_{-\infty}^{+\infty} S_{11}(\omega)e^{-j\omega x}d\omega$$

2. Solve the integral equations (known as Gelfand-Levitan-Marchenko equations) for its unknown kernels $A_1(x,y)$ and $A_2(x,y)$:

$$A_1(x,y) + \int_{-y}^{x} A_2(x,s)\rho(y+s)ds = 0$$

$$A_2(x,y) + \rho(x+y) + \int_{-y}^{x} A_1(x,s)\rho(y+s)ds = 0$$

3. Compute the heterogeneity function through

$$\frac{1}{Z_{\infty(x)}}\frac{d}{dx}Z_{\infty(x)} = 2A_2(x,x)$$

Simulations and Validations

In order to validate the proposed method for post-tensioned cable diagnosis, results of numerical simulation are presented in this section. To simulate reflectometry measurements, reflection coefficients are computed by solving the Riccati's equation (2).

In the simulation, we consider a duct filled with cement, white paste and air. A material widths profile (Figure 3) is considered together with the permittivity's values shown in Table 1.

For each excitation frequency in ω the reflection coefficient of a duct was calculated using (2) and (3). A $Z_\infty(z)$ profile is simulated in both *z* and *x* coordinates in Figure 4. The simulated reflection coefficient $S_{11}(f)$ (modulus and phase) is shown in Figure 5.

ISTL software was designed to retrieve the characteristic impedance for a lossless transmission line. Nevertheless, the algorithm is robust and it works also for lossy transmission line, that means it is capable of finding the impedance defined in (1). The Z_∞ profile computed through ISTL (Figure 6) is compared to the original simulated profile in Figure 4: oscillations of retrieved impedance are due to the terminal impedance mismatch.

[1] INRIA Institut National de Recherche en Informatique et en Automatique, Domaine de Voluceau-Rocquencourt- 78153 Le Chesnay, France

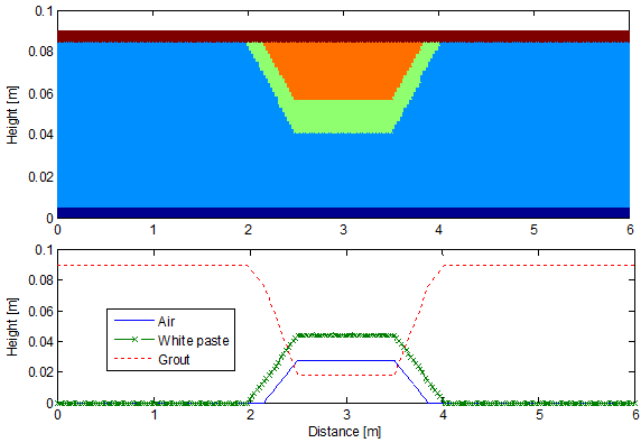

Figure 3: Post-tensioned duct modeled

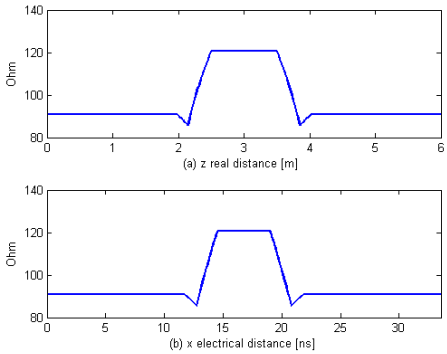

Figure 4: Simulated reflection coefficient $\boldsymbol{S_{11}}$

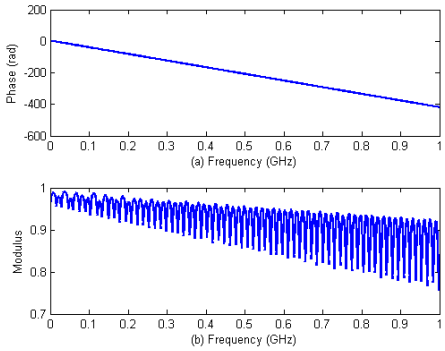

Figure 5: Simulated $\boldsymbol{Z}_{\infty}$profile : z vs x.

We remind that the inverse scattering transform computes the high frequency as a function of x. In practice it would be more useful to inspect the ratio as a function of z, the true spatial coordinate of the transmission line. Like all reflectometry methods, the information obtained by observing incident and reflected waves is related to the wave propagation time x.

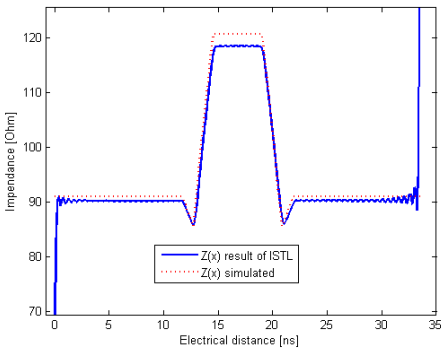

Figure 6: The impedance profile computed by ISTL and compared to the simulated profile

Experimental results

Experiments were carried out to check the validity of the numerical simulations.
Two mockup ducts of 6 *m* length and with a diameter of 90 *mm* have been considered. They are equipped with 12 steel cables of 15 *mm* diameter (Figure 7).
These ducts were fixed on a frame reproducing the curvature of pre-tensioned ducts on a stack. The vents are positioned on either side of the top point, i.e. in practice each side of the deviator. Moreover, wooden wedges were inserted between the metal structures supporting the ducts. The cement was injected into duct A using a standard *Superstresscem* with a ratio Water/Cement 0.35. In duct B it has

been injected with cement together with a *ChrysoGT* adjutant (Water/Cement 0.65) in order to promote the appearance of white paste.

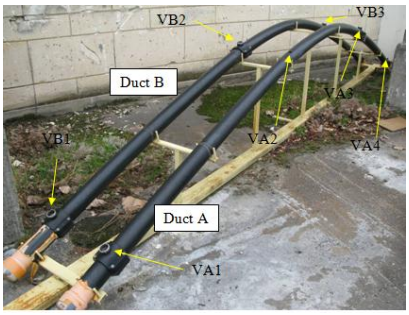

Figure 7: External post stressed duct (IFSTTAR laboratoires, France)

S_{11} measurements are performed using a VNA of *Anritsu MS2026*. Ducts are equipped with metal strips on the upper and lower parts of the ducts. The strip is composed of adhesive aluminum rubber (thickness 0,1*mm* and width 50*mm*). This pair of strips is connected to a coaxial cable through clips. The coaxial cable is linked to the VNA port. The measurements are performed on a frequency range of 1 MHz to 1 GHz with a frequency step of 1 MHz (1000 points).
The VNA coaxial cable is connected to the duct through clips and at the end of duct another pair of clips connects the metallic strips to known terminal impedance (Z_T).
On each cable, we performed three different experiences connected to three different terminal impedances branched at the end of the ducts (open circuits, short circuits and an impedance of 50 Ohms).
The ducts have been inspected by hammer auscultation. Figure 8 shows the location of void areas and vents on ducts. Cables have not been open so the exact profile of the heights of materials is unknown.

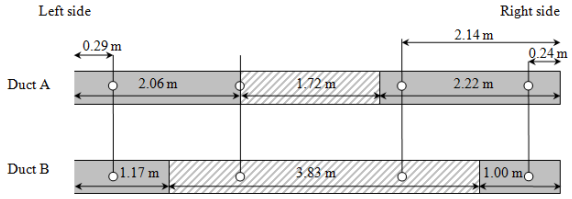

Figure 8: Location of void areas (hatched) and vents (o) on ducts A and B

Data inversion

$S_{11}(f)$ measurements of VNA has been fed to ISTL software. Results of the inversion software are in figure 9. Each figure shows a comparison between the three different experiences: the impedance profiles match until the end of the line where the terminal impedances are. ISTL is capable of detecting these three terminations. Both figures shows two bumps of impedance profile at both ends of the cable (around 5 *ns* and 40 *ns*): these variations of impedance correspond to the ruptures of impedance caused by the connection between the coaxial cable and tapes. On the other side, ISTL retrieve the impedance profile as a function of electrical distance. The physical end of the electric line is determined by adjusting the terminal impedance (Z_T).
From the impedance profile, we deduced the real part of the apparent permittivity and consequently lossless wave velocity. We were able to plot the impedance profiles as functions of physical distance. These inversion results have been compared to hammer auscultation (see Figure 9). The presence of void is detected clearly as an increment of the retrieved impedance: we can see a rise of impedance's values in the middle part of duct, where the void is supposed to be.
The oscillations at the beginning of the duct are also due to the ruptures of impedance caused by the connection. Moreover, the vents create a bump of impedance.

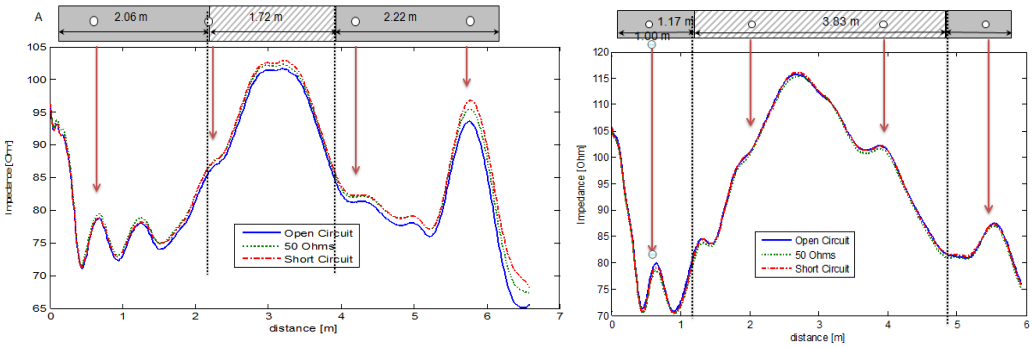

a) on duct A b) on duct B

Figure 9: The impedance profile computed by ISTL compared to hammer auscultation

Conclusion and further direction

In this paper, we have presented a new non destructive testing method based on FDR method. Associated to FDR measurement, we used the software Inverse Scattering Transmission Line (ISTL) as robust inversion algorithm.
This method is validated to diagnosis the external post-tensioned duct. This diagnostic method is able to detect the heterogeneities (void, white paste) of materials along a cable. We have developed an equivalent permittivity model taking the dispersion electromagnetic properties into account, allowing us a reflection coefficient simulation using the Telegrapher's model. Theoretical work, taking the properties of the materials and propagation phenomenon into account, enables one to predict the signal measured. Moreover, once the duct equipped with a strip line, the diagnosis can be done remotely to improve the safety of personnel in the event of a cable break. As the capacitive method, the method presented here, is able to distinguish a shrinkage and a void, which is not possible with classical inspection method using a hammer.
Further research of the FDR method concerns the nuclear applications to measure the water content of the concrete of containment, cooling tower or also nuclear waste repositories. The ideas is to take electromagnetic dispersion properties of the concrete into account to improve the measurement of a water content and to measure the moisture profile along the TDR probe.

Acknowledgements

The authors wish to thank the team SISYPHE of INRIA for the development of software ISTL and the team of CEREMA from Trappes for the use of the post-tensioned duct mockups.

Bibliography

[1] P. Stephan, J. Salin, Ageing management of concrete structure: Assessment of EDF methodology in comparison with SHM and AIEA guides, Constr. And Build Mat. 2012, 37 924-933.
[2] R. Le Roy, Rhéologie et stabilité des matrices cimentaires et des coulis, Etudes et recherches des Laboratoires des ponts et chaussées, LCPC Paris, 2006.
[3] T. Bore, D. Placko, F. Taillade, M. Himbert, Capacitive sensor for measuring the filled of post-tensioned ducts: experimental set-up, modelling and signal processing, IEEE Sensors Journal, 2012, 13 457-465.
[4] H. Tang and Q. Zhang, Inverse scattering for lossy electric transmission line soft fault diagnosis, Antennas and Propagation Society International Symposium (APSURSI), 2010.
[5] Q. Zhang, M. Sorine, and M. Admane, Inverse Scattering for Soft Fault Diagnosis in Electric Transmission Lines, In 48th IEEE Conference on decision and Control, Shanghai, China, 2009.
[6] D. M. Pozar, Microwave engineering, Wiley, New York, 3rd ed. edition, 2005.
[7] G. L. Lamb, Elements of Soliton Theory. John Wiley and sons, 1980.

CONDITION ASSESSMENT OF PRESSURE PIPELINES IN NUCLEAR POWER PLANTS: A CASE FOR NON-DESTRUCTIVE EVALUATION OF CONCRETE PRESSURE PIPES

E. Padewski, III, P.E., Pure Technologies, USA,
M. Wrigglesworth, A. Somani, Pure Technologies, Canada

ABSTRACT

Many nuclear power plants use pressurized concrete pipes to distribute cooling and service water throughout the plant. Large diameter pipes form the backbone of a plant's cooling water system and work reasonably well in a buried environment. However, over a period of time, either due to internal or external factors, these pipes deteriorate and may result in catastrophic failures. These failures are cause for interruption in service, property damage, and repair costs.

Earlier methods for evaluating buried pressurized concrete pipes included internal visual inspection or external excavation of the line. Based on the number of cracks and delaminations, these methods help to identify pipeline sections close to failure. However, a true non-destructive evaluation method based on electromagnetics was developed that accesses the actual condition of these critical buried pressure pipes. Specialized in-line leak detection tools are also now able to find leaks in these large pipelines, which can be an early indicator of joint and corrosion problems. An acoustic fiber optic cable is capable of monitoring the deterioration of pipes in real time. By combining these technologies with a visual inspection, a comprehensive risk management program can be developed.

This paper will present the nuances of visual and sounding, electromagnetic, and in-line acoustic leak detection inspection techniques, factors affecting service life, case studies of actual inspections of pressurized concrete pipes in nuclear power plants, and how to tie all these processes together to effectively manage a pressurized concrete pipeline in a nuclear power plant.

JUSTIFICATION

Large diameter circulating water mains are a crucial component in the operation of nuclear power plants. These pipelines distribute cooling and service water throughout the plant, without which the plant would not be able to operate. Over time, as with any material, these pipes deteriorate and unless properly inspected and repaired will fail. A failure in a circulating water main could force a nuclear power plant to shut down, result in energy shortage, and cause large economic losses. Therefore, monitoring and inspecting water mains in nuclear power plants is extremely important. This paper focuses on the effectiveness of inspection techniques for pressurized concrete pipe in nuclear power plants, and how these inspections can help to prolong the lifespan of the circulating water mains.

INSPECTION METHODOLOGIES

While distress rates are low for most concrete or ferrous pipe, a single deteriorating section is all that is required for a pipeline failure. Inspection and condition assessment of cooling mains is a sound pipeline management task. Assessing issues in cooling mains and addressing areas of concern is a pipeline management alternative to capital replacement projects for aging mains. This method relies on assessing the condition of a pipeline to quantify damage/risk and performing isolated repairs on sections of pipe experiencing advanced deterioration[i].

Visual and Sounding Inspection

Internal visual and sounding inspections are time tested methods for evaluation of the condition of concrete pipe with the intent of finding individual pipe sections in a state of incipient failure.

During an internal inspection, the inner concrete core of the pipeline is visually examined for cracking, spalling, pitting and other possible indications of distress. Certain crack patterns in the concrete of the pipe can be an indicator of structural deterioration, excessive loading conditions or possibly transient pressure issues. Additionally, each joint is visually inspected for cracking and spalling of the joint mortar. Over time, mortar can spall away and expose the steel joint ring leading to corrosion of the steel. Water flowing over a spalled joint can lead to deterioration of the inner core. When the cooling water of a nuclear power plant consists of seawater or brackish water the corrosion of the joint ring can be severe and possibly lead to the corrosion of the steel cylinder.

In the case of prestressed concrete pipe ("PCP") and prestressed concrete cylinder pipe ("PCCP"), as prestressing wire wraps break, the pipe begins to expand. As concrete has a low threshold for tensile stress, either a delamination or crack will form prior to a pipe approaching failure. Under normal operating conditions, the concrete core can separate from the steel cylinder. The sounding inspection of PCCP relies on the use of a steel rod, approximately 25cm shorter than the internal diameter of the pipe, to impact the inner lining of each pipe in order to detect "hollow" areas. Hollow areas in the lining of embedded cylinder pipe typically represent the separation of the lining from the steel cylinder, which is usually the result of a loss of prestress due to broken prestressing wire wraps, the most common form of distress in PCCP. When the prestress is lost and compression of the concrete is released, the internal pressure causes the cylinder and core to further expand. Since the internal pressure acts against the steel cylinder, the concrete lining separates and does not expand after its residual concrete compression is relieved. This separation is not completely reversible when the internal pressure is removed and can be detected as a hollow when the lining is sounded[ii].

Reinforced concrete pipe ("RCP") or bar-wrapped ("BWP") pipe rely on the steel reinforcement encapsulated in concrete core for their strength. As the reinforcement corrodes, the concrete core may expand and crack, leading to failure or leakage.

In addition to visually inspecting and sounding the pipeline, a surveyor's distance wheel is used to measure the distance of each pipe length in order to provide documentation of the in-ground pipe layout, which often differs from the "as-built" records, and provides an accurate lay schedule. Measurements are also taken from known features (e.g. a joint) to any distressed areas, which allows the inspection team to develop a full inventory of every pipe that can be correlated to the available pipe laying schedules, as built drawings, and specifications to establish a comprehensive layout of the line.

Electromagnetic Inspection Technologies

Electromagnetic inspection is a nondestructive method of evaluating the baseline condition of the prestressing wire in PCP and PCCP or the reinforcing bars in BWP. Electromagnetic inspections ascertain a magnetic signature for each pipe to identify anomalies that are produced by zones of broken prestressing wire wraps. Various characteristics associated with an anomaly (length, magnitude, phase shift, etc.) are evaluated to provide an estimate of the number of broken wire or bar wraps. This inspection method is able to quantify the amount of damage and is the best method available to determine the baseline condition of a pipeline. Electromagnetic inspection provides an estimation of the level of prestressing wire or bar damage

Electromagnetic pipe inspection technologies work by inducing a varying electrical field in the prestressing wire and measuring the corresponding magnetic field response. The main components of the electromagnetic equipment consist of a transmitter coil to generate the field, a receiver coil to pick up the induced response, and a data logger to record the data. This equipment is moved through the pipeline, or along the external pipe surface, and the resulting data is recorded on the data acquisition system. By evaluating this data, wire breaks can be identified on pipe sections and the position and number of broken wire wraps can be estimated.

A common analogy used to describe the physics of an electromagnetic inspection is to view the prestressing wire as a coiled inductor. If the prestressing wire, acting as an antenna, is intact, the receiver coil detects a signal with certain characteristics. When the end of a pipe is reached, the

polarity of the detected field reverses because the coiled inductor ends. However, if the inductor is broken (i.e., the prestressing wire wrap is broken), the signal is altered and a new pole reversal occurs part way through the pipe. These unexpected reversals delay the arrival of the signal at the receiver and can be quantified to estimate the number of broken wire wraps.

Multiple platforms consisting of manned or in-line unmanned options now exist that allow various degrees of preparation prior to performing an internal inspection. The various electromagnetic platforms provide the most thorough and accurate assessment available as data and, in the case of the manned inspection, can be correlated to the results of the internal visual and sounding inspection. For the unmanned electromagnetic inspections, options include the robotic and free-swimming inspection platforms for large diameter mains which can operated under depressurized or live operating conditions, respectfully, providing an electromagnetic inspection with the possibility of limited service disruption.

The main variables that should be analyzed in determining whether to use the manned technology, the robotic tool or the unmanned free-swimming platform is whether or not the utility would like the electromagnetic inspection to be correlated with the visual and sounding inspection and whether or not the pipeline can be shut down and dewatered. If the client is able to shut down the pipeline for a short period of time, and is interested in the visual and sounding evaluation in conjunction with the electromagnetic inspection, the manned electromagnetic technology is recommended providing the greatest level of detail.

In-line Acoustic Leak Detection

In-line leak detection services allow water utilities to proactively locate water main leaks that may otherwise have gone unnoticed, thereby minimizing costs associated with potential ruptures and water loss. Although not necessarily an indicator of structural damage, often times leakage is a precursor of larger problems in a pipe. Acoustic leak detection sensors are most successful when inserted into the pipelines, bringing the sensor to the leak, rather than relying on the sound of the leak to find the sensor. In-line surveys work exceptionally well on large-diameter water mains, which are often poor at transmitting leak sounds to external sensors and have limited access points to the pipe. In-line leak detection services have been proven to reliably identify very small leaks on water transmission mains with pinpoint precision, without requiring the water main to be taken out of service.

Two successful types of in-line acoustic leak detection tools can be utilized in the larger diameter cooling water mains are the “free swimming” or “tethered” listening devices. Both systems are in-line, meaning that neither requires that the main be shut down for the inspection.

The free swimming tools detect anomalous acoustic activity associated with leaks or pockets of trapped gas in pressurized pipelines. As the tool is free swimming, it can traverse and inspect very long distances with only two access points are required for insertion and extraction.

The tethered in-line acoustic leak detection tools can pinpoint the location of leaks in a pipeline. Unlike the free swimming tool, the apparatus, it is connected to the surface by a cable through a 50mm or larger tap. A small drag chute uses the flow of the water to draw the sensor through the pipeline while a trained technician evaluates results in real time. As the tool is tethered, when a leak is detected, the technician can stop the tool and locate the leak, typically within 50cm.

POST-INSPECTION SERVICES

Structural Analysis

In addition to the various pipeline inspection techniques, a post-inspection structural evaluation is advisable to analyze any specific pipe designs. In the case of PCCP, the evaluation would be based on the European (“EN”) Standard EN642, similar in nature to the American Water Works Association (“AWWA”) C301 and AWWA C304 standards used to define the design requirements. Additional concrete pipe designs can be evaluated based on either the current design standards or the standards in place at the time of manufacture.

A finite element analysis non-linear three dimensional model is an accurate method for modeling complex geometry under different loading conditions. The finite element analysis model has been developed to determine the structural consequence of a deteriorating concrete pipe either due to cracking of the concrete, corrosion or breaking of the steel members, excessive external loading or

varying internal pressure. The evaluation is based on the available design standards, by utilizing pipe design specifications, design parameters, and the assumed current condition of the concrete and steel. In the analysis, the model of a pipe is subjected to internal pressure, pipe and fluid weights, and external loads while varying the level of damage. A performance curve, displaying the effects of the damage, is formulated and used to determine the acceptable deterioration the concrete pipe can withstand prior to experiencing theoretical loading limits. The finite element analysis offers the client the most accurate and comprehensive analysis of their pipeline by determining how a specific level of damage will affect the remaining useful of the asset.

Examples of finite element performance risks curves are shown in Figure 1. Figure 1 is an embedded cylinder pipe that was design for a maximum combined operational and surge pressure of 483 kPa. At the maximum design pressure, once the damage reaches 61 broken wire wraps, the pipe, theoretically, will no longer be in compression and will be in danger of failure. Similar curves can be created for non-cylinder pipe as well as metallic pipe.

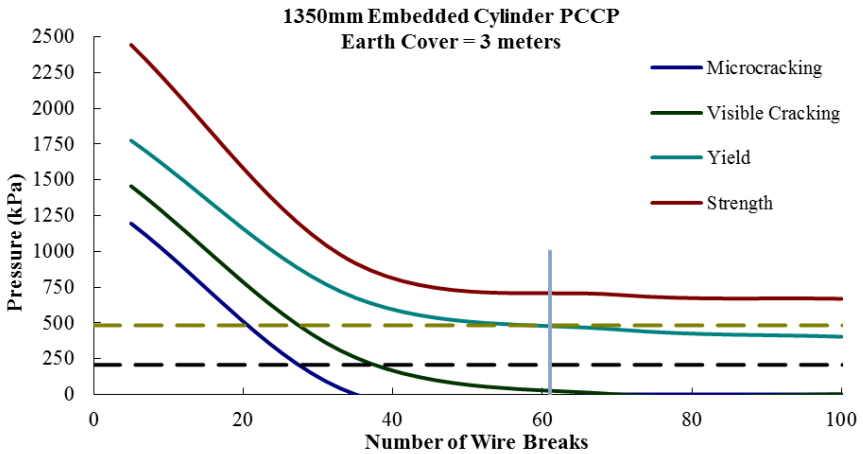

Figure 1: Performance risk curve for embedded cylinder PCCP

Acoustic Fiber Optic Cable

In North America, Acoustic Fiber Optic Cable ("AFO") systems are being deployed in water mains as a method to detect and locate prestressing wire wrap break events in PCCP while the pipeline is in service. When developing a management program for a PCCP pipeline, such as pipelines that are found in nuclear power plants, there are two important variables to consider: the baseline condition of the pipeline and the rate of deterioration. The visual and sounding inspection, electromagnetic inspection, and the in-line leak detection services will provide an in depth and comprehensive evaluation of the baseline condition of a pipeline. However, this is simply a "snapshot" of the pipeline condition. To evaluate and track the deterioration of various PCCP water mains, an AFO system can listen for actively deteriorating pipes.

AFO technology continuously monitors the acoustic activity in a pipeline to identify the acoustic events associated with the failure of prestressing wires. The AFO system continuously tracks the condition of each pipe in the line and reports the time and location of breaking prestressing wires. Thus, acoustic monitoring can identify actively deteriorating pipe sections and determine the rate of deterioration. The AFO system offers the client a unique insight into the real time status of their pipeline. Continuously monitoring the system provides information that could be invaluable to a nuclear power plant, because a pipe failure in a crucial line such as a large diameter cooling main could be catastrophic.

CASE STUDIES

Case Study 1

Visual, sounding, and electromagnetic inspections were performed on a cooling water pipeline located at a nuclear power generating station in North America. The pipeline carried cooling water that was critical to the power generation process. It was comprised of 2100mm PCCP manufactured by in three stages in the late 1960s and early 1970s. A relatively short pipeline, the approximate distance inspected was 280m for a total of 61 pipes.

The visual inspection observed eight joints without mortar protecting the steel joint ring, and, therefore, were in need of repair. An additional thirteen joint has the spalling had yet to expose the steel rings. The sounding inspection detected a single pipe with a hollow sounding area in the barrel near mid-pipe. Review of the pipe laying schedule indicated an anchor ring embedded in the pipe and the concrete foundation. As a result, no pipes were found to be in a state of failure.

During the same shutdown, an electromagnetic inspection was performed on the pipeline. Of the 57 lengths of PCCP available for evaluation, three (3) had electromagnetic signals indicative of distress. Though based on a limited sample size, the approximately 5.3% of damaged pipes the cooling pipeline exceeded the 3.9% average typically observed during other inspections of PCCP pipelines[1]. Two pipes had anomalies representing 10 and 40 broken prestressing wire wraps while a third pipe had an anomaly where the electromagnetic signal could not provide quantifiable distress. As the electromagnetic inspection results did not correlate with the visual and sounding inspection, it was determined that the pipes with the electromagnetic anomalies did not have a loss of compression in the concrete core. Table 1 summarizes the results of the electromagnetic inspection.

Table 1: Electromagnetic Pipes of Interest

Pipe Number	Pipe Class	Inspection Distance	Pipe Length	Break Region[1]	Number of Wire Wrap Breaks by Region	Total Number of Wire Wrap Breaks
4	IV-84C	46m	4.88m	2.6; 4.1	25; 15	40
5	III-84C2	100m	4.88m	0.8; 1.2–2.9	5; Shifted[3]	5; Shifted[3]
6	III-84D	168m	4.88m	1.7	10	10

[1] *Wire break regions were reported as meters from the upstream joint.*
[2] *Shifted indicates a region where the electromagnetic signal indicated an anomalous area, though the exact number of broken wire wraps could not be determined.*

In addition to the joint damage and pipes with electromagnetic anomalies, marine growth was observed throughout the pipeline, and corrosion on a blind flange in a pipe. It was recommended that the marine growth and locations of the corrosion be monitored or reevaluated during future internal inspections. A structural evaluation will determine the threshold of damage prior to rehabilitation as well as re-inspection during the next scheduled outage to determine if the pipe deterioration is an ongoing issue.

Case Study 2

Electromagnetic, visual, and sounding inspections were conducted in the supply and return lines for a nuclear power generating station in North America. The supply and return lines were comprised of 1800mm, 2100mm, 2900mm, and 3000mm diameter PCCP that were manufactured in 1982. The inspection covered 1,660m as a total of 365 pipes were inspected. The cooling lines had been inspected and repair following an earlier inspection. The intent of the recent inspection was to determine the current condition of the pipe as well as estimating the rate of deterioration. The inspection findings are summarized as follows:

- Four pipes of the return main had hollow areas detected; however, no pipes of the supply main had any hollow areas.
- Of the four pipes of the return main, three hollow areas were located in the 3000mm portion of the return line and one hollow area was located in the 2100mm portion of the return line.

- The hollow areas were believed to be consistent with a loss of compression in the concrete core.
- A total of 122 pipes were previously repaired using an internal carbon fiber lining. Of the 122 repairs, 60 had defects as a result of the operating conditions or were not adequately installed and in need of repair.
- A joint between two pipes in the 3000mm portion of the return line had moisture present from the 1 o'clock position to the invert, indicating the potential of a leak. The joint was observed to be a wide, welded joint with faint cracks extending from the 3 o'clock position up to the crown. These cracks were visible near the area where the water was observed to be seeping through the joint.
- Analysis of the electromagnetic data identified 167 of the 365 pipes (45.8%) with electromagnetic anomalies consistent with broken prestressing wire wraps. However, multiple pipes had been previously repaired by means of a carbon fiber liner.

Part of the structural analysis was to evaluate the risk of PCCP structural failure due to reduced structural capacity as a result of broken prestressing wire wraps. The prestressing wire is a principal structural component of PCCP and each individual class of PCCP installed in a pipeline was designed specifically for the maximum hydraulic operating pressure and earth covers expected along the route. Therefore, any amount of wire wrap damage poses some level of risk to PCCP and should be carefully evaluated. In an effort to quantify risk, a structural analysis and risk evaluation was performed, similar to shown in Figure 1 above, to determine the pipes in need of repair. The evaluation determined the nuclear power plant needed to repair eight pipes prior to returning the supply and return Lines to service. As the pipeline continues to deteriorate, re-inspection of the cooling lines was recommended within the next three to five years in an effort to identify additional pipes of concern.

Case Study Conclusions

Case Study #1 and Case Study #2 are examples of successfully manned internal inspections where the utility was able and chose to shut down their pipeline. The results showed that the level of damage in a given system can vary drastically, yet still can be adequately managed using current techniques and engineering evaluations. In Case Study #2, a considerably higher than average level of distress for PCCP water mains was encountered, yet the internal inspection schedule will allowed the utility to minimize the overall cost of rehabilitation when compared to complete replacement of the cooling lines.

The pipes that were in need of repair were listed to the client as well as pipes that should be carefully monitored for the future. In the case of Case Study #2, comparisons of the results of the most recent inspection to those of a prior inspection, were available and provided to the client who was then able to determine not only the current state of their pipeline, but also the rate of deterioration. Neither client in Case Study #1 or Case Study #2 opted to utilize and install a leak detection system or an AFO monitoring system, though, if they continue to include an inspection program in with their scheduled outages, the risk of failure should remain low.

Overall, an increased level of deterioration was found in the return lines compared to the supply lines. The reason may be the higher temperature of the return flow as steel corrosion rates as well as other chemical reactions are directly affected by temperature.

CONCLUSIONS

Large diameter circulating water mains are vital components in the operation of nuclear power plants. These pipelines distribute cooling and service water throughout the plant, without which the plant would not be able to run. Over time, as with any material, these pipes deteriorate and in extreme cases can fail. A failure in a circulating water main could force the nuclear power plant to shut down, result in energy shortage, and cause large economic losses. Therefore, monitoring and inspecting circulating water mains in nuclear power plants is extremely important.

Internal inspections can be utilized to gain a comprehensive understanding of the state of PCCP in a nuclear power plant. A visual and sounding inspection provides a thorough inventory of the

condition of the interior of the pipeline and is a time tested method for detecting pipes with severe damage that are a severe risk of failure. Electromagnetic inspections are able to detect broken prestressing wire wraps in PCCP, which is important because detecting broken wire wraps early allows for the utility to track the deterioration of a pipe and act before a failure occurs. In-line acoustic leak detection can locate leaks in the pipeline which cause water loss and in some cases are indicators of structure deterioration.

In addition to the various pipeline inspection techniques that are available for a nuclear power plant, a post-inspection structural evaluation is advisable for the pipe designs that make up the pipeline. Structural evaluation consists of a design evaluation, investigation into possible operating issues, and a finite element analysis. Structural analysis in accordance with an internal inspection is an invaluable tool in evaluating the condition of a pipeline. Long term acoustic monitoring or reinspection and rehabilitation at regularly scheduled intervals provides a utility the adequately assess the condition of their pipeline minimizing the likelihood of failure.

---

[i] Higgins, M.S., Stroebele, A., Zahidi, S., "Numbers Don't Lie, PCCP Performance and Deterioration Based on a Statistical Review of a Decade of Condition Assessment Data", Pipelines Conference 2012, Miami Beach, Florida, American Society of Civil Engineers, 2012.

[ii] Price, R.E., Brooks, M.B., "Evaluation of Concrete Pressure Pipelines and Prevention of Failures", Pipelines Conference 1995, San Diego, California, American Society of Civil Engineers, 1995.

REMOTE CONTROLLED VEHICLE FOR INSPECTION OF VERTICAL CONCRETE STRUCTURES

J. Lindberg, M. Guimaraes, EPRI

INTRODUCTION

The infrastructure in the energy industry includes several types of large, curved vertical structures such as cooling towers, nuclear containments and hydroelectric dams, as shown in Figure 1. Inspections of these structures are often performed manually by means of scaffolds. Automating such inspections will reduce time and costs, make them more efficient, increase inspection frequency and reduce safety risks.

EPRI has evaluated different types of technologies and their technology readiness level and concluded with the selection of a device that could be adapted to a variety of needs. The device identified did not include a positioning system or an NDE device, which was integrated into the crawler by modifying existing technologies. During the fall of 2012, a demonstration took place of the crawling device with a mapping and positioning system and an attached air-coupled NDE device. This presentation highlights the process of searching for a suitable device and concludes with the demonstration of its capabilities.

DEPLOYMENT

The current inspection practice requires manual access to the structures, typically via scaffolding. The process is difficult, time consuming and potentially unsafe. Improved concrete inspections are a high value to coal plants, nuclear plants and hydroelectric concrete dams. The availability of automated concrete inspections will translate into faster and less costly inspections of vertical structures. This will allow for easier and more frequent inspections that will be probably needed as plants age.

Figure 1 – Large, curved, vertical structures are common in the energy industry

Technology exists to inspect horizontal concrete structures such as bridges and roads with a rolling automated device [1]. However, the challenge lies in vertical and curved concrete structures. These structures could be inspected by using an automated device that moves on the surface attached to it by using some adhesion mechanism such as vacuum. Such a device could expedite the inspection process and reduce its costs.

The ideal device should be rugged enough to withstand field use outdoors, have a battery or independent power supply, be able to carry a device for non destructive tests in concrete, and be able to move over a rough concrete surface.
The objective of this project is to evaluate the feasibility of using an automated device for NDE tests in vertical concrete structures, perform a small scale field test and develop a strategy for demonstration of the technology.

SEARCH FOR AVAILABLE TECHNOLOGIES

The first step in automating large civil infrastructure inspections was to search on other industries, in the US as well as internationally, for devices that could be adapted to this need. For this purpose, a request for proposals was launched.
The request for proposals invited proposals for a remote controlled vehicle to inspect the surface of large vertical concrete structures. Furthermore, the ideal technology would:
• Be able to move *vertically* on a concrete surface;
• Be able to move over a *rough concrete surface;*
• Be able to move over *concave and convex surfaces;*
• Have *positional control* over surface including record of coordinate data;
• Be able to *carry a device* to perform nondestructive examination (NDE) tests;
• Be rugged enough to withstand field use outdoors resisting some exposure to some rain and humidity
• Preferably have a battery or independent power supply for 3-4 days of use.

EVALUATED TECHNOLOGIES

Forty three responses were submitted after the period of open request. These included 18 replies from industry and 15 from academia. Figure 2 shows pie charts with the detailed distribution of all respondents and the geographic distribution of the answers.
The request for proposal required that the technology readiness be disclosed. The technologies rediness of the responses ranged from conceptual to prototypes, and with several responses having technologies that were already commercialized.
The request for proposal described the requirements without specifying the approach. The respondents provided three basic approaches: a) flying vehicles; b) crawling vehicles; and c) cable-guided or cable driven vehicles. Figure 3 shows the responses classified according to the basic approach used to contact the vertical structure.

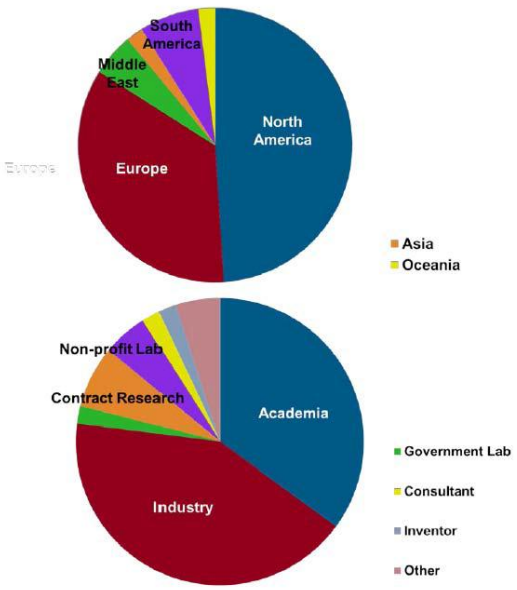

Figure 2 – Types of responses and geography

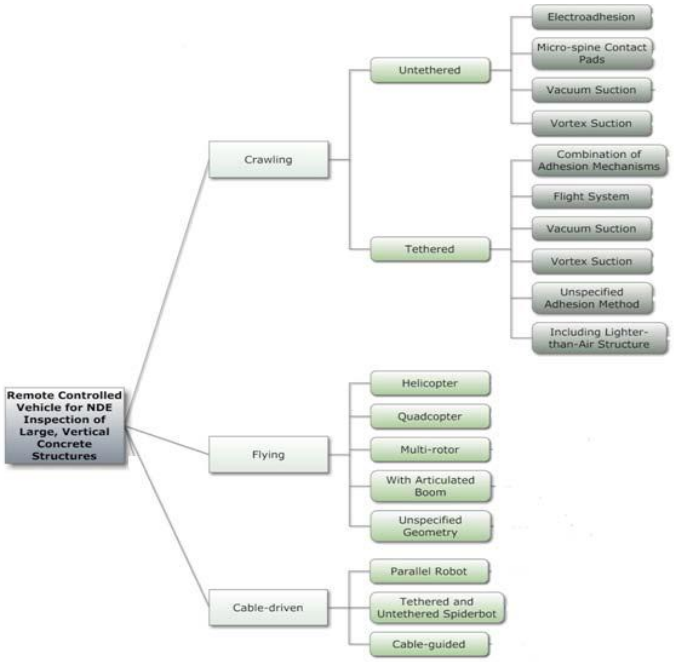

Figure 3 – Types of responses by approach

SELECTED APPROACH

The team composed of SouthWest Research Institute (SWRI) and International Climbing Machines (ICM) was selected among the 43 respondents. The selected approach met most of the requirements in the request for proposal and it was chosen due to its robustness and its potential.

The mechanism used by ICM's device to attach to the concrete wall is vacuum. This patented system uses a central vacuum chamber surrounded by a rolling foam seal that provides both a seal and propulsion. The vacuum chamber generates in excess of 225 pounds of adhesive force on a wide range of surface materials. The system is capable of traversing most surface types, including ferrous and non-ferrous metal, composites, and concrete and brick structures. It can adhere to convex, concave, and overhanging surfaces, and can even navigate gaps, seams, and obstacles on the surface such as conduit. Example applications are shown in Figure 4.

The ICM Climber is operated via a hand-held remote controller and requires a tether with a fall protector (heights less than ten feet may not require a fall-protector). ICM has developed several versions of their fall-protector and belay system that automatically maintains proper tension on the safety cable. The climber is inherently a remote-controlled device, but for large-scale inspection tasks, precision position information is needed to be able to map the location and path of the vehicle.

Figure 4 – Example applications of selected device

LOCATION AND POSITIONING SYSTEM

SwRI developed and integrated a Simultaneous Localization and Mapping (SLAM) system for the ICM Climber that is capable of generating and displaying the vehicle position and a 2D map of the structure. The SLAM code is an open source code developed by UT Darmstadt.

The SLAM system includes an Inertial Measurement Unit (IMU) fused with a scanning laser range finder (LIDAR) that provides high accuracy measurements. The system is modular so that it could be installed on any platform and be battery powered.

DEMONSTRATION

The objectives of the demonstration were to verify the core mobility technology that permits controlled access to a wide range of concrete structures and geometries; and to verify the positioning and tracking system that provides location information.

Additionally, the University of Texas at Austin (UT) demonstrated their air-coupled impact echo inspection technology mounted in the crawler. This system is relatively simple to implement on the Climber since it is non-contact (except for the impact hammer) and only requires a parabolic microphone be attached to the machine. For this demonstration, the impacts were generated manually using a small hammer and data was collected via an existing UT data acquisition system. The position information provided by the SLAM system could be correlated to the inspection data to generate defect maps.

The ICM climber with the positioning device (SLAM) and the air-coupled impact echo is shown in Figure 5. A video of the demonstration can be seen by scanning the QRcode or at www.youtube.com/EPRIvideos.

Figure 5 - ICM climber with the positioning system and the air-coupled impact echo device installed – Use QR code to see the video of the demonstration.

CONCLUSIONS

The demonstrated climber and NDE sensor system seem to be well suited to large, relatively flat, concrete structure inspection. The mobility of the platform is good and capable of traversing rough surfaces and even small obstacles. The NDE sensor was shown to be tolerant of variable positioning, operational while moving, and insensitive to ambient and vacuum noise. The positioning system was shown to be accurate enough for structural mapping. The integrated platform appears to have strong potential to significantly improve the efficiency, cost and safety of concrete structure inspection.

The demonstration system is considered to be a prototype feasibility demonstrator, with a system technology readiness level of approximately TRL 5. The climber is commercially available (TRL 9), but the positioning and sensing subsystems are TRL 4 or 5. Thus, further testing and development is needed.

The demonstration was conducted in a controlled environment. A follow-up demonstration at a hydro dam took place in July 2014, with excellent results and allowing EPRI to move forward with this concept.

Acknowledgments

The cooperation by NineSigma, South West Research Institute and the University of Texas at Austin are gratefully acknowledged.

REFERENCES

[1] BETOSCAN – An instrumented mobile robot system for the diagnosis of reinforced concrete floors, Herbert Wiggenhauser, Markus Stoppel, Gerd Dobmann, Jochen Kurz, Michael Raupach, and Kenji Reichling, Chapter 90 in Concrete Repair, Rehabilitation and Retrofitting II, Pages 255–256.

ADVANCED METHODS FOR SAMPLING AND ANALYSIS OF POST-TENSIONED CONCRETE TENDON GREASES

R. Wurzbach, MRG Labs, USA

Abstract

Post-tensioned concrete tendons in nuclear containment are often ungrouted, relying on a protective coating of grease to prevent corrosion of tendons and anchor components. In these installations, regulations such as ASME Section XI, subsection IWL, and Reg. Guide 1.35 provide guidance for testing of this grease to ensure continued protection of the tendon components. Advances in grease sampling and analysis technique allow for the possibility of obtaining samples without removal of the anchor can assemblies, significantly reducing the level of effort required to effectively monitor grease condition. These small sample size methods, utilizing sampling techniques outlined in ASTM D7718 standard, allow for selective sampling from close to the anchor head surface, and without the invasive process of removal of the enclosure can that holds the grease. This means that the grease will not be partially replenished during sampling, which could subsequently create a non-homogeneous grease mixture that could lead to sampling errors. Additional new analysis methods such as red-oxide quantification, ion-selective electrochemistry, and electrophoresis, may enhance the predictive capability of such monitoring, and improve maintenance practices to protect and extend tendon component life in containment applications.

Keywords: Corrosion, grease analysis, concrete structures

DETERMINING MATERIAL PROPERTIES OF CONCRETE COMPONENTS: ELASTIC PARAMETERS AND COMPRESSIVE STRENGHT

D. Algernon, S. Feistkorn, M. Schrrer
SVT Swiss Association for Technical Inspections, Switzerland

Abstract

In the condition assessment of concrete components of nuclear power plants, knowledge of the material properties is crucial. In many cases, the concrete strength and the elastic properties including modulus of elasticity, Poisson's ratio and shear modulus will be of particular interest. The elastic properties can be estimated based on their relationship with the propagation of elastic waves. The key is to use a combination of different wave modes. While most current applications are based on ultrasonic pulse velocity (transmission), a technique using the impact-echo method is introduced here, which provides significant advantages for the application in the field. Impact-Echo is normally used for thickness measurements using multiple reflections of longitudinal waves that are generated by the elastic impact of a small steel ball. However, in addition to the longitudinal waves, the impact causes strong surface waves. Whereas these surface waves are unwanted in conventional impact-echo applications, the combined analysis of longitudinal and surface waves provides the elastic parameters, which is demonstrated here. The concrete strength can be estimated using a rebound hammer, a traditional NDE method that can be very powerful if it is applied correctly. It is crucial to take into account the carbonation depth, perform a thorough calibration and provide a meaningful statistical basis. Since a thorough evaluation can therefore become quite complex, a software program has been developed that guides the analyst through the process and makes the evaluation reliable, time-efficient and practical.

Keywords: Materials characterization, Concrete, Impact-Echo, Rebound Hammer

NON-DESTRUCTIVE EVALUATION OF STEEL-CONCRETE MOCK-UPS

H. Wiggenhauser, J. Wöstmann, S. Schulze, BAM, Germany
K. Barry, M. Guimaraes, D. Scott, J. Lindberg, EPRI
J. Lareau, Westinghouse

INTRODUCTION AND MOTIVATION

The ability to inspect new constructions of nuclear power plants (NPP) is getting more attention, this is true also for concrete structures. Quality control of newly built structures is a pre-requisite for low maintenance during service life. It also provides a base for future service life extensions in order to keep NPPs in safe operation.

EPRI and BAM cooperated in a project to carry out a performance demonstration of non-destructive testing methods on two mock-up specimens provided by an industrial partner. The specimens were of the new modular construction type called Steel-Concrete (SC) which is used in new plants. These modules consist of two steel liners connected with steel rods. Concrete is poured between these liners which serve as form work in this process. Nelson studs ensure a good connection between the steel liners and the concrete [1].

The objectives of the project were to test two mock-ups with acoustic techniques in order to:

a) *identify embedded voids*
b) *identify further possibilities to improve the investigation techniques in these types of composite structures*

The NDT methods applied were Ground Penetrating Radar (GPR) (only for the concrete exposed surface) and ultrasound with two ultrasonic echo devices. Both ultrasonic systems had point contact transducers which can be coupled to the structure by pressing them against the surface. Additionally, a scanner system was used to record ultrasonic scans in a dense grid.

SPECIMENS

Two mock-up specimens of concrete-steel construction were tested. The small mock-up shown in Figure 1 (left) contains steel plates covering 5 sides with concrete between those plates. Horizontal rebars (tie rods) hold the long sides together and Nelson studs are placed between the rods. The voids, which were placed in the small specimen during construction, are made of styrofoam balls held together with a thin net.

The large mockup, also shown on Figure 1 (right), contains embedded pipes in addition to the Nelson studs and tie rods. Voids made of Styrofoam balls were placed at different locations during construction of the large mockup.

Figure1 Small Mock-Up during concreting (left).

Large mock-up before concrete placement (right)

NON-DESTRUCTIVE METHODS

The two methods applied are GPR and Ultrasound Pulse Echo (UPE) with dry point contact transducers [2].

Ground Penetrating Radar

Radar uses the reflection of electromagnetic waves from dielectric discontinuities or metal surfaces. Using this effect radar is a NDT tool for the investigation of civil engineering structures, such as reinforced concrete and masonry buildings, pavement or underground utilities. Radar in civil engineering was derived from the geophysical method of GPR to image the subsurface using short electromagnetic pulses. Following the impulse echo principle, radar data is handled similarly to the way as ultrasonic data is processed [3].

For radar testing, the polarization of the electromagnetic waves has to be taken into account. Reinforcing bars which are aligned parallel to the polarization direction (E-vector) show much higher reflection amplitudes than perpendicular ones. To be able to produce an even image of reinforcing bars in all directions, it is necessary to scan the surface in two perpendicular directions and to combine the measurements (data fusion).

Ultrasound Pulse Echo

UPE is based on the propagation of elastic waves in concrete. Due to high attenuation and scattering at pores and aggregates, low frequency ultrasound must be used. Shear waves do have a low signal to noise ratio. Longitudinal shear waves of frequencies around 55 kHz have proven to be of practical use for UPE measurements on concrete [4].

Ultrasound T/R Probe A1220. For single point measurements, there are generally two types of equipment: transducers with planar contact to the measuring surface and dry point contact transducers. For quick measurements of large concrete areas, usually dry contact transducers are used. The A1220 transducer consists of two arrays of 12 individual point contact transducers. One group acts as transmitter of shear waves while the other receives the ultrasonic signals.

Figure 2, right, shows as an example a typical A-scanning when the transducer is positioned above a tendon duct. The echo signals of both the tendon duct and the back wall are visible. The first strong signal on the time axis, belongs to the surface wave signals (arrow).

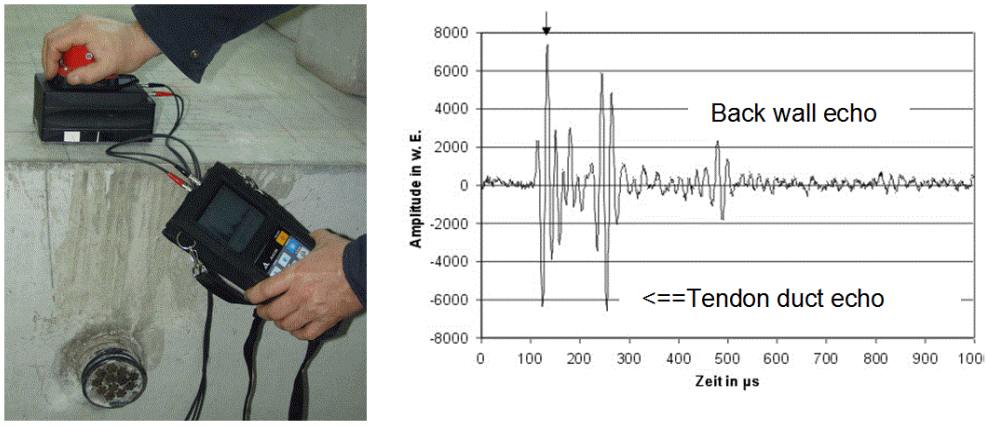

Figure 2 Principle of ultrasonic testing, left: photograph of test with A1220 equipment, right: A-scan of measurement with surface wave signal and duct and backwall echo.

Ultrasound Tomographer MIRA A1040. In order to accelerate and enhance the ultrasonic data acquisition, a linear array was developed in co-operation between BAM and ACSYS [5]. It consists of 12 lines of 4 dry contact shear wave transducers each generating ultrasound of a frequency of 55 kHz. The distance between the lines is 3,5 cm. The transducers and the electronics are mounted in a handheld box to be applied easily at concrete surfaces (Figure 3 left).

The 12 lines are configured as a multistatic array, which means that one line acts as transmitter and the other as receiver, after this, the second line acts as transmitter, and so forth as indicated in Figure 3 right). The data transfer of a complete data set is recorded and stored in less than 1 second per test location.

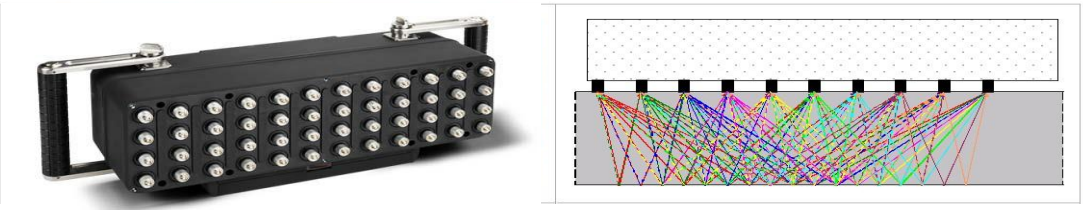

Figure 3 Multistatic tomographer A1040 with 12 rows of 4 shear wave transducers each (left). Right: principle of data acquisition each row acts subsequently as transmitter, while all other rows function are receiver (12 x11 individual sound paths in one measurement)

Scanner. An automated scanner was used to measure areas on the specimens with the A1220 transducers [9]. The automated process guarantees highly accurate measurements under reproducible and uniform conditions (spacing, orientation, applied contact pressure). The scanner is mounted on the surface using vacuum suction caps. The scan area is approximately 100 x 120 cm². The grid spacing typically ranges between 2 and 5 cm in both directions and the contact pressure is approximately 50 N.

MEASUREMENTS AND RESULTS

Small mock-up – concrete side

GPR measurements. Three antennas with different mean frequencies (2 GHz, 1,5 GHz and 900 MHz) were applied. Antennas with lower frequency have a larger penetration depth, while the resolution is reduced in comparison to an antenna with higher frequency. With increasingly higher frequency of the radar waves the resolution increases, but the penetration depth is lower. The software RADAN was used to process and analyse the data. For each line, a surface correction was carried out, the data was reconstructed and a Hilbert transformation was carried out. The velocity of the electromagnetic wave in concrete was considered to be equal to v = 12 cm/ns. In a next step horizontal and vertical data sets were superpositioned to create a resulting data set.

UT using A1220 probe. Measurements were carried out using the scanner system. Step width in both directions was 2 cm (2500 point measurements per square meter). Due to the space requirements of the vacuum attachment, not the whole surface could be reached by the transducers. A strip of 30 cm at both ends along the long axis of the specimen was left out.

UT using A1040 system. Measurements were taken in both polarization directions, parallel and perpendicular aligned to the long dimension of the specimen. Best results were obtained from the ones with parallel polarization. In perpendicular polarization, the wide aperture limits the area where all points have the same amount of measurements. Only a small volume can therefore be reconstructed in this configuration.

Figure 4 shows C-scans from all tested methods at 5 and 20 cm depth. Main observations follow:

- GPR. The results at a depth of 5 cm where steel rods connect the liners clearly show how resolution improves with frequency of radar waves. Also the Nelson studs can be identified; in the 2 GHz image even the heads of the studs can be clearly seen.
- GPR. The embedded void at 20 ± 2 cm depth on the left side at x = 25 cm can clearly be identified in all three measurements. This void (labelled void 4 in the drawings) also contains an undocumented steel bar perpendicular to the tie rods.
- UT 1220 probe. At a depth of 5 cm, in the place of the first tie rods, all of them are clearly identified. In addition, the Nelson studs are also visible with high contrast.
- UT 1220 probe. At depth 20 cm, the tie rods and the Nelson studs are localized. There are two additional reflections at position (25 cm, 40 cm, void 4) and (260 cm, 40 cm, void 1).

These two corresponded to void 4 and in the case of void 1 to a non-documented bar shaped reflector. Void 4 is highly reflectable and only partially visible, because it is at the edge of the scan area. The bar shaped reflector (void 1) is non-metallic, because it is not detected by radar.

- UT A1040 probe. The corresponding C-scan image shows the tie rods of the second layer along with void 1. Also an indication of void 4 is visible, although this void is located higher and therefore out of focus. The corresponding image confirms the nature of void 4 as air filled. UT cannot see the bar because it is inside of the air filled void 4.
- The void number 4 (at 20cm depth) is highly reflective for both, radar and ultrasound. Also, the GPR signals indicate the presence of a steel rod inside the defect. This is also confirmed by the phase analysis of the A1040 data.
- The phase evaluation of the ultrasonic signal helps to qualify the interface at which the ultrasound has been reflected: at steel a positive phase shift is observed, at air (or an acoustic soft material) the phase shift is positive. In the phase evaluation of the C-scan at depth 20, void 4 is obviously air filled. The rod shaped void 1 is indicated as acoustic hard material, but it should be non-metallic, because GPR does not see this void.

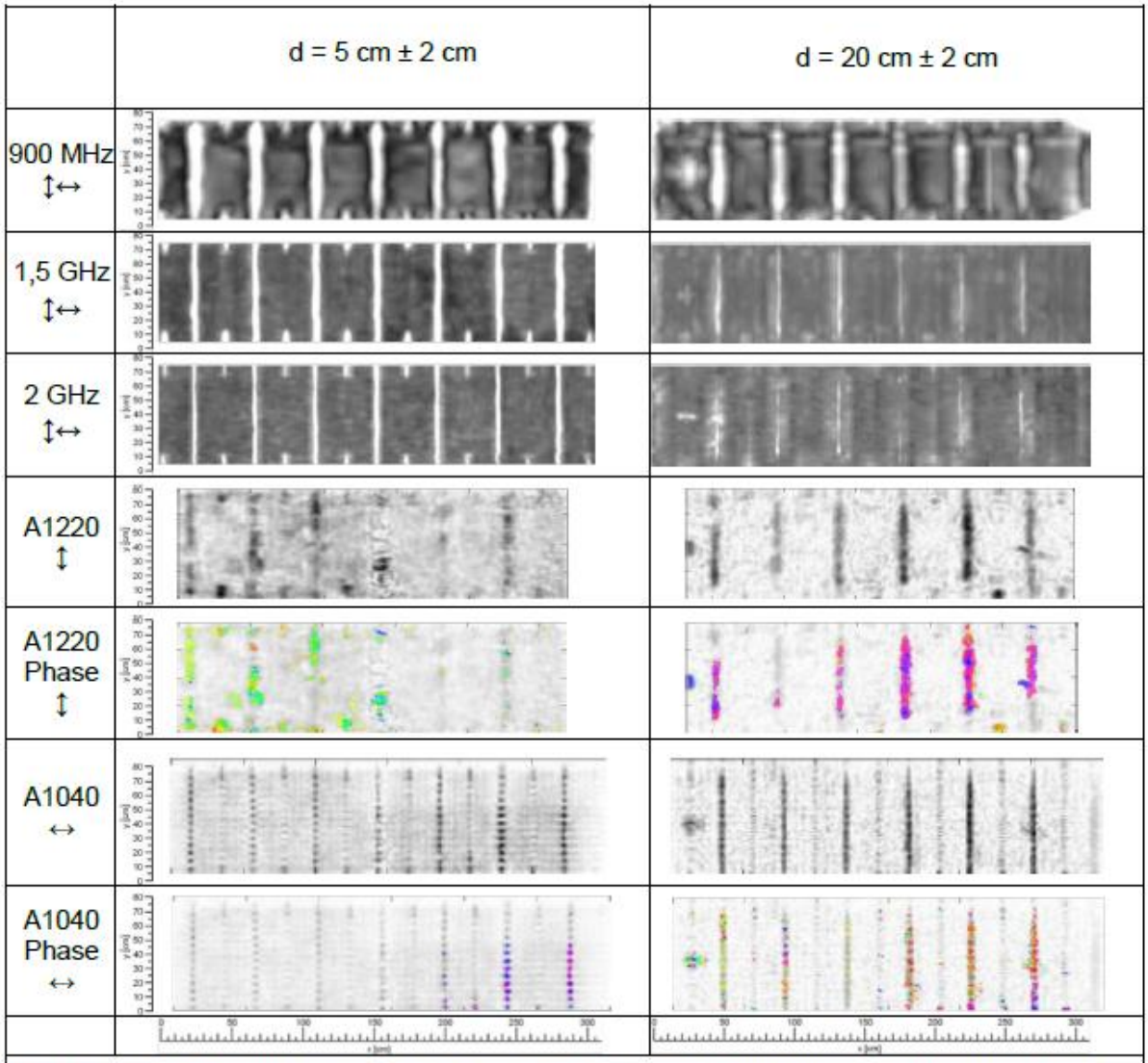

Figure 4 Summary of multimethod experiments at the small mock-up from the concrete side (see text). Columns hold C-scans at same depth. Rows represent data from different instruments and methods. Arrows indicate polarization of electromagnetic waves (E-vector) and shearwaves, respectively. Phase coloring may be read relative to known steel reflection at the same depth.

Small mock-up – steel side

Both the A1220 and A1040 probes were used. The steel liner at the concrete significantly affects the ultrasonic measurements. The surface waves, reflected from the nearby edges of the steel plate, have a much higher intensity then any signal reflected from the inside of the concrete behind the liner.

- UT 1220. Surface reflections of tie rods and reflections of shear stud heads are visible. Neither the back wall nor the voids are detectable.
- UT 1040. The back wall is is likely partly shadowed by the void located within the measuring field. Thus, this void can be detected indirectly but without information about depth or exact location. In contrast, there are no tie rod or shear stud reflections visible.

Large Mock up - steel side

Several areas of the large mock-up were tested including one area as reference, where no intentional defects have been placed. Two of those areas are shown here.

Area 1

All measurements with the A1220 transducers were taken with a step width of 2,5 cm in both directions. Figure 5 shows an example of the results. The steel liner has a large influence on the tests. Most signals can be attributed to surface effects. There are also distinguished disc shaped features at the location of the Nelson studs or tie rods. Also the weld joint obviously affects the signal. The surface or steel related signals are so strong that any ultrasonic reflection signal from the concrete behind the liner is indistinguishable.

Neither the results of the measurements with the A1220 nor the A1040 show enough evidence of the embedded faults.

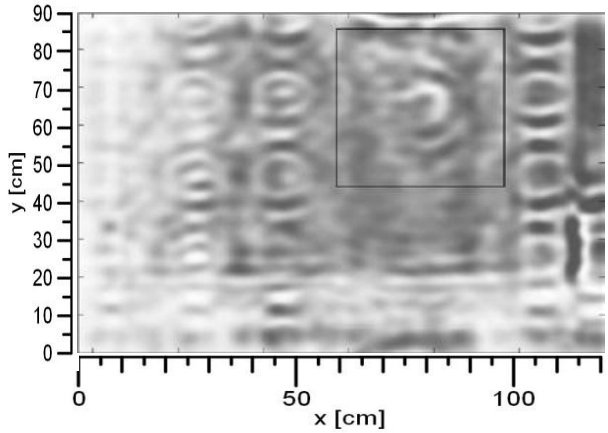

Figure 5 A1220 measurements of test area 1 on the large mock-up. Signals are due to surface reflections at nearby welds or edges. In addition, circular reflections from Nelson studs can be identified.

Area 2

Again, measurements were taken using the A1220 and A1040 instruments. At the bottom of this area, the steel surface follows an incline, the thickness of the specimen gets smaller. At this edge, an intentional defect has been placed. This defect is visible in the A1220 data analysis with both horizontal and vertical polarization. This is most likely due to the fact that the defect was placed directly on the steel, with no concrete in between.

All steel parts connected directly with the steel case are detectable due to surface wave reflection, and the same applies to boundary reflections. Both voids located close to the surface are detectable. The back wall is not detectable in any of the measuring fields, probably due to high attenuation and/or poor bonding conditions at steel-concrete interface and/or high loss of intensity at the steel-concrete interface.

CONCLUSIONS

The measurement results from the concrete side of the small mock-up define the present technical state of NDE of reinforced concrete. Defects up to a depth of 30 cm can be located together with the detailed identification of tie rods and Nelson studs. Beyond 30 cm, GPR data is difficult to interpret especially in a mock-up of such limited size.

Ultrasonic measurements were also successful to a depth of 30 cm. In B-scans the backside at a depth of 100 cm could be identified. The test from the steel side clearly showed that this type of construction is a big challenge for any ultrasonic testing attempt. This is caused by the mismatch of the acoustic properties of steel and concrete.

The tests were carried out using a scanner system with high repeatability and uniform testing conditions, assuring a data quality at the limit of present on-site conditions.

With the present technology, it seems highly unlikely that unknown defects embedded in concrete behind a steel liner can be identified with needed reliability.

Improvements to the tests should be possible through R&D efforts in the following areas:

- In order to increase the detectability of irregular shaped objects, bi-static measurements with a large aperture need to be tested. These tests would collect more echos than just the reflection in the direction of the transmitter.
- Phase evaluation of ultrasonic signals needs to be investigated further. This additional identification of the nature of an interface which reflects ultrasound is very helpful. Usability needs to be improved.
- Mock-ups with a larger variety of defects with well known properties (shape, orientation, density, homogeneity) are needed for thorough research. Also, the mock-ups should have a size which is big enough that surface effects do not play any mayor role.
- The effect of delamination between a liner and concrete needs detailed research.
- Software for the analysis of ultrasonic echo data needs further improvement. The analysis in this study was done using laboratory software in development, which is not available to the public.
- Data fusion may be helpful to improve reliability of tests.
- Tests were performed utilizing commercially available test equipment. The ultrasonic transducers were developed for concrete inspection. For steel liner covered concrete, new equipment must be developed in order to address this testing problem.

Acknowledgments

The cooperation by Dr. Klaus Mayer (Uni Kassel) in developing the software for ultrasonic data analysis is highly appreciated.

REFERENCES

[1] Lareau, J. P., Inspection of a Composite Steel-Concrete Shield Building for the AP1000TM Nuclear Power Plant Construction, 8th International Conference on NDE in Relation to Structural Integrity for Nuclear and Pressurised Components (2010), Berlin, Germany

[2] Wiggenhauser, H., Helmerich, R., Taffe, A., Krause, M., Kind, Th., Lai, W.-L., Scheel, H., Wilsch, G. and E. Niederleithinger, Nondestructive Testing in Civil Engineering, NDT Handbook, Nondestructive Testing, 6. Nondestructive Testing in Civil Engineering, Wiley-VCH Verlag GmbH & Co. KGaA, Weinheim (2011) 32 p.

[3] DGZfP B10 (2008). Leaflet about the Radar method for Non-Destructive Testing in Civil Engineering (in German: Merkblatt über das Radarverfahren zur zerstörungsfreien Prüfung im Bauwesen). www.dgzfp.de/Fachausschüsse/ZfPimBauwesen/Publikationen.aspx

[4] DGZfP B04 (1999). Leaflet about the Ultrasonic-Impulse Method for Non-Destructive Testing of mineral building materials and structural elements, (In German: Merkblatt für das Ultraschallimpuls-

Verfahren zur Zerstörungsfreien Prüfung mineralischer Baustoffe und Bauteile). www.dgzfp.de/Fachausschüsse/ZfPimBauwesen/Publikationen.aspx

[5] Kozlov, V.N., Samokrutov, A.A. and V.G. Shevaldykin, Ultrasonic Equipment for Evaluation of Concrete Structures Based on Transducers with Dry Point Contact, In: Al-Quadi, I. and G. Washer (eds.); Proceedings of the NDE Conference on Civil Engineering, 14.-18. August 2006, St. Louis, MO, USA, pp. 496-498 , 2006-08-14

[6] Schickert M., Krause M., Müller W. (2003) Ultrasonic Imaging of Concrete Elements Using Reconstruction by Synthetic Aperture Focusing Technique. Journal of Materials in Civil Engineering (JMCE), ASCE Vol. 15, 3, pp. 235-246.

[7] Krause, M., Milmann, B., Mielentz, F., Streicher, D., Redmer, B., Mayer, K., Langenberg, K.-J. and M. Schickert , Ultrasonic Imaging Methods for Investigation of Post-Tensioned Concrete Structures: A Study of Interfaces at Artificial Grouting Faults and its Verification, Journal of Nondestructive Evaluation 27 (2008) 1-3, pp. 67-82

[8] Mayer, K., Langenberg, K.-J., Krause, M., Milmann, B. and F. Mielentz, Characterization of Reflector Types by Phase-Sensitive Ultrasonic Data Processing and Imaging, Journal of Nondestructive Evaluation 1-3 (2008) 27, pp. 35-45

[9] Wiggenhauser H., Streicher D., Algernon D., Wöstmann J., Behrens M. (2007) Automated Application and Combination of Non-Destructive Echo Methods for the Investigation of Post-Tensioned Concrete Bridges. In: Long, A. and J. Bungey (eds.); Proceedings of Concrete Platform, Belfast, 19.-20.04.2007, Proc. and CD-ROM, pp. 261-270

CONCRETE – CANISTER (T8.2)

APPLICABILITY EVALUATION OF ULTRASONIC TESTING FOR LID WELDING OF STAINLESS STEEL CANISTER OF CONCRETE CASK

H. Shohji, M. Goto, K. Shirai

Central Research Institute of Electric Power Industry, Japan

ABSTRACT

Concrete cask storage for spent nuclear fuel (SNF) has been implemented worldwide. Japanese utilities plan to use concrete cask storage as one of the alternative methods [1].

For dry storage of SNF using concrete casks, a major function of the stainless steel canister housed within the concrete body is to serve as the final barrier for the encapsulation of spent fuel and radioactive materials. Canister lid welding, particularly with high reliability, is required because the lid welding is performed from outside of the lid and the canister contains SNF. Japanese nuclear safety regulations regarding SNF storage requires inspection of the canister lid weld by liquid penetrant testing. The regulations also require additional inspection by ultrasonic testing (UT). Yet, it is quite difficult to examine the integrity of the canister lid weld by UT.

This research reports on the evaluation of the applicability of UT of the lid weld integrity of stainless steel canisters storing SNF. In this study, typical full-scale canister lid models made of stainless steel which included the deliberate introduction of artificial flaws were fabricated to perform several UT techniques. It was determined that it is possible to detect cracks located in the weld root area in addition to performing UT on a lid weld at high temperature using the corresponding instruments.

INTRODUCTION

The Japan Atomic Energy Commission identified three potential nuclear fuel cycle policy options (reprocessing, reprocessing plus direct disposal, or direct disposal), which are considered according to the possible share of nuclear energy supply in the future. Regardless of the nuclear fuel cycle policy option chosen, the needs for interim storage of spent nuclear fuel (SNF) are ever-increasing. To realize the early utilization of economical and large capacity storage methodologies, the Japan Society of Mechanical Engineers (JSME) had already developed and issued a Code for Construction of SNF Facilities - Rules on Concrete Cask (**Figure 1**) - (JSME S FB1-2003) in 2003 [2]. On the other hand, the former competent authority (Nuclear and Industrial Safety Agency: NISA) issued safety requirements for concrete cask design in 2004 [3]. For confinement requirements, although continuous monitoring of the confinement of the canister system is not required, two key regulatory issues remain for maintaining an inert environment within the canister cavity and the welded enclosure as a confinement boundary, as follows.

* UT should be used to inspect the lid welding in addition to the liquid Penetrant Test (PT).
*Chloride induced Stress Corrosion Cracking (SCC) of the canister under a marine environment should be evaluated.

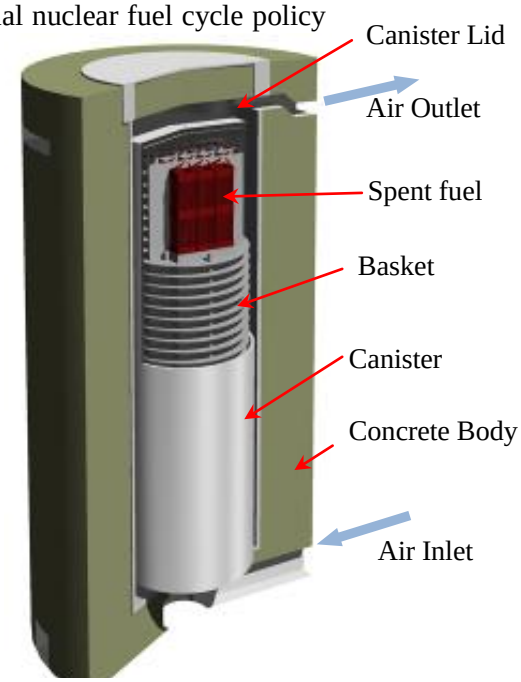

Figure 1 A schematic overview of the Concrete Cask

Of these two key issues, this study is focused on the evaluation of the applicability of UT of the lid weld of stainless steel canisters [4]. The inspection concept for the welded lid is written in the technical requirements of NISA (**Figure 2**) [5].

UT for the stainless steel canister suffers from the following problems.

(1) One-side welding and partial penetration welding.
- Geometrical echoes appear in the non-flawed area.

(2) Welded surface cannot be flushed, because grinding is not acceptable.
- The UT probe cannot access the weld crown area.

(3) The canister contains spent fuel, such that
- The radiation level of the area is high.
- The canister is at a high temperature owing to the decay of spent fuel.
- UT examination should be performed in minimum time.

In this study, several UT techniques were performed to measure the artificial flaws in the lid welding of a typical full-scale canister under both room temperature and high temperature conditions. From the measurement results, we discuss the applicability of UT as a method for investigating the integrity of the canister lid weld.

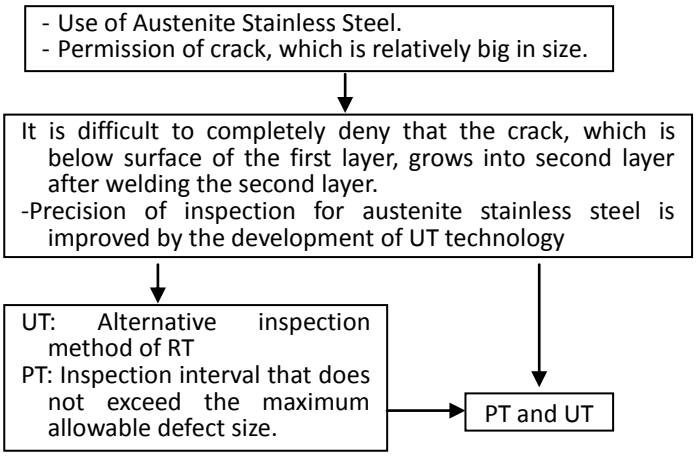

Figure 2 Inspection Concept of the welded lid

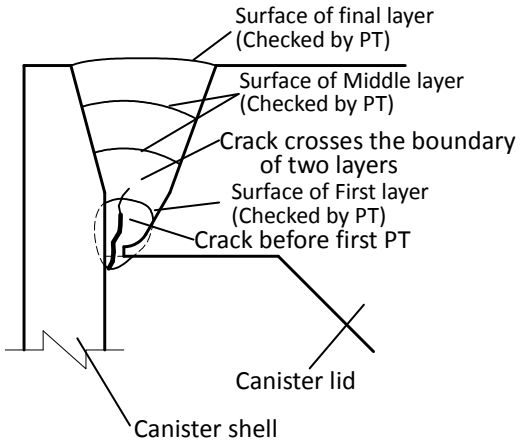

Figure 3 Schematic diagram of a crack on the stainless steel weld

TEST SPECIMEN

To confirm whether flaws in the welded lid can be measured by UT techniques, two weld mockups of full-scale canister lids were fabricated to include artificial flaws as shown in **Figure 4**. The two test specimens were made of stainless steel 304L, which is a typical canister material. The groove shapes of the lid depend on the canister design, and a typical groove shape was chosen. To simulate flaws, EDM (electro discharge machining) was used to introduce notches into one mockup, as shown in **Figure 4** at left, and faulty weld defects were introduced into the other, as shown in **Figure 4** at right. Square and round shaped EDM notches having depths of 2–6 mm were introduced in both the weld root and the weld surface (**Figure 4** at left). The faulty weld defects (**Figure 4** at right) are characterized as follows:

- Lack of fusion (fabricated by low heat input);
- Lack of fusion (fabricated by wrong weld metal);
- Porosity (poor back shield gas and poor preparation cleaning).

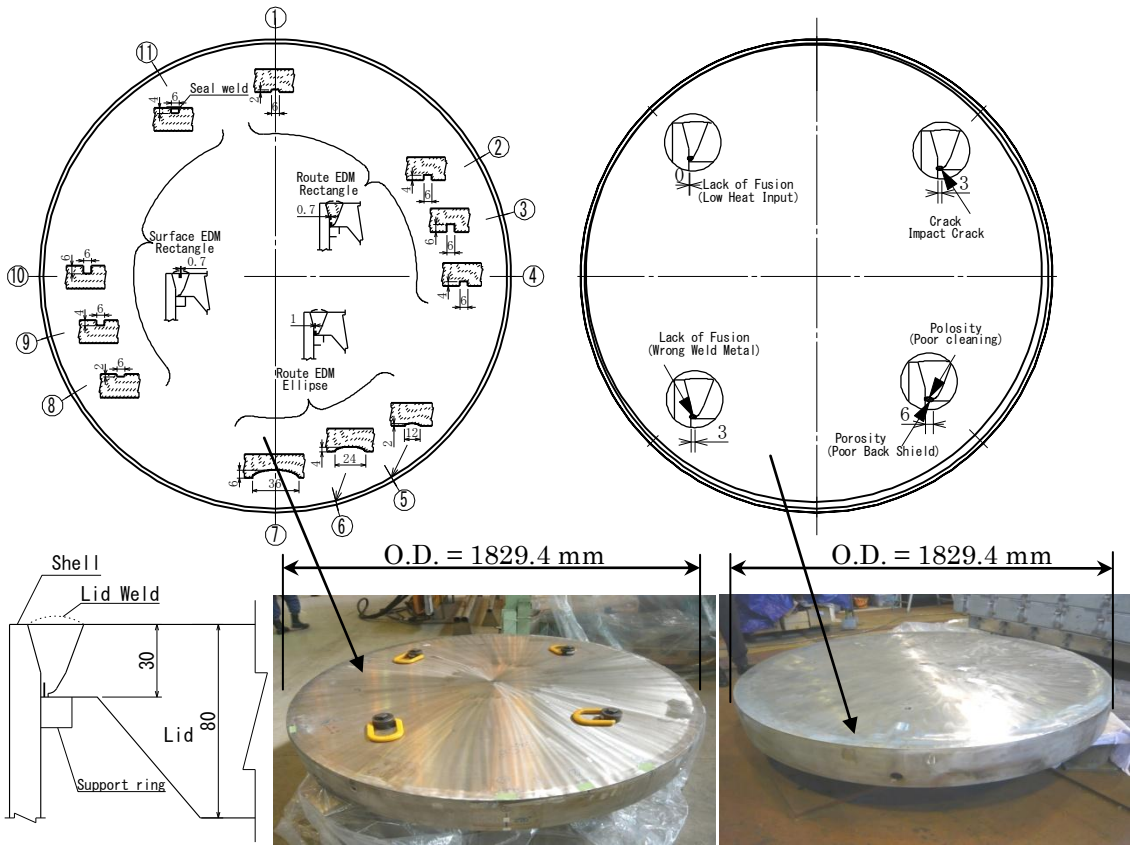

Figure 4 Canister Lid Mockups including EDM notch placements and welding flaw regions

EXAMINATION

UT techniques were applied to the mockups. Three types of UT techniques were chosen:

- Phased array
- Angled beam from the lid top
- Straight beam from the shell side

The straight and angled beam methods are conventionally implemented (**Figure 5**). For the angled beam method, the probe is placed on the lid surface. For the straight beam method, the probe is placed on the side surface of the canister. The phased array method is a relatively new method. Using the phased array method, two dimensional data is obtained and image processing is performed. The test parameters of the probe are the wave mode, frequency, and angle.

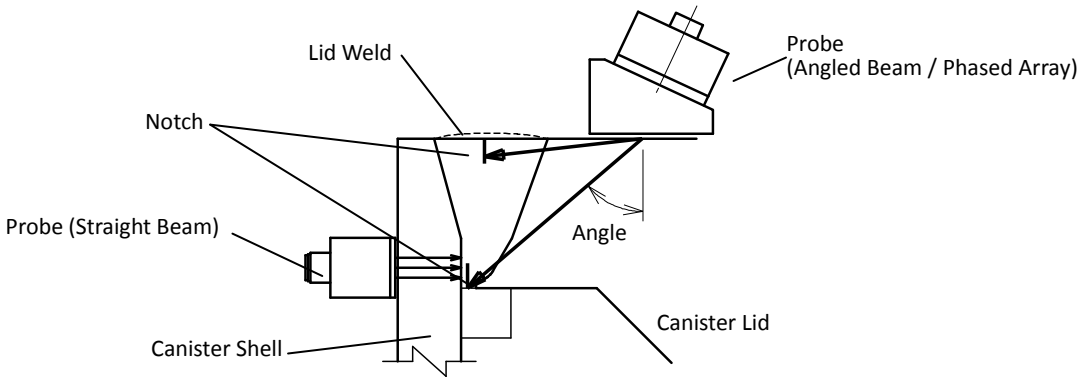

Figure 5 Layout of the EDM notches and the probes for UT measurement of the lid weld

Another examination parameter must be the temperature because, in practice, the canister surface is heated from the decay of spent nuclear fuel. We performed UT at room temperature and 200 °C (the expected maximum temperature of the canister surface, depending on canister design), respectively.

RESULTS

Examination-1, room temperature test

UT Examination was performed under the following conditions and labeled as Examination-1.

- Temperature: Room temperature;
- UT Technique: Phased array and Conventional UT;
- Scanning area: Lid Top;
- Data acquisition: Automated;

Table-1 lists the test results of Examination-1 for notch detection and **Figure 6** shows some typical results. As shown in Table-1, the technique having the highest detectability was the 45° angled beam technique using a 2 MHz share wave. Therefore, as shown in **Figure 7**, in the case of the 45° angled beam technique, the scanning area is limited by the weld crown. Under these conditions, the 60° share wave angled beam technique and share wave phased array techniques yielded good results. Both techniques showed better detectability in visual analysis even if the signal-to-noise ratio is low.

Figure 8 shows a sample of the weld defect detection results. The longitudinal wave phased array technique is good for detecting weld defects like porosity, and the share wave phased array technique is good for detecting weld defects like root cracks. Additionally, we attempted UT examination from the shell side (side wall). But, because the lid weld was only partial welded, it was difficult to discriminate between the echo of a good weld and the defect (**Figure 9**). Therefore, these results indicate that the best techniques are as follows:

- For weld root defects: share wave, 60° angled beam or phased array, from lid top.
- For porosity: longitudinal wave, 60° angled beam or phased array, from lid top.

Table-1 Results of the EDM detection test (from lid top)

UT Technique	Mode	Freq. (MHz)	Ref. Angle (°)	EDM	Shape	Rectangle at root area			Ellipse at root area			With weld Crown
					Depth	2 mm	4 mm	6 mm	2 mm	4 mm	6 mm	
					Length	6 mm	6 mm	6 mm	12 mm	24 mm	36 mm	
					Def. ID	1	2	3	5	6	7	
Phased Array	Shear	2	45			◎	◎	◎	◎	◎	◎	No
			60			◎	○	○	○	◎	◎	OK
			*1			◎	◎	◎	◎	◎	◎	OK
		5	45			○	○	○	◎	◎	◎	No
			60			○	○	○	○	○	◎	OK
			*1			○	○	○	◎	◎	◎	OK
	Longitudinal	2	45			△	△	○	△	△	○	No
			60			△	△	○	△	△	○	OK
			*1			△	△	○	△	△	○	OK
		5	45			△	△	△	△	△	◎	No
			60			△	△	△	△	△	○	OK
			*1			△	△	△	△	△	◎	OK
Conventional	Shear	2	45			◎	◎	◎	◎	◎	◎	OK
			60			△	○	◎	○	◎	◎	OK
		5	45			○	△	○	○	○	◎	OK
			60			△	△	△	△	△	○	OK

*1: Sector Scan ◎: Excellent (> DAC 100%) ○: Good (> DAC 20%) △: Poor (< DAC 20%) ×: Not detected

Table-2 Results of the EDM detection tests

UT Technique	Mode	Freq. (MHz)	Ref. Angle (°)	EDM	Shape	Rectangle at lid surface				With weld Crown	UT from
					Depth	2 mm	4 mm	6 mm	4 mm		
					Length	6 mm	6 mm	6 mm	6 mm		
					Def. ID	8	9	10	11 *2		
Phased Array	Shear	2	70			◎	◎	◎	◎	No	Lid Top
			80			◎	◎	◎	◎	No	Lid Top
			*1			◎	◎	◎	◎	No	Lid Top
		5	70			◎	◎	◎	◎	No	Lid Top
			80			◎	◎	◎	◎	No	Lid Top
			*1			◎	◎	◎	◎	No	Lid Top
			0			×	×	×	×	OK	Shell side
Conventional	Long	2	70			◎	◎	◎	◎	No	Lid Top

*1: Sector Scan *2: Seal weld ◎: Excellent (> DAC 100%) ○: Good (> DAC 20%) △: Poor (< DAC 20%) ×: Not detected

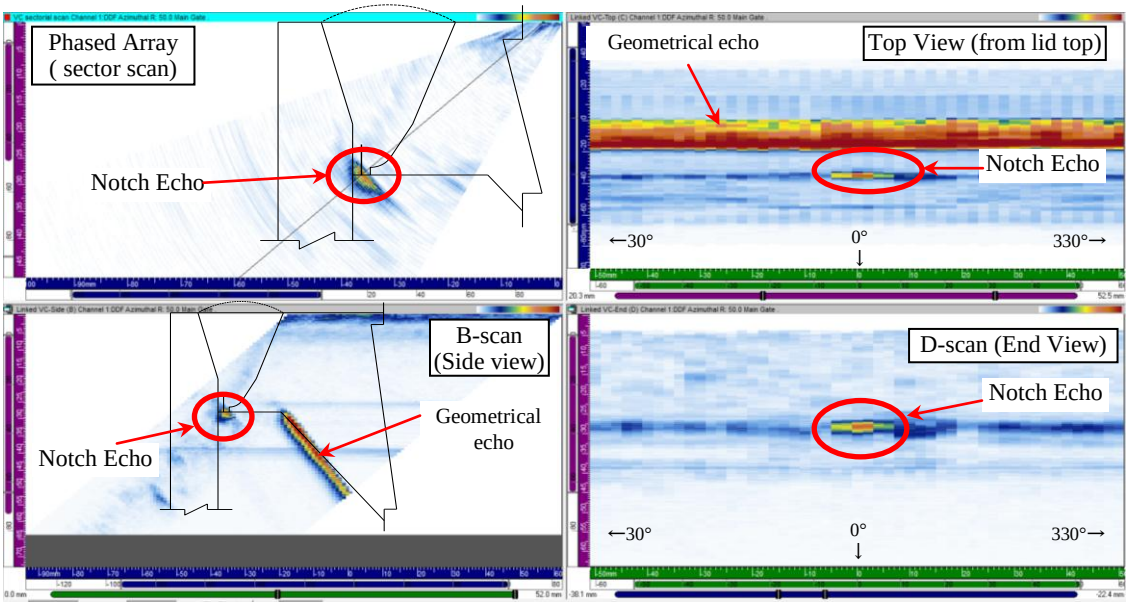

Figure 6 Typical UT examination results for a rectangular EDM notch
(depth = 2 mm and width = 6 mm)

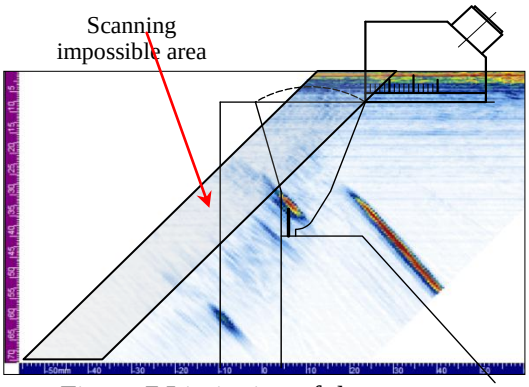

Figure 7 Limitation of the scan area by the weld crown

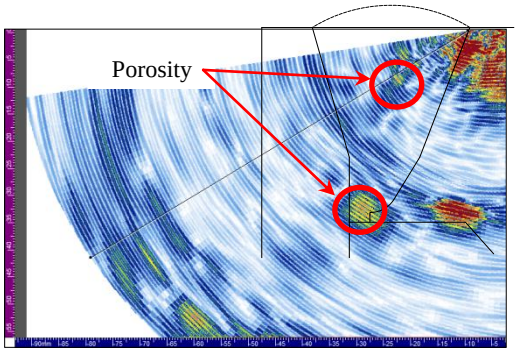

Figure 8 Typical results of the longitudinal wave

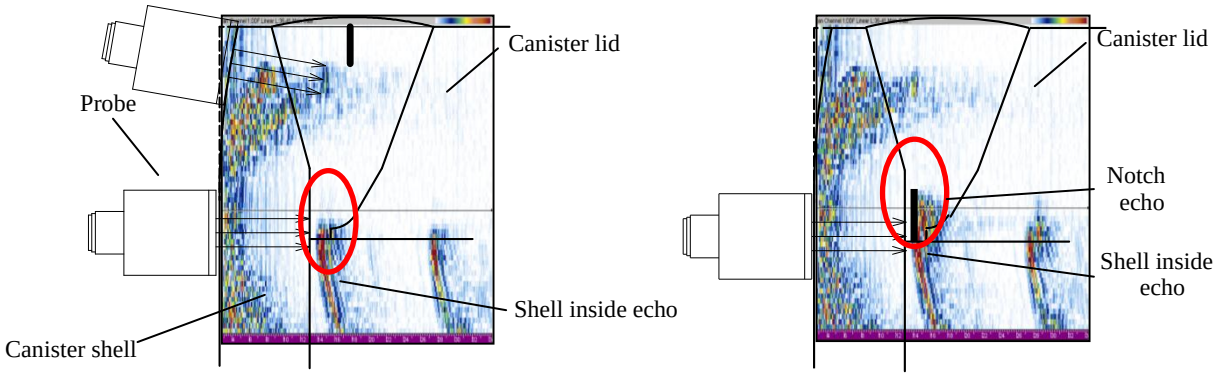

Figure 9 UT result from shell side

Examination-2, High Temperature test

When the lid weld is complete, it is necessary to finalize the inspection as soon as possible because the canister contains SNF. Owing to heat generated by the decay of the contained SNF, the canister temperature maintains a maximum temperature of approximately 200 °C [6]. As a result, UT examination was performed under the following conditions and labeled as Examination-2:

- Temperature: 200 °C;
- UT Technique: Conventional UT (high temperature probe with polyimide wedge);
- Scanning Area: Lid top;
- Data Acquisition: Automated;
- Couplant: Special couplant for high temperature.

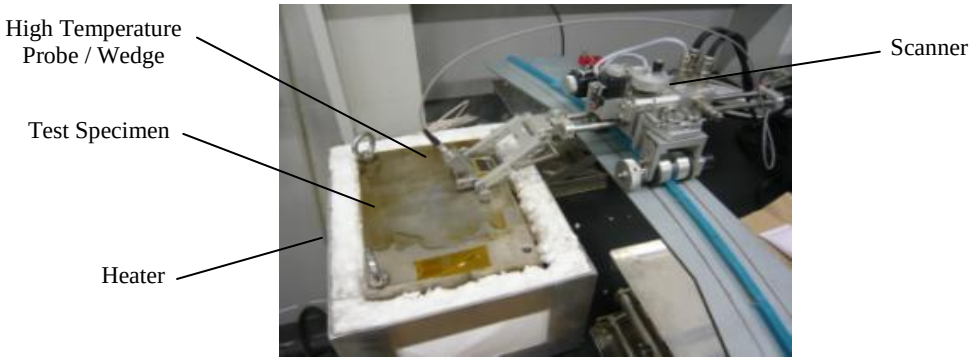

Figure 10 Overview of the high temperature UT Examination

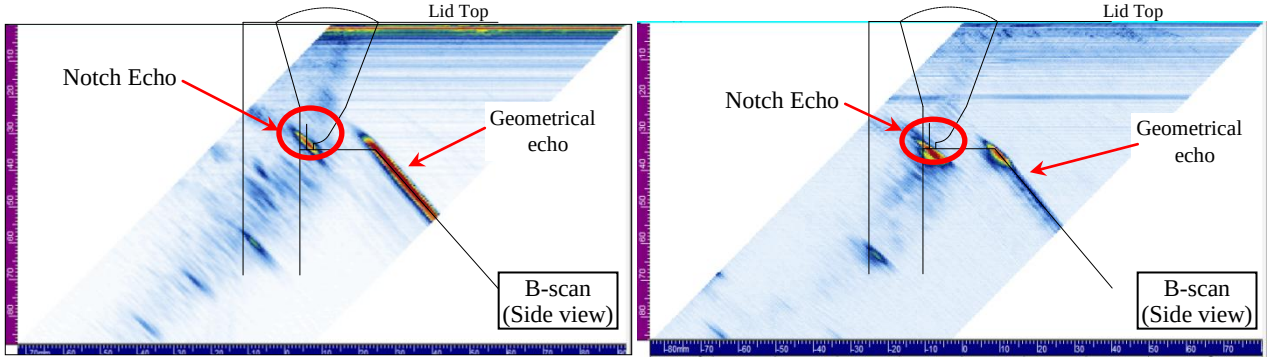

(a) Room temperature (Conventional angled beam probe)

(b) High temperature (200 deg. Celsius) (High temperature probe with polyimide wedge)

Figure 11 UT results under the high temperature condition.

UT examination was performed as shown in **Figure 10**. The test specimens were cut out and placed in the heating device, and UT examination was performed on the heated test specimen.

Figure 11 shows a sample of the results of the high temperature test.

There is no difference in the signal-to-noise ratio between the room temperature and high temperature test results, and this indicates the absence of any significant difference in detectability.

Additionally, the high temperature probe generally has a good radiation resistance, and it is good for limiting radiation damage to the UT system from the contained nuclear fuel.

CONCLUSION

The concrete cask storage system is one of the alternative methods for SNF storage. The safety requirements for concrete cask design indicate that UT should be used to inspect the stainless steel canister lid weld in addition to utilizing PT. However, it is difficult to examine the integrity of the canister lid weld by means of UT.

We performed UT examination trials to evaluate the applicability of UT for examination of stainless steel canister lid weld integrity. In this study, typical full-scale canister lid models made of stainless steel (SUS304L) containing artificial flaws were fabricated.

UT was performed under conditions of changing test parameters, such as probe, wave mode, wave frequency, angle, position of the probe, and specimen temperature, to detect deliberately introduced artificial notches and other flaws in the lid weld. A summary of the results are as follows.

- ✓ It is possible to detect cracks located in the weld root area.
- ✓ It is important to discriminate between geometrical and defect echoes. Image analysis is suitable for this purpose.
- ✓ It is possible to perform UT on a lid weld at high temperature using high temperature UT instruments.

ACKNOWLEDGEMENT

The authors wish to thank to Japanese utilities for their assistance.

REFERENCES

[1] Atomic Energy Commission of the Japanese Government, "Nuclear Fuel Cycle Policy Options," AEC Decisions (http://www.aec.go.jp), (2012).
[2] Japan Society of Mechanical Engineers, "Code for Construction of Spent Nuclear Fuel Storage Facilities‐Rule on Concrete Casks, Canister Transfer Machines and Canister Transport Casks for Spent Nuclear Fuel –," JSMES FB1-2003, (2003).
[3] Nuclear and Industrial Safety Agency of the Japanese Government, "Technical Requirements on Interim Spent Fuel Storage Facility Using Dry Concrete Cask," NISA-314c-06-01, (in Japanese), (2006).
[4] Goto M., Shohji H, Shirai K, "Study on Spent Fuel Storage by Concrete Cask for Practical Use - Applicability Evaluation of Ultrasonic Test with Imaging Analysis for Type 304L Stainless Steel Canister Lid Weldment- ," CRIEPI Report N11057 (2012).
[5] Ogawa K., Miura M., "Hydrogen Cracking in Duplex Stainless Steel Weldment," Quarterly journal of the Japan Welding Society Vol.8 No.4 p45-51 (1990).
[6] Wataru M., Shirai K., Saegusa T., "Study on Concrete Cask for Practical Use - Heat Removal Test under Normal Condition -," CRIEPI Report N04029 (2004).

DEVELOPMENT OF PHASED ARRAY ULTRASONIC TECHNIQUES FOR THE CAST IRON INSERT FOR THE SWEDISH SPENT NUCLEAR FUEL

U. Ronneteg, T. Grybäck, SKB, Sweden
R. Risberg, Barend van den Bos, Exova Materials Technology, Sweden
M. Bertovic, BAM, Germany

Abstract

The Swedish KBS-3 design for the disposal of spent nuclear fuel is based on encapsulation of the fuel in canisters consisting of a nodular cast iron insert surrounded by an outer 5 cm thick shield of copper. The insert is the vital component to withstand the mechanical loads in the repository while the copper shell serves as a corrosion barrier. To make sure that the canisters will fulfil the requirements, an extensive program for quality control is developed. In this program the use of non-destructive testing (NDT) is vital and for the insert the use of ultrasonic inspection, primarily phased array techniques, are dominant.

At the Canister Laboratory in Oskarshamn the inspection techniques are developed and tested in full-scale on manufactured components. For the cast iron insert several different inspection techniques are combined to achieve an extended coverage and detectability. The development includes optimisation of existing preliminary inspection techniques and definition of complementary new techniques. As a part of this work ultrasonic modelling with the CIVA software is used to determine suitable array designs and to tune the inspections with respect to choice of angles and focussing parameters. Furthermore, the techniques are applied in full-scale by construction of probe fixtures, definition of ultrasonic settings and scan parameters. Finally, the inspection procedures are developed from the human factor point of view which has led to significant improvements resulting in more user-friendly and thereby more reliable instructions.

1. INTRODUCTION

The Swedish Nuclear Fuel and Waste and Management Company (SKB) is responsible to take care of all radioactive waste produced in Sweden. This includes first of all of the waste produced by the nuclear power plants but also from the traditional industries, research and from the medical field (see figure 1). The spent nuclear fuel, which is the most critical portion of the waste, is stored for minimum 30 years in the central interim storage (Clab). The fuel is stored in water basins 30 metres below ground. The water works both as radiation shield and as coolant for the fuel. The operational waste is stored, surrounded by concrete, some tens of metres below ground in the final repository for operational waste (SFR). These two storages together with a specially build ship, used for transportation of the fuel, have been running for more than 20 years.

What still needs to be built is an encapsulation plant where the fuel will be encapsulated and a final repository for the spent nuclear fuel. During 20 years SKB has been working on finding a place for the final repository. To begin with, feasibility studies were conducted in eight areas spread out within Sweden. From year 2002 site investigations were conducted in the areas of Forsmark and Oskarshamn. Results from these site investigations, were carefully compared. This resulted in that SKB in the beginning of June 2009 could decide, based on the long-term safety, to choose Forsmark as the site for the final repository. The next step in the program was to submit an application for building of the encapsulation plant in connection with Clab in Oskarshamn and the final repository in Forsmark. The application was sent to the authorities in spring 2011. After approval from the authorities the construction work will start in 2019 and finally the deposition of canisters will start in 2027.

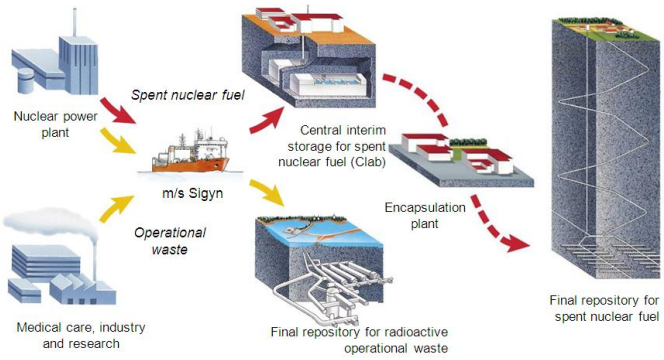

Figure 1. SKB's system for managing the radioactive waste in Sweden.

SKB is developing a method, called the KBS-3 method, for final disposal of the spent nuclear fuel. The method is based on three protective barriers, see figure 2. The first barrier is the canister composed of a nodular cast iron insert surrounded by a copper shell. The impermeable copper canisters are then embedded in bentonite clay that serves as the second buffer and finally placed in the third barrier, the crystalline basement rock at a depth of about 500 metres. Finally after the canisters have been disposed, the tunnels and rock caverns will be sealed.

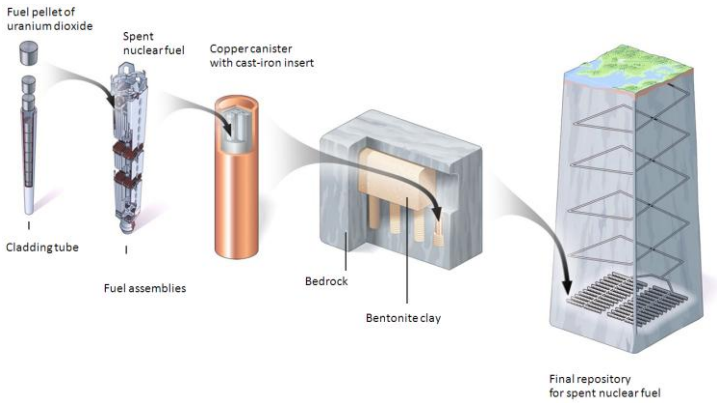

Figure 2. The KBS-3 system with the different barriers.

To be able to develop the techniques that will be used for building the deep repository and deposit the canisters as well as to make research on the properties of the bed-rock, SKB has built a full scale laboratory (Äspö hard rock laboratory) in Oskarshamn with tunnels down to 450 metres below ground. For developing the encapsulation technique, SKB has built the Canister Laboratory in Oskarshamn.

2. THE CANISTER LABORATORY

The Canister Laboratory (CL), see figure 3, in Oskarshamn was initially, in 1998, built to develop techniques for full size welding of the copper lid to the copper tube by electron beam welding, develop non-destructive testing (NDT) techniques for weld inspection and test the handling of the canister in a similar way as for the planned encapsulation plant. Over the years the activities at the laboratory have been expanded. It now works as the centre for encapsulation techniques for the canister. This means that the work also includes detailed construction and verifying calculations of the canister as well as development of both the manufacturing processes (together with external suppliers) and the NDT techniques for the canister components.

Figure 3. The Canister Laboratory.

In the Canister Laboratory full-scale inspection systems for the canister components and welds have been built up. This includes systems for digital radiography and ultrasonic testing of the friction stir welds as well as systems for ultrasonic testing of the canister components, i.e. the copper tube, lid and base as well as the cast iron insert. The manipulators used for ultrasonic inspections have been built in a flexible way, meaning they are not fixed to the inspection equipment to be used. This means that the systems can be used in combination with various inspection instruments, i.e. different ultrasonic instruments, eddy current instruments etc. To increase the reliability of the inspection of the large components (copper tube and cast iron insert), the reference blocks are integrated in the inspection system (see figure 4), using the same geometry for the reference blocks as for the real components.

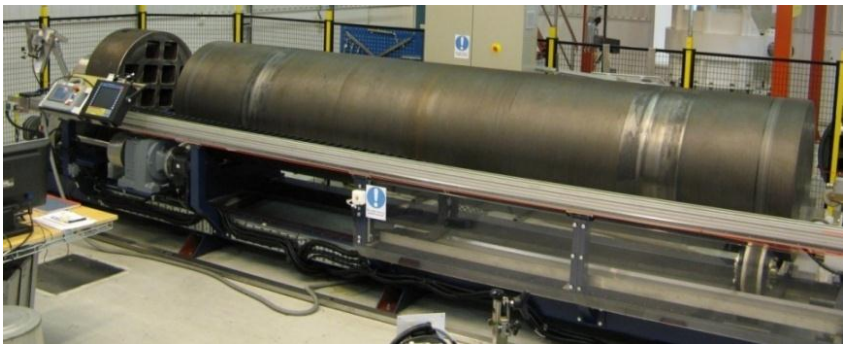

Figure 4. Manipulator for the cast iron insert with the reference block to the left.

3. THE CANISTER

The copper canisters that will encapsulate the spent nuclear fuel are nearly five metres long and over one metre in diameter (REF 1). The weight is between 25 and 27 tonnes including about 2 tons of spent nuclear fuel. The canister, see figure 5, is composed of a nodular cast iron insert surrounded by a five centimetre thick copper shell. The insert is manufactured in two different types, the PWR (pressure water reactor) type with four steel channels and the BWR (boiling water reactor) type with twelve steel channels. The main functions of the insert are to contain the fuel and withstand the mechanical loads in the repository. The copper shell, which serves as the corrosion barrier, consists of a lid and a base that are welded to the tube by means of friction stir welding (FSW).

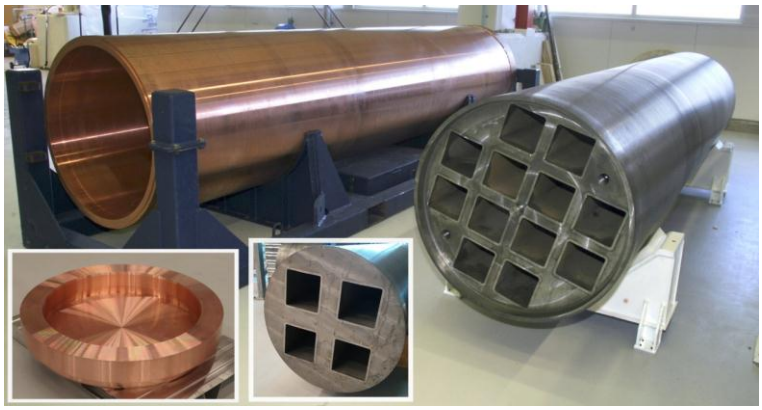

Figure 5. The canister components.

4. INSPECTION STRATEGY

A general strategy has been developed for the future inspection of inserts. This strategy rests on three major pillars:

- The use of mechanized inspections to get reliable and repeatable results.
- To overcome the problems of UT with its limited near surface sensitivity, inspections are to be performed at a specific pre-machined stage in the production. At this pre-machined stage, there is additional material that will be removed later in the process.
- After final machining the surface will be inspected using dedicated surface inspection techniques.

This strategy has been applied and verified during development of the NDT techniques used for inspection of the inserts from the trial manufacturing.

5. DEVELOPMENT OBJECTIVES

The development of NDT techniques for the canister is done with several objectives. First of all it shall result in techniques that shall be used to verify the canisters produced in the future. Secondly, it will form the base for projecting the future facilities where the final NDT will be done. Finally, and maybe at the moment, the most important, is to support the development of the casting process for the inserts with inspections of the presently manufactured trial components using inspection techniques that are reliable enough. Based on this, the inspection techniques have been tailored to detect a multitude of possibly occurring casting defects, as well as giving information on the general structure of the insert.

6. DEVELOPMENT OF NDT TECHNIQUES FOR THE CAST IRON INSERT

The development of NDT techniques at SKB follows a process described in figure 6. As shown, ultrasonic modelling is an integrated part of the development.

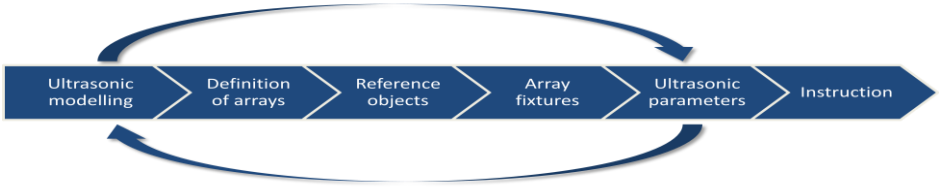

Figure 6. Principal development process

6.1 Inspection techniques

The purpose of the inspection as well as the insert geometry are the basis for development of the following three inspection techniques:

- Phased array pulse echo 70° incidence angle, shear waves for the outer volume.
- Phased array pulse echo 0° incidence angle for the outer volume.
- Phased array pulse echo and through transmission, sector scan, for the central sections.

The developed techniques used for inspection of the main volume of the insert, as well as the development steps to reach to those techniques, are described in the following sub-chapters.

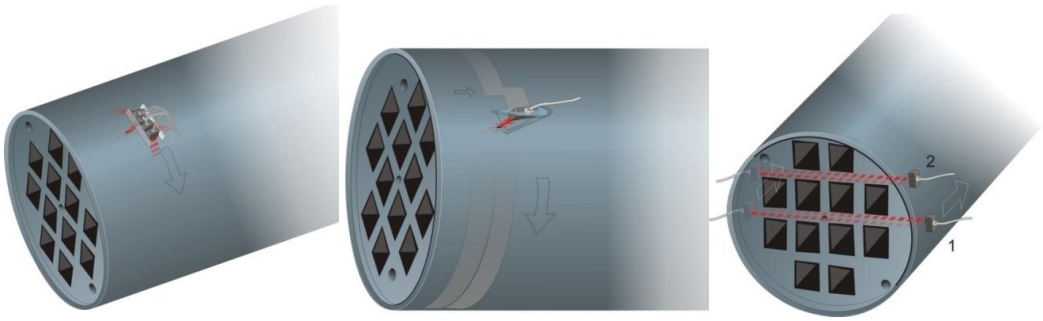

Figure 7. Angular ultrasonic inspection (left), local immersion normal ultrasonic inspection (middle) and ultrasonic transmission inspection (right) of a BWR-insert.

6.1.1 Angular inspection technique

The angular inspection technique covers the outer 45 mm of the insert and is performed by the use of four 32 elements linear curved contact arrays with mechanical focus in the passive direction. The arrays have a centre frequency of 1.7 MHz and a nominal shear wave angle of 70°. Two of the arrays are directed in opposite axial directions while the other two are directed in opposite circumferential directions. In order to get a narrow homogeneous sound beam along the whole inspection depth, two different ultrasonic channels are used. One covers the depth range 0-15 mm using an aperture of 22 elements focused at the depth of 7-10 mm and the other covers the depth range 15-45 mm using an aperture of 32 elements focused at the depth of 30 mm. A further description of the techniques is shown in the ultrasonic modelling section below.

6.1.2 Normal incidence technique

The normal inspection technique covers the depth range 5-210 mm of the insert and is performed by the use of one 128 elements linear array, with centre frequency of 3.5 MHz, aligned along the insert. In order to get a good coupling a local immersion technique with a water path of 65 mm is used. In order to get good sensitivity along the whole inspection depth, three different ultrasonic channels are used. One for the depth range 5-45 mm using an aperture of 18 elements focused at the depth of 12 mm, one for the depth range 45-110 mm using an aperture of 32 elements focused at the depth of 80 mm and the third one using an aperture of 40 elements focused at the depth of 160 mm.

6.1.3 Pulse echo and transmission technique

The inspection between the fuel channels in the insert is performed by the use of two 64 elements linear curved contact arrays with centre frequency of 2 MHz. The arrays are positioned on each side of the insert and aligned along the circumference of the insert. The pulse echo inspection is done from both sides using a sector scan within the angle range ±20°. The pulse echo inspection is done down to 480 mm depth meaning that each array covers half of the insert thickness while the transmission inspection is done in both directions using the arrays as both transmitters and receivers. A further description of the techniques is shown in the ultrasonic modelling section below.

6.2 Ultrasonic modelling

Ultrasonic modelling with the CIVA software has been used in order to determine suitable array designs and to tune the inspections with respect to choice of angles and focussing parameters.

6.2.1 Angular inspection technique

The goal with the ultrasonic modelling of the angular inspection technique was to define an inspection technique that gives a homogeneous and narrow sound field with high sensitivity along the whole inspection depth 0-45 mm at the desired inspection angle of 70°. In order to achieve this also in the passive direction the effect of mechanical focusing has been studied. These simulations (see figure 8) show that the mechanical focussing results in clearly better focus along the inspection depth. Based on the results, suitable probe parameters where defined and two pair of arrays were manufactured; one pair for inspection in axial directions and one pair for inspection in circumferential directions. The initial modelling showed that it not was possible to get a uniform sensitivity along the whole inspection range by using only one focus depth and therefore a setup with two ultrasonic channels with different focusing parameters were created. In order to test the sensitivity both simulations and inspection of an insert segment with side drilled holes at different depths have been performed. The results (see figure 9) show that all five holes are clearly seen with a uniform sensitivity and that there is a good agreement between the simulations and the inspection results.

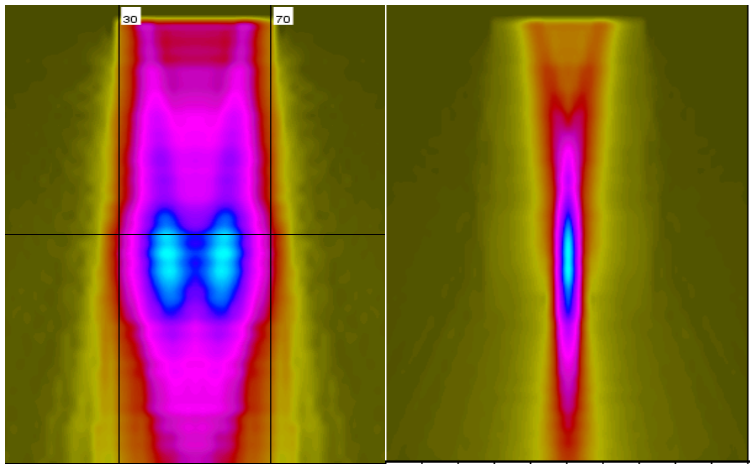

Figure 8. Ultrasonic sound field in passive direction without mechanical focusing (left) and with mechanical focusing (right).

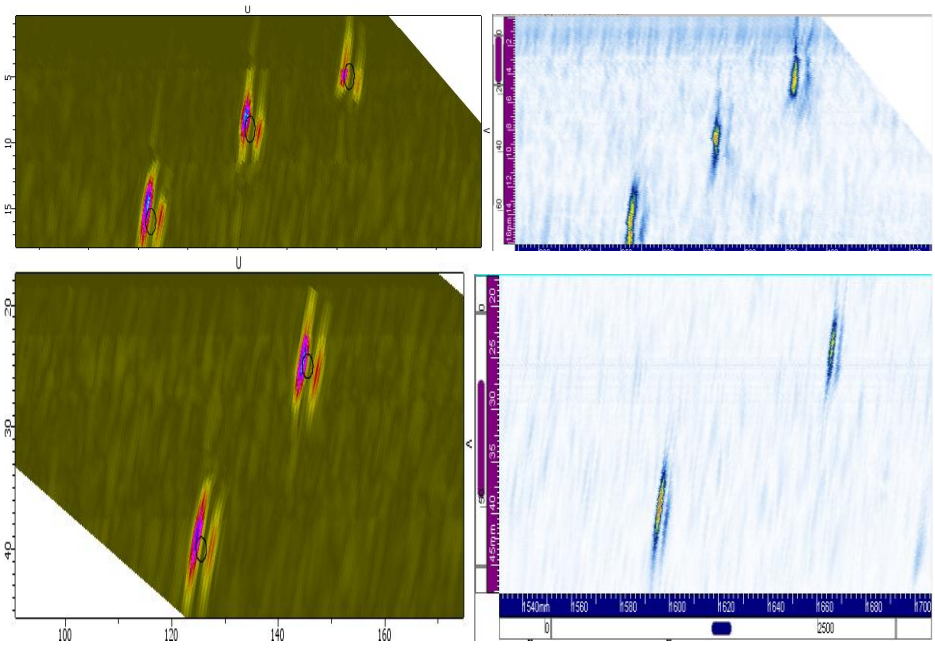

Figure 9. Comparison of simulations (left) and inspection results (right) on side drilled holes at various depths.

6.2.3 Pulse echo and transmission inspection technique

Ultrasonic simulations have been done to define suitable inspection parameters for the volume between the fuel channels for both the BWR and PWR insert: As the concept for the developed inspection techniques is similar for both insert types only the simulations for the PWR insert is presented. The basis for the simulations was to define techniques that covered the whole volume between the fuel channels. To achieve the possibility to detect both individual and clustered defects as well as a generally inhomogeneous material, a combined pulse echo and transmission setup was defined. The pulse echo inspections are done from both arrays for the depth range 170-480 mm by using sector scans within the angle range ±20° with 0.4° resolution. The accumulated ultrasonic beams are shown in the left image in figure 10.

For the transmission inspection the ultrasonic modelling showed that the best way to achieve a well focused beam with limited beam spreading was to set a rather deep focus point. Based on this a sector scan sequence with a focus depth of 600 mm was created within the angle range ±3.15° with 0.25° resolution. In order to get optimal sensitivity each receiving aperture was programmed with the same incidence angle as the corresponding transmitting aperture (see figure 10).

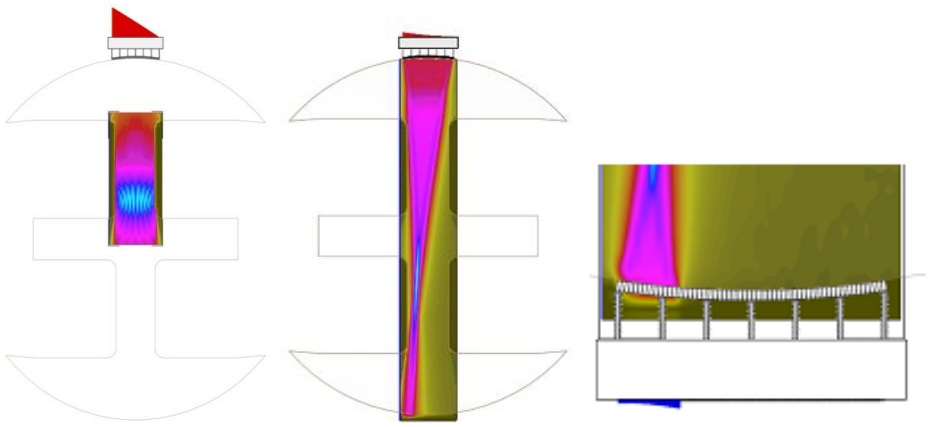

Figure 10. Modelling of the inspection between the fuel channels. The image to the left show the summarized field from the pulse echo channels. The middle image show one of the transmitted beam in the transmission while the image to the right shows the principles for the receiving aperture.

6.3 Practical aspects

In order to develop robust inspection techniques a number of practical aspects have been considered. Reference objects (see figure 11), with various artificial defects like side drilled holes and notches, were manufactured to verify the results from the ultrasonic modelling and to get the opportunity to achieve the same sensitivity along the whole inspection range for every inspection. The reference objects were manufactured from real insert segments giving the same inspection geometry and material structure as for the component.

As all inspection techniques use the advantage of mechanized inspection it has been of high importance to develop robust fixtures (see figure 12) dedicated for each technique. For the local immersion technique it has been important that the array position and the water column are constant. This is achieved using a rigid seal on the water tub adapted to the insert geometry. For the angular inspection it has been important that the relatively heavy contact arrays get good contact without too high friction.

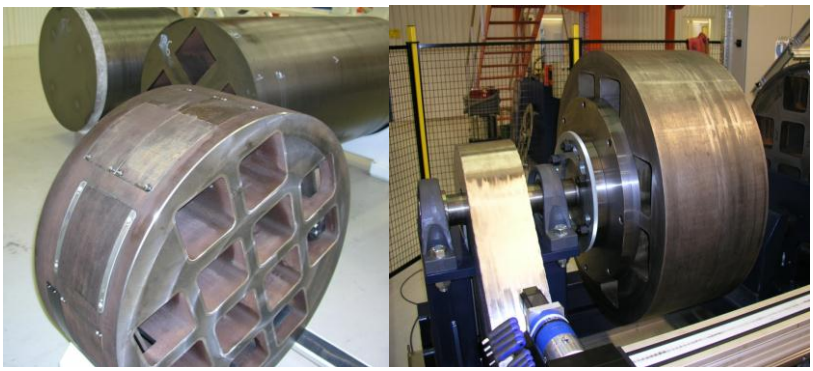

Figure 11. Reference objects used for sensitivity settings for ultrasonic inspection of the insert.

Figure 12. Fixture for the local immersion technique (left) and with the four 70° linear arrays (right).

6.4 Instructions for inspection

The developed inspection techniques are used as one tool in evaluation of each manufactured insert to provide input for further development of the manufacturing process. As the numbers of inserts manufactured are, and will be, limited during several years the importance of having good and reliable instructions has been noticed. Special attention has been given to describe the complex evaluation process of the collected data. Based on this a study have been conducted in order to develop reliable instructions. The study was performed both in a theoretical and experimental way.

The theoretical way was to study the PANI 3 study performed within the Health and Safety Executive, UK (REF 2). Based on this study some suggestions were taken into account; the instructions should be clearly structured and be written in active voice, only one action per step and the steps should be written in the order they are to be performed.

The experimental part was performed using the eye tracking (REF 3, REF 4) methodology during data evaluation. The experiments were conducted by four operators, whose task was to evaluate a set of data according to the inspection procedure available on the screen. During the experiments, the operators were observed to see how they followed the instruction and whether they made any mistakes. Afterwards, the reported indications were compared and, with the help of the recorded data, the causes for errors were identified. During the observations, additional errors were identified and analyzed in order to determine the possible consequences. After this first study the instruction was re-worked into another format where the PANI3 guidelines were taken into account and after this the experiments were repeated (a follow up study). The preliminary evaluation of the two experiments showed almost no improvement in the data evaluation performance. Further evaluation of the results showed that the reason for it was that the main effort was invested into changing the format of the instruction, rather than reviewing the tasks that have to be done (e.g. missing information). Based on the findings of these two studies the instruction was again optimized and reviewed both by several operators (reviewing by doing), as well as by several reviewers looking into the usability and structure of the written text. The ongoing work aims at the comparison of the initial instruction and the newest instruction version, in terms of instruction information (Is the instruction understandable? Does the instruction support the operator in decision making and problem solving?), and the instruction format (Does the change in formatting lead to a more efficient, i.e. faster, search for information and, in general, use of the instruction?).

7. CONCLUSIONS

Three ultrasonic phased array techniques have been developed for full-scale inspections of BWR- and PWR inserts. The development has included ultrasonic modelling, design and manufacturing of transducers, reference objects and fixtures as well as definition of ultrasonic parameters and composition of instructions. The inspection techniques have been used for inspection of three complete inserts. The results have been used as a tool in the development of the casting process. Some needs for optimisation have been identified, but in general the techniques can be seen to be “on the road to the final inspection techniques”. Of special interest is the concept of inspection instructions that has been developed that has the major goal to increase the reliability.

What still needs to be done is to complement the techniques with development of technique for inspection of the final machined surface and specific techniques required for the top and base of the insert.

8. REFERENCES

1) SKB (2010). Design, production and initial state of the canister, SKB Report TR-10-14.
2) McGrath, B. A. (2008). Programme for the Assessment of NDT in Industry. PANI 3. Prepared by Serco Assurance for the Health and Safety Executive. Research Report RR617.
3) Bertovic, M., Fahlbruch, B., Müller, C. Pitkänen, J., Ronneteg, U. (2012). Human Factors Approach to the Acquisition and Evaluation of NDT Data. Proceedings of the 18th WCNDT, 16-20 April 2012, Durban, South Africa.
4) Bertovic, M., Fahlbruch, B., & Müller, C. (2013). Human factors perspective on the reliability of NDT in nuclear applications. Materials Testing, 55(4), 243–253.

TEST BLOCK FOR INSPECTION TRIALS OF DISPOSAL CANISTER OF SPENT FUEL

R. Paussu, Fortum Power and Heat Oy, Finland
J. Pitkänen, Posiva Oy, Finland

ABSTRACT

Posiva Oy will take care of spent nuclear fuel disposal in Finland. Spent fuel of Loviisa NPP of Fortum Oyj and Olkiluoto plants of TVO Oyj will be disposed in the same disposal site in Olkiluoto. Disposal canister components are nodular cast iron insert providing strength and fracture toughness, and copper tube and lid providing corrosion protection. Sealing weld of copper tube and lid will be welded either with electron-beam welding (EBW) or friction stir welding (FSW). Posiva Oy has mainly investigated EB welds, but nowadays also friction stir welds.

Posiva Oy has realized wide sampling investigation of EB sealing weld flaws, detected by using different non-destructive examination (NDE) methods. Sampling has discovered the nature and sizes of certain flaw types and also given feedback for detection and sizing inaccuracy and capability of NDE methods. This sampling investigation has given information to continue development of NDE techniques, and gathered input data for future qualification action of NDE methods.

Several NDE methods are investigated and developed by Posiva Oy to ensure the quality of copper components and sealing weld. Knowledge of fabrication defects of copper components and sealing weld are the key points for NDE development and in simulation of flaw types, typical in copper material and sealing weld. Also the test blocks for the next development phase are described in the paper.

INTRODUCTION

The Finnish disposal solution (multibarrier disposal system KSB-3) is based on packing of spent nuclear fuel into nodular cast iron insert and copper over pack with welded lid. Canisters are located into deep underground disposal tunnels surrounded by bentonite clay in the bedrock at Olkiluoto, Figure 1. The internal canister of nodular cast iron, with steel canals around fuel assemblies and steel cover, will withstand the mechanical loads acting on the canister in the bedrock. The external copper canister tightly encloses the internal nodular cast iron canister, and protects it from the corrosive influence of groundwater, Figure 2.

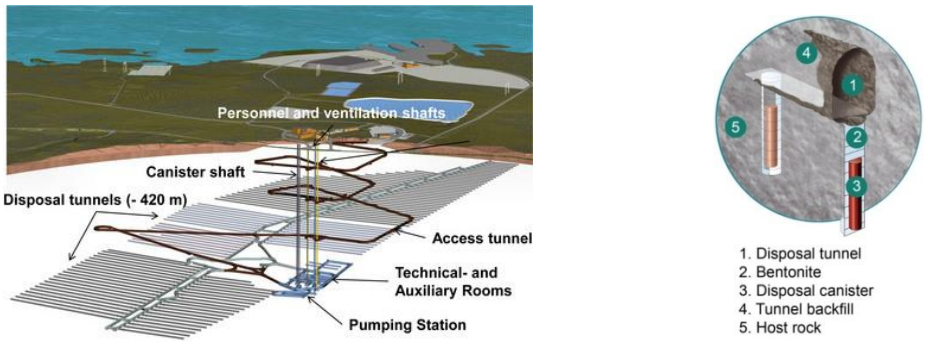

Figure 1 - Repository layout including Onkalo research area /
Copper canister in tunnel hole surrounded with bentonite clay blocks.

Figure 2 - Structures of spent fuel canister.

Posiva Oy is an expert organization responsible for the final disposal of spent nuclear fuel of its owners; Teollisuuden Voima Oyj (TVO) and Fortum Power and Heat Oy (Fortum Oyj). Posiva is responsible for research and development, construction, operation and eventual decommissioning and dismantling of the final disposal facility. Fortum Power and Heat Oy consults in layout design of encapsulation plant as nuclear engineering company, and in this case, helping Posiva to deliver and manufacture flaws into reference test blocks for inspection trials of copper components and welds (EBW and FSW). Experience gained in test block manufacturing together with Mekelex Oy for in-service inspection qualifications for Loviisa NPP has enabled also the manufacturing of challenging test blocks and flaws for Posiva.

Copper material itself is a challenge for NDE. Investigation of inspection methods was needed in order to optimize a proper manufacturing inspection of copper components and electron beam welding (EBW) of the lid to canister weld (friction stir welding, FSW will be later researched). Reference test blocks are used for calibration of inspection systems. Full size test blocks are used for simulation of fabrication flaws, demonstration and optimization of inspection capability of different inspection techniques for detection and sizing of different flaw types. Probability of detection (POD) blocks are fabricated for detection trials of certain flaw types. The basic ideas of reflector design of Posiva and fabrication methods are presented in the paper.

The designed and fabricated reference test blocks will be used for improving and justifying the capability of inspection techniques. The flaw population of test blocks is designed by Posiva to fulfill also the needs of qualification requirements. Many of test blocks are real size portion of component and whole welds. Heavy weight and large dimensions has to be considered before flaw fabrication. Flaw fabrication trials are needed to guarantee proper flaws for inspection trials. Challenges in flaw fabrication are described in the paper.

INVESTIGATIONS OF COPPER COMPONENTS AND EBW WELD

Posiva has investigated eddy current testing (ET), ultrasonic testing (UT) and visual testing (VT) methods for copper tube and copper lid. EB sealing weld of copper tube to lid is tested with radiographic testing (RT), ET, UT and VT methods. Investigation on inspection methods are going on for figuring out their capabilities for detection and sizing of typical flaws of copper components and welds. Development of inspection techniques was needed to improve detection and sizing capability.

Method specific inspection trials have been performed with pre-fabrication components and with test blocks and their flaws. The results of those trials and studies will be used as evidence documentation for qualification and preparing method specific POD curves. The final goal is to qualify the manufacturing inspection systems for disposal of spent nuclear fuel according to Finnish qualification rules based on Methodology and Recommended Practices of European network of inspection qualification (ENIQ). Special attention is put for mechanizing of the inspections by construction of proper manipulators also for trials considering the remote controlled implementation of final inspections of components and the weld inspections in radioactive environment in the encapsulation plant.

Posiva is collecting input data for qualification and defining the acceptance criteria for all components and sealing weld (EBW / FSW). Posiva will define the proper inspection strategy for all canister components and define the proper inspection methods and techniques and their combination for each inspection target. The final qualification will be in 2018.

The next issue after that is to design the devices and ways to control inspections to be performed during fabrication phase of components before installing nuclear fuel assemblies. The remote canister weld inspections in the encapsulation plant in radioactive environment will need special arrangements when designing inspection devices and inspection performance. The planned commissioning of encapsulation plant will start in 2019 and operation will be in 2020.

REFERENCE FLAWS

Component specific flaws will be generated during manufacturing of copper components depending on the manufacturing process. The main idea for development of test blocks is to simulate the manufacturing flaws. This approach has been realized in different cases for copper test blocks - copper tube, lid and weld.

One important issue is to select representative material for test blocks (typical attenuation, electrical and magnetic properties of material). Considering the flaws, for each NDT method has to be found a similarity for response of used flaw type. The intensity variations in radiography are giving different possibilities: geometrical changes, flaw generated in the welding process, beam divergence from possible presence of flaws. The acoustic response in ultrasonic inspection reacts to phase, amplitude or frequency changes. Also the geometry of material, focus point, active element size of probe, wave mode and material properties (etc.) has to be taken into account in UT. These effects have be considered in the design of reference flaws similarly like the defect types originated from the manufacturing. Electrical and magnetic properties of material shall be considered in ET as well as effect of flaw. Also the probe positions versus flaw positions in the material are important and they shall be followed in flaw fabrication.

Fabrication methods for flaws in copper are mechanical and electro discharge machining (EDM) due to material properties. Small size holes (side drilled holes, SDH and flat bottom holes, FBH), and specially deep holes, are hard to produce by drilling or milling in sizes under Ø 2 mm due to soft and adhesive material and lack of proper drills and milling cutter, and those tools will break and get blocked into hole easily. One solution was to use EDM machining with rotating tube electrodes. The accurate depth control is difficult due to large erode (wear) of electrode while EDM machining. Bending of long tube electrode will easily widen the hole mouth area while EDM machining, Figure 3.

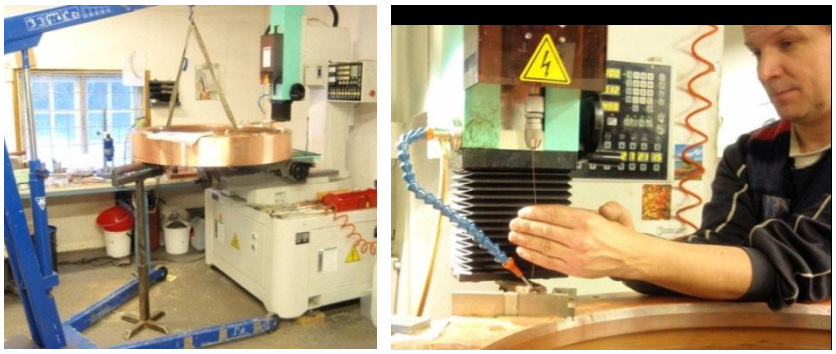

Figure 3 - Arrangements for producing small size holes into EBW weld using rotating tube electrodes.

EDM machining in pool requires copper-wolfram electrodes. The electrodes of this material will not erode (wear) so heavily during EDM machining, but the copper-wolfram electrodes must be fabricated from proper material piece with EDM wire cutting. This takes extra time, but it is also benefit, when you have to fabricate different groove shapes or defined shapes into test blocks like horse shoe shape flaws for EB sealing weld, Figure 4.

The EDM machining parameters have to be defined by trials beforehand in order to control the defined depth measures. One difficulty was producing narrow grooves close each other for calibration piece of VT camera inspection. Thin electrodes will easily bend due to feeding liquid, spooling the dirt out of grooves while sparkling. Calibration block for VT camera inspections was one challenging task to produce, Figure 5.

Figure 4 - Trials before fabrication of real flaws in test blocks.

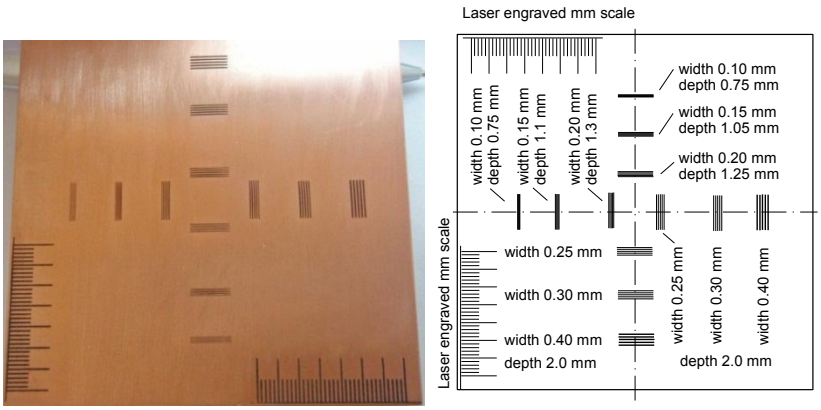

Figure 5 - Test piece for calibration and adjustment of camera image.

The basic problem in EDM and machining of real size component is the large weight and size not suitable to pool size or on work table (Figure 3). The solution is to place component on support or rotation wheels beside the EDM pool or machine (see Figure 7). Special arrangements, tools and careful handling of heavy and soft copper material is needed to avoid surface damages while lifting and moving of component parts.

TEST BLOCKS OF COPPER INGOT (2013)

Posiva will be inspect copper billet with VT and ET method reaching into depth of 20 mm. UT inspection is not possible due to high attenuation level of billet. First phase will be implemented on cast surface and 2nd phase after machining of billet piece. Test blocks with both surface conditions were fabricated in 2013. Test block with cast surface has axial and radial notch series and flat bottom hole lines of Ø 5 and Ø 10 mm with different depths, Figure 6.

Cast copper billet block will be machined for acceptance inspection. Test block includes axial and circumferential notch lines with two widths and depth series on outer circumference and on plane surface of the disc. The sizes of reflectors are the same as with ingot block, Figure 7. The inspection methods are the same as with ingot inspection (VT + ET surface areas). The heavy weight of blocks was a problem to be considered.

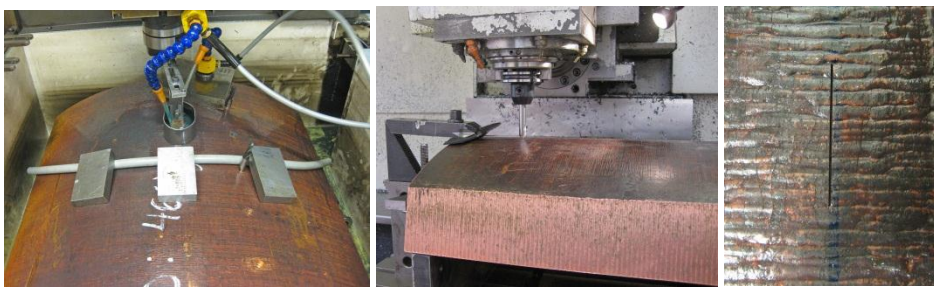

Figure 6 - Fabrication of flaws for test block of copper billet (466 kg).

Figure 7 - Fabrication of for billet disc - arrangements (1012 kg).

TEST BLOCKS OF COPPER TUBE (2008)

Test block (T42-5) was fabricated in 2007-2008 for reference block for UT and ET inspection of copper tubes. Test block includes axial and circular EDM surface notch and V-groove series with different depths and shapes in inner and outer and edge surfaces. Machined flat bottom holes and side drilled holes were machined also for calibration. Posiva has rented SKB's manipulator for copper tube inspections at Oskarshamn. Flange was fixed later into test block in Sweden for rotation of tube reference block in SKB manipulator, Figure 8. Totally new software was designed and tailored for ET inspections for Posiva to be used for tube, lid and weld inspections. Also the inspection techniques had to be improved to get more inspection coverage in depth direction.

Figure 8 - Reference block of copper tube (T42-5) / Calibration before inspection of copper tube.

UT inspection is also under investigation and new matrix probes will be used for UT inspection trials of copper tube, lid and sealing weld. First trials will be carried out in Finland using new test blocks designed and fabricated for matrix probes. Half ball reference block with flat bottom holes Ø 2.0 mm with different angle steps and wedge lines is fabricated in 2012 for basic calibration, Figure 9. New test blocks were fabricated for matrix probes: flat surface block, axial and circumferential curved blocks, all with half ball ends and FBH Ø 2 mm and four wedge lines with different angles of FBH Ø 3 mm on tube, Figures 10-12.

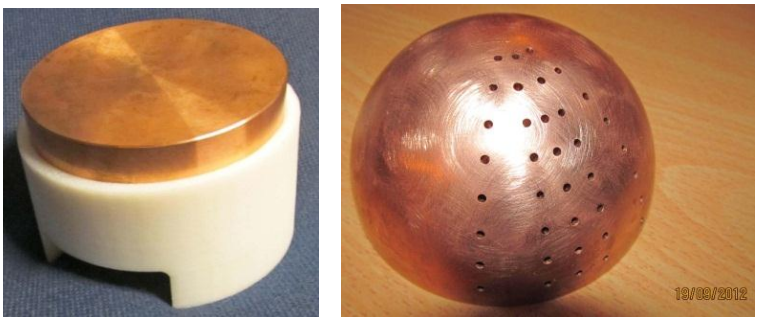

Figure 9 - Half ball reference block for check and calibration of matrix probes.

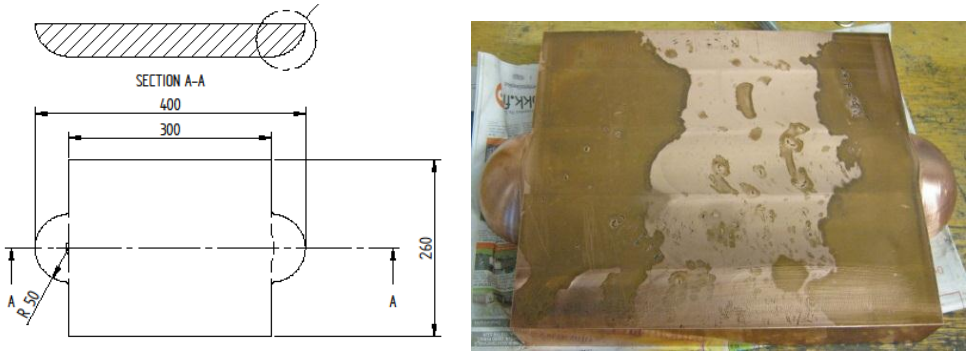

Figure 10 - Flat surface block

Figure 11 - Axial curved test block with flat bottom holes in axial wedge series and half ball ends.

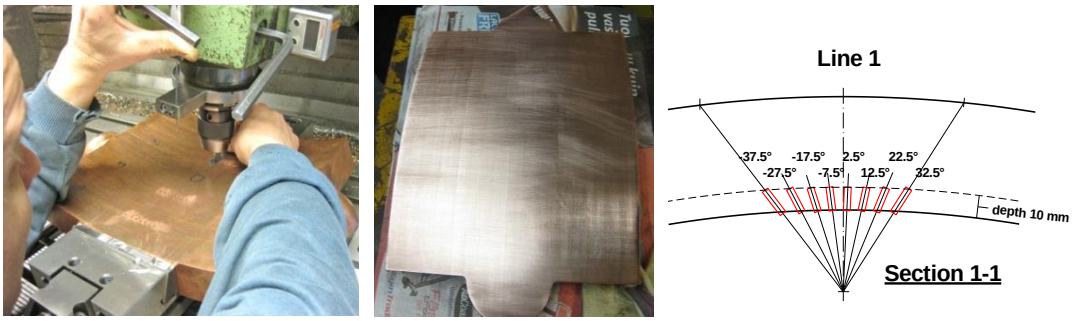

Figure 12 - Circ. curved test block with FBH Ø 3 mm in circular wedge series, FBH Ø 2 in half ball ends.

TEST BLOCKS OF COPPER LID (2008)

Test block (PL100) was fabricated in 2008 for reference block for UT and ET inspection of copper lid. Test block includes totally 116 flaws, 81 notches and 35 flat bottom holes in different flaw series in radial and circumferential direction. Machined flat bottom holes on cylinder surfaces had to be machined using a special angle head, Figure 13. The most challenging flaws to produce were the tilted notches, Figure 14. Lid inspection is carried out in Finland using rotation table manipulator of Posiva.

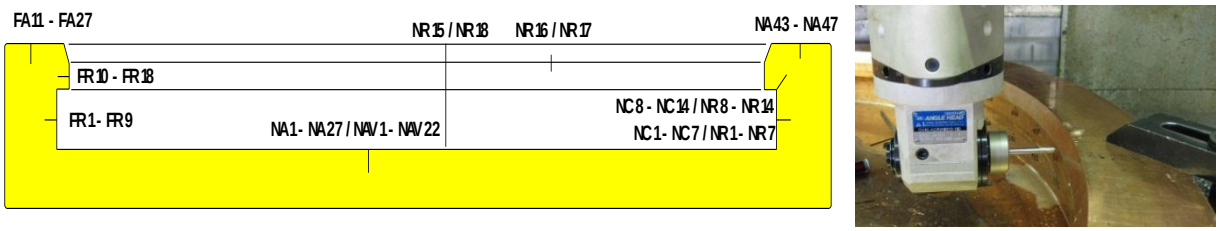

Figure 13 - Flaw set locations in copper lid (PL100)

Figure 14 - EDM machining of different notches and grooves.

CROSSCUTTING OF EB TEST WELDS

Four test welds were selected for investigation of detected manufacturing flaws to verify the real sizes, directions and types of flaws. This information is used for further improvement of inspection techniques and as collection of input data for qualification. The raw sampling of sections of sealing welds was carried out by sawing pieces out from weld. The samples were cut out with EDM wire cutting. The samples were inclined marked and sliced in depth direction into thin samples with EDM wire cutting. After marking and arranging the slices in order, the observed flaws were verified and documented.

Thin samples were melt into plastic and polished as micro section of welds and photographed. The flaws to be seen on sample surfaces were measured and sized. In order to keep samples as identified and thin sections in right thickness order, the sampling had to be designed carefully beforehand. Clear marking code system was the solution to keep all slices in order, Figure 15.

Figure 15 - Sawing of EB weld, EDM wire cutting of samples, marking and slicing.

POD BLOCK (2009) AND TEST BLOCKS OF COPPER WELD (2011)

POD block was designed for UT, ET and VT inspections to investigate detection capabilities of techniques to be used and later for qualification actions. Flaw population includes notch series using stable 2 mm depth and varying both length series and different notch width series. Triple notch population includes notch series using stable 2 mm depth and varying both length series and notch width series.

Hole series with stable 3 mm depth was fabricated with different diameters starting from 0.10 mm. In addition hole depth variation with three hole size series were fabricated with different depth series. The most challenging task was to fabricate 50 mm deep serial with different hole sizes, Figure 16.

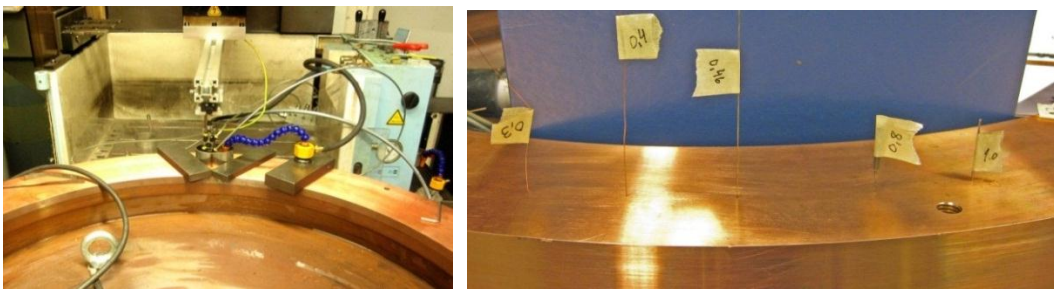

Figure 16 - POD weld block (Posiva code XK048) - fabrication of notches / ready small size holes

One sector of test weld block (Posiva code XK053) for UT and ET inspection includes welding flaws. The rest of weld circumference is full of small size cylindrical hole series. Fabrication of small diameter holes was a challenging job using EDM with rotating tube electrodes. Flaw population along the center line of weld includes 10 + 10 hole series of Ø 0.5 and 1.0 mm with different depths, Figure 17.

In addition to full size weld blocks, segment blocks are fabricated to include several more typical flaws for calibration and comparison of inspection methods.

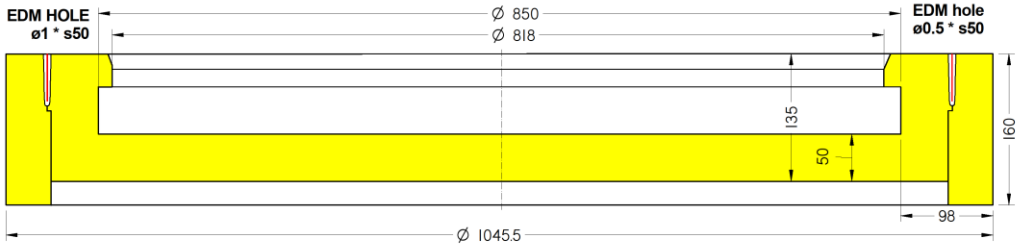

Figure 17 - Test weld block (XK053)

CONCLUSIONS

The external copper canister face challenging conditions in spent nuclear fuel disposal. The challenges for NDT in copper canisters are the material and wide variety of different flaws, which require special artificial flaw manufacturing techniques. The response of the artificial flaws must be applicable for several NDT techniques at the same time. The size of the full size mock-ups caused challenges for the flaw manufacturing. These challenges were expected and resolved during the fabrication.

Inspection of the steel structures and welds of cast iron insert will be challenging task to perform. Reference flaws and test blocks for inspection trials will be needed.

FUTURE JOBS FOR POSIVA

The EB weld has already been inspected with test blocks and POD blocks. The first sealing welds using friction stir welding (FSW) are now available for fabrication of test block and flaw population. The weld location of FSW locates on outer cylinder surface of copper tube and so the shape of lid is also different, Figure 18. Posiva has designed the flaw population for those welds to be fabricated in test block. The steel channel welds and cover of cast iron insert need new test blocks with flaws for inspection trials.

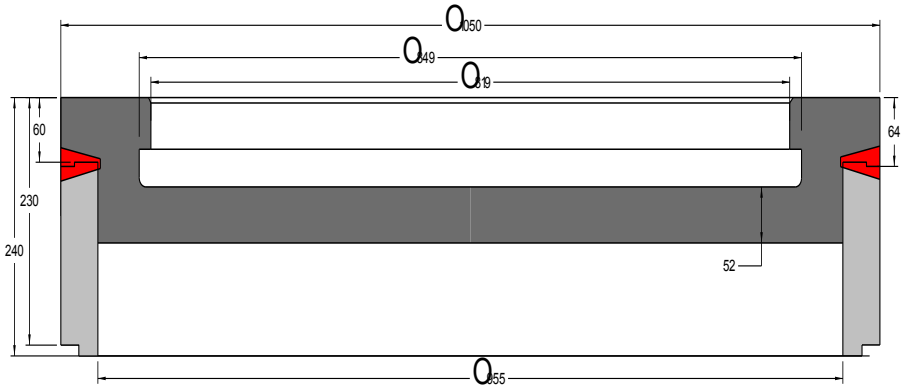

Figure 18 - Canister construction with FSW sealing weld.

INVESTIGATION OF DETECTABILITY OF CRACKS IN ANCHOR BOLTS FOR APPLICATION OF PHASED ARRAY ULTRASONIC TESTING

S. Lin, Hiroyuki Fukutomi
Central Research Institute of Electric Power Industry, JAPAN

ABSTRACT

It is necessary to assess the integrity of anchor bolts used in nuclear power plants after a massive earthquake to check for any cracks that may be present in the bolts. Reliable detection of fatigue cracks in anchor bolts in aging nuclear and thermal power plants is a major concern. Phased array ultrasonic testing (PAUT) is an effective technology for the detection of such cracks and determining their size. However, it is necessary to first determine if the cracks are actually detectable by PAUT when this technology is applied to anchor bolts. We prepared different types of bolt specimens with different fatigue cracks introduced. Linear array probes with frequencies of 5 and 10 MHz were used to test the bolt specimens. The test results show the following: (1) it is difficult to detect a crack that has a depth of less than 2 mm at 5 MHz, but 1-mm-deep cracks are detectable when a 10-MHz linear array probe is used; and (2) the concrete surrounding a bolt and the mark engraved on the bolt end scarcely affect the detectability of cracks.

KEYWORDS: Ultrasonic testing, Anchor bolts, Crack, Phased array technique, Detectability

INTRODUCTION

Massive earthquakes may result in cracks in anchor bolts that are used to fix components to foundations in nuclear power plants. Moreover, numerous fatigue cracks have previously been found in aging nuclear and thermal power plants [1-2]. To assess the integrity of anchor bolts, we need to reliably detect cracks and determine their size. Presently, hammering and visual testing are used to detect cracks in bolts. It is impossible for a visual test to detect underground defects. Meanwhile, the results of hammering testing are strongly influenced by environmental and human factors. However, in contrast with hammering and visual tests, ultrasonic tests offer an effective technique for detecting cracks in bolts [3]. Because the tip echo from a crack is overwhelmed by the reflection echo, it is difficult to determine the crack size by the conventional tip echo technique. Phased array ultrasonic testing (PAUT) is a promising candidate for determining crack size because it provides a measurement result corresponding to different propagation directions at the same time. However, before applying PAUT to anchor bolts, it is necessary to check the detectability of the cracks in the anchor bolts.

In this study, four types of bolt specimens with different size fatigue cracks were prepared to investigate the detectability of cracks. Three linear array probes were used, whose respective frequencies were 2 MHz, 5 MHz, and 10 MHz. Variation in the crack echo intensity due to the concrete surrounding the anchor bolts and the engraved marks on bolt ends were also studied.

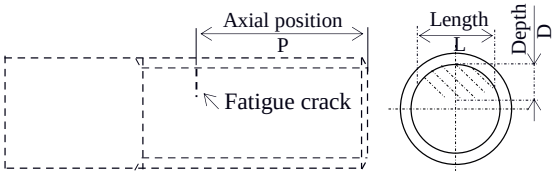

Figure 1 Definition of fatigue crack parameters

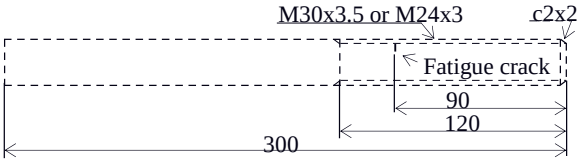

Figure 2 Geometry of bare specimen

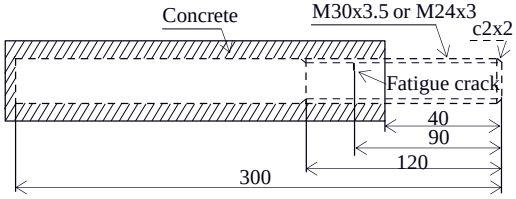

Figure 3 Concrete specimen

Figure 4 Engraved mark specimen

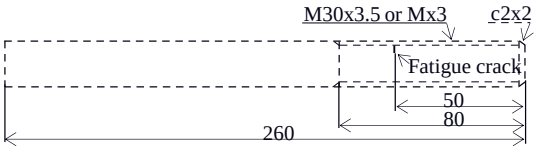

Figure 5 Short specimen

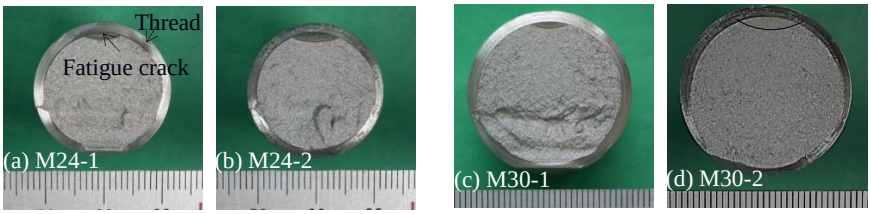

Figure 6 Fracture surface of fatigue crack

SPECIMEN and PAUT for anchor bolts

Specimens

For convenience, parameters related to the definition of a crack are shown in Figure 1. The geometry of bolt specimens made of SS400 carbon steel is shown in Figure 2. Bolt specimens were 300-mm long and their thread lengths were 120 mm. Taking the dimensions of a base plate and nut into consideration, the axial position of a crack was determined to be 90 mm. Fatigue cracks were introduced to M30 or M24 bolts with the bending fatigue test. The targeted crack depths were 1 mm, 2 mm, 4 mm, and 6 mm. Specimens shown in Figure 1 are called bare specimens.

To investigate how the concrete surrounding bolts influence the detectability of cracks in bolts, concrete specimens were prepared as shown in Figure 3. The length of the concrete segment was 260 mm so that the cracks could be embedded in the concrete.

Sometimes, identification numbers are engraved on bolt ends in manufacture processes. To clarify the influence of engraving on the detectability of cracks, concrete specimens with engravings of numbers on the bolt ends were prepared as shown in Figure 4. The depths of the engraved marks ranged from 0.35 mm to 0.83 mm.

With the reduction in axial position, a crack echo superimposed the thread echoes, which caused some difficulty in differentiating the crack echo from thread echoes. Figure 5 shows the geometry of short specimens whose axial positions were 50 mm after cutting a part of the thread off the bare specimens.

In our experiment, symbols such as M30-4 were introduced to differentiate bolt specimens from each other. M30-4 indicates a bolt with a diameter of 30 mm and a 4-mm-deep crack. Figure 6 shows fracture surfaces of fatigue cracks corresponding to M24-1, M24-2, M30-1, and M30-2 whose true depths were 1.03 mm, 1,70 mm, 1.35 mm, and 2.13 mm, respectively.

PAUT for anchor bolts

Before applying PAUT to bolt specimens, the detectability of cracks by longitudinal normal beam techniques was investigated. The frequency and diameter of the probe used here were 5 MHz and 10 mm, respectively. Figure 7 shows the measurement result for M30 where TP, TE, BW, FE, and DE represent the transmission pulse, thread echo, backwall echo, crack echo, and delayed echo, respectively. As shown in this figure, it is easy to detect a crack with a depth larger than 4 mm, but it is difficult for a crack with a depth smaller than 2 mm because its crack echo is overwhelmed by thread echoes. For M24, the result is the same.

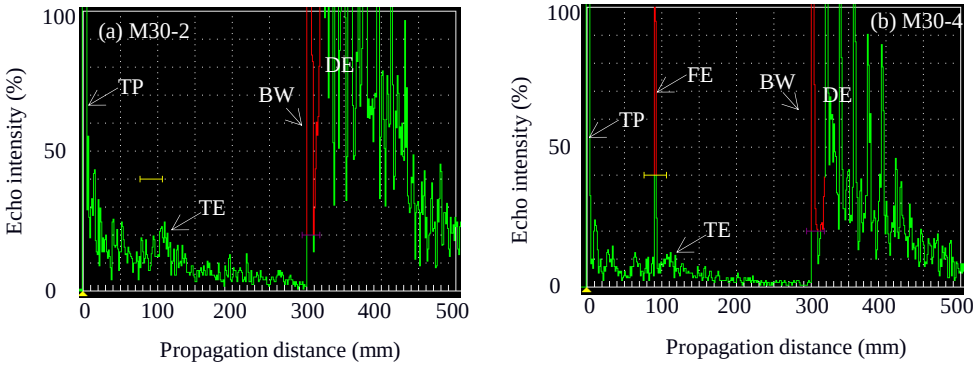

Figure 7 Snapshot of results by conventional UT

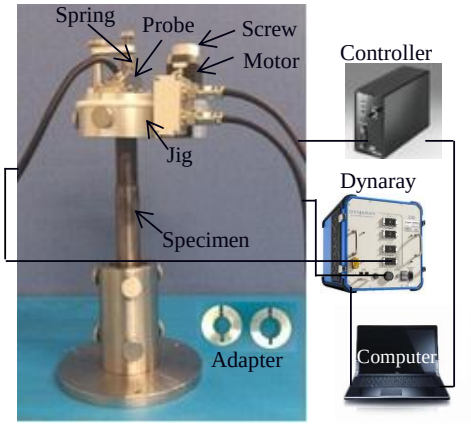

Figure 8 Measurement set-up

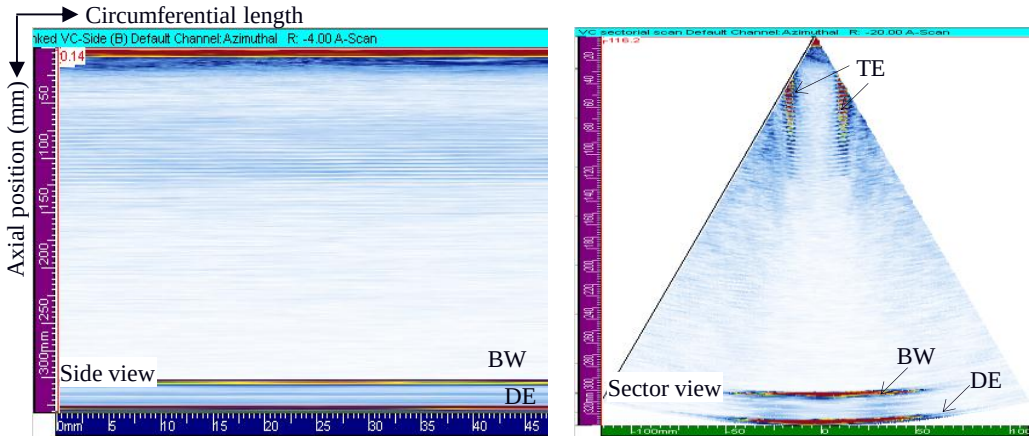

(a) 5MHz

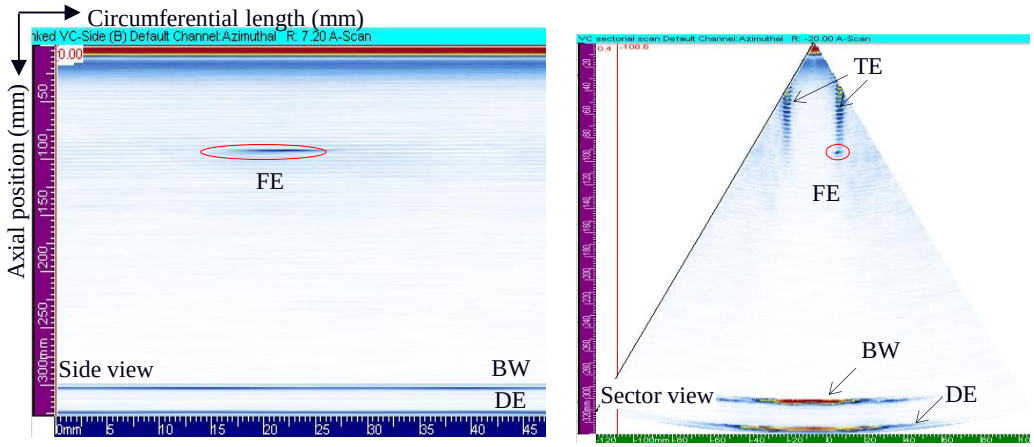

(b) 10MHz

Figure 9 Measurement result for bare specimen M30-1

Obviously, the detectability by the longitudinal beam techniques is not adequate for guaranteeing the integrity of anchor bolts. PAUT is a promising solution to this problem because it can potentially obtain information regarding various propagation directions and focusing positions in one measurement. Figure 8 shows the system used to detect cracks in bolt specimens, which consisted of a jig, a probe, a controller, a phased array instrument, and a computer. Different adapters are used for bolts with different diameters. In this study, two 64-ch probes were used that had respective frequencies of 5 MHz and 10 MHz. The active aperture was set to be 32 and the refraction angle was set to be in −20–20° range. The focusing depth for transmission was 60 mm, but it ranged from 10 to 150 mm for reception in the dynamic depth focusing mode.

MEASUREMENT RESULTS AND DISCUSSION

Bare specimen

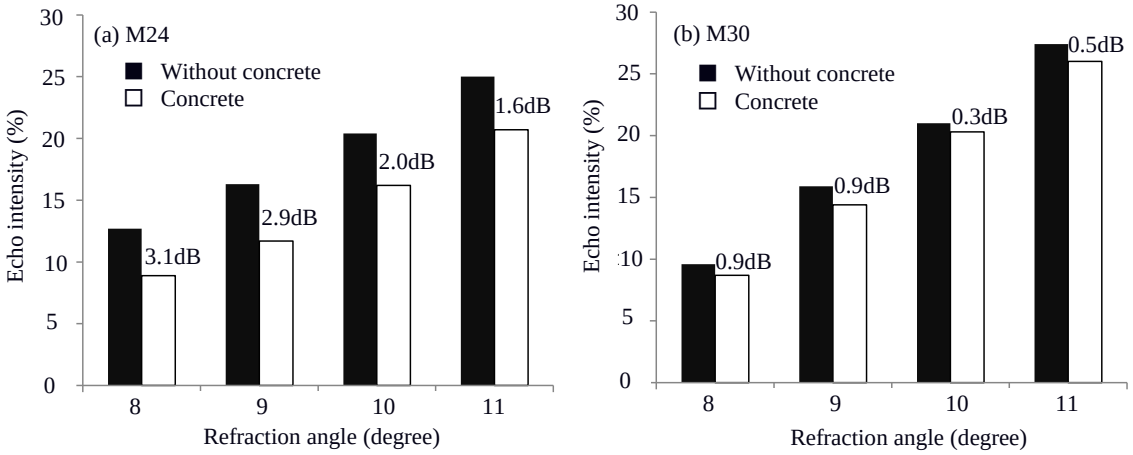

Figure 10 Comparison of echo intensity between before and after bolt embedded in concrete

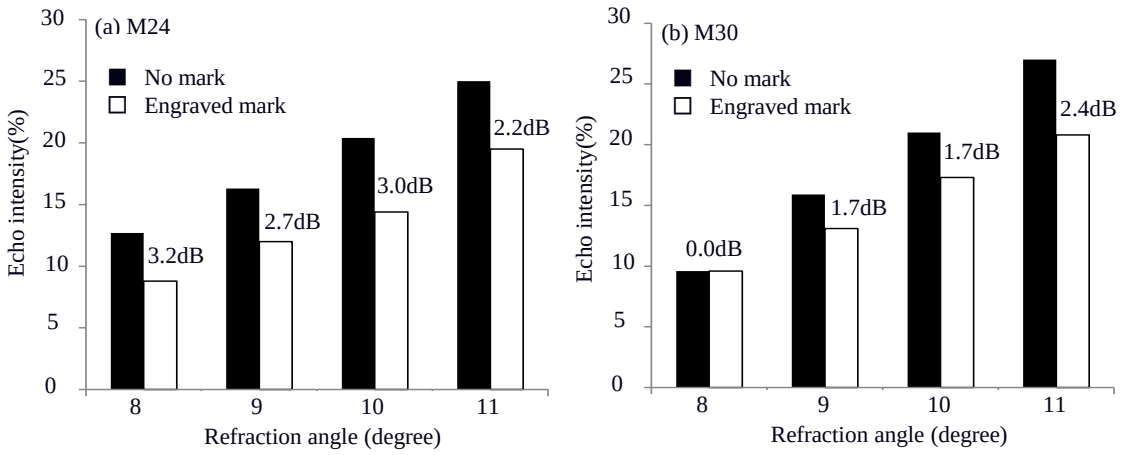

Figure 11 Comparison of echo intensity between before and after mark engraved on head end

Figure 9 shows the measurement results for the M30-1 bare specimen at 5 MHz and 10 MHz. At 5 MHz, the thread, backwall, and delayed echoes were observed, but no echo from the 1-mm-deep crack was detected. In contrast, the 1-mm-deep crack was easily detected at 10 MHz. It was also verified that the echo from a crack with a depth greater than 2 mm can be easily detected at 5 MHz and 10 MHz. The same results were obtained for the M24 sample. These results suggest that a probe with a frequency of at least 10 MHz should be used if we want to detect a crack with a depth smaller than 1 mm.

Concrete specimen

Measurements were performed for bare specimens and concrete specimens at 5 MHz under same conditions for both specimens. From the measurement results, we easily obtained the intensities of thread echoes corresponding to different refraction angles for the M30 and M24 bolts. The average thread echo intensities for the M24 and M30 bolts are shown in Figure 10. Compared to bare specimens, the thread echo intensities for concrete specimens are lower.

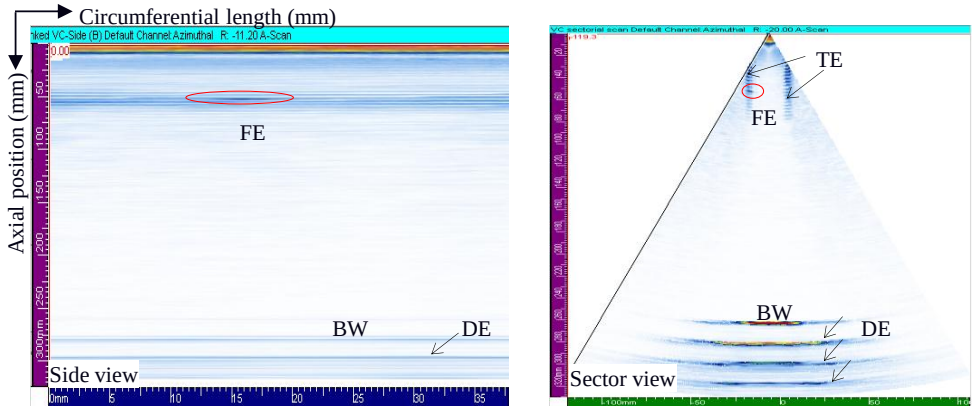

(a) M24-1

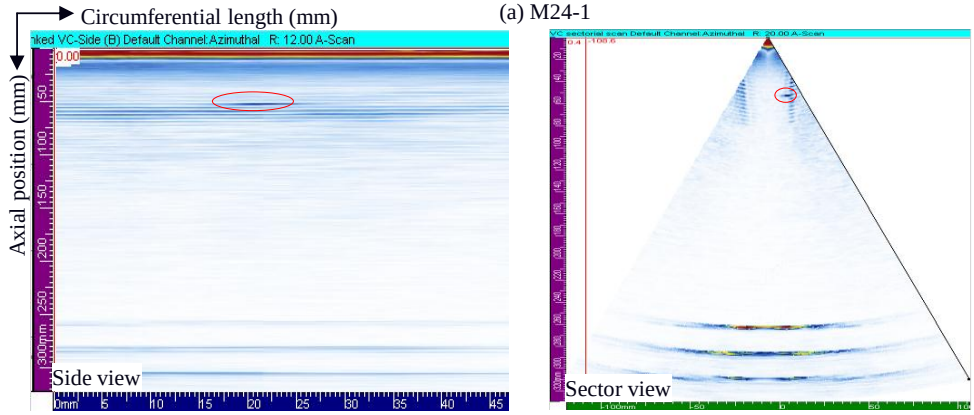

(b) M30-1

Figure 12 Measurement result for short bolt specimen with 1-mm-deep crack at the frequency of 10MHz

This decrease is dependent on the refraction angle and bolt diameter. The maximum decrease in the M24 bolts was 3.1 dB, and for the M30 bolts, it was 0.9 dB. From this result, we can also conclude that the crack echo intensities for concrete specimens are slightly lower than those of bare specimens.

However, it was confirmed that cracks in the M24-2 and M30-2 concrete specimens could easily be detected at 5 MHz and 10 MHz, and even 1-mm-deep cracks were detected at 10 MHz. This means that a small reduction in the intensity of a crack echo does not greatly affect the detectability of cracks in bolts.

Engraved mark specimen

The thread echo intensity comparison between engraved mark specimens and bare specimens is shown in Figure 10. On account of the engraved marks, the thread echo intensity of the M24 bolts was 2.2 dB to 3.2 dB lower compared to the bare bolts. For M30 bolts, the reduction ranged from 0.0 dB to 2.4 dB.

Measurements were performed for the engraved mark specimens with 5 and 10 MHz probes. Cracks with a depth of 2 mm were easily detected at 5 MHz and 10 MHz; specifically, at 5 MHz, the intensity of the 2-mm-deep crack echo was approximately 3 dB lower than that of the bare specimens. It was also verified that it is not difficult to detect 1-mm-deep cracks at 10 MHz.

Short specimen

Figure 12 illustrates measurement results corresponding to M30-1 at 10 MHz and results corresponding to M30-2 at 5 MHz for short specimens. As predicted, crack echoes are superimposed with thread echoes in the results. However, it is possible to differentiate a crack echo from thread echoes. Therefore, there is no issue with detecting a crack whose depth is larger than 1 mm if the axial position of the crack is between 50 mm to 90 mm.

CONCLUSIONS

Because the detectability of cracks must be determined before utilizing PAUT, the detectability of cracks in anchor bolts was investigated. Two linear phased array probes with respective frequencies of 5 MHz and 10 MHz were used to detect cracks in bare specimens, concrete specimens, engraved mark specimens, and short specimens. Measurement results show the following: (1) 1-mm-deep cracks are detectable at 10 MHz, but are undetectable at 5 MHz; (2) the concrete surrounding anchor bolts and the engraved number mark on bolt ends cause the intensity of crack echoes to decrease slightly, but they scarcely affect the detectability of cracks in anchor bolts; and (3) no difference was observed in detectability of cracks when the axial position varies from 50 mm to 90 mm.

ACKNOWLEDGEMENTS

Authors gratefully acknowledge Mr. Shimomura for his assistance in measuremnts.

REFERENCES

1) Yi-Bin Chen, Shen-Yu Lai, Ta-Kang Hsiung and Ting Chow, “Degradation and Failure of RPV Support Skirt Anchor Bolts at Taipower’s Kuosheng Nuclear Power Station,” 1st ICMST Conference 2012, 2012, pp.63-64.

2) Resolution of Generic Safety Issue: Issue 29: Bolting Degradation or Failure in Nuclear Power Plants (Rev.2) (NUREG-0933, Main Report with Supplements 1-34), http://www.nrc.gov/reading-rm/doc-collections/nuregs/staff/sr0933/sec3/029r2.html.

3) D. M. Suh and W. W. Kim, Journal of Nondestructive Evaluation, Vol. 14, No. 4, 1995, pp. 201-206.

DEFECT SIZING USING PA-ULTRASONIC TESTING AND ACCEPTANCE IN COPPER LIDS, TUBES AND WELDS FOR DISPOSAL CANISTER

J. Pitkänen, Posiva Oy, Finland
A. Lipponen, H. Raiko, D. Braddock, VTT, Finland
G. Brekow, BAM, Germany

ABSTRACT

Posiva Oy will take care of spent nuclear fuel disposal canisters. Spent fuel of Loviisa NPP of Fortum Oyj and Olkiluoto Plants of TVO Oyj will be stored in the same disposal site in Olkiluoto. Disposal canister components are nodular cast iron inserts providing strength and fracture toughness, with copper tube and lid providing corrosion protection. The canisters will be sealed with electron beam welding or friction stir welding.
Several NDT methods are applied and developed by Posiva Oy to ensure the quality of copper components and sealing welds. This paper describes some phased array ultrasonic inspection techniques of disposal canister copper components and welds. More advanced ultrasonic evaluation can be carried out using PA-SAFT or using matrix PA. Both approaches are also discussed for evaluation of these components. The evaluation of the indications is a demanding task for sizing and a basis for the right acceptance. The defects to be inspected are related to different manufacturing methods of the defects. The defect types form a basis for the design of non-destructive testing because the defect types, which occur in the inspected components affect to the choice of inspection methods. The results from other NDT-methods (ET, RT and VT) will be also used to guide sizing in different areas of components. Some of the UT results will be compared to radiographic results.
The practical inspection of the copper material is challenging due to the anisotropic properties of the material and local changes in the grain size of the copper material. The copper properties for testing must be taken into consideration in inspection and this will be also discussed.

1. INTRODUCTION

The disposal canister should hold its tightness large at least 100 000 years. A good and long lasting tightness is requiring /1/:

A good original tightness (with high quality requirements and extensive inspections)
A good corrosion resistance (use oxygen-free copper as a copper material)
Sufficient mechanical strength (ensure with tensile tests or similar).

Canister must limit the radiation exposure on the outer surface of the canister, in order not to limit excessively the handling or transport of the canister.
The NDT inspection of copper tube, lid and lid weld plays important role in the acceptance of nuclear fuel disposal canister. There are two main reasons for inspection of these components: manufacturing and handling defects of components. To accept and reject the copper components and welds the defect sizing is necessary process in order to compare the inspection results to requirements and inspection specifications. The inspection procedure has been produced during the development of the inspection techniques. The aim of the inspection method development is to qualify the inspection methods defect detection and sizing procedures according to ENIQ in order to show the inspection capability. At the moment the study of technical justification for the qualification purposes is going on. At the same time the defect catalogue will be gathered and gained experience from Posiva's test manufacturing and welding by doing NDT measurements. To inspect copper tubes, lids and welds ultrasonic and eddy current testing techniques are applied. Basic ultrasonic inspection will be carried out with linear phased array probes. For sizing different ultrasonic techniques will be applied and all sizing tasks are carried out with the phased array probes. Typical sizing techniques have been applied like 6 dB method, tip diffraction and TOFD. Additionally phased array SAFT has been applied to large amount of reference specimen and welds containing both reference and real defects. The grain size variation gives additional challenges to ultrasonic testing and this can make sizing more difficult. The inspection requirement concerning the defects of components and welds and also the basics of the applied ultrasonic sizing techniques will be discussed.

The acceptance and rejection process based on the NDT is necessary. The acceptance criteria are mainly under development. Some preliminary criteria have been given for the thick copper weld inspection in the /2/ but this work continues. The sizing of the defects will be most important phase in acceptance of the components and welds based on NDT results.

2. DEFECT TYPES OF COPPER COMPONENTS

The inspection of copper components will be started with the surface inspection of the copper billet. The designed spent nuclear fuel canister consist of copper tube, copper lid (see Figure 1), nodular cast iron insert, steel lid and closure copper weld between copper tube and and copper lid. All copper components and closure weld will be inspected by the ultrasonic testing except copper billet. These components contain different types of manufacturing and handling defects.

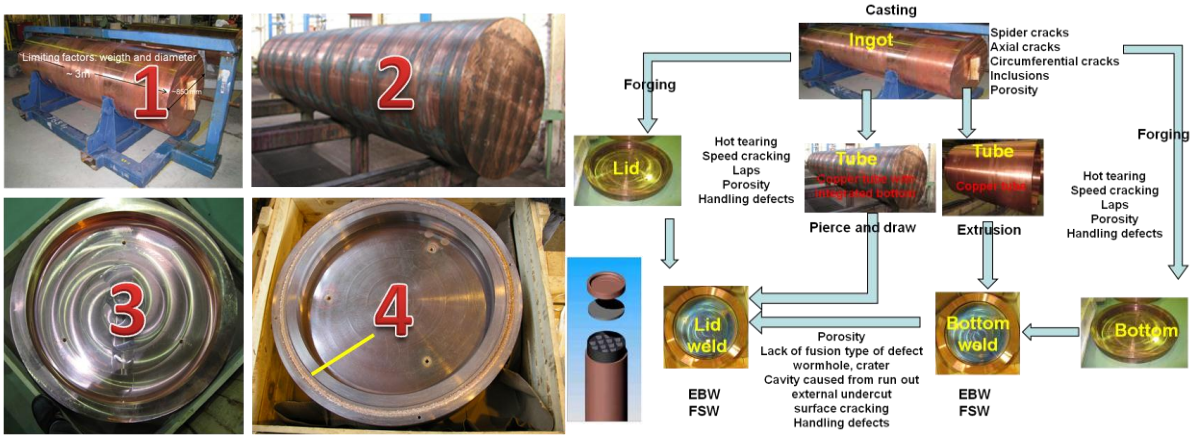

Figure 1. Copper billet (1), copper tube with integrated bottom (2), lid (3) and EB-weld (4) combines the copper tube and the lid (on the left). The possible defect types are mentioned based on the manuf.acturing method as shown in the right image.

In Figure 1 on the right mentioned possible manufacturing defect types of different copper components, which can occur in the ultrasonic inspection. Defect types are discussed in the litterature /3,4,5,6/. Basic rules are that for copper billet the detectability of inner defects is impossible and also not necessary. Large voids in ingot can be detected through the mass and dimensions variations. The surface of copper components will be more sensitive after metal working (forging, extrusion, pierce and draw) and after final machining. This means that one has to avoid all kind of handling defects to final surface of the copper components as well as for the weld surface after final machining. Typical defect types are gathered defect in Figure 1. The detectability of the different defect types in ultrasonic testing can vary based on the properties of the defect. Planar defects are typically difficult to detect if they are inclined to ultrasonic beam. There are also 3D defects in the copper welds which can be difficult to detect in normal PA- ultrasonic testing mainly based on the orientation of the defect. Typical defects in copper tubes can be porosities, delaminations, large grain size variations and in some special cases cracking, In copper lid there can be laps from the forgings and also porosities and voids. In copper lid the grain size can vary depending on the working grade. In copper weld are defects related to welding method. There can be 3D-defects which are mainly lack of fusion type defects. Also larger voids can occur in welds if parameter are outside of the normal range. Main defect types in friction stir (FSW) and electron beam welding (EBW) are discussed in /2/.

3. DEFECT SIZING ULTRASONIC TECHNIQUES APPLIED TO COPPER TESTING

In this study have been applied 4 methods: 6 dB drop method, tip diffraction, TOFD and phased array SAFT.

3.1 6 dB method with Linear PA and Matrix PA

The half drop of the amplitude is mainly used sizing method in ultrasonic testing. Still it is known to be the most unreliable sizing of the surface breaking defects. For the inner defects sizing it is usable when no other method is available. In this method the indication amplitude is maximized and probe is moved on the other direction as long the amplitude is reducing to the half of the maximum amplitude. Same procedure is repeated in the opposite direction and the size of the defect is gained from measurement. This method has been applied to measure the LOP defects and also in sizing of one internal defect of weld shown in Figure 2.

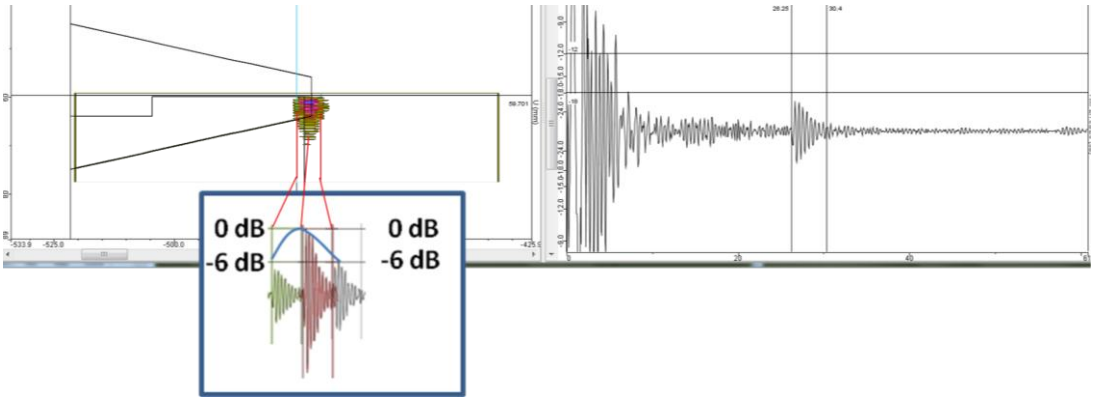

Figure 2 Sizing by 6 dB drop method for the weld defect.

3.2 Tip diffraction with matrix PA-TRL and Linear PA

The tip diffraction method is based on the diffraction phenomena at the defect upper or lower edge. It is known as one of the most accurate sizing method. This has been proven in different round robin trials. The method has been used in Finnish nuclear power plants since 1980s as one sizing method for detected indications. TOFD is special application if sizing based on diffraction and for that reason it will be regarded and discussed separately.

Because of existence of the 3D-defects in copper welds using either EB-welding or FS-welding, matrix phased array offers possibility to improve defect detectability by adjusting ultrasound field in optimal direction to receive maximum response in spite of defect orientation, Figure 3. Other important improving factor in defect detection in matrix phased array is that better focus can be achieved when focusing in two active directions. In linear phased array there is one passive direction, which cannot be focused. That passive direction acts like in conventional ultrasonic probes. In our case matrix phased array technology has been applied for thick copper plate (60 mm) inspection containing EB-weld and also in copper FS-weld inspection. For thick plate EB-weld was manufactured a reference specimen which contains defects having 2.5 mm and 5 mm depths in front of weld and behind the weld shown in Figure 3. In this thick copper plate the reference notch 2.5 mm in depth behind the weld was detected by about 20 dB Signal to noise ratio and the tip was also detectable. These types of thick copper plates are used for parametric study of EB-welding.

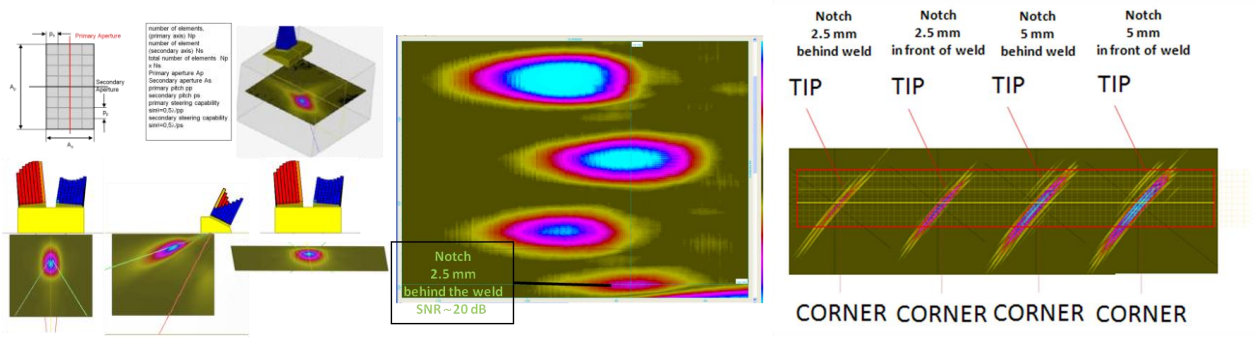

Figure 3 TRL matrix PA-array configuration and Measurement results from thick copper plate having different depths of notches in the front and back of the EB-weld.

3.3 TOFD technique

Measuring the amplitude of the reflected signal can be an unreliable method of sizing defects because the amplitude strongly depends on the orientation of the crack. Instead of amplitude, TOFD (Time of Flight Diffraction) uses the time of flight of an ultrasonic pulse to determine the position of a reflector/7/. In a typical TOFD system, a pair of probes is turned against each other. One of the probes transmits an ultrasonic pulse that is received by the other probe. In undamaged material, the signals picked up by the receiver probe are from two waves: first one that travels along surface - lateral wave and second one back wall response (longitudinal wave). TOFD technique is well explained in /8/. TOFD-application using linear phased array probe can simply realized by choosing a group of elements for example 7 elts as in our case as a sender and choosing corresponding receiver group (7 elts). The distance of 2S can be varied in applied cases from 20 mm to 40 mm. For focal law computation the angle incidence of 60° was applied for receiver and sender, see Figure 4. To optimize for TOFD linear phased array has to go some structural changes which has been realized by different companies /9, 10/. In our cases we have satisfied with the ordinary linear phased array in TOFD sizing trials.

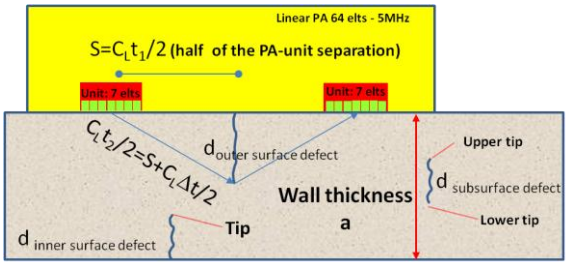

Figure 4 Linear phased array set up for sizing with TOFD technique surface breaking defects

The depth d of the surface breaking defect can be computed from 3 input in TOFD method according to equation 1:

$$d_{Outer\,surface\,defect} = \sqrt{(S + (\frac{C_L \Delta t}{2}))^2 - S^2} \qquad (1),$$

where S is half of the probe separation 2S, C_L is velocity of the lateral wave and Δt is time difference between lateral wave response and diffraction wave response. If it is a question of the defect in the inner surface defect its depth can be computed according to equation 2:

$$d_{Inner\,surface\,defect} = a - d_{Tip} \qquad (2),$$

where a is the wall thickness and the size of a subsurface defect is received according to equation 3:

$$d_{Subsurfacedefect} = d_{Lowertip} - d_{Uppertip} \quad (3)$$

To calibrate TOFD it is possible to use either back wall response or lateral wave response. Lateral wave is not normally present when a surface breaking defect is a sufficient deep more than 1.0 mm and long on the surface. Additionally defect must be open. In case of closed cracks for instance the lateral wave can go through closed crack and defect is not detectable. The lateral wave can go underneath the defect and it is not detected clearly before 2 mm defect depth in our measurements. In any case TOFD is easy technique and quick way to produce reliable information from a defect, its depth and length which is normally needed for ordinary sizing. In Figure 5 is shown the principle of defect sizing using TOFD by comparing lateral wave time of flight to defect diffraction response time of flight. In Figure 5 case the time of flight is 0.7 µs corresponds 1.8 mm defect depth. The calibration curve for different defect depths is shown in Figure 5 on the right. Blue dots show calibration used which extends from 1 mm to 10 mm. for deeper defect will used different setup for phased array this is shown as red dots in calibration curve. According to calibration curve the sizing error will be less than 0.3 mm when defect depth is less than 10 mm. By using C-scan the length of the defect can be measured as shown in Figure 5 on the right. The measurement has been carried out along axial direction but scanning along circumferential direction so that the weld center line is in the middle of the PA-probe. In the measured case the defect starts from 2129 mm and its length is 285 mm.

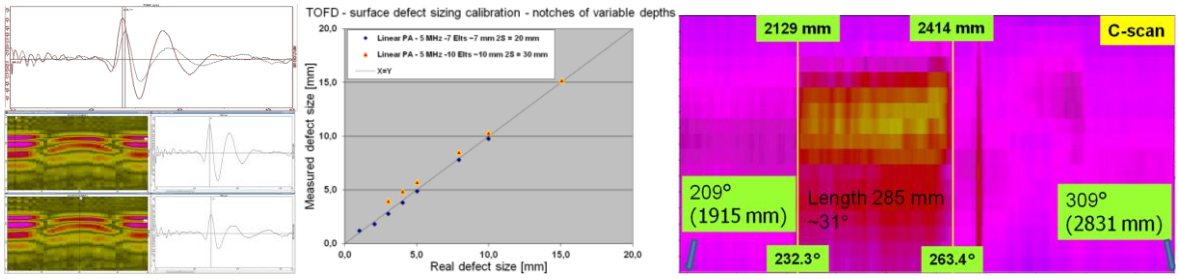

Figure 5 The depth sizing based on using lateral way time of flight calibration for surface breaking defects (on the left and in the middle of the image). The length sizing is based on 6 dB drop (on the right).

3.4 PA-SAFT

In SAFT reconstruction Signal noise ratio from defects will be improved with help of signal averaging. Typically for SAFT measurements small conventional probes has been used. With the help of phased array by angular scanning enables to use SAFT reconstruction for data evaluation. This technology has been developed and reported for many applications by the BAM Berlin, who applies the phased array SAFT (PA-SAFT). In PA-SAFT several angles of incidence are computed together producing large sound field as shown in Figure 6. Each angle of incidence can be separately computed in order to improve signal noise ratio. Along one measurement line can thus produce a sufficient large aperture for SAFT reconstruction. In Figure 6 are modelled both conventional small conventional probe (on the left) and linear phased array (on the right) both having large aperture /11/.

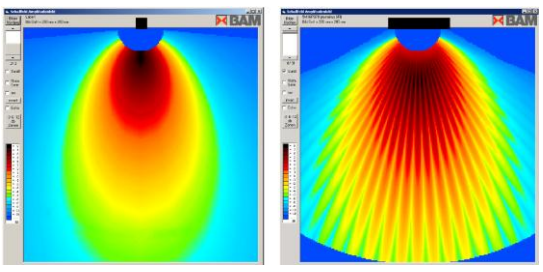

Figure 6 The sound field of a small conventional probe and phased array probe using angular scanning /11/

Posiva applied in the measurement the linear phased array probes having frequencies of 3.5 MHz or 5 MHz. The PA-probes were guided along horizontal circumferential scanning tracks at the outer surface of selected copper lids with welds and a part of a copper tube, Figure 7. The specimen under test were mounted on a turn table and totally immersed in water so that all the circumference water was available for probe coupling. The probes were fixed to a probe holder and the measurements occurred along comb-shaped scanning tracks so that the data acquisition only happened during a turn table movement in clock wise or counter clock wise direction in dependence of probe alignment. The increasing summing of increments by the encoder was applied for recording of measurement positions. Measurement point distances as well as distances between adjacent scanning tracks had an amount of 0.2 mm or 2 mm. The beam angles were changed between -40° and +40°. For the measurement16 transducer elements were always used. For best coupling conditions the elements with number 56 until number 71 were activated in transmitter and receiver mode. In some cases the elements with number 113 until number 128 were activated for data recording. The arrangement is shown in Figure 7 is shown the weld positioning in the measurement arrangement. There were inspected several copper tube and several copper EB-welds using PA-SAFT. The reference copper tube T42-5 was used also for sizing measurements. This reference specimen contains about 60 reference defects. The measured copper welds were containing both reference as well real defects. Reference defect types were small EDM side drilled holes having different depths. With this arrangement the smallest (5 mm deep) side drill holes were not detected. But all other were detected in spite of the diameter. The EDM side drilled hole diameter varied from about 0.3 mm to 2 mm (reference specimen Xk048, and Xk053).

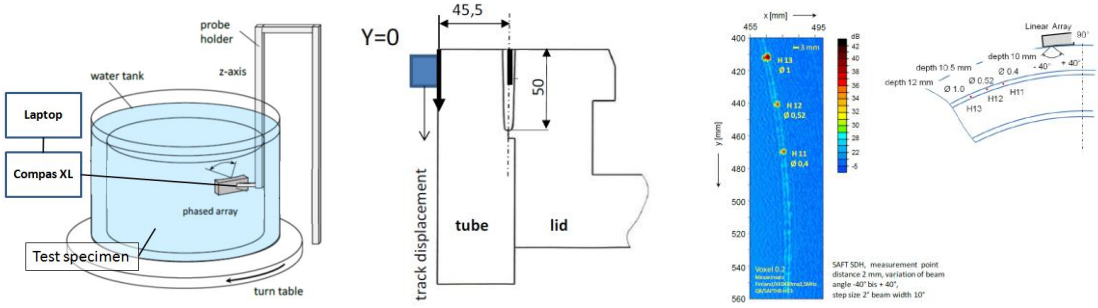

Figure 7 Measurement set up for PA-SAFT trials and copper weld positioning in phased array SAFT.

4 SIZING TRIALS AND EXPERIENCE IN COPPER INSPECTIONS

The NDT acceptance of the component can be divided into the requirements caused by defects for the choice of inspection technique (1), the defect detection analysis after inspection (2), the defect sizing (3), the comparison of the inspection results to acceptance criteria (4).
The final disposal canister master requirement is shown in Figure 8. According to it defect size should not exceed 15 mm or remaining wall thickness should be at least 35 mm.

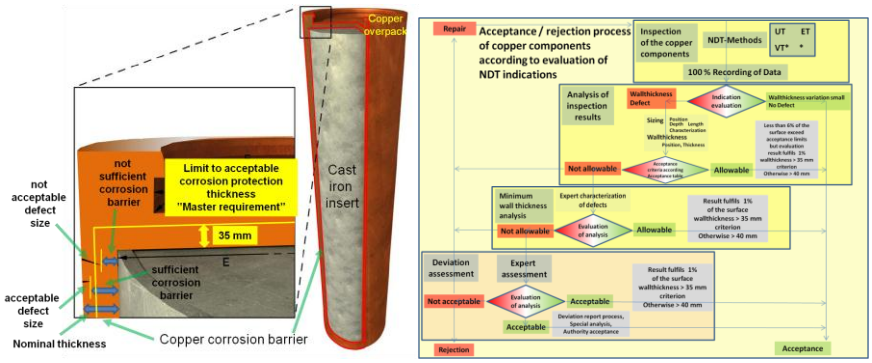

Figure 8 Master requirement of the disposal canister for acceptance rejection process (on the left). Acceptance and rejection process of copper components according to evaluation of NDT indications (on the right)

The preliminary acceptance / rejection process of copper components and copper welds is divided in four sections, Figure 8. In copper components will be done defect detection applying 3 methods: visual, eddy current and ultrasonic testing. In the weld inspection is applied additionally radiographic testing. After measurement the analysis is based on the raw data analysis. If indications are clear and acceptable the component or weld can be accepted. In case of indication exceeding the acceptance criteria further analysis will be carried out in order to measure the minimum wall thickness and the defect more accurate by suitable method. Some of these methods have been mentioned in previous chapters. If indication is acceptable after this analysis component will be accepted. In case the indication i not acceptable and it is not clearly rejectable deviation assessment will be carried out. The material experts will be also involved in the deviation assessment besides the NDT experts before final acceptance or rejection. In special cases if the defect exceeds the acceptance criteria but is situated so that it's presence does not cause problems in long term safety issues. In this case the component deviation assessment will be guided to authority handling. If in the deviation assessment process can be stated the component fulfils acceptance criteria the component can be accepted by the licensee.
In our sizing trials it was tested the acceptance criteria process. Among others following sizing trials were carried out sizing with linear and matrix phased array using 6 dB sizing, TOFD using linear phased array probe and linear phased array SAFT method.
An internal defect was found in the weld and sized using normal linear phased array probe (LPA) and matrix phased array probe (MPA), Figure 9. The radial size was measured to 11.2 mm by using LPA in total after combining two near indications. The measured axial length was 14.0 mm and in circumferential direction the length was about 1° which corresponds about 9.1 mm. So the defect size according to ASME XI was gained a x l = 5.6 mm x 9.1 mm. This is still acceptable size of the defect. This indication will be investigated also with help of metallographic study.

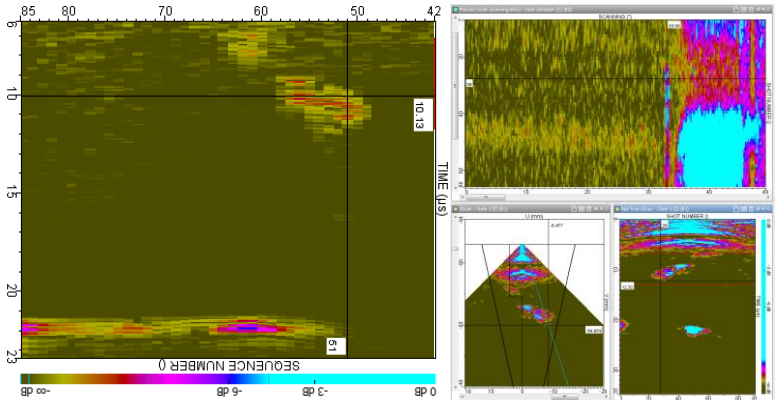

Figure 9 Internal weld defect sizing using linear phased array and matrix phased array probes. The size of the defect was measured in three different directions.

For copper weld inspection the angular scanning in 2 directions was realized by using matrix phased array having 11 x 11 elements. The size of the weld defect was determined in the axial angular scanning: the radial size was measured to be 13 mm in total after combining two near indications. The measured axial length was 14.1 mm and in circumferential direction the length was about 1° which corresponds about 9.1 mm. So the defect size according to ASME XI was gained a x l = 6.5 mm x 9.1 mm. This is still acceptable size of the defect. This indication will be investigated with help of the metallographic study. The size of the indication was about the same as measured with linear phased array probe or matrix phased array probe. The size of the defect was a bit smaller in circumferential angular scanning direction using matrix phased array probe: 8.2 mm and in radial direction 11.8 mm which gives a x l =5.9 mm x 8.2 mm.

In TOFD inspection there were measured different types of defects: reference defects as well also real defects in copper weld, tubes and plates. The variation of defect depth from the surface varied from 1 mm to 44 mm. The known maximum distance to surface was about 37 mm. The real defects were not sized by metallographic studies, but later on will be carried out some metallographic studies on the some of these measured indications. The amount of the known distance of defect depths was about 30 reference defects. The measurement of those defects is shown in the curve of Figure 10. Based on this information the sizing error was about ±1 mm of the true value.

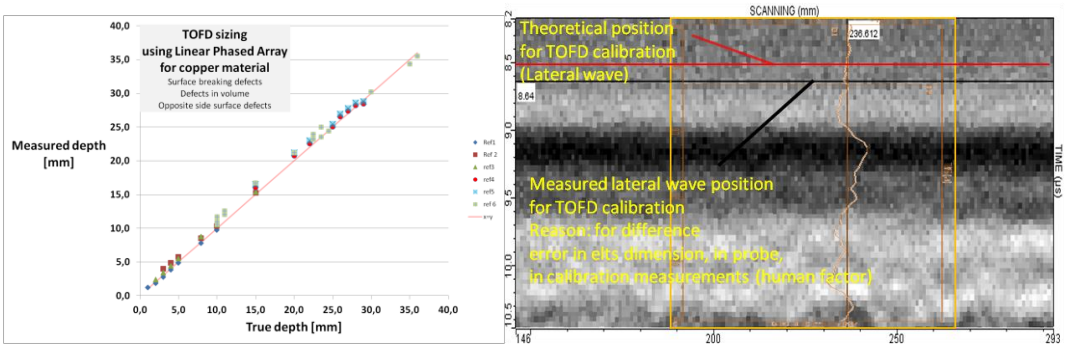

Figure 10 The results of the analysis TOFD surface breaking defects on the left and lateral wave measurement

To minimize the sizing error is based on the accurate measurement of arrival time of the lateral wave and back wall response. In our measurements in was seen that theoretical lateral wave arrival time was smaller than measured which is probably related to the probe information accuracy of the PA-pitch and (or) index position accuracy. In TOFD measurements the variation of the lateral wave was about 0.2 µs bigger from the theoretical value. Also the used linear phased array probe was not optimized for TOFD measurements, which can cause some error is measurements. This was seen in weak lateral wave and back wall response. When analyzing surface breaking defects it was seen that 1 mm defect depth was not seen clearly because the defect signal was mixed with lateral wave signal. It is obvious that lateral wave will go underneath the defect when defect's depth is 1 mm or smaller in our probe setup. When the probe separation was chosen to be 20 mm from 40 mm, there was small amplitude weakening in lateral wave C-scan from 1 mm deep notch, but it was hardly detectable in the C-scan. In Figures 11 - 12 is shown additional results from our TOFD measurements.

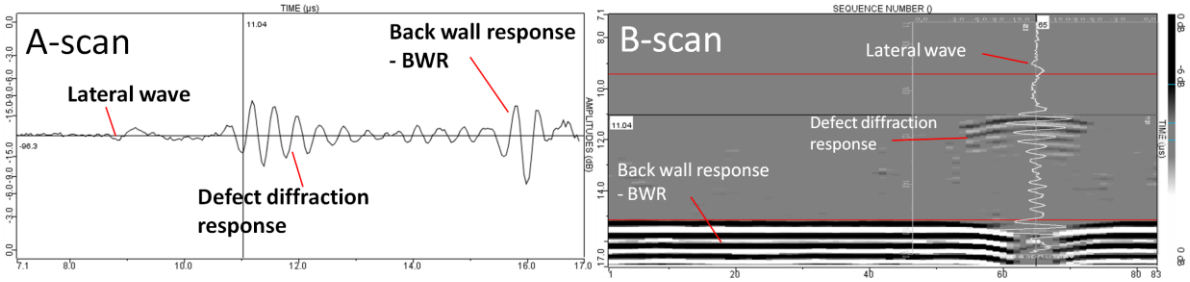

Figure 11 Diffraction responses from a 15 mm deep notch locating in the opposite surface. Lack of back wall response is also detectable. A-scan is on the left and B-scan on the right.

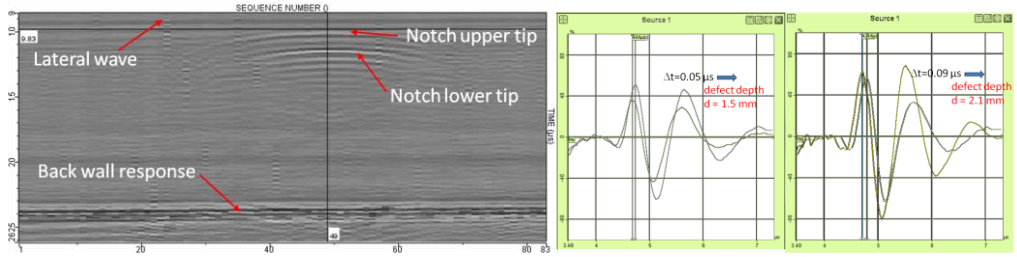

Figure 12 TOFD image from the internal notch in wall thickness direction is showing upper and lower tip of the notch on the left. On the right is shown A-scans from the sizing of the two long surface breaking defect in the copper weld.

In copper weld detected surface defects - voids. They were measured with TOFD method. The depths of defects were in the measurements 1.5 mm and 2.1 mm. Both defects were long more than 100 mm. The possible sizing error will be caused by the geometry of the defect, while it is about 5 mm wide, Figure 12 on the right.

In the phased array SAFT measurement one reference specimen (XK053) was measured as a blind and PA-SAFT found all 80 reference defects. The diameter of the side drilled holes varied from 0.5 mm to 1 mm and the depths varied from 10 to 50 mm. some of the defects ware deeper than 50 mm. The Figure 13 shows similar EDM side drilled holes in the reference specimen XK048. In Figure 14 has been shown the sizing of a real defect. The sizing gives as a result the depth in axial direction 15.7 mm, in radial direction 10 mm and in circumference direction about 9.2 mm. Some sizing properties was programmed after Posiva's measurement trial's to BAM's analyzing software in order to be able size in all three directions.

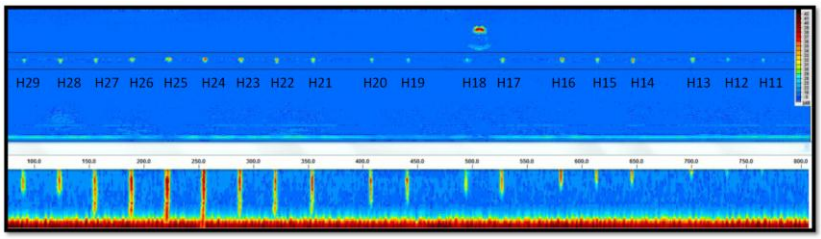

Figure 13 Visualizing PA-SAFT measurement from several EDM side drilled holes having different depths.

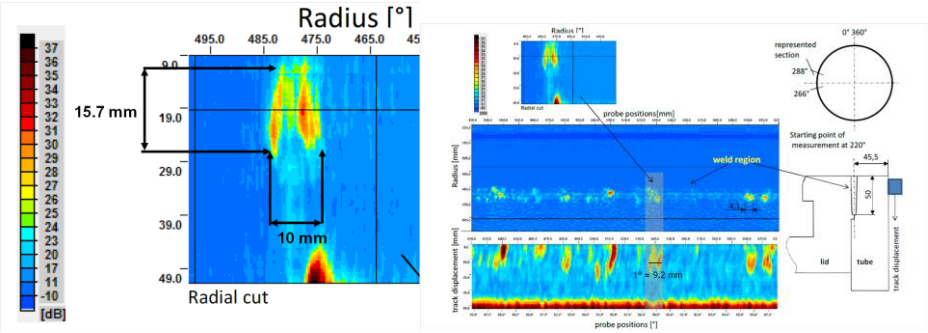

Figure 14 Real weld defects detected and sized using PA-SAFT from the weld specimen Xk033.

Same specimen (Xk033) was also X-rayed with 9 MeV linear accelerator. About same defects was detected with both methods. Some extra indications were seen in phased array SAFT result as seen in Figure 15. At the moment in metallographic testing some small defects has not been detected using linear phased array measurements and they are typically in radial direction. Phased array SAFT provides also for detection of these defect types. These defects are quite thin and also 3-dimensional which means that in X-ray inspection they are not necessary optimal for detection. Phased array SAFT can be improved by using matrix phased array so that angular scanning can be performed in two axis directions (circumference and axial directions).

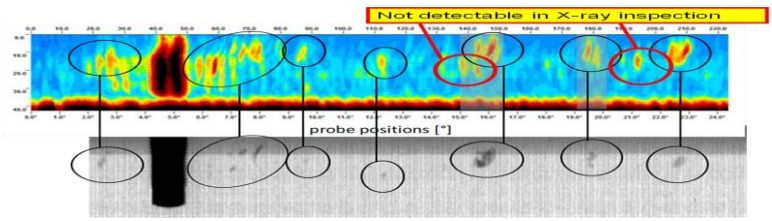

Figure 15 Comparison between Xray and PA-SAFT results from a copper weld containing several weld defects

5 SUMMARY AND CONCLUSIONS

Several sizing methods were applied successfully to copper components of the disposal canister. The sizing error could not be fully estimated because all metallographic studies have not yet been carried out for all measured defects. In generally PA-SAFT was shown to be really extremely good in detection of weld defects compared to normal linear phased array measurements. Some results PA-SAFT were compared to X-ray measurements. Ultrasonic PA-SAFT detected even more defects than X-ray using 9 MeV linear accelerator. PA-array SAFT provides also the possibility to evaluate both defects in front and back of the weld, which is not possible in X-ray inspection. TOFD method showed to be simple and quick for defect sizing. The inaccuracy of the sizing in TOFD was sensitive to lateral wave calibration for small surface breaking defects. When the surface breaking defect depth is more than 2 mm the applicability of the TOFD was good. In order to improve our accuracy of the method the probe configuration must be changed for phased array applications as it has been realized by some inspection companies. The acceptance rejection process was applied to these sizing trials and it showed to function successfully. Copper anisotropy was not a problem in EB-weld for ultrasonic sizing. One should not forget other methods possibility to give aid for sizing and for improved acceptance and rejection.

6 REFERENCES

1. Raiko, H., 2012. Canister Design 2012, Posiva report 2012-13.
2. Pitkänen J., 2010, Inspection of Bottom and Lid welds of disposal canisters, Posiva report 2010-04, 98 p.
3. Pitkänen, J., Salonen, J., Sandlin, S. & Ronneteg, U., 2007, Defect Detectability in EB-welded Copper Disposal Canister with 9 MeV Accelerator, 6th International Conference on NDE in Relation to Structural Integrity for Nuclear and Pressurized Components, Budapest 12th -14th October 2007, 14p.
4. Savolainen, K., 2004, Friction Stir Weldability of Copper Alloys. M.Sc. Thesis. Helsinki University of Technology, Laboratory of Engineering Materials, 115p + 3 appendices.
5. SKB, 2006, Kapsel för använt kärnbränsle, Tillverkning av kapselkomponenter, SKB Report R-06-03, 2006, 67p.
6. Müller, C., Elagin, M., Scharmach, M., Bellon, C., Jaenisch, G.-R., Bär, S., Redmer, B., Goebbels, J., Ewert, U., Zscherpel, U., Böhm, R., Brekow, G., Erhard, A., Heckel, T., Tessaro, U., Tscharntke D. & Ronneteg, U., 2006, Reliability of nondestructive testing (NDT) of the copper canister seal weld, SKB report R-06-08, 158p.
7. SFS-EN 583-6, 2008, Non-destructive testing, Ultrasonic examination, Time-of-flight diffraction technique as a method for detection and sizing of discontinuities 26p.
8. Charlesworth J. P. & Temple J. A. G., 2001, Engineering application of ultrasonic Time-of Flight diffraction, Second Edition, Research Studies Press LTD, 254 p.
9. Yamada, H., Yano, Y. & Udagawa T., 2004, Development of the phased array system for angle beam testing, Nippon Steel Technical report N089 January 2004, pp. 28-32
10. Böhm, R., 2012, internal communication,
11. Kitze J., 2009, Ultraschalluntersuchungen zur Fehleranalyse mit SAFT unter Anwendung der Gruppenstrahlertechnik, Diplomarbeit (Master of science study), 109 p

APPLICATION OF ULTRASONIC STRESS MEASUREMENT TO PRELOAD ASSESSMENT ON ALREADY TIGHTENED BOLTS

H. Walaszeka, P. Bouteilleb, CETIM, France

KEYWORDS:

Bolt, screw, tightening control, ultrasonic assessment of preload , already tightened bolts, torque control, ultrasonic method, ultrasound, acoustic wave, longitudinal wave, compressional wave, shear wave, acoustoelastic constants, differential method, mono-wave method, bi-wave method**.**

ABSTRACT

When a material is under mechanical load, the stresses modify the velocity of acoustic waves. This consists in acoustoelastic effect. This property can be exploited for stress measurement in the material itself when the stress concerns the surface of the material, or in the bulk material, as in bolts.
The ultrasonic bolt tightening control allows knowledge of preload stress in bolts. The accuracy is much better than in the case of torque wrench. In fact, the use of this mechanical-based measurement equipment leads to uncertainties due to random resistant torques, induced by mechanical manufacturing tolerances. The ultrasonic measurement of the pre-load gives the information about the tension inside of the bolt, independently of mechanical uncertainties. This consists in an in-situ measurement. More, in some cases, the ultrasonic method allows knowledge of the preload on bolts already tightened, without untightening. This method is called bi-wave method, and exploits compressive and shear ultrasonic waves.
Examples of application of the method are presented about the differential mode case, which is largely known and industrialized, and in the case of bi-wave method, which lead to several on site applications, performed by CETIM with a portable equipment.
The good performances obtained on carbon steel bolts are presented, and limitations observed on non-ferritic steels are discussed, with possible ways to overcome these limitations.

1. THEORETICAL BASIS OF ULTRASONIC STRESS MEASUREMENT

The ultrasonic method of stress measurement is based on the application of the theoretical results developed in the articles [1] and [2]. The elastic waves which are propagated in isotropic solids are characterized by their propagation velocity in material (Fig. 1). This velocity is given for the waves of compression (longitudinal) and transverse (shear) modes by :

$$\rho V_L^2 = \lambda + 2\mu = K + \frac{3}{4}\mu \qquad \rho V_T^2 = \mu$$

where λ, μ, and K are the elastic constants and ρ the density.

We can thus write this velocity variation according to the deformation for each mode. The following expression is given for the longitudinal mode,

$$\frac{\frac{dV_{11}}{V_{11}}}{d\varepsilon} = 2 + \frac{(\mu + 2m) + \nu\mu\left(1 + \frac{2l}{\lambda}\right)}{\lambda + 2\mu} = A_{11} \qquad \text{with} \quad \varepsilon = \frac{\sigma}{E} \qquad (1)$$

where A_{11}, ε, E and σ are respectively acoustoelastic constant corresponding to the longitudinal mode, deformation, Young modulus and stress or constraint.

Thus, according to (1), the relative velocity variation is proportional to the constraint. The constant of proportionality is a coefficient which depends on considered material and its metallurgical state.
The velocity dependence versus stress slopes (Fig. 1) is given by quasi-linear curves having different according to propagating modes, as described by Egle and Bray [3].

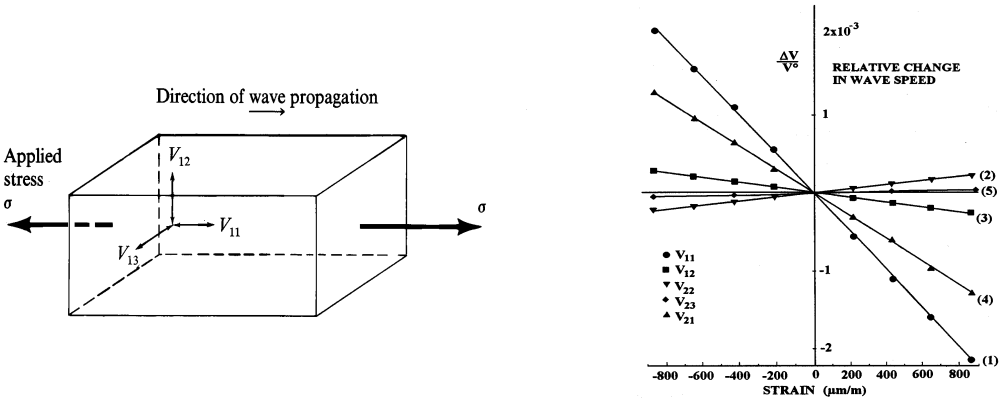

Fig 1: Propagation of acoustic waves in a solid against various modes and Sensitivity of ultrasonic velocity versus stress, according to the propagating mode considered

Some laboratory trials and studies show the interest of ultrasonic technique for measuring the residual stresses [1] [2] [3] [5] [6] [7] [8]. We now will describe the application of the acoustoelastic effect on the determination of the stresses for bolt tightening control.

2. APPLICATION OF THE ULTRASONIC METHOD IN ULTRASONIC CONTROL OF BOLT TIGHTENING

2.1. The need.

The presence for a sufficient prestressing in the screw of an assembly allows to ensure the good behaviour in the time of this one, as well as good performances in fatigue. The oldest and most usually used technique to control the tension in the assemblies consists in measuring the tightening torque. However, the parameters linking the tightening torque to the effective tension in the material of the bolt or screw are difficult to control. Indeed, coefficient of friction, state of lubrication, surface quality of the plans in contact, quality of machining, assembly alignment, and manufacturing tolerances result in important resistant torques, with a very dispersed value. Thus the torque wrench which uses a mechanical principle measures only the total applied torque to the assembly. This torque results in the addition of the useful part of the torque, producing longitudinal stress in the bolt, and a resistant torque, which value is random, as explained in the last lines. A torque wrench gives in best case an uncertainty on the tension introduced into the material of the screw about ± 20 %.
The ultrasonic measurement of the mechanical tension provides a solution to this problem, as the measurement is performed in the bulk material of the bolt or screw, where the wave propagates.

The tightening process produces bolt length increase plus stress increase also. This results in ultrasonic time of flight (T.O.F.) increase in the bolt. Calibration of T.O.F. measurement versus load applied enables the knowledge of the load on bolts.

Two ultrasonic methods can be used:

- the mono-wave method, using only the longitudinal waves. It is of differential type because it requires a measurement of time at null constraint T_{0L} (on an unstressed bolt) and thus loosening if value T_{0L} is not filed, which is almost always the case. This method is employed industrially (existence of measuring apparatus), generally when the tightening is operated.

- the bi-wave method exploits two types of waves of different nature : longitudinal waves and transverse waves. It can be called “absolute” because it applies during or after tightening without needing a measurement with null constraint. So, it is applicable on already tightened bolts or screws.

This method is not industrialized yet. Presently, CETIM uses it in provision of services with prototype portable equipment.

2.2. Description of the method

2.2.1. Mono-wave method or differential method

In practice, the control of the tightening of the screws in differential mode is carried out in two successive phases :

- the phase of calibration where a standard screw (which is representative of that to be measured) is loaded (i.e. tightened) with the same conditions as the screw to be controlled. The screws are of the same material, have the same geometry and the same tight length. The calibration test is carried out, generally in a laboratory by measuring times of transit of the ultrasonic waves on the screw standard on which are applied simple traction efforts, in the elastic range. So are obtained calibration curves (abacuses) representing the variation of times of transit according to the tensions, or load applied.
- the phase of measurement during which ultrasonic time of transit journey in the screw are measured, before tightening and after tightening. The report of the so-measured differential time on the calibration curve enables establishing the constraint of tightening.

So, the mono-wave method, which represents a widely industrialized method, is operated in differential mode.

The principles of the control of differential tightening, used industrially, are summarized below in Fig. 2.

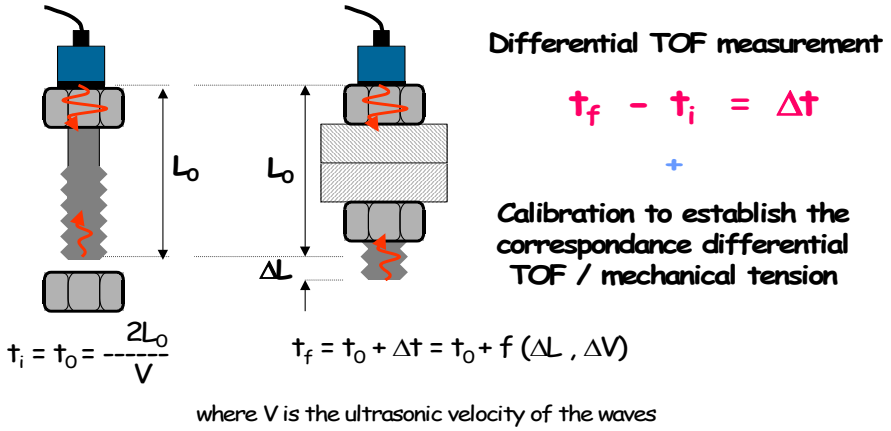

Fig 2: Principles of ultrasonic tightening control in differential mode

2.2.2. Bi-wave method.

The control of tightening in bi-wave mode exploits the longitudinal and transverse waves. The use of these two waves enables to eliminate the need from the knowledge of exact length of the unstressed screw, which is necessary in differential mode. The measurement mode is summarized hereafter (Fig. 4).

Electromagnetic transducers are used to generate for the need, the wave L (compressional) and the wave T (shear). These transducers enable reliable coupling, very difficult to guarantee in wave T with traditional piezoelectric transducers. The electromagnetic coupling suppresses the need of coupling agent traditionally used to transmit the ultrasonic mechanical pulse from the probe to the head of the bolt. On Fig. 3 are displayed the description of electromagnetic generation of ultrasound, and the Fourier transform of the echoes, obtained on a 30 mm thick 35NCD16 block part. It appears that the ultrasonic spectrum is centred near 6,5 MHz , which meets the frequency range used in N.D.T.

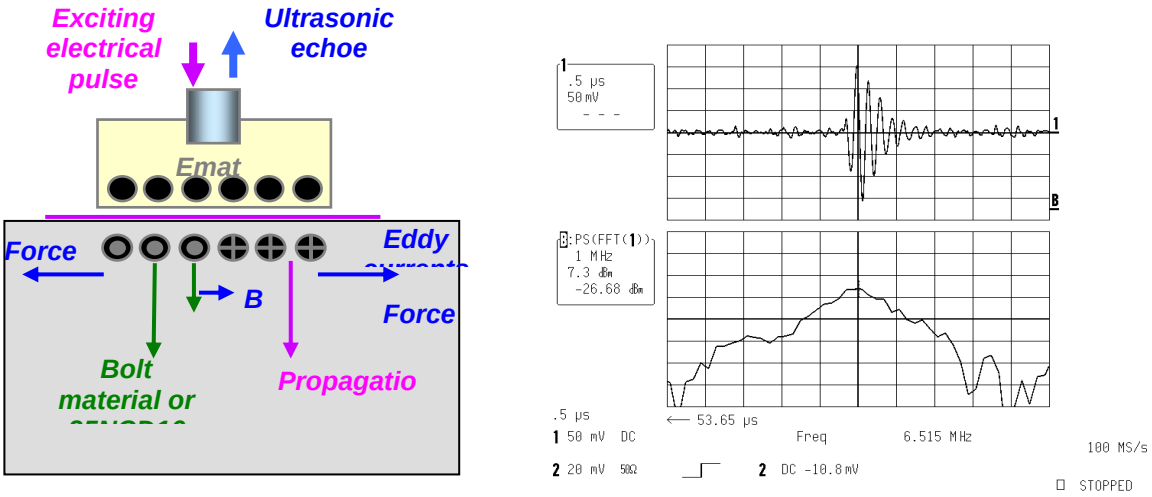

Fig 3: Principles of EMAT generation of ultrasound and typical ultrasonic spectrum

On Fig.4 are displayed the typical echoes produced by EMAT transducers, for both compressional and shear mode. The echoes are very similar to those obtained with piezoelectric technology.

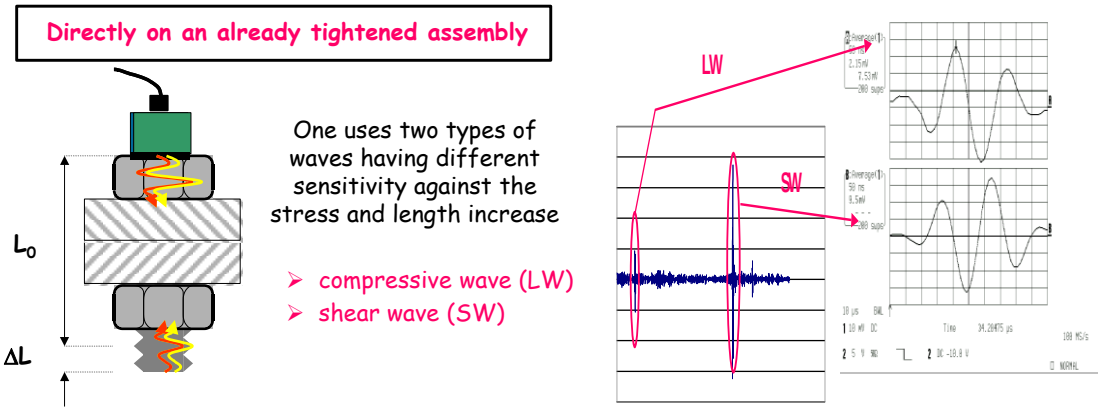

Fig 4: Principles of ultrasonic tightening control with bi-wave mode, and echoes obtained with electromagnetic transducers (E.M.A.T.)

Here are examples of calibration obtained on 520 mm length M30 bolts. The curves display T.O.F. ratio for shear and compressional waves versus load (Fig.5) or temperature (Fig.6).

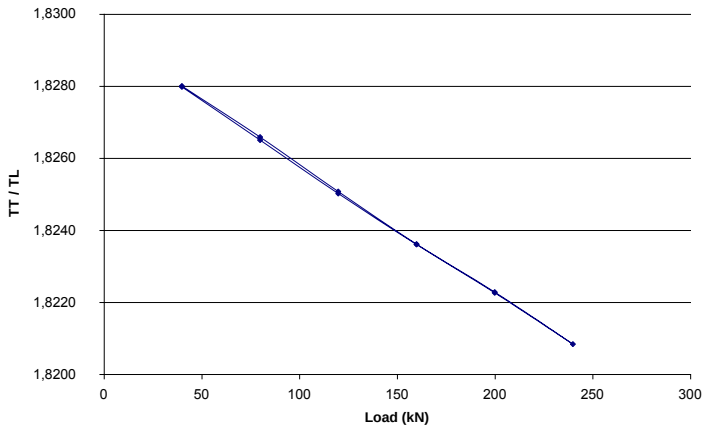

Fig 5: Tension calibration curve

The influence of temperature is measured in an oven on an unstressed bolt. The following curve (Fig.6) establishes the load correction factor versus temperature.

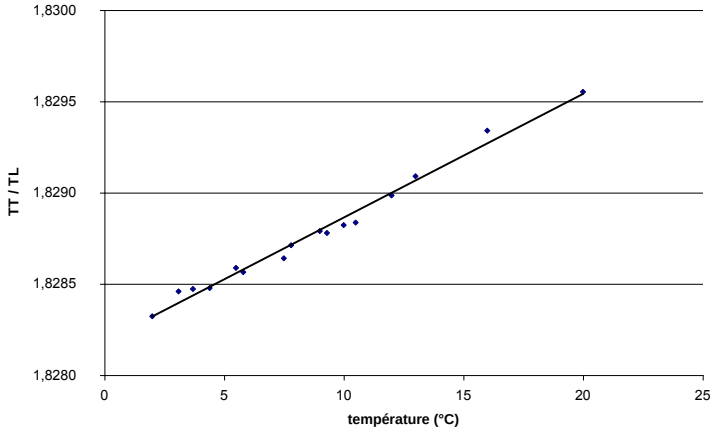

Fig 6: Temperature calibration curve

The main characteristic of the acquisition is oversampling with 100 MHz frequency. This leads to 500 MHz equivalent frequency. The time of flight is measured on the peak of compressional and shear wave echoes. The sampling resolution (2 ns) gives a maximum measured stress resolution of 1kN on typical industrial applications.
Practically, the measurement dispersion observed in industrial conditions is about ± 5%, which is a great measurement improvement if we compare with torque wrench.

2.2.3.Application of the Bi-wave method

The bi-wave methodology was used on the structures which maintain the glazed frontages of the Airport of Paris [9],[10].

Fig 7: Bolt tightening control on the air terminal 2F of the Airport Roissy Charles of Gaulle (France)

The ultrasonic measurements were performed with prototype equipment adapted by CETIM for the present operation. The control of the glazed frontage of the terminal 2F of the Air terminal of Roissy-Charles-of-Gaulle, relates to several hundred of bolts.
Inaugurated in 1998, this terminal consists of an architectural structure of almost 400 meters length, whose principal frontage consists of glass plate assembled on a framework metal, and maintained by stiffeners out of glass. More than one thousand of pins with a diameter 18 mm fix these plates on metal amounts. Vertical stiffeners out of glass ensure the behaviour the wind of the frontage. They are assembled by metal fish-plates which grip glass, which implies a very precise adjustment of the force exerted not to damage the plates.
Taken measurements allowed, several years after the installation, to plan the maintenance actions of the frontage.

3. CONCLUSION

The methodology of tightening control by ultrasounds enables to know prestressing in the heart itself of the assembly, within the centre even of the bolt or the screw. This methodology is proved and reliable in its differential version, which is largely industrialized.
The method bi-wave, although not yet to date industrialized, is very promising within sight of the first results obtained. Now, this last technique still requires work to be usable on the majority of the existing bolts to meet the needs of industry.

4. REFERENCES

[1] D. S. Hughes and J. L. Kelly, 1953, "Second-order elastic deformation of solids", *Phys. Rev*, 92, 5, pp 1145-1149

[2] T. D. Murnaghan, 1951, *Finite Deformation of an elastic solid*, John Wiley, New York

[3] D. M. Egle and D. E. Bray, 1976, "Measurement of acoustoelastic and third-order elastic constants for rail steels", *Journal of Acoustical Society of America*, 60, 3, pp 741-744

[4] D. E. Bray, "Current directions of Ultrasonic Stress Measurement Techniques", 2000, 15th WCNDT, Rome, Paper n°647

[5] H. Walaszek, H.P. Lieurade, C. Peyrac, J. Hoblos, J. Rivenez, 2002, "Potentialities of ultrasonics for evaluating residual stresses : Influence of microstructure", *Journal of Pressure Vessel Technology*, Vol. 124, August 2002, pp 349-353

[6] H. Walaszek, J. Hoblos, G. Bourse, C. Robin, 2002, "Effect of microstructure on ultrasonic measurements of residual stresses in welded joints", 6th European Conference on Residual Stresses (E.C.R.S. 6), 10-13 July 2002, Coimbra, Portugal

[7] J. Hoblos, G. Bourse, C. Robin, H. Walaszek, 2003, "Ultrasonic stress in welded joints by using Lcr Waves : An approach to separate microstructure and stress effects" (WCU2003), 7-10 September, Paris, France, pp 701-704.

[8] H. Walaszek, J. Hoblos, G. Bourse, C. Robin, HP. Lieurade, 2004, "Ultrasonic stress measurement in welded component by using L_{CR} waves : analysis of the microstructure effect", Conference ASME PVP, July 2004, San Diego CA, USA

[9] Cetim-Info n° 181, december 2002 "Les assemblages contrôlés en direct"

[10] H. Walaszek, J. Hoblos, G. Bourse, C. Robin, H.P. Lieurade, P. Bouteille, 2005, "Ultrasonic stress measurement : application to welded joints and to bolt tightening assessment", COFREND Congress, May 2005, Beaune, France

REACTOR PRESSURE VESSEL IV

ARCHER – ADVANCED SYSTEM FOR RPVH INSPECTION AND REPAIR

S. Galošić, T. Tomašić, I. Vuković, A. Bakić, INETEC,Croatia

ABSTRACT

The reactor pressure vessel head (RPVH) is an integral part of the reactor coolant pressure boundary. Its integrity is important for the safe and reliable operation of the nuclear power plants (NPP). After detection of the leakage and cracks on the RPVH in a French NPP, followed by another that occurred in a NPP in the USA, methods and frequency of inspections were defined, and are strictly regulated by the US NRC Order EA-03-009 (substituted lately by ASME Code Case N-791-1) since 2003.

ARCHER, INETEC's new manipulator, is designed to provide full scope inspection of the RPVH, by using various test modules and by performing the surface repair action on J-groove weld. It is adjustable to work with different types of penetration nozzles and thermal sleeves on both VVER and PWR types of NPPs.

The paper describes the system's capabilities and features, and its advantages compared to other systems for performing the RPVH inspection and repair activities on PWR and VVER reactors.

1. INTRODUCTION

The reactor pressure vessel head (RPVH) has penetration nozzles for instrumentation systems and control rod drive mechanisms (CRDM). A typical configuration of the reactor vessel head penetration nozzles, used in most of the PWR's worldwide, is shown in Figure 1. The joint between the RPV head and a penetration nozzle is achieved by the so called J-Groove weld. It ensures the mechanical fixture and sealing of the pressure boundary.

Operating conditions of PWR plants and primary coolant water can cause cracking of the nickel-based alloys through a process called primary water stress corrosion cracking (PWSCC). The susceptibility of RPVH penetrations to PWSCC appears to be strongly linked to the temperature of the RPVH and the operating time. Problems related to PWSCC therefore increase as plants are operating for a longer period of time.

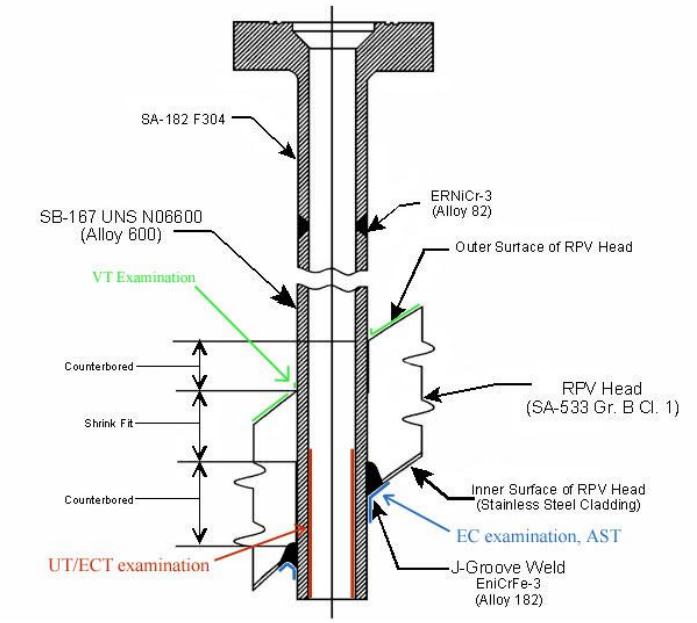

Figure 1: Control Rod Drive Mechanism (CRDM) penetration

The discovery of leaks and nozzle cracking at an US NPP and some other PWR plants [1] has made clear the need for more effective inspections of RPV heads and associated penetration nozzles [2, 3].

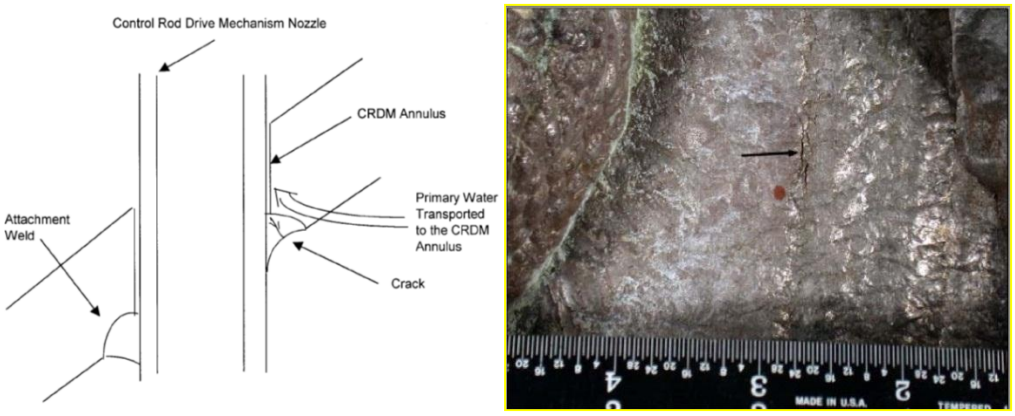

Figure 2: Actual flaw and flaw mechanism [4]

Usual scope of inspection from inner side of RPVH comprises of:

- Visual inspection of the surface,
- Ultrasonic testing (UT) and eddy current testing (ET) of the penetration nozzle
- Eddy current testing (ET) of the J-groove weld and nozzle outside surface below the weld.

In order to perform the needed in-service inspection per procedure, the ARCHER manipulator has been developed. The base manipulator has interchangeable modules (End effectors) that allow different inspection methods. The schematic representation of the entire ARCHER system concept is given on Figure 3.

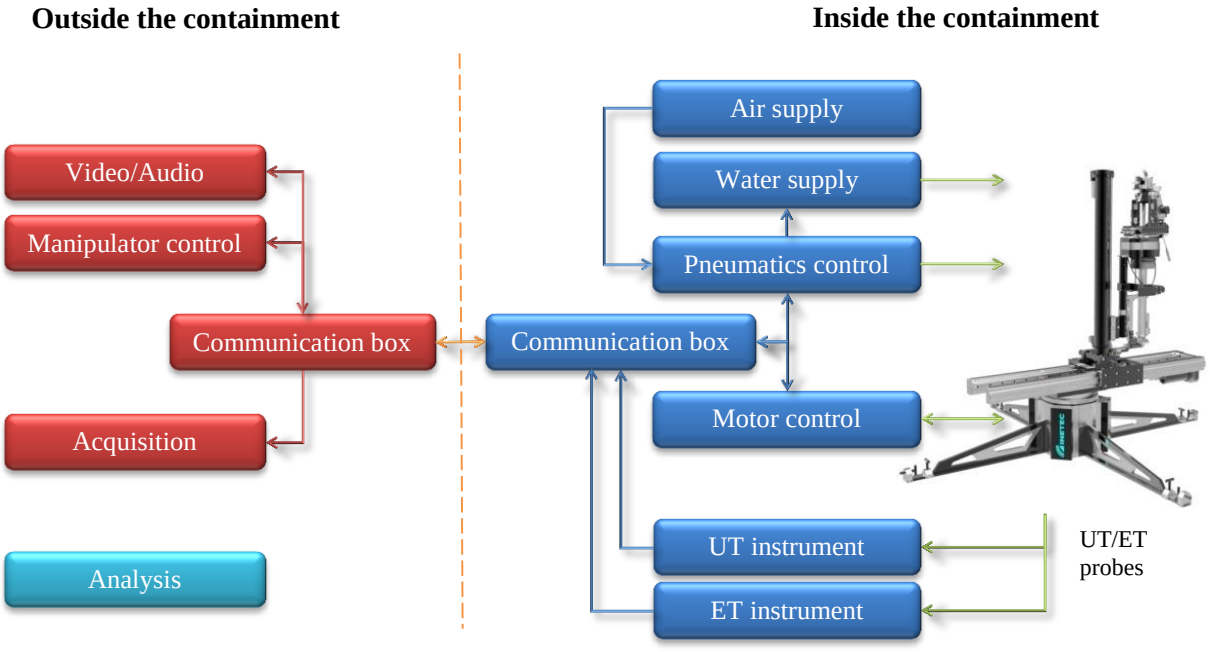

Figure 3: Schematic representation of the ARCHER system

2. HARDWARE

The manipulator has 7 axes that can be moved independently. The first 4 axes are the manipulator axes used for positioning of the modules under the selected penetration, while the remaining 3 are used for driving the module's axes.

Maximum velocities of the manipulator are 20 °/s for the main rotation axis and 100 mm/s for the horizontal and vertical axes. Because the electronics are sensitive to radiation exposure, the absolute position of the axes is measured with the resolvers.

Figure 4: ARCHER - RPVH inspection manipulator

The motor control box is located outside of the manipulator, and is connected to it in such a way that the motor (power) and the data (resolver and data) wires are physically separated to minimize the interference and ensure the best quality of the data signals. Cable management has been conducted inside the manipulator – there are no wires hanging for the operator to think about while operating the manipulator.

In comparison with the older system, the number of cables between the and the outside of the containment area has been significantly reduced. All control, video, audio and tester signals go into one communication box located inside the containment. From there they are connected to the outside of the containment communication box with only two optical cables. The first one is used for the tester instruments (MIZ and DYNARAY), while the other one carries everything else (video, audio, control…).

3. SOFTWARE

The RPVH manipulator is controlled by a new version of the Manipulator Control (MC) software, which utilizes the possibilities given by the next generation of motion controllers.

Previous versions of the MC and firmware (FW) used the Modbus communication that made sending complex commands difficult to implement. To solve that, a standard TCP/IP server has been implemented on the controller side. In addition, the whole communication is formatted in the JSON format which further simplifies and standardizes the communication.

Using this approach, complex commands and data (error descriptions, configuration files, status data…) can be easily sent to the controller without the need for additional tools and restarts. For example, the axis configuration file can be sent to the controller which can then reconfigure its parameters and structure on the fly.

Communication between the controller and drives (status and command data) is performed over the CAN protocol. The schematic of the control section of the system is given on Figure 5.

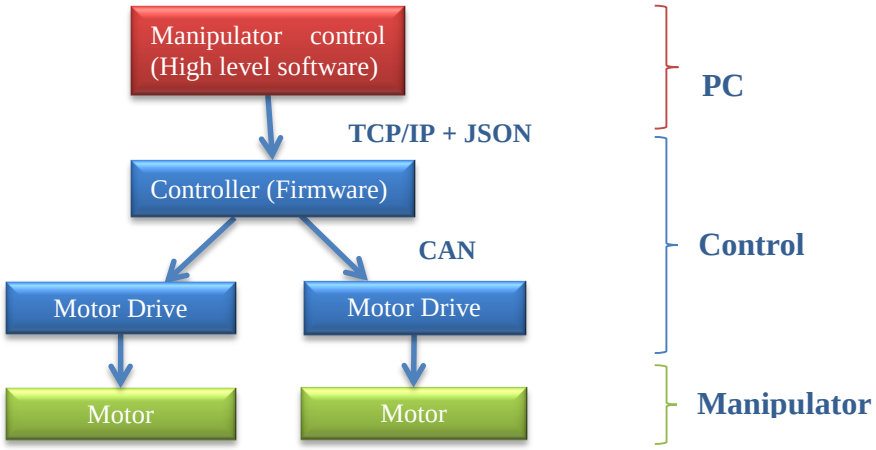

Figure 5: ARCHER control system schematic view

Commonly used manipulator commands (e.g. enabling and disabling of the axes, driving the axes …) have been mapped to the keyboard which allows for a simpler and faster control of the manipulator. A 3D model of the manipulator has been added to the program to simplify the process of positioning the manipulator under the selected penetration. Also, a double click on a penetration automatically drives the manipulator to the selected penetration, reducing the complexity of driving the multi-axis system.

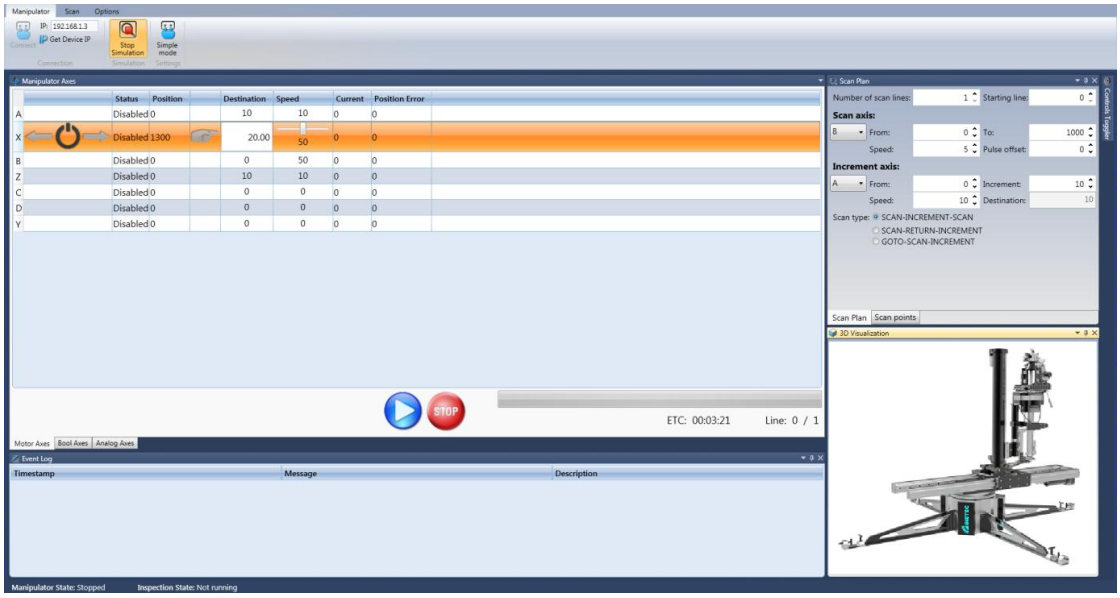

Figure 6: RPVH Manipulator control high level software

While driving the manipulator, the user can select between the axis coordinate system (each axis is operated independently) and the tool coordinate system, where the rotation and translation of the first two axes have been transformed to the X and Y tool translations which makes positioning easier for the user.

4. MODULES

Due to complex geometry, each module is specially designed for particular type of examination. Modules are exchanged through the docking system without need for personnel to enter under the head region, thus reducing the personnel's exposure to the ionizing radiation. Three different module types are used in the RPVH inspection and repair procedure.

4.1 GAP module

The GAP Module is used to determine the surface flaws or cracks on inner diameter surface of penetration nozzle gap. It guides a slim sword-like probe (Figure 7) which carries a pair of Time-of-flight diffraction (TOFD) transducers for detection and sizing of circumferential and axial cracks, an eddy current cross-wound coil, and a zero-degree UT probe through a gap between the penetration nozzle and thermal sleeve. In the case of a non-sleeved penetration nozzle, an open housing module is used.

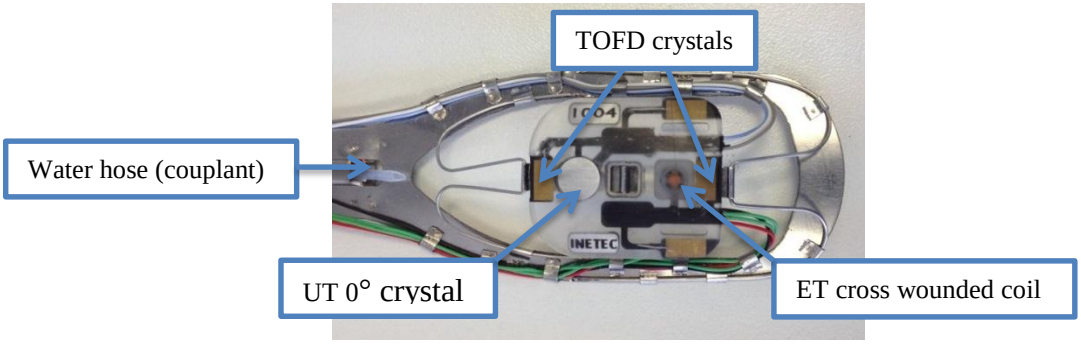

Figure 7: Pro Ultra Sabre probe

The Gap Module, shown in Figure 8, guides the described eddy current and ultrasonic probes into the gap (approximately 3 mm) between the inner surface of the penetration nozzle and the thermal sleeve. It also manipulates the probes to scan the inner surface area.

Figure 8: Gap module

4.2 J-Groove module

The J-Groove module (Figure 9) is designed to fit the geometry of the J-groove weld of the penetration nozzle, vent pipe and funnel guide. The whole weld area (2" on shell side and ½" on nozzle side) is covered by two specially designed arrays of eddy current probes.

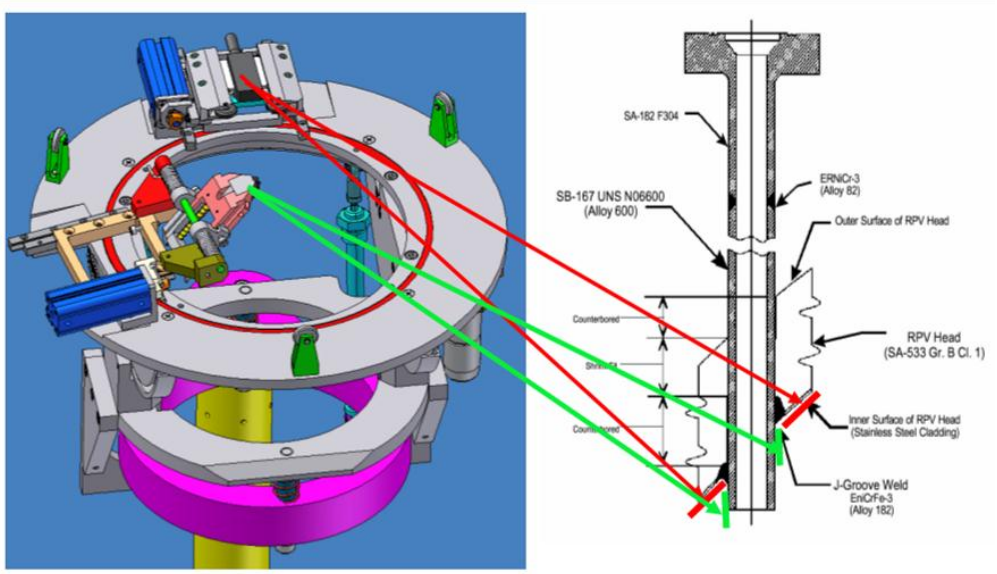

Figure 9: J-Groove module

4.3 ASR module

Surface flaws that were discovered by eddy current examination of the J-groove weld define the scope of the grinding for the automated surface repair module (ASR module).

A specially developed grinding procedure, based on the surface probing and UT results, ensures that the treatment does not affect the originally designed structural integrity basis. When compared with the other repairing methods, the ASR module significantly reduces the inspection time and radiation exposure of the personnel, and does not introduce residual stresses into the structural material. The grinding is performed with a grinder head that is powered remotely via a flexible shaft. The holder for grinding head is fixed on the ASR module. The ASR module has three axes of movement which ensure the position and remote drive of the grinding head. The C-axis is rotational and it is used to position the grinding head angularly around the penetration axis. The Linear X-axis is used for the radial positioning of the grinding tool head with respect to the penetration axis. The Z-axis positions the grinding tool head by height (measured from penetration's bottom surface).

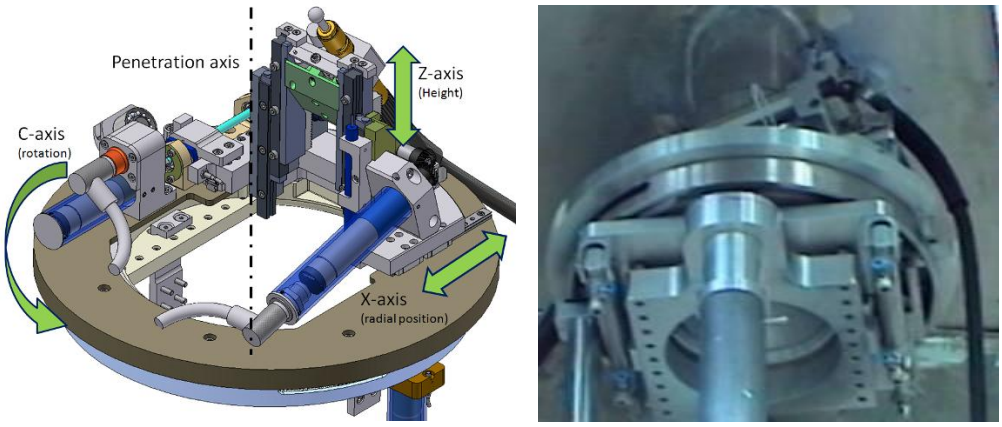

Figure 10: ASR module

5. CONCLUSION

To obtain safer functioning of nuclear power plants for longer periods of time the various inspection methods of the reactor pressure vessel head need to be performed. This article presented the ARCHER system - INETEC's solution for efficient and quick PWR's RPVH inspection and repair. Modules available for the ARCHER manipulator cover the full scope of inspection and repair methods for the RPVH.

REFERENCES

1) S.E. Cumblidge, S.R. Doctor, G.J. Schuster, R.V. Harris, S.L. Crawford, "NDE and DE of PWSCC Found in the J-Groove Weld of a Removed-From-Service Control Rod Drive Mechanism", 6th International Conference on NDE in Relation to Structural Integrity for Nuclear and Pressurized Components, Budapest, 2007, pp. 723-733
2) NRC Order EA-03-009, United States of America Nuclear Regulatory Commission, Office of Nuclear Regulation, Washington, D. C. 20555-0001, February 20, 2004.
3) Maintenance, Surveillance and In-Service Inspection in Nuclear Power Plants, Safety Standards Series No. NS-G-2.6, IAEA, Vienna, 2002.
4) M. Pajnić, D. Novosel, "Examination of VVER-1000 Reactor Pressure Vessel Head", 6th International Conference Nuclear Option in Countries with Small and Medium Electricity Grids, Dubrovnik, 2006.

EVALUATION OF THE PERFORMANCE OF COMPUTED RADIOGRAPHY SYSTEMS WITH DIFFERENT SOURCES AND DIFFERENT CONFIGURATIONS

J. Banchet, A. Peterzol, B. Bader, AREVA, France
C. Caperaa, V. Didier, EDF - CEIDRE, France

ABSTRACT

Computed radiography (CR) is a digital radiographic technique, which uses very similar equipment to conventional radiography except that in place of a film to create the latent image, an imaging plate (IP) made of a photostimulable phosphor is used [1]. CR systems are commonly used in medical applications since they have proven reliability over more than two decades. Conversely, the NDT community has discussed the efficacy of film replacement by CR for more than 15 years. Though some standards were introduced in 2005 [ASTM E 2033, CEN EN 14784-2] and in 2013 [ISO 17636-2], CR is currently not included within the French RCCM although the technique is commonly used in US for nuclear applications according to ASME (Section V, article 2).
Since 2006, AREVA has had a research and development project on this issue. This project aims to evaluate the performance differences between these two techniques within the framework of the NF standard EN 14784 for the CR and the RCCM for the film. The objective was to build a technical justification report to eventually support introduction of CR into the RCCM.
In 2009 the subject gave rise to collaboration between AREVA NP – NETEC and EDF- CEIDRE, for a joint project to establish performance limits of CR towards EN 14784 specifications and RCCM image quality indicator (IQI) requirements [2]. In this paper, we present performance comparison results of four different CR systems. The measurements were conducted in 2012 and they demonstrate the current states of achievable image quality in CR. Benchmark comparisons included two gamma sources (Selenium 75 and Iridium 192), and three different material thicknesses. Image quality was assessed in terms of EN 462 and ASTM (E 747, E 1742) IQI. The results have been scored considering ISO 17636-2, RCCM 2007, and ASME V-2010. This also permitted comparison among the different standards. Additionally, detectability measurements have been performed with the Selenium 75 gamma source and one system. Trials considered a real mock-up and different geometry configurations.

1. INTRODUCTION

Computed radiography is based on the use of photo-stimulable storage phosphor (PSP) [1]. By absorption of X-ray, a latent image is generated in PSP detector (also known as Imaging Plate), and latterly using a laser scanner, the latent image stored in IP can be read out and releases photo-stimulated luminescence (PSL) which can be collected by a light guide for reconstructing a digital image. Once the image acquisition is completed, by applying intense light, all the residual signals are removed, and the imaging plate is ready for reuse.

CR systems are commonly used in medical applications since they have proven reliability over more than two decades. Conversely, the NDT community has discussed the efficacy of film replacement by CR and Digital Detector Arrays (DDA) for more than 15 years. Several standards were published by CEN, ASTM and ASME [3][4][5][6] to support the application of phosphor imaging plates in lieu of X-ray film in the year 2005 and a set of standards for DDA application was published by ASTM in 2010 [7][8][9].

The European Community funded the project "FilmFree" (www.filmfree.eu.com), where thirty three companies and institutes tested the ability of the new technologies and developed guidelines and standards (2005-2009) [10]. The new ISO 17636-2 [11] was proposed as result of this project and a joined work group of CEN/TC121 and ISO/TC44 was set up for replacement of the EN 1435 [12]. The content of EN 1435 was transferred into ISO 17636-1 (radiographic testing of welds with films) and a new part ISO 17636-2 (radiographic testing of welds with digital detectors) was added for new digital film replacement methods. One of the key concepts is the usage of signal-to-noise (SNR) measurements as equivalent to the optical density of film. The standard has been recently published (Jan. 2013).

However, nowadays, CR is not included within the French RCCM [13], while the technique is commonly used in US for nuclear applications according to ASME (Section V, article 2).

Since 2006, AREVA has been evaluating the performance of CR in comparison to conventional RT in the framework of EN 14784 for the digital part and the RCCM for the conventional part. The objective was to build a technical justification report to eventually support introduction of CR into the RCCM.

In 2009 the subject gave rise to collaboration between AREVA NP – NETEC and EDF-CEIDRE, for a joint project to establish performance limits of CR towards EN 14784 specifications and RCCM image quality indicator (IQI) requirements [2].

It has been pointed out that computed radiographs, taken with imaging plates, achieve similar IQI visibility than film radiographs when considering X-ray tube expositions and small steel thickness (< 30 mm). But, for the gamma-graphic inspections, conventional RT achieves typically much better IQI visibility than CR; in many cases only class A (basic) of EN 14784 is achieved.

In this paper, we present performance comparison results of four different CR systems. Measurements were conducted in 2012 and demonstrate the current state of achievable image quality in CR. Performance has been evaluated for steel with thicknesses equal to 21, 26 and 41 mm using Iridium 192 (Ir192) and Selenium 75 (Se75) gamma sources. Image quality has been assessed in terms of EN 462 [14][15][16] and ASTM [17][18] IQI. And results have been scored considering the ISO 17636-2, RCCM 2007, and ASME V-2010.

In addition, for one of the investigated system and for the Se75 gamma source case, also detectability measurements have been performed with a real mock-up and for different geometry configurations.

2. METHODS AND MATERIALS

2.1. Image quality evaluation

Performance evaluation concerned four different CR systems. Due to confidentiality agreements, in the following text, the CR models are referred to as S1, S2, S3, and S4. Image quality obtained with the different systems was assessed accordingly to ISO 17636-2, RCCM 2007, and ASME V-2010. The following IQI were used:

- Wire IQI reference W6 FE EN 462-1
- Hole IQI reference H5 FE EN 462-2
- Duplex IQI in conformity with NF EN 462-5
- ASTM (Hole type 25, 30 and 35)

Measurements were carried out with and without a test object. For trials aiming at evaluating system performance, different uniform steel blocks with 21, 26 and 41 mm thicknesses were used. These test objects were placed in contact with the complete CR system formed by; the front filter (if applicable), the cassette, (which contains the metal front screen, the phosphor imaging plate (IP) and the back screen) and the back scatter filter. IQIs were positioned on the source side of the object as depicted in Figure 1, except for the duplex IQI witch was positioned directly on the image receptor (the cassette) without any test piece. Finally, when used, a pre-filter was positioned near the source between the source and the test object.

Measurements were carried out with Ir192 and Se75 gamma sources with the following characteristics:

- Ir192 size - 2.5 mm with source activity of 3,4 TBq (91.6 Ci).
- Se75 size - 3.2 mm anwith source activity of 2.16 TBq (58.5 Ci).

When performing measurements with the Duplex IQI, the source to detector distance was set to 1500 mm in order to minimize source unsharpness versus detector spatial resolution. Exposure time was adjusted to obtain, a grey level between ½ and ¾ of the max available signal in the image region containing the test object. CR scanner parameters were selected by the operator according to the vendor recommendations excepted for the pixel size, i.e. the nominal spatial resolution, which was fixed at 100 μm.

The source-to-object distance (SOD) and the source-to-detector distance (SDD) were selected accordingly to [11].
In the following table the SDD values are reported as function of the test object thickness.

OBJECT THICKNESS (mm)	SDD (mm)	
	Ir192	Se75
21	483	559
26	508	610
41	610	711

Table 1. SDD values for various sources & thicknesses

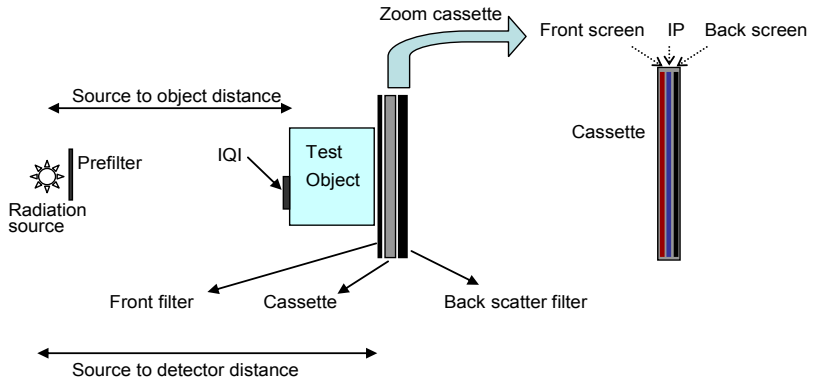

Figure 1. Schematic (not to scale) set-up representation in section 2.1. Cassette contains the metal front screen, the imaging plate (IP) and the back screen.

Obtained images were evaluated according to the monitor viewing conditions described in reference [11]. In particular, no processing of original data was considered and performed; only the contrast/brightness were adjusted by the operator. All radiographic images were interpreted by a COFREND Level 2 operator [19].
In the following, a description of each test measurement is reported for a single detector. The series of measurements were applied for each detector under investigation.

2.1.1. Measurements list for a single detector

	Object Thickness (mm)	Pixel Size	Prefilter	Penetrameter (IQI)	Front filter Pb	Front Screen Pb	Back Screen	BS filter Pb
Ir192	21	100µm	No	All on source side	0,5 mm	0,25 mm	0,5 mm Fe + 2mm Pb	4 mm
	26							
	41							
Se75	21	100µm	No	All on source side	0,20 mm	0,20 mm	0,5 mm Fe+ 2mm Pb	4 mm
	26							
	41							

Table 2. Image acquisition conditions for tests objects with the selected thicknesses in section 2.1

2.2. Detectability measurements

Detectability measurements were performed with S3 and for the Se75 gamma source case. Image quality was assessed using an Inconel mock-up (MU) 19 mm thick with 64 embedded notches. These rectangular notches are distributed at different radial distances from the MU centre and had variable sizes, as described in table 3:

Notch	Width (mm)	Depth (mm)	Length (mm)
Type 1	0,015	1,9	5,7
Type 2	0,015	3,8	11,4
Type 3	0,015	5,7	11,4
Type 4	0,023	7,6	11,4
Type 5	0,051	9,5	12,7
Type 6	0,102	9,5	12,7

Table 3. Sizes of the 64 notches embedded in the mock-up

Additional plain steel blocks were used to evaluate performance with total thicknesses equal to 19, 24, 29 and 89 mm. Several relative positions of the steel blocks and the MU were used, as depicted in Figure 2.

Similarly to image quality measurements (section 2.1), these test objects were placed in contact with the system formed by the front filter, the cassette and the back scatter filter.

Measurements were carried out with 3 mm/1.7 TBq (46 Ci) activity Se75 gamma source. Source to detector distances (SDD) were selected according to [11], except for the configuration with an 89 mm total thickness (Test 7).

Exposure time, CR scanner parameters and image processing were performed similarly to image quality measurements (see section 2.1), except for the 89 mm configuration (Test 7), for which the exposure time was adjusted down to 100 min. A description of each test measurement is reported in table 4.

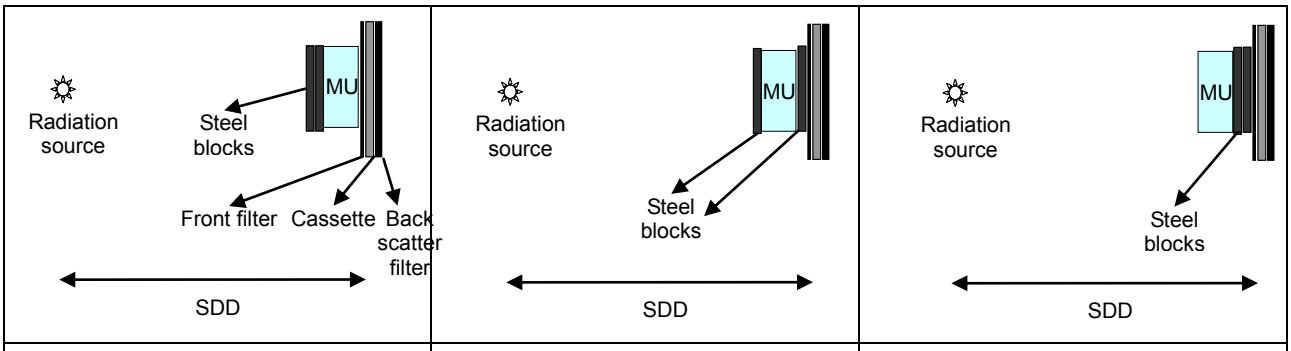

Object position case (a)	Object position case (b)	Object position case (c)

Figure 2. Schematic (not to scale) setups as described in section 2.2. The cassette contains a metal front screen, an imaging plate (IP) and a back screen. The plain steel blocks can be positioned at the source side of MU (a), the MU can be "sandwiched" between two steel blocks (b), or the steel blocks can be positioned behind the MU in contact with the front filter and the cassette (c).

	Test Object	Object position case	Total Thickness	Source to detector distance	Front filter	Front Screen	Back Screen	BS filter
Test 1	MU in contact with FC	none	19 mm	340 mm	0,2 mm Pb	0,2 mm Pb	0,5 mm Fe + 0,2 mm Pb	4 mm Pb
Test 2	(5 mm of Fe + MU) in contact with FC	(a)	24 mm	400 mm				
Test 3	(MU + 5mm of Fe) in contact with FC	(c)						
Test 4	(10 mm of Fe + MU) in contact with FC	(a)	29 mm	460 mm				
Test 5	(5 mm of Fe + MU + 5 mm of Fe) in contact with FC	(b)						
Test 6	(MU + 10 mm of Fe) in contact with FC	(c)						
Test 7	(MU + 70 mm of Fe) in contact with FC	(c)	89 mm	533 mm				

Table 4. Image acquisition conditions for tests objects with the selected thicknesses in section 2.2. FC is unit composed by the Front filter and the Cassette.

3. RESULTS

Before presenting the results, some explanations/definitions concerning the symbols used in the following tables must be introduced:

- 1) Letter Y is used when conformity to the code/standard is achieved, N when not.
- 2) In the ISO 17636-2 it is stated that "In the case where Ir192 or Se75 sources are used, IQI values worse than listed in tables B.1 to B.12 may be accepted by agreement of contracting parties as follows (single wall single image and double wall single image techniques, class B):

– 10 mm < w ≤ 40 mm 1 wire or step-hole value less for Ir192
– 5 mm < w ≤ 20 mm 1 wire or step-hole value less for Se75"

When the conformity to the standard requirements is achieved by invoking this rule, the symbol "*" is added to the letter Y, which indicates the conformity being respected.
- 3) When scoring the IQI values, it has been noted also if the obtained value is equal to the minimum required by the standard or the code (Y) or is larger (Y(+1), Y(+2), …).
- 4) During an examination, the operator can choose between a wire and a hole IQI type. It is not mandatory to use both. As a consequence, an X-ray image satisfies the standard requirements if the value of at least one of the IQI (wire or hole) is ≥ than that listed in the standard reference tables.
However, in order to make a detailed analysis of the results, it was decided to distinguish between two cases: if both IQI values satisfy the standard requirements, then the phrase "conformity is achieved" is used, whereas if one of the IQI values satisfies the standard requirements, then the phrase "conformity is partially achieved" is used. It is important to underline that the second sentence does not make sense in the standards context. It is only used in order to better characterize/compare the performance of the different investigated systems. First, image quality results obtained for each investigated system
will be presented. Then, the systems are compared using the ISO 17636-2, RCCM and ASME image quality criteria, and also the exposure time. Finally, detectability results using the measurements carried with the mock-up are commented.

3.1. System performance comparisons

With Ir192

Ir 192	Thick mm	Wire IQI required by ISO 17636	Wire IQI required by RCCM	Wire IQI saw	Hole IQI required by ISO 17636	Hole IQI required by RCCM	Hole IQI saw	Wire IQI required by ASME	Wire IQI saw	Hole IQI required by ASME	Hole IQI saw	Duplex IQI required by ISO 17636	Duplex IQI saw	SNR_N required by ISO 17636	SNR_N meas.
S1	21	**0,25mm/W12**	**0,25mm**	0,25mm/W12	**0,50mm/H7**	**0,63mm**	0,63mm/H8	**0,51mm**	0,25mm	**25/2T**	20/1T	**10D**	9D	**100**	455
	26	**0,25mm/W12**	**0,32mm**	0,25mm/W12	**0,50mm/H7**	**0,80mm**	0,63mm/H8	**0,64mm**	0,25mm	**30/2T**	25/1T	**10D**	9D	**100**	524
	41	**0,40mm/W10**	**0,50mm**	0,32mm/W11	**0,80mm/H9**	**1,25mm**	0,80mm/H9	**0,81mm**	0,33mm	**35/2T**	1T	**9D**	9D	**100**	532
S2	21	**0,25mm/W12**	**0,25mm**	0,4mm/W10	**0,50mm/H7**	**0,63mm**	0,80mm/H9	**0,51mm**	0,41mm	**25/2T**	20/1T	**10D**	9D	**100**	80
	26	**0,25mm/W12**	**0,32mm**	0,4mm/W10	**0,50mm/H7**	**0,80mm**	0,80mm/H9	**0,64mm**	0,41mm	**30/2T**	25/2T	**10D**	9D	**100**	68
	41	**0,40mm/W10**	**0,50mm**	0,32mm/W11	**0,80mm/H9**	**1,25mm**	0,80mm/H9	**0,81mm**	0,33mm	**35/2T**	1T	**9D**	9D	**100**	93
S3	21	**0,25mm/W12**	**0,25mm**	0,32mm/W11	**0,50mm/H7**	**0,63mm**	0,63mm/H8	**0,5 mm**	0,33mm	**25/2T**	20/2T	**10D**	10D	**100**	837
	26	**0,25mm/W12**	**0,32mm**	0,32mm/W11	**0,50mm/H7**	**0,80mm**	0,63mm/H8	**0,64mm**	0,33mm	**30/2T**	25/1T	**10D**	10D	**100**	511
	41	**0,40mm/W10**	**0,50mm**	0,50mm/W09	**0,80mm/H9**	**1,25mm**	0,80mm/H9	**0,81mm**	0,51mm	**35/2T**	1T	**9D**	10D	**100**	513
S4	21	**0,25mm/W12**	**0,25mm**	0,32mm/W11	**0,50mm/H7**	**0,63mm**	0,50mm/H7	**0,51mm**	0,33mm	**25/2T**	20/1T	**10D**	9D	**100**	49
	26	**0,25mm/W12**	**0,32mm**	0,4mm/W10	**0,50mm/H7**	**0,80mm**	0,63mm/H8	**0,64mm**	0,41mm	**30/2T**	25/1T	**10D**	9D	**100**	125
	41	**0,40mm/W10**	**0,50mm**	0,4mm/W10	**0,80mm/H9**	**1,25mm**	0,80mm/H9	**0,81mm**	0,41mm	**35/2T**	1T	**9D**	9D	**100**	47

Table 5. All Systems performance evaluation results

With Se75

Se75	Thick mm	Wire IQI required by ISO 17636	Wire IQI required by RCCM	Wire IQI saw	Hole IQI required by ISO 17636	Hole IQI required by RCCM	Hole IQI saw	Wire IQI required by ASME	Wire IQI saw	Hole IQI required by ASME	Hole IQI saw	Duplex IQI required by ISO 17636	Duplex IQI saw	SNR_N required by ISO 17636	SNR_N meas.
S1	21	**0,25mm/W12**	**0,25mm**	0,25mm/W12	**0,50mm/H7**	**0,63mm**	0,5mm/H7	**0,51mm**	0,25mm	**25/2T**	20/1T	**10D**	9D	**100**	595
	26	**0,25mm/W12**	**0,32mm**	0,32mm/W11	**0,50mm/H7**	**0,80mm**	0,63mm/H8	**0,64mm**	0,33mm	**30/2T**	1T	**10D**	9D	**100**	643
	41	**0,40mm/W10**	**0,50mm**	0,32mm/W11	**0,80mm/H9**	**1,25mm**	0,8mm/H9	**0,81mm**	0,33mm	**35/2T**	1T	**9D**	9D	**100**	421
S2	21	**0,25mm/W12**	**0,25mm**	0,32mm/W11	**0,50mm/H7**	**0,63mm**	0,63mm/H8	**0,51mm**	0,33mm	**25/2T**	20/1T	**10D**	10D	**100**	96
	26	**0,25mm/W12**	**0,32mm**	0,32mm/W11	**0,50mm/H7**	**0,80mm**	0,63mm/H8	**0,64mm**	0,33mm	**30/2T**	1T	**10D**	10D	**100**	125
	41	**0,40mm/W10**	**0,50mm**	0,5mm/W9	**0,80mm/H9**	**1,25mm**	0,8mm/H9	**0,81mm**	0,51mm	**35/2T**	2T	**9D**	10D	**100**	94
S3	21	**0,25mm/W12**	**0,25mm**	0,32mm/W11	**0,50mm/H7**	**0,63mm**	0,5mm/H7	**0,51mm**	0,33mm	**25/2T**	20/1T	**10D**	10D	**100**	478
	26	**0,25mm/W12**	**0,32mm**	0,32mm/W11	**0,50mm/H7**	**0,80mm**	0,63mm/H8	**0,64mm**	0,33mm	**30/2T**	1T	**10D**	10D	**100**	550
	41	**0,40mm/W10**	**0,50mm**	0,63mm/W8	**0,80mm/H9**	**1,25mm**	1mm/H10	**0,81mm**	0,63mm	**35/2T**	2T	**9D**	10D	**100**	354
S4	21	**0,25mm/W12**	**0,25mm**	0,4mm/W10	**0,50mm/H7**	**0,63mm**	0,5mm/H7	**0,51mm**	0,25mm	**25/2T**	20/1T	**10D**	9D	**100**	141
	26	**0,25mm/W12**	**0,32mm**	0,5mm/W9	**0,50mm/H7**	**0,80mm**	0,8mm/H9	**0,64mm**	0,33mm	**30/2T**	1T	**10D**	9D	**100**	229
	41	**0,40mm/W10**	**0,50mm**	0,4mm/W10	**0,80mm/H9**	**1,25mm**	0,8mm/H9	**0,81mm**	0,41mm	**35/2T**	1T	**9D**	9D	**100**	177

Table 6. All Systems performance evaluation results

3.2. Systems comparison in terms of wire/hole IQI ISO 17636-2 requirements

In the following table, image quality evaluation results via conformity to the wire/hole IQI ISO 17636-2 requirements are reported.

	Conformity to ISO 17636-2 W/H IQI															
	S1				S2				S3				S4			
Thickness (mm)	W		H		W		H		W		H		W		H	
	Se75	Ir192	Se75	Ir192	Se75	Ir192	Se75	Ir192	Se75	Ir192	Se75	Ir192	Se75	Ir192	Se75	Ir192
21	Y	Y	Y	Y*	N	N	N	N	N	Y*	Y	Y*	Y	Y*	Y	Y
26	N	Y	N	Y*	N	N	N	N	N	Y*	N	Y*	N	N	N	Y*
41	Y(+1)	Y(+1)	Y	Y	N	Y(+1)	Y	Y	N	N	N	Y	Y	Y	Y	Y

Table 7. Systems comparison in terms of wire/hole IQI ISO 17636-2 requirements with the two gamma sources

From table 7, it emerges that:

With Ir192:

S1 satisfies the conformity for 3/3 thicknesses, (both IQI 3/3)
S4 satisfies the conformity for 2/3 thicknesses (partially 3/3),
S3 satisfies the conformity for 2/3 thicknesses (partially 3/3),
S2 satisfies the conformity for 1/3 thicknesses (both IQI 1/3).

With Se75:

S1 satisfies the conformity for 2/3 thicknesses, (both IQI 2/3)
S4 satisfies the conformity for 2/3 thicknesses (both IQI 2/3),
S3 satisfies the conformity for 0/3 thicknesses (partially 1/3),
S2 satisfies the conformity for 0/3 thicknesses (partially 1/3)

3.3. Systems comparison in terms of wire/hole IQI RCCM requirements

In the following table, image quality evaluation results via conformity to the wire/hole IQI RCCM requirements are reported.

	Conformity to RCCM W/H IQI Requirements															
	S1				S2				S3				S4			
Thickness (mm)	W		H		W		H		W		H		W		H	
	Se75	Ir192	Se75	Ir192	Se75	Ir192	Se75	Ir192	Se75	Ir192	Se75	Ir192	Se75	Ir192	Se75	Ir192
21	Y	Y	Y(+1)	Y	N	N	Y	N	N	N	Y(+1)	Y	Y	N	Y(+1)	Y(+1)
26	Y	Y(+1)	Y(+1)	Y(+1)	Y	N	Y(+1)	Y	Y	Y	Y(+1)	Y(+1)	Y	N	Y	Y(+1)
41	Y(+2)	Y(+2)	Y(+2)	Y(+2)	Y	Y(+2)	Y(+2)	Y(+2)	N	Y	Y(+1)	Y(+2)	Y(+1)	Y(+1)	Y(+2)	Y(+2)

Table 8. Systems comparison in terms of wire/hole IQI RCCM requirements with the two gamma sources

From table 8, it emerges that:
With Ir192:
S1 satisfies the conformity for 3/3 thicknesses, (both IQI 3/3)
S3 satisfies the conformity for 2/3 thicknesses (partially 3/3).
S4 satisfies the conformity for 1/3 thicknesses (partially 3/3),
S2 satisfies the conformity for 1/3 thicknesses (partially 3/3),
With Se75:
S1 satisfies the conformity for 3/3 thicknesses, (both IQI 3/3)
S4 satisfies the conformity for 3/3 thicknesses (both IQI 3/3),
S2 satisfies the conformity for 2/3 thicknesses (partially 3/3)
S3 satisfies the conformity for 1/3 thicknesses (partially 3/3),

3.4. Systems comparison in terms of wire/hole IQI ASME requirements

In the following table, image quality evaluation results via conformity to the wire/hole IQI ASME requirements are reported.

	Conformity to ASME IQI Requirements															
	S1				S2				S3				S4			
Thickness (mm)	W		H		W		H		W		H		W		H	
	Se75	Ir192	Se75	Ir192	Se75	Ir192	Se75	Ir192	Se75	Ir192	Se75	Ir192	Se75	Ir192	Se75	Ir192
21	Y(+3)	Y(+3)	Y(+5)	Y(+3)	Y(+2)	Y(+1)	Y(+5)	Y(+3)	Y(+2)	Y(+2)	Y(+5)	Y(1)	Y(+3)	Y(+2)	Y(+5)	Y(+3)
26	Y(+3)	Y(+4)	Y(+4)	Y(+3)	Y(+3)	Y(+2)	Y(+4)	Y(+1)	Y(+3)	Y(+3)	Y(+4)	Y(+3)	Y(+3)	Y(+2)	Y(+4)	Y(+3)
41	Y(+4)	Y(+4)	Y(+4)	Y(+2)	Y(+2)	Y(+4)	Y	Y(+2)	Y(+1)	Y(+2)	Y	Y(+2)	Y(+3)	Y(+3)	Y(+4)	Y(+2)

Table 9. Systems comparison in terms of wire/hole IQI ASME requirements with the two gamma sources

From table 9, it emerges that: all systems largely satisfy the conformity to ASME IQI requirements, with both gamma sources.

3.5. Systems comparison in terms of ISO 17636 Duplex IQI and SNR_N

In the following table, image quality evaluation results via conformity to the ISO 17636 Duplex IQI and SNR_N requirements are reported.

	Conformity to ISO 17636-2 DUPLEX IQI and SNR_N requirements															
	S1				S2				S3				S4			
Thickness (mm)	Duplex		SNR_N		Duplex		SNR_N		Duplex		SNR_N		Duplex		SNR_N	
	Se75	Ir192	Se75	Ir192	Se75	Ir192	Se75	Ir192	Se75	Ir192	Se75	Ir192	Se75	Ir192	Se75	Ir192
21	N	N	Y	Y	Y	N	N	N	Y	Y	Y	Y	N	N	Y	N
26	N	N	Y	Y	Y	N	Y	N	Y	Y	Y	Y	N	N	Y	Y
41	Y	Y	Y	Y	Y	Y	N	N	Y	Y	Y	Y	Y	Y	Y	N

Table 10. Systems comparison in terms of ISO 17636 Duplex IQI and SNR_N with the two gamma sources

From table 10, it emerges that:
With both gamma sources:
S3 satisfies the conformity to both Duplex IQI and SNR_N,
S1 does not satisfy the conformity to the Duplex IQI in two cases out of 3 (2/3 cases), but it does for the SNR_N
With Ir192:
S4 does not satisfy the conformity to Duplex IQI in 2/3 cases, and does not for the SNR_N in 2/3 cases,
S2 does not satisfy the conformity to Duplex IQI in 2/3 cases, and does not satisfy conformity to SNR_N in 0/3 cases.
With Se75:
S4 does not satisfy the conformity to Duplex IQI in 2/3 cases, but it does for the SNR_N in 3/3 cases,
S2 satisfy the conformity to the Duplex IQI in 3/3 cases, and does satisfy conformity to SNR_N in 1/3 cases.

3.6. Systems comparison in terms of exposure time

In the following table, systems comparison in terms of exposure time is reported. To ease a direct comparison between Se75 and Ir192 trials, exposure times were recalculated for Ir192 in taking into account an equivalent activity and distance than for the Se75 source. Results are presented in Table 11.

Thick in mm	S1		S2		S3		S4	
	Ir192	Se 75	Ir192	Se 75	Ir192	Se 75	Ir192	Se 75
21	2	9	2	5	3,1	12	5,1	11
26	7,1	12	3,1	15	4,3	12	17	22
41	20,4	24	15,5	27	14,4	15	46	50

Table 11. Systems comparison in terms of exposition time with the two gamma sources

Regarding the exposure time, it is apparent that each system operates differently. If we consider the exposure time mean value for the three considered thicknesses, we can list the systems from the fastest to the slowest as follows:

With Ir192:
S2 presents a mean exposure time of 6,8 min
S1 presents a mean exposure time of 7,2 min
S3 presents a mean exposure time of 9,8 min
S4 presents a mean exposure time of 22,7 min
With Se75 :
S3 presents a mean exposure time of 13 min
S1 and S2 present a similar mean exposure time of 15 min and 15,6 min
S4 presents a mean exposure time of 27,6 min

3.7. Detectability performance of a single system

In these trials using a mock-up, it was shown that the notches' visibility was not very dependent on the object position and thickness. In general, visibility degradation was observed when the additional 10 mm of steel were positioned in contact with the FC (moving from Test 5 to Test 6).

The image quality obtained in Test 7 (89 mm total thickness) did not allow for the detection of any IQI or any notch.

Except for Test 7, type 4 and type 5 notches were detected in all situations.
Detection of type 1, 2, 3 and 6 notches is not systematic and depends on the different tests. The relation between radial distance to mock-up centre (i.e. source axe) and detectability is not linear.

4. DISCUSSION

It has been pointed out that if we use the ISO 17636-2 wire/hole IQI requirements to "score" system performance, we obtain the following grading:
From table 5, with Ir192 it emerged that:
S1 satisfies the conformity for 3/3 thicknesses, (both IQI 3/3)
S4 satisfies the conformity for 2/3 thicknesses (partially 3/3),
S3 satisfies the conformity for 2/3 thicknesses (partially 3/3),
S2 satisfies the conformity for 1/3 thicknesses (partially 1/3).
From table 6, with Se75 it emerged that:
S1 satisfies conformity for 2/3 thicknesses, (both IQI 2/3)
S4 satisfies conformity for 2/3 thicknesses (both IQI 2/3),
S3 satisfies conformity for 0/3 thicknesses (partially 1/3),
S2 satisfies conformity for 0/3 thicknesses (partially 1/3),
On the other hand, if we consider the SNR_N for the three thicknesses as criterion, the grading is as follows:
With Ir192:
S3 presents a mean SNR_N of 620,
S1 presents a mean SNR_N of 503,
S2 presents a mean SNR_N of 80,
S4 presents a mean SNR_N of 73.
With Se75:
S1 presents a mean SNR_N of 553,
S3 presents a mean SNR_N of 460,
S4 presents a mean SNR_N of 182,
S2 presents a mean SNR_N of 105

These rankings are not consistent. Indeed, system S3 which presents the best SNR and spatial resolution, in many cases, does not detect the required wire/hole IQI. A possible explanation may be associated with a high level of the so-called structured noise affecting the imaging plates. Two systems presenting the same SNR, can be characterized by a different content of the structured noise giving rise to different performance. A method to verify this hypothesis could be to measure the noise power spectrum. On the other hand, with Se75, the system S1 is the best, respecting both ISO and SNR criteria. The S3 results are equivalent with the Ir192. We see, in any cases, that the SNR for Se75 is higher than the required reference (100).

As far as spatial resolution is concerned, in general, though systems were set at 100 µm pixel size (100 µm corresponds to the Duplex IQI D10, i.e. the value required by the ISO 17636-2 for a thickness comprised between 12 and 40 mm), in practice, the effective measured pixel size is slightly larger: D9, i.e. 130 µm. Rigorously, we shall say that it is comprised between 100 and 130 µm. Besides, it was pointed out that systems achieving the best image quality in terms of the wire/hole IQI are those which do not completely satisfy the IQI Duplex requirement (one value less). Combining this outcome with the SNR results, it seems that two of the outstanding parameters are the noise level (compared to the signal) and its "quality" (namely a good white noise versus a bad structured one).

It emerged also that to satisfy Duplex IQI along the ISO standard, imaging system has to be set at a nominal spatial resolution smaller than required.

It has been also highlighted that the ISO standard is the most severe, followed by the RCCM and then by ASME. The latter does not include a SNR and spatial resolution evaluation criteria since only the wire/hole IQI are used to assess image quality. On the other hand, it emerged that in some cases it was not possible to outline a "linear" correspondence between wire/hole IQI results, SNR and duplex IQI values.

From section 3.7, a modeling study using MODERATO code was deemed necessary in the future, in order to understand the notches' visibility degradation that was observed for types 1, 2, 3 and 6 notches.

5. CONCLUSIONS

All the investigated systems satisfy the ASME IQI requirements for all the tested thicknesses. From the RCCM and the ISO perspective, S1 was in conformity and S3 and S4 were in partial conformity using the Ir192 source. With Se75, S1 and S4 are fully in conformity to the RCCM, and partially for the others, while from the ISO point of view only S1 and S4 are partially in conformity.

It must be reiterated that measurements were performed with a spatial resolution set at 100 µm. It is realistic to predict that with a smaller pixel size, conformity would be more easily achieved.

It can be said that, in most cases, two of the considered systems (S1 and S4) satisfy the ISO standard at 100 µm, and that at 50 µm they would probably be three (S1, S4 plus S3). For all the thicknesses, three systems, S1, S3 and S4, satisfy the RCCM requirements at 100 µm. This is an important result supporting the introduction of CR into the RCCM.

In general, and for the considered thickness range, it is not evident to establish which source furnishes best results. For S1, the two sources are almost equivalent in terms of IQI values. For S2, better results are obtained with the Se75 gamma source, while the opposite trend is observed for S4. For S3, slightly better results are obtained with Ir192, but only for the 41 mm thickness case. These results are quite surprising since the energy spectrum of Se75 contains lower energies than that of Ir192. It would be very useful to investigate this outcome in detail both experimentally and theoretically via X-ray image simulation tools.

As expected, exposure time is larger with the Se75 source. However the ratio between Se75 and Ir192 exposure time is not constant for the considered thickness range (21-41 mm). When moving from the Se75 to the Ir192 source, exposure time is multiplied by a factor 2,5-6 at 21 mm, and by a factor 1-3,5 at 41 mm. Exposure time ratio decrease with test piece thickness increase could arise from the increased similarity of the transmitted photon spectrum. With the thicker the sample, the spectrum is more filtered resulting in a more high energy spectrum.

The detectability results obtained on mock-up with notches gave a first quantitative approach using a Se75 source with a CR system.
Finally, it is thought that the existing discrepancy between the different standards poses non negligible difficulties in the process of introducing CR into nuclear inspection practice.
Harmonization among these standards and codes would certainly benefit manufacturers, in enabling them to fulfil all requirements and end-users, who could then choose a CR system to comply with their applications and needs.

REFERENCES

[1] The physics of computed radiography J.A. Rowlands Phys. Med. Biol. 47(2002) R123-R166.

[2] Digital radiography performance study in the nuclear context D. Tisseur, J. Banchet, E. Martin, and C. Luc COFREND 2011 conference.

[3] EN 14784-1:2005: Non destructive testing- industrial computed radiography with storage phosphor imaging plates. Part 1 : Classification of system

[4] EN 14784-2:2005: Non destructive testing- industrial computed radiography with storage phosphor imaging plates. Part 2 : General principles for testing of metallic materials using X-rays and gamma rays

[5] ASTM E2033 - 99(2006) Standard Practice for Computed Radiology (Photostimulable Luminescence Method)

[6] ASME Section V Article 2: Radiographic examination (2005)

[7] ASTM E2698 - 10 Standard Practice for Radiological Examination Using Digital Detector Arrays

[8] ASTM E2736 - 10 Standard Guide for Digital Detector Array Radiology

[9] ASTM E2737 - 10 Standard Practice for Digital Detector Array Performance Evaluation and Long-Term Stability

[10] Strategies for Film Replacement in Radiography - Approaches Used in the New Standards, Uwe ZSCHERPEL, Uwe EWERT, Klaus BAVENDIEK, Mirko JECHOW, DIR2011 Conference

[11] ISO 17636-2 : Non-destructive testing of welds- Radiographic testing – Part 2 : X and gamma ray techniques with digital detector

[12] EN 1435:1997 Non-destructive examination of welds. Radiographic examination of welded joints

[13] RCCM – Edition 2007- MC 3000

[14] EN 462-1 : Non destructive testing – Image quality of radiographs – Part 1 : Image quality indicators (wire type), determination of image quality value

[15] EN 462-2 : Non destructive testing – Image quality of radiographs – Part 2 : Image quality indicators (step/step hole)

[16] EN 462-5 : Non destructive testing – Image quality of radiographs – Part 5 : Image quality indicators (duplex wire type), determination of image unsharpness value

[17] ASTM E747 - 04(2010) Standard Practice for Design, Manufacture and Material Grouping Classification of Wire Image Quality Indicators (IQI) Used for Radiology

[18] ASTM E1025 - 11 Standard Practice for Design, Manufacture, and Material Grouping Classification of Hole-Type Image Quality Indicators (IQI) Used for Radiology

[19] ISO 9712 : Qualification and certification of the NDT personnel – general principles

RESULTS FROM NONDESTRUCTIVE EXAMINATION OF PWR VESSEL INTERNALS

Jack Spanner, EPRI, USA

Introduction

This paper describes the initial results obtained to date from examining pressurized water reactor (PWR) vessel internals in accordance with the requirements of the EPRI Material Reliability Program (MRP) inspection and evaluation guidelines. These examinations have been performed at seven nuclear plants. The objective of this aging management program for internals is to provide utilities a systematic approach to monitor potential degradation of internals components, support power up-rate activities, and meet license renewal requirements. An accompanying inspection standard for PWR internals is implemented with the guideline. The inspection standard contains requirements specific to the inspection methodologies involved as well as requirements for qualification of the NDE systems used to perform those inspections.

The Electric Power Research Institute's Materials Reliability Program (MRP) has developed an Inspection and Evaluation (I&E) Guideline (MRP-227-A) [1] to meet the requirements for aging management of pressurized water reactor vessel internals and license renewal activities. To support the guidelines MRP has also developed an Inspection Standard (MRP-228, Rev 1) [2] that provides the inspection requirements. Generally, visual examinations will be used to detect evidence of age related degradation mechanisms for all components, except ultrasonics are used to volumetrically examine some of the bolts. During development of the I&E Guidelines several components were identified as being potential areas to consider for inspection. Most of these components are not typically included in a nuclear in-service inspection program with the pressure boundary components. MRP-227 addresses the following damage mechanisms:

- Stress Corrosion Cracking (Cracking)
- Irradiation-Assisted Stress Corrosion Cracking (Cracking)
- Wear (Loss of Material)
- Fatigue (Cracking)
- Thermal Aging Embrittlement (Loss of Toughness > Cracking)
- Irradiation Embrittlement (Loss of Toughness > Cracking)
- Void Swelling and Irradiation Growth (Dimensional Change/Distortion > Cracking)
- Thermal and Irradiation-Enhanced Stress Relaxation or Irradiation- Enhanced Creep (Loss of Preload > Wear/Cracking)

NDE System Qualification

The process for NDE system qualification described herein is based on the use of technical justifications as described in the American Society of Mechanical Engineers Boiler and Pressure Vessel Code, Section V, Article 14 [3] and is similar to the original version of the European Network for Inspection Qualification (ENIQ). The Technical Justification is a detailed explanation of the procedure including the method, and any laboratory or field experience that support the procedure capabilities. The Technical Justification provides the technical basis and rationale for the qualification. This qualification process builds on the field experience and previous work performed by the inspection vendors and other inspection organizations to develop the examination systems already in use today throughout industry and does not mandate any new performance demonstrations. Where there is a need to simulate performance specific examinations for the purpose of preparing the Technical Justifications required by the Inspection Standard, or for other reasons, such as to qualify improved techniques, new or existing vendor mockups may be used or, where mockups of such components are not otherwise available, mockups developed by the MRP may be used. The Technical Justification is a required written report providing the detailed explanation of the examination process, including the theory of the examination technique as applied to reactor internals inspections, the essential variables of the procedure, other influential parameters important to the overall performance of the examination system, and field experience and/or mockup demonstrations supporting the capabilities of the NDE system.

The Technical Justification includes a description of the active or anticipated material damage mechanisms and the NDE evaluation process used to interpret the results of the applied examination technique. Prior to use of an NDE system for reactor internals inspections, the Technical Justification report shall be reviewed and approved by the utility.

Visual Inspection of Reactor Pressure Vessel (RPV) Internals, Components

The Inspection Standard is to be used by pressurized water reactor utilities when performing visual examination (Enhanced VT-1 (EVT-1), detailed VT-1 and general VT-3) of reactor vessel (RPV) internals, components, and associated repairs to meet the recommendations set forth in applicable Materials Reliability Program documents. As used in this paper, the EVT-1 and VT-1 techniques are used for detecting surface imperfections and flaws such as cracks, wear, erosion, and corrosion. Specifically, EVT-1 is used for the detection of surface breaking flaws, whereas VT-1 is used to detect surface conditions such as gaps. VT-3 is used for detecting general degradation conditions. ASME Section XI [4] describes VT-1 and VT-3 while MRP-228 provides the requirements for EVT-1. The EVT-1 and VT-1 need to resolve the same .044 inch (1 mm) characters. However, the EVT-1 requires .5 inch/sec (13 mm/sec) maximum scan speed, cleaning assessment and a viewing angle within 30 degrees perpendicular to the surface.

Utilities shall also conduct site specific training for all personnel evaluating inspection data. The training shall include utility-specific procedural requirements, configuration details, previous inspection results, operation of inspection equipment, specific outage inspection scope, and any other pertinent information related to inspection, evaluation and reporting, as applicable. The training is to be conducted prior to inspections for each refueling outage. Personnel evaluating inspection data shall have a minimum of ten (10) hours of work time experience performing EVT-1, VT-1 and/or VT-3 remote visual inspections of reactor internals

Ultrasonic Examination of Bolting in Reactor Pressure Vessel Internals

This section describes requirements and recommendations for the performance of ultrasonic examination of bolts in reactor vessel internal components.

UT Technical Justifications and Demonstrations Ultrasonic examination systems are required to be qualified by a Technical Justification (TJ) as described earlier. The organization that prepared the procedure will also be responsible for preparing the Technical Justification. The utilities are responsible for approving the Technical Justification.

Equipment Requirements The equipment included in the UT procedure as an essential variable or range of variables as described in this section must be used for the examinations and be included in the technical justification and demonstration, as applicable (Figure 1). Examination coverage should be reported as the number or percentage of the bolts that were successfully examined out of the population of bolts that were scheduled for examination.

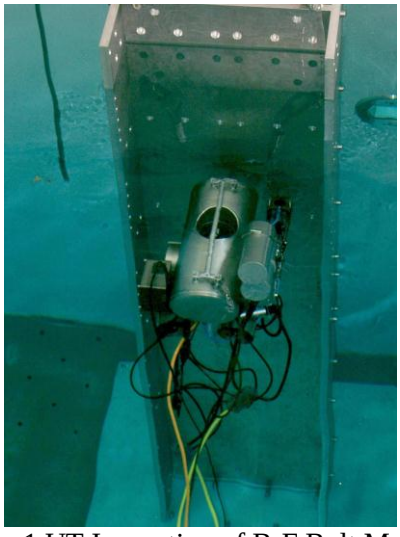

Figure 1 UT Inspection of B-F Bolt Mockup

Application

The accompanying Inspection Standard is intended for the use of individual plant owners in preparing inspection procedures and qualifying NDE systems used to perform inspections needed for their PWR internals aging management programs. As a companion to the I & E Guidelines of MRP-227, this standard is required for compliance with one of the mandatory requirements of MRP-227. These requirements are applicable to internals in the three Nuclear Steam Supply System pressurized water reactor designs currently operating in the United States: Babcock & Wilcox (B&W), Combustion Engineering (CE), and Westinghouse Nuclear, respectively.

PWR Internals Inspection Results

Seven PWR units have completed or partially completed inspections of their internals in accordance with MRP-227. Some owners decided to perform the inspections during one, two or three refueling outages so some of the owners that decided to inspect over multiple outages have not completed their inspections yet. The inspections so far have essentially met the minimum extent of inspections with very few detections of flawed components. Almost all of the detections have been located in bolting, including the locking devices such as locking bars and welds, The following list summarizes the results of the inspections conducted to date:

- Unit 1:
    - Each CRGT Guide Card is acceptable until the next scheduled inspection required by MRP-227-A based upon wear projections performed
    - Observed volumetric Guide Card wear ranging from 21%-51%.
- Unit 2 :
    - Baffle to Former Bolts –Replace or UT of plant specific minimum bolt pattern or alternate bolts as selected by analysis; 1 bolt (or 1%) identified with a relevant UT indication
    - Guide Card Wear –100% VT-3 Inspection; no appreciable wear seen

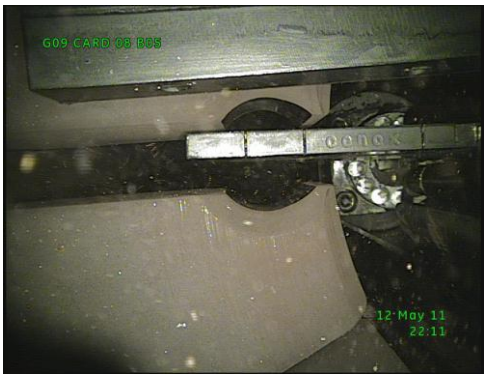

    - CRGT Flange Welds –100% EVT-1 Inspection; no relevant indications identified

- Core Barrel Upper Flange Weld –100% EVT-1 Inspection; no relevant indications identified
- Thermal Shield Flexures –100% VT-3; no relevant conditions
- Core Barrel Baffle Edge Bolts & Seams –100% VT-3 (all 16 high fluence seams for full length); no relevant conditions
- Baffle Former Assembly –100% VT-3; no relevant conditions

- Unit 3:
  - Only one UT detection of a likely flaw in one bolt.
  - VT-3 identified two bolts deformed at the hex head points
  - VT-3 also identified one baffle to former bolt with one missing locking bar weld

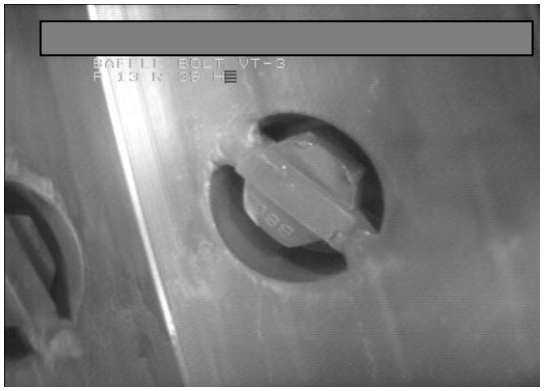

  - VT-3 also identified one edge bolt with one missing locking bar weld

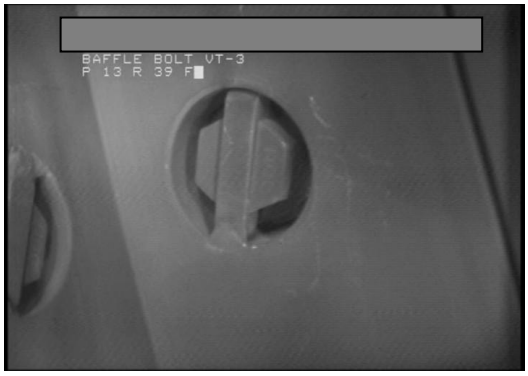

- Unit 4:
  - All 1088 baffle to former bolts were UT and VT-3 examined. All accessible 936 baffle edge bolts were VT-3 examined.
  - Baffle former bolt UT detected indications in two bolts located at the head to shank region of the bolt.
  - With only two assumed failed bolts out of 1088, there is significant margin above the industry evaluation guideline for reactor internals
- Unit 5:
  - No relevant indications
- Unit 6:
  - UT – 5 lower core barrel (LCB) with crack like indications
  - VT – 1 LCB locking device with a missing weld on one side and a small weld on the other.
  - The coverage for the VT-3 examination of 7 of the LCB bolts and their locking devices was 40% to 50% due to the partial obstruction from the stand, although 100% of the accessible surfaces were examined.
  - UT – 1 flow distributor bolt with crack like indication.
  - 860 out of 864 baffle-to-former bolts
  - 4 baffle-to-former bolts were un-inspectable due to large welds on locking bars.

- Unit 7
    - Guide Cards - 93 of 297 guide cards with recordable indications (wear) were identified.
    - Based on Operation Curve Method – 2 CRGTs yellow in ~ 7 EFPY, 3 CRGTs yellow in 17 to 20 EFPY, and 28 yellow in 20+ EFPY
    - Based on Operation Curve Method – 1 CRGT red in ~ 7 EFPY and 32 CRGTs red in 20+ EFPY
    - CRGT Flange Welds
    - 110 of 118 (93%) accessible welds in 24 Peripheral CRGTs

Note: Missed welds attributed to interference from RV Flange Protector Ring
    - CB Lower Girth Weld
    - (Covered by thermal shield)
    - 78% of exterior surface
    - Weld features not visible
    - CB Lower Flange Weld
    - 92% of exterior surface (RV Flange Protector Ring interference)
    - Weld features not visible

References

1. Materials Reliability Program: PWR Internals Inspection and Evaluation Guidelines (MRP-227-A), Electric Power Research Institute, Palo Alto, CA, 2011. 1022863
2. Materials Reliability Program: Inspection Standard for PWR Internals (MRP-228, Rev 1), EPRI, Palo Alto, CA 2012. 1025147
3. ASME Boiler and Pressure Vessel Code, Section V, Nondestructive Examination, American Society of Mechanical Engineers, New York, NY, 2007 Edition through 2008 Addenda
4. ASME Boiler and Pressure Vessel Code, Section XI, Inservice Inspection, American Society of Mechanical Engineers, New York, NY, 2004 Edition through 2008 Addenda

FLAW HANDBOOK DEVELOPMENT FOR VVER-1000 RPV INLET NOZZLE AREA

N. Sakhno, O. Kharytonov, I. Kadenko
Nondestructive Examination Training and Certification Facility, Ukraine
O. Kharytonov, O. Kutzenko, Taras Shevchenko National University of Kyiv, Ukraine

1. INTRODUCTION

As in general not any NDT instrument is applicable to detect all defect types, orientations and sizes in equipment component, base metal or in a structural weld, and there is always a possibility that a defect will remain undetected in the component even after up-to-date inspection and repair. The probability of this occurring depends on many parameters, such as the equipment fabrication technology, NDT methods and requirements, NDE reliability, the qualification of operators etc.

Thus, two criteria can be used for the setting in-service NDE target and problem definition. The first criterion deals with a detection probability, NDE equipment characteristics and inspection techniques, while the second one is a criterion of necessity and it is based on a conception of critical, acceptable and allowable flaw sizes. These sizes are determined based on fracture mechanics analysis and crack growth rate evaluation. The ASME Section XI is considered to address second criterion.

The best international practices provide the way for NPP personnel to simply using the data about acceptable and the allowable crack sizes for specific equipment. It is the concept of the Flaw Evaluation Handbook for future service without repair.

In this paper all the steps of the above procedure are considered to develop the Flaw Handbook for the VVER-1000 reactor pressure vessel (RPV) inlet nozzle area.

As a limiting emergency condition transient the step cooldown scenario was chosen. In accordance with such scenario the coolant temperature is dropped immediately from the normal operation value to selected limiting temperatures. For RPV region the most conservative factor is the hydraulic tanks water temperature of Emergency Core Cooling System (ECCS). In the same time as we considered, the primary circuit pressure is not reduced and equals to normal operating pressure value. Conservative value of the heat transfer coefficient is to be applied. Such a scenario has a maximum available conservatism from the point of view of cool-down rate and pressure value. We consider the "hydrotest – heatup – cooldown" normal operation cycle. This cycle is used for calculation of crack growth while unit is under operation.

Real data obtained during NDE In-Service Inspection (ISI) performance from Ukraine NPP were used for our calculations.

For the determination of critical/acceptable crack sizes only the worst case of the emergency conditions was considered. The linear-elastic model of the material behavior was applied.

Determination of critical crack sizes was performed using fracture mechanics calculations. With this aim the conditions of critical crack size were determined. For calculations the RPV material properties from VERLIFE code were used.

The acceptable and allowable crack depths were determined for each crack parameters ratio.

Also we developed the recommendations for Flaw Handbook utilization. Some of the developed forms of the diagrams are simpler in making decision about flaw allowability and other ones can be used to determine time left to necessary repair.

2. LINK BETWEEN ISI AND FRACTURE MECHANICS CALCULATIONS

As it is well known, ISI results in flaws detection, schematization and sizing, namely: equivalent area, length, height or combinations.

Fracture mechanics calculations results are presented in acceptance criteria whether the specific crack is acceptable/allowable or not for NPP equipment or pipe specific component operation.

To reduce a scope of NDT ISI without reducing the NPP safe operation level, there was received a request from Ukraine NPPs: to develop the concept for linking ISI results and Fracture mechanics calculations to enable NPP ISI staff with effective utilization of existing ISI systems/manual NDE and future NDE development planning.

3. TERMINOLOGY APPLIED

A critical crack size - the largest size of the crack for which the crack stability is guaranteed for the worst loading conditions (Fig. 1 – critical level).

An acceptable crack size – a critical crack size that is reduced using appropriate safety factor (Fig. 1 – acceptable defect).

An allowable crack size – the initial size of the crack for which the conditions of crack acceptability are guaranteed to the end of crack growth period (so, the final allowable crack size is less than acceptable one) (Fig. 1 – allowable defect).

A qualification crack size – an allowable crack size minus detection tolerance (Fig. 1 – qualification defect).

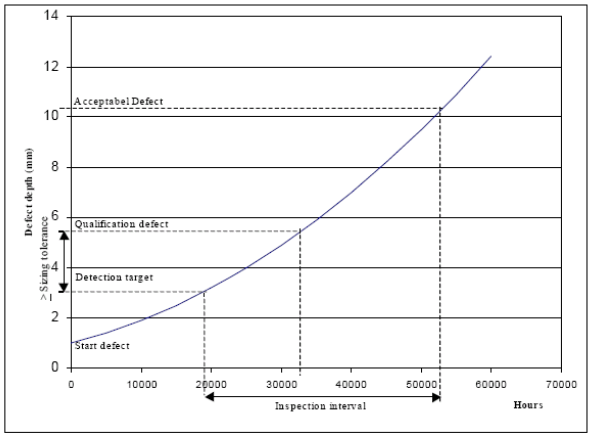

Figure 1 - An example of crack growth diagram [PBM2. Rules for Qualification of NDT Systems in Sweden. Edition 4]

4. FLAW HANDBOOK CONCEPT

The best international practices provide the way for NPP personnel to simple using the data on acceptable and the allowable crack sizes for specific equipment. It is the concept of the Flaw Evaluation Handbook for Future Service without Repair. The Flaw Handbook concept gives the following advantages:

- Handbook can be usable directly during inspection results analysis and doesn't require any additional information;
- when the flaw is observed, no calculation should be needed except flaw schematization.

Such possibility takes place when all necessary calculations were carried out during Handbook development. The steps of the Flaw Handbook development are as follows:

1 Determination of the scope of work. A set of the safety-significant segments must be selected for flaw evaluation procedure.

2 For each segment the list of normal operational conditions, operational transients, hydraulic testing, emergency conditions and their occurrences must be specified. The structural and fracture mechanics analyses should be done to determine the governing transient for critical/acceptable crack size calculation.

3 Crack postulation for the determination of the critical/acceptable crack dimensions.

4 The fracture mechanics calculations are used to define the critical/acceptable crack dimensions for end of life conditions. So, for each crack ratio value $a/2c$ the critical/acceptable crack depth is defined, where a is crack depth defined as semi-axis: perpendicularly to free or interface surface; $2c$ is crack length defined as semi-elliptical crack axis oriented perpendicularly to a (Fig. 2).

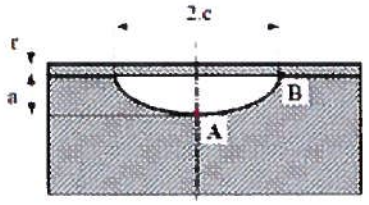

Figure 2 - Configuration of undercladding defect

The allowable crack sizes are determined based on operational modes that are specific for this equipment type. These sizes are defined as initial sizes that result in acceptable sizes for the end of life conditions. For the crack growth assessment all degradation mechanisms must be considered. Mechanisms depend on the material and environment.

5. FLAW HANDBOOK DEVELOPMENT

5.1 The scope of analysis

VVER-1000 RPV inlet nozzle area is considered.

5.2 The list of normal operational conditions, operational transients, hydraulic testing, emergency conditions and their occurrences

Worst case of emergency conditions scenario. As a limiting emergency condition transient the step cooldown scenario was chosen. In accordance with such scenario the coolant temperature is dropped immediately from the normal operation temperature to the selected limiting values. For the RPV region the most conservative value is the hydraulic tanks water temperature of ECCS. At the same time primary circuit pressure is not reduced and equals to the normal operating pressure value. Conservative value of the heat transfer coefficient should be applied. Such a scenario has a maximum available conservatism from the point of view of cool-down rate and pressure value.

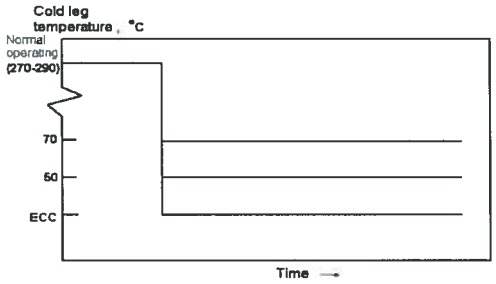

Figure 3 - Step cooldown scenario

Normal operation transients. In our case we consider the hydrotest-heatup-cooldown normal operation cycle. This cycle is used for calculation of crack growth during unit operation.

The parameters of the normal operation loading cycle are shown in Figs. 4, 5.

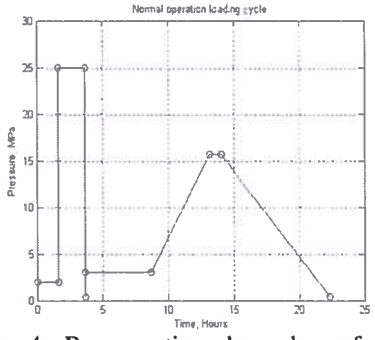

Figure 4 - Pressure-time dependence for the normal operation loading cycle

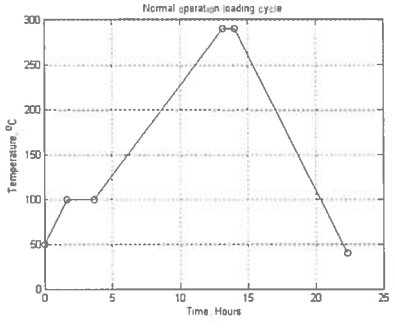

Figure 5 - Temperature-time dependence for the normal operation loading cycle

The conservative value of cycle frequency is n=3.24 per year (real NPP data).

The value of cycle frequency for cycles of all types is n=11 per year (real NPP data).
In our case for the determination of the critical/acceptable crack sizes only the worst case of the emergency conditions was considered. It is a step cooldown scenario with the temperature drop from 290°C (VVER-1000 reactor cold leg normal operating temperature) to 10°C and 20°C (ECCS temperature for nominated NPP considered by OKB Gidropress [1 - 3]), constant pressure value (15.7MPa, normal operating pressure) and with conservative value of heat transfer coefficient 20,000 Wt/(m^2·K). The linear-elastic model of the material behavior was applied.

5.3 Crack postulation

The crack is postulated in the equipment segment that is included into the scope of the analysis. The longitudinal crack orientation was selected because in nozzle area the circumferential stresses are much higher than longitudinal ones. Surface cracks should be considered for the assessment of the critical crack size for the normal operation conditions [4].

ISI of RPV is carried out using the NDE system, qualified by the Ukrainian Qualification Body. The defects in RPV wall were not detected by previous and current inspections. The cladding integrity is verified by the NDE testing. Based on this the undercladding longitudinal semielliptical cracks were postulated in our case. The following semi-axis ratios are considered: a/c = 0.1; a/c = 0.3; a/c = 0.5; a/c = 0.7; a/c = 1.0. The sketch of the postulated crack is presented in Fig.2.

The lower value of the crack ratio a/c = 0.1 gives the approximation to the crack with infinite length, because of the crack front has the form that is very close to the straight line.

5.4 The conditions of critical crack size determination using fracture mechanics calculations

For the determination of the critical crack sizes the conditions of the resistance against fast fracture can be used.

$$K_{I\max} \le [K_{IC}], \tag{1}$$

Where $K_{I\max}$ - is the maximum from the stress intensity factor (SIF) values, calculated at the points on the crack front (only the points in the base metal were taken into account) at all the time points of the transient; $[K_{IC}]$ - critical stress intensity factor.

For each fixed value of the crack ratio a/c the critical crack depth a_c is determined from the condition below:

$$K_{I\max} = [K_{IC}]. \tag{2}$$

To calculate SIF values for the set of points of the crack front, the finite-element (FE) analysis should be performed. Then a set of FE models of the equipment element with cracks embedded into the FE mesh should be developed.

For VVER-1000 RPV base metal and welds the following temperature dependence for the $[K_{IC}]$ should be used:

$$[K_{IC}] = \min\{26 + 36\exp(0.02(T - T_k)), 200\}, \text{MPa}/\sqrt{\text{m}}, \tag{3}$$

where T - is current temperature value at the point on the crack front; T_k - is critical temperature of brittleness calculated according to approach from PNAE G [5] was used:

$$T_k = T_{k0} + \Delta T_N + \Delta T_T + \Delta T_F, \tag{4}$$

where T_{k0} - is initial critical brittle fracture temperature; ΔT_N - shift in T_k due to fatigue damage; ΔT_T - shift in T_k due to thermal ageing; ΔT_F - shift in T_k due to neutron irradiation.

For nozzle area of VVER-1000 RPV the following dependence for ΔT_T can be used:

$$\Delta T_T = \left[\Delta T_{\text{inf}} + b_T \exp\left(\frac{t_T - t}{t_{OT}}\right)\right] \tanh\left(\frac{t}{t_{OT}}\right) \tag{5}$$

where ΔT_{inf} - shift of critical temperature of brittleness due to temperature aging while $t \to \infty$; b_T, t_T, t_{OT} - material parameters; t - unit operation time, hour, the values of the parameters can be used from the VERLIFE document [4].

For determination of critical crack size the end-of-life value of critical temperature of brittleness has to be used, taking into account real conditions of RPV operation.

The conditions (1) and (2) can be rewritten in terms of an allowable critical temperature of brittleness. The corresponding conditions are:

$$T_k \le T_k^a, \tag{6}$$

$$T_k = T_k^a, \quad (7)$$

where T_k - critical temperature of brittleness; T_k^a - is an allowable critical temperature of brittleness.

6. RESULTS OF FLAW HANDBOOK DEVELOPMENT

In our case the most dangerous crack location in inlet nozzle area was estimated based on the stress and temperature fields. Those fields were calculated using full WWER-1000 RPV model without crack embedded into the mesh (Fig. 6). It was found, that the highest stresses correspond to the center of nozzle fillet. Therefore, in this analysis all the cracks were postulated in such a position that provides the angle of 45° between axis of crack symmetry and RPV axis.

To determine the critical depth for the crack with given aspect ratio five depth values were considered. They are a = 10, 20, 30, 40, 50mm, or a/s=0.035, 0.07, 0.11, 0.14, 0.18, where s - is nominal value of the wall thickness, (s =285 mm for the nozzle area). So, the twenty five finite-element models with the crack embedded into the mesh were generated. The examples of the finite-element models (the region near crack) are shown in Figs. 7 - 9.

6.1 Determination of the critical crack sizes

For the calculations the RPV material properties from VERLIFE [4] were used.

The values of an allowable critical temperature of brittleness for different crack sizes were calculated for value of ECCS water temperature T_{ECCS} = 20ºC.

For the calculation of T_k value we used the dependence (4) where for the nozzle area T_{k0}=-10ºC, ΔT_F=0ºC and ΔT_T is defined using the dependence (5) within the time interval t ∈[24·365·8; 24·365·40] hours (corresponds to the operation period 8-40 years). The maximal value of T_k within given time interval is 3ºC.

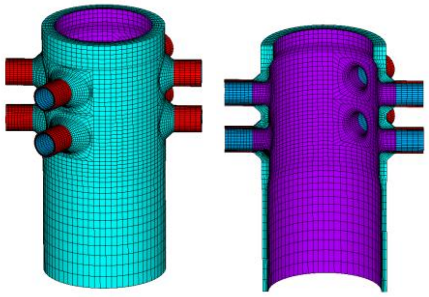

Figure 6 - General view of VVER-1000 RPV FE –model

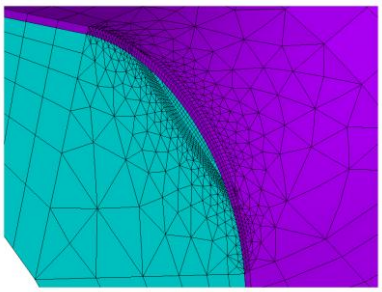

Figure 7 - The FE-model with the crack embedded into the mesh. Crack depth a=20mm, a/c=1.0

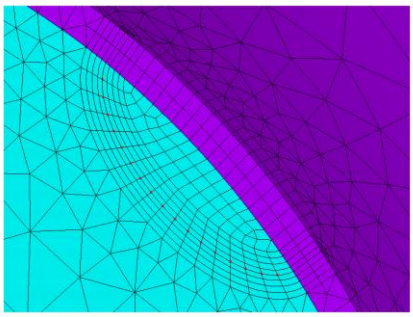

Figure 8 - The FE-model with the crack embedded into the mesh. Crack depth a=20mm, a/c=0.5 The calculation points on the crack front are marked

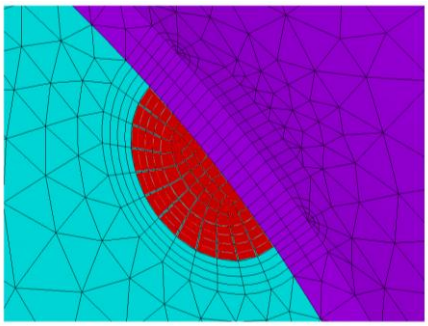

Figure 9 - The FE-model with the crack embedded into the mesh. Crack depth a=20 mm, a/c=1.0. The crack face is marked

The T_k^a values were determined for ECCS water temperature T_{ECCS} =20ºC of the step cool-down scenario for each crack sizes a and c using condition (7). The results are presented in Table 1.

Table 1 - The values of an allowable critical temperature of brittleness for different crack sizes

Crack aspect ratio, *a*/*c*	**Crack depth *a*, mm**				
	10	**20**	**30**	**40**	**50**
0.1	17.09	1.95	-3.85	-7.19	-
0.3	19.18	4.32	-1.73	-4.84	-
0.5	22.45	7.68	1.67	-2.02	-
0.7	26.64	11.78	5.09	-0.72	-
0.9	-	14.87	5.52	-1.18	-6.42
1.0	33.06	15.78	5.52	-1.52	-
1.2	-	15.94	5.53	-1.50	-7.02

The dependence $a_c(T_k^a)$ was developed using the linear interpolation of the data from Table 1. The critical depth a_c for the crack with given crack ratio can be defined using the condition (7), namely – by the linear interpolation of Table 1 data for the value $T_k^a = T_k$ =3ºC. The results of critical crack size calculations are presented in Table 2 for the T_{ECCS} = 20ºC.

Table 2 - Critical depth values. T_{ECCS} =20ºC

a*/*c	**0.1**	**0.3**	**0.5**	**0.7**	**0.9**	**1.0**	**1.2**
a_c, mm	18.93	21.49	26.88	34.13	33.32	33.34	33.36

6.2 Determination of the acceptable crack sizes

The acceptable crack depth is determined for each value of the crack ratio *a*/*c*. The following approach has to be used [6]:

$$a_{ac} = \min(a_c / 2, a_i / 10), \tag{8}$$

where a_c - is the critical crack depth determined for the emergency conditions; a_i - is the critical crack depth determined for the normal operation conditions.

In our case only the critical crack depth determined for the emergency conditions, a_c, was used for the calculation of an acceptable crack depth.

The acceptable depth values for cracks with above crack ratios are presented in Table 3 ECCS temperature T_{ECCS} =20ºC.

Table 3 - Acceptable depth values. T_{ECCS} =20ºC

a*/*c	**0.1**	**0.3**	**0.5**	**0.7**	**0.9**	**1.0**	**1.2**
a_{ac}, mm	9.466	10.746	13.433	16.661 (17.065)	16.661	16.661 (16.668)	16.661 (16.683)

6.3 Determination of an allowable crack size

An allowable crack depth was determined for each value of the crack ratio *a*/*c*. A set of time points at the NPP in-service operation time interval was considered. For cracks in RPV it can be supposed that the active degradation mechanism is the fatigue. The crack growth due to SCC degradation mechanism can be neglected.

To determine an allowable crack depth the crack growth process due to cyclic loading was considered. For given time point an allowable crack depth is determined by the backward integration of the Paris equation:

$$\frac{\mathrm{da}}{\mathrm{dN}} = 2.1\cdot 10^{-17}\left(\frac{\Delta \mathrm{K}}{(1-\mathrm{R})^{0.5}}\right)^{7.2}, \text{for}\ \frac{\Delta \mathrm{K}}{(1-\mathrm{R})^{0.5}} < 31.8,$$

$$\frac{\mathrm{da}}{\mathrm{dN}} = 1.08\cdot 10^{-8}\left(\frac{\Delta \mathrm{K}}{(1-\mathrm{R})^{0.5}}\right)^{1.4}, \text{for}\ \frac{\Delta \mathrm{K}}{(1-\mathrm{R})^{0.5}} \geq 31.8, \qquad (9)$$

$$\Delta \mathrm{K} = \mathrm{K}_{I\max} - \mathrm{K}_{I\min}, \mathrm{R} = \frac{\mathrm{K}_{I\min}}{\mathrm{K}_{I\max}}$$

with the initial condition

$$a(t_{eol}) = a_{ac}, \qquad (10)$$

where N - is the number of cycles; $K_{I\max}$, $K_{I\min}$ - are the maximal and minimal SIF values in the cycle; a_{ac} - is an acceptable crack depth.

Only normal operation cycles have to be assessed.

Calculations were carried out for acceptable crack depth values corresponding ECCS temperature T_{ECCS} =20ºC. Two values of cycle frequency were considered: n=3.24 cycle per year as a conservative value of the frequency for a hydrotest-heatup-cooldown normal operation cycle and n=11 cycle per year for all types of normal operation cycles.

The diagrams of allowable crack sizes developed for the step cooldown scenario loading conditions with T_{ECCS} =20ºC for n=3.24 are presented in the Figs. 10, 11, and for n=11 in the Figs. 12, 13. The numerical data correspondent to the cycle frequency values n=3.24 and n=11 are presented in the Tables 4 and 5, respectively.

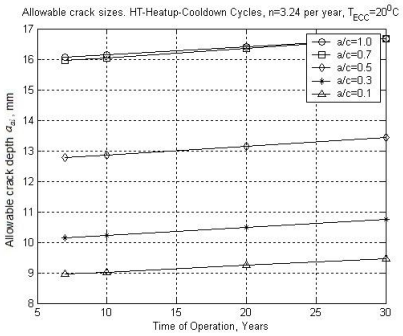

Figure 10 - Allowable crack sizes for the HT-Heatup-Cooldown cycles. An allowable depth with time dependence

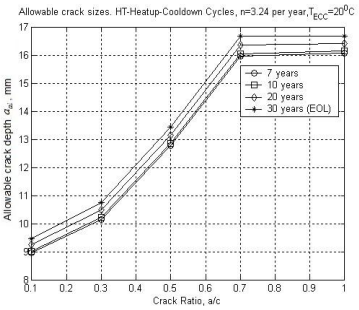

Figure 11 - Allowable crack sizes for the HT-Heatup-Cooldown cycles. An allowable depth with crack ratio dependence. T_{ECCS} =20ºC

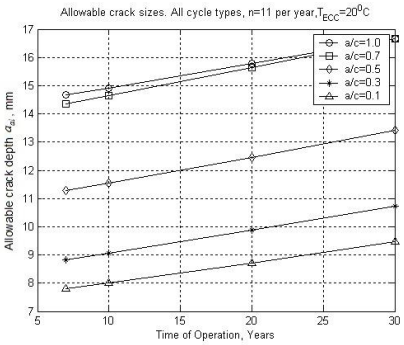

Figure 12 - Allowable crack sizes for all the cycles, considered as a HT-Heatup-Cooldown cycle. An allowable depth with time dependence

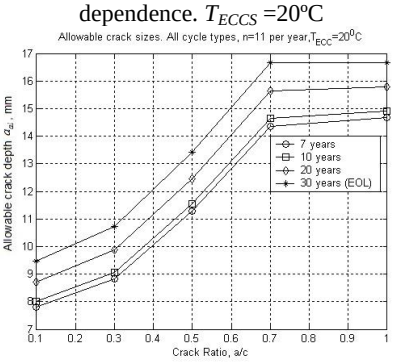

Figure 13 - Allowable crack sizes for all the cycles, considered as a HT-Heatup-Cooldown cycle. An allowable depth with crack ratio dependence

Table 4 - Allowable crack depth values a_{al} for HT-Heatup-Cooldown cycles (n=3.24)

Crack aspect ratio, *a*/*c*	**Years of operation**			
	7	**10**	**20**	**30**
0.1	8.95	9.02	9.24	9.46
0.3	10.15	10.23	10.48	10.74
0.5	12.77	12.86	13.14	13.43
0.7	15.96	16.05	16.35	16.66
1.0	16.06	16.14	16.40	16.66

Table 5 - Allowable crack depth values a_{al} for all the cycles considered as a HT-Heatup-Cooldown cycle (n=11)

Crack aspect ratio, *a*/*c*	**Years of operation**			
	7	**10**	**20**	**30**
0.1	7.81	8.01	8.71	9.46
0.3	8.82	9.05	9.87	10.74
0.5	11.27	11.54	12.46	13.43
0.7	14.36	14.65	15.63	16.66
1.0	14.68	14.92	15.78	16.66

7. FLAW HANDBOOK UTILIZATION

As we may see "Crack ratio – Allowable depth" form of the diagrams is simpler in using to determine flaw allowability. At the same time form "Operational time - allowable depth" can be used to determine time left up to necessary repair performance. Let's consider Fig.13 and suppose that for t_p-th year of operation a certain flaw is detected. This defect is schematized towards undercladding semi-elliptical crack with the depth a_p and one half length, equal to c_p. The following steps should be carried out to estimate whether this crack size is an allowable.

From time points t =7; 10; 20; 30 years choose the maximum value to keep $t_p > t$.

Consider at the diagram a point with coordinates (a_p/c_p, a_p). If this point is located above the curve $a(a/c)$, corresponding to value t chosen, then this flaw is considered as unallowable, i.e. immediately or suspended repair is requested; if this point is located below the curve, then such flaw is considered as an allowable one.

For example, after the t_p =10.5 years of operation the defects with the depth a_{p1} =12.9 mm and a_{p2} =13.2 mm and crack ratio a_p/c_p=0.6 is detected (Fig.14).

The nearest to t = 10.5 years time t, calculated in Flaw Handbook and which meets the condition $t_p > t$, is a point with coordinate t = 10 years. Therefore, estimation of flaw allowability is carried out relative to curve that corresponds to t = 10 years (marked by "squares"). Consequently, first flaw is an allowable, second one – not.

To determine time period left up to repair, "Operational time - Allowable depth" dependence is to be used (Fig.15).

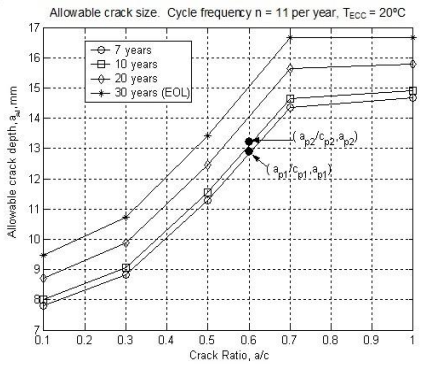

Figure 14 - Estimation of flaw allowability

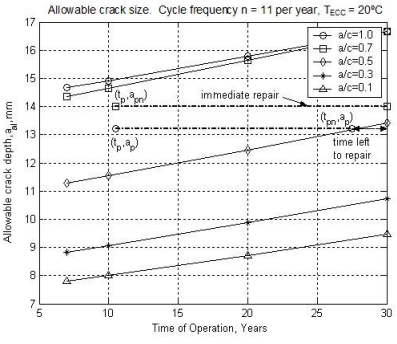

Figure 15 - Estimation of the residual time before repair

With this aim maximum value that satisfies condition $a/c < a_p/c_p$ must be selected from the following crack size ratios a/c= 0.1; 0.3; 0.5; 0.7; 1.0 (remember, that crack area is increased when crack sizes ratio is reduced, therefore, more conservative allowable size corresponds to smaller value of crack sizes ratio).

Therefore, using the conservative approach, we consider it as a crack with crack ratio a_p/c_p=0.5.

Such defect is unallowable, because the correspondent point with coordinates (t_p, a_p) at the diagram (Fig.15) is located higher than the point with the same value of t_p, but located at the curve that corresponds to the crack ratio 0.5 and determines limit values of crack depths in different time moments. From another hand, the defect with such sizes is an allowable one if it is detected for another time of operation: t_{pn} = 27.5 years or later. This time t_{pn} is defined by the intersection of the horizontal line $a = a_p$ with the limiting curve that corresponds to the crack ratio 0.5.

As point (t_{pn}, a_p) is on the limiting curve, the defect with the sizes a_p, a_p/c_p (under condition a_p/c_p=0.5) reaches an acceptable depth by the end of life time operation. So, the time period of crack growth to the acceptable size equals 30-27.5=2.5 years.

If detected crack depth is higher than acceptable (as it is for the flaw with a_{pn} = 14 mm in Fig.15) the defect must be repaired immediately.

8. CONCLUSIONS

1. The best world experience gives the possibility for the safe operation of the equipment with defects detected under the ISI program at Ukraine NPPs.

2. Such possibility provided by the minimum flaw indication standards (allowable defects without calculation), the procedures of the analysis of the defects detected during the ISI and flaw handbooks.

3. Advanced calculation methods based on the Finite Element analysis were used.

4. The best way to provide the safe operation of the equipment with defects is the online assessment based on preventive calculations (Flaw Handbook concept, the monitoring and diagnostics systems).

5. Full 3D models of primary and secondary loops must be developed for each NPP unit to support such an approach.

9. REFERENCES

1. Reactor Pressure Vessel. Structural Analysis. Part 10. Calculation of Fields of Temperature, Stresses and Available Critical Brittle Fracture Temperature. OKB “Gidropress”, 320.100.08.01.000 PP06.09, 2007.
2. Reactor Pressure Vessel. Structural Analysis. Part 12. Resistance to Brittle Fracture of Reactor Pressure Vessel of Rivno NPP, Unit 4. OKB “Gidropress”, 320.100.08.01.000 PP06.11, 2007.
3. The Increasing of Reliability of NPP Unit V-320. Thermalhydraulics Analysis. Part 68. Determination of Boundary Conditions for the Demonstration of the Resistance to Brittle Fracture of the Reactor Pressure Vessel. OKB “Gidropress”. 320.100.08.01.000 PP02.67, 2007.
4. Unified Procedure for Lifetime Assessment of Components and Piping in WWER NPPs VERLIFE – Version 2011, v.2
5. PNAEG-G7-002-86, Rules and Regulations for Design and Stress Analysis for Components and Piping of Nuclear Installation/Moscow, Energoatomizdat,1989.PNAE G-7-002-86.
6. ASME Boiler and Pressure Vessel Code. Section XI. Rules for Inservice Inspection of Nuclear Power Plant Components. 2010.

CORE MAPPING PROCESS

L. Blondel, European PWR Reactor Services, France
Rob Wheeler, Newton Research Labs, USA

Abstract

Problem:
Correct placement of FA is a constant concern for the industry. The control of FA positions requires a tool able to produces accurate results, quickly usable by outage refuelling personnel.
Method:
Tool head is located above the reloaded FA and take pictures. The system performs automated televisual inspection on these images and locates the FA "S" holes and the baffles. Then it can determine the FA positions and their spatial relationship to the baffles. The system then measures and records all of the distances between the FA and the baffles and turns in the information to the operator in real time.
Principal result:
The system overcomes the issues due to thermals effect using specifically development algorithms that compensate for the visually distorting thermal turbulence. It also deals with differences between old and new bundles. These abilities have been recognized during its US implementations. It produces real time positioning information for each FA compared to its theoretical position under a green-yellow-red map for immediate usage by outage personnel.

Keywords: Application areas of NDT (RPV-SG-Internals and primary circuit-Other component)

DEVELOPMENT OF HIGH RESOLUTION X-RAY CT TECHNIQUE FOR IRRADIATED FUEL ASSEMBLY

A. Ishimi, K. Katsuyama, H. Kodaka, H. Furuya
Japan Atomic Energy Agency, Japan

1. Abstract

In order to observe the structural change in the interior of irradiated fuel assembly, the non-destructive post irradiation examination technique using X-ray computer tomography (X-ray CT) was developed. In this X-ray CT system, the 12 MeV X-ray pulses were used in synchronization with the switch-in of the detector to minimize the effects of the gamma ray emissions from the irradiated fuel assembly. This method was applied to a fuel assembly irradiated in the experimental fast reactor "JOYO," and images were successfully obtained of transverse cross sections at different heights of fuel assembly along its axis for the first time in the world.

This X-ray CT technique can substitute non-destructive PIEs for a number of destructive PIEs. This has a great advantage to enhance efficiency of PIE.

2. Introduction

In the field of post irradiation examination (PIE), the information on the structural changes of nuclear fuel assembly during irradiation in nuclear reactor is basically important to the safety of nuclear reactor. These data have generally obtained by the non-destructive and destructive PIE in hot cell[1), 2)].

At the beginning of 21st century in our Institute, a powerful X-ray computer tomography (X-ray CT) technique was installed as a non-destructive PIE tecniques of irradiated fuel assembly. This technique has been improved year by year. In this paper, the basic concept of this technique and its improvement are discribed.

3. Development of high resolution X-ray CT technique

3-1. Basic concept[3), 4)]

Until the development of this X-ray CT technique, it had been believed among many researchers over the world that X-ray CT technique cannot be applied to the PIE of irradiated materials because of strong intensity of radioactivity (especially gamma ray). We have succeeded in the application of X-ray CT technique to the PIE of irradiated fuel assembly by using the following techniques.

An outline of X-ray CT apparatus developed in our Institute is shown in Fig.1. X-ray CT apparatus is set up in a hot cell and a CT test room, which protect workers from strong intensity radioactivity. The irradiated fuel assembly is inserted into a guide tube by an elevator.

The introduced fuel assembly is irradiated by the pulsed X-ray of maximum energy 12 MeV. The X-ray transmitted through the irradiated fuel assembly are divided into 30 channels by the collimator of 0.3 mm in the width and 2 mm in height and then each X-ray intensity are measured by a detector of $CdWO_4$ scintillator. The system of X-ray source, the collimator and detector can rotate around the guide tube and move laterally from one end to the other of the irradiated fuel assembly.

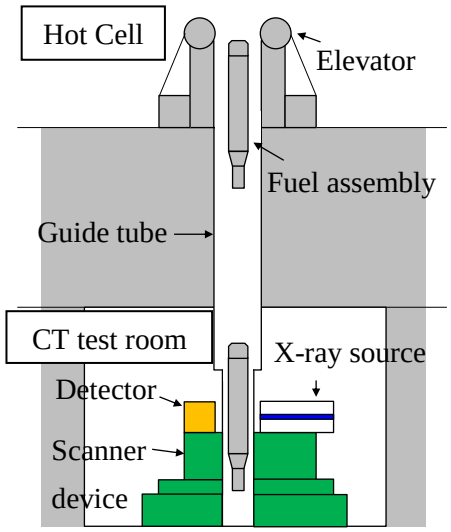

Fig.1 The X-ray CT apparatus composed of elevator, detector, X-ray source and scanner device

It is generally considered that the strong intensity of gamma-ray emitted from the irradiated fuel assembly interferes so much the X-ray CT measurement. From the reason, it is necessary to reduce the effect of the gamma-ray in order to obtain a clear X-ray CT image. We succeeded in a drastic reduction of the gamma-ray effect by using the pulsed X-ray of high energy 12MeV. The pulse width of X-ray is 4.5 microseconds and its interval is 10 milliseconds. In addition, the detection of X-ray passed through the collimator is synchronized with the emission of X-ray by the linear accelerator.

3-2. Upgrading[5)]

In order to obtain the high resolution X-ray CT image, previous X-ray CT technique was upgraded. First, the collimator slit width was decreased from 0.3 mm to 0.1 mm. Secondly, the material of X-ray detector was changed from a $CdWO_4$ scintillator to a high sensibility of silicon semiconductor, and the number of detector was increased from 30 channels to 100 channels. Finally, the X-ray focus shape was fitted to the collimator slit shape to increase the detected X-ray intensity. These upgrades made it possible to obtain the high resolution X-ray CT image.

The X-ray CT image is constructed by analyzing many digital data (CT values). This analytical method was innovated to observe the more accurate fuel performance.

4. Result and discussion

4.1 Examination specimen

The outline of fuel assembly that was irradiated in the fast reactor "JOYO" is shown in Fig.2. 127 fuel rods were assembled as a fuel assembly. The main specifications of a fuel assembly are shown in table 1. The fuel pellets loaded into the fuel rod were mixed oxide (MOX) fuel of uranium and plutonium which had the diameter of 4.63 mm and the high of 5 mm. The fuel rod has the length of 1533 mm and its cladding is made of the stainless steel. The total length of the mixed oxide fuel pellet is 550 mm. In the other parts in the fuel rod, the blanket UO_2 fuel pellets are inserted and the remaining part is plenum where fission gas can be accumulated.

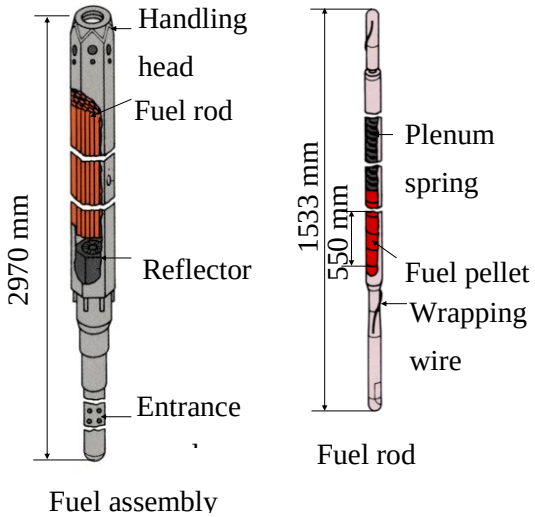

Fig.2 Outlines of "JOYO" fuel assembly and fuel rod

Table 1 Main specifications of fuel assembly

Item	Description
Specification data	
Number of fuel rod	127
Diameter of cladding	5.5mm
Diameter of fuel pellet	4.63mm
Pellet density	94%T.D.
Plutonium content	16wt%
Irradiation data	
Average burn-up (assembly)	53.5GWd/t
Maximum linear heat rating	401W/cm

The average burn-up of fuel assembly was 53.5 GWd/t, and maximum linear heat rating of the fuel pellet was 401W/cm in the fast reactor.

4.2 X-ray CT image of the irradiated fuel assembly

When the fuel rod is irradiated at a high linear heat rating, the steep temperature gradient along the radial direction appears, leading to the formation of cracks. In addition, pores in the sintered fuel pellet moves towards its radial centre, resulting in the redistribution of density and volution of central void. Fig.3 shows an X-ray CT image obtained on the transverse cross section of the irradiated fuel assembly (Fig.3 (a)), together with an enlarged image (Fig.3 (b)) and its metallographical microstructure (Fig.3 (c)) obtained on the transverse cross section of fuel rod located in the centre of fuel assembly. In the X-ray CT image of Fig.3 (a) and 3 (b), the fuel pellet, cladding tubes of 0.4 mm in thickness, wrapping wires of 0.9 mm in diameter and wrapper tube of fuel assembly can be clearly distinguished from each other.

The central void and crack in the fuel pellet on the X-ray CT image (Fig.3 (b)) can be clearly as same as metallographical microstructure (Fig.3 (c)).

The knowledge on the central void size and density redistribution along the radial direction are very important to evaluate the irradiation performance of fuel rod. Until now, the central void size and density redistribution have been evaluated on only the metallographical

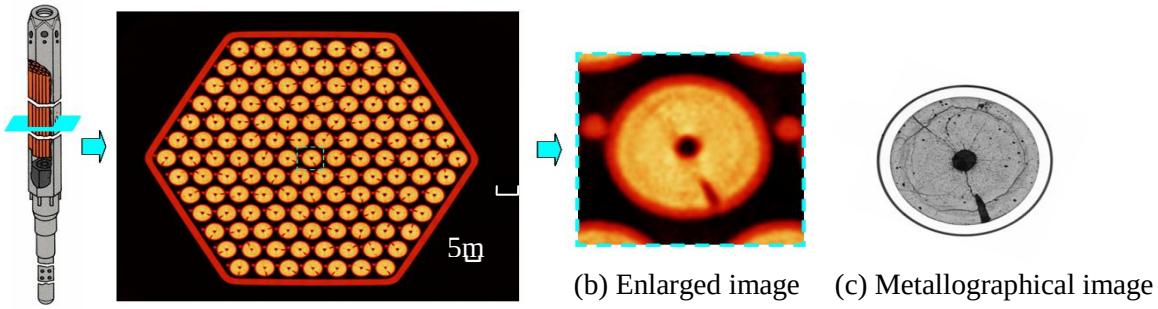

(a) X-ray CT (b) Enlarged image (c) Metallographical image

Fig.3 X-ray CT image of fuel assembly obtained on the transverse cross section at the axially central position, together with the X-ray CT image obtained in the transverse cross section of fuel rod and the metallographical microstructure as the destructive examinations.

Since it needs a long time to carry out destructive examinations, the number of results obtained by destructive examination is limited. In the other hand, a number of data on the central void sizes can early be obtained in a short time by the X-ray CT technique. 2413 central void sizes obtained on 19 traverse cross sections of all fuel rods as a function of linear heat rating during irradiation is shown in Fig.4. It can be seen that the central void begins to evolve at nearly 300 W/cm and the sizes increases with the linear heat rating.

Also, the radial redistribution of density in the fuel pellet after irradiation could be evaluated more accurately by the X-ray CT technique than by metallographical method. Generally in the metallographical microstructure, the irradiated fuel region excluding the central pore has been radially divided into three regions from the low temperature side, the undisturbed, equiaxial, and columnar regions. Since it is assumed that the density of each region is constant, the radial redistribution of density is discontinuous evaluated.

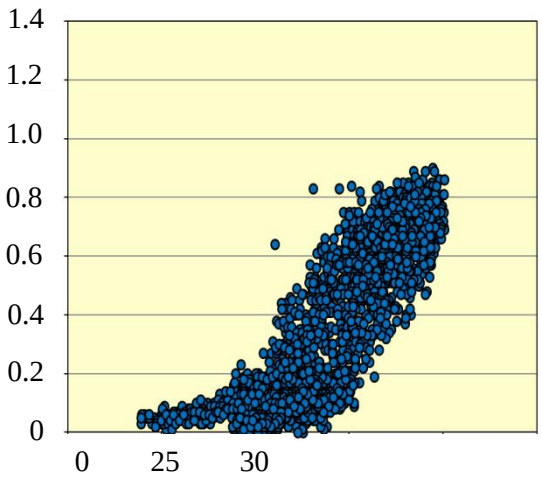

Fig.4 2413 central void sizes on a function of linear heat

While in the evaluation by the X-ray CT technique, the radial redistribution of density could be continuously evaluated from the relationship between the densities and CT values, which was obtained by plotting the CT values of 11 standard materials having known densities as their densities. A typical examples evaluated using a transverse cross section of irradiated fuel rod and the metallographical image are shown in Fig.5.

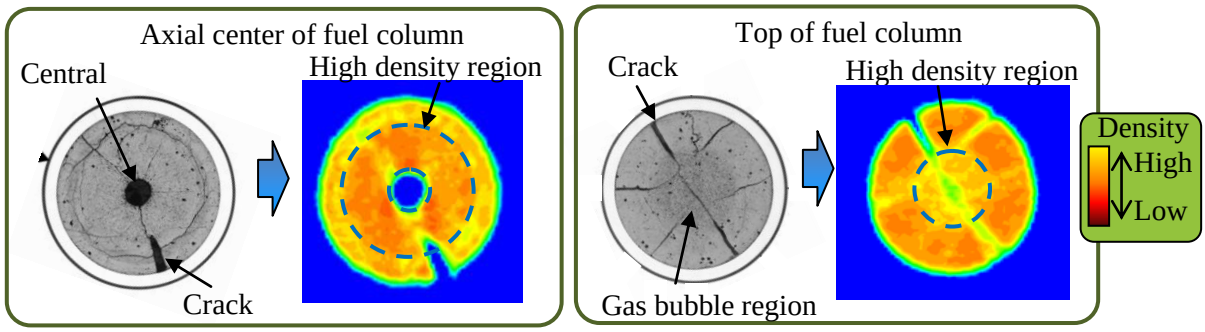

Fig.5 Radial redistributions of density evaluated using the transverse cross sections of fuel rod at axially central and top position.

A splendid merit of this X-ray CT technique is to be able to obtain three dimensional X-ray CT image (3D image) of irradiated fuel assembly. This 3D image could be obtained by combining several two dimensional X-ray CT images. A typical examples of irradiated fuel assembly are shown in Fig.6. This 3D image can be observed from various angles as shown in Fig.6 (a) , and can be observed without wrapper tube and cladding tube as shown in Fig.6 (b). Therefore, the 3D image made it possible to observe the surface of cladding tube and fuel pellet and the central void in fuel pellet.

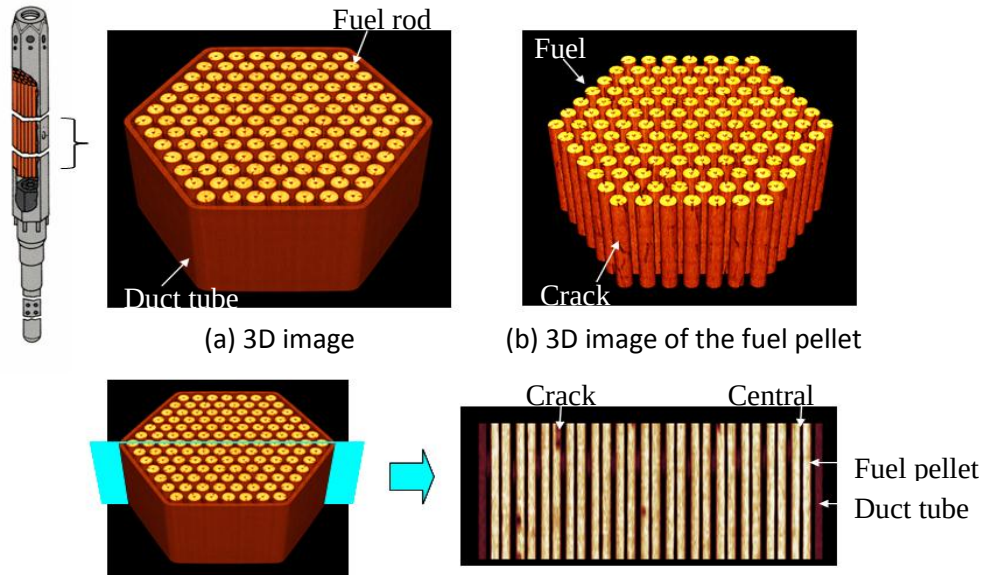

Fig.6 X-ray CT images obtained at the axially central region of fuel assembly

In addition, fine and large 3D images of fuel assembly can be obtained by changing the interval between transverse cross sections on which X-ray CT image is obtained. Using these 3D images, many fuel performances such as the deformation of fuel rod, the bundle-duct interaction and so on can be examined.

5. Conclusion

A high resolution of X-ray CT technique, which can be applied to the irradiated fuel assembly, could be successfully developed in our Institute.

Using this high resolution X-ray CT technique, a number of central voids evolved in the fuel pellet during irradiation could be observed and the more reliable relationship between their size and linear heat rating could be obtained. The radial redistribution of density after irradiation could be continuously evaluated. In addition, 3D image could be obtained by combining several 2D images, from which many fuel performances can be evaluated.

A further improvement of this X-ray CT apparatus is under progress. It is greatly expected in a near future that the more detail data on the fuel performance can be obtained.

6. References

1) P.R. Betten and D.M. Tow, “Cat Reconstruction and Potting Comparison of a LMFBR Fuel Bundle”, Trans. Am. Nucl. Soc. 1984 46 779–780.
2) M. Inoue, K. Maeda, K. Katsuyama, K. Tanaka, K. Mondo, and M. Hisada, “Fuel-to-cladding gap evolution and its impact on thermal performance of high burnup fast reactor type uranium–plutonium oxide fuel pins”, J. Nucl. Mat. 2004 326 59–73.
3) K. Katsuyama, T. Nagamine, S. Matsumoto, and M. Ito, “Application of X-ray computer tomography for observing the deflection and displacement of fuel pins in an assembly irradiated in FBR”, J. Nucl. Sci. Technol. 2003 40(4/12) 220-226.
4) K. Katsuyama, T. Nagamine, S. Matsumoto, M. Ito, and H. Furuya, “Development of a non-destructive post irradiation examination technique using high-energy X-ray computed tomography”, Trans. Am. Nucl. Soc. 2004 91 481-482.
5) A. Ishimi a , K. Katsuyama a , K. Maeda a , T. Nagamine a , T. Asaga and H. Furuya, “Upgrading of X-ray CT technique for analyses of irradiated FBR MOX fuel”, J. Nucl. Sci. Technol. 2012 49(12/12) 1144-1155.

SURFACE EXAMINATION

ASESSING RELIABILITY OF REMOTE VISUAL TESTING – RESULTS OF A ROUND ROBIN EXERCISE

P. Ramuhalli, Pacific Northwest National Laboratory, USA
J. Lindberg, J. Landrum, EPRI, USA
A. Diaz, M. T. Anderson, Pacific Northwest National Laboratory, USA

Abstract

Remote Visual Testing (VT) is a commonly used method for the inspection of reactor internals components in nuclear power plants. The advantages of remote VT are that these generally involve less radiation exposure and time to perform the examinations than do comparable volumetric or surface examinations. Remote VT with radiation-hardened submersible closed-circuit video system has been used by nuclear utilities to find degradation in both pressurized and boiling water reactor internals, and to investigate leaks in piping and other components. These visual tests are performed using a variety of procedures and equipment. The wide range of potential applications and personnel skill levels requires that issues relative to the capabilities and limitations of remote VT in determining the structural integrity of reactor components be assessed. PNNL and the Electric Power Research Institute cooperated to conduct a series of round-robin exercises and parametric studies to assess remote VT procedures, and to identify significant variables impacting their reliability. In two phases of blind testing, multiple operators, using both standard definition and high-definition cameras, examined a set of specimens. The specimen set included both cracked and blank specimens. Tested variables included crack opening displacement (COD), crack length, procedure variability, camera resolution, and magnification. The results of these round robin studies are presented in this paper.

Keywords: Remote visual examination, round robin test, NDE reliability, visual examination, reactor internals, vessel internals examination

ADVANCES IN THREE DIMENSIONAL MEASUREMENTS IN REMOTE VISUAL INSPECTION

J. J. Le Corre, GE Measurement&Controls, France
E. Hubben, GE Measurement&Controls, USA

Abstract

Recent developments in industrial video borescope technology have enabled three-dimensional surface scanning of equipment internal spaces. Named 3D Phase Measurement, the optical metrology techniques of structured light and optical phase shifting has been adapted to the size restrictions of a six millimeter diameter video borescope, to allow the 3D visualisation benefits to be transferred to Remote Visual Inspection (RVI). By combining this projection system with high-quality viewing optics and sophisticated, proprietary processing algorithms, it is now possible to view a full 3D map, or point cloud, of the inspected surface, which is used in conjunction with measurement to obtain more precise information about an indication.

Keywords: Development in surface examination, Remote Visual Inspection (RVI), 3D, video borescope, structured light, phase shifting, 3D phase measurement, point cloud.

ADVANCED DC-PULSE TECHNOLOGY FOR MT TESTING AND DEMAGNETIZATION OF STEEL COMPONENTS

P. Hirsch, HPT Hirsch Prueftechnik GmbH, Germany

HPT Hirsch Prueftechnik GmbH in Zweibrücken supplies small low weight and mobile DC-pulse MT testing devices with a DC power peak up to 30.000 A (picture 2) in combination with an equipment carrier (picture 3) for surface crack detection and demagnetization of steel components. Magnetic connectors with high adhesive force are in use to attach the cables at the part under test.

An UV-LED-lamp illuminates the surface and provides some greenish crack indications (picture 1). The measuring device for current-, magnetically field- and residual field strength needed to make sure that testing is carried out properly.

MT-testing with DC-pulse technology can be applied in many industries like submarine ship yards, machine building, foundries, forging shops, mobile cranes, for offshore equipment, hydroelectric and wind power plants, armoured vehicles, tanks, casted GGG40-blades (picture 1) etc..

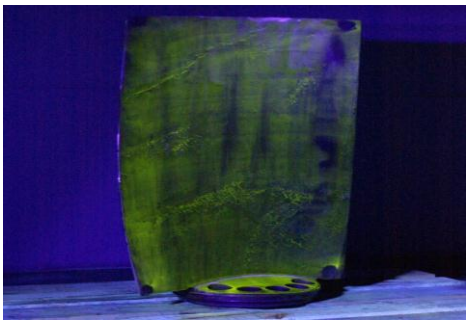

Picture 1: GGG40-blades with cracks from a industrial fan for an power plant

Picture 2: 4-pol-DC-pulse unit, type Multipuls-1003-E2-1 (DC power peak= 30.000 A) with UV-lamp, remote control, test cables and magnetic connectors

Picture 3: Equipment carrier, type Multipuls-1003-V

The MT-testing devices generate short, fierce direct current pulses (picture 4) in order to magnetize the parts under test.

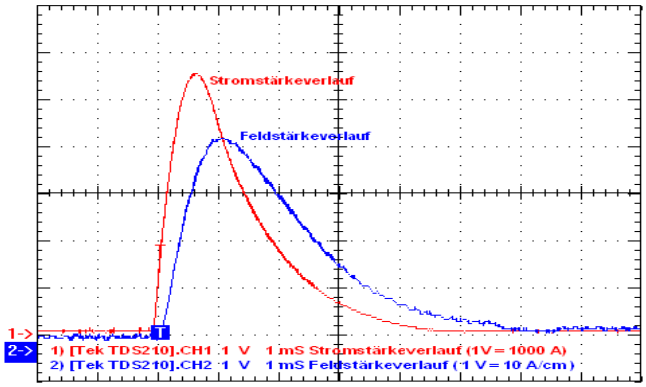

Picture 4: DC current flow (red) and magnetically field strength (blue), Multipuls-1003-C (6.000 A)

Like all other MT-testing methods MT-testing with DC-pulse technology takes advantage of the effect, that at the location of surface cracks magnetic stray fields are escaping from magnetized parts. Once testing liquid mixed with iron or iron oxide particles has sprayed on the surface of the parts, the magnetic stray fields accumulate the particles at the cracks.

One important advantage of MT-testing with DC-pulse-technology is the fact, that it produces very clear crack indications without false indications within very short time.

Large components i.e. tooth wheels, shafts, castings or welded components can be tested quickly and economically.

The DC-pulse-technology is used in combination with the following magnetization methods:

- Direct current flow for MT testing and demagnetization (picture 5 - 8)
- Combined MT testing with direct current flow and coil (picture 9 - 10)
- Non-contact MT testing and demagnetization with double coil (picture 11- 13)
- Demagnetization with double coil (picture 14)

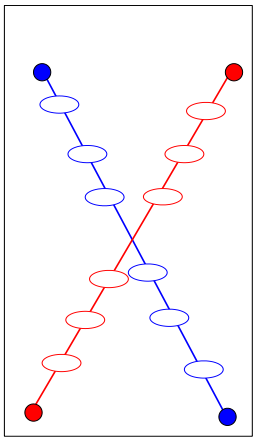

Picture 5: MT testing and demagnetization of a GGG40 blade for an industrial fan for a power plant with direct current flow

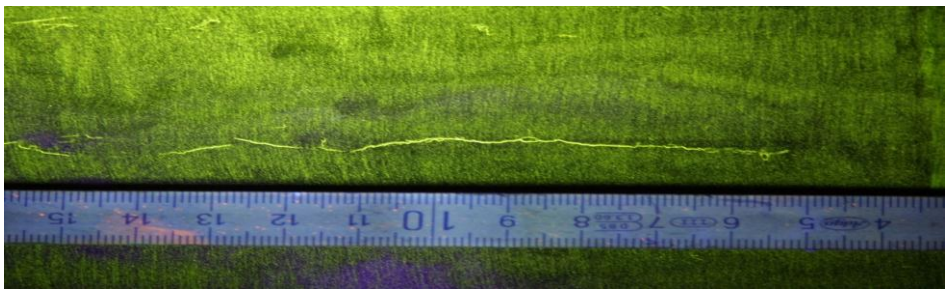

Picture 6: Crack indications in a GGG40 blade for an industrial fan for a power plant

Picture 7: MT testing of a blade for a hydroelectric power plant (W= 4.5 m; H= 3.0 m) with direct current flow

Picture 8: MT testing of a safety valve with direct current flow

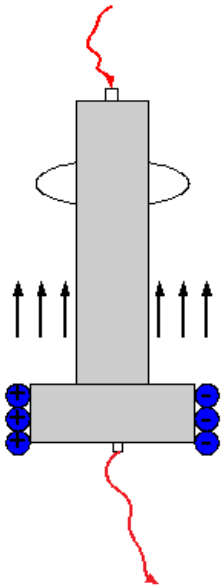

Picture 9: Combined MT testing of a blade shaft for an industrial fan for a power plant

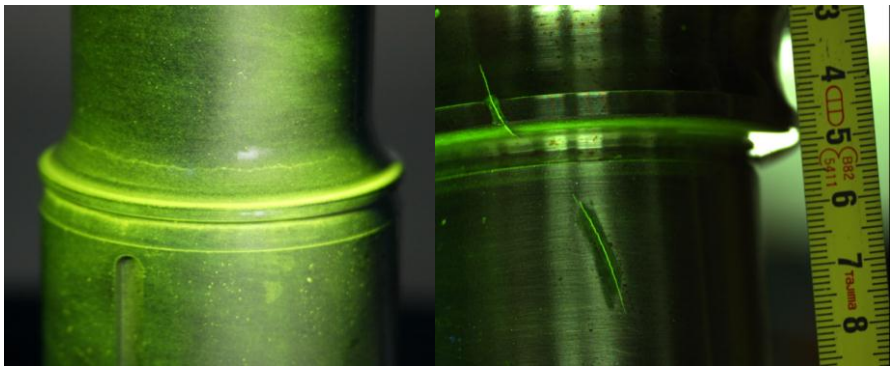

Picture 10: Crack indication in blade shafts for industrial fans for a power plant

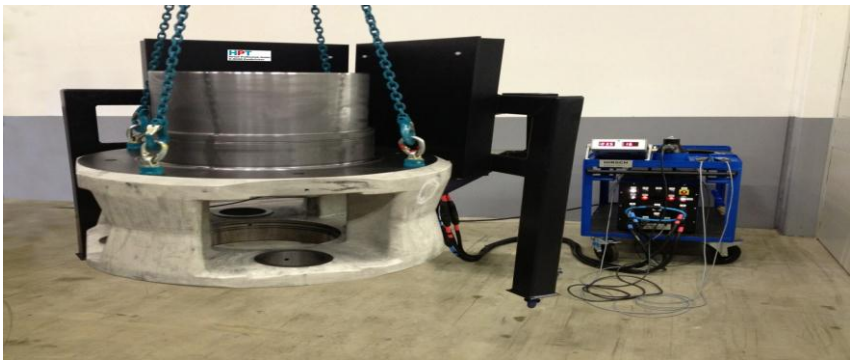

Picture 11: Non contact MT testing and demagnetization of a planet-wheel carrier with two coils and Multipuls-1003-E2-1 (30.000 A)

Picture 12: Non-contact MT testing and demagnetization with two coils and Multipuls-1003-E2 (25.000 A)

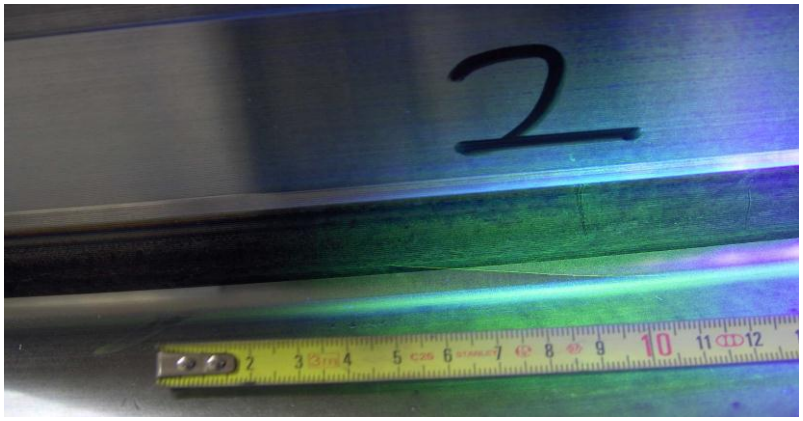

Picture 13: Results of non contact MT-testing with two coils and Multipuls-1003-E2 (25.000 A)

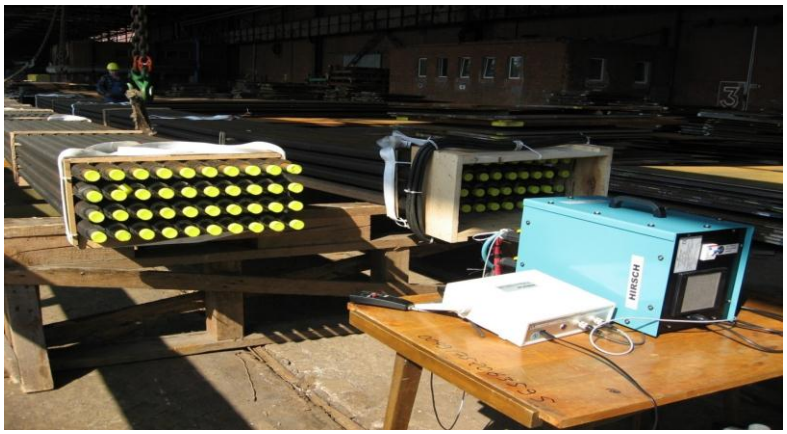

Picture 14: Demagnetization of 40 pieces of heat exchanger pipes for a power plant within 2 minute with double coil

DEFECT DETECTION USING AN OPTIMIZED AND INNOVATIVE PROCESSING TECHNIQUE OF THERMOGRAPHY IMAGES

M. S. Benmoussat, K. Spinnler, Fraunhofer iis, Erlangen, Germany
M. S. Benmoussat, M. Guillaume, Ecole Centrale Marseille, Institut Fresnel, CNRS, France
Y. Caulier, AREVA, France

Abstract

The vision technology and in particular the thermography testing (TT) is a rapid developing NDE method within the nuclear industry. This paper proposes a new approach based on TT and anomaly detection algorithms for the detection of defects in nuclear components. The novelty of the approach consists of using a processing method, originally developed for multi- and hyperspectral imagery, for the automatic and unsupervised processing of thermography images. Practicability of the lock-in and pulsed thermography (LT and PT, respectively) are experimentally investigated by using reference samples containing different surface and sub-surface anomalies such as open cracks, and closed notches with different sizes and depths. The heating is carried out with Eddy current approach.

The generated Eddy-current is launched on the specimen for different time periods and frequencies. Both, heating and cooling parts of the temporal signals are used. Principal component thermography is used to reduce the data space dimension of the acquired thermal sequences, and thus permits the decrease of the processing time. After the reduction of the data space dimension, anomaly detection algorithms are applied on the reduced data cubes. The influence of the size of the reduced data spaces on the anomalies detection is studied using the false alarm rate as evaluation criterion of the detection results obtained from two anomaly detection algorithms: the well-known Reed and Xiaoli Yu detector (RX) and a spatially adaptive version, the regularized adaptive RX (RARX).

The investigations show that; in the case where the targets are small and have significant temperature values, their signal spaces are kept after the reduction of the data cube dimensionality; the optimal false alarm rates are obtained when 80 – 86 % of the variance proportion of the projected data is considered. Indeed, with a detection of 80 – 90 % of the anomalies, we obtain optimal false alarm rates with a dimensionality which does not exceed 10 components, for both surface and subsurface defects.

Keywords: Anomaly detection, Surface inspection, NDT, Infrared thermography

1. INTRODUCTION

Different kinds and shapes of metallic parts (steel, stainless steel, aluminium, etc.) are used in several industrial areas such as the automotive, aviation, and nuclear domains. These components are very often inspected during the production or maintenances steps for quality control purposes. Inspection, which is a quality control task, is defined by Newman and Jain [1] as a process of determining if a product deviates from a given set of specifications. The inspectors are provided with lists and descriptions of unacceptable product defects such as cracks or surface blemishes for example.

Depending on the quality control requirements (number of parts to be examined, size of defects to be detected, etc.), the products are examined manually or automatically during the production or the manufacturing processes. Various non-destructive testing (NDT) techniques exist in the literature [2]. The choice of the appropriate technique primary depends on the type of anomalies to be detected (for metal parts, e.g., anomalies are often either surface defects (scratches, dents, etc.) or subsurface defects (certain types of cracks or porosities, etc.) which are internal discontinuities and cannot be seen visually).

Automated visual testing (AVT) concerns surfaces and also the subsurfaces parts of components. As an example, the examination weld structures of nuclear componants encompasses the early detection of inter-dentrictic propagating cracks.

Inspection of surface and sub-surface defects has become a critical task for manufacturers who strive to improve product quality and production efficiency.

Such kind of defects can affect the functionality, stability, safety of the components and therefore of complete installations. Large and obvious surface defects such as cracks, indents, scraps and scratches are usually inspected by AVT systems, where image processing techniques play a crucial role.

The detection of surface and sub-surface defects has been the subject of several researches for the inspection of metallic industrial components by means of NDT techniques. NDT is an examination, test, or evaluation performed on an object of any type, size, shape or material without changing or altering that object in any way, in order to determine the absence or presence of discontinuities that may have an effect on the usefulness or serviceability of that object. NDT may also be conducted to measure other test object characteristics, such as size; dimension; configuration; or structure, including alloy content, hardness, and grain size [2]. Nondestructive Evaluation (NDE) is a term that is often used interchangeably with NDT. NDE may be used to determine material properties such as fracture toughness, formability, and other physical characteristics [3]. Nondestructive testing and evaluation NDT&E methods are required to be reliable, economical, sensitive, user friendly and fast [4]. Although, NDT cannot guarantee that failures will not occur, it plays a significant role in minimizing the possibilities of failure. Several NDT techniques such as liquid penetrant testing, magnetic particle testing (MT), radiographic testing (RT), ultrasonic testing (UT), and thermography testing (TT) have been used for material inspection. Each of these NDT techniques has appropriate and adequate treatments to inspect the objects. In liquid penetrant testing, only surface breaking defects can be detected; surface preparation is critical as contaminants can mask defects; relatively smooth and nonporous surface are required; and chemical handling precautions are necessary (toxicity, fire, waste). In MT, only ferromagnetic materials can be inspected; smooth surfaces are relatively required; paint or other nonmagnetic coverings adversely affect sensitivity; and demagnetization and post cleaning is usually necessary. In RT, access to both sides of the structure is usually required; relatively expensive equipment investment is required; and possible radiation hazard for personnel. In UT, skill and training required is more extensive than other technique; surface finish and roughness can interfere with inspection; thin parts may be difficult to inspect; and linear defects oriented parallel to the sound beam can go undetected. TT is an imaging technology, which is contactless and completely non-destructive and secure. Since the temperature is one of the most useful parameter that indicates the structural health of an object, TT is used to detect surface and sub-surface defects by determining the surface temperature of the object using an IR camera.

We focus in this paper on infrared thermography (IRT) techniques. IRT is a non-intrusive temperature measuring technique for producing an image of the infrared light – invisible to our eyes – emitted by objects due to their thermal condition. IRT is a NDT method, with the advantages of being fast; easy to apply; applicable to all situations as long as there is a temperature difference on the surface of the inspected object; and providing non-contact, non-interaction, real-time measurements over a large detection area – instead of point or line – with a long range. IRT can only detect defects which cause a change in heat flow or the surface temperature of the item.

Defects detection and material inspection methods in IRT have gone through several progressive steps. Classical thermography is based on the visual interpretation of the thermographic images. The heating or the cooling anomalies are observed after the application of the heat. Defects that produce subtle temperature differences in the thermal images are generally not detected. Furthermore, this technique is based on temperature information only and can be susceptible to emissivity or uneven heating variations. Detection of subsurface defects can be greatly enhanced by the real time capture of a series of thermal images and the subsequent analysis of these images using various image processing algorithms, where defects not readily observable can be detected and quantitatively characterized [5]. Various techniques including: image normalization [6], thermal contrast calculations [7], pulsed phase thermography (PPT) [8] and principal component thermography (PCT) [9, 10] have been developed to remove emissivity or uneven heating variations so as to increase defect contrast and inspection depths.

We propose in this paper a new approach for the inspection of surface and sub-surface metallic parts. The proposed approach is based on the use of IRT techniques, PCT and hyperspectral imagery (HSI) algorithms. Lock-in and pulsed thermography (LT and PT, respectively) techniques are used to heat the inspected specimen and its thermal behaviour recorded during the heating and the cooling periods.

PCT is then used to reduce the data space of the acquired data cubes, where a subspace signal is estimated in order to work on space of smaller dimension than the original space of the data. After the dimensionality reduction of the data cube, HSI algorithms – dedicated to remote sensing applications – are applied on the reduced dataset images, where the anomalies are detected in an unsupervised way.

The novelty of this paper consists of the combination of these two techniques, TT and HSI detection algorithms. It is shown that this approach leads to a new unsupervised and generic examination procedure, as different defect types can be revealed with one processing method. We illustrate our purpose with experiences on two metallic parts containing respectively open notches with different sizes, and open cracks. Two thermography techniques, LT and PT, were applied to the samples and dataset of thermal images were created. The goal of this paper is to apply anomaly detection algorithms on the elaborated dataset images in order to detect surface and subsurface existing anomalies within the inspected samples. Only unsupervised algorithms are investigated, where no prior knowledge about the defects is known.

The remainder of this paper is organized as follows. Section 2 recalls the main thermography techniques dedicated to faults detection in IRT images. The proposed approach is described in Section 3. Section 4 reviews some existing algorithms from HSI literature dedicated to anomaly detection. Section 5 shows the experimental procedure and the used setup. The results are discussed there and Section 6 concludes this work.

2. INFRARED THERMOGRAPHY

Since the early 1960s, thermal testing has been successfully used, in many applications as a NDT&E technique to measure the surface temperature variations in response to induced energy. The energy creates a temperature contrast at material discontinuities that can be detected by an infrared (IR) camera [6]. The IR cameras detect radiation in the IR range of the electromagnetic spectrum (roughly $3 - 5\,\mu m$ and $8 - 14\,\mu m$) and generate false color images of IR or thermal emission called thermograms, allowing very sensitive non-contact temperature measurement [11]. IRT is also used for defect characterization and material property evaluation and inspection since it is completely noncontact and may be faster than many other techniques that are being used. Due to its noncontact character that allows for quick 2D surface mapping, it represents a powerful tool for NDE of materials and structures.

IRT is being used in a wide range of areas, such as in agriculture, civil engineering and architecture, diagnosing electrical and mechanical equipment, automotive industry, medicine and biology, manufacturing industry, food quality control and protection of historic heritage.

IRT can be divided into two approaches usually indicated as passive and active thermography. The passive approach tests materials and structures, which are naturally at different (often higher) temperature than ambient. The temperature is monitored without employing any heating of the sample induced by the measurement procedure. Features of the temperature distribution, like differences with respect to a reference level, allow to obtain qualitative information about the specimen under examination. Important applications of the passive approach are in production, predictive maintenance, medicine, fire forest detection, building thermal efficiency survey programs, road traffic monitoring, agriculture and biology. Contrary to the passive approach, in the active approach, an external stimulus is necessary to induce relevant temperature differences not present otherwise. Knowing the characteristics of this external stimulus (example: time t_0 when it is applied), active thermography allows to obtain both qualitative and quantitative evaluations by monitoring the transient of the temperature change induced in the anomalies by means of adequate artificial light emitting heating techniques, such as e.g. flashes or direct current (DC) lamps, lasers or other light sources [12].

Currently commonly used infrared thermography methods are active methods. Depending on the way of thermal excitation, different approaches of active thermography have been developed, such as step heating, PT and LT [13]. In step heating, the temperature rise is monitored in the transient domain, where a long heating pulse is applied. In PT, a short heating pulse is applied to the specimen and the cooling data is monitored in the transient domain. LT is carried out in stationary domain, where a modulated heat wave is launched on the sample, travels through the bulk by diffusion and reflects back from the defect sites. PT is being routinely used for quantitative evaluation of defect in both metallic and composite specimens.

LT has been extensively used to find quantitative information of subsurface defects, corrosion protective paints, morphologies of defects (like circular, square-like, etc.).

3. PROPOSED METHOD

The acquired thermal images are grouped in a sequence of thermograms, (Fig. 1a), where the first two dimensions represent the spatial information (pixel positions) and the third dimension represents the variation of the temperature for each pixel over the time, and gives the temperature profile (Fig. 1b). This data structure is remindful of the hyperspectral cubes which have the same data structure except that the third dimension represents the spectral response of each pixel with respect to the wavelength position. Fig. 1 shows a thermogram sequence with respect to the acquisition time and the temperature profile for the pixel p on coordinates (i, j). Δt is the sampling time. Hence, the use of multi- and hyperspectral imaging algorithms on thermographic data for defect detection is possible. Actually, the thermal response of a material can be considered as representative of this material. It has been already shown in [14] that is possible to apply HSI algorithms, such as target and anomaly detection algorithms and spectral distance measures, for surface defect detection of metal parts on such pseudo-spectral-cubes corresponding to the different lighting modalities: white light and monochromatic lights in combination with polarization.

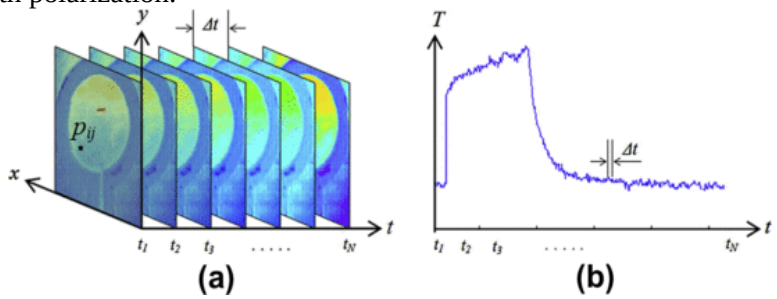

Fig. 1: (a) thermograms sequence and (b) temperature profile for the pixel p on coordinates (i, j).

We propose in this paper a new defect detection approach based on anomaly detection algorithms for thermography images. The acquired thermal images are arranged in a 3D matrix, called cube or data cube, in ascending order of acquisition time (Fig. 2a). The defect detection is based on the time behaviour of each pixel, where the anomalies are defined as observations that deviate in some way from the background from a statistical point of view.

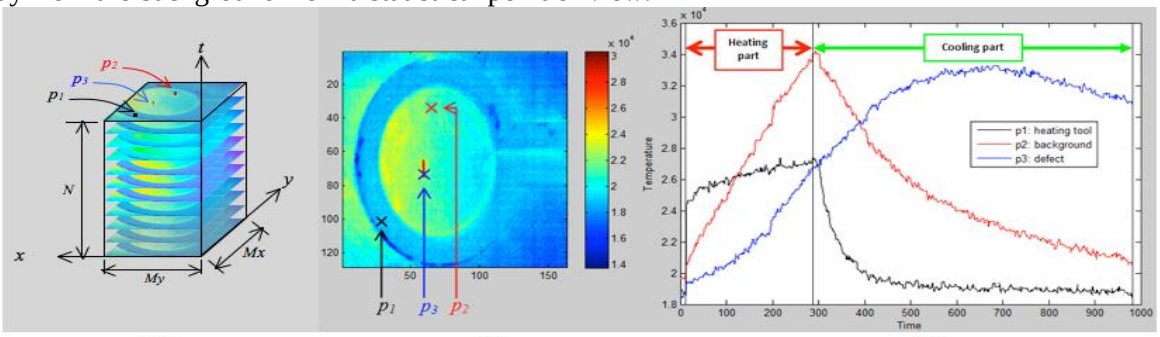

Fig. 2: (a) data cube dimensions, (b) thermogram at t_{500} *and (c) temperature rise and decay curves for three different objects.*

The observed temporal responses are composed of two main successive components corresponding, respectively, to the heating (temperature rise) and the cooling (temperature decay) processes of the specimen (Fig. 2c). Usually, the behaviour of the specimen is analyzed only either during the rising surface temperature or during the decay [8]. Most often, in PT the temperature decay part is used to analyze the inspected parts [12]. Basically, the specimen is briefly heated for a certain period of time and then it is allowed to cool. In parallel, its temperature profile is recorded. At time t_1, before heat reaches the specimen's surface, a cold image is captured. The temperature of the material rises during the pulse. After the pulse, it decays because the thermal energy propagates by diffusion under the surface.

Later, the presence of a subsurface defect reduces the diffusion rate so that when observing the surface temperature, such a subsurface defect appears as an area of higher temperature with respect to the surrounding sound area. Fig. 2 shows the data cube construction from the thermograms sequence. It also shows a thermogram example at t_{500} and plots the temperature rise and decay curves for three pixels of different parts: the heating tool, background and defect. The limit between the heating and cooling parts (HP and CP, respectively) is plotted with respect to the heating tool (black curve). The limits of the background and defect pixels, red and blue curves respectively, are slightly shifted with respect to the heating tool pixel, due to the thermal front propagations and to the distance separating them from the heating tool.

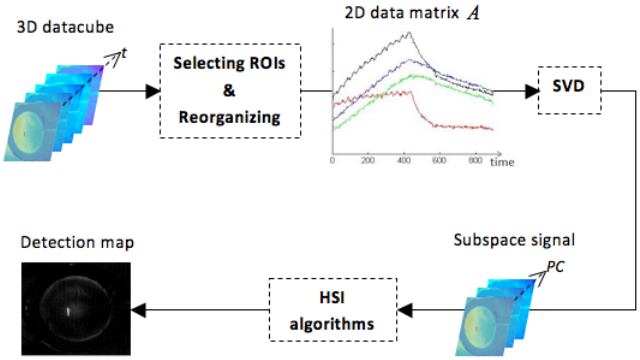

Fig. 3: proposed scheme of the presented approach based on SVD and HSI algorithms.

The proposed approach can now be schematized. Fig. 3 illustrates the main steps involved in this approach. As a first step, either the entire datacube, recorded by the IR thermal camera, is treated or spatial and temporal regions of interest (ROIs) can be selected. The spatial ROI corresponds to the desired area to be inspected, while the temporal ROI corresponds to HP and/or CP (Fig. 2c), or to any part of the temporal profile want to be considered. Once the desired ROIs are chosen, the datacube is unfolded into a matrix A and singular value decomposition (SVD) is applied, allowing to decompose it into N components, arranged in a descending order of the corresponding singular values (SVs), where the first components contain the maximum variance.

In PCT, the thermographic data is projected from its original space to its eigenspace to increase its variance and reduce its covariance [9, 10, 13]. SVD extracts the spatial and temporal information from the thermographic matrix in a compact manner. SVD is close to principal component analysis (PCA) with the difference that SVD simultaneously provides the PCAs in both row and column spaces. The 3D thermogram cube representing time and spatial variations is reorganised as a 2D $M \times N$ matrix A, where M is the total number of pixels and N is the total number of images. Under this configuration, the matrix A can be decomposed into three matrices U, S and V as follows [9, 10]:

$$A = \sum_{i=1}^{N} U_i \, S_i V_i^T \qquad (1)$$

The columns of matrix U consists of singular vectors that represent the spatial variation of the data set. The matrix S is a diagonal matrix with the singular values on its diagonal, which are reordered in descending order based on their values. The columns of matrix V are the right singular vectors that represent the temporal variation of the data set. Usually, original data can be adequately represented with only a few components. Typically, a 1000 thermograms sequence can be replaced by 10 or less components [13].

A reduction of the data space is often used, where a subspace signal is estimated in order to work on smaller dimension than the original space of the data. In general, the space reduction leads to a loss of information, especially for targets that have low spatial dimensions (represented by only a few pixels). In our case, the targets are small, but due to the fact that they have significant temperature values, their respective signal spaces are preserved after the reduction of the data cube dimensionality.

Anomaly detectors are then applied on the reduced datacube in order to detect the defects with a non-supervised approach. This means that no prior knowledge about the defects is used. The detection results are given as 2D maps which will be used next to evaluate and compare the detection algorithms by means of the receiver operating characteristic (ROC) curves.

4. ANOMALY DETECTION ALGORITHMS

The observed data cube is considered as a set of $M = M_x \times M_y$ vectors in the full multidimensional space (Fig. 2a). More often, the task of a detection algorithm is to decide, by means of a statistical hypothesis test, whether a target of interest **s** is present or not in a pixel-under-test with observed pixel vector **x** [15]. To take a decision, we calculate a test value $y = D(\mathbf{x})$, and compare it to a threshold η. A practical question of paramount importance for a detection algorithm user is how to set the threshold to keep the total number of detection errors (target misses and false alarms) small. Indeed, there is always a compromise between choosing a low threshold to increase the probability of (target) detection (PD) and a high threshold to keep the probability of false alarm (PFA) low. For any given detector, the trade-off between PD and PFA is described by the ROC curve, which plots PD (η) versus PFA (η), as a function of threshold.

In the literature, many algorithms for detection and classification are proposed, applied in multi- and hyperspectral imagery. The most popular unsupervised detectors are the anomaly detection algorithms, which do not require any knowledge of the spectral signatures of the target of interest (defect). Anomalies are defined with reference to a model of the background. Background models are developed adaptively using reference data from either a local neighbourhood of the test pixel or a large section of the image. Anomalies are defined as observations that deviate in some way from the neighbouring clutter background or the image-wide clutter background, respectively [16].

The problem of anomaly detection is typically formulated as a binary test between two hypotheses: background only (H_0) or target and background (H_1):

$$y = D(\mathbf{x}) \underset{H_0}{\overset{H_1}{\gtrless}} \eta \qquad (2)$$

The most common used anomaly detector is the Reed and Xiaoli Yu detector (RX) given by [16, 17]:

$$D_{RX}(\mathbf{x}) = (\mathbf{x} - \mu)^T \hat{\Gamma}^{-1} (\mathbf{x} - \mu) \underset{H_0}{\overset{H_1}{\gtrless}} \eta \qquad (3)$$

where $\hat{\Gamma}$ and μ are respectively the estimated covariance matrix and mean vector of the reference background data. In order to obtain good estimations of the mean and the covariance matrix, using the whole data, the background must be homogeneous and the target must be small. Basically, $D_{RX}(\mathbf{x})$ estimates the Mahalanobis distance between the pixel vector **x** and the mean background, which is zero for centred data [15]. This algorithm has the constant false alarm rate (CFAR) property, it assumes that the background follows a local Gaussian multivariate distribution, that the spatial signature of the target is known, and that the covariance matrix is unknown [18].

Recently, a new approach of RX, A regularized adaptive RX (RARX), was proposed in [18] to estimate the spatial distribution conjointly with the detection algorithm. Its expression is given by:

$$D_{RARX}(\mathbf{x}_i) = \frac{1}{\hat{\mathbf{s}}\,\hat{\mathbf{s}}^T} \left[\|\tilde{\mathbf{x}}_i\|^2 + 2 \sum_{l \in v(i)} \hat{s}_l \tilde{\mathbf{x}}_i^T \tilde{\mathbf{x}}_l \right] \qquad (4)$$

where $\hat{s}_l$ is an estimation of the abundance of the tested pixel $\mathbf{x}_i$ in its neighbour $\mathbf{x}_l$, which can be calculated by the following expression:

$$\hat{s}_l = \left(\frac{\tilde{\mathbf{x}}_i^T \tilde{\mathbf{x}}_l}{\|\tilde{\mathbf{x}}_i\| \, \|\tilde{\mathbf{x}}_k\|} \right)^2, k = 1..V$$

$\tilde{\mathbf{x}}$ is the whitened vector, and $\mathbf{s} = [s_1, s_2, \ldots, s_V]^T$, where V is the number of neighbour pixels.

The first term in Eq. (4) is similar to Eq. (3), and the second one is a linear correlation between $\mathbf{x}_i$ and its neighbours, weighted by the estimated spatial distribution of the target in the neighbourhood. This term linearly depends on $\hat{s}_l$.

5. APPLICATION

Two samples, containing different anomalies, were used in order to validate our proposed approach. The considered samples are listed in Table 1. A dataset of thermography images was elaborated with different anomalies, where two recording processes, PT and LT, were considered.

The recording setup is made of an IR-camera, an inductor (for eddy-current excitation) and a sample. The camera is placed at a certain distance and angle to the surface in order to have constant lateral resolution and avoiding disturbing reflections (in case of high emissive surfaces, e.g.). Fig. 4 depicts the recording setup.

Sample name	S1	S2
Sample photo	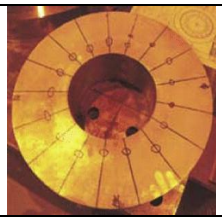	
Anomaly type	Open notches with different sizes	Open cracks
Material	Inconel 600	Inconel 600
Defect size	Length: 5 mm Depth: 2 mm	Length: 8 mm Width: 20 µm (approximately)

Table 1: considered samples for the thermography reference dataset.

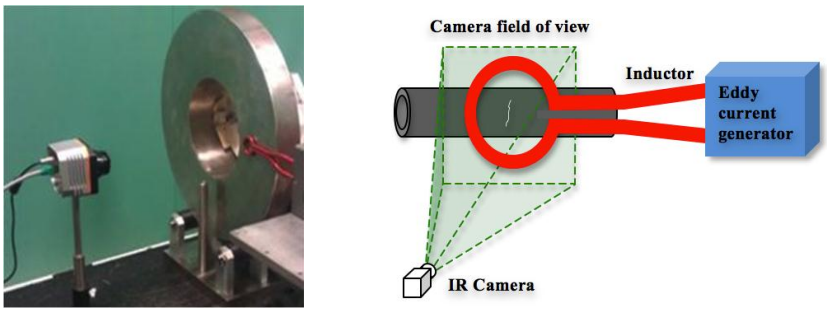

(a) (b)

Fig. 4: considered recording setup for both samples (a) S1 and (b) S2.

The current generator is used to generate eddy currents (also called Foucault currents), which are electric currents induced within conductors by a changing magnetic field induced by the conductor. The heating effect is caused by the effective resistance of the conductor through which the eddy current is flowing. During the heating process, the currents propagate in the vicinity of the inductor. They are propagating in the upper part of the sample, and they also are disturbed by the presence of the defects.

In PT, a short heating pulse is generated and launched for a few seconds (from 1 to 10 s) on the specimen through the inductor and in LT, a sinusoidal wave of low frequency (form 1 to 5 Hz) is generated and applied for 5 to 10 s. In both processes, LT and PT, the specimen is left to cool for 5 to 10 s. The IR camera images the temperature variations as thermograms during the heating and cooling phases with a frequency of acquisition of 62 fps and sends the acquired images to the computer, where the output data of each sequence is stored as a cube of size $[Mx \times My \times N]$, i.e. ($Mx \times My$ signal vectors of length N).

Usually, the behaviour of the inspected object is analyzed only either during the surface temperature rise or during its decay [8]. As the anomaly detection is based on the temporal behaviour of the pixels, it is very important to choose the relevant part (heating and/or cooling parts), where the anomaly pixels are well separated from the other pixels. A comparative study was done in [19] based on the criterion of false alarm rate (FAR). For automated inspections, it has been suggested to keep the whole provided information about each pixel and to choose both regions: heating and cooling parts, of the temperature profile. This will avoid the problems of how to choose the temporal ROI and how to find the limits between the heating and cooling parts. In addition, dimensionality reduction methods will be applied on the data cubes in order to work with cubes in reduced data spaces, where only relevant components will be kept and the anomalies can be easily detected, for sufficient temperatures. We have kept the totality of the cube in order to have the best estimation of the data subspace.

We have chosen for this study two cubes, corresponding to LT and PT, for each sample. For the two used samples, S1 and S2, (Lock-in 4 Hz and Pulsed 4s) and (Lock-in 1 Hz and Pulsed 5s) cubes were selected, respectively.

SVD is then applied on the selected data cubes, where the original data are projected in subspaces of dimension K. The images in the resulting cubes are arranged in descending order of the variance r. $r = \frac{\sum_{i=1}^{K} e_i}{\sum_{i=1}^{N} e_i}$, where e_i is the i^{th} eigenvalue on the diagonal matrix S described in Eq. (1). In this experiment, we varied the values of K from 2 to 15. This corresponds to a variance r of 80 – 86%. The described algorithms in Eqs. (4) and (5) are then applied on the reduced data cubes with different values of K, where the detection results are given as 2D masks after thresholding the detection maps. We varied the probabilities of detection from 40% to 90% and we calculated the corresponding false alarm rates. The results are shown in Fig. 5. Since both algorithms RX and RARX have given similar results, we show only the results of RARX.

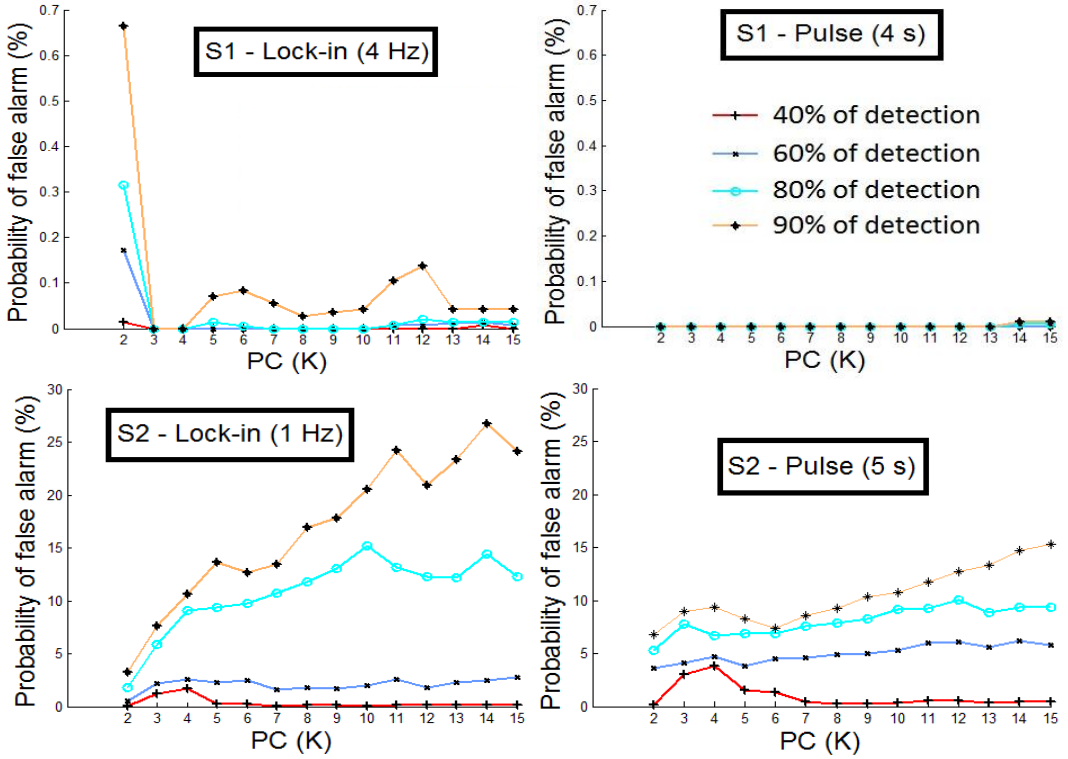

Fig. 5: probabilities of false alarm for $K = 2{:}15$ and detection rates for two specimens acquired with LT and PT.

The false alarm rates vary from 0 % to 0.66 % for S1-Lock-in and from 0 % to 0.03 % for S1-Pulse. The anomalies present in S1 are mostly detected with very low false alarm rates in both lock-in and pulse cubes only with a detection of 40 % of the pixels of the defect. These anomalies are easily detected with low false alarm rates because the defects are located on the surface of the sample and are visible in all the acquired thermograms, which means that after data space reduction step, they are present and with high energy. Also, their thermal profiles are different from those of the pixels of the background and the heating tool, which make easy to detect them with the used anomaly detection algorithms.

Concerning S2, the false alarm rates vary alot from each detection rate. But, the optimal rates are obtained with a detection of 40 % of the pixels of the defect. The false alarm rates vary from 0.06 % to 1.68 % and from 0.19 % to 3.84 % for S2-Lock-in and S2-Pulse respectively. These rates can reach, respectively, 26.74 % and 15.32 % for S2-Lock-in and S2-Pulse when high detection rates (80 – 90%) are fixed. The main reason of these high false alarm rates is that, there is an additional, compared to S1, class of pixels (the pixels where the heating tool is reflected on the surface); in addition to the other classes (background, defect and heating tool); which have also significant temperature values.

In fact, the signal spaces of both classes defect and reflexion are kept after the reduction of the data cube dimensionality. This is the reason why the pixels of these 2 classes appear in the detection masks, as shown in Table 2.

Table 2 shows the detection masks (binary cards) for different detection rates (30 – 90 %) with the optimal value of K.

Probability of detection	30 %	40 %	60 %	80 %	90 %
S1 Lock-in	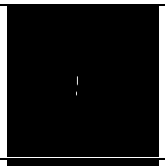	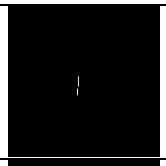	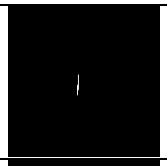	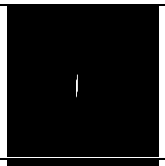	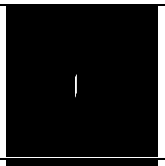
S1 Pulse	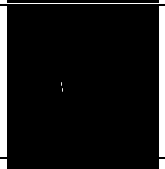	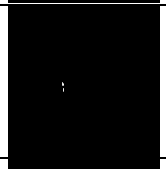	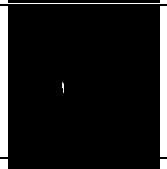	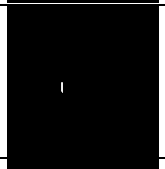	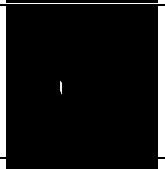
S2 Lock-in	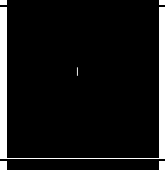	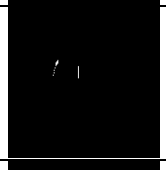		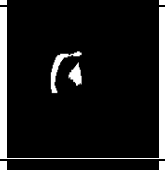	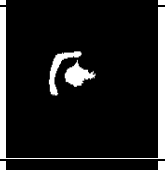
S2 Pulse	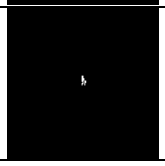	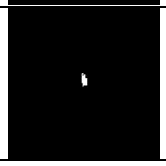		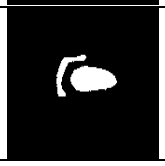	

Table 2: detection masks for different probabilities of detection.

Knowing that we are looking for linear anomalies corresponding to linear defects and in order to detect only the pixels corresponding to the anomaly, the probability to detect all the pixels of the anomaly should be kept low (30 – 40 %). In such cases, the pixels of the defect can be easily detected with very low false alarm rates.

A comparison study has been done between the use of the original and reduced data cubes. The results in Table 3 show that the detection times are approximately 10 times greater when reduced data cubes are used compared to when original data cubes are used, however the false alarm rates are greatly reduced. The computational burden of the used anomaly detection algorithms depends directly on the size ($Mx \times My \times N$) of the input data cube, which is expressed in terms of big O notation for both algorithms, RX and RARX, as: $O\ (Mx\ My\ N)$ after calculation of the covariance matrix. This means that these algorithms scale to increasing amounts of data. For a data cube of size $120 \times 160 \times 900$; the detection time is about 9 s, the dimension reduction time is about 90 s and the detection after reduction with $K = 2$ is about 2 s. However, the SVD calculation time could be reduced by using a reduced version of SVD, such as truncaded SVD to determine only the first components.

	Original data cube			**Reduced data cube**			
	Size (pixels)	**Detection time (s)**	**Probability of false alarm (%)**	**Size (pixels)**	**Reduction time (s)**	**Detection time (s)**	**Probability of false alarm (%)**
S1-LT	88x163x927	7.84	19.69	88x163x3	56.06	2.06	0
S1-PT	128x163x959	10.96	24.94	128x163x2	114.62	2.95	0
S2-LT	124x163x824	9.45	48.56	124x163x2	94.31	2.87	0.56
S2-PT	124x163x952	10.94	98.17	124x163x2	101.87	2.84	3.58

Table 3: Comparison between original and reduced data cubes.

6. CONCLUSION

In this paper, an unsupervised approach of surface and sub-surface defects detection for the inspection of nuclear metallic components has been proposed. It is based on the use of thermography images and anomaly detection algorithms, basically dedicated to remote sensing applications. A dataset of thermal cubes, where the thermal profile of the inspected surface is recorded, has been established for two metallic parts containing different types of anomalies by means of LT and PT techniques. Both rising and decay parts of the temperature profile have been considered, which means that the whole information about the temporal behaviour of each pixel have been used. The space dimensions of the data cubes were then reduced by means of SVD in order to work with smaller data spaces than the original ones. The reduced data cubes have been analyzed by means of anomaly detection algorithms to obtain the existing anomalies within the inspected parts with no prior knowledge about the defects. The detection maps, resulting from the used algorithms RX and RARX, have been compared for different dimensions of the reduced dataspaces and different detection rates of the anomaly pixels. The results show that the detection strategy allows to detect compact anomalies with very low false alarm rates when low detection rates are fixed. The results are better when there is only three main classes: background, heating tool and defect pixels and no additive perturbation pixels are present on the scene corresponding the reflexion of the heating tool on the surface. Compared to detection on original data cubes, the inspection time in the proposed approach is significantly increased, but the detection performances are substantially improved with the use of dimension reduction. Moreover, the use of the reduced version of SVD, such as truncaded SVD to determine only the first components, should be much quicker and more economical than the full SVD.

ACKNOWLEDGMENT

The authors would like to thank the Bavarian Research Foundation (BFS: Bayerische Forschungsstiftung) for supporting this researches done at the Fraunhofer IIS in Fürth, Germany.

REFERENCES

[1] Timothy S. Newman, Anil K. Jain, “A Survey of Automated Visual Inspection”, Computer Vision and Image Understanding, Volume 61, Issue 2, March 1995, Pages 231-262.
[2] Hellier C.J., “Handbook of Nondestructive Evaluation”, McGRAW-HILL, 2001.
[3] IAEA, “Non-destructive testing for plant life assessment”, 2005 IAEA-TCS-26, ISSN 1018–5518.
[4] Liu J., Yang W., Dai J., “Research on thermal wave processing of lock-in thermography based on analyzing image sequences for NDT”, Infrared Physics & Technology, Vol. 53, Issue 5, Sep. 2010, Pages 348-357.
[5] Joseph N. Zalameda, Nikolas Rajic, William P. Winfree, “A comparison of image processing algorithms for thermal nondestructive evaluation”. Proc. SPIE 5073, Thermosense XXV, 374, April 3, 2003.
[6] C.Ibarra-Castanedo, D.González, M. Klein, M. Pilla, S. Vallerand, X. Maldague, “Infrared image processing and data analysis”, Infrared Physics & Technology, Volume 46, Issues 1-2, Dec. 2004, Pages 75-83.
[7] Maldague X., “Theory and practice of Infrared thechnology for nondestructive Testing”, John Wiley-Interscience, 2001.
[8] Maldague X., Marinetti S., “Pulse phase infrared thermography”, Journal of Applied Physics, vol.79, no.5, pp. 2694-2698, Mar. 1996.
[9] N. Rajic, “Principal component thermography for flaw contrast enhancement and flaw depth characterisation in composite structures”, Composite Structures, Vol. 58, Issue 4, Dec. 2002, Pages 521-528.
[10] V. Vrabie, E. Perrin, J.L. Bodnar, K. Mouhoubi, V. Detalle, “Active IR thermography processing based on higher order statistics for non-destructive evaluation”, European Signal Processing Conference, Aug. 2012.
[11] Rogalski A., Chrzanowski K., “Infrared devices and techniques”. Opto-Electronics Review 2002, 111 – 136.

[12] Maldague X.P.V., “Introduction to NDT by active infrared thermography”. Materials Evaluation 2002; 60(9): 1060–1073.
[13] C. Ibarra-Castanedo, A Bendada, Maldague , “Thermographic Image Processing for NDT”, Proc. IV Pan American Conference in END, Oct. 2007.
[14] Benmoussat M.S., Spinnler K., Guillaume M., "Surface defect detection of metal parts: Use of multimodal illuminations and hyperspectral imaging algorithms," Imaging Systems and Techniques (IST), 2012 IEEE International Conference on, vol., no., pp.228, 233, 16-17 Jul. 2012.
[15] Manolakis D., “Detection algorithms for hyperspectral imaging applications: a signal processing perspective”. In: Advances in Techniques for Analysis of Remotely Sensed Data, p. 378 – 384, 2003.
[16] Stein D., Beaven S., Hoff L., Winter E., Schaum A., Stocker A., “Anomaly detection from hyperspectral imagery”. Signal Processing Magazine, IEEE 2002; 19(1): 58 –69.
[17] Reed I., Yu X., “Adaptive multiple-band CFAR detection of an optical pattern with unknown spectral distribution”. Acoustics, Speech and Signal Processing, IEEE Transactions on 1990; 38(10):1760 –1770.
[18] Gaucel J.M., “Méthodes tridimensionnelles pour la compression, restauration et détection en imagerie hyperspectrale”. Ph.D. thesis, Université Paul Cézanne Aix-Marseille (France), 2007.
[19] M.S. Benmoussat, M. Guillaume, Y. Caulier, K. Spinnler, “Automatic metal parts inspection: Use of thermographic images and anomaly detection algorithms”, Infrared Physics & Technology, Vol. 61, Nov. 2013, Pages 68-80.

NEW SYSTEM "SOKRAT" FOR WWER-1000 REACTOR PRESSURE VESSEL VISUAL TESTING FROM OUTER SURFACE

I. Kadenko, R. Iermolenko, V. Petryshyn, N. Sakhno
Nondestructive Examination Training and Certification Facility, Ukraine

1. INTRODUCTION

Reactor pressure vessel (RPV) of WWER-1000 unit as a part of NPP main equipment comprises a second physical barrier of NPP defence in depth concept. To ensure structural integrity of RPV there was established a set of technical means and organizational measures. Periodical in-service visual testing (VT) of RPV outer surface is a mandatory requirement for WWERs in Ukraine [1].

Until recently the only available inspection system SK-187 with modifications was applicable to perform reactor WWER-1000 RPV VT from outer surface. SK-187 was designed and manufactured back to 80-th last century and nowadays requires either deep upgrade or replacement.

Till nowadays for Units 3 and 4 of Rivne NPP, Ukraine, the visual survey of WWER-1000 RPV from outer surface with SK-187 old fashioned system faces with the following problems:

- overlapping of maintenance schedules of RNPP and ZNPP (the owner of SK-187 system);
- transportation of contaminated SK-187 equipment between ZNPP and RNPP with corresponding police guidance;
- loading operations of SK-187 system equipment do require waiting for the polar crane availability;
- assembling and disassembling of SK-187 system under limited room conditions;
- decontamination of SK-187 system equipment afterwards.

To address all the above listed problems and also taking into account the growing demands to meet the up-to-date operational safety it was made the technical decision (No.TP-530/2005) to develop a brand new system "SOKRAT" [5] for visual testing/survey of WWER-1000 RPV from outer surface.

Therefore, to meet current safety requirements for carrying out WWER-1000 RPV VT from outer surface, the VT system "SOKRAT" was designed and manufactured based on modern components and engineering solutions.

System "SOKRAT" is dedicated for VT of the outer surface of the cylindrical part of the WWER-1000/V-320 RPV between weld joints Nos. 2 – 4. VT system "SOKRAT" serves as up-to-date manipulator with elements of robot-technology. VT is performed with application of radiation-resistant TV camera being delivered to the inspection area by automated manipulator with remote control. Manipulator is developed to inspect RPV cylindrical part metal and RPV bottom area.

Opposite to inspection system SK-187 [2, 3, 4] with a mass about 6 tons, the system "SOKRAT" weight is less than 400 kg. VT system "SOKRAT" consists of the following components: mechanical equipment of manipulator, control equipment subsystem, coordinate subsystem with absolute and relative encoders, laser positioning subsystem, VT equipment subsystem. Delivery of manipulator to working location beneath RPV is performed with rail wheels. Direct drive engine and electro-magnetic brakes are built in into each of 4 wheels. Even in case of 3 wheels failed one wheel left would be sufficient to drive system "SOKRAT" from reactor vault premise to neighbouring room with acceptable working conditions. Remote operation of manipulator is performed with own developed software. System "SOKRAT" has "3 + 1" axis of movement. Global positioning uncertainty doesn't exceed 5 mm. Minimal step of camera movement is 5 mm.

VT system "SOKRAT" provides inspection in two modes: manual control mode and fully automated survey mode. Laser positioning subsystem allows carrying out an initial installation and positioning the manipulator in reactor vault without staff presence.

Assembling / disassembling of system "SOKRAT" can be done with application either of cargo-handling facilities or manually by 3 - 4 persons. System "SOKRAT" was designed to be easily decontaminated when needed.

VT system “SOKRAT” went through the factory acceptance and functional testing at NPP site and was commissioned. It is planned to perform first full scope VT of the outer surface of WWER-1000 RPV with application of VT system “SOKRAT” during outage in 2014.

2. SYSTEM “SOKRAT” DESCRIPTION

The system “SOKRAT” manipulator sketch is presented in Fig.1. This system comprises of the following main parts: platform; rotating rod; hoist; module for bottom testing, control system; VT system. The manipulator is positioned on rails in under reactor rooms G301 and G302 (Fig.2).

Figure 1 - Appearance of the system “SOKRAT”

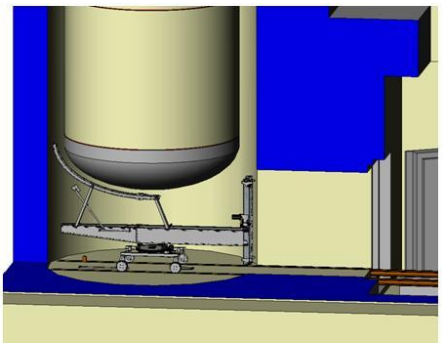

Figure 2 - Stationing the system “SOKRAT” manipulator in G301 room (module for RPV bottom VT lifted)

The design of system “SOKRAT” is similar to SK-187 system to some extent, but utilization of up-to-date light alloy materials allowed reducing a total weight from 5,700 kg (system SK-187) up to 400 kg (system “SOKRAT”). The Tec specs are given in Table 1.

Table 1 – System “SOKRAT” technical characteristics

	Parameter	Value
1	Operational mode:	Manual/Automated
2	No. of axis for manipulator movement	3+1
3	Min/Max velocity of the platform movement, mm/s: Velocity along H axis, mm/s: Rotational speed F, rotations/min: Velocity along R axis, mm/s:	20/100 10÷30 0,25 10÷30
4	Uncertainty of video camera positioning, mm	1
5	Minimal step of video camera movement, mm	1
6	Temperature of environment, °C	+10 ÷ +45
7	Relative humidity, %	≤ 85%
8	Maximum dose rate at video-camera, Gy/hour	up to 3
9	Power supply	220 V, 50 Hz, 15 A

2.1 The platform

The platform serves as a base unit of this manipulator and presented in Fig. 3.

This platform is assembled on the frame made of stainless steel welded of rectangular pipes mm. The platform is driven with 4 wheels-direct drive motors without any transmission nodes. The motor’s control is executed with PID controller to achieve a very smooth ride for manipulator, approaching RPV, and the coordinate accuracy (±6 mm).

Figure 3 - The platform of system “SOKRAT”

All 4 motors are equipped with parking electromagnetic brakes to remotely block the translational movement of system “SOKRAT” while VT is being performed. The system “SOKRAT” motors/wheels mounting let control the alignment of manipulator rotational axis and RPV symmetry axis. The rotary support with outer ring gear is installed on the manipulator frame to provide 365° angle rotation and exclude the “dead” zones. The rotary support is being revolved thorough the rotational drive by stepping motor. Such a design makes it accurately possible the setting up the angle of rotation, the speed of rotation and to utilize a turn encoder as additional monitoring device. Design of the platform includes the option to remotely rotate the rotary support with emergency rod in case of stepping motor failure.

2.2 The hoist

The hoist is dedicated to deliver the radiation-resistance camera to the necessary zone for RPV cylindrical part VT (survey). The hoist is a telescope device consisting of 4 sections (Fig.4). The radiation resistant camera is installed on upper part of section 4 of the hoist. Video signals, control signals, supply and lightning control are transmitted via spring cables. When black out of stepping motor occurred with the hoist in up position, then the hoist softly returns to the folded position with emergency brake system based on stepping motor. For this particular case the stepping motor operates in the generation mode. Also the design of drive allows remotely returning the hoist in the folded position with emergency rod when the hoist stepping motor failed.

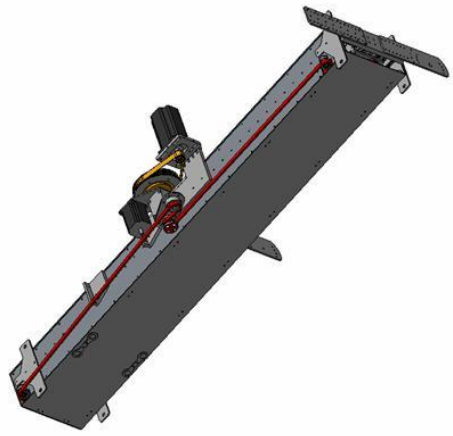

Figure 4 - The hoist in the folded position

2.3 Module for bottom testing

The module for bottom testing is dedicated for the delivery of radiation-resistant video camera to the zone for visual testing/survey of RPV elliptical bottom and presented in Fig. 5. The module for bottom testing consists of elliptical guide and carriage (Fig.6).

Figure 5 - The module for bottom testing (in lifted position)

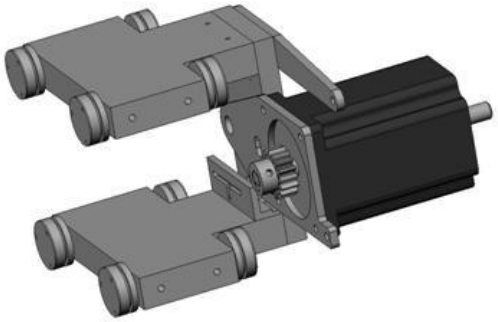

Figure 6 - The carriage of the module for bottom testing

The radiation-resistant video camera is mounted on carriage and follows the elliptical trajectory (parallel /equidistant from RPV bottom) while a carriage moves along a guide. Carriage itself is being set in a motion with the stepping motor through a rack wheel (installed on the motor shaft) and elliptical rack (mounted on guide). Similar to the hoist the video signals, control signals, power supply, and lightening control signals are being transmitted via spring cables.

The movement of system "SOKRAT" manipulator to room G301 beneath RPV is carried on with a module for bottom testing in the folded position. When manipulator approaches the dedicated position under RPV, the electromagnetic breaks of wheels are switched on and a module for elliptical bottom testing is to be lifted by means of actuator. The mechanism for lifting/folding of this module for bottom testing is adapted for the folding of this module with emergency rod when actuator fails.

2.4 Radiation resistant video camera

The VT/survey of RPV from outside assumes considerable dose loadings at video camera even if fuel is discharged (first of all, due to activation of RPV and internals metal). To get a qualitative video picture a radiation resistant digital video camera PTZ-100, comprising the visual testing system Everest Ca-Zoom 6.2 (Fig. 7) was mounted on system "SOKRAT".

Figure 7 - VT system Everest Ca-Zoom 6.2

The camera is equipped with a 4 LED lightening system, 2 axis rotation drives and laser device for calibration of linear dimensions of images. VT system Everest Ca-Zoom 6.2 is applicable to get a video picture both at local control unit and at PC for data acquisition.

2.5 Control system

The control system of system "SOKRAT" includes 2 PCs: PC1 is for data acquisition and PC2 – for manipulator control (Fig.8).

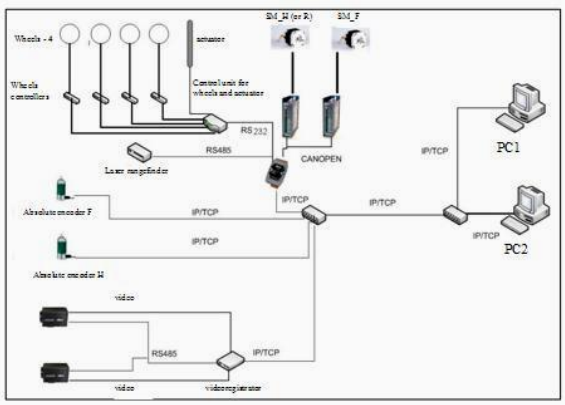

Figure 8 – System "SOKRAT" control system

PC2 controls all the system "SOKRAT" functions via Ethernet IP/TCP protocol and operates a controller. Controller generates control and supply voltages for motors. Data about the video camera position gets to controller and further to PC2. Controller also receives data about positions of end switchers and in case of their work out a corresponding motor will be switched off.

2.6 Software for control of platform motion

The original software is developed for control of longitudinal displacement of manipulator along rails (in manual or remote mode) and lifting or folding a module for bottom testing. The software interface consists of some specific windows (Fig. 9).

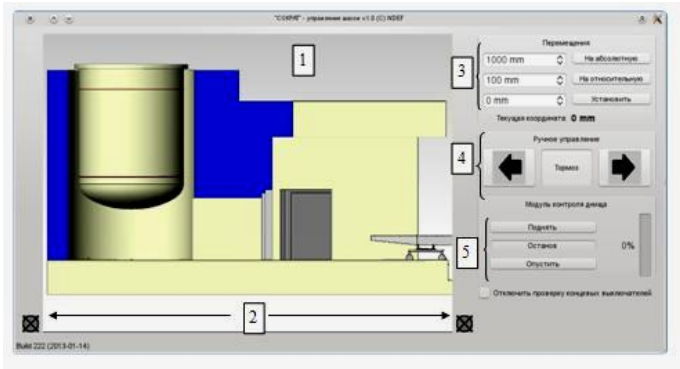

Figure 9 - The software interface for platform motion control

In left half of the screen a sketch of manipulator is shown with it's coordinates assigned to real positioning (1). In a lower part of a screen the indicators of end switch states are given (2). In right half of this window there are fields to set up coordinates and motion control buttons (3). Manual operation of manipulator can be performed with button (4). And finally, in a lower right corner of this screen the buttons for operation of module for RPV vessel are available (5).

2.7 The system "SOKRAT" software for VT/survey performance

The software for VT/survey performance is dedicated for RPV VT/survey both in manual and automated modes. The software interface allows to control a current location of manipulator and it's parts relative to RPV vault and includes necessary fields to set the VT/survey parameters and operational mode (Fig.10).

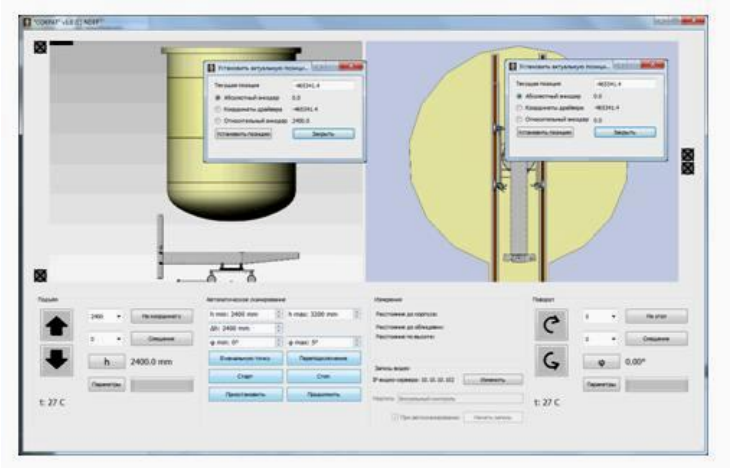

Figure 10 - Software interface for VT/survey performance

This interface is necessary to set main settings of stepping motor controllers (current, step, acceleration etc.) and parameters of absolute encoders. Also auxiliary information about system “SOKRAT” (end switch states, connection/disconnection with stepping motors controllers and absolute encoders, working temperature of stepping motors controllers, distance to RPV, etc.) is available at any time.

3. CONCLUSIONS

The system “SOKRAT” for WWER-1000 RPV visual testing/survey from outer surface is designed, developed and manufactured by NDEF Company. Intensive factory acceptance testing and functional testing showed:

- the system is very reliable and user friendly;
- can ensure essential reducing radiation doses at NPP personnel;
- system “SOKRAT” has necessary values of positioning inaccuracies and repeatability;
- UT system for WWER-1000 RPV can be developed at the base of system “SOKRAT”.

4. REFERENCES

1) PM-T.0.03.061-04 «Typical program of periodical in-service inspection of the state of base metal, weldings and overlays of equipment and pipes at WWER-1000 NPPs », (in Russian).
2) 104-11-TC-CKM. Technical specification. Manufacturing and supply of visual examination/survey system SOKRAT for WWER-1000/320 reactor pressure vessel from outer surface.
3) Manipulator moveable. Operational manual CK187MYu.01.01.00.00.00 RE, (in Russian).
4) Multi channel UT instrument. Operational manual. CK27.60.00.00.00.00 PE, (in Russian).
5) Equipment for UT data acquisition and processing. Operational guidelines CK187MYu1.01.80.00.00.00 RE.

NEW APPROACH OF CLEAN NDT FOR APPLICATIONS IN NUCLEAR INDUSTRY

A. Pelletier, S. Besson, IXTREM, France
E. A. Crescenzo, CONVERGENCE INNOVATIONS, France

Abstract
There is a need in the nuclear industry to have at disposal both alternative technologies for magnetic particle inspection and penetrant testing as well as noncontact techniques to detect and characterize cracks on welded structures.
It is proposed in this paper to comment the results obtained through the ANR project "ECO CND" and LIFE+ European Project "GREEN TESTING" regarding to inductive thermography, laser/EMAT and laser/dry coupled piezoelectric transducer as receiver techniques, applied to the detection and characterization of surface cracks in welded structures.
After a short introduction on the objectives of these two projects and of the approach used; we will describe both the two corresponding demonstrators developed and the mock ups manufactured for the demonstration trials (with artificial and natural defects).
We arrive to the following conclusion:

- Inductive thermography is able to detect cracks with sufficient length and depth (5 mm length and 500µm depth seems to be the actual limit of the technique).
- Laser / dry coupled piezoelectric transducer as receiver seems to be an attractive technique not only for surface defects detection but also for deeper defects in the thickness of the material with the advantage to generate ultrasonic waves directly on the welded area avoiding grinding operations.

Key words: clean NDT, thermography, laser, EMAT, dry coupled transducer, welded structure

1. Introduction

This conference follows the R & D realized in part in the ANR project "ECO CND": "The ultrasonic guided waves precursors of new environmental NDT technologies", and the other in the framework of the European LIFE + GREEN TESTING entitled "Make your non Destructive Testing greener by new eco-friendly practices and technologies".
In the ANR project "ECO CND", it is to develop new technologies based on the use of guided waves and surface plate (Lamb and SH).
For the European LIFE + project "GREEN TESTING", the approach is twofold:

- Develop an inventory of good practices and of new existing ways to significantly reduce the environmental impact of magnetic particle and dye penetrant inspection.
- Develop and implement demonstrators related to new technologies such as those developed in the "ECO CND" project or being validated in our laboratories as infrared thermography excited induction

One of the main objective that we have set ourselves to achieve through these two programs is to reduce up to 90% the energy based on the implementation of alternative techniques as ultrasonic guided waves or infrared thermography.
This conference will present more particularly these alternative techniques: ultrasonic guided waves High Frequency, and the infrared thermography with excitation by induction.

2. Summary of the unconditional NDT techniques

2.1. Ultrasonic guided waves HF *(High Frequency)*

The NDT ultrasonic guided waves have been developed in recent years mainly for the control of pipes and piping systems in the frequency range from 20 kHz to 250 kHz. Industrial equipment are already available on the market but are very expensive, cumbersome and difficult to implement at the interpretation of results. Given the very low frequencies, this method is not suitable for the searching of surface or sub-cutaneous defects. Therefore, we directed towards the development of this technique to higher frequency (500 kHz to 10 MHz) based on the use of variable angle transducers, piezoelectric patches and finally a laser to generate ultrasonic waves in a broadband frequency. The advantage of the laser is to better control the generation and propagation of ultrasonic waves by controlling the geometry of the impact. For example, a linear impact will limit the dispersion of ultrasonic surface waves, and therefore focus mainly ultrasonic energy in a specific direction.

2.2. Infrared Thermography *(IR)*

IR Thermography is used mainly in aviation for the control of composite structures for cracks or defects collages.

For metallic materials, the IR thermography is used prospectively mainly in laboratories and research centers. IXTREM, in collaboration with CETIM and HOLO3 within the European LIFE + project, sought to make improvements to this technique by comparing their expertise in the field of thermal excitation by electromagnetic induction effect, of the use of thermal imaging cameras and appropriate softwares for image processing.

3. Synthesis and results of work using unconventional NDT techniques

3.1. Infrared thermography with excitation by electromagnetic induction

3.1.1. Description of the demonstrator

The demonstrator consists of the following elements:

IR Camera “Low cost” :

- 160*120 pixels
- 120Hz
- 80mK
- 7.5~13µm

IR Camera High Resolution - Sensibility:

- 320*290 pixels
- 300Hz
- 20mK
- 2.5~5µm

Fig. 1. The choice of the IR camera is adapted to the intended application

Inductor control unit developed by IXTREM

Fig. 2. Induction heating system

Advantages of this method:

- This process is a non-contact process and permits examinations where it is practically impossible to achieve it by Magnetic Particle Inspection (MPI) and Dye Penetrant Inspection (DPI), for example : contaminated rooms (nuclear), very hot or very cold parts with retention areas for magnetic liquor or penetrants ; control over the vertical walls ...
- This process is well suited for serial control and reduce costs and environmental pressures associated with the use of cleaning products and products for MPI and DPI. This process doesn’t
- generate waste and thus simplifies facility design (*no extraction systems for fumes or gaseous products or wastewater treatment system).*

- The results obtained by infrared thermography with excitation by induction, permit in some cases to obtain a similar detection of defects to that obtained by MPI.

Limitations of this method:

- The necessity to adapt the shape of the inductor to the geometry of the test piece
- The heating of the test piece by the Eddy Currents (EC) depends on its magnetic permeability and its electrical conductivity. Some materials are more difficult to control with this excitation mode, even impossible if they are not or very poor conductors of electricity.

3.1.2. Examples of comparative results

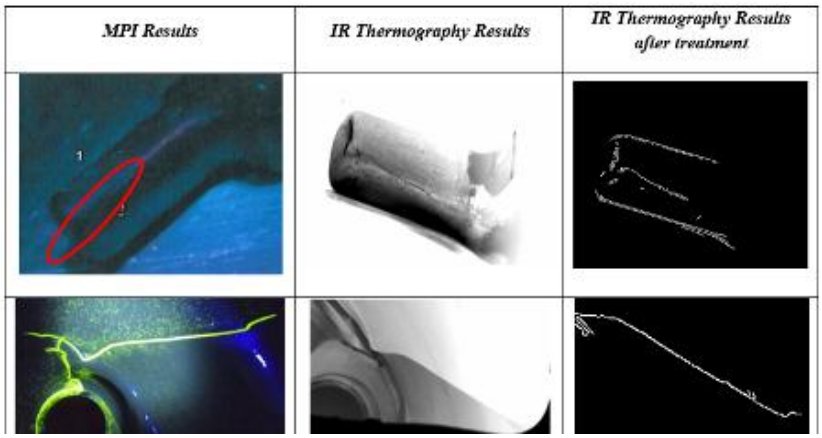

Fig.3. Comparative results between MPI and Infrared Thermography

3.2. Control by Ultrasonic guided waves HF

3.2.1. Description of the demonstrator

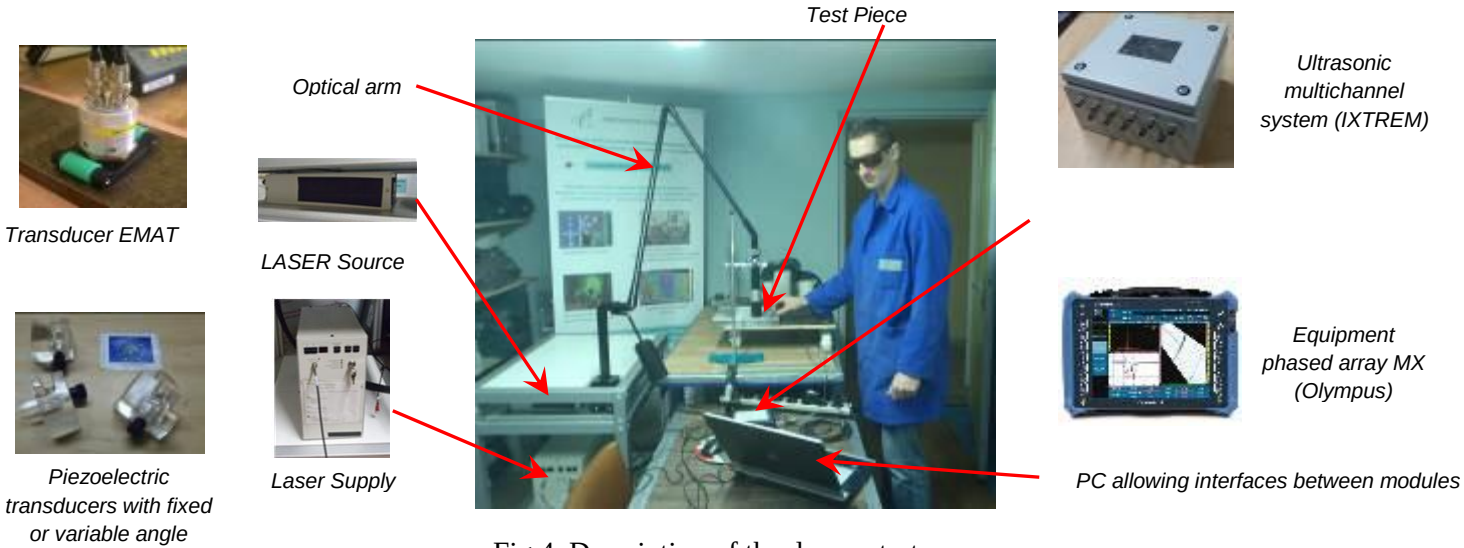

Fig.4. Description of the demonstrator

The demonstrator above consists :

- Of a compact laser source with optical for shaping of the laser beam *(for example: linear impact).*
  Laser source: Wavelength: 1064nm; Energy: 12mJ per pulse, Frequency 1Hz to 15Hz.
- Of an optical arm enabling an impact on parts of complex geometry in a global space of about $1m^3$.
- A set of piezoelectric transducers with adapted shoes to generate and detect ultrasonic waves inclined OL / OT of different refraction angles (0 to 90 °), including sabots continuously variable angle. These piezoelectric transducers have frequencies ranging from 1 to 5 MHz, and fixed or variable angle. For transducers with fixed angles, the value of the angle of refraction has been previously determined by tests using variable angle transducers.
- A set of transducers EMAT (ElectroMagnetic Acoustic Transducer) associated with appropriate electronics of acquisition and signal treatment.
- A set of ultrasonic and Phased Array platforms including associated electronic packaging and signal processing.

This demonstrator was designed to be more flexible in its use to cover a wide frequency range (20 kHz – 10 MHz). Thus this analysis platform has been made compatible with a set of piezoelectric transducers and EMAT to generate and receive ultrasonic guided wave modes of propagation (Rayleigh waves, creeping, Lamb and different symmetric modes, anti-symmetric; guided SH waves).

3.2.2.Results

The following tables summarize the main results obtained using piezoelectric transducers with surface waves according a variant implementing of a generation of ultrasonic by a linear laser impact. This form of the impact allows to make the ultrasonic beam more directional than that resulting from the use of a piezoelectric transducer with surface wave.

Modeling of the propagation of the Rayleigh wave - directivity function of the geometry of the source

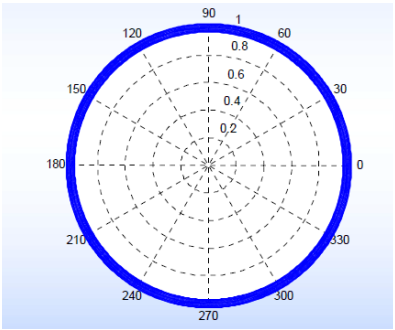

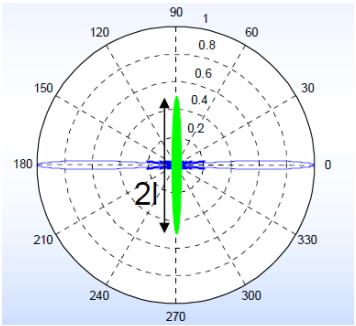

Directivity for punctual circular impact ***Directivity for a line source***

Fig.5. Results of the modeling of the HEMP-DOAE - ANR ECO CND Project

3.2.3 Welded Structures

a) *Results obtained by piezoelectric transducers with variable angles to generate ultrasonic surface waves (pulse / echo technical) :*

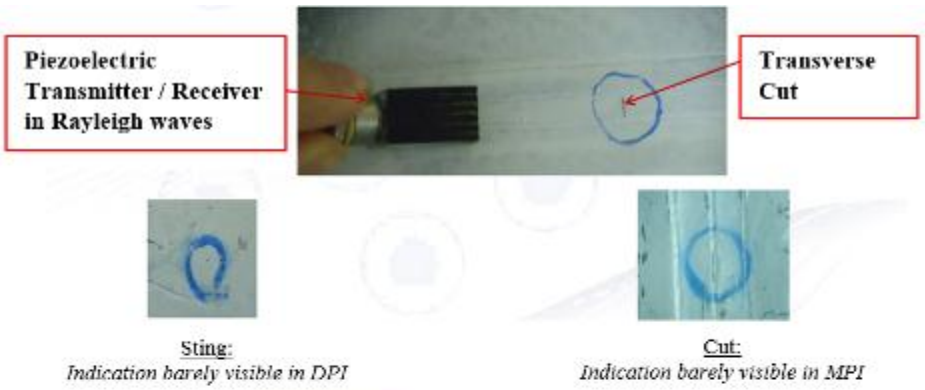

Type	Dimensions	HAZ (Heat Affected Zone) Echo	HAZ (Heat Affected Zone) Gain (dB)	IN THE WELD Echo	IN THE WELD Gain (dB)
Cut	Length : 5 mm Depth : 1 mm		18		21
STING	Length : 0,3 mm Depth : 0,5 mm		33		32

b) *Results obtained with the laser emission source and a piezoelectric transducer with guided surface waves used in reception; Case where the laser shot is performed in the weld:*

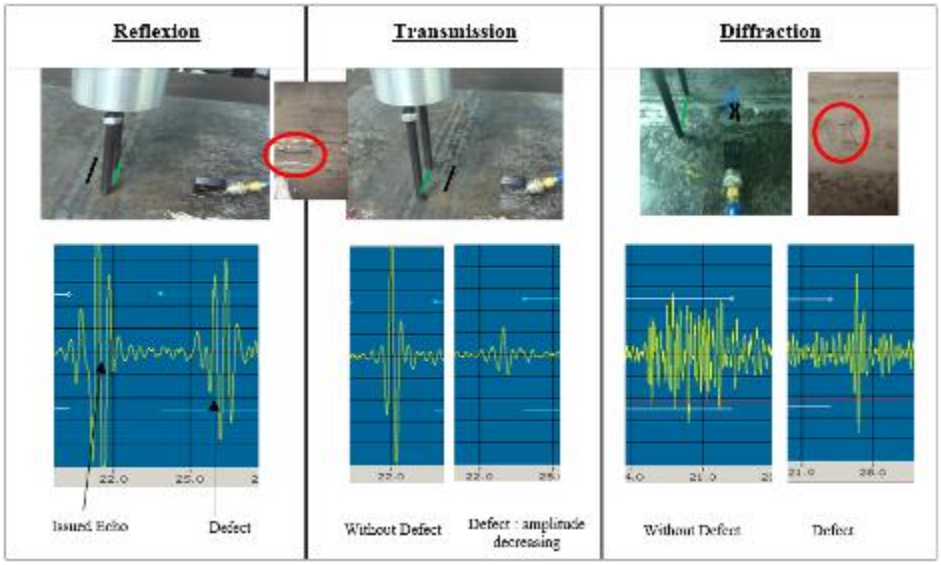

c) *Similarly to above, results in reflection but by positioning the laser impact on the base metal*

Detection of defects in the HAZ and in the weld seam, in reflection:

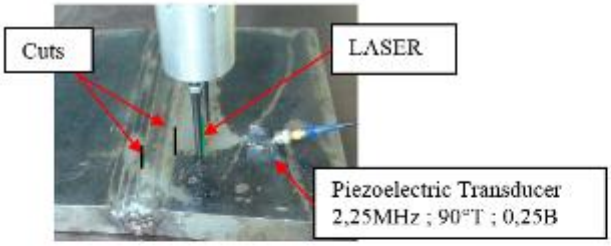

Type	Dimensions and Orientation of the defect	Laser emission – Piezoelectric transducers reception		Piezoelectric transducers Emission / Reception	
		Echo	Gain (dB)	Echo	Gain (dB)
Cut in the HAZ	Length: 5 mm Depth: 1 mm *Defect parallel to the weld seam*		52		24
Cut in the weld seam	Length: 5 mm Depth: 1 mm *Defect parallel to the weld seam*	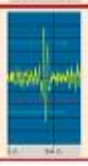	72	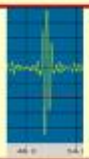	41

d) B-Scan obtained in transmission with two piezoelectric transducers with Rayleigh waves

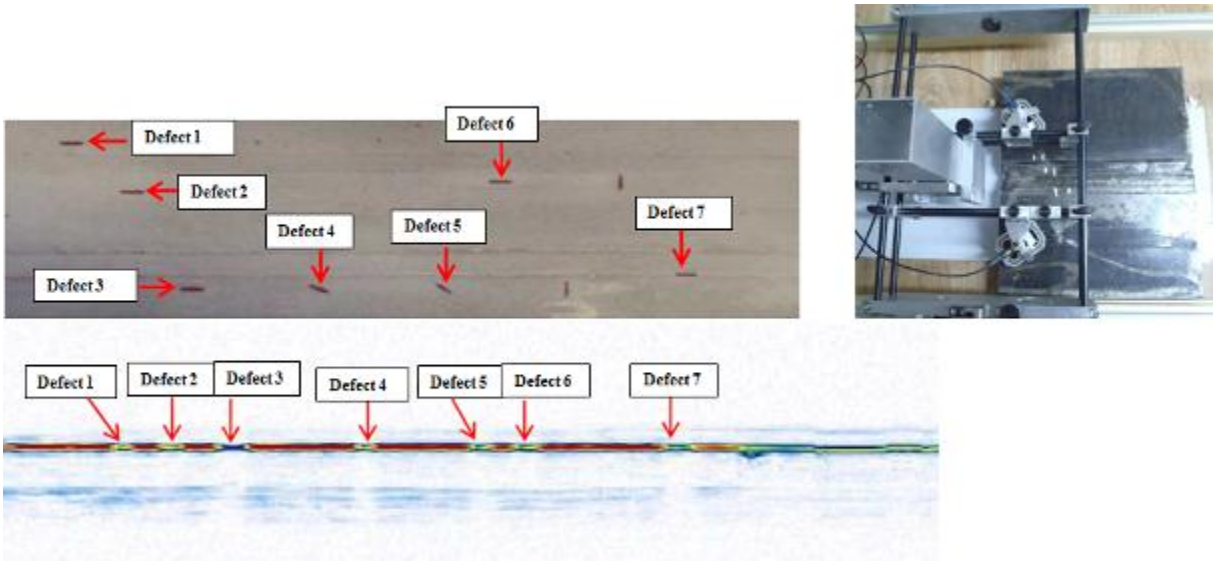

Fig.6. B-Scan in transmission on a test block with electro-eroded cuts

As shown in Figure 6 above, the transmission mode analysis does not allow the positioning of defects on the surface of the piece, because it focuses only on the amplitude of the coupling echo. For cons, the B-scan analysis in transmission mode is much less sensitive to the disorientation of defects compared to the pulse-echo technique.

e) *Results on a test piece used in the nuclear industry*

On a weldment – Comparison with conventional MPI :

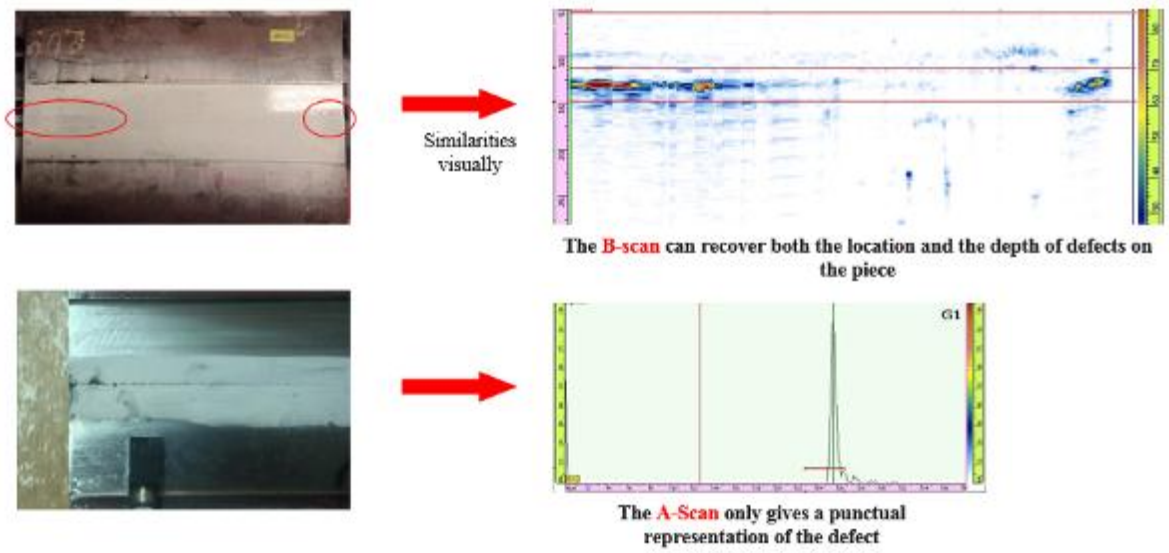

Fig.7. A-Scan and B-Scan in reflection on a test piece (nuclear industry)

3.2.4 Results on a steel sheet

Results obtained in reflection with a piezoelectric transducer with Rayleigh Waves

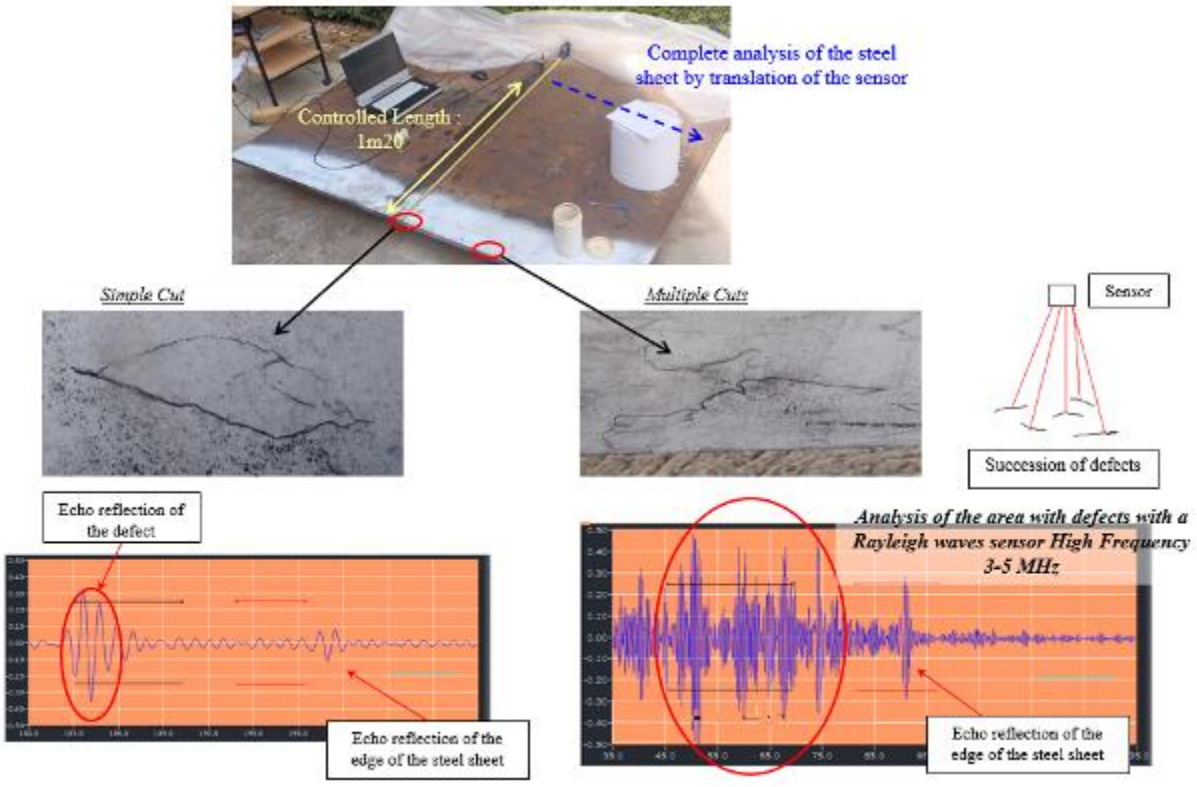

Fig.8. A-Scan in reflection on a steel sheet

3.2.5 Corroded structure

a) *Results obtained on coupons of steel sheets with artificial defects:*

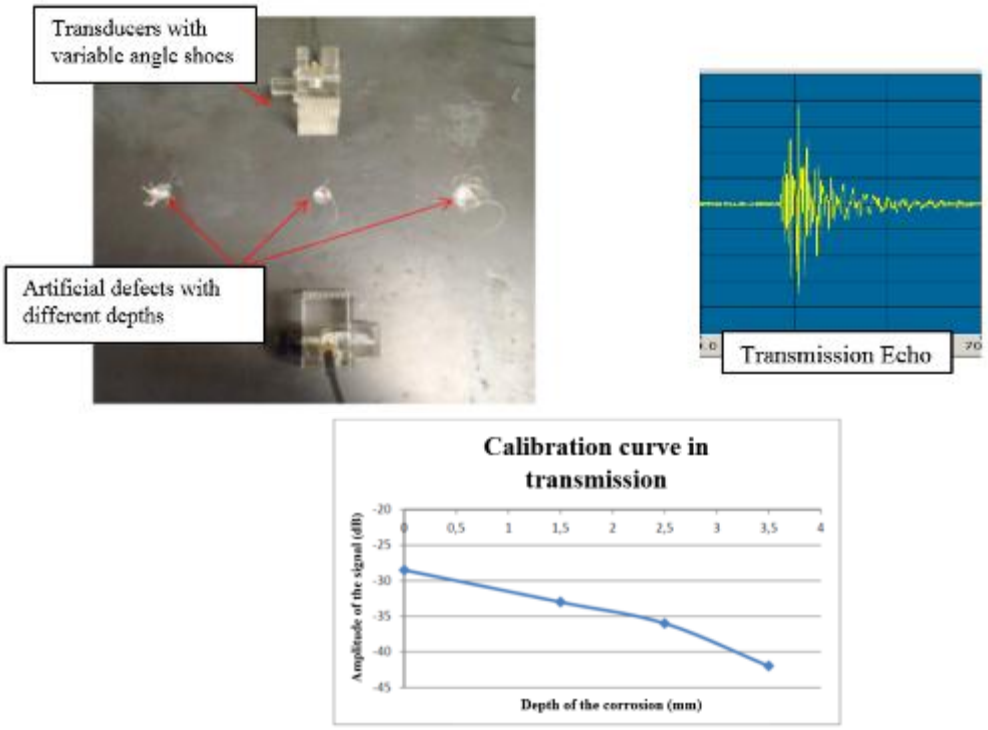

Fig.9. A-Scan calibration on a corroded structure

We notice a substantially linear response of the amplitude of the coupling echo with the loss of thickness up to 2.5 mm. For excessive depths of corrosion, the appearance of nonlinear phenomena could be explained by the integration of changing of propagation modes, in particular the appearance of surface waves.

b) *Results obtained on coupons of steel sheets with natural corrosions:*

Fig.10. Pictures with natural corrosions on steel sheet

To determine the residual thickness of the steel sheet coupons with natural corrosion, we used the calibration curves established on samples of plates with artificial defects using ultrasonic technique by guided Lamb waves in transmission mode *(spacing between transmitter and receiver transducers: 150mm).*

Conclusion on the use of ultrasonic guided waves HF:

U.S. Guided Wave HF (> 1MHz), and in particular the Rayleigh waves are an attractive and effective alternative to DPI and MPI.

They offer the possibility to remote control and examine hidden areas *(avoid removing components)*. The technique of ultrasonic generation by laser is now made available to be used in an industrial environment *(cost and compactness of acceptable equipment)* and provides the ability to impact pieces of complex geometry and weld seam.

Although still complex implementation, guided waves can already apply for the control of weldment, bars and rods, rails or certain pieces of complex geometry, mainly of revolution. Compared to Eddy Currents, there are no problems formatting of transducers to the curvatures of pieces *(guided ultrasonic waves follow the contour of the piece).*

4. Ecological impacts of these alternative techniques compared with MPI and DPI

In MPI or DPI, most of the used products are either harmful or hazardous for the environment (as magnetic liquors, solvents, penetrants…), while in ultrasonic guided waves we use only a biodegradable gel which serve of coupling. In the other side, no products are used for thermography!
Regarding the energy sources of this technique, MPI consumes on average 31kW per year and DPI up to 6kW per year. We will note Ultrasonic Guided Waves doesn't exceed 500W and 3kW for the thermography.
Then, look at the carbon balance. For MPI, quantity of carbon released in the nature per year exceeds 200 kg, and 150 kg for the DPI. Whereas for the alternative technologies, the quantity of carbon rejected reach 40 kg for ultrasonic guided waves and 60 kg for infrared thermography.
To finish, we must be taken into account the presence of magnetic fields and volatile organic compounds with the use of the conventional techniques. And apart from the risk of burns with the inductor used in thermography, it appears no other major risk with the use of these alternative techniques

5. Conclusions

In the short run, we think that ultrasonic guided waves could substitute the DPI and MPI techniques. Indeed, for the most of defects, US present sensitivity similar to this conventional NDT. Furthermore, relative to the MPI, US can detect both cuts and stings and the time of control decreases with the use of a translation scan system by piezoelectric transducers.
About the infrared thermography, it applies only on small areas. So its performance is optimum when we know where the defect could be, and particularly for the control of small pieces or control on production line knowing that this technology offers significant opportunity for change and improvement.

---

6. References

[1] - Eric CRESCENZO – IXTREM, Daniel CHAUVEAU – IS SERVICES, Dee DULAY – NDT Consultants - "Utilisation des ondes guidées exploitant des transducteurs à effet magnétostrictif pour la détection de corrosion" - MATERIAUX 2006
[2] - E. CRESCENZO (IXTREM) ; D. DULAY et R. TANEJA (NDT Consultants) ; D. CHAUVEAU (Institut De Soudure) - « Utilisation des ondes ultrasonores guidées pour le contrôle non destructif » - Journées COFREND à Toulouse du 20 au 22 mai 2008
[3] - E. CRESCENZO (IXTREM) - « Main interest of guided waves for NDT applications » - Conférence ICSAAM à Tarbes du 07 au 10 septembre 2009
[4] - E. CRESCENZO (IXTREM) ; A. PELLETIER (IXTREM) ; JL. IZBICKI (FANO CNRS) ; JP. CHAMBARD –(HOLO3) ; S. BITTENDIEBEL (INSTITUT DE SOUDURE) ; H. WALASZEK

(CETIM SENLIS) - « Les ondes ultrasonores guidées - L'une des technologies clé des CND pour la prochaine décennie » - Journées COFREND 2011 du 24 au 27 mai 2011 à Dunkerque
[5] – Site GREEN TESTING www.greentesting.fr - Rubrique « Outils » – Accès à des conférences sur le sujet
[6] – Site IXTREM www.ixtrem.fr - Rubrique « Documentation » – Accès à des documents et textes de conférences sur le sujet

PARTICIPANT LIST

AKIHIRO	Ishimi	JAPAN ATOMIC ENERGY AGENCY	ishimi.akihiro@jaea.go.jp	JAPAN
ALGERNON	Daniel	SVTI SWISS ASSOCIATION FOR TECHNICAL INSPECTIONS	daniel.algernon@svti.ch	SWITZERLAND
ALGHAMDI	Sami	SABIC-SADAF	ghamdish2@sadaf.sabic.com	SAUDI ARABIA
AL-SHAMMARI	Nasser	SADAF	shammarinf@sadaf.sabic.com	SAUDI ARABIA
ALZARIB	Mohammed	SABIC	ZARIBMA@SADAF.SABIC.COM	SAUDI ARABIA
AMZIANE	Ahmed	GRTGAZ	ahmed.amziane@grtgaz.com	FRANCE
ANCRENAZ	Patrick	AREVA	patrick.ancrenaz@areva.com	FRANCE
ARZHAEV	Alexey	JSC "ATOMTECHENERGO'	alex.arj@yandex.ru	RUSSIAN FEDERATION
ASHWIN	Philip	EPRI	pashwin@epri.com	USA
ATHANASIADIS	Lisel	CEGELEC	*	SWEDEN
AUBERT	Philippe	AREVA NDE SOLUTIONS	philippe.aubert@areva.com	FRANCE
BÄCKSTRÖM	Tommy	FORSMARKS KRAFTGRUPP AB	tommy.backstrom@forsmark.vattenfall.se	SWEDEN
BANCHET	Julien	AREVA NDE SOLUTIONS/NETEC	julien.banchet@areva.com	FRANCE
BARRERA	Carlos	IHI SOUTHWEST TECHNOLOGIES, INC.	cbarrera@ihiswt.com	USA
BECKER	Ingo	EC-WORKS GMBH	becker@ecworks.de	GERMANY
BECKERICH	Nadia	COFREND	n.beckerich@cofrend.com	FRANCE
BEGAT	Delphine	MISTRAS	dbegat@ascot.fr	FRANCE
BELLIARD	Pascal	EDF	pascal.belliard@edf.fr	FRANCE
BENITEZ	Jorge	DEKRA INDUSTRIALL AB	jorge.benitez@dekra.com	SWEDEN
BENMOUSSAT	Mohammed	FRAUNHOFER IIS	mohammed-seghir.benmoussat@iis.fraunhofer.de	GERMANY
BENOIST	Philippe	M2M	p.pichard@m2m-ndt.com	FRANCE
BERGALONNE	Patrick	COMEX NUCLEAIRE	bergalonne@comex-nucleaire.com	FRANCE
BERTOLIS	Didier	ELECTRABEL GDF SUEZ	didier.bertolis@electrabel.com	BELGIUM
BERTOVIC	Marija	BAM FEDERAL INSTITUTE FOR MATERIALS RESEARCH AND TESTING	marija.bertovic@bam.de	GERMANY
BIANCHI	Stefano	KERNKRAFTWERK LEIBSTADT	stefano.bianchi@kkl.ch	SWITZERLAND
BIENENTREU	Robert	WESTINGHOUSE ELECTRIC GERMANY GMBH	bienenrj@westinghouse.com	GERMANY
BIETH	Michel	EUROPEAN COMMISSION - JRC	michel.bieth@ec.europa.eu	NETHERLANDS
BILLON	François	ONET TECHNOLOGIES	*	FRANCE
BIRD	Colin	DOOSAN POWER SYSTEMS	colin.bird@doosan.com	UNITED KINGDOM
BISIAUX	Bernard	VALLOUREC	bernard.bisiaux@vallourec.fr	FRANCE
BJURLING	Per Arne	AREVA NP UDDCOMB	perarne.bjurling@areva.com	SWEDEN
BLOMBERGSSON	Pär	FORSMARKS KRAFTGRUPP AB	par.blombergsson@forsmark.vattenfall.se	SWEDEN
BLONDEL	Lucile	WESTINGHOUSE	*	FRANCE
BOLANDER	Martin	WESDYNE EUROPE	bolandms@westinghouse.com	GERMANY
BOND	Leonard	CENTER FOR NDE AT IOWA STATE UNIVERSITY	bondlj@iastate.edu	USA
BOOLER	Russ	AMEC	*	UNITED KINGDOM
BOSCH	Philippe	CEGELEC PSC	philippe.bosch@cegelec.com	FRANCE
BOUTTIER	Bertrand	VEOLIA	bertrand.bouttier@veolia.com	FRANCE
BRACONNIER	Dominique	DB	dominique@braconnier.com	FRANCE
BREDIF	Philippe	CEA LIST	philippe.bredif@cea.fr	FRANCE
BUDIMIR	Marko	INETEC - INSTITUTE FOR NUCLEAR TECHNOLOGY LTD.	marko.budimir@inetec.hr	CROATIA
BURAT	Olivier	AREVA - INTERCONTROLE	olivier.burat@areva.com	FRANCE
CABEZA	Antonio	ENSA	cabeza.antonio@ensa.es	SPAIN

CAILLAT	Lionel	SRA SAVAC	lionel.caillat@sita.fr	FRANCE
CALMON	Pierre	CEA LIST	pierre.calmon@cea.fr	FRANCE
CAPERAA	Claire	EDF - CEIDRE	claire.caperaa@edf.fr	FRANCE
CARDILLO	Nicholas	ZETEC, INC	ncardillo@zetec.com	USA
CARRERE	Renaud	SRA SAVAC	renaud.carrere@sita.fr	FRANCE
CARTER	Luke	AMEC	luke.carter@amec.com	UNITED KINGDOM
CARTIER	Francois	CEA	francois.cartier@cea.fr	FRANCE
CASSIER	Olivier	SONATEST	cassier@sofranel.com	FRANCE
CASTIN	Pascal	AREVA INTERCONTROLE	pascal.castin@areva.com	FRANCE
CAULIER	Yannick	AREVA	yannick.caulier@areva.com	FRANCE
CHAMPIGNY	François	EDF CEIDRE	françois.champigny@edf.fr	FRANCE
CHAPUIS	Bastien	CEA	bastien.chapuis@cea.fr	FRANCE
CHARDOME	Vincent	VINÇOTTE	vchardome@vincotte.be	BELGIUM
CHARPIOT	Laurent	CEGELEC PSC	laurent.charpiot@cegelec.com	FRANCE
CHASSIGNOLE	Bertrand	EDF	bertrand.chassignole@edf.fr	FRANCE
CHATELLIER	Laurence	EDF CEIDRE	laurence.chatellier@edf.fr	FRANCE
CHAUVEAU	Daniel	INSTITUT DE SOUDURE INDUSTRIE	c.daniel@institutdesoudure.com	FRANCE
CHAUVEAU	Thomas	BOUYGUES CONSTRUCTION	t.chauveau@bouygues-construction.com	FRANCE
CHAUX	Philippe	OLYMPUS INDUSTRIAL SYSTEMS EUROPA	gert.vandemieroop@olympusndt.com	UNITED KINGDOM
CHERRABEN	Toufik	DOOSAN POWER SYSTEMS	toufik.cherraben@doosan.com	UNITED KINGDOM
CHOI	Evan	CANDU OWNERS GROUP	evan.choi@candu.org	CANADA
CHOI	Wonjae	IMPERIAL COLLEGE LONDON	w.choi@imperial.ac.uk	UNITED KINGDOM
COASTER	Donald	ROLLS-ROYCE	donald.coaster@rolls-royce.com	UNITED KINGDOM
COLOMBIE	Tamara	DEKRA	barbara.pidoux@dekra.com	FRANCE
CORAK	Dusko	INETEC	zrinka.corak@inetec.fr	CROATIE
CORAK CVJETICANIN	Zrinka	INETEC	zrinka.corak@inetec.fr	CROATIE
CORDEIRO	Sara	EDF CEIDRE ET R&D	sara.cordeiro@edf.fr	FRANCE
CORNATON	Philippe	EDF	philippe.cornaton@edf.fr	FRANCE
CRAULAND	Jean Marc	AREVA NP SAINT MARCEL	jeanmarc.crauland@areva.com	FRANCE
DALPE	Colombe	EDDYFI	cdalpe@eddyfi.com	CANADA
DANIELS	Will	AMEC	Will.Daniels@amec.com	UNITED KIGDOM
DANIELSSON	Johan	WESDYNE SWEDEN AB	danieljl@westinghouse.com	SWEDEN
D'ANNUCCI	Filippo	WESTINGHOUSE ELECTRIC GERMANY	dannucf@westinghouse.com	GERMANY
DAO	Gavin	ADVANCED OEM SOLUTIONS	gavin.dao@aos-ndt.com	USA
DE ROUMILLY	Loïc	EDF-CEIDRE	loic.de-roumilly@edf.fr	FRANCE
DE SCHEPPER	Xavier	GE	xavier.de_schepper@ge.com	FRANCE
DEBROISE	Mikael	PNB (PÔLE NUCLÉAIRE BOURGOGNE)	mikael.debroise@polenucleairebourgogne.fr	FRANCE
DEHLAU	Steffi	GERMAN SOCIETY FOR NON-DESTRUCTIVE TESTING (DGZFP) E.V.	mz@dgzfp.de	GERMANY
DEHOUVE	Dominique	CTE NORDTEST	dominique.dehouve@socotec.com	FRANCE
DELANNOY	Lionel	GE	lionel.delannoy@ge.com	FRANCE
DELAUNAY	Bastien	EDF UTO	bastien.delaunay@edf.fr	FRANCE
DELEMONTEZ	Jerome	EDF DIV. TECH. GEN.	jerome.delemontez@edf.fr	FRANCE
DENEUVILLE	François	VALLOUREC RESEARCH AULNOYE	francois.deneuville@vallourec.fr	FRANCE
DENNIS	Mark	ELECTRIC POWER RESEARCH INSTITUTE	mdennis@epri.com	USA
DESPREZ	Damien	DOOSAN POWER SYSTEMS	damien.desprez@doosan.com	UNITED KINGDOM
DEYDIER	Sebastien	EDF	sebastien.deydier@edf.fr	FRANCE

DIB	Mustapha	EDF/CEIDRE	mustapha.dib@edf.fr	FRANCE
DOBMANN	Gerd	FRAUNHOFER-IZFP	gerd.dobmann@izfp.fraunhofer.de	GERMANY
DOH	Euisoon	KPS	*	SOUTH KOREA
DOMBRET	Philippe	TRACTEBEL ENGINEERING	philippe.dombret@gdfsuez.com	BELGIUM
DORMOY	Benjamin	ALSTOM POWER	benjamin.dormoy@power.alstom.com	FRANCE
DOVERSPIKE	Paul	GE HITACHI NUCLEAR ENERGY	Paul.Doverspike@ge.com	USA
DRESSLER	Klaus	EC-WORKS GmbH	info@ecworks.de	GERMANY
DUBOIS	Philippe	EXTENDE	*	FRANCE
DUGUE	Christian	AREVA NDE SOLUTIONS	christian.dugue@areva.com	FRANCE
DUMAS	Philippe	INETEC	phd@imasonic.com	FRANCE
DUMONT	Emmanuel	LUZIESA EXCELDEF	edumont@luziesa.com	FRANCE
DUMONT	Pascal	LUZIESA EXCELDEF	sdumont@luziesa.com	FRANCE
DUPOND	Olivier	EDF R&D	olivier.dupond@edf.fr	FRANCE
DUPONT	Benoit	CETIM	benoit.dupont@cetim.fr	FRANCE
DUSCH	Pascal	EDF - CEIDRE	pascal.dusch@edf.fr	FRANCE
ERHARD	Anton	BAM BUNDESANSTALT FÜR MATERIALFORSCHUNG UND -PRÜFUNG	Anton.Erhard@bam.de	GERMANY
ESPEILLAC	Benjamin	EDF	benjamin.espeillac@edf.fr	FRANCE
FARENBAUGH	Neal	FRAUNHOFER-IZFP	fhall@curtisswright.com	USA
FASHAM	Jack	EDF ENERGY	jack.fasham@edf-energy.com	UNITED KINGDOM
FEHRENBACH	Nicolas	AREVA NDE SOLUTIONS	nicolas.fehrenbach@areva.com	FRANCE
FELIUS	Hans	ACOUSTICEYE	hans.felius@acousticeye.com	USA
FERNANDEZ	Ricardo		*	FRANCE
FERNANDEZ	Roman	EXTENDE	roman.fernandez@extende.com	FRANCE
FERNANDEZ	Francisco	TECNATOM	ffernandez@tecnatom.es	SPAIN
FERRANDIS	Jean-Yves	SOUTHERN ELECTRONIC INSTITUTE, CNRS	jean-yves.ferrandis@univ-montp2.fr	FRANCE
FISHER	Jay	SOUTHWEST RESEARCH INSTITUTE	jay.fisher@swri.org	USA
FLEURY	Alain	IMASONIC	alf@imasonic.com	FRANCE
FLEURY	Gérard	IMASONIC	gf@imasonic.com	FRANCE
GAC	Hervé	SG NDT	hgac@sgndt.com	FRANCE
GALLEZOT	Benjamin	MINISTÈRE DU REDRESSEMENT PRODUCTIF	*	FRANCE
GALOSIC	Sergio	INETEC	sergio.galosic@inetec.hr	CROATIE
GARBOUD	Sylvain	CEGELEC NDT	sylvain.garboud@cegelec.com	FRANCE
GARCÍA ROLDÁN	Giselle	SWEDISH RADIATION SAFETY AUTHORITY	giselle.garciaroldan@ssm.se	SWEDEN
GARCIA(BUENO)	Angel	TECNATOM	agarcia@tecnatom.es	SPAIN
GARZINO	Geoffrey	AREVA NDE SOLUTIONS	geoffrey.garzino@areva.com	FRANCE
GAUTHIER	Karine	AREVA NDE SOLUTIONS FRANCE	karine.gauthier@areva.com	FRANCE
GELEBART	Yann	EDF / CEIDRE	yann.gelebart@edf.fr	FRANCE
GEORGSSON	Hans Ake	NRG ARNHEM	*	NETHERLANDS
GERARD	Pascal	VALTIMET	pascal.gerard@valtimet.com	FRANCE
GIBERT	Christophe	EDF / CEIDRE	christophe.gibert@edf.fr	FRANCE
GILLES	Michel	ELECTRABEL	michel.gilles@electrabel.com	BELGIUM
GILLOT	Josselin	WESTINGHOUSE / ASTARE	gillotj@westinghouse.com	FRANCE
GIRAUD	Florence	COFREND	f.giraud@cofrend.com	FRANCE
GLASS	Samuel	AREVA	Bill.Glass@areva.com	USA
GOBERT	Jean Luc	AREVA	jeanluc.gobert@areva.com	FRANCE
GOODFELLOW	Jamie	BABCOCK & WILCOX ENERGIE NUCLÉAIRE	jgoodfellow@babcock.com	FRANCE

GOURDIN	Gregory	VINÇOTTE	ggourdin@vincotte.be	BELGIUM
GRANDSIR	Marc-Olivier	OLYMPUS INDUSTRIAL SYSTEMS EUROPA	marc-olivier.grandsir@olympusndt.com	UNITED KINGDOM
GREENER	Chris	ROLLS-ROYCE	chris.greener@rolls-royce.com	UNITED KINGDOM
GRIBI	Markus	AXPO POWER AG	markus.gribi@axpo.com	SWITZERLAND
GRYBÄCK	Thomas	SVENSK KÄRNBRÄNSLEHANTERING AB	thomas.gryback@skb.se	SWEDEN
GUEY	Jean-Luc	IMASONIC	jlg@imasonic.com	FRANCE
GUSTIN	Jean-Pierre	COFREND	president@cofrend.com	FRANCE
GUY	Alan	AXPO POWER AG	alan.guy@axpo.com	SWITZERLAND
HAGEN	Markus-Friedrich	VECTOR TUB	hagen@vector-tub.com	GERMANY
HALL	JOHN	ANATEC LMT	*	USA
HAMANO	Toshiaki	IHI CORPORATION	toshiaki_hamano@ihi.co.jp	JAPAN
HAMMAR	Lars	CHALMERS UNIVERSITY OF TECHNOLOGY	lars.hammar@chalmers.se	SWEDEN
HANKINSON	Neil	PHOENIX INSPECTION SYSTEMS LTD	nhankinson@phoenixisl.co.uk	UNITED KINGDOM
HAREL	Yoav	ACOUSTICEYE	info@acousticeye.com	USA
HÄRKÖLÄ	Jukka	STUK	jukka.harkola@stuk.fi	FINLAND
HARRISON	Tim	ROLLS-ROYCE NUCLEAR	timothy.harrison@rolls-royce.com	UNITED KINGDOM
HARSÁNY	Jozef	SLOVENSKÉ ELEKTRÁRNE, A.S., ?LEN SKUPINY ENEL	vzdelavanie@enel.com	SLOVAKIA
HASEBE	Takashi	MITSUBISHI HEAVY INDUSTRIES, LTD.	takashi_hasebe@mhi.co.jp	JAPAN
HASELDEN	Chris	ROLLS-ROYCE	chrishaselden@hotmail.com	UNITED KINGDOM
HE CHEN	Yuxin	WESTINGHOUSE	hecheny@westinghouse.com	FRANCE
HERVAULT	Vincent	EDF CEIDRE	vincent.hervault@edf.fr	FRANCE
HIRSCH	Peter	HPT HIRSCH PRÜFTECHNIK GMBH	info@hirsch-prueftechnik.de	GERMANY
HORACEK	Ladislav	UJV REZ, A.S.	hor@ujv.cz	CZECH REPUBLIC
HUBERT	Christophe	EDF CEIDRE	christophe.hubert@edf.fr	FRANCE
HUKKANEN	Kari	TEOLLISUUDEN VOIMA OY	kari.hukkanen@tvo.fi	FINLAND
HUSAREK	Pierre	COFREND	husarek@sofranel.com	FRANCE
HUYNEN	Henk	HQ SONICS BV	HHuynen@HQsonics.com	NETHERLANDS
INCERA PÉREZ	Pablo	EQUIPOS NUCLEARES, S.A.	incera@ensa.es	SPAIN
IWAMATSU	Fuminori	HITACHI, LTD.	fuminori.iwamatsu.vt@hitachi.com	JAPAN
JACKSON	Benjamin	INTERTEK AIM	ben.jackson@intertek.com	USA
JAMBON	Michel	AREVA NP	michel.jambon@areva.com	FRANCE
JANSSENS	Anneloes	NRG ARNHEM	janssens@nrg.eu	NETHERLANDS
JANSSON	Anders	RINGHALS AB	anders.jansson4@vattenfall.com	SWEDEN
JAOUEN	Claude	AREVA	*	FRANCE
JÄPPINEN	Tarja	VTT TECHNICAL RESEARCH CENTER OF FINLAND	tarja.jappinen@vtt.fi	FINLAND
JARDET	Patrice	EDF CEIDRE	patrice.jardet@edf.fr	FRANCE
JENSON	Frédéric	CEA LIST	frederic.jenson@cea.fr	FRANCE
JEUNE	Evelyne	COOPERATION INTERNATIONAL EVY'S	ajemces.org@hotmail.com	MEXICO
JIAN	John	EDF Energy	john.jian@edf-energy.com	UNITED KINGDOM
JINNESTRAND	Jonas	TÜV-NORD Swden AB	jjinnestrand@tuv-nord.com	SWEDEN
JOLLY	Bernard	SFEN	bjolly@sfen.fr	FRANCE
JONSSON	Alf	FORSMARKS KRAFTGRUPP AB	afj@forsmark.vattenfall.se	SWEDEN
JONSSON	Ake	ORG AB	*	SWEDEN
JULIEN	Alexandre	GE	alexandre.julien@ge.com	FRANCE
KADENKO	Igor	NONDESTRUCTIVE EXAMINATION TRAINING AND CERTIFICATION FACILITY	NDEF.Office@gmail.com	UKRAINE
KANG	Sung-Sik	SOUTH KOREA INSTITUTE OF NUCLEAR SAFETY	sskang@kins.re.kr	SOUTH KOREA

KANZLER	Daniel	FEDERAL INSTITUTE FOR MATERIALS RESEARCH AND TESTING	daniel.kanzler@bam.de	GERMANY
KATSUMATA	Ryosuke	NUCLEAR ENGINEERING, LTD.	rkatsumata@neltd.co.jp	JAPAN
KELB	Wilhelm	KONTROLLTECHNIK GMBH	w.kelb@kontrolltechnik.com	GERMANY
KERNIN	Yann	AREVA NDE SOLUTIONS	yann.kernin@areva.com	FRANCE
KIM	Hak-Joon	SUNGKYONKWAN UNIVERSITY	*	SOUTH KOREA
KIM	Ki-Bok	SOUTH KOREA RESEARCH INSTITUTE OF STANDARDS AND SCIENCE	*	SOUTH KOREA
KIMURA	Tadashi	MITSHIBISHI HEAVY INDUSTRIES	tadashi1_kimura@mhi.co.jp	JAPAN
KOLAR	Jan	CEZ, A.S. - TEMELIN NPP	jan.kolar@cez.cz	CZECH REPUBLIC
KOSKINEN	Ari	VTT TECHNICAL RESEARCH CENTRE OF FINLAND	ari.koskinen@vtt.fi	FINLAND
KOUBAYDATT	Firas	ARMINES	firas.koubaydatt@cetim.fr	FRANCE
KRAMARZ	Gerhard	FEDERAL MINISTRY FOR THE ENVIRINMENT, NATURE CONSERVATION AND NUCLEAR SAFETY	gerhard.kramarz@bmu.bund.de	GERMANY
KURDI	Jamal	EDF	jamal.kurdi@edf.fr	FRANCE
KUUSINEN	Petri	TEOLLISUUDEN VOIMA OYJ	petri.kuusinen@tvo.fi	FINLAND
KVARNSTRÖM	Magnus	RINGHALS AB	magnus.kvarnstrom@vattenfall.com	SWEDEN
LAMARRE	André	OLYMPUS	andre.lamarre@olympusndt.com	CANADA
LASSERRE	Frédéric	AREVA E&P	frederic.lasserre@areva.com	FRANCE
LE BER	Laurent	M2M	l.leber@m2m-ndt.com	FRANCE
LE LOSTEC	Nechtan	AREVA NDE SOLUTIONS	nechtan.lelostec@areva.com	FRANCE
LE CORRE		GE MEASUREMENT & CONTROLS, - FRANCE	Jean-Jacques.LeCorre@ge.com	FRANCE
LE QUERRE	Jean Claude	WESTINGHOUSE	*	FRANCE
LECOUR	Eric	WESTINGHOUSE	lecoure@westinghouse.com	FRANCE
LEDRU	Alain	EDF/CEIDRE	alain.ledru@edf.fr	FRANCE
LEE	Boyoung	SOUTH KOREA AEROSPACE UNIVERSITY	bylee@kau.ac.kr	SOUTH KOREA
LEE	Jinyi	CHOSUN UNIVERSITY	jinyilee@chosun.ac.kr	SOUTH KOREA
LEJON	Anders	RINGHALS AB	a.lejon@vattenfall.com	SWEDEN
LELEU	Jean Marc	WESTINGHOUSE	leleujm@westinghouse.com	FRANCE
LEMAIRE	Sophie	WESTINGHOUSE	lemairs@westinghouse.com	FRANCE
LENAIN	Jean-Claude	MISTRAS	jclenain@mistrasgroup.eu	FRANCE
LENNARTSSON	Eric	SWEDISH QUALIFICATION CENTRE AB	eric.lenartsson@sqc.se	SWEDEN
LESAFFRE	Cyril	CEA	cyril.lesaffre@cea.fr	FRANCE
LESAGE	Frédéric	WESTINGHOUSE	lesagef@westinghouse.com	FRANCE
LESKELÄ	Esa	VTT TECHNICAL RESEARCH CENTRE OF FINLAND	esa.leskela@vtt.fi	FINLAND
LEVEQUE	Gerard	SOUTHERN ELECTRONIC INSTITUTE	gerard.leveque@univ-montp2.fr	FRANCE
LEVIVIEN	Pascale	AREVA NDE SOLUTIONS	pascale.levivien@areva.com	FRANCE
LEVY	Robert	ERELEX	erelex.sarl@sfr.fr	FRANCE
LHEUREUX	Mathieu	VALTIMET	mathieu.lheureux@valtimet.com	FRANCE
LHUILLIER	Pierre-Emile	EDF R&D	pierre-emile.lhuillier@edf.fr	FRANCE
LIN	Shan	CENTRAL RESEARCH INSTITUTE OF ELECTRIC POWER INDUSTRY	shanlin@criepi.denken.or.jp	JAPAN
LINDBERG	John	ELECTRIC POWER RESEARCH INSTITUTE	jlindberg@epri.com	USA
LIPKE	Harald	KERNKRAFTWERK LEIBSTADT AG	harald.lipke@kkl.ch	SWITZERLAND
LIPPONEN	Aarne	VTT TECHNICAL RESEARCH CENTRE OF FINLAND	Aarne.Lipponen@vtt.fi	FINLAND
LONNE	Sébastien	EXTENDE	*	FRANCE
LOURME	Hugues	CEA	hugues.lourme@cea.fr	FRANCE
MAES	Guy	ZETEC	gmaes@zetec.com	CANADA
MAHAUT	Steve	CEA LIST	steve.mahaut@cea.fr	FRANCE

MANNESSIEZ	Gilles	BUREAU VERITAS - CEP INDUSTRIE	gilles.mannessiez@fr.bureauveritas.com	FRANCE
MARCHAND	Benoit	CEA LIST	benoit.marchand@cea.fr	FRANCE
MARES	Pavel	CENTRUM VYZKUMU REZ, S.R.O. (RESEARCH CENTRE REZ)	mpa@cvrez.cz	CZECH REPUBLIC
MARTENS	Dirk	GDF SUEZ	Dirk.Martens@electrabel.com	BELGIUM
MARTENS	Joel	AREVA IBN-F INTERCONTROLE	joel.martens@areva.com	FRANCE
MARTIN	Etienne	COFREND	etienne.martin@edf.fr	FRANCE
MARTÍNEZ-OÑA	Rafael	TECNATOM, S.A.	rmo@tecnatom.es	SPAIN
MARTINOTTI	Badea	INTERCONTROLE	badea.martinotti@areva.com	FRANCE
MARTINSEN	Hans	RINGHALS AB	hans.martinsen@vattenfall.com	SWEDEN
MASSOL	Vincent	SAFRAN - SNECMA	vincent.massol@snecma.fr	FRANCE
MATLACK	Kathryn	GEORGIA INSTITUTE OF TECHNOLOGY	katie.matlack@gatech.edu	USA
MAURICE	Heikki	INSPECTA SERTIFIOINTI OY	heikki.myohanen@inspecta.com	FINLAND
MAURICE	Léa	EDF CEIDRE	lea.maurice@edf.fr	FRANCE
MAYOS	Michel	EDF/DPN	michel.mayos@edf.fr	FRANCE
MC NEIL	Colin	DOOSAN POWER SYSTEMS	colin.mcneil@doosan.com	UNITED KINGDOM
MELBI	Mikael	WESDYNE SWEDEN	melbiml@westinghouse.com	SWEDEN
MEMBRE	Arnaud	IMASONIC	am@imasonic.com	FRANCE
MEQUIES	Philippe	EDF-CEIDRE	philippe.mequies@edf.fr	FRANCE
MERLE	Jean-Philippe	ROLLS ROYCE	bruno.pernot@rolls-roycenuclear.com	UNITED KINGDOM
MEYNET	Alain	ZETEC	ameynet@zetec.com	USA
MISTRAL	THOMAS	AREVA INTERCONTROLE	thomas.charret@areva.com	FRANCE
MISTRAL	Quentin	EDF	quentin.mistral@edf.fr	FRANCE
MOHR	Friedrich	INTELLIGENDT SYSTEMS & SERVICES GMBH	friedrich.mohr@intelligendt.de	GERMANY
MOLPECERES	Diego	TECNATOM, S.A.	dmolpeceres@tecnatom.es	SPAIN
MONTERO	Manuel	CEGELEC NDT	manuel.montero@cegelec.com	FRANCE
MOULIN	Olivier	AREVA NDE SOLUTIONS	olivier.moulin@areva.com	FRANCE
MOUSSEBOIS	Dominique	LABORELEC	dominique.moussebois@laborelec.com	BELGIUM
MUELLER	Christina	BAM FEDERAL INSTITUTE OF MATERIALS RESEARCH AND TESTING	Christina.Mueller@bam.de	GERMANY
NAGAI	Masaki	CENTRAL RESEARCH INSTITUTE OF ELECTRIC POWER INDUSTRY	nagai@criepi.denken.or.jp	JAPAN
NAGASHIMA	Yoshiaki	HITACHI, LTD., HITACHI RESEARCH LABORATORY	yoshiaki.nagashima.ka@hitachi.com	JAPAN
NESEVSKI	Zlate	FORCE TECHNOLOGY	zn@force.dk	DENMARK
NEUPAUER	Juraj	SLOVENSKÉ ELEKTRÁRNE, A.S., SUBSIDIARY OF ENEL	vzdelavanie@enel.com	SLOVAKIA
NOEL	Christian	CEGELEC PSC	christian.noel@cegelec.com	FRANCE
OBRUTSKY	Laura	AECL	obrutskyl@aecl.ca	CANADA
O'DELL	Tom	ZETEC INC.	todell@zetec.com	USA
OLIVOTTO	Silvia	ENEL INGEGNERIA E RICERCA S.P.A	silvia.olivotto@enel.com	ITALY
O'REGAN	Patrick	EPRI	poregan@epri.com	USA
PACKALÉN	Tapani	INSPECTA SERTIFIOINTI OY	tapani.packalen@inspecta.com	FINLAND
PADEWSKI	Ed	PURE TECHNOLOGIES LTD.	Ed.Padewski@puretechltd.com	CANADA
PAILLARD	Severine	CEA TECH	severine.paillard@cea.fr	FRANCE
PARK	Duck-Gun	SOUTH KOREA ATOMIC ENERGY RESEARCH INSTITUTE	dgpark@kaeri.re.kr	SOUTH KOREA
PARK	Jaeseok	DOOSAN HEAVY INDUSTRY & CONSTRUCTION	jaeseok.park@kaist.ac.kr	SOUTH KOREA
PASQUIER	Thierry	INTERCONTROLE	thierry.pasquier@areva.com	FRANCE
PAUSSU	Raimo	FORTUM POWER AND HEAT OY, POWER DIVISION	raimo.paussu@fortum.com	FINLAND

PEARCE	John	EDF ENERGY	john.pearce@edf-energy.com	UNITED KINGDOM
PELLETIER	Arnaud	IXTREM - INNOVATIONS EXTRÊMES, TECHNOLOGIES & RECHERCHE	ixtrem@wanadoo.fr	FRANCE
PETTERSSON	Sara	FORSMARKS KRAFTGRUPP AB	sara.pettersson@forsmark.vattenfall.se	SWEDEN
PICHARD	Patrick	M2M	*	FRANCE
PIRINEN	Jani	FORTUM	jani.pirinen@fortum.com	FINLAND
PITKÄNEN	Jorma	POSIVA OY	jorma.pitkanen@posiva.fi	FINLAND
PLATEAU	Manuel	VINÇOTTE	mplateau@vincotte.be	BELGIUM
POGUET	Jérôme	IMASONIC	jp@imasonic.com	FRANCE
POIDEVIN	Clarisse	CEA/LIST	clarisse.poidevin@cea.fr	FRANCE
POIRIER	Jérome	ZETEC	jpoirier@zetec.com	USA
PONTON	Jimmy	CEGELEC PSC	jimmy.ponton@cegelec.com	FRANCE
POULET	Jean-Paul	CLEMESSY NDT	jp.poulet@clemessy.fr	FRANCE
POZNIC	Milan	WESDYNE SWEDEN AB	poznicm@westinghouse.com	SWEDEN
PRADALIE	Emilie	CEGELEC PSC	emilie.pradalie@cegelec.com	FRANCE
PURNELL	Thomas	ROLLS-ROYCE	Rolls-Roycetom.purnell@rolls-roycenuclear.com	UNITED KINGDOM
PURONTAKANEN	Reijo	DEKRA INDUSTRIAL OY	reijo.purontakanen@dekra.com	FINLAND
QUEEN	Harold	STRUCTURAL INTEGRITY ASSOCIATES, INC.	hqueen@structint.com	USA
QUIRK	Karl	PHOENIX INSPECTION SYSTEMS LTD	kquirk@phoenixisl.co.uk	UNITED KINGDOM
RAILLON	Raphaele	CEA-LIST	raphaele.raillon@cea.fr	FRANCE
RAPIN	Mireille	AREVA NDE SOLUTIONS	mireille.rapin@areva.com	FRANCE
RASMUSSEN	Viggo	FORCE TECHNOLOGY	kvr@force.dk	DENMARK
REAL	Ignacio	IBERDROLA GENERATION SPAIN	*	SPAIN
REECE	Christopher	EDF CEIDRE	christopher.reece@edf.fr	FRANCE
REFFS	Joan Ascanius	FORCE TECHNOLOGY	jhr@force.dk	DENMARK
RENAUD	Jean Luc	WESTINGHOUSE	renaudjl@westinghouse.com	FRANCE
RICHNAU	Anders	VATTENFALL	anders.richnau@vattenfall.com	SWEDEN
RIEDER	Hans	FRAUNHOFER-INSTITUT FÜR TECHNO- UND WIRTSCHAFTSMATHEMATIK ITWM	hans.rieder@itwm.fraunhofer.de	GERMANY
RIGAUD	Nicole	EDF UTO	nicole.rigaud@edf.fr	FRANCE
RISHEL	Rick	WESDYNE INTERNATIONAL	rishelrd@westinghouse.com	USA
RONNETEG	Ulf	SWEDISH NUCLEAR FUEL AND WASTE MANAGEMENT CO	ulf.ronneteg@skb.se	SWEDEN
ROY	Anne-Marie	COFREND	contact@amroy-consulting.com	FRANCE
ROY	Olivier	M2M	o.roy@m2m-ndt.com	FRANCE
ROYER	Roger	STRUCTURAL INTEGRITY ASSOCIATES, INC.	rroyer@structint.com	USA
RUHA	Matti	INSPECTA OY	matti.ruha@inspecta.com	FINLAND
RUMMEL	Ward	D&W ENTERPRIESES, LTD.	ndter2001@yahoo.com	USA
RUPIN	Fabienne	EDF R&D	fabienne.rupin@edf.fr	FRANCE
RYF	Martin	ENSI	martin.ryf@ensi.ch	SWITZERLAND
SAILLANT	Jean-Francois	INTERCONTROLE	jean-francois.saillant@areva.com	FRANCE
SAINTOT	Franck	ZETEC	fsaintot@zetec.com	USA
SAKHNO	Nadiia	NONDESTRUCTIVE EXAMINATION TRAINING AND CERTIFICATION FACILITY	NDEF.Office@gmail.com	UKRAINE
SALIN	Jean	EDF R&D	jean.salin@edf.fr	FRANCE

SANCHEZ	Violette	COMEX NUCLEAIRE	*	FRANCE
SANCHEZ	Jose-Luis	TECNATOM, S. A.	jlsanchez@tecnatom.es	SPAIN
SAPIA	Mark	GE HITACHI NUCLEAR ENERGY	mark.sapia@ge.com	USA
SARETE	Jean	WESTINGHOUSE	*	FRANCE
SARTEEL	Jean-Marc	CAP TECH	jmsarteel@captech.fr	FRANCE
SARUTA	Koichi	JAPAN ATOMIC ENERGY AGENCY	saruta.koichi@jaea.go.jp	JAPAN
SASAHARA	Toshihiko	NDI RESEARCH	sasahara_home@nifty.com	JAPAN
SAURIAT	Florent	AREVA	florent.sauriat@areva.com	FRANCE
SAUZET	Thierry	SRA SAVAC	thierry.sauzet@sita.fr	FRANCE
SCHADITZKI	Frédéric	DEKRA	frederic.schaditzki@dekra.com	FRANCE
SCHERRER	Michael	SVTI, SWISS ASSOCIATION FOR TECHNICAL INSPECTIONS	michael.scherrer@svti.ch	SWITZERLAND
SCHMIDBAUER	Jan	E.ON KERNKRAFT GMBH, NPP GROHNDE	jan.schmidbauer@eon.com	GERMANY
SCHMITT	Gregor	WESTINGHOUSE ELECTRIC GERMANY GMBH	schmitgh@westinghouse.com	GERMANY
SCHORS	Jörg	KERNKRAFTWERK LEIBSTADT AG	joergvolker.schors@kkl.ch	SWITZERLAND
SCHULZ	Susanne	ENSI	Susanne.Schulz@ensi.ch	SWITZERLAND
SCHUMACHER	Eric	EXTENDE	erica.chumacher@extende.com	FRANCE
SCHUMM	Andreas	EDF R&D	andreas.schumm@edf.fr	FRANCE
SCHWAMMBERGER	Rudolf	KKL	rudolf.schwammberger@kkl.ch	SWITZERLAND
SELBY	Greg	ELECTRIC POWER RESEARCH INSTITUTE (EPRI)	dcampbell@epri.com	USA
SEVRAIN	Pascal	COMEX-NUCLEAIRE	sevrain@comex-nucleaire.com	FRANCE
SHOHJI	Hajime	CENTRAL RESEARCH INSTITUTE OF ELECTRIC POWER INDUSTRY	shohji@criepi.denken.or.jp	JAPAN
SIDNEY	Ron	SONATEST	ron@sonatest.com	UNITED KINGDOM
SIPPU	Esa	FORTUM	esa.sippu@fortum.com	FINLAND
SIROIS	Michael	EDDYFI	msirois@eddyfi.com	CANADA
SJO	Torbjorn	DEKRA INDUSTRIAL	torbjorn.sjo@dekra.com	SWEDEN
SKELTON	Elizabeth	IMPERIAL COLLEGE	e.a.skelton@imperial.ac.uk	UNITED KINGDOM
SOMVILLE	Frederic	GDF SUEZ - TRACTEBEL ENGINEERING	frederic.somville@gdfsuez.com	BELGIUM
SONG	Sung-Jin	SUNGKYONKWAN UNIVERSITY	*	SOUTH KOREA
SPANNER	Jack	EPRI	jspanner@epri.com	USA
SPEAS	Christopher	ANATEC-LMT, CURTISS WRIGHT FLOW CONTROL	Cspeas@curtisswright.com	USA
SRDIC	David	ROLLS-ROYCE PLC	Dave.Srdic@Rolls-Royce.com	UNITED KINGDOM
STAAT	Stéphane	CEGELEC NDT	stephane.staat@cegelec.com	FRANCE
STEPNICK	David	WESTINGHOUSE ELECTRIC CO	stepnidg@westinghouse.com	USA
SULLIVAN	Paul	STRUCTURAL INTEGRITY ASSOCIATES, INC.	psullivan@structint.com	USA
SUTZ	Pascal	BUREAU VERITAS	*	FRANCE
TAGGART	John	AMEC	John.taggart@amec.com	UNITED KINGDOM
TAKAGI	Toshiyuki	Tohoku University	takagi@ifs.tohoku.ac.jp	JAPAN
TAKAHIRO	Miura	TOSHIBA CORPORATION	takahiro.miura@toshiba.co.jp	JAPAN
TANIOKA	Shuji	E-TECHNO LTD.	shuji_tanioka@mhi.co.jp	JAPAN
TEN GROTENHUIS	Raymond	ONTARIO POWER GENERATION INC.	ray.tengrotenhuis@opg.com	CANADA
THERIAULT	Martin	EDDYFI	mtheriault@eddyfi.com	CANADA
THIBAULT	Adrien	ASN	adrien.thibault@asn.fr	FRANCE
THOMAS	Pierre	EDF	pierre.thomas@edf.fr	FRANCE

TISSEUR	David	CEA	david.tisseur@cea.fr	FRANCE
TOCHE	Philippe	COMEX NUCLEAIRE	toche@comex-nucleaire.com	FRANCE
TOOMA	Masahiro	HITACHI LABORATORY, HITACHI, LTD.	masahiro.toma.hb@hitachi.com	JAPAN
TRAMPUS	Peter	TRAMPUS CONSULTING & ENGINEERING	trampusp@trampus.axelero.net	HUNGARY
TRAUTMANN	Harald	SWISS QUALIFICATION BODY QST	harald.trautmann@svti.ch	SWITZERLAND
TREMBLAY	Patrick	ZETEC	ptremblay@zetec.com	CANADA
TRICHET	Serge	AREVA INTERCONTROLE	serge.trichet@areva.com	FRANCE
TSURUTA	Takayoshi	MITSUBISHI HEAVY INDUSTRIES, LTD.	takayoshi_tsuruta@mhi.co.jp	JAPAN
TSVETKOV	Elenko	AREVA GMBH	elenko.tsvetkov@areva.com	GERMANY
TULAZA	Bruno	BABBCO	apptechcom.babbco@orange.fr	FRANCE
VAN DE VIJVERE	Johan	GE MEASUREMENT AND CONTROLS	*	FRANCE
VANHOYE	Arnaud	CEA LIST	arnaud.vanhoye@cea.fr	FRANCE
VICAT	François	OLYMPUS INDUSTRIAL SYSTEMS EUROPA	thierry.couturier@olympusndt.com	UNITED KINGDOM
VIERSTRAETE	Hans-Peter	NRG ARNHEM	vierstraete@nrg.eu	NETHERLANDS
VILLAGOMEZ	Rosey	IHI SOUTHWEST TECHNOLOGIES, INC.	rosey@ihiswt.com	USA
VINZELBERG	Ingo	WESTINGHOUSE ELECTRIC GERMANY	vinzeli@westinghouse.com	GERMANY
VIRKKUNEN	Iikka	TRUEFLAW LTD.	iikka@trueflaw.com	FINLAND
VIRTANEN	Ilpo	INSPECTA SERTIFIOINTI OY	ilpo.virtanen@inspecta.com	FINLAND
VISSERS	Stief	GDF SUEZ	Stief.Vissers@electrabel.com	BELGIUM
VIVIER	Florian	EDF CEIDRE	florian.vivier@edf.fr	FRANCE
VOLLMER	Bob	ZETEC	bvollmer@zetec.com	USA
WALASZEK	Henri	CETIM	henri.walaszek@cetim.fr	FRANCE
WALKER	Stan	EPRI	swalker@epri.com	USA
WALL	James	ELECTRIC POWER RESEARCH INSTITUTE	jwall@epri.com	USA
WARNES	Michael	HEALTH & SAFETY EXECUTIVE	mike.c.warnes@hse.gsi.gov.uk	UNITED KINGDOM
WEBER	Patrick	AREVA GMBH	doreen.seifert@areva.com	GERMANY
WEDGE	Samuel	AMEC	sam.wedge@amec.com	UNITED KINGDOM
WEISS	Anne	AREVA INTERCONTROLE	anne.weiss@areva.com	FRANCE
WIGGENHAUSER	Herbert	FEDERAL INSTITUTE FOR MATERIALS RESEARCH AND TESTING (BAM)	cathleen.hickstein@bam.de	GERMANY
WIRDELIUS	Håkan	CHALMERS UNIVERSITY OF TECHNOLOGY	hakan.wirdelius@chalmers.se	SWEDEN
WLODARZYCK	François	ZETEC FRANCE	fwlodarzyck@zetec.com	FRANCE
WOISEL	Lionel	BUREAU VERITAS - CEP INDUSTRIE	lionel.woisel@fr.bureauveritas.com	FRANCE
WOLF	Céline	ROLLS ROYCE	celine.wolf@brooksrc.fr	UNITED KINGDOM
WURZBACH	Richard	MRG LABS	rwurzbach@mrgcorp.com	USA
YAACOUBI	Slah	INSTITUT DE SOUDURE	s.yaacoubi@insitutdesoudure.com	FRANCE
YAMAMOTO	Toshihiro	JAPAN POWER ENGINEERING AND INSPECTION CORPORATION	yamamoto-toshihiro@japeic.or.jp	JAPAN
ZETTERVALL	Tommy	SQC SWEDISH QUALIFICATION CENTRE	tommy.zetterwall@sqc.se	SWEDEN

EXHIBITORS LIST

Exhibitors List			
First Name	**Last name**	**Email**	**Company**
Delphine	Begat	dbegat@ascot.fr	Mistras
Patrick	Bergalonne	bergalonne@comex-nucleaire.com	Comex Nucleaire
Colin	Bird	colin.bird@doosan.com	Doosan Power Systems
Olivier	Cassier	cassier@sofranel.com	Sonatest
Philippe	Chaux	gert.vandemieroop@olympusndt.com	Olympus Industrial Systems Europa
Dusko	Corak	zrinka.corak@inetec.fr	Inetec
Colombe	Dalpe	cdalpe@eddyfi.com	Eddyfi
Lionel	Delannoy	lionel.delannoy@ge.com	GE Sensing & Inspection Technologies
Philippe	Dumas	phd@imasonic.com	Inetec
Emmanuel	Dumont	edumont@luziesa.com	Luziesa
Pascal	Dumont	sdumont@luziesa.com	Luziesa
Roman	Fernandez	roman.fernandez@extende.com	Extende
Gérard	Fleury	gf@imasonic.com	Imasonic
Sergio	Galosic	sergio.galosic@inetec.hr	Inetec
Sylvain	Garboud	sylvain.garboud@cegelec.com	Cegelec NDT
Neil	Hankinson	nhankinson@phoenixisl.co.uk	Phoenix Inspection Systems Ltd
Alexandre	Julien	alexandre.julien@ge.com	GE Inspection Technologies
Laurent	Le ber	l.leber@m2m-ndt.com	M2M
Jean-Claude	Lenain	jclenain@mistrasgroup.eu	Mistras
Colin	Mc neil	colin.mcneil@doosan.com	Doosan Power Systems
Jean-Philippe	Merle	bruno.pernot@rolls-roycenuclear.com	Rolls Royce Nuclear Services
Alain	Meynet	ameynet@zetec.com	Zetec
Karl	Quirk	kquirk@phoenixisl.co.uk	Phoenix Inspection Systems Ltd
Olivier	Roy	o.roy@m2m-ndt.com	M2M
Franck	Saintot	fsaintot@zetec.com	Zetec
Violette	Sanchez		Comex Nucleaire
Frédéric	Schaditzki	frederic.schaditzki@dekra.com	Dekra
Eric	Schumacher	erica.chumacher@extende.com	Extende
Ron	Sidney	ron@sonatest.com	Sonatest
Torbjorn	Sjo	torbjorn.sjo@dekra.com	Dekra Industrial
Stéphane	Staat	stephane.staat@cegelec.com	Cegelec Ndt
Martin	Theriault	mtheriault@eddyfi.com	Eddyfi
Philippe	Toche	toche@comex-nucleaire.com	Comex Nucleaire
Bruno	Tulaza	apptechcom.babbco@orange.fr	Babb Co
François	Vicat	thierry.couturier@olympusndt.com	Olympus Industrial Systems Europa
Bob	Vollmer	bvollmer@zetec.com	Zetec
Céline	Wolf	celine.wolf@brooksrc.fr	Rolls Royce Nuclear Services

European Commission
EUR 26577 EN – Joint Research Centre – Institute for Energy and Transport
Title: Proceedings of the tenth International Conference on NDE in Relation to Structural Integrity for Nuclear and Pressurized Components, 1 – 3 October 2013 – Cannes, France
Edited by: M. Bièth (EC JRC - IET Petten, The Netherlands)
Luxembourg: Publications Office of the European Union
2014-1112pp.–17x24cm
EUR – Scientific and Technical Research series – ISSN 1831-9424(online); ISSN 1018-5593(print)

ISBN 978-92-79-36758-8(pdf)
ISBN 978-92-79-36759-5(print)

Doi 10.2790/17225(online)

Abstract

This conference, the tenth in a series on NDE in relation to structural integrity for nuclear and pressurized components, was held from 1st October to 3rd October 2013, in Cannes, France. The scientific programme was co-produced by the European Commission's Joint Research Centre, Institute for Energy and Transport (EC-JRC/IET). The Conference has been coordinated by the Confédération Française pour les Essais Non Destructifs (COFREND). The first conference, under the sole responsibility of EC-JRC was held in Amsterdam, 20-22 October 1998. The second conference was locally organized by the EPRI NDE Center in New Orleans, 24-26 May 2000, the third one by Tecnatom in Seville, 14-16 November 2001, the fourth one by the British Institute of Non-Destructive Testing in London, 6-8 December 2004, the fifth by EPRI in San Diego, 10-12 May 2006, the sixth by Marovisz in Budapest, 8-10 October 2007, the seventh by the University of Tokyo and JAPEIC in Yokohama, 12 -14 May 2009, the eight by DGZfP in Berlin, 29 September to 1st October 2010, the ninth by EPRI NDE Center in Seattle 22-24 May 2012.

The theme of this conference series is to provide the link between the information originated by NDE and the use made of this information in assessing structural integrity. In this context, there is often a need to determine NDE performance against structural integrity requirements through a process of qualification or performance demonstration. There is also a need to develop NDE to address shortcomings revealed by such performance demonstration or otherwise. Finally, the links between NDE and structural integrity require strengthening in many areas so that NDE is focussed on the components at greatest risk and provides the precise information required for assessment of integrity. These were the issues addressed by the papers selected for the conference.

LD-NA-26577-EN-N

Doi 10.2790/17225(online)
ISBN 978-92-79-36758-8(pdf)